1999

Genetic vaccine encoding secreted glutamic acid decarboxylase prevents autoimmune diabetes in NOD mice

Running Title: Genetic vaccine for Type 1 diabetes

Maria Filippova[1], Jingxue Liu[1,2,3], and Alan Escher[1,2]

[1]Center for Molecular Biology & Gene Therapy, [2] Department of Microbiology & Molecular Genetics, Loma Linda University, Loma Linda, California, USA.

Correspondence: Alan Escher, Center for Molecular Biology and Gene Therapy, 11085 Campus Street, Loma Linda University, California 92350, USA. E-mail: aEscher@som.llu.edu

[3] Current Address: Bio-Rad Laboratories, 2000 Alfred Nobel Drive, Hercules, California 94547

20010215 101

Summary

Type 1 diabetes results from the destruction of insulin producing beta cells by the immune system. Several immunization methods based on autoantigenic proteins or peptides have been used to prevent autoimmune diabetes in the non-obese diabetic (NOD) mouse. In the work presented here, a gene-based approach was taken for a similar purpose. Intramuscular injection of "naked" plasmid DNA was used to determine the efficacy of genes encoding different versions of a beta cell-associated autoantigen for prevention of cyclophosphamide-accelerated diabetes in female NOD mice. Four-week old animals received injections of DNA encoding either intracellular or secreted human glutamic acid decarboxylase (GAD), an enzyme found in beta cells and whose recognition by the immune system is thought to be necessary for disease onset. Monitoring of glycosuria and hyperglycemia showed that DNA encoding intracellular GAD did not suppress diabetes, but that, in contrast, DNA encoding secreted GAD could prevent its onset. Analysis of IgG1 antibody levels from animal sera suggested that disease prevention was associated with increased T helper 2 cell activity. These results indicate that plasmid DNA encoding secreted GAD can be used effectively as part of a genetic vaccine protocol for prevention of autoimmune diabetes in NOD mice.

Key words: DNA-based vaccine; Type 1 diabetes; glutamic acid decarboxylase; secreted protein

Type 1 diabetes is a complex autoimmune disease caused by multiple genetic and environmental

factors. Diabetes onset is believed to begin with antigen presenting cells display of autoantigen(s) synthesized by insulin-secreting beta cells in the pancreas, which results in destructive insulitis specifically targeted to beta cells. Insulitis is promoted by T helper type 1 (Th1) lymphocytes, and leads to apoptotic cell death of beta cells mediated by CD8+ cytotoxic T lymphocytes and macrophages (Yoon and Jun 1999).

The non obese diabetic (NOD) mouse is an animal model system that is often used to study Type 1 diabetes, because it develops a form of the disease with an etiology remarkably similar to Type 1 diabetes in humans, with important common susceptibility factors such as loci in the major histocompatibility complex (Wicker 1995). Studies of humans and NOD mice have indicated that two proteins synthesized in the pancreas play determining roles as autoantigens responsible for diabetes occurrence. They are the hormone insulin, a secreted protein, and the enzyme glutamic acid decarboxylase (GAD), an intracellular protein found either in a soluble form (GAD67), or membrane-bound to microvesicles (GAD65) in beta cells. The importance of the role of these two autoantigens during diabetes onset in NOD mice is underlined by the findings that most pathogenic CD8+ T cells recognize a single insulin epitope (Wong *et al.*,1999), and that mice with pancreas-specific reduced expression of *gad65/67* genes do not develop diabetes (Yoon *et al.*, 1999). These reports have confirmed that insulin and GAD proteins are molecules of choice for the development of antigen-specific immunosuppressive forms of therapy aimed at preventing and treating type 1 diabetes.

Delivery of insulin and GAD proteins/peptides into NOD mice through a variety of routes has been shown to prevent and/or delay diabetes onset significantly (Simone et al., 1999). Recently, plasmid DNA encoding these two proteins was used in genetic vaccination protocols aimed at

preventing Type 1 diabetes in animal models. In one study, intramuscular (i.m.) injection of plasmid DNA encoding an intracellular form of the insulin B chain could reduce diabetes incidence after lymphocytic choriomeningitis virus (LCMV) infection of transgenic mice expressing the LCMV nucleoprotein in their beta cells (Coon et al., 1999). In another study, plasmid DNA encoding rat GAD65 or rat GAD67 protein did not cause significant protection against diabetes onset after i.m. injection in NOD mice (Wiest-Ladenburger et al., 1998). However, we reported that i.m. injection of plasmid DNA encoding human GAD65 or a secreted form of the protein could prevent insulitis in the pancreas of the same animal model (Liu et al., 1999). Therefore, in the work presented here, the DNA constructs used in our previous study were injected into NOD mice to determine whether plasmid encoding human GAD65 or its secreted form could also prevent diabetes.

Three groups of 4-week old animals received i.m injections of plasmid DNA carrying the following genes: *gad65*, a cDNA encoding human GAD65 protein; *sgad55*, a modified *gad65* cDNA encoding a secreted truncated form of human GAD65 (Liu et al, 1999); and *sruc3*, a modified cDNA encoding a secreted version of the soft coral *Renilla reniformis* luciferase (Liu and Escher, 1999). All animals received a second set of injections five days after the first set. In addition, plasmid-treated mice and a group of untreated control animals received cyclophosphamide (CY) injections at 10 and 12 weeks of age to accelerate disease onset. Animals were killed when diagnosed as diabetic, or at the end of the observation period at 18 weeks of age.

Each of the three plasmid DNAs used for injection had a different effect on diabetes onset (Fig.1). Mice that received injections of plasmid carrying full-length human *gad65* cDNA (800 μg/mouse total) did not show decreased diabetes when compared with untreated control mice. This result was similar to those obtained previously by other investigators who injected plasmid DNA

carrying rat *gad65* or *gad67* cDNAs (100 μg/mouse total) into female NOD mice (Wiest-Ladenburger et al., 1998). Another group of mice received injections of plasmid carrying the *sgad55* gene construct, which encodes the human interleukin-2 signal peptide fused to human GAD65 protein truncated at its N-terminus. The deletion removes an 88 amino acids region containing a palmitoylation sequence and a Golgi targeting signal that prevents secretion of full-length GAD65 protein (Liu et al., 1999). This truncated GAD65 protein contains all of the epitopes recognized by antibodies from patients suffering from Type 1 diabetes (Richter et al., 1993). Figure 1 shows that in contrast with *gad65*, injection of *sgad55* could prevent diabetes in NOD mice significantly. The levels of protection attained after this treatment were similar to those reported by others with female NOD mice receiving injection (Tisch et al., 1993; Petersen et al.,1994; Ramiya et al., 1997), nasal spraying (Tian et al., 1996), or feeding (Ramiya et al., 1997)of GAD proteins/peptides from murine or human origin. However, the protocol used in our study included an additional treatment, consisting in the injection of the immunosuppressant CY. CY injection suppresses activity of both Th1 and Th2 lymphocytes, but with a faster subsequent recovery of Th1 cells (Ablamunits et al., 1999). As a result, CY injection causes acceleration of diabetes in NOD mice, since Th1 cells mediate autoimmune diabetes onset, and Th2 cells suppress the activity of Th1 cells. Due to its effects, CY injection can be used to test the robustness of preventative therapies for Type 1 diabetes (French et al., 1997, Nicoletti et al., 1999). It is therefore possible that injection of the *sgad55* gene construct in the absence of CY could result in even more efficient suppression of diabetes than was observed here.

A third group of mice received injections of plasmid DNA carrying the *sruc3* gene construct, which encodes a secreted form of the soft coral *Renilla reniformis* luciferase. This group was used

as a control for the non-specific effect of a non-autoantigenic secreted protein on diabetes onset. Although injection of the *sruc3* gene did not prevent diabetes, it could delay its onset significantly. This is in contrast with results from immunization studies that use protein/peptide, where foreign control antigens generally do not affect diabetes onset. The reason for the delay in diabetes onset after *sruc3* injection in the NOD mouse is not known, but could reflect a property particular to genetic vaccines encoding secreted proteins when applied in the context of autoimmune diabetes.

It is known that i.m. injection of plasmid DNA encoding a secreted antigen generally tends to induce a humoral response against the antigen, and injection of plasmid encoding the membrane bound or cytosolic form of the same antigen induces a cell mediated response (Robinson, 1999). The finding that the plasmid DNA encoding secreted GAD could prevent diabetes, but that its membrane-bound form could not would support this view. Injection of plasmid encoding secreted GAD would induce a Th2-mediated humoral response that would suppress the Th1-mediated cellular response mounted against pancreatic beta cells, while injection of plasmid encoding membrane-bound GAD would induce a Th1-mediated cell response which would either exacerbate or not affect the disease. However, results obtained by other investigators suggest that i.m. injection of plasmid DNA encoding intracellular antigens can induce a Th2-mediated response that can prevent disease onset in animal models for autoimmune diseases. For example, injection of plasmid DNA encoding a myelin basic protein peptide or porcine insulin B chain can prevent respectively experimental autoimmune encephalomyelitis in the Lewis rat (Lobell et al., 1998), or hyperglycaemia in the RIP-LCMV transgenic mouse (Coon et al., 1999). Therefore, there may be some characteristic properties of GAD65 that prevent its encoding gene from being effective as a genetic vaccine for prevention of Type 1 diabetes, since neither injection of DNA encoding rat GAD65, 67, nor human GAD65

appear to prevent diabetes. This conclusion is further supported by the finding that NOD mice expressing full-length murine *gad65* cDNA as a transgene fail to develop tolerance to GAD65 and show no decrease in diabetes (Bridgett et al., 1998; Geng et al., 1998), which is in contrast with NOD mice transgenic for a gene encoding intracellular proinsulin and not developing diabetes (French et al., 1997). This failure of DNA encoding intracellular GAD proteins to prevent diabetes when expressed *in situ* does not appear to be correlated with GAD cellular localization, because neither membrane bound GAD65 nor cytosolic GAD67 is effective in that respect (Wiest-Ladenburger et al., 1998).

Levels of anti-GAD IgG antibodies in mice sera were determined using ELISA to detect a possible immune response to GAD after injection of *gad*-carrying plasmids (Fig. 2). There were no significant increases in levels of anti-GAD IgG antibodies in mice that had received injections of plasmids carrying *gad65* or *sgad55* genes when compared with untreated controls. These results were in contrast with those obtained in another study, where female NOD mice that had received i.m. injection of rat *gad65* or *gad67* genes had shown a strong humoral response against plasmid-encoded GAD protein (Wiest-Ladenburger et al., 1998). The reason for the difference between the two studies could have been due to CY injection, since this treatment suppresses activity of Th2 cells which are known to activate B lymphocytes, or to the use of different DNA isolation protocols, or NOD strains. However, absence of increased levels of anti-human GAD antibody after injection of human GAD-encoding plasmid DNA and prevention of diabetes are not necessarily contradictory, since a similar lack of anti-GAD antibody response concomitant with a preventative effect on diabetes has been observed previously after injection of GAD protein/peptide into NOD mice (Ramiya et al., 1997).

Another ELISA was performed to determine levels of anti-GAD IgG1 antibodies in mice sera. Because Th2 cells mediate a process that leads to production of IgG1 antibodies, IgG1 levels have been used in studies of immunization and tolerization to determine whether a humoral response is induced. Protection of pancreatic beta cells after tolerization for GAD or insulin is believed to be due in most cases to local suppression of Th1 cells via "by-stander suppression" by antigen-specific activated Th2 cells, and several tolerization studies that used insulin or GAD as autoantigens have shown an increase in Th2 cell activity associated with prevention of diabetes (Homann et al., 1999; Maron et al., 1999; Tisch et al., 1999). An increase in IgG1 levels was readily observed in several non-diabetic mice that had received injection of plasmid carrying the *sgad55* gene construct (Fig. 3). In contrast, none of the non-diabetic mice in other groups showed a comparable increase. It is likely that the non-diabetic mice with low IgG1 levels represented the approximately 20% of the population of NOD/MrkTac mice which is expected to be diabetes-free for undefined reasons. The finding that non-diabetic mice that received injections of *sgad55*-carrying plasmid showed the highest levels of anti-GAD IgG1 antibodies suggests that prevention of diabetes in these animals was associated with increased Th2 cell activity, which would be in agreement with a "by-stander suppression" mechanism of diabetes prevention.

We have reported previously that i.m injection of plasmid encoding SGAD55 or GAD65 significantly reduces insulitis in 10-week old non-diabetic female NOD mice, but that plasmid encoding SRUC3 does not (Liu et al., 1999). Data presented here indicate that only plasmid encoding SGAD55 could significantly prevent diabetes in female NOD mice with an accelerated form of the disease induced by CY injection. Surprisingly, plasmid encoding SRUC3 caused a delay in diabetes, while plasmid encoding GAD65 did not have a detectable effect on the disease.

Altogether these data indicate that i.m. injection of plasmid carrying *sgad55* had a consistent protective effect against both insulitis and diabetes, suggesting that *sgad55* is the most potent gene construct for diabetes prevention among those used in our studies. The effects of i.m injection of plasmid DNA carrying *gad65* or *sruc3* genes on diabetes in NOD mice not treated with CY and on insulitis in CY-treated NOD mice remain to be determined to establish whether CY injection was responsible for the observed discrepancy between our insulitis and diabetes studies.

To our knowledge, this is the first report of the successful use of a GAD-based genetic vaccine for diabetes prevention in NOD mice. Together with the finding by Coon et al. that an insulin-based genetic vaccine can prevent hyperglycaemia in RIP-LCMV transgenic mice, our results suggest that injection of plasmid DNA encoding beta cell-associated autoantigens may be a promising approach to prevent Type 1 diabetes. Several therapies have already been used to prevent diabetes in the NOD mice with success (Atkinson and Leiter, 1999). However, the established and potential advantages of genetic vaccines over other methods of immunization are significant (Tuteja, 1999). For example, genetic vaccines can be obtained in large quantities at low cost, and can be readily modified at the gene level for improved results, as demonstrated in the work presented here. Further improvements, such as cell-targeting of vaccine and co-expression of tolerization-enhancing genes, could make genetic vaccines a powerful and practical means to prevent and treat Type 1 diabetes in the future.

Acknowledgements

This work was sponsored by the Department of the Army and the National Medical Technology Testbed Inc., Cooperative Agreement Number DAMD17-97-2-7016. The content of the information does not necessarily reflect the position or the policy of the government or the National Medical Technology Testbed, Inc.

References

Ablamunits V *et al.*, Acceleration of autoimmune diabetes by cyclophosphamide is associated with an enhanced IFN-gamma secretion pathway. *J Autoimmun* 1999;13:383-392.

Atkinson MA, Leiter EH. The NOD mouse model of type 1 diabetes: as good as it gets? *Nat Med* 1999; 5:601-4.

Bridgett M *et al.* Differential protection in two transgenic lines of NOD/Lt mice hyperexpressing the autoantigen GAD65 in pancreatic beta-cells. *Diabetes* 1998;47:1848-56.

Coon B, An LL, Whitton JL, von Herrath MG. DNA immunization to prevent autoimmune diabetes. *J Clin Invest* 1999; 104:189-94.

French MB *et al.* Transgenic expression of mouse proinsulin II prevents diabetes in non-obese diabetic mice. *Diabetes* 1997;46:34-9.

Geng L, Solimena M, Flavell RA, Sherwin RS, Hayday AC. Widespread expression of an autoantigen-GAD65 transgene does not tolerize non-obese diabetic mice and can exacerbate disease. *Proc Natl Acad Sci USA* 1998;95:10055-60.

Homann D, Holz A, Bot A, Coon B, Wolfe T, Petersen J, Dyrberg TP, Grusby MJ, von Herrath MG. Autoreactive CD4+ T cells protect from autoimmune diabetes via bystander suppression using the IL-4/Stat6 pathway. *Immunity* 1999;11:463-72.

Liu J *et al.* Intramuscular injection of plasmid DNA encoding intracellular or secreted glutamic acid decarboxylase causes decreased insulitis in the non-obese diabetic mouse. *Gene Ther Mol Biol* 1999; 3:197-206.

Liu J, Escher A. Improved assay sensitivity of an engineered secreted Renilla luciferase. *Gene* 1999; 237:153-9.

Lobell A, Weissert R, Storch MK, Svanholm C, de Graaf KL, Lassmann H, Andersson R, Olsson T, Wigzell H. Vaccination with DNA encoding an immunodominant myelin basic protein peptide targeted to Fc of immunoglobulin G suppresses experimental autoimmune encephalomyelitis. *Exp Med* 1998;187:1543-8.

Maniatis T, Fritsch EF, Sambrook J. *Molecular Cloning. A Laboratory Manual*, second edition. Cold Spring Harbor Laboratory: Cold Spring Harbor, NY, 1989.

Maron R, Melican NS, Weiner HL. Regulatory Th2-type T cell lines against insulin and GAD peptides derived from orally- and nasally-treated NOD mice suppress diabetes. J Autoimmun 1999 Jun;12(4):251-8.

Nicoletti F, Zaccone P, Conget I, Gomis R, Moller C, Meroni PL, Bendtzen K, Trepicchio W, Sandler S. Early prophylaxis with recombinant human interleukin-11 prevents spontaneous diabetes in NOD mice. Diabetes 1999; 48:2333-9.

Petersen JS, Karlsen AE, Markholst H, Worsaae A, Dyrberg T, Michelsen B. Neonatal tolerization with glutamic acid decarboxylase but not with bovine serum albumin delays the onset of diabetes in NOD mice. *Diabetes* 1994; 43:1478-84.

Ramiya VK, Shang XZ, Wasserfall CH, Maclaren NK. Effect of oral and intravenous insulin and glutamic acid decarboxylase in NOD mice. *Autoimmunity* 1997;26:139-51.

Richter W, Shi Y, Baekkeskov S. Autoreactive epitopes defined by diabetes-associated human monoclonal antibodies are localized in the middle and C-terminal domains of the smaller form of glutamate decarboxylase. *Proc Natl Acad Sci USA* 1993;90:2832-6.

Robinson HL. DNA vaccines: basic mechanism and immune responses (Review). *Int J Mol Med* 1999; 4:549-55.

Simone EA, Wegmann DR, Eisenbarth GS. Immunologic "vaccination" for the prevention of autoimmune diabetes (type 1A). *Diabetes Care* 1999;22 Suppl 2:B7-15.

Tian J, Atkinson MA, Clare-Salzler M, Herschenfeld A, Forsthuber T, Lehmann PV, Kaufman DL Nasal administration of glutamate decarboxylase (GAD65) peptides induces Th2 responses and prevents murine insulin-dependent diabetes. *J Exp Med* 1996;183:1561-7

Tisch R, Yang XD, Singer SM, Liblau RS, Fugger L, McDevitt HO. Immune response to glutamic acid decarboxylase correlates with insulitis in non-obese diabetic mice. *Nature* 1993; 366:72-5.

Tisch R, Wang B, Serreze DV. Induction of glutamic acid decarboxylase 65-specific Th2 cells and suppression of autoimmune diabetes at late stages of disease is epitope dependent. *J Immunol* 1999; 163:1178-87.

Tuteja R. DNA vaccines: a ray of hope. *Crit Rev Biochem Mol Biol* 1999;34:1-24.

Wicker LS, Todd JA, Peterson LB. Genetic control of autoimmune diabetes in the NOD mouse. *Annu Rev Immunol* 1995;13:179-200.

Wiest-Ladenburger U *et al.* DNA vaccination with glutamic acid decarboxylase (GAD) generates a strong humoral immune response in BALB/c, C57BL/6, and in diabetes-prone NOD mice. *Horm Metab Res* 1998 ;30:605-9.

Wong FS *et al.* Identification of an MHC class I-restricted autoantigen in type 1 diabetes by screening an organ-specific cDNA library. *Nat Med* 1999; 5:1026-31.

Yoon JW et al. Control of autoimmune diabetes in NOD mice by GAD expression or suppression in beta cells. *Science* 1999; 284:1183-7

Yoon JW, Jun HS. Cellular and molecular roles of beta cell autoantigens, macrophages and T cells in the pathogenesis of autoimmune diabetes. *Arch Pharm Res* 1999; 22:437-4.

Titles and legends to figures

Figure 1. Effects of plasmid DNA injection on diabetes incidence. Female NOD/MrkTac mice (Taconic Laboratories, Germantown, NY) received injections of plasmid DNA into each quadriceps muscle (200 μg/leg) at the age of four weeks, and an identical set of injections 2 days afterwards, for a total of 800 μg plasmid DNA/mouse. Mice received injections of plasmid DNA encoding either full-length, membrane-bound human GAD65 (n=10); SGAD55, a secreted form of truncated human GAD65 (n=8); or SRUC3, a secreted form of a soft coral luciferase (n=11). A group of mice was left untreated as control (n=9). All mice received an intra-peritoneal injection of cyclophosphamide (200 mg/kg) at the age of 10 and 12 weeks to accelerate diabetes onset. Mice that received injection of plasmid DNA encoding SGAD55 or SRUC3 showed respectively a significant reduction($p=0.05$, log-rank test) or delay ($p=0.01$, Mann-Whitney U test) in diabetes when compared with controls. Plasmid DNA was amplified from *Escherichia coli* strain DH5-α using the alkaline lysis method, and isolated after two rounds of cesium chloride purification (Maniatis et al., 1989). Both amounts and quality of plasmid DNA were determined after ultraviolet spectrophotometry (A_{260}/A_{280} greater than 1.8) and agarose gel electrophoresis. Plasmid DNA was dissolved under sterile conditions in phosphate buffer saline (PBS) solution at a final concentration of 2 μg/μl and stored at -20°C. Mice kept at Loma Linda University animal facilities under non-pathogenic free conditions received injection of DNA under general anaesthesia using Ketamine, 66 mg/kg body weight (Phoenix Scientific, S^t Joseph, MO), 7.5 mg/kg body weight oxylazine (Lloyd Laboratories, Shenandoa, IO), and 1.5 mg/kg body weight acepromazine maleate (Fermenta Animal Health Co., MO). Glycosuria was monitored twice a week with Clinistix Reagent Strips for urine analysis (Bayer

Corporation, Elkhart, IN). When positive, mice were confirmed diabetic when blood glucose levels were greater than 300mg/dl on two consecutive days, using Accucheck Advantage (Boehringer Mannheim Corporation, Indianapolis, IN).

Figure 2. Levels of anti-GAD IgG antibodies in mice sera. Blood was harvested when NOD mice were diagnosed as diabetic (black circles), or at the end of the observation period when non-diabetic (white circles). The broken line represents the highest levels of anti-GAD IgG antibodies observed among sera from six 3-4 month old CD1 mice, as negative control. Sera were obtained from collected blood after two centrifugations at 3,000 x g for 10 min at 4°C; 10 µl of 1% sodium azide was added to each sample. Ninety-six wells microtiter plates (Dynex Technologies Inc., Chantilly, VA) were coated overnight at 4°C with 100 µl of 10 µg/ml recombinant human GAD55 protein isolated from *E.coli* (data not shown) or BSA, in PBS containing 5 mM DTT and 100 mM beta-mercaptoethanol. Blocking was done using 0.5% BSA in PBS for 2 hr at 37°C, and mouse sera diluted 1:100 were added and allowed to incubate for 2 hr at 37°C. Unbound proteins and antibodies were removed with 4 washes with PBS + 0.1% Triton X100 for 5 minute at room temperature after each reaction. Alkaline phosphatase-conjugated Fab-specific anti-mouse IgG monoclonal antibodies (Sigma, St Louis, MO) were diluted in 1:40,000 in blocking buffer, added to the wells, and incubated for 2 hrs at 37°C. The relative amounts of bound antibodies were determined after addition of 100 µl alkaline phosphatase substrate Lumi-Phos Plus (Lumigen Inc., Southfield, MI) to each well. Light emission catalyzed by alkaline phosphatase was measured in a ML3000 Luminometer (Dynex Technologies Inc., Chantilly, VA) after allowing the reaction to develop for 30 min at 37°C.

Figure 3. Levels of anti-GAD IgG1 antibodies in mice sera. A protocol identical to the one described in Fig. 2 was used to detect levels of IgG1 antibodies, except that alkaline phosphatase-conjugated IgG1-specific anti-mouse IgG monoclonal antibodies (Zymed Laboratories Inc., South San Francisco, CA) were used for detection at a dilution of 1:2,000. Black circles: diabetic mice;

white circles: non-diabetic mice. RLU: relative light units. The broken line represents the highest levels of anti-GAD IgG1 antibodies observed among sera from six 3-4 month old CD1 mice, as negative control.

FIGURE 1

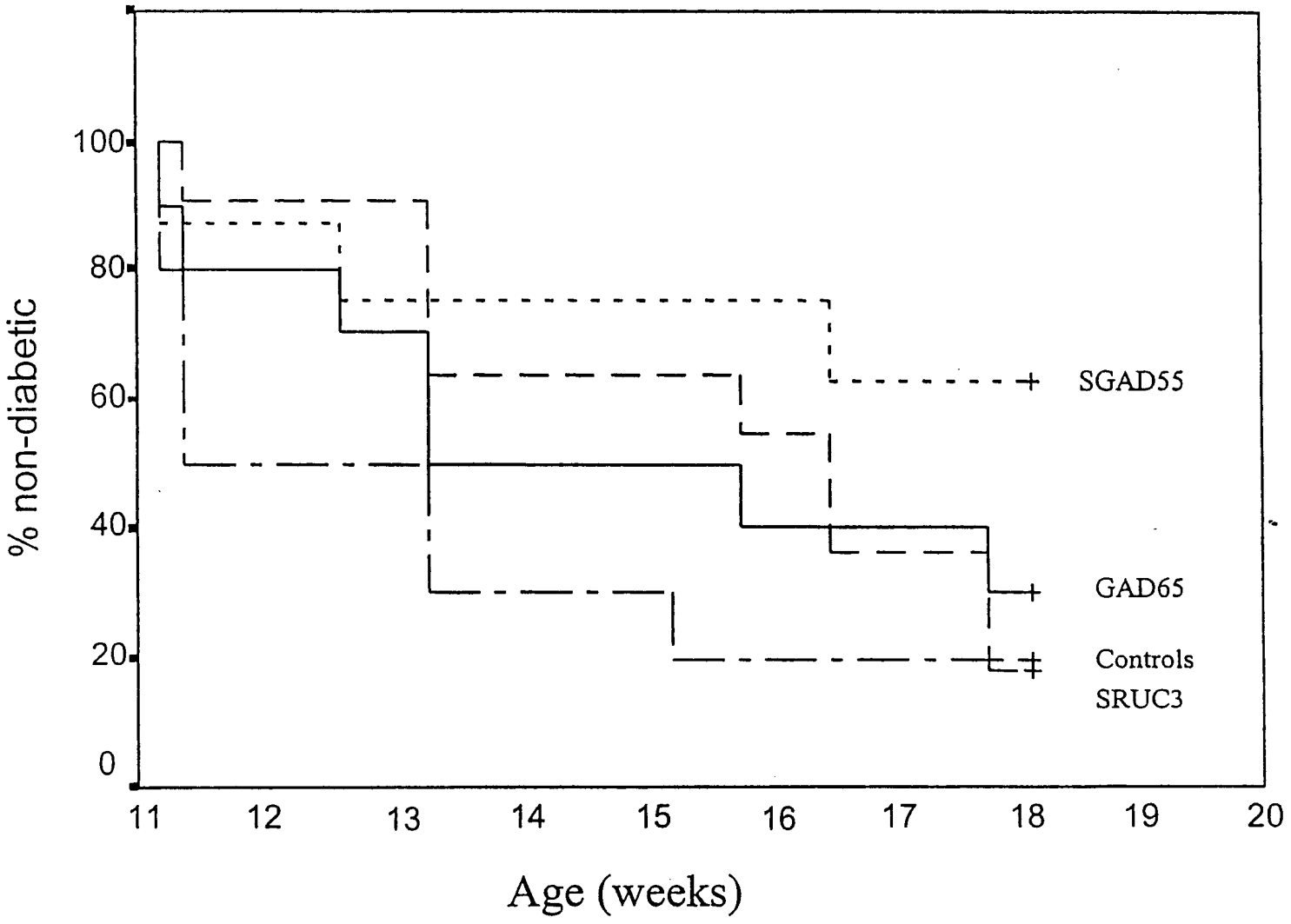
100
80
60
40
20
0
% non-diabetic
11
12
13
14
15
16
17
18
19
20
Age (weeks)
SGAD55
GAD65
Controls
SRUC3

FIGURE 2

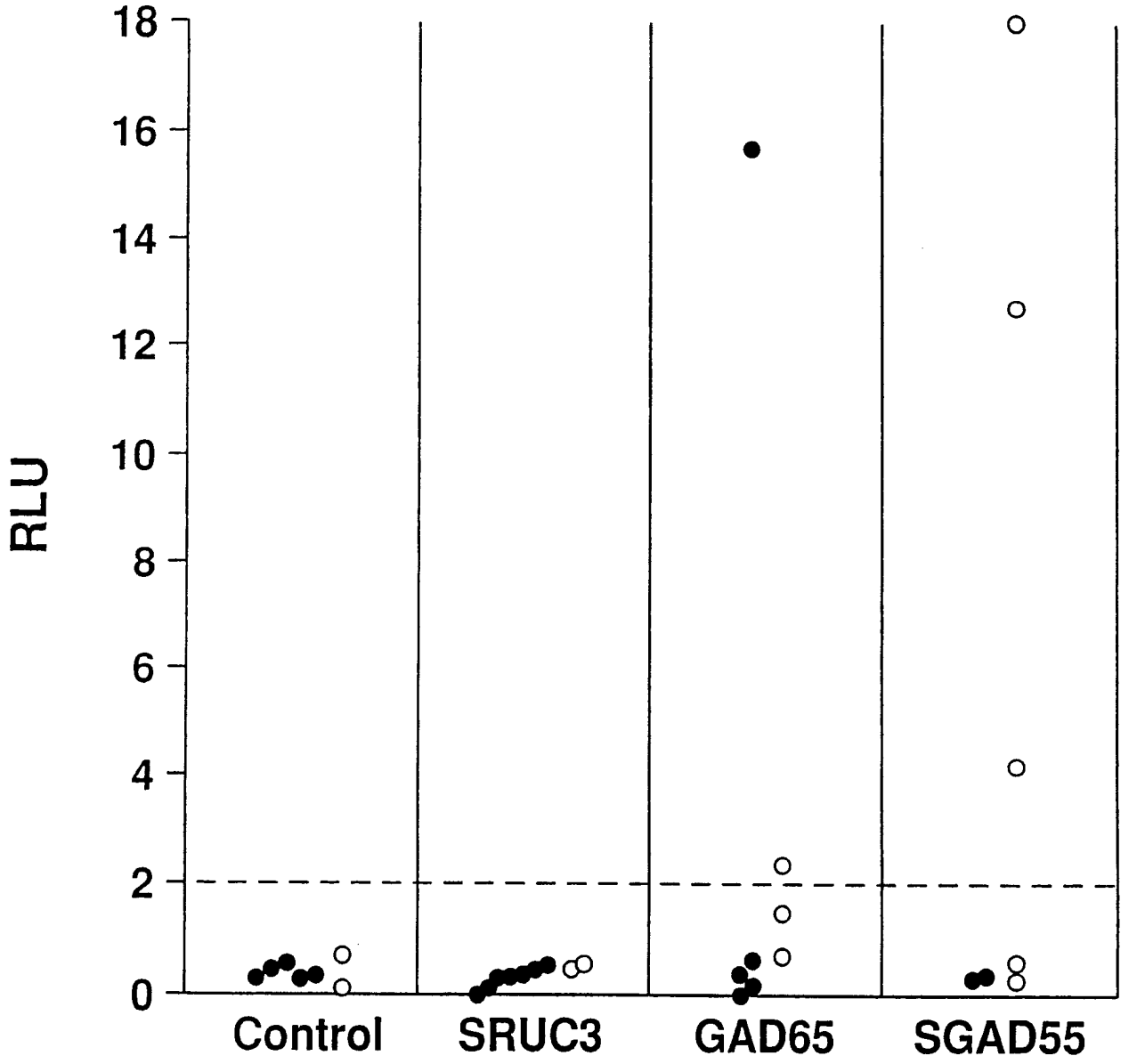

FIGURE 3

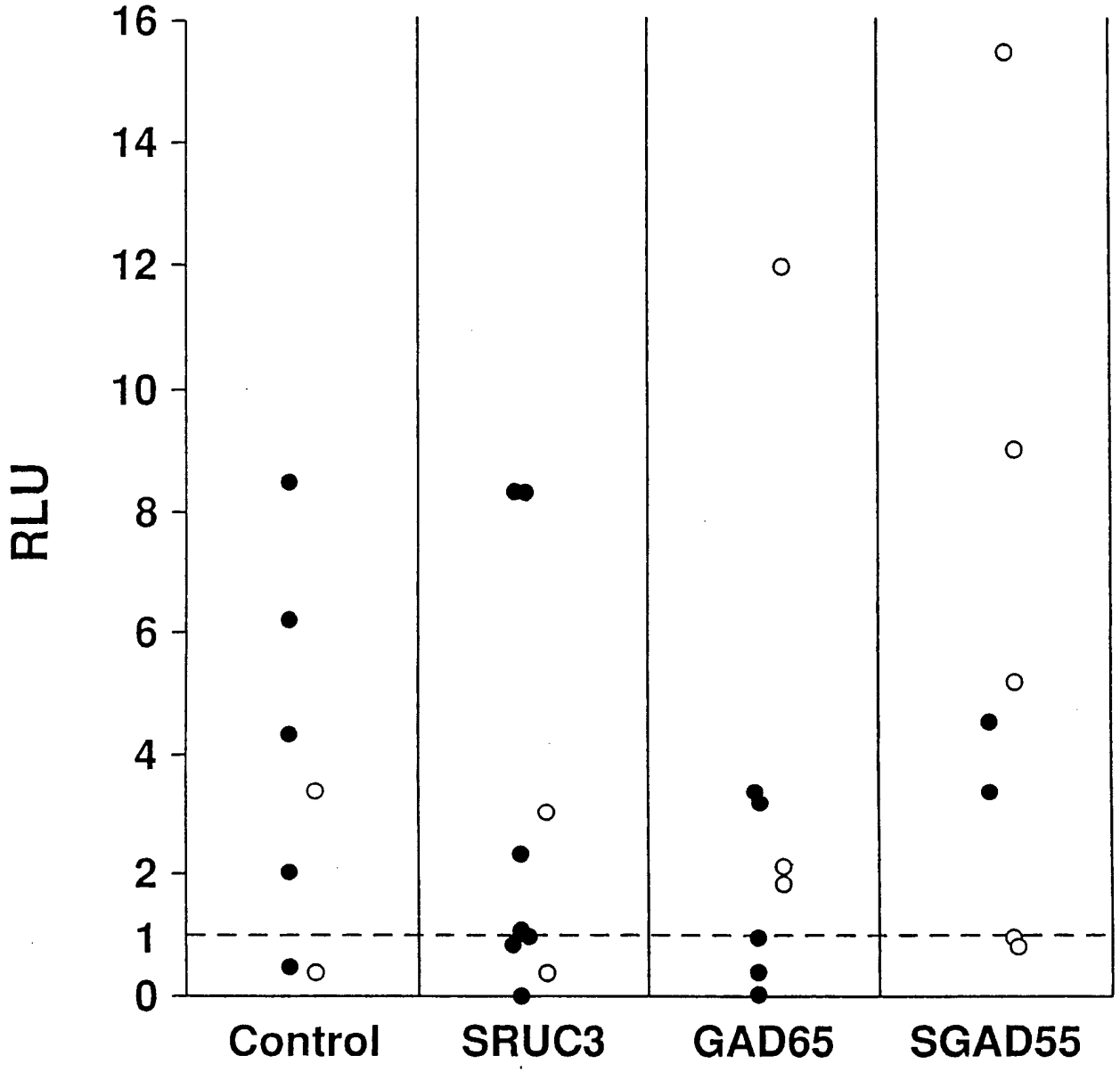

Volume 6, Number 6 November/December 1999

No. 19
Loma Linda University/Fodor

A CONFERENCE SUPPLEMENT TO

CANCER GENE THERAPY

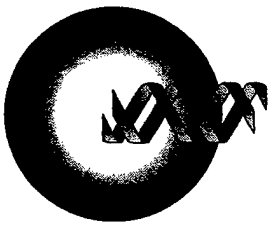

Gene Therapy of Cancer VIII

San Diego, California
December 9–11, 1999

STOCKTON

No. 19
Loma Linda University/Fodor

International Journal Of Molecular Medicine

ISSN 1107-3756

VOLUME 4, SUPPLEMENT 1, 1999

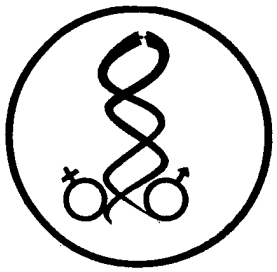

Proceedings of the Abstracts of

The 4th World Congress on Advances in Oncology, and 2nd International Symposium on Molecular Medicine

7-9 October, 1999, Vouliagmeni, Athens, Greece

Low dose vaccinia virus-mediated cytokine therapy of glioma

Bing Chen[1,2], Tatyana M Timiryasova[1], Peyman Haghighat[1,2], Daila S Gridley[2,3], Melba L Andres[3], Eric Kajioka[3], Rhoda D Roy[3], and Istvan Fodor[1,2]

[1]Center for Molecular Biology and Gene Therapy, [2]Departments of Microbiology & molecular Genetics, and [3]Radiation Medicine, Loma Linda University School of Medline, Loma Linda, California

running title: virus-mediated cancer immunotherapy

Correspondence and reprint requests: Dr. Istvan Fodor, Center for Molecular Biology and Gene Therapy, Mortensen Hall, Loma Linda University School of Medicine, Loma Linda, CA 92350, USA. Tel: [1] 909-824-4300 ext. 81398; Fax: [1] 909-478-4177; E-mail: ifodor@som.llu.edu

Abstract. Recombinant viruses can produce cytokines in tumors mobilizing an immune response to tumor cells. In this study we investigated gene expression, *in vivo* antitumor efficacy and safety of attenuated recombinant vaccinia virus (rVV) carrying murine cytokine genes IL-2 (rVV-mIL2), IL-12 (rVV-mIL12) and both IL-2 and IL-12 (rVV-2-12) in athymic nude mice model. Significant tumor inhibition ($P<0.05$) was observed in a pre-established subcutaneously C6 glioma model using rVVs at doses in the range of 10^2-10^7 PFU. Anti-tumor effect did not depend on the dose of the rVV-mIL2 and rVV-mIL12 viruses. All constructed rVVs showed high level of cytokine expression *in vitro* and *in vivo*. Most cytokine groups with the high dose of virus treatment (10^5-10^7 PFU) showed signs of cytokine toxicity while in low dose treatment groups (10^2-10^3 PFU) toxicity was greatly reduced. The VV control vector *per se* induced tumor inhibition, but the antitumor effect was less effective as compared to rVV carrying cytokine genes ($P<0.05$). These results suggest that attenuated recombinant strains of VV at low doses may potentially be efficient vectors for the cancer immunotherapy.

Key words: vaccinia virus, IL-2, IL-12, glioma, cancer immunotherapy

INTRODUCTION

Virus-mediated cytokine therapy has been proved effective against tumors inducing local and systemic immune response (2,7,10,15,22,25-27). Potential vectors of gene delivery for humans include adenovirus, herpes simplex virus (HSV), adeno-associated virus (AAV), poxvirus, or non-viral plasmid DNA. Compared to other virus vectors vaccinia virus (VV), a poxvirus, is a particularly attractive vector due to its wide host range, large cloning capacity, cytoplasmic site of viral replication, and high efficiency of foreign gene expression [3]. The safety and efficacy of live vaccine strains of VV was successfully demonstrated in the smallpox eradication program and in vaccine trials for a number of animal and human infectious diseases [3].

Recent preclinical studies on VV-mediated cytokine treatment is emerging as a promising approach for cancer gene therapy. Recombinant VV expressing different cytokines have been proved to produce authentic proteins both *in vitro* and *in vivo,* and induce anti-tumor effect in various animal tumor models [4-7, 42]. Compared to adenoviral vector which is used in gene therapy studies at high dose, VV can be applied at considerably lower dose to achieve similar antitumor effect. Low dose VV therapy may reduce the risk of systemic inflammatory response syndrome caused by high dose of virus vector (Hollon, 2000), and toxicity induced by overexpressed cytokines [36-41].

Currently, in most of tumor therapy studies laboratory strain Western Reserve (WR) of VV is used [10-13] which is known to be neurotropic and virulent to mice [14]. However, several attenuated VV strains were developed which proved to be safe in different animal models [3]. Patient treated by intratumoral injection of attenuated VV strain expressing cytokines showed no evidence of systemic spread of the virus or of organ dysfunction or other major hematological or biochemical changes [9 15]. Recent study on animals immunized with VV demonstrated that VV-specific protein expression in tumors was as effective as in non-vaccinated animals [8]. This important finding was confirmed by Robinson and colleagues [9] in clinical study demonstrating that VV can infect and replicate in tumor cells despite the presence of systemic neutralizing antibodies.

In our laboratory, the attenuated strain Lister has been used for many years. The safety and efficacy of this VV strain has been confirmed in our previous animal and human vaccination studies [16-18] and in studies on cancer gene therapy [19,20]. In this study, the efficacy of Lister VV as a vector of IL-2 and IL-12 delivery for low dose cancer immunotherapy has been investigated in athymic mice C6 glioma model. The C6 cell line demonstrates astrocytic morphology and has been widely used in neurobiology showing high homology to human glioma in terms of parenchymal invasion, neovascularity, and necrosis [23,24]. Athymic nude mice model may simulate immuno-deficient individuals or cancer patients

particularly at advanced stages which often develop impaired T cell response similar to nude mice due to the disease itself, radiotherapy and/or chemotherapy [25]. This animal model is also convenient for studying of the safety of the virus vectors. We performed a dose-escalation experiment (10 PFU to 10^7 PFU) to determine the effective dose of this attenuated VV for the inhibition of tumor growth. For the first time we have demonstrated that low-dose VV-mediated cytokine delivery can be an effective strategy for immunotherapy of glioblastomas in vivo.

MATERIALS AND METHODS

Cell lines. CV-1 cells, African green monkey kidney fibroblasts, were obtained from the American type Culture Collection (ATCC, Rockville, MD) and maintained in Dulbecco's modified Eagle's medium containing 5% fetal bovine serum and antibiotic-antimycotic solution (Sigma Chemical Co., St. Louis, MO). The Rat C6 nitrosourea-induced glioma cell line, originally established by Benda *et al* [21] was cultured in RPMI-1640 medium (Cellgro/Mdiatech, Inc., Herndon, virginia) supplemented with 5% fetal bovine serum and antibiotic-antimycotic solution.

Animals. Athymic nude mice (male, nu/nu) were purchased from Charles River Breeding Laboratories, Inc. (Wilmington, MA) at 5-6 weeks of age. The animals were housed in self-contained filter-top cages in a room controlled for temperature, humidity, and a 12 h day-night cycle. Autoclaved bedding, food and water were provided. At the time of

sacrifice, rapid CO_2 asphyxiation was performed in compliance with the NIH Guide for the Care and Use of Laboratory Animals. The study was approved by our institutional Animal Research Committee.

Construction of recombinant vaccinia virus expressing IL-2 and IL-12. LIVP variant of the attenuated Lister strain of VV has been used in this study. The plasmid (VR1110) containing mouse IL-2 (mIL-2) gene and plasmid (pSFG.IL-12.p40.L.Δp35) carrying mouse IL-12 (mIL-12) fusion gene were obtained from Dr. Parker (Vical, Inc., San Diego) and Dr. Mulligan (Howard Hughes Medical Institute, Boston), respectively. The constructions of recombinant viruses rVV-mIL2, rVV-mIL12 and rVV-2-12, which carrying mIL-2, mIL-12 or both genes, are described in Fig.1. The control virus rVV_4 has the insertion of two genes encoding *Photinus pyralis luciferase (luc)* and the *Escherichia coli lacZ* at the TK region of the wild-type VV (wt VV) (Fig. 1d). All recombinant viruses contained a copy of reporter *lacZ* gene.

Recombinant clones were selected by growth on CV-1 cells, in the presence of 5-bromo-4-chloro-indolyl-β-D-galactosidase (X-gal) using the *lacZ* reporter gene. The recombinant viruses were then purified over a sucrose gradient. Virus concentration was determined by plaque titration on CV-1 cells and expressed as plaque-forming units (PFU) per milliliter.

Kinetic analysis of cytokines expression *in vitro*

The efficacy of cytokine expression was performed on rat C6 glioma cells by enzyme-linked immuno-sorbent assay (ELISA). C6 cells

($1x10^6$ cells/well) were plated on 6-well plate and infected with rVV-mIL2, rVV-mIL12 or rVV-2-12 respectively at different multiplicity of infection (MOI). Supernatants were collected at specified time points and cytokines assayed by ELISA kits (Douset kit, Genzyme, Cambridge, MA).

Animal model. C6 glioma cells ($5x10^5$/mouse) were injected subcutaneously (s.c.) at right hind of the nude mice. On day 5 after cell inoculation when palpable tumor had formed, animals were injected intratumorally (i.t) with increasing doses of rVV4, rVV-mIL2, rVV-mIL12 or rVV-2-12 in a volume of 50μl. The lowest dose for these viruses was 10PFU while the highest dose was 10^7PFU for rVV-mIL2 and rVV-mIL12, and 10^5PFU for rVV-2-12. Animals were weight twice a week and tumor dimensions were measured with vernier calipers. All animals were euthanized at the same time, when mean tumor volume for the control group reached ~2,500 mm^3.

Tumors were removed and cut into small pieces in PBS with 100 μM phenylmethylsulfomyl fluoride (PMSF). After centrifuged at 2000 rpm, 5 min, supernatant were collected and stored at -80°C before assayed by ELISA for mIL-2 and mIL-12 expression.

Western blot analysis for IL-12 fusion protein in tumor. To confirm the authenticity of the fused subunit of IL-12 gene expression by rVV *in vivo*, tumors treated with 10^5 PFU rVVs on day 7 after virus injection were homogenized and extracts were analyzed for IL-12 fusion protein expression by Western blot. Eighty μg of protein were separated on a 12%

polyacrylamide/SDS gel and transferred to Immunobilon-P membrane (Millipore, Bedford, MA). The membrane was blocked with 5% non-fat milk and probed with primary antibody: Goat anti-mouse IL-12 monoclonal antibody (R&D systems Inc., MN), and then incubated with the secondary antibody conjugated with horseradish peroxidase (Jackson ImmunoResearch Lab. Inc., PA). The membrane development was performed according to the manufacturer's instructions.

Virus *in vivo* infection efficiency. Forty μm thick sections from frozen tumors (two/group) were dried, fixed in 2% formaldehyde (v/v) and 0.2% glutaraldehyde (v/v) in PBS for 30 min and washed in PBS for 2 times. Then, sections were stained in X-gal solution for 4 h at 37°C. X-gal solution was prepared by combining the following: 5 mM potassium ferricyanide, 5 mM potassium ferrocyanide, 2 mM $MgCl_2$, 1 mg/ml X-gal in PBS.

Spontaneous blastogenesis in peripheral blood and spleen. Seven days after virus infection, whole blood samples of animals treated with control virus (rVV4) of different dosage (10, 10^2, 10^3 and 10^7 PFU) were collected in heparinized tuberculin syringes via cardiac puncture immediately after euthanasia. Spleens were removed and smashed in RPMI-1640 medium before filtrated. The leukocyte counts in blood and spleen samples were performed on HESCA Hematology Analyzer (ABX Hematologie, France). Fifty μl aliquots of whole blood or spleen samples were mixed with 150 μl of complete RPMI 1640 medium and 1 μCi ^{3}H-

thymidine in 50 μl of medium was immediately added. The cells were incubated for 4 h at 37°C, harvested with a multiple-sample harvester, and the amount of ^{3}H-thymidine incorporated into cell DNA was counted in a liquid β-scintillation counter (E&G Wallac Inc., MD). The results are expressed as disintegrations per minute (dpm)/10^{6} cells.

Flow cytometry analysis. Blood and spleen samples were prepared as described above. Fifty μl of each sample was then stained with appropriate fluorescent-conjugated monoclonal antibodies (CD_{45}, PAN-NK) (PharMingen, San Diego, CA). Stained cells were washed and analyzed using a FACSCalibur machine with CellQuest software (Becton Dickinson, Manfield, MA).

Virus dissemination. The dissemination of VV in immuno-compromised nude mice was assessed using the highly sensitive β-galactosidase luminometric assay. Tumor and organs were removed at day 2 and 9 after virus injection and smashed in appropriate volume of lysis buffer. The extract was centrifuged at 13,000 rpm for 5min to remove tissue debris. A 20 μl sample of extract was assayed using Galacto-light Plus™ kit (Tropix, Bedford, MA). Bioluminescence was measured by ML300 microplate luminomiter (Dynatech Laboratories, Inc., Chantilly, VA). Results are expressed as light units (LU)/mg organ wet weight [22].

Statistical analysis. The data were analyzed using one-way analysis of variance, Tukey's HSD test (SPSS). A P value of <0.05 was considered to indicate significant differences among groups.

RESULTS

Cytokine expression *in vitro* and *in vivo.* The recombinant vaccinia viruses induced efficient synthesis of mIL-2 and mIL-12 in infected cells both *in vitro* and *in vivo.* In C6 glioma cells infected *in vitro* proteins were measured as early as 6 h after virus infection reaching the peak of cytokine production between 24 and 48 h with the yield of 600ng/10^6cells of mIL-2 and 1800ng/10^6cells of mIL-12 (Fig.2). Cytokine expression was still detectable at 96 h. The efficiency of cytokine expression of the construct rVV-2-12 carrying both mIL-2 and mIL-12 genes in different regions of the same VV genome was similar to that after infection with virus rVV-mIL2 or rVV-mIL12 alone. Thus, the rVV-2-12 virus expressed both cytokines at the same time without influencing the gene expression. The expression of two reporter genes (*lacZ and luc*) incorporated into the rVV-2-12 genome along with cytokine genes were not interfered either.

Local intratumoral injection of rVVs in some animals directed cytokine expression even at doses as low as 10 and 10^2 PFU of viruses. In higher dose groups, almost all tumor extracts showed efficient cytokine expression measured by ELISA assay. Highest level of IL-2 (56 pg/mg) and IL-12 (825 pg/mg) at tumor site and in circulation (5.5 ng/ml and 88.7 ng/ml, respectively) was observed on day 2 after injection of 10^7 PFU viruses (Table 1, 2). On days 8, IL-2 was still detectable in the tumor but at lower level, while IL-12 was found both in tumor and blood. The difference

in cytokine expression levels at high doses of 10^5–10^7 PFU was insignificant. At the same MOI, IL-12 expression in terms of protein production was found to be significantly higher than IL-2. In control groups, IL-2 and IL-12 on days 2 and 8 were barely detectable, if any (data not shown).

Western blot analysis confirmed that IL-12 fusion protein expressed by rVV-mIL12 in tumor remained authentic and intact under reducing condition, whereas control recombinant IL-12 (rIL-12) with heterodimer structure dissociated to p35 and p40 subunits (Fig. 3). No endogenous mIL-12 was detected in Hank's, rVV4 and rVV-mIL2 groups.

Tumor inhibition in nude mice glioma model. To determine the efficacy of different doses of VV administered by *i.t.* injection we used seven graded doses from 10 to 10^7 PFU on an established nude mice glioma model. Dosage from 10^2 to 10^7 PFU of both rVV-mIL2 and rVV-mIL12 demonstrated significant growth inhbition of subcutaneous glioma ($P<0.05$) with tumor volumes near or over 50% smaller than that treated with the control virus (Fig.4). No significant difference was observed between IL-2 and IL12 treatment groups. Injection of 10 PFU of rVVs did not produce anti-tumor effects. High dose of control virus also exhibited an effective inhibition of tumor growth.

Except for animals animal treated with 10 PFU of rVV-mIL12, in all rVV-mIL2 or rVV-mIL12 treated groups we observed signs of cytokine-associated toxicity. High dosage groups (10^5 to 10^7 PFU) resulted in high

mortality rate with an approximately 60% survival on 8 day after rVV injection. Low virus doses (10 to 10^4 PFU) resulted in 100% survival at the same time but some animals failed to gain weight indicating on possible cytokine mediated side effect. Combination therapy with rVV-2-12 was lethal for mice even at 10^3-10^5 PFU with 100% mortality on day 5. At 10 PFU, 30% animals died on day 5. Further data on cytokine toxicity will be presented elsewhere (manuscript in preparation).

Virus infection *in vivo*. To examine the efficiency of low dose (10-10^2 PFU) VV infection, on day 7 after *i.t.* injection of rVV tumor sections were prepared and stained with X-gal. No positive staining was found in all 10 PFU groups, indicating that either virus particles were cleared from the tumor by host immune system, or the level of gene expression was very low. Sections of tumors treated with 10^2 PFU rVV4, rVV-mIL2 and rVV-mIL12 exhibited *lacZ* activity within 2 h after adding the substrate (Fig.5). These findings showed that as low as 100 viral particles of VV constructs were sufficient to detect productive infection of tumor tissues.

Immune response to vaccinia virus vector. The immune response induced by rVV4 vector itself was characterized by blood and spleen blastogenesis study and NK cell analysis. Peripheral blood leukocytes from 10^7 PFU group exhibited significantly greater spontaneous blastogenesis compared to saline tumor control ($P<0.05$), while lower doses (10-10^3 PFU) produced some increase but the difference was statistically insignificant (Fig.6). High increase in NK cells ($P<0.05$) was

detected in blood after treatment with 10^3 PFU of rVV4 (Fig.7). However, no obvious changes in number of NK cells and in spontaneous blastogenesis were found in spleen after *i.t.* injection of rVV4 at any doses (data not shown).

Virus dissemination. Using a virus titration method we previously demonstrated that this strain of VV is safe for nude mice even after *s.c.* inoculation of 10^8 PFU [19]. Here, we used a sensitive chemiluminescent method to detect β-galactosidase expression in different organs and tumors after *i.t.* injection of 10^7 PFU of VV. All recombinant viruses in this experiment carried *lacZ* gene driven by VV promoter p11. Measured level of β-galactosidase expression showed that the viral proliferation at tumor injection site could be detected on day 2 after virus injection (rVV4: 12.1 LU/mg; rVV-mIL2: 17.9 LU/mg; rVV-mIL12: 11.9 LU/mg). Virus replication significantly decreased by day 9 (rVV4: 3.83 LU/mg; rVV-mIL2: 0.61 LU/mg; rVV-mIL12: 4.45 LU/mg).

Although on day 2 the *lacZ* gene expression was detected in organs (lung, liver, kidney), but the reporter expression was several orders of magnitude less than in tumor tissue. On day 9, the virus replication was barely detectable in these organs and animals showed no signs of side effects or disease.

DISCUSSION

The present study describes an application of immunotherapy by local delivery of low dose recombinant Lister VV carrying IL-2 or fused

subunits of IL-12 in an athymic mice and C6 glioma xenograft model. Our *in vitro* experiments demonstrate that the constructed rVVs efficiently infect tumor cells resulting in production of authentic cytokines. The peak of cytokine synthesis was observed at 24-48 h after infection producing 600ng/10^6cells of IL-2 and 1800ng/10^6cells of IL-12. Incorporation of as many as four foreign genes into vaccinia virus did not interfere with the expression level of these genes.

In nude mouse model we found that single intratumoral injection of as low virus dose as 10^2 or 10^3 PFU of rVV-mIL2 or rVV-mIL12 can induce significant inhibition of C6 tumor growth. Higher virus doses (10^5-10^7 PFU) also exhibited antitumor effect, however treated animals showed signs of toxicity and high mortality apparently associated with high cytokine production (manuscript in preparation). Thus, virus doses of 10^2-10^3 PFU may result in sufficient production of therapeutic cytokines and immune responses for tumor immunotherapy.

Antitumor effect of virus- mediated IL-2 and IL-12 immunotherapy has also been demonstrated in other tumor models. It was suggested that the produced cytokines activate lymphokine-activated killer (LAK) cells, NK cells and tumor infiltrating lymphocytes (TILs) [26-28]. IL-12 was also reported to inhibit angiogenesis indirectly through the stimulating of IFN-γ and chemokine IP-10 [29].

By analyzing the cytokine production *in vivo*, the maximum level of gene expression in tumors and in plasma was observed on day 2 after

virus treatment. Surprisingly, the cytokine expression levels in tumors and plasma at 10^5-10^7 PFU of virus treatment varied but the differences were not significant. IL-2 expressed by rVV *in vivo* seemed to facilitate the virus elimination from the animal. The efficiency of virus reporter gene (*lacZ)* expression in tumors on day 8 after virus injection was significantly lower in IL-2 groups (0.61 LU/mg) than that with the control virus (3.83 Lu/mg) and IL-12 groups (4.45 LU/mg). This result is in agreement with data previously reported by other researchers [30-32] on IL-2-mediated inhibition of VV infection in nude mice presumably via elevated NK activity.

Since the safety of virus-based therapy is a great concern and virus dissemination is usually related to high dose of applied recombinant virus [12,12,22], low-dose therapy of VV may be advantageous in cancer immunotherapy by minimizing the risk of virus spread and pathogenicity. In other vector systems the applied virus doses are very high. The effective dose of the WR strain of VV in tumor immunotherapy study was 10^5 PFU [7,7,33], while the dose of adenovirus mediated IL-2 and IL-12 treatment was in the range of 10^7- $5x10^8$ PFU [2,2,26,27]. Our rVV viruses can achieve tumor inhibition at 10^2 PFU, a dose that is much lower as compared with that using WR VV and adenovirus vectors. Safety of our virus vector was previously demonstrated on human [16,18]. Here we confirmed that as a highly attenuated virus vector it did not exhibit obvious systemic dissemination after *i.t.* injection at dose as high as 10^7 PFU per mouse, and VV particles mostly remained localized at the injection site.

In this study, we also confirmed our previous finding that high dose of the VV vector itself can cause tumor inhibition effects [19], although its efficiency is much lower as compared to recombinant VV carrying genes of cytokines. Others reported similar results using adenovirus vector in P815 murine tumor model[27]. General increase of blood leukocytes by blastogenesis analysis and the significant increase in blood NK cell population may indicate an important role of these cells in vaccinia-mediated tumor suppression. Immunogenic virus itself may act as an adjuvant for cancer immunotherapy augmenting stronger antitumor immune response by enhancing the presentation or recognition of tumor-specific antigens and inducing the production of cytokines [34]. Preferential infection of tumor cells by virus may also contribute to stimulation of host antitumor immune response [1,13,35].

Our results indicate that low dose VV-mediated IL-2 and IL-12 delivery may induce therapeutic effects against pre-established glioma. To our knowledge, this is the first report on use of Lister strain of VV as a vector in cancer immunotherapy. Previously, we demonstrated that p53-mediated gene therapy based on this virus vector might be a new promising antitumor strategy [19]. However, single treatments itself either with cytokines or tumor suppressors may not be sufficient for elimination of tumors. Combination of immunotherapy with other antitumor gene therapy strategies, like tumor suppressor treatment, or virus-mediated inhibition of vascularization may further enhance the antitumor efficacy

and contribute to the translation of these promising experimental systems into clinical practice. Combination of VV-mediated immunotherapy and p53 tumor gene therapy will be addressed in our future experiments.

Acknowledgments

This work was supported by grant from National Military test bed # . We thank Dong-won Kim, Glen M Miller, Jun Li and Xiao W Mao for help in animal study. We thank Drs Susan Parker and Richard C Mulligan for providing IL-2 and IL-12 plasmid DNA.

Sponsored by the US Department of the Army and NMTB. The view, opinions and/or finding contained in this report are those of the authors and should not be construed as a position, policy, decision or endorsement of the federal Government or the National Medical Technology Testbed, Inc.

References

1. Webb HE, Smith CE. Viruses in the treatment of cancer. *Lancet* 1970;1:1206-1208.

2. Nasu Y, Bangma CH, Lee HM, Hu J, Wang J, McCurdy MA, Shimura S, Yang G, Timme TL, Thompson TC. Adenovirus-mediated interleukin-12 gene therapy for prostate cancer: suppression of orthotopic tumor growth and pre-established lung metastases in an orthotopic model. *Gene Therapy* 1999;6:338-349.

3. Moss B. Genetically engineered poxviruses for recombinant gene expression, vaccination, and safety. *Proc Natl Acad Sci USA* 1996;93:11341-11348.

4. Peplinski GR, Tsung K, Whitman ED, Meko JB, and Norton JA. Construction and Expression in Tumor Cells of a Recombinant Vaccinia Virus Encoding Human Interleukin-1Beta. *Annals of Surgical Oncology* 1995;2:151-159.

5. Uzendoski K, Kantor JA, Abrams SI, Schlom J, and Hodge JW. Construction and Characterization of a Recombinant Vaccinia Virus Expressing Murine Intercellular Adhesion Molecule-1: Induction and Potentiation of Antitumor Responses. *Human Gene Therapy* 1997;8:851-860.

6. Whitman ED, Tsung K, Paxson J, Norton JA. In vitro and in vivo kinetics of recombinant vaccinia virus cancer-gene therapy. *Surgery* 1994;116:183-188.

7. Meko JB, Yim JH, Tsung K, Norton JA. High cytokine production and effective antitumor activity of a recombinant vaccinia virus encoding murine interleukin 12. *Cancer Research* 1995;55:4765-4770.

8. Lee SS, Eisenlohr LC, McCue PA, Mastrangelo MJ, and Lattime EC. Intravesical Gene Therapy: In vivo Gene Transfer Using Recombinant Vaccinia Virus Vectors. *Cancer Research* 1994;54:3325-3328.

9. Robinson BW, Mukherjee SA, Davidson A, Morey S, Musk AW, Ramshaw I, Smith D, Lake R, Haenel T, Garlepp M, Marley J, Leong C, Caminschi I, Scott B. Cytokine gene therapy or infusion as treatment for solid human cancer. *J Immunother* 1998;21:211-217.

10. Qin H, Chatterjee SK. Recombinant vaccinia expressing interleukin-2 for cancer gene therapy. *Cancer Gene Ther* 1996;3:163-167.

11. Ramshaw I, Ruby J, Ramsay A, Ada G, Karupiah G. Expression of cytokines by recombinant vaccinia viruses: a model for studying cytokines in virus infections in vivo. *Immunol Rev* 1992;127:157-182.

12. Gnant MFX, Puhlmann M, Alexander HR Jr, Bartlett L. Systemic administration of a recombinant vaccinia virus expressing the cytosine deaminase gene and subsequent treatment with 5-fluorocytosine leads to tumor-specific gene expression and prolongation of survival in mice. *Cancer Research* 1999;59:3396-3403.

13. Puhlmann M, Gnant M, Brown CK, Alexander HR, Bartlett DL. Thymidine kinase-deleted vaccinia virus expressing purine nucleoside phosphorylase as a vector for tumor-directed gene therapy. *Human Gene Therapy* 1999;10:649-657.

14. Buller RML, Smith GL, Cremer K, Notkins AL, Moss B. Decreased virulence of recombinant vaccinia virus expression vectors is associated with a thymidine kinase-negative phenotype. *Nature* 1985;317:813-815.

15. Mastrangelo MJ, Maguire HCJ, Eisenlohr LC, Laughlin CE, Monken CE, McCue PA, Kovatich AJ, Lattime EC. Intratumoral recombinant GM-CSF-encoding virus as gene therapy in patients with cutaneous melanoma. *Cancer Gene Ther* 1999;6:409-422.

16. Chernos VI, Cheliapov NV, Antonova TP, Rakhilina LE, Unanov SS, Al'tshtein AD, Zakharova LG, Fodor II, Bendukidze KA, Komarov FI. Verification of the safety, inoculability, reactogenicity and antigenic properties of a live recombinant smallpox-hepatitis B vaccine in an experiment in volunteers. *Vopr Virusol* 1990;35:132-135.

17. Timiryasova TM, Kopylova-Sviridova TN, Fodor I. Analysis of expression of the reporter genes in different regions of vaccinia virus genome. *Mol Biol* 1993;27:392-401.

18. Fodor I. Live recombinant vaccines for humans. *Acta Biotechnol Acad Verlag* 1991;11:215-221.

19. Timiryasova TM, Chen B, Haghighat P, Fodor I. Vaccinia virus-mediated expression of wild-type p53 suppresses glioma cell growth and induces apoptosis. *Int J Oncol* 1999;14:845-854.

20. Gridley DS, Andres ML, Li J, Timiryasova TM, Chen B, Fodor I. Evaluation of radiation effects against C6 glioma in combination with vaccinia virus-p53 gene therapy. *Int J Oncol* 1998;13:1093-1098.

21. Benda P, Lightbody J, Sato G, Levine L, Sweet W. Differentiated rat glial cell strain in tissue culture. *Science* 1968;161:370-371.

22. Bui LA, Butterfield LH, Kim JY, Ribas A, Seu P, Lau R, Glaspy JA, McBride WH, Economou JS. In vivo therapy of hepatocellular carcinoma with a tumor-specific adenoviral vector expressing interleukin-2. *Human Gene Therapy* 1997;8:2173-2182.

23. Vajkoczy P, Schilling L, Ullrich A, Schmiedek P, Menge M. Characterization of angiogenesis and microcirculation of high-grade glioma: an intravital multifluorescence microscopic approach in the athymic nude mouse. *J cereb Blood Flow Metab* 1998;18:510-515.

24. Peterson DL, Sheridan PJ, Brown WE. Animal models for brain tumors: historical perspectives and future directions. *J Neurosurg* 1994;80:865-876.

25. Kimura M, Yoshida Y, Narita M, Takenaga K, Takenouchi T, Yamaguchi T, Saisho H, Sakiyama S, Tagawa M. Acquired immunity in nude mice induced by expression of the IL-2 or IL- 4 gene in human pancreatic carcinoma cells and anti-tumor effect generated by in vivo gene transfer using retrovirus. *Int J Cancer* 1999;82:549-555.

26. Addison CL, Bramson JL, Hitt MM, Muller WJ, Gauldie J, Graham FL. Intratumoral coinjection of adenoviral vectors expressing IL-2 and IL-12 results in enhanced frequency of regression of injected and untreated distal tumors. *Gene Therapy* 1998;5:1400-1409.

27. Fernandez N, Levraud JP, Haddada H, Perricaudet M, Kourilsky P. High frequency of specific $CD8^+$ T cells in the tumor and blood is associated with efficient local IL-12 gene therapy of cancer. *J Immunol* 1999;162:609-617.

28. Gollob JA, Schnipper CP, Murphy EA, Ritz J, Frank DA. The functional synergy between IL-12 and IL-2 involves p38 mitogen-activated protein kinase and is associated with the augmentation of STAT serine phosphorylation. *J Immunol* 1999;162:4472-4481.

29. Yao L, Sgadari C, Furuke K, Bloom ET, Teruya-Feldstein J, Tosato G. Contribution of natural killer cells to inhibition of angiogenesis by interleukin-12. *Blood* 1999;93:1612-1621.

30. Ramshaw IA, Andres ML, Phillips SM, Boyle DB, Coupar BEH. Recovery of immunodeficient mice from a vaccinia virus/IL-2 recombinant infection. *Nature* 1987;329:545-546.

31. Karupiah G, Coupar BEH, Andrew ME, Boyle DB, Phillips SM, Mullbacher A, Blanden RV, Ramshaw I. Elevated natural killer cell responses in mice infected with recombinant vaccinia virus encoding murine IL-2. *J Immunol* 1990;144:290-298.

32. Flexner C, Hugin A, Moss B. Prevention of vaccinia virus infection in immunodefecient mice by vector-directed IL-2 expression. *Nature* 1987;330:259-262.

33. Peplinski GR, Tsung K, Meko JB, Norton JA. In vivo gene therapy of a murine pancreas tumor with recombinant vaccinia virus encoding human interleukin-1 beta. *Surgery* 1995;118:185-191.

34. Reichard KW, Lorence RM, Cascino CJ, Peeples ME, Walter RJ, Fernando MB, Reyes HM, Greager JA. Newcastle disease virus selectively kills human tumor cells. *J Surg Res* 1992;52:448-453.

35. Martuza RL. Experimental therapy of human glioma by means of a genetically engineered virus mutant. *Science* 1991;252:854-856.

36. Rachmilevich AL, Timmins JG, janssen K, Pohlmann, Sheehy MJ, Yang N-S. Gene gun-mediated IL-12 gene therapy induces

antitumor effects in the absence of toxicity: a direct comparison with systemic IL-12 protein therapy. J. Immunother. 22, 135-144, 1999

37. Orange JS, Salazar-Mather TP, Opal SM. Et al., mechanism of interleukin 12-mediated toxicities during experimental viral infectons: rle of tumor necrosis factor and glucocorticids.J. Exp. Med. 1995, 181: 901-14.

38. Coughlin CM, Wysocka M., Kurzawa WM, Lee G., Trinchieri G. Eck SL. B7-1 and interleukin 12 synergistically induce effective antitumor immunity. Cancer Res. 1995, 55: 4980-7.

39. Marshall E. Cancer trial of interleukin-12 halted. Science 1995, 268, 1555.

40. Lamont AG and Adorini L. IL-12: a key cytokine in immune regulation. Immunol.Today 1966 17:214-7.

41 Carson WE, Yu H., Dierksheide J. Pfeffer K., Bouchard P., Clark R., Durbin R., Baldwin AS. Peschon J., Johnson PR., Ku G, Baumann H, Caligiuri MA. A fatal cytokine-induced systemic inflammatory response reveals a critical role for NK cells. J. Immunol. 1999, 162: 4943-51.

42. Kaufman HL, rao JB, Irvine KR, Bronte V., Rosenberg SA and Restifo NP. Interleukin-10 enhances the therapeutic effectiveness of a recombinant poxvirus-based vaccne in an experimental murine tumor model. J. Immunother. 22: 489-496, 1999

Legends

Fig.1. Construction of recombinant vaccinia viruses. (a, b) The mouse IL-2 or IL-12 cDNA fragment was cloned into the VV transfer vector pSC-11 downstream of the early/late VV p7.5 promoter, resulting in pSC-mIL2 or pSC-mIL12, respectively. The reporter gene *lacZ* was under the control of VV late p11 promoter. Recombinant rVV-mIL2 and rVV-mIL12 was generated by homologous recombination between TK region flanking mIL-2 or mIL-12 on plasmid and the TK region of the wild type VV genome. The IL-12 gene we used was a fusion gene, containing both p40 and p35 subunits. (c) mIL-12 cDNA was ligated into the SmaI site of a VV expression vector, pNL5Sma, which contained the *luc* reporter gene. The resulting mIL-12 expression vector, pN-mIL12, was inserted into the N region of rVV-mIL2 genome by homologous recombination. The rVV-2-12 contained four foreign genes, mIL-12, *luc* genes at N region and mIL-12, *lacZ* genes at TK region. (d) control virus rVV4 had the two reporter genes, *lacZ* and *luc*, inserted into the TK region of wild type VV.

Fig. 2. Kinetic analysis of mIL-2 or mIL-12 expression by different recombinants. Rat C6 glioma cells were seeded in 24-well plate at $1x10^6$ cells/well. The next day, cells were infected with rVV-mIL2, rVV-mIL12 or rVV-2-12 at the indicated MOI. Supernatants were collected at 6, 24, 48, 72 and 96 h. The secretion of cytokine was measured by ELISA.

Fig. 3. Authentic expression of IL-12 fusion protein in tumor. Recombinant heterodimeric and fusion protein forms of mouse IL-12 were analyzed by

Western blot under reducing condition (β-mercaptoethanol). Heterodimeric IL-12 separated into two subunits, while the fusion IL-12 maintained an intact protein. rIL-12: recombinant heterodimeric IL-12.

Fig. 4. *In vivo* dose response. Rat C6 glioma cells ($5x10^6$) were injected s.c. in the right hind of the nude mice. After 5 days of initial inoculation, all animals attained palpable tumors, at which time Hank's, rVV4, rVV-mIL2, or rVV-mIL12 were administrated i.t. for a single injection at seven different doses ($10\text{-}10^7$ PFU). Significant difference ($P<0.05$) was observed in $10^2\text{-}10^7$ PFU groups when compared with saline and virus control groups.

Fig. 5. *In vivo* virus infection. Frozen tumor section from Hank's, rVV4, rVV-mIL2 or rVV-mIL-12-treated groups were dried and fixed in fixative buffer. After rinsed in PBS for 2 times, sections were stained in X-gal solution for 4 h at 37°C.

Fig. 6. Spontaneous blastogenesis in peripheral blood from mice injected with rVV4. Aliquots (50 μl) of whole blood were incubated in medium containing 1 μCi ^{3}H-thymidine per well for 4 h before counting the amount of radioactivity taken up by cells. * significant difference between two groups ($P<0.05$).

Fig. 7 NK cell proliferation in peripheral blood from mice injected with rVV4. Aliquots (50 μl) of whole blood were labeled with antibody (pan-NK) and analyzed by flow cytometry. . * statistically significant difference between two groups ($P<0.05$).

FIGURE 1

a

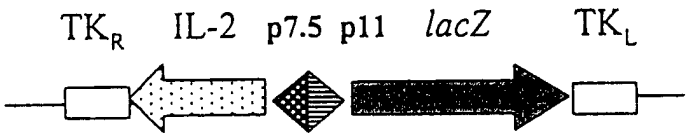

b

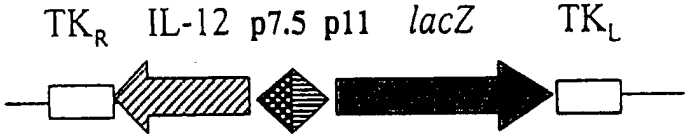

c

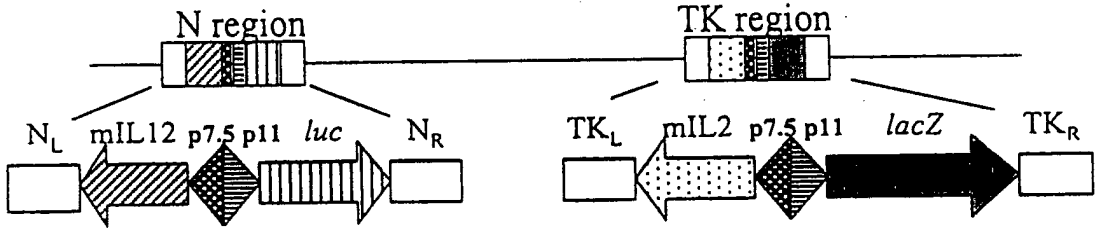

d

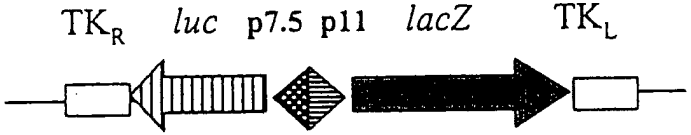

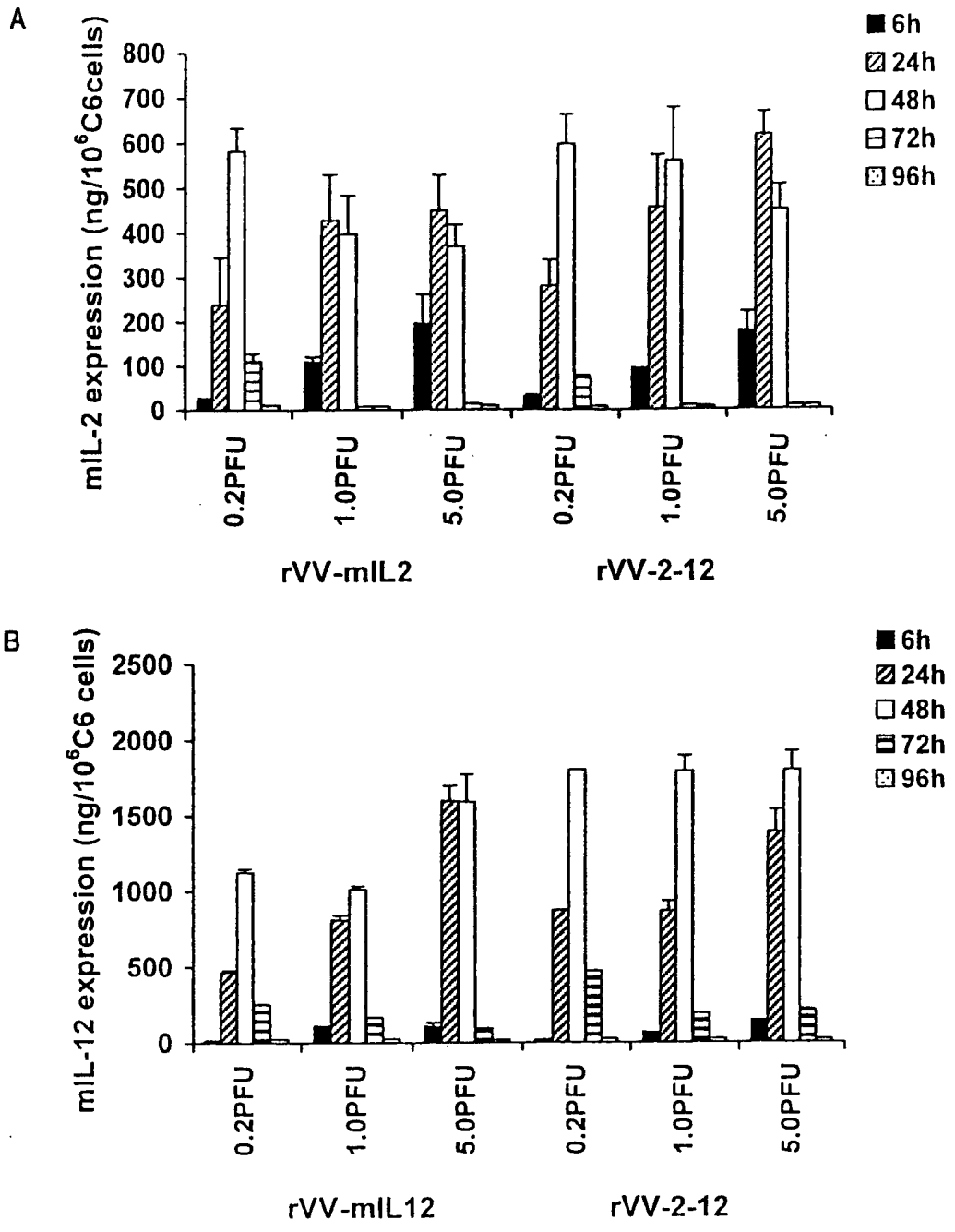
A
mIL-2 expression (ng/10^6C6cells)
800
700
600
500
400
300
200
100
0
6h
24h
48h
72h
96h
0.2PFU
1.0PFU
5.0PFU
0.2PFU
1.0PFU
5.0PFU
rVV-mIL2
rVV-2-12
B
mIL-12 expression (ng/10^6C6 cells)
2500
2000
1500
1000
500
0
6h
24h
48h
72h
96h
0.2PFU
1.0PFU
5.0PFU
0.2PFU
1.0PFU
5.0PFU
rVV-mIL12
rVV-2-12

FIGURE 2

FIGURE 3

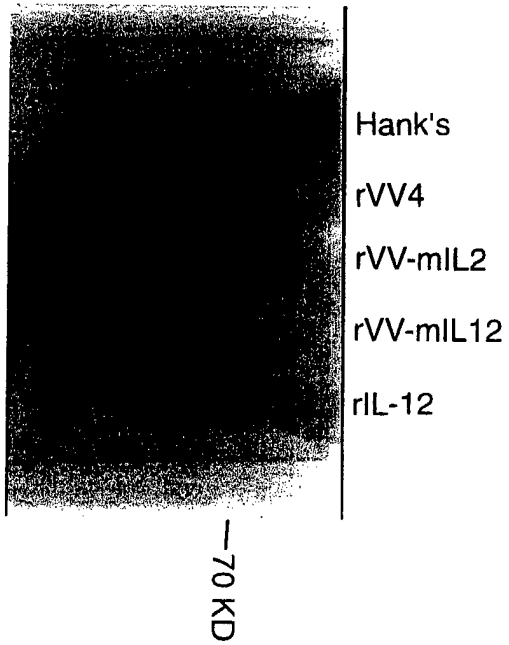

FIGURE 4

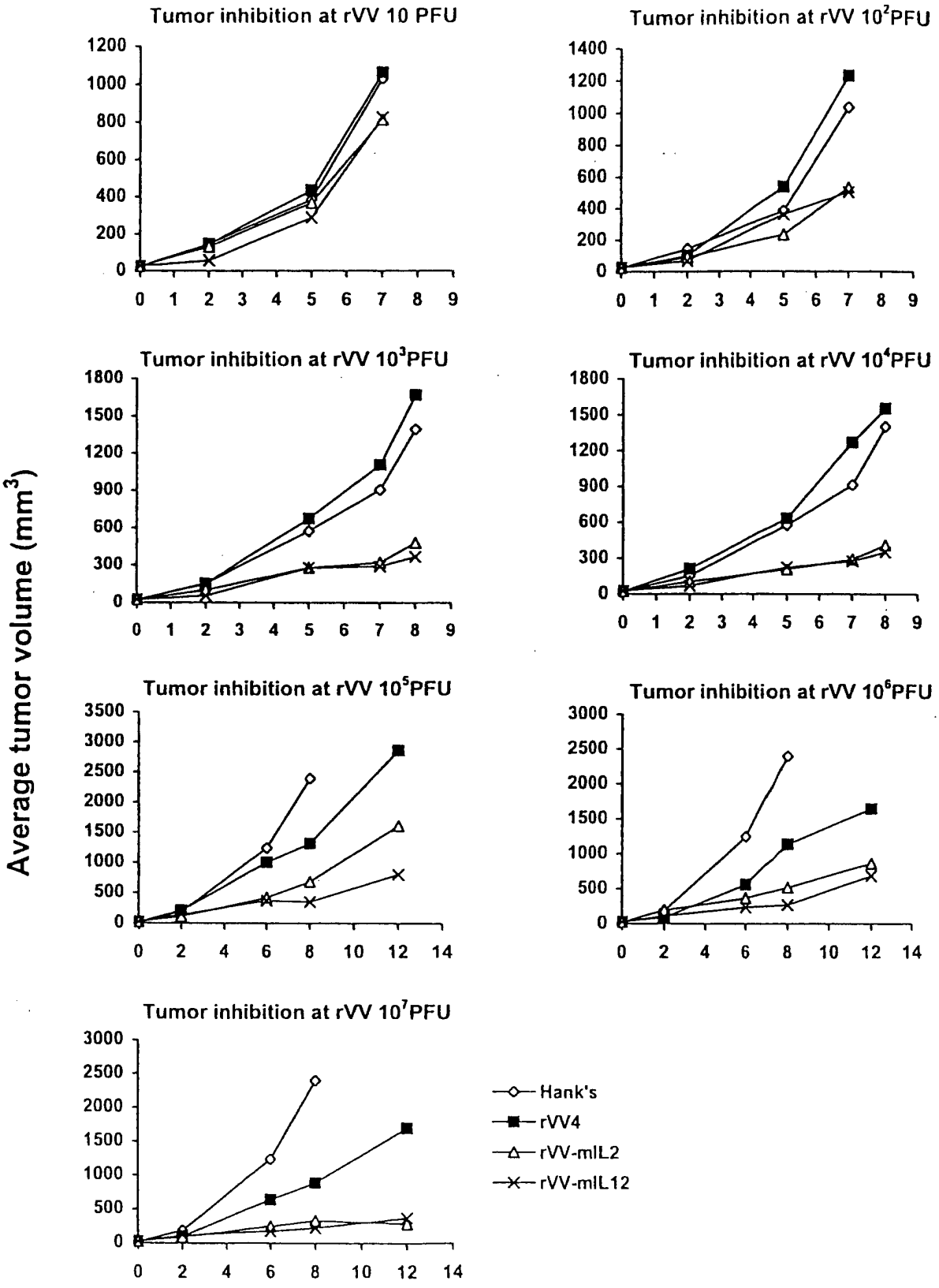
Tumor inhibition at rVV 10 PFU
Tumor inhibition at rVV 10²PFU
Tumor inhibition at rVV 10³PFU
Tumor inhibition at rVV 10⁴PFU
Tumor inhibition at rVV 10⁵PFU
Tumor inhibition at rVV 10⁶PFU
Tumor inhibition at rVV 10⁷PFU
Average tumor volume (mm³)
Days after virus injection
Hank's
rVV4
rVV-mIL2
rVV-mIL12

0.5 cm

Hank's

rVV4 100 PFU

rVV-mIL2 100 PFU

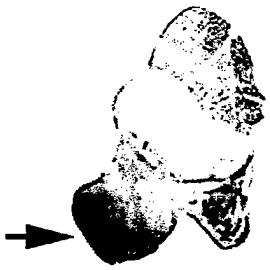

rVV-mIL12 100 PFU

FIGURE 5

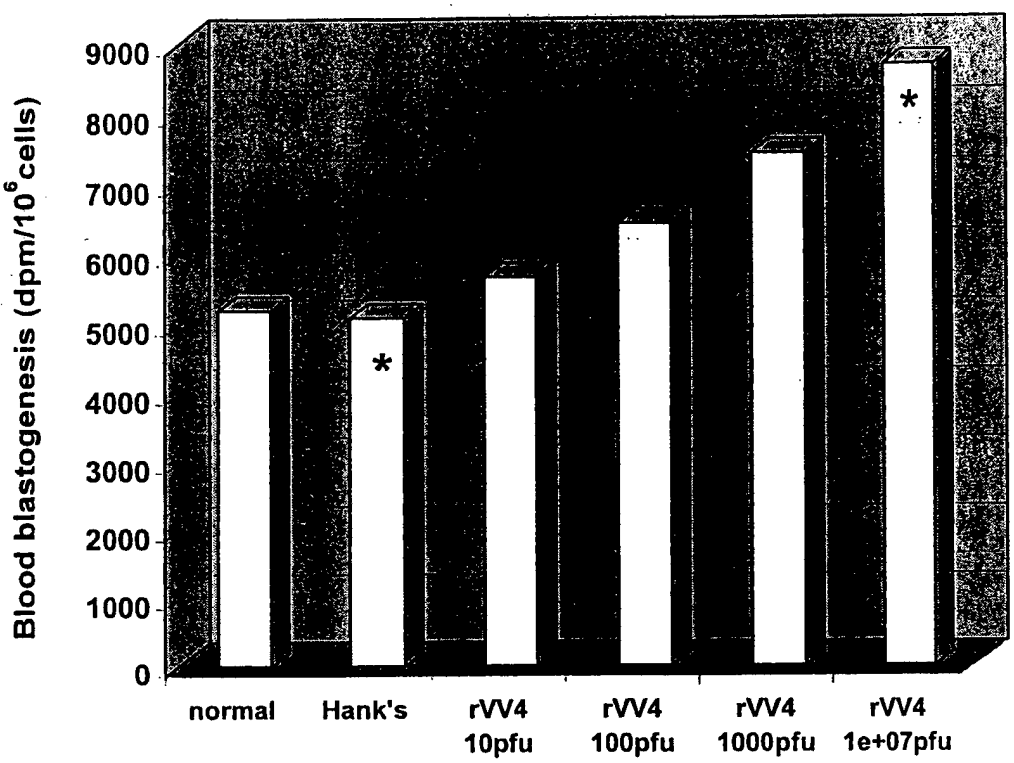
Blood blastogenesis (dpm/10^6 cells)
9000
8000
7000
6000
5000
4000
3000
2000
1000
0
*
*
normal
Hank's
rVV4 10pfu
rVV4 100pfu
rVV4 1000pfu
rVV4 1e+07pfu

FIGURE 6

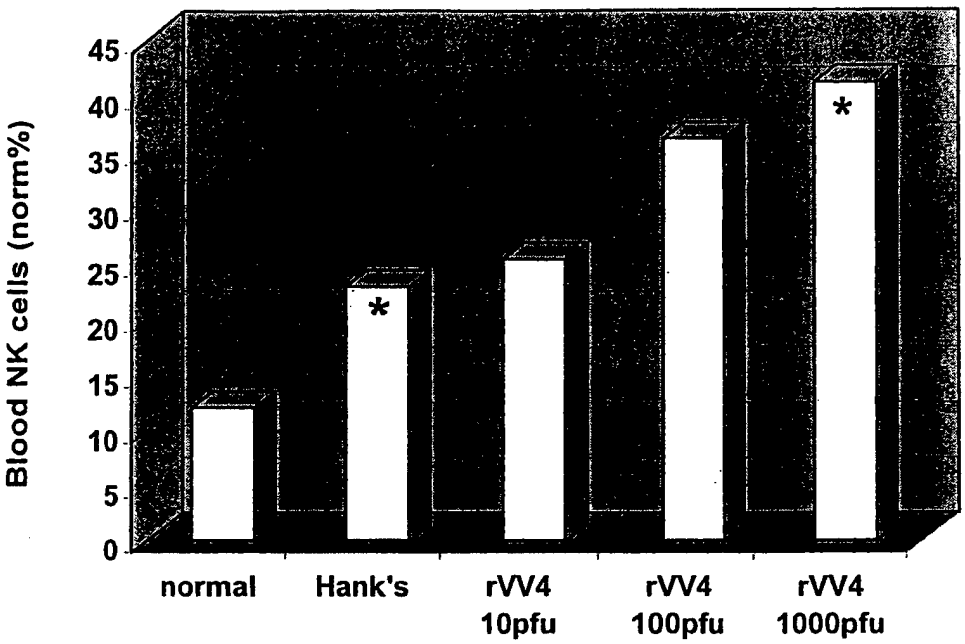
Blood NK cells (norm%)
45
40
35
30
25
20
15
10
5
0
*
*
normal
Hank's
rVV4 10pfu
rVV4 100pfu
rVV4 1000pfu

FIGURE 7

Evaluation of combined vaccinia virus-mediated antitumor gene therapy with p53, IL-2 and IL-12 in glioma model

Bing Chen[1,2], Tatyana M Timiryasova[1], Melba L Andres[3], Eric Kajioka[3], Rhoda D Roy[3], Daila S Gridley[2,3] and Istvan Fodor[1,2]

[1]Center for Molecular Biology and Gene Therapy, [2]Departments of Microbiology & molecular Genetics, and [3]Radiation Medicine, Loma Linda University School of Medicine, Loma Linda, California

running title: combined therapy using p53, IL-2 and IL-12

Address Correspondence and reprint requests: Dr. Istvan Fodor, Center for Molecular Biology and Gene Therapy, Mortensen Hall, Loma Linda University School of Medicine, 11085 Campus Street, Loma Linda, CA 92354, USA. Tel: (909) 824-4300 Ex. 81398; Fax: (909) 478-4177; E-mail: ifodor@som.llu.edu

Key words: vaccinia virus, p53, IL-2, IL-12, glioma, gene therapy

ABSTRACT

Previously, we have shown that vaccinia viruses (VV) expressing p53, IL-2 and IL-12 results in an effective inhibition of subcutaneous glioma growth in mice. We suggest that combination therapy of tumors with virus-mediated p53 and cytokine genes may offer the prospect of synergistic antitumor response. In this work, we evaluate the antitumor efficacy of combined VV-mediated combination of p53, IL-2 and IL-12 genes in nude mice model. To minimize cytokine-associated toxicity as low virus dose as 10 PFU of VV expressing IL2 and IL12 per animal was used. Local treatment of established C6 glioma with recombinant viruses rVV-p53, rVV-mIL2, rVV-mIL12 and rVV-2-12 induced prolonged expression of p53, IL-2, IL-12 and both cytokines, respectively, in tumors. Combination rVV-p53/rVV-mIL12 or rVV-p53/rVV-2-12 treatments resulted in synergistic tumor inhibition compared to the single modality treatment ($P<0.05$). rVV-p53/rVV-2-12 therapy was found to be associated with striking elevation of NK cells in blood and IFN-γ expression in tumors. The difference in the inhibition of tumor growth with rVV-p53/rVVmIL2 combination and rVV-p53 treatments was statistically insignificant. These data demonstrate that gene therapy based on VV-mediated combination of p53, IL-2 and IL-12 treatment may be a promising alternative strategy for glioma treatment.

INTRODUCTION

Glioblastoma is a common tumor derived from glial precursors and the second leading cause of cancer death in children younger than 15 years of age. The median survival from these tumors is less than one year (Dietrich, 1994). p53 mutation was found in 63 to 65% of high grade and 63% of low-grade astrocytomas (Lang, 1994; Newcomb, 1993). The documented p53 functions include cell growth arrest that is partially mediated by p21 and the apoptosis that may involve the apoptosis regulating genes Bcl-2 and Bax (Wang, 1997). Several studies have demonstrated that virus-mediated delivery of wild-type p53 can suppress growth in a number of human cancer cell lines *in vitro* and *in vivo* (Fujiwara, 1996, Qazilbash, 1997, Kim, 1999, Aspinall, 1999). Therefore, therapeutic strategies designed to restore wild-type p53 protein activity in cancer cells are particularly appealing.

Recently, it has been demonstrated that delivery and overexpression of wild-type p53 gene induced apoptosis in rat and human glioma cell lines *in vitro* (Gomez-Manzano, 1997, Shinoura, 1999 Timiryasova, 1999) which was independent of the endogenous p53 status (Li, 1997, Timiryasova, 1999). p53 transduced into established intracranial rat 9L glioma suppressed the tumor growth by 40% (Badie, 1995). In a nude mice model, injection of adenovirus (Li, 1999) or vaccinia virus (Timiryasova, 1999) expressing p53 also resulted in an effective inhibition of glioma growth. Although these studies demonstrated the potential of p53 gene therapy, the efficacy of p53 treatment is

far from ideal, and further improvements of anticancer strategies are needed. For example, strategies of multiple modalities of therapy may provide more effective approach for treatment of cancer. Indeed, it was demonstrated that overexpressed p53 rendered the tumor cells more sensitive to irradiation (Lang, 1998; Gridley, 1998) and cisplatin-induced apoptosis (Dorigo, 1998), while each agent alone failed to achieve a significant antitumor effect. Other therapeutic genes, like cytokine genes, combined with p53 treatment may also augment an antitumor effect. Recently, Putzer et al (Putzer, 1998) have shown that combined delivery of p53 and IL-2 genes into murine breast tumors resulted in significant tumor regressions in 65% of animals. Interleukin-2 (IL-2) and interleukin-12 (IL-12) are two potent agents that have been demonstrated to possess antitumor activity through their ability to stimulate cytotoxic T lymphocyte (CTLs), to enhance natural killer cell (NK) activity and to activate tumor infiltrating lymphocytes (TILs) **(???)**. In addition, IL-12-mediated antitumor effect is also related to its antiangiogenesis activity and increase of IFN-γ secretion (Yao, 1999). Previous studies in both xenogeneic and syngeneic glioma models showed that intratumoral IL-2 production might stimulate an immune antitumor response with predominance of CD_4, CD_8 lymphocytes, NK cells, neutrophils and activated macrophages (Palu, 1999, Okada, 1996). IL-12 has been recently shown to produce antiglioma immune activity in rodent models (Toda et al., 1998; Kikuchi et al., 1999).

To increase the efficacy of antitumor therapy, we are studying vaccinia viruses (VV) as vectors for gene therapy. Recently, we have shown that VV expressing p53 (rVV-p53) was effective in tumor therapy of nude mice in *ex vivo* experiment and in established subcutaneous glioma model (Timiryasova, 1999). We also found that VV

carrying mouse IL-2 (rVV-mIL2) or IL-12 (rVV-mIL12) gene could induce significant tumor inhibition in a pre-established C6 glioma model by the virus dose as low as 100 plaque forming unit (PFU) (Chen et al, manuscript in preparation). However, like most other cytokine therapies, toxicity is a major limitation of the strategy. To achieve better antitumor efficacy and minimize cytokine toxicity, in the present study we investigate the ability of tumor inhibition by combination of low dose rVV-mIL2 or rVV-mIL12 and high dose rVV-p53 in a C6 glioma model. We found that treatment with recombinant viruses combined at ratio 10 to $2x10^7$ PFU effectively expressed their transgenes *in vivo* and synergistically inhibited the tumor growth.

MATERIALS AND METHODS

Vaccinia virus constructions

Construction and characterization of recombinant virus rVV_2, rVV_4, rVV-p53, rVV-mIL2, rVV-mIL12 and VV containing both IL-2 and IL-12 genes (rVV-2-12) were performed as previously described (Timiryasova et al., 1999; Chen *et al.,* manuscript in preparation). rVV_2 was the control virus for rVV-p53, while rVV_4 was the control for recombinant viruses carrying genes encoding cytokines. Instead of therapeutic gene, In rVV_2 and rVV_4, reporter genes *lacZ* of *E.coli* and firefly luciferase (*luc*) were inserted into the same position of the genome that carried therapeutic genes in recombinant viruses.

Cell lines, animals.

CV-1 cells, African green monkey kidney fibroblasts, were obtained from the American type Culture Collection (ATCC, Rockville, MD) and maintained in Dulbecco's modified Eagle's medium containing 5% fetal bovine serum and antibiotic-antimycotic solution (Sigma Chemical Co., St. Louis, MO). The Rat C6 nitrosourea-induced glioma cell line, originally established by Benda *et al* (Benda, 1968) was cultured in RPMI-1640 medium (Cellgro/Mdiatech, Inc.,Herndon, virginia) supplemented with 5% fetal bovine serum and antibiotic-antimycotic solution.

Athymic nude mice (male) were obtained from Charles River Breeding Laboratories, Inc. (Wilmington, MA) at 4-6 weeks of age. All animal studies were conducted in accordance with the animal care policy of the Loma Linda University.

Infection of cells in vitro

To determine whether transgene expression could be mutually interfered after coinfection with two different rVVs, equal amount of rVV-p53 and rVV-mIL2 were used to infect C6 glioma cells *in vitro* at a multiplicity of infection (MOI) 0.2 plaque forming unit (PFU) per cell. The virus was added to the cell monolayer ($1x10^6$ cells/well) and incubated at 37°C for 1 h. Then, a complete RPMI 1640 medium was added, and samples of specific time points were taken and frozen at -80°C. Level of IL-2 secreted into the medium was measured by ELISA using mouse IL-2 Duoset ELISA kit (Genzyme, USA???). p53 expression was detected by western blot as previously described (Timiryasova, 1999).

Since in the combined therapy the ratio of cytokine- and p53-producing viruses was 10 to $2x10^7$ PFU, we did not rule out the possibility that high dose virus could inhibit the infection and replication of the low dose virus. To test it C6 cells were coinfected with rVV_4 expressing *lacZ* gene and wild-type VV (wtVV) at ratio 1 to 100. Cells were then fixed with 2% formaldehyde (v/v) and 0.2% glutaraldehyde (v/v) in PBS for 30 min. Fixed cells were washed 2 times with PBS and stained in X-gal solution for 4 hr at 37°C. X-gal solution contained 5 mM potassium ferricyanide, 5 mM potassium ferrocyanide, 2 mM $MgCl_2$, 1 mg/ml X-gal in PBS.

The level of *lacZ* gene expression was also determined by chemoluminescent assay. C6 cells were coinfected with wtVV and/or rVV_4 as described above. 24 h later, cells were lysed in lysis buffer and assayed using Galacto-light Plus™ kit (Tropix, Bedford, MA). Bioluminescence was measured by ML300 microplate luminomiter (Dynatech Laboratories, Inc., Chantilly, VA).

Functional assay of p53

p53 function was analyzed by DNA fragmentation assay. $9x10^6$ C6 cells were plated in 10 cm^2 dish 24 h before virus infection. Cells were then infected with rVV_2, rVV_4, rVV_2/rVV_4, rVV-mIL2, rVV-p53 and rVV-p53/rVV-mIL2 by 0.2 PFU of each virus. Cells were harvested at 48 h post infection and lysed in 10 mM Tris-HCl pH 7.5, 1 mM EDTA and 0.2% Triton X-100. After incubated on ice for 50 min, debris was centrifuged and supernatant was sequentially digested with 400 μg/ml RN_{ase} and 400 μg/ml Protease K for 30 min at 37°C. Samples were then extracted with phenol/chloroform/isoamyl alcohol three times. DNA was precipitated and dissolved in

30 μl H_2O, and 4 μg of DNA from each sample was analyzed by electrophoresis in 2% agarose gel.

Inhibition of tumor growth in vivo

An aliquot of $5x10^5$ C6 glioma cells were injected subcutaneously (s.c.) in the right hind of athymic nude mice. Animals were then randomly divided into 11 groups: normal control, saline tumor control, rVV_4 control, rVV_2 control, rVV-mIL2, rVV-mIL12, rVV-2-12, rVV-p53, rVV-p53/rVV-mIL2, rVV-p53/rVV-mIL12, rVV-p53/rVV-2-12. Approximately 5 days later, when palpable tumors had developed in all recipients, a single intratumoral injection of Hank's medium, 10 PFU of rVV_4 or recombinant VV was performed in a volume of 50 μl. Twenty four hours later, mice in rVV_2 and p53 treatment groups received rVV_2 or rVV-p53 at the dose of $2x10^7$ PFU. Animal weight was measured twice a week; tumor dimensions were measured with calipers. All animals were euthanized at the same time, when mean tumor volume of control group reached ~2,500 mm^3.

Tumors were removed and one half was fixed in 10% buffered formalin. The other half was snap frozen in liquid nitrogen and stored at -80°C.

Detection of p53 and cytokine expression in tumor

Frozen tumors were thawed and cut into small pieces in PBS with 100 μM phenylmethylsulfomyl fluoride (PMSF). After centrifugation at 2000 rpm, 5 min, supernatant was collected and assayed for IL-2, IL-12 (Duoset kit, Genzyme), IFN-γ and TNF-α (Quantikine, R&D system) expression by ELISA.

P53 expression was detected by immunohistochemistry as previously described (Timiryasova, 1999). Briefly, formalin fixed tumors were embedded in paraffin and sectioned (5 μm). Monoclonal antibody against human p53 (1:100, clone DO-7, Novocastra Lab, Ltd., Newcastle, UK) and Cy 3-conjugated anti-mouse antibody (1:1000, Jackson Immuno-Research Lab., West Grove, PA) were used as primary and secondary antibodies, respectively. After immunohistochemical reactions, sections were counterstained with DAPI for nuclear detection. Expression of p53 was analyzed using fluorescence microscopy.

in situ TUNEL assay

Apoptosis-associated DNA cleavages were detected using terminal deoxynucleotidyl transferase-mediated dUTP nick end-labeling of DNA (TUNEL, *in situ* cell death detection kit, fluorescein, Boehringer Mannheim, IN). Tumor sections on day 9 after virus infection were deparaffinized and permeabilized with 0.1% Triton X-100 in 0.1% sodium citrate for 2 min on ice. After several washes in PBS, the sections were incubated with the TUNEL reaction mixture containing fluorescein-conjugated dUTP for 60 min at 37°C in the dark as specified by the manufacturer (Boehringer Mannheim). Following three washes with PBS, samples were directly analyzed using a fluorescence microscope.

Flow cytometry analysis

Four and nine days after virus infection, whole blood sample from each animal was collected in heparinized tuberculin syringes via cardiac puncture immediately after

euthanasia. Spleens were removed and smashed in RPMI-1640 medium before filtration. The leukocyte counts in blood and spleen samples were performed on HESCA Hematology Analyzer (ABX Hematologie, France). 50 μl of each sample was then stained with appropriate fluorescent-conjugated monoclonal antibodies (CD_{45}, CD_{19}, PAN-NK, NK1.1, TCR-β, MAC-1) (PharMingen, San Diego, CA). Stained cells were washed and analyzed using a FACSCalibur machine with CellQuest software (Becton Dickinson, Manfield, MA).

Data analysis

The data were analyzed using one-way analysis of variance, Tukey's HSD test (SPSS). A P value of <0.05 was considered to indicate significant differences among groups.

RESULTS

The interference of transgene expression by coinfection with two different rVVs

Cells infected with rVV-p53 or rVV-mIL2 overexpressed p53 or IL-2 with the peak of expression around 24-48 h. postinfection. However, the expression of these recombinant proteins was reduced when cells were co-infected with rVV-p53 and rVV-mIL2 at same multiplicity of infection (MOI)(Fig.1, 2) although the p53 function remained to be active. Indeed, DNA fragmentation pattern induced by rVV-p53/rVV-mIL2 infection did not differ from that of rVV-p53 treatment (Fig.3). Cells infected by control virus (rVV_2,

rVV_4) also showed certain level of apoptosis, but it was significantly lower compared with the rVV-p53-treated cells.

To determine the influence of high dose virus on the infection and replication ability of the low dose virus strain, C6 cells were coinfected with the combination rVV_4/wtVV at ratio 1 to 100. After exposing the cell to viruses for 24 h cells were found to express low level of rVV_4-derived lacZ expression (Fig.4), while infection of cells with rVV_4 alone at the same MOI resulted in a significant increase in the reporter expression (111.9±1.31 RLU/10^6 cells). These data indicate that high dose virus can inhibit infection or replicaton of the low dose virus if two viruses are combined.

Effect of p53 and cytokine combined therapy

The experiment was designed to test whether low doses of virus-mediated cytokine treatment can enhance the antitumor effect of p53. Athymic nude mice carrying established C6 tumor xenografts were *i.t.* treated with different p53/cytokine combinations. On day 9 post-injection, animals treated with rVV-p53/rVV-mIL12 and rVVp53/rVV-2-12 showed significant tumor growth inhibition ($P<0.05$) compared with those treated with single construct (Fig.5). Combination therapy rVV-p53/rVV-mIL2, compared with rVV-p53 treatment, had no significant increase in therapeutic effect ($P=0.078$), but compared with rVV-mIL2 group the inhibition of tumor growth was statistically significant ($P<0.05$). No significant differences in mean tumor volume were noted between rVV-p53 and control rVV_2 groups at all time points (1537.3±309.9 mm^3 and 1745.5±355.9 mm^3, respectively, on day 9), although in comparison with the saline control group they showed significantly reduced tumor growth.

Treatment with single injection of 10 PFU of rVV-mIL2, rVV-mIL12 or rVV-2-12 did not result in tumor inhibition. rVV-mIL2 and rVV-mIL12 induced low, if any, cytokine toxicity, but the construct rVV-2-12 expressing both cytokines showed signs of toxicity in nude mice. Twenty five percent of animals injected with rVV-2-12 died by day 5-6 after virus treatment. Interestingly, in rVV-p53/rVV-2-12 combination group, all animals survived the treatment until the end of experiment.

rVV-mediated production of recombinant proteins in tumors

Overexpressed p53 protein could be detected by immunohistochemistry at least 9 days after injection of rVV-p53 or p53/cytokine expressing combination viruses (Fig.6A). Strong signal was mostly found around or in the necrotic area visualized by H&E staining. p53 expression was not found to be impaired in combined p53/cytokine therapy. Tumors treated with the control rVV_2 virus in this experiment showed little antitumor effect.

On day 4 after virus injection, IL-2 expression was detected in tumors of 2 of 4 animals treated with rVV-2-12 (18.3 ng/g, 3.4 ng/g) and in 1 of 4 animals treated with rVV-p53/rVV-2-12 (5.67 ng/g). On day 9, only one animal treated with rVV-p53/rVV-2-12 showed IL-2 expression in tumor (6.6 ng/g).

IL-12 expressed in tumors of almost all animals treated with rVV-mIL12, rVV-2-12, rVV-p53/rVV-mIL12 and rVV-p53/rVV-2-12, reaching the highest level, 57.3 ng/g, on day 4. Only half of the animals expressed the cytokine on day 9, with the highest value 41.6 ng/g.

Apoptosis induced by recombinant VV

On day 9 after virus injection TUNEL-stained cells were detected in rVV_2, rVV-p53, and p53/cytokine-treated groups (Fig.6B). These cells exhibited apoptotic morphology, containing strongly labeled condensed nuclei and micronuclei. TUNEL-positive cells mostly gathered around the tumor necrosis area. Surprisingly, we could not observe any difference in tumor cell apoptosis between control rVV_2 and rVV-p53 groups. Staining of saline-treated tumor cells showed few apoptotic cells.

Characterization of host antitumor immune response

Involvement of macrophages and NK cells in tumor rejection was analyzed by flow cytometry. On day 4 after single i.t. injection of rVV-p53/rVV-2-12, blood samples showed a distinct increase in NK cell population as compared with all other treatment groups ($p<0.05$). No statistically significant difference in NK cells was noted among saline control, rVV_2 control, rVV-mIL2, rVV-mIL12, rVV-2-12, rVV-p53/rVV-mIL2 and rVV-p53/rVV-mIL12 groups. On day 9, no difference was observed among all groups. Compared to saline control, the percentage of macrophage (MAC-1 positive cells) doubled in all high dose ($2x10^7$ PFU) rVV-treated animals on days 4 and 9, indicating that macrophage stimulation was caused by high dose application of VV vector *per se*. Cell suspensions isolated from spleen showed no significant differences in NK cells and macrophages among groups at all observed time points. NKT cell ($NK1.1^+$ TCR-β^+), which was previously reported to contribute to IL-12-induced tumor inhibition (Kitamura, 1999), did not exhibit obvious changes in our tumor model. No proliferation of B cells was observed either in all groups.

Intratumoral induction of IFN-γ and TNF-α

High production of IFN-γ was measured only in some tumors on day 4 after treatments with rVV-mIL12 (891.4 pg/g), rVV-2-12 (5000 pg/g), rVV-p53/rVV-mIL12 (600 pg/g) and rVV-p53/rVV-2-12 (1227.3 pg/g), whereas all tumors treated with saline control rVV_2, rVV-mIL2 and rVV-p53/rVV-mIL-2 showed low level of IFN-γ expression (less than 30 pg/g). The striking difference in IFN-γ expression of IL-12 therapy versus IL-2 therapy supported the fact that induction of IFN-γ is a characteristic feature of IL-12 treatment.

At least 6-fold increase in TNF-α expression was detected in few animals following rVV-2-12 (74.1 pg/g), rVV-p53/rVV-mIL2 (91.2 pg/g), rVV-p53/rVV-mIL12 (70.5 pg/g) and rVV-p53/rVV-2-12 (332.9 pg/g) treatment compared with the control rVV-mIL-2 and rVV-mIL12 groups expressing less than 10 pg/g. Some increase was found in rVV-p53 group (23.1 pg/g) as well.

DISCUSSION

Combination gene therapy offers the therapeutic advances through the additive or synergistic effect induced by two or more therapeutic genes. P53, IL-2 and IL-12 are well-known proteins that have been proved to be the potent antitumor agents in animal studies and clinical trials. Here we suggested that combined vaccinia virus-mediated delivery of these genes into tumors might elicit synergistic antitumor effect by augmenting immune response against cancer cells and tumor cell apoptosis. Expected synergistic effect may be explained by several molecular mechanisms: 1) Antitumor

effect of p53 and IL-12 may occur through inhibition of angiogenesis. p53 was shown to regulates the release of antiangiogenic factors, such as thrombospondin 1 (Dameron, 1994). Overexpression of p53 may also inhibitor the expression of vascular endothelial growth factor (Nishizaki, 1999). IL-12 can inhibit angiogenesis by inducing IFN-γ, chemokine IP-10, and NK-cells of endothelial cells (Yao, 1999). 2) Formation of apoptotic bodies in tumor cells by overexpressed p53 may activate the macrophages and induce local inflammatory response, which can be amplified by VV induced intratumoral IL-2 and/or IL-12 production. 3) TNF-α released from activated macrophages and NK cells can induce hemorrhagic necrosis of tumors *in vivo* through destruction of tumor vasculature (Carswell, 1975) and induce apoptosis in sensitive tumor cells (Rubin, 1988). 4) IL-2 and IL-12 may enhance the immune response to p53 protein overexpressed in rVV-p53-infected tumor cells by activating NK cells, macrophages and B cells (Topalian, 1994).

In this study we demonstrated that rVV-p53/rVV-2-12 combination therapy induced a statistically significant tumor growth arrest ($P<0.01$) as compared with rVV-p53 and rVV-2-12-treated alone. Previously, we showed that glioma therapy with 10 PFU rVV-mIL2 or rVV-mIL12 caused little, if any, cytokine-associated side effects, but had no anti-tumor effect either (Chen et al., manuscript ion preparation). Although treatment with rVV-p53/rVV-mIL12 also produced inhibition of tumor growth (1110.8 ± 543.2 mm^3, day 9) compared to single modality groups ($P<0.05$), rVV-p53/rVV-2-12 showed the greatest antitumor effect (624.2 ± 165.7 mm^3, day 9). rVV-p53/rVV-2-12 therapy induced a substantial increase of NK cell population in blood. In other treatment groups, NK activation in blood was not detected suggesting that early

proliferation of NK cells in blood on day 4 played an important role in antitumor effect. High level of IFN-γ production was also detected in the tumor following rVV-p53/rVV-2-12 treatment that may indicate on the local activation of NK cells. Previously, it was shown that combination of IL-2 and IL-12 induced IFN-γ production by NK cells (Ross and Caligiuri, 1997), and recombinant IL-12 administration induced IFN-γ production and tumor regression (Nastala, 1994; Brunda, 1995). Virus-mediated delivery of IFN-γ had also antiangiogenic effect in murine brain tumor model (J. Immunol. 2000; 164: 217-222). Induction of IFN-γ is an important condition but it may not be sufficient for effective tumor therapy. Indeed, induction of IFN-γ we also observed in tumors of rVV-2-12-treated animals although it failed to result in tumor growth retardation. Other cytokines and chemokines may be also involved in tumor inhibition.

Although we did not observe the expected increase in apoptosis using VV-p53-treated versus control virus, p53-mediated antitumor effect may be explained by different mechanism. High proliferation of NK cells in the blood after the VV-p53/rVV-2-12, but not rVV-p53 or rVV-2-12 treatment, and an increased level of intratumoral TNF-α production in p53/cytokine-treated animals compared with single modality treatment suggests an important role of rVV-p53-mediated p53 synergistically potentiating the immune response of rVV-2-12 therapy. Further study is necessary to shed light on molecular mechanisms of combined p53/cytokine-mediated induction of NK cell proliferation and TNF-α production, and the role of p53 in this process.

In contrast to VV-p53/rVV-2-12 and rVV-p53/rVV-mIL12 treatments, intratumoral injection of rVV-p53/rVV-mIL2 did not induce marked reduction of tumor volume compared with rVV-p53 single modality treatment. Our *in vitro* and *in vivo* data

also demonstrated that rVV-mIL2-mediated expression of IL-2 in terms of synthesized protein was greatly reduced compared with rVV-mIL12-mediated production of IL-12 at equal MOI. The low level of IL-2 production is apparently insufficient to induce efficient antitumor immune response. We also found that rVV-p53/rVV-mIL2-mediated synthesis of intratumoral IFN-γ was considerably lower compared with rVV-p53/rVV-mIL12 treatment, which may partially explain the difference in therapeutic efficiency between two combination therapies. Antiangiogenic effect could also account for antitumor activity of combined p53/IL-12 therapy.

Tumor growth was also inhibited after injection of control virus (rVV_2) ($2x10^7$ PFU) although the antitumor efficiency was lower than that with p53/cytokine combination. This is apparently associated with the oncolytic effect of VV as it was discussed in previously (Timiryasova et al., 1999). Noteworthy, an increase in number of blood macrophages was found in rVV_2 and other high rVV dose treated groups. It suggests that high dose of VV vector *per se* is a strong inducer of macrophages, which might proliferate in response to cell infection and/or lysed tumor cells. C6 glioma cells infected with the rVV_2 *in vitro* showed little signs of apoptosis while rVV-p53 and combined p53/cytokine constructs induced effective apoptosis. However, therapy of tumors with rVV_2, rVV-p53 and p53/cytokine *in vivo* induced similar level of apoptosis of tumor cells suggesting that activation of immune system by high dose of viruses may be an important factor of apoptosis.

In combination therapy, especially when the dose of one virus construct is several orders of magnitude greater, the efficacy of therapy depends on the ability of the administered viruses to replicate after coinfection. Our *in vitro* data showed reduction in

the gene expression of one virus even when the ratio of MOI of two co-infecting recombinant viruses was equal to 1. At the ratio of co-infection 1:100, the gene expression of low-dose virus was greatly reduced. In animal study, to minimize the cytokine toxicity we used extremely low dose of VV expressing cytokines (10 PFU). Previously we found that 10 PFU rVV-mIL2 or rVV-mIL12 caused little, if any, cytokine toxicity in vivo, but the treatments did not induce reduction of tumor size either (Chen et al, manuscript in preparation). To avoid suppression of replication of low dose (10 PFU) rVV carrying IL-2 or IL-12 by rVV-p53 *in vivo*, the cytokine-expressing virus was injected into tumor 24 h prior the rVV-p53 treatment. Unlike *in vitro* results, expression of IL-2 and IL-12 in tumors was not inhibited by high-dose of rVV-p53. As expected, rVV-p53-mediated expression of p53 was not suppressed by low-dose virus either. Thus, our data revealed that for tumor therapy 10 infectious viral particles of recombinant cytokine-producing VV can be combined with $2x10^7$ viral particles of rVV-p53, and the replication of these viruses and transgene expression was not interfered.

We also found that rVV-p53/rVV-2-12 combination decreased the cytokine-associated side effects caused by rVV-2-12. Interestingly, 100% animals survived the combination treatment and minimal, if any, cytokine toxicity was observed in treated animals, while rVV-2-12-treatment alone resulted in 25% mortality during the experimental period. Thus, it suggests that combination gene therapy may be safer strategy than cytokine therapy alone. It is not excluded that some increase of the ratio of rVV-2-12 in combination therapy could result in greater therapeutic effect.

In summary, using nude mice subcutaneous C6 glioma model combined rVV-p53/rVV-2-12 and rVV-p53/rVV-mIL12 treatments elicited significant antitumor effect.

In our future study, the strategy will be tested in orthotopic, syngeneic brain tumor model induced in specific central nervous system environment.

ACKNOWLEDGEMENT

We thank Glen M. Miller, Dong-won Kim, Jun Li, Xiao W Mao for help in animal study. We are grateful to Drs Susan Parker and Richard C Mulligan for providing plasmids encoding IL-2 and IL-12.

This work was sponsored by the US department of the Army and NMTB. The view, opinions and/or finding contained in this report are those of the authors and should not be construed as a position, policy, decision or endorsement of the federal Government or the National Medical Technology Testbed, Inc.

Legends

Fig.1 Reduction of IL-2 expression in cells coinfected by rVV-p53/rVV-mIL2 *in vitro*. C6 glioma cells ($1x10^6$/well) were plated in 6-well plate and infected with rVV-mIL2 or rVV-p53/rVV-mIL2 at 0.2 PFU of each virus. Supernatants were collected at 6, 24, 48, 72 and 96 h and measured for IL-2 by ELISA.

Fig. 2. Reduction of p53 expression in cells coinfected by rVV-p53/rVV-mIL2 *in vitro*. C6 glioma cells ($1x10^6$/well) were plated in 6-well plate and infected with rVV-mIL2 or rVV-p53/rVV-mIL2 at 0.2 PFU of each virus. Cells were harvested and homogenized in lysis buffer at 6, 24, 48, 72 and 96 h. Proteins (80 μg) were separated by 12% SDS-polyacrylamide gel electrophoresis and probed with primary antibody (DO-7, vector laboratories, Inc.). The blot was then incubated with horseradish peroxidase-conjugated secondary antibody and developed in color regent. P53 expression by SW480 cell line served as positive control and wild type VV served as negative control.

Fig. 3. DNA fragmentation analysis. C6 glioma cells were infected with different recombinant viruses at 0.2 PFU of each virus. After 48 h, DNA was extracted and subjected to 2% agarose gel. Lane 1: C6 cell mock-infected; Lane 2: rVV_2 ; Lane 3: rVV_4; Lane 4: rVV_2/rVV_4; Lane 5: rVV-mIL2; Lane 6: rVV-p53; Lane 7: rVV-p53/rVV-mIL2.

Fig. 4 Reduction of *lac Z* expression in C6 cells co-infected with wtVV/rVV_4. C6 glioma cells were infected with wtVV, rVV_4, or wtVV/rVV_4 at indicated MOI. 24 h later, *lac Z* production was visualized by X-gal staining (A) and the level of expression was measured by chemoluminescent method (B).

Fig. 5 Tumor growth inhibition mediated by p53/cytokine combination therapy. Mice bearing s.c. C6 tumors of similar sizes were treated with recombinant VVs alone and in combination. Tumor growth in combination groups was compared with saline, virus control and single agent treated groups. rVV-p53/rVV-2-12 and rVV-p53/rVV-mIL12 combination therapy showed statistically significant antitumor effect ($P<0.01$ and $P<0.05$, respectively).

Fig. 6 In situ detection of p53 expression and apoptosis. (A) Paraffin-embedded tumor sections obtained from saline, rVV_2 control and rVV-p53 treated animals 9 days after virus injection, were stained for p53 expression by immunohistochemistry. (B) Tumor sections from these groups were also stained for apoptosis by TUNEL assay as described in Material and Methods. Original magnification x100

References

1. Webb HE, Smith CE. Viruses in the treatment of cancer. *Lancet* 1970; **1**: 1206-8.

2. Wang XW, Harris CC. p53 tumor-suppressor gene: clues to molecular carcinogenesis. *J.Cell Physiol.* 1997; **173**: 247-55.

3. Fujiwara T, Kagawa S, Ogawa N *et al.* [Recombinant virus-mediated transfer of the wild-type p53 gene is a potent therapeutic strategy for human cancer]. *Hum Cell* 1996; **9**: 25-30.

4. Qazilbash MH, Xiao X, Seth P *et al.* Cancer gene therapy using a novel adeno-associated virus vector expressing human wild-type p53. *Gene Ther.* 1997; **4**: 675-82.

5. Kim J, Hwang ES, Kim JS *et al.* Intraperitoneal gene therapy with adenoviral-mediated p53 tumor suppressor gene for ovarian cancer model in nude mouse. *Cancer Gene Ther.* 1999; **6**: 172-8.

6. Aspinall RJ, Lemoine NR. Gene therapy for pancreatic and biliary malignancies. *Ann.Oncol.* 1999; **10 Suppl 4**: 188-92.

7. Lang FF, Miller DC, Pisharody S *et al.* High frequency of p53 protein accumulation without p53 gene mutation in human juvenile pilocytic, low grade and anaplastic astrocytomas. *Oncogene* 1994; **9**: 949-54.

8. Newcomb EW, Madonia WJ, Pisharody S *et al.* A correlative study of p53 protein alteration and p53 gene mutation in glioblastoma multiforme. *Brain Pathol.* 1993; **3**: 229-35.

9. Dietrich PY, Walker PR, Saas P *et al.* Immunobiology of gliomas: new perspectives for therapy. *Ann.N.Y.Acad.Sci.* 1997; **824:124-40**: 124-40.

10. Timiryasova TM, Chen B, Haghighat P *et al.* Vaccinia virus-mediated expression of wild-type p53 suporesses glioma cell growth and induces apoptosis. *Int J Oncol* 1999; **14**: 845-54.

11. Gomez-Manzano C, Fueyo J, Kyritsis AP *et al.* Characterization of p53 and p21 functional interactions in glioma cells en route to apoptosis. *J.Natl.Cancer Inst.* 1997; **89**: 1036-44.

12. Shinoura N, Muramatsu Y, Nishimura M *et al.* Adenovirus-mediated transfer of p33ING1 with p53 drastically augments apoptosis in gliomas. *Cancer Res.* 1999; **59**: 5521-8.

13. Li H, Lochmuller H, Yong VW *et al.* Adenovirus-mediated wild-type p53 gene transfer and overexpression induces apoptosis of human glioma cells

independent of endogenous p53 status. *J.Neuropathol.Exp.Neurol.* 1997; **56**: 872-8.

14. Badie B, Drazan KE, Kramar MH *et al.* Adenovirus-mediated p53 gene delivery inhibits 9L glioma growth in rats. *Neurol.Res.* 1995; **17**: 209-16.

15. Li H, Alonso-Vanegas M, Colicos MA *et al.* Intracerebral adenovirus-mediated p53 tumor suppressor gene therapy for experimental human glioma. *Clin.Cancer Res.* 1999; **5**: 637-42.

16. Lang FF, Yung WK, Raju U *et al* . Enhancement of radiosensitivity of wild-type p53 human glioma cells by adenovirus-mediated delivery of the p53 gene. *J Neurosurg* 1998; **89**: 125-32.

17. Dorigo O, Turla ST, Lebedeva S *et al.* Sensitization of rat glioblastoma multiforme to cisplatin in vivo following restoration of wild-type p53 function. *J.Neurosurg.* 1998; **88**: 535-40.

18. Putzer BM, Bramson JL, Addison CL *et al.* Combination therapy with interleukin-2 and wild-type p53 expressed by adenoviral vectors potentiates tumor regression in a murine model of breast cancer. *Hum.Gene Ther.* 1998; **9**: 707-18.

19. Addison CL, Bramson JL, Hitt MM *et al.* Intratumoral coinjection of adenoviral vectors expressing IL-2 and IL-12 results in enhanced frequency of regression of injected and untreated distal tumors. *Gene Therapy* 1998; **5**: 1400-9.

20. Fernandez N, Levraud JP, Haddada H *et al.* High frequency of specific $CD8^+$ T cells in the tumor and blood is associated with efficient local IL-12 gene therapy of cancer. *J Immunol* 1999; **162**: 609-17.

21. Gollob JA, Schnipper CP, Murphy EA *et al.* The functional synergy between IL-12 and IL-2 involves p38 mitogen-activated protein kinase and is associated with the augmentation of STAT serine phosphorylation. *J Immunol* 1999; **162**: 4472-81.

22. Yao L, Sgadari C, Furuke K *et al.* Contribution of natural killer cells to inhibition of angiogenesis by interleukin-12. *Blood* 1999; **93**: 1612-21.

23. Palu G, Cavaggioni A, Calvi P *et al.* Gene therapy of glioblastoma multiforme via combined expression of suicide and cytokine genes: a pilot study in humans. *Gene Ther.* 1999; **6**: 330-7.

24. Okada H, Miyamura K, Itoh T *et al.* Gene therapy against an experimental glioma using adeno-associated virus vectors. *Gene Ther* 1996; **3**: 957-64.

25. Toda M, Martuza RL, Kojima H *et al.* In situ cancer vaccination: an IL-12 defective vector/replication- competent herpes simplex virus combination induces local and systemic antitumor activity. *J Immunol* 1998; **160**: 4457-64.

26. Kikuchi T, Joki T, Akasaki Y *et al.* Antitumor activity of interleukin 12 against interleukin 2-transduced mouse glioma cells. *Cancer Lett.* 1999; **135**: 47-51.

27. Parker JN, Gillespie GY, Love CE *et al.* Engineered herpes simplex virus expressing IL-12 in the treatment of experimental murine brain tumors. *Proc.Natl.Acad.Sci.U.S.A* 2000; **97**: 2208-13.

28. Andl T, Kahn T, Pfuhl A *et al.* Etiological involvement of oncogenic human papillomavirus in tonsillar squamous cell carcinomas lacking retinoblastoma cell cycle control. *Cancer Res.* 1998; **58**: 5-13.

29. Timiryasova TM, Li J, Chen B *et al.* Antitumor effect of vaccinia virus in glioma model. *Oncology Research* 1999; **11**: 133-44.

30. Benda P, Lightbody J, Sato G *et al.* Differentiated rat glial cell strain in tussue culture. *Science* 1968; **161**: 370-1.

31. Kitamura H, Iwakabe K, Yahata T *et al.* The natural killer T (NKT) cell ligand alpha-galactosylceramide demonstrates its immunopotentiating effect by inducing interleukin (IL)- 12 production by dendritic cells and IL-12 receptor expression on NKT cells. *J Exp.Med.* 1999; **189**: 1121-8.

32. Dameron KM, Volpert OV, Tainsky MA *et al.* Control of angiogenesis in fibroblasts by p53 regulation of thrombospondin-1. *Science* 1994; **265**: 1582-4.

33. Nishizaki M, Fujiwara T, Tanida T *et al.* Recombinant adenovirus expressing wild-type p53 is antiangiogenic: a proposed mechanism for bystander effect. *Clin.Cancer Res.* 1999; **5**: 1015-23.

34. Carswell EA, Old LJ, Russel RL *et al.* An endotoxin induced serum factor that causes necrosis of tumors. *Proc.Natl.Acad.Sci.USA* 1975; **72** : 3600-70.

35. Rubin BY, Smith LJ, Hellerman GR *et al.* Correlation between anticellular and DNA-fragmentation activities of TNF. *Cancer Res* 1988; **48**: 6006-10.

36. Topalian SL. MHC class II restricted tumor antigens and the role of CD4+ T cells in cancer immunotherapy. *Curr.Opin.Immunol* 1994; **6**: 741-5.

37. Ross HJ, Canada AL, Antoniono RJ *et al.* High and low dose rate irradiation have opposing effects on cytokine gene expression in human glioblastoma cell lines. *Eur.J.Cancer* 1997; **33**: 144-52.

38. Nastala CL, Edington HD, McKinney TG *et al.* Recombinant IL-12 administration induces tumor regression in association with IFN-gamma production. *J Immunol* 1994; **153**: 1697-706.

39. Brunda M, Luistro L, Hendrzak J *et al.* Role of interferon-gamma in mediating the antitumor efficacy of interleukin-12. *J Immunotherapy* 1995; **17**: 71-7.

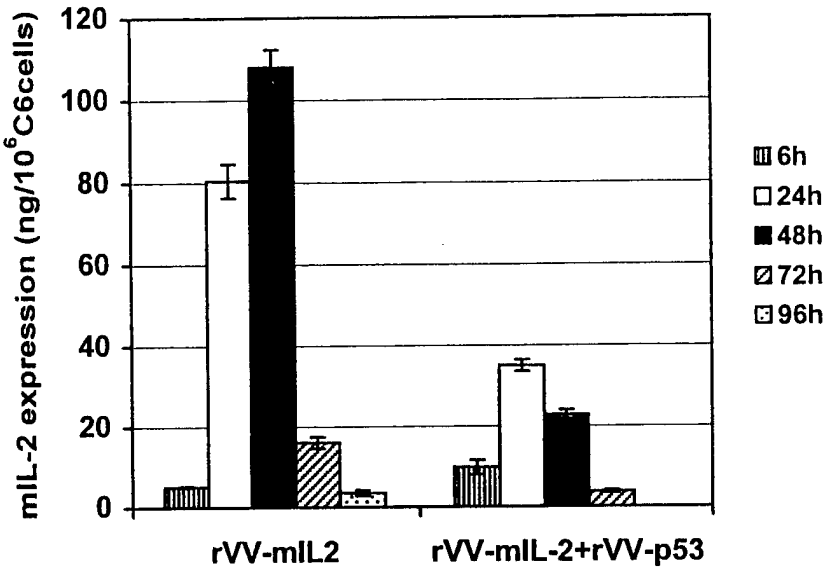
mIL-2 expression (ng/10^6C6cells)
120
100
80
60
40
20
0
rVV-mIL2
rVV-mIL-2+rVV-p53
6h
24h
48h
72h
96h

FIGURE 8

FIGURE 9

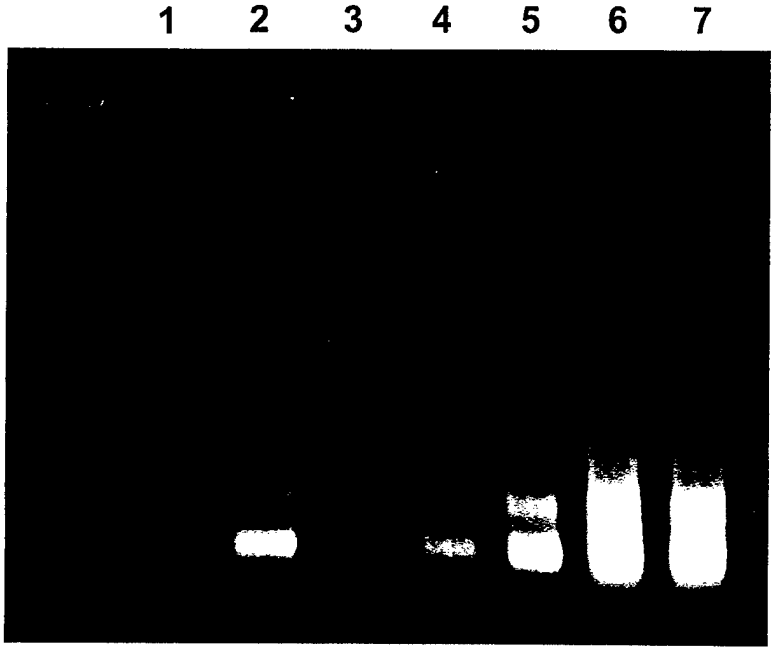

FIGURE 10

A

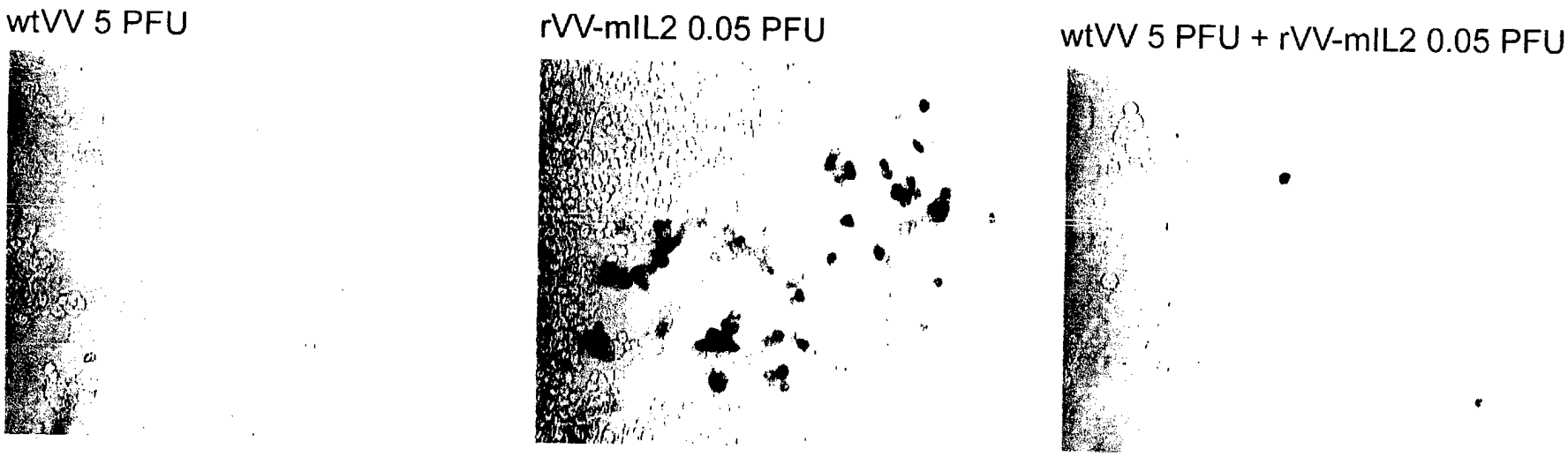
wtVV 5 PFU
rVV-mIL2 0.05 PFU
wtVV 5 PFU + rVV-mIL2 0.05 PFU

B

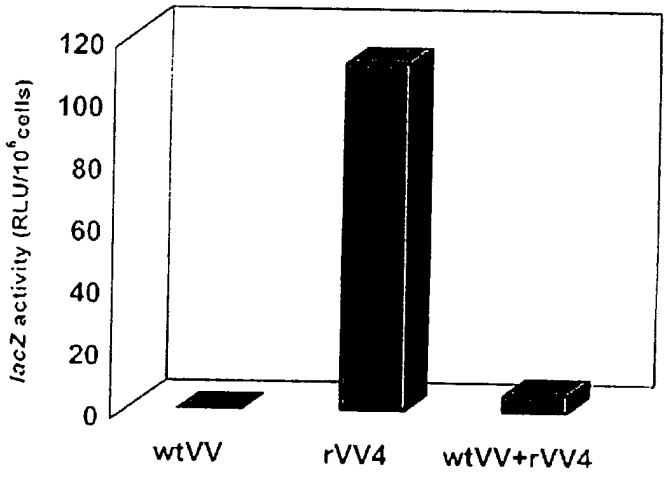
120
100
80
60
40
20
0
lacZ activity (RLU/10^6 cells)
wtVV
rVV4
wtVV+rVV4

FIGURE 11

Inactivated vaccinia virus mediated gene delivery into cancer cells

Tatyana M. Timiryasova[1], Bing Chen[1], and Istvan Fodor[1, 2]

[1]Center for Molecular Biology and Gene Therapy, [2]Departments of Microbiology & Molecular Genetics, Loma Linda University School of Medicine, Loma Linda, CA , USA

Running title: Nonreplicating Vaccinia Virus

Correspondence: Istvan Fodor, Ph.D.,
Center for Molecular Biology & Gene Therapy
Loma Linda University School of Medicine
11085 Campus Street,
Mortensen Hall
Loma Linda, CA 92350
Tel: (909) 824-4300, ext. 81398
Fax: (909) 478-4177
E-mail: ifodor@som.llu.edu

ABSTRACT

The generation of non-replicating recombinant vaccinia viruses (VV) may facilitate the use of poxviral vectors in research and clinical use as a safe vector of recombinant vaccines and gene therapy. In this study, we analyze the gene expression by VV after mild treatment with psoralen and UV-irradiation (PUV) that introduces cross-linking of double-stranded DNA. The treatment inactivates the viral replication and the cell lysis without abolishing the ability of the virus to infect cells. Recombinants VVs expressing either reporter genes ß-galactosidase (*lacZ*) and firefly luciferase (*luc*), or tumor suppressor p53 under the control of early (P13) and synthetic early/late (PE/L) vaccinia promoters have been constructed and investigated. CV-1 cells infected with PUV-inactivated virus iL-15 effectively expressed reporter under the control of the PE/L viral promoter. Overproduction of p53 protein in C6 glioma cells was demonstrated by ELISA assay in the cells infected with non-replicating iVV-TK-53 virus. Approximately 40% and 88% of C6 glioma cells infected with iVV-TK-53 virus underwent apoptosis on day 2 and 7, respectively, while 80% of cells infected with control virus iL-15 or mock-infected cells remained viable on day 7. In *ex vivo* experiment, infection of C6 cells with non-replicating iVV-TK-53 inhibited the tumor growth in nude mice. This method of generation of non-replicating vaccinia virus vectors may be applied to any attenuated or virulent vaccinia virus strain for infection of wide host range.

Key Words: vaccinia virus; gene therapy; p53

INTRODUCTION

Most of currently used gene delivery vectors based on viruses, such as adenoviruses, retroviruses, herpesviruses, or adeno-associated viruses, have been manipulated to provide safe, replication-deficient versions of the virus for gene therapy (see review by Boulikas, 1998). Vaccinia virus (VV) has been successfully used in gene therapy in several studies (Meko *et al.*, 1995; Qin and Chatterjee, 1996; Uzendoski *et al.*, 1997) its potential remains to be investigated in various therapy models. Previously, we have demonstrated that live VV can be used for cancer gene therapy purposes (Gridley *et al.*, 1998; Timiryasova *et al.*, 1999b). VV has certain advantages over other viral vectors, like large cloning capacity, efficient gene expression, cytoplasmic site of replication. In addition, VV infects a broad spectrum of human and animal tumor cells. A specific feature of VV development is that all enzymes necessary for early gene transcription are packaged in the infecting virus particle (Moss, 1996) and therefore, early genes expression is independent of viral replication. Apparently, it depends only on previous assembly of a competent viral particle and a subsequent partial uncoating of the infecting virus after entry into infected cell.

The lytic activity of vaccinia virus may contribute to enhanced anti-tumor immunity by providing a source of tumor antigens that can lead to anti-tumor effect against both localized and metastasized tumors. However, the infectious and cytopathic nature of VV limits its further use in individuals suffering from immune dysfunction or in infants with eczema (Fenner *et al.*, 1988; Graham *et* al., 1993; McElrath *et al.*, 1994; Johnson *et al.*, 1994). It is obvious that safer, non-replicating and non-cytopathic forms of VV are required for these potential users. Several

approaches have recently been reported to enhance the safety of VV as vectors of immunizations (Taylor *et al.*, 1991; Belyakov *et al.*, 1998; Blanchard *et al.*, 1998). Safety concerns of VV vectors have been addressed by the engineering of host range-restricted poxviruses, like MVA strain of VV (Carrol and Moss, 1997). Recombinant avipox viruses, such as canarypox virus, could be also useful vector system that, while restricted for productive replication to avian species, yet significant gene expression occurs (Taylor and Paoletti, 1988; Wang *et al.*, 1995; Paoletti, 1996; Fischer *et al.*, 1997; Kawakita *et al.*, 1997; Roth *et al.*, 1996). Varies degrees of attenuation can be achieved by deletion of one or more genes not required for replication in tissue culture (Kotwal *et al.,* 1989). However, genetically constructed non-replicating poxviral vectors require special host cells for manipulation, and little is known about their efficacy in inoculated mammals.

Recently, it has been shown that the mild treatment of VV with psoralen and long-wave UV light (PUV) may inactivate viral replication but the virus is able to infect cells and express viral early genes (Tsung *et al.*, 1996; Meko *et al.*, 1996; Puhlmann *et al.*, 1999). In this report, we optimized the PUV-treatment of recombinant VV strains expressing a tumor suppressor gene *p53 and* reporter genes, and investigated the effectiveness of non-replicating virus-mediated *p53* gene therapy of cancer cells.

RESULTS AND DISCUSSION

Replication-deficient VV

Theoretically, a few cross-links in the large genome of VV should be sufficient to inhibit replication without impairing the locally confined viral early transcription. To make VV

replicative deficient, the recombinant viruses were treated with psoralen and irradiated with long-wave UV-light as described under Materials and Methods. Inactivation of VV replication and abolishing of cytopathic effect were achieved by incubating of virus ($3x10^8$ pfu/ml) with 1 μg/ml of psoralen and UV irradiation for 5 min, resulting in almost 100% inhibition of replication. Lytic effects of replicating rL-15 and inactivated iL-15 viruses were analyzed by plaque assay on CV-1 cells (Fig. 1). No virus plaques were observed in the cells infected with iL-15 virus even at m.o.i. 30 pfu/cell as well as in mock-infected cells. Non-replicating viruses did not cause cytopathic effects either. Numerous viral plaques were visualized in the cells infected with live rL-15 virus after 10^{-5} dilution (m.o.i. = 0.0003 pfu/cell). These data are in agreement with known effect of psoralen on viral genome (Hanson *et al.*, 1978) and with recent studies on PUV-inactivated VV (Tsung *et al.*, 1996; Puhlmann *et al.*, 1999).

Replication-deficiency of UVP-inactivated viruses was confirmed by experiment with incorporation of [^{3}H]-thymidine. As shown in Fig. 5, no significant difference in mean dpm of incorporated [^{3}H]-thymidine was observed in mock-infected cells (10942.51) and cells infected with iVV-TK-53 (11247.45). However, statistically significant difference ($p=0.003$) was found in the cells infected with replicating control virus as compared to mock-infected and iVV-TK-53-infected cells.

The ability of PUV-inactivated VV to replicate was also investigated plaque assay in C6 cells infected at a m.o.i. 5. On day 6 after infection, the C6 cells were harvested and samples were titered in duplicate on monolayers of CV-1 cells. No virus plaques were observed on CV-1 cells at 72 h after infection.

Expression of luciferase by inactivated vaccinia virus

To compare the promoter strength and duration of luciferase expression by replicating versus inactivated virus we constructed VV recombinants expressing reporter genes under the control of either early (P13) or early/late (PE/L) promoters (Fig. 2). CV-1 cells were infected either with replicating or inactivated viruses at an m.o.i. 5, and at indicated time post-infection the luciferase activity was measured (Fig. 3). In cells infected with non-replicating iL-5 virus the expression of P13-driven luciferase was obviously higher during 8-72 h post-infection as compared with the replicating rL-5 virus, reaching the highest value at 18 h ($2.8x10^3$ versus $1.3x10^2$ RLU).

There were no significant differences in PE/L-driven *luc* gene expression during 72 h post-infection in cells infected with either replicating or non-replicating forms of L-15 virus except at 2 h post-infection when the luciferase activity of rL-15 was significantly higher ($p=0.008$; $2.3x10^3$ versus $3.6x10^2$). Comparing two constructs, PE/L-driven expression of the *luc* gene mediated by iL-15 at all time points was found to be significantly higher. These results confirmed the effective functioning of the early promoter of the PUV-inactivated VV which is in accordance with previously reported data (Tsung *et al.*, 1996; Pulman *et al.,* (1999). Enzymes and protein factors required for early transcription are presented within the virus particles that are activated after the penetration of the cell. Therefore, early VV genes are express immediately upon entry of the virus into the host cell. Early transcription, among other factors, requires the viral RNA polymerase and the transcription factor VETF. VETF exhibits early promoter-specific DNA-binding activity and it is responsible for the recruiting of the RNA polymerase (Broyles *et al.*, 1991; Li and Broyles, 1993).

Expression of p53 protein *in vitro* and its effects on the cells

The strong PE/L vaccinia promoter was chosen to construct the VV expressing wild-type human *p53* gene (Fig. 2). The DNA sequence of the vaccinia PE/L promoter contains tandem early and late promoters allowing a continuous moderate level of gene expression (Mackett *et al*, 1984). Kinetics of virus-mediated p53 expression in C6 glioma cells was analyzed using ELISA. Maximum expression of the p53 protein by replicative rVV-TK-53 virus was observed on day 1 with the mean yield 6650 ng/ml (Fig. 4). The decline in p53 protein synthesis correlated with the decrease in number of living cells on the plate due to cytopathic effect induced by the rVV-TK-53. Kinetics of p53 synthesis mediated by replication-deficient iVV-YK-53 showed striking differences. During first 3 days after infection the yield of the p53 was very low, around 50 ng/ml. However, during 5-7 days post-infection rapid increase of p53 protein expression was measured with the mean maximal production of 9042 ng/ml (Fig. 4). These results suggest that in iVV-TK-53-infected cells a highly stable p53 protein with a long half life are synthesized and accumulated, especially on days 5-7 post-infection. This is in an agreement with previously reported data on high stability of recombinant p53 overexpressed by VV (Ronen *et al.,* 1992). Although PUV-inactivated virus-mediated expression is limited to early genes, surprisingly, Th extended synthesis of p53 driven by early promoter is surprising because expression kinetics of early genes of replicating vaccinia virus usually ceases at the onset of DNA replication, at 3-4 h postinfection. Thus, our data suggest that PUV-inactivated VV effectively penetrate the cells and induce early gene expression. After that the infection process must terminate due to lack DNA replication that plays a key role in the regulatory process and is required for expression of the intermediate and late stage genes (Moss, 1996). After entry of the virus into the cytoplasm, virus-associated enzymes transcribe the early virus genes. The membrane-bound viral core remains

intact and the encapsidated transcriptional machinery directs the synthesis of early mRNAs. These genes encode factors that uncoat the virus core, transcription factors, enzymes of nucleotide biosynthesis and DNA replication. A few hours after the initiation of infection, the viral core undergoes a secondary uncoating process, which releases the genome into the cytoplasm and DNA replication occurs. During the late phase of infection most early genes are repressed most probably mediated by some late gene product(s). Lack of these late functions may maintain early genes active. The half life of RNA polymerase and VETF transcription factor delivered by the virion may determine the kinetics of early gene expression. Long-lasting early transcriptions may indicate on long life time of the virus transcripts and transcription machinery delivered by the virion. Prevention of virus DNA replication by cross-linking may support extended expression of early gene, and overexpression of certain viral early protein(s) may mediate this process. Alternatively, in spite of lack of DNA replication, the mechanism of late transcription factors are synthetized activating the late function of the PE/L promoter. Future studies are needed to elucidate the molecular mechanisms of early gene expression of inactivated VV.

To test the inhibition of C6 glioma cell growth in vitro by inactivated recombinant vaccinia virus carrying the human *p53* gene the trypan blue exclusion assay was used. Normally, VV virus infection is lethal and is followed by extensive cytopathic effects. However, despite the fact that UVP-inactivated virus infection is accompanied by early gene expression, the infected cells failed to exhibit any cytopathic effects, suggesting that infected cells survived the infection. To asses the effects of iVV-TK-53 on cell viability, C6 cells were incubated with iVV-TK-53 or iL-15 control viruses (m.o.i. =5) and the number of live C6 cells was determined. Cells infected with iVV-TK-53 by day 2 showed reduced survival (Fig. 6), and by day 7 less than 20% of all

plated cells remained live. In contrast, C6 cells infected with iL-15 control virus or mock-infected cells continued to divide. iVV-TK-53-mediated growth inhibition correlated with the pattern and kinetics of p53 expression.

Since *p53* gene-mediated cell growth inhibition is realized mainly through induction of apoptosis (Li *et al.*, 1997; Timiryasova *et* al., 1999a), C6 cells following infection with iVV-TK-53 were examined by *in situ* labeling of fragmented DNA (TUNEL). Cells infected with iVV-TK-53 virus showed numerous apoptotic bodies (Fig. 7), while mock-infected cells failed to show morphological changes at all; some apoptosis was observed in the cells infected with control iL-15 virus. These data are in agreement with our previous observations on apoptosis induced by live VV expressing p53 protein: apoptosis induction correlated with the level of p53 protein production (Timiryasova et al., 1999a). Data rule out necrosis as a possible reason of observed morphological changes of cells, and strongly argue for apoptosis as a predominant underlying mechanism.

Tumor growth inhibition

To determine the antitumor effect of iVV-TK-53 in animals, C6 cells were infected *ex vivo* with different m.o.i. of PUV-inactivated viruses, and injected subcutaneously into nude mice. The control mice were inoculated with mock-infected cells or infected with control iL-15 virus. On day 12, the mean tumor volume in iVV-TK-53 (m.o.i.=10) group was 331.13 mm^3, while in mock-infected group the tumor volume reached 1345 mm^3 (Fig. 8). Thus, iVV-TK-53-infected cells showed significant tumor growth inhibition compared with mock ($p=0.0001$) or iL-15 (m.o.i.=1, $p=0.0001$; m.o.i.=10, $p=0.002$). No significant difference was found between two iL-

15-infected groups with different m.o.i., and between iVV-TK-53 (m.o.i.=1) and iVV-TK-53 (m.o.i.=10) groups.

Thus, infection the C6 glioma tumor cells with non-replicating VV expressing tumor suppressor p53 caused an effective tumor growth inhibition in athymic mice. We have previously demonstrated that injection of C6 glioma cells infected *ex vivo* with live VV into athymic mice at an m.o.i. of 1 delayed tumor growth due to effective oncolytic effect of live VV by itself (Timiryasova et al., 1999, in vivo). The results of this experiment indicate on effective p53-mediated inhibition of tumor growth although none of the animals were eventually cured from the tumor. Apparently, further improvements of non-replicating VV vectors are needed to ensure stable and high level of expression of therapeutic genes in cell culture and *in vivo*. The strategy of combined, e.g. p53 and radiation, or p53 and cytokine, treatments based on PUV-inactivated VV seems to be an attractive, especially for cancer gene therapy.

In summary, we developed a non-replicating recombinant VV vector encoding and overproducing wild type human p53 in infected cells. *The recombinant virus* inhibits glioma cell growth, induces cell apoptosis and significantly delayed the tumor growth. Unique properties of VV can be exploited for construction of improved safe vectors for gene therapy.

MATERIALS AND METHODS

Cell culture

Cell lines were obtained from the American Type Culture Collection (Rockville, MD). The rat C6 nitrosourea-induced glioma cell line, originally established by (Benda *et al.,* 1968) was cultured in RPMI - 1640 medium (Cellgro/Mediatech, Inc., Herndon, Virginia) supplemented

with 10% fetal bovine serum and antibiotic-antimycotic solution (Sigma Chemical Co., St. Louis, MO). CV-1 African green monkey kidney fibroblasts were maintained in Dulbecco's modified Eagle's medium containing 5% fetal bovine serum and antibiotic-antimycotic solution (Sigma).

Constructions of plasmids

p*VNP13-luc.* The cDNA encoding luciferase gene (*luc*) of firefly *Photinus pyralis* was isolated by digestion with restriction enzymes *Bam*HI and *Hind*III from plasmid p19pL27 (Krausova *et al.,* 1991) and cloned into the *Sma*I-*Sal*I sites of pWS4 kindly provided by Dr. R. Dornburg (Sheay *et al.,* 1993), resulting in pWL7. The DNA sequence of early vaccinia virus promoter P13, containing in 5'-end site of *Sac*I and in 3'-end site of *Bam*HI (43bp) for easy cloning (GATCCAATAAAAATAAATTTTTTTCATTTATCTATATGAGGT) was synthesized and inserted into pUC28 (Benes *et al.,* 1993) digested with *Sac*I and *Bam*HI, resulting in pUCP13. *Sac*I-*Bam*HI fragment from pUCP13 was cloned into pWL7 digested with *Sac*I and *Bam*HI, resulting in pWLP13. The *luc* gene was isolated from pWLP13 by digestion with *Sac*I and *Bgl*II and cloned into the *Sma*I site of pVN1, a transfer vector for homologous recombination with the *Hind*III-N locus of the vaccinia (Timiryasova *et al.,* 1999 in vivo), resulting in pVNP13-luc, which was used for construction of recombinant vaccinia virus L-5.

pSC15. Transfer vector pSC65 for insertion of foreign genes into TK-region of vaccinia was kindly provided by Dr. B.Moss (Chakrabarti *et al.*, 1997). cDNA of luciferase was isolated from p1914 (Krausova *et al.,* 1986) by *Hind*III and *Sma*I and inserted into *Sal*I site of pSC65. New plasmid pSC15 was used for construction of recombinant virus L-15.

*pSCp53. Bam*HI-*Bgl*II fragment from pWS-53 (Timiryasova *et al.,* 1999 in vitro) encoding the human wild-type *p53* gene was cloned into the *Sal*I site of pSC65, resulting in pSCp53. New plasmid pSCp53 was used for construction of recombinant virus VV-TK-53.

Viruses

Lister (LIVP) strain of vaccinia virus (Timiryasova *et al.,* 1993) was used in these experiments as a parental virus. The recombinant vaccinia viruses (VV) (Fig. 2) were constructed by homologous recombination. L-5 virus encodes the luciferase and β-galactosidase genes at the *HindIII*-N-locus of the genome. L-15 contains two reporter genes (*luc* and *lac Z*) inserted into thymidine kinase region of VV. Recombinant virus VV-TK-53 is similar to L-15 differing only in the expression of foreign gene. VV-TK-53 encodes the human wild-type *p53* gene instead of *luc* gene in the L-15 construct. Infection of the cells was carried out at a multiplicity of infection (m.o.i.) of 5 or 10 plaque-forming units (pfu) per cell. Virus suspension was added to cell monolayers (0.5 ml/60-mm dish; 0.25ml/well on 6-well plate) and incubated at 37^{0}C for 1 h with brief agitation every 10 min. Then, the virus was removed, cells were washed once with serum free medium, complete growth medium was added, and the cells were incubated at 37^{0}C.

Inactivation of VV by PLWUV treatment

Vaccinia virus with the titer of $3x10^8$ pfu/ml was incubated with 1μg/ml of psoralen at room temperature for 10 min, and then irradiated for 5 minutes in a Stratalinker 1800UV-cross-linking unit (Stratagene, La Jolla, CA) equipped with five 365 nm long-wave UV bulbs as described (Tsung, 1996). The remaining viral infectivity has been determined by viral plaque forming

assay on CV-1 cell monolayer and was expressed as $\log_{10}$ pfu/ml. At 72 h postinfection the cells were stained with 50% of crystal violet solution in ethanol.

[^{3}H]-Thymidine uptake assay

Inactivation of viral DNA replication was assessed in 96-well plates on CV-1 cells mock-infected or infected with replicating, or psoralen-UV-treated viruses at an m.o.i. 5 pfu/cell. The plates were incubated at 37^{0}C in 5 % CO_2 for 1, 6, 7 days. During the last 4 h the cells were incubated in the medium containing [^{3}H]-thymidine at 1 μCi/well. The cells were harvested with a multiple sample harvester, and the amount of [^{3}H]-thymidine incorporated into cell DNA was counted in a liquid β-scintillation counter. CV-1 cells used in the assay were rendered nonreplicating by treatment with 100 ng/ml of psoralen and with UV-irradiation for 10 min. The results are expressed as disintegrations per minute (dpm).

Luciferase assay

CV-1 cells were infected with replicating (rL-5 or rL-15) or inactivated (iL-5 or iL-15) viruses at an m.o.i. 5 pfu/cell. At specified time points following infection, the cells were harvested and resuspend in a reporter lysis buffer (Luciferase assay kit, Promega, Madison, WI) as described previously (Timiryasova, 1999 in vivo). Luciferase activity was measured in the supernatants using ML300 microplate luminometer (Dynatech Lab., Inc., Chantilly, VA). Results are expressed as relative light units (RLU) normalized to 1x10^6 cells.

ELISA of p53 protein

Quantitation of p53 protein in C6 rat glioma cells infected with replicating (rVV-TK-53) or inactivated (iVV-TK-53) viruses was determined by ELISA assay (Pantropic p53 rapid format ELISA, Oncogene Research Products, Cambridge, MA) according to the instructions of the manufacturer. In brief, C6 rat glioma cells grown in 6-well plate were mock-infected or infected with viruses at an m.o.i. of 5 pfu/cell. The culture medium was changed every two days. At specific time point, supernatant from cells was removed and the cells were harvested by scraping. Pellet was washed by phosphate buffer and resuspend in lysis buffer (50 mM tris, pH 7.4, 5 mM EDTA, 0.2 mM PMSF, 1 μg/ml aprotinin) containing antigen extraction agent (provided in kit), and incubated 30 min on ice with occasional vortexing. Then the extract was centrifuged for 5 min and the supernantant was used for ELISA. Absorbance was measured using a spectophotometric plate reader (MRX Revelation, DYNEX Technologies, Inc., Chantilly, VA) at dual wavelengths of 450/570 nm. Experiments were repeated three times. The results were expressed as ng/ml.

Analysis of the cell viability

The viability of C6 rat glioma cells was determined using trypan blue exclusion assay. Glioma cells ($6x10^4$ cells/well) were seeded in 24-well plates for 18 h before infection. The cells were mock-infected or infected with nonreplicating control virus (iL-15) or expressing p53 virus (iVV-TK-53) at an m.o.i. of 5 pfu/cell. At specific time point, cells were trypsinized and counted. Duplicated samples of each treatment were counted.

TUNEL assay

Apoptosis-related DNA strand breaks were detected by terminal deoxynucleotidyl transferase-mediated dUTP nick end labeling of DNA (TUNEL; *in situ* cell death detection kit, fluorescein, Roche Molecular Biochemicals, Indianapolis, USA) as described previously (Timiryasova *et al.,* 1999 in vitro) with some modifications. Glioma cells were seeded on coverslips 24 h prior to infection with 5 pfu/cell of recombinant viruses. Six days after virus infection, the air-dried cells were fixed with 4% paraformaldehyde for 30 min at room temperature, washed three times with PBS, and then permeabilized with 0.1% triton X-100 in 0.1% sodium citrate for 2 min at room temperature and for 2 min on ice. After several washes in PBS, the cells were incubated with the TUNEL reaction mixture containing fluorescein-conjugated dUTP for 60 min at 37°C in a humidified atmosphere in the dark as specified by the manufacturer (Roche Molecular Biochemicals). After three times washes with PBS samples were directly analyzed using a fluorescence microscope.

Animals and tumor induction

Athymic nude mice (*nu/nu*; Charles River Lab., Inc., Wilmington, MA) at 6-7 weeks of age were used for animal's studies. Biosafety level 2 precautions were implemented during housing and handling of the animals, as described in *Guidelines for Research Involving Recombinant DNA Molecules* (NIH Guidelines, 1994). Euthanasia by rapid CO_2 asphyxiation was performed in compliance with the NIH *Guide for Care and Use of Laboratory Animals.* All animals care was performed under the direction of a licensed veterinarian. The study was approved prior to initiation by the University Animal Research Committee.

For *ex vivo* experiments, C6 glioma cells were infected with the inactivated (1 μg/ml of psoralen and 5 min UV-irradiation) viruses (iVV-TK-53 or iL-15) at an m.o.i. 1 or 10 pfu/cell at 37 ^{0}C for 60 min, washed with PBS to remove free viral particles, and cultured. At 24 h post-infection, cells were collected, counted, and injected sc in the right hind flank of athymic mice (3 x 10^5 viable cells/animal). Mock-infected cells were injected into mice and used as a positive control. The tumor volume was calculated as described previously (Gridley *et al.,* 1998; Timiryasova *et al.,* 1999 in vivo). All mice were euthanized when the mean tumor volume in control group reached 2000 mm^3.

Statistical analysis

The data were assessed by one-way analysis of variance (ANOVA) Tukey's HSD test and student t-test. A p-value of <0.05 was considered to indicate significant differences. These analyses were performed using Statgraphics software version 9.0 (SPSS, Inc. Rockville, MD).

ACKNOWLEDGMENTS

The authors express their gratitude to Dr. B. Moss for providing plasmid pSC65, to Dr. D.S. Gridley for the helpful comments and to Melba Andres for help in [^{3}H]-thymidine uptake assay.

This work was supported by the US department of the Army and NMTB. The view, opinions and/or finding contained in this report are those of the authors and should not be construed as a position, policy, decision or endorsement of the federal Government or the National Medical Technology Testbed, Inc.

REFERENCES

Belyakov, I. M., Wyatt, L. S., Ahlers, J. D., Earl, P., Pendleton, C. D., Kelsall, B. L., Strober, W., Moss, B., and Berzofsky, J. A. (1998). Induction of a mucosal cytotoxic T-lymphocyte response by intrarectal immunization with a replication-deficient recombinant vaccinia virus expressing human immunodeficiency virus 89.6 envelope protein. *J. Virol.* **72**, 8264-8272.

Benda, P., Lightbody, J., Sato, G., Levine, L., and Sweet, W. (1968). Differentiated rat glial cell strain in tissue culture. *Science* **161**, 370-371.

Benes, V., Hostomsky, Z., Arnold, L., and Paces, V. (1993). M13 and pUC vectors with new unique restriction sites for cloning. *Gene* **130**, 151-152.

Blanchard, J., Alcami, A., Andrea, P., and Smith, G. L. (1998). Modified vaccinia virus Ankara undergoes limited replication in human cells and lacks several immunomodulatory proteins: applications for use as a human vaccinie. *J. Gen. Virol.* **79**, 1159-1167.

Boulikas, T. (1998). Status of gene therapy in 1997: molecular mechanisms, disease targets, and clinical applications. *Gene The.r Mol. Biol.* **1**, 1-172.

Broyles, S. S., Li, J., and Moss, B. (1991). Promoter DNA contacts made by the vaccinia virus early transcription factor. *J. Biol. Chem.* **263**, 15539-15544.

Carroll, M. W., and Moss, B. (1997). Host range and cytopathogenicity of the highly attenuated MVA strain of vaccinia virus: propagation and generation of recombinant viruses in a nonhuman mammalian cell line. *Virology* **238**, 198-211.

Chakrabarti, S., Sisler, J. R., and Moss, B. (1997). Compact, synthetic, vaccinia virus early/late promoter for protein expression. *BioTechn.* **23**, 1094-1097.

Fischer, L., Legros, F. X., Mason, P. W., and Paoletti, E. (1997). A recombinant canarypox virus protects rabbits against a lethal rabbit hemorrhagic disease virus (RHDV) challenge. *Vaccine* **15**, 90-96.

Graham, B. S., Matthews, T. J., Belshe, R. B., Clements, M. L., Dolin, R., Wright, P. F., Gorse, G. J., Schwartz, D. H., Keefer, M. C., and Bolognesi, D. P. (1993). Augmentation of human immunodeficiency virus type 1 neutralizing antibody by priming with gp160 recombinant vaccinia and boosting with rgp160 in vaccinia-naive adults. The NIAID AIDS Vaccine Clinical Trials Network. *J. Infect. Dis.* **167**, 533-537.

Gridley, D. S., Andres, M. L., Li, J., Timiryasova, T. M., Chen, B., and Fodor, I. (1998). Evaluation of radiation effects against C6 glioma in combination with vaccinia virus-p53 gene therapy. *Int. J. Oncol.* **13**, 1093-1098.

Hanson, C. V., Riggs, J. L., and Lennette, E. H. (1978). Photochemical inactivation of DNA and RNA viruses by psoralen derivatives. *J. Gen. Virol.* **40**, 345-358.

Johnson, R. P., Hammond, S. A., Trocha, A., Siliciano, R. F., and Walker, B. D. (1994). Induction of a major histocompatibility complex class I-restricted cytotoxic T-lymphocyte response to a highly conserved region of human immunodeficiency virus type 1 (HIV-1) gp120 in seronegative humans immunized with a candidate HIV-1 vaccine. *J. Virol.* **68**, 3145-3153.

Kawakita, M., Rao, G. S., Ritchey, J. K., Ornstein, D. K., Hudson, M. A., Tartaglia, J., Paoletti, E., Humphrey, P. A., Harmon, T. J., and Ratliff, T. L. (1997). Effect of canarypox virus (ALVAC)-mediated cytokine expression on murine prostate tumor growth. *J. Natl. Cancer Inst.* **89**, 428-436.

Kotwal, G. J., Hugin, A. W., and Moss, B. (1989). Mapping and insertional mutagenesis of a vaccinia virus gene encoding a 13,800-Da secreted protein. *Virology* **171**, 579-587.

Krausova, V. I., Kopylova-Sviridova, T. N., Timiryasova, T. M., and Fodor, I. (1991). Expression of the genes for Glowworm luciferase in mammalian cells with the use of vaccinia viral vectors. *Mol.Genet., Microbiol., Virol.* **2**, 23-28.

Li, H., Lochmuller, H., Yong, V. W., Karpati, C., and Nalbantoglu, J. (1997). Adenovirus-mediated wild-type *p53* gene transfer and overexpression induces apoptosis of human glioma cells independent of endogenous *p53* status. *J. Neuropathol. Exp. Neurol.* **56**, 872-878.

Li, J., and Broyles, S. (1993). Recruitment of vaccinia virus RNA polymerase to early gene promoters by the viral early transcription factor. *J. Biol. Chem.* **268**, 2273-2280.

Mackett, M., Smith, G. L., and Moss, B. (1984). General method for production and selection of infectious vaccinia virus recombinants expressing foreign genes. *J. Virol.* **49**, 857-864.

McElrath, M. J., Corey, L., Berger, D., Hoffman, M. C., Klucking, S., Dragavon, J., Peterson, E., and Greenberg, P. D. (1994). Immune responses elicited by recombinant vaccinia-human immunodeficiency virus (HIV) envelope and HIV envelope protein: analysis of the durability of responses and effect of repeated boosting. *J. Infect. Dis.* **169**, 41-47.

Meko, J. B., Yim, J. H., Tsung, K., and Norton, J. A. (1995). High cytokine production and effactive antitumor activity of a recombinant vaccnina virus encoding murine interleukin 12. *Cancer Res.* **55**, 4765-4770.

Meko, J. B., Tsung, K., and Norton, J. A. (1996). Cytokine production and antitumor effect of a nonreplicating, noncytopathic recombinant vaccinia virus expressing interleukin-12. *Surgery* **120**, 274-281.

Moss, B. (1996a). Poxviridae: The viruses and their replication. *In* "Fields Virology" (D. M. Knippe, B. N .Fields, , and P. M. Howley, Eds.), Vol. 3, pp. 2637-2672. Lippincott-Raven, Philadelphia.

Moss, B. (1996b). Genetically engineered poxviruses for recombinant gene expression, vaccination, and safety. *Proc. Natl. Acad. Sci. USA* **93**, 11341-11348.

Paoletti, E. (1996). Application of poxvirus to vaccination: An update. *Proc. Natl. Acad. Sci. USA* **93** , 11349-11353.

Puhlmann, M., Gnant, M., Brown, C. K., Alexander, H. R., and Bartlett, D. L. (1999). Thymidine kinase-deleted vaccinia virus expressing purine nucleoside phosphorylase as a vector for tumor-directed gene therapy. *Hum. Gene Ther.* **10**, 649-657.

Qin, H. and Chatterjee, S. K. (1996). Cancer gene therapy using tumor cells infected with recombinant vaccinia virus expressing GM-CSF. *Hum. Gene Ther.* **7**, 1853-1860.

Ronen, D., Teitz, Y., Goldfinger, N., and Rotter, V. (1992). Expression of wild-type and mutant p53 proteins by recombinant vaccinia viruses. *Nucl. Acids Res.* **20**, 3435-3441.

Roth, J., Dittmer, D., Rea, D., Tartaglia, J., Paoletti, E., and Levine, A. J. (1996). p53 as a target for cancer vaccines: recombinant canarypox virus vectors expressing p53 protect mice against lethal tumor cell challenge. *Proc. Natl. Acad. Sci. U.S.A* **93**, 4781-4786.

Sheay, W. E., Nelson, S., Martinez, I., Chu, T.-H. T., Bhatia, S., and Dorndurg, R. (1993). Downstream insertion of the adenovirus tripartite leader sequence enhances expression in universal eukaryotic vectors. *BioTechn.* **15**, 856-862.

Taylor, J. and Paoletti, E. (1988). Fowlpox virus as a vector in non-avian species. *Vaccine* **6**, 466-468.

Taylor, J., Trimarchi, C., Weinberg, R., Languet, B., Guillemin, F., Desmettre, P., and Paoletti, E. (1991). Efficacy studies on a canarypox-rabies recombinant virus. *Vaccine* **9**, 190-193.

Timiryasova, T. M., Kopylova-Sviridova, T. N., and Fodor, I. (1993). Analysis of expression of the reporter genes in different regions of vaccinia virus genome. *Mol. Biol.* **27**, 392-401.

Timiryasova, T. M., Li, J., Chen, B., Chong, D., Langridge, W. H. R., Gridley, D. S., and Fodor, I. (1999a). Antitumor effect of vaccinia virus in glioma model. *Oncol. Res.* **11**, 133-144.

Timiryasova, T. M., Chen, B., Haghighat, P., and Fodor, I. (1999b). Vaccinia virus-mediated expression of wild-type p53 suppresses glioma cell growth and induces apoptosis. *Int. J. Oncol.* **14**, 845-854.

Tsung, K., Yim, J. H., Marti, W., Buller, R. M. L., and Norton, J. A. (1996). Gene expression and cytopathic effect of vaccinia virus inactivated by psoralen and long-wave UV light. *J. Virol.* **70**, 65-171.

Uzendoski, K., Kantor, J. A., Abrams, S. I., Schlom, J., and Hodge, J. W. (1997). Construction and characterization of a recombinant vaccinia virus expressing murine intercellular adhesion molecule-1: induction and potentiation of antitumor responses. *Hum. Gene Ther.* **8**, 851-860.

Wang, M., Bronte, V., Chen, P. W., Gritz, L., Panicali, D., Rosenberg, S. A., and Restifo, N. P. (1995). Active immunotherapy of cancer with a nonreplicating recombinant fowlpox virus encoding a model tumor-associated antigen. *J.Immunol.* **154**, 4685-4692.

FIGURE LEGENDS

FIG. 1. Analysis of inactivated virus by titration. The remaining viral infectivity of the PUV inactivated virus was determined on CV-1 cell monolayer. rL-15, replicating virus; iL-15, nonreplicating virus; n/d, 30 pfu/cell; -1, 3 pfu/cell; -2, 0.3 pfu/cell; -3, 0.03 pfu/cell; -4, 0.003 pfu/cell; -5, 0.0003 pfu/cell.

FIG. 2. Schematic representation of the recombinant viruses. L-5 virus contains the luciferase gene (*luc*) of firefly *Photinus pyralis* and β-galactosidase (*lac Z*) of *E. coli* at the *Hind*III-N-locus of VV. L-15 contains two reporter genes (*luc* and *lac Z*) inserted into thymidine kinase region of VV. Recombinant virus VV-TK-53 is similar to L-15 differing only in the expressed foreign gene. VV-TK-53 contains the human wild-type *p53* gene instead of *luc* gene in the L-15 construct. Abbreviations: P7.5, vaccinia early/late promoter; P11, vaccinia late promoter; P13, synthetic vaccinia early promoter; PE/L, synthetic vaccinia early/late promoter; N_L and N_R; TK_L and TL_R, refer to segments of vaccinia genome that include the left and right portions of *Hind*III-N- and TK-regions, respectively; *luc*, luciferase gene; *lac Z*, β-galactosidase gene; *p53*, human wild-type *p53* gene.

FIG. 3. Luciferase expression. CV-1 cells were infected with replicating (rL-5 or rL-15) or inactivated (iL-5 or iL-15) viruses at an m.o.i. of 5 pfu/cell. At specified time points following infection, the cells were harvested, lysed and analyzed by luminometer.

FIG. 4. p53 expression. Cells were infected at an m.o.i. of 5 pfu/cell and harvested at the indicated times. Quantitation of p53 protein in C6 rat glioma cells infected with replicating (rVV-TK-53) or inactivated (iVV-TK-53) viruses was determined by ELISA assay.

FIG. 5. [^{3}H]-Thymidine uptake. Inactivation of viral DNA replication was assessed on CV-1 cells mock-infected or infected with replicating, or PUV inactivated viruses at an m.o.i. of 5 pfu/cell in 96-well plates. The plates were incubated at 37^{0}C in 5 % CO_2 for 1, 6, 7 days. During the last 4 h the cells were incubated in the medium containing [^{3}H]-thymidine at 1 μCi/well. The amount of ^{3}H-TdR incorporated into cell DNA was counted in a liquid β-scintillation counter. Average values of two independent experiments are shown; a, statistically significant difference compared with other two groups.

FIG. 6. Viability of C6 cells. Effect of the tumor suppressor p53 expressed by nonreplicating VV-TK-53 virus on the viability of C6 rat glioma cells was determined using trypan blue exclusion assay. Duplicated samples of each treatment were counted.

FIG. 7. Detection of apoptosis *in situ.* C6 rat glioma cells were seeded on glass coverslips, and on next day were mock-infected, or infected with nonreplicating control (iL-15) or p53-expressing (iVV-TK-53) virus at an m.o.i. of 5 pfu/cell. In 6 days after the infection, apoptosis-related DNA strand breaks were detected by TUNEL assay. The samples were directly analyzed using a fluorescence microscope. Brightly stained green cells were undergoing apoptosis. Magnification x1000.

FIG. 8. Tumor growth inhibition. Athymic mice were injected sc with $3x10^5$ of mock-infected C6 glioma cells or infected with iL-15 or iVV-TK-53 at m.o.i. of 5 and incubated for 24 h prior injection. Results of a representative experiment are shown.

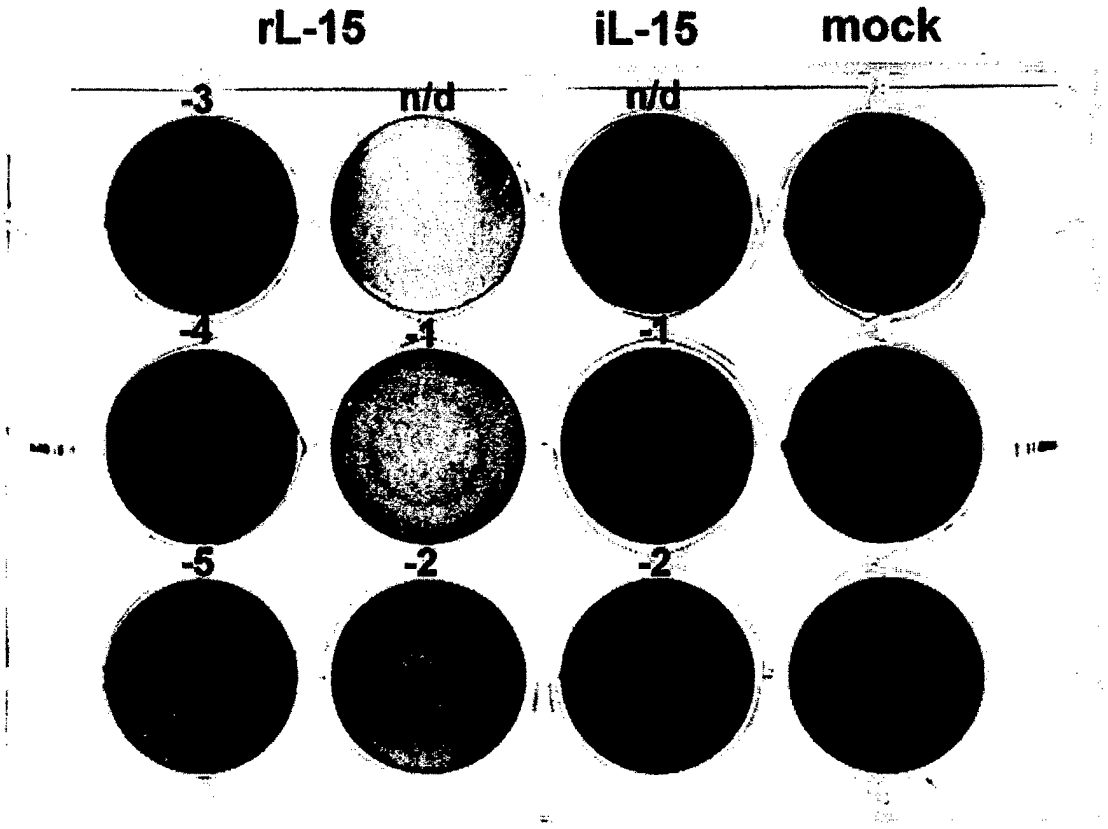

FIGURE 1

FIGURE 2

L-5

L-15

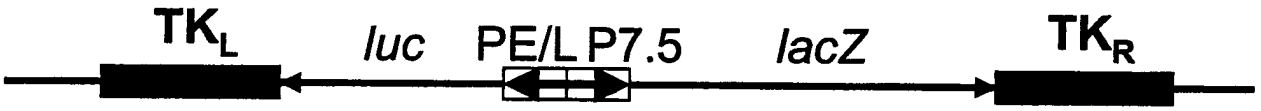

VV-TK-53

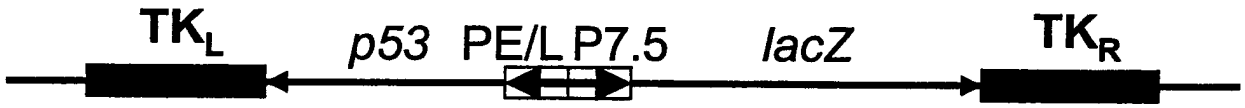

FIGURE 3

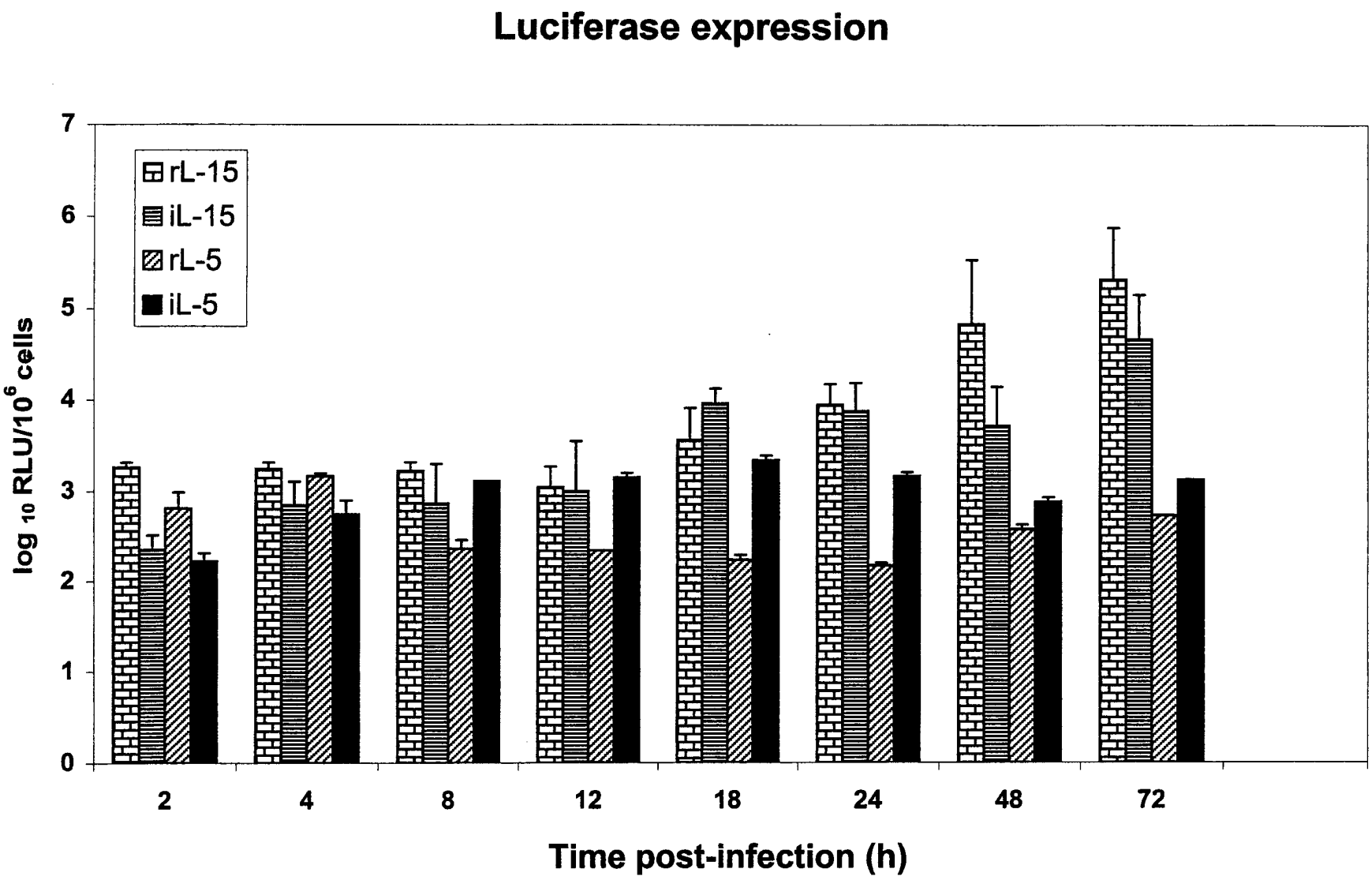
Luciferase expression
rL-15
iL-15
rL-5
iL-5
log 10 RLU/10^6 cells
0
1
2
3
4
5
6
7
2
4
8
12
18
24
48
72
Time post-infection (h)

FIGURE 4

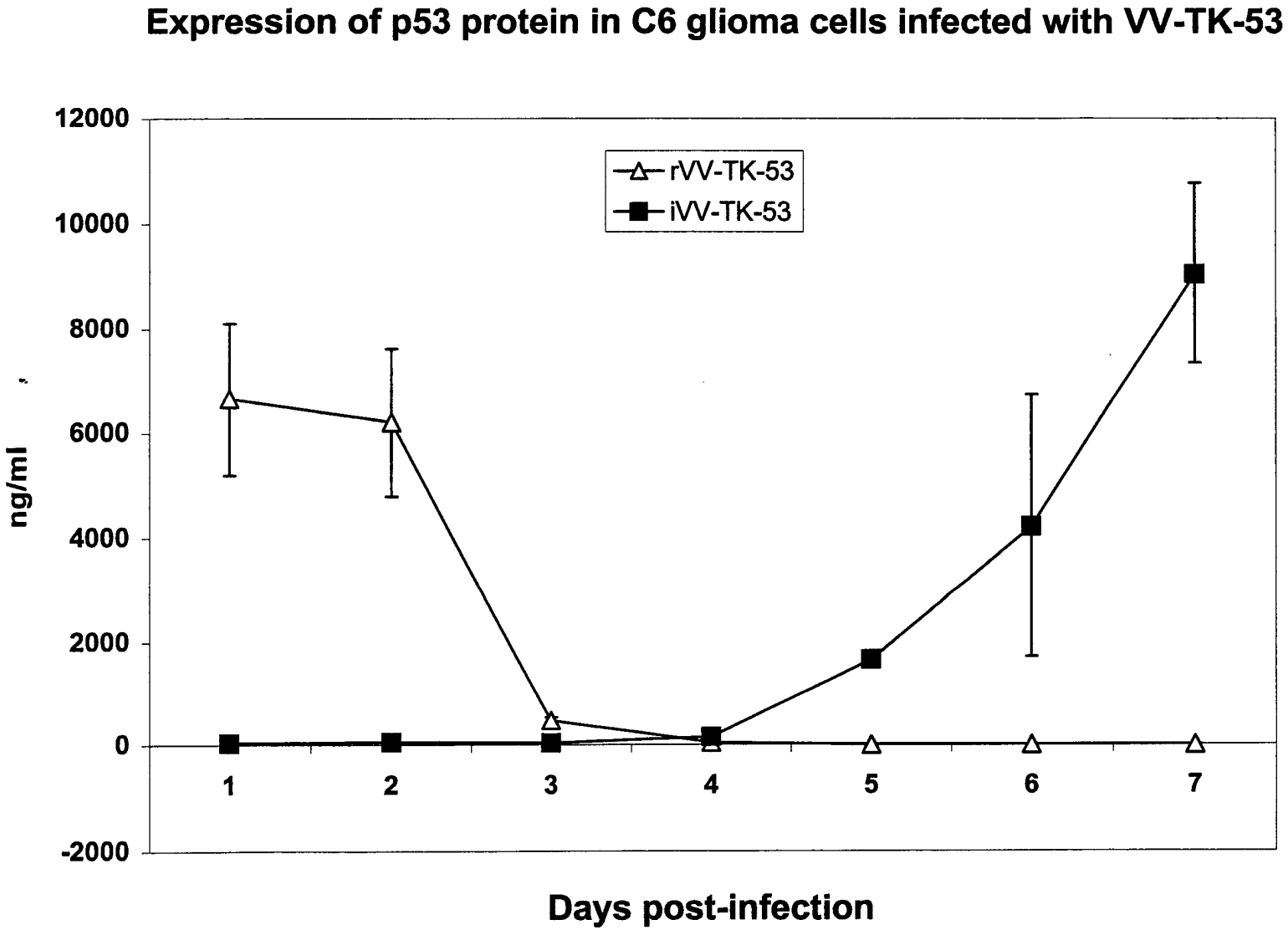
Expression of p53 protein in C6 glioma cells infected with VV-TK-53
12000
10000
8000
6000
4000
2000
0
-2000
ng/ml
rVV-TK-53
iVV-TK-53
1
2
3
4
5
6
7
Days post-infection

FIGURE 5

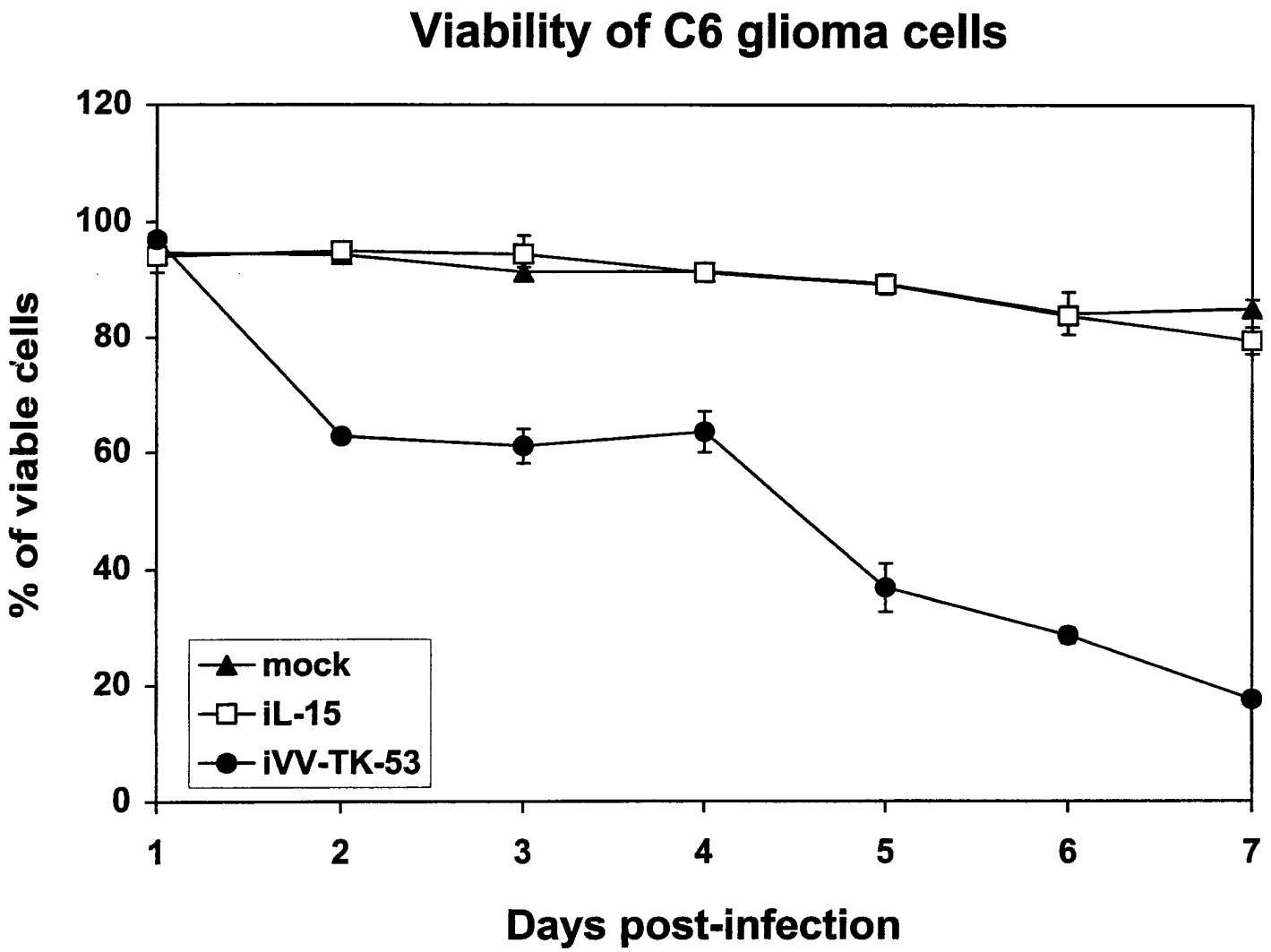
Viability of C6 glioma cells
% of viable cells
120
100
80
60
40
20
0
1
2
3
4
5
6
7
Days post-infection
mock
iL-15
iVV-TK-53

FIGURE 6

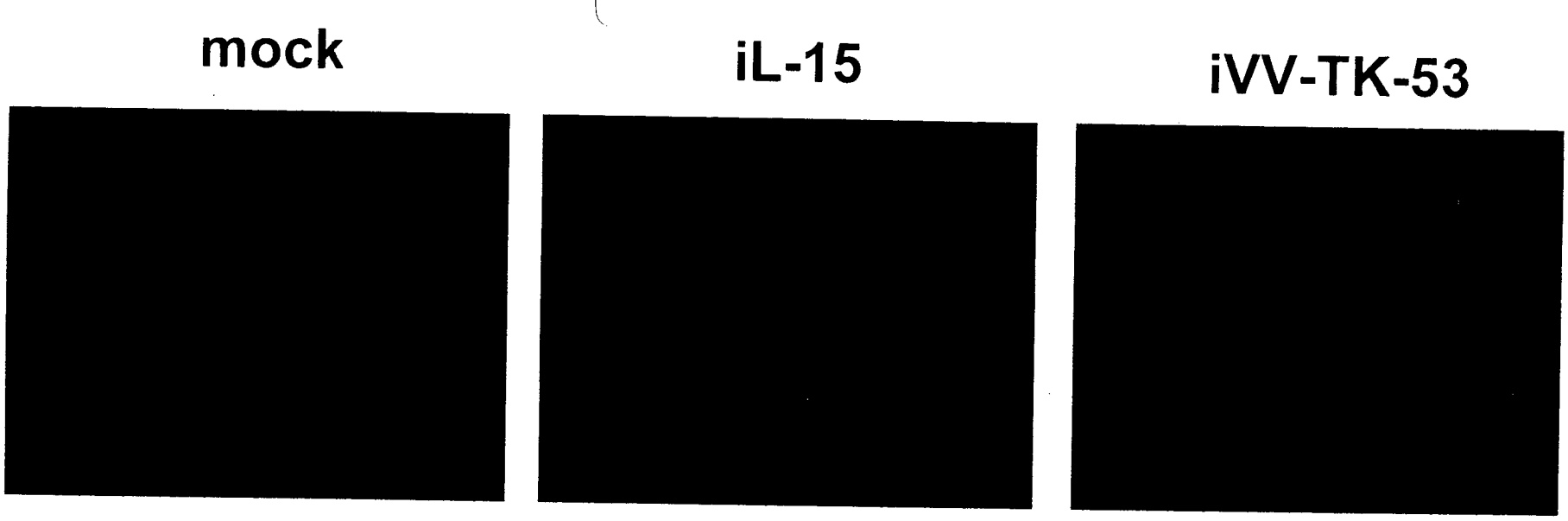

Poject Director: Istvan Fodor, Ph.D.

DESCRIPTION AND PERFORMANCE SITES (Form B)

DESCRIPTION:

The project goal is to determine the efficacy and safety of recombinant vaccinia treatment combined with radiation therapy against a highly malignant tumor in a cost-effective preclinical model. The ultimate goal of our research program is to help increase the survival and quality of life for children and adults diagnosed with cancer in this country and around the world. *Our preclinical research addressing innovative combined therapies can be rapidly translated into clinical protocols and thus, funding should be a priority for cancer research.* In this project, the most common primary tumor arising in the human brain will be investigated in an animal model.

Previously, we proposed a novel strategy of glioblastoma treatment based on combined gene therapy and immunotherapy of tumors using vaccinia viruses expressing tumor suppressor gene p53, and cytokines IL-2 and IL-12. The effectiveness of this combined approach currently is under investigation and mid-year results have been included in this application (*see* Progress Report); the project is funded by NMTB (1998). Here, we propose to develop a new strategy of increasing the sensitivity of malignant cells to the lethal effects of radiation using therapeutic vaccinia viruses. Our recent data indicate that virus-mediated gene therapy combined with ionizing radiation may drastically reduce the tumor growth. *This innovative strategy is expected to increase both the efficacy and safety of gene (and immune-) therapy and radiotherapy for brain tumors and other highly malignant forms of cancer.*

Specific aim 1 of the project is to determine the molecular mechanisms and efficacy of combined virus and radiation treatment in vitro, which will be accomplished by conducting five consecutive experiments on two glioma cell lines. Specific aim 2 is to determine the efficacy and safety of combined vaccinia and ionizing radiation treatment of subcutaneous tumors, which will be accomplished by two separate experiments. Specific aim 3 is to evaluate the anti-tumor effect of combined treatment in an intracranial glioma model.

The project will contribute to gene therapy and radiotherapy researches for cancer in two ways which may ultimately improve national health care. First, we are developing a safer and more efficacious gene therapy vector system which can deliver any desired combination of several therapeutic genes. And second, we are evaluating for the first time the combination of vaccinia-mediated gene therapy and radiotherapy.

PROJECT SITES

Loma Linda University and Medical Center,

Loma Linda, CA

Table 2. Hematological variables in blood from mice in Phase A

Time[a]	Group	Erythrocytes: No. of cells ($x10^6$/ml)	Erythrocytes: Hemoglobin (g/dl)	Erythrocytes: Hematocrit (%)	Platelets ($x10^3$/ml)	WBC ($x10^6$/ml)
-	No tumor	7.61+/ 0.34[b]	13.3+/-0.5	40.1+/-1.7	383+/-67	6.97+/-0.96
18 hr	Tumor-bearing: PBS	7.60+/-0.56	13.7+/-0.9	41.6+/-2.8	450+/-114	4.16+/-0.56
	pGL1-TNF (15μg)	6.99+/ 0.14	12.8+/-0.3	38.3+/-0.9	368+/-79	6.09+/-0.68
	pGL1-TNF (150μg)	7.33+/ 0.18	13.1+/-0.3	39.3+/-0.9	391+/-77	5.91+/-0.71
	pGL1-TNF (450μg)	7.16+/-0.09	13.2+/ 0.2	39.1+/-0.4	193+/-33	5.84+/-0.49
72 hr	PBS	6.94+/-0.12	12.6+/-0.2	37.8+/-0.5	620+/-23	5.88+/-0.37
	pGL1-TNF (15μg)	6.01+/ 0.62	11.2+/-1.1	32.8+/-3.4	603+/-104	5.26+/-0.17
	pGL1-TNF (150μg)	6.85+/-0.15	12.5+/-0.3	36.8+/ 0.8	465+/- 43	7.70+/-0.27[f]
	pGL1-TNF (450μg)	6.23+/-0.68	11.5+/-1.2	33.9+/-3.7	237+/- 54[e]	7.71+/-0.90
168 hr	PBS	6.05+/ 0.36[c]	11.2 +/- 0.6	32.2+/-1.9[c]	226+/-59	8.62+/-0.69
	pGL1-TNF (15μg)	5.53+/ 0.31[c]	10.5 +/- 0.5[c]	30.9+/-1.5[c]	302+/-29	6.97+/-0.67
	pGL1-TNF (150μg)	6.33+/-0.11[c]	11.8 +/- 0.2	34.4+/-0.6	328+/-64	8.21+/-0.66
	pGL1-TNF (450μg)	4.89+/-0.40[c,d]	9.4 +/- 0.7[c,d]	26.9+/-2.0[c,d]	379+/-34	8.08+/-1.01

[a]Time after i.t. injection of pGL1-TNF-α.

[b]Mean +/- SEM; n = 5-7 mice/group/time point.

[c]$P<0.05$ vs no tumor.

[d]$P<0.05$ vs pGL1-TNF (150 μg) at 168 hr.

[e]$P<0.01$ vs PBS and pGL1-TNF (15 μg) at 72 hr.

[f]$P<0.05$ vs pGL1-TNF (150μg) at 72 hr.

ORIGINAL MAR 22 2000

VACCINIA VIRUS-BASED CANCER GENE THERAPY

Final Report

NMTB, February 1, 1999 – February 1, 2000

Principal investigator: Istvan Fodor, Ph.D.

Phone: 909-824-4300/ext.82398
FAX: 909-478-4177
E-mail: ifodor@som.llu.edu

P.I. signature: Istvan Fodor

Date: March 20, 2000

INTRODUCTION

Transformation of a normal cell to its malignant counterpart is the result of multiple genetic changes that include inactivation of tumor-suppressor genes. P53 gene is the mostly studied tumor suppressor gene and the most frequent target of genetic alterations in human cancers. P53 mutation or protein inactivation was found in 63 to 65% of high grade and 63% of low-grade astrocytomas [1,2]. The malignant form, glioblastoma multiforme, is the commonest tumors derive from glial precursors and the second leading cause of cancer death in children younger than 15 years of age.

Therapeutic strategies designed to restore wild-type p53 protein activity in cancer cells are particularly appealing. Indeed, several studies have demonstrated that introduction of wild-type p53 by virus-mediated delivery can suppress growth in a number of human cancer cell lines *in vitro* and *in vivo*[3-5]. Replacement of mutated p53 genes may present alternatives to conventional therapy, although p53 treatment alone may not be sufficient to cure the patients. Strategy of combined therapy by p53 with other antitumor agents, like cytokine, may be more effective approach for *in vivo* treatment of cancer. Potential vectors of gene delivery for human gene therapy include adenovirus, herpes simplex virus, adeno-associated virus, poxvirus, or non-viral plasmid DNA. Compared to other virus vectors vaccinia virus (VV), a poxvirus, is a particularly attractive vector due to its wide host range, large cloning capacity, cytoplasmic site of viral replication, and high efficiency of foreign gene expression[6]. The safety and efficacy of live vaccine strains of VV was successfully demonstrated in the smallpox eradication program and in vaccine trials for a number of animal and human infectious diseases[6]. In our laboratory, the attenuated VV strain Lister has been used for many years. The safety and efficacy of this VV strain has been confirmed in our previous animal and human vaccination studies [7-10] and in studies on cancer gene therapy[11-13]. Recombinant VV expressing immune modulators, such as interleukin-2 [14-18], interleukin-12[18-21] and other cytokines [17,22-25], have been proved to produce authentic proteins both *in vitro* and *in vivo* and induce anti-tumor immunity in

various animal tumor models. Interleukin 2 (IL-2) and interleukin 12 (IL-12) seem to be potent cytokines that possess antitumor activity through their ability to stimulate the cell-mediated killing activity of cytotoxic T lymphocyte (CTLs), to enhance natural killer cell (NK) activity and to activate tumor infiltrating lymphocytes (TILs). Recently, Putzer et al [26] have shown that combined intratumoral delivery of p53 and IL-2 genes resulted in significant regressions in 65% of treated murine breast cancer. Previous studies in both xenogeneic and syngeneic glioma models showed that intratumoral IL-2 and IL-12 production might stimulate an immune antitumor response, with predominance of CD_4, CD_8 lymphocytes, NK cells, neutrophils and activated macrophages [27-30].

In this study, the efficacy of Lister VV as a vector of IL-2 and IL-12 delivery for low dose cancer immunotherapy has been investigated in athymic mice C6 glioma model. Athymic nude mice model may simulate immuno-deficient individuals or cancer patients particularly at advanced stages which often develop impaired T cell response similar to nude mice due to the disease itself, radiotherapy and/or chemotherapy[17]. We performed a dose-escalation experiment (10 PFU to 10^7 PFU) to determine the effective dose of this attenuated VV for the inhibition of tumor growth. For the first time we have demonstrated that low-dose VV-mediated cytokine delivery can be an effective strategy for immunotherapy of glioblastomas *in vivo*.

To augment an antitumor efficacy and minimize cytokine toxicity, a study was performed to investigate the ability of tumor inhibition by combination of low dose rVV-mIL2 and rVV-mIL12 and high dose rVV-p53 in a C6 glioma model. For the first time, we have demonstrated that two different recombinant viruses, when combined at ratio 10 to $2x10^7$, could still express their own transgene *in vivo* and synergistically inhibit tumor growth.

Specific Aim 1: To determine the efficacy and safety of *live* recombinant vaccinia mediated cytokine immunotherapy combined with tumor suppressor p53 gene therapy in a preclinical model of highly malignant cancer. To achieve the goal three experiments were planned and performed.

Experiment 1. Construction of recombinant vaccinia virus vectors expressing cytokines IL-2 and IL-12, individually and combined.

Experiment 2. Determination of the dose response for vectors producing IL-2 or IL-12.

Experiment 3. Determine the efficacy and safety of combined p53 gene therapy and IL-2 and IL-12 immunotherapy.

Specific Aim 2: To determine the efficacy and safety of *inactivated* recombinant vaccinia-mediated gene therapy in a preclinical model of highly malignant cancer.

EXPERIMENTAL METHODS

Cell lines. CV-1 cells, African green monkey kidney fibroblasts, were obtained from the American type Culture Collection (ATCC, Rockville, MD) and maintained in Dulbecco's modified Eagle's medium containing 5% fetal bovine serum and antibiotic-antimycotic solution (Sigma Chemical Co., St. Louis, MO). The Rat C6 nitrosourea-induced glioma cell line, originally established by Benda *et al* [31] was cultured in RPMI-1640 medium (Cellgro/Mdiatech, Inc., Herndon, virginia) supplemented with 5% fetal bovine serum and antibiotic-antimycotic solution.

Animals. Athymic nude mice (male, nu/nu) were purchased from Charles River Breeding Laboratories, Inc. (Wilmington, MA) at 5-6 weeks of age. The animals were housed in self-contained filter-top cages in a room controlled for temperature, humidity, and a 12 h day-night cycle. Autoclaved bedding, food and water were provided. At the time of sacrifice, rapid CO_2 asphyxiation was performed in compliance with the NIH Guide for the Care and Use of Laboratory Animals. The study was approved by the institutional Animal Research Committee.

Construction of recombinant vaccinia viruses. *Details were presented in the Progress Report.* LIVP variant of the attenuated Lister strain of VV has been used in this study. The plasmid (VR1110) containing mouse IL-2 (mIL-2) gene and plasmid (pSFG.IL-12.p40.L.Δp35) carrying mouse IL-12 (mIL-12) fusion gene were obtained from Dr. Parker (Vical, Inc., San Diego) and Dr. Mulligan (Howard Hughes Medical Institute, Boston), respectively. Recombinant viruses rVV-mIL2, rVV-mIL12 and rVV-2-12 carrying mIL-2, mIL-12 or both genes, are described in Fig.1. The rVV_2 strain has lacZ gene and served as a control virus for rVV-p53. rVV_4 has the insertion of two genes encoding *Photinus pyralis luciferase (luc)* and the *Escherichia coli lacZ* at the TK region of the wild-type VV (wt VV) (Fig. 1d). All recombinant viruses contained a copy of reporter *lacZ* gene.

p*VNP13-luc.* The cDNA encoding luciferase gene (*luc*) of firefly *Photinus pyralis* was isolated by digestion with restriction enzymes *Bam*HI and *Hind*III from plasmid p19pL27 [32] and cloned into the *Sma*I-*Sal*I sites of pWS4 kindly provided by Dr. R. Dornburg [33], resulting in pWL7. The DNA sequence of early vaccinia virus promoter P13, containing in 5'-end site of *Sac*I and in 3'-end site of *Bam*HI (43bp) for easy cloning (GATCCAATAAAAATAAATTTTTTTCATTTAT CTATATGAGGT) was synthesized and inserted into pUC28 [34]. Then, the plasmid was digested with *Sac*I and *Bam*HI resulting in pUCP13. *Sac*I-*Bam*HI fragment from pUCP13 was cloned into pWL7 digested with *Sac*I and *Bam*HI, resulting in pWLP13. The *luc* gene was isolated from pWLP13 by digestion with *Sac*I and *Bgl*II and cloned into the *Sma*I site of pVN1, a transfer vector for homologous recombination with the *Hind*III-N locus of the vaccinia [8], resulting in pVNP13-luc, which was used for construction of recombinant vaccinia virus L-5.

pSC15. Transfer vector pSC65 for insertion of foreign genes into TK-region of vaccinia was kindly provided by Dr. B.Moss [35]. cDNA of luciferase was isolated from p1914 [32] by *Hind*III and *Sma*I and inserted into *Sal*I site of pSC65. New plasmid pSC15 was used for construction of recombinant virus L-15.

*pSCp53. Bam*HI-*Bgl*II fragment from pWS-53 [36] encoding the human wild-type *p53* gene was cloned into the *Sal*I site of pSC65, resulting in pSCp53. New plasmid pSCp53 was used for construction of recombinant virus VV-TK-53.

Recombinant vaccinia viruses (Fig. 1) were constructed by homologous recombination. L-5 virus encodes the luciferase and β-galactosidase genes at the *HindIII*-N-locus of the genome. L-15 contains two reporter genes (*luc* and *lac Z*) inserted into thymidine kinase region of VV. Recombinant virus VV-TK-53 is similar to L-15 differing only in the expression of foreign gene. VV-TK-53 encodes the human wild-type *p53* gene instead of *luc* gene in the L-15 construct. Infection of the cells was carried out at a multiplicity of infection (m.o.i.) of 5 or 10 plaque-forming units (pfu) per cell. Virus suspension was added to cell monolayers (0.5 ml/60-mm dish; 0.25ml/well on 6-well plate) and incubated at 37^0C for 1 h with brief agitation every 10 min. Then, the virus was removed, cells were washed once with serum free medium, complete growth medium was added, and the cells were incubated at 37^0C.

Recombinant clones of VV were selected by growth on CV-1 cells, in the presence of 5-bromo-4-chloro-indolyl-β-D-galactosidase (X-gal) using the *lacZ* reporter gene. The recombinant viruses were then purified over a sucrose gradient. Virus concentration was determined by plaque titration on CV-1 cells and expressed as plaque-forming units (PFU) per milliliter.

Kinetic analysis of cytokines expression *in vitro*. The efficacy of cytokine expression was performed on rat C6 glioma cells by enzyme-linked immuno-sorbent assay (ELISA). C6 cells ($1x10^6$ cells/well) were plated on 6-well plate and infected with rVV-mIL2, rVV-mIL12 or rVV-2-12 respectively at different multiplicity of infection (MOI). Supernatants were collected at specified time points and cytokines assayed by ELISA kits (Douset kit, Genzyme, Cambridge, MA).

***In vitro* studies.** *Other details were presented in the Progress Report.* To determine whether transgene expression level might be interfered by coinfection

with two different rVVs, equal amount of rVV-p53 and rVV-mIL2 were used to infect C6 glioma cells. Infection of cells was carried out at a multiplicity of infection (MOI) of 0.2 plaque forming unit (PFU) per cell. Virus suspension was added to cell monolayer ($1x10^6$ cells/well) and incubated at 37°C for 1 h before adding complete RPMI 1640 medium. Samples were taken at specific time points and froze at -80°C. Levels of secreted IL-2 in the medium were quantitated by enzyme-linked immunosorbent assay (ELISA) using mouse IL-2 Duoset ELISA kit from Genzyme. P53 expression was detected by western blot as previously described [36].

Since the ratio of cytokine viruses and p53 virus we used in this combined therapy is 10 to $2x10^7$, it is possible for high dose virus inhibit the infection and replication of low dose virus. To test this hypothesis, we coinfected the C6 cells with rVV_4 expressing *lacZ* gene and wild-type VV (wtVV) carrying no reporter gene at ratio 1 to 100. Cells were then fixed in 2% formaldehyde (v/v) and 0.2% glutaraldehyde (v/v) in PBS for 30 min, After washed in PBS for 2 times, cells were stained in X-gal solution for 4 hr at 37°C. X-gal solution was prepared by combining the following: 5 mM potassium ferricyanide, 5 mM potassium ferrocyanide, 2 mM $MgCl_2$, 1 mg/ml X-gal in PBS.

The level of *lacZ* gene expression was also determined by chemoluminescent assay. C6 cells were coinfected with wtVV and/or rVV_4 as described above. 24 h later, cells were lysed in lysis buffer and assayed using Galacto-light Plus™ kit (Tropix, Bedford, MA). Bioluminescence was measured by ML300 microplate luminomiter (Dynatech Laboratories, Inc., Chantilly, VA).

P53 function *in vitro* was analyzed by DNA fragmentation assay. $9x10^6$ C6 cells were plated in 10 cm^2 dish 24 h before virus infection. Cells were then infected with rVV_2, rVV_4, rVV_2/rVV_4, rVV-mIL2, rVV-p53 and rVV-p53/rVV-mIL2 at 0.2 PFU of each virus. Cells were harvested at 48 h post infection and lysed in 10 mM Tris-HCl pH 7.5, 1 mM EDTA and 0.2% Triton X-100. After incubated on ice for 50 min, debris was centrifuged down and supernatant was sequentially digested with 400 μg/ml RN_{ase} and 400 μg/ml Protease K for 30 min at 37°C. Samples were then extracted with phenol/chloroform/isoamyl alcohol for

three times. DNA was precipitated and dissolved in 30 µl H_2O. Total 4 µg of DNA from each sample was analyzed by electrophoresis in 2% agarose gel.

Inactivation of VV by PLW-UV treatment. Vaccinia virus with the titer of $3x10^8$ pfu/ml was incubated with 1µg/ml of psoralen at room temperature for 10 min, and then irradiated for 5 minutes in a Stratalinker 1800UV-cross-linking unit (Stratagene, La Jolla, CA) equipped with five 365 nm long-wave UV bulbs as described [37]. The remaining viral infectivity has been determined by viral plaque forming assay on CV-1 cell monolayer and was expressed as $\log_{10}$ pfu/ml. At 72 h postinfection the cells were stained with 50% of crystal violet solution in ethanol.

***Ex vivo* experiments**. C6 glioma cells were infected with the inactivated (1 µg/ml of psoralen and 5 min UV-irradiation) viruses (iVV-TK-53 or iL-15) at an m.o.i. 1 or 10 pfu/cell at 37 ^{0}C for 60 min, washed with PBS to remove free viral particles, and cultured. At 24 h post-infection, cells were collected, counted, and injected sc in the right hind flank of athymic mice (3×10^5 viable cells/animal). Mock-infected cells were injected into mice and used as a positive control. The tumor volume was calculated as described previously [8,9]. All mice were euthanized when the mean tumor volume in control group reached 2000 mm^3.

***In vivo* studies.** *Experiment 1. Details were presented in the Progress Report.*
Experiment 2. C6 glioma cells ($5x10^5$/mouse) were injected subcutaneously (s.c.) at right hind of the nude mice. On day 5 after cell inoculation when palpable tumor had formed, animals were injected intratumorally *(i.t)* with increasing doses of rVV4, rVV-mIL2, rVV-mIL12 or rVV-2-12 in a volume of 50µl. The lowest dose for these viruses was 10PFU while the highest dose was 10^7PFU for rVV-mIL2 and rVV-mIL12, and 10^5PFU for rVV-2-12. Animals were weight twice a week and tumor dimensions were measured with vernier calipers. All animals were euthanized at the same time, when mean tumor volume for the control group reached ~2,500 mm^3. Tumors were removed and cut into small pieces in PBS with 100 µM phenylmethylsulfomyl fluoride (PMSF). After centrifuged at 2000

rpm, 5 min, supernatant were collected and stored at -80°C before assayed by ELISA for mIL-2 and mIL-12 expression.

Experment 3. An aliquot of $5x10^5$ C6 glioma cells were injected subcutaneously (s.c.) in the right hind of athymic nude mice. Animals were then randomly divided into 11 groups: normal control, saline tumor control, rVV_4 control, rVV_2 control, rVV-mIL2, rVV-mIL12, rVV-2-12, rVV-p53, rVV-p53/rVV-mIL2, rVV-p53/rVV-mIL12, rVV-p53/rVV-2-12. Approximately 5 days later, palpable tumors had developed in all recipients. At that time, mice in corresponding groups were given a single intratumoral injection of Hank's, 10 PFU of rVV_4 or 10 PFU of different cytokine recombinant viruses in a volume of 50 μl, respectively. 24 h later, mice in rVV_2 and p53 groups were received rVV_2, rVV-p53 at the dose of $2x10^7$ PFU. Animals were weight twice a week and tumor dimensions were measured with calipers. All animals were euthanized at the same time, when mean tumor volume of control group reached ~2,500 mm^3. Tumors were removed and cut in half. Half was fixed in 10% buffered formalin. The other half was snap frozen in liquid nitrogen and stored at -80°C.

All animal studies were conducted in accordance with the animal care policy of the Loma Linda University. Athymic nude mice (male) were obtained from Charles River Breeding Laboratories, Inc. (Wilmington, MA) at 4-6 weeks of age.

Detection of p53 and cytokine expression in tumor. Frozen tumors were thawed and cut into small pieces in PBS with 100 μM phenylmethylsulfomyl fluoride (PMSF). After centrifuged at 2000 rpm, 5 min, supernatant were collected and assayed by ELISA for IL-2, IL-12 (Duoset kit, Genzyme), IFN-γ and TNF-α (Quantikine, R&D system) expression.

P53 expression was detected by immunohistochemistry as previously described [8]. Briefly, formalin fixed tumors were embedded in paraffin and sectioned (5 μm). Monoclonal antibody against human p53 (1:100, clone DO-7, Novocastra Lab, Ltd., Newcastle, UK) and Cy 3-conjugated anti-mouse antibody (1:1000, Jackson Immuno-Research Lab., West Grove, PA) were used as primary

and secondary antibodies, respectively. After immunohistochemical reactions, sections were counterstained with DAPI for nuclear detection. Expression of p53 was analyzed using fluorescence microscopy.

***In situ* TUNEL assay.** Apoptosis-related DNA strand breaks were detected by terminal deoxynucleotidyl transferase-mediated dUTP nick end-labeling of DNA (TUNEL, *in situ* cell death detection kit, fluorescein, Boehringer Mannheim, IN). Tumor sections 9 days after virus infection were deparaffinized and permeabilized with 0.1% Triton X-100 in 0.1% sodium citrate for 2 min on ice. After several washes in PBS, the sections were incubated with the TUNEL reaction mixture containing fluorescein-conjugated dUTP for 60 min at 37°C in the dark as specified by the manufacturer (Boehringer Mannheim). Following three washes with PBS, samples were directly analyzed using a fluorescence microscope.

Western blot analysis for IL-12 fusion protein in tumor. To confirm the authenticity of the fused subunit of IL-12 gene expression by rVV *in vivo*, tumors treated with 10^5 PFU rVVs on day 7 after virus injection were homogenized and extracts were analyzed for IL-12 fusion protein expression by Western blot. Eighty μg of protein were separated on a 12% polyacrylamide/SDS gel and transferred to Immunobilon-P membrane (Millipore, Bedford, MA). The membrane was blocked with 5% non-fat milk and probed with primary antibody: Goat anti-mouse IL-12 monoclonal antibody (R&D systems Inc., MN), and then incubated with the secondary antibody conjugated with horseradish peroxidase (Jackson ImmunoResearch Lab. Inc., PA). The membrane development was performed according to the manufacturer's instructions.

Efficiency of *in vivo* infection. Forty μm thick sections from frozen tumors (two/group) were dried, fixed in 2% formaldehyde (v/v) and 0.2% glutaraldehyde (v/v) in PBS for 30 min and washed in PBS for 2 times. Then, sections were stained in X-gal solution for 4 h at 37°C. X-gal solution was prepared by

combining the following: 5 mM potassium ferricyanide, 5 mM potassium ferrocyanide, 2 mM $MgCl_2$, 1 mg/ml X-gal in PBS.

Spontaneous blastogenesis in peripheral blood and spleen. Seven days after virus infection, whole blood samples of animals treated with control virus (rVV4) of different dosage (10, 10^2, 10^3 and 10^7 PFU) were collected in heparinized tuberculin syringes via cardiac puncture immediately after euthanasia. Spleens were removed and smashed in RPMI-1640 medium before filtrated. The leukocyte counts in blood and spleen samples were performed on HESCA Hematology Analyzer (ABX Hematologie, France). Fifty μl aliquots of whole blood or spleen samples were mixed with 150 μl of complete RPMI 1640 medium and 1 μCi ^{3}H-thymidine in 50 μl of medium was immediately added. The cells were incubated for 4 h at 37°C, harvested with a multiple-sample harvester, and the amount of ^{3}H-thymidine incorporated into cell DNA was counted in a liquid β-scintillation counter (E&G Wallac Inc., MD). The results are expressed as disintegrations per minute (dpm)/10^6 cells.

Flow cytometry analysis. Four and nine days after virus infection, whole blood sample from each animal was collected in heparinized tuberculin syringes via cardiac puncture immediately after euthanasia. Spleens were removed and smashed in RPMI-1640 medium before filtrated. The leukocyte counts in blood and spleen samples were performed on HESCA Hematology Analyzer (ABX Hematologie, France). 50 μl of each sample was then stained with appropriate fluorescent-conjugated monoclonal antibodies (CD_{45}, CD_{19}, PAN-NK, NK1.1, TCR-β, MAC-1) (PharMingen, San Diego, CA). Stained cells were washed and analyzed using a FACSCalibur machine with CellQuest software (Becton Dickinson, Manfield, MA).

Virus dissemination. The dissemination of VV in immuno-compromised nude mice was assessed using the highly sensitive β-galactosidase luminometric assay. Tumor and organs were removed at day 2 and 9 after virus injection and smashed

a

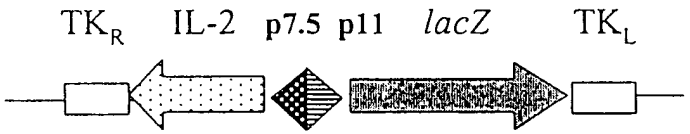
TK$_R$ IL-2 p7.5 p11 *lacZ* TK$_L$

b

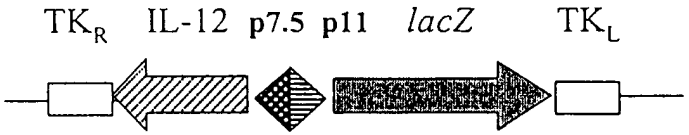
TK$_R$ IL-12 p7.5 p11 *lacZ* TK$_L$

c

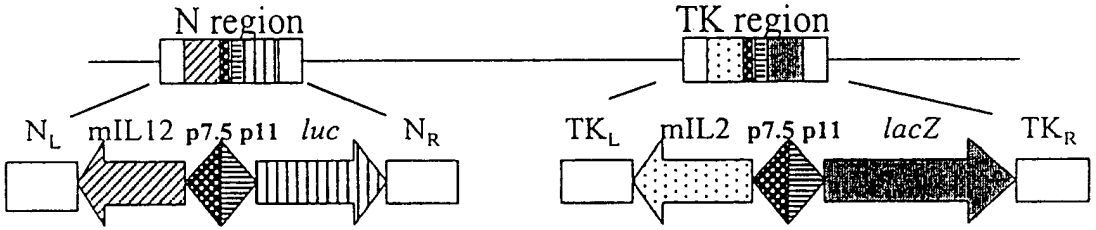
N region
TK region
N$_L$ mIL12 p7.5 p11 *luc* N$_R$
TK$_L$ mIL2 p7.5 p11 *lacZ* TK$_R$

d

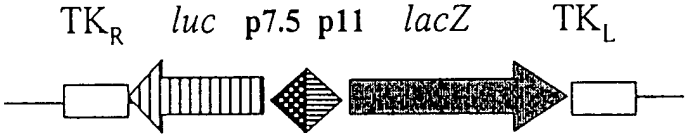
TK$_R$ *luc* p7.5 p11 *lacZ* TK$_L$

in appropriate volume of lysis buffer. The extract was centrifuged at 13,000 rpm for 5min to remove tissue debris. A 20 µl sample of extract was assayed using Galacto-light Plus™ kit (Tropix, Bedford, MA). Bioluminescence was measured by ML300 microplate luminomiter (Dynatech Laboratories, Inc., Chantilly, VA). Results are expressed as light units (LU)/mg organ wet weight [16].

Statistical analysis. The data were analyzed using one-way analysis of variance, Tukey's HSD test (SPSS). A P value of <0.05 was considered to indicate significant differences among groups.

RESULTS

Cytokine expression *in vitro* and *in vivo*. Recombinant vaccinia viruses induced efficient synthesis of mIL-2 and mIL-12 in infected cells both *in vitro* and *in vivo*. In C6 glioma cells infected *in vitro* proteins were measured as early as 6 h after virus infection reaching the peak of cytokine production between 24 and 48 h with the yield of 600ng/10^6cells of mIL-2 and 1800ng/10^6cells of mIL-12 (Fig.2). Cytokine expression was still detectable at 96 h. The efficiency of cytokine expression of the construct rVV-2-12 carrying both mIL-2 and mIL-12 genes in different regions of the same VV genome was similar to that after infection with virus rVV-mIL2 or rVV-mIL12 alone. Thus, the rVV-2-12 virus expressed both cytokines at the same time without influencing the gene expression. The expression of two reporter genes (*lacZ and luc*) incorporated into the rVV-2-12 genome along with cytokine genes were not interfered either.

Local intratumoral injection of rVVs in some animals directed cytokine expression even at doses as low as 10 and 10^2 PFU of viruses. In higher dose groups, almost all tumor extracts showed efficient cytokine expression measured by ELISA assay. Highest level of IL-2 (56 pg/mg) and IL-12 (825 pg/mg) at tumor site and in circulation (5.5 ng/ml and 88.7 ng/ml, respectively) was observed on day 2 after injection of 10^7 PFU viruses (Table 1, 2). On days 8, IL-2 was still detectable in the tumor but at lower level, while IL-12 was found both in

Table 1. mIL-2 expression in tumor and plasma

Groups	Tumor (pg/mg) Day 2	Tumor (pg/mg) Day 8	Plasma (ng/ml) Day 2	Plasma (ng/ml) Day 8
rVV-mIL2 10^5PFU	44.6±5.7	2.5±1.0	6.9±0.5	0
rVV-mIL2 10^6 PFU	60.6±10.2	5.8±0.7	6.4±1.1	0
rVV-mIL2 10^7 PFU	56.6±7.2	4.9±1.1	5.5±0.8	0

A

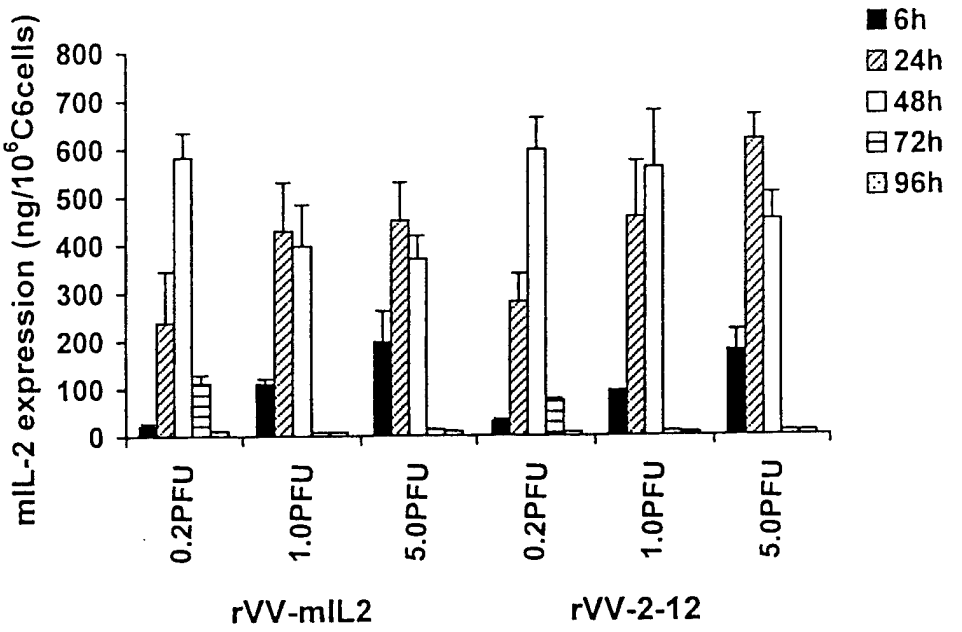
mIL-2 expression (ng/10^6C6cells)
800
700
600
500
400
300
200
100
0
6h
24h
48h
72h
96h
0.2PFU
1.0PFU
5.0PFU
0.2PFU
1.0PFU
5.0PFU
rVV-mIL2
rVV-2-12

B

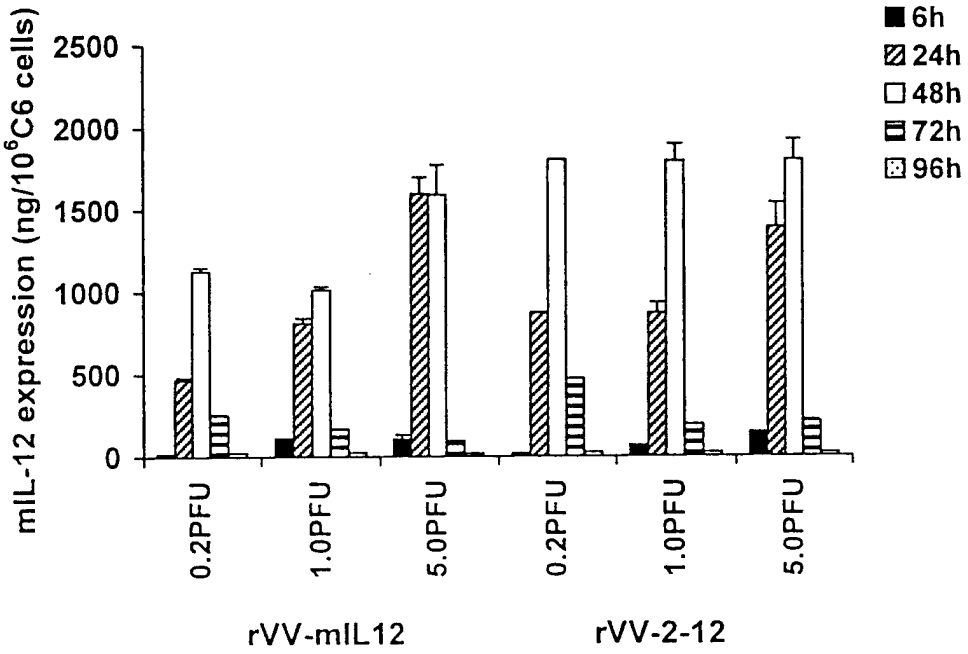
mIL-12 expression (ng/10^6C6 cells)
2500
2000
1500
1000
500
0
6h
24h
48h
72h
96h
0.2PFU
1.0PFU
5.0PFU
0.2PFU
1.0PFU
5.0PFU
rVV-mIL12
rVV-2-12

Table 2. mIL-12 expression in tumor and plasma

Groups	Tumor (pg/mg) Day 2[a]	Tumor (pg/mg) Day 8	Plasma (ng/ml) Day 2	Plasma (ng/ml) Day 8
rVV-mIL12 10^5PFU	474.9±54.5[b]	98.9±26.0	62.3±25.0	28.1±14.0
rVV-mIL12 10^6 PFU	285.3±25.4	94.5±26.5	31.8±8.4	41.1±0.7
rVV-mIL12 10^7 PFU	825.2±106.2	105.3±2.1	88.7±4.5	41.4±7.0

a days after rVV i.t injection
b Mean ± SEM

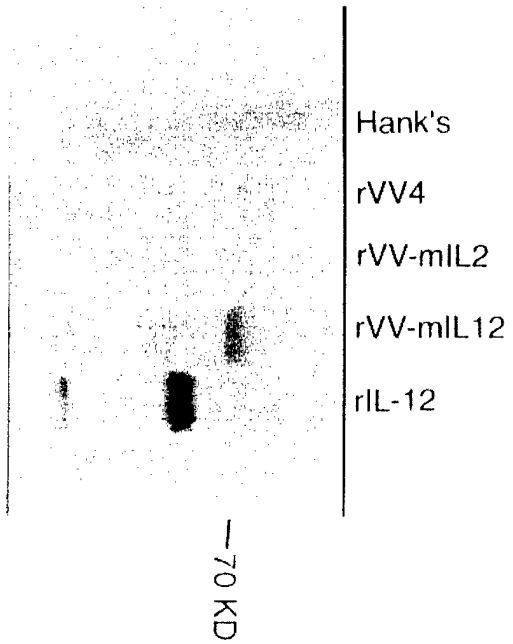
Hank's
rVV4
rVV-mIL2
rVV-mIL12
rIL-12
70 KD

tumor and blood. The difference in cytokine expression levels at high doses of 10^5–10^7 PFU was insignificant. At the same MOI, IL-12 expression in terms of protein production was found to be significantly higher than IL-2. In control groups, IL-2 and IL-12 on days 2 and 8 were barely detectable, if any.

Western blot analysis confirmed that IL-12 fusion protein expressed by rVV-mIL12 in tumor remained authentic and intact under reducing condition, whereas control recombinant IL-12 (rIL-12) with heterodimer structure dissociated to p35 and p40 subunits (Fig. 3). No endogenous mIL-12 was detected in Hank's, rVV4 and rVV-mIL2 groups.

Cytokines cause tumor inhibition. To determine the efficacy of different doses of VV administered by *i.t.* injection we used seven graded doses from 10 to 10^7 PFU on an established nude mice glioma model. Dosage from 10^2 to 10^7 PFU of both rVV-mIL2 and rVV-mIL12 demonstrated significant growth inhibition of subcutaneous glioma ($P<0.05$) with tumor volumes near or over 50% smaller than that treated with the control virus (Fig.4). No significant difference was observed between IL-2 and IL12 treatment groups. Injection of 10 PFU of rVVs did not produce anti-tumor effects. High dose of control virus also exhibited an effective inhibition of tumor growth.

Except for animals treated with 10 PFU of rVV-mIL12, in all rVV-mIL2 or rVV-mIL12 treated groups we observed signs of cytokine-associated toxicity. High dosage groups (10^5 to 10^7 PFU) resulted in high mortality rate with an approximately 60% survival on 8 day after rVV injection. Low virus doses (10 to 10^4 PFU) resulted in 100% survival at the same time but some animals failed to gain weight indicating on possible cytokine mediated side effect. Combination therapy with rVV-2-12 was lethal for mice even at 10^3-10^5 PFU with 100% mortality on day 5. At 10 PFU, 30% animals died on day 5.

Virus infection *in vivo*. To examine the efficiency of low dose (10-10^2 PFU) VV infection, tumor sections were prepared on day 7 after *i.t.* injection of rVV and stained with X-gal. No positive staining was found in all 10 PFU groups,

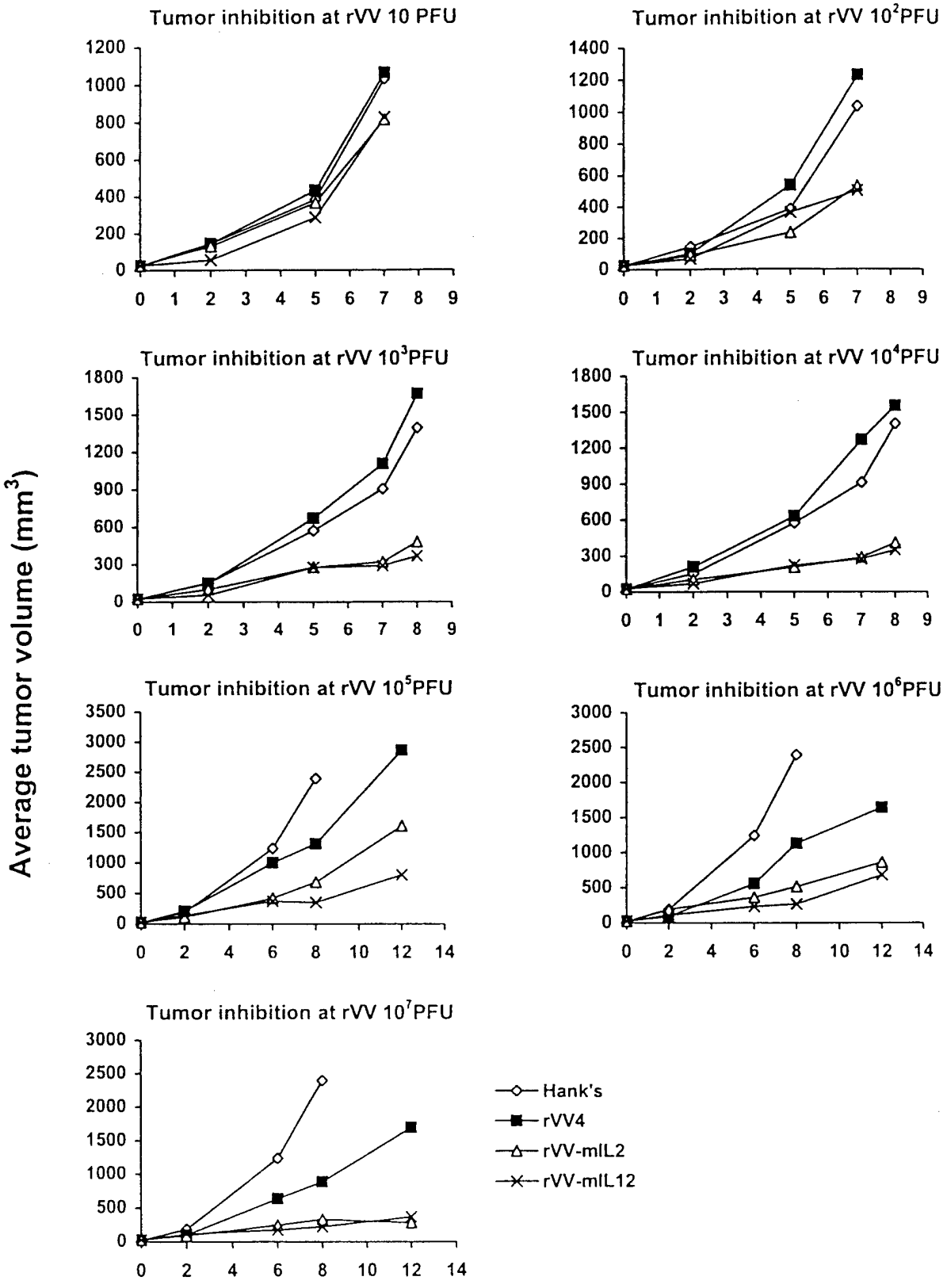
Tumor inhibition at rVV 10 PFU
Tumor inhibition at rVV 10²PFU
Tumor inhibition at rVV 10³PFU
Tumor inhibition at rVV 10⁴PFU
Tumor inhibition at rVV 10⁵PFU
Tumor inhibition at rVV 10⁶PFU
Tumor inhibition at rVV 10⁷PFU
Average tumor volume (mm³)
Days after virus injection
Hank's
rVV4
rVV-mIL2
rVV-mIL12

0.5 cm

Hank's

rVV4 100 PFU

rVV-mIL2 100 PFU

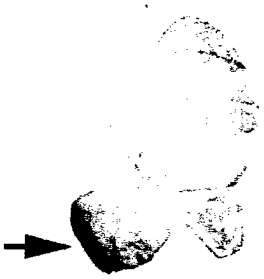

rVV-mIL12 100 PFU

indicating that either virus particles were cleared from the tumor by host immune system, or the level of gene expression was very low. Sections of tumors treated with 10^2 PFU rVV4, rVV-mIL2 and rVV-mIL12 exhibited *lacZ* activity within 2 h after adding the substrate (Fig.5). These findings showed that as low as 100 viral particles of VV constructs were sufficient to detect productive infection of tumor tissues.

Immune response to vaccinia virus vector. The immune response induced by rVV4 vector itself was characterized by blood and spleen blastogenesis study and NK cell analysis. Peripheral blood leukocytes from 10^7 PFU group exhibited significantly greater spontaneous blastogenesis compared to saline tumor control ($P<0.05$), while lower doses (10-10^3 PFU) produced some increase but the difference was statistically insignificant (Fig.6). High increase in NK cells ($P<0.05$) was detected in blood after treatment with 10^3 PFU of rVV4 (Fig.7). However, no obvious changes in number of NK cells and in spontaneous blastogenesis were found in spleen after *i.t.* injection of rVV4 at any doses.

Virus dissemination. Using a virus titration method we previously demonstrated that this strain of VV is safe for nude mice even after *s.c.* inoculation of 10^8 PFU[36]. Here, we used a sensitive chemiluminescent method to detect β-galactosidase expression in different organs and tumors after *i.t.* injection of 10^7 PFU of VV. All recombinant viruses in this experiment carried *lacZ* gene driven by VV promoter p11. Measured level of β-galactosidase expression showed that the viral proliferation at tumor injection site could be detected on day 2 after virus injection (rVV4: 12.1 LU/mg; rVV-mIL2: 17.9 LU/mg; rVV-mIL12: 11.9 LU/mg). Virus replication significantly decreased by day 9 (rVV4: 3.83 LU/mg; rVV-mIL2: 0.61 LU/mg; rVV-mIL12: 4.45 LU/mg).

Although on day 2 the *lacZ* gene expression was detected in organs (lung, liver, kidney), but the reporter expression was several orders of magnitude less than in tumor tissue. On day 9, the virus replication was barely detectable in these organs and animals showed no signs of side effects or disease.

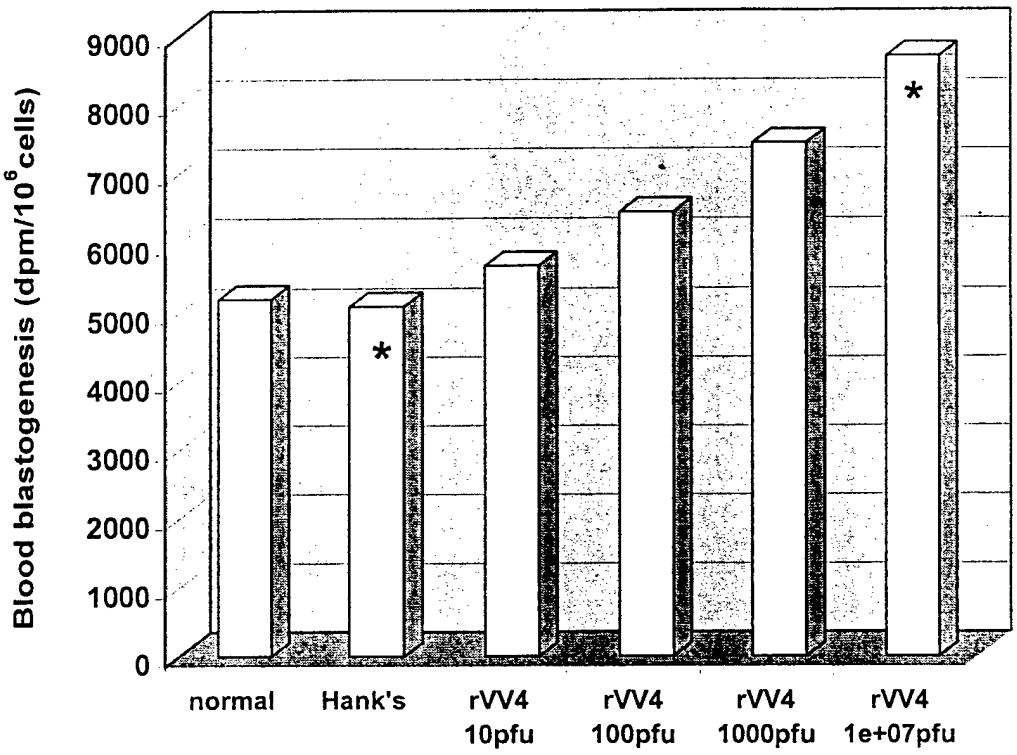
Blood blastogenesis (dpm/10^6cells)
9000
8000
7000
6000
5000
4000
3000
2000
1000
0
*
*
normal
Hank's
rVV4 10pfu
rVV4 100pfu
rVV4 1000pfu
rVV4 1e+07pfu

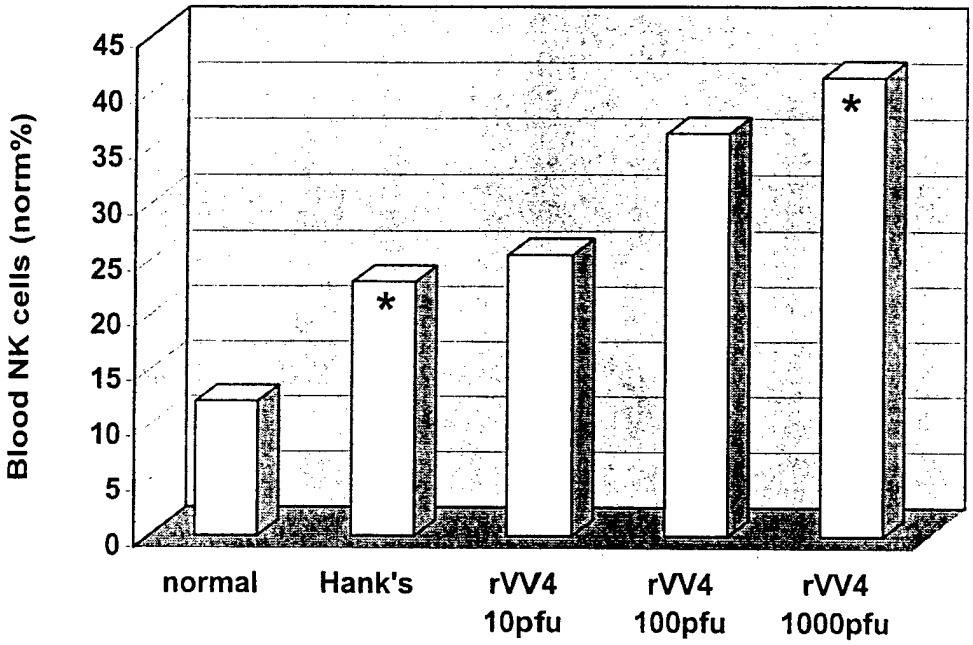
Blood NK cells (norm%)
45
40
35
30
25
20
15
10
5
0
*
*
normal
Hank's
rVV4 10pfu
rVV4 100pfu
rVV4 1000pfu

The interference of transgene expression by coinfection with two different rVVs. Over expressed p53 or IL-2 was found in cells infected with rVV-p53 or rVV-mIL2, with peak expression around 24-48 h. The expression of these two proteins was reduced when cells were coinfected with rVV-p53 and rVV-mIL2 at the same multiplicity of infection (Fig.8, 9). Interestingly, the p53 function seemed not to be interfered. As shown in Fig.10, DNA fragmentation induced by rVV-p53/rVV-mIL2 had no significant difference as compared with rVV-p53 treatment alone. Cells infected by control virus (rVV_2, rVV_4) also showed certain level of apoptosis, but several magnitudes lower than rVV-p53-treated cells.

To determine the influence of high dose virus on the infection and replication ability of low dose virus, C6 cells were co-infected with rVV_4/wtVV at ratio 1 to 100. After exposed to viruses for 24 h, only a tiny proportion of cells were infected by rVV_4 and showed β-galactosidase expression (5.70±0.04 RLU/10^6 cells) (Fig.11). Infection of cells with rVV_4 alone, however, resulted in a significant increase in the expression level of β-galactosidase (111.9±1.31 RLU/10^6 cells). These data indicate that high dose virus could inhibit low dose virus replication if two viruses were combined.

Combined p53 and cytokine therapy of glioma. Our previous data showed 10 PFU rVV-mIL2 or rVV-mIL12 caused minimum cytokine side effect, but did not induce reduction of tumor size. This study was designed to test whether this low dose cytokine treatment can enhance the antitumor effect of p53.

Different p53/cytokine combinations were injected i.t. to athymic nude mice. At 9 days post-injection, tumors treated with rVV-p53/rVV-mIL12 and rVVp53/rVV-2-12 were significantly growth inhibited than those treated with single agent ($P<0.05$). The mean tumor volumes of these groups are shown in Fig.12. rVV-p53/rVV-mIL2 therapy did not show advantage over rVV-p53 treatment alone ($P=0.078$), but tumor size was significant smaller than that in rVV-mIL2 group ($P<0.05$). No significant differences in mean tumor volume were noted between rVV-p53 (1537.3±309.9 mm^3) and rVV_2 control

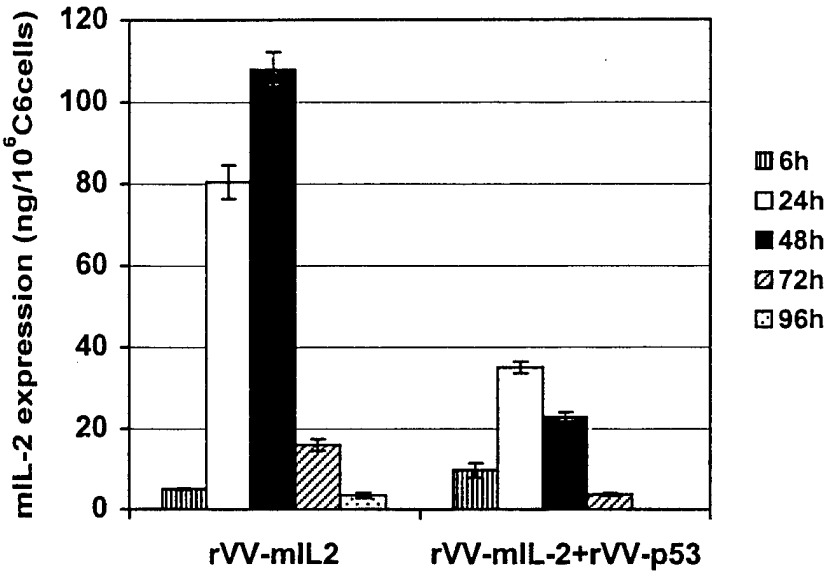
mIL-2 expression (ng/10^6C6cells)
120
100
80
60
40
20
0
rVV-mIL2
rVV-mIL-2+rVV-p53
6h
24h
48h
72h
96h

A

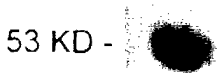

B

(1745.5±355.9 mm^3) group at any time point, although these two groups showed significantly reduced tumor growth in comparison with saline control.

Treatment with single injection of 10 PFU rVV-mIL2, rVV-mIL12 or rVV-2-12 appeared to result in no tumor inhibition. rVV-mIL2 and rVV-mIL12 i.t. injection induced light cytokine side effect at the dose of 10 PFU, but rVV-2-12 was still toxic to nude mice. 25% animals in rVV-2-12-treated group died 5-6 days after virus injection. Interestingly, in rVV-p53/rVV-2-12 combination group, 100% animals survived until the day of euthanasia.

rVV-mediated production of transgenes in tumors. Overexpressed p53 protein could be detected at least 9 days after virus injection by immunohistochemistry in rVV-p53 and p53/cytokine combination groups (Fig.13A). Strong signal was mostly around or in the area corresponding to necrosis area by H&E staining. P53 expression level was not interfered by p53/cytokine combined therapy. Tumor treated with rVV_2 control virus showed negative result.

IL-2 expression was detected in tumor 4 days after virus injection in 2 of 4 animals treated with rVV-2-12 (18.3 ng/g, 3.4 ng/g) and 1 of 4 animals treated with rVV-p53/rVV-2-12 (5.67 ng/g). At day 9, only one animal in rVV-p53/rVV-2-12 showed IL-2 expression in tumor (6.6 ng/g).

IL-12 expressed in tumor could be measured in almost all animals treated with rVV-mIL12, rVV-2-12, rVV-p53/rVV-mIL12 and rVV-p53/rVV-2-12, with the highest level 57.3 ng/g at day 4. Expression could still be detected in half of the animals in these groups at day 9, with the highest 41.6 ng/g.

Apoptosis induced by recombinant VV. A portion of TUNEL-stained cells was clearly observed in rVV_2, rVV-p53, and p53/cytokine-treated groups 9 days after virus injection (Fig.13B). These cells exhibited apoptotic morphology, containing strongly labeled condensed nuclei and micronuclei. TUNEL-positive cells mostly gathered around the tumor necrosis area. There is no significant difference between control rVV_2 group and VV carrying p53 groups. Saline tumor control showed few apoptotic staining.

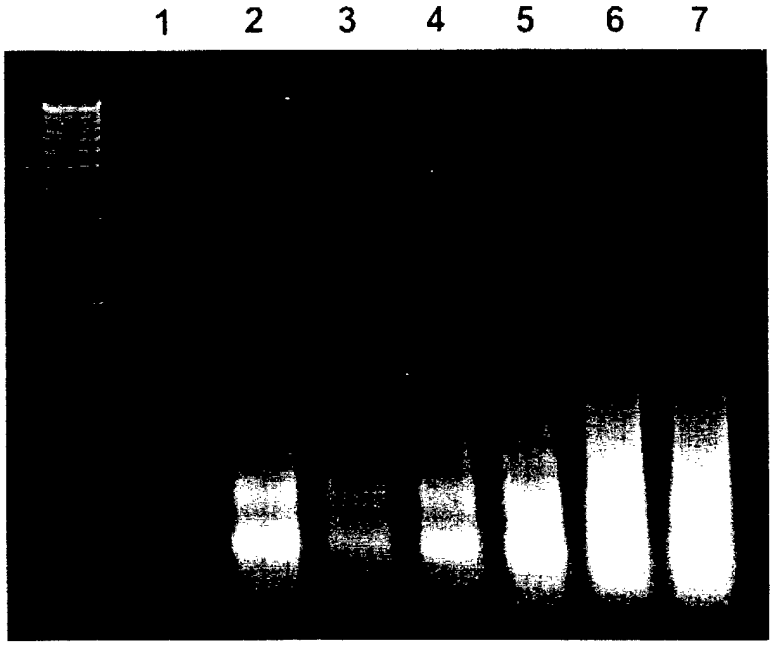
1
2
3
4
5
6
7

Characterization of host antitumor immune response. The involvement of macrophages and NK cells in tumor rejection was analyzed by flow cytometry. Blood samples 4 days following single i.t. injection of rVV-p53/rVV-2-12 showed a distinct increase in NK cell population as compared with all other treatment groups ($p<0.05$). No statistical difference in NK cells was noted among saline control, rVV_2 control, rVV-mIL2, rVV-mIL12, rVV-2-12, rVV-p53/rVV-mIL2 and rVV-p53/rVV-mIL12 groups. At day 9, no difference was observed among all groups. Compared to saline control, the percentage of macrophage (MAC-1 positive cells) doubled in all high dose ($2x10^7$ PFU) rVV-treated animals both at day 4 and day 9, indicating that macrophage stimulation was caused by high dose application of VV vector *per se*. Cell suspensions isolated from spleen showed no significant differences in NK cells and macrophages among groups at any observed time points. NKT cell ($NK1.1^+$ $TCR\text{-}\beta^+$), which was previously reported to contribute to IL-12-induced tumor inhibition[17], did not have obvious changes in our specific tumor model. No proliferation of B cells was observed in all groups.

Intratumoral induction of IFN-γ and TNF-α. An obvious local IFN-γ production was found in some tumors 4 days after treated with rVV-mIL12 (891.4 pg/g), rVV-2-12 (5000 pg/g), rVV-p53/rVV-mIL12 (600 pg/g) and rVV-p53/rVV-2-12 (1227.3 pg/g), whereas saline control, rVV_2, rVV-mIL2 and rVV-p53/rVV-mIL-2 showed low expression (less than 30 pg/g). The striking difference in IFN-γ expression of IL-12 therapy versus IL-2 therapy supported the fact that IFN-γ is a characteristic of IL-12 treatment.

Compared with control groups and rVV-mIL-2, rVV-mIL12 groups (less than 10 pg/g), at least 6-fold increase in TNF-α expression was detected in some of animals following rVV-2-12 (74.1 pg/g), rVV-p53/rVV-mIL2 (91.2 pg/g), rVV-p53/rVV-mIL12 (70.5 pg/g) and rVV-p53/rVV-2-12 (332.9 pg/g) treatment. A slight increase was found in rVV-p53 group (23.1 pg/g).

A

wtVV 5 PFU

rVV-mIL2 0.05 PFU

wtVV 5 PFU + rVV-mIL2 0.05 PFU

B

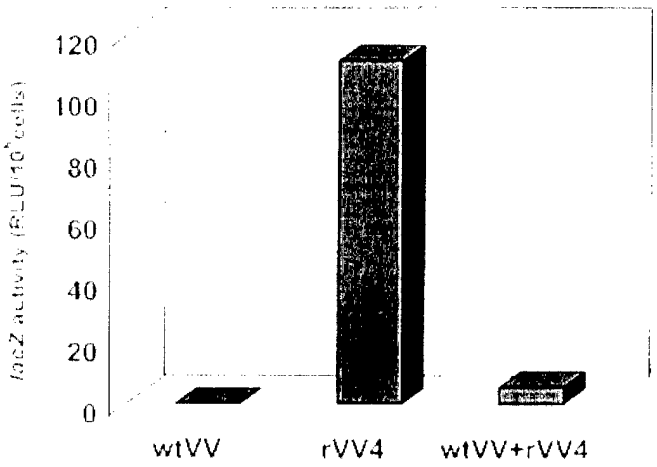

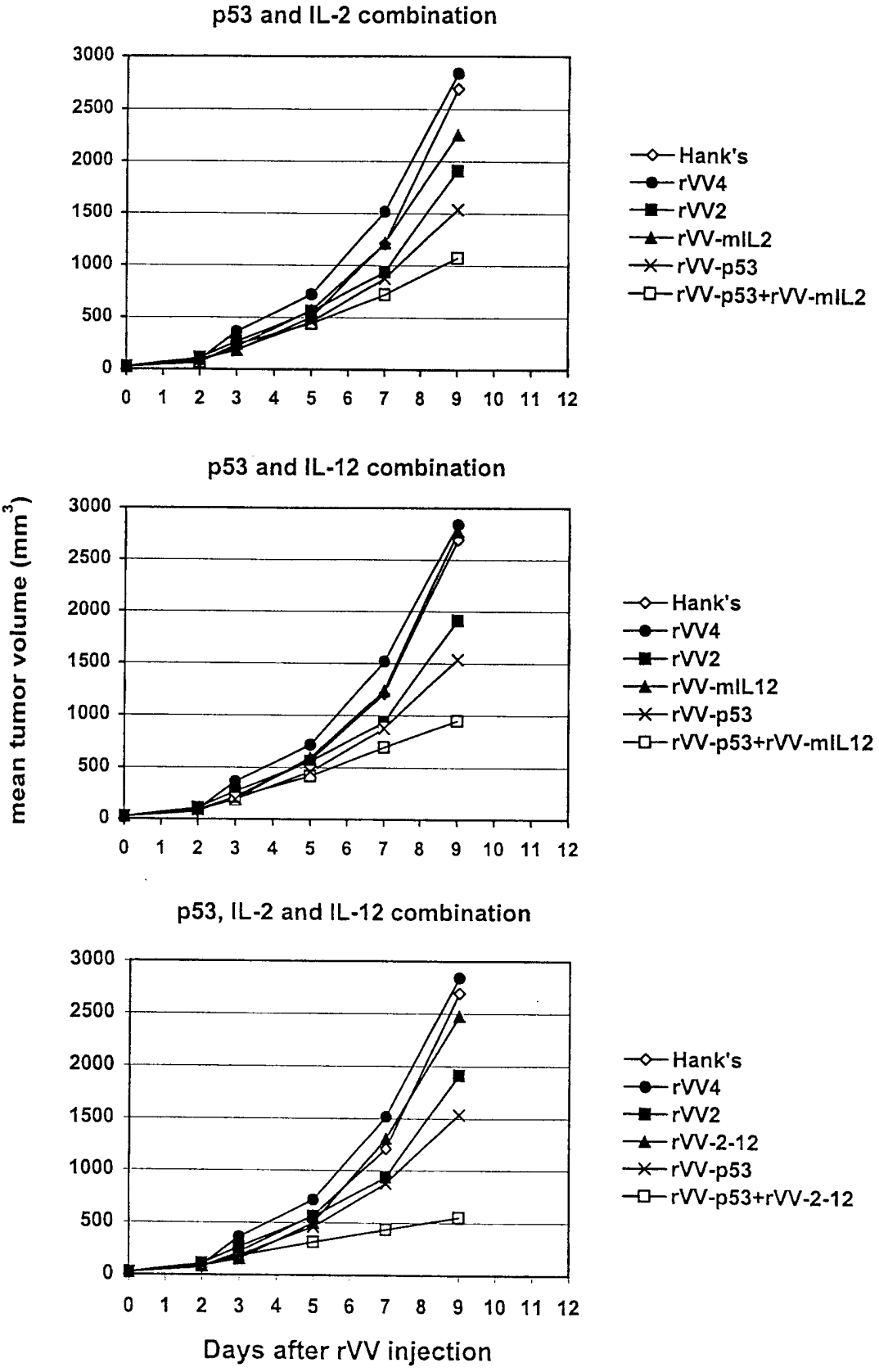
p53 and IL-2 combination
3000
2500
2000
1500
1000
500
0
0 1 2 3 4 5 6 7 8 9 10 11 12
Hank's
rVV4
rVV2
rVV-mIL2
rVV-p53
rVV-p53+rVV-mIL2
p53 and IL-12 combination
mean tumor volume (mm3)
3000
2500
2000
1500
1000
500
0
0 1 2 3 4 5 6 7 8 9 10 11 12
Hank's
rVV4
rVV2
rVV-mIL12
rVV-p53
rVV-p53+rVV-mIL12
p53, IL-2 and IL-12 combination
3000
2500
2000
1500
1000
500
0
0 1 2 3 4 5 6 7 8 9 10 11 12
Hank's
rVV4
rVV2
rVV-2-12
rVV-p53
rVV-p53+rVV-2-12
Days after rVV injection

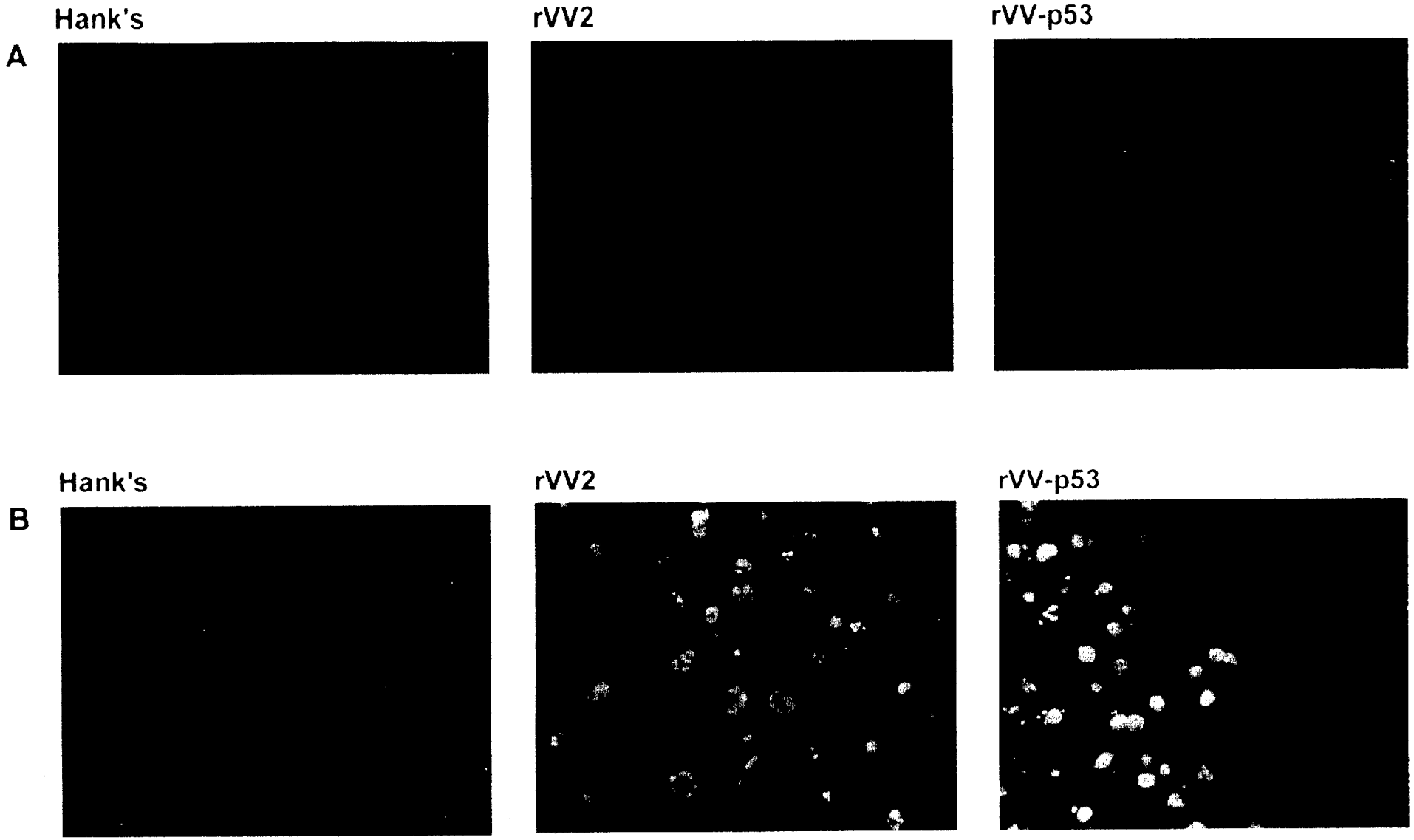
Hank's
rVV2
rVV-p53
A
Hank's
rVV2
rVV-p53
B

Inactivated vaccinia virus-mediated gene therapy. To make VV replicative deficient, the recombinant viruses were treated with psoralen and irradiated with long-wave UV-light as described in the Materials and Methods. Inactivation of VV replication and abolishing of cytopathic effect were achieved by incubating of virus ($3x10^8$ pfu/ml) with 1 μg/ml of psoralen and UV irradiation for 5 min, resulting in almost 100% inhibition of replication. Cytopathic effects of replicating rL-15 and inactivated iL-15 viruses were estimated by plaque assay on CV-1 cells (Fig. 14). No virus plaques were observed in the cells infected with iL-15 virus even at m.o.i. 30 pfu/cell as well as in mock-infected cells. A numerous viral plaques were visualized in the cells infected with live rL-15 virus after 10^{-5} dilution (m.o.i. = 0.0003 pfu/cell).

To compare the promoter strength and duration of luciferase expression by replicating versus inactivated viruses, we constructed VV recombinants with reporter genes under the control of either early P13 or early/late PE/L promoters (Fig. 15). CV-1 cells were infected either with replicating or inactivated viruses at an m.o.i. 5, and, at indicated time post-infection, cells were evaluated for luciferase activity (Fig. 16). Surprisingly, after infection of cells with non-replicating iL-5 virus the expression of P13-driven luciferase was higher as compared to the expression by replicating rL-5 virus demonstrating high efficiency of the early promoter in the cells infected with PUV-inactivated VV. Thus, the UV-inactivation enhanced the early gene expression. Cells infected with either replicating or non-replicating form of L-15 construct exhibited similar level of efficacy of the *luc* gene expression driven by vaccinia promoter PE/L. However, at 18 h post-infection, luciferase activity in iL-15 virus infected cells was higher than in rL-15 infected cells. Constructs containing *luc* gene under the control of P13 promoter expressed low level of the reporter compared with PE/L promoter. Therefore, the potent PE/L vaccinia promoter was chosen to construct a virus expressing wild-type human *p53* gene (Fig. 15).

ELISA was used to analyze PUV-vaccinia-mediated expression of the p53 in C6 glioma cells. High level of p53 protein production was observed on days 3-7 after the infection iVV-TK-53 virus (Fig. 17). Although PUV-inactivated virus-

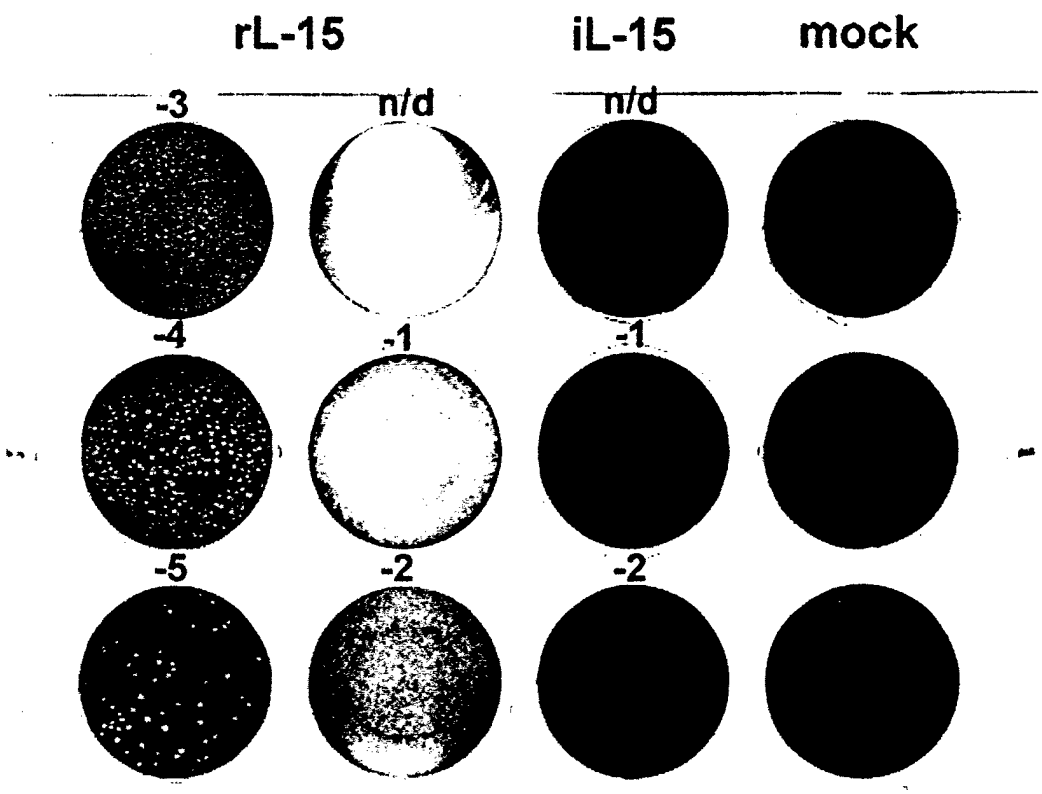
rL-15
iL-15
mock
-3
n/d
n/d
-4
-1
-1
-5
-2
-2

L-5

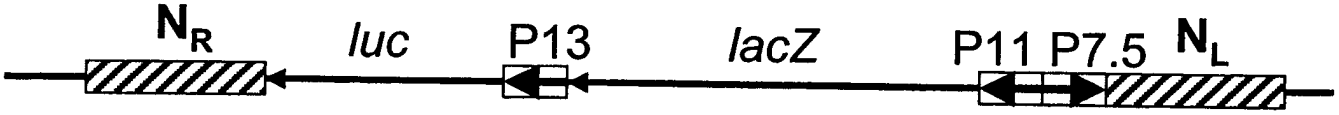

L-15

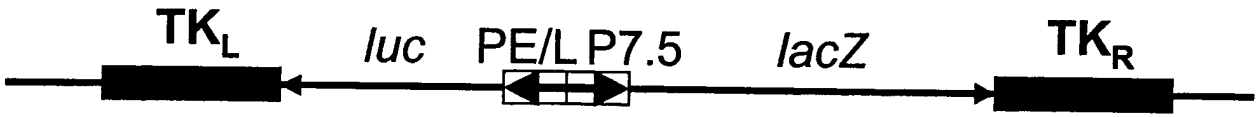

VV-TK-53

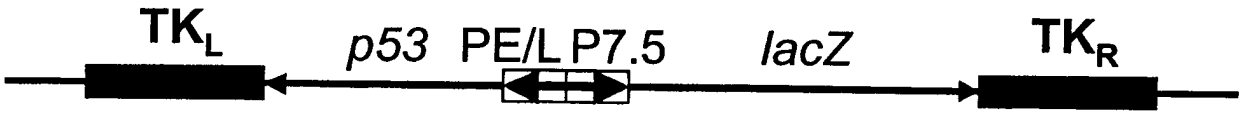

Luciferase expression

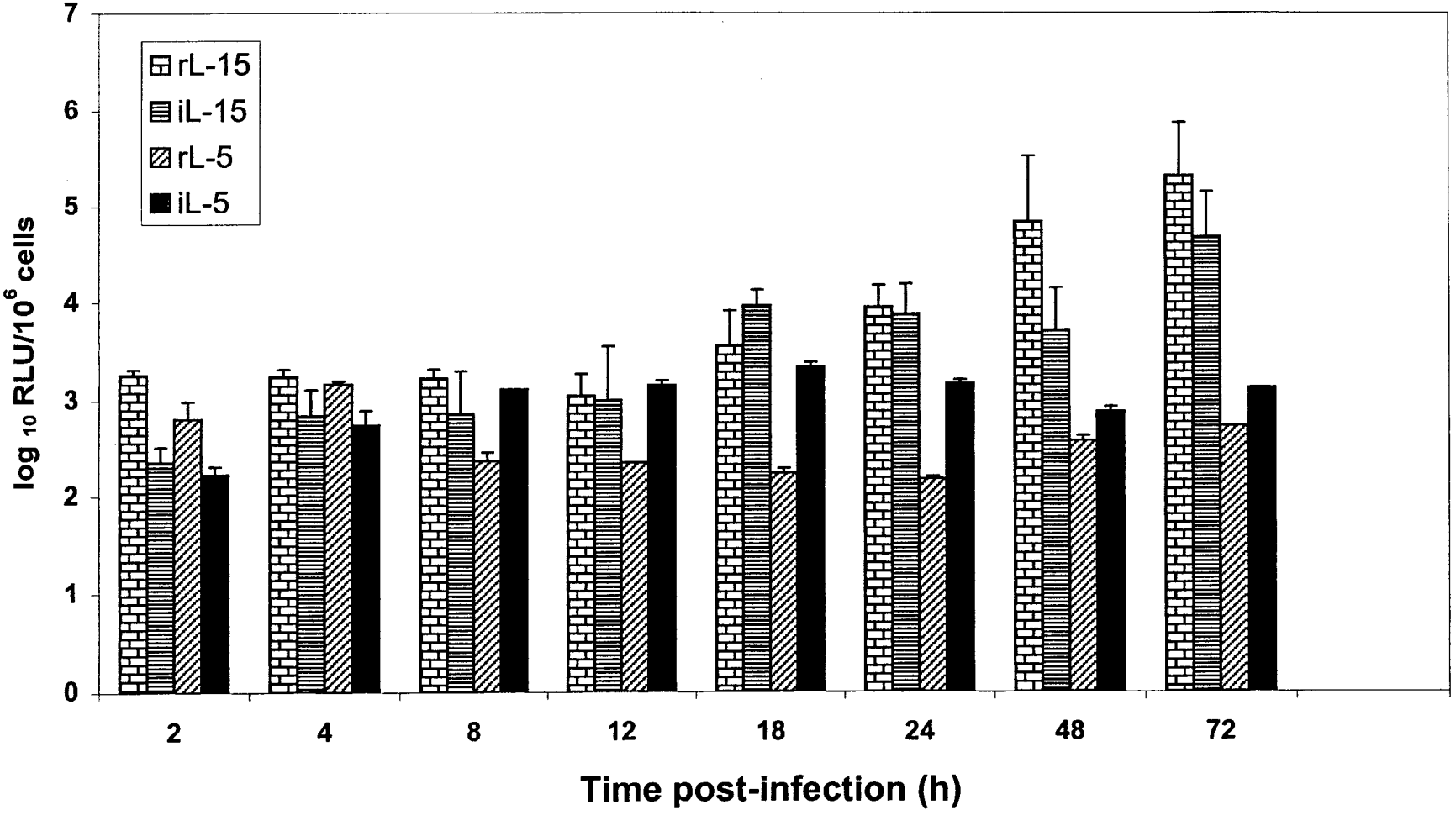

mediated expression is limited to early genes, the expression continues for extended period of time, up to 7 days and was still detectable on day 9.

To test the inhibition of C6 glioma cell growth *in vitro* by inactivated recombinant vaccinia virus carrying the human *p53* gene the trypan blue exclusion assay was used. C6 cells were incubated with iVV-TK-53 or iL-15 control viruses (m.o.i. =5) and the number of live C6 cells were determined. The number of iVV-TK-53-infected live cells by day 2 significantly dropped (Fig. 18), and by day 7 less than 20% of all plated cells survived the treatment. In contrast, C6 cells infected with iL-15 control virus or mock-infected cells continued to divide. The pattern and kinetics of p53 expression correlated with iVV-TK-53-mediated cell growth inhibition.

Apoptosis was determined by *in situ* labeling of fragmented DNA (TUNEL). Cells infected with iVV-TK-53 virus showed numerous apoptotic bodies (Fig. 19), while mock-infected cells failed to show morphological changes at all; some apoptosis was observed in the cells infected with control iL-15 virus.

To determine the effect of iVV-TK-53 in animals, $3x10^6$ C6 cells infected *ex vivo* with different m.o.i. of PUV-inactivated viruses were injected subcutaneously into nude mice. The control mice were inoculated with mock-infected cells or infected with control iL-15 virus. Infection the C6 glioma tumor cells *ex vivo* with iVV-TK-53 virus moderately inhibited the tumor growth in athymic mice (Fig. 20).

DISCUSSION

In the first part of the study we analyzed the efficacy of immunotherapy by local delivery of low dose of recombinant Lister VV carrying IL-2 or fused subunits of IL-12 in an athymic mice and C6 glioma xenograft model. Our *in vitro* experiments demonstrate that the constructed rVVs efficiently infect tumor cells resulting in production of authentic cytokines. The peak of cytokine synthesis was observed at 24-48 h after infection producing 600ng/10^6cells of IL-2 and 1800ng/10^6cells of IL-12. Incorporation of as many as four foreign genes into vaccinia virus did not interfere with the expression level of these genes.

Expression of p53 protein in C6 glioma cells infected with VV-TK-53

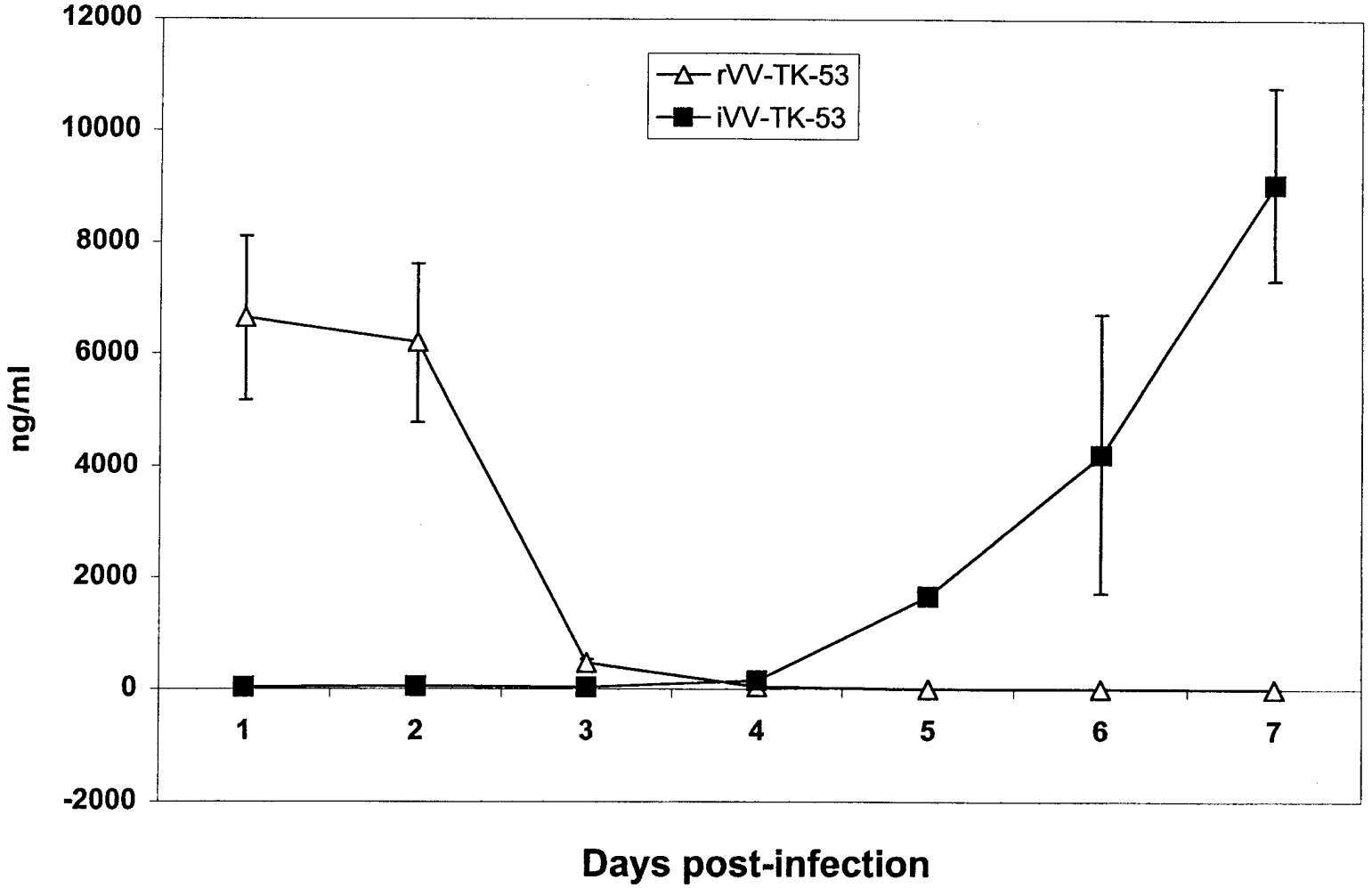

In nude mouse model we found that single intratumoral injection of as low virus dose as 10^2 or 10^3 PFU of rVV-mIL2 or rVV-mIL12 can induce significant inhibition of C6 tumor growth. Higher virus doses (10^5-10^7 PFU) also exhibited antitumor effect, however treated animals showed signs of toxicity and high mortality apparently associated with high cytokine production. Thus, virus doses of 10^2-10^3 PFU may result in sufficient production of therapeutic cytokines and immune responses for tumor immunotherapy.

Antitumor effect of virus- mediated IL-2 and IL-12 immunotherapy has also been demonstrated in other tumor models. It was suggested that the produced cytokines activate lymphokine-activated killer (LAK) cells, NK cells and tumor infiltrating lymphocytes (TILs) [18,21,38]. IL-12 was also reported to inhibit angiogenesis indirectly through the stimulating of IFN-γ and chemokine IP-10 [39]. Analyzing the cytokine production *in vivo* we found that the maximum level of gene expression in tumors and in plasma was observed on day 2 after virus treatment. Surprisingly, the cytokine expression levels in tumors and plasma at 10^5-10^7 PFU of virus treatment varied but the differences were not significant. IL-2 expressed by rVV *in vivo* seemed to facilitate the virus elimination from the animal. The efficiency of virus reporter gene (*lacZ)* expression in tumors on day 8 after virus injection was significantly lower in IL-2 groups (0.61 LU/mg) than that with the control virus (3.83 Lu/mg) and IL-12 groups (4.45 LU/mg). This result is in agreement with data previously reported by other researchers [40-42] on IL-2-mediated inhibition of VV infection in nude mice presumably via elevated NK activity.

Since the safety of virus-based therapy is a great concern and virus dissemination is usually related to high dose of applied recombinant virus [16,43], low-dose therapy of VV may be advantageous in cancer immunotherapy by minimizing the risk of virus spread and pathogenicity. In other vector systems the applied virus doses are very high. The effective dose of the WR strain of VV in tumor immunotherapy study was 10^5 PFU [22,44], while the dose of adenovirus mediated IL-2 and IL-12 treatment was in the range of 10^7- $5x10^8$ PFU [18,19,21]. Our rVV viruses can achieve tumor inhibition at 10^2 PFU, a dose that is much

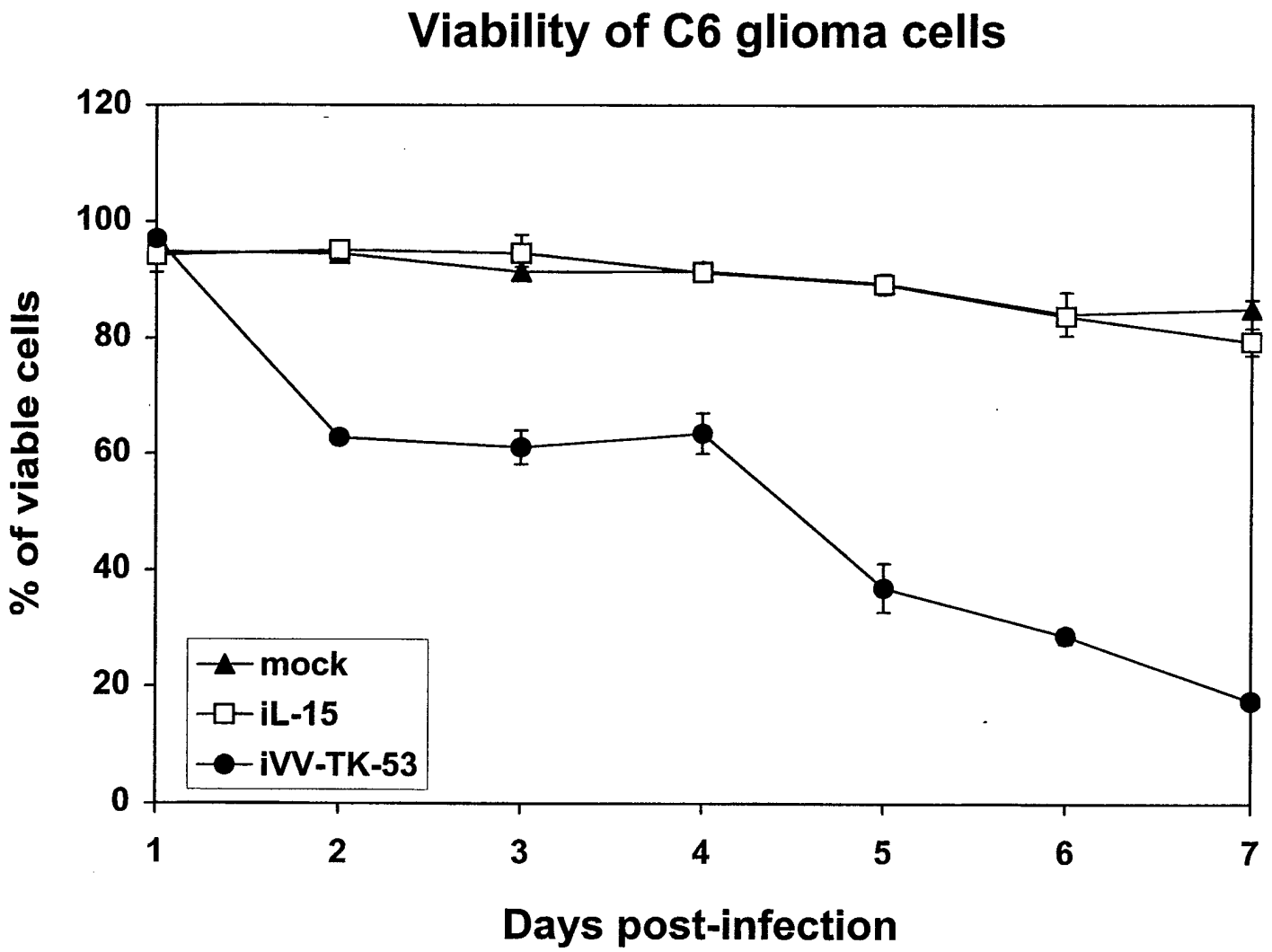
Viability of C6 glioma cells
120
100
80
60
40
20
0
% of viable cells
mock
iL-15
iVV-TK-53
1
2
3
4
5
6
7
Days post-infection

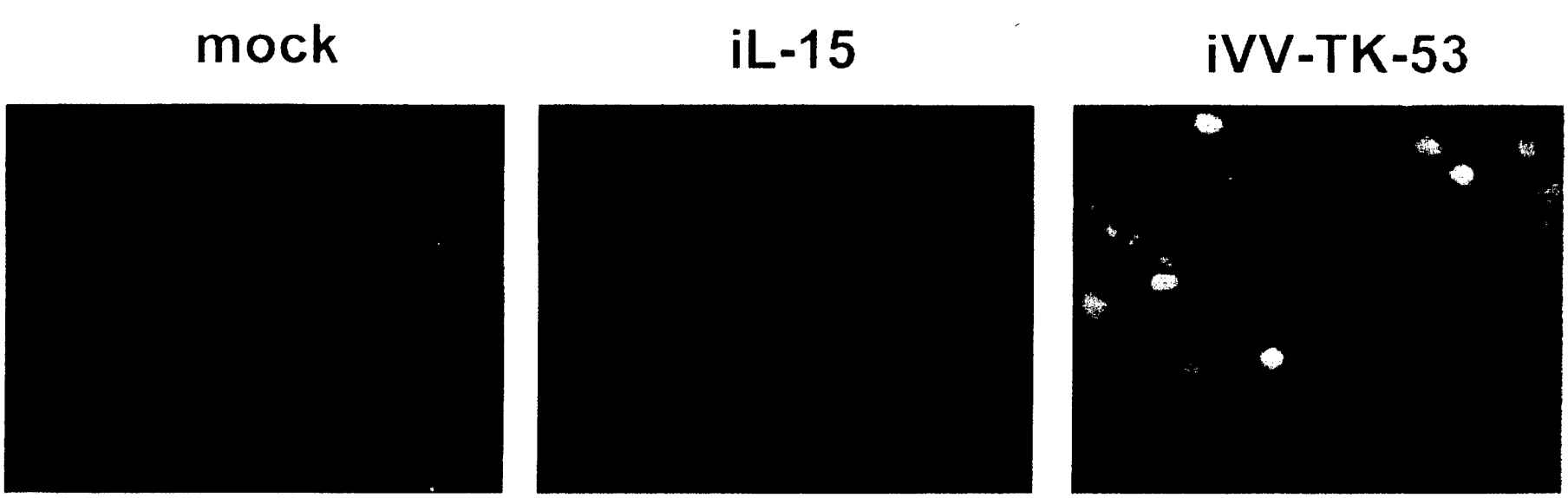
mock
iL-15
iVV-TK-53

lower as compared with that using WR VV and adenovirus vectors. Safety of our virus vector was previously demonstrated on human [4,6]. Here we confirmed that as a highly attenuated virus vector it did not exhibit obvious systemic dissemination after *i.t.* injection at dose as high as 10^7 PFU per mouse, and VV particles mostly remained localized at the injection site.

We also confirmed our previous finding that high dose of the VV vector itself can cause tumor inhibition effects [8], although its efficiency is much lower as compared to recombinant VV carrying genes of cytokines. Others reported similar results using adenovirus vector in P815 murine tumor model [21]. General increase of blood leukocytes by blastogenesis analysis and the significant increase in blood NK cell population may indicate an important role of these cells in vaccinia-mediated tumor suppression. Immunogenic virus itself may act as an adjuvant for cancer immunotherapy augmenting stronger antitumor immune response by enhancing the presentation or recognition of tumor-specific antigens and inducing the production of cytokines [45]. Preferential infection of tumor cells by virus may also contribute to stimulation of host antitumor immune response [46,47,48].

Our results indicate that low dose VV-mediated IL-2 and IL-12 delivery may induce therapeutic effects against pre-established glioma. To our knowledge, this is the first report on use of Lister strain of VV as a vector in cancer immunotherapy. Previously, we demonstrated that p53-mediated gene therapy based on this virus vector might be a new promising antitumor strategy [8]. However, single treatments itself either with cytokines or tumor suppressors may not be sufficient for elimination of tumors. Combination of immunotherapy with other antitumor gene therapy strategies, like tumor suppressor treatment, or virus-mediated inhibition of vascularization may further enhance the antitumor efficacy and contribute to the translation of these promising experimental systems into clinical practice. Combination of VV-mediated immunotherapy and p53 tumor gene therapy was addressed in our following study.

Combination gene therapy offers the therapeutic advances through the additive or synergistic effect of the therapeutic genes. P53, IL-2 and IL-12 are

Tumor growth inhibition

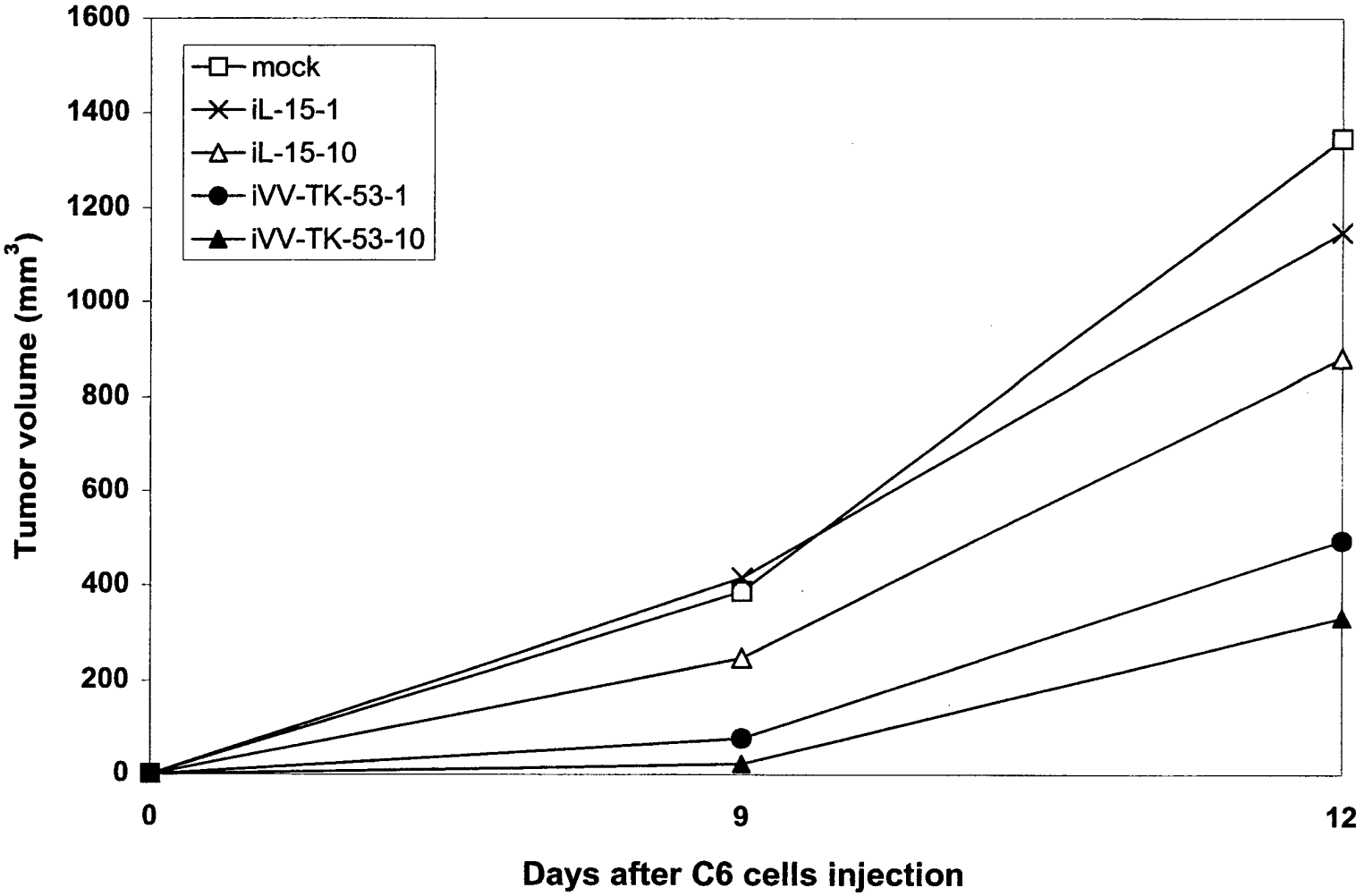

three well-known genes that have been proved to be the potent antitumor agents in animal studies and clinical trials. The combined therapy using these three genes may elicit stronger antitumor effect by synergistic interaction that increases both immune cells cytotoxicity and tumor cell apoptosis. We hypothesize several possible mechanisms of the synergistic antitumor effects. 1) Both p53 and IL-12 may decrease tumor growth through the inhibition of angiogenesis. Antiangiogenesis induced by p53 was found to be associated with the release of antiangiogenic factors, such as thrombospondin 1 and the inhibition of angiogenic factors, such as vascular endothelial growth factor [49,50]. Others have noted that IL-12 could inhibit angiogenesis by inducing IFN-γ, chemokine IP-10, and NK-cell cytotoxicity of endothelial cells [39]. 2) Formation of apoptotic bodies due to p53 over expression in tumor cells may activate the macrophages and induce local inflammatory response, which can be amplified by VV induced intratumoral IL-2 and/or IL-12 production. 3) TNF-α released from activated macrophages and NK cells can induce hemorrhagic necrosis of tumors *in vivo* through destruction of tumor vasculature [51] and induce apoptosis in sensitive tumor cells [52]. 4) IL-2 and IL-12 may enhance the immune response to p53 peptide presented by rVV-p53 infected tumor cells by activating NK cells, macrophages and B cells [53].

In this study, we demonstrated that rVV-p53/rVV-2-12 combination therapy induced a statistically significant tumor growth arrest ($P<0.01$) as compared with rVV-p53 and rVV-2-12-treated alone. Although rVV-p53/rVV-mIL12 also significantly inhibited the tumor growth (1110.8 ± 543.2 mm^3, day 9) compared to single agent-treated groups ($P<0.05$), rVV-p53/rVV-2-12 showed the strongest antitumor effect (624.2 ± 165.7 mm^3, day 9). Four days after initiation of the treatment, a significant increase of NK cell population in blood achieved with rVV-p53/rVV-2-12 therapy, but not with other treatment groups, suggested this early and short proliferation of NK cells played an important role in tumor reduction. At same time, high level of IFN-γ was detected in the tumor following rVV-p53/rVV-2-12 treatment, indicating the local activation of NK cells. It is in accordance with results of Ross and Caligiuri [54] showing that IL-2 and IL-12 combination provide a strong stimulus for IFN-γ production by NK cells. But

IFN-γ was also found in tumors of rVV-2-12-treated animals that failed to retard the tumor growth. As previous studies reported, induction of IFN-γ is necessary but not sufficient for the tumor regression [55,56].

It is possible that other cytokines and chemokines involved in significant tumor inhibition following rVV-p53/rVV-2-12 combination therapy, but the contribution of rVV-p53 is also evident. Although our study indicated that apoptosis in tumor induced by rVV-p53 did not show improvement over the control virus (rVV_2), high proliferation of NK cells in the blood related to VV-p53/rVV-2-12 treatment, but not to rVV-p53 or rVV-2-12-treated alone, played a major role in the antitumor activities of combination therapy. Even though both IL-2 and IL-12 are strong stimulus for NK cells, rVV-2-12-treated alone shows no efficiency on blood NK cell proliferation at the low dose 10 PFU. In addition, intratumoral TNF-α production was detected in p53/cytokine-treated animals, whereas p53 and cytokine single agent treatment only showed the background expression. Together, these results support a role for rVV-p53 as an antitumor effector that potentiate the immune response synergistically with rVV-2-12.

In contrast to rVV-p53/rVV-mIL12, which had a clear impact on tumor growth, rVV-p53/rVV-mIL2 did not show marked reduction of tumor volume over rVV-p53 treatment alone. Our *in vitro* and *in vivo* data demonstrated that IL-2 expression directed by rVV-mIL2 was much lower than IL-12 expressed by rVV-mIL12 when used at same MOI. The low level of IL-2 production is probably not sufficient to induce strong antitumor immune response. We found a considerable elevation of intratumoral IFN-γ in rVV-p53/rVV-mIL12 group, but not in rVV-p53/rVV-mIL2 group, which may partially explain the difference in therapeutic efficiency between two combination therapies. The possible synergistic antiangiogenesis effect by combined p53/IL-12 therapy could also partly account for the antitumor activity.

Tumor growth was also inhibited by injection of control virus (rVV_2) ($2x10^7$ PFU), although the efficiency was much lower than p53/cytokine combination. Noteworthy that an increase of blood macrophages was found in rVV_2 and all other high dose rVV-treated groups. Therefore, high dose of VV

vector *per se* is a strong inducer of macrophages, which might proliferate by responding to tumor lysis induced by oncolytic VV. The strong stimulation of macrophages may correlate with reduced tumor masses in rVV_2 control group, since this phenomena was not observed in saline control. We demonstrated in *in vitro* study that rVV-p53 and p53/cytokine could induce apoptosis in C6 glioma cell line, whereas control virus (rVV_2) had little effect. However, animal study showed the similar apoptosis effect by rVV_2, rVV-p53 and p53/cytokine treatment *in vivo*, indicating the activation of immune response by high dose virus vector may play a factor.

The ratio of the two viruses used in combination therapy may influence the therapeutic outcome, especially when the ratio of one virus is higher. Our *in vitro* data showed the great reduction in gene expression even when two recombinant viruses coinfected the cells at same MOI. When two viruses were used at higher ratio, like 1 to 100, the gene expression mediated by the low dose virus was suppressed. In animal study, we used extremely low dose (10 PFU) rVV carrying IL-2 or IL-12 to minimize the cytokine toxicity. The ratio between cytokine- and p53-expressing VV recombinant was still high although the cytokine-expressing virus was injected 24 h prior to p53-expressing VV. Surprisingly, both IL-2 and IL-12 were detectable in tumors of some treatment groups at least 9 days after virus injection. Although apparent individual difference existed, these data revealed that it is possible to combine 10 viral particles of cytokine VV recombinant with $2x10^7$ viral particles of rVV-p53. As expected, the p53 expression was not interfered by p53/cytokine combination therapy. We also found that rVV-p53/rVV-2-12 combination decreased the cytokine side effect caused by rVV-2-12. 100% animals survived and showed minimum, if any, cytokine toxicity. But rVV-2-12-treated alone resulted in 25% death during the experimental period. Our results also indicate that combination gene therapy may be much safer than cytokine therapy alone, and new combination ratio can be designed in which higher dose of cytokine-producing VV recombinants could achieve higher efficacy of antitumor therapy.

Thus, using a nude mice subcutaneous C6 glioma model, we observed the synergistic antitumor effect elicited by rVV-p53/rVV-2-12 and rVV-p53/rVV-mIL12 and also, the possibility of combining two recombinant viruses with great virus dose differences. Based on these promising data, in our future study we will test the potential of p53/cytokine combination therapy in orthotopic, syngeneic brain tumor model in central nervous system environment.

Although **PUV-inactivated virus-mediated expression** must be limited to early genes, high level of p53 protein production in infected cells was observed by ELISA assay for extended period of time, up to 7-9 days. This is in contrast with expression kinetics of early genes of replicating vaccinia virus, which is limited to early step of infection and usually ceases at the onset of DNA replication (3 to 4 h). The DNA sequence of the vaccinia PE/L promoter contains tandem early and late promoters allowing a continuous moderate level of gene expression [57]. The persistence of the early transcriptions after infection with PUV-inactivated VV shown to last as long as 7-9 days may represent the lifetime of the virus transcription machinery delivered by the virion. Apparently, PUV-inactivated VV penetrate the cells and induce core-mediated early gene expression, after which the infection process terminates probably due to lack DNA replication required for further virus development and maturation. Normally, VV virus infection is lethal and is followed by extensive cytopathic effects. However, despite the fact that UVP-inactivated virus infection is accompanied by early gene expression, the infected cells failed to exhibit any cytopathic effects, suggesting that infected cells might have survived the infection.

Apoptosis induction was correlated with increased level of p53 protein. These results rule out necrosis as a possible reason for the morphological changes of cells observed in the experiment, and argue strongly for apoptosis as the predominant underlying mechanism.

Although infection the C6 glioma tumor cells *ex vivo* with iVV-TK-53 virus was effective in inhibition of tumor growth in athymic mice, however,

comparing with live rVV-p53 the anti-tumor effect could be considered as moderate.

Conclusions

Aim 1A. Recombinant viruses can produce cytokines in tumors mobilizing an immune response to tumor cells. In this study we investigated gene expression, *in vivo* antitumor efficacy and safety of attenuated recombinant vaccinia virus carrying murine cytokine genes IL-2, IL-12 and both IL-2 and IL-12 in athymic nude mice model. Significant tumor inhibition was observed in a pre-established subcutaneously C6 glioma model using rVVs at doses in the range of 10^2-10^7 PFU. Anti-tumor effect did not depend on the dose of the rVV-mIL2 and rVV-mIL12 viruses. All constructed rVVs showed high level of cytokine expression *in vitro* and *in vivo*. Most cytokine groups with the high dose of virus treatment (10^5-10^7 PFU) showed signs of cytokine toxicity while in low dose treatment groups (10^2-10^3 PFU) toxicity was greatly reduced. The VV control vector *per se* induced tumor inhibition, but the antitumor effect was less effective as compared to rVV carrying cytokine genes. These results suggest that attenuated recombinant strains of VV at low doses may potentially be efficient vectors for the cancer immunotherapy.

Aim 1B. Combination gene therapy offers the prospect of greater therapeutic response through the synergistic effect of therapeutic genes. The aim of this study was to evaluate the efficacy of a combination of recombinant vaccinia viruses (rVV) expressing p53, IL-2 or IL-12 gene (rVV-p53, rVV-mIL2, rVV-mIL12, rVV-2-12) for the treatment of glioma. Localized treatment of subcutaneous C6 glioma in athymic mice with rVV-p53/ rVV-mIL12 or rVV-p53/rVV-2-12 resulted significant tumor inhibition compared to the single agent treatment ($P<0.05$). rVV-p53/rVVmIL2 combination did not statistically slow tumor growth. A striking elevation of NK cells in blood and IFN-γ expression in tumor were related to rVV-p53/rVV-2-12 therapy. Despite the antitumor effect of rVV-p53/rVV-mIL12, no significant immune response was detectable in circulation

but IFN-γ could be measured in tumor. The expression of IL-2, IL-12 and p53 could be detected in tumors in some treatment groups at least 9 days after virus injection, indicating 10 viral particles of cytokine VV recombinants could replicate and function despite the existence of $2x10^7$ rVV-p53 viral particles. P53 expression was not interfered by p53/cytokine combination. These data demonstrate that combination gene therapy using VV-directed p53, IL-2 and IL-12 can be a promising alternative method for glioma treatment.

Aim 2. Cells infected with PUV-inactivated virus iL-15 effectively expressed reporter under the control of the PE/L viral promoter. Non-replicating iVV-TK-53 virus overproduced p53 protein in infected cells as demonstrated by ELISA. Approximately 40% and 88% of C6 glioma cells infected with iVV-TK-53 virus underwent apoptosis on day 2 and 7, respectively, while 80% of cells infected with control virus iL-15 or mock-infected cells remained viable on day 7. In *ex vivo* experiment, infection of C6 cells with non-replicating iVV-TK-53 inhibited the tumor growth in nude mice. This simple method of generation of non-replicating vaccinia virus vectors may be applied to any attenuated or virulent vaccinia virus strain.

Additional comment:

We have successfully completed the project according to the schedule and achieved main objectives of the project:

(1) We have constructed several recombinant viruses (live and inactivated) that are effective in gene delivery and expression of therapeutic genes *in vitro* and *in vivo.* These constructs will be useful tools in further research, preclinical and clinical studies on cancer immunotherapy;

(2) We have demonstrated that vaccinia virus-mediated gene delivery cytokines is a promising alternative of anti-tumor immunotherapy. Previously we have found that vaccinia-mediated p53 treatment is effective in glioma treatment. Combination of virus-mediated immunotherapy and p53 therapy has produced a synergistic anti-tumor effect. Further studies are needed to

clarify the molecular mechanisms of cytokine- and p53-mediated anti-tumor effects.

(3) We have found that inactivated versions of vaccinia virus can effectively express foreign genes and induce therapeutic effects in treated cells. It may provide a new alternative strategy of gene therapy of genetic and somatic diseases. For tumor cancer gene therapy further studies are needed to optimize the gene delivery and expression to achieve greater anti-tumor effects.

Problems and questions raised in this study will be addressed in our following NMTB-supported studies.

References

1. Lang FF, Miller DC, Pisharody S, Koslow M, Newcomb EW. High frequency of p53 protein accumulation without p53 gene mutation in human juvenile pilocytic, low grade and anaplastic astrocytomas. *Oncogene* 1994;9:949-954.

2. Newcomb EW, Madonia WJ, Pisharody S, Lang FF, Koslow M, Miller DC. A correlative study of p53 protein alteration and p53 gene mutation in glioblastoma multiforme. *Brain Pathol* 1993;3:229-235.

3. Fujiwara T, Kagawa S, Ogawa N, Yasuda T, Tanaka N, Orita K, Cai DW, Zhang WW, Roth JA. [Recombinant virus-mediated transfer of the wild-type p53 gene is a potent therapeutic strategy for human cancer]. *Hum Cell* 1996;9:25-30.

4. Kim J, Hwang ES, Kim JS, You EH, Lee SH, Lee JH. Intraperitoneal gene therapy with adenoviral-mediated p53 tumor suppressor gene for ovarian cancer model in nude mouse. *Cancer Gene Ther* 1999;6:172-178.

5.Aspinall RJ, Lemoine NR. Gene therapy for pancreatic and biliary malignancies. *Ann Oncol* 1999;10 Suppl 4:188-192.3.

6. Moss B. Genetically engineered poxviruses for recombinant gene expression, vaccination, and safety. *Proc Natl Acad Sci USA* 1996;93:11341-11348.

7. Chernos VI, Cheliapov NV, Antonova TP, Rakhilina LE, Unanov SS, Al'tshtein AD, Zakharova LG, Fodor II, Bendukidze KA, Komarov FI. Verification of the safety, inoculability, reactogenicity and antigenic properties of a live recombinant smallpox-hepatitis B vaccine in an experiment in volunteers. *Vopr Virusol* 1990;35:132-135.

8. Timiryasova TM, Kopylova-Sviridova TN, Fodor I. Analysis of expression of the reporter genes in different regions of vaccinia virus genome. *Molecular Biology* 1993;27:392-401.

9. Fodor I. Live recombinant vaccines for humans. *Acta Biotechnol Acad Verlag* 1991;11:215-221.

10. Timiryasova TM, Kopylova-Sviridova TN, Fodor I. Analysis of expression of the reporter genes in different regions of vaccinia virus genome. *Mol Biol* 1993;27:392-401.

11. Timiryasova TM, Li J, Chen B, Chong D, Langridge WHR, Gridley DS, Fodor I. Antitumor effect of vaccinia virus in glioma model. *Oncology Research* 1999;11:133-144.

12.Gridley DS, Andres ML, Li J, Timiryasova TM, Chen B, Fodor I. Evaluation of radiation effects against C6 glioma in combination with vaccinia virus-p53 gene therapy. *International Journal of Oncology* 1998;13:1093-1098.

13. Gridley DS, Andres ML, Li J, Timiryasova TM, Chen B, Fodor I. Evaluation of radiaiton effects against C6 glioma in combinatin with vaccinia virus-p53 gene therapy. *Int J Oncol* 1998;13:1093-1098.

14. Whitman ED, Tsung K, Paxson J, Norton JA. In vitro and in vivo kinetics of recombinant vaccinia virus cancer-gene therapy. *Surgery* 1994;116:183-188.

15. Qin H, Chatterjee SK. Recombinant vaccinia expressing interleukin-2 for cancer gene therapy. *Cancer Gene Ther* 1996;3:163-167.

16. Bui LA, Butterfield LH, Kim JY, Ribas A, Seu P, Lau R, Glaspy JA, McBride WH, Economou JS. In vivo therapy of hepatocellular carcinoma with a tumor-specific adenoviral vector expressing interleukin-2. *Human Gene Therapy* 1997; 8:2173-2182.

17. Kimura M, Yoshida Y, Narita M, Takenaga K, Takenouchi T, Yamaguchi T, Saisho H, Sakiyama S, Tagawa M. Acquired immunity in nude mice induced by expression of the IL-2 or IL- 4 gene in human pancreatic carcinoma cells and anti-tumor effect generated by in vivo gene transfer using retrovirus. *Int J Cancer* 1999; 82:549-555.

18. Addison CL, Bramson JL, Hitt MM, Muller WJ, Gauldie J, Graham FL. Intratumoral coinjection of adenoviral vectors expressing IL-2 and IL-12 results in enhanced frequency of regression of injected and untreated distal tumors. *Gene Therapy* 1998;5:1400-1409.

19. Nasu Y, Bangma CH, Lee HM, Hu J, Wang J, McCurdy MA, Shimura S, Yang G, Timme TL, Thompson TC. Adenovirus-mediated interleukin-12 gene therapy for prostate cancer: suppression of orthotopic tumor growth and pre-established lung metastases in an orthotopic model. *Gene Therapy* 1999;6:338-349.

20. Meko JB, Yim JH, Tsung K, Norton JA. High cytokine production and effactive antitumor activity of a recombinant vaccnina virus encoding murine interleukin 12. *Cancer Research* 1995;55:4765-4770.

21. Fernandez N, Levraud JP, Haddada H, Perricaudet M, Kourilsky P. High frequency of specific $CD8^+$ T cells in the tumor and blood is associated with efficient local IL-12 gene therapy of cancer. *J Immunol* 1999;162:609-617.

22. Peplinski GR, Tsung K, Meko JB, Norton JA. In vivo gene therapy of a murine pancreas tumor with recombinant vaccinia virus encoding human interleukin-1 beta. *Surgery* 1995;118:185-191.

23. Uzendoski K, Kantor JA, Abrams SI, Schlom J, and Hodge JW. Construction and Characterization of a Recombinant Vaccinia Virus Expressing Murine Intercellular Adhesion Molecule-1: Induction and Potentiation of Antitumor Responses. *Human Gene Therapy* 1997;8:851-860.

24. Kaufman HL, Rao JB, Irvine KR, Bronte V, Rosenberg SA, Restifo NP. Interleukin-10 enhances the therapeutic effectiveness of a recombinant poxvirus-based vaccine in an experimental murine tumor model. *J Immunother* 1999;22:489-496.

25. Mastrangelo MJ, Maguire HCJ, Eisenlohr LC, Laughlin CE, Monken CE, McCue PA, Kovatich AJ, Lattime EC. Intratumoral recombinant GM-CSF-encoding virus as gene therapy in patients with cutaneous melanoma. *Cancer Gene Ther* 1999;6:409-422.

26. Putzer BM, Bramson JL, Addison CL, Hitt M, Siegel PM, Muller WJ, Graham FL. Combination therapy with interleukin-2 and wild-type p53 expressed by adenoviral vectors potentiates tumor regression in a murine model of breast cancer. *Hum Gene Ther* 1998;9:707-718.

27. Okada H, Miyamura K, Itoh T, Hagiwara M, Wakabayashi T, Mizuno M, Colosi P, Kurtzman G, Yoshida J. Gene therapy against an experimental glioma using adeno-associated virus vectors. *Gene Ther* 1996;3:957-964.

28. Toda M, Martuza RL, Kojima H, Rabkin SD. In situ cancer vaccination: an IL-12 defective vector/replication- competent herpes simplex virus combination induces local and systemic antitumor activity. *J Immunol* 1998;160:4457-4464.

29. Kikuchi T, Joki T, Akasaki Y, Abe T, Ohno T. Antitumor activity of interleukin 12 against interleukin 2-transduced mouse glioma cells. *Cancer Lett* 1999;135:47-51.

30. Parker JN, Gillespie GY, Love CE, Randall S, Whitley RJ, Markert JM. Engineered herpes simplex virus expressing IL-12 in the treatment of experimental murine brain tumors. *Proc Natl Acad Sci U S A* 2000;97:2208-2213.

31. Benda P, Lightbody J, Sato G, Levine L, Sweet W. Differentiated rat glial cell strain in tissue culture. *Science* 1968;161:370-371.

32. Krausova VI, Kopylova-Sviridova TN, Timiryasova TM, Fodor I. Expression of the genes for Glowworm luciferase in mammalian cells with the use of vaccinia viral vectors. *Mol Genetetics, Microbiol , Virol* 1991;2:23-28.

33. Sheay WE, Nelson S, Martinez I, Chu T-HT, Bhatia S, Dorndurg R. Downstream insertion of the adenovirus tripartite leader sequence enhances expression in universal eukaryotic vectors. *Biotechniques* 1993;15:856-862.

34. Benes V, Hostomsky Z, Arnold L, Paces V. M13 and pUC vectors with new unique restriction sites for cloning. *Gene* 1993;130:151-152.

35. Chakrabarti S, Sisler JR, Moss B. Compact, synthetic, vaccinia virus early/late promoter for protein expression. *Biotechniques* 1997;23:1094-1097.

36. Timiryasova TM, Chen B, Haghighat P, Fodor I. Vaccinia virus-mediated expression of wild-type p53 suppresse glioma cell growth and induces apoptosis. *International Journal of Oncology* 1999;14:845-854.

37. Tsung K, Yim JH, Marti W, Buller RML, Norton JA. Gene expression and cytopathic effect of vaccinia virus inactivated by psoralen and long-wave UV light. *Journal of Virology* 1996;70:165-171.

38. Gollob JA, Schnipper CP, Murphy EA, Ritz J, Frank DA. The functional synergy between IL-12 and IL-2 involves p38 mitogen-activated protein kinase and is associated with the augmentation of STAT serine phosphorylation. *J Immunol* 1999;162:4472-4481.

39. Yao L, Sgadari C, Furuke K, Bloom ET, Teruya-Feldstein J, Tosato G. Contribution of natural killer cells to inhibition of angiogenesis by interleukin-12. *Blood* 1999;93:1612-1621.

40. Ramshaw IA, Andres ML, Phillips SM, Boyle DB, Coupar BEH. Recovery of immunodeficient mice from a vaccinia virus/IL-2 recombinant infection. *Nature* 1987;329:545-546.

41. Karupiah G, Coupar BEH, Andrew ME, Boyle DB, Phillips SM, Mullbacher A, Blanden RV, Ramshaw I. Elevated natural killer cell responses in mice infected with recombinant vaccinia virus encoding murine IL-2. *J Immunol* 1990;144:290-298.

42. Flexner C, Hugin A, Moss B. Prevention of vaccinia virus infection in immunodefecient mice by vector-directed IL-2 expression. *Nature* 1987;330:259-262.

43. Gnant MFX, Puhlmann M, Alexander HR Jr, Bartlett L. Systemic administration of a recombinant vaccinia virus expressing the cytosine deaminase gene and subsequent treatment with 5-fluorocytosine leads to tumor-specific gene expression and prolongation of survival in mice. *Cancer Research* 1999;59:3396-3403.

44. Meko JB, Yim JH, Tsung K, Norton JA. High cytokine production and effective antitumor activity of a recombinant vaccinia virus encoding murine interleukin 12. *Cancer Research* 1995;55:4765-4770.

45. Reichard KW, Lorence RM, Cascino CJ, Peeples ME, Walter RJ, Fernando MB, Reyes HM, Greager JA. Newcastle disease virus selectively kills human tumor cells. *J Surg Res* 1992;52:448-453.

46. Webb HE, Smith CE. Viruses in the treatment of cancer. *Lancet* 1970;1:1206-1208.

47. Puhlmann M, Gnant M, Brown CK, Alexander HR, Bartlett DL. Thymidine kinase-deleted vaccinia virus expressing purine nucleoside phosphorylase as a vector for Tumor-direted gene therapy. *Human Gene Therapy* 1999;10:649-657.

48. Martuza RL. Experimental therapy of human glioma by means of a genetically engineered virus mutant. *Science* 1991;252:854-856.

49. Dameron KM, Volpert OV, Tainsky MA, Bouck N. Control of angiogenesis in fibroblasts by p53 regulation of thrombospondin-1. *Science* 1994;265:1582-1584.

50. Nishizaki M, Fujiwara T, Tanida T, Hizuta A, Nishimori H, Tokino T, Nakamura Y, Bouvet M, Roth JA, Tanaka N. Recombinant adenovirus expressing wild-type p53 is antiangiogenic: a proposed mechanism for bystander effect. *Clin Cancer Res* 1999;5:1015-1023.

51. Carswell EA, Old LJ, Russel RL, Green G, Williamson B. An endotoxin induced serum factor that causes necrosis of tumors. *Proc Natl Acad Sci USA* 1975;72:3600-3670.

52. Rubin BY, Smith LJ, Hellerman GR, Lunn RM, Richardson NK, Anderson SL. Correlation between anticellular and DNA-fragmentation activities of TNF. *Cancer Res* 1988;48:6006-6010.

53. Topalian SL. MHC class II restricted tumor antigens and the role of CD4+ T cells in cancer immunotherapy. *Curr Opin Immunol* 1994;6:741-745.

54. Ross ME, Caligiuri MA. Cytokine-induced apoptosis of human natural killer cells identifies a novel mechanism to regulate the innate immune response. *Blood* 1997;89:910-918.

55. Nastala CL, Edington HD, McKinney TG, Tahara H, Nalesnik MA, Brunda MJ, Gately MK, Wolf SF, Schreiber RD, Storkus WJ. Recombinant IL-12 administration induces tumor regression in association with IFN-gamma production. *J Immunol* 1994;153:1697-1706.

56. Brunda M, Luistro L, Hendrzak J, Fountoulakis M, Garotta GaGM. Role of interferon-gamma in mediating the antitumor efficacy of interleukin-12. *J Immunotherapy* 1995;17:71-77.

57. Mackett M, Smith GL, Moss B. General method for production and selection of infectious vaccinia virus recombinants expressing foreign genes. *J Virol* 1984;49:857-864.

Legends

Fig.1. Construction of recombinant vaccinia viruses. (a, b) The mouse IL-2 or IL-12 cDNA fragment was cloned into the VV transfer vector pSC-11 downstream of the early/late VV p7.5 promoter, resulting in pSC-mIL2 or pSC-mIL12, respectively. The reporter gene *lacZ* was under the control of VV late p11 promoter. Recombinant rVV-mIL2 and rVV-mIL12 was generated by homologous recombination between TK region flanking mIL-2 or mIL-12 on plasmid and the TK region of the wild type VV genome. The IL-12 gene we used was a fusion gene, containing both p40 and p35 subunits. (c) mIL-12 cDNA was ligated into the SmaI site of a VV expression vector, pNL5Sma, which contained the *luc* reporter gene. The resulting mIL-12 expression vector, pN-mIL12, was inserted into the N region of rVV-mIL2 genome by homologous recombination. The rVV-2-12 contained four foreign genes, mIL-12, *luc* genes at N region and mIL-12, *lacZ* genes at TK region. (d) control virus rVV4 had the two reporter genes, *lacZ* and *luc*, inserted into the TK region of wild type VV.

Fig. 2. Kinetic analysis of mIL-2 or mIL-12 expression by different recombinants. Rat C6 glioma cells were seeded in 24-well plate at $1x10^6$ cells/well. The next day, cells were infected with rVV-mIL2, rVV-mIL12 or rVV-2-12 at the indicated MOI. Supernatants were collected at 6, 24, 48, 72 and 96 h. The secretion of cytokine was measured by ELISA.

Fig. 3. Authentic expression of IL-12 fusion protein in tumor. Recombinant heterodimeric and fusion protein forms of mouse IL-12 were analyzed by Western blot under reducing condition (β-mercaptoethanol). Heterodimeric IL-12 separated into two subunits, while the fusion IL-12 maintained an intact protein. rIL-12: recombinant heterodimeric IL-12.

Fig. 4. *In vivo* dose response. Rat C6 glioma cells ($5x10^6$) were injected s.c. in the right hind of the nude mice. After 5 days of initial inoculation, all animals attained palpable tumors, at which time Hank's, rVV4, rVV-mIL2, or rVV-mIL12

were administrated i.t. for a single injection at seven different doses (10-10^7 PFU). Significant difference ($P<0.05$) was observed in 10^2-10^7 PFU groups when compared with saline and virus control groups.

Fig. 5. *In vivo* virus infection. Frozen tumor section from Hank's, rVV4, rVV-mIL2 or rVV-mIL-12-treated groups were dried and fixed in fixative buffer. After rinsed in PBS for 2 times, sections were stained in X-gal solution for 4 h at 37°C.

Fig. 6. Spontaneous blastogenesis in peripheral blood from mice injected with rVV4. Aliquots (50 μl) of whole blood were incubated in medium containing 1 μCi ^{3}H-thymidine per well for 4 h before counting the amount of radioactivity taken up by cells. * significant difference between two groups ($P<0.05$).

Fig. 7. NK cell proliferation in peripheral blood from mice injected with rVV4. Aliquots (50 μl) of whole blood were labeled with antibody (pan-NK) and analyzed by flow cytometry. . * significant difference between two groups ($P<0.05$).

Fig. 8. *In vitro* suppression of IL-2 expression by rVV-p53/rVV-mIL2 coinfection. C6 glioma cells ($1x10^6$/well) were plated in 6-well plate and infected with rVV-mIL2 or rVV-p53/rVV-mIL2 at 0.2 PFU of each virus. Supernatant were collected at 6, 24, 48, 72 and 96 h and measured for IL-2 by ELISA.

Fig. 9. P53 expression was reduced by rVV-p53/rVV-mIL2 coinfection. C6 glioma cells ($1x10^6$/well) were plated in 6-well plate and infected with rVV-mIL2 or rVV-p53/rVV-mIL2 at 0.2 PFU of each virus. Cells were harvested and homogenized in lysis buffer at 6, 24, 48, 72 and 96 h. Proteins (80 μg) were separated by 12% SDS-polyacrylamide gel electrophoresis and probed with primary antibody (DO-7, vector laboratories, Inc.). The blot was then incubated with horseradish peroxidase-conjugated secondary antibody and developed in

color regent. P53 expression by SW480 cell line served as positive control and wild type VV served as negative control.

Fig. 10. DNA fragmentation analysis. C6 glioma cells were infected with different recombinant viruses at 0.2 PFU of each virus. After 48 h, DNA was extracted and subjected to 2% agarose gel. Lane 1: C6 cell mock infection Lane 2: rVV_2 Lane 3: rVV_4 Lane 4: rVV_2/rVV_4 Lane 5: rVV-mIL2 Lane 6: rVV-p53 Lane 7: rVV-p53/rVV-mIL2

Fig. 11. Reduction of *lac Z* expression by $wtVV/rVV_4$ coinfection. C6 glioma cells were infected with wtVV, rVV_4, or $wtVV/rVV_4$ at indicated MOI. 24 h later, *lac Z* production was visualized by X-gal staining (A) and the level of expression was measured by chemoluminescent method (B).

Fig. 12. *In vivo* tumor inhibition by p53/cytokine combination therapy. Mice with similar size s.c. glioma were treated with different recombinant VVs individually or in combination. Tumor growth in combination groups was compared with saline, virus control and single agent treated groups. rVV-p53/rVV-2-12 and rVV-p53/rVV-mIL12 combination therapy showed statistically significant antitumor effect ($P<0.01$ and $P<0.05$, respectively).

Fig. 13. In situ detection of p53 expression and apoptosis. (A) Paraffin-embedded tumor sections obtained from saline, rVV_2 control and rVV-p53 treated animals 9 days after virus injection, were stained for p53 expression by immunohistochemistry. (B) Tumor sections from these groups were also stained for apoptosis by TUNEL assay as described in Material and Methods. Original magnification x100

FIG. 14. Analysis of inactivated virus by titration. The remaining viral infectivity of the PUV inactivated virus was determined on CV-1 cell monolayer. rL-15,

replicating virus; iL-15, nonreplicating virus; n/d, 30 pfu/cell; -1, 3 pfu/cell; -2, 0.3 pfu/cell; -3, 0.03 pfu/cell; -4, 0.003 pfu/cell; -5, 0.0003 pfu/cell.

FIG. 15. Schematic representation of the recombinant viruses. L-5 virus contains the luciferase gene (*luc*) of firefly *Photinus pyralis* and β-galactosidase (*lac Z*) of *E. coli* at the *Hind*III-N-locus of VV. L-15 contains two reporter genes (*luc* and *lac Z*) inserted into thymidine kinase region of VV. Recombinant virus VV-TK-53 is similar to L-15 differing only in the expressed foreign gene. VV-TK-53 contains the human wild-type *p53* gene instead of *luc* gene in the L-15 construct. Abbreviations: P7.5, vaccinia early/late promoter; P11, vaccinia late promoter; P13, synthetic vaccinia early promoter; PE/L, synthetic vaccinia early/late promoter; N_L and N_R; TK_L and TL_R, refer to segments of vaccinia genome that include the left and right portions of *Hind*III-N- and TK-regions, respectively; *luc*, luciferase gene; *lac Z*, β-galactosidase gene; *p53*, human wild-type *p53* gene.

FIG. 16. Luciferase expression. CV-1 cells were infected with replicating (rL-5 or rL-15) or inactivated (iL-5 or iL-15) viruses at an m.o.i. of 5 pfu/cell. At specified time points following infection, the cells were harvested, lysed and analyzed by luminometer.

FIG. 17. p53 expression. Cells were infected at an m.o.i. of 5 pfu/cell and harvested at the indicated times. Quantitation of p53 protein in C6 rat glioma cells infected with replicating (rVV-TK-53) or inactivated (iVV-TK-53) viruses was determined by ELISA assay.

FIG. 18. Viability of C6 cells. Effect of the tumor suppressor p53 expressed by nonreplicating VV-TK-53 virus on the viability of C6 rat glioma cells was determined using trypan blue exclusion assay. Duplicated samples of each treatment were counted.

FIG. 19. Detection of apoptosis *in situ.* C6 rat glioma cells were seeded on glass coverslips, and on next day were mock-infected, or infected with nonreplicating control (iL-15) or p53-expressing (iVV-TK-53) virus at an m.o.i. of 5 pfu/cell. In 6 days after the infection, apoptosis-related DNA strand breaks were detected by TUNEL assay. The samples were directly analyzed using a fluorescence microscope. Brightly stained green cells were undergoing apoptosis. Magnification x1000.

FIG. 20. Tumor growth inhibition. Athymic mice were injected sc with $3x10^5$ of mock-infected C6 glioma cells or infected with iL-15 and iVV-TK-53 at m.o.i. of 1 or 10 (iL-15-1, iL-15-10, iVV-TK-53-1, iVV-TK-53-10, respectively). Results of a representative experiment are shown.

Publications (see *Appendix*):

Abstracts Attached to 12. Appendix 4

1. B Chen, TM Timiryasova, P Haghighat, DS Gridley, ML Andres, E Kajioka, R-D Roy and I Fodor. Vaccinia virus as a vector for immunotherapy.8th International Conference on Gene Therapy of Cancer, Dec. 9-11, 1999, San Diego, PD-104.

2. István Fodor, Tatyana M. Timiryasova, Bing Chen, Jun Li, Peyman Haghighat and Daila S.Gridley .Vaccinia virus-mediated expression of wild-type p53 suppresses glioma cell growth and induces apoptosis. Intern. J. Molec. Med. V.4, Suppl. 1, 1999. The 4th World Congr. on Adv. in Oncol.; 2nd Intern. Symp. on Molec. Med., October 7-9, 1999, Vouliagmeni, Athens, Greece.

Manuscripts:

Bing Chen, Tatyana M Timiryasova, Peyman Haghighat, Daila S Gridley, Melba L Andres, Eric Kajioka, Rhoda D Roy and Istvan Fodor. Low dose vaccinia virus-mediated cytokine therapy of glioma (manuscript is prepared for publication in J. Immunotherapy).

Bing Chen, Tatyana M Timiryasova, Melba L Andres, Eric Kajioka, Rhoda D Roy, Daila S Gridley and Istvan Fodor. Evaluation of combined vaccinia virus-mediated antitumor gene therapy with p53, IL-2 and IL-12 in glioma model (manuscript has been prepared for publication in J. Immunology).

Tatyana M. Timiryasova, Bing Chen and Istvan Fodor. Inactivated vaccinia virus mediated gene delivery into cancer cells (manuscript has been prepared for publication in Virology).

SEP - 6 2000

COPY

No. 20
Loma Linda University/Gridley

Lymphocyte activation with localized pGL1-TNF-α gene therapy in a glioma model

Daila S. Gridley[1,2], Jun Li[2], Eric H. Kajioka[1] Radha Dutta-Roy[1], Melba L. Andres[1], Tatyana M. Timiryasova[2], and Istvan Fodor[2]

Departments of [1]Radiation Medicine, Radiobiology Program, and [2]Microbiology & Molecular Genetics

Loma Linda University and Medical Center, Loma Linda, CA 92354 U.S.A.

Running Title: pGL1-TNF-α gene therapy and glioma

Corresponding author: Daila S. Gridley, Ph.D.

Chan Shun Pavilion, Room A-1010

11175 Campus Street

Loma Linda University School of Medicine

Loma Linda, CA 92354

Phone: (909)558-8361

Fax: (909)558-0825

E-mail: dgridley@dominion.llumc.edu

Key words: TNF-α gene therapy; lymphocytes; C6 glioma; brain tumor; radiation

Previous studies have shown that tumor necrosis factor-α (TNF-α) can augment the antitumor effect of radiation. The major goal of this study was to evaluate the effects of naked pGL1-TNF-α, a plasmid containing the human TNF-α gene, on hematological and leukocyte variables, as well as C6 tumor growth in athymic mice treated with radiation. pGL1-TNF-α was administered intratumorally at low to high doses (15μg, 150μg, and 450μg) in all three phases of this study. In Phase A, pGL1-TNF-α expression within tumors was dose-dependent and transient, with highest levels seen at 18 hr post-injection, whereas no TNF-α protein was detected in plasma. Low erythrocyte counts, hemoglobin, and hematocrit were associated with tumor presence, but the reduction in these variables was most striking in the group receiving 450μg of pGL1-TNF-a and that also exhibited thrombocytopenia by 168 hr. In Phase B, treatment with pGL1-TNF-α at 15μg or 150μg resulted in the highest leukocyte and lymphocyte numbers in the spleen and the greatest degree of splenomegaly at 64 and 88 hr post-injection. In these same two groups, flow cytometry analyses showed that up to 26% of spleen lymphocytes and up to 84% of blood lymphocytes expressed the CD71 activation marker; increased expression of the CD25 activation marker was also seen ($P<0.05$). The highest levels of natural killer cells (panNK+) were observed in blood, whereas B lymphocytes (CD19+) were increased in spleens from these mice. An enhancing effect was also noted in some of the measurements with parental plasmid pWS4 and tumor presence. In Phase C, the slowest tumor progression was observed in the groups receiving 15μg and 150μg pGL1-TNF-α together with radiation; tumor volumes were 51% and 43% smaller, respectively, than for PBS-injected controls by the end of the study. Collectively, these results show that localized treatment with pGL1-TNF-α is effective and non-toxic at low doses and support the premise that activation of lymphocytes may contribute to the antitumor effects of radiation against a highly aggressive brain tumor.

INTRODUCTION

Although current treatment protocols for malignant glioma (surgical resection followed by radiation and/or chemotherapy) are tumor-reductive, the prognosis for patients with high grade brain tumors remains dismally poor.[1] Attempts to increase the dose of radiation or drugs or perform more radical surgery have had little or no effect on survival time and have increased the risk for serious side effects. The failure to increase survival may be, at least partly, related to the immunodepression observed in these patients.[2] Thus, the administration of cytokines that activate leukocyte populations with antitumor properties may prove to be beneficial as an adjunctive form of therapy.

Gene therapy offers new and innovative techniques by which cytokine genes could be safely administered. Currently, there is no single gene delivery system that is considered to be best, as all are limited in one respect or another. Viral vectors (e.g., retrovirus, adenovirus, and adeno-associated virus) generally have higher gene transfer efficiency and longer gene expression than non-viral vectors.[3] However, viral vectors are often immunogenic, especially with repeated administration, making the study of immunological responses induced by cytokine gene expresssion difficult and may also compromise therapeutic efficacy. Non-viral vectors complexed to cationic liposomes and similar carriers do not induce specific immune responses, but may stimulate a strong inflammatory response that inhibits gene expression and/or confounds interpretation of the results.[4,5] Naked plasmid DNA is not limited by many of these drawbacks and the transient nature of gene expression is not a major concern when the intended purpose requires short-term production of the protein of interest. To date, investigations utilizing non-viral vectors in gene therapy for brain tumors are virtually nonexistant.

The most widely used gene therapy approach for brain tumors has been based on viral

vectors, expecially the transduction of tumor cells with the herpes simplex virus type-1 thymidine kinase (HSV-*tk*) gene, followed by ganciclovir treatment.[6-12] These investigations have resulted in varying degrees of success. Interestingly, Kim et al.[13] showed that glioma cells expressing the HSV-tk gene in culture exhibited increased radiosensitivity when treated with bromovinyldeoxyuridine (BVdUrD). Unfortunately, previous clinical trials have demonstrated that BVdUrD, at the doses required for radiation sensitization, are too toxic to normal tissues such as bone marrow and intestine.[14]

Tumor necrosis factor-α (TNF-α) has received much attention due to its direct cytostatic and cytotoxic effects against many tumor types. The cytokine also has multiple indirect activities that may contribute to tumor response *in vivo*, including recruitment and activation of leukocytes and upregulation of cell surface molecules that are important in immunological responsiveness.[15,16] However, clinical trials utilizing high-dose systemically administered TNF-α have generally been disappointing and frequently plagued with dose-limiting toxicities.[17,18] The use of low-dose TNF-α in combination with other therapeutic modalities has great potential due to its potent immunomodulatory properties even at very low doses and potential to radiosensitize tumor cells.

We and others have previously shown that TNF-α protein can augment radiation-induced control of both TNF-α-sensitive and TNF-α-resistant tumors *in vivo*.[19-23] More recently, we have combined plasmid pGL1-TNF-α treatment (with and without transfection agent) together with radiation with some success.[24,25] The major goals of the present study were to determine the kinetics of pGL1-TNF-α expression *in vivo*, quantify hematological and immunological changes that may occur due to pGL1-TNF-α expression, and evaluate tumor progression when varying doses of pGL1-TNF-α are combined with radiation.

MATERIALS AND METHODS

Animals

Athymic male mice (outbred background, nu/nu; n = 300) were purchased from Charles River Breeding Laboratories, Inc. (Wilmington, MA) at 5-6 weeks of age and acclimatized in self-contained filter-top cages (7-8 mice/cage) for 2 weeks under appropriate conditions for immunocompromised rodents. Autoclaved bedding, food, and water were provided. Rapid CO_2 euthanasia was performed in compliance with the *NIH Guide for the Care and Use of Laboratory Animals*. The study was approved by the Institutional Animal Care and Use Committee.

Tumor cell line, tumor induction, and volume measurements

The rat C6 nitrosourea-induced glioma cell line, originally derived by Benda et al.[26] was obtained from the American Type Culture Collection (ATCC; Rockville, MD). The tumor cells were cultured in Dulbecco's minimal essential medium (DMEM; Irvine Scientific, Santa Ana, CA) containing 10% bovine calf serum (BCS; Hyclone Laboratories, Logan, UT), and antibiotics (Sigma Chemical Co., St. Louis, MO). The cells were harvested, washed, counted, adjusted to a concentration of 2.5×10^6 cells/ml in phosphate buffered saline (PBS), and injected subcutaneously (s.c.) in the right hind flank (5×10^5 cells/0.2 ml/mouse). Tumor dimensions were measured with vernier calipers and volumes were calculated: tumor volume (mm^3) = (H · W · L)/2, where H = height, W = width, and L = length of the tumor.

pGL1-TNF-α and pWS4

The human recombinant TNF-α coding sequence in plasmid pUC18 was purchased from R & D

Systems, Inc. (Minneapolis, MN). The TNF-α coding sequence was then ligated into the polylinker region of plasmid pWS4, a universal eukaryotic gene expression vector originally developed by Sheay et al.[27] The details of pGL1-TNF-α construction and expression by transfected C6 cells in culture have been previously reported.[25]

Phase A: Experimental design

Mice (n = 76) were injected s.c. with C6 tumor cells that were allowed to become established for 7 days (tumor volume: ~300 mm^3) before intratumoral (i.t.) injection of pGL1-TNF-α. The plasmid was administered at 15μg, 150μg, and 450μg in a single injection using a Hamilton syringe with a 3/4-inch needle. The animals were euthanized at 18 hr, 72 hr, and 168 hr thereafter.

Phase A: *Measurement of hematological variables*

Whole blood was collected in heparin-containing syringes by cardiac puncture at the time of euthanasia. Aliquots (12 μl) from all of the mice were then evaluated using the Vet ABC Hematology Analyzer (Heska Corp., Waukesha, WI) programmed to analyze murine blood. The measurements included white blood cell (WBC), red blood cell (RBC) and thrombocyte counts, hemoglobin, and hematocrit (% of whole blood composed of RBC).

Phase A: *pGL1-TNF-α expression in vivo*

At each time of testing, representative tumors were excised (n = 3/group/timepoint) and cut into small pieces in PBS with 100 μM phenylmethylsulfomyl fluoride (PMSF). After centrifugation for 5 min, the supernatants were collected and stored at -70°C. Whole blood was centrifuged, and plasma was frozen. Immediately before quantification of human TNF-α protein, the tumor

supernatants and plasma samples were thawed and analyzed using a commercially available enzyme-linked immunosorbent assay (ELISA) kit (Quantikine™, R&D Systems, MN).

Phase B: Experimental design

In this phase, additional mice (n = 180) were treated similarly to those in Phase A and assigned to 6 different groups: a) no tumor control; b) PBS-treated tumor; c) pWS4 (150μg); d) pGL1-TNF-α (15μg); e) pGL1-TNF-α (150μg); and f) pGL1-TNF-α (450μg). The animals were weighed, and blood and spleens were collected for a series of *in vitro* assays (described below) at 16 hr, 64 hr and 88 hr after pGL1-TNF-α injection. This phase was performed in two identical experiments. There were a total of 30 mice with no tumor, euthanized in sets of 10 at each time point, and 10 tumor-bearing mice/group/time point.

Phase B: Relative spleen weight (RSW) and leukocyte counts in blood and spleen

Whole blood was collected in syringes containing anticoagulant by cardiac puncture at the time of euthanasia and erythrocytes were lysed (Unopette Microcollection System, Becton Dickinson and Co., Rutherford, NJ). Spleen weights were determined and RSW values were calculated: RSW = [weight of spleen (g) x 10^3]/body weight (g). The spleens were then processed into single-celled suspensions, erythrocytes were lysed in 2 ml of lysing buffer, and the remaining leukocytes were washed and suspended in 1 ml of RPMI 1640 medium (Irvine Scientific) containing 10% heat-inactivated fetal calf serum (FCS; Hyclone), antibiotics, and mercaptoethanol. Viable leukocytes from both blood and spleen were counted with a hemocytometer using the trypan blue exclusion method.

Phase B: Spontaneous and mitogen-induced blastogenesis

These assays have been previously described in detail.[28,29] Briefly, to quantify the basal proliferation of leukocytes, aliquots of whole blood were diluted with supplemented RPMI 1640 medium (Irvine Scientific) and dispensed into wells of microculture plates. One μCi of ^{3}H-thymidine (^{3}H -TdR; specific activity = 46 Ci/μmol; ICN Biochemicals, Costa Mesa, CA) was immediately added, and incubation was for 3 hr at 37°C. Spleen leukocytes (2 x 10^{6}/ml in medium) were dispensed into microtiter plates either with or without lipopolysaccharide (LPS; Sigma), incubated for 48 hr, and pulse-labelled with ^{3}H-TdR (1 μCi/50 μl/well) for the final 4 hr. In both assays, cells were harvested with a multiple sample harvester and the incorporated radioactivity was quantified. For spleen cells incubated with mitogen, the counts per minute (cpm) were used to calculate a stimulation index (SI): SI = (cpm with LPS – cpm without LPS)/cpm without LPS. The spontaneous uptake of ^{3}H-TdR was adjusted to cpm/10^{6} cells, based on the total leukocyte count.

Phase B: Flow cytometry analysis of spleen and blood lymphocyte populations

Immunophenotyping was carried out using a 4-color FACSCalibur™ flow cytometer (Becton Dickinson, Inc., San Jose, CA) and standard techniques. A rapid 2-tube procedure was employed using custom-monoclonal antibody (MAb) conjugates specially designed for investigators in the LLU Radiobiology Program by Pharmigen (San Diego, CA) in collaboration with Becton Dickinson. Briefly, the MAb were labeled with FITC, PE, APC, or PerCP and directed against: natural killer (NK) cells (PanNK+), B cells (CD19+), mature T (CD3+), T helper (CD4+ Th), and T cytotoxic (CD8+ Tc) cells. Additional tests were performed on gated lymphocytes to quantify cells with CD71, CD25, CD3/CD71, and CD3/CD25 markers. Analysis was performed using CellQuest™ software version 3.1 (Becton Dickinson). A total of 10,000

lymphocyte events/tube were acquired. To obtain the number of cells for each lymphocyte population, the following formula was used: no. of cells in population/ml = no. of leukocytes/ml x percentage of population.

Phase C: Experimental design

C6 cells were injected as described above and on day 9 after tumor cell implantation the mice (n = 44) were assigned to groups: a) no tumor control, b) PBS-treated tumor, c) pGL1-TNF-α (150μg), d) radiation, e) pWS4 (150μg) + radiation, f) pGL1-TNF-α (15μg) + radiation, g) pGL1-TNF-α (150μg) + radiation, and h) pGL1-TNF-α (450μg) + radiation. Irradiation of tumors was performed using a ^{60}Cobalt (^{60}Co) source and an Eldorado Model "G" gamma irradiation machine (Atomic Energy of Canada, Ltd., Commercial Products Division, Ottawa, Canada). The γ-rays were delivered at 2 gray (Gy) per exposure at a dose rate of 0.8 Gy/min. Lipowitz metal alloy blocks of 3-inch thickness shielded the bodies of the mice and the tumors were covered with a 0.5-cm superflab bolus. The treatment sequence consisted of i.t. injection of plasmid at 5 μg, 50 μg and 150 μg/mouse/injection followed by tumor irradiation 16-18 hr later; each modality was administered three times over a period of 9 days. All animals were euthanized when mean tumor volume in the tumor-bearing PBS-treated controls reached ~2300 mm^3.

Statistical analysis

The data were assessed using one-way analysis of variance (ANOVA) and Tukey's HSD (honestly significant difference) test. These analyses were performed using SigmaStat™

software version 2.03 (SPSS, Inc., Chicago, IL). A p value of <0.05 indicated significant differences among groups.

RESULTS

Phase A: pGL1-TNF-a expression in tumors and plasma

Table 1 shows that human TNF-α protein was present in C6 tumors at highest levels at 18 hr after pGL1-TNF-α injection. Injection of the plasmid at a dose of either 150 μg or 450 μg resulted in similar levels of the protein at both the 18 hr and 72 hr time points. TNF-α was still detectable at 168 hr after injection at all three doses, but the levels had declined substantially. The cytokine was not detected in plasma at any time of testing.

Phase A: Hematological variables

Erythrocyte characteristics and the numbers of thrombocytes and leukocytes in blood are presented in Table 2. Red blood cell counts were significantly reduced in all tumor-bearing mice by 168 hr compared to mice with no tumor ($P<0.05$). At this same time point, hemoglobin content was low in pGL1-TNF-α (15μg/450μg)-injected groups and hematocrit values were low in the groups receiving pGL1-TNF-α (15μg/450μg) and PBS ($P<0.05$). The reduction in erythrocyte number, hemoglobin, and hematocrit was most striking in the high-dose (450μg) pGL1-TNF-α-treated mice. At 72 hr the platelet count was significantly reduced in the pGL1-TNF-α (450μg) group, whereas leukocytes were elevated after the 150μg dose.

Phase B: Body weights, leukocyte and lymphocyte counts, RSW, and tumor volumes

There were no significant differences in mouse body weights at all measured time points. Mean

values ranged from 26.3 +/- 0.7g (pGL1-TNF-α, 450μg) to 29.0 +/- 0.7g (PBS) at 16 hr and 29.2 +/- 1.0g (PBS) to 31.3 +/- 1.2g (pGL1-TNF-α, 450μg) by 88 hr. The leukocyte and lymphocyte numbers obtained for both blood and spleen and relative spleen weight (RSW) values are shown in Table 3. In the blood, significantly increased leukocyte, but not lymphocyte, counts were noted only at 64 hr in the PBS- and pGL1-TNF-α (150μg)-treated groups when compared to normal mice with no tumor ($P<0.05$). At this same time, significantly elevated leukocyte numbers were found in spleens from all tumor-bearing mice compared to controls without tumor; lymphocyte and RSW values were increased in the groups injected with 15μg and 150μg of pGL1-TNF-α ($P<0.01$). By 88 hr, leukocyte and lymphocyte numbers in the spleen were high in pGL1-TNF-α (15μg/150μg)- and pWS4-treated groups and splenomegaly was noted in all groups receiving plasmid (pGL1-TNF-α or pWS4). In general, the mice injected with 15μg or 150μg of pGL1-TNF-α tended to exhibit the greatest increases in these measurements. Tumor volumes were not significantly different among the groups throughout this phase. Mean tumor volumes at 16 hr after injection ranged from 219 +/- 50mm^3 (PBS) to 356 +/- 49mm^3 (pGL1-TNF-α, 15μg); at 88 hr the mean values ranged from 1,746 +/- 163mm^3 (pGL1-TNF-α, 150μg) to 1,993 +/- 239mm^3 (PBS).

Phase B: Spontaneous and mitogen-induced blastogenesis

Significant 2.7- to 4.1-fold increases in spontaneous blastogenesis were observed in the blood from pGL1-TNF-α (150μg/450μg)- and pWS4-treated groups at 16 hr after plasmid injection compared to mice with no tumor ($P<0.001$), but there were no differences among groups at 64 hr and 88 hr (Table 4). In the spleen, a significant increase in spontaneous incorporation of ^{3}H-TdR

into DNA was observed only at 64 hr in the group receiving 15μg of pGL1-TNF-α. The response of spleen cells to LPS stimulation was similar among all groups (Table 4).

Phase B: Flow cytometry analysis lymphocyte populations

Figure 1 presents the numbers of NK (panNK+) cells in the blood and spleen. Injection with 150μg and 450μg pGL1-TNF-α and pWS4 resulted in significantly increased NK cell numbers in blood at 16 hr compared to mice with no tumor ($P<0.001$). The mean for the pWS4 group was also significantly higher than that for the PBS-injected control group. In the spleen, the groups treated with 15μg and 150μg of pGL2-TNF-α exhibited the highest NK cell levels at 64 hr, although statistical significance was not obtained. Figure 2 shows that mice injected with pGL1-TNF-a (450mg) and pWS4 had lower B cell numbers in the blood at 16 hr compared to the no tumor and PBS-injected mice ($P<0.005$). In contrast, the number of splenic B cells was significantly elevated at both the 64 hr and 88 hr time points in the groups receiving 15μg and 150μg of pGL1-TNF-α ($P<0.001$). A high B cell count was also noted with pWS4 injection by 88 hr. CD4+ Th and CD8+ Tc subsets were detectable in both blood and spleen, however the numbers and percentages were very low and no specific pattern of changes was observed with treatment (data not shown).

The numbers of blood and spleen lymphocytes expressing the CD71 activation marker are shown in Figure 3. In the blood, mice treated with pGL1-TNF-α at 15μg and 150μg had significantly increased levels of CD71+ cells at 64 hr and 88 hr post-injection compared to mice with no tumor ($P<0.01$); mean values were 2.1- to 2.7-fold greater. In the spleen, increases in CD71+ lymphocytes were also evident in these two groups at 64 hr and 88 hr and were more dramatic than in blood, e.g. 6.2- and 8.2-fold above normal controls at 64 hr, ($P<0.005$). The

pGL1-TNF-α (15μg/150μg) groups also had significantly more splenic CD71+ lymphocytes than the PBS- and pWS4-injected mice at 64 hr. Several additional differences were noted.

Figure 4 presents the numbers of CD25+ lymphocytes in the blood and spleen. In the blood, a significant increase was noted in the pGL1-TNF-α (150μg) group compared to the group with no tumor ($P<0.005$). The data also show that all tumor-bearing mice, except those treated with 450 μg of pGL1-TNF-α, had significantly increased numbers of CD25+ cells at 88 hr in relation to animals without tumor ($P<0.001$). In addition, the groups treated with 15μg and 150μg pGL1-TNF-α had the highest levels of these cells at that time. Figure 5 shows that the numbers of splenic lymphocytes expressing CD3 and either CD71 (CD3+/CD71+) or CD25 (CD3+/CD25+) were significantly increased in mice treated with 150μg of pGL1-TNF-α compared to nearly all other groups at 64 hr ($P<0.001$). Need blood CD3/CD71 and CD3/CD25 stats

Phase C: *Tumor progression after pGL1-TNF-a and radiation*

Figure 6 shows that pGL1-TNF-α at doses of 15 μg and150 μg, in combination with ^{60}Co radiation, significantly slowed C6 tumor progression compared to mice injected with PBS or pGL1-TNF-α (450μg) at nearly all times of measurement. By 18 days after C6 cell implantation, mean tumor volumes in these two groups were 43-51% smaller than those for the PBS-injected control group and 56-62% smaller compared to the group receiving only pGL1-TNF-α (150μg). There was no significant difference in tumor volume between these two combination groups at any time. Tumor growth in the mice treated with pGL1-TNF-α (450μg) + ^{60}Co and pWS4 + ^{60}Co was similar to that of radiation alone.

DISCUSSION

In Phase A of this study, the kinetics of pGL1-TNF-α expression was determined after i.t. injection at varying concentrations. The results show that human TNF-α protein was present in C6 tumors, with peak levels found at the earliest time point of measurement (18 hr post-injection), and that the expression was dose-dependent and temporary. The transient nature of pGL1-TNF-α expression could be considered as an advantage, since continuous production of the cytokine would increase the risk for severe side effects associated with administration of TNF-α protein.[17,18,30,31] Furthermore, a major purpose of TNF-α in the proposed combined regimen is to enhance radiation efficacy during therapy. Mechanisms by which the cytokine may accomplish this include the induction of wild-type p53 expression,[32] damage to tumor vasculature resulting in ischemic tumor necrosis,[34,35] induction of apoptosis,[35] and augmentation of oxygen radical production by either the tumor cells themselves[36] or by phagocytic cells of the host.[37]

In the present study, the human TNF-α protein was not detected in the plasma at all times of testing, yet systemic changes were observed. Blood analyses were performed in Phase A to detect possible hematological toxicities. TNF-α has been implicated as the mediator of erythropoiesis suppression, anemia, weight loss, and hypercalcemia associated with cancer.[38-40] Studies have also shown that thrombocytopenia and leukopenia can occur after TNF-α administration.[41-44] Furthermore, since suppression of normal hematopoiesis is often a dose-limiting factor in radiation therapy,[45] the combination of two modalities with a similar toxicities may lead to serious consequences. We found that by 168 hr post-injection, the number of RBC in peripheral blood had declined significantly in all tumor-bearing groups and consistently low hemoglobin and hematocrit values were obtained for these mice. The most dramatic reductions,

however, were seen in the group treated with the highest dose of pGL1-TNF-α (450μg). Platelet counts were significantly low at 72 hr in the pGL1-TNF-α (450μg) group, but leukocyte counts remained close to normal in most groups. The thrombocytopenia seen with high-dose pGL1-TNF-α may be due to platelet migration into tumor and/or decreased survival due to mast cell release of platelet agonists.[43,46-48] Overall, these findings indicate that pGL1-TNF-α, when used in relatively low amounts (15μg and 150μg), is nontoxic to the hematopoietic system, but that a high dose (450μg) may be contraindicated.

Given the transient nature of pGL1-TNF-α expression, in Phase B we focused on the 16-88 hr time period after injection. Although increased spontaneous blastogenesis, based on ^{3}H-TdR uptake, was noted at 16 hr and a modest elevation in leukocyte numbers occurred in the blood at 64 hr after pGL1-TNF-α injection, similar increases occurred in the PBS- and pWS4-treated groups. In contrast to the blood, striking changes in the spleen were associated with pGL1-TNF-α treatment, especially when administered at the 15μg and 150μg doses. Splenomegaly, high leukocyte and lymphocyte counts, and increased spontaneous blastogenesis were noted at various times post-injection, indicating that a significant degree of activation was occurring in the spleen. TNF-α can recruit non-specific immune effector cells and, in a syngeneic host, facilitate the development of specific anti-tumor responses. The finding that the combination of TNF-α together with granulocyte/macrophage colony-stimulating factor induces the maturation of dendritic cells (the most effective antigen presenting cells) supports this latter possibility.[49]

The results from Phase B also show that the number of circulating NK (panNK+) cells were significantly elevated after pGL1-TNF-α (150μg/450μg) injection, although pWS4 also induced this effect. In the spleen, the highest levels of NK cells were found after pGL1-TNF-α (15μg/150μg) treatment. NK cells are lymphocytes that kill tumor targets in a non-specific

manner. It has been demonstrated that the tumoricidal activity of spleen cells in athymic mice includes NK cells, as well as other non-specific cytotoxic cell types.[50] He et al.[51] recently showed that i.v. injection of naked plasmid DNA encoding various genes can enhance NK cell numbers in spleen and lymph nodes within a few days. Mechanisms of tumor rejection in athymic mice xenotransplanted with human head and neck carcinomas have been correlated with NK cell activation.[52] The data also show that significant increases occurred in CD19+ B cells in the spleen, but not blood, after pGL1-TNF-α (15μg/150μg) injection. However, spleen cell response to LPS, a B cell mitogen, was similar among groups. Overall, B lymphocytes are thought to play a relatively minor role in tumor defense.

Our previous studies in the C6 tumor – athymic mouse model demonstrated an increase in leukocyte populations, especially granulocytes expressing the CD69 activation marker, when pGL1-TNF-α complexed to a cationic polyamine was injected intratumorally.[24] Histological evaluation of stained tumor sections showed presence of a granulocytic, as well as lymphocytic, infiltrate. In assessing cellular modulations in the present study, we focused on the lymphocytes by gating on these cells during flow cytometry analysis. The data show that the number of lymphocytes expressing the CD71 (transferrin receptor) activation marker were elevated in both the blood and spleen after pGL1-TNF-α injection. The most striking increase (818% compared to non-tumor bearing mice; 275% and 365% compared to pWS4- and PBS-injected mice, respectively) occurred in the spleens of animals treated with the 150μg dose of pGL1-TNF-α. CD71 is a non-lineage restricted marker that is expressed by activated lymphocytes, monocyte-macrophages, and neutrophils.[53] Interestingly, it has been shown that whole-body irradiation up to 7 Gy results in mononuclear cell activation and expression of CD71 that is dose- and time-dependent.[54] The results also show that CD25+ splenic lymphocytes were greatly increased by

pGL1-TNF-α expression. Historically, CD25 (IL-2 receptor α chain) was often used as a T cell activation marker, but it is now known to also be present on activated NK and B cells.[55] CD25 and CD71are also found on the surface of activated CD3+ T cells. Although present in very small numbers, athymic mice are not entirely devoid of this cell population.[56] Furthermore, it has been demonstrated that post-thymic T cells show extensive self-renewal, expansion, and functional activity in the absence of the thymus.[57] Because of these and other similar observations, we chose to evaluate T cells in the present study. CD3+ T lymphocytes were significantly increased in the spleen after pGL1-TNF-α (150μg) injection and increases in CD3+/CD25+ and CD3+/CD71+ cells were observed in these mice. Approximately 40% of the CD3+ cells also expressed CD71, whereas only 7% of these cells also expressed CD25. However, it remains to be determined whether the activated T cells were functionally competent.

We have previously demonstrated that i.t. injection of 150μg of naked pGL1-TNF-α can enhance the effects of radiation against C6 glioma when tumor irradiation is performed at 16-18 hr after administration.[25] In Phase C of the present study we compared the efficacy of the 15μg and 450μg doses to that of the 150μg dose. The data show that pGL1-TNF-α at a total of either 15μg or 150μg in combination with radiation significantly slowed C6 tumor progression, and that the degree of tumor growth inhibition was virtually identical between the two doses. This indicates that a beneficial effect can be achieved with pGL1-TNF-α at doses as low as 15 μg (given at 5μg/injection over a period of 9 days). In contrast, when 450μg of pGL1-TNF-α was administered together with radiation, tumor growth inhibition was similar to that of radiation alone. The reasons for the lack of any further effect with the highest amount of pGL1-TNF-α are not known. However, it is possible that an increase in soluble TNF-α receptors (i.e., sTNF-RI and sTNF-RII) may have occurred, which, upon binding to TNF-α, can inhibit its effects.[58]

In addition, there is evidence that platelets infiltrating into tumors may reduce tumor response to TNF-α, limit antitumor activity of infiltrating macrophages, and shield tumor cells from NK cell attack.[406,47] Based on the above reports and our data showing a decrease, albeit transient, in circulating platelets after 450μg of pGL1-TNF-α, it is tempting to speculate that the platelets in the mice may have accumulated within tumors, resulting in reduced tumor response.

In summary, the present study shows that i.t. injection of pGL1-TNF-α results in transient expression of TNF-α *in vivo* and that relatively low doses induce marked lymphocyte activation, especially in the spleen. There were no toxicities associated with 15μg and 150μg pGL1-TNF-α treatment, based on hematological assays and body weights. The data also demonstrate that C6 tumor progression was significantly inhibited when pGL1-TNF-α was administered together with radiation. This latter experiment showed that the pGL1-TNF-α dose of 15μg could achieve the same effect as the 10-fold higher dose of 150μg. Taken together, the results demonstrate that low-dose pGL1-TNF-a is non-toxic and suggest that it may contribute tp the anti-tumor effects of radiation, at least partly, by activation of lymphocyte populations. Experiments ongoing in our laboratories are designed to determine whether this combination approach will prove to be beneficial in the control of intracranial glioma growth.

ACKNOWLEDGMENTS

The authors thank Gregory A. Nelson, Ph.D. for use of equipment and facilities and Bing Chen, Gregory A. Abell, and Erben Bayeta for expert technical assistance. This study was supported by the U.S. Department of the Army and the National Medical Technology Testbed, Inc. The view, opinions and/or findings contained in this report are those of the authors and should not be

construed as a position, policy, decision, or endorsement of the Federal Government or the National Medical Technology Testbed, Inc.

REFERENCES

1. Salcman M, Kaplan R. Intracranial tumors in adults. In: Moosa AR, Schimpff SC, Robson MC, eds. *Comprehensive Textbook of Oncology*, 2nd ed. vol II. Baltimore MD: Williams & Wilkins; 1991:1339-1352.
2. Dix AR, Brooks WH, Roszman TL, Morford LA. Immune defects observed in patients with primary malignant brain tumors. (review) *J. Neuroimmunol.* 1999;100:216-232.
3. Anderson WF. Human gene therapy. *Nature (Lond.)* 1998;392:25-30.
4. Wolff JA, Budker V. Cationic lipid-mediated gene transfer. In: Sobol RE, Scanlon KJ, eds. *The Internet Book of Gene Therapy. Cancer Therapeutics.* Stamford, CN: Appleton & Lange; 1995:65-73.
5. Yew NS, Wang KX, Przybylska M, Bagley RG, Stedman M, Marshall J, Scheule RK, Cheng SH. Contribution of plasmid DNA to inflammation in the lung after administration of cationic lipid:pcDNA complexes. *Hum. Gene Ther.* 1999;10:223-234.
6. Kramm CM, Breakfield XO, Chiocca EA. Genetic strategies for brain tumor therapy. In: Sobol RE, Scanlon KJ, eds. *The Internet Book of Gene Therapy. Cancer Therapeutics.* Stamford, CN: Appleton & Lange; 1995:235-245.
7. Oldfield EH, Ram Z, Culver KW, Blaese RM, DeVroom RL, Anderson WF. Gene therapy for the treatment of brain tumors using intera-tumoral transduction with the thymidine kinase gene and intravenous ganciclovir. *Hum. Gene Ther.* 1993;4:39-69.

8. Culver KW, Van Gilder J, Link CJ, Carlstrom T, Buroker T, Yuh W, Koch K, Schabold K, Doornbas S, Wetjen B, et al. Gene therapy for the treatment of malignant brain tumors with in vivo tumor transduction with the herpes simplex thymidine kinase gene/ganciclovir system. *Hum. Gene Ther.* 1994;5:343-379.

9. Raffel C, Culver K, Kohn D, Nelson M, Siegel S, Gillis F, Link CJ, Villablanca JG, Anderson WF. Gene therapy for the treatment of recurrent pediatric malignant astrocytomas with in vivo tumor transduction with the herpes simplex thymidine kinase gene/ganciclovir system. *Hum. Gene Ther.* 1994;5:863-890.

10. Vincent AJ, Vogels R, Someren GV, Esandi MC, Noteboom JL, Avezaat CJ, Vecht C, Bekkum DW, Valerio D, Bout A, Hoogerbrugge PM. Herpes simplex virus thymidine kinase gene therapy for rat malignant brain tumors. *Hum. Gene Ther.* 1996;7:197-205.

11. Moriuchi S, Oligino T, Krisky D, Marconi P, Fink D, Cohen J, Glorioso JC. Enhanced tumor cell killing in the presence of ganciclovir by herpes simplex virus type 1 vector-directed coexpression of human tumor necrosis factor-α and herpes simplex virus thymidine kinase. *Cancer Res.* 1998;58:5731-5737.

12. Alemany R, Gomez-Manzano C, Balague C, Yung WK, Curiel DT, Kyritsis AP, Fueyo J. Gene therapy for gliomas: molecular targets, adenoviral vectors, and oncolytic adenoviruses *Exp. Cell Res.* 1999;252:1-12.

13. Kim JH, Kim SH, Brown SL, Freytag SO. Selective enhancement by an antiviral agent of the radiation-induced cell killing of human glioma cells transduced with HSV-tk gene. *Cancer Res.* 1994;54:6053-6056.

14. Kinsella T, Mitchell J, Russo A, Morstyn G, Glatstein E. The use of halogenated thymidine analogues as clinical radiosensitizers. Rationale, current status, and future prospects. *Int. J. Radiat. Oncol. Biol. Phys.* 1984;10:139-146.

15. Tada M, Sawamura Y, Sakuma S, Suzuki K, Ohta H, Aida T, Abe H. Cellular and cytokine responses of the human central nervous system to intracranial administration of tumor necrosis factor α for the treatment of malignant gliomas. *Cancer Immunol. Immunother.* 1993;36:251-259.

16. Hernandez-Caselles T, Stutman O. Immune functions of tumor necrosis factor. *J. Immunol.* 1993;151:3999-4012.

17. Feinberg B, Kurzrock R, Talpaz M, Blick M, Saks S, Gutterman JU. A phase I trial of intravenously administered tumor necrosis factor-alpha in cancer patients. *J. Clin. Oncol.* 1988; 6:1328-1334.

18. Gamm H, Lindemann A, Martelsmann R, Herrmann F. Phase I trial of recombinant human tumor necrosis factor-α in patients with advanced malignancy. *Eur. J. Cancer* 1991;27:856-863.

19. Gridley DS, Hammond SN, Liwnicz B. Effects of tumor necrosis factor-α and radiation on human tumor xenografts. *Anticancer Res.* 1994;14:1107-1112.

20. Gridley DS, Andres ML, Garner C, Mao XW, Slater JM. Evaluation of tumor necrosis factor-α and radiation efficacy in a human lung adenocarcinoma model. *Oncol. Res.* 1997;8:484-495.

21. Gridley DS, Archambeau JO, Andres ML, Mao XW, Slater JM. Tumor necrosis factor-α enhances the anti-tumor effects of radiation against glioma xenografts. *Oncol. Res.* 1997;9:217-227.

22. Sersa G, Willingham V, Milas L. Anti-tumor effects of tumor necrosis factor alone or combined with radiotherapy. *Int. J. Cancer* 1988;42:129-134.

23. Hallahan DE, Vokes EE, Rubin SJ, O'Brien S, Samuels B, Vijaykuman S, Kufe DW, Phillips R, Weichselbaum RR. Phase I dose-escalation study of tumor necrosis factor-α and concomitant radiation therapy. *Cancer J.* (from Scientific American) 1995;1:204-209.

24. Baher AG, Andres ML, Folz-Holbeck J, Cao JD, Gridley DS. A model using radiation and plasmid-mediated tumor necrosis factor-β gene therapy for treatment of glioblastoma. *Anticancer Res.* 1999;19:2917-2924.

25. Li J, Andres ML, Fodor I, Nelson GA, Gridley DS. Evaluation of pGL1-TNF-α therapy in combination with radiation. *Oncol Res.* 1998;10:379-387.

26. Benda P, Lightfoot J, Sato G, Levine L, Sweet W. Differentiated rat glial cell strain in tissue culture. *Science* 1968;161:370-371.

27. Sheay W, Nelson S, Martinez I, Chu THT, Bhatia S, Dornburg R. Downstream insertion of the adenovirus tripartite leader sequence enhances expression in universal eukaryotic vectors. *Biotechniques* 1993;15:856-862.

28. Gridley DS, Andres ML, Slater JM. Enhancement of prostate cancer xenograft growth with whole-body radiation and vascular endothelial growth factor. *Anticancer Res.* 1997;17:923-928.

29. Kajioka EH, Andres ML, Li J, Mao XW, Moyers MF, Nelson GA, Slater JM, Gridley DS. Acute effects of whole-body proton irradiation on the immune system of the mouse. *Radiat. Res.* 2000;153:587-594.

30. Moritz T, Niederle N, Baumann J, May D, Kurchel E, Osieka R, Kempeni J, Schlick E, Schmidt CG. Phase I study of recombinant human tumor necrosis factor α in advanced malignant disease. *Cancer Immunol. Immunother.* 1989; 29:144-150.

31. Sidhu RS, Bollon AP. Tumor necrosis factor activation and cancer therapy – a perspective. *Pharmacol. Ther.* 1993; 57:79-128.

32. Yin D, Kondo S, Barnett GH, Morimura T, Takeuchi J. Tumor necrosis factor-α induces p53-dependent apoptosis in rat glioma cells. *Neurosurg.* 1995; 37:758-763.

33. Mauceri HJ, Hanna NN, Wayne JD, Hallahan DE, Hellman S, Weichselbaum RR. Tumor necrosis factor α (TNF-α) gene therapy targeted by ionizing radiation selectively damages tumor vasculature. *Cancer Res.* 1996; 56:4311-4314.

34. Srinivasan JM, Fajardo LF, Hahn GM. Mechaism of antitumor activity of tumor necrosis factor a with hyperthermia in a tumor necrosis factor α-resistant tumor. *J. Natl. Cancer Inst.* 1990; 82:1904-1910.

35. Jarvis WD, Grant S, Kolesnick RN. Ceramide and the induction of apoptosis. (minireview) *Clin. Cancer Res.* 1996; 2:1-6.

36. Yamauchi N, Karizana H, Watanabe H, Neda H, Maeda M, Nutsu Y. Intracellular hydroxyl radical production induced by recombinant human tumor necrosis factor. *Cancer Res.* 1989; 49:1671-1675.

37. Steadman R, Petersen, MM, Topley N, Williams D, Matthews , Spur B, Williams JD. Differential augmentation by recombinant human tumor necrosis factor-α of neutrophil responses to particulate zymosan and glucan. *J. Immunol.* 1990; 144:2712-2718.

38. Oliff A, Defea-Jones D, Boyer M, Martinez D, Kiefer D, Vuocola G, Wolfe A, Socker SH. Tumors secreting human TNF/cachectin induce cachexia in mice. *Cell* 1987;50:555-563.

39. Johnson RA, Boyce BF, Mundy GR, Roodman GD. Tumors producing human TNF induce hypercalcemia ad osteoclastic bone resorption in nude mice. *Endocrinol.* 1989;124:1424-1427.

40. Fossa A, Brandhorst D, Myklebust JH, Seeber S, Nowrousian MR. Relation between S-phase fraction of myeloma cells and anemia in patients with multiple myeloma. *Exp. Hematol.* 1999;27:1621-1626.

41. Chapman PB, Lester TJ, Casper ES, Gabrilove JL, Wong GY, Kempin SJ, Gold PJ, Welt, Warren RS. Clinical pharmacology of recombinant human tumor necrosis factor in patients with advanced cancer. *J. Clin. Oncol.* 1987;5:1942-1951.

42. Bauer KA, Ten Cate H, Barzegar S, Spriggs DR, Sherman ML, Rosenberg RD. Tumor necrosis factor infusions have a procoagulant effect on the hemastatic mechanism of humans. *Blood* 1989;74:165-172.

43. Piguet PF, Vesin C, Guo J, Donati Y, Barazzone C. Role of mast cells and monoamines in the thrombocytopaenia and mortality elicited by tumour necrosis factor in mice. *Immunol.* 1998;95:111-116.

44. Renard N, Nooijen PTGA, Schalkwijk L, De Waal RMW, Eggermont AMM, Lienard D, Kroon BBR, Lejeunes FJ, Ruiter DJ. VWF release and platelet aggregation in human melanoma after perfusion with TNFα. *J Pathol.* 1995;176:279-287.

45. Shen S, DeNardo GL, Jones TD, Wilder RB, O'Donnell RT, DeNardo SJ. A preliminary cell kinetics model of thrombocytopenia after radioimmunotherapy. *J. Nucl. Med.* 1998;39:1223-1229.

46. Phillippe C, Phillippe B, Fouqueray B, Perez J, Lebret M, Baud L. Protection from tumor necrosis factor-mediated cytolysis by platelets. *Am J. Pathol.* 1993;143:1713-1723.

47. Nieswandt B, Hafner M, Echtenacher B, Mannel DN. Lysis of tumor cells by natural killer cells in mice is impeded by platelets. *Cancer Res.* 1999;59:1295-1300.

48. Tacchini-Cottier F, Vesin C, Redard M, Buurman W, Piguet PF. Role of TNF receptors I and II in TNF-induced platelet consumption in mice. *J. Immunol.* 1998;160:6182-.6186

49. Caux C, Dezutter-Dambuyant C, Schmitt D, Banchereau J. GM-CSF and TNF-α cooperate in the generation of dendritic Langerhans cells. *Nature (Lond.)* 1992; 360:258-261.

50. Radzikowski C, Rygaard J, Budzynski W, Salwa J, Stenvang JP, Schou M, Lorenzen L, Zeuthen J. Cytotoxicity and proliferation of splenocytes and lymph node cells from adjuvant-treated nude mice. Studies of natural and in vitro activation. *A.P.M.I.S.* 1996;104:647-658.

51. He Y, Pimenov AA, Nayak J, Plowey J, Falo LD, Huang L. Intravenous injection of naked DNA encoding secreted flt3 ligand dramatically increases the number of dencritic cells and natural killer cells in vivo. *Hum. Gene Ther.* 2000;11:547-554.

52. Mizuno M, Yoshida J, Oyama H, Sugita K. Growth inhibition of glioma cells by liposome-mediated cell transfection with tumor necrosis factor-alpha gene – its enhancement by prior gamma-interferon treatment. *Neurol. Med. Chir. (Tokyo)* 1992;32:873-876.

53. Lai L, Alaverdi N, Maltais L, Morse HC 3rd. Mouse cell surface antigens: nomenclature and immunophenotyping. *J. Immunol.* 1998;160:3861-3868.

54. Harrington NP, Chambers KA, Ross WM, Filion LG. Radiation damage and immune suppression in splenic mononuclear cell populations. *Clin. Exp. Immunol.* 1997;107:417-424.

55. Janeway CA, Bottomly K. Signals and signs for lymphocyte responses. *Cell* 1994;76:275-285.

56. Holub M. T cells. I. T-cell differentiation and function. In: *Immunology of Nude Mice*. Boca Raton, FL: CRC Press, Inc. 1989;53-66.

57. Stutman O. Postthymic T-cell development. *Immunol. Rev.* 1986;91:159-194.

58. Aderka D. The potential biological and clinical significance of the soluble tumor necrosis factor receptors. *Cytokine Growth Factor Rev.* 1996;7:231-240.

Table 1. Expression of TNF-α protein in C6 tumor with time after intratumoral injection of pGL1-TNF-α in Phase A

Amount of	pg/g tumor		
pGL1-TNF-α[a] hours:	16	72	168
0 μg	0 +/- 0[b]	0 +/- 0	0 +/- 0
15 μg	404 +/- 60	135 +/- 68	7 +/- 5
150 μg	714 +/- 182	301 +/- 59	60 +/- 32
450 μg	765 +/- 201	294 +/- 55	146 +/- 51

[a]Single i.t. injection of pGL1-TNF-α, 7 days after s.c. implantation of 5 x 10^5 C6 cells; mean tumor volume at this time was 300-500 mm^3.

[b]Mean +/- SEM; n = 3/group/time point. Sensitivity of assay: 0.18 pg/ml.

Table 3. Relative spleen weight (RSW) and leukocyte and lymphocyte numbers in blood and spleen from mice in Phase B

		Blood		Spleen		
Time[a]	Group[b]	leukocytes ($x10^6$/ml)	lymphocytes ($x10^6$/ml)	RSW	leukocytes ($x10^6$/ml)	lymphocytes ($x10^6$/ml)
-	No tumor	4.2+/-0.2[c]	2.8+/-0.2	41.5+/-1.8	55.4+/-3.0	30.1+/-2.5
	Tumor-bearing:					
16 hr	PBS	5.4+/-0.6	3.0+/-0.4	42.6+/-2.7	49.7+/-6.3	29.6+/-5.0
	pWS4 (150μg)	5.2+/-0.4	2.1+/-0.1	53.0+/-4.5	57.6+/-9.4	28.8+/-5.4
	pGL1-TNF (15μg)	4.5+/-0.3	2.3+/-0.2	46.7+/-2.6	45.4+/-9.0	25.6+/-6.0
	pGL1-TNF (150μg)	5.1+/-0.3	2.4+/-0.2	53.3+/-5.0	60.1+/-9.0	31.3+/-5.4
	pGL1-TNF (450μg)	4.8+/-0.4	2.0+/-0.2	54.3+/-3.4	72.2+/-8.9	37.7+/-6.3
64 hr	PBS	6.0+/-0.5[d]	3.2+/-0.3	55.3+/-3.1	120.2+/-17.3[e]	42.1+/-3.7
	pWS4 (150μg)	5.9+/-0.5	3.2+/-0.3	53.2+/-2.6	125.4+/-13.3[e]	43.2+/-5.3
	pGL1-TNF (15μg)	5.5+/-0.3	2.5+/-0.1	69.9+/-7.1[e]	140.0+/-9.8[e]	57.8+/-5.1[f]
	pGL1-TNF (150μg)	6.4+/-0.6[d]	2.7+/-0.1	74.2+/-9.0[e]	162.9+/-14.0[e]	62.7+/-7.9[e]
	pGL1-TNF (450μg)	5.2+/-0.4	2.7+/-0.3	57.5+/-5.5	146.3+/-13.2[e]	49.1+/-7.9
88 hr	PBS	4.5+/-0.3	2.4+/-0.2	50.7+/-1.5	78.7+/-7.3	53.2+/-5.1
	pWS4 (150μg)	5.4+/-0.3	3.2+/-0.2	59.7+/-4.0[d]	100.2+/-10.6[d]	63.7+/-65[e]
	pGL1-TNF (15μg)	5.0+/-0.4	2.6+/-0.2	77.4+/-5.7[e,g]	118.0+/-13.0[e]	73.3+/-8.9[e]
	pGL1-TNF (150μg)	5.8+/-0.7	3.0+/-0.3	65.9+/-3.4[e]	99.3+/-9.1[d]	65.6+/-7.8[e]
	pGL1-TNF (450μg)	4.8+/-0.7	2.2+/-0.2	62.9+/-6.5[f]	86.9+/-7.0	53.9+/-5.4

[a]Time after i.t. injection of pGL1-TNF-α.

[b]n = 30 mice with no tumor; n = 10 mice with tumor/group/time point.

[c]Mean +/- SEM.

[d]$P<0.05$ compared to no tumor.

[e]$P<0.001$ compared to no tumor.

[f]$P<0.01$ compared to no tumor

[g]$P<0.01$ compared to PBS at 88 hr.

Table 4. Spontaneous and mitogen-induced blastogenesis in mice from Phase B

Time[a]	Group[b]	Spontaneous blastogenesis (cpm/10^6cells) blood	spleen	Spleen LPS - SI[c]
-	No tumor	6,652 +/- 756[d]	26,318 +/- 2,670	161 +/- 23
	Tumor-bearing:			
16 hr	PBS	2,444 +/- 553	29,220 +/- 3,236	248 +/- 20
	pWS4 (150μg)	27,095 +/- 3,684[e,f]	33,700 +/- 4,700	199 +/-31
	pGL1-TNF (15μg)	5,230 +/-1 ,175	25,910 +/- 4,610	194 +/- 36
	pGL1-TNF (150μg)	18,192 +/- 2,906[e]	35,275 +/- 3,884	137 +/- 23
	pGL1-TNF (450μg)	24,833 +/- 6,754[e,f]	43,819 +/- 12,827	141 +/- 23
64 hr	PBS	4,933 +/- 809	39,324 +/- 3,489	114 +/- 16
	pWS4 (150μg)	7,626 +/- 1,159	36,961 +/- 3,344	130 +/- 16
	pGL1-TNF (15μg)	7,017 +/- 1,039	50,212 +/- 5,727[g]	131 +/- 30
	pGL1-TNF (150μg)	8,831 +/- 1,465	49,680 +/- 4,343	68 +/- 20
	pGL1-TNF (450μg)	13,513 +/- 2,779	38,897 +/- 3,908	129 +/- 46
88 hr	PBS	3,528 +/- 569	26,699 +/-2,199	176 +/- 17
	pWS4 (150μg)	3,760 +/- 579	27,372 +/- 2,461	161 +/- 13
	pGL1-TNF (15μg)	7,595 +/- 735	34,707 +/- 3,639	207 +/- 20
	pGL1-TNF (150μg)	5,968 +/- 589	28,918 +/- 5,024	162 +/- 14
	pGL1-TNF (450μg)	7,618 +/- 1,379	27,278 +/- 2,955	163 +/- 17

[a]Time after i.t. injection of pGL1-TNF-α.

[b]n = 30 mice with no tumor; n = 10 mice with tumor/group/time point.

[c]Stimulation index (SI) after activation with lipopolysaccharide (LPS): (cpm with LPS – cpm without LPS)/cpm without LPS.

[d]Mean +/- SEM.

[e]$P<0.001$ compared to no tumor and PBS.

[f]$P<0.001$ compared to pGL1-TNF-α (15μg) at 16 hr.

[g]$P<0.005$ compared to no tumor.

LEGENDS FOR FIGURES

Figure 1. NK cells in Phase B mice. Each bar represents the mean +/- SEM; n = 30 mice with no tumor, n = 10 tumor-bearing mice/group/time point. a: $P<0.001$ vs. no tumor and PBS, $P<0.05$ vs pGL1-TNF-α (150μg); b: $P<0.001$ vs. no tumor, $P<0.05$ vs. pGL1-TNF-α (15μg).

Figure 2. B lymphocytes in Phase B mice. Each bar represents the mean +/- SEM; n = 30 mice with no tumor, n = 10 tumor-bearing mice/group/time point. a: $P<0.005$ vs. PBS; b: $P<0.005$ vs. no tumor and PBS; c: $P<0.001$ vs. no tumor.

Figure 3. Lymphocytes expressing the CD71 activation marker in Phase B mice. Each bar represents the mean +/- SEM; n = 30 mice with no tumor, n = 10 tumor-bearing mice/group/time point. a: $P<0.01$ vs. no tumor; b: $P<0.05$ vs. pGL1-TNF-α (450μg); c: $P<0.001$ vs no tumor; d: $P<0.01$ vs all other groups except pGL1-TNF-α (150μg); e: $P<0.05$ vs. all other groups except pGL1-TNF-α (15μg); f: $P<0.05$ vs. no tumor, pGL1-TNF-α (15μg) and pGL1-TNF-α (150μg); g: $P<0.05$ vs. no tumor and PBS.

Figure 4. Lymphocytes expressing the CD25 activation marker in Phase B mice. Each bar represents the mean +/- SEM; n = 30 mice with no tumor, n = 10 tumor-bearing mice/group/time point. a: $P<0.005$ vs. no tumor; b: $P<0.005$ vs. no tumor and PBS; c: $P<0.05$ vs. no tumor, PBS, and pGL1-TNF-α (450μg); d: $P<0.001$ vs. no tumor; e: $P<0.001$ vs. no tumor, pGL1-TNF-α (15μg), and pGL1-TNF-α (150μg).

Figure 5. Lymphocytes expressing CD3/CD71 and CD3/CD25 in Phase B mice. Each bar represents the mean +/- SEM; n = 30 mice with no tumor, n = 10 tumor-bearing mice/group/time point. a: $P<0.0$ vs. need stats to finish

Figure 6.. Tumor volume with time after pGL1-TNF-α and radiation treatment in Phase C mice. Each point represents the mean +/- SEM for 5-6 animals/group. a: $P<0.05$ compared to pGL1-TNF-α; b: $P<0.05$ compared to PBS.

FIGURE 1

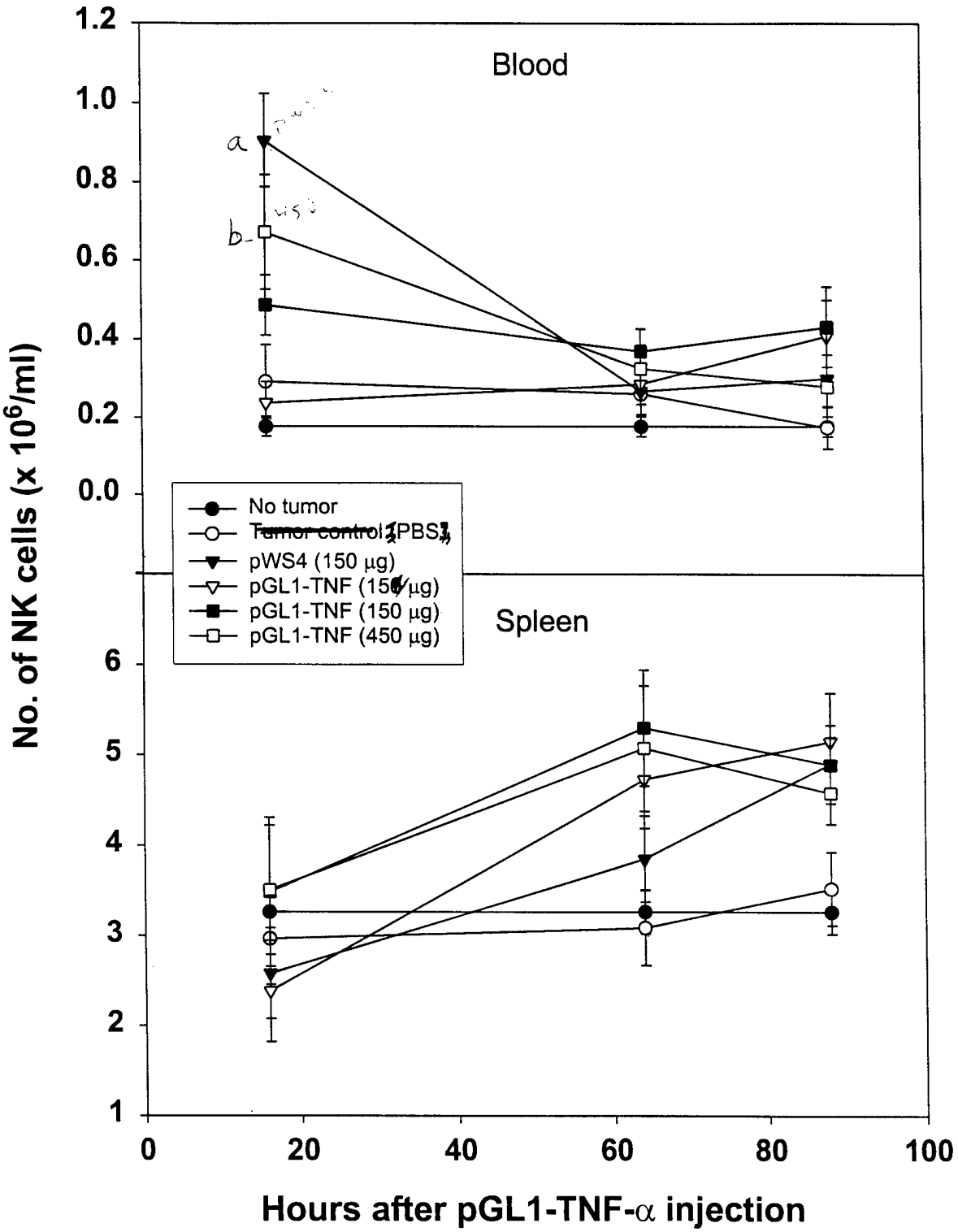

a $p<0.001$ vs no tumor, and tumor control (PBS); $p<0.05$ vs pGL1-TNF-α (15 μg)

b $p<0.001$ vs no tumor; $p<0.05$ vs pGL1-TNF-α (15 μg).

FIGURE 2

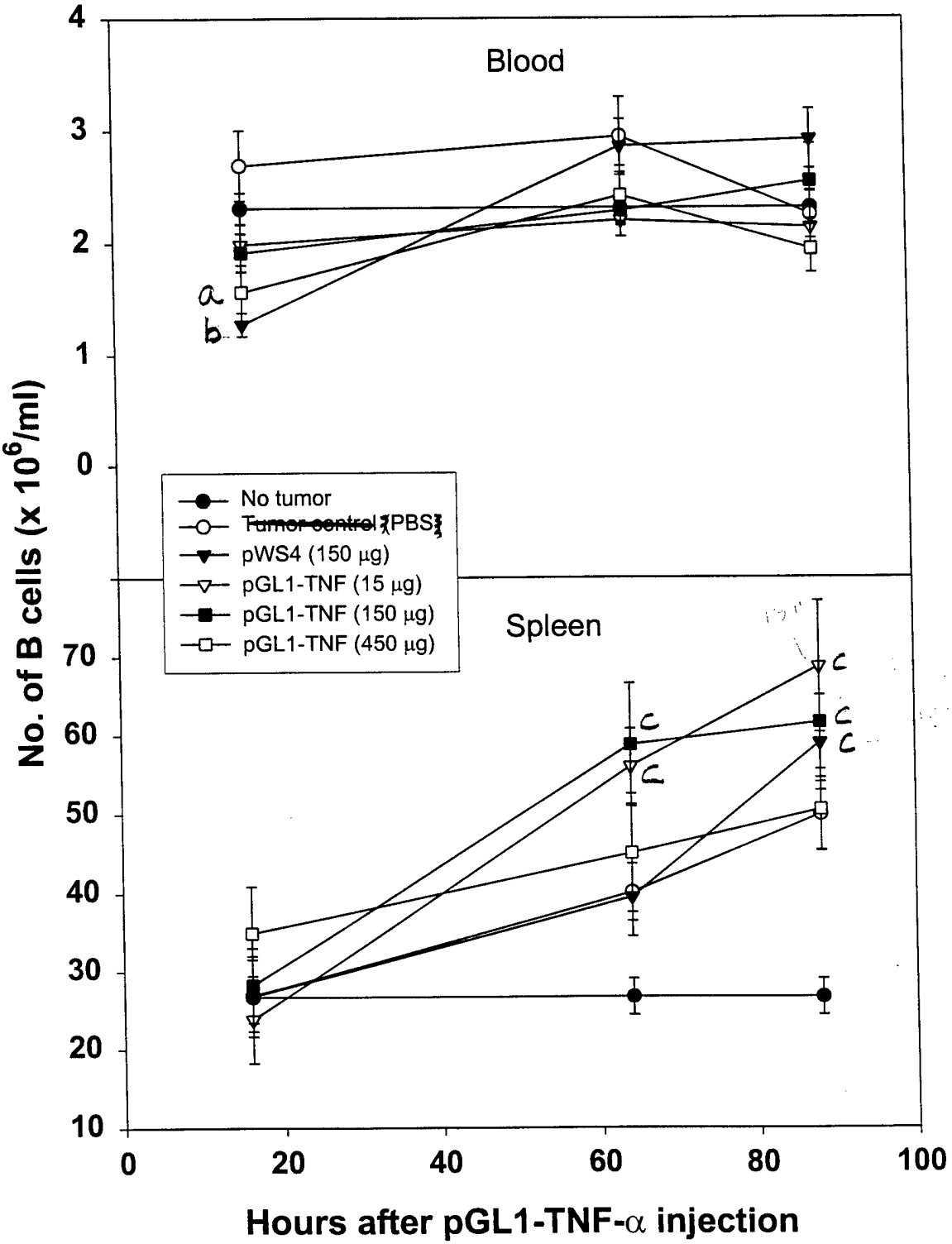

a $p < 0.005$ vs no tumor and ~~tumor control~~ (PBS)

b $p = 0.001$ vs no tumor,

[illegible] vs PBS

FIGURE 3

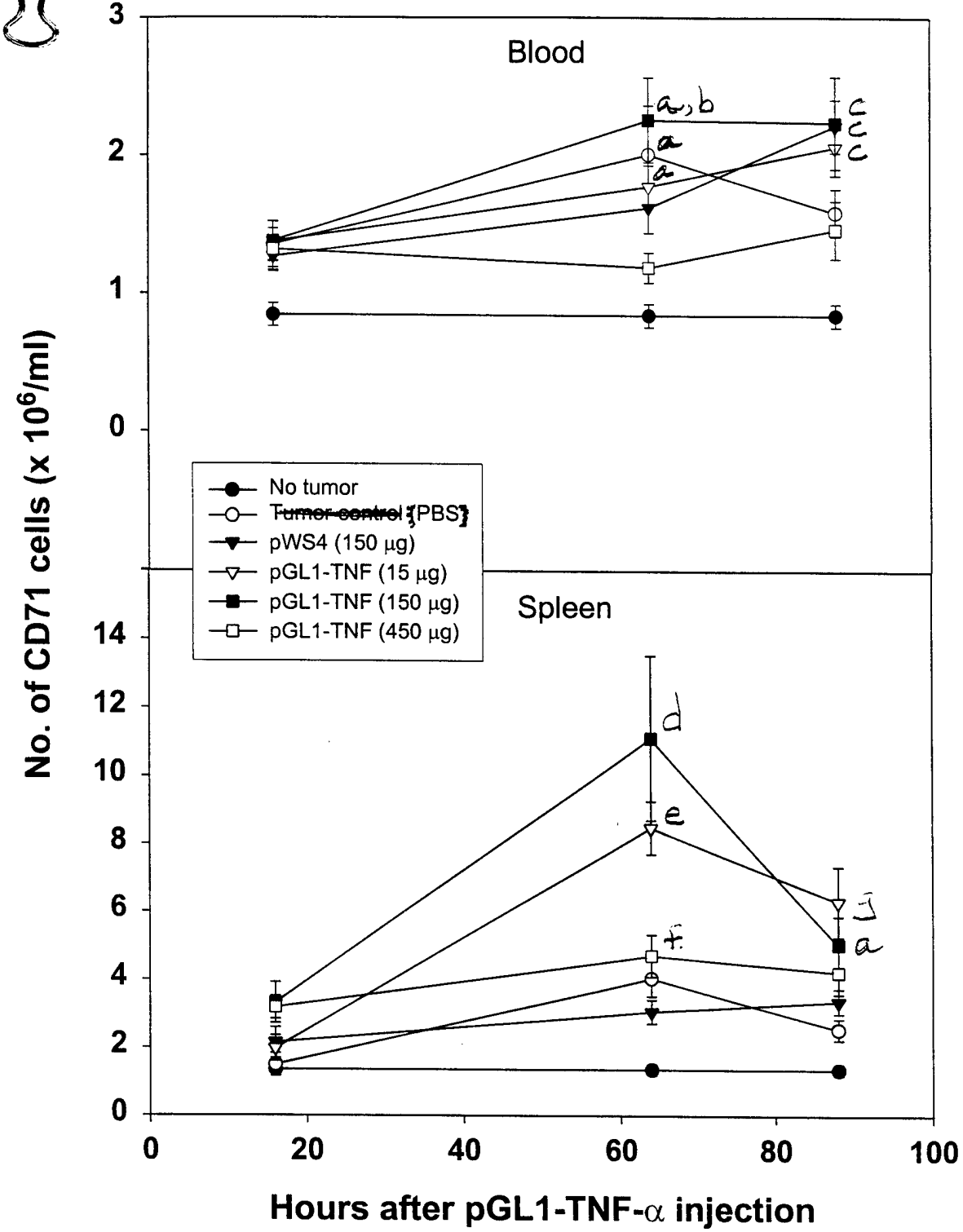

a $p < 0.01$ vs no tumor,

b $p < 0.05$ vs pGL1-TNF-α (450 mg)

c $p < 0.001$ vs no tumor,

d $p < 0.01$ vs ~~no tumor~~ all other groups except pGL1-TNF-α (150 mg)

e $p < 0.05$ vs ~~no tumor~~ all other groups except pGL1-TNF-α (15 mg)

f $p < 0.05$ vs no tumor, pGL1-TNF-α (15 mg), and pGL1-TNF-α (150 mg)

g $p < 0.05$ vs no tumor and tumor control (PBS).

FIGURE 4

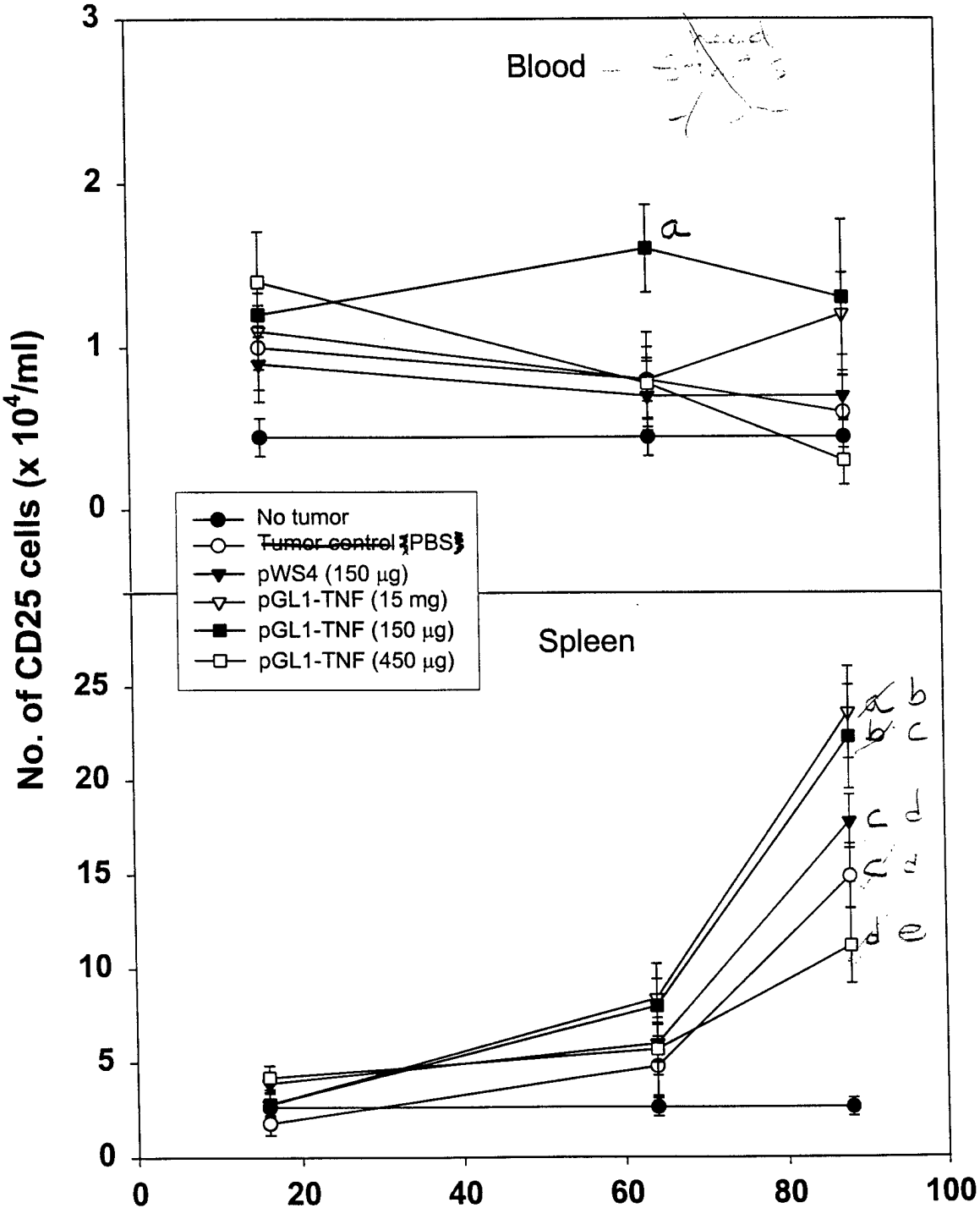

a $p < 0.005$ vs no tumor.

b a $p < 0.005$ vs no tumor, b, c, d, e $p < 0.05$ vs tumor control (PBS), pGL1-TNF-α (450 µg)

c a, b $p < 0.01$ vs " " " " " " " "

d a, b, c $p < 0.001$ vs " " " " " " " "

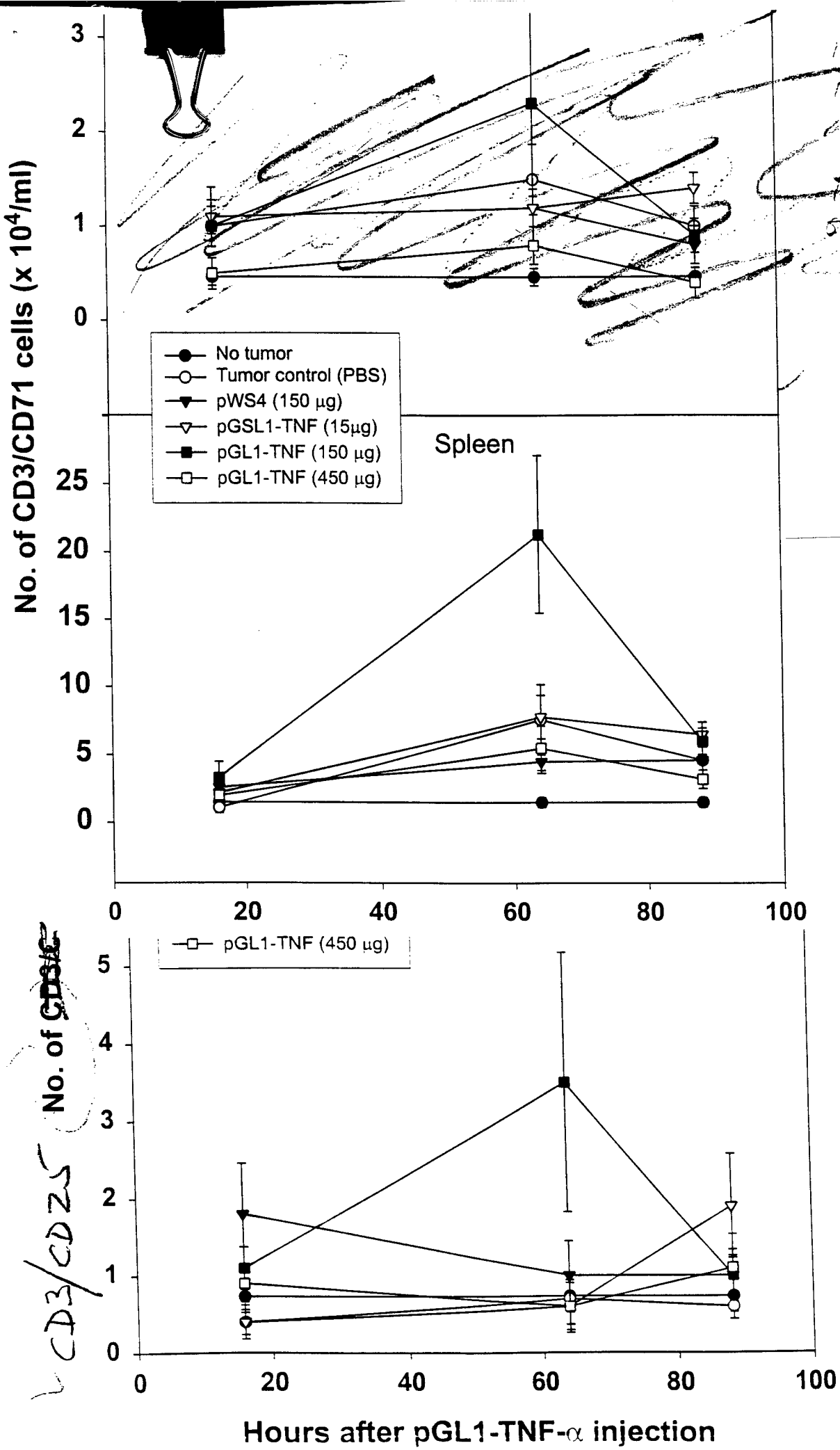
No. of CD3/CD71 cells (x 10⁴/ml)
No tumor
Tumor control (PBS)
pWS4 (150 µg)
pGSL1-TNF (15µg)
pGL1-TNF (150 µg)
pGL1-TNF (450 µg)
Spleen
No. of CD3/CD25
pGL1-TNF (450 µg)
Hours after pGL1-TNF-α injection

FIGURE 5A

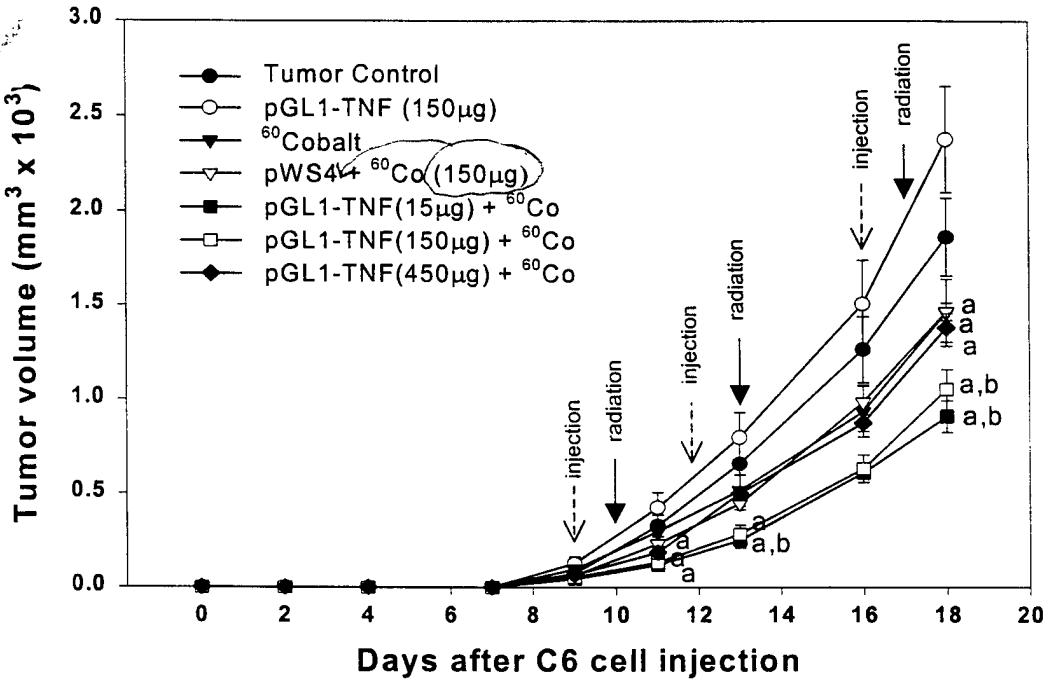
Tumor Control
pGL1-TNF (150μg)
60Cobalt
pWS4 + 60Co (150μg)
pGL1-TNF(15μg) + 60Co
pGL1-TNF(150μg) + 60Co
pGL1-TNF(450μg) + 60Co
Tumor volume (mm3 x 10^3)
Days after C6 cell injection
injection
radiation
injection
radiation
injection
radiation
a
a
a
a,b
a,b
a
a
a
a,b
3.0
2.5
2.0
1.5
1.0
0.5
0.0
0
2
4
6
8
10
12
14
16
18
20

FIGURE 6

Name of Project Director: Daila S.

DESCRIPTION AND PERFORMANCE SITES (FORM B)

DESCRIPTION: State the goal of the research project including how it relates to improving health care for the nation's people. Use succinct language to describe how the project goals will be achieved. Do Not exceed the space provided on this page.

The American Cancer Society estimates that 1,382,400 Americans were diagnosed with cancer and 560,000 Americans suffered cancer-related deaths during 1997. Approximately half of patients diagnosed with cancer receive radiation treatment. However, efficacy is limited by the dose which can be safely delivered to the tumor without damaging normal tissue and, thereby, causing life-threatening or debilitating side effects. This is especially true for highly malignant, radiation-resistant cancers, such as brain tumors — currently the leading cause of cancer death in children under 15 years of age.

The Loma Linda University Medical Center & Children's Hospital are recognized as a leader in radiation treatment of cancer by establishment of the world's first, largest, and most comprehensive hospital-based proton treatment facility. More precise tumor targeting, made possible by this advanced technology, has significantly improved patient survival and decreased side effects. However, successful treatment of highly malignant, radiation-resistant tumors requires an innovative adjunct strategy.

Our cancer research team (a collaboration between Radiation Medicine and Microbiology & Molecular Genetics) has reported promising preclinical results from recombinant human tumor necrosis factor-alpha (TNF-α) protein administration prior to radiotherapy. Immunomodulation and synergistic reduction of lung, colon, and brain (glioma) tumor volumes were achieved in the athymic/nude mouse.

The *project goal* is to increase the efficacy and safety of combined TNF-α/radiotherapy for cancer using the emerging biotechnology of gene therapy. We have collaborated with the Center for Molecular Biology & Gene Therapy to construct a plasmid for local, high level production of human TNF-α within tumors. We have chosen subcutaneous and intracranial implantation of rat C6 glioma cells into Sprague Dawley rats to simulate highly malignant, radiation-resistant human cancers of the body and brain, respectively. This cost-effective preclinical model facilitates intracranial tumor implantation, *in vivo* gene therapy, proton radiotherapy, and provides a more complete analysis of immunomodulation.

The *specific aims* are to determine: **1)** the optimal dose of plasmid (pWS4-TNF-α) to administer prior to radiotherapy; **2)** whether plasmid-mediated TNF-α gene therapy enhances the antitumor effects of conventional radiotherapy and stimulates immunological response in the subcutaneous glioma model; and **3)** whether plasmid-mediated TNF-α gene therapy enhances the antitumor effects of proton radiotherapy and stimulates immunological responses in the intracranial glioma model.

PROJECT SITE(s) (*Organization, City, State*):

Loma Linda University and Medical Center
Loma Linda, CA

Name of Project Director: Daila S.

DESCRIPTION AND PERFORMANCE SITES (FORM B)

DESCRIPTION: State the goal of the research project including how it relates to improving health care for the nation's people. Use succinct language to describe how the project goals will be achieved. Do Not exceed the space provided on this page.

The American Cancer Society estimates that 1,382,400 Americans were diagnosed with cancer and 560,000 Americans suffered cancer-related deaths during 1997. Approximately half of patients diagnosed with cancer receive radiation treatment. However, efficacy is limited by the dose which can be safely delivered to the tumor without damaging normal tissue and, thereby, causing life-threatening or debilitating side effects. This is especially true for highly malignant, radiation-resistant cancers, such as brain tumors — currently the leading cause of cancer death in children under 15 years of age.

The Loma Linda University Medical Center & Children's Hospital are recognized as a leader in radiation treatment of cancer by establishment of the world's first, largest, and most comprehensive hospital-based proton treatment facility. More precise tumor targeting, made possible by this advanced technology, has significantly improved patient survival and decreased side effects. However, successful treatment of highly malignant, radiation-resistant tumors requires an innovative adjunct strategy.

Our cancer research team (a collaboration between Radiation Medicine and Microbiology & Molecular Genetics) has reported promising preclinical results from recombinant human tumor necrosis factor-alpha (TNF-α) protein administration prior to radiotherapy. Immunomodulation and synergistic reduction of lung, colon, and brain (glioma) tumor volumes were achieved in the athymic/nude mouse.

The *project goal* is to increase the efficacy and safety of combined TNF-α/radiotherapy for cancer using the emerging biotechnology of gene therapy. We have collaborated with the Center for Molecular Biology & Gene Therapy to construct a plasmid for local, high level production of human TNF-α within tumors. We have chosen subcutaneous and intracranial implantation of rat C6 glioma cells into Sprague Dawley rats to simulate highly malignant, radiation-resistant human cancers of the body and brain, respectively. This cost-effective preclinical model facilitates intracranial tumor implantation, *in vivo* gene therapy, proton radiotherapy, and provides a more complete analysis of immunomodulation.

The *specific aims* are to determine: **1)** the optimal dose of plasmid (pWS4-TNF-α) to administer prior to radiotherapy; **2)** whether plasmid-mediated TNF-α gene therapy enhances the antitumor effects of conventional radiotherapy and stimulates immunological response in the subcutaneous glioma model; and **3)** whether plasmid-mediated TNF-α gene therapy enhances the antitumor effects of proton radiotherapy and stimulates immunological responses in the intracranial glioma model.

PROJECT SITE(s) (*Organization, City, State*):

Loma Linda University and Medical Center
Loma Linda, CA

ORIGINA

FINAL REPORT
Subagreement No. 15-FY98-LLU-GRIDLEY

Period covered: January 25, 1999 – April 30, 2000

Dale S. Gridley 6/27/00
Signature of P.I. / Date

(909)558-8361 (909)558-0825 dgridley@dominion.llumc.edu
Phone fax e-mail

INTRODUCTION

The American Cancer Society estimates that 1,221,800 Americans were diagnosed with cancer and 563,100 Americans suffered cancer-related deaths in 1999. Although approximately one-half of cancer patients receive radiation treatment, efficacy is limited by the dose that can be safely delivered to the tumor without causing life-threatening or debilitating side effects. The Loma Linda University Medical Center (LLUMC) is recognized as a leader in radiation treatment of cancer through its establishment of the world's first, largest, and most comprehensive hospital-based proton treatment facility. More precise tumor targeting made possible by this advanced technology has significantly improved patient survival and decreased side effects. However, successful treatment of highly malignant tumors, requires adjunct strategies to enhance tumor response to proton (or conventional) radiotherapy. Our multi-disciplinary research team within the Department of Radiation Medicine (LLUMC) and the Department of Microbiology & Molecular Genetics (LLU) has reported a series of preclinical studies showing immunomodulation and a synergistic reduction in the volume of malignant tumors (brain, lung, and colon) by low-dose tumor necrosis factor-α (TNF-α) in athymic/nude (immunocompromised) mice when administered prior to radiotherapy. To achieve complete tumor regression without adverse side effects, however, we propose to increase TNF-α protein within the tumor. The *project goal* is to improve the efficacy and safety of a combined radiotherapy/TNF-α protocol using the emerging biotechnology of gene therapy. In collaboration with the Center of Molecular Biology & Gene Therapy (LLU), we have constructed a plasmid that expresses TNF-α protein (pGL1-TNF-α) in rat C6 glioma cells, both *in vitro* and *in vivo*. In the present study, athymic rodents will be used for both subcutaneous (s.c., in hind flank) and intracranial implantation of C6 glioma cells to simulate highly malignant tumors of the body and brain, respectively. The *primary hypothesis* is: Combined radiation and plasmid-mediated TNF-α gene therapy will produce a synergistic inhibition of tumor progression. The *secondary hypothesis* is: The mechanism of action will include not only the lethal effects of radiation and TNF-α within the tumor, but also their mutual stimulation of systemic antitumor immune responses. In testing these hypotheses, the following *specific aims* will be addressed: 1) measure the level and kinetics of TNF-α expression in s.c. C6 tumors after treatment with varying doses of pGL1-TNF-α; 2) determine if pGL1-TNF-α can enhance the antitumor effects of radiation against s.c. C6 tumor development and if immune system parameters are upregulated by the treatments; and 3) determine if pGL1-TNF-α can enhance the antitumor effects of proton radiation against intracranial C6 tumors and if immunesystem modification is similar to what is observed in Aim 2. The results of this study should provide valuable information that will be applicable to more common tumor types (e.g., those of the colon, breast, prostate, and lung) and thus may lead to improved management of many different types of cancers.

EXPERIMENTAL METHODS/RESULTS/DISCUSSION

In the original grant application submitted on 10/1/1998, the Sprague-Dawley rat was to be used as the host for C6 rat glioma. However, new information, published in 1/1999, described genetic disparity between Sprague-Dawley rats (and all other rat strains currently available) and the C6 rat glioma cells. Therefore, evaluating the effects of gene therapy in the C6 tumor/Sprague-Dawley rat model would be comprised due to rejection of the tumor cells in this non-syngeneic model. Because of these new findings, a request was made to NMTB to consider changing the animal model from rats to athymic mice. A revised 'Research Involving Animals' form was submitted on 3/8/1999 and notification of approval was received approximately two months later (letter to Mr. J. Patrick Yhip dated 5/6/1999). Thus, initiation of the study was delayed. However, since limited funding was available from other sources that allowed subcutaneous (s.c.) implantation of C6 tumors into athymic mice and treatment with radiation and plasmid-mediated TNF-α gene therapy, related experiments were proceeding. For the present study, athymic mice (outbred background, male, nu/nu) were utilized.

Data from all of Aim 1 and a *portion* of Aim 2 (performed in a series of *in vivo* phases) have been analyzed, compiled and, with the approval of NMTB, presented at a scientific meeting, as well as submitted for publication. The contents of the submitted manuscript (formatting of references and other sections are as specified by the International Journal of Cancer) and a poster presentation are included below.

Submitted to the International Journal of Cancer (in review):

MODEL OF pGL-1-TNF-α GENE AND RADIATION (PROTON AND γ-RAY) THERAPY AGAINST BRAIN TUMOR

Daila S. GRIDLEY[1,2], Jun LI[2], Eric H. KAJIOKA[1], Melba L. ANDRES[1], Michael F. MOYERS[1], and James M. SLATER[1]

Departments of [1]Radiation Medicine (Radiobiology Program) and [2]Microbiology & Molecular Genetics
Loma Linda University and Medical Center, Loma Linda, CA 92354 U.S.A.

Running Title: TNF-α GENE THERAPY AND RADIATION AGAINST GLIOMA

Corresponding author: Daila S. Gridley, Ph.D.
Chan Shun Pavilion, Room A-1010
11175 Campus Street
Loma Linda University School of Medicine
Loma Linda, CA 92354
Phone: (909)558-8361
Fax: (909)558-0825
E-mail: dgridley@dominion.llumc.edu

Key words: TNF-α, gene therapy, ionizing radiation, proton radiation, brain tumor

The major goal of this study was to determine if treatment with the newly constructed plasmid vector for tumor necrosis factor-α (pGL1-TNF-α) could enhance the radiation-induced growth reduction of C6 rat glioma. In addition, two different forms of ionizing radiation (^{60}cobalt photons and protons) were utilized. Body and spleen mass, leukocyte blastogenesis, and flow cytometry analysis of cell populations in blood and spleen were performed to detect toxicity, if any, and to identify mechanisms that may correlate with the anti-tumor action of combination therapy. C6 tumor cells were implanted subcutaneously into athymic mice and allowed to become established before treatment initiation. pGL1-TNF-α was injected into the implanted tumors, which were then irradiated 16-18 hr later; each modality was administered three times over 8-9 days. The addition of pGL1-TNF-α significantly enhanced the anti-tumor effect of radiation ($p<0.05$). The effect was more than additive, since pGL1-TNF-α alone did not slow tumor progression and radiation alone had only a modest effect. Administration of pGL1-TNF-α together with proton radiation resulted in tumor volumes that were 23% smaller than those following pGL1-TNF-α/γ-ray treatment; a similar differential in tumor size was observed in the groups receiving only radiation. Body weights and blood and spleen cell analyses did not reveal treatment-related toxicity. High basal proliferation of blood leukocytes and increased B cell levels in the spleen were associated with pGL1-TNF-α + ^{60}Co or proton treatment. Overall, the results suggest that the pGL1-TNF-α/radiation combination is effective and safe under the conditions employed. This is the first study to combine gene and proton radiation therapy and to show, under controlled experimental conditions, that proton radiation may have a greater effect against malignant tumors compared to the same physical dose of γ-radiation.

INTRODUCTION

According to American Cancer Society estimates, approximately 16,800 brain and other nervous system cancers were newly diagnosed and 13,100 individuals with these diseases died in the U.S.A. in 1999 (Landis *et al.*, 1999). Although high-grade brain tumors are not frequent in the human population, they are among the most deadly malignancies in humans. Furthermore, there is considerable evidence that the incidence of primary brain tumors is increasing in the elderly population (Laws, 1993). In children, tumors of the central nervous system (CNS) are the leading solid neoplasms, being second only to leukemias in their overall frequency (Cohen *et al.*, 1994). Curative therapy for high-grade brain tumors, such as glioblastoma multiforme, is extremely rare and overall survival time is only 1 year from the time of diagnosis (Loeffler *et al.*, 1992; Prados *et al.*, 1998).

Approximately 50% percent of all cancer patients in the U.S.A. receive radiation at some time during their treatment (Coia *et al.*, 1994). This includes the great majority of individuals with malignant gliomas. However, because of the inability to selectively irradiate the tumor mass, normal adjacent tissues are frequently injured. High doses of brain irradiation can result in radio-necrosis, edema, and serious intellectual, motor and sensory impairment (Hawkins *et al.*, 1987 Pollack, 1994). As a consequence, a less than optimal total dose is frequently used to reduce the possibility of unacceptable damage to normal tissue. In ~90% of children with high-grade brain tumor, the tumor recurs within the irradiated field because the prescribed dose was insufficient (Leibel and Sheline, 1985; Archambeau *et al.*, 1991). It is clear that new therapeutic approaches are needed to augment existing therapies for improved management of these neoplasms.

Radiotherapy with heavy charged particles, such as protons, provide a superior method of tumor targeting. The dose distribution generated by a proton beam allows the radiation oncologist to reduce the dose delivered to normal tissues by a factor of 2 to 5 compared to conventional radiotherapy, thereby allowing a higher total dose to be delivered to the tumor target (Archambeau and Bennet, 1972; Archambeau *et al.*, 1994). Thus, proton beam therapy has the potential to

realize higher cure rates with fewer side effects than conventional photon beams. Loma Linda University Medical Center established the world's first hospital-based proton treatment center in 1990 (Slater *et al.* 1988; Slater *et al.* 1991). More than 5,000 patients have now received proton therapy at the facility. The proton accelerator is also available for biological and physics research.

We and others have recently demonstrated that tumor necrosis factor-α (TNF-α), a multi-functional polypeptide produced primarily by activated macrophages, can enhance the anti-tumor effects of radiation (Sersa *et al.*, 1988; Gridley *et al.*, 1994a, 1994b, 1997b, 1997c; Seung *et al.*, 1995; Mauceri *et al.*, 1996). The biological effects of TNF-α include induction of hemorrhagic necrosis in tumors, direct cytotoxicity against tumor cells, and activation of effector cells with tumoricidal activity (Carswell *et al.*, 1975; Talmadge *et al.*, 1988; Hernandez-Caselles and Stutman 1993). However, serious side effects (e.g. hypotension, metabolic acidosis and respiratory distress) have been noted with systemic administration of high-dose TNF-α, thereby limiting its use as a sole therapeutic agent (Creaven *et al.*, 1987; Hersh *et al.*, 1991).

Tumor-localized gene therapy studies are now being conducted, with most efforts thus far concentrating on viruses as vectors for TNF-α and other genes of interest (Kramm *et al.*, 1995). Unfortunately, clinical trials employing virus-based gene therapies have shown very little or no success with varying degrees of toxicity (Alemany *et al.*, 1999; Melvor 1999). Plasmid-mediated gene transfer offers several advantages compared to viral vectors: dividing cells are not required, insertional mutagenesis is minimized, there is virtually no size limitation, and immunological problems should be less likely, in as much as DNA is a very poor antigen (Li and Huang 2000). Furthermore, interpretation of results is facilitated with naked plasmid vectors by the absence of liposomes, which by themselves can mediate potent effects.

The major goals of the present study were to determine the effects of our newly constructed plasmid, pGL1-TNF-α, when injected into tumors as naked DNA and administered together with ionizing radiation (proton or γ-ray), against a brain tumor type that is among the most radioresistant and is virtually incurable. *This is the first study to employ a combination of gene therapy and proton radiation therapy.* Since both TNF-α and ionizing radiation have profound effects on leukocyte populations and can lead to serious side effects, we performed *in vitro* assays of blood and spleen. These data were also evaluated to determine if changes in leukocyte populations could be correlated with enhanced anti-tumor efficacy.

MATERIAL AND METHODS

Animals

Athymic mice (n = 56; outbred background, male, nu/nu) were purchased from Charles River Breeding Laboratories, Inc. (Wilmington, MA) at 5-6 weeks of age and housed in filter-top cages under conditions controlled for temperature, humidity, and a 12-12 hr day-night cycle. Autoclaved bedding, food, and water were provided and the animals were acclimatized for 2 weeks prior to experimentation. The mice were euthanized by rapid CO_2 asphyxiation in compliance with the National Institutes of Health (NIH) Guide for the Care and Use of Laboratory Animals when mean tumor volume in the nontreated tumor control group reached a maximum of ~2500 mm^3. This study was approved by our institutional Animal Research Committee.

C6 tumor cell line

The rat C6 nitrosourea-induced glioma cell line (Benda *et al.* 1968), was obtained from the American Type Culture Collection (ATCC; Rockville, MD). The cells were cultured in Dulbecco's minimal essential medium (DMEM; Irvine Scientific, Santa Ana, CA) supplemented with 10% bovine calf serum (Hyclone Laboratories, Logan, UT), 100 μg/ml fungizone (E.R. Squibb & Sons, Princeton, NJ), and 50 μg/ml gentamicin (Sigma Chemical Co., St. Louis, MO). The cells were incubated at 37°C in 5% CO_2 until near confluence, harvested with 0.25% trypsin solution, washed, counted, and adjusted to the appropriate concentration.

Tumor induction and volume measurements

The C6 tumor cells were harvested, washed, counted, and injected subcutaneously (s.c.) in the right hind flank at 5×10^5 cells/0.2 ml PBS/mouse. Tumor dimensions were measured with

vernier calipers and volumes were calculated: tumor volume (mm^3) = (H · W · L)/2, where H = height, W = width, and L = length of the tumor.

pGL1-TNF-α

The human recombinant TNF-α coding sequence in plasmid pUC18 was purchased from R&D Systems, Inc. (Minneapolis, MN) and ligated into the polylinker region of plasmid pWS4, a universal eukaryotic gene expression vector that contains the cytomegalovirus promoter (Sheay *et al.*, 1993). Details of construction and preliminary testing of pGL1-TNF-α have been previously reported (Li *et al.*, 1999). Large amounts of pGL1-TNF-α and the parental pWS4 plasmid for the present experiments were obtained by transformation into competent *E. coli* (strain DHα5) and standard purification techniques.

Tumor irradiation with protons and γ-rays

Tumors were irradiated with γ-rays (photons) using an Eldorado gamma radiation machine (Atomic Energy of Canada, Ltd., Commercial Products Division, Ottawa, Canada) containing a ^{60}Co source. Lipowitz metal alloy blocks were used to shield normal tissues and a 0.5 cm 'superflab' bolus was placed on top of each tumor during irradiation to achieve full electronic equilibrium. Proton irradiation was performed in the Proton Treatment Center, located within Loma Linda University Medical Center. Protons were delivered at an energy of 250 MeV with 60 mm of range modulation. The tumor surface was placed at the center of the modulated region. Tumors were irradiated with the same physical dose of either γ-rays or protons at 2 gray (Gy) x 3 fractions, giving a total dose of 6 Gy per tumor. The dose rate for γ-rays was ~0.32 Gy/min; protons were delivered as a pulsed beam in 0.3 sec pulses every 2.2 s, giving an average dose rate of ~0.90 Gy/min. Prior to irradiation, the mice were lightly anesthetized with a ketamine/xylazine combination; animals not scheduled for treatment were also anesthetized to equalize the stress factor. Tumors in up to 8 mice were irradiated simultaneously.

Treatment protocol

This study was performed in two separate experiments. In both experiments, the treatments were initiated when palpable tumors first appeared in all C6 cell-injected animals (days 7-8 post-injection). Mice were euthanized 1 day after the last irradiation (day 17). The animals were assigned to test and control groups immediately before the first treatment. Intratumoral injections of pGL1-TNF-α and pWS4 were administered at a dose 50 μg/injection using a 10 μl Hamilton syringe with a 1/2 inch needle; total volume injected was 225 μl. The solution was delivered to a single location, approximately in the center of the tumor mass. Sixteen to 18 hr thereafter, tumors were irradiated with 2 Gy of either ^{60}Co γ-rays or protons. Plasmid injection and radiation were each delivered three times over a period of 8-9 days. Mice were weighed and the blood and spleens were collected for *in vitro* assays.

Body and spleen mass and spleen and blood leukocyte counts

At the time of euthanasia, the animals and spleens were weighed. Spleens were processed into single-celled suspensions, erythrocytes were lysed with lysing buffer, and the remaining cells were counted using an ABC Hematology Analyzer (Heska Corporation, Waukesha, WI). To determine leukocyte concentration in blood, erythrocytes were lysed by using the Unopette Microcollection System (Becton Dickinson Co., Rutherford, NJ) and the remaining cells were counted with a hemocytometer.

Spontaneous and mitogen-induced blastogenesis

These assays have been previously described in detail (Gridley *et al.*, 1997b; Kajioka *et al.*, 1999). Briefly, the incorporation of ^{3}H-thymidine (^{3}H-TdR; ICN Biochemicals, Costa Mesa, CA) into cell DNA was used to quantify the basal proliferation of leukocytes and the response of spleen cells to lipopolysaccharide (LPS; Sigma Chemical Co., St. Louis, MO). In the spontaneous blastogenesis assay, the disintegrations per minute (dpm) were adjusted to 10^6 leukocytes/ml, based on the blood

volume tested and cell counts. Response of spleen cells to LPS is expressed as a stimulation index (SI): SI = (dpm with mitogen – dpm without mitogen)/dpm without mitogen.

Flow cytometry analysis of blood and spleen lymphocytes

Immunophenotyping of peripheral blood and spleen samples was carried out to quantify specific lymphocyte populations using a FACSCalibur™ 4-channel dual laser flow cytometer (Becton Dickinson, Inc, San Jose, CA). A lyse-no wash, 2-tube procedure was employed using custom-monoclonal antibody (MAb) conjugates specially designed for investigators in the LLU Radiobiology Program by Pharmingen (San Diego, CA) in collaboration with Becton Dickinson. The MAb were conjugated with fluorescein isothiocyanate (FITC), phycoerythrin (PE), allophycocyanin (APC), or peridinin chlorophyll protein (PerCP); one tube contained CD3*FITC/CD8*PE/CD45*PerCP/CD4*APC, whereas the other tube contained CD3*FITC/pan-NK*PE/CD45*PerCP/B220*APC. T (CD3+), T helper (CD4+), T cytotoxic (Tc), B (B220+) and natural killer (NK; panNK+) cell populations were identified. An aliquot (20 µl) of each custom MAb mixture was added to 50 µl of undiluted blood and filtered spleen cell samples. The tubes were vortexed and incubated for 20 min in the dark at room temperature. Prewarmed lysing buffer (450 µl) was added to each tube. The tubes were then vortexed, incubated in a 37-40°C water bath for 20 min, and placed on ice until analysis. A total of 10,000 lymphocyte events/tube were acquired and analyzed using CellQuest™ software version 3.1 (Becton Dickinson).

Statistical analysis

Data were assessed with one-way analysis of variance (ANOVA) and Tukey's HSD (honestly significantly difference test) using SigmaStat™ software version 2.03 (SPSS, Inc., Chicago, IL). A p value of <0.05 indicated statistical significance and $p<0.10$ a trend.

RESULTS

Tumor progression in experiment 1

Figure 1 shows that pGL1-TNF-α in combination with ^{60}Co radiation significantly slowed C6 tumor progression compared to the non-treated tumor-bearing control group. By day 16, there was a tendency ($p = 0.072$) for the mice treated with pGL1-TNF-α + ^{60}Co to have smaller tumors compared those treated only with ^{60}Co. Preliminary experiments with intratumoral injections of the parental pWS4, at the same dose used in the present study, showed no significant effect on tumor growth (data not shown).

Body mass and analyses of blood and spleen from mice in experiment 1

Mouse body and spleen weights and blood leukocyte counts are summarized in Table 1. Significantly higher body and spleen masses were noted in the non-treated tumor-bearing and ^{60}Co-treated groups when compared to the normal mice with no tumor. Although no significant differences were found in blood leukocyte counts, Figure 2 shows that the white blood cells from animals treated with pGL1-TNF-α together with radiation had increased ^{3}H-TdR incorporation into cell DNA compared to the normal controls, non-treated tumor-bearing mice, and those treated only with ^{60}Co. The mean value for the group treated with pWS4 + ^{60}Co was higher only than that for the normal control group.

Tumor progression in experiment 2

Figure 3 shows C6 tumor growth with time after treatment with pGL1-TNF-α when used in combination with either ^{60}Co γ-rays or protons. The groups receiving pGL1-TNF-α together with either form of radiation had significantly smaller tumor volumes compared to the non-treated tumor control and pGL1-TNF-α treated groups on days 11-16 after tumor cell implantation. Significantly smaller tumors were also observed on day 9 in the pGL1-TNF-α + proton group when compared to the non-treated tumor group and the groups treated with ^{60}Co or pGL1-TNF-α; at this same time the pGL1-TNF-α + ^{60}Co group had significantly smaller tumors than did mice treated with pGL1-

TNF-α. No statistically significant differences in mean tumor size were obtained when comparing the γ-ray- and proton-irradiated groups with their respective counterparts receiving combination therapy. However, when the two irradiated groups were pooled into one group and the two combination groups were pooled into one group, pGL1-TNF-α + radiation therapy resulted in significantly smaller tumors than did radiation alone on days 11-16.

Body and spleen mass and analyses of spleen and blood from mice in experiment 2

Table II shows that body and spleen weights were similar among all groups, although non-treated tumor-bearing mice had the largest spleens. In tumor-bearing animals, the mean SI values in response to LPS stimulation of splenocytes were 20% (non-treated tumor-bearing controls) to 50% (pGL1-TNF-α + protons) lower compared to normal mice, but statistical support was lacking due to the relatively large variation within groups (Table II). Blood leukocyte counts in tumor-bearing animals ranged from 100% (^{60}Co) to 170% (pGL1-TNF-α) of the mean obtained for mice without tumor (Table II); groups with non-treated tumors and tumors treated with pGL1-TNF-α had elevated counts compared to no-tumor and ^{60}Co-treated groups

Figure 4 presents the mean dpm values for spontaneous blastogenesis of blood leukocytes when adjusted to 10^6 cells/ml. Although no statistically significant differences were found among groups, the mice receiving pGL1-TNF-α + proton radiation exhibited the highest mean value.

Figures 5 and 6 show B and NK cell data obtained by flow cytometry analyses of blood and spleen, respectively. The numbers of B lymphocytes were significantly elevated in the blood from the group treated with pGL1-TNF-α compared to mice with no tumor and those treated with ^{60}Co, protons, and pGL1-TNF-α + ^{60}Co. This group also had the highest B cell percentage. In the spleen, B cell numbers in the non-treated tumor-bearing controls were significantly depressed compared to all treated groups; ^{60}Co-treated mice had lower counts in relation to the pGL1-TNF-α-treated animals. NK cell counts and percentages in spleens from mice in all tumor-bearing groups were significantly lower than in the control group with no tumor; significantly lower percentages were also observed for the pGL1-TNF-α and pGL1-TNF-α + proton groups when compared to the group treated with ^{60}Co.

CD3+, CD4+, and CD8+ T lymphocytes were detected at very low levels in both blood and spleen. No significant differences in these cells were observed in the blood among the various groups (data not shown). However, as shown in Table III, spleens from mice treated with pGL1-TNF-α + protons had significantly increased CD3+ T cell numbers compared to non-treated tumor-bearing mice. Elevated CD3+ T cell percentages were also observed in the groups receiving protons alone and pGL1-TNF-α + ^{60}Co with respect to controls with no tumor; the relatively high T cell percentages in the pGL1-TNF-α + proton group approached statistical significance ($p<0.1$). Mice treated with pGL1-TNF-α together with either form of radiation had a 4.5- to 4.8-fold increase in the CD4:CD8 ratio when compared to mice with no tumor; a 3.0- to 3.2- increase in the ratio was observed in relation to the non-treated tumor-bearing animals.

DISCUSSION

A number of investigators have reported that TNF-α enhances radiation effects against tumors. Early *in vitro* studies with human tumor cell lines demonstrated that combined treatment could induce synergistic or additive cell killing (Hallahan *et al.*, 1990). Sersa *et al.* (1988) found that TNF-α protein, when given systemically together with radiation, resulted in a more than additive increase in the radioresponse of two murine tumors, as well as reduced radiation damage to bone marrow progenitor cells. A phase I clinical trial by Hallahan and colleagues (1995) showed that in some patients, locally advanced tumors can be controlled by lower than expected doses of radiation when combined with intravenously (i.v.) administered TNF-α. However, major toxicities that were independent of the cytokine dose required termination of the regimen in a number of subjects.

Previous studies conducted in our laboratory have demonstrated that low, non-toxic doses of i.v.-administered TNF-α protein enhanced radiation effects against human colon and lung adenocarcinoma xenografts in nude mice (Gridley *et al.*, 1994a, 1997a). These tumor cells were

shown to be directly susceptible to the effects of the cytokine and represent relatively radiosensitive tumor types. In subsequent studies, we found that TNF-α protein in combination with radiation also significantly slowed the progression of C6 glioma in athymic mice, in spite of the findings that the cells in culture were not sensitive to TNF-α at doses ranging from 5 to 500 units/ml and the cytokine did not enhance tumor cell susceptibility to radiation *in vitro* (Gridley *et al.*, 1997c). Relatively low doses of TNF-α protein were administered i.v. in these studies in order to avoid systemic toxicity. Although promising results were obtained when treatments were initiated very early after tumor cell implantation, regression of large, established tumors was not observed and there were no cures. Increasing the dose of the cytokine was an option, but that would also increase the possibility of side effects. TNF-α toxicity was of paramount concern, since the maximum tolerated dose in humans is approximately 40-fold less compared to the mouse on a weight-by-weight basis (Rosenberg 1991). The potential of using the cytokine as an adjunctive therapy has been recognized, as evidenced by efforts to develop virus-based and other vectors for the TNF-α gene (Blankenstein *et al.* 1991; Mauceri *et al.*, 1996; Seung *et al.*, 1995; Vanhoesebroeck *et al.*, 1991).

These and other observations, prompted us to construct a plasmid-mediated delivery system for TNF-α. Results from *in vitro* assays and a pilot evaluation of pGL1-TNF-α in combination with γ-radiation in the C6 glioma-athymic mouse model were promising (Li *et al.*, 1999). The major aim of the present study was to further explore the effects of this combination regimen *in vivo*. The results demonstrate that intratumoral injection of pGL1-TNF-α enhanced the anti-tumor tumor effects of radiation against C6 glioma, a tumor type that is considered to be among the most radioresistant and is virtually impossible to cure. Treatments were initiated after the tumors were well established. Indeed, the 8-9 day time period between tumor cell implantation and beginning of treatment is relatively long considering the aggressive nature of C6 glioma. However, the presence of a readily detectable tumor mass ensured the accuracy of plasmid injection.

The slowest tumor growth was noted after pGL1-TNF-α and proton radiation treatment; by day 16 after C6 cell implantation, mean tumor volume in this group was 21-23% smaller on days 11-16 than in the combination group that received γ-radiation (Fig. 3). In the two groups receiving only radiation, proton-irradiated tumors were 15-33% smaller (days 11-16) compared to γ-rays. The observation that proton-irradiated tumors grew more slowly than those treated with γ-rays (photons) is not entirely surprising, since it is generally assumed in radiation oncology that protons have a greater biological effect in relation to γ-rays (i.e. a relative biological effectiveness or RBE of 1.1) (Gerwick and Kozin 1999). However, very few studies have directly compared the efficacy of proton and γ-radiation against *in vivo* growing tumors under controlled conditions. A wide range of RBE values for proton radiation can be found in the literature, based primarily on non-tumorigenic cell lines cultured *in vitro* and colony survival assays. The greater biological effectivness of protons, as compared to photons, is thought to be due to differences in the intrinsic properties of these two forms of radiation (Paganetti *et al.*, 1997). This property and the ability to focus protons more precisely to a target volume (thus sparing normal tissues) give proton radiotherapy an advantage over conventional radiotherapy. Clinical use of proton beams is rapidly increasing world-wide for cancer, as well as other pathological conditions, and very encouraging results have been reported (Levin 1991; Yonemoto *et al.*, 1996, 1997; Slater *et al.*, 1998; Hug *et al.*, 1999; Moyers *et al.*, 1999).

Our data also show that there was very little difference in mouse body weight among the various groups. This indicates that normal eating habits and activity were maintained during treatment. Results from assays of blood and spleen did not show deficiencies that were associated with combination treatment. A slight, but generally non-significant, tendency for splenomegaly, depressed response of splenocytes to mitogenic stimulation, and low NK cell numbers and percentages in the spleen were observed in all tumor-bearing groups compared to the control mice with no tumor. In contrast, the significantly elevated basal proliferation of leukocytes (Fig. 2) and high B lymphocyte counts in the blood (Fig. 5) from mice treated with pGL1-TNF-α (+/- radiation) suggest that some degree of systemic activation may have occurred as a result of treatment. Whether or not the observed changes are involved in the anti-tumor effect of the combination therapy requires further study. TNF-α is well known for induction of tumor necrosis through its selective action on tumor vasculature. However, our previous studies using TNF-α protein and γ-radiation in the C6 model did not reveal an increase in thrombotic blood vessels above what was observed with either modality alone (Gridley *et al.*, 1997c). Preliminary evaluation of stained tumor

sections following pGL1-TNF-α/radiation treatments (data not shown) appear to confirm these earlier observations. TNF-α also has potent pro-inflammatory properties (Hernandez-Casseles and Stutman, 1995). Several studies have correlated tumor-inhibitory effects with TNF-α-induced activation and recruitment of specific and non-specific leukocyte populations (Blankenstein *et al.*, 1991; Mizuguchi *et al.*, 1998).

It was demonstrated many years ago that the athymic mouse is not entirely devoid of the T cell lineage (Raff, *et al.*,1973; Holub,1989). Furthermore, it has been observed that post-thymic T cells show extensive self-renewal, expansion, and functional activity in the absence of the thymus (Stutman *et al.* 1986). Because of these observations, we chose to evaluate these cells in the present study. Although the overall numbers were very low, a significant increase was found in the CD3+ T cell counts in the spleens from mice in some of the treated groups (Table III). The highest level was observed in the group treated with pGL1-TNF-α and proton radiation (3.3-fold higher compared to the non-treated group with tumor). These mice, as well as the pGL1-TNF-α + ^{60}Co-treated group, also had the highest CD4:CD8 cell ratios. However, the significance of these findings, if any, remains to be determined.

Collectively, the results support the premise that low, non-toxic doses of pGL1-TNF-α in combination with radiation is a promising therapeutic strategy and that the utilization of proton radiation may provide increased tumor control compared to γ-rays at the same physical dose, while reducing damage to normal tissues. Studies are currently on-going to elucidate the possible interactions between TNF-α and ionizing radiation and to explore the efficacy of this combination treatment in an orthotopically implanted brain tumor model.

ACKNOWLEDGEMENTS

The authors thank Tatyana Timiryasova, Ph.D., Radha Dutta-Roy, M.S., Gregory A. Abell, M.S., and Bing Chen, B.S. for various aspects of this study and William Preston, Ed.D. for editorial review of the manuscript. This study was supported by grants from Loma Linda University School of Medicine and the U.S. Department of the Army, National Medical Technology Testbed, Inc., subcontract #15-FY98. The view, opinion, and/or findings contained in this report are those of the authors and should not be construed as a position, policy, decision or endorsement of the federal government or the National Medical Technology Testbed, Inc.

REFERENCES

ALEMANY, R., GOMEZ-MANZANO, C., BALAGUE, C., YUNG, W.K., CURIEL, D.T., KYRITSIS, A.P. and FUEYO, J., Gene therapy for gliomas: molecular targets, adenoviral vectors, and oncolytic adenoviruses *Exp. Cell Res.*, **252**, 1-12 (1999).

ARCHAMBEAU, J.O. and BENNETT, G.W., Potentialities of proton radiotherapy. Report of Symposium Aug. 9-10, 1972. Brookhaven National Laboratory Report #BNL-50365, 1972.

ARCHAMBEAU, J.O., SLATER, J.D., SLATER, J.M. and TANGEMAN, R., Role for proton beam irradiation in treatment of pediatric CNS malignancies. *Int. J. Radiat. Oncol. Biol. Phys.*, **22**, 287-294 (1991).

ARCHAMBEAU, J.O., SLATER, J.M., COUTRAKON, G.B., MILLER, D.W., PRESTON, W. and SLATER, J.D., Proton-beam irradiation for the cancer patient: An approach to optimal therapy and normal-tissue sparing. *Adv. Radiat. Biol.*, **18**, 53-89 (1994).

BENDA, P., LIGHTFOOT, J., SATO, G., LEVINE, L. and SWEET, W., Differentiated rat glial cell strain in tissue culture. *Science*, **161**, 370-371 (1968).

BLANKENSTEIN, T., QIN, Z., UBERLA, K., MULLER, W., ROSEN, H., VOLK, H.-D. and DIAMANTSTEIN, T., Tumor suppression after tumor cell-targeted tumor necrosis factor a gene transfer. *J. Exp. Med.*, **173**, 1047-1052 (1991).

CARSWELL, E.A., OLD, L.J., RUSSEL, R.L., GREEN, G. and WILLIAMSON, B., An endotoxin induced serum factor that causes necrosis of tumors. *Proc. Natl. Acad. Sci. USA*, 7, 3600-3670, (1975).

CREAVEN, P.J., PLAGER, J.E., DUPERE, S., HUBEN, R.P., TAKITA, K., MITTELMAN, A., PROEFROCK, A., Phase I clinical trial of recombinant human necrosis factor. *Cancer Chemother. Pharmacol.* **20**, 137-144, (1987).

COHEN, M.E. and DUFFNER, P.K., Brain tumors in children. Principles of Diagnosis and treatment. 2nd ed., Raven Press: New York, (1994).

COIA, L.R. and MOYLAN, D.J., Introduction to clinical radiation oncology, 2nd ed. Baltimore: Williams & Wilkins Co. (1994).

GERWICK, L.E. and KOZIN, S.V., Relative biological effectiveness of proton beams in clinical therapy. *Radiother. Oncol.*, **50**, 135-142 (1999).

GRIDLEY, D.S., ANDRES, M.L., GARNER, C., MAO, X.W. and SLATER, J.M., Evaluation of tumor necrosis factor-α and radiation efficacy in a human lung adenocarcinoma model. *Oncol. Res.*, **8**, 485-493 (1997a).

GRIDLEY, D.S., ANDRES, M.L. and SLATER, J.M., Enhancement of prostate cancer xenograft growth with whole-body radiation and vascular endothelial growth factor. *Anticancer Res.* **17**, 923-928, (1997b).

GRIDLEY, D.S., ARCHAMBEAU, J.O., ANDRES, M.L., MAO, X.W. and SLATER, J.M., Tumor necrosis factor-α enhances the anti-tumor effects of radiation against glioma xenografts. *Oncol. Res.*, **9**, 217-227 (1997c).

GRIDLEY, D.S., GLISSON, W.C. and UHM, J.-R., Interaction of tumor necrosis factor-α and radiation against human colon tumor cells. *Therapeutic Immunol.*, **1**, 25-31 (1994a).

GRIDLEY, D.S., HAMMOND, S.N. and LIWNICZ, B., Effects of tumor necrosis factor-α and radiation on human tumor xenografts. *Anticancer Res.*, **14**, 1107-1112, (1994b).

HALLAHAN, D.E., BECKETT, M.A., KUFE, D. and WEICHSELBAUM, R.R., The interaction between human recombinant tumor necrosis factor and radiation in 13 human tumor cell lines. *Int. J. Radiat. Oncol. Biol. Phys.*, **19**, 60-74 (1990).

HALLAHAN, D.E., VOKES, E.E., RUBIN, S.J., O'BRIEN, S., SAMUELS, B., VIJAYKUMAN, S., KUFE, D.W., PHILLIPS, R. and WEICHSELBAUM, R.R., Phase I dose-escalation study of tumor necrosis factor-α and concomitant radiation therapy. *Cancer J.*, **1**, 204-209 (1995).

HAWKINS, M.M., DRAPER, G.J. and KINGSTON, J.E., Incidence of second primary tumors among childhood cancer survivors. *Br. J. Cancer*, **56**, 339-347 (1987).

HERNANDEZ-CASELLES, T. and STUTMAN, O., Immune functions of tumor necrosis factor. *J. Immunol.*. **151**, 3999-4012,(1993).

HERSH, E.M., METCH, B.S., MUGGIA, F.M., BROWN, T.D., WHITEHEAD, R.P., BUDD, G.T., RINEHART, J.J., CRAWFORD, E.D., BONNET, J.D. and BEHRENS, B.B., Phase II studies of recombinant

human tumor necrosis factor alpha in patients with malignant disease: A summary of the southwest oncology group experience. *J. Immunother.*, **10**, 426-431 (1991).

HOLUB, M., T cells. I. T-cell differentiation and function. *In:* Immunology of Nude Mice. Boca Raton, FL: CRC Press, Inc. pp. 53-66 (1989).

HUG, E.B., LOREDO, L.N., SLATER, J.D., DEVRIES, A., GROVE, R.I., SCHAEFER, R.A., ROSENBERG, A.E. and SLATER, J.M., Proton radiation therapy for chordomas and chondrosarcomas of the skull base. *J. Neurosurg.*, **91**, 432-439 (1999).

KAJIOKA, E.H., GHEORGHE, C., LI, J., ANDRES, M.L., FOLZ-HOLBECK J., ABELL, G.A., SLATER, J.M., NELSON, G.A. and GRIDLEY, D.S., Effects of proton and gamma radiation on lymphocyte population and acute response to antigen. *In Vivo.* In press (1999).

KRAMM, C.M., SENA-ESTEVES, M., BARNETT, F.H., RAINOV, N.G., SCHUBACK, D.E., YU, J.S., PECHAN, P.S., PAULUS, W., CHIOCCA, E.A. and BREAKFIELD, X.O., Gene therapy for brain tumors (review). *Brain Path.*, **5**, 345-381 (1995)

LAWS, E.R. JR., Brain tumors. *CA Cancer J. Clin.*, **43**, 263-271 (1993).

LANDIS, S.H., MURRAY, T., BOLDEN, S. and WINGO, P.A., Cancer statistics, 1999. *CA Cancer J. Clin.*, **49**, 8-31 (1999).

LEIBEL, S.A. and SHELINE, G.E., Tolerance of the central and peripheral nervous system to therapeutic irradiation. *Adv. Radiat. Biol.*, **12**, 257-293 (1987).

LEVIN, C.V., Potential for gain in the use of proton beam boost to the para-aortic lymph nodes in carcinoma of the cervix. *Int. J. Radiat. Onc. Biol. Phys.*, **22**, 355-359 (1991).

LI, J., ANDRES, M.L., FODOR, I., NELSON, G.A. and GRIDLEY, D.S., Evaluation of pGL1-TNF-α therapy in combination with radiation. *Oncol. Res.*, **10**, 379-387 (1999).

LI, S. and HUANG, L., Nonviral gene therapy: promises and challenges. *Gene Ther.*, **7**, 31-34 (2000).

LOEFFLER, J.S., ALEXANDER, E., SHEA, W.M., WEN, P.Y., FINE, H.A., KOOY, H.M., BLACK, P.M. and ALEXANDER, E., Radiosurgery as part of the initial management of patients with malignant gliomas. *J. Clin. Oncol.*, **10**, 1379-1385 (1992).

MAUCERI, H.H., HANNA, N.N., WAYNE, J.D., HALLAHAN, D.E., HELLMAN, S. and WEICHSELBAUM, R.R., Tumor necrosis factor-α (TNF-α) gene therapy targeted by ionizing radiation selectively damages tumor vasculature. *Cancer Res.*, **56**, 4311-4314 (1996).

MELVOR, R.S., Gene therapy of genetic diseases and cancer. *Pediatr. Transplant.*, **3**, 116-121 (1999).

MIZUGUCHI, H., NAKAGAWA, T., TOYOSAWA, S., NAKANISHI, M., IMAZU, S., NAKANISHI, T., TSUTSUMI, Y., NAKAGAWA, S., HAYAKAWA, T., IJUHIN, N. and MAYUMI, T., Tumor necrosis factor α-mediated tumor regression by the in vivo transfer of genes into the artery that leads to tumors. *Cancer Res.*, **58**, 5725-5730 (1998).

MOYERS, M.F., GALINDO, R.A., YONEMOTO, L.T., LOREDO, L., FRIEDRICHSEN, E.J., KIRBY, M.A., SLATER, J.D. and SLATER, J.M., Treatment of macular degeneration with proton beams. *Med. Phys.*, **26**, 777-782 (1999).

PAGANETTI, H., OLKO, P., KOBUS, H., BECKER, R., SCHMITZ, T., WALIGORSKI, M.P.R., FILGES, D. and MULLER-GARTNER, H.-W., Calculation of relative biological effectiveness for proton beams using biological weighting functions. *Int. J. Radiat. Oncol, Biol. Phys.*, **37**, 719-729 (1997).

POLLACK, I.F., Brain tumors in children. *N. Engl. J. Med.*, **331**, 1500-1507 (1994).

PRADOS, M.D., BERGER, M.S. and WILSON, C.B., Primary central nervou system tumours: Advances in knowledge and treatment. *CA Cancer J. Clin.*, **48**, 331-360 (1998).

RAFF, M.C. Theta-bearing lymphocytes in nude mice. Nature, 246, 350-351 (1973).

ROSENBERG, S.A., Immunotherapy and gene therapy for cancer. *Cancer Res.*, **51**, 5074s-5079s (1991).

SERSA, G., WILLINGHAM, V. and MILAS, L., Anti-tumor effects of tumor necrosis factor alone or combined with radiotherapy. *Int. J. Cancer.*, **42**, 129-134 (1988).

SEUNG, L.P., MAUCERI, H.J., BECKETT, M.A., HALLAHAN, D.E., HELLMAN, S. and WEICHSELBAUM, R.R., Genetic radiotherapy overcomes tumor resistance to cytotoxic agents. *Cancer Res.*, **55**, 5561-5565 (1995).

SHEAY, W., NELSON, S., MARTINEZ, I., CHU, T.H.T., BHATIA, S. and DORNBURG, R., Downstream insertion of the adenovirus tripartite leader sequence enhances expression in universal eukaryotic vectors. *Biotechniques*, **15**, 856-862 (1993).

SLATER, J.D., YONEMOTO, L.T., ROSSI, C.J., REYES-MOLYNEUX, N.J., BUSH, D.A., ANTOINE, J.E., LOREDO, L.N., SCHULTE, R.W., TEICHMAN, S.L. and SLATER, J.M., Conformal proton therapy for prostate carcinoma. *Int. J. Radiat. Oncol. Biol. Phys.*. **42**, 299-304 (1998).

SLATER, J.M., ARCHAMBEAU, J.O., MILLER, D.W., NOTARIUS, M.I., PRESTON, W. and SLATER, J.D., The proton treatment center at Loma Linda University Medical Center: Rationale for and description of its development. *Int. J. Radiat. Oncol. Biol. Phys.*, **22**, 383-389 (1991).

SLATER, J.M., MILLER, D.W. and ARCHAMBEAU, J.O., Development of a hospital-based proton beam treatment center. *Int. J. Radiat. Onc. Biol. Phys.* **14**, 761-775 (1988).

STUTMAN, O., Postthymic T-cell development. *Immunol. Rev.* **91**, 159- (1986).

TALMADGE, J., PHILLIPS, H., SCHNEIDER, M., Immunomodulatory properties of recombinant murine and human tumor necrosis factor. *Cancer Res.*, **48**, 544-550 (1988).

VANHOESEBROECK, B., MARCEL, M., VAN ROY, F., GROOTEN, J. and FRIERS, W. Expression of the tumor necrosis factor gene in tumor cells correlates with reduced tumorigenicity and reduced invasiveness in vivo. *Cancer Res.*, **51**, 2229-2238 (1991).

YONEMOTO, L.T., SLATER, J.D., FRIEDRICHSEN, E.J., LOREDO, L.N., ING, J., ARCHAMBEAU, J.O., TEICHMAN, S., MOYERS, M.F., BLACHARSKI, P.A. and SLATER, J.M., Phase I/II study of proton beam irradiation for the treatment of subfoveal choroidal neovascularization in age-related macular degeneration: treatment techniques and preliminary results. *Int. J. Radiat. Oncol. Biol. Phys.*, **36**, 867-871 (1996).

YONEMOTO, L.T., SLATER, J.D., ROSSI, C.J., ANTOINE, J.E., LOREDO, L., ARCHAMBEAU, J.O., SCHULTE, R.W.M., MILLER, D.W., TEICHMAN, S.L. and SLATER, J.M., Combined proton and photon conformal radiation therapy for locally advanced carcinoma of the prostate: preliminary results of a phase I/II study. *Int. J. Radiat. Oncol. Biol. Phys.*, **27**, 21-29 (1997).

TABLE I
Body and Spleen Mass and Blood Leukocyte Counts in Mice from Experiment 1

Groups	Body mass (g)	Spleen mass (g)	Leukocytes ($\times 10^6$/ml)
No tumor	24.1 +/- 0.1[a]	0.118 +/- 0.021	4.91 +/- 0.89
Tumor			
Non-treated	26.8 +/- 0.2[b]	0.199 +/- 0.011[d]	7.01 +/- 1.00
^{60}Cobalt	27.2 +/- 0.8[c]	0.208 +/- 0.016[d]	5.56 +/- 0.73
pWS4 + ^{60}Co	24.3 +/- 0.4	0.153 +/- 0.010	4.25 +/- 0.80
pGL1-TNF-α + ^{60}Co	26.0 +/-0.4	0.170 +/- 0.011	4.06 +/- 0.31

[a]Mean +/- SE of 4 mice/group.
[b]$p<0.05$ vs. no tumor and pWS4 + ^{60}Co.
[c]$p<0.01$ vs. no tumor and pWS4 + ^{60}Co.
[d]$p<0.05$ vs. no tumor.

TABLE II
Body and Spleen Mass and Spleen and Blood Variables in Mice from Experiment 2

Groups	Body mass Mass (g)	Spleen (g)	Spleen SI with LPS[a]	Blood leukocytes ($\times 10^6$/ml)
No tumor	24.2+/-0.6[b]	0.131+/-0.009	568+/-78	5.30+/-0.19
Tumor				
Non-treated	26.2+/-0.5	0.188+/-0.028	457+/-86	8.90+/-0.53[c]
^{60}Cobalt	25.9+/-0.9	0.133+/-0.008	307+/-26	5.30+/-1.03
Protons	26.0+/-0.5	0.147+/-0.006	324+/-82	6.50+/-0.54
pGL1-TNF-α	26.6+/-1.3	0.171+/-0.007	327+/-78	9.00+/-0.71[c]
pGL1-TNF-α + ^{60}Co	23.6+/-0.8	0.148+/-0.009	333+/-61	6.40+/-0.55
pGL1-TNF-α + protons	23.9+/-1.0	0.155+/-0.014	286+/-62	7.30+/-0.98

[a]Stimulation indices (SI) after lipopolysaccharide (LPS) stimulation.
[b]Mean +/- SE (n = 4-7/group).
[c]$p<0.05$ vs. no tumor and ^{60}Co.

TABLE III

T Lymphocytes in Spleens from Mice in Experiment 2

Groups	Number of cells (x 10^5/ml) T cells (CD3+)	Th cells (CD4+)	Tc cells (CD8+)	CD4:CD8 ratio
No tumor	9.70 +/- 1.41[a] (2.2 +/- 0.3)[b]	2.37 +/- 0.85 (0.6 +/- 0.2)	3.02 +/- 0.50 (0.7 +/- 0.1)	0.78
Tumor				
Non-treated	7.20 +/- 3.26 (2.9 +/- 0.1)	0.92 +/- 0.17 (0.5 +/- 0.1)	0.78 +/- 0.49 (0.4 +/- 0.2)	1.18
^{60}Cobalt	9.65 +/- 3.10 (3.7 +/- 0.3)	1.00 +/- 0.46 (0.4 +/- 0.1)	2.55 +/- 0.94 (0.9 +/- 0.2)	0.39
Protons	18.86 +/- 4.49 (4.4 +/- 0.4)[c]	5.66 +/- 1.89 (1.3 +/- 0.3)	2.84 +/- 0.52 (0.7 +/- 0.1)	1.99
pGL1-TNF-α	18.83 +/- 3.50 (3.1 +/- 0.6)	2.68 +/- 0.79 (0.5 +/- 0.2)	2.20 +/- 0.70 (0.4 +/- 0.1)	1.22
pGL1-TNF-α + ^{60}Co	16.99 +/- 2.67 (4.0 +/- 0.3)[c]	2.66 +/- 0.98 (0.6 +/- 0.2)	0.71 +/- 0.16 (0.2 +/- 0.03)	3.75
pGL1-TNF-α + protons	24.03 +/- 4.90 (3.8 +/- 0.6)	5.88 +/- 1.72 (1.70 +/- 0.3)	1.68 +/- 0.54 (0.2 +/- 0.1)	3.50

[a]Mean +/- SE of total mononuclear cell population.
[b]Numbers in parentheses denote mean percentage +/- SE of all mononuclear cells.
[c]$p<0.05$ vs. non-treated tumor.
[d]$p<0.05$ vs. no tumor

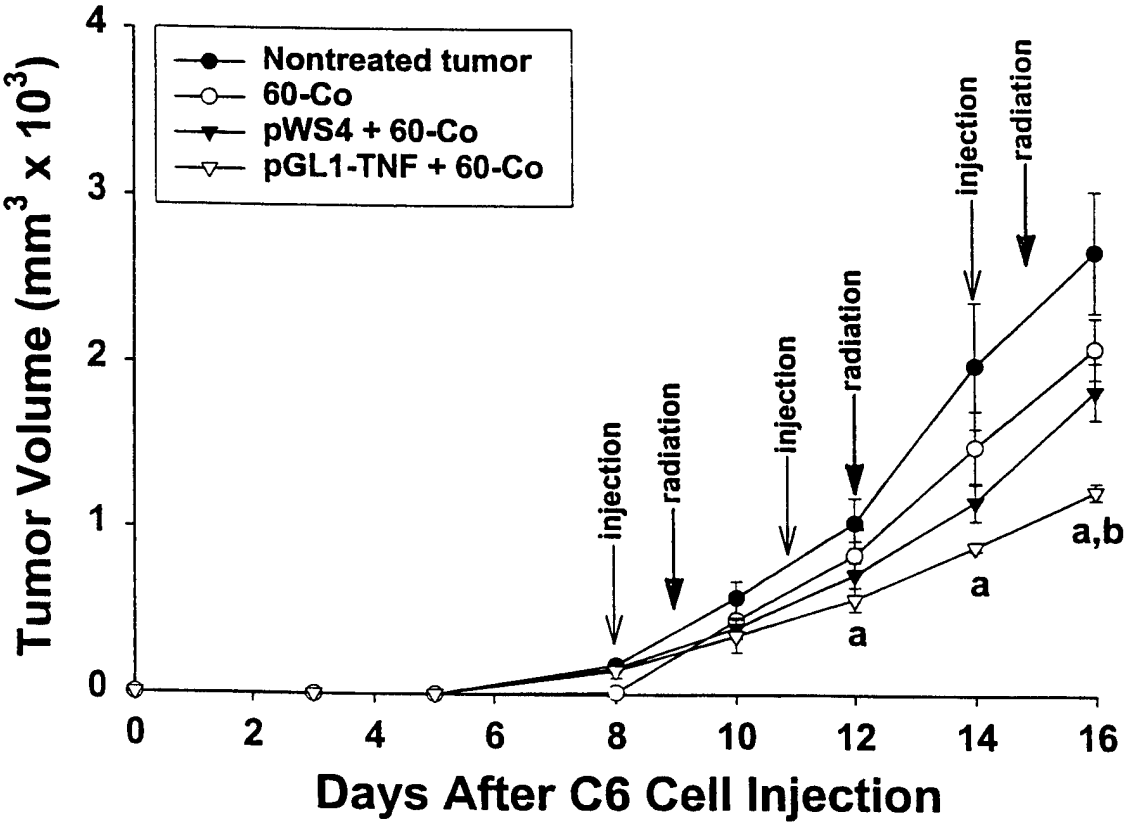

Figure 1 - Tumor growth with time after C6 tumor cell injection in mice from experiment 1. Each point represents the mean +/- SE (n = 4/group). Vertical arrows indicate times of intratumoral injection of pGL1-TNF-α or pWS4 (both at 50 μg/injection) and tumor irradiation (2 Gy/fraction) in the appropriate groups. a: $p<0.05$ vs non-treated tumor; b: $p = 0.072$ vs. ^{60}Co. ANOVA on days 12 and 14, $p<0.05$. ANOVA on day 16: $p = <0.001$.

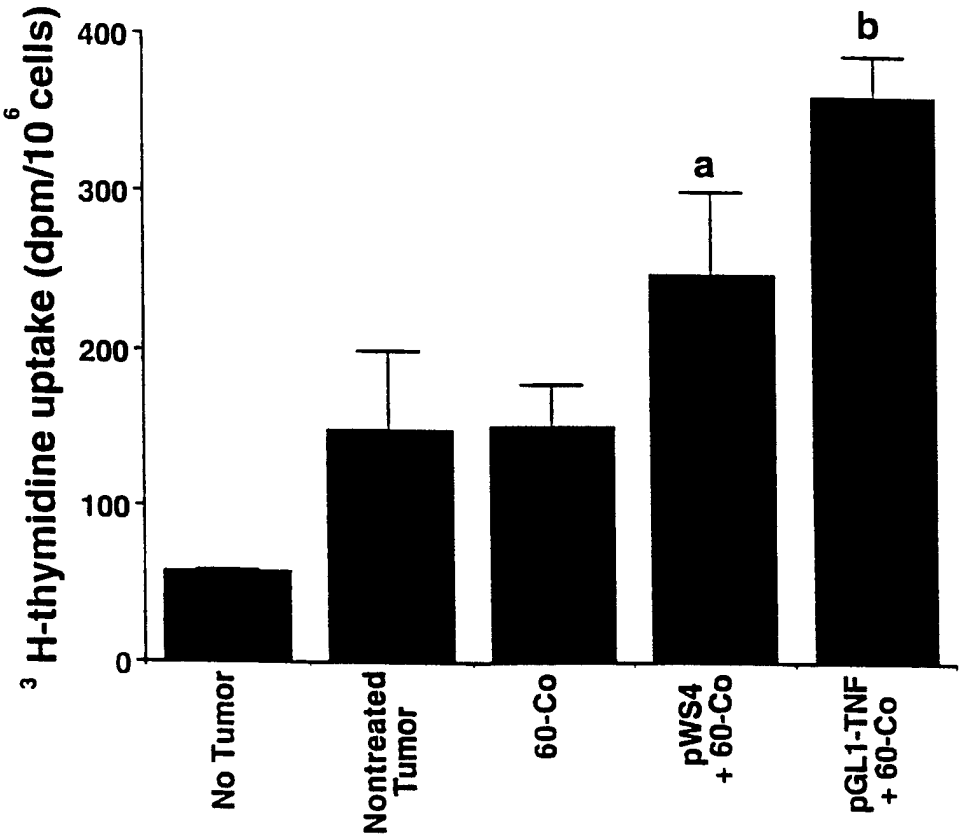

Figure 2 - Spontaneous blastogenesis of blood leukocytes from mice in experiment 1 at the time of euthanasia. Each bar represents the mean +/- SE (n = 4/group). a: $p<0.05$ vs. no tumor; b: $p<0.05$ vs. no tumor, non-treated tumor, and ^{60}Co.

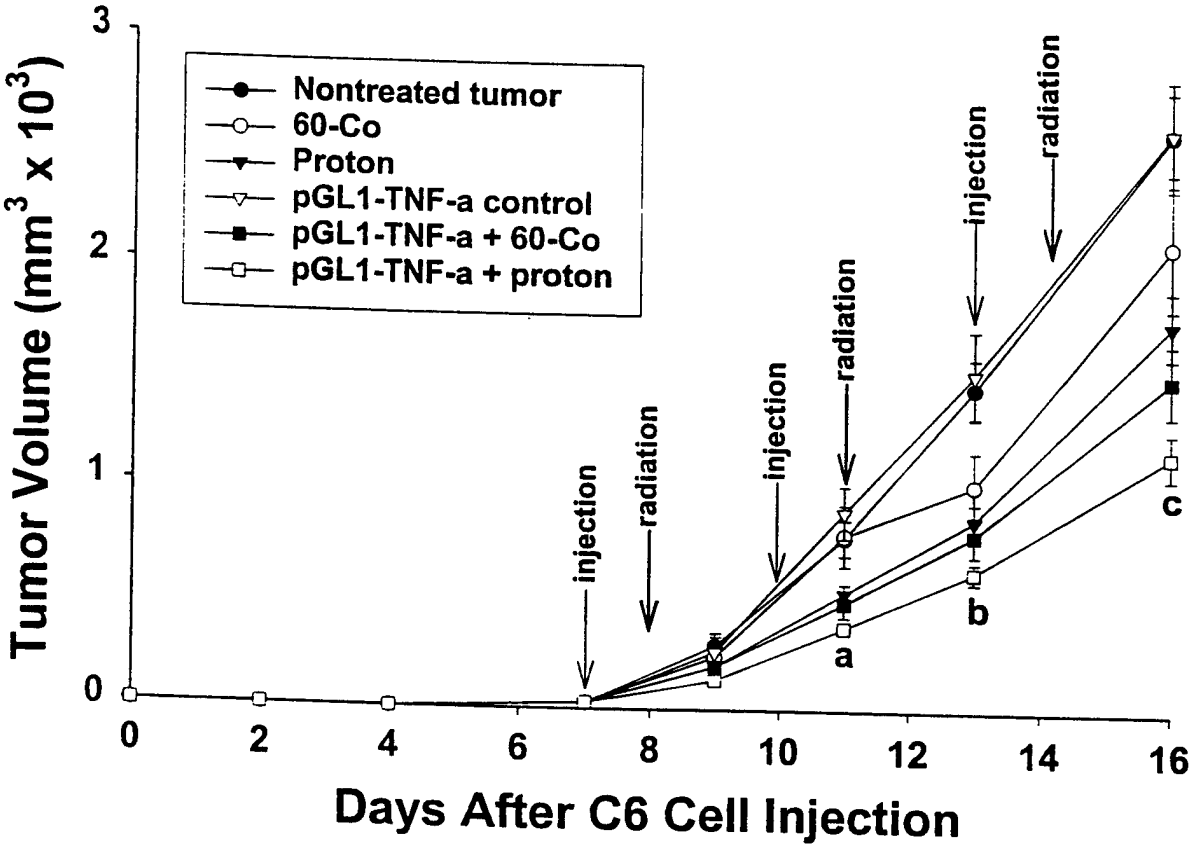

Figure 3 - Tumor growth with time after C6 tumor cell injection in mice from experiment 2. Each point represents the mean +/- SE (4-7/group). Vertical arrows indicate times of intratumoral injection with pGL1-TNF-α 50 μg/injection) and tumor irradiation (2 Gy/fraction) in the appropriate groups. a: day 11, pGL1-TNF-α + proton versus ^{60}Co, pGL1-TNF-α and non-treated tumor ($p<0.05$); pGL1-TNF-α + ^{60}Co versus pGL1-TNF-α ($p<0.01$). b: day 13, pGL1-TNF-α + proton versus pGL1-TNF-α and non-treated tumor ($p<0.01$); pGL1-TNF-α + ^{60}Co versus pGL1-TNF-α and non-treated tumor ($p<0.01$). c: day 16, pGL1-TNF-α + proton versus ^{60}Co, pGL1-TNF-α, and non-treated tumor ($p<0.05$); pGL1-TNF-α + ^{60}Co versus pGL1-TNF-α and non-treated control ($p<0.01$). ANOVA on days 11, 13 and 16: $p<0.001$. When pGL1-TNF-α + radiation (proton/^{60}Co) were compared to radiation (proton/^{60}Co), $p = 0.043$.

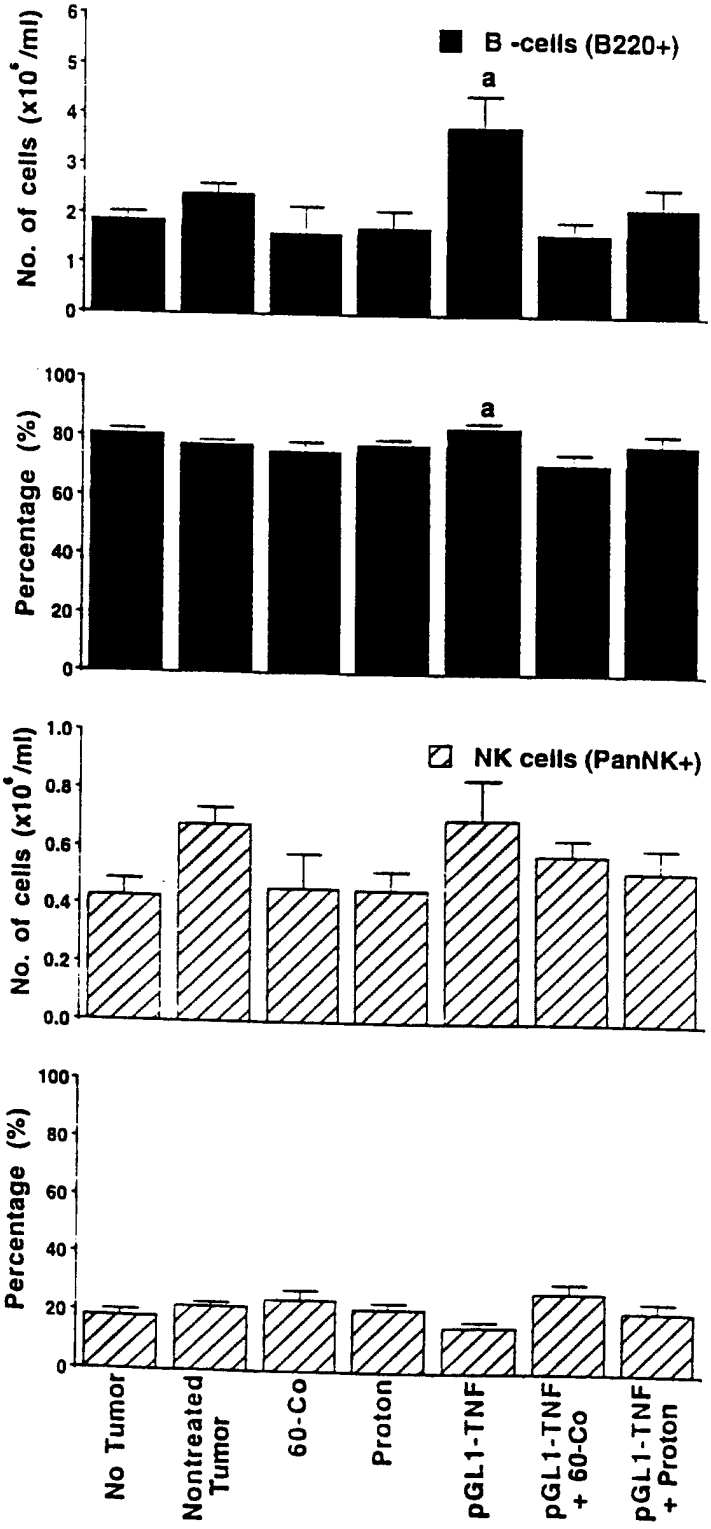

Figure 4 - B and NK cell numbers and percentages in blood from mice from experiment 2. Each bar represents the mean +/- SE (n = 4-7/group). a: $p<0.05$ vs. no tumor, ^{60}Co, protons and pGL1-TNF-α + ^{60}Co. b: $p<0.05$ versus no tumor, ^{60}Co, proton and pGL1-TNF-α + ^{60}Co.

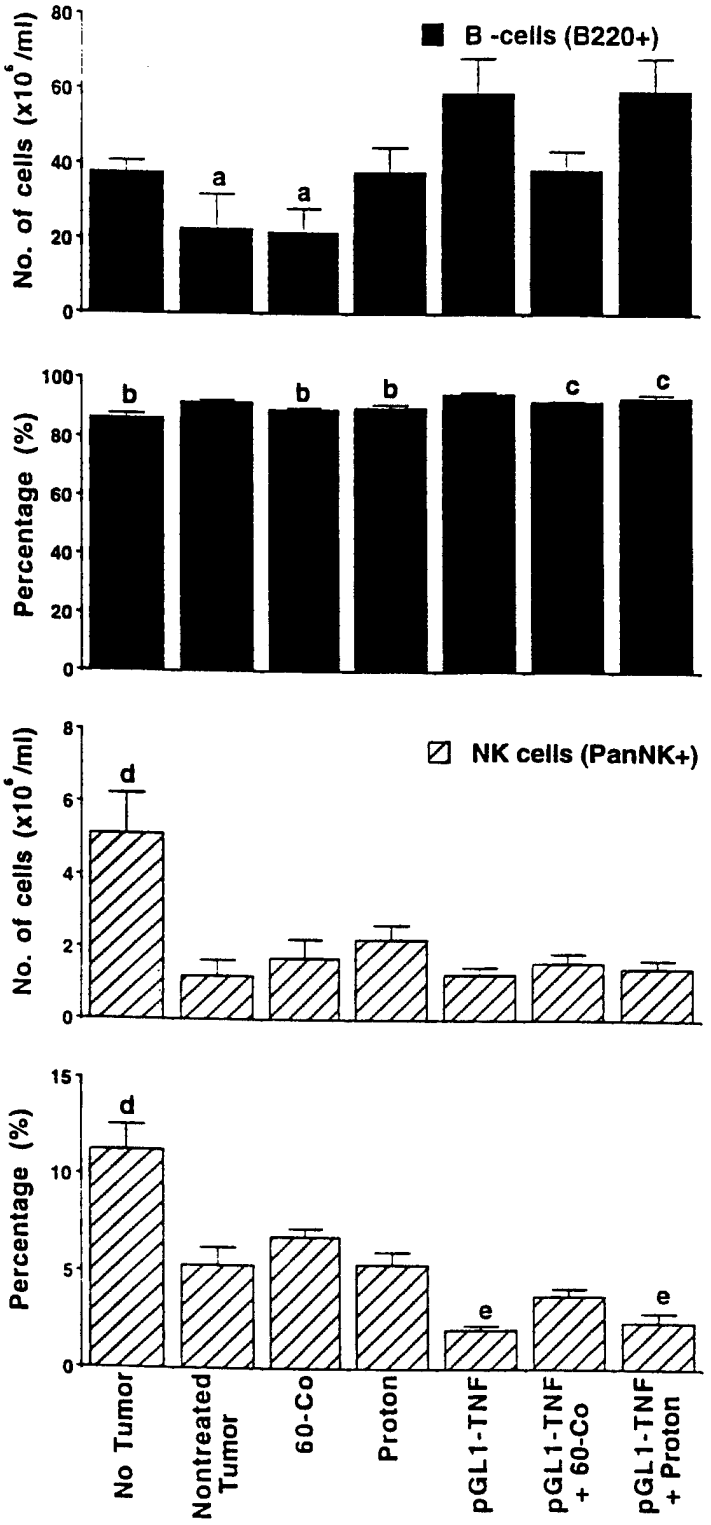

Figure 5 - B and NK cell numbers and percentages in spleens from mice from experiment 2. Each bar represents the mean +/- SE (4-7/group). a: $p<0.05$ versus pGL1-TNF-α + proton; b: $p<0.05$ versus pGL1-TNF-α; c: $p<0.05$ versus no tumor; d: $p<0.05$ versus all tumor-bearing groups; e: $p<0.05$ versus ^{60}Co.

Presented at 8th International Conference on Gene Therapy of Cancer December 9-11, 1999, San Diego, CA

pGL1-TNF-α Gene Therapy and Radiation in a Malignant Brain Tumor Model. J. Li, M.L. Andres, E.H. Kajioka, T. Timiryasova, I. Fodor, J.M. Slater and D.S. Gridley. Departments of Radiation Medicine and Microbiology & Molecular Genetics. Loma Linda University and Medical Center, Loma Linda, CA 92354.

High-grade brain tumors are among the most difficult types of cancers to control with current therapeutic regimens. The major goal of this study was to determine if a unique plasmid-human tumor necrosis factor-α gene construct (pGL1-TNF-α) could augment the antitumor effects of radiation in the C6 glioma/athymic mouse model. In addition, possible mechanisms of pGL1-TNF-α action were investigated. C6 glioma cells (5×10^5) were subcutaneously implanted into the right hind leg of mice. When tumors became palpable, pGL1-TNF-α was administered intratumorally 3 times over a 9-day period at three different doses (15 μg, 150 μg, or 450 μg), 18 hr before radiation (^{60}Co, 2 Gy x 3 fractions). A modest decrease in tumor volume was observed with radiation, whereas no effect was seen with pGL1-TNF-α, when each modality was used alone. Combination treatment, however, resulted in significantly ($p<0.05$) slower tumor progression. The smallest mean tumor volumes were obtained with the 15 μg and 150 μg of pGL1-TNF-α + radiation. Additional groups of mice with established C6 tumors were treated with the same 3 doses of pGL1-TNF-α each dose given in one injection) and euthanized at 18, 72, and 168 hr thereafter. TNF-α expression in tumors and plasma was determined and leukocyte populations were analyzed for spontaneous blastogenesis (^{3}H-TdR incorporation) and by flow cytometry using fluorescence-labelled monoclonal antibodies. TNF-α protein was detected in tumors at all 3 times points, with highest levels seen at 18 hr post-injection (404 - 765 pg/g tumor after 15 - 450 μg pGL1-TNF-α); no TNF-α was found in plasma. The greatest immunomodulatory effects of pGL1-TNF-α treatment were observed at 18 hr and included increased blastogenesis of leukocytes and high levels of natural killer (NK) cells and monocytes/granulocytes. At this same time, low levels of B lymphocytes were noted. These data indicate that low-dose pGL1-TNF-α in combination with radiation may be useful in the treatment of malignant brain tumors and suggest that the mechanisms of pGL1-TNF-α action include the upregulation of nonspecific effector cells.

[The view, opinion, and/or findings contained in this report are those of the author(s) and should not be construed as a position, policy, decision or endorsement of the federal government or the National Medical Technology Testbed, Inc.]

Materials & methods and results presented at conference, but not described in the submitted manuscript:

Tumor processing for TNF-α quantification. Tumor were excised and weighed immediately after euthanasia. PBS was added at a volume equal to tumor mass, (wt:vol) and the tumor was cut into small pieces with sharp scalpels and scissors. The pieces were rapidly expelled through a 1 ml syringe with a small gauge needle several times and centrifuged at ~13,000 rpm for 5 min. The supernatant was removed, volume was measured, and the samples were frozen (-65°C) until testing for TNF-α by ELISA.

Quantification of TNF-α protein in tumors. Tumor supernatants were thawed and human TNF-α protein was quantified by high-sensitivity ELISA using a commercially available kit (Quantikine™, R & D Systems, Minneapolis, MN). The procedure was performed according to the manufacturer's instructions. The amount of TNF-α was expressed using the formula below:

pg of TNF-α/mg of tumor = (pg/ml x total volume of supernatant in ml)/tumor mass in mg.

Table IV. Level of TNF-α protein in C6 tumor and plasma with time after intratumoral injection of pGL1-TNF-α

Amount of pGL1-TNF-α[a]	pg/g tumor			pg/ml plasma		
	16 hr	72 hr	168 hr	16 hr	72 hr	168 hr
0 μg	0 +/- 0[b]	0 +/- 0	0 +/- 0	0 +/- 0	0 +/ -0	0 +/- 0
15 μg	404 +/- 60	135 +/- 68	7 +/- 5	0 +/- 0	0 +/- 0	0 +/- 0
150 μg	711 +/- 182	301 +/- 59	60 +/- 32	0 +/- 0	0 +/- 0	0 +/- 0
450 μg	765 +/- 201	294 +/- 55	146 +/- 51	0 +/- 0	0 +/- 0	0 +/- 0

[a]Single intratumoral injection of pGL1-TNF-α, 7 days after s.c. implantation of 5 x 10^5 C6 cells; mean tumor volume at this time was approximately 300 mm^3. [b]Mean +/- SEM. Sensitivity of the assay: 0.18 pg/ml.

Results in Table IV above show that the TNF-α protein is expressed at relatively high levels within C6 tumors, even after injection of the lowest pGL1-TNF-α dose (15 μg). The highest levels were observed at 16 hr after treatment. TNF-α protein was not detected in plasma.

Additional results from this presentation are to be included in a manuscript that is currently in preparation.

CONCLUSIONS

The data obtained so far support the *primary hypothesis* that combined radiation and pGL1-TNF-α gene therapy produces a synergistic inhibition of C6 glioma progression. A smaller than expected dose of pGL1-TNF-α was needed in order to achieve significant enhancement of radiation effects. The combination regimen was effective against well-established s.c. tumor. The combination of pGL1-TNF-α plus proton radiation may be somewhat more effective than pGL1-TNF-α plus ^{60}Co γ-radiation.

Data that impact the *secondary hypothesis* (i.e. the mechanism of action includes interaction of TNF-α protein expressed by plasmid pGL1-TNF-α and tumor-localized radiation, resulting in the upregulation of systemic antitumor immune responses) has also been obtained. Results of assays that were performed several days after the end of the last treatment indicate that presence of tumor and localized tumor irradiation have a significant impact on systemic immune system parameters. Data obtained at early time points after injection of pGL1-TNF-α (without radiation and when tumor volumes in all mice were similar) have been obtained. Statistical analyses, although still in progress, suggest increased leukocyte activity early after intratumoral injection of pGL1-TNF-α.

Little or no weight loss occurred, indicating that normal feed consumption and activity were maintained, even in mice receiving multiple pGL1-TNF-α injections together with fractionated tumor irradiation. No prohibitive treatment-related toxicities were noted. Taken together, the data are very promising and support our goal in the development of a safer and more effective treatment for cancer, especially highly malignant cancers (such as those of the brain).

In the continuation of this project (FY-99) we will determine the effects of pGL1-TNF-α/proton radiation treatment in rats with intracranial C6 tumor. This should demonstrate that that the combination therapy approach is effective and safe for animals with intracranial (and not only animals with s.c.) tumors. We also plan to include normal, euthymic C57BL/6 mice (not athymic) injected s.c. in the right hind limb with Lewis Lung carcinoma cells that were originally derived from the C57BL/6 mouse. Based on our previous results, we hypothesize that the antitumor effects of pGL1-TNF-α/radiation treatments may be even greater in a normal mouse-syngeneic tumor model (one that more closely resembles the cancer patient population) than in the athymic mouse-xenograft model. Furthermore, we will combine proton radiotherapy with gene

therapy that will deliver not only TNF-α, but also Bax (a cell death regulator). Thus, the *commercial product(s)* my research team is working to make possible are a novel method (treatment protocol) and unique combination of therapeutic substances [proton beam radiation and plasmid vector(s) encoding these two anti-tumor proteins]. The utility we hope to achieve with this potentially proprietary approach is increased safety and efficacy in the treatment of cancer, especially highly aggressive cancers for which current therapies are non-curative and/or cancers that have already metastasized at the time of diagnosis.

There is clearly still an unmet need to cure cancer according to the American Cancer Society (webiste at www.cancer.org). The potential target market for cancer treatment in the U.S.A. is 1 out of 2 men and 1 out of 3 women (based on lifetime risk of cancer). At present the 5-year relative survival rate for all cancers combined is ~60% which translates to more half a million Americans dying of cancer each year. The National Institutes of Health (NIH) has estimated overall direct medical costs for cancer at $37 billion annually. As yet there is no single therapeutic approach that will likely provide a cure for highly malignant cancers. Thus, the need is great for the development of novel combinations of therapeutic approaches, especially those that offer additive and potentially synergistic antitumor responses with fewer adverse side effects.

APPENDICES

Recently obtained data (including flow cytometry quantification of leukocytes with the CD25 and CD71 activation markers) in athymic mice have been partially analyzed and are currently being compiled into a second manuscript. These results will be presented in the FY-99 progress report.

Patents - None at this time
Abstracts and Manuscripts – reported above

This project came to a close because of the unavailability of athymic rats (for intracranial tumor irradiation with the proton beam) and, with the permission of NMTB, was transferred to the new award which started on May 1, 2000. Athymic rats will arrive in 3 sets over a 3-month period, beginning on June 27, 2000. In addition, permission has been requested from NMTB to include evaluation of the pGL-1-TNF-α/radiation regimen in C57BL/6 mice with Lewis Lung tumor, a syngeneic pre-clinical model that more closely resembles (compared to athymic mice) the cancer patient population in terms of immunological responsiveness (approval pending).

ANIMAL USE REPORTING

Activity Name & Address: Daila S. Gridley, Ph.D.; Chan Shun Pavilion, A-1010
11175 Campus Street; Loma Linda University
Loma Linda, CA 92354

Contract number: Subagreement #15-FY98-LLU-GRIDLEY

Animal Type Genus/Species	Animals Purchased or Bred	Animals Used	USDA Pain Column C	USDA Pain Column D	USDA Pain Column E	AAALAC Accreditation
Mouse, athymic (nu/nu)	256	256	42	214		
Rat, athymic (nu/nu)	156	0	12	144		

04-15

DEPARTMENT OF THE ARMY
US ARMY MEDICAL RESEARCH ACQUISITION ACTIVITY
820 CHANDLER STREET
FORT DETRICK, MARYLAND 21702-5014

April 14, 1998

REPLY TO ATTENTION OF
Special Projects Branch

SUBJECT: Cooperative Agreement Number DAMD17-97-2-7016

Ms. Lydia M. Pearson
Contracts Administrator
National Medical Technology Testbed
11165 Mountain View Avenue, Suite 121
Loma Linda, CA 92354

Dear Ms. Pearson

Animal Care and Use Approval is hereby granted for the following protocol:

1. "Preclinical Model Proton Beam Radiation/TNG Gene Therapy (Cancer)," PI Dr. Daila S. Gridley.

If you have any questions concerning this matter, please contact L. Joan Wilson, Contract Specialist, at (301) 619-2387.

Sincerely,

Michael A. Younkins

Michael A. Younkins
Contracting Officer

DESCRIPTION: State the goal of the project, including how it relates to improving health care and noting the advanced technology that will be developed or tested . Use succinct language to describe how the project goals will be achieved. **Do not exceed the space provided.**

This application proposes three sets of related experiments that will determine the role that growth factors have in the ability to transform undifferentiated stem cells (cells that have the ability to become one of several types of cells found in adult animals) into ganglion cells of the adult retina. The first two sets of specific aims will determine the ability of fibroblast growth factors 8 and 15 (FGF-8, FGF-8) to transform stem cells into retinal ganglion cells using tissue culture techniques. Additionally, these experiments will determine the time and location in the developing retina of the expression of the mRNA of these two growth factors, thereby correlating the effect in culture conditions with the timing and location of their expression in the developing retina. These two specific aims will also determine the factors that inhibit, or turn off, the developmental actions of FGF-8 and FGF-15. This is important for understanding the mechanisms that stop stem cell differentiation during normal development, but can also be used for the third and final specific that will determine the ability of transplanted stem cells, exposed to FGF growth factors, to replace cells in blind adult animals. The third specific aim will use stem cells that have been exposed to FGF growth factors. These cells will be injected into the retina of blind adult rodents in an attempt to establish a new population of retinal ganglion cells. The retina is an immune privileged area and therefore is minimally susceptible to rejection. Examination will be made of the number, location, morphology and function of the transplanted cells in the host animal.

Although technically challenging, these experiments hold the promise for extending our current understanding of the genetic role of growth factors in determining cell fate during development, and perhaps more importantly, the ability of stem cells to grow and replace damaged cells in the adult.

PROJECT SITE(S) (organization, city, state):

All tissue culture and tansplant experiments will be performed in room A534 of the Loma Linda University Medical Center, Loma Linda, CA. Physiological examination of transplanted animals will be performed in the basement of the Anatomy building (Shyrock Hall) on the Loma Linda University Campus, Loma Linda, CA.

NO. 21

LLU/Kirby

Genetic Regulation of Neuron Proliferation and Differentiation in the CNS. I.FGF-15 and Ganglion Cell Differentiation

Recently begun project with first report due October 2000

No report at this time

DESCRIPTION: State the goal of the project, including how it relates to improving health care and noting the advanced technology that will be developed or tested . Use succinct language to describe how the project goals will be achieved. **Do not exceed the space provided.**

This project addresses the process by which a conceptual model is entered into a computer program to build a computer simulation. A pilot version of a multi-domain model entry system will be designed, built, and tested. The model entry system has three parts: a database to store hierarchical model descriptions in the form of mathematical equations; front-end programs to convert various types of domain descriptions into equations; and back-end programs to convert the equations into computer code for simulation computations. The equation database serves as common storage for model descriptions from a variety of domains and this method of storage permits us to take advantage of highly-developed database software technology. The new model entry software will become a part of the SCoP simulation package, a rapid application development system for building computer simulation programs. The hypothesis is that multi-domain entry will advance computer simulation because users will be able to describe models in the domain language most familiar: chemical reaction, compartmental model, electrical circuit diagram, etc. Experienced simulators will be able to produce programs more rapidly and accurately and novices will find it easier to learn to use computer simulations. We will test our hypothesis by giving the pilot version of the program to both novice and experienced simulators and recording their reactions and results. Computer simulation is now widely recognized as an important tool for understanding and learning about complex biological systems. This project will thus advance health care because it has the potential to contribute to understanding at all levels of biomedicine from biochemistry to epidemiology.

PROJECT SITE(S) (organization, city, state):

Loma Linda University
11234 Anderson Street
Loma Linda, CA 92354

NO. 22

LLU/Kootsey

Multi-Domain Model for Computer Simulation

Recently begun project with first report due October 2000

No report at this time

DESCRIPTION AND PERFORMANCE SITES (FORM B)

DESCRIPTION: State the goal of the research project including how it relates to improving health care for the nation's people. Use succinct language to describe how the project goals will be achieved. Do Not exceed the space provided on this page.

Our goal is to construct a *novel vaccine production and delivery system* employing transgenic food plants to protect our military personnel and indigenous civilians from epidemic cholera, enterotoxigenic *E. coli* (ETEC) and rotavirus encountered during natural disaster or political unrest. This goal will be realized by the transformation of potato and tomato plant cells with plant expression vectors containing DNA encoding a combination of enteric bacterial and viral pathogen antigens: cholera enterotoxin B and A_2 subunits (CTB,CTA_2), ETEC colonization factor CFA/I, rotavirus NSP4 enterotoxin 24 amino acid epitope and capsid proteins VP2 and VP6. The antigen levels produced in potato tubers from the transgenic plants will be measured by immunoblot and ELISA and antigen production will be optimized, if necessary. Antigen containing potato tissues will then be fed to mice to achieve mucosal immunization in the intestinal tract. Serum (IgG) and intestinal (IgA) antibody levels for each antigen will be determined in the immunized animals. Antibody memory cell numbers will be measured from the digestive tracts of immunized animals by ELISPOT assay to determine the duration of immunologic memory after plant-based vaccine immunization. Lastly, the efficacy of serum and intestinal antibody protection will be determined in animals immunized with potato delivered CTB, CFA/I , NSP4 and rotavirus capsid proteins. Achieving this objective will prepare the basis for future clinical studies and the production of analogous tomato based vaccines.

PROJECT SITE(s) (*Organization, City, State*):

Our plant molecular biology laboratory is situated in the Center for Molecular Biology and Gene Therapy, on the campus of Loma Linda University, Loma Linda CA, 92350. Our laboratory is equipped to conduct all the molecular biology, cell culture and plant growth aspects of the proposed project. A greenhouse located adjacent to our laboratory enables the growth of recombinant potato and tomato tissues sufficient to determine the efficacy of our plant-based mucosal vaccines in animal systems. We are equipped to test the efficacy of our plant-based multicomponent vaccines in mammalian model systems. Animal care and operative procedures are provided in the adjacent facilities of the University Medical Center supervised by Loma Linda University resident veterinarian Dr. Charles Kean. Harry Greenberg, M.D., Stanford University School of Medicine, will assist in the design and performance of our rotavirus *in vivo* efficacy studies in his laboratories at Stanford. Dr. Greenberg, is a world authority on human rotavirus vaccines. He believes these studies may lead to clinical trials which he is prepared to help facilitate.

UNITED STATES PROVISIONAL PATENT APPLICATION

for

PRODUCTION OF A CHOLERA TOXIN B SUBUNIT-ROTAVIRUS NSP4 ENTEROTOXIN FUSION PROTEIN IN POTATO

by

William H.R. LANGRIDGE and Takeshi ARAKAWA

STATEMENT REGARDING FEDERALLY SPONSORED RESEARCH OR DEVELOPMENT

This invention was made with Government support under subcontract number 010-FY97-LLU-LANGRIDGE with the National Medical Test Bed, United States Department of the Army. The Government has certain rights in this invention.

PART I

INTRODUCTION

Human rotavirus is the most important cause of infantile gastroenteritis throughout the world. This virus has a tremendous public health impact worldwide, infecting nearly every child in the first few years of life (Kapikian *et al.*, 1985). Rotavirus infection is responsible for approximately 1 million deaths each year, and an estimated 18 million hospitalizations of which 20 to 40% of the hospitalizations are for childhood diarrhea, making this virus the most important single cause of diarrheal mortality among children (Glass *et al.*, 1994). Rotavirus caused acute gastroenteritis is second only to acute respiratory disease as a source of child illness in the USA (Jawetz *et al.*, 1989). Although mortality rates in the USA are relatively low (75 to 125 deaths each year) compared to developing countries, direct medical expenses exceed $500 million and total costs exceed $1 billion (Glass *et al.*, 1994).

Rotavirus belongs to family Reoviridae which includes six genera; reovirus, rotavirus, and orbivirus as well as three additional genera which infect only plants and insects (Jawetz *et al.*, 1989). Human rotavirus belongs to the genus rotavirus which contains 11 segments of double-stranded RNA, each encoding a viral protein. Two important viral glycoproteins for neutralizing the virus are the outer capsid protein VP7 and VP4 (hemagglutinin). Serological studies revealed four common types of VP7 glycoprotein (G1 through G4) and two VP4 serotypes (P4 and P8); all of these serotypes are found in children with diarrhea (Glass *et al.*, 1994). Theoretically an effective vaccine should protect against rotavirus encoding all of these common neutralization antigens. However, a live bovine strain of rotavirus vaccine (RIT) with serologically distinctive VP7 and VP4 has been found to be protective both in adults and in children, significantly reducing

the incidence of gastroenteritis (Vesikari *et al.*, 1986). Therefore, a vaccine strain marginally immunogenic in humans might prevent the disease process through heterotypic protection. Alternatively, an independent study done by a research group in Japan showed that protection against rotavirus gastroenteritis was serotype specific and seemed to be related to levels of antibodies to homotypic virus (Chiba *et al.*, 1993). Recent discovery of a rotavirus non-structural protein, NSP4 and its 22-amino acid peptide which functions as a viral enterotoxin may provide new insights into the development of effective rotavirus vaccines (Ball *et al.*, 1996). Induction of antibody against NSP4 alone may confer cross protection from clinical disease without the need for induction of antibodies against viral structural proteins (Conner *et al.*, 1996). Induction of antibodies against NSP4 or its 22-amino acid peptide conferred protection in pups born to immunized dams, and decreased incidence and severity of diarrhea (Ball *et al.*, 1996).

Although medical treatment for rotavirus gastroenteritis is routine in hospitals in the USA, early epidemiological studies conducted in Finland indicated that rotavirus might best be controlled through vaccination (Vesikari *et al.*, 1986). Natural passive immunity seems to protect children under 2 years of age. Reinfection with the same rotavirus occurs infrequently, and repeated illness tend to be less severe or even asymptomatic. Thus, even though immunity against rotavirus is not fully protective against reinfection neonatal rotavirus infection confers protection from the development of clinically severe disease later in life (Bishop *et al.*, 1983).

We have previously demonstrated that oral immunization of CD-1 mice with transgenic potato plants producing cholera toxin B subunit (CTB) induced anti-cholera toxin antibody both in serum and the intestine and conferred approximately 50% level of protection against cholera toxin challenge in the ligated ileal loop assay (Arakawa *et al.*, 1997; 1998). Here we demonstrate that food plants are capable of producing substantial amounts of CTB fusion peptide for oral vaccine purposes. Such recombinant transgenic food vaccine would be cost-effective so that countries which can not presently afford conventional animal cell-based rotavirus reassortant vaccines may be able to produce oral vaccine plants in their own countries for protection of their children from this enteric virus.

FIGURES

Figure 1.

Plant transformation vector pPCV701FM4-CTBH:NSP4(113-135):SEKDEL. Four genes located within the T-DNA sequence flanked by the right and left border (RB and LB), 25 bp direct repeats required for integration of the T-DNA into plant genomic DNA: 1.) CTBH:NSP4(113-135):SEKDEL coding sequence under control of the *mas* P2 promoter; 2.) the bacterial luciferase AB fusion gene (*luxF*) under control of the *mas* P1 promoter as a detectable marker; 3.) an NPT II expression cassette for resistance to kanamycin in plants; 4.) a β -lactamase cassette for resistance to ampicillin in *E. coli* and carbenicillin in *A. tumefaciens*. The g7pA polyadenylation signal is from the *A. tumefaciens* T_L-DNA gene 7; the OcspA polyadenylation signal is from the octopine synthase gene; Pnos is the promoter of the nopaline synthase gene; g4pA is the polyadenylation signal from T_L-DNA gene 4; OriT is the origin of transfer derived from pRK2; OriV is the wide host range origin of replication for multiplication of the plasmid in *A. tumefaciens* derived from pRK2; and Ori pBR322 is the replication origin of pBR322 for maintenance of the plasmid in *E. coli*.

Figure 2.

Luciferase activity in transformed potato leaf tissues. Three kanamycin resistant potato plants (#1 - #3) showed bacterial luciferase activity in leaves and microtubers detected by low-light image analysis after induction on high auxin medium for 48 hours. No luciferase activity was detected in leaves of untransformed potato plants. Photon detection period was five minutes.

Figure 3.

CTB fusion gene detection in genomic DNA of transformed potato leaves. lane 1, 1 Kb DNA ladder (Gibco Life Technologies) DNA templates used for PCR amplification reaction of the CTB gene were; lane 2, pPCV701FM4-CTBH:NSP4(113-135):SEKDEL plasmid DNA (10 ng); lane 3, untransformed potato plant genomic DNA (500 ng); lane 4-6, transformed potato plant genomic DNA (500 ng) from plants #1, #2, and #3.

Figure 4.

Immunoblot detection of plant CTB chimeric peptide. Auxin induced microtuber tissues

derived from transgenic potato plant #1 were analyzed for the expression of multimeric CTB fusion peptide which dissociated to monomers by heat treatment. **A. multimeric chimera.** lane 1, 100 ng bacterial CTB; lane 2, total protein (100 μg) from untransformed potato plant tuber tissue; lane 3 - 5, total protein (100 μg) from tuber tissues of transgenic potato plants #1 - #3; lane 6, total protein (100 μg) from tuber tissue of transformed potato plant producing CTB:SEKDEL fusion peptide (Arakawa *et al.*, 1997). **B. monomeric CTB.** lane 1, 100 ng bacterial CTB multimer (M_r ~ 45 kDa) partially dissociated to monomer (M_r ~ 12 kDa); lanes 2 (boiled) and 3 (unboiled), total protein (100 μg) from untransformed potato plant callus tissue; lanes 4 (boiled) and 5 (unboiled), total protein (100 μg) from #4 transgenic potato plant leaf callus tissue. Arrow indicates the band (M_r ~ 15 kDa) corresponding to leaf callus CTB monomer. **C. CTB in tuber tissues.** lane 1, 100 ng bacterial CTB (boiled); lane 2, total protein (150 ng) from #4 transgenic potato plant microtuber tissue (boiled); lane 3, total protein (150 ng) from untransformed potato plant microtuber tissue (boiled); lanes 4-6, identical to lanes 1-3, respectively, except samples were not boiled prior to SDS-PAGE. Arrow indicates microtuber CTB monomer (M_r ~15 kDa).

Figure 5.

Determination of fusion peptide levels in transgenic potato plants. The G_{M1}-ELISA detection of plant-synthesized CTB indicates that the chimeric peptide showed specific binding affinity for the natural receptor of cholera toxin, G_{M1}-ganglioside and that its level in tuber tissues from transgenic potato plant #1 is approximately 0.1% of total soluble plant protein. The relative light units (RLU) was plotted against dilutions of plant homogenate.

MATERIALS AND METHODS

Construction of plant expression vector pPCV701FM4-CTB:NSP4(114-135):SEKDEL. The plant expression vector pPCV701FM4, a derivative of plasmid pPCV701 was digested with *Xba*I and *Sac*I restriction endonucleases within the multiple cloning site to insert a gene encoding the cholera toxin B subunit from plasmid pRT42 containing the *ctxAB* operon (provided by Dr. J. Mekalanos, Harvard Medical School). The oligonucleotide 5' primer (5'-GC**TCTAGA**GCCACCATGATTAAATTAAAATTTGGTG-3') and the 3' primer (5'-CTG**GAGCTC**GGGCCCCGGCCCATTTGCCATACTAATTGCGG-3') were synthesized

with *Xba*I and *Sac*I restriction endonuclease recognition sites (bold) for amplification and cloning of the CTB-hinge coding sequence, in a model 394 DNA/RNA Synthesizer (Applied Biosystems, Inc.). The oligonucleotide sequence surrounding the translation initiation codon of the CTB gene was altered to a preferred nucleotide context for translation in eukaryotic cells (Kozak, 1981), and a putative Shine-Dalgarno sequence (AGGA) present in the *ctxAB* operon in plasmid pPT42 was removed. The DNA sequence encoding the 21 amino acid leader peptide of the CTB was retained to direct the nascent CTB fusion peptide into the lumen of the ER. The 3' primer was designed to contain a nucleotide sequence encoding a Gly-Pro box (Gly-Pro-Gly-Pro) with relatively less frequently used codons in plants to allow the ribosomes to halt for proper folding of CTB moiety before translation of the downstream message sequence. An additional function of the Gly-Pro box would be to act as a flexible hinge between CTB and the conjugated peptide. The methods for cloning the CTBH fusion gene into the multiple cloning site immediately downstream of the *mas* P_2 promoter and the DNA sequence confirmation were as follows. After PCR amplification (Perkin Elmer Gene Amp PCR System 9600) according to the following reaction parameters; 94 °C, 45 sec.: 55 °C for 60 sec.: 72 °C for 45 sec., a total of 30 cycles), the ligated vector and PCRed fragment (T4 ligase at 16 °C for 20 hrs.) were electroporated into *Escherichia coli* strain HB101 (250 μFD, 200 Ω , and 2,500 volts; Gene Pulser, Bio-Rad, Inc.) and ampicillin resistant colonies were isolated after overnight growth at 37 °C. To confirm the presence of the correct CTBH fusion gene sequence in transformed *E. coli* cells, the plasmid was isolated from individual colonies of transformants and subjected to DNA sequence analysis with the forward primer (5'-ACCAATACATTACACTAGCATCTG-3') specific for the *mas* P_2 promoter and the reverse primer (5'-GACTGAGTGCGATATTATGTGTAATAC-3') specific for the gene 7 poly(A) signal (model 373A DNA Sequencer Applied Biosystems, Inc.). This plant transformation vector was designated as pPCV701FM4-CTBH.

To insert the rotavirus enterotoxin NSP4(114-135) epitope gene, two overlapping primer sequences were sysnthesized and equimolar amounts of both single-stranded deoxyribonucleotide fragments were subjected to PCR amplification (94 °C 45 sec.: 55 °C for 60 sec.: 72 °C for 60 sec.: 30 cycles total) to created double stranded 103 bp length synthetic

gene. The 5' oligonucleotide and the 3' oligonucleotide were designed to contain 17 bp complementary sequence for the thermostable Vent DNA polymerase (New England Biolabs) attachment site for the initial cycle of the PCR reaction. The 3' oligonucletide contains DNA sequence encoding endoplasmic reticulum retention signal (SEKDEL) (underlined) with codons most frequently found in potato plants. Both oligonucleotides contains *Sac*I recognition sites (bold) to clone the synthetic gene fragment into *Sac*I site immediately downstream of the hinge sequence of the vector to create vector pPCV701FM4-CTBH:NSP4(114-135):SEKDEL.

Following confirmation of the correct fusion gene sequence, the shuttle vector was transferred into *A. tumefaciens* recipient strain GV3101 pMP90RK by the same electroporation conditions used for *E. coli* transformation. *A. tumefaciens* transformants were grown at 29 °C on YEB solid medium containing the antibiotics carbenicillin (100 μg/ml), rifampicin (100 μg/ml), kanamycin (25 μg/ml), and gentamycin (25 μg/ml) for selection of transformants. The plasmid was isolated from an *A. tumefaciens* transformant and transferred back into *E. coli* HB101 by electroporation to confirm by restriction endonuclease analysis that no significant deletion had occurred in the vector. Structural confirmation of the plasmid was required because recombination events within the *rec*$^+$ *A. tumefaciens* strain could alter the T-DNA sequence. Transfer of the plasmid from *A. tumefaciens* back to the *E. coli* host was necessary because significant amounts of plasmid are difficult to isolate directly from *A. tumefaciens*. Agrobacteria carrying the plant expression vector were grown on YEB solid medium containing all four antibiotics for 48 hours at 29 °C and directly used for transformation of sterile potato leaf explants.

Plant transformation. Sterile potato plants *S. tuberosum* cv. Bintje were grown in Magenta boxes (Sigma Chemical, Co.) on solid Murashige and Skoog (MS) complete organic medium (JRH Biosciences) containing 3.0% sucrose and 0.2% gelrite. Leaf explants excised from the young plants were laterally bisected in a 9 cm diameter culture dish containing an overnight culture of *A. tumefaciens* suspension (1 x 10^{10} cell/ml) harboring pPCV701FM4-CTBH:NSP4(113-135):SEKDEL. Bacterial suspension was supplemented with acetosyringone (370 μM) to increase transformation efficiency. The explants were incubated in the bacterial suspension for 5 minutes, blotted on sterile filter paper, and transferred to MS solid medium,

pH 5.7, containing 0.1 μg/ml naphthalene acetic acid (NAA) and 1.0 μg/ml trans-zeatin. The leaf explants were incubated for 48 hours at room temperature on MS solid medium to permit T-DNA transfer into the plant genome. For selection of transformed plant cells and for counter selection against continued *Agrobacterium* growth, the leaf explants were transferred to MS solid medium containing the antibiotics kanamycin (100 μg/ml) and claforan (300 μg/ml). Transformed plant cells formed calli on the selective medium after continuous incubation for 2 to 3 weeks at room temperature in a light room under cool white fluorescent tubes on a 12 hour photoperiod regime. When transformed calli grew to 5 - 10 mm in diameter, the leaf tissue was transferred to MS medium containing 1.0 μg/ml trans-zeatin, 50 μg/ml kanamycin and 400 μg/ml claforan for shoot induction. Regenerated shoots were excised and transferred to MS solid medium without plant hormones or antibiotics to stimulate root formation. Plantlets were allowed to grow and form microtubers under sterile conditions to characterization.

Detection of luciferase activity in transformed *A. tumefaciens* and transgenic plants. The presence of the plant expression plasmid in agrobacteria, *luxF* gene expression under control of the *mas* P1 promoter was monitored by low-light image analysis (Langridge *et al.*, 1991). To perform the bioluminescent assay, bacterial culture grown for 24 hours on YEB solid culture medium was covered with a glass culture plate lid swabbed with substrate n-decyl aldehyde (Sigma) and analyzed by the Argus-100 intensified camera system (Hamamatsu Photonics, K.K.).

Expression of *luxF* gene was also monitored to confirm the presence of the T-DNA sequence in the plant genome and to estimate the level of CTB fusion gene expression by *mas* P2 promoter. Leaves excised from putative transformants were wounded by scalpel blade followed by incubation on MS solid medium containing naphthalene acetic acid (5 μg/ml) and 2,4-dichlorophenoxy acetic acid (6 μg/ml) for 48 hours. Light emission from the wounded leaf tissues was detected as described for agrobacteria.

Detection of the CTB gene in transformed plant genomic DNA. Genomic DNA was isolated from transformed potato leaf tissues. Presence of the CTB fusion gene was determined by PCR analysis using the oligonucleotide primers specific for the T-DNA

sequence. Transformed plant genomic DNA (500 ng) was used as a template to detect the CTB gene by PCR amplification (94 °C for 45 seconds, 55 °C for 60 seconds, and 62 °C for 60 seconds for a total of 30 cycles).

CTB fusion protein detection in transformed potato tissues. Transgenic potato leaf and microtuber tissues were analyzed for the CTB fusion gene expression by immunoblot analysis. Callus tissues were derived from leaf or tuber tissues incubated for 4 weeks on MS solid medium containing 5.0 mg/l NAA and 6.0 mg/l 2,4-D. Tissues were homogenized by grinding by a mortar and pestle at 4 °C in extraction buffer (1:1 w/v) (200 mM Tris-Cl, pH 8.0, 100 mM NaCl, 400 mM sucrose, 10 mM EDTA, 14 mM 2-mercaptoethanol, 1 mM phenylmethylsulfonyl fluoride, 0.05% Tween-20). The tissue homogenate was centrifuged at 17,000 × g in a Beckman GS-15R centrifuge for 15 minutes at 4 °C to remove insoluble cell debris. An aliquot of supernatant containing 100 μg of total soluble protein, as determined by Bradford protein assay (Bio-Rad, Inc.), was separated by 15% sodium dodecylsulfate polyacrylamide gel electrophoresis (SDS-PAGE) at 125 volts for 30 to 45 minutes in Tris-glycine buffer (25 mM Tris, 250 mM glycine, pH 8.3, 0.1% SDS). Samples were either loaded directly on the gel or boiled for 5 minutes prior to electrophoresis.

The separated protein bands were transferred from the gel to approximately 80 cm^2 Immun-Lite membranes (Bio-Rad, Inc.) by electroblotting on a semi-dry blotter (Labconco) for 60 minutes at 15 V. and 100 mA. Nonspecific antibody reactions were blocked by incubation of the membrane in 25 ml of 5% non-fat dry milk in TBS buffer (20 mM Tris pH 7.5 and 500 mM NaCl) for 1 hour with gentle agitation on a rotary shaker (40 rpm), followed by washing in TBS buffer for 5 minutes. The membrane was incubated overnight at room temperature with gentle agitation in a 1:5,000 dilution of rabbit anti-cholera antiserum (Sigma C-3062) in TTBS antibody dilution buffer (TBS with 0.05% Tween-20 and 1% non-fat dry milk) followed by washing three times in TBST washing buffer (TBS with 0.05% Tween-20). The membrane was incubated for 1 hour at room temperature with gentle agitation in a 1:10,000 dilution of mouse anti-rabbit IgG conjugated with alkaline phosphatase (Sigma A-2556) in antibody dilution buffer. The membrane was washed three times in TTBS buffer as before and once with TBS buffer, followed by incubation in 1 × chemiluminescent substrate

CSPD™ (Bio-Rad, Inc.) for 5 minutes at room temperature with gentle agitation. The membrane was wrapped with transparent plastic membrane and placed in a photocassette on Kodak X-OMAT film (cat# 1651454). (The membrane was also used to image chemiluminescent light intensity in both the numerical and graphic form by the Argus-100 video image analysis.) The film was subjected to 1 - 10 minutes exposure and developed in a Kodak M35A X-OMAT Processor.

Quantitation of CTB fusion protein level in transgenic potato tissues. Pentameric CTB fusion protein levels in transgenic potato plants and its affinity for G_{M1}-ganglioside were evaluated by quantitative chemiluminescent G_{M1}-ELISA assays. The microtiter plate was coated with 100 μl/well of monosialoganglioside G_{M1} (3.0 μg/ml) (Sigma G-7641) in bicarbonate buffer, pH 9.6 (15 mM Na_2CO_3, 35mM $NaHCO_3$) and incubated at 4 °C overnight. Wells were loaded with 100 μl/well of 10-fold serial dilutions of total soluble potato leaf or tuber protein in phosphate buffered saline (PBS) and incubated overnight at 4 °C. The plate was washed three times in PBST (PBS containing 0.05% Tween-20). The wells were blocked by adding 300 μl/well of 1% bovine serum albumin (BSA) in PBS and incubated at 37 °C for 2 hours followed by washing three times with PBST. The wells were loaded with 100 μl/well of 1:5,000 dilution of rabbit anti-cholera toxin antibody (Sigma C-3062) and incubated for 2 hours at 37 °C, followed by washing the wells three times with PBST. The plate was incubated with 100μl/well of 1:50,000 dilution of alkaline phosphatase-conjugated anti-rabbit IgG (Sigma A-2556) for 2 hours at 37 °C and washed three times with PBST. The plate was finally incubated with 100 μl/well of Lumi-Phos® Plus (Lumigen, Inc. P-701) for 30 minutes at 37 °C and the enzyme-substrate reaction was measured in a Microlite™ ML3000 Microtiter® Plate Luminometer (Dynatech Laboratories).

RESULTS

Detection of luciferase activities from putative transgenic potato plants. After *Agrobacterium* mediated transformation of potato leaf explants with the plant expression vector pPCV701FM4-CTBH:NSP4(113-135):SEKDEL (Fig. 1), more than 40 independent kanamycin-resistant plants were regenerated. Of those only three plants were found to express luciferase activities above background levels from untransformed plants (Fig. 2). Thus, only

less than 10% of kanamycin-resistant plants were found to express luciferase activities in this plant transformation experiment. However, in additional potato plant transformation experiments, transformation efficiencies were found to vary considerably experiment to experiment, suggesting the possibility that differences in aspects of the transformation method such as physiological state of leaf explants and the growth state of the agrobacteria used for transformation may result in substantial differences in transformation efficiency. In addition, the number of kanamycin-resistant plants regenerated per transformation experiment varied dramatically ranging from 0 to 200 per 50 leaf explants transformed. Therefore, the presence of a convenient detectable marker gene such as luciferase in addition to selectable marker gene significantly enhances the process of screening large numbers of antibiotic resistant putative transformants.

PCR detection of CTB fusion gene in transgenic potato plants. Three transformed potato plants showing luciferase activities were analyzed for the presence of the fusion gene in plant genomic DNA isolated from young leaf tissues (Fig. 3). A 650 bp DNA fragment, including both 5' and 3' flanking sequences of the fusion gene, was amplified. The PCR amplification was very specific probably due to high specificity of the primers used for the PCR reaction. The DNA fragments amplified from plasmid vector pPCV701FM4-CTBH:NSP4(114-135):SEKDEL and from transgenic plant genomic DNA were identical in molecular weight. Although, identical amounts of template genomic DNA (500 ng) was used for the PCR reaction, the plant exhibiting the highest luciferase activity (Fig. 2) also demonstrated the highest level of PCR amplification (Fig. 3). The correlation between PCR product level and luciferase activity suggests the possibility of increased T-DNA copy number in this transformant.

Immunoblot analysis of plant synthesized CTB fusion protein. The three transformed plants were analyzed for the presence of CTB-NSP4 fusion peptide by immunoblot analysis (Fig. 4). Transgenic potato tuber tissues were shown to contain CTB fusion protein (~ 60 kDa) that strongly reacted with anti-cholera toxin antibody which predominantly recognized pentameric form of cholera toxin or its B subunit (Fig. 4). Vector transfomed potato plants did not show this protein bands (lane 2). Plants #1 showed approximately 3 to 5 fold higher

chimeric protein level than other two (#2 and #3, lanes 4 and 5). Potato-synthesized CTB-NSP4 fusion peptide exhibited higher molecular weight than both pentameric bacterial CTB subunit (45 kDa, lane 1) and potato-synthesized pentameric CTB subunit with ER retention signal (50 kDa, lane6).

CTB protein levels in transformed potato plants. To obtain quantitatively measure the CTB protein level in tubers of transgenic plant #1, both chemiluminescent G_{M1}-ELISA and chemiluminescent immunoblot assays were employed.

In the chemiluminescent G_{M1}-ELISA method, the amount of plant CTB fusion protein was measured by comparison of chemiluminescent intensities from a known amount of bacterial CTB protein-antibody complex with that emitted from a known amount of transformed plant soluble protein. Two standard curve (1% and 0.1%) were generated based on the relative light units (RLU) measured for different amount of bacterial CTB. The RLU generated from serial dilutions of transgenic potato plant homogenates were plotted into the graph, and found to reside within the 0.1% and 0.01% curves, indicating that the fusion protein level in the transgenic potato tissue is slightly less than 0.1%.

In the chemiluminescent immunoblot method, luminescent intensities of bacterial and plant CTB protein bands blotted on Immun-Lite membranes after SDS-PAGE were measured by the Argus-100 low-light imager Data Analysis Program. The number of photons emitted from either bacterial CTB (Fig. 4, lane 1) or plant CTB (Fig. 4, lane 6) or plant CTB-NSP4 fusion protein bands was quantified, and their values compared to provide a semi-quantitative estimate of the amount of plant synthesized CTB fusion protein. Based on the amount of light emission detected from a known amount of bacterial CTB protein (100 ng), the amount of plant CTB fusion protein was calculated to be approximately 100 ng. The % of chimeric protein in the plant was calculated based on the amount of soluble plant protein (100 μg) used in the assay. Based on this method, the % of plant CTB protein was found to be approximately 0.1% of total soluble plant protein, a value in close agreement with measurements made by the chemiluminescent G_{M1}-ELISA method. Based on the results of the chemiluminescent ELISA and immunoblot assays, 1 g of callus tissues (fresh weight) obtained from auxin-induced potato leaves contained 10 μg of recombinant plant CTB-NSP4 fusion

protein.

DISCUSSION

The combination of a convenient method for screening large numbers of transformants via the bacterial luciferase reporter gene and the hormone-inducible *mas* promoter system provides us with the potential for rapid screening for large numbers of transgenic plants to obtain those with the highest transgene expression levels. In our potato transformation experiments, the luciferase reporter gene was important for identification of transformants as only less than 10% of kanamycin-resistance plants were transformed. The *mas* dual promoter system provides a distinct advantage when simultaneous expression of marker gene and another gene were desired in plant.

Addition of polypeptide at the N-terminus of CTB subunits has been shown to reduce its affinity for G_{M1}-ganglioside (Dertzbaugh and Elson, 1993) probably because of the steric hindrance or conformational changes induced within the CTB molecules. In contrast, C-terminus of the CTB subunits has been shown to well tolerate addition of relatively large polypeptide without disrupting its affinity for the ligand (reference********). The leader peptide of this fusion protein required to translocate the conjugates into the lumen of ER was presumably provided by the original CTB leader peptide. Presence of Gly-Pro box between CTB and NSP4(114-135) peptide may function as a flexible hinge between the two moieties of the chimera, allowing maximal movement between them to reduce steric hindrance which may reduce G_{M1} affinity (Jagusztyn-Krynicka *et al.*, 1993). In addition, relatively less frequently used codons in plants were used for the hinge to allow ribosome to halt elongation process, thus possibly facilitating CTB subunit folding prior to translation of the downstream message. The C-terminus of the CTB fusion proteins contain hexapeptide ER retention signal to sequester the chimeric protein, which may facilitate pentamerization process. Presence of the SEKDEL hexapeptide at the C-terminus of proteins has been shown by other investigators to significantly increase protein accumulation within plant tissues such as potato leaves and tubers, tobacco and alfalfa leaves as well as in COS cells (Munro and Pelham, 1987; Wandelt *et al.*, 1992; Haq *et al.*, 1995), thereby facilitating protein subunit oligomerization. Production of pentameric CTB chimeric protein in transgenic potato tissues suggest that the

plant endoplasmic reticulum, similar to the periplasmic space of Gram-negative bacteria (Hirst and Holmgren, 1987), provides an intracellular environment in which chimeric monomers are accumulated and assembled into pentamers.

Pentamerization of CTB subunits is essential for its affinity for the natural receptor. In G_{M1}-ELISA binding assays, plant-produced chimeric protein and bacterial CTB demonstrated a strong affinity for G_{M1}-ganglioside but not for BSA, which was the bases of protein production level measurement. The ability of plant-derived CTB to bind G_{M1}-ganglioside indicates that the specific protein-ganglioside binding interactions between amino acid residues forming the G_{M1} binding sites and the oligosaccharide moiety of G_{M1}-ganglioside are conserved. Tryptophan residue at position 88 of the CTB protein is essential for both pentamerization of the B monomer as well as binding of the pentamer to the oligosaccharide moiety of G_{M1} (de Wolf *et al.*, 1981; de Wolf *et al.*, 1981). The strong binding efficiency of plant CTB conjugate for G_{M1} indicate that molecular configurations of CTB moiety is well conserved. In addition, the absence of monomeric form of chimera by immunoblot analysis indicates that predominant molecular species of chimeric protein is in the pentameric form, because monomeric CTB is unable to bind to G_{M1}-ganglioside. Those observations suggest that monomeric B subunit fusion polypeptide accumulates within the lumen of the ER of plant cells where self-assembly into pentameric G_{M1} binding forms takes place.

The production in edible plants of pentameric CTB protein conjugated with neutralizing epitopes from microbial pathogens may provide protective immunity by simply ingesting transgenic edible plant tissues. Palatable food plant species of tropical and semi-tropical origin such as bananas, tomatoes and avocados which are consumed without heat treatment must be evaluated for their abilities to produce CTB-fusion protein for vaccine purposes. These food plants would be practically useful for production of heat-labile CTB-conjugated vaccine protein. In addition, they would be particularly advantageous as oral vaccines for children due to their palatability. Development of edible transgenic plants with high expression levels of pentameric CTB fusion peptide with strong G_{M1}-ganglioside affinity, which presumably achieve effective delivery and presentation of conjugate epitopes to gut-associated lymphoid tissues, would provide low-cost and convenient food-plant based oral vaccines for prevention

of infectious diseases in regions of the developing world where conventional vaccines are difficult to afford.

Although the present invention has been discussed in considerable detail with reference to certain preferred embodiments, other embodiments are possible. Therefore, the scope of the appended claims should not be limited to the description of preferred embodiments contained in this disclosure. All references cited herein are incorporated by reference in their entirety.

REFERENCES

Arakawa, T., D. K. X. Chong, J. L. Merritt, and W. H. R. Langridge. Expression of cholera toxin B subunit oligomers in transgenic potato plants. Transgenic Res., in press.

Ball, J. M., P. Tian, C. Q.-Y. Zeng, A. P. Morris, and M. K. Estes. 1996. Age-dependent diarrhea induced by a rotavirus nostructural glycoprotein. Science 272:101-104.

Bishop, R. F., G. L. Barnes, E. Cipriani, and J. S. Lund. 1983. Clinical immunity after neonatal rotavirus infection: a prospective longitudinal study in young children. N. Engl. J. Med. 309:72-76.

Dertzbaugh, M. T., and C. O. Elson. 1993. Comparative effectiveness of the cholera toxin B subunits and alkaline phosphatase as carrier for oral vaccines. Infect. Immun. 61:48-55.

Dertzbaugh, M. T., and C. O. Elson. 1993. Reduction in oral immunogenicity of cholera toxin B subunits by N-terminal peptide addition. Infect. Immun. 61: 384-390.

de Wolf, M. J. S., M. Fridkin, M. Epstein, and L. D. Kohn. 1981. Structure-function studies of cholera toxin and its A and B protomers: modification of tryptophan residues. J. Biol. Chem. 256: 5481-5488.

de Wolf, M.J.S., M. Fridkin, and L. D. Kohn. 1981. Tryptophan residues of cholera toxin and its A and B protomers: intrinsic fluorescence and solute quenching upon interacting with the ganglioside G_{M1}, oligo-G_{M1}, or dansylated oligo-G_{M1}. J. Biol. Chem. 256: 5489-5496.

Escher, A., D. J. O'Kane, J. Lee, and A. A. Szalay. 1989. Bacterial luciferase alpha-beta fusion protein is fully active as a monomer and highly sensitive *in vivo* to elevated temperature. Proc. Natl. Acad. Sci. USA 86: 6528-6532.

Glass, R. I., J. Gentsch, and J. C. Smith. 1994. Rotavirus vaccine: success by reassortment? Science 265:1389-1392.

Jagusztyn-Krynicka, E. K., J. E. Clark-Curtiss, and R. Curtiss III. 1993. *Escherichia coli* heat-labile toxin subunit B fusions with *Streptococcus sobrinus* antigens expressed by *Salmonella typhimurium* oral vaccine strains: importance of the linker for antigenicity and biological activities of the hybrid proteins. Infect. Immun. 61:1004-1015.

Jawetz, E., J. L. Melnick, and E. A. Adelberg. 1989. Medical Microbiology. Connecticut: Appleton & Lange, p482-486.

Hardy, S. J. S., J. Holmgren, S. Johansson, J. Sanchez, and T. R. Hirst. 1988. Coordinated assembly of multisubunit proteins: oligomerization of bacterial enterotoxins *in vivo* and *in vitro*. Proc. Natl. Acad. Sci. USA 85:7109-7113.

Hirst, T.R. and J. Holmgren. 1987. Conformation of protein secreted across bacterial outer membranes: a study of enterotoxin translocation from *Vibrio cholerae*. Proc. Natl. Acad. Sci. USA 84:7418-7422.

Haq, T.A., H. S. Mason, J. D. Clements, and C. J. Arntzen. 1995. Oral immunization with a recombinant bacterial antigen produced in transgenic plants. Science 268:714-716.

Kapikian, A. Z. and R. M. Chanock. 1985. Norwalk group of viruses: agents associated with epidemic viral gastroenteritis. Virology. New York: Raven Press. p1495-1518.

Langridge, W. H. R., K. L. Fitzgerald, C. Koncz, J. Schell, and A. A. Szalay. 1989. Dual promoter of *Agrobacterium tumefaciens* mannopine synthase gene is regulated by plant growth hormones. Proc. Natl. Acad. Sci. USA 86:3219-3223.

Munro, S. and H. R. B. Pelham. 1987. A C-terminal signal prevents secretion of luminal ER proteins. Cell 48:899-907.

Vesikari, T., A. Z. Kapikian, and G. Zissis. 1986. A comparative trial of rhesus monkey (RRV-1) and bovine (RIT4237) oral rotavirus vaccines in young children. J. Infct. Dis. 153:832-839.

Wandelt, C. I., M. R. I. Khan, S. Craig, H. E. Schroeder, D. Spencer, and T. J. V. Higgins. 1992. Vicilin with carboxy-terminal KDEL is retained in the endoplasmic reticulum and accumulates to high levels in the leaves of transgenic plants. Plant J. 2:181-192.

PART II

A. Goal, Objectives and Research Phases

The goal of our NMTB subcontract is to generate increased efficacy of plant-based vaccines by: a) targeting multiple antigens to the gut associated lymphoid system (GALT) and b) by generating rotavirus capsid protein conformational epitopes in plant cells. Achievement of these goals is based on the following research objectives: 1. Generation of transformed potato plants containing the genes encoding the cholera toxin A and B subunits (CTA2,CTB), the enterotoxigenic *E. coli* fimbrial antigen (CFA/I) and the rotavirus VP2, VP6 capsid and NSP4 enterotoxin antigen proteins. 2. Assembly of CTB-antigen fusion protein - CTA2-antigen fusion protein heterohexameric complexes in plant cells. 3. Generation of rotavirus-like particles (VLPs) in transformed tuber cells. Accomplishment of the research objectives is divided into four phases:

Phase 1: *Plant Transformation with plant expression vectors*. Construction of plant expression vectors containing enterotoxigenic *E. coli* (ETEC) fimbrial antigen CFA/I, rotavirus capsid proteins VP2 and VP6, the rotavirus enterotoxin peptide NSP4 and the cholera CTA2 and CTB subunits was accomplished in FY97-98. Transgenic potato plants have been regenerated which carry the genes encoding the CFA/I-CTB-NSP4 multicomponent vaccine antigens and VP2-VP6 rotavirus capsid protein antigens. Based on the loss of previous transformed plants and recent technical problems with plant transformation methods, neither the VP6-CTB-NSP4 multicomponent vaccine vector or the VP2 alone will be able to provide multicomponent vaccine containing plants prior to the end of FY98-99. Therefore, if it is agreed upon, measurement of rotavirus antigen expression levels in transformed plants based on these two vectors will be placed on hold to focus increased attention on accomplishment of the oral immunization and efficacy testing of tuber tissues containing the "proof of concept" GALT targeted multicomponent and rotavirus conformational epitope vectors, CFA/I-CTB-NSP4 and VP6-VP2.

Phase 2: *Determination of antigen protein levels in transformed plants*. ELISA experiments for measurement of antigen expression levels in potato plants transformed with

the CFA/I-CTB-NSP4 multicomponent vaccine vector, the VP6-VP2 rotavirus capsid protein vector and the rotavirus VP6 capsid protein vector were completed during the second quarter of FY98-99. These results complete Phase 2 of our subcontract.

Phase 3: *Determination of antibody titers following oral immunization.* ELISA measurements of mouse serum (IgG) and mucosal (IgA) antibody titers generated by the plant-based vaccines following oral immunization with tuber tissues synthesizing the multiple antigens has been completed solely on VP6 containing plants. The results of the antibody titration experiments will provide the experimental basis for determining the amounts of antibody required to generate protective efficacy against the pathogen. Through vegetative propagation, we are generating additional transformed tubers synthesizing CFA/I-CTB-NSP4 and mouse oral immunization experiments will be initiated in the second week of the third quarter. Oral immunization with tubers synthesizing the two rotavirus capsid proteins VP6-VP2 will be initiated during the third quarter, following continued vegetative amplification of transformed tubers.

Phase 4: *Protective efficacy of the plant-based multicomponent and rotavirus vaccines.* Assessment of protective immunity generated by the plant-based vaccines by measurement of reduction in diarrhea volume, reduced ETEC binding to enterocytes, or reduction in rotavirus shed in immunized mice following rotavirus challenge, is contingent on ELISA detection of significant mucosal and (or) serum antibody titers against the pathogen antigens after Phase 3 oral immunization experiments. With the exception of plants synthesizing VP6 capsid protein, no additional Phase 3 mouse immunization experiments have so far been initiated. Depending on the presence of detectable amounts of IgG and IgA levels in orally immunized animals determined in the third quarter, ETEC will be used to challenge CFA/I antigen protection against bacterial cell attachment to Caco enterocyte cells in culture. Wild type rotavirus (strain ECW), will be used to challenge VP2 and VP6 immunization in the fourth quarter of the subcontract. Our progress towards the completion of Phase 3 and 4 objectives during the second quarter (October through December 1999), is outlined in Table 1 and in detail on a vector by vector basis in Section B.

Table 1. ENHANCEMENT OF PLANT-BASED VACCINE EFFICACY

Expression Vector[x]	Phase 1. Transformed plants[#]	Phase 2. Antigen in tuber	Phase 3. Antigen titration	Phase 4. Vaccine efficacy
A. GALT Targeted Vaccines				
1. pPCV701- **CFA/I-CTB-NSP4**	P,T^{ip}	+	ip	-
2. pPCV701- **VP6-CTB-NSP4**	P^{ip},T^{ip}	-	-	-
B. Rotavirus VLP Vaccines				
3. pPCV701- **VP6, VP2**	P	ip	-	-
4. pPCV701- **VP6**	P	+	+	-
5. pPCV701- **VP2**	P^{ip}	-	-	-

x - Plant expression vectors #1 and #2 were designed to test CTA2-CFA/I and CTA2-VP6 fusion gene expression and fusion protein assembly with CTB pentamers to form heterohexameric cholera subunit complexes in plants capable of targeting to the GALT. Vector #3 contains cDNAs encoding rotavirus capsid proteins VP2 and VP6, for detection of multicomponent capsid protein gene expression and VLP assembly in plants. Vectors #4 and #5 contain cDNAs encoding single rotavirus capsid proteins VP6 and VP2 for electron microscopic study of rotavirus capsid protein assembly into VLP structures.

- P = potato; T = tomato

ip - in progress

B. Progress Toward Completion of Phase Three and Phase Four Objectives

1. Plant Expression Vector 1: pPCV701-CFA/I-CTB-NSP4 (J.Y.)

The multicomponent vaccine plant expression vector RB---(KDEL)-CTA_2-CFA/I-leader<-P_1-*mas*-P_2->leader-**CTB -NSP4**-(SEKDEL)---LB, is based on our cholera toxin heterohexamer approach to plant-based mucosal immunization, and is designed to express

three individual antigen proteins from three different enteric pathogens. In this vector, the CTB subunit gene is fused to the rotavirus enterotoxin (NSP4) gene 22 amino acid epitope and the ETEC fimbrial antigen CFA/I gene is fused to the 5' end of the cholera CTA2 gene. In the first quarter report, we determined through immunoblot experiments that transformed potato plants containing this construct synthesize the CTB-NSP4 fusion protein at levels of 0.01% of total soluble protein (TSP). In contrast, ELISA experiments suggested that the CFA/I protein was present at ten fold lower levels(0.001% TSP). Anti-CFA/I antibodies obtained from Dr. Myron Levine, NIH Vaccine Institute, Baltimore, MD, were generated against the entire fimbria rather than the portion which binds to enterocytes. Thus their sensitivity for detection of the CFA/I subunit was found to be inadequate to detect the amounts of CFA/I synthesized in the plant.

As an alternative, we decided to use the GM1 ganglioside binding sandwich ELISA assay method for detection of CFA/I-CTA2 fusion protein-CTB hexamer aggregates. We found that we were only able to detect 0.001% TSP in transformed plant homogenates. This level of CFA/I-CTA2 fusion protein which binds to CTB pentamers may be only a fraction of the CFA/I protein synthesized in the cell (underscored by the substantial CFA/I mRNA signal detected in transformed plant cells by RT-PCR hybridization methods) and may account for the more than 10 fold reduction expected in antigen detection.

To circumvent the problem of lack of CFA/I antibody binding specificity, and to more accurately determine the level of CFA/I protein produced in transformed potato tuber tissues, we are generating our own antibodies to the peptide sequence of the CFA/I cell attachment site as well as against CFA/I fimbrial protein subunit monomers generated by heating intact CFA/I fimbria. Dr. Levine's laboratory is in the process of generating more intact CFA/I fimbria for us for the rabbit immunization experiments. Within the next three months, we expect to have specific anti-CFA/I antibodies which can provide us with a more sensitive indication of the amount of CFA/I protein synthesized in transformed tuber tissues and whether the CFA/I-CTA2 fusion protein is linked to the CTB pentamer in the plant. If increased antibody specificity for the CFA/I protein does not permit unequivocal detection of heterohexamer formation in the plant cells, we will attempt to increase the level of CFA/I protein synthesized

in the plant by expressing the CFA/I cDNA fragment from the *mas* P2 promoter and the enhanced CaMV 35S promoter as part of a request for an additional year of NMTB contract support.

An alternative possibility for our inability to detect significant plant synthesized CFA/I protein in the GM1 ganglioside ELISA experiments may be that the CTA subunit does not associate to a significant extent with the CTB pentamer. To explore this possibility further, a multicomponent vaccine expression vector pPCV701-**CTA-CTB** was constructed by D.C.

This vector was recently introduced into potato cells and transgenic plants regenerated. Preliminary immunoblot experiments with transformed potato tuber tissues suggest that the CTA and CTB gene products are both synthesized in the transformed tuber cells and that the two subunits associate in plant tissues to form the heterohexamer holotoxin conformation. While CTB protein was easily detected in the transformed tuber tissues, anti-CTA polyclonal antibodies obtained from several sources, (R. Finkelstein - Univ. of Missouri, and John Mekalanos - Harvard School of Medicine), cross reacted to different extents with the CTB subunit protein. Thus, while the molecular size of the putative CT detected in transformed potato tissues is approximately correct for the holotoxin, at present it is impossible to unambiguously identify the CTA subunit linked with the CTB pentamer in transformed tuber tissues. During the last week in December, in agreement with our University, we signed a Material Transfer Agreement with the University of Colorado, to obtain monoclonal antibodies specific for the CTA subunit from the laboratory of Dr. Randall Holmes, University of Colorado. Based on the specificity of the monoclonal antibodies specific for the CTA subunit, we hope to resolve the problem of CTA protein detection within the plant synthesized holotoxin in transformed potato tissues before the end of the third quarter.

In the third quarter, we will initiate a Phase 3 oral immunization experiment to determine whether significant levels of anti CFA/I, CTB and NSP4 protein IgG can be detected in immunized mice. Generation of a significant antibody response to the CFA/I, CTB and NSP4 antigens will provide the basis for Phase 4 protective efficacy studies. To accomplish these studies, Caco-2 enterocyte cell cultures available in our laboratory will be used to test the reduction of ETEC binding after incubation in the serum of CFA/I immunized

animals. Based on earlier studies (Arakawa et.al., 1998), the detection of anti-CTB antibodies in immunized mice will confirm protection against cholera infection. Finally, detection of anti-NSP4 antibodies in the serum or intestinal contents of immunized mice will permit us to carry out mouse immunization experiments with Dr. Greenberg or Dr. Mary Estes, to demonstrate plant-based vaccine protection against rotavirus infection in mice.

Although we have not yet demonstrated protective efficacy of any of our plant-based vaccine constructs, to fulfill the goal of tomato transformation with the plant based vaccine, during the second quarter, D.C. initiated transformation experiments with multicomponent vaccine vector #1 in *Lycopersicon esculentum* var. Tiny Tim tomato plants. In contrast to potato, tomato has several major advantages over potato for the expression of vaccine antigens: 1). fruit ripening does not require exogenous auxin treatment for maximum activation of the *mas* dual promoters and 2). the fruit does not require cooking prior to consumption. Putative transformed shoots present on transformed leaf callus tissues will during the course of the third quarter be transferred to rooting medium to regenerate intact plants. In the fourth quarter, the amounts of CFA/I, CTB and NSP4 protein synthesized in the transformed tomato leaf and fruit tissues will be determined by immunoblot and ELISA methods. Due to the time required to regenerate transformed plants, we will not be able to test the immunogenic nature of the transformed tomato fruit tissues in mice before the end of the fourth quarter, July, 2000. However, if the tomato tissues produce significant amounts of the antigen proteins, further analysis of the immunogenicity and protective efficacy of transformed tomato tissues could be explored if given the opportunity of a third year of NMTB funding.

2. Vaccine Expression Vector 2: pPCV701-VP6-CTB-NSP4 (D.C.)

Plant expression vector RB--(KDEL)-CTA_2-**VP6**-leader<- P_1-*mas*-P_2 ->leader-**CTB-NSP4**$^{114-135}$-(SEKDEL)--LB was constructed to generate a hexameric subunit cholera toxin capable of delivery of the rotavirus capsid protein VP6 and CTB-NSP4 antigens to the GALT. As previously reported, transformed plants regenerated earlier were destroyed in FY97-98, by growth room temperature regulation malfunction. To regain these transformed plants, we attempted to transform potato explants several times. However, due to apparent contamination

of our Agrobacterium stock with claforan resistant bacterial mutants, transformed plants have not yet been obtained.

Experiments for re-selection of claforan sensitive Agrobacterium transformants are in process. If contamination of our Agrobacterium stock turns out to be the reason for our failure to produce transformed plants, potato transformation experiments may be completed before the end of the third quarter. Selection and regeneration of transgenic plantlets containing this multicomponent vaccine vector could be accomplished by the end of the fourth quarter. At this time, we will collect tubers for the possibility of analysis of the second multicomponent vaccine in a possible third year of NMTB support.

If however, contamination is not the sole problem with the abortive transformation experiments, we will terminate further transformation experiments until we are able to resolve the problem by alternative means. As the VP6-CTB-NSP4 vector represents a second multicomponent vaccine, and is not essential to the proof of concept, we will concentrate the remainder of our efforts on Phase 3 and 4 assessment of antigenicity and vaccine protective efficacy of the CFA/I-CTB-NSP4 and VP2-VP6 vaccines.

Transformation experiments with tomato plants *Lycopersicon esculentum* var. Tiny Tim, with the multicomponent vaccine vector containing the VP6 and CTB-NSP4 antigen genes are currently in progress (D.C.). Putative transformed shoots have regenerated on the transformed callus and will soon be transferred to rooting medium to regenerate plantlets during the course of the third quarter. In the last quarter of our NMTB contract, the transformed tomato plants will be grown to maturity and tomato fruit harvested. The transformed tomato tissues will be freeze dried and stored at freezer temperatures for later (possible third year) quantification of VP6, CTB and NSP4 proteins antigens by immunoblot and ELISA methods.

3. Vaccine Expression Vector 3: pPCV701-VP6,VP2 (D.C.)

To generate an effective multivalent vaccine for mammalian rotaviruses, plant expression vector RB--**VP6**<--P_1-*mas*-P_2-> **VP2** --LB, was constructed and introduced into potato leaf tissues and potato plants regenerated. The amounts of VP6 and VP2 proteins contained within leaf tissues were quantified by immunoblot and ELISA methods. The amount

of VP2 protein detected in the transformed plant tissues is approximately 0.001% TSP while the amounts of VP6 protein are in the range of 0.01% TSP. Capsid protein expression levels have not yet been measured in tuber tissues. Transformed tubers are being grown under sterile conditions over the next three months to obtain sufficient transformed tuber tissues to permit initiation of oral immunization experiments in the fourth quarter to determine whether the transformed tuber tissues can generate serum and mucosal immune responses against VP6 and VP2 in CD-1 mice.

Previous Norwalk virus capsid protein biosynthesis studies using a baculovirus capsid protein biosynthesis system, have demonstrated that the empty capsids termed virus like particles (VLP's), contain conformational epitopes which generate a significantly stronger immune response in comparison with linear capsid protein epitopes. Transformed potato tissues synthesizing VP6 and VP2 detected by immunoblot experiments are being vegetatively propagated prior to attempts at multicapsid VLP visualization by electron microscopic staining methods. We will attempt E.M visualization of VLP's during the third and fourth quarters to provide the first opportunity for detection of coordinated assembly of multicapsid (VP2/ VP6),VLPs in plant tissues.

4. Vaccine Expression Vector 4: pPCV701-VP6 (J.Y.)

This plant expression vector RB---<--P_1-*mas*-P_2->**VP6**---LB, contains the murine rotavirus capsid protein VP6 and was constructed to test the ability of transformed potato cells to synthesize and assemble rotavirus capsid protein. The VP6 protein has been identified in transformed plants by immunoblot assay using anti-VP6 antibodies obtained from Dr. Mary Estes. Levels of VP6 protein have been determined by ELISA to be in the range of 0.01% total soluble protein. Preliminary electron microscopic studies of VP6 protein assembly into virus like particles (VLP's) in transformed potato tubers and leaves have been initiated to detect rotavirus capsid protein self-assembly in the tissues of transformed potato plants. Phosphotungstic acid stained E.M. grids containing VP6 transformed tuber extracts were subjected to transmission electron microscopy. In the first preliminary experiment, tubular structures resembling polymerized capsid proteins observed by other investigators were detected in the transformed cell extracts however, no VLPs were observed in these

preparations. Experiments will be conducted in the third and fourth quarters to concentrate the extracts of auxin stimulated potato tissues to improve the possibilities for detection of VLP structures.

Based on the presence of significant amounts of VP6 protein (seen on western blots), and tubular virus protein-like structures in the transformed tuber tissues, oral immunization experiments were initiated in CD-1 mice late in the second quarter to determine the level of anti-VP6, IgG and IgA generated in the transformed cells. After three feedings of VP6 protein containing tuber tissues, ELISA measurements detected the presence of anti-VP6 antibodies in the serum but not in the intestinal contents (fecal pellets), of the orally immunized mice. The oral immunizations will be continued through 5 feedings to generate the highest titer of anti-VP6 antibodies which can be detected prior to sacrifice of the animals for final collection of serum for end point titration experiments.

In these immunogenicity experiments, no estimation of the contribution of cytotoxic lymphocytes to the immune response has been considered. Therefore, if time permits, spleen tissues will be excised from the immunized mice, the cells dissociated from the tissues and subjected to fluorescent cell counting of CD8+ and CD4+ lymphocytes to determine the relative distribution of the immune response between T helper and cytotoxic cell lymphocytes (CTL) in the immunized animals. This data will provide information on the likelihood of successful protection against rotavirus attack. Finally, protective efficacy (virus shed reduction) experiments will be performed in the fourth quarter on orally immunized animals to provide further information on the amount of rotavirus protein which must be synthesized in the plant to obtain detectable protection against rotavirus infection. Detection of IgA and IgG will provide an indication of T helper cell stimulation of antibody formation.

5. Vaccine Expression Vector 5: pPCV701-VP2 (D.C.)

The plant expression vector RB---<--P_1-*mas*-P_2->**VP2**---LB carries the core rotavrius capsid protein VP2. This vector was used to transform potato leaf explants.

WHAT IS CLAIMED IS:

1. A method for the production of a cholera toxin B subunit-rotavirus NSP4 enterotoxin fusion protein in a plant as disclosed herein.

ABSTRACT

A fusion gene encoding the cholera toxin B subunit (CTB) linked to the 22 amino acid neutralizing epitope (114-135) of the human rotavirus enterotoxin protein (NSP4) was inserted adjacent to the bi-directional mannopine synthase (*mas*) P_2 promoter in a plant expression vector which contains a LuxF reporter gene (a bacterial luciferase AB subunit fusion gene *fab2*) linked to the *mas* P_1 promoter. The CTB leader peptide encoding sequence was retained and an oligonucleotide sequence encoding a microsomal retention signal (SEKDEL) was added to the 3' end of the fusion gene to permit accumulation and pentamerization of the fusion gene product within the plant endoplasmic reticulum (ER). To permit flexibility between the CTB and NSP4 protein moieties, a CNA sequence encoding a tetrapeptide hinge was inserted between the CTB and NSP4 DNA sequences. Potato plants carrying the plant expression vector were generated by *Agrobacterium tumefaciens* mediated *in vivo* plant transformation . Immunoblot analysis of tuber tissues proteins from the transformed potato indicated that the molecular size of the CTB-NSP4 fusion protein was the predominant molecular species. The CTB-NSP4 fusion protein retained specific binding affinity for G_{M1} ganglioside, a cell surface receptor for CTB protein, and was synthesized in amounts up to 0.1% of total soluble potato protein. Pentameric CTB molecules linked to antigens synthesized in food plants may provide edible subunit mucosal vaccines for protection against infectious diseases.

Synthesis and Assembly of Cholera Holotoxin In Potato Plants

Daniel K.X. Chong[1] and William H.R. Langridge [1,2,*]

1. Center for Molecular Biology and Gene Therapy
2. Department of Biochemistry, Loma Linda University, Loma Linda, CA 92350

Telephone number: (909) 824-4300 Extension 81362

Fax number: (909) 478-4177

E-mail: blangridge@som.llu.edu

* To whom the correspondence should be addressed.

Keywords: cholera holotoxin assembly, edible vaccine, potato, transgenic plants

Abstract

DNA fragments encoding the cholera toxin (CTX) A subunit (CTA) and B subunit (CTB) were transferred into *Solanum tuberosum* leaf cells under control of the bi-directional mannopine synthase P1P2 promoters by *Agrobacterium tumefaciens*-mediated leaf disc transformation methods. The presence of both CTA and CTB genes in the transformed plant genome was confirmed by PCR methods. Recombinant CTA and CTB proteins were detected in transformed tuber tissue extracts by immunoblot analysis. Plant synthesized CTA migrated on SDS-PAGE gels identically to purified bacterial CTA. In contrast to bacterial CTA, plant synthesized CTA was resistant to thiol-reduction. The oligomeric form of recombinant CTB was detected on SDS-PAGE gels by immunoblotting. A large protein band with a molecular mass (MW ~ 80 kDa) equivalent to the sum of CTA and pentameric CTB molecules was detected in transformed plant tuber extracts by both anti-CTX and anti-CTA antibodies. In contrast to bacterial CTX, this protein complex was relatively stable in the presence of SDS. Similar to bacterial CTX, the 80 kDa oligomeric protein was not detected in the presence of β-mercaptoethanol. Taken together the estimated molecular mass of the ologomeric protein, the strong immunological reaction with both CTA and CTB specific antibodies, and disassociation of the ologomer in the presence of reducing agents strongly indicate that the 80 kDa protein synthesized in transformed potato cells is homologous to cholera holotoxin.

Introduction

The diarrhea causing cholera holotoxin (CTX) secreted by *Vibrio cholerae* is an extremely potent immunogen when administered orally. Further studies have demonstrated that CTX acts as a strong immunological adjuvant for co-administered antigens (Czerkinsky *et al.*, 1999; Holmgren, *et al.*, 1993). Based on its strong adjuvant effect, CTX has been used in mucosal vaccines against a variety of infectious agents (Williams *et al.*, 1999). However, the toxicity of CTX has until recently prevented its use for human vaccination.

To overcome this problem, recent work has focused on separating CTX toxicity from adjuvant activity (Holmgren *et al*, 1993). Cholera holotoxin is composed of a single A (CTA) subunit and five identical B (CTB) subunits. A single CTA subunit is located in the center of a doughnut-shaped pentameric ring formed by five identical CTB subunits. The CTA subunit can be readily nicked by exogenous proteases to yield two fragments, a globular toxic molecule CTA_1 (MW ~ 21 kD) and a helical stalk peptide CTA_2 (MW ~ 7 kD), linked via a single disulphide bond (Rappuoli *et al.*, 1999). A variety of mucosal vaccines have been generated by chemical conjugation or genetic fusion of protein antigens to the CTB subunit. These recombinant vaccines have proven to be effective in eliciting secretary IgA antibodies, which provide protection at mucosal surfaces by interfering with microbial adherence and colonization or invasion of intestinal epithelial cells (Dertzbaugh and Macrina, 1989; Dertzbaugh et al., 1990). Based on CTA_2 subunit insertion into the CTB pentamer ring structure to form a non-covalent association of CTA_1 with CTB, Hajishengallis and his colleagues were able to construct an effective vaccine against *Streptococcus mutants* by genetically fusing a streptococcal protein antigen to the n-terminus CTA2 subunit (Hajishengallis

et al., 1995). This result demonstrated for the first time that protein antigens could be genetically fused to the N-terminal of CTA_2 to form chimerical molecules with CTB to create novel toxoid immunogens capable of inducing a mucosal immune response.

During the last decade, genetically engineered plants have been used for production of protein antigens for use as edible vaccines for a variety of human diseases, such as Hepatitis B surface antigen (Mason et al., 1992; Thanavala *et al.*, 1995), heat labile enterotoxic *E. coli.* toxin B subunit (Haq *et al.*, 1995; Tacket *et al.*, 1998), rabies virus glycoprotein (McGarvey *et al.*, 1995; Modelska *et al.*, 1998) and Norwalk virus capsid protein (Mason *et al.*, 1996). In our laboratory, we were able to synthesize the non-toxic CTB subunit in potato plants (Arakawa *et al.*, 1997). The plant CTB subunits formed oligomers of pentameric size that were biochemically and immunologically similar to bacterial CTB. The plant synthesized CTB subunits also induced serum and intestinal CTB-specific antibodies in orally immunized mice (Arakawa *et al.*, 1998). Following intraileal injection with bacterial CTX, the plant-immunized mice showed approximately a 60% reduction in diarrheal fluid accumulation in the small intestine.

To take advantage of the adjuvant effects of the CTA subunit and the multicomponent vaccine construction dependent on genetic coupling of antigens to the CTA_2 subunit, both cholera CTA and CTB subunits must be synthesized in the same plant to ensure the opportunity for holotoxin assembly. Previous experiments have demonstrated that CTA and CTB can be synthesized in separate plants (Hein *et al.*, 1996). Through sexual crossing experiments, a certain percentage of F1 progeny might be expected to synthesize both CTA and CTB in the same plant leading to holotoxin assembly. However, progeny demonstrating synthesis of both subunits and assembly of the holotoxin in the same plant have not been yet reported. In the following experiments, we have used the mannopine synthase (*mas*) dual promoters (P1P2), to express both CTA and CTB subunits in the same potato plant. Further, we report for the first time successful assembly of the CTA and CTB subunits into a CTX holotoxin like molecule.

Materials and Methods

*Construction of plant expression vector pPCV701CTAB encoding CTA and CTB subunits.*DNA fragments encoding CTA and CTB were inserted into the plant expression vector pPCV701 under control of the *Agrobacterium tumefaciens* mannopine synthase (*mas*) P1P2 dual promoters. A DNA fragment encoding the CTA gene was amplified by the polymerase chain reaction method from the plasmid pRT42 kindly provided to us by Dr. John Mekalanos, Harvard Medical School. The 793 bp CTA fragment was amplified using primer CTA-SAL5: (5'- CDC CDA ACC ATG GTA AAG ATA TTT-3') and CTA-SAL3: (5'- CGC CGT GAC TCA TAA TTC ATC CTT AAT TCT-3'). A *Sal* I restriction enzyme site was incorporated into both primers for simplification of cloning. The CTA fragment was inserted into the *Sal* I site downstream of the *mas* P1 promoter in vector pPCV701FM4-CTB:SEKDEL replacing the bacterial luciferase fusion gene (Arakawa *et al.*, 1997). A DNA fragment containing the CTB gene was excised from plasmid pPCV701FM4CTB (Arakawa *et al.*, 1997), and inserted immediately downstream of the *mas* P2

promoter in plasmid pPCV701. DNA sequences encoding a flexible glycine - proline hinge tetrapeptide (GPGP) and a microsomal retention signal (SEKDEL) were fused sequentially at the 3'-end of the CTB gene (Arakawa *et al.*, 1997). The resultant plasmid was named pPCV701CTAB (Figure 1). Plant expression vector pPCV701CTAB also contains the β-lactamase gene conferring ampicillin resistance in *E. coli* and carbenicillin resistance in *A. tumefaciens*. In addition, the neomycin phosphotransferase II gene (NPT II) linked to the nopaline synthase (NOS) promoter provides antibiotic selection for transformed plant cells.

Plant transformation. *In vivo* mediated plant cell transformation with *Agrobacterium tumefaciens* was performed as described by Chong *et al.* (1997). Sterile leaf explants of *S. tuberosum* cv. Bintje were infected by *A. tumefaciens* strain GV3010 MP90RK harboring plasmid pPCV701CTAB. Plant cell transformation was carried out by incubating leaf explants in approximately 1 x 10^9 *Agrobacterium tumefaciens* cells in log stage of growth per ml of Murashige and Skoog (MS) medium for 10 minutes at room temperature. The explants were transferred onto solid MS medium containing naphthalene acetic acid (NAA, 1 mg/L) and 0.2 % gelrite for 2 to 3 days to achieve T-DNA transfer into the plant genome. The leaf explants were then placed on callus growth medium containing plant growth hormones and antibiotics, (0.1 mg/L NAA and 1.0 mg/L trans zeatin, 50 mg/L kanamycin and 300 mg/L claforan). The explants were incubated in a light room at 27 °C with an illumination intensity of approximately 12 mE and a 12 h photoperiod for 2-3 weeks to generate callus tissue. Leaf explants containing friable callus tissues were transferred to callus growth medium minus NAA for an additional 2-3 weeks to facilitate shoot regeneration. Regenerated shoots were rooted in the callus medium without plant growth hormones. Roots regenerated from the shoots after 2-3 weeks incubation and the small plantlets were transferred to polycarbonate "Magenta" boxes for tuberization, or alternatively to sterile soil for growth to maturity in the greenhouse (3 mo).

Detection of the CTA and CTB genes in transformed plant genome. The CTA and CTB genes were detected in the genomic DNA of the putative transgenic plants using a polymerase chain reaction method with sets of primers flanking each gene as described by Chong et al. (1997). The DNA primers were designed to amplify DNA inserts placed under the control of the *mas* P1 and P2 promoters. The 5' forward primers are located upstream of the *mas* P2 promoter for amplification of the CTB gene and upstream of the *mas* P1 promoter for amplification of the CTA gene. The 3' reverse primers are located within the polyadenylation region of the T_L DNA gene 7 sequence poly A site (g7pA) for amplification of the CTB gene and the octopine synthase gene polyadenylation signal (OcspA) for amplification of the CTA gene (Figure 1). Plant genomic DNA was isolated from both leaf and tuber tissues of transgenic potato plants using a plant DNA isolation kit (Boehringer-Mannheim Cat # 1667-319).

Immunoblot detection of CTA and CTB protein in transformed potato tissue. Prior to analysis, microtuber tissue slices from transgenic potato plants were wounded by cutting into approximately 2 mm thick sections with a sterile razor blade. The tuber sections were incubated for 3 days on solid culture medium containing 3 mg/L NAA and 5 mg/L 2,4-D to activate the *mas*

promoters. Total soluble protein was extracted from transformed potato tuber tissues by homogenization with a mortar and pestle on ice at 4 °C in an extraction buffer containing 50 mM Tris-HCl (pH 7.5), 2 mM EDTA, 0.5 mM EGTA, 1 mM PMSF and 1% Triton X-100. The homogenates were centrifuged in a Beckman GS-15R tabletop centrifuge at 14,000 rpm for 10 min at 4 °C. The soluble protein concentration in the homogenate supernatant was determined (Bradford, 1976). Samples containing approximately 100 μg total tuber protein were boiled for 5 min and loaded into the wells of a 10% polyacrylamide gel. The protein bands were separated by polyacrylamide gel electrophoresis,**(voltage, time?)** and transferred onto a nitrocellulose membrane by electroblotting **(voltage, time?)** with a semi-dry blotter (Labconco Inc.). The damp membrane was blocked with 1% BSA and 20% fetal calf serum in TBST buffer (10 mM Tris-HCl pH 8.0, 150 mM NaCl and 0.05% Tween 20) for at least 1 hour at room temperature. The blocked membrane was incubated for 3 hours to overnight in TBST solution containing a 1:1000 dilution of either commercially available rabbit anti-Cholera holotoxin antibody (Sigma) or a goat anti-CTA polyclonal antibody provided by provided by Dr. Richard A. Finkelstein, University of Missouri. The anti-cholera primary antibody/recombinant Cholera protein antigen complex was reacted with a secondary antibody by incubating the membrane in a 1:3000 TBST dilution of an anti-rabbit or anti-goat IgG alkaline phosphatase conjugate (BioRad Inc). The recombinant protein was visualized by a colorimetric reaction in which the membrane was incubated in a BCIP/NBT (5-bromo-4-chloro-3indolyl phosphate/nitro blue tetrazolium) substrate solution for 10-30 min at room temperature prior to photography of the purple reaction product.

Results and Discussion

Detection of CTA and CTB genes in transgenic potato plants. After transformation of potato leaf explants with expression vector pPCV701CTAB, three independent kanamycin-resistant plants were regenerated although more shoots were generated from callus tissue. The presence of CTA and CTB genes in the genomic DNA isolated from all three-regenerated potato transformants was detected by PCR amplification of inserts with 5' and 3' flanking primers. The separation pattern of the PCR products amplified from the transgenic plant genome is shown in Figure 2. The expected PCR products included a 892 bp DNA fragment for the CTA gene and a 408 bp DNA fragment for the CTB gene. The CTB gene fragment was amplified from a transgenic plant (Fig 2, lane 3) and from the positive control vector plasmid DNA (Fig 2, lane 1). No DNA band was detected in untransformed plant genomic DNA lane (Fig 2, lane 2). Similar DNA amplification and separation patterns were observed for CTA gene fragments (Fig 2, lane 5-7).

Expression of cholera toxin genes and assembly of cholera holotoxin in transgenic plants. Both CTA, CTB and multimeric CTA-CTB structures were detected in transformed tuber extracts by SDS polyacrylamide gel electrophoresis using a commercially available anti-CTX rabbit polyclonal antibody (Sigma) and an anti-CTA goat polyclonal antibody provided by Dr. Richard A.

Finkelstein, University of Missouri. Transgenic plant homogenates contained two protein bands of a molecular mass of ~ 80 kDa and ~55 kDa, which reacted with anti-CTX rabbit polyclonal antibody on SDS-PAGE gels under non-reducing (minus b-mercaptoethanol) conditions (Figure 3A, lane 5). However, when the anti-CTA antibody was used, an extra band with a lower molecular mass of ~ 28 kDa was detected (Figure 3B, lane 5). Cell extracts from untransformed potato plants showed no immunologically reactive protein bands with either antibody (lane 4 in Figures 3A and 3B).

Synthesis of the CTA protein in transgenic tuber tissues was demonstrated by immunoblot experiments using anti-CTA goat polyclonal antibody. In addition to the two protein bands detected by the anti-CTX antibody, transformed plants contained a protein band of approximately 28 kDa detected by SDS-PAGE (Figure 3B, lane 5). This band migrated with a mobility identical to the CTA band detected from *Vibrio cholerae* (Figure 3B, lane 1) under non-reducing conditions. The CTA subunit of bacterial cholera toxin, although synthesized as a single polypeptide chain, is usually 'nicked' between its two-cysteine residues by bacterial protease(s) (Holmgren, 1981). Thus,when treated with thiol-reducing agents with or without boiling, the CTA peptide chain of *V. cholerae* CTX splits into two peptide fragments A_1 (MW ~ 21 kd), and A_2 (MW~7 kd) (Figure 3B, lanes 2 and 3). In this experiment, the small CTA_2 fragment runs off the 10% SDS-PAGE gel during electorphoresis. However, the plant synthesized CTA showed no evidence of further processing into CTA_1 and CTA_2 peptides, as reduction with b-mercaptoethanol did not result in an altered migration pattern on SDS-PAGE gels (Figure 3B, lanes 6 and 7). Resistance of CTA to thiol-reduction was also observed when the CTA gene was expressed in tobacco plant cells (Hein *et al.*, 1996). The observed resistance of plant-synthesized CTA peptide to thiol-reduction might be due to the absence of bacterial proteases capable of nicking the CTA single polypeptide chain. In 1996, Hein and his colleagues found that heating transgenic plant extracts in the presence of β-mercaptoethanol resulted in a significant loss of both plant synthesized and exogenous, added CTA. However, upon heating transformed plant homogenates we observed no significant loss of CTA. Boiling transformed plant homogenates had no effect on the separation of CTA subunits (Figure 3B, lane 7). Due to the relatively low level of tuber cholera toxin protein gene expression, plant synthesized CTA was undetectable with less sensitive commercially available rabbit polyclonal anti-CTX antibodies (Fig. 3A,lanes 5-7).

Synthesis of CTB and formation of putative pentameric structures was confirmed by SDS-PAGE with both anti-CTX and anti-CTA antibodies. Previously, our laboratory demonstrated that potato plants stably transformed with the CTB gene not only synthesized CTB protein monomers but also assembled them into a multimeric structure capable of binding GM_1 ganglioside, a characteristic specific to CTB pentamers only (Arakawa *et al.*, 1997). In the present study, the same CTB gene-containing cassette was used in the construction of pPCV701CTAB. A protein band (Figure 3A, lane 5) with a molecular mass higher than the bacterial CTB pentamer (Figure 3A, lane 1) was obtained. This band was equal in size (~55 kDa) to our previously reported plant synthesized CTB pentamer. The increased molecular mass of this peptide is likely due to the presence of the hexapeptide ER retention signal, or possibly to the failure of plant cells to remove the leader peptide

during processing in the ER (Arakawa *et al.*, 1997). Similar to the bacterial CTB pentamer the plant synthesized CTB pentamer was resistant to thiol-reduction (Figure 3A, lanes 2 and 6). Boiling for 5 minutes disassociated the multimeric structure of both bacterial and plant CTB pentamers (Figure 3A, lanes 3 and 7). Heating also resulted in a significant loss of bacterial CTB monomer both in amount and in immunological reactivity, as the anti-CTX antibody failed to detect the CTB monomer from either boiled bacterial or plant samples (Figure 3A, lanes 3 and 7). Heavy loading (300 μg per lane), combined with increased antibody concentration (1:500) permitted detection of the monomeric form of CTB from boiled transformed tuber extracts (data not shown).

Assembly of cholera holotoxin-like structures in transformed plant cells was indicated by the protein band separation patterns detected on immunoblots with both anti-CTX and anti-CTA antibodies. The bacterial cholera holotoxin structure was unstable in the presence of SDS and did not appear on SDS-PAGE gels detected with the anti-CTX antibody (Figure 3A, lane 1). However, in addition to the CTA and oligomeric CTB products, transformed potato plant homogenates contain an additional large protein with a molecular weight above 80 kDa which is equivalent to the sum of the plant synthesized pentamer and the CTA peptide (lane 5 in Figures 3A and B). This protein was detected by SDS-PAGE under non-reducing conditions with both anti-CTX and anti-CTA antibodies. Bacterial CTX separated into pentameric CTB and CTA components upon thiol-reduction (Figure 3A, lane 2). Similarly, when transformed tuber homogenates were treated with β-mercaptoethanol prior to electrophoresis, the 80 kDa protein was no longer detectable with either anti-CTX or anti-CTA antibodies (lane 6 in Figures 3A and 3B). Based on its estimated molecular weight, its thiol-reducing capability, and its strong immunological reaction with both CTA and CTB specific antibodies, it is likely that the 80 kDa protein structure represents assembled cholera holotoxin in transformed plant cells.

The demonstration that a genetically altered CTX holotoxin including a foreign antigen linked to the CTA_2 subunit can be synthesized and assembled in *E. coli* (Hajishengallis *et al.*, 1995) raises the possibility for synthesis and assembly of CTX in eukaryotic cells. For CTX assembly to occur in plants, not only must the plant cell be able to express both CTA and CTB subunit proteins but the plant must also possess the machinery for their assembly into a holotoxin-like structure. In this study, we have demonstrated that potato plants stably transformed with both CTA and CTB subunit encoding genes successfully synthesize both subunits and assemble them into a holotoxin-like structure. Our transformed potato plants synthesizing the putative cholera holotoxin demonstrated no unusual morphological features and grew at a normal rate displaying no apparent toxic effects.

Acknowledgements:

We would like to thank Dr. John Mekalanos, Harvard University School of Medicine, for the gift of the CTX gene and Dr. Richard Finkelstein, University of Missouri, Department of Microbiology, for providing us with the cholera holotoxin protein and antiserum against the cholera toxin CTA subunit. This work was supported by a subcontract to WL by the National Medical Technology Testbed Inc., and in part by an intramural grant to WL by Loma Linda University

References

Arakawa,T., Chong,D.K., and Langridge,W.H. (1998) Efficacy of a food plant-based oral cholera toxin B subunit vaccine *Nat.Biotechnol.* **16**: 292-297.

Arakawa,T., Chong,D.K., Merritt,J.L., and Langridge,W.H. (1997) Expression of cholera toxin B subunit oligomers in transgenic potato plants *Transgenic.Res.* **6**: 403-413.

Bradford,M.M. (1976) A rapid and sensitive method for the quantitation of microgram quantities of protein utilizing the principle of protein-dye binding *Anal.Biochem.* **72**: 248-254.

Chong,D.K., Roberts,W., Arakawa,T., Illes,K., Bagi,G., Slattery,C.W., and Langridge,W.H. (1997) Expression of the human milk protein beta-casein in transgenic potato plants *Transgenic.Res.* **6**: 289-296.

Czerkinsky,C., Anjuere,F., McGhee,J.R., George-Chandy,A., Holmgren,J., Kieny,M.P., Fujiyashi,K., Mestecky,J.F., Pierrefite-Carle,V., Rask,C., and Sun,J.B. (1999) Mucosal immunity and tolerance: relevance to vaccine development *Immunol.Rev.* **170**: 197-222.

Dertzbaugh,M.T., Macrina,F.L. (1989) Plasmid vectors for constructing translational fusions to the B subunit of cholera toxin *Gene* **82**: 335-342.

Dertzbaugh,M.T., Peterson,D.L., and Macrina,F.L. (1990) Cholera toxin B-subunit gene fusion: structural and functional analysis of the chimeric protein *Infect.Immun.* **58**: 70-79.

Hajishengallis,G., Hollingshead,S.K., Koga,T., and Russell,M.W. (1995) Mucosal immunization with a bacterial protein antigen genetically coupled to cholera toxin A2/B subunits *J.Immunol.* **154**: 4322-4332.

Haq,T.A., Mason,H.S., Clements,J.D., and Arntzen,C.J. (1995) Oral immunization with a recombinant bacterial antigen produced in transgenic plants [see comments] *Science* **268**: 714-716.

Hein,M.B., Yeo,T.C., Wang,F., and Sturtevant,A. (1996) Expression of cholera toxin subunits in plants *Ann.N.Y.Acad.Sci.* **792**: 50-56.

Holmgren,J., Lycke,N., and Czerkinsky,C. (1993) Cholera toxin and cholera B subunit as oral-mucosal adjuvant and antigen vector systems *Vaccine* **11**: 1179-1184.

Mason,H.S., Ball,J.M., Shi,J.J., Jiang,X., Estes,M.K., and Arntzen,C.J. (1996) Expression of Norwalk virus capsid protein in transgenic tobacco and potato and its oral immunogenicity in mice *Proc.Natl.Acad.Sci.U.S.A* **93**: 5335-5340.

Mason,H.S., Lam,D.M., and Arntzen,C.J. (1992) Expression of hepatitis B surface antigen in transgenic plants *Proc.Natl.Acad.Sci.U.S.A* **89**: 11745-11749.

McGarvey,P.B., Hammond,J., Dienelt,M.M., Hooper,D.C., Fu,Z.F., Dietzschold,B., Koprowski,H., and Michaels,F.H. (1995) Expression of the rabies virus glycoprotein in transgenic tomatoes *Biotechnology (N.Y.)* **13**: 1484-1487.

Modelska,A., Dietzschold,B., Sleysh,N., Fu,Z.F., Steplewski,K., Hooper,D.C., Koprowski,H., and Yusibov,V. (1998) Immunization against rabies with plant-derived antigen *Proc.Natl.Acad.Sci.U.S.A* **95**: 2481-2485.

Rappuoli,R., Pizza,M., Douce,G., and Dougan,G. (1999) Structure and mucosal adjuvanticity of cholera and Escherichia coli heat-labile enterotoxins *Immunol.Today* **20**: 493-500.

Tacket,C.O., Mason,H.S., Losonsky,G., Clements,J.D., Levine,M.M., and Arntzen,C.J.

(1998) Immunogenicity in humans of a recombinant bacterial antigen delivered in a transgenic potato *Nat.Med.* **4**: 607-609.

Thanavala,Y., Yang,Y.F., Lyons,P., Mason,H.S., and Arntzen,C. (1995) Immunogenicity of transgenic plant-derived hepatitis B surface antigen *Proc.Natl.Acad.Sci.U.S.A* **92**: 3358-3361.

Williams,N.A., Hirst,T.R., and Nashar,T.O. (1999) Immune modulation by the cholera-like enterotoxins: from adjuvant to therapeutic *Immunol.Today* **20**: 95-101.

Figure Legends

Figure 1. Linear map of the plant expression vector pPCV701CTAB. This vector carries the *Agrobacterium tumefaciens* left and right 25 bp direct repeats (LB and RB) of the transferred DNA (T-DNA) bordering the DNA fragment which will be incorporated into the potato genome. The CTB gene was placed immediately downstream of the *mas* P2 promoter and is followed by the polyadenylation sequence of T_L-DNA gene 7 (g7pA). The CTA gene DNA fragment was placed under control of the *mas* P1 promoter and is followed immediately by the polyadenylation signal of the octopine synthase gene (ocspA). Arrows indicate the direction of transcription. NPTII, is the neomycin phosphotransferase gene from transposon Tn5 used for kanamycin selection of transformed plants. Bla, is the β-lactamase gene conferring resistance to ampicillin for selection in *E. coli*.

Figure 2. PCR detection of the bacterial CTA and CTB genes in transgenic potato plants. The predicted PCR DNA fragment for CTA is 892 bp and 408 bp for CTB containing the entire gene and two flanking primers. Lanes 1 (CTB) and 5 (CTA) are the PCR products amplified from plasmid pPCV701CTAB. Lanes 2 and 6 are the PCR products from untransformed potato leaf tissues. Lanes 3 (CTB) and 7 (CTA) are the PCR products amplified from transgenic potato **(tuber tissues?)** and lane 4 is the sample containing **water?**. Lane M is the DNA molecular weight marker ladder.**(Where is Lane M?)**

Figure 3. Immunodetection of CTA, CTB and putative CTX protein in transformed potato **tuber?** tissue homogenates. Total soluble protein from potato tuber extracts (100 μg /lane), were fractionated by SDS-PAGE and the bands transferred to a nitrocellulose membrane. The membrane was probed with rabbit anti-CTX primary antibodies (panel A) or goat anti-CTA primary antibodies (panel B), followed by an alkaline phosphatase conjugated secondary antibody. Protein samples in lanes 5 – 7 on panels A and B are from transformed tissue homogenates. Untransformed potato tuber homogenates are located in lane 4 on panel A and B. Lanes 1 – 3 in panel A contain purified bacterial CTX protein (Sigma) and lanes 1 –3 in panel B contain purified bacterial CTA protein. The tissue samples were prepared under three different conditions (1), non-reducing conditions in the absence of β-mercaptoethanol; (2), reducing conditions with β-mercaptoethanol **(how much?- Perhaps you say somewhere else?)**, and (3), boiling in the presence of β-mercaptoethanol **(how**

much?). Samples in lanes 1 and 5 in panels A and B contain no β-mercaptoethanol, while samples in lanes 2 and 6 contain β-mercaptoethanol in the sample buffer. Samples boiled 5 minutes in the presence of β-mercaptoethanol are located in lanes 3 and 7 on panels A and B.

Figure 1

pPCV701CTAB 11.00 kb

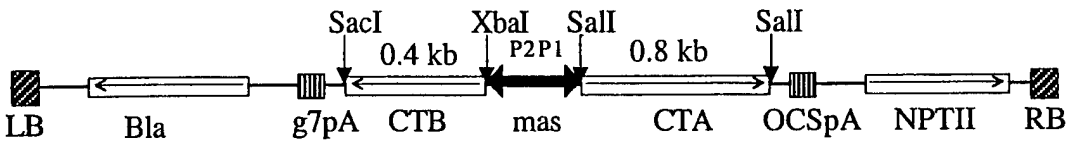

Figure 2.

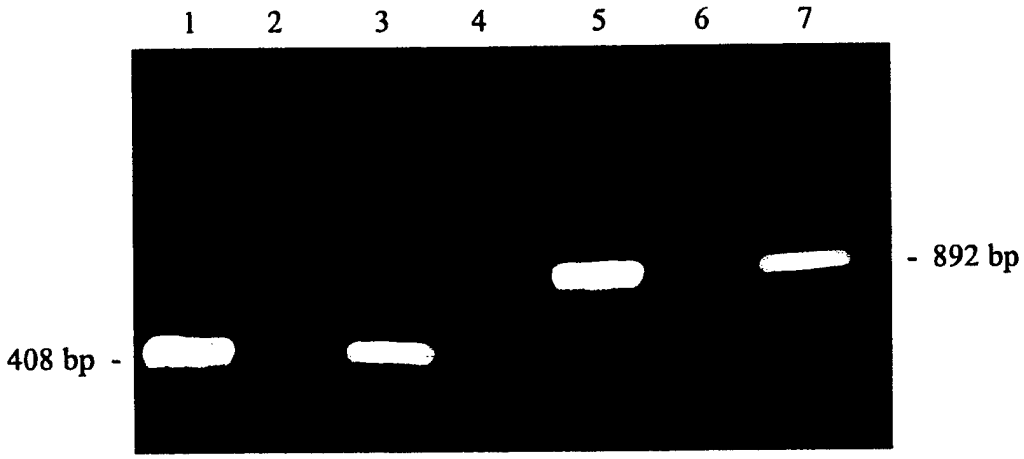

Figure 3

A

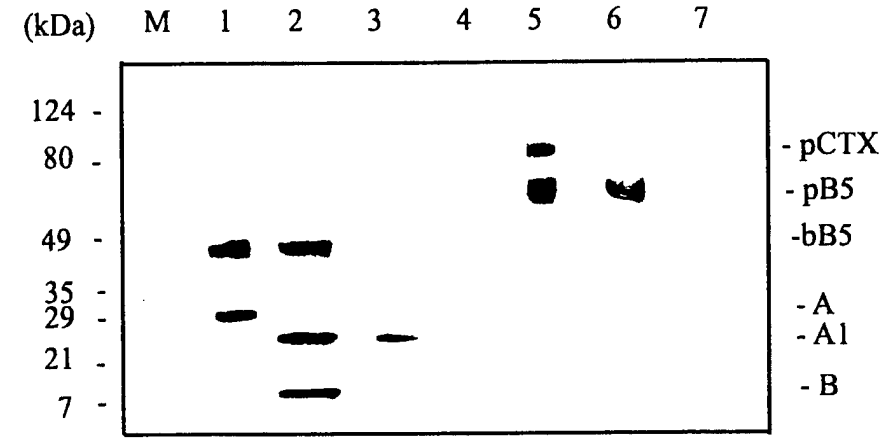
(kDa)
M
1
2
3
4
5
6
7
124
80
49
35
29
21
7
- pCTX
- pB5
-bB5
- A
- A1
- B

B

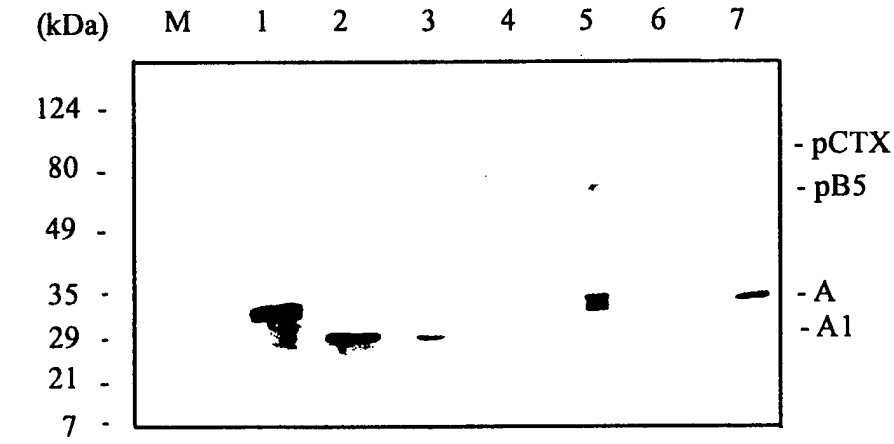
(kDa)
M
1
2
3
4
5
6
7
124
80
49
35
29
21
7
- pCTX
- pB5
- A
- A1

Assembly of Cholera Toxin-Antigen Fusion Proteins in Potato

Jie Yu, [1,2] Takeshi, Arakawa[2] and William H.R. Langridge [1,2]

Department of Biochemistry[1] and Center for Molecular Biology and Gene Therapy[2], Loma Linda University, Loma Linda CA, 92350.

Abstract

Solanum tuberosum cv. Bintje leaf explants were transformed with a plant expression vector containing the mannopine synthase (*mas*) dual P1,P2 promoters in which a cholera toxin B subunit – rotavirus enterotoxin epitope gene fusion (CTB-NSP4) was linked to the P2 promoter and an enterotoxigenic *E.coli* fimbrial antigen – cholera toxin A2 subunit fusion (CFA/I-CTA2), was linked to the P1 promoter. Following transformation and regeneration of transformed plants, the cholera toxin fusion proteins were detected in transformed potato leaf and tuber tissues by immunoblot assay and quantitated by enzyme linked immunosorbent assay (ELISA) methods. The CTB-NSP4 protein expression level was found to be approximately 0.01% of total soluble tuber protein. Assembly of the CFA/I-CTA2 subunit fusion peptide monomer into the CTB-NSP4 fusion pentamer was detected by immunoblot staining methods. The CFA/I-CTA2-CTB-NSP4 pentameric fusion protein complex retained an affinity for binding GM1 ganglioside enterocyte membrane receptor molecules. The experimental results demonstrate that cholera toxin fusion proteins can be synthesized in edible plants. and assemble into cholera holotoxin like molecules. The results demonstrate for the first time that plant synthesized cholera toxin A and B subunit fusion proteins can interact in a coordinated fashion in a plant to generate a carrier complex for targeted delivery of multiple pathogen antigens to the mucosal immune system.

Introduction

Cholera, rotavirus and ETEC are the three major causes of acute gastroenteritis worldwide (Jawez et al., 1989). Vaccination and eventually eradication of these endemic diseases depends on the development of inexpensive oral vaccines accessible to the developing world. Recombinant DNA technology has now made it possible to express foreign antigens in plants for creating food plant based vaccines. Recent examples are the expression of hepatitis B surface antigens in potatoes and tobacco, heat sensitive enterotoxin (LTB), expression in potatoes, and Norwalk virus capsid protein biosynthesis in both tobacco and potatoes. However, oral immunization requires a relatively large dose of antigen to stimulate an efficient immune response due to acid digestion of the antigen in the stomach, intestinal digestion of the antigen by proteolytic enzymes and dilution of

of antigen to stimulate an efficient immune response due to acid digestion of the antigen in the stomach, intestinal digestion of the antigen by proteolytic enzymes and dilution of the antigen by food and mucosal secretions. The generally low expression levels of foreign proteins in plants has limited the practical application of transgenic plants as production and delivery vehicles for oral vaccines. One attractive solution to the necessity for antigen overproduction in plants is the development of carrier molecules, which can target fusion antigens to the mucosal immune system. Cholera toxin is known to be such a carrier molecule possessing strong immunogenicity as well as adjuvant activity **(REFERENCES)**. The cholera holotoxin is made of 5 copies of the CTB subunit and one copy of the CTA subunit. The CTB subunits assemble to form pentameric multimers which can bind to the GM1 ganglioside receptors embedded in the surface of intestinal epithelial cells and especially in M cells. Following translation, the CTA subunit is postranslationally cleaved into a CTA1 and a A2 subunit. The small 6.3 kDa helical CTA2 subunit is inserted into the central core of the CTB pentamer and becomes linked to the CTA1 subunit by hydrogen and disulfide bonds. Chemically or genetically fusing small molecules to the CTB subunit was found to stimulate antibody production against both antigens (Dertzbaugh and Elson, 1993). Alternatively, replacement of CTA1 with streptococcal adhesion protein was also found to stimulate a mucosal immune response against the fusion protein. Here we report the expression of a double fusion protein in potato plants: a twenty amino acid epitope of rotavirus nonstructural enterotoxin protein NSP4 fused to the CTB subunit, and the ETEC fimbrial colonization factor CFA/I linked to the CTA2 subunit and the assembly in the plant of the two fusion proteins into a cholera holotoxin like structure.

Materials and Methods

Construction of plant expression vectors. In the first plant expression vector construct, the CTB gene including its leader peptide was PCR amplified from the ctxAB operon in plasmid pPT42(provided by J. Mekalanos, Harvard Medical School). The 3' primer was designed to contain an oligonucleotide encoding the endoplasmic reticulum (ER)-retention signal in frame downstream from the CTB gene. The amplified DNA fragment encoding the CTB:SEKDEL fusion gene was inserted into the plant expression vector pPCV701 under control of the P2 mannopine synthase(*mas*) promoter. The plant expression vector was designated pPCV701-CTB. In a second construction, the CTB gene and its leader peptide was obtained by PCR amplification from the same ctxAB operon. The 3' primer was designed to contain a nucleotide sequence encoding the tetrapeptide hinge(Gly-Pro-Gly-Pro) to increase the flexibility of the conjugated protein. The CTB:hinge sequence was inserted into plant transformation vector pPCV701under control of the *mas* P2 promoter. The plant expression vector was designated pPCV701 CTBh. A double stranded DNA fragment encoding the rotavirus enterotoxin NSP4 (114-135) epitope was synthesized (model 394 DNA/RNA Synthesizer Applied Biosystems, Inc.), in our laboratory at Loma Linda University. The 3'end of the NSP4 DNA fragment contains the endoplasmic reticulum (ER) retention signal, SEKDEL. The NSP4:SEKDEL sequence was cloned into vector pPCV701CTBh, immediately downstream of the CTB: hinge sequence to create the fusion gene CTB:hinge-NSP4: SEKDEL. The plant

expression vector was designated pPCV701CTB-NSP4. In the third expression vector construct, The CTA leader sequence and CTA2 gene, which has its own KDEL signal sequence was amplified by PCR from the ctxAB operon, and inserted into the vector pPCV701 CTB-NSP4 under control of the *mas* P1 promoter. A DNA fragment encoding the ETEC colonization factor CFA/I was amplified from plasmid pIGx15A(provided by Dr. M. Levine, University of Maryland), and was inserted in frame between the CTA leader sequence and the CTA2 gene. The resultant plant expression vector was designated pPCV701 CFA-CT-NSP4 and contains the CTA2-CFA/I fusion gene driven by the *mas* P1 promoter and CTBh-NSP4 fusion gene driven by the *mas* P2 promoter. The plant expression vectors pPCV701-CTB, pPCV701CTB-NSP4 and pPCV701 CFA-CT-NSP4 were introduced into *Agrobacterium tumefaciens* strain GV3101 pMP90RK by electroporation **(REF)**. Potato leaf discs were transformed with agrobacteria harboring the plant expression vectors and transgenic potato plants were regenerated as described **(REF)**.

Analysis of DNA/RNA from transformed potato. Plant genomic DNA was isolated from transformed potato leaf tissues using DNeasy Plant Mini Kit (Qiagen Inc). Presence of the CTB, NSP4 and CFA/I genes were determined by PCR analysis using transformed plant genomic DNA(500ng) as a template and primers specific for each gene. The PCR products were separated by electrophoresis on a 1% agarose gel and stained with ethidium bromide. Total RNA from leaves of transformed plants was isolated using Rneasy Plant Mini kit (Qiagen Inc.). The presence of CFA/I mRNA was determined by RT-PCR analysis following the instructions from Omniscript Reverse Transcriptase kit (Qiagen Inc.). The RT-PCR samples were separated by electrophoresis on a 1% agarose gel and stained with ethidium bromide.

Immunoblot analysis of protein from transformed potato. Approximately 1g of leaf tissue was homogenized on ice in 1ml of extraction buffer (200mM Tris-HCL, pH 8.0, 100 mMNaCl, 400mM sucrose, 10 mM EDTA, 14 mM 2-mercaptoethanol, 1mM phenyl-methylsulfonyl fluoride, 0.05% Tween-20). The tissue homogenates were centrifuged twice at 17,000 G for 15min at 4^0 C to remove insoluble debris. A 10-20 aliquot of supernatant fluid containing 100-200 ug of total soluble protein, as determined by protein assay (Bio-Rad Inc.), was analyzed by 12% SDS-PAGE. Plant homogenate samples were either boiled 5 min prior to electrophoresis or loaded directly on the gel. The expression of CTB, NSP4 and CFA/I protein were detected by rabbit anti CTB antiserum (Sigma1:5000 dilution), rabbit anti NSP4(114-135) antiserum (provided by M. Estes, Balyor College of Medicine, at 1:1000 dilution) and rabbit anti CFA/I antiserum (1:1000 dilution). The second antibody was an alkaline phosphatase-conjugated mouse antirabbit IgG (Sigma,1:10,000 dilution).

Quantification of CTB-NSP4, CFA-CTA2 proteins' levels in transformed potato. The amount of plant-synthesized CTB-NSP4 fusion protein was measured by chemiluminescent GM1 ELISA assay (Arakawa et al., 1997). Briefly, the wells of a 96-well microtiter plate (Dynatech Laboratories) were coated with 100ul/well of monosialoganglioside GM1 (3.0ug/ml) (Sigma) in pH9.6 bicarbonate buffer (15mM Na2CO3, 35mM NaHCO3), and incubated at 4^0 C overnight. The plate was washed three

times with PBST (phosphate buffered saline (PBS) containing 0.05% Tween-20). The background was blocked by incubation in 1% bovine serum albumin (BSA) in PBS (300ul/well) at 37^0 C for 2h followed by washing three times with PBST. The microtiter plate was incubated with 2ug of transformed plant total soluble protein per well in PBS (100ul/well). Alternatively, a known amount of bacterial CTB (Sigma) plus 2ug untransformed plant total soluble protein in PBS (100ul/well) was added to the plate and incubated overnight at 4^0 C. The plate was washed three times with TBST and then incubated in a 1:8000 dilution of rabbit anti-cholera toxin antibody (Sigma, 100ul/well) for 2h at 37^0 C, followed by washing three times with PBST. The plate was incubated with a 1:80,000 dilution of anti-rabbit IgG alkaline phosphatase conjugate (Sigma, 100ul/well) for 2h at 37^0 C and washed three times with PBST. The plate was finally incubated with 100ul/well Lumi-Phos Plus substrate (Lumigen) for 30 min at 37^0 C. The plate was cooled for 5 min and measured in a Dynatech 3000 Microtiter Plate Luminometer (Dynatech Laboratories). The amount of plant-synthesized CFA-CTA2 fusion protein in each well was measured by the same chemiluminescent ELISA assay, except that 2ug of transformed plant total soluble protein was directly coated to the plate in pH9.6 bicarbonate buffer and the first antibody used was rabbit anti-CFA/I in 1:3000 dilution. The rest of the assay procedure was identical to the ELISA assay described above.

Detection of CFA-CTA2 and CTB-NSP4 assembly in plant tissues. The folding of CFA-CTA2 subunit with the CTB-NSP4 pentamer in transformed plant tissues was detected by a chemiluminescent GM1 ELISA assay procedure. The analysis procedures were the same as the GM1 ELISA for quantification of CTB-NSP4 fusion protein except that the first antibody used was rabbit anti-CFA/I in a 1:3000 dilution.

Results and Discussion

Construction of plant expression vectors. The plant expression vector pPCV701 CFA-CT-NSP4 (Figure 1)was generated by inserting the CTB-NSP4 gene behind the *mas* P2 promoter and inserting the CFA/I-CTA2 gene behind the *mas* P1 promoter. The *mas* promoter is a bidirectional promoter capable of driving the expression of two genes in opposite directions in plants at the same time. A hinge region (GPGP), was added between CTB and NSP4 epitope to provide increased flexibility of the fusion peptide. The CTA2 gene was fused to the 5' end of the CFA/I gene as a linker to facilitate the association of CFA/I-CTA2 peptide with CTB pentamer structure.**(The Description is confusing, show the structure of the construct in diagram)** Each fusion gene has its bacterial leader sequence and an ER retention signal. As controls, plant expression vectors contain CTB or CTB-NSP4 gene under the mas P2 promoter were included. *Agrobacterium tumifaciens* meditated stable transformation of potato leaf tissues generated fifteen kanamycin resistant transgenic potato plants.

DNA/RNA analysis of transformed plants. The transformed potato plants were analyzed by PCR for the presence of the CTB-NSP4 gene and the CFA/I-CTA2 gene (Figure 2). A 560bp DNA fragment which included both the CTB and the NSP4 sequence was amplified from transformed potato genomic DNA. Nonspecific

amplification was not observed in untransformed plant samples, indicating the high specificity of annealing of the 5' CTB primer and the 3' NSP4 primer. Using primers including 5' flanking sequence of CFA/I gene and 3' flanking sequence of CTA2 gene, we detected a specific amplification of a 590bp DNA fragment, which is the correct size for the CFA/I-CTA2 gene. Because the P1 promoter is 5 to 10 times weaker than P2 promoter, we chose to study the mRNA transcription of CFA/I gene at the P1 side of the *mas* promoter. Both 5' and 3' CFA/I primers were used in the RT-PCR assay. A 430bp mRNA fragment was detected, which is the exact size of CFA/I cDNA. Samples without the addition of reverse transcriptase showed no band, which indicated that no DNA contamination was present in the total RNA sample preparation.

Detection of foreign proteins in transformed plants. The presence of the CTB gene product was identified by immunoblot analysis using antiserum against cholera toxin (Figure 3A). Bacterial CTB formed 45kD pentamer structure, partially dissociated into 11kD monomers. Gel electrophoretic separation results indicated that the plant derived CTB pentamers had a higher molecular weight than the bacterial CTB by about 50kD. The 5kD molecular mass increase was due to the additional SEKDEL sequence and probably the improper cleavage of the bacterial CTB leader sequence. Plant derived CTB-NSP4 fusion protein also formed the pentamer structure about the same size of plant derived CTB pentamer. The transgenic plant containing CFA/I-CTA2 and CTB-NSP4 genes displayed a 70kD band, which was higher in molecular weight than the plant derived CTB-NSP4 pentamer. The additional increase in molecular mass was due to the presence of CFA/I-CTA2 fusion protein. Heat treatment dissociated the multimeric structures into monomers. Plant derived CTB-NSP4 fusion protein had a 18kD monomer. The CTB-NSP4 fusion protein maintained the antigenicity of bacterial cholera toxin and its ability to associate into pentamers which is essential for maintenance of its biological function. The bacterial colonization factor CFA/I is made up of 6000 copies of a 20kD monomer. A multimer ladder of bacterial CFA/I was detected in SDS-PAGE gels (Figure 3B, lane 1). Anti-CFA/I antiserum reacts with the same 70kD band detected by anti-CT antiserum from the plant transformed with the CFA/I-CTA2: CTB-NSP4 double fusion genes. The control plant, transformed only with the CTB-NSP4 gene did not cross react with the anti-CFA/I antiserum (Figure 3B lanes 5 and 6). The cholera toxin A2 subunit passes through the central pore of the B pentamer as a continuous helix. The hydrophobic interaction between the A2 and B subunits stabilize the B pentamer structure. The presence of CFA/I-CTA2 peptide made the chimeric protein more resistant to heat degradation (Figure3B, lane 3 and 4). Immunoblot analysis using antiserum against the NSP4 peptide detected the NSP4 moiety of the CTB-NSP4 fusion protein in monomer form. The reaction was specific and did not cross react with plant derived CTB protein. The inability to detect the small NSP4 moiety in its CTB-NSP4 multimeric form may be due to steric hindrance generated by the CTB pentameric structure.

Quantitation of protein expression levels. The CTB-NSP4 fusion protein expression levels in transformed potato tissues were determined by quantitative chemiluminescent ELISA. The amount of plant CTB-NSP4 protein was measured by comparison of the relative light units (RLU) from a known amount of bacterial CTB protein (Figure 4). The amount of CTB-NSP4 detected was expressed as a percentage of total soluble plant

protein in samples. Plant #15 had the highest expression level about 0.01% of total soluble protein. This is roughly equivalent to 5-10ug of CTB-NSP4 protein in 3.0g of transgenic potato tuber tissues. Plant #3 had the lowest expression level, about one tenth of plant #15 (0.001%). Five minutes of boiling dissociated the CTB multimers, we failed to detect the light emission from the boiled samples.

Assembly of subunit foreign proteins. The association of CFA/I-CTA2 with CTB-NSP4 pentamer was further demonstrated by the results obtained by the GM1 ELISA using anti-CFA/I antibody as the first antibody. Plants #1 and #2 were control plants transformed with CTB and CTB-NSP4 genes respectively. Plants #3 through #7 were transformed with CFA/I-CTA2: CTB:NSP4 genes (Figure 5A). The Student's t-test revealed significant differences among the control plants and CFA/I-CTA2 transformed plants ($p<0.05$). When we increased the amount of total soluble protein from 20ug to 60ug, the RLU signal from the CTB-NSP4 control plant remained the same at the background level (Figure 5B). In comparison, the CFA/I transformed plant showed a increased slope, statistically significant above the control plant ($p<0.05$).

Future experiments. The *mas* promoters are known to be induced auxin inducible promoters. The expression levels are equivalent to or greater than constitutively expressed promoters such as the cauliflower mosaic virus 35S promoter (Mason et al,1992, Haq et al 1995), the patatin promoter. The bidirectional nature of the *mas* promoters enable us to express two foreign proteins simultaneously. This may a benefit for the production of large functional foreign proteins in plants, which are made of two or more subunits. The correlated expression levels between *mas* P1 and P2 promoters provide options for the production of different amounts of subunits, which may in turn achieve optimal ratios for subunit association. Assembly of the CFA/I-CTA2 protein with the CTB-NSP4 pentamer protein to form a multimeric structure in plants, similar to the natural form of cholera holotoxin demonstrates that cholera toxin can be used as a carrier molecule for large peptides and for multiple antigens. The expression of three antigens CFA/I, CTB, NSP4 from three infectious enteric disease cholera, rotavirus and ETEC in one transgenic plant paved the road for developing multi-component oral vaccine in edible plants. Further study of how the immune system responds to oral administration of multi-component antigens may provide further information about how our immune system maintains a balanced immune response against multiple pathogens in the environment. To our knowledge this is the first report of expression of three antigens in individual transgenic plants.

Maryland School of Medicine for the gift of the CFA/I gene and *E. coli* CFA/I fimbrial protein, Dr. John Patton, NIAID Laboratory of Infectious Diseases, Bethesda, Maryland, for the simian rotavirus gene 2 encoding the rotavirus capsid protein VP2, and Dr. Richard Finkelstein, University of Missouri, Department of Microbiology for providing us with cholera holotoxin and antisera against the cholera toxin CTA subunit. This work was supported by a subcontract to WHRL by the National Medical Technology Testbed Inc. and in part by an intramural grant awarded to WHRL by Loma Linda University.

References

Arakawa, T., D. K. X. Chong, and W. H. R. Langridge. 1998. Efficacy of a food plant-based oral cholera toxin B subunit vaccine. Nat. Biotechnol. **16:**292–297.

Arakawa, T., D. K. X. Chong, J. L. Merritt, and W. H. R. Langridge. 1997. Expression of cholera toxin B subunit oligomers in transgenic potato plants. Transgenic Res. **6:**403–413.

Ball, J. M., P. Tian, C. Q.-Y. Zeng, A. P. Morris, and M. K. Estes. 1996. Age-dependent diarrhea induced by a rotavirus nonstructural glycoprotein. Science **272:**101–104.

Bishop, R. F., G. L. Barnes, E. Cipriani, and J. S. Lund. 1983. Clinical immunity after neonatal rotavirus infection: a prospective longitudinal study in young children. N. Engl. J. Med. **309:**72–76.

Clements, J. D. 1990. Construction of a nontoxic fusion peptide for immunization against *Escherichia coli* strains that produce heat-labile and heat-stable enterotoxins. Infect. Immun. **58:**1159–1166.

Dertzbaugh, M. T., and C. O. Elson. 1993a. Comparative effectiveness of the cholera toxin B subunits and alkaline phosphatase as carrier for oral vaccines. Infect. Immun. **61:**48–55.

Dertzbaugh, M. T., and C. O. Elson. 1993b. Reduction in oral immunogenicity of cholera toxin B subunits by N-terminal peptide addition. Infect. Immun. **61:**384–390.

Escher, A., D. J. O'Kane, J. Lee, and A. A. Szalay. 1989. Bacterial luciferase alpha-beta fusion protein is fully active as a monomer and highly sensitive *in vivo* to elevated temperature. Proc. Natl. Acad. Sci. USA **86:**6528–6532.

Glass, R. I., J. Gentsch, and J. C. Smith. 1994. Rotavirus vaccine: success by reassortment? Science **265:**1389–1392.

Haq, T.A., H. S. Mason, J. D. Clements, and C. J. Arntzen. 1995. Oral immunization with a recombinant bacterial antigen produced in transgenic plants. Science **268:**714–716.

Hardy, S. J. S., J. Holmgren, S. Johansson, J. Sanchez, and T. R. Hirst. 1988. Coordinated assembly of multisubunit proteins: oligomerization of bacterial enterotoxins *in vivo* and *in vitro*. Proc. Natl. Acad. Sci. USA **85:**7109–7113.

Hirst, T.R. and J. Holmgren. 1987. Conformation of protein secreted across bacterial outer membranes: a study of enterotoxin translocation from *Vibrio cholerae*. Proc. Natl. Acad. Sci. USA **84:**7418–7422.

Jagusztyn-Krynicka, E. K., J. E. Clark-Curtiss, and R. Curtiss III. 1993. *Escherichia coli* heat-labile toxin subunit B fusions with *Streptococcus sobrinus* antigens expressed by *Salmonella typhimurium* oral vaccine strains: importance of the linker for antigenicity and biological activities of the hybrid proteins. Infect. Immun. **61:**1004–1015.

Jawetz, E., J. L. Melnick, and E. A. Adelberg. 1989. Medical Microbiology. Connecticut: Appleton & Lange, p482–486.

Kapikian, A. Z. and R. M. Chanock. 1985. Norwalk group of viruses: agents associated with epidemic viral gastroenteritis. Virology. New York: Raven Press. p1495–1518.

Langridge, W. H. R., K. L. Fitzgerald, C. Koncz, J. Schell, and A. A. Szalay. 1989. Dual promoter of *Agrobacterium tumefaciens* mannopine synthase gene is regulated by plant growth hormones. Proc. Natl. Acad. Sci. USA **86:**3219–3223.

Lipscombe, M., I. G. Charles, M. Roberts, G. Dougan, J. Tite, and N. F. Fairweather. 1991. Intranasal immunization using the B subunit of the *Escherichia coli* heat-labile toxin fused to an epitope of the *Bordetella pertussis* P.69 antigen. Mol. Microbiol. **5:**1385–1392.

Munro, S. and H. R. B. Pelham. 1987. A C-terminal signal prevents secretion of luminal ER proteins. Cell **48:**899–907.

Purvis, I. J., A. J. Bettany, T. C. Santiago, J. R. Coggins, K. Duncan, R. Eason, and A. J. Brown. 1987. The efficiency of folding of some proteins is increased by controlled rates of translation in vivo. A hypothesis. J. Mol. Biol. **193:**413–417.

Vesikari, T., A. Z. Kapikian, and G. Zissis. 1986. A comparative trial of rhesus monkey (RRV-1) and bovine (RIT4237) oral rotavirus vaccines in young children. J. Infct. Dis. **153:**832–839.

Wandelt, C. I., M. R. I. Khan, S. Craig, H. E. Schroeder, D. Spencer, and T. J. V. Higgins. 1992. Vicilin with carboxy-terminal KDEL is retained in the endoplasmic reticulum and accumulates to high levels in the leaves of transgenic plants. Plant J. **2:**181–192.

Plant Expression Vectors

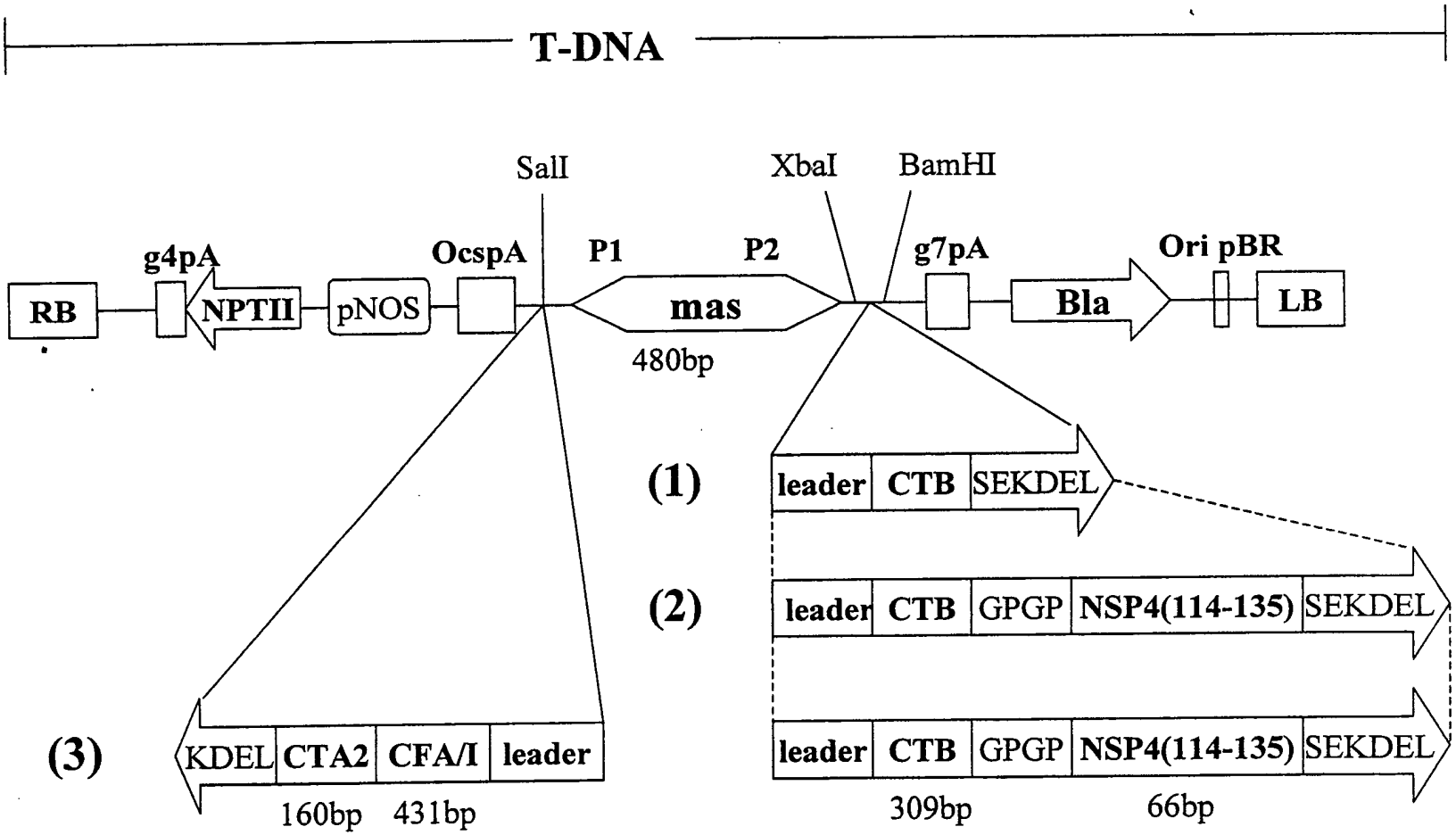

Figure 1. Plant transformation vectors

Construct (3) pPCV701CFA-CT-NSP4. Four genes located within the T-DNA sequence flanked by the right and left border (RB and LB), 25bp direct repeats required for integration of the T-DNA into plant genomic DNA:1) CTBH:NSP4(114-135):SEKDEL coding sequence under control of the *mas* P2 promoter; 2) CFA/I:CTA2 coding sequence under control of the *mas* P1 promoter;3) an NPT II expression cassette for resistance to kanamycin in plants; 4) a β-lactamase cassette for resistance to ampicillin in *E.coli* and carbenicillin in *A.tumefaciens*. The g7pA polyadenylation signal is from the *A.tumefaciens* T_L-DNA gene 7; the OcspA polyadenylation signal is from the octopine synthase gene; Pnos is the promoter of the nopaline synthase gene; g4pA is the polyadenylation signal from T_L-DNA gene 4; Ori pBR is the replication origin of pBR322 for maintenance of the plasmid in *E.coli*. Construct (2), which has only CTBH:NSP4:SEKDEL under the *mas* P2 promoter, and construct (1), which has only CTB:SEKDEL under *mas* P2 promoter, were included as controls.

A

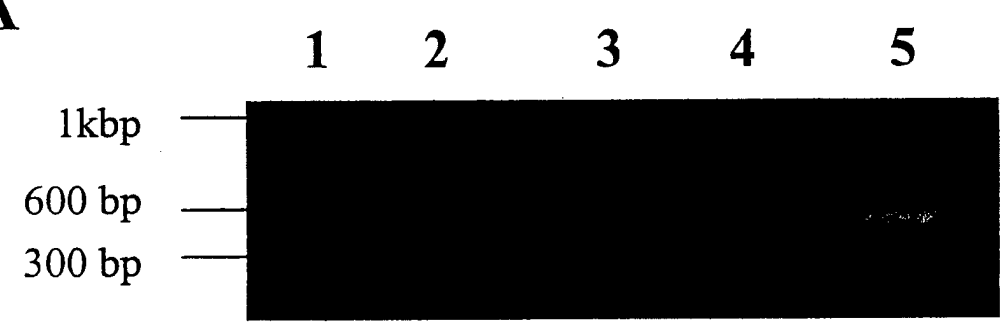
1 2 3 4 5
1kbp
600 bp
300 bp

B

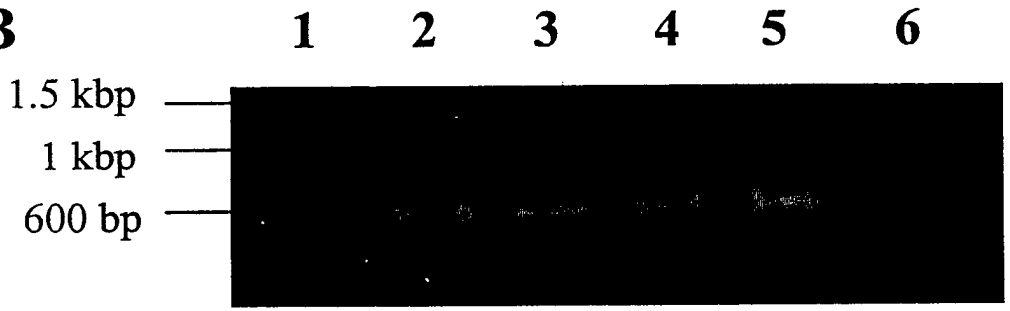
1 2 3 4 5 6
1.5 kbp
1 kbp
600 bp

C

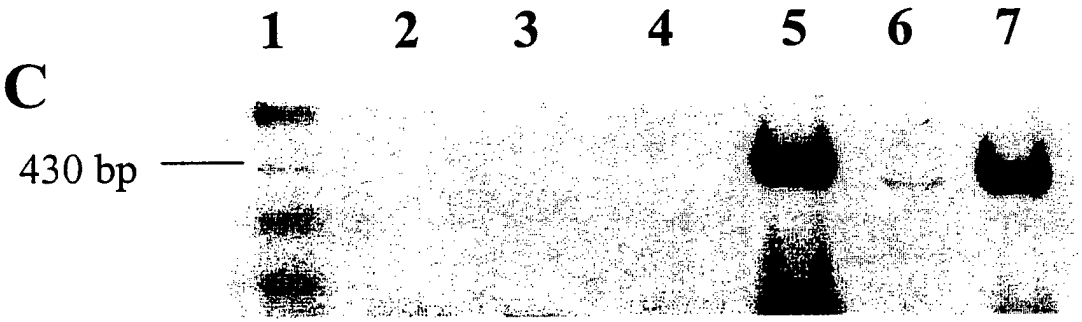
1 2 3 4 5 6 7
430 bp

Figure 2. DNA/RNA analysis of transformed potato

A. PCR detection of CFA/I-CTA2 cDNA in potato genomic DNA: lane 1, 1kb molecular weight marker; lane 2, genomic DNA from untransformed potato leaf tissues; lanes 3 through 5, genomic DNA isolated from potato leaf tissues transformed with plant expression vector pPCV701 CFA-CT-NSP4. **B.** PCR detection of CTBH-NSP4 cDNA in potato genomic DNA: lane 1, 1kb molecular weight marker; lanes 2 through 5, genomic DNA from potato leaf tissues transformed with plant expression vector pPCV701 CFA-CT-NSP4; lane 6, genomic DNA from untransformed potato leaf tissues. **C.** RT-PCR detection of CFA/I mRNA: lane 1, 100bp molecular weight marker; lanes 2 and 3, total RNA preparations from untransformed potato leaf tissues; lanes 4 through 7, total RNA preparations from potato leaf tissues transformed with plant expression vector pPCV701 CFA-CT-NSP4. Lanes 4 and 6, the PCR reaction only, without the reverse transcription step.

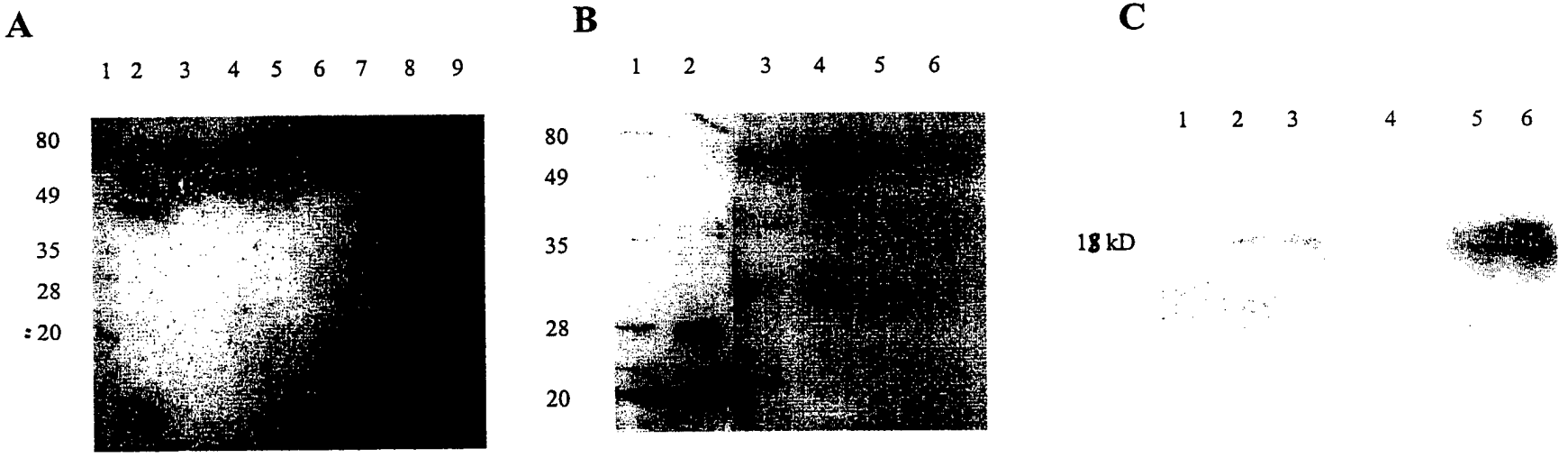
A
1 2 3 4 5 6 7 8 9
80
49
35
28
20
B
1 2 3 4 5 6
80
49
35
28
20
C
1 2 3 4 5 6
18 kD

Figure 3. Immunoblot detection of CTB-NSP4 and CFA/I-CTA2 fusion proteins in transformed potato tuber tissues. **A.**Immunoblot with anti-CT antiserum. Lane 1. Molecular weight markers; Lane 2 through 5 ~~were~~ unboiled samples. Lane 6 through 9 ~~were~~ boiled samples. Lane 2 and 6, 100ng bacterial CTB; Lane 3 and 7, 100ug total soluble protein from potato plant transformed with CTB gene; lane 4 and 8, 100ug total soluble protein from potato plant transformed with CTB-NSP4 fusion gene; Lane 5 and 9, 100ug total soluble protein from potato plant transformed with CFA/I-CTA2 and CTB-NSP4 double fusion genes. **B.** Immunoblot with anti-CFA/I antiserum. Lane 1. Molecular weight markers; 100ng boiled bacterial CFA/I protein; Lane 3 and 4 ~~were~~ unboiled and boiled 200ug total soluble protein from potato plants transformed with CFA/I-CTA2:CTB-NSP4 double fusion genes; Lane 5 and 6 ~~were~~ unboiled and boiled 200ug total soluble protein from potato plants transformed with CTB-NSP4 gene. **C.** Immunoblot with anti-NSP4 antiserum. Lane 1 through 3 were unboiled samples; lane 4 through 6 were boiled samples. Lane 1 and 4, 200ug total soluble protein from potato plants transformed with CTB gene; lane 2 and 5, 200ug total soluble protein from potato plants transformed with CTB-NSP4 fusion gene; lane 3 and 6, 200ug total soluble protein from potato plants transformed with CFA/I-CTA2: CTB-NSP4 double fusion genes.

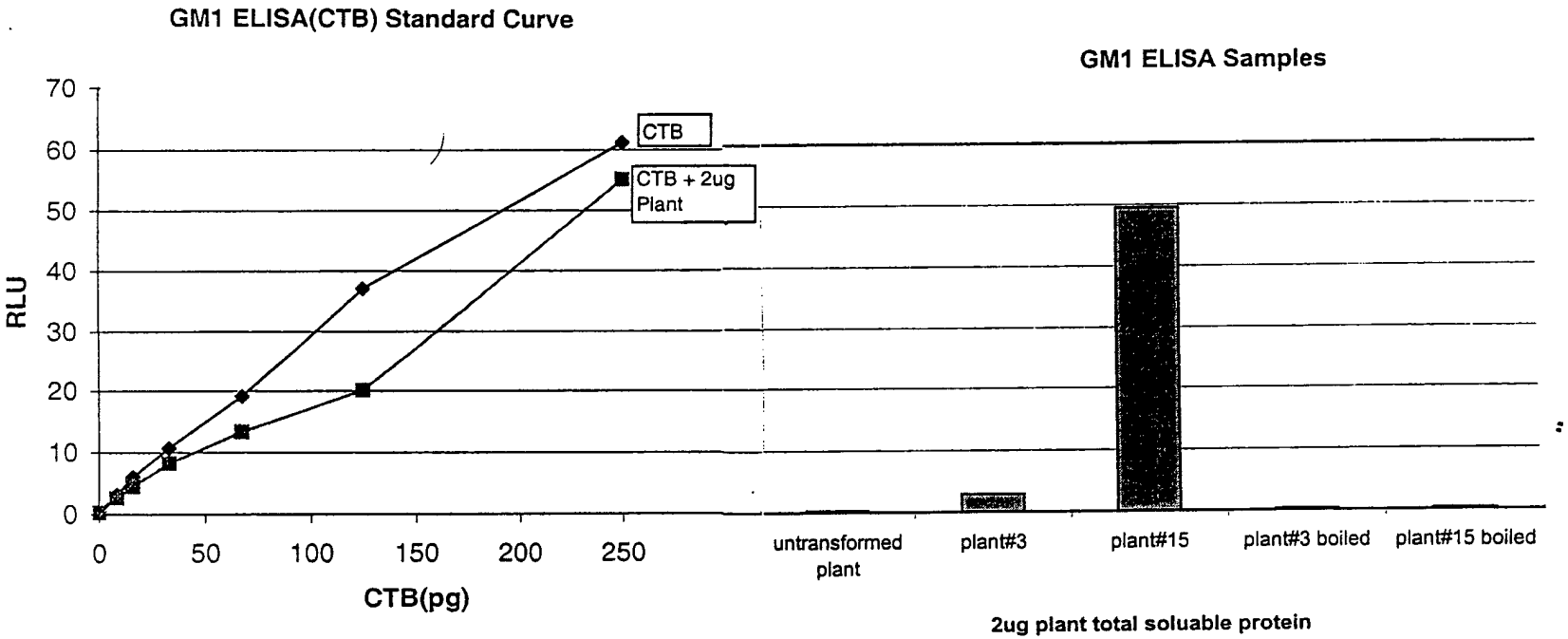
GM1 ELISA(CTB) Standard Curve
GM1 ELISA Samples
RLU
70
60
50
40
30
20
10
0
CTB
CTB + 2ug Plant
0
50
100
150
200
250
CTB(pg)
untransformed plant
plant#3
plant#15
plant#3 boiled
plant#15 boiled
2ug plant total soluable protein

Figure 4. Quantitation of CTB-NSP4 fusion protein levels in transformed potato tissues. Anti-CT antiserum was used as primary antibody in GM1 ELISA assay. Known amounts of bacterial CTB protein plus 2ug total soluble protein from untransformed potato tissues were used to generate standard curves. 2ug total soluble protein from transformed potato plant #3 and #15 were either boiled or directly used for GM1 ELISA assay. An untransformed plant was used as a negative control. The relative light units (RLU) obtained from the sample assay were compared with the standard curve to calculate CTB-NSP4 fusion protein expression level.

A

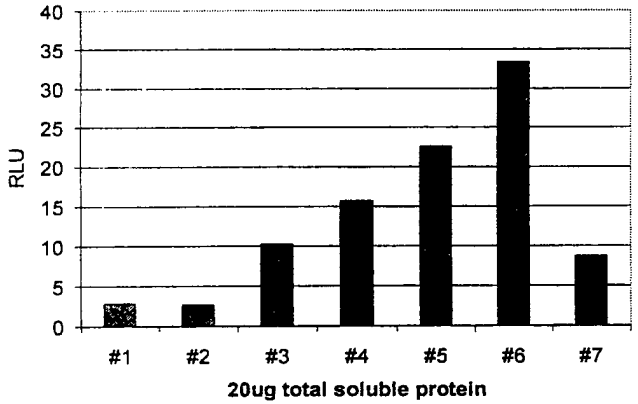
40
35
30
25
20
15
10
5
0
RLU
#1
#2
#3
#4
#5
#6
#7
20ug total soluble protein

B

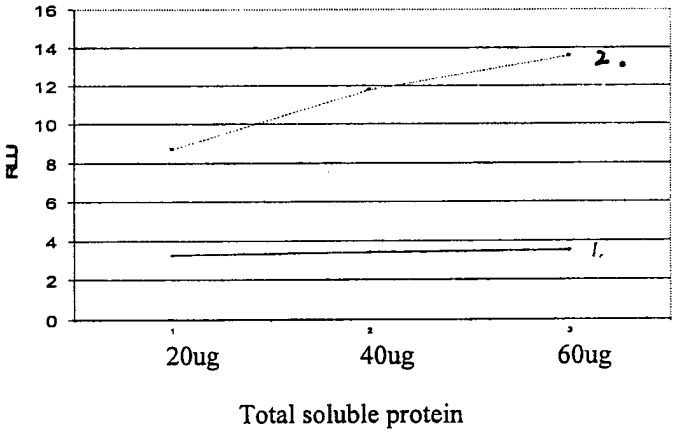
16
14
12
10
8
6
4
2
0
RLU
2.
1.
20ug
40ug
60ug
Total soluble protein

Figure 5. Detection the association of CFA/I-CTA2 fusion protein with CTB-NSP4 fusion protein in transformed potato plants.

A. Plant homogenate containing 20ug total soluble protein was used to perform the GM1 ELISA. Rabbit anti-CFA/I antiserum was used as the primary antibody. #1 ~~was~~ control plant transformed with CTB gene only; #2 ~~was~~ control plant transformed with CTB-NSP4 gene only; #3 through#7 were plants transformed with CFA/I-CTA2: CTB-NSP4 double fusion genes. **B.** various amount of total soluble protein from transformed plant tissues was used to perform the GM1 ELISA. Rabbit anti-CFA/I antiserum was used as the primary antibody. Rabbit anti-CFA/I antiserum was used as the primary antibody. Curve #2 ~~was~~ RLU obtained from plant transformed with CFA/I-CTA2: CTB-NSP4 double fusion genes; curve #1 ~~was~~ a control ~~from~~ plant transformed with CTB-NSP4 gene only.

One day children may get immunized by munching on foods instead of enduring shots. More important, food vaccines might save millions who now die for lack of access to traditional inoculants

EdibleVaccines

by William H. R. Langridge

1. painting
FOODS UNDER STUDY as alternatives to injectable vaccines include, among others, bananas, potatoes and tomatoes, lettuce, rice, wheat, soybeans and corn[?].

Vaccines have accomplished near miracles in the fight against infectious disease. They have consigned smallpox to history and should soon do the same for polio. By the late 1990s an international campaign to immunize all the world's children against six devastating diseases was reportedly reaching 80 percent of infants (up from about 5 percent in the mid-1970s) and was reducing the annual death toll from those infections by roughly three million.

Yet these victories mask tragic gaps in delivery. The 20 percent of infants still missed by the six vaccines—against diphtheria, pertussis (whooping cough), polio, measles, tetanus and tuberculosis—account for about two million unnecessary deaths each year, especially in the most remote and impoverished parts of the globe. Upheavals in many developing nations now threaten to erode the advances of the recent past, and millions still die from infectious diseases for which immunizations are nonexistent, unreliable or too costly.

This situation is worrisome not only for the regions that lack health care but for the entire world. Regions harboring infections that have faded from other areas are something like bombs ready to explode. When environmental or social disasters undermine sanitation systems or displace communities—bringing people with little immunity into contact with carriers—infections that might have been long gone from a population come roaring back. Further, as international travel and trade make the earth a smaller place, diseases that arise in one locale are increasingly popping up continents away. Until everyone has routine access to vaccines, no one will be entirely safe.

In the early 1990s Charles J. Arntzen, then at Texas A&M

DES/THEIR PRESENCE MAGNIFIES the risk that dengue and yellow fever may follow. Dengue fever itself has struck at the mile mark in Taxco, Mexico. The patterns of insect migration

University, conceived of a way to solve many of the problems that bar vaccines from reaching all too many children in developing nations. Soon after learning of a World Health Organization call for inexpensive, oral vaccines that needed no refrigeration, Arntzen visited Bangkok, where he saw a mother soothe a crying baby by offering a piece of banana. Plant biologists had already devised ways of introducing selected genes (the blueprints for proteins) into plants and inducing the altered, or "transgenic," plants to manufacture the encoded proteins. Perhaps, he mused, food could be genetically engineered to produce vaccines in their edible parts, which could then be eaten when inoculations were needed.

The advantages would be enormous. The plants could be grown locally—and cheaply—with standard growing methods of a given region. Because food plants can be regenerated readily, the crops could potentially be produced indefinitely without the growers having to purchase more seeds or plants year after year. Home-grown vaccines would also avoid the logistical and economic problems posed by having to transport traditional preparations over long distances, keeping them cold all along the way and at their destination. And, being edible, the vaccines would require no syringes—which, aside from costing something, can lead to infections if they become contaminated.

Efforts to make Arntzen's inspired vision a reality are still quite preliminary and could be slowed by opposition to genetically altered foods in general. Yet studies carried out in animals in the past 10 years—and small tests in people—encourage hope that edible vaccines can work. The research has also fueled speculation that certain food vaccines might help suppress autoimmunity—in which the body's defenses wrongly attack normal, uninfected tissues. Among the autoimmune disorders that might be prevented or eased are type I diabetes (the kind that commonly arises during childhood), multiple sclerosis and rheumatoid arthritis.

By Any Other Name ...

Regardless of how vaccines for infectious diseases are delivered, they all have the same aim: priming the immune system to swiftly destroy specific disease-causing agents, or pathogens, before the agents can multiply enough to cause symptoms. Classically, this priming has been achieved by presenting the immune system with whole viruses or bacteria that have been killed or made too weak to proliferate much.

On detecting the presence of a foreign organism in a vaccine, the immune system behaves as if the body were under attack by a fully potent antagonist. It mobilizes its various forces to root out and destroy the apparent invader—targeting the campaign to specific antigens (proteins recognized as foreign). The acute response soon abates, but it leaves behind sentries, known as "memory" cells, that remain on alert, ready to unleash whole armies of defenders if the real pathogen ever finds its way into the body. Some vaccines provide life-long protection; others (such as those for cholera and tetanus) must be readministered periodically.

Classic vaccines pose a small but troubling risk that the vaccine microorganisms will somehow spring back to life, causing the diseases they were meant to forestall. For that reason, vaccine makers today favor so-called subunit preparations, composed primarily of antigenic proteins divorced from a pathogen's genes. On their own, proteins have no way of establishing an infection. Subunit vaccines, however,

2.PHOTO
BANANA TREES in a greenhouse at the Boyce Thompson Plant Research Center, in Ithaca, NY, have been genetically engineered to produce an experimental vaccine against [TO COME]. Although newly planted banana trees take three years to produce food, they offer several advantages as a sources of vaccines: they grow widely parts of the developing world and their fruit, which usually appeals to children, can be eaten raw.

DES. THEIR PRESENCE MAGNIFIES the risk that dengue and yellow fever may follow. Dengue fever itself has struck at the mile mark in Taxco, Mexico. The patterns of insect migration change faster in the mountains than they do at sea level. Those alterations can thus serve as indicators of climate change and of diseases likely to extend their range.

are expensive, in part because they are produced in cultures of bacteria or animal cells and have to be purified out; they also need to be refrigerated.

Food vaccines are like subunit preparations in that they are engineered to contain antigens but bear no genes that would enable whole pathogens to form. Ten years ago Arntzen understood that edible vaccines would therefore be as safe as subunit preparations while sidestepping their costs and demands for purification. But before he and others could study the effects of food vaccines in people, they had to obtain positive answers to a number of questions. Would plants engineered to carry antigen genes produce functional copies of the proteins? When the food plants were fed to test animals, would the antigens be degraded in the stomach before having a chance to act? (Typical subunit vaccines have to be delivered by injection precisely because of such degradation.) If the antigens did survive, would they, in fact, attract the immune system's attention? And would the response be strong enough to defend the animals against infection?

Additionally, researchers wanted to know whether edible vaccines would elicit what is known as mucosal immunity. Many pathogens enter the body through the nose, mouth or other openings. Hence, the first defenses they encounter are those in the mucous membranes that line the airways, the digestive tract and the reproductive tract; these membranes occupy a huge 4,300 square feet of area and constitute the biggest pathogen-deterring surface in the body. When the mucosal immune response is effective, it generates molecules known as secretory antibodies that dash into the cavities of those passageways, neutralizing any pathogens they find. An effective reaction also activates a systemic response, in which circulating cells of the immune help to destroy invaders at distant sites.

Injected vaccines, being delivered into muscles or the bloodstream, initially bypass mucous membranes and typically do a poor job of stimulating mucosal immune responses. But ed-

ible vaccines come into contact with the lining of the digestive tract. In theory, then, they should activate mucosal immunity as well as systemic immunity. That dual effect should, in turn, help improve protection against many dangerous microorganisms, including, importantly, the kinds that cause diarrhea after colonizing the small intestine.

Those of us attempting to develop food vaccines place high priority on combating diarrhea. Together the main causes—the Norwalk virus, rotavirus, *Vibrio cholera* (the cause of cholera) and enterotoxigenic *Escherichia coli* (a toxin-producing source of "traveler's diarrhea")—account for some three million infant deaths a year, mostly in the developing nations. These pathogens disrupt intestinal cells in ways that cause water to flow from the blood and tissues into the intestine. The resulting dehydration may be combated by feeding patients an electrolyte solution, but it often turns deadly when rehydration therapy is not available. No vaccine practical for wide distribution in the developing nations is yet available to prevent these ills.

Green Lights on Many Fronts

When investigators began addressing the questions before them, they took some encouragement from past research. In the late 1980s Julian K.-C. Ma and his colleagues at Guy's Hospital in London had coaxed genetically altered tobacco plants (which are

BOXED DIAGRAM TITLE

SIDEBAR SUBTITLE GOES HERE

Isn't it an exaggeration to call this teleportation? After all, it is only a quantum state that is teleported, not an actual object. This question raises the deeper philosophical one of what we mean by identity. How do we know that an object— say, the car we find in our garage in the morning—is the same one we saw a while ago? When it has all the right features and properties. Quantum physics reinforces this point: particles of the same type in the same quantum state are indistinguishable even in principle. If one could carefully swap all the iron atoms in the car with those from a lump of ore and reproduce the atoms' states exactly, the end result would be identical, at the deepest level, to the original car. Identity cannot mean more than this: being the same in all properties.

Isn't it more like "quantum faxing"? Faxing produces a copy

DIAGRAM

3. How Edible Vaccines Provide Protection

Antigens in food vaccines begin their work after being taken up by "M" cells in the intestinal lining and passed to other cells of the immune system immune system cells (*left detail*). The antigens trick the recipient cells into launching a defensive attack, as if the antigen were a true disease-causing agent. The response leads to the production of long-lasting "memory" cells (*right detail*) that ward off disease by promptly quashing any disease-causing agents bearing the antigens used in the vaccine (*second detail*).

DIAGRAM

2. Making an Edible Vaccine
One way of generating edible vaccines relies on bacteria to deliver into plant cells the genetic blueprints for viral or bacterial "antigens"—proteins that elicit an immune response in the recipient. The example shows the production of a vaccine potato, containing an antigenic protein.

not edible) to produce normal-looking versions of a mammalian secretory antibody. Much later, in 1998, the group showed that application of the purified antibodies to the teeth of human volunteers prevented a cavity-causing bacterium, *Streptococcus mutans*, from colonizing the dentition. Such passive immunization—direct delivery of immune system components—might be extremely valuable for some uses (such as for enhancing the cavity-fighting power of toothpaste).

Those recent findings are certainly exciting, but back in the early 1990s scientists were particularly impressed by the demonstration that plants could construct complex foreign proteins properly. That ability had to be in place if plant-derived antigens were to be used for "active" immunization—for inducing the body to build its own, long-lasting immune shield against invasion by pathogens.

By 1995 researchers had established that plants could, indeed, manufacture foreign antigens in their proper conformations. For instance, Arntzen and his colleagues had introduced into tobacco plants the gene for a protein derived from the hepatitis B virus and had gotten the plants to synthesize the protein. When *they injected the antigen into* mice, it activated the same immune system components as are activated by the virus itself. (Hepatitis B can damage the liver and contribute to liver cancer.)

But injection is not the aim; feeding is. In the past five years, experiments conducted by Arntzen (who moved to the Boyce Thompson Institute for Plant Research at Cornell University in 1995) and his collaborators and by my group at Loma Linda University have demonstrated that tomato or potato plants can synthesize antigens from the Norwalk virus, enterotoxigenic *E. coli*, *V. cholerae* and the hepatitis B virus. Moreover, feeding antigen-laced tubers or fruits to test animals can evoke mucosal and systemic immune responses that fully or partly protect animals from subsequent exposure to real pathogens or, in the case of *V. cholerae* and enterotoxigenic *E. coli*, to microbial toxins. Edible vaccines have also provided laboratory animals with some protection against challenge by the rabies virus, *Helicobacter pylori* (a bacterial cause of ulcers) and the mink enteric virus (a disease that does not affect humans but is important in mink).

It is not entirely surprising that antigens delivered in plant foods survive the trip through the stomach well enough to reach and activate the immune system, even though typical subunit vaccines would not. The tough outer wall of plant cells apparently serves as temporary armor for the antigens, keeping them relatively safe from gastric enzymes. ~~Only~~ When the wall finally begins to break down in the intestines, the cells gradually release their antigenic cargo.

Of course, the key question is whether food vaccines can be useful in people. The era of clinical trials for this technology is just beginning. Nevertheless, Arntzen and his collaborators obtained reassuring results in the first published human trial, involving 11 subjects. In 1997 volunteers who ate pieces of peeled, raw potatoes containing a benign segment of the *E. coli* toxin (the B subunit) displayed both mucosal and systemic immune responses. Since then, the group has also seen immune reactivity in 19 or 20 people who ate potato vaccines aimed at the Norwalk virus. Similarly, after Hilary Koprowski of Thomas Jefferson University fed transgenic lettuce carrying a hepatitis B antigen to three volunteers, two of the subjects displayed a good systemic response. Whether edible vaccines can actually protect against human disease remains to be determined, however.

DES, THEIR PRESENCE magnifies the risk that dengue and yellow fever may follow. Dengue fever itself has struck at the mile mark in Taxco, Mexico. The patterns of insect migration change faster in the mountains than they do

Still to Be Accomplished

In short, the studies completed so far in animals and people have provided a proof of principle. They indicate that the strategy is feasible, yet many issues must still be addressed.

For one, the amount of vaccine made by the plants is low. Production can be increased in different ways—for instance, by linking antigen genes with regulatory elements known to help switch on the genes more readily. As researchers solve that challenge, they will also have to ensure that any given portion of a vaccine food provides a predictable dose of antigen.

Efforts are also under way to enhance the odds that antigens will interact with the immune system instead of passing out of the body unused. Better targeting to the immune system can compensate in part for low antigen production.

One strategy involves linking antigens to molecules that bind readily to immune system components known as M cells in the intestinal lining. M cells take in samples of material that has entered the small intestine (including pathogens) and pass them to other cells of the immune system, including antigen-presenting cells and B lymphocytes (the antibody-producing cells). The antigen-presenting cells chop up their acquisitions and display the resulting protein fragments on the cell surface for perusal by white blood cells called helper T lymphocytes. If the T lymphocytes recognize the fragments as foreign, they help to activate the B lymphocytes and may initiate a full-blown immune attack on

can omit → this is not work but only tangential to plant vaccines

Antibodies are passive immuniz
Antigens cause Active immuniz

If we keep this ¶ we need a "but" statement indicating drawbacks of passive immun relative to active immun

degraded ? is not

M cell take up gut contents intact easier to recognize pathogen Antigens

Amount

Are cells part of immune system? yes → they are the interface cells between the intestin and the macrophage (APCs). Hard to do challenge exists in humans. No one wants to take a chance to become ill.

↑ is this paragraph up to date? (yes) OK? yes

help to systemic Antibody Inflammatory response

chalera holotoxin challenge

* making Antibodies in humans is not enough. Protection of humans against pathogen challenge is the critical point. Our lab is

Sidebar Intro Title

Sidebar Title

This is sidebar text. This is sidebar text. This is sidebar text.

methods of preserving these foods—such as drying—might overcome the spoilage problem. Among the other food choices under consideration are lettuce, carrots, peanuts, rice, wheat, corn and soybeans.

In another concern, scientists need to be sure that vaccines meant to enhance immune responses do not backfire and suppress immunity instead. Research into a phenomenon called oral tolerance teaches that feeding of certain proteins can at times cause the body to shut down its responses to those proteins. To determine safe, effective doses and feeding schedules for edible vaccines, manufacturers will need to have a better handle on the manipulations that influence whether an orally delivered antigen will stimulate or depress immunity.

A final issue worth studying is whether food vaccines can indirectly vaccinate babies who are too young for anything but breast milk. In theory, the mothers could ingest the bananas or whatever, triggering production of antibodies that would travel to the baby via the breast milk. Eating one or two bananas in a sitting might be sufficient.

Nonscientific challenges accompany the technical ones. Most pharmaceutical makers shy away from vaccines, partly out of fear over lawsuits. And few vaccine makers are eager to support research for products targeted to markets outside the lucrative West. International aid organizations and some national governments and philanthropies are striving to fill the gap, but the effort to develop edible vaccines remains underfunded.

In addition, edible vaccines fall under the increasingly unpopular rubric of "genetically modified" plants. Recently a British company (Axis Genetics) that was supporting studies of edible vaccines failed; one of its leaders lays at least part of the blame on investor worry about companies involved with genetically engineered foods. I hope, however, that these vaccines will avoid serious controversy because they are intended to save lives and would probably be planted over much less acreage than other food plants (if they are raised outside of greenhouses at all). Also, as drugs, they would be subjected to closer scrutiny by regulatory bodies.

Fighting Autoimmunity

Consideration of one of the challenges detailed above—the risk of inducing oral tolerance—has recently led my group and others to pursue edible vaccines as tools for quashing autoimmunity. Although oral delivery of antigens derived from infectious agents often stimulates the immune system, oral delivery of "autoantigens" (proteins derived from uninfected tissue in a treated individual) can sometimes suppress immune activity—a phenomenon seen frequently in test animals. No one fully understands the reasons for this difference.

Some of the evidence that ingesting autoantigens, or "self-antigens," might suppress autoimmunity comes from studies of type I diabetes, which results from autoimmune destruction of the insulin-producing cells (the beta cells) of the pancreas. This destruction progresses silently, often for years, before symptoms arise. Eventually, though, the loss of beta cells leads to a drastic shortage

DIAGRAM

SEE CAPTION on next page

The Author

WILLIAM H. R. LANGRIDGE, a leader in the effort to develop edible vaccines for infectious and autoimmune diseases, is professor [?] at the Center for Molecular Biology and Gene Therapy at the Loma Linda University School of Medicine. After receiving his doctorate in biology from the University of Massachusetts at Amherst in 1973, he conducted genetic research on plants for several years at the Boyce Thompson Institute at Cornell University. In 1987 he became associate professor in the Plant Biotechnology Center of the University of Alberta in Edmonton. Langridge joined Loma Linda in 1993.

Further Information

ORAL IMMUNIZATION WITH A RECOMBINANT BACTERIAL ANTIGEN PRODUCED IN TRANSGENIC PLANTS. Charles J. Arntzen in *Science*, Vol. 268, No. TK, pages 714–716; May 5, 1995.

IMMUNOGENICITY IN HUMANS OF A RECOMBINANT BACTERIAL ANTIGEN DELIVERED IN A TRANSGENIC POTATO. Carol O. Tacket, Hugh Mason, G. Losonosky, J. D. Clements, M. M. Levine and Charles J. Arntzen in *Nature Medicine*, Vol. 4, No. TK, pages 607–609; April 1998.

A PLANT-BASED CHOLERA TOXIN B SUBUNIT-INSULIN FUSION PROTEIN PROTECTS AGAINST THE DEVELOPMENT OF AUTOIMMUNE DIABETES. Takeshi Arakawa, Jie Yu, D. K. Chong, John Hough, Paul C. Engen and William H. R. Langridge in *Nature Biotechnology*, Vol. 16, No. TK, pages 934–938; October 16, 1998.

PLANT-BASED VACCINES FOR PROTECTION AGAINST INFECTIOUS DISEASES. Jie Yu and William H. R. Langridge in *[to come]*

of insulin, a hormone needed to help cells take up sugar from the blood for energy. The loss results in high blood sugar levels and, if left untreated, coma and death. Insulin injections help to control diabetes, but they are not a cure; diabetics face an elevated risk of kidney failure, blindness, foot ulcers that lead to gangrene, and other complications.

In the past 15 years, investigators have identified several beta cell proteins that can elicit autoimmunity in people predisposed to type I diabetes. The main culprits, however, are a protein called GAD (glutamic acid decarboxylase) and insulin. Researchers have also made progress in detecting when diabetes is "brewing." The next step, then, is to find ways to stop the underground process before any symptoms arise.

To that end, my colleagues and I, as well as other groups, have developed plant-based vaccines, such as potatoes consisting of GAD or insulin linked to the innocuous B subunit of the cholera toxin (to enhance uptake of the antigens by M cells). Feeding of the vaccines to a mouse strain that becomes diabetic helped to suppress the immune attack and to prevent or delay the onset of high blood sugar.

Transgenic plants cannot yet produce the amounts of self-antigens that would be needed for a viable vaccine against human diabetes or other autoimmune diseases. But, as is true for infectious diseases, investigators are exploring a number of promising schemes to overcome that and other challenges.

Even though the precise way that ingestion of autoantigens leads to suppression of autoimmunity is murky, immunobiologists have proposed some reasonable explanations. At least in some instances, the display of self-antigens by intestinal macrophages seems to preferentially activate a subset of white blood cells capable of suppressing other immune system cells. These suppressor cells then travel through the blood to the site of the autoimmune activity. There they secrete a cocktail of small proteins that force their tissue-destroying cousins to quiet down [*see illustration on page 00*].

Edible vaccines for combating autoimmunity and infectious diseases have a long way to go before they will be ready for large-scale testing in people. But the technical obstacles all seem surmountable. Nothing would be more satisfying than to protect the health of many millions of now defenseless children around the globe.

severe yes!!

note:
I deleted mention of MS studies. I didn't understand your corrections, & we don't need that data to get your point across.

(almost 50% reduction!)

absolutely ☺

(MS is more complex:
① - autoantigen ill defined
② more than one organ affected)

4. Stopping Autoimmunity

AUTOIMMUNE REACTION responsible for type I diabetes arises when the immune system mistakes proteins that are made by pancreatic beta cells (the insulin producers) as foreign. The resulting attack, targeted to the offending proteins, or "autoantigens," destroys the beta cells (*left panel*). Eating autoantigens sometimes quiets the process in diabetic mice, perhaps in part by switching on "suppressor" cells of the immune system, which then repress the destructive activities of their cousins (*right panel*).

- I might delete this (it'll be a tricky one to put in the art, Boo!)

A the trick is to provide a small amount of autoantigen to induce & activation of suppressor T cells

called cytokines

point of interest
not all bacteria will work
need specialized bacteria = Agrobacterium tumefaciens is typically one ↑ a modified plant pathogen which can transfer genes into plant cells

7/5

HOW TO MAKE AN EDIBLE VACCINE

One method for generating edible vaccines relies on bacteria to deliver into plant cells the genetic blueprints for viral or bacterial "antigens"—proteins that elicit an immune response in a person. The diagram below illustrates the production of vaccine potatoes.

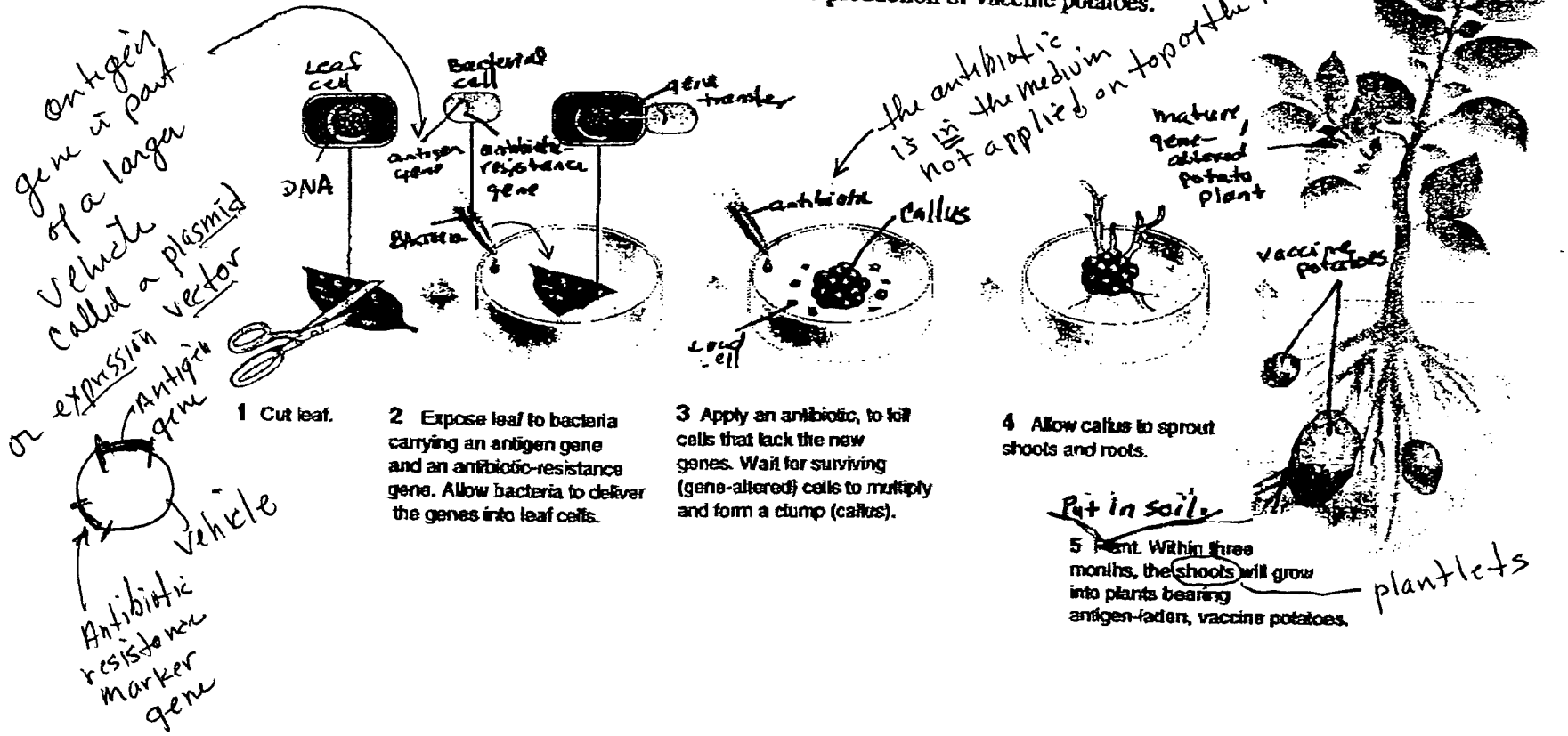

1 Cut leaf.

2 Expose leaf to bacteria carrying an antigen gene and an antibiotic-resistance gene. Allow bacteria to deliver the genes into leaf cells.

3 Apply an antibiotic, to kill cells that lack the new genes. Wait for surviving (gene-altered) cells to multiply and form a clump (callus).

4 Allow callus to sprout shoots and roots.

5 Plant. Within three months, the shoots will grow into plants bearing antigen-laden, vaccine potatoes.

SCI AMER EDIT

3. How Edible Vaccines Provide Protection

Antigens in food vaccines get taken up by so-called M cells in the intestine and passed to various immune-system cells. Those cells then launch a defensive attack (*left panel*), as if the antigen were a true infectious agent, not just part of one. That response leaves behind long-lasting "memory" cells able to promptly neutralize the real infectious agent should it attempt a later invasion (*right panel*).

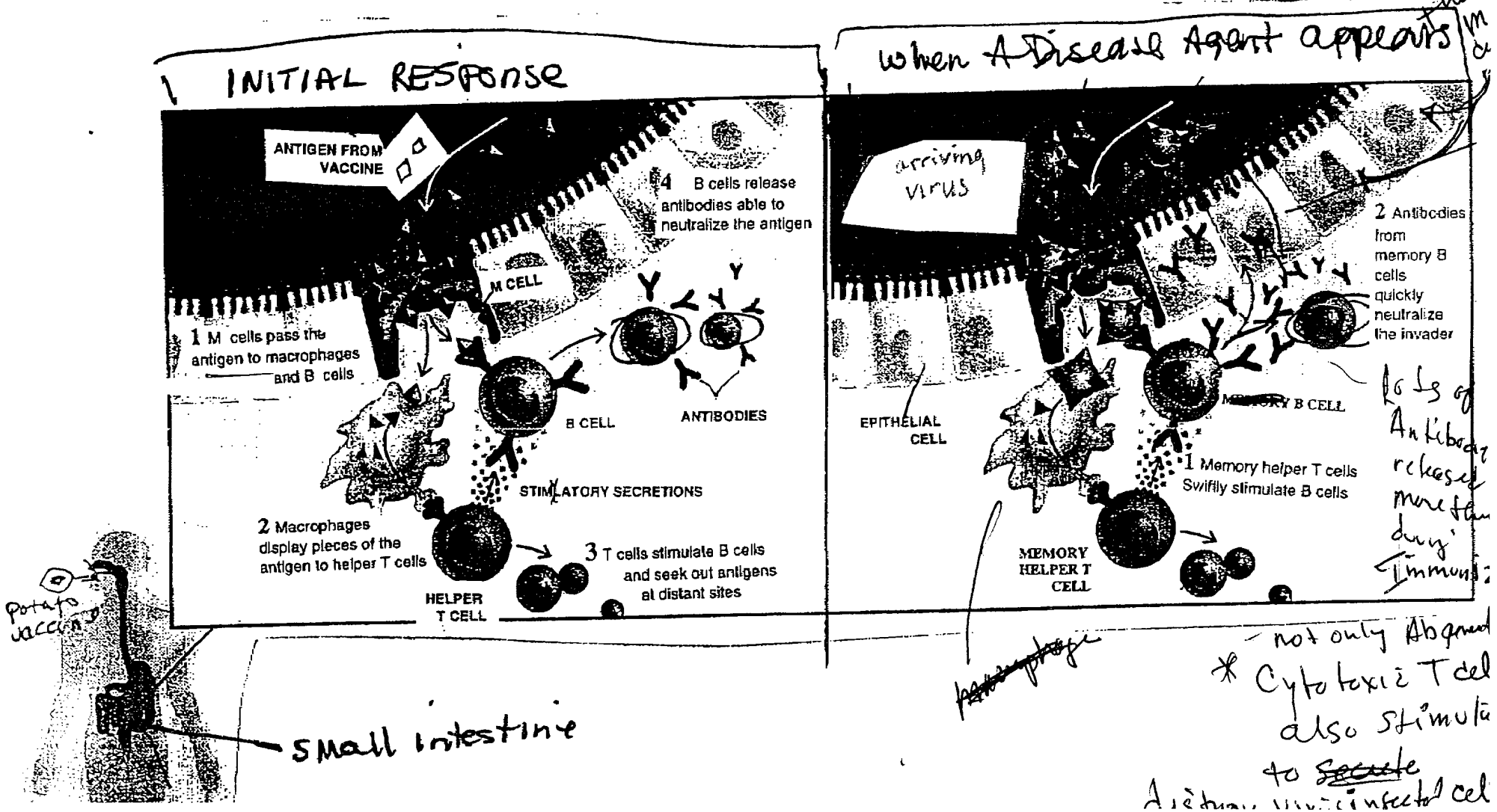

Moving Against Malnutrition [ROUGH DRAFT 7/3]

As research into edible vaccines is progressing, so too are gene-based efforts to make foods more nutritious. Like those vaccines, certain of these foods are being devised with the developing nations in mind—to combat malnutrition.

One entry takes aim at deficiencies of vitamin A, which are rampant in impoverished regions. Lack of this vitamin can lead to blindness and can worsen diarrhea and other diseases, thereby contributing to the deaths of perhaps two million children each year. Rice would be a convenient way to deliver the needed vitamin, since half of all the people on earth eat it daily as a staple. But standard forms do not supply it.

Enter "golden" rice, which contains high amounts of beta-carotene, a pigment the body converts to vitamin A. A team lead by Ingo Potrykus, of the Swiss Federal Institute of Technology, and Peter Beyer, of the University of Freiburg (Germany), announced its creation this past January. In May a biotech company, Astra Zeneca, bought the rights and agreed to distribute the seeds at no cost to impoverished nations once the product is perfected and fully tested. (Testing is expected to last at least until 2003.)

Related research is seeking ways to enrich rice with other vitamins and with minerals, including zinc and iron. (More than 2 billion people are iron deficient). Investigators are attempting to enrich other foods as well. In June, for instance, a group of British and Japanese investigators reported producing tomatoes that contained three times the usual amount of beta carotene.

Not everyone is thrilled by these announcements, however. Some opponents of genetically modified crops contend that malnutrition can be combated right now in other ways, say by constructing supply routes. Further, they worry that companies will tout the benefits of the new foods to deflect attention from worries over other genetically modified crops, most of which so far offer few clear advantages for consumers (such as plants designed to resist damage from pesticides). High on the list of concerns are risk to the environment and to people.

Supporters of the new, nutritionally improved foods hope, however, that the rice won't be thrown out with the rinse water. –*Ricki Rusting, staff writer*

possible mention could be our ~~the~~ human beta casein/lactoferrin producing potatoes for more nutritious, hypoallergenic infant formulae and baby goods to protect infants who are not breast fed from bacterial infection and to promote healthy brain development and prevent autism as

COPY JUL 24 2000

Preclinical Evaluation of A Plant-based Multi-Component Oral Vaccine Against Enteric Diseases

Subcontract No. 10-FY97-LLU-LANGRIDGE
Cooperative Agreement No. DAMD 17-97-2-7016

tel: 909-558-4300, xt. 81362
fax: 909 - 558-04177
email: blangridge@som.llu.edu

NMTB Progress Report 4, FY98-00

(4th quarter report: 4/18/00-7/11/00)

Personnel

1. William H.R. Langridge, Ph.D., Project Director, Department of Biochemistry and Center for Molecular Biology and Gene Therapy, (30%)

2. Dr. Daniel Chong, Ph.D., Research Associate, Center for Molecular Biology and Gene Therapy, (100%),

3. Mr. Jie Yu, Senior Graduate Student, Department of Biochemistry, Center for Molecular Biology and Gene Therapy (100% time commitment, funded by an LLU graduate student stipend),

William H.R. Langridge William H.R. Langridge. **Date: 7/11/00.**

Introduction

The goal of our NMTB subcontract remains determination of the feasibility of a *novel vaccine production and delivery system* employing edible plant-delivered mucosal vaccine technology to protect our armed forces personnel and indigenous civilian population from the enteric diseases cholera, enterotoxigenic *E. coli* (ETEC) and rotavirus which cause extensive mortality when the social infrastructure of a country is fragmented during natural disaster, or political unrest.

Subcontract Outline

The specific goals of our subcontract for the 5th report are:

- Construction of plant expression vectors containing fusion proteins between the cholera toxin A or B subunits (CTA2 and CTB), with the ETEC fimbrial antigen CFA/I or the rotavirus capsid VP2, VP6 and NSP4 enterotoxin antigen proteins. (This goal was completed during the six month no cost extension following the first funding cycle).

- Construction of plant expression vectors containing the rotavirus capsid protein genes VP2 and VP6 together in the same vector and in individually in separate vectors to determine the most effective combination for vaccine delivery. (This goal was completed during the six month no cost extension following the first funding cycle).

- Transformation of potato tissues and detection of assembly of CTB-NSP4 antigen fusion protein and CTA2-CFA/I antigen fusion protein oligomeric cholera holotoxin-like protein complexes in regenerated transformed potato plants. (Construction of the vectors, transformation and regeneration of transformed plants and expression studies completed at the end of the six month no cost extension period following the first funding cycle).

- Generation of empty virus capsids, rotavirus-like particles (VLP's) in transformed tuber cells and detection of the VLP's in transformed plant extracts by electron microscopy. (Immunoblot and ELISA evidence indicated that the rotavirus VP2 and VP6 capsid proteins are synthesized at the level of approximately 0.01% of total soluble plant protein. Electron microscopic detection of VLPs showed the presence of tubular structures frequently observed in rotavirus capsid protein transformed plant tissues which are evidence of low cell levels of capsid protein synthesis. During the final quarter of the second funding cycle sucrose gradient separation methods will be used to concentrate VLP structures which may be present at low levels in transformed plant extracts. Concentration of the VLPs may permit detection by transmission electron microscopy).

- Determination of CTA2 and CTB-antigen fusion protein levels generated in leaf and tuber tissues of the developing transgenic potato plants. (During the later part of the first year and the first quarter of the second funding year, using chemiluminescent ELISA and

immunoblot methods, we were able to detect both the CFA/I- CTA2 and CTB-NSP4 fusion proteins in transformed potato plant extracts. Since potato is easier to regenerate than tomato, it was adopted as the plant of choice for initial multiple antigen plant vaccine "proof of concept" experiments).

- Serum and intestinal IgA and IgG antibody titers against CTB-NSP4, CTA2-CFA/I and VP6 were measured in orally immunized CD-1 outbred mice by chemiluminescent ELISA methods. The mice were fed transgenic potato tuber tissues expressing CTB-NSP4 and CTA2-CFA/I fusion proteins for targeting fusion antigens to intestinal M cells mediated by cholera toxin B subunit-antigen fusion protein pentameric complexes (This work completed during the third and fourth quarters of the second year funding period, showed significant measurable levels of IgG and IgA antibody titers in the mice which remained up to 56 days following the last immunization. No antibody titers were detected in unimmunized mice).

- The protective efficacy generated by plant delivered CTB-NSP4 fusion protein, mouse pups passively immunized *in utero* by oral immunization of the dams with transformed tuber tissues was determined by challenging the passively immunized mouse pups with simian rotavirus SA-11. (These experiments were completed during the current funding cycle and a show a significant protective effect against development of diarrhea symptoms in the passively immunized mouse pups. A manuscript is currently under construction to demonstrate the protective efficacy in the immunized pups and will be submitted for NMTB approval before the deadline of the final report).

- Protection against rotavirus infection in adult mice immunized with VP6 capsid protein can be determined by measurement of reduction in rotavirus shed following rotavirus challenge. (Unfortunately, the virus shed experiments are not trivial to perform, a concept also reinforced by our prospective collaborator Dr. Harry Greenberg, Department of Urology, Stanford University). The virus shed experiments require antisera which are available only in Dr. Greenberg's laboratory. Therefore due to the complexity of the VP6 virus shed experiments, coupled with the lack of a detailed protocol from Dr Greenberg and finally the lack of funds to carry out the experiments in Dr. Greenberg's laboratory, as well as the inability to obtain a second no-cost extension, we will be unable to complete the virus shed experiments during this funding cycle).

- The protective efficacy of serum and mucosal anti-CFA/I antibody can be determined by measuring bacterial adhesion in mammalian cell culture infected with ETEC. (The ETEC binding protection efficacy experiments were not initiated during the current funding cycle due to the small amounts of CFA/I antigen detected in transformed plant extracts by the relatively insensitive antiserum previously acquired from our colleagues. However, new anti-CFA/I antibodies recently prepared commercially against the CFA/I protein can reliably detect CFA/I at levels from 0.001 to 0.05% of total soluble protein. Thus, we know that CFA/I protein is generated in the transformed potato plants. Since we know that from earlier studies in the literature that the small amounts of CFA/I protein produced in the transformed

plants would be unlikely to provide measurable results in the ETEC binding experiments, an alternative approach was taken to determine the protective efficacy of the CFA/I protein. Cytokine analysis of splenocytes isolated from mice immunized with CTB, NSP4 and CFA/I and stimulated with the purified homologous antigen will provide information on the type of T lymphocyte response (Th1 or Th2 and or cytotoxic T lymphocyte), generated by oral immunization with plant-based antigens (While these experiments were not a part of the original subcontract goals, they were considered to be an alternative approach to gathering immunological information on protective efficacy of our plant based vaccines when small amounts of the antigen were synthesized in the plant. These experiments have been partially completed and a manuscript is presently under construction pending conformation of the initial experimental results).

- Protection against cholera toxin induced diarrhea is measured by reduction in ileal loop fluid retention in mice immunized with plant delivered CTB and has demonstrated a positive result in of diarrhea reduction in previous experiments by Arakawa et. al. 1998 (1). Since the amounts of CTB protein produced in the CTB-NSP4 fusion protein were several times greater than the amounts of CTB generated in previous experiments we have decided not to repeat the ileal loop CTX inoculation experiments based on the judgement that we are likely to obtain similar data and results as obtained in the previous experiments and we could avoid additional unnecessary pain to the immunized experimental animals.

- Fluorescent antibody cell staining flow cytometric analysis (FACS) experiments have been initiated with unstimulated and antigen stimulated splenocytes isolated from unimmunized and orally immunized mice. These experiments while not originally a part of the subcontract will provide us with quantitative information on the relative numbers of CD4+ or CD8+ T lymphocytes generated in response to the plant-delivered antigens. This information will be indicative of the extent of T cell help and cytotoxic T cell (CTL), amplification as well as providing information on the presence of memmory cells generated in response to plant-based mucosal immunization.(Although these FACS experiments were not originally a part of our subcontract agreement, they compliment the splenocyte cytokine analysis providing a quantitative measurement of protective efficacy of plant-based mucosal immunization and are currently underway. The information obtained will be presented in manuscript form prior to the end of the second years subcontract funding cycle).

Body

During the course of our first two NMTB subcontract funding cycles, we constructed a variety of plant expression vectors containing cDNAs encoding cholera A and B subunit, rotavirus capsid and enterotoxin epitope peptides and an ETEC fimbrial antigen. During the first funding cycle and the following 6 month no-cost extension, we succeeded in transforming and regenerating transformed potato plants synthesizing the cholera toxin B subunit-rotavirus enterotoxin 22 aa epitope fusion protein (CTB-NSP4), the cholera toxin A2 subunit -ETEC, fimbrial antigen fusion protein (CTA2-CFA/I) (1). During the six month no-cost extension following the first funding cycle

we constructed two additional plant expression vectors containing the auxin up regulated mannopine synthase dual P1,P2 promoters (2,3), *mas* P2- VP2 and *mas* P1-VP6 rotavirus capsid protein-promoter fusions expressed together in the same vector or *mas* P2-VP6 alone, for the purpose of studying self-assembly of capsid proteins into multi capsid virus-like antigenic particles (VLPs). Transformed potato plants generated quantifiable levels of antigen (4,5). During the second year funding cycle, SA-11 rotavirus challenge experiments conducted with passively immunized CD-1 mouse pups indicated that anti-NSP4 IgG and IgA antibodies produced in adult mice immunized with NSP4 antigen protein containing tuber tissues were able to provide significant passive protection of their offspring against development of rotavirus induced diarrhea. We have raised antiserum with high sensitivity and specificity for CFA/I subunit protein. This antiserum has permitted us to detect significant levels of CFA/I protein in transformed tuber tissues. The tuber-synthesized CFA/I antigen induced detectable antibody levels in orally immunized mice.

To circumvent time consuming cell culture and animal efficacy experiments while obtaining similar information on the protective efficacy of our plant based multicomponent vaccines, we decided to substitute for pathogen challenge experiments, immunized animal splenocyte assays to detect the protective efficacy of our multicomponent plant-based vaccines. During the later part of the present second year funding cycle we have performed splenocyte cytokine analysis and flow cytometry experiments not previously outlined in our subcontract, to shed light on the nature of the plant-based vaccine protective response. We have isolated splenocytes from mice orally immunized with tuber tissues generating CTB, NSP4 and CFA/I antigens. The splenocytes were separated, transferred into cell culture and challenged with CTB, NSP4 or CFA/I. Following antigen challenge, the cytokines produced by the challenged splenocytes were isolated and quantified. The results of these splenocyte challenge experiments revealed significant increases in IL-2 and INF-gamma cytokine levels and reduced IL-4 cytokine levels in comparison with the control unimmunized animals. This result provides conclusive evidence of the presence of Th1 helper lymphocyte mediated immunity against each of the plant delivered antigens.

The first flow cytometry analysis experiments on spleen cells from immunized mice have shown the presence of significant CD4+ memory cell populations in the plant vaccine immunized animals. The flow cytometry experiments will be continued to the end of the second funding cycle and a manuscript describing the nature of the multicomponent plant vaccine immune response at the cellular level will be constructed to show the extent of the protective immune response generated by the multicomponent plant-based vaccines produced in potato.

Following application of specific antibodies against purified CFA/I protein, we were able to detect CTA2-CFA/I fusion protein association with the CTB-NSP4 pentamer in transformed plant extracts. This result suggests the synthesis and assembly of a cholera holotoxin-like molecule in the transformed plant tissues. In recent experiments not previously described in our subcontract, we were able to demonstrate synthesis and assembly of the cholera toxin CTA and CTB subunits in transformed potato cells (6). Toxicity contributed from the CTA1 subunit was not detected in the transformed plants which grew normally and set tubers in a normal fashion. This result could be possibly associated with the low level of expression from the *mas* promoters in the absence of

exogenous auxin stimulation. The apparent assembly of cholera holotoxin (CTX) (7), in plant cells is a land mark experiment which in the future, may permit us to increase the number of antigenic proteins the plant can deliver to the GALT. A provisional patent application was constructed based on the production of enterocyte targeted antigen fusion proteins in edible plants for protection against infectious diseases was filed with the US patent office by Loma Linda University in the early part of the second funding cycle to protect this intellectual property for the NMTB.

Conclusions

We have demonstrated that individual transformed potato plants are able to synthesize quantifiable amounts (from 0.001 to 0.3% of total soluble protein), of two or three antigens which provide a mucosal immune response (antibody formation or T cell help), against cholera toxin, CFA/I the ETEC fimbrial antigen, the rotavirus capsid protein VP6 and the rotavirus NSP4 enterotoxin 22 amino acid epitope. Mouse oral immunization experiments with transformed tuber tissues demonstrated significant mucosal and serum antibody titers against all three pathogen proteins. Cytokine analysis of antigen stimulated splenocytes from immunized mice showed plant delivered antigens generated a strong Th1 helper cell response. FACS phenotype analysis of the splenocytes indicated the presence of cytotoxic lymphocytes (CTL's) and protective memory cells. Rotavirus and cholera challenge experiments have demonstrated protection against cholera toxin and rotavirus toxin symptom development in immunized mice. Thus, even in the light that only small amounts of antigen can be produced in plants, targeting of the antigen protein to the mucosal immune system permits the generation of useful vaccines against single antigens in plants and indicates that the production of multiple vaccine antigens in individual food plants is clearly a feasible goal. Experiments not previously part of the subcontract recently demonstrated that the cholera toxin A subunit can be synthesized and assembled with cholera toxin B subunit pentamers in the plant to form a structure immunologically identical to the holotoxin. Further, we have demonstrated that CFA/I-CTA2 fusion protein is synthesized in transformed potato tuber tissues and appears to assemble with the CTB-NSP4 pentamer in the plant to form a holotoxin-like hetero-oligomeric molecule indicating the feasibility of generating enterocyte targeted multi subunit complexes capable of delivering three or more antigens to the GALT. The most significant impediment to plant vaccine development remains the relatively low amounts of antigen protein (0.001% to 0.3% of total soluble protein) synthesized in the plant. These low levels of antigen in combination with concomitantly low levels of antibodies generated by mucosal immunization methods could result in the lower levels of protective secretory antibody synthesis following oral immunization seen in comparison with parenteral introduction of antigens.

To establish a baseline for estimating the contribution of alternative methods for increasing plant based vaccine protection against the three enteric pathogens, antigen dose - immune response curves should be generated. However, these experiments are presently beyond the time available during the second year of our subcontract. To increase the protective efficacy of our plant based vaccines, in addition to increasing the synthesis of antigen protein in plant tissues, methods could be explored to increase the delivery of available antigen to the GALT e.g., through specific targeting of antigens to receptor molecules on the intestinal cell surface or through adjuvant stimulated

immunogenicity of individual or multicomponent plant synthesized antigens (8). Information gathered from the enterocyte targeting and adjuvant enhancement experiments will continue to increase the protective efficacy of plant-based vaccines and will facilitate health care delivery for military personnel and provide increased protection against infectious enteric diseases for civilian populations in economically emerging countries.

References

1. de Block, M. (1988) Genotype-independent leaf disc transformation of potato (*Solanum tuberosum*) using *Agrobacterium tumefaciens*. *Theor. Appl. Genet.* 76, 767-774.

2. Langridge, W.H.R., Fitzgerald, K.J., Koncz, C., Schell, J., and Szalay, A.A. (1989) The dual promoter of *A. tumefaciens* mannopine synthase genes is regulated by plant growth hormones. *Proc. Natl. Acad. Sci., U.S.A.* 86, 3219-3223.

3. Velten, J., Velten, L., Hain, R. and Schell, J. (1984), Isolation of a dual plant promoter fragment from the Ti plasmid of *Agrobacterium tumefaciens*. *EMBO J.* 3:2723-2730.

4. Arakawa, T, Chong, D.K., Merritt, J.L. and Langridge, W.H., (1997),Expression of cholera toxin B subunit oligomers in transgenic potato plants. *Transgenic Res.* 6(6):403-13.

5. Arakawa, T, Chong,D.K., Langridge, W.H., (1998), Efficacy of a food plant-based oral cholera toxin B subunit vaccine. *Nat. Biotechnol.* 16(3):292-7.

6. Chong, K.X.D. and Langridge, W.H.R. (2000), Synthesis and Assembly of Cholera Holotoxin in Potato Plants. *Transgenic Research*, to be submitted, Appendix II.

7. Gill, D.M. (1976) The arrangement of subunits in cholera toxin. *Biochemistry* 15(6), 1242-1248.

8. Holmgren, J., Czerkinsky, C., Lycke, N. and Svennerholm, A..M.,(1994), Strategies for the induction of immune responses at mucosal surfaces making use of cholera toxin B subunit as immunogen, carrier, and adjuvant. *Am. J. Trop. Med. Hyg.* 50(5 Suppl):42-54.

Patents and Publications

No new patent applications have been applied for since the fourth progress report was submitted as the multicomponent plant-based vaccines are currently protected under the priority date established by the Provisional Patent Application entitled "Production of a Cholera Toxin B Subunit-Rotavirus NSP4 Enterotoxin Fusion Protein in Potato" submitted to the US patent office in January 2000 (see report # 4). This data has been condensed into two manuscripts which the NMTB gave the authors permission to publish. We have now submitted the first manuscript with Dr Chong as

principal author, (Appendix II, fourth quarterly report.), presenting our data on the cloning, synthesis and assembly of the cholera A and B subunits in potato plants which has been sent to the journal *Transgenics*. The second manuscript with a senior graduate student Mr. Jie Yu as the senior author describes the basis for expression of three antigens in an enterocyte targeted vaccine molecule, presents our data on construction of multicomponent vaccine plant expression vectors, the transformation of potato leaf explants with these vectors and the regeneration of transformed potato plants. The measurement of multicomponent vaccine protein expression levels in regenerated transformed potato plant leaf and tuber tissues is also described (Appendix III, fourth quarter report). Permission was given from the NMTB to publish this manuscript and it has been sent to the journal *Transgenics*. We recently heard from the editor that the manuscript has been accepted and we expect to see publication of this information within the next several months. A manuscript approved earlier for publication by the NMTB dealing with the construction and expression in the plant of the CTB-NSP4 fusion protein was not submitted for publication due to the desire to obtain a provisional patent covering this intellectual property before it became public domain. This manuscript has been recently sent for publication to the Journal *Transgenics*. A fourth manuscript describing the protective efficacy of the plant generated multicomponent vaccine incorporating the results of the passive immunization experiments against rotavirus infection, the splenocyte cytokine assays demonstrating protective efficacy against CTB, NSP4 and CFA/I antigens and the fluorescent cell sorting experiments. This manuscript is in the second draft stage and will be submitted to the NMTB for consideration regarding publication in early October. Due to the ground breaking information contained in this work, we intend to submit this manuscript to the journal *Nature biotechnology*. Finally, The PI was asked to write a feature article on edible plant based vaccines for *Scientific American* for the October issue. The NMTB gave conditional approval for publication of this article provided that the proper disclaimer was added to the manuscript prior to publication. The article was published in the September issue of Scientific American with the appropriate disclaimer. The principal investigator will provide a copy of the *Scientific American* article to the NMTB office as soon as *Scientific American* provides the author with the requested reprints.

DESCRIPTION: State the goal of the project, including how it relates to improving health care and noting the advanced technology that will be developed or tested . Use succinct language to describe how the project goals will be achieved. **Do not exceed the space provided.**

Transplantation of engineered cells is an emerging therapeutic intervention for a wide variety of diseases, including cancer, autoimmune disorders, and neurodegenerative conditions. Central to the development of these treatments is the ability to produce and modify transplantable cells *ex-vivo*. We propose the development of new methods for manipulating cells in culture without the need for DNA transfer. This approach relies on the transfer of cell-permeable *proteins* (rather than *genes*) into cells to effect increased proliferation, or decreased differentiation or death. Proteins will be rendered competent to enter cells by their being coupled (through genetic means) to a small peptide vector sequence. We refer to such vectored proteins as "vecteins." Our studies will utilize FDCP1 cells, a model of primitive hematopoietic progenitors, to address two critical issues to the development of vecteins as tools for manipulation of cells. *First*, we will construct vecteins incorporating the product of the *bcl-2* gene, a known cell survival gene. We will treat FDCP1 cells with vecteins targeted to either the cytoplasm or nucleus, and compare the biologic effects of the exogenously added proteins with that of retrovirally expressed Bcl-2, a known effector of enhanced cell survival. Successful completion of these studies will demonstrate the feasibility of delivering biologically active proteins to suppress cell death, without genomic modification of the target cells. *Secondly*, we will develop additional vector sequences to effect improved nuclear and membrane targeting of vecteins. These studies could potentially expand the range of cellular targets to be manipulated by vecteins in *ex-vivo* treated cells. Successful vectein technologies could be immediately applied to treatment programs involving cell transplantation and gene therapy.

PROJECT SITE(S) (organization, city, state):

Center for Molecular Biology and Gene Therapy
Loma Linda University
Loma Linda, CA 92354

FORM B

COPY

JUL - 3 2000

SEMI-ANNUAL REPORT

CELL-PERMEABLE PROTEINS FOR CELL REGULATION

Michael B. Lilly, MD, Principal Investigator
Phone (909) 558-8777
FAX (909) 558-0177
e-mail: mlilly@som.llu.edu

Cooperative Agreement No. DAMD17-97-2-7016

Subagreement No. 76-FY99-LLU-Lilly

Michael B. Lilly, MD

6/30/00
Date

INTRODUCTION

This contract provides funds for the development of methods to introduce proteins into cells to reversibly regulate cellular processes such as proliferation and differentiation. The basic technology involves the development of cell-permeabilization sequences, which will allow the delivery of exogenous proteins to various intracellular locations. The original aim was to identify proteins that could permit the expansion of hematopoietic progenitor cells in culture. The use of exogenous, cell-permeable proteins ("vecteins") would avoid genomic modification, such as would occur with typical gene therapy methods. Additional aims were to identify methods for delivery of exogenous proteins directly to the plasma membrane. These methodologies probably do not have a role in telemedicine, and are not derived from known defense technologies.

SPECIFIC AIMS/OBJECTIVES

The funded proposal had three specific aims:

1. **Specific Aim #1. Produce a variety of Bcl-2 vecteins that incorporate different vector sequences.** Create an artificial protein, similar to the human Bcl-2 protein, which can enter cells. The protein would be produced by standard molecular engineering methods in bacteria.

2. **Specific Aim #2. Evaluate Bcl-2 vecteins for their ability to inhibit cell death in a primitive hematopoietic cell line.** Determine if the cell-permeable Bcl-2 protein can enter mouse white blood cells and prevent their death.

3. **Specific Aim #3. Develop novel vector sequences that may confer on vecteins the ability to accumulate in different intracellular locations.** Create methods for delivering foreign proteins to the cell surface following addition of the protein to the culture medium, as well as an improved vector sequence for nuclear targeting of proteins. These tools may expand the range of transforming proteins we can introduce into cells to effect reversible immortalization.

WORK ACCOMPLISHED (12/01/99 – 6/01/00)

Substantial progress has been made during the initial six month funding period on all of the specific aims outlined in the original proposal (see page 12/section A1-3 of research plan). Multiple bacterial expression plasmids have been constructed in the process of exploring specific aims #1, 2 and biologically active proteins are being produced and evaluated. Specific aim #3b has been essentially completed. Specific aim #3a, the construction of a bacterial expression plasmid incorporating our "CTCF" vector sequence, has been incorporated into studies to develop a new, modular protein construction system, and will be part of our 02 year proposal. During the remaining six

months of the 01 year we will focus on additional biologic studies under specific aim #1, 2, and expect to demonstrate production of cell-permeable vecteins which can mediate both gain-of-function and loss-of-function phenotypes in murine hematopoietic cell lines.

1. Specific Aim #1. Produce a variety of Bcl-2 vecteins that incorporate different vector sequences. This specific aim incorporated the construction of a new bacterial expression plasmid for N- or C-terminal vector fusions, and the use of this plasmid to produce human Bcl-2 protein in cell permeable form (Bcl-2 "vectein").

a. Creation of pOMNITAT, a versatile bacterial expression vector for production of cell-permeable proteins. Our original expression plasmids only permitted C-terminal fusions, and the Bcl-2 protein, which was our initial protein of interest, contained a C-terminal transmembrane domain that was necessary for biologic activity. The bacterial expression plasmid pET15b (Novagen) was modified by insertion of an alternate polylinker, which containing the 11-amino acid HIV-Tat vector sequence (Fig. 1). The new DNA sequences were produced as synthetic oligonucleotides (sense and antisense), which were annealed *in vitro*, then ligated into the cut plasmid between the *Nde I* and *Bam HI* (*Bgl II*) sites.

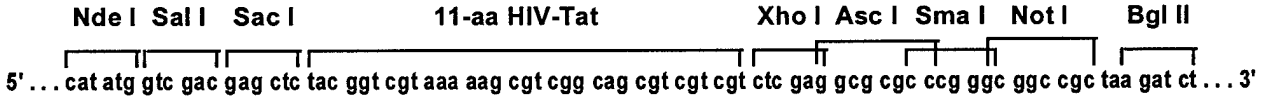

Fig. 1. Polylinker region of pOMNITAT. Nde I and Bgl II (BamHI) sites identify the ligation sites to the pET15b backbone.

The resulting plasmid, pOMNITAT has new 5' and 3' restriction sites for insertion of cDNAs. The former include *Sal I* and *Sac I* sites, while the latter are *Xho I*, *Asc I*, *Sma I*, and *Not I*. In addition, the many arginine codons in the HIV-Tat vector sequence have been optimized for bacterial usage.

b. Expression of cell-permeable Pim-1 proteins as alternatives to Bcl-2 vecteins. Our original intention was to use Bcl-2 as a model protein to demonstrate the ability of appropriate cell-permeable proteins (vecteins) to inhibit cell death in hematopoietic cells. However, we have been unable to express Bcl-2 vecteins when prepared in pOMNITAT as N-terminal fusions with the HIV-Tat vector sequence. This failure appears due to toxicity of the recombinant protein for the host bacteria. The toxicity results from the presence of the C-terminal transmembrane domain of the wild-type Bcl-2 sequence, since *bcl-2* cDNAs lacking this sequence are expressed well. However, this transmembrane region is needed for full biologic activity. Thus Bcl-2 protein appears to show the same difficulties with bacterial expression that other transmembrane proteins exhibit. Colleagues who are interested in cell permeable proteins have recently reported to us their failure to express full-length Bcl-2 protein in cell-permeable form (Steve Dowdy, Washington University, personal communication). Because of the potential importance of membrane-targeted proteins we are taking steps to develop efficient methods for production of these proteins in recombinant form (see below, and proposal for 02 year funding). In the

meantime, however, we have proceeded to investigate alternative proteins for use in a cell death model, to demonstrate the feasibility of death- and differentiation-inhibiting vecteins.

We have recently reported that the *pim-1* gene product inhibits death in hematopoietic cells through a *bcl-2* dependent mechanism [1]. Because *pim-1* can apparently regulate *bcl-2* expression and acts through *bcl-2* to inhibit cell death, we have begun to produce Pim-1 vecteins to "side step" the troublesome issues of production of Bcl-2 vecteins, while producing a similar biologic effect. To this end we have begun to prepare a series of Pim-1 vecteins, to include both wild type and dominant negative forms. The later is based on an N-terminal truncation of the wild-type sequence (NT81; Fig. 2)[1]. We have made initial bacterial expression constructs for the active and inactive forms of Pim-1 using our original plasmids pMTS and pTAT. These express recombinant proteins with C-terminal vector domains. The pMTS plasmid affixes a 12-amino acid hydrophobic vector sequence found in keratinocyte growth factor [2] while pTAT fuses a 30-amino acid polybasic sequence derived from the HIV-Tat protein[3].

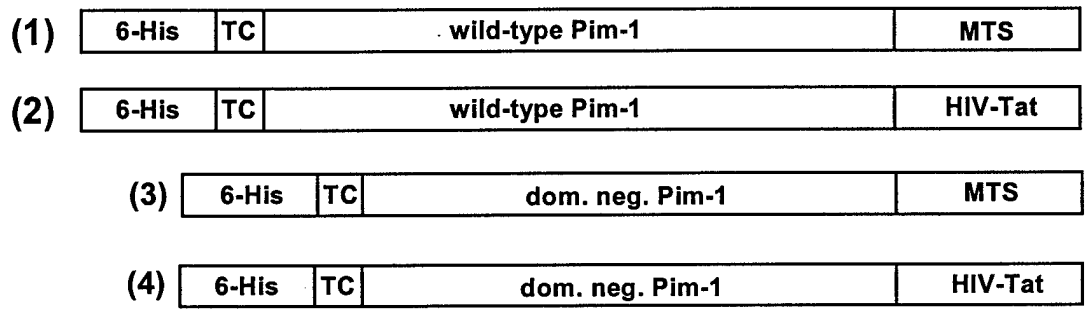

Fig. 2. Pim-1 vectein proteins. 6-His = purification motif; TC = thrombin cleavage site; wild-type Pim-1 = human 33kd protein sequence; dom. neg. Pim-1 = NT 81 mutant pim-1 sequence; MTS = hydrophobic vector (cell penetration) domain; HIV-Tat = polybasic vector (cell penetration) domain.

Unlike the Bcl-2 vectein constructs, each of these four recombinant proteins were easily produced in quantity (several milligrams/liter; Fig. 3). However, all were almost

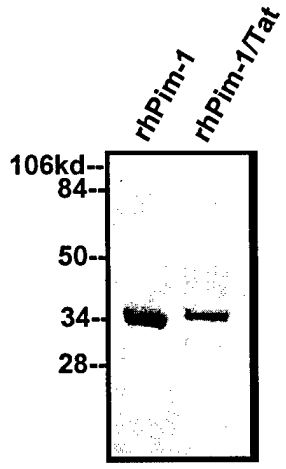

Fig. 3. Expression of recombinant human Pim-1 proteins that lack (rhPim-1) or contain (rhPim-1/Tat) HIV-Tat vector sequences. Proteins were expressed in bacteria, and the purified proteins were purified by metal chelate affinity chromatography. SDS:PAGE, stained with Coomasie Blue stain.

exclusively insoluble. Protein could be solubilized and purified easily under denaturing conditions (8M urea or 6M guanidine HCl), but when transfer to a physiologic buffer was attempted, near-quantitative precipitation occurred. We tried a variety of methods to produce a degree of solubility, such as renaturation on metal chelate resin, rapid or slow buffer exchange by dialysis or desalting columns in the presence or absence of carrier proteins, glycerol, or non-detergent sulfabetaines. Because of persistent failures to solubilize the purified protein, we explored the effect of molecular variants. Initially two additional constructs were prepared. These fused the dominant-negative NT81 Pim-1 mutant cDNA or a full-length Pim-1 protein cDNA to a N-terminal, shortened HIV-Tat sequence, using an expression plasmid described by Dowdy's group at Washington University (Fig. 4)[4]. This plasmid differs from our original Tat plasmid in that the vector sequence is shorter (11 amino acids compared to 30 in our construct) and is exclusively expressed as an N-terminal fusion.

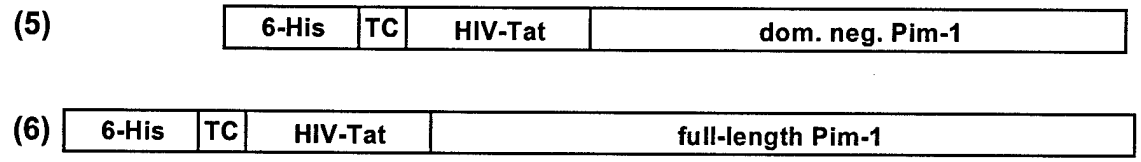

Fig. 4. Pim-1 vectein proteins. 6-His = purification tag; TC = thrombin cleavage site; HIV-Tat = cell penetration domain; dom.neg. Pim-1 = NT81 mutant Pim-1 sequence; full-length Pim-1 = wild-type protein sequence.

Both of these recombinant proteins were substantially insoluble in aqueous buffers under physiologic conditions, but could be dissolved at high concentration in 0.5% acetic acid.

We made a further construct by fusing *pim-1* sequences to the C-terminus of GFP (Fig. 5). We have previously successfully produced GFP vecteins, and so hoped that the favorable structure of this molecule would negate the tendency of the Pim-1 sequences to aggregate. For this construct we used our new pOMNITAT plasmid.

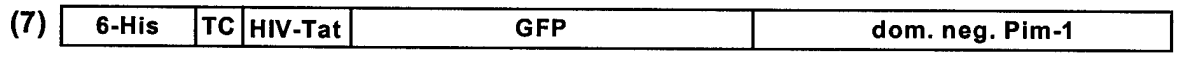

Fig. 5. GFP/Pim-1 chimeric vectein protein. 6-His = purification tag; TC = thrombin cleavage site; HIV-Tat = cell penetration domain; GFP = green fluorescent protein; dom.neg.Pim-1 = NT81 mutant Pim-1 sequence.

Again, this recombinant protein was substantially insoluble in aqueous solution under standard purification conditions (solubilization of intracellular inclusion bodies in guanidine, affinity purification under denaturing conditions, followed by renaturation through dialysis).

While each of these recombinant vecteins has shown a substantial tendency to aggregate, we have still been able to produce small amounts of soluble protein in physiologic buffers. This has most reliably been achieved by allowing the protein to precipitate, washing the pellet extensively to eliminate denaturants, and then solubilizing the proteins in 0.5-5% acetic acid. When the protein solution is then added dropwise

into tissue culture medium (DME/0.1% BSA) with at least a 20-to-1 dilution, with rapid vortexing of the solution, some solubility has been achieved. We estimate a final concentration of approximately 150nM. Other cell permeable proteins show biologic activities at this concentration[4]. In addition, we are exploring purification methods involving submaximal protein expression followed by careful extraction and purification of the recombinant proteins under native conditions.

Specific Aim #2. Evaluate cell-permeable vecteins for their ability to modulate cell death in a primitive hematopoietic cell line. As an alternative to Bcl-2 vecteins, we have begun to examine recombinant Pim-1 vecteins for biologic activity. Since *pim-1* is a survival gene the wild-type protein inhibits cell death, while the dominant negative form enhances death[1]. We have been able to achieve slightly better solubility of the dominant negative vectein protein than the wild-type fusion protein; hence, we have been able to begin preliminary experiments with the former protein. We have treated FDCP1 murine hematopoietic cells with the N-terminal HIV-Tat fusion dominant-negative Pim-1 protein (construct (5) above) and examined survival and death.

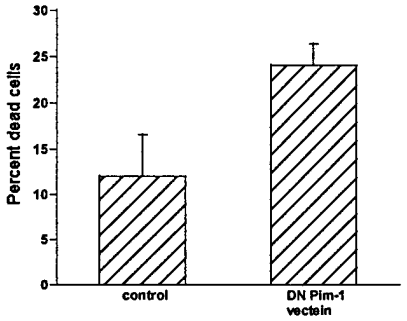

Fig. 6. Effect of DN Pim-1 vectein on FDCP1 viability. Cells were removed from IL-3 and cultured with or without DN Pim-1 vectein 150nM x 24hr. Percent dead cells were determine by Trypan Blue dye exclusion. Bar represents mean +/- SD of triplicate measurements from one of three similar experiments. Treated cultures contain significantly more dead cells than control (p<.05 for no difference, by T test)

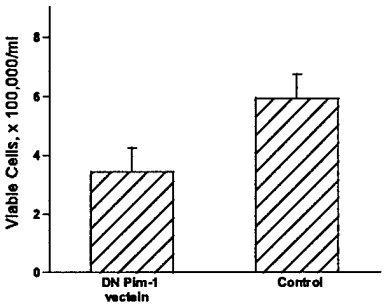

Fig. 7. Effect of DN Pim-1 vectein on FDCP1 viability. Cells were removed from IL-3 and cultured with or without DN Pim-1 vectein 150nM X 24hr. 600,000 cells per well at start of experiment. Bar represents mean +/- SD of triplicate measurements from one of three similar experiments. Treated cultures contain significantly fewer live cells than control (p<.05 for no difference, by T test)

Twenty-four hours after IL-3 removal FDCP1 cells are beginning to die by apoptosis. Cells treated with the dominant-negative Pim-1 vectein showed twice as many dead cells as were present in cultures treated with buffer controls (Fig. 6). In addition, there were half as many live cells after 24hrs in the vectein-treated wells as were present in the control cultures (Fig. 7). These data are consistent with the known effects of the dominant negative Pim-1 protein.[1] Although our primary goal is to enhance survival with a wild-type Pim-1 vectein this result is important because we show for the first time that a biologically active vectein can be delivered to murine hematopoietic cells in culture.

Specific Aim #3. Develop novel vector sequences that may confer on vecteins the ability to accumulate at different intracellular locations. There were two goals of this specific aim. The first was to develop a vectein expression plasmid for enhanced delivery of proteins to the nucleus, based on our "CTCF" sequence. We have not yet produced this plasmid. We now feel it may be more efficient to develop a "modular" system for assembly of cell-permeable proteins, rather than creating multiple different expression plasmids for different vector systems. Studies for this purpose are proposed under the 02 year application.

The other goal was to develop vector sequences for delivery of proteins or other payloads to the cell membrane. The HIV-Tat and MTS vectors utilized thus far can effect delivery of proteins to cytoplasm, and at times, to the nucleus. However, many situations may call for delivery of proteins to the cell membrane. We initially proposed to develop a membrane-targeting system by fusing to the C-terminus of a recombinant protein a hydrophobic transmembrane domain, and then an HIV-Tat penetration domain.

We initially prepared a bacterial expression plasmid for a fusion protein containing green fluorescent protein (GFP) fused on its C-terminus to the transmembrane domain of the Mil-1 protein, followed by the HIV-Tat penetration sequence (Fig. 8):

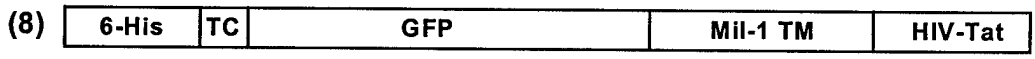

Fig. 8. Membrane-targeted vectein protein. 6-His = purification tag; TC = thrombin cleavage site; GFP = green fluorescent protein; Mil-1 TM = 23aa transmembrane domain of Mil-1 protein; HIV-Tat = cell penetration domain.

Unfortunately, like the Tat/Bcl-2 fusion protein, which has an endogenous transmembrane domain at the C-terminus, the GFP/Mil-1/Tat fusion was toxic to bacteria, resulting in no expression. Thus we were required to develop an alternate test system.

The alternative test system has utilized a pair of fluorescein-labelled synthetic peptides, Tat-FITC and Mil-Tat-FITC.

FITC – YGRKKRRQRRR (= Tat-FITC)

FITC – SILLFGGAAAVAILAVAIGVALALYGRKKRRQRRR (= Mil-Tat-FITC)

The first is the known 11-amino acid HIV-Tat vector or cell-penetration domain of HIV-Tat[4]. The latter is a fusion between that sequence (at the C-terminus) and the transmembrane domain of Mil-1, a recently described mitochondrial protein. Our hypothesis is that the Tat domain acts as an "arrow" to penetrate the plasma membrane, while the Mil-1 transmembrane domain would act as a "stopper" to hold the protein in the membrane and prevent transmembrane passage.

To evaluate the ability of these peptide vectors to localize to the cell membrane, or to effect delivery of a large protein "payload" in an oriented manner to the cell membrane,

we prepared complexes of the peptides with a monoclonal antibody to fluorescein (anti-FITC; Sigma). One microliter of peptide (approximately 1 microgram) in 0.1% acetic acid was mixed with 10 microliters Tris buffer (pH 8.0) and 10 microliters of anti-FITC (as ascitic fluid), followed by a 10 min incubation at room temperature. The sample thus contained both free peptide (MW about 1700) and peptide complexed with anti-FITC antibody (MW about 150,000). LNCaP prostate cancer cells were previously grown in 6-well plates on coverslips. The peptide/antibody complexes were then added to the cells in 2ml of RPMI-1640 medium with 0.1% BSA, followed by incubation at 37°C for 1hr. The coverslips were then washed extensively with PBS, followed by fixation in cold methanol. After a PBS rinse the coverslips with treated LNCaP cells were then incubated with PBS/0.1% BSA to block non-specific protein binding sites, followed by incubation with an anti-mouse IgG-phycoerythrin conjugate. After a final wash, the coverslips were dried and mounted for fluorescent microscopy.

Cell treated with Tat-FITC/antibody mixture showed both nuclear and cytoplasmic green fluorescence (Fig. 9) demonstrating that the peptide was able to penetrate all regions of the cell. The nuclear staining was much more prominent however. When the same field was examined for red fluorescence (reflecting the presence of the peptide-antibody complex) only cytoplasmic staining was seen. Thus the Tat vector domain was able to effect intracellular delivery of a protein complex of at least 150kd. The peptide vector sequence was unable to deliver a protein of this size to the nucleus however.

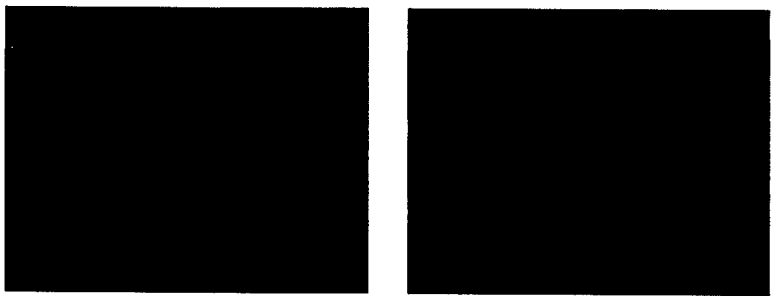

Fig. 9. Uptake of FITC-Tat/anti-FITC complexes in LNCaP cells. Left panel: green fluorescence; Right panel: Red fluorescence. Free peptide (green only) localizes primarily in the nucleus, while peptide/antibody complexes (red and green) localize in a granular pattern in the cytoplasm.

The Mil-Tat-FITC peptide showed markedly different behavior (Fig. 10). Staining of the cells was primarily localized to cell membrane and intracellular granular structures

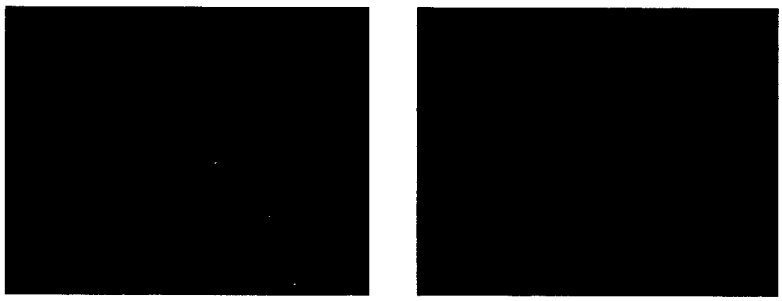

Fig. 10. Uptake of FITC-Mil-Tat/anti-FITC complexes in membranes and organelles of LNCaP cells. Free peptide and peptide/antibody complexes localize primarily on the plasma membrane. Lesser amounts of free peptide or complexes are found in intracellular structures resembling Golgi or lysosomes.

suggestive of lysosomes or golgi. The peptide-antibody complexes showed a higher proportion of membrane staining, and lower accumulation in granular intracellular structures. Nuclear accumulation was not seen with either peptide or peptide-antibody complexes. These data demonstrate the feasibility of delivering exogenous peptides or proteins, which contain the proposed membrane targeting structure, to the cell membrane and membrane-bound intracellular structures. The appearance of the complexes in lysosome-like granules also suggests that membrane-bound exogenous proteins are internalized in part through endocytosis. These data also demonstrate that non-peptide structures in the construct—such as the bond between the FITC molecule and its antibody—do not prevent internalization.

CONCLUSIONS

Substantial progress has been made in the first six months towards achieving the stated goals. Development of methods to regulate cell behaviour or function by exogenous, cell-permeable proteins ("vecteins") remains an attractive goal which would bypass the major problem of gene therapy—inefficient delivery of the genetic material and expression of the transgene in the target cells. While cell-permeable proteins would not be suitable for all applications, they are particularly attractive for *ex vivo* use. Our application of these technologies to reversible immortalization of hematopoietic stem cells still shows significant promise.

Our initial efforts in this field have clarified several issues to be resolved. First is the need for a modular system for assembling recombinant proteins with various vector domains. We have had to produce several bacterial expression plasmids for relatively minor changes in the final protein product. We envision the need for a system of

semisynthesis, whereby a recombinant protein can be fused to any of several synthetic peptides encoding potential vector sequences. Possible approaches to the development of this system will be outlined in the proposal for 02 year funding. Second, an additional insight from our extensive modification of the dominant-negative Pim-1 vecteins is that simply rearranging the pieces of the vectein construct, or fusing to a soluble partner, is unlikely to completely solve problems of aggregation and precipitation. Thus additional attention to purification and expression procedures which increase the amount of soluble protein may be helpful. Exploration of additional fusion partners could be useful in this regard, but at lest some traditional partners such as glutathione-S-transferase or thioredoxin may have biologic activities when introduced into mammalian cells. Furthermore we have noted a strong tendency for multiple aborted sequence proteins being produced from GST fusions, leading to the possibility of a mixture of active and inactive vecteins. This could obscure any biologic effect. A serious consideration will also need to be production of reagents in insect or mammalian cells, where the lower production may be offset by higher biologic activity.

During the next six months we expect to complete studies under specific aims #1 and #2 of the funded proposal—to produce and evaluate a prototype vectein which has biologic activity toward inhibiting the death or differentiation of hematopoietic cells in culture. These studies will utilize kinase-active as well as the kinase-inactive forms of Pim-1 vectein. Many potential target molecules, which regulate death or differentiation, are being identified. We may need to evaluate additional molecules as well. Nevertheless, the practical experience which we expect to gain from the *pim-1* model will be highly valuable as we explore other, more relevant regulatory vecteins to achieve our ultimate goal of expanding hematopoietic stem cells *ex vivo*.

Our studies of membrane-targeted vecteins (specific aim #3b) may also be useful for our ultimate goal of reversible immoralization of hematopoietic progenitor cells. We envision introducing transforming proteins into progenitors. Several potentially transforming proteins are localized to the cell membrane; hence, development of tools to deliver a vectein to either side of the plasma membrane may allow us to use a wider spectrum of molecular tools to achieve reversible immortalization of stem cells. In addition membrane-targeted exogenous proteins could be extremely useful for modifying cellular immunogenicity or susceptibility to viral gene transfer.

REFERENCES

1. Lilly M, Sandholm J, Cooper JJ, Koskinen PJ, Kraft A: The PIM-1 serine kinase prolongs survival and inhibits apoptosis- related mitochondrial dysfunction in part through a bcl-2-dependent pathway. Oncogene 18:4022, 1999

2. Hawiger J: Cellular import of functional peptides to block intracellular signaling. Curr Opin Immunol 9:189, 1997

3. Fawell S, Seery J, Daikh Y, Moore C, Chen LL, Pepinsky B, Barsoum J: Tat-mediated delivery of heterologous proteins into cells. Proc Natl Acad Sci U S A 91:664, 1994

4. Nagahara H, Vocero-Akbani AM, Snyder EL, Ho A, Latham DG, Lissy NA, Becker-Hapak M, Ezhevsky SA, Dowdy SF: Transduction of full-length TAT fusion proteins into mammalian cells: TAT-p27Kip1 induces cell migration. Nat Med 4:1449, 1998

PATENTS/INTELLECTUAL PROPERTY

Because only the first six months of the project have been completed, no public disclosure of our findings has been made or is planned at this time. Thus, no patent application has been filed regarding an invention emerging from this research. However, we feel that the potential commercial uses of our method for membrane targeting of exogenous proteins could represent a substantial intellectual property once the technology is more fully developed and evaluated. We will contact NMTB for permission to disclose our findings and request that Loma Linda University seek patent protection as soon as we obtain sufficient data to fully describe the invention and its best method of use. We anticipate that the filing of a provisional US patent application could occur during the second year of the project.

COMMERCIALIZATION

Development of techniques for reversible immortalization of stem cells are of great potential interest to companies in the field of cell-based therapies. Refer to the 02 year proposal for more details. Several biotechnology companies could be interested in a general method for delivering exogenous proteins to cell surfaces. Immediate applications could include increasing the number of receptors for gene-transfer viruses, thus enhancing the gene transfer efficiency.

PUBLICATIONS

No publications have resulted from the initial 6 months work on this project.

2. DESCRIPTION AND PERFORMANCE SITES (FORM B)

DESCRIPTION: State the goal of the research project, including how it relates to improving health care for the nation's people. Use succinct language to describe how the project goals will be achieved. Do not exceed the space provided on this page.

The treatment of disease with radiation therapy requires beams that enter the patient from multiple directions. Mechanical devices, including those used to deliver radiation, flex when rotated. The most time consuming and costly process in the delivery of radiation beams is the alignment of each beam with the patient. The quality of alignment directly influences the success of the treatment because precise alignment can separate diseased tissue from critical normal tissues. When good separation is achieved, high doses can be delivered to the target and small doses to normal tissue. This leads to high cure rates and minimal treatment related complications. If the time for alignment can be reduced, the comfort of the patient will increase and better alignment can be achieved. Reduced alignment times will also increase the number of patients per day that can be treated, reducing the cost per patient and ostensibly allowing more patients to take advantage of the treatment modality.

The purpose of this work is to achieve better alignment of radiation treatment beams while reducing overall treatment times. Two methods have been proposed to automatically compensate the position of the patient for each beam without requiring a new alignment procedure to be performed. The first method utilizes precise mechanical measurements of the delivery system at different positions made prior to patient treatment to predict the necessary compensation. The second method utilizes sensor measurements of the delivery system made during patient treatment. This project will acquire the measurements required by the first method and investigate the technology required for the second method. The ability to compensate will be tested by building a computer-driven test platform and test jigs to simulate patient treatments. At the end of the project, the preferred method of data acquisition and specifications for a clinical patient positioner will be provided.

PROJECT SITE(S) (organization, city, state):

Applicant organization:
Department of Radiation Medicine
Loma Linda University Medical Center
Loma Linda, California

Sub-contract organization to build test devices:
Optivus Technology, Inc.
San Bernadino, California

NMTB Second Semi-annual Report

COPY

Document Name: NMTB_ann.doc

Project: Computer Compensated Positioning for Multiple Field Alignment

Sub-agreement Number: 19-FY98-LLU-MOYERS

Period: January 26, 1999 through January 25, 2000

Principal Investigator: Michael F. Moyers, Ph.D.
Radiation Medicine

Michael F. Moyers

Date Prepared: February 24, 2000

Telephone: 909-478-4552
Facsimile: 909-824-4083
e-mail: moyers@proton.llumc.edu

I. Introduction

The hypothesis of this project is that better alignment of radiation treatment beams can be achieved while simultaneously reducing the time for a treatment session. In the clinic, this could be accomplished by automatically repositioning the patient to compensate for rotation induced deflections in the beam delivery equipment. This project will test the hypothesis by measuring beam delivery deflections, building a highly precise computerized positioning platform, developing a compensation algorithm and user interface, and measuring the ability of the total system to correctly align a test jig. Application of this method to patients will require registration and immobilization devices that complement the positioning device and thus models of new devices will also be made.

II. Body

The project described in the introduction can be broken into six distinct projects or specific aims.

II.1 Measure and Analyze Beam Delivery Equipment Deflections

Notwithstanding the better treatment that occurs when a radiation beam is accurately aligned with a patient, the alignment process is a major cost in delivering radiotherapy. The large amount of time invested by both therapists and physicians in aligning patients prevents large numbers of patients from receiving treatment and makes the treatments for those patients that are treated expensive. More efficient methods of aligning patients with beams can not currently be used because of: 1) differential sag in the gantry/nozzle system when rotated to different positions; 2) skew in the snout when extended or retracted from the reference position; 3) fabrication of the beam defining aperture; 4) installation of the aperture at the appropriate position in the snout; 5) positioning of the x ray tube on the central axis of the proton beam when preparing to make an exposure; and 6) differential sag in the image receptor system when rotated to different positions. This project measured the errors that would be produced by items 1 and 2 using a surveyor's theodolite and a dial indicator. The fabrication of the aperture for each patient's portal, item 3, is always checked before use. Current operating procedures check item 5 once each day at one gantry angle while item 6 is believed to be predictable.

The procedure for measuring the radial component of item 1 was previously described in a manuscript submitted with the grant application. Before performing the set of measurements in this study, the theodolites were sent for re-calibration. Scale illumination packages were also installed on the theodolites which made the collection of data much easier and faster in the dimly lit treatment room. Results from the gantry #2 measurements yielded the same general shape as the previous

measurements on gantry #1 with an overall size approximately the same. Initial analysis of the data indicate that any point along the path of the radial component can be predicted within 0.4 mm.

The axial component of the isocenter path was measured with a dial indicator. The path found for gantry #2 was almost identical to gantry #1. Any point along the path of the axial component can be predicted to within 0.3 mm using general gantry data while data specific to a particular gantry could be used to predict the path within 0.2 mm.

The sag of the snout was investigated for different aperture weights at 90° and 270° gantry angles. As long as the brakes were applied to the snout extension ballscrews, gantry rotation did not result in more than a 0.05 mm deviation of the frontpointer. When the brakes were released and the gantry rotated 180°, a deviation of 0.1 mm was observed. This deviation was correlated with a change in the difference between the encoders reading out the position of the ballscrews. The difference in encoder readings, referred to as delta snout, could be used to calculate the change in the beam pointing direction for different extensions and gantry angles.

II.2 Investigate Sensor Technology

Five different uses of sensors for increasing the accuracy of patient alignment were identified. These included: 1) measuring the deflection of the cone relative to the gantry/nozzle frame; 2) measuring the position of the aperture cone in the room; 3) measuring the position of the cone relative to the patient; 4) measuring the position of the patient positioner in the room; and 5) measuring the position of the patient in the room. A number of different sensor technologies were reviewed. These included systems using optical cameras, radiofrequency, ultrasound, magnetic, and laser ranging sensors. Severe doubt is cast upon the use of magnetic systems due to the stray magnetic fields produced by the large beam transport magnets. Representatives from a company specializing in radiosurgery treatments came to Loma Linda to present their multiple optical camera system for realignment. None of the systems have matured to the point of being readily available for multi-field patient alignment. Use of any of the sensor systems would require an extensive research and development project. As discussed in section II.1, the encoders already installed on the snout extension ballscrews appear to offer a quick and inexpensive solution to predicting the snout skewness and aperture projection.

II.3 Design and Build Test Platform

The funding allocated to this project was smaller than the amount initially requested so, in order to complete the project, funds from another project are being used to purchase the hardware for the test platform. The Henry Guenther Foundation is supporting an effort to develop proton

treatments for Parkinson's disease and other functional disorders. These types of treatments require a rotational capability not available with the current patient positioners. A major fraction of the funds for the Guenther grant are being used to purchase a new positioner with rotational capabilities. In exchange for the funds for the test platform, this NMTB grant was used to develop the specifications for the new positioner. The test platform will be an integral aspect of the new positioner but its use for compensating deflections in the beam delivery system is not required and, in fact, not allowed until extensive testing has proven its usefulness and reliability.

A survey of potential manufacturers was performed and specifications for a positioner negotiated. Precitron AB of Uppsala, Sweden was found to have a device that could serve both as the new patient positioner and, with modifications, as a base for the test platform. This device, called the Hercules, is an FDA approved patient positioner. A drawing of this device is included in Appendix 1. The specifications developed under this grant for the modified device are also included in Appendix 1 along with a conceptual drawing of the new positioner. Before the order was finalized, an invention disclosure was made with LLU and an agreement with Precitron reached over potential intellectual property rights. Because a large amount of funds from another project were being allocated to the purchase of the positioner, numerous committee meetings were held during 1999 in order to satisfy all parties involved. The purchase order was released the last week of December 1999 with delivery of the positioner expected in June of 2000. Initial testing of associated registration and immobilization devices is expected to proceed in a test location during the summer of 2000 with final installation in the treatment room expected in the fall of 2000.

II.4 Develop Compensation Algorithm and User Interface

The control system of the positioner will be broken into two sub-systems, a coarse base part and a fine alignment part. Although the two sub-systems will communicate, they will have separate electronic controllers. The coarse base sub-system will not be modified locally so as not to effect the FDA approval of the product. This component will be used by the therapists in the treatment room in much the same manner as the current positioner except for its increased range of motions. The fine alignment sub-system will come from the manufacturer with a basic set of commands but the user interface and compensation algorithm will be developed locally. Because the motions of the fine alignment subsystem are small, slow, and do not change the intended purpose of the device, no additional FDA application is anticipated.

Small orientation errors inevitably occur during the patient alignment process. These errors can, in general, be corrected by small

rotations of less than 5° in pitch, roll, and yaw. The fine alignment sub-system has rotational capabilities in the pitch and roll directions. The base sub-system has a yaw capability. Restrictions on the height of the table top above the floor and the desire to simplify the logic in aligning patients drove the design of the fine alignment sub-system. A decision was made to force the correction of rotational alignment errors in the patient's orientation to be made first and afterwards perform the fine translational movements necessary to correct the positioning errors. This allowed the fine translational movements to be independent of the pitch and roll adjustment mechanisms. Philosophically, all rotations will be made by the coarse (base) sub-system although, technically, the pitch and roll are controlled by the fine alignment sub-system. Fine translational movements for initial alignment or beam delivery system deflection compensation will then be limited to the alignment sub-system.

The deflection compensation algorithm will reside wholly on the fine alignment sub-system although it must receive information from the base sub-system to understand its location and orientation within the treatment room. The Department of Radiation Medicine has requested that the user interface for the alignment sub-system also be capable of allowing the therapists to make small controlled moves even when the deflection compensation algorithm is not being used. A user interface has thus been designed to accommodate both purposes. An automatic positioning capability has also been included to reduce initial set-up time. A picture of the proposed user interface, written in Visual C++, is included in Appendix 2. Detailed design of the low level compensation software must wait until the vendor of the positioner supplies the motion driver software.

II.5 Test Compensation for Alignment

The positioner will initially be installed in a test location rather than in the treatment room. The control system, user interface, and deflection algorithm will be tested at this location for functionality and safety. Registration and immobilization devices currently under use as well as possible new devices (see section II.6) will also be fitted during the time testing is being performed at this location. The positioner will likely remain at this location from three to four months. After the initial testing and fitting is complete, the positioner will be relocated to the Gantry 2 treatment room. The theodolites will be used to acquire data that will be input into the positioner control system to correct for deviations as the positioner translates and rotates around the room. The compensation tests will then be performed with the real deflections from the gantry and snout. A standard five mm diameter tungsten ball pointer used for stereotactic radiosurgery alignment checks has been bought using funds from the Guenther Foundation. This ball will be positioned at the virtual isocenter to simulate a target point within a patient. The proton beam will then be directed at

the ball from different directions to verify correct compensation by the alignment algorithm. Still to be manufactured is a small, precisely milled brass aperture that will collimate the proton beam to a circular field with a diameter just slightly larger than the ball. The alignment of the ball shadow with the outside of the proton field from each direction will indicate the ability of the algorithm to correctly compensate the deflections. Testing of the compensation algorithm should be completed by February 2001.

II.6 Registration and Immobilization

The precise multi-field alignment technique can only be advantageous if better registration and immobilization of the patient to the positioner is also performed. Several conceptual models of registration and immobilization apparatus for targets in the pelvis and head have been built. The key feature to each of these devices is that perturbation of the proton beam in transit to the patient is kept to a minimum. A seminar was given to the Department of Radiation Medicine in August of 1999 to present these new devices. A copy of the overheads presented at this seminar and a few pictures of the devices are included in appendix 3. Current effort in this area is directed towards finding an industrial partner to help fund further development.

III. Conclusions

Preliminary data indicate that the error in patient alignment using an efficient multi-field technique can be reduced from the current 2 mm value to 0.5 mm by utilizing a predictive model for deflections and computerized repositioning of the patient. The delay in approval of the new positioner purchase has resulted in only about half of the work scope having been performed. This translates to only half of the funds being expended. All of the major pieces to the project have now been addressed. The current proposed time frame to complete the project is approximately one year but no additional funds beyond what has already been allocated will be required. Further development of registration and immobilization devices to a prototype stage, not in the original proposed scope of work, would require additional funds or industrial partners.

Appendix 1

Diagram of standard Hercules patient positioner.

Patient Positioner Requirements- Modifications for Hercules Solution

Conceptual drawing of modified Hercules positioner with alignment sub-system

HERCULES
Side view with hand pendant and arms for position readout

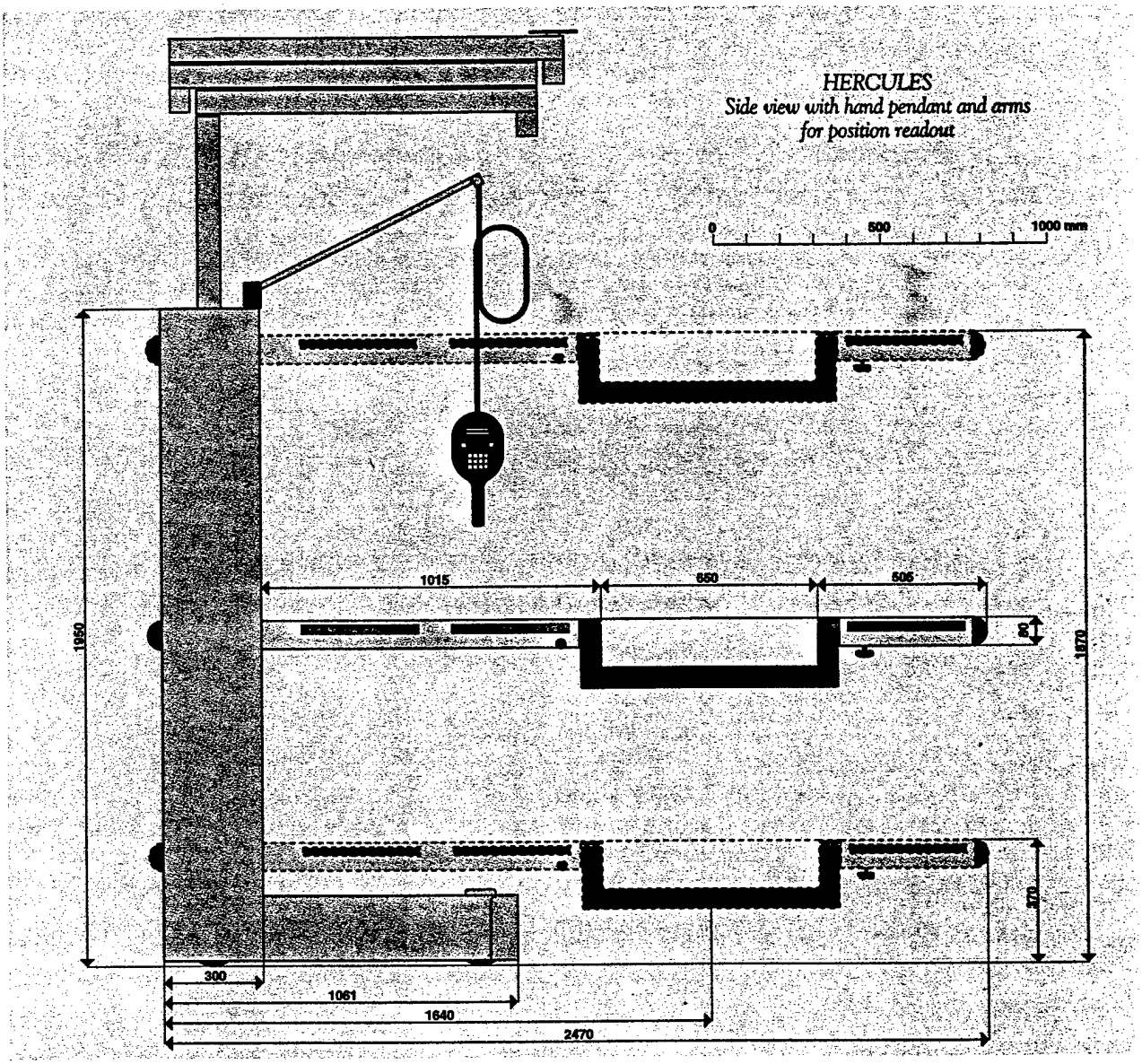

HERCULES
Top view with hand pendants and arms for position readout

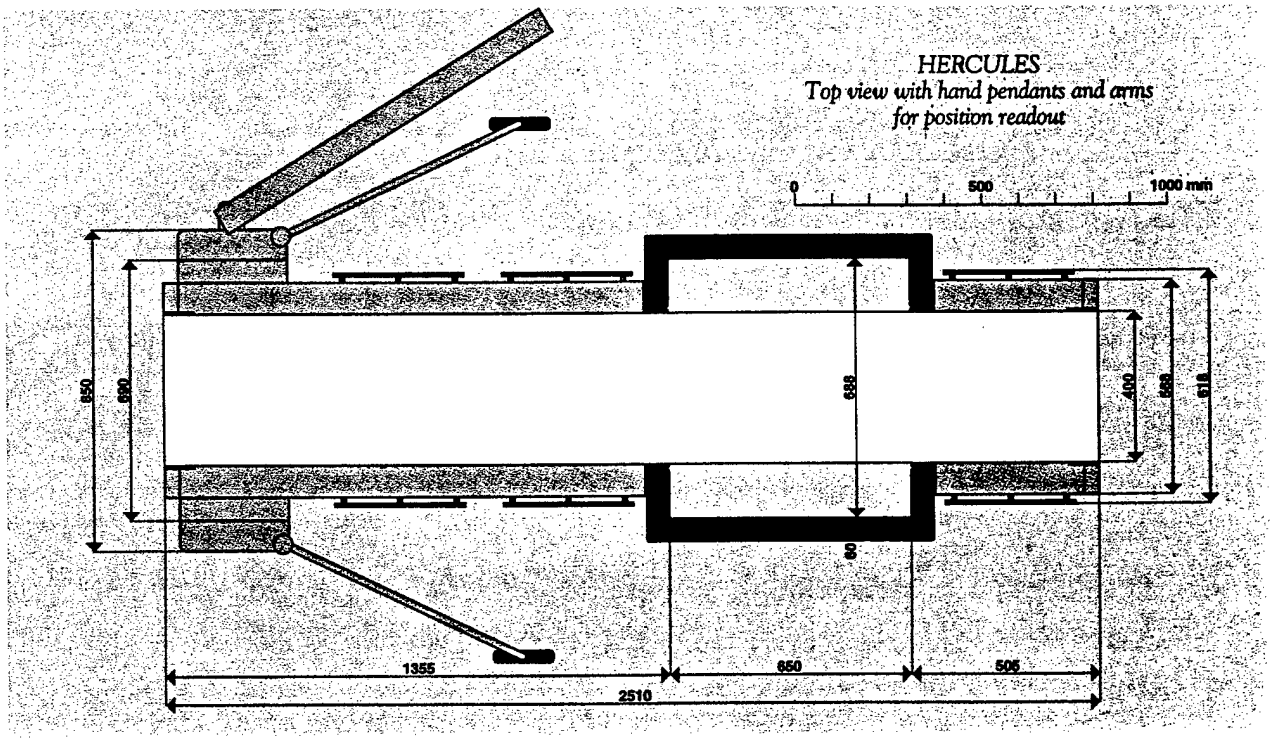

Patient Positioner Requirements - Modifications for Hercules Solution

document: PPS-Rqrmnts.doc; 17-Feb-99; MFM
revised: PPS-Rqrmnts.doc; 23-Jun-99; MFM
revised: PPS-Rqrmnts.doc; 5-Aug-99; MFM

Introduction

The patient positioner (PP) shall consist of two subsystems. The base subsystem will provide coarse moves to facilitate loading and registration of the patient and to locate the patient at the treatment position in the room. The alignment subsystem will provide adjustments in the patients position to properly align the patient with the proton beam. This alignment is performed using information from the imaging system and knowledge about the mechanics of the beam delivery system.

1. Base Subsystem Translational Capabilities

1.1 The base subsystem shall support movements in the lateral, longitudinal, and vertical directions.

1.2 The minimum distance for which a translational movement can be made shall be 0.5 mm or less.

1.3 The resolution of the position readout for all translational movements shall be 0.1 mm or better.

1.4 The accuracy of the position readout in room coordinates for all translational movements shall be 1.0 mm or better.

1.5 The reproducibility of position readout in room coordinates for all translational movements shall be 0.5 mm or better.

1.6 The reproducibility of achieving a requested position in room coordinates for all translational movements shall be 0.5 mm or better.

1.7 Motion perpendicular to a commanded motion (tracking) shall be less than 0.001 of the commanded distance or 1 mm, whichever is greater.

2. Base Subsystem Rotational Capabilities

2.1 The base subsystem shall support a rotational movement about a vertical axis located between the lifting columns.

2.2 The base subsystem shall support a rotational movement about a vertical axis located by the user at an arbitrary location within the room (subject to envelope of base subsystem). This motion must simulate a rotation about the isocenter of the proton gantry of at least ±55°. This type of rotation is referred to as yaw.

2.3 The minimum angle for which a rotational movement can be made shall be 0.1° or less.

2.4 The resolution of the angular readouts for rotational movements shall be 0.1° or better.

2.5 The accuracy of the angular readouts for rotational movements shall be 0.5° or better.

2.6 The reproducibility of the angular readouts for rotational movements shall be 0.1° or better.

2.7 The reproducibility of achieving a requested angular position for all rotational movements shall be 0.5° or better.

3. Alignment Subsystem Translational Capabilities

3.1 The alignment subsystem shall support movements of ±20 mm in the lateral, longitudinal, and vertical directions.

3.2 The lateral and longitudinal motions of the alignment subsystem shall be parallel to the floor (horizontal in the room coordinate frame).

3.3 The vertical motion of the alignment subsystem shall be perpendicular to the floor (vertical in the room coordinate frame).

3.4 The minimum distance for which a translational movement can be made shall be 0.05 mm or less.

3.5 The resolution of the position readout for all translational movements shall be 0.01 mm or better.

3.6 The accuracy of the position readout relative to the base system for all translational movements shall be 0.05 mm or better.

3.7 The reproducibility of position readout in room coordinates for all translational movements shall be 0.05 mm or better.

3.8 The reproducibility of achieving a requested position in room coordinates for all translational movements shall be 0.05 mm or better.

3.9 The acceleration and deceleration for traveling the 40 mm stroke length should not result in an alteration of the patient's location or orientation relative to the tabletop.

4. Alignment Subsystem Rotational Capabilities

4.1 The alignment subsystem shall support a minimum ±5° rotational movement of the table top about a horizontal axis parallel to the longitudinal axis of the table top and located by the user at an arbitrary location within the vertical boundaries of the table top. This type of rotation is referred to as roll.

4.2 The alignment subsystem shall support a minimum ±5° rotational movement about a horizontal axis perpendicular to the longitudinal axis of the table and located by the user at an arbitrary location within the vertical boundaries of the table top. This type of rotation is referred to as pitch.

4.3 The minimum angle for which a rotational movement can be made shall be 0.1° or less.

4.4 The resolution of the angular readouts for rotational movements shall be 0.1° or better.

4.5 The accuracy of the angular readouts for rotational movements shall be 0.2° or better.

4.6 The reproducibility of the angular readouts for rotational movements shall be 0.1° or better.

4.7 The reproducibility of achieving a requested angular position for all rotational movements shall be 0.1° or better.

5. Table Top

5.1 The table top of the PP shall have a an adjustable C-arm configuration to allow unobstructed access of proton beams to the patient from any direction.

This requirement does not allow the presence of a polyester or Mylar belt that is a standard feature of this table.

5.2 An insert shall be provided for the table top of the PP to support a full scanning water phantom above the C-arm opening. This table insert shall support a minimum weight of 135 kg. The insert will register in a single position and be securely fastened.

5.3 The center of the C-arm area shall be located a minimum of 942 mm from the closet approach of the base legs.

This is an extension of 363 mm to the standard location.

5.4. The vertical motion of the table top shall allow the top of the table to have a maximum elevation above the floor of at least 914 mm and a minimum elevation above the floor of no more than 530 mm.

6. Registration and Immobilization Devices

6.1 An attachment interface shall be provided for whole body pods. (Pods shall be supplied by the customer.)

6.2 An attachment interface shall be provided for a face mask/head pod.

6.3 An attachment interface shall be provided for a foam cradle.

6.4 An attachment interface shall be provided for a cranial ring.

6.5 An attachment interface shall be provided for a maxilla vacuum lock.

6.6 Exchange of registration and immobilization devices shall be accomplished by one person in less than 5 minutes.

6.7 All immobilization and registration devices must be compatible with XCT and MR imaging.

7. Control Interface

7.1 All positions will be displayed both in the treatment room and in the treatment control room.

7.2 The display of the positions will be updated at a frequency no less than once per second.

7.3 Control over all motions will be possible both in the treatment room and in the treatment control room.

7.4 Motion enable buttons will be supplied both in the treatment room and in the treatment control room.

7.5 Emergency off buttons will be supplied both in the treatment room and in the treatment control room.

7.6 A built in command for the alignment subsystem should be "go to center". This command should be performed before the initial set-up of each patient.

7.7 A built in command for the base subsystem should be "point wheels toward isocenter". This command should be performed before fine alignment for extended field segmental therapy.

7.8 A built in command for the base subsystem should be "point wheels for isocentric rotation". This command should be performed before fine alignment for multiple angle segmental therapy.

7.9 A built in command for the both the base and alignment subsystems should be "set isocenter coordinates". This command should be performed before fine alignment.

8. Delivery and Installation

8.1 The PP will be delivered and installed at a test site for development and testing of the alignment compensation algorithms. Final installation in the treatment room will occur only after all registration

and immobilization devices have been tested and alignment algorithm tests have passed.

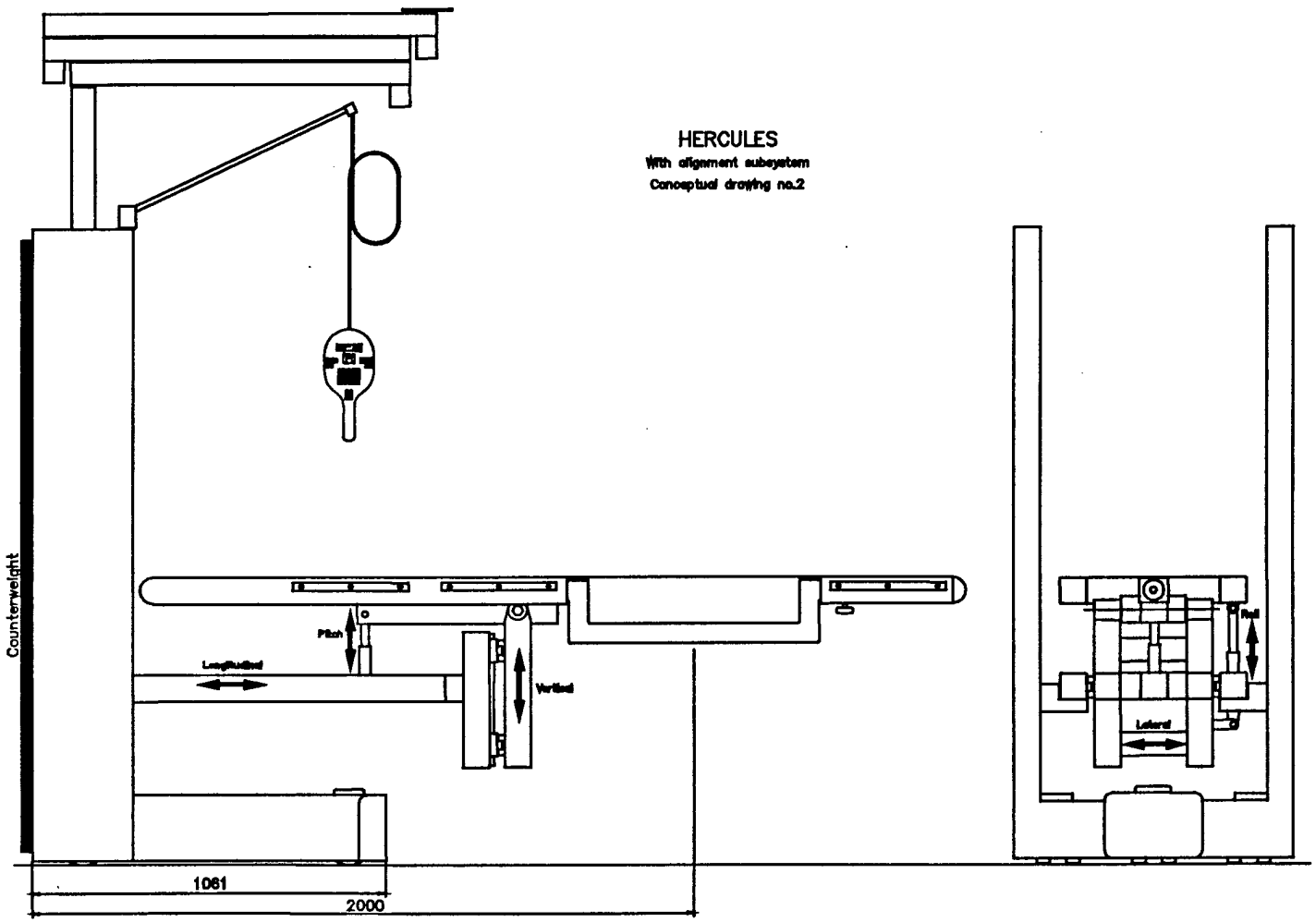
HERCULES
With alignment subsystem
Conceptual drawing no.2
Counterweight
Pitch
Longitudinal
Vertical
Roll
Lateral
1061
2000

Appendix 2

Picture of user interface for patient positioner.

Proposed procedure for patient alignment entitled "Phased Approach to Beam Alignment".

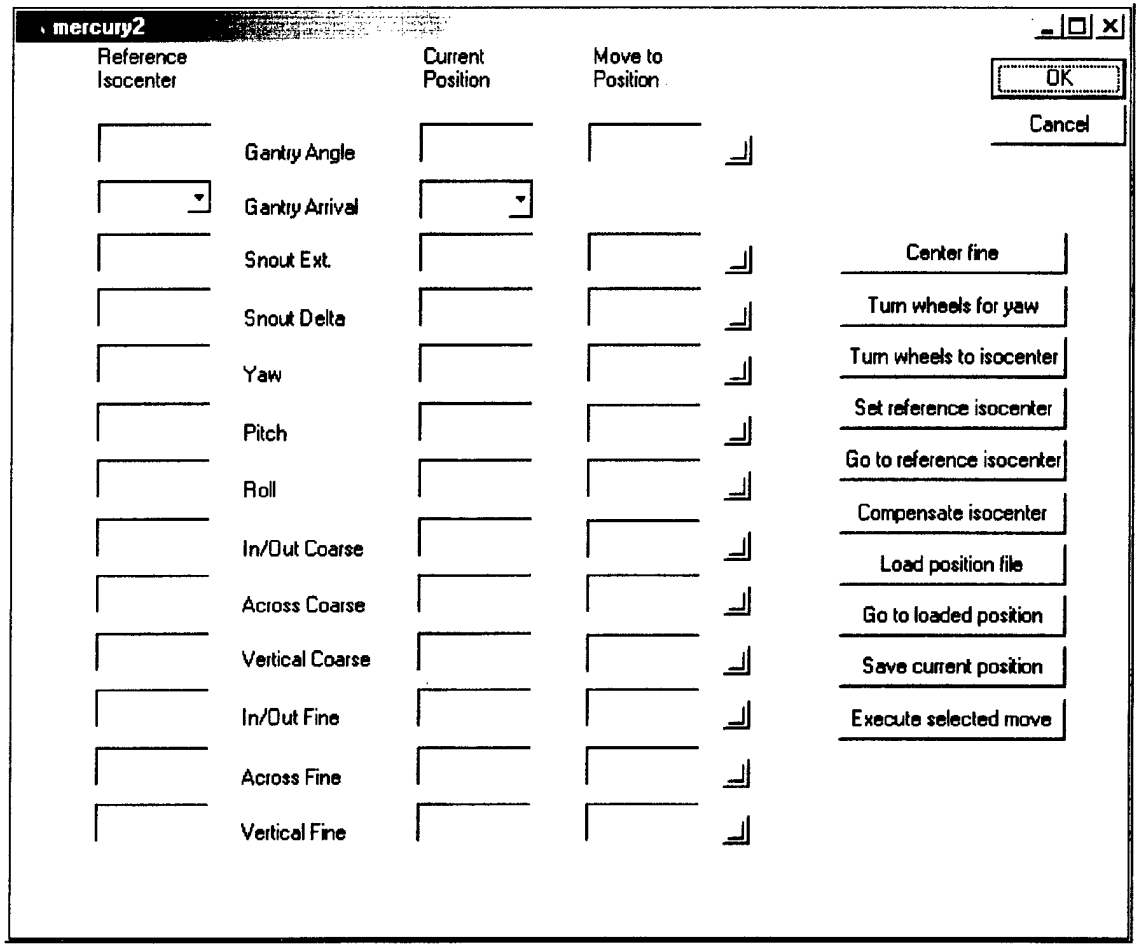
mercury2
Reference Isocenter
Current Position
Move to Position
OK
Cancel
Gantry Angle
Gantry Arrival
Snout Ext.
Snout Delta
Yaw
Pitch
Roll
In/Out Coarse
Across Coarse
Vertical Coarse
In/Out Fine
Across Fine
Vertical Fine
Center fine
Turn wheels for yaw
Turn wheels to isocenter
Set reference isocenter
Go to reference isocenter
Compensate isocenter
Load position file
Go to loaded position
Save current position
Execute selected move

Phased Approach to Beam Alignment

document: AlnAprch.doc
revised: 13-Feb-00; MFM

1. The snout is retracted to avoid a possible collision with the patient or equipment and the gantry is rotated to a beam delivery angle of 0°.

2. The fine alignment system of the patient positioning system (PPS) is centered.

3. The patient is registered to the PPS using an appropriate registration device.

4. The patient is immobilized on the PPS using an appropriate registration device.

5. Using the PPS base sub-system, the patient is moved to place the target within the patient within a few centimeters of the virtual isocenter of the gantry. The orientation of the PPS at this time should roughly match the prescribed orientation.

6. The patient's position file, previously generated, is loaded.

7. The base sub-system is commanded to go to the loaded position thereby placing the target within the patient within a few millimeters of the virtual isocenter.

8. The base sub-system is commanded to either "turn wheels for yaw" or "turn wheels to isocenter" dependent upon the anticipated move required to align the next field.

9. A localization x ray picture is taken. The gantry is rotated to 90°. Another x ray picture is taken.

10. The patient alignment algorithm computes the discrepancy between the current location and orientation of the patient and the prescribed location and orientation.

11. Upon verification and activation of the enable switch, the fine alignment sub-system automatically rotates and translates the patient to correct for the difference in location and orientation. This repositioning accounts for the current table yaw angle but does not correct for yaw rotation differences. (The x ray localization system is currently not linked to the alignment system and therefore the repositioning is not now automatic.)

12. The alignment system is commanded to "set reference isocenter". This command queries the gantry rotation angle, gantry arrival direction, snout extension, snout delta, and all positioner positions.

13. The aperture and bolus are installed into the snout, the gantry rotated to the treatment angle, and the snout extended to its treatment position.

14. The therapist commands the fine alignment sub-system to "compensate isocenter". This command queries the gantry rotation angle, gantry arrival direction, snout extension, snout delta, and all positioner positions. Upon activation of the enable switch, the alignment subsystem then automatically translates the patient in all three directions to compensate for the gantry sag, gantry arrival direction, snout sag, and snout skewness.

15. Treatment beam is delivered.

16. The snout is retracted and the gantry rotated to 90°.

17. Steps 13 through 16 are repeated for each additional field.

Appendix 3

Visuals from seminar delivered to LLUMC Department of Radiation Medicine, August 25, 1999 entitled "New Devices for Registration and Immobilization".

New Devices for Registration and Immobilization

Michael F. Moyers and Roberto Arellano

Loma Linda University Medical Center
Department of Radiation Medicine
11234 Anderson St.
Loma Linda, CA 92354

supported by a grant from:
National Medical Technology Testbed

Outline

I. Goals of Project

II. Definitions

III. Head Problems

IV. Head Solutions and Model Devices

V. Potential Pelvic Mis-registrations and Solutions

VI. Pelvic Registration and Immobilization Device

VII. Future Activity

Goals of Project

improve beam alignment

decrease storage space for R/I devices

increase solid angle for beam entry

decrease perturbations of beam

decrease time for set-up

Patient alignment is the process by which a patient is reproducibly interfaced with equipment for the purposes of:

1. obtaining anatomical, morphological, or physiological information

2. performing treatment simulations

3. delivering treatments

The 4 goals for patient alignment are to provide:

1. accurate aiming of beams (targeting and avoidance)
   entry angle
   entry position

2. accurate dose delivery
   depth of beam penetration

3. unrestricted access to the patient by radiation beams
   4π geometry
   non-perturbing

4. safety and comfort of patient
   no un-natural positions or motions
   quick un-assisted egress

The patient alignment process ideally consists of five separate tasks:

1. **registration - The patient is placed on a patient positioner (PP) in a reproducible manner.**
   Generally the patient positioner is a movable table. This task is the most difficult and time consuming process in radiotherapy.

2. **immobilization - The registered patient is fixated and attached to the PP so that they move together as a single unit in a controlled fashion.**
   Sometimes true immobilization is not possible such as when allowance for breathing is necessary. Immobilization may not be needed for special techniques such as frameless radiosurgery in which the beam follows the patient movements.

3. **localization - The location of the target relative to the diagnostic, simulation, or treatment unit is determined.**
   This task can be as simple as visualizing a light field or as complex as three-dimensional radiographic triangulation.

4. **positioning - The PP is moved to place the target in the desired orientation at the desired location.**
   Patient positioners typically have three mutually perpendicular translational motions and one or two rotational motions. High precision treatments require three independent rotational motions.

5. **verification - The patient's orientation and location are verified.**
   The technique used for this task may or may not be the same technique used for localization.

Any of these five tasks may require iteration to succeed.

Example R/I Devices

Registration Devices	Immobilization Devices
standard contoured pillows	masking tape
Plaster of Paris casts	belts
fiberglass tape and resin	Velcro® straps
low density foam mold	vacuum form mold
belly boards	vacuum bead bag
scaled, multi-jointed supports	thermoplastic mold
external ring adaptor	external ring
	bite block
	rectal probe
	water, urine

Head Problems

non-custom registration

not reproducible
uncomfortable

immobilization sheet shrinkage

treatment does not match CT

limited beam access

plastic pillow
table supports
mask frame

Head Solutions

single C-arm with foam head cradle and mask

no interference for co-axial beams
no interference with anterior vertex beams
posterior vertex beams possible?

double C-arm with foam head cradle and mask

no interference for co-axial beams
no interference with anterior vertex beams
posterior vertex beams possible?

pod with foam head cradle and mask

minimal interference for co-axial beams
minimal interference for vertex beams

blue mask material

1/3 shrinkage compared to standard material
foam more comfortable to skin
less elastic

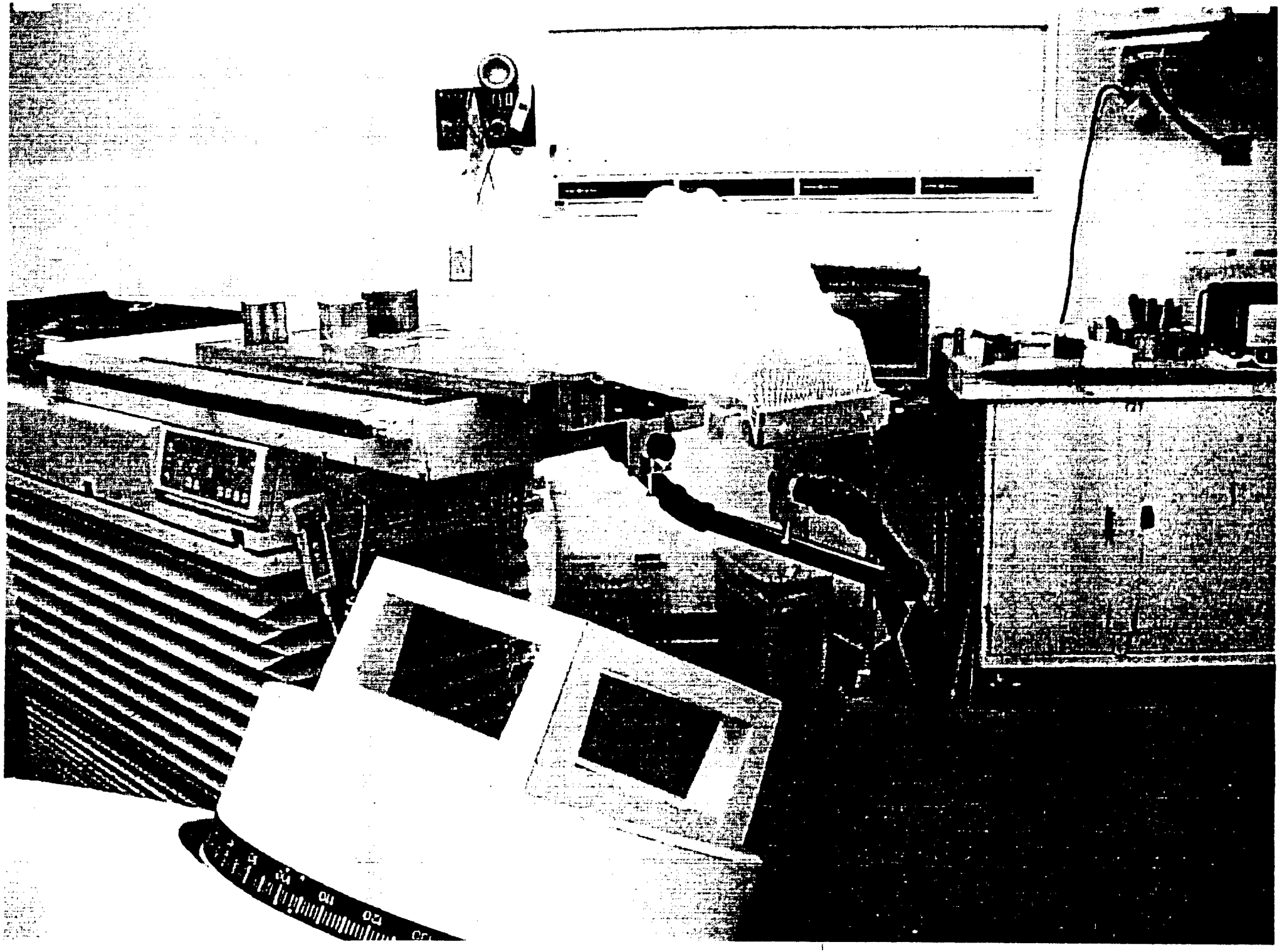

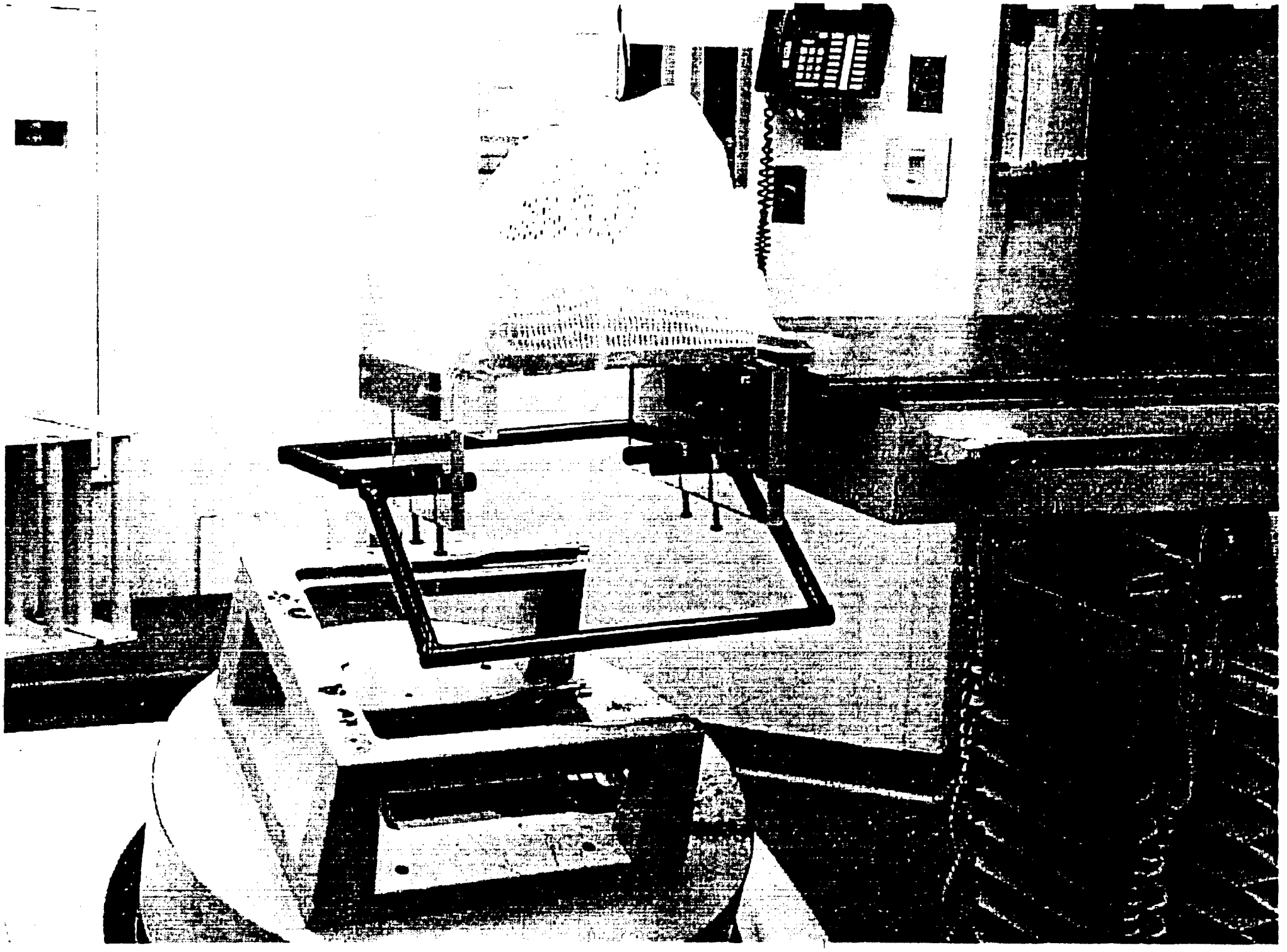

8B

Potential Pelvic Mis-Registrations and Solutions

1. body axis roll - use a knee support to provide an angulation between the femur and the spine thereby defining a plane

2. double leg roll, congruent - bend the knee to prevent roll

3. double leg roll, opposite - bend the knee to prevent roll

4. leg scissors (one up, one down) - use knee supports with the vertical positions scaled

5. leg opening (distance between knees) - use knee supports with the horizontal positions scaled

6. caudal/cranial slide - use a heel support with the longitudinal and lateral positions scaled

7. jack-knife (abdomen vs. legs) - use side panels to straighten abdomen with lateral positions scaled

Pelvis Alignment Board

Parts:
Base plate
Adjustable position foot rest slant board
Adjustable position heel cups (left and right)
Adjustable elevation knee support
Adjustable position knee rests (left and right)
Adjustable position side limit plates (left and right)
Velcro® straps at knees and feet

Advantage:
1. One device per room.

Disadvantage:
1. Limits solid angle at which beams may enter.

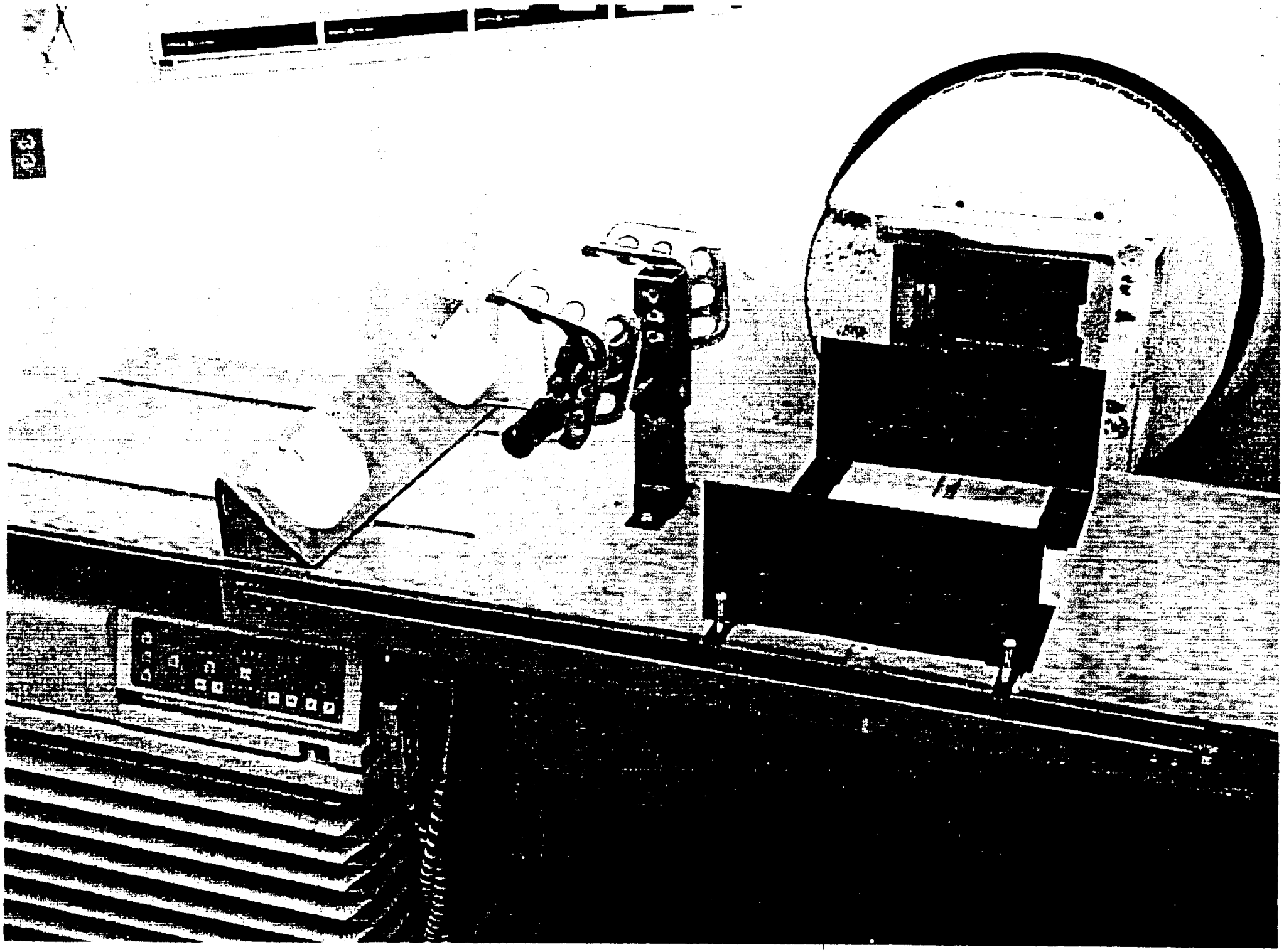

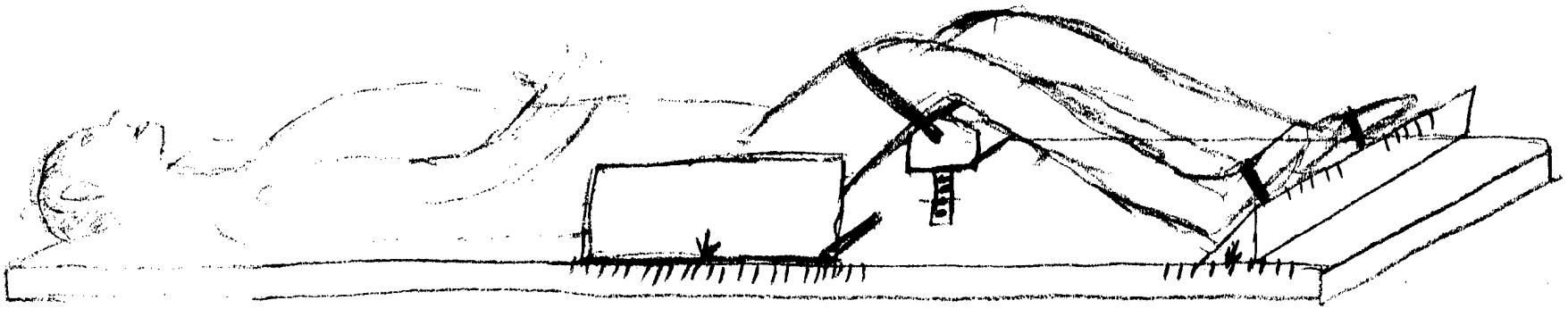

SET-UP SHEET

LL-001 Pelvis Board

Patient:_____

_____

Date:_____

Notes:_____

_____

_____

1. *Elevation*

Peg #_____

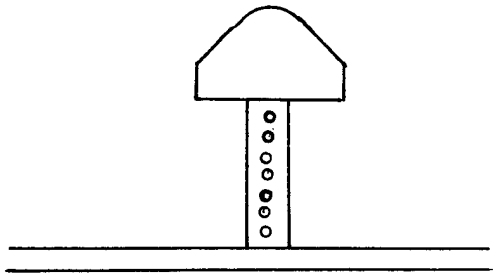

2. *Foot Rest Longitudinal*

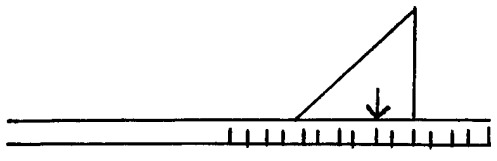

Position:_____

3. *Limit Board Left* *Limit Board Right*

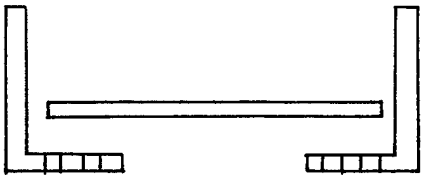

Position:_____ Position:_____

4. *Heel Cup Left* *Heel Cup Right*

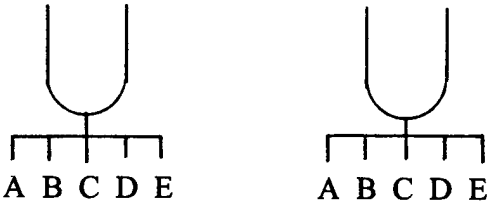

5. *Knee Rest Left* *Knee Rest Right*

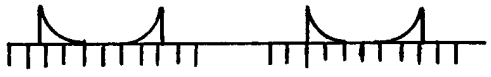

Position:_____ Position:_____

Future Activity

money to build actual devices?

industrial partners?

- Optivus Technology?
- Precitron?
- Med-Tec?
- Soule?
- Bionix?

clinical testing?

DESCRIPTION: State the goal of the project, including how it relates to improving health care. Use succinct language to describe how the project goals will be achieved. **Do not exceed the space provided.**

Morning sickness is a troublesome and at times serious condition that affects more than one million women in this country at an given moment in time. It has been little investigated and its cause remains unknown. In this application it is reported for the first time, based on new findings using the advanced technology of *thermography*, that nonshivering thermogenesis becomes active in brown adipose tissue of patients with morning sickness and then regresses as symptoms abate. There is an associated increase in thyroid hormones (thyroxine, T_3 and rT_3) and increased turnover of fatty acids. The hypothesis is put forward that the fatty acids, products of lipolysis in brown fat, known to be highly toxic when not bound to albumin, cause the nausea and vomiting, anorexic and weight loss of severe morning sickness. It is proposed to measure nonshivering thermogenesis by *thermography*, a noninvasive method, wherein infrared emission from the nape of the neck, the site shown to be thermogenic, is compared with the lower back, a quiescent region. Measurements will be made in pregnant women with symptoms, after a light carbohydrate meal, after gentle stimulation (cold exposure of the hands) and suppression of the sympathetic nervous system, after symptoms subside later in pregnancy, and after delivery and also in symptom-free pregnant and nonpregnant individuals to serve as controls. Blood samples will be analyzed for fatty acids and a number of hormones and metabolites to learn how the control of brown fat metabolism differs in pregnancy. Although a clinical trial is not proposed here, the findings will be highly relevant to the rational treatment of morning sickness.

PROJECT SITE(S) (organization, city, state):

School of Medicine
Loma Linda University
Loma Linda, California

COP U

JAN 19 2000

Year-end final Progress Report for "**Morning sickness: Investigation of cause and mechanisms by thermography**"

Gordon G. Power, MD, Principal Investigator

Subcontract #007-FY97-LLU-POWER (year 2)

This report covers the period from May 30, 1999 to November 14, 1999

Table of Contents

	Page
Introduction	3
Body	3-8
Conclusions	8
Listing of workers receiving financial support from NMTB	9
Appendix	Attached
Report of inventions	Attached
Awardee's assignment	Attached

Introduction:

Even during the last two years the incidence and severity of morning sickness has been worsening in this country and throughout the world. The reason for this increase in the symptoms of morning sickness among pregnant women remains unknown, as does the underlying fundamental cause of this disorder and its more severe form hyperemesis gravidarum. Paradoxically, interest in research about this disorder remains minimal. It is a disease largely ignored by men and accepted by many women with surprising equanimity. Its fundamental cause remains completely unknown, and at last count at least 14 causes have been put forward.

Morning sickness and its more severe form, hyperemesis gravidarum, are distinct syndromes. Hyperemesis occurs in 0.5 to 10 per 100 pregnancies. It is characterized by vomiting starting in the first half of pregnancy that results in weight loss, metabolic disturbances and electrolyte imbalance. It may become so severe as to require hospitalization and termination of pregnancy. As noted above, despite 40 years of rigorous investigation and despite our efforts during the past two years its cause remains unknown, though we will show in this report a distinct role for thyroid abnormalities and our growing speculation for a role for leptin. The goal of this project has been to determine if morning sickness is a result of metabolic alterations during pregnancy related to thermogenesis, in particular nonshivering thermogenesis in brown adipose tissue. We have carried out in collaboration with Japanese colleagues the largest study of morning sickness yet undertaken in the world. A preprint of this work is enclosed here as an appendix.

The heat-sensing technology which makes this research possible was originally developed for military purposes. It is this technology application that makes the project relevant to NMTB. Infra-red thermography provides us with a tool for measuring surface temperatures with extremely high precision. During the two years of NMTB support, continuing to use this technology, we have further demonstrated that brown adipose tissue becomes active in early human pregnancy. We have monitored the activity of subcutaneous brown adipose tissue in human subjects after eating and during exposure of the hands to cold (cold-pressor test). We have obtained strong evidence of local thermogenesis at the nape of the neck in particular, and thermograms documenting this new finding will be published during the coming year. Infrared thermography allows real-time observation of the spatial distribution of heat generation in a non-invasive manner and so provides a completely new and powerful window into the metabolism of pregnancy and a tool to investigate the cause of morning sickness. Despite an ending of NMTB support in November 1999, we are continuing our work and two manuscripts are in preparation.

Body of Report:

During the past year of Testbed support we made progress along several lines. This progress is related to specific aims later in this report.

1) We confirmed that nonshivering thermogenesis becomes activated in early pregnancy. In the past year we studied an additional 15 women at San Bernardino County Hospital (now Arrowhead) and an additional 40 women at Nippon Medical School Hospital in Japan.

2) We observed a correlation between the severity of symptoms of morning sickness and the extent of thermogenesis.

3) We noted changes in metabolic hormones, particularly of the thyroid axis, which are involved in the control of thermogenesis. The paper submitted six months ago has now been accepted and is in press (See

Appendix). It relates morning sickness to elevated levels of reverse triiodothyronine, a metabolic diversion product away from the physiologically active triiodothyronine T3.

4) We have analyzed blood samples from pregnant women with and without the symptoms of morning sickness for a variety of metabolites. Graphs of these results are included here.

As noted in the six-month report of last June we originally proposed that brown adipose tissue becomes activated during early pregnancy and produces heat which could be detected by infra-red thermography. This has been confirmed, now both in this country and in Japan where morning sickness is a more serious and prevalent problem. It was further postulated that as lipid stores are broken down they release excess fatty acids into the circulation whose concentration rises to toxic levels and cause the symptoms of morning sickness. We have largely discarded this hypothesis now as untenable because fatty acids, while increasing 2- to 4-fold do not reach seriously toxic levels. Despite this setback, many new lines of work have opened up and we are pursuing these vigorously. A number of these relate to leptin, a hormone released by fat that has actions on the brain. Indeed, levels of leptin are known to be elevated in early pregnancy, and of most importance elevated levels of leptin tend to induce nausea. We hypothesize that morning sickness is caused by exaggerated and inappropriate responses to leptin. This idea of causation is not particularly related to commercial product and becomes outside the purposes of NMTB. Nevertheless these ideas will be pursued vigorously without financial support from the Testbed. Should commercial product, perhaps in the form of antilipolytic or anti-leptin therapy, become available NMTB will be notified.

The specific aims put forward in the second year application were to obtain thermograms of pregnant women and record changes after eating, activation of the sympathetic nervous system by cold stress, and at different times during gestation, to measure selected hormones and metabolites in these various conditions, and to measure the bound and unbound fractions of fatty acids (FAs) in plasma and their binding properties with albumin. The progress made toward these goals is described below.

I. Japanese studies. One major group of studies was carried out at the First Hospital in Tokyo Japan in collaboration with Drs. Hirobumi Asakura and Atsuko Oya. The purpose of these studies was to test whether increased sympathetic activity would stimulate nonshivering thermogenesis in brown fat of pregnant women and nonpregnant controls. The goal was to compare patients with hyperemesis gravidarum, those with mild morning sickness and asymptomatic women. It was elected to begin by stimulating the sympathetic system by a cold stress in which the women placed their hands in moderately cold water. This was to fulfil part of *Specific Aim #1* in the proposed work schedule.

Subjects. Three groups of subjects were studied. The first group consisted of 17 women with severe hyperemesis gravidarum in whom there was an average weight loss of 2.66 $\pm$ 0.42 kg. The second group consisted of nine pregnant women with less severe nausea and vomiting who were gaining weight normally, an average gain of 1.38 $\pm$ 0.98 Kg. The third group consisted of six nonpregnant women with stable weight. The gestational age of the pregnant groups were comparable, 10.7 and 11.4 weeks for the hyperemesis and morning sickness groups, respectively. The women with hyperemesis and morning sickness were studied while they were hospitalized.

Protocol. After informed consent was obtained, subjects were dressed in a hospital gown that exposed their back and neck. Subjects were seated and allowed to become accustomed for 5 min or more in a room maintained at 26-27° C. Thereafter thermograms were recorded every 5 seconds. The thermal system

consisted of an infra-red camera, a color display, a frame recorder, and a disk system for storage of the data (Thermal Video System 3000ME,Japan Avionics, Tokyo). It provided a thermal map of the back, shoulders, and neck of the subject by translating infrared emission from the skin into a scale that was internally calibrated for temperature. The instrument was adjusted to display 16 colors, each color representing 0.3° C, spanning the range from 29 to 33.8° C.

After a two minute control period the subject was asked to place her hands in cool water (12 °C) for 50 seconds. This was done to provide a cold stimulus for sympathetic stimulation and a challenge to thermoregulation. The woman's hands were then towel dried, and observations continued for another 3 to 4 min.

Blood samples were collected immediately before the start of the thermographic observations and 20 min after the cold stimulus. Samples were analyzed for free T_3, thyroxine, and reverse T_3 and fatty acids.

Statistical analysis. Because we just recently completed this study the statistical analysis remains incomplete. We are expressing results as mean ± SEM. We are analyzing differences between the three groups using ANOVA with repeated measures followed by Scheffe's F-test. We propose to examine the influence of individual factors using multiple linear regression with heat flux and symptoms as dependent variables, but this has not been done yet. We accept significance at the traditional $P<0.05$ level. A paper is being written in Japan which I will edit for publication in the *Am J Ob Gyn*.

Results and Comment. Brown fat is located between the scapulae and at the nape of the neck in humans. During the control period 82% (14 of 17) of those patients with hyperemesis showed a central region between the scapulae that was appreciably warmer than other regions of the back and shoulders. Thermograms comparing differences in this basal state are shown in color as appendices to this report. This result may be contrasted with 56% (5 of 9) of patients with milder morning sickness showing the warm regions and 33% of non-pregnant women showing the warm regions. The difference was statistically significant by Chi square ($P<0.025$). We interpret these results as indicating a strong association between active nonshivering thermogenesis in brown fat and morning sickness. We think this is a new and potentially important finding. It does not, however, establish a caused link, and there is the alternative hypothesis that the sympathetic system becomes activated as a consequence of vomiting and stress rather than being its cause.

After immersion of the hands in cold water the average temperature of the entire back decreased in all study groups. Then, after about 30 seconds, the temperature began to increase. This result is consistent with blood cooled by its passage through the hands returning to the central circulation and then, soon thereafter, thermoregulatory compensations such as vasoconstriction coming into play.

During cooling of the hands the central warm region between the scapulae expanded in area in most patients with morning sickness and hyperemesis. An example of this type of response in an individual patient with hyperemesis gravidarum is shown on the next page. We interpret this response as indicating an increased heat flux across the skin in regions of brown fat depots during sympathetic stimulation, and hence to be consistent with a further activation of nonshivering thermogenesis in this region.

To compare patients beginning from different basal temperatures we used our measurements of heat dissipation provided by the thermal camera. We expressed heat flux as calories dissipated per unit area (cm^2) per hour. Then, to obtain a numerical index of thermogenic activity, we calculated the ratio of heat flux in the interscapular warm area divided by heat flux from other areas of the back and multiplied the result by 100.

We interpret these data as indicating greater basal thermogenic activity in the patients experiencing the symptoms of morning sickness, especially in those patients with hyperemesis. The data also strongly suggest greater increases in thermogenic activity after sympathetic stimulation in patients with morning sickness. This also is a new and potentially important finding, but again does not establish a causal link. A second paper is being prepared which will report changes in heat production in morning sickness which should be ready in about 6 months. Our findings suggest changes in metabolic control in early pregnancy that may be related to the mobilization of energy stores for placental and embryonic use, especially protein synthesis.

The results of blood sampling for thyroid hormone and fatty acid concentrations in the three groups are given in the following table. The data are for samples collected during the initial control period. Their values did not change measurably in the samples collected after cold stimulation.

	Hyperemesis	Morning sickness	Non-pregnant
Thyroxine (pg/ml)	4.01 + 0.62*	3.04 + 0.12	3.06 + 0.10
T_3, triiodo-thyronine, (pg/dl)	1.44 + 0.22*	1.00 + 0.10	1.19 + 0.04
Reverse T_3 (ng/ml)	459 + 68*	405 + 29	262 + 16
Non-esterified fatty acids, (mEq/l)	0.0.45 + 0.14*	0.22 + 0.05	0.32 + 0.07

* Significantly higher than non-pregnant control.

To summarize the thyroid data we can note that all thyroid hormones are elevated despite a low thyroid stimulating hormone TSH signal from the pituitary. This is especially true for reverse T_3. We interpret these findings as indicating an increased release of thyroxine into the circulation. The reason for this is not clear because TSH has actually declined, perhaps as part of efforts at control by negative feedback. Most provocatively, the data are consistent with peripheral conversion of thyroxine to T_3 in brown fat which occurs by virtue of Type II 5'-deiodinase, a special enzyme found in this tissue. This type of 5'-deiodinase is also found in the brain, and one may speculate about possible links to altered cerebral metabolism, nausea, weight loss, and other findings of hyperemesis. In any case, the elevated thyroid hormones demonstrated in this study are consistent with increased metabolic rate throughout the body and in brown fat in particular. These changes occur despite what appears to be a compensation, effect in part, that diverts thyroxine from the metabolically active T_3 to the inert reverse T_3.

This conclusion is further supported by the negative correlation between weight loss and the heat dissipation ratio. The figure in the appended paper indicates that those patients with greatest thermogenic activity tended to experience the most weight loss.

Such responses have not been reported previously to our knowledge, and we believe they provide hints towards understanding thermoregulation in early human pregnancy and possibly the cause of morning sickness.

The elevations in plasma levels of fatty acids we measure are statistically significant and of possible physiologic importance. However, the fatty acid concentrations are not particularly high and do not extend into

the range of > 1.0 Meq/L wherein FAs would saturate their binding sites on albumin. These modest elevations in *total* fatty acids do not preclude greater increases in the *unbound* fraction of the fatty acids. This fraction must be measured directly before the fatty acid-toxicity hypothesis can be further supported or refuted. This work remains for the future. Nonetheless, the modest increases of FAs after sympathetic stimulation have dampened my enthusiasm for the earlier hypothesis.

II. USA-based studies.

Thermal camera and accessories. These studies are being carried out with a thermal infra-red camera purchased with NMTB funds that has a higher spatial resolution and higher temperature sensitivity than the one we are currently using in Japan. In the past year's work we have been able to discriminate between areas of thermogenic activity and areas of non-activity where the temperature difference is only 0.1-0.2° C.

Assays and other analytical methods. We have continued to develop the assays and other analytical methods needed for these studies. In the past six months we analyzed plasma samples for thyroxine, T$_3$, reverse T$_3$, and TSH. The thyroid hormones are elevated, but not so much so as our studies in Japan. In our initial analysis the elevation of these hormones and metabolites correlated directly with the severity of morning sickness (the latter based on patients subjective reporting of the severity of her nausea). Then with reassessment of patients severity these direct correlations could no longer be demonstrated. We are studying additional patients, especially in the severe hyperemesis group, in an effort to resolve these statistical uncertainties.

Human studies. We have carried on these studies for the past year with NMTB funds and to date have studied about 30 patients at the Arrowhead Medical Center. We are now obtaining follow-up studies of patients with morning sickness later in pregnancy and after delivery. We began studying the effects of a carbohydrate meal, as this intervention is most readily accepted by the patients experiencing nausea. We are currently beginning our study of sympathetic stimulation (cold pressor test), as we have been doing in Japan. To date we have studied two women in this manner. We have not yet begun our studies of caffeine intake in coffee and tea drinkers. We showed these results as color printouts from the thermal camera as an appendix to our report 6 months ago. The thermograms showed a marked difference between non-pregnant and pregnant women with morning sickness. These differences are regarded as perhaps the most important discovery made with NMTB support because they indicate changes in adult metabolic controls in early pregnancy, increased lipolysis, increased heat production, increased oxygen consumption, all of which may be associated with mobilization of maternal energy stores for placental and embryonic synthesis.

Evolution of concepts and recent information regarding leptin.

Based on our results during Testbed support and recent advances reported in the literature we will increasingly direct our focus on interactions between leptin, brown adipose tissue activation, and morning sickness.

Background. We have observed that women with morning sickness have significantly increased thermogenically active brown adipose tissue along with a concomitant increase in plasma free fatty acids. This activation of brown adipose tissue during early pregnancy removes maternal energy stores. Because the mitochondria of brown adipose tissue contain uncoupling protein, there is a dissociation between mitochondrial oxidation and energy formation. The uncoupling protein disrupts the normal proton gradient across the inner mitochondrial membrane and causes a large fraction of mitochondrial oxidation to result in heat production rather than ATP formation. This system is an important thermoregulatory response that allows animals to use

stored fatty acids to generate heat. Brown fat activation has also been thought of as a mediator of full-body metabolism, effectively reducing fat stores in an effort to maintain body weight limits.

It would seem paradoxical that women with morning sickness would possess active brown fat. In early pregnancy, energy expenditure is higher than normal, as there is the need for synthesis of embryonic, placental and well as new maternal tissues. It is possible that the increase of free fatty acids in plasma and brown fat activation represent a state of altered energy homeostasis.

Recently, other investigators have established a link between the hormone leptin and the regulation of brown fat activation. These investigators found that leptin increases energy expenditure and sympathetic outflow to brown fat. In addition, leptin was found to increase levels of mRNA rat uncoupling protein transcription. These results are consistent with the role of leptin acting as a mediator of body fat stores. Leptin has also been shown to directly increase the production of active thyroid hormones, which are active in regulating whole-body metabolism and brown fat activation.

Until recently, the production of leptin has been thought to be directly linked to the amount of stored fat in the body, with increases in the synthesis and secretion of leptin as fat mass grows. Now, however, several biochemical mediators have been shown to increase leptin without a corresponding increase in fat mass. Increases in leptin production have been observed with the addition of insulin, estrogen, and the thyroid hormones and inhibited by cortisone. Significantly, Highman et al. found that serum leptin concentrations were increased without corresponding increases in metabolic rate during early pregnancy. They concluded that the increases of leptin levels were due to factors other than the amount of body fat in pregnant subjects. They suggest that pregnancy represents a leptin-resistant state, which would be a necessary metabolic adaptation for maintaining a viable pregnancy.

In light of this new evidence, we are pursuing the hypothesis that women with morning sickness have increased plasma leptin concentrations and are not leptin resistant. Thus, leptin would, we hypothesize, increase whole-body metabolic rate, activate brown adipose tissue and suppress appetite. This increase in metabolism and decrease in food intake would increase lipolysis. Because pregnancy requires nutrients and energy for proper growth and formation of the embryo and later the fetus, the mother is in a state of caloric debt. We postulate these alterations in leptin homeostasis would affect whole-body hormone production and metabolic rate resulting in illness, in short we hypothesize that hyperemesis is *caused by inappropriate responses to the normal increase in leptin that occurs in early pregnancy.*

In the coming year, without NMTB support, we propose to measure brown fat activation, plasma leptin concentrations, the thyroid hormones, human chorionic gonadotrophin, and fatty acid production. We will correlate these responses with one another and note changes with time. Our broad goal will continue to be to seek a cause-and-effect relationship that could explain the genesis of morning sickness.

Conclusions:

Two years is too short a period of time for significant biomedical research. Nonetheless wee have shown for the first time that there is localized heat production at the nape of the neck where brown fat is located in human beings. This is a fundamental new discovery that merits further work. This site becomes thermogenically active in pregnant women and especially in pregnant women with morning sickness. Although this activation is a new discovery with regards to pregnancy, similar responses have been found in patients with sepsis, those with pheochromocytoma, and in Eskimos living in cold environments. We also find increases in

the circulating levels of thyroid hormones despite low levels of TSH, suggesting a non-thyroid origin of the hormones--perhaps in brown fat itself. And finally we observe a correlation between increased thermogenic activity and weight loss in patients with hyperemesis gravidarum. These are important leads to pursue to understand the genesis of morning sickness. They do not necessarily establish a causal relationship between activation of nonshivering thermogenesis and morning sickness.

In the next two years the principal investigator proposes to write two papers further describing results obtained with NMTB support. Copies will be submitted for clearance. There is a patient base for follow-up studies.

In conclusion I would like to publicly thank NMTB for its financial support. I would like to express appreciation to all who made these time-consuming and difficult clinical studies possible. These include many workers in Japan, and also at San Bernardino County Hospital (Arrowhead), and at Loma Linda University Medical Center. Among those receiving financial support from the Testbed are the following: Gordon Power, MD; Shannon Bragg, MS; Tomoaki Murata, MD; Jiang Lan, MS; Hirobumi Asakura, MD; Atsuko Oya, MD; and Jan Craig. Last of all I would like to thank the pregnant women and control subjects for allowing themselves to be studied.

As I noted in the six month progress report a rational treatment of morning sickness will be possible one day. In particular, treatment with propranolol (Inderol), a long-acting adenosine analogue, and prostaglandin-related drugs would be reasonable, as these are all potent inhibitors of brown adipose tissue activation. In addition, it may become possible to modify responses to leptin. As I noted before, much caution is required because the embryo is at the critical organogenesis stage when morning sickness is at its worst and any drug treatment must require an ardent balancing of therapy and risk.

c:\office\arpa\morn_sic\apply_98\final_rp.doc

Arch Gynecol Obstet (200[illegible]

COPY

© Springer-Verlag 2000

ORIGINAL ARTICLE

JAN 19 2000

Hirobumi Asakura · Syouiti Watanabe
Atsuko Sekiguchi · Gordon G. Power · Tsutomu Araki

Severity of hyperemesis gravidarum correlates with serum levels of reverse T_3*

Received: June 1999 / Accepted: 29 November 1999

Abstract To investigate the possible physiological relevance of extra-thyroidal production of reverse T_3 (rT_3) in hyperemesis gravidarum, measurements of serum rT_3, free T_3 (FT_3), free T_4, (FT_4), and nonesterified fatty acids (NEFA) were correlated with weight loss of hyperemetic women. All the thyroid hormones, NEFAs and weight loss were significantly higher in hyperemesis gravidarum than in control subjects, and also higher than in those with milder symptoms of morning sickness ($p < 0.05$). Elevations of FT_3, FT_4 and NEFAs correlated with the extent of weight loss, the latter taken as the index of the severity of hyperemesis gravidarum ($p < 0.05$). Only rT_3 correlated with both weight loss and the rate of lipolysis, as reflected by elevations of NEFAs ($p < 0.05$). The data are consistent with a shift from T_3 to rT_3 as products of 5′-monodeiodination of thyroxine in hyperemesis gravidarum. Because reverse T_3 is physiologically inactive a control mechanism may be postulated wherein T_3 production is minimized, thereby reducing weight loss and lipolysis in patients with hyperemesis gravidarum.

Key words Hyperemesis gravidarum · Thyroxin · T_3 · Reverse T_3 · Fatty acids

* The project, work or effort depicted was sponsored by the U.S. Department of the Army and NMTB. The view, opinions and/or findings contained in this report are those of the authors and should not be construed as a position, policy, decision or endorsement of the federal government or the National Medical Technology Testbed, Inc.

H. Asakura · S. Watanabe · A. Sekiguchi · T. Araki
Department of Obstetrics and Gynecology, Nippon Medical School, Tokyo, Japan

G.G. Power (✉)
Center for Perinatal Biology,
Loma Linda University School of Medicine,
Loma Linda CA 92350, USA
Tel.: 909-824-4325, Fax: 909-824-4029

Introduction

Hyperemesis gravidarum, is a distinct syndrome occurring in 0.5–10 per 100 pregnancies. It is characterized by vomitig starting in the first half of pregnancy that results in weight loss, metabolic disturbances and electrolyte imbalance. It may become so severe as to require hospitalization and termination of pregnancy. In view of the structural similarities between human chorionic gonadotropin (hCG) and thyroid stimulating hormone (TSH). links between hCG, and thyroid stimulation have been proposed [12]. Endocrine abnormalities in hyperemesis gravidarum have been postulated and evidence presented [6]. However, there remains controversy concerning the pathogenic role of the thyroid axis in hyperemesis gravidarum and morning sickness [2, 10, 18, 19, 21].

Juras *et al.* [8] showed increased conversion of T_4 to reverse T_3 (rT_3) in hyperemesis gravidarum. This conversion occurs largely in the peripheral tissues without apparent over-activity of thyroid gland itself. During fasting in nonpregnant subjects T_3 gradually decreases while there is an associated increase of the biologically inactive rT_3 [13, 15]. This shift to rT_3 is potentially useful to the body because it reduces the physiological active metabolite of thyroxine T_3, and thereby, together with other changes in the growth hormone and adrenal axes in fasting [13], maintains energy stores and causes less stimulation of metabolic rate.

In many respects hyperemesis gravidarum resembles fasting. There is, for instance, reduced food intake and hence limited availability of energy sources, fluids, ~~vi-~~ ~~mentins~~ and other nutrients. Thus circulating levels of rT_3 may be postulated to increase in hyperemesis as in fasting, and its concentration would provide an index of the severity of hyperemesis gravidarum. Alternatively. there may be fundamental differences in the thyroid axis during hyperemesis, but this remains speculative because Juras *et al.* [8] reported thyroid function is normal in patients with hyperemesis gravidarum.

In this study we hypothesized that serum levels of rT_3 would provide a useful index of the severity of hypere-

Ms. No. 052 Author Asakura Ms. 14 Pages 6
Springer-Verlag, Heidelberg / H. Stürtz AG, Würzburg
Provisorische Seitenzahlen / Provisional page numbers 1. Korr.: Date: 5.1.2000

P

vitamins

mesis gravidarum. We selected weight loss as an independent and quantifiable measure of the severity of hyperemesis. We also determined non-esterified fatty acids (NEFAs) as an estimate of the increased lipolysis that accompanies weight loss and hyperemesis. Lipolysis is known to be stimulated by hyperthyroidism.

Methods

The group of patients with hyperemesis consisted of 80 pregnant women who were admitted to Nippon Medical School hospital and three regional hospitals from January 1993 until December 1998. The indications for their admission were severe weight loss in recent weeks, chronic weight loss of more than 5 kg from their weight before conception, or their inability to retain food because of intractable vomiting persisting for several days. The patients' ages ranged from 22–37 years and gestational ages ranged from 7–16 weeks.

A second study group of patients consisted of 30 pregant women with morning sickness admitted during the same time period. The symptoms in this group were not as severe as in those with hyperemesis. These women suffered from nausea, but their vomiting was less frequent and not so severe that they required medical treatment. In these pregnant women the abnormalities of electrolytes and liver function were absent or the tests were not performed.

A third group of women served as a control population. It consisted of 30 non-vomiting, healthy pregnant women who were matched for age, ideal body weight, and gestational age with patients with hyperemesis gravidarum.

During their study patients from all groups were admitted to the hospital. Venous blood was typically sampled for hematocrit, electrolyte values, and liver function chemistries. Those patients with hyperemesis typically evidenced ketonuria and required intravenous fluid therapy with multivitamins. In some instances this treatment was necessary to correct electrolyte abnormalities and liver function abnormalities.

None of the patients was given β-agonists. Those patients and control subjects with thyroid disease, detected by characteristic clinical and laboratory findings including abnormal levels of antithyroid antibodies, were excluded from the study. One subject required termination of pregnancy and all subjects but one were improved within several weeks by the intravenous fluid therapy and hospitalization described above.

Blood sampling

Blood was withdrawn from a cubital vein early in the morning (before breakfast in those ingesting food). Assays were performed using plasma separated from blood after centrifugation. Measurements included the thyroid hormones free T_3 (FT_3), free T_4 (FT_4), and rT_3 and NEFAs. The thyroid hormones and NEFAs were measured by RIA as described in earlier work [4, 9].

Statistical analysis

The severity of hyperemesis gravidarum was estimated by weight loss from the preconception period or, if a clinic visit was made within six weeks after conception, from the weight recorded at the time of that clinic visit. Weight loss was used as the independent variable and thyroid hormones and NEFAs were taken as dependent variables. Least-squares regression methods were used to analyze the relation among these parameters. Students *t*-test was used to test the significance of differences between control and experimental groups. The level of significant was set at $p < 0.05$.

Results

Weight loss and gestational weeks in subjects

The weight loss in hyperemesis patients averaged 4.57 ± 3.38 kg, as shown in Table 1. The loss varied widely from 14.8–3.8 kg. The weight loss of this group was appreciably higher than those with morning sickness (0.85 ± 1.41 kg) and may be contrasted with the weight gain of 0.78 ± 1.89 kg in control subjects.

Hyperemesis patients were studied after 5–14 weeks of gestation, mean 11.7 weeks, a somewhat longer period than study of patients with morning sickness (9.7 weeks) and control subjects (10.9 weeks). In hyperemetic patients weight loss tended to be more severe in those patients studied later in their pregnancy ($r = 0.32$, $p < 0.05$), and thus their weight loss reflected both the severity and duration of hyperemesis gravidarum.

Thyroid hormones and NEFA in different groups

Both $[T_3]$ and $[T_4]$ were measurably higher in serum of patients with hyperemesis gravidarum as compared with control subjects and morning sickness patients ($p < 0.001$). Patients with morning sickness also showed chemical evidence of hyperthyroidism when compared with control subjects ($p < 0.01$) (Table 1).

Serum levels of NEFAs was significantly higher in hypremesis gravidarum patients than in the control wom-

Table 1 Variation of gestational weeks, weight loss, thyroid hormones and non-esterified fatty acid (NEFA) in different subjects and control

	Gestational Weeks	Weight Loss [kg]	FT4 [ng/dL]	FT3 [pg/mL]	Reverse T3 [pg/mL]	NEFA [mEQ/L]
Hyperemesis gravidarum ($n = 80$)	11.7 ± 3.0 **	–4.57 ± 3.38 **	2.11 ± 1.13 **	4.69 ± 2.44 **	720.6 ± 433.7 **	0.60 ± 0.36 **
Morning sickness ($n = 30$)	9.7 ± 2.6	–0.85 ± 1.41 *	1.39 ± 0.53 *	3.23 ± 0.84 *	439.7 ± 162.8	0.43 ± 0.38
Control ($n = 30$)	10.9 ± 2.5	0.78 ± 1.89	1.27 ± 0.21	2.75 ± 0.46	381.1 ± 57.53	0.24 ± 0.15

** and * indicate $p < 0.001$ and $p < 0.01$ vs. control. Values are given as mean ± SEM

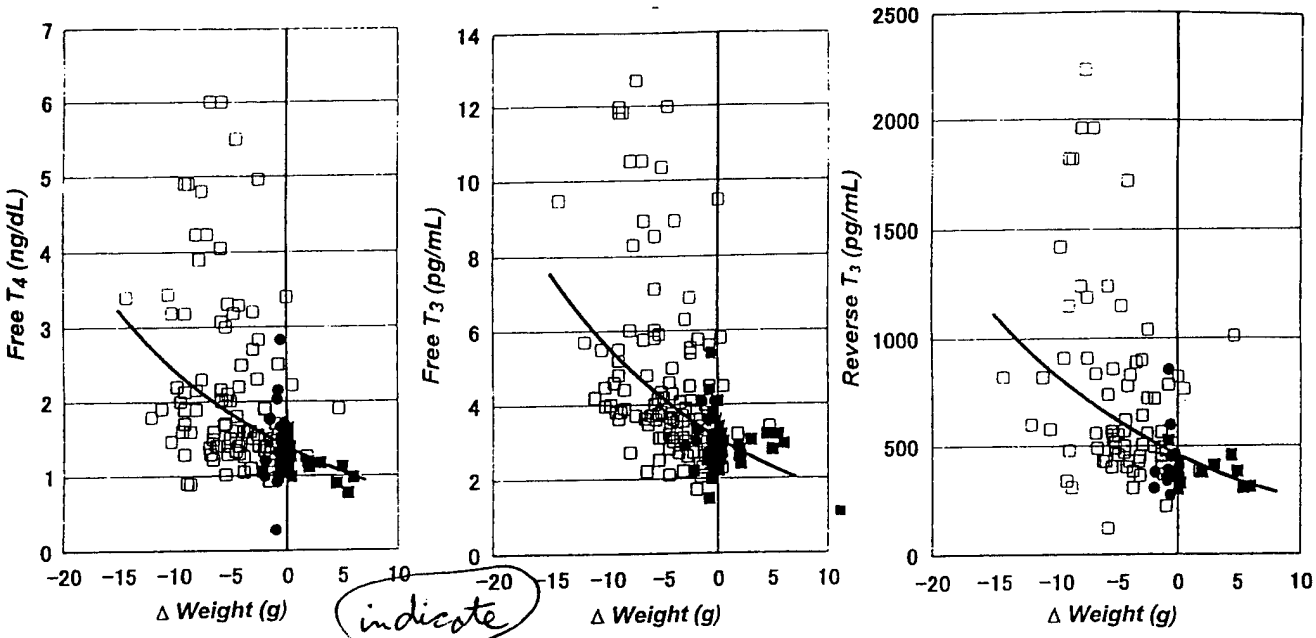

Fig. 1 Correlation between thyroid hormones and weight change in early pregnancy. Open squares indicate patients with hyperemesis gravidarum, closed circles those with morning sickness, and closed squares asymptomatic pregnant women. Regression curves are as follows: Free $T_4 = 1.39\ e^{(-0.0561X)}$, ($r = 0.46$, $n = 158$, $p < 0.05$); Free $T_3 = 3.09\ e^{(-0.0596X)}$, ($r = 0.52$, $n = 177$, $p < 0.05$); reverse $T_3 = 460\ e^{(-0.059X)}$, ($r = 0.44$, $n = 103$, $p < 0.05$), where X is weight loss in kg

en ($p < 0.001$). No measurable differences of NEFAs were found between patients with morning sickness and hyperemesis gravidarum (Table 1).

Interrelationships among weight loss, thyroid hormones, and NEFAs

A negative correlation was observed between weight change and each of thyroid hormones that was measured ($p < 0.05$) (Fig. 1). Correlation coefficients were 0.46, 0.52, and 0.44 for FT_4, FT_3, and rT_3, respectively. A negative correlation was also observed between weight change and NEFAs ($r = 0.35$, $p < 0.05$) (Fig. 2).

Relationship between NEFAs and thyroid hormones

NEFAs were higher in those women with elevated levels of rT_3 ($p < 0.05$), as shown in Fig. 3. The levels of NEFAs were not correlated with FT_3 and FT_4. The levels of NEFAs correlated weakly with the ratio of FT_3 to FT_4 ($r = 0.39$, $p < 0.05$) (Fig. 4), a result that indicates a shift in the peripheral conversion of T_4 away from the physiological active T_3. No measurable correlation was found between NEFAs and the ratio of rT_3 to T_4.

Comment

The elevation of serum levels of thyroxine [T_4] and triiodothyronine [T_3] in hyperemesis gravidarum have been reported previously [3, 12, 17], although not found by all investigators [8], and not always interpreted as indicative of a hyperthyroid condition [12]. The findings of increased reverse triiodothyronine [rT_3] and its correlation with the severity of hyperemesis gravidarum are new in this report and provide further insights into the role of thyroid hormones in hyperemesis gravidarum.

Role of peripheral tissues

Thyroxine is metabolized by 5′-monodeiodination to either T_3 or reverse T_3. This process occurs largely in extra-thyroidal sites. In the case of the rT_3 found in serum, more than 97% has its origin in extra-thyroidal sits [5]. Wolf and Keck [22] have emphasized the importance of local intracellular generation of T_3 in cells of human adipose tissue. Some 76% of the body's T_3 is located in the muscle, skin, and gut as a slow pool. Nineteen percent is found in liver and kidney as a fast pool, and only 5% is located in the plasma. This partitioning among various peripheral tissues has not been worked out for pregnancy, either with or without hyperemesis. In particular, the role of the placenta and fat are largely unexplored. Fat is of special interest because brown adipose tissue converts T_4 to T_3 in rats [14], and there is preliminary evidence that brown adipose tissue may become active in early human pregnancy (unpublished results).

Usefulness of rT_3 as an index of the severity of hyperemesis

In the present study weight loss was taken as an index of the severity of hyperemesis. It correlated as shown in Fig.

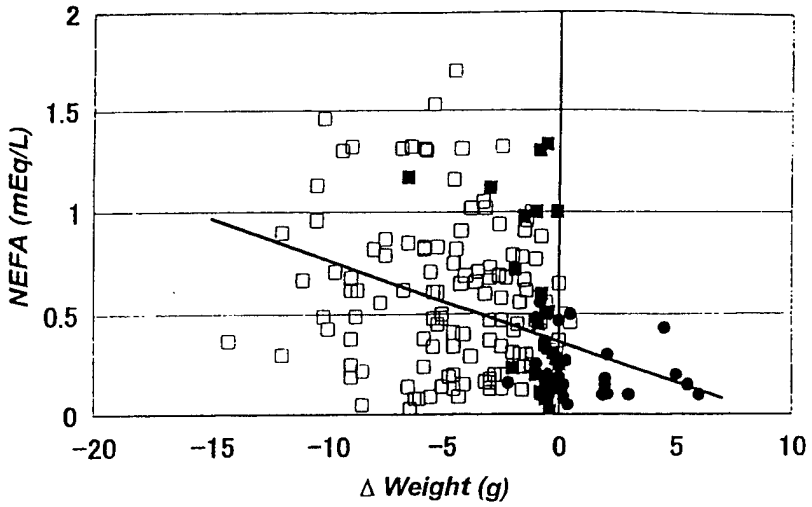

Fig. 2 Correlation between non-esterified fatty acids (NEFAs) and weight change in early pregnancy. The regression curve is: NEFA – 0.396 – 0.0364 X, where x is weight loss, ($r = 0.35$, $n = 180$, $p < 0.05$). Open squares indicted results of patients with hyperemesis gravidarum, closed circles those with morning sickness, and closed squares those with morning sickness, and closed squares those of asymptomatic pregnant women

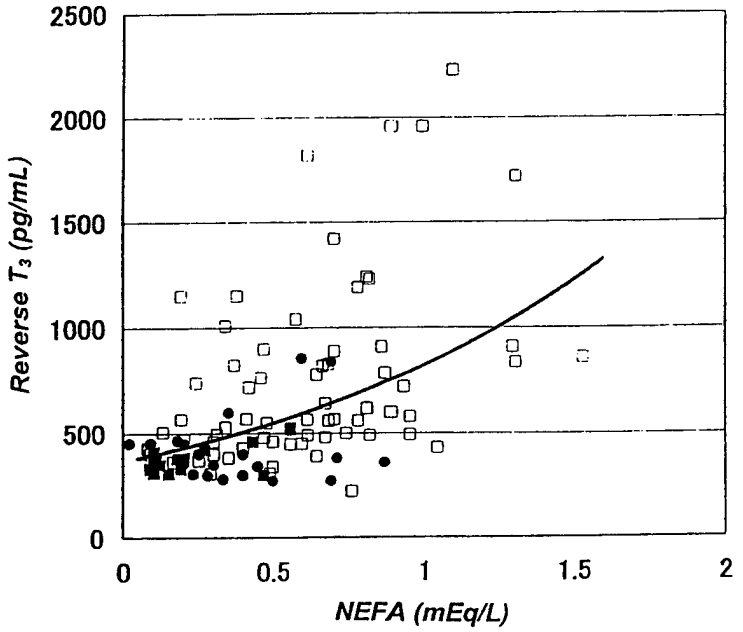

Fig. 3 Correlation between reverse T_3 and non-esterified fatty acids (NEFAs). The regression curve is: reverse $T_3 = 376\ e^{(0.81X)}$, where x is NEFA, ($r = 0.53$, $n = 103$, $p < 0.01$)

1 with [rT_3]. The correlation was tighter than observed for either [T_3] or [T_4], whose results are also shown in Fig. 1. Reverse [T_3] may be a particularly useful as an index of the severity of hyperemesis gravidarum because it is cleared about threefold faster from the serum than T_3 [5], yet its serum level remains some 100-fold greater. Thus there is a far more rapid production of rT_3 as well as a more rapid clearance than is the case of T_3. This rapid turnover of rT_3 indicates its serum concentration is a rapid responding index of thyroid axis activity.

Comparison between fasting and hyperemesis gravidarum

Although similarities exist between fasting and hyperemesis gravidarum there are also important differences. Fasting, malnutrition and acute illness are known to be associated with a decreased conversion of T_4 to T_3 [16] and reduced concentrations of T_3 in serum [13, 15]. This reduction of [T_3] avoids the metabolic stimulation that would otherwise tend to further deplete energy stores. In hyperemesis the mean dietary intake of most nutrients, including energy sources and vitamins, falls below 50% of recommended dietary allowances [20]. In hyperemesis, however, [T_3] as well as [T_4] increase, as shown by the data in the Table. Because this increase of physiological active thyroid hormones has the potential to aggravate the severity hyperemesis gravidarum and contribute to weight loss, it may be postulated to play a role in its genesis, rather than its moderation. These divergent results strongly suggest fundamental differences between hyperemesis and fasting despite the limitation of energy sources in both.

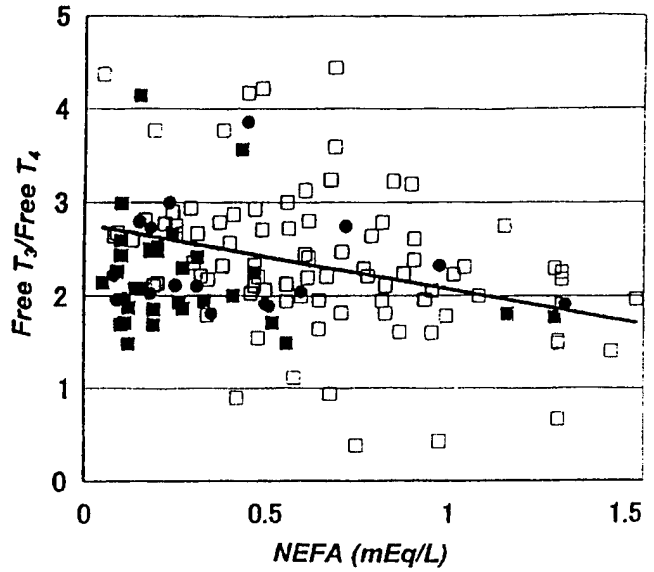

Fig. 4 Correlation between the ratio of free T_3 to free T_4 and non-esterified fatty acids (NEFA)

It would appear therefore that elevations of T_3 and T_4 may aggravate the hyperemetic condition, particularly the weight loss, but other studies are at variance with this conclusion [19, 21]. This difference of interpretation may arise in part because of the wide variation in the severity of symptoms of morning sickness and hyperemesis gravidarum, difficulties defining the condition, and the limited number of patients in some earlier studies.

Interpretation of increased [rT_3]

Elevated levels of rT_3 in patients with hyperemesis gravidarum and to a less extent in those with morning sickness may simply represent an accumulation of the inactive metabolite that comes about because of accelerated metabolism of thyroxine. This would be an anticipated response caused by mass action once [T_4] becomes increased. Alternatively, the measured increases of [rT_3] may be postulated to be a consequence of metabolic controls, whereby the body would divert the products of thyroxine away from the stimulation that would come if T_3 were the principal 5′-monodeiodination product rather than the inert rT_3. A compensatory diversion of this sort would be consistent with the finding that the T_3 to T_4 ratio declined when concentrations of NEFAs became higher and hyperemesis became more severe.

Stimuli for increased thyroid levels

The reason for increased levels of thyroid hormones in hyperemesis gravidarum and to a lesser extent in morning sickness is largely unknown. It may be related to the dietary factors, especially the carbohydrate deficit, that has been shown to influence serum T_3 and rT_3 [1, 15].

Increase of serum NEFAs

During times of fasting, glucose is released from glycogen, but glycogen stores are not large and cannot provide an adequate amount of glucose to meet requirements for both maternal energy and fetal growth. Cleavage of triacylglycerols stored in adipose tissue provides the mother with energy in the form of NEFAs especially when oral intake is limited. Lipolysis and the attendant increase of NEFAs also occur prominently when carbohydrate energy scores are insufficient for other reasons. This stimulation of lipolysis may be attributed in part to thyroxine [7], which increased about 66% above control in hyperemetic patients in the present study, and which appears to act in part by modulating and increasing the sensitivity of adrenergic responses [11]. The 5′-monodeiodination of thyroxine to rT_3 and the latter's attendant 90% rise (Table 1) may account for the correlation between rT_3 and NEFAs shown in Fig. 3.

In summary, serum levels of the active thyroid hormones increase 66–70% in patients with hyperemesis gravidarum and to a lesser extent in those with morning sickness. The physiologically inert rT_3 also increases and to a greater extent, about 90%, especially in hyperemesis, possibly due to a redirection of the deiodination pathway leading from T_4 to this inert by-product. Fatty acid levels also increase markedly in patients with hyperemesis consistent with accelerated lipolysis. Fatty acids are likely to become an increasingly important energy source as the severity of hyperemesis increases.

This study was supported in part by an award to Dr. Power from the National Medical Technology Testbed.

References

1. Azizi F (1978) Effect of dietary composition on fasting-induced changes in serum thyroid hormones and thyrotropin. Metabolism 27:935–942
2. Bouillon R, Naesens M, Assche FA van, Keyser L de, Moor P de, Renaer M, Vos P de, Roo M de (1982) Thyroid function in patients with hyperemesis gravidarum. Am J Obstet Gynecol 143:922–926
3. Chin RKH, Lao TTH (1988) Thyroxine concentration and outcome of hyperemetic pregnancies. Br J Obstet Gynaecol 95: 507–509
4. Chopra IJ (1974) A radioimmunoassay for measurement of 3,3′,5′-triiodothyronine (reverse T_3). J Clin Invest 54:583–592
5. Chopra IJ (1976) An assessment of daily production and significance of thyroidal secretion of 3,3′,5′-triiodothyronine (reverse T3) in man. J Clin Invest 58:32–40
6. Fairweather DV (1968) Nausea and vomiting in pregnancy. Am J Obstet Gynecol 102:135–175
7. Hales CN, Luzio JP, Siddle K (1978) Hormonal control of adipose-tissue lipolysis. Biochem Soc Symp 43:97–135
8. Juras N, Banovac K, Sekso M (1983) Increased serum reverse triiodothyronine in patients with hyperemesis gravidarum. Acta Endocrinol 102:284–287
9. Kasagi K, Kousaka T, Misaki T, Miyamoto S, Takeuchi R, Konishi J (1994) A new one-step, labeled-antibody assay for measuring free thyroid hormone concentrations. Kaku Igaku 31: 1525–1537
10. Kennedy RL, Darne J, Davies R; Price A (1992) Thyrotoxicosis and hyperemesis gravidarum associated with a serum activity which stimulates human thyroid cells in vitro. Clin Endocrinol 36:83–89

11. Landsberg L, Young JB (1987) Catecholamines and the sympathoadrenal system. In: Ingbar SH, Braverman LE (eds) Werner's the thyroid. Lipincott, Philadelphia
12. Mori M, Amino N, Tamaki H, Miyai K, Tanizawa O (1988) Morning sickness and thyroid function in normal pregnancy. Obstet Gynecol 72:355–359
13. Palmblad J, Levi L, Burger A, Melander A, Westgren U, Schenck H von, Skude G (1977) Effects of total energy withdrawal (fasting) on the levels of growth hormone, thyrotropin, cortisol, adrenaline, noradrenaline, T_4, T_3, and rT_3 in healthy males. Acta Med Scand 201:15–22
14. Silva JE, Larsen PR (1986) Interrelationships among thyroxine, growth hormone, and the sympathetic nervous system in the regulation of 5′-iodothyronine deiodinase in rat brown adipose tissue. J Clin Invest 77:1214–1223
15. Spaulding SW, Chopra JJ, Sherwin RS, Lyall SS (1976) Effect of caloric restriction and dietary composition of serum T_3 and reverse T_3 in man. J Clin Endocrinol Metab 42:197–200
16. Surks HI, Oppenheimer JJ (1964) Postoperative changes in the concentration of thyroxine binding prealbumin and serum free T_4. J Clin Endocrinol Metab 24:794
17. Tareen AK, Baseer A, Jaffry HF, Shafiq M (1995) Thyroid hormone in hyperemesis gravidarum. J Obstet Gynaecol 21: 497–501
18. Thomson JA, Wilson R, Gray CG, Glen ACA, Mack D (1989) Hyperemesis gravidarum and thyrotoxycosis – A diagnostic and therapeutic problem. Scott Med J 34:472–473
19. Valbo A, Jerve F (1987) A study of thyroid hormones in women suffering from vomiting in pregnancy. Acta Eur Fertil 18: 381–383
20. Van Stuijvenberg ME, Schabort I, Labadarios D, Nel JT (1995) The nutritional status and treatment of patients with hyperemesis gravidarum. Am J Obstet Gynecol 172:1585–1589
21. Wilson R, McKillop JH, MacLean M, Walker JJ, Fraser WD, Gray C, Dryburgh F, Thomson JA (1992) Thyroid function tests are rarely abnormal in patients with severe hypremesis gravidarum. Clin Endocrinol 37:331–334
22. Wolf CF, Keck FS (1991) Thyroxine and reverse T_3 5′deiodination in the cells of human adipose tissue. Thyroidology 3: 47–50

DESCRIPTION: State the goal of the project, including how it relates to improving health care and noting the advanced technology that will be developed or tested . Use succinct language to describe how the project goals will be achieved. Do not exceed the space provided.

Although cerebral blood flow research extends over the past 40 years little is known about regulation of cerebral blood flow during fetal life. A number of factors have contributed to this problem, many related to technical limitations. The standard method used to measure cerebral flow in the chronically instrumented mammalian fetus has been radioactive microspheres. Although this method provides an accurate description of flow at one moment in time, it is limited by the number of measurements available per experiment. Laser Doppler flowmetry has been established as an effective method for measuring blood perfusion in microvascular beds of various organs in adults. However it has not been used for the fetus due to the sensitivity of the flow probe to movement. We have addressed this concern and present here our adaptation of this method to measure cerebral blood flow in a representative animal model. Cerebral blood flow is of fundamental importance because oxygen stores of the body are minimal yet cerebral metabolic rate is high, and thus prompt adjustments of flow are necessary to match oxygen supply with oxygen need. Inadequate blood flow and oxygen delivery in the perinatal period cause tragic lifelong consequences including cerebral palsy and mental retardation.

Our first specific aim is to adapt laser Doppler flowmetry to measure the cerebral blood flow using the chronically prepared, near-term fetal sheep. Under halothane anesthesia a laser Doppler flow probe will be placed in the parietal cortex of the brain. The probe will be encased in a custom-molded, bivalve plastic probe-holder, shaped to the fetal skull, which will be secured to the skull with tissue glue. The probe-holder is designed to stabilize the probe. In preliminary experiments we find it reduces movement artifact from 40% to 5% of total flow signals. Various experiments will be done to further validate the methodology. These will include testing the usefulness of adding a reference probe that is sensitive only to movement artifact and noting changes after fetal and maternal death.

Our second specific aim is to examine the role of a possible mediator of the cerebral circulation. Nitric oxide is a powerful vasodilator in many vascular beds in the adult and it may be hypothesized to help maintain oxygen delivery to the fetal brain during times of stress. Fetal hypoxia will be induced by giving the ewe 10-11% oxygen to breathe. Cerebral flow responses will be compared with and without inhibition of the effects of nitric oxide using the drug L-NAME. Preliminary experiments to date indicate that nitric oxide does indeed increase brain blood flow during hypoxia and thus protects the brain. Finally, our third specific aim is to begin to test the roles of carbon dioxide, oxygen lack, adenosine and selected prostaglandins in modulating fetal cerebral blood flow.

In summary, the proposed work will test whether laser Doppler flowmetry can provide continuous, real-time measurements of blood flow in the fetal brain for the first time. The results may help guide therapy to optimize brain development and function.

PROJECT SITE(S) (organization, city, state):

Perinatal Biology Center
Loma Linda University
School of Medicine
Loma Linda CA 92350

COPY AUG 15 2000

Six month progress report for Subagreement No. 61-FY99-LLU-Power

as part of Cooperative Agreement Nol DAMD17-97-2-7016

USE OF LASER DOPPLER FLOWMETRY TO MEASURE CEREBRAL BLOOD FLOW IN THE FETUS

Principal Investigator: Gordon Power, MD

Center for Perinatal Biology

Loma Linda University School of Medicine

Loma Linda CA 92350

Phone: 909-824-4325

FAX: 909-824-4029

E-mail: gpowerjr@aol.com

This progress report covers the interval from February 1, 2000 until August 1, 2000

Gordon Power — August 14, 2000

Principal investigator — Date

A. INTRODUCTION

Cerebral blood flow is of fundamental importance for normal development of the brain during fetal life. Oxygen stores of the body are minimal yet cerebral metabolic rate is high, and thus prompt adjustments of flow are necessary to match oxygen supply with oxygen need. Inadequate blood flow and oxygen delivery in the perinatal period cause tragic lifelong consequences including cerebral palsy and mental retardation. Until the present time there has not been any method to measure cerebral blood flow in utero on a continuous basis. During the past six months with Testbed support we have successfully adapted laser Doppler flowmetry to measure cerebral blood flow in the chronically prepared, near-term fetal sheep. The new method is able to reduce movement artifacts to less than 5% of total flow signals. Using the method we have shown that nitric oxide mediates about 60% of the increase in flow that occurs in response to hypoxic stress. We have also obtained early evidence that the brain enters a state of *regulated hypometabolism* upon hypoxic stress, presumably by curtailing nonessential metabolic activities, and thereby rations oxygen use. Our broad goal remains to establish the control factors for oxygen delivery and use by the fetal brain and thereby to optimize brain development and minimize hypoxic injury.

B. OUTLINE

1. Specific Aims

a) *Specific aim #1* was to demonstrate that laser Doppler flowmetry can be used to provide a continuous signal of perfusion in a localized region of the fetal brain. The new methodology has enabled recording of the changes in cerebral hemodynamics in the unanesthetized fetus on a moment-to-moment basis in response to an hypoxic stress. This was the first time this has been achieved. This Specific Aim was completed.

b) *Specific Aim #2* was to demonstrate that nitric oxide, a fundamental controller of vascular reactivity and metabolic processes, mediates much of the increase in brain blood flow that occurs in response to hypoxia in the fetal sheep. This also was accomplished successfully for the first time.

2. There were no uncompleted specific aims

C. BODY

The following is taken largely from the reapplication made to the Testbed for a second year of funding.

As indicated above in the outline much progress was made toward completing the aims of the proposed work during the first six months. We completed both specific aims of the project. We have submitted two papers describing this work, one outlining the new methodology to the *Journal of Applied Physiology* and the second describing the role of nitric oxide to the *American Journal of Physiology*. The first was completed before Testbed support could begin, but the second receives full Testbed recognition, was preapproved, and includes appropriate disclaimer language.

The most important scientific lead to emerge during the first 6 months of this project is that the fetal brain may enter a period of *regulated hypometabolism* soon after exposure to hypoxia. The slowing of metabolic rate allows time for other compensations, such as further

increases of brain blood flow, to take place. The mediators initiating regulated hypometabolism are unknown and of great interest to us. We now propose studies to investigate possible candidates. From the methodological point of view the most significance advance has been the development of a new method to measure O_2 use in a localized region of the brain based on heat production. Our proposed studies will enable us to establish this method for the first time. The new method depends on accurate measurements of temperature of blood entering the brain and of brain tissue itself, and from the difference, together with measurement of local flow, calculating the calories of heat produced and hence of the ml of O_2 consumed.

In summary, for the next six months we propose to further develop a new method to measure O_2 consumption in a localized region of the brain and test its usefulness. We propose to examine the role of adenosine in mediating changes in cerebral blood flow and in the induction of regulated hypometabolism. We will continue negotiations with Biopac (Biopac, Inc., Santa Barbara CA) to develop a marketable, patentable hardware kit in which the laser Doppler probe and two thermocouples are packaged together and sold as a commercial product. With appropriate software the unit will provide a continuous write-out of brain metabolic rate for the first time.

Our broad goals remain the same. They are to provide new techniques to evaluate brain function and to minimize brain injury in the mammalian fetus.

Progress towards Specific Aim #1.

Fabrication of the Probe Holder. A key step to the successful application of laser Doppler flowmetry in the fetus was the reduction of movement artifact. We accomplished this by fabricating a probe holder which was custom molded to fit the contours of the fetal skull. By securing the holder to the fetal skull the tip of the probe is held stationary in regards to its position in the brain.

Laser Doppler Flowmetry. In our experiments we apply laser Doppler methodology by directing a continuous laser beam into brain tissue via an optical fiber, which then receives and carries the backscattered light to a photo-detector. Measurement of cerebral perfusion was performed with a Biopac 100A laser Doppler flowmeter (Biopac Systems, Inc. Santa Barbara, CA). The perfusion signal provides an index of relative blood perfusion at the tip of the probe that is calculated by an algorithm that analyzes the Doppler shift of backscattered light. The magnitude and frequency distribution of the Doppler-shifted light are proportional to the number and velocity of blood cells moving within the illuminated volume of tissue. An analog-to-digital converter system, MP100, Biopac Systems, was used for data acquisition. The laser Doppler flow probes used in the study were calibrated with a motility standard, an aseptically prepared, colloidal solution of suspended latex spheres undergoing Brownian motion, as supplied by the manufacturer.

Experimental procedures. A series of animal experiments were carried out to test the usefulness of laser Doppler technology in fetal life. Western ewes carrying singleton fetuses at 125-130 days of gestation were used for these feasibility studies. Hypoxia was used as a means to change cerebral blood flow during development of the method. The details of the surgical preparation are given below.

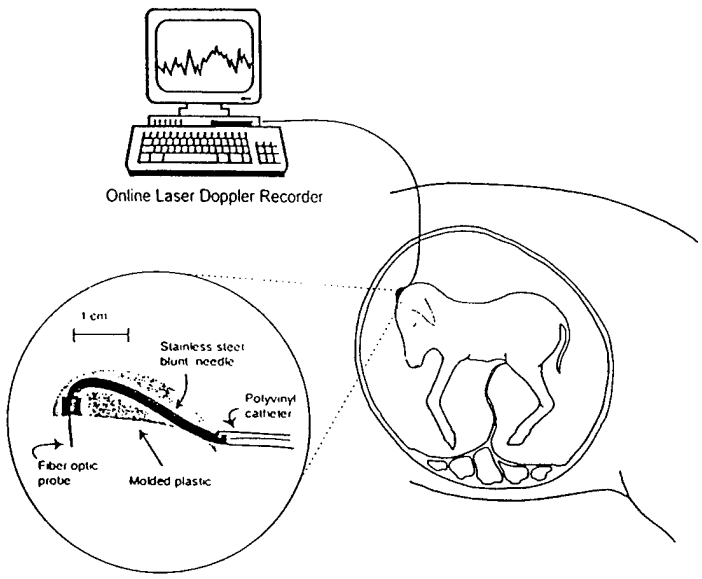

Experiments were carried out three to ten days after surgery with the fetus unanesthetized. Five fetuses were studied in these preliminary experiments. Experiments began with a 30-min baseline control period. A 30-min episode of hypoxia was then induced by allowing the ewe to breathe 10-11% O_2 in a balance of nitrogen. This was followed by a 30-min recovery period.

After completion of the experiment, the fetus was humanely killed with an overdose of T-61 (Hoechst-Roussel Co.), a proprietary euthanasia solution. Flow signals were monitored for an hour after fetal death to assess the importance of fetal movement artifact in perfusion readings. The ewe was then killed with the same agent, and any remaining flow signal was monitored for an additional hour to assess maternal-movement-induced artifacts.

Data handling. Laser Doppler flowmetry signals, backscatter, fetal blood pressure, heart rate and temperature were recorded using the data acquisition software Acqknowledge. The data were collected continuously and averages were calculated during three-minute time spans. Before averaging, spikes in apparent flow signal, often associated with changes in maternal or fetal position, were removed. The criteria for rejection were abrupt increases of more than 100 percent above baseline lasting less than 2 seconds, and thus outside the physiologic range. Mean values of arterial blood pressure and heart rate during the three minute intervals were calculated using the wave-form analysis functions of the Acqknowledge software program. Percentage changes in O_2 delivery were calculated as the product of relative perfusion and the O_2 content of arterial blood. Further details of the procedures are given in the appended papers.

Results. Residual signals persisting after fetal and then maternal death were used to assess movement artifacts. Early in development of the methodology these residual signals accounted for as much as 40% of the apparent total flow signals indicating a large *baseline zero* that would have had to be subtracted to estimate the true flow signal. However, as time progressed during the year with better probe design and better fixation technique, movement artifacts and baseline zero decreased until, at the present time, *baseline zero* averages less than 5%, and usually less than 3%, of the total recorded signal. This marked improvement has greatly simplified data handling. Abrupt spikes, often associated with changes in maternal posture, still must be edited from the flow record before analysis.

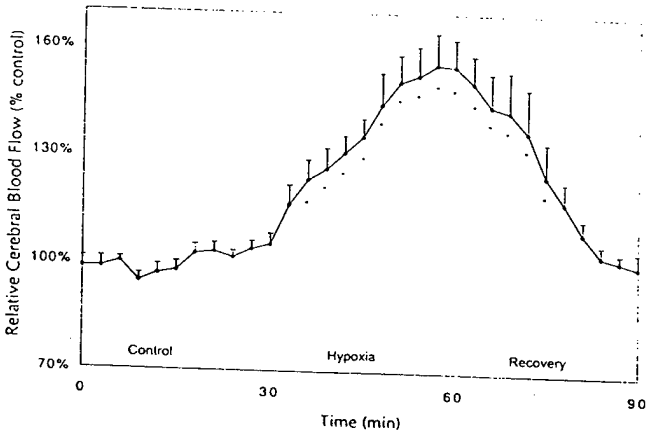

Cerebral flow responses were measured during hypoxia induced by giving the ewe 10% O_2 in nitrogen to breathe for 30 min. This exposure led to decreases in fetal preductal arterial O_2 tension from 21.2 $\pm$ 0.5 to 10.7 $\pm$ 0.4 Torr. During the hypoxic exposure cerebral perfusion increased progressively and came to average 56 $\pm$ 8% above baseline, as shown in the figure above. The relatively slow rise in flow was an unanticipated finding, and its implications will be discussed more fully below. When normal oxygenation was restored, perfusion returned to baseline levels during a 30-min recovery period. This recovery was also relatively slow.

In conclusion, the work under this specific aim has shown that laser Doppler methodology can be successfully used to measure brain perfusion in the unanesthetized, chronically prepared fetal sheep. With custom-fabricated probe holders and other advances in technique, movement artifacts can be reduced to less than 5% of measured flow values. The method provides only relative changes of perfusion from a small volume of the fetal brain, roughly 2 mm^3. It does this on a continuous basis, however, which is an important advantage for future studies inquiring into mechanisms. This work is in press for the *Journal of Applied Physiology* with a publication date scheduled for mid-summer.

Progress towards Specific Aim #2.

The second specific aim of the first year was to measure fetal cerebral blood flow during hypoxia with and without inhibition of nitric oxide. The objective was to determine the protective effect of NO on fetal O_2 delivery and use. Nitric oxide is a powerful vasodilator in

most organs of the adult and a suppressor of metabolic rate (12,33,37), and thus of possible importance in maintaining a balance between O_2 need and O_2 supply in the brain.

Using the methodology described under *Specific Aim #1* two groups of animals were studied. One served as a control group and the second received a nitric oxide synthase inhibitor (L-NAME). This drug was given at the beginning of the second hypoxic episode that was identical in time sequence to the first. It was given an intravenous bolus of 45 mg/kg iv followed by a continuous infusion (1.5 mg/kg/min).

Results. Maternal hypoxia led to a decline of fetal arterial PO_2 from 21.1 ± 0.5 to 10.7 ± 0.4 Torr with little change in arterial pH or PCO_2. There was no significant difference in blood gas data between those fetuses receiving L-NAME and those not.

The changes in mean arterial blood pressure for the two groups are shown in the figure to the right. Blood pressure increased similarly in both groups during the first hypoxic period. During the second period of hypoxia, however, blood pressure of the unmedicated fetuses increased as it had during the first hypoxic episode, whereas in the group given L-NAME the response was greater after infusion of L-NAME.

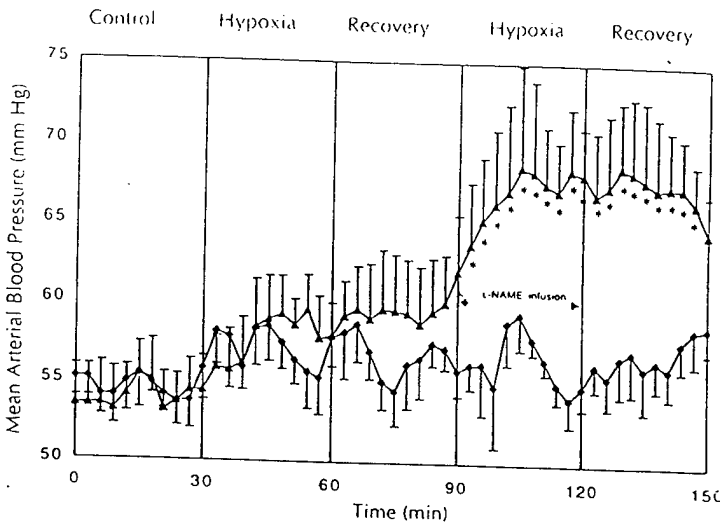

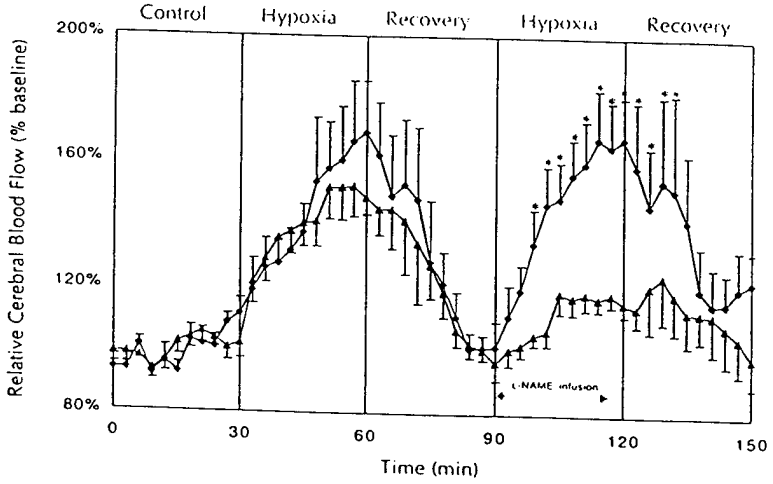

The changes in cerebral blood flow are shown in the figure to the left. Without L-NAME hypoxia led to an increase of about 55% in cerebral perfusion after 30 min (n=5). In the group of animals treated with L-NAME during the second hypoxic period, the increases of cerebral blood flow during hypoxia were diminished, rising only ~20% above control levels.

Changes in O_2 delivery to the brain were calculated as the product of blood flow and arterial O_2 content, and the results are shown in the figure at the top of the next page. Average changes in arterial O_2 content, cerebral blood flow, and cere-bral O_2 delivery are shown. Arterial O_2 content decreased rapidly after initiation of hypoxia, from 8.0 ± 0.24 to 4.8 ± 0.92 ml/dL.

However, the increase of cerebral blood flow was comparatively slow, reaching a maximum 15-20 min after hypoxia was induced.

These results show that nitric oxide is necessary for a major portion of the compensatory increase in cerebral blood flow that occurs in the fetus during hypoxia. The severe blunting of the flow response after L-NAME strongly supports this conclusion. The results show that O_2 delivery to the fetal brain falls rapidly and does not recovery completely until 25-30 min after the beginning of moderately severe hypoxia. They also show that O_2 delivery is increased above baseline during recovery. This appears to be the first time these observations have been made.

Despite continued infusion of L-NAME throughout the hypoxic interval, cerebral flow eventually rose to ~20% above baseline. This relatively small, delayed increase may indicate that blockade of nitric oxide synthase was inadequate to prevent nitric oxide synthesis during hypoxia. However, the sustained increase of fetal blood pressure shown earlier suggests that the blockade remained effective throughout the hypoxic exposure. We speculate, therefore, that other vasoactive mediators such as adenosine may be responsible for the remaining increase in cerebral blood flow. One of the specific aims for the next six months' work will be to investigate whether adenosine plays such a role, and if so, whether it acts independently of NO, and whether it acts continuously or only when the nitric oxide system is reduced or absent.

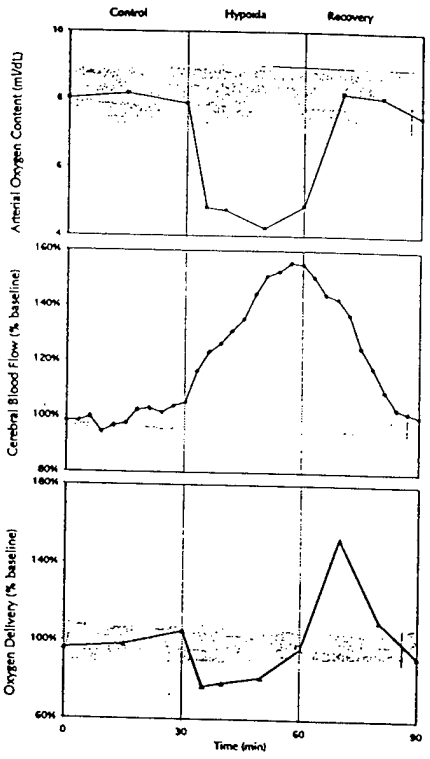

D. CONCLUSIONS.

These studies have provided continuous measurements of cerebral perfusion from a small region of the fetal brain for the first time. The control of the cerebral circulation is of great importance in preventing hemorrage into the brain which is a devastating complication in the perinatal period. The present results and future results will provide a rational basis for administering drugs, in particular nitric oxide and adenosine agonists and antagonists, that would reduce the tendency to hemorrage, form edema and other pathophysiological processes.

There are two deliverable products. The first is purely basic science. It is the knowledge of what drugs to administered to alter cerebral blood flow favorably. The second is a hardware item that may be patentable. It is a dual probe containing both a laser Doppler window and a temperature sensor. It will be developed in collaboration with BioPac and marketed by them. Further details are provided in the special information section below.

E. REFERENCES

1. Albera, R., Magnano, M., De Siena, L., Orecchia, C., Bolognese, P., Pignocchino, P., and Cortesina, G. [The measurement of cochlear flow by laser Doppler in man: the preliminary results]. *Acta Otorhinolaryngol Ital* 12(6), 553-564, 1992.
2. Anderson, P. A. W., C. S. Kleinman, G. Lister, and N. S. Talner. Cardiovascular Function During Normal Fetal and Neonatal Development and with Hypoxic Stress. In Polin, R. A. and W. W. Fox, eds. Fetal and Neonatal Physiology. Philadelphia, W.B. Saunders Company. 1998, 876-890.
3. Arbit, E. and G. R. DiResta. Application of laser Doppler flowmetry in neurosurgery. *Neurosurg Clin N Am* 7: 741-8, 1996.
4. Archer, S. Measurement of nitric oxide in biological models. *Faseb J* 7: 349-60, 1993.
5. Asakura, H., K. T. Ball and G. G. Power. Interdependence of arterial PO_2 and O_2 consumption in the fetal sheep. *J. Develop. Physiol.* 13: 205-213, 1990.
6. Asano, H., Homan, J., Carmichael, L., Korkola, S., and Richardson, B. Cerebral metabolism during sustained hypoxemia in preterm fetal sheep. Am J Obstet Gynecol 170(3), 939-944. 94.
7. Ashwal, S., Majcher, J. S., Vain, N., and Longo, L. D. Patterns of fetal lamb regional cerebral blood flow during and after prolonged hypoxia. *Pediatr Res* 14(10), 1104-1110, 1980.
8. Ball, K. T., Gunn, T. R., Power, G. G. Asakura, H., and Gluckman, P. D. A potential role for adenosine in the inhibition of nonshivering thermogenesis in the fetal sheep. *Pediatr Res*. 37: 303-309, 1995.
9. Barfod, C., Akgören, N., Fabricius, M., Dirnagl, U., and Lauritzen, M. Laser-Doppler measurements of concentration and velocity of moving blood cells in rat cerebral circulation. *Acta Physiol Scand* 160(2), 123-132, 1997.
10. Bocking, A. D., S. E. White, J. Homan, and B. S. Richardson. Oxygen consumption is maintained in fetal sheep during prolonged hypoxaemia. *J Dev Physiol* 17: 169-74, 1992.
11. Bolognese, P., Miller, J. I., Heger, I. M., and Milhorat, T. H. Laser-Doppler flowmetry in neurosurgery. *J Neurosurg Anesthesiol* 5(3), 151-158, 1993.
12. Brown, G. C., McBride, A. G., Fox, E. J., McNaught, K. S., and Borutaite, V. Nitric oxide and oxygen metabolism. *Biochem Soc Trans* 25(3), 901-4, 1997.
13. Browne, V. A., Stiffel, V. M., Pearce, W. J., Longo, L. D., and Gilbert, R. D. Cardiac beta-adrenergic receptor function in fetal sheep exposed to long-term high-altitude hypoxemia. *Am J Physiol* 273(6 Pt 2), R2022-R2031, 1997.
14. Bruno, V. M., Goldberg, M. P., Dugan, L. L., Giffard, R. G., and Choi, D. W. Neuroprotective effect of hypothermia in cortical cultures exposed to oxygen-glucose deprivation or excitatory amino acids. *J Neurochem* 63(4), 1398-1406, 1994.
15. Buchanan, J. E. and J. W. Phillis. The role of nitric oxide in the regulation of cerebral blood flow. *Brain Res* 610: 248-55, 1993.
16. Cohen, R. A. The potential clinical impact of 20 years of nitric oxide research [editorial]. *Am J Physiol* 276: H1404-7, 1999.
17. Czosnyka, M., Guazzo, E., Iyer, V., Kirkpatrick, P., Smielewski, P., Whitehouse, H., and Pickard, J. D. Testing of cerebral autoregulation in head injury by waveform analysis of blood flow velocity and cerebral perfusion pressure. Acta Neurochir Suppl (Wien) 60, 468-471. 94.
18. Czosnyka, M., H. Whitehouse, P. Smielewski, P. Kirkpatrick, E. P. Guazzo, and J. D. Pickard. Computer supported multimodal bed-side monitoring for neuro intensive care. *Int J Clin Monit Comput* 11: 223-32, 1994.

19. de Haan, H. H., Ijzermans, A. C., de Haan, J., Van Belle, H., and Hasaart, T. H. Effects of surgery and asphyxia on levels of nucleosides, purine bases, and lactate in cerebrospinal fluid of fetal lambs. *Pediatr Res* 36(5), 595-600, 1994.

20. Dietrich, W. D. The importance of brain temperature in cerebral injury. *J Neurotrauma* 9 Suppl 2: S475-85, 1992.

21. Dreier, J. P., K. Korner, A. Gorner, U. Lindauer, M. Weih, A. Villringer, and U. Dirnagl. Nitric oxide modulates the cerebral blood flow response to increased extracellular potassium. *J Cereb Blood Flow Metab* 15: 914-9, 1995.

22. Eyre, J. A., Essex, T. J., Flecknell, P. A., Bartholomew, P. H., and Sinclair, J. I. A comparison of measurements of cerebral blood flow in the rabbit using laser Doppler spectroscopy and radionuclide labelled microspheres. *Clin Phys Physiol Meas* 9(1), 65-74, 1988.

23. Fabricius, M. and Lauritzen, M. Laser-Doppler evaluation of rat brain microcirculation: comparison with the [14C]-iodoantipyrine method suggests discordance during cerebral blood flow increases. *J Cereb Blood Flow Metab* 16(1), 156-161, 1996.

24. Faraci, F. M. Role of nitric oxide in regulation of basilar artery tone in vivo. *Am J Physiol* 259: H1216-21, 1990.

25. Faraci, F. M. Role of endothelium-derived relaxing factor in cerebral circulation: large arteries vs. microcirculation. *Am J Physiol* 261: H1038-42, 1991.

26. Faraci, F. M. and D. D. Heistad. Regulation of the cerebral circulation: role of endothelium and potassium channels. *Physiol Rev* 78: 53-97, 1998.

27. Faraci, F. M. and Sobey, C. G. Role of potassium channels in regulation of cerebral vascular tone. *J Cereb Blood Flow Metab* 18(10), 1047-1063, 1998.

28. Fasano, V. A., Urciuoli, R., Bolognese, P., and Mostert, M. Intraoperative use of laser Doppler in the study of cerebral microvascular circulation. *Acta Neurochir (Wien)* 95(1-2), 40-48, 1988.

29. Fukuda, O., Endo, S., Kuwayama, N., Harada, J., and Takaku, A. The characteristics of laser-Doppler flowmetry for the measurement of regional cerebral blood flow. *Neurosurgery* 36(2), 358-364, 1995.

30. Gautier, H. Invited editorial on "oxygen transport in conscious newborn dogs during hypoxic hypometabolism". *J. Appl. Physiol.* 84: 761-762, 1998.

31. Gilbert, R. D., Pearce, W. J., Ashwal, S., and Longo, L. D. Effects of hypoxia on contractility of isolated fetal lamb cerebral arteries. *J Dev Physiol* 13(4), 199-203, 1990.

32. Gleason, C. A., C. Hamm, and M. D. Jr. Jones. Effect of acute hypoxemia on brain blood flow and oxygen metabolism in immature fetal sheep. *Am J Physiol* 258: H1064-9, 1990.

33. Goadsby, P. J., Kaube, H., and Hoskin, K. L. Nitric oxide synthesis couples cerebral blood flow and metabolism. *Brain Res* 595(1), 167-170, 1992.

34. Green, L. R., Bennet, L., and Hanson, M. A. The role of nitric oxide synthesis in cardiovascular responses to acute hypoxia in the late gestation sheep fetus. J Physiol Lond 497(Pt 1), 271-7. 96.

35. Gunn, A. J. and Gunn, T. R. The 'pharmacology' of neuronal rescue with cerebral hypothermia. *Early Hum Dev* 53(1), 19-35, 1998

36. Haberl, R. L., Heizer, M. L., and Ellis, E. F. Laser-Doppler assessment of brain microcirculation: effect of local alterations. *Am J Physiol* 256(4 Pt 2), H1255-H1260, 1989.

37. Heales, S. J., Barker, J. E., Stewart, V. C., Brand, M. P., Hargreaves, I. P., Foppa, P., Land, J. M., Clark, J. B., and Bolanos, J. P. Nitric oxide, energy metabolism and neurological disease. *Biochem Soc Trans* 25(3), 939-43, 1997.

38. Hemingway, A., and L. Birzis. Effect of hypoxia on shivering. *J. Appl. Physiol.* 8: 577-579, 1956.

39. Heymann, M. A., B. D. Payne, J. I. Hoffman, and A. M. Rudolph. Blood flow measurements with radionuclide-labeled particles. *Prog Cardiovasc Dis* 20: 55-79, 1977.

40. Hill, J. R. The oxygen consumption of new-born and adult mammals. Its dependence on the oxygen tension of the inspired air and on the environbmental temperature. *J. Physiol. (Lond.)* 149: 346-373, 1959.

41. Hoffman, J. I., M. A. Heymann, A. M. Rudolph, and B. D. Payne. Uses and abuses of the radioactive microsphere method of measuring regional blood flow. *Bibl Anat* (15: 20-3, 1977.

42. Hope, I. D., F. J. Huikeshoven, R. D. Gilbert, G. G. Power, and L. D. Longo. Errors in microsphere determination of cardiac output: a computer simulation in fetal sheep. *Am. J. Physiol* 256: H302-310, 1989.

43. Hudetz, A. G. Regulation of oxygen supply in the cerebral circulation. *Adv Exp Med Biol* 428, 513-520, 1997.

44. Hudetz, A. G., Shen, H., and Kampine, J. P. Nitric oxide from neuronal NOS plays critical role in cerebral capillary flow response to hypoxia. *Am J Physiol* 274(3 Pt 2), H982-H989, 1998.

45. Hylland, P., Nilsson, G. E., and Lutz, P. L. Role of nitric oxide in the elevation of cerebral blood flow induced by acetylcholine and anoxia in the turtle. *J Cereb Blood Flow Metab* 16(2), 290-295, 1996.

46. Iadecola, C. Does nitric oxide mediate the increases in cerebral blood flow elicited by hypercapnia? *Proc Natl Acad Sci USA* 89: 3913-6, 1992.

47. Iadecola, C., Pelligrino, D. A., Moskowitz, M. A., and Lassen, N. A. Nitric oxide synthase inhibition and cerebrovascular regulation. *J Cereb Blood Flow Metab* 14(2), 175-192, 1994.

48. Jensen, A. and R. Berger. Fetal circulatory responses to oxygen lack. *J Dev Physiol* 16: 181-207, 1991.

49. Jensen, A., Y. Garnier, and R. Berger. Dynamics of fetal circulatory responses to hypoxia and asphyxia. *Eur J Obstet Gynecol Reprod Biol* 84: 155-72, 1999.

50. Jensen, A., M. Hohmann, and W. Kunzel. Redistribution of fetal circulation during repeated asphyxia in sheep: effects on skin blood flow, transcutaneous PO2, and plasma catecholamines. *J Dev Physiol* 9: 41-55, 1987.

51. Karimi, A., Ball, K. T., and Power, G. G. Exogenous infusion of adenosine depresses whole body O_2 use in fetal/neonatal sheep. *J Appl Physiol* 81(2), 541-547, 1996.

52. Kirkeby, O. J., Rise, I. R., Nordsletten, L., Skjeldal, S., Hall, C., and Risöe, C. Cerebral blood flow measured with intracerebral laser-Dopplerflow probes and radioactive microspheres. *J Appl Physiol* 79(5), 1479-1486, 1995.

53. Kirkpatrick, P. J., Smielewski, P., Czosnyka, M., and Pickard, J. D. Continuous monitoring of cortical perfusion by laser Doppler flowmetry in ventilated patients with head injury. *J Neurol Neurosurg Psychiatry* 57(11), 1382-1388, 1994.

54. Kobari, M., Fukuuchi, Y., Tomita, M., Tanahashi, N., and Takeda, H. Role of nitric oxide in regulation of cerebral microvascular tone and autoregulation of cerebral blood flow in cats. *Brain Res* 667(2), 255-262, 1994.

55. Koos, B. J., Chau, A., and Ogunyemi, D. Adenosine mediates metabolic and cardiovascular responses to hypoxia in fetal sheep. *J. Physiol (Lond)* 488: 761-766, 1995.

56. Kubonoya, K. and G. G. Power. Plasma adenosine responses during repeated episodes of umbilical cord occlusion. *Am J Obstet Gynecol* 177: 395-401, 1997.

57. Kubonoya, K., Y. Yoneyama, R. Sawa, T. Araki, and G. G. Power. Brain temperature and metabolic responses during umbilical cord occlusion in fetal sheep. *Pflugers Arch* 436: 667-72, 1998.

58. Lassen, N. A. Autoregulation of cerebral blood flow. *Circ Res* 9 and 10(Supplement I), I-201-204, 1964.

59. Lindsberg, P. J., Jacobs, T. P., Frerichs, K. U., Hallenbeck, J. M., and Feuerstein, G. Z. Laser-Doppler flowmetry in monitoring regulation of rapid microcirculatory changes in spinal cord. *Am J Physiol* 263(1 Pt 2), H285-H292, 1992.

60. Lindsberg, P. J., O'Neill, J. T., Paakkari, I. A., Hallenbeck, J. M., and Feuerstein, G. Validation of laser-Doppler flowmetry in measurement of spinal cord blood flow. *Am J Physiol* 257(2 Pt 2), H674-H680, 1989.

61. Longo, L. D. and S. Packianathan. Hypoxia-ischaemia and the developing brain: hypotheses regarding the pathophysiology of fetal-neonatal brain damage. *Br J Obstet Gynaecol* 104: 652-62, 1997.

62. Longo, L. D. and Pearce, W. J. Fetal and newborn cerebral vascular responses and adaptations to hypoxia. *Semin Perinatol* 15(1), 49-57, 1991.

63. Lundar, T., K. F. Lindegaard, and H. Nornes. Continuous recording of middle cerebral artery blood velocity in clinical neurosurgery. *Acta Neurochir* 102: 85-90, 1990.

64. Meyerson, B. A., L. Gunasekera, B. Linderoth, and B. Gazelius. Bedside monitoring of regional cortical blood flow in comatose patients using laser Doppler flowmetry. *Neurosurgery* 29: 750-5, 1991.

65. Morikawa, E., M. D. Ginsberg, W. D. Dietrich, R. C. Duncan, S. Kraydieh, M. Y. Globus, and R. Busto. The significance of brain temperature in focal cerebral ischemia: histopathological consequences of middle cerebral artery occlusion in the rat. *J Cereb Blood Flow Metab* 12: 380-9, 1992.

66. Newby, A. C., Y. Worku, P. Meghji, J. Nakazawa, and A. C. Skladanowski. Adenosine: A retaliatory Metabolite or Not? *News Physiol. Sci.* 5: 67-70, 1990

67. Newson, T. P., Obeid, A., Wolton, R. S., Boggett, D., and Rolfe, P. Laser Doppler velocimetry: the problem of fibre movement artefact. *J Biomed Eng* 9(2), 169-172, 1987.

68. Nilsson, G. E. and Söderström, V. Comparative aspects on nitric oxide in brain and its role as a cerebral vasodilator. *Comp Biochem Physiol* 118(4), 949-958, 1997.

69. Obeid, A. N. In vitro comparison of different signal processing algorithms used in laser Doppler flowmetry. *Med Biol Eng Comput* 31(1), 43-52, 1993.

70. Obeid, A. N., Barnett, N. J., Dougherty, G., and Ward, G. A critical review of laser Doppler flowmetry. *J Med Eng Technol* 14(5), 178-181, 1990.

71. Obeid, A. N., Dougherty, G., and Pettinger, S. In vivo comparison of a twin wavelength laser Doppler flowmeter using He-Ne and laser diode sources. *J Med Eng Technol* 14(3), 102-110, 1990.

72. Palmer, R. M., D. S. Ashton, and S. Moncada. Vascular endothelial cells synthesize nitric oxide from L-arginine. *Nature* 333: 664-6, 1988.

73. Papile, L. A., Rudolph, A. M., and Heymann, M. A. Autoregulation of cerebral blood flow in the preterm fetal lamb. *Pediatr Res* 19(2), 159-161, 1985.

74. Paulson, O. B., Strandgaard, S., and Edvinsson, L. Cerebral autoregulation. *Cerebrovasc Brain Metab Rev* 2(2), 161-192, 1990.

75. Pearce, W. J. Mechanisms of hypoxic cerebral vasodilatation. *Pharmacol Ther* 65(1), 75-91, 1995.

76. Pearce, W. J. and Longo, L. D. Developmental aspects of endothelial function. *Semin Perinatol* 15(1), 40-48, 1991.

77. Pearce, W. J., A. M. Reynier-Rebuffel, J. Lee, P. Aubineau, L. Ignarro, and J. Seylaz. Effects of methylene blue on hypoxic cerebral vasodilatation in the rabbit. *J Pharmacol Exp Ther* 254: 616-25, 1990.

78. Peeters, L. L., R. E. Sheldon, M. D. Jr. Jones, E. L. Makowski, and G. Meschia. Blood flow to fetal organs as a function of arterial oxygen content. *Am J Obstet Gynecol* 135: 637-46, 1979.

79. Pelligrino, D. A., H. M. Koenig, and R. F. Albrecht. Nitric oxide synthesis and regional cerebral blood flow responses to hypercapnia and hypoxia in the rat. *J Cereb Blood Flow Metab* 13: 80-7, 1993.

80. Pohl, U. and de Wit, C. A Unique Role of NO in the Control of Blood Flow. *New Physiol. Sci.* 14, 74-80, 1999.

81. Power, G. G. Biology of temperature: the mammalian fetus. *J Dev Physiol* 12: 295-304, 1989.

82. Power, G. G., P. S. Dale, and P. S. Nelson. Distribution of maternal and fetal blood flow within cotyledons of the sheep placenta. *Am. J. Physiol* 241: H486-496, 1981.

83. Purves, M. J. The Physiology of the Cerebral Circulation. Cambridge, England, Cambridge University Press. 1972.

84. Raab, S., E. Thein, A. G. Harris, and K. Messmer. A new sample-processing unit for the fluorescent microsphere method. *Am J Physiol* 276: H1801-6, 1999.

85. Richards, H. K., Czosnyka, M., Kirkpatrick, P. J., and Pickard, J. D. Estimation of laser-Doppler flux biological zero using basilar artery flow velocity in the rabbit. *Am J Physiol* 268(1 Pt 2), H213-H217, 1995.

86. Richardson, B., Nodwell, A., Webster, K., Alshimmiri, M., Gagnon, R., and Natale, R. Fetal oxygen saturation and fractional extraction at birth and the relationship to measures of acidosis. Am J Obstet Gynecol 178(3), 572-579. 98.

87. Richardson, B. S. Fetal adaptive responses to asphyxia. *Clin Perinatol* 16: 595-611, 1989.

88. Rohlicek, C.V., C. Saiki, T. Matsuoka, and J. P. Mortola. Oxygen transport in conscious newborn dogs during hypoxic hypometabolism. *J. Appl. Physiol* 84: 763-768, 1998.

89. Rosenblum, B. R., R. F. Bonner, and E. H. Olaser Doppler flowield. Intraoperative measurement of cortical blood flow adjacent to cerebral AVM using laser Doppler velocimetry. *J Neurosurg* 66: 396-9, 1987.

90. Rurak, D. W., Richardson, B. S., Patrick, J. E., Carmichael, L., and Homan, J. Blood flow and oxygen delivery to fetal organs and tissues during sustained hypoxemia. Am J Physiol 258(5 Pt 2), R1116-R1122. 90.

91. Schneider, S. J., A. D. Rosenthal, B. M. Greenberg, and J. Danto. A preliminary report on the use of laser-Doppler flowmetry during tethered spinal cord release. *Neurosurgery* 32: 214-7; discussion 217-8, 1993.

92. Skarphedinsson, J. O., H. Harding, and P. Thoren. Repeated measurements of cerebral blood flow in rats. Comparisons between the hydrogen clearance method and laser Doppler flowmetry. *Acta Physiol Scand* 134: 133-42, 1988.

93. Stern, M. D., D. L. Lappe, P. D. Bowen, J. E. Chimosky, G. A. Jr. Holloway, H. R. Keiser, and R. L. Bowman. Continuous measurement of tissue blood flow by laser-Doppler spectroscopy. *Am J Physiol* 232: H441-8, 1977.

94. Thompson, B. G., Pluta, R. M., Girton, M. E., and Olaser, E. H. Nitric oxide mediation of chemoregulation but not autoregulation of cerebral blood flow in primates. *J Neurosurg* 84(1), 71-78, 1996.

95. Todd, M. M., B. Wu, M. Maktabi, B. J. Hindman, and D. S. Warner. Cerebral blood flow and oxygen delivery during hypoxemia and hemodilution: role of arterial oxygen content. *Am J Physiol* 267: H2025-31, 1994.

96. van Bel, F., A. Sola, C. Roman, and A. M. Rudolph. Role of nitric oxide in the regulation of the cerebral circulation in the lamb fetus during normoxemia and hypoxemia. *Biol Neonate* 68: 200-10, 1995.

97. van Bel, F., Sola, A., Roman, C., and Rudolph, A. M. Perinatal regulation of the cerebral circulation: role of nitric oxide and prostaglandins. *Pediatr Res* 42(3), 299-304, 1997.

98. von Lubitz, D. K. J. E. Adenosine and cerebral ischemia: therapeutic future or death of a brave concept? Eur. J. Pharmacol. 371: 85-102, 1999

99. Ward, M. E. Dilation of rat diaphragmatic arterioles by flow and hypoxia: roles of nitric oxide and prostaglandins. *J Appl Physiol* 86: 1644-50, 1999.

100. Watkins, L. D. Nitric oxide and cerebral blood flow: an update. *Cerebrovasc Brain Metab Rev* 7: 324-337, 1995.

101. Winn, H. R., G. R. Rubio, and R. M. Berne. The role of adenosine in the regulation of cerebral blood flow. *J Cereb Blood Flow Metab* 1: 239-44, 1981.

102 Wood, S. C., and R. Gonzales. Hypothermia in hypoxic animals: mechanisms, mediators, and functional significance. *Comp. Biochem. Physiol.* 113B:37-43, 1996.

103. Yamashita, N., Kamiya, K., and Nagai, H. CO_2 reactivity and autoregulation in fetal brain. *Childs Nerv Syst* 7(6), 327-331, 1991.

104. Zhang, L., Xiao, D., and Bouslough, D. B. Long-term high-altitude hypoxia increases plasma nitrate levels in pregnant ewes and their fetuses. *Am J Obstet Gynecol* 179(6 Pt 1), 1594-8, 1998.

105. Zhong, J., Seifalian, A. M., Salerud, G. E., and Nilsson, G. E. A mathematical analysis on the biological zero problem in laser Doppler flowmetry. *IEEE Trans Biomed Eng* 45(3), 354-364, 1998.

SPECIAL INFORMATION

Patents-

Patent protection for the custom-made, probe-holding device is possible. However, the use of the fixation device in the human fetus in utero is problematic because of the risk of abortion, intracrancial bleeding and infection. Whether the device might be patented for use in the perinatal period immediately after birth remains for future work.

Publications--

A paper describing NMTB-supported work is currently in review and was approved before submission. A copy is included here as an appendix.

Publications pending approval-- None

Commercialization--

Laser Doppler probes and flowmeters are currently manufactured by several companies. These include Perimed Inc, North Royalton, OH and BioPak Systems Inc., Santa Barbara, CA as leaders.

Laser Doppler is increasingly used to measure brain perfusion in the neurosurgical intensive care unit. It is used to judge the need for surgery and to guide therapy, especially with regards to the need to lower intracranial pressure. In the future laser Doppler may prove useful in the neonatal intensive care unit. Improvements in technology to reduce movement artifacts as described in this application will speed this application.

There is no currently available means to measure oxygen consumption of the brain continuously on-line. Such measurements are directly relevant monitoring cerebral welfare and the need for treatment and surgery. The proposed technology using thermocouples in conjunction with laser Doppler flow recording is new and novel, and is likely to find application first in neurosurgical intensive care units.

Commercial planning is currently underway with Biopac Systems, Inc. to develop and test the proposed unit. We believe the critical element will be to record perfusion and temperature in the same localized region of the brain. We propose to do this with a composite probe with both sensors fabricated together. The two sensing elements must be placed sufficiently far apart (perhaps 3 mm as an initial estimate) to avoid cross-talk and sufficiently close together to sample information from a physiologically discrete region of the brain.

DESCRIPTION: State the goal of the project, including how it relates to improving health care and noting the advanced technology that will be developed or tested. Use succinct language to describe how the project goals will be achieved. **Do not exceed the space provided.**

In America today, half of all men and one third of all women will develop cancer during their lifetime. Surgery is used to treat 60% of cancer patients, but only a minority are cured by surgery alone. Radiation and chemotherapy improve outcomes but the persistent morality from this disease suggests a need for continued innovation. Cancer immunotherapy uses the body's defenses to recognize and destroy tumor cells and is a promising adjunct therapy.

Human $CD8^+$ 'killer' T cells have been shown to recognize and kill tumor cells from melanoma, breast, colon, and prostate cancer, leading to the search for methods to immunize patients against their own tumors. Dendritic cells (DC) are promising vehicles for immunization as they can potently activate T cells both *in vitro* and *in vivo.*

Current strategies and clinical trials for DC immunotherapy have focused solely on the delivery of antigens to DC, but not strategies for their activation. The proposed work will develop chimeric proteins that carry immunizing antigens, but also serve to activate dendritic cells to increase their immunostimulatory properties and their lifespan.

Freshly isolated or 'immature' DC stimulate T cells poorly, and can in some cases inactivate them. The ligation of CD40 on DC is the most potent stimuli for their maturation, causing an increase in theirimmunostimulatory function and lifespan. Adaptor proteins of the TRAF (TNF Receptor Adaptor Factors) family mediate CD40 signaling, and their over-expression mimics CD40 function. A truncated version of TRAF2, lacking its C-terminal TRAF regulatory domain, has been shown to be constitutively active and will be the basis of strategies to activate dendritic cells.

Adenoviral vectors will be constructed expressing a chimeric protein composed of a constitutively active TRAF2 protein fused to a gene segment coding for the immunizing antigen. Murine DC will then be treated with the viral vectors, and their ability to stimulate $CD8^+$ T cells in vitro and in vivo measured. An murine tumor model using defined model tumor antigens will then be used to assess the efficacy of these DC in tumor protection and eradication

Clinical trials are currently underway using DC in the therapy of melanoma and breast, colon, and prostate cancers, diseases that account for 450,000 new cases annually. Of these cancers, the most promising application for dendritic cell vaccines is the adjuvant therapy of high-risk melanoma, for which the only FDA approved therapy is interferon-α, for which the annual market is estimated at $151 million (wholesale US sales) and is expected to increase as the incidence of melanoma in this country continues to rise

PROJECT SITE(S) (organization, city, state):

Loma Linda Cancer Research Institute
Loma Linda University
Loma Linda CA 92354

NO. 28

LLU/Salo

Chimeric Vaccines for Dendritic Cell Activation

Recently begun project with first report due October 2000

No report at this time

DESCRIPTION AND PERFORMANCE SITES (FORM B)

DESCRIPTION: State the goal of the research project including how it relates to improving health care for the nation's people. Use succinct language to describe how the project goals will be achieved. Do not exceed the space provided on this page.

The current prostate cancer screening methods, prostatic specific antigen (PSA) and digital rectal examination (DRE), have limitations in the detection of early curable prostate cancer. The positive predictive value of these two screening methods is in the range of 25-35%. A more informative non-invasive screening method is continually being sought. The recent discovery of presence of telomerase activity in prostate cancer tissue suggests that the telomeric repeat amplification protocol, TRAP, assay may be of clinical value in the screening and detection of prostate cancer. We established a collaboration between the departments of Biochemistry, Urologic Surgery, and Pathology of Loma Linda University and obtained specimens from patients receiving care at four local institutions, including the university hospital, a veterans administration hospital, and two county hospitals serving the indigent population. We explored the novel use of the TRAP assay as a prostate cancer screening procedure using non-invasively obtained prostatic fluid rather than tissue. Our preliminary data indicate that the TRAP assay detects telomerase activity in prostatic fluid (PF) of patients with prostate cancer, but does not detect any telomerase activity in normal patients. The positive preditive value of PF TRAP assay appears to be in the range of 80-90% suggesting that this assay fulfills the need for a more informative non-invasive prostate cancer screening procedure. A larger sample size now needs to be investigated in order to optimize the sensitivity and specificity of this assay. Our ultimate goal is to develop a clinically relevant telomerase assay on prostatic fluid which can be used as a screening tool either alone or in conjunction with other screening methods to improve the detection of prostate cancer in its early curable stages.

PROJECT SITE(s) ***(Organization, City, State)*****:**

Loma Linda University
Loma Linda, CA

CO

MAR 6 2000

ROLE OF TELOMERASE IN GENITOURINARY MALIGNANCIES

FINAL REPORT

Subagreement #14-FY98-LLU-SANDS Loma Linda University

Period Covered: 01/26/1999-01/26/2000

Principal Investigator: John F. Sands, Ph.D.

Report Submitted By: Charles W. Slattery, Ph.D.

Voice: 909-558-1000 X48656

FAX: 909-558-4887

E-mail: cslattery@som.llu.edu

Signature: Charles W. Slattery Date Prepared: 3/2/00

During the project over 100 prostatic fluid samples were examined. Approximately 2/3 of the samples were collected in attempts to determine the best conditions for the assay. The remaining 1/3 are described below in a format that is similar to a submitted article and in a format that is close to that requested by NMTB. The second part describes our efforts to determine the utility of the ELISA for examining prostatic fluid and tissue.

The analysis of prostatic fluid using the TRAP assay to detect prostate cancer

INTRODUCTION

Prostate cancer is the most common noncutaneous malignancy in men and is second only to lung cancer in causing cancer-related deaths of males in the United States (1). It is believed by most urologists that the early detection of prostate cancer increases the probability of successful treatment (1). Diagnostic techniques, including the serum prostate specific antigen (PSA) test and transrectal ultrasound, have a low incidence of complications and have increased the sensitivity of cancer detection over digital rectal examination, thus benefiting many patients (2). Telomerase activity has been detected in tissue specimens from prostate cancer patients (3-8), raising the possibility that telomerase activity in tissue may be an independent marker for prostate cancer. However, an even more significant clinical use of detecting telomerase activity would be in the detection of prostate cancer through the analysis of readily accessible body fluids such as urine, semen, or prostatic secretions. Collection of such fluid specimens has the advantage of avoiding surgical invasion of the prostate gland. In this research, we have used the TRAP assay to measure telomerase activity in freshly collected prostatic fluid specimens with the goal of developing the TRAP assay into a reliable diagnostic tool for prostate cancer detection.

MATERIALS AND METHODS

Cell Culture and CHAPS Protein Extraction

A human prostate cancer cell line derived from a bone metastasis, PC-3, with a doubling time of 2.7 days in tissue culture (9) and obtained from the ATCC (Rockville, MD), was grown in RPMI 1640 medium supplemented with 10% new-born calf serum. The cells were harvested when 90% confluent using trypsin. After the cells were collected by centrifugation, the cell pellet was washed twice with cold phosphate-buffered saline, re-suspended in ice-cold Buffer A [10 mM HEPES-KOH (pH 7.5), 1.5 mM $MgCl_2$, 10 mM KCl, 1 mM dithiothreitol] and recentrifuged. The pellet was lysed in Buffer B (Lysis Buffer) [0.5% 3-(3-cholamidopropyl-dimethylammonio)-1-propanesulfonate (CHAPS), 5 mM β-mercaptoethanol, 0.1 mM phenylmethanesulfonyl fluoride (PMSF), 10% glycerol, 10 mM Tris-HCl (pH 7.5), 1 mM $MgCl_2$] for 30 min on ice. Then, the lysate was centrifuged at 16,000 x g for 20 min at 4 °C. Aliquots of the supernatant fluid were immediately stored at -80 °C. The protein concentration was determined by ultraviolet spectrophotometry (10).

Collection of Prostatic Fluid

Prostatic fluid specimens were collected from 30 prostrate cancer (PCa) patients and from

9 patients clinically confirmed as cancer-free, including 6 benign prostatic hyperplasia (BPH) patients. In brief, siliconized microcentrifuge tubes were prepared in advance to contain 1.18 ml of a master mix of protease inhibitors (see below). A few minutes prior to specimen collection, 20 µl of an ethanol solution of PMSF was added to each microcentrifuge tube. Prostatic fluid was collected from each patient by palpating the prostate and milking the fluid through the urethra. Approximately 300 µl of the extruded fluid was transferred immediately into the microtube, mixing the specimen with protease inhibitors by inversion three times. The final concentrations of the added protease inhibitors were 10 mM disodium EDTA, 5 mM benzamidine-HCl, 20 mM sodium caproate, and 0.2 mM PMSF. The microtube was then centrifuged 5 min in an Eppendorf table-top centrifuge at 4 °C. The supernatant fluid was divided into aliquots, which together with the pellet were placed on dry ice and transferred to the laboratory. The aliquots of the supernatant fluid were stored at -80°C, while the pellet was further treated by the CHAPS protein extraction method as described above. This extract was also divided into aliquots for freezing and storage at -80 °C. The protein concentrations of the CHAPS extracts were determined by ultraviolet spectrophotometry (10).

TRAP Assay

Each specimen was assayed for telomerase activity using supernatant fluid samples (1 µl) and aliquots of the CHAPS protein extract of the pellet that contained 6 µg protein. An aliquot of CHAPS protein extract of PC-3 cells, containing 6 µg of protein corresponding to approximately 3,000 PC-3 cells, was assayed along with specimen samples as a positive control. An identical aliquot inactivated by heat (85 °C for 15 min) or by exposure to RNase A (0.2 µg/µl at 37 °C for 30 min) was assayed as a negative control. CHAPS lysis buffer was also used as a negative control. Aliquots of PC-3 cell extracts corresponding to 1,000, 100, 10, and 1 cells were assayed to standardize the telomerase activity and estimate how much telomerase was present in each specimen.

The TRAP assay for telomerase activity was performed as described by Kim et al. (3) with minor modifications. In brief, an appropriate aliquot of either a prostatic specimen or a protein extract of PC-3 cells was assayed in 50 µl of reaction mixture containing 50 µM deoxynucleotide triphosphates, 0.1 µg of TS primer (5'-AATCCGTCGAGCAGAGTT-3'), 2 Units of *Taq* polymerase, 1 µl of [α-^{32}P]dCTP (10 mCi/ml, 3,000 Ci/mmol), 20 mM Tris-HCl (pH 8.3), 1.5 mM $MgCl_2$, 63 mM KCl, 1 mM EGTA, 0.005% Tween-20 in a 0.5 ml tube that contained 0.1 µg of CX primer (5'-CCCTTACCCTTACCCTTACCCTAA-3') sequestered at the bottom of the 0.5 ml tube by a wax barrier (Ampliwax, Perkin Elmer, Foster City, CA). After 45 min of incubation at room temperature, the reaction mixture was subjected to 34 PCR cycles consisting of 94 °C for 30 s, 50 °C for 30 s, and 72 °C for 90 s. The PCR product was then subjected to electrophoresis on a 10% non-denaturing polyacrylamide gel, dried, and exposed to X-ray film, or developed in a Bio-Rad Molecular Imager in conjunction with the Molecular Analyst software (Bio-Rad Laboratories, Hercules, CA). Typical products of telomerase activity were shown by the 6-bp ladder bands starting from 40 bp. Telomerase activity was graded on a scale of 0 to 3 (0, no activity; 3, highest activity). The following standards were used to judge a sample telomerase positive: 1) the presence in a sample lane of more than four bands of the 6-bp telomerase repeat, which could be eliminated by either RNase A or heat, and 2) repetition of the result with two or more repeat samplings.

Statistical analysis

Differences were evaluated by means of the chi-square test. *P* values less than or equal to 0.05 were considered statistically significant.

RESULTS

In agreement with previously reported data (5), substantial telomerase activity was observed in lysates of the PC-3 human prostate cancer cell line. In a serial dilution study of the PC-3 CHAPS lysate, telomerase activity could be detected in a protein extract corresponding to as little as one PC-3 cell when using a 34-PCR cycle (Fig. 1), confirming the high sensitivity of this assay system to detect telomerase activity in immortal cells.

Telomerase activity was detected in the supernatant fluid and/or the pellet extract of specimens obtained from 25 of 30 PCa patients (83%), whereas no activity was detectable in specimens taken from 8 of 9 patients (89%) with either a normal prostate gland or BPH (Table 1). The telomerase signals from the CHAPS protein extracts of the pellets were stronger than those from the supernatant fluids (Fig. 2). The telomerase ladder obtained from most of the prostate fluid specimens suggested that each assayed aliquot contained the telomerase equivalent of approximately 10 PC-3 cancer cells (Fig. 1 and Fig. 2). The positive rate (80%) from the CHAPS extracts of the pellets was significantly higher than that (53%) from the supernatant fluids (Table 1). Furthermore, in some specimens the telomerase activity was increased after heating at 85 °C for 15 min (Fig. 2, lanes 3, 7), while in other specimens the telomerase activity was diminished but could not be abolished by such heating (Fig. 2, lane 1). This is in contrast to the effect of heating a CHAPS extract of PC-3 cells to 85 °C for 15 min, which essentially eliminated telomerase activity (Fig. 2, lane 11). This phenomenon was further investigated by heating the aliquots of protein extract from a prostate cancer patient specimen to 85 °C for 60, 15, and 5 min and then determining the amount of telomerase activity that remained after the heat treatment (Fig. 3, lanes 2, 3, 4). Telomerase activity was still detectable after an hour at 85 °C. A double pretreatment was performed which involved heating at 85 °C for 15 min followed by exposure to RNase A (0.2 μg/μl) for 30 min at 37 °C (Fig. 3, lane 1). No telomerase activity was detectable in the specimens pretreated with both heat and RNase A. Our results suggest that a heat-pretreatment is not always an appropriate negative control for telomerase activity in prostatic fluid specimens. On the contrary, heat-pretreatment of some of the specimens improves the ability to detect telomerase activity.

We also analyzed the relationship between telomerase activity in the prostatic fluid specimens and the PSA values of patients, and found that telomerase activity had a strong correlation with the PSA levels (Table 2A). Patients with PSA values >4 ng/ml had telomerase activity in their prostatic fluid specimens 84% of the time, while only 29% of the patients with PSA values ≤4 ng/ml had telomerase activity in their prostatic secretions. Using this comparison, the positive predictive value (PPV) of the TRAP assay for an elevated PSA was 84%.

Telomerase activity was also correlated with the Gleason scores of PCa patients (Table 2B). Telomerase activity could be detected in 85% of prostatic fluid specimens from PCa patients with Gleason scores >4, and half of PCa patients with Gleason scores ≤4 also had telomerase activity in their prostatic fluid specimens. Using the Gleason score of 4 as the dividing point for these two groups produced a PPV of 92% for the higher group.

DISCUSSION

Since the development of the TRAP assay by Kim et al. (3), telomerase activity has been detected in a wide variety of malignant tumors, including prostate cancer (3,4). Therefore, telomerase shows promise as a cancer marker. Telomerase activity is detectable in surgically collected tissue specimens from PCa patients, indicating that the TRAP assay can be used as a diagnostic tool for PCa (5-8). However, telomerase detection in nonsurgically obtained body fluids, such as prostatic fluid, would likely be more practical for the diagnosis of prostate cancer because of easier patient compliance and lower expense.

Clinically, prostatic adenocarcinoma arises in the acinar and proximal ductal epithelium of the prostate gland and accounts for over 95% of prostatic cancers (11). Prostatic fluid contains proteases, lipids, metal ions and amines secreted daily from acinar cells of the prostate gland (12). Furthermore, a few exfoliated cells from the prostate and telomerase from those cancer cells might be in prostatic fluid. Telomerase activity has been detected in exfoliated cells present in urine from bladder carcinoma patients (13,14), as well as in colonic luminal washings from colon carcinoma patients (15).

The present study focuses on determining the diagnostic value of the TRAP assay applied to prostatic fluid specimens. More than 80% of 30 PCa patients showed positive telomerase activity in their prostatic fluid specimens. The PPV for prostate cancer was 96%. Almost 90% of the normal and BPH patients were negative for telomerase activity. These results indicate that telomerase activity in prostatic fluid is a useful diagnostic marker for prostate cancer. The pellets from centrifuged fresh prostatic fluid specimens, which probably contain exfoliated cancer cells, were shown to be better for detecting telomerase activity than supernatant fluids.

Telomerase is a ribonucleoprotein enzyme whose activity depends on both its RNA and protein components. Numerous data have shown that its activity can be eliminated by a pretreatment with either RNase A or heat (16,17). However, the results from some specimens showed that the telomerase activity could be increased after heat-pretreatment. In other specimens, the telomerase signals became weakened, but could not be totally abolished by pre-heating. This hints that inhibitors of telomerase are present in pure prostatic fluid specimens which bind tightly to the telomerase enzyme. Heat pretreatment appears to be inactivating the inhibitors rather than inactivating telomerase.

Serum PSA is commonly used as a marker for prostate cancer. In general, the higher the PSA level, the greater is the likelihood of an advanced pathologic stage (18). Serum PSA level has been found to correlate with tumor volume and is an important predictor of tumor progression and prognosis (19). In this study, we demonstrated that telomerase activity is highly correlated with PSA levels. In addition, we showed that a strong correlation exists between the presence of telomerase and a Gleason score greater than 4. Therefore, the detection of telomerase in prostatic fluid appears to serve as a prognostic marker as well as a diagnostic marker for prostate cancer. In our study, 96% of patients who showed positive telomerase activity in their prostatic fluid specimens also had prostate cancer. In contrast, only about 35% of males with serum PSA levels above 4 ng/ml are found to have prostate cancer (20). Therefore, the presence of telomerase in prostatic fluid is a more specific marker than serum PSA for diagnosing prostate cancer.

In conclusion, the PCR-based TRAP assay was sensitive enough to detect telomerase activity in prostatic fluid. Telomerase activity was detectable in more than 80% of prostatic fluid specimens obtained from prostate cancer patients, but it was not detectable in close to 90% of

specimens taken from prostate-normal or BPH patients. The prostatic fluid specimens can be collected easily and with minimal discomfort or risk to patients. The ability to detect telomerase activity in those specimens strongly suggests that the TRAP assay of prostatic fluid has the potential of playing a key role in the clinical diagnosis of prostate cancer.

CONCLUSIONS

Telomerase is a ribonucleoprotein enzyme that is able to add telomeric repeats to the ends of eukaryotic DNA to stabilize chromosomes. Telomerase is active in germline cells, stem cells and immortalized or malignant tumor cells, but not in most human somatic cells. In this study we report the extended use of the Telomeric Repeat Amplification Protocol (TRAP) assay for the detection of telomerase activity in freshly collected prostatic fluid. Out of 30 prostatic fluid specimens from patients with confirmed prostate cancer (PCa), 25 had positive telomerase activity (sensitivity 83%), while only 1 of 9 samples from patients with benign prostatic hyperplasia or prostate-normal subjects tested negative (specificity 89%). The positive predictive value (PPV) of the TRAP assay for prostate cancer was 96%. We found a strong correlation between telomerase activity in prostatic fluid specimens and serum prostate specific antigen (PSA) values. Telomerase activity was found in 79% of specimens from patients with PSA values >4 ng/ml, while in specimens from patients with PSA values ≤4 ng/ml only 29% tested positive for telomerase activity. In patients with PSA values above the standard 0-4 ng/ml reference range, the PPV of the TRAP assay was 84%. Furthermore, telomerase activity could be detected in 85% of the specimens from PCa patients with Gleason scores >4. In prostatic fluid from PCa patients with Gleason scores of ≤4, telomerase activity was detected 50% of the time. The PPV was 92% when a Gleason score of 4 was used as the lower limit. The use of the TRAP assay to detect telomerase activity in prostatic fluid is a novel approach to diagnosing prostate cancer. This method of detecting prostate cancer is promising, considering the correlation between telomerase expression and cancer. The TRAP assay has the potential of becoming an effective assay for the diagnosis of prostate cancer.

REFERENCES

1. Naitoh J, Zeiner RL, Dekernion JB (1998): Diagnosis and treatment of prostate cancer. Am. Fam. Physician 57:1531-1547.
2. Gohagen JK, Prorok PC, Kramer BS, Cornett JE (1994): Prostate cancer screening in the prostate, lung, colorectal and ovarian cancer screening trial of the National Cancer Institute. J. Urol. 152:1905-1909.
3. Kim NW, Piatyszek MA, Prowse KR, *et al* (1994): Specific association of human telomerase activity with immortal cells and cancer. Science 266:2011-2015.
4. Shay JW, Wright WE (1996): Telomerase activity in human cancer. Curr. Opin. Oncol. 8:66-71.
5. Sommerfeld H-J, Meeker AK, Piatyszek MA, Bova GS, Shay JW, Coffey DS (1996): Telomerase activity: a prevalent marker of malignant human prostate tissue. Cancer Res. 56:218-222.
6. Lin Y, Uemura H, Fujinami K, Hosaka M, Harada M, Kubota Y (1997): Telomerase activity in primary prostate cancer. J. Urol. 157:1161-1165.
7. Takahashi C, Miyagawa I, Kumano S, Oshimura M (1997): Detection of telomerase

activity in prostate cancer by needle biopsy. Eur. Urol. 32:494-498.
8. Lin Y, Uemura H, Fujinami K, *et al* (1998): Detection of telomerase activity in prostate needle-biopsy samples. Prostate 36:121-128.
9. Kaighn ME, Narayan KS, Ohnuki Y, Lechner JF, Jones LW (1979): Establishment and characterization of a human prostatic carcinoma cell line (PC-3). Invest. Urol. 17:16-23.
10. Robyt JF, White BJ: Biochemical Techniques: Theory and Practice. U.S.A., Waveland Press, 1990.
11. Trump DL, Shipley WU, Dillioglugil O, Scardino PT: Neoplasms of the Prostate. In Holland JF, Frei III E, Bast, Jr. RC, Kufe DW, Morton DL, Weichselbaum RR (eds): Cancer Medicine 1997. U.S.A., Williams & Wilkins, 1997.
12. Grover PK, Resnick MI (1995): Analysis of prostatic fluid: Evidence for the presence of a prospective marker for prostatic cancer. Prostate 26:12-18.
13. Yoshida K, Sugino T, Tahara H, *et al* (1997): Telomerase activity in bladder carcinoma and its implication for noninvasive diagnosis by detection of exfoliated cancer cells in urine. Cancer 79:362-369.
14. Kinoshita H, Ogawa O, Kakehi Y, *et al* (1997): Detection of telomerase activity in exfoliated cells in urine from patients with bladder cancer. J. Natl. Cancer Inst. 89:724-730.
15. Yoshida K, Sugino T, Goodison S, *et al* (1997): Detection of telomerase activity in exfoliated cancer cells in colonic luminal washings and its related clinical implications. Br. J. Cancer 75:548-553.
16. Greider CW, Blackburn EH (1987): The telomere terminal transferase of *Tetrahymena* is a ribonucleoprotein enzyme with two kinds of primer specificity. Cell 51:887-898.
17. Morin GB (1989): The human telomere terminal transferase enzyme is a ribonucleoprotein that synthesizes TTAGGG repeats. Cell 59:521-529.
18. Stamey TA, Kabalin JN (1989): Prostate-specific antigen in the diagnosis and treatment of adenocarcinoma of the prostate. I. Untreated patients. J. Urol. 141:1070-1075.
19. Ohori M, Wheeler TM, Dunn JK, Stamey TA, Scardino PT (1994): The pathological features and prognosis of prostate cancers detectable with current diagnostic tests. J. Urol. 152:1714-1720.
20. Catalona WJ, Smith DS (1994): Comparison of different serum prostate specific antigen measures for early prostate cancer detection. Cancer 74:1516-1518.

TABLES

Table 1. Diagnostic significance of telomerase activity in prostatic fluid specimens from a hospital-based patient population.

	Carcinoma	Sample Source *	Telomerase Activity: Positive (n)	Negative	Total	Sensitivity	Specificity	Positive Predictive Value
PF	Present	Sup	16	14	30	53% (16/30) ❶		
		E	24	6	30	80% (24/30) ❶		
	Total (n)		**25 ❷ ❹**	**5 ❷**	**30**	**83%** (25/30)		
	Absent	Sup	0	9	9			
		E	1	8	9			
	Total (n)		**1 ❸ ❹**	**8 ❸**	**9**		**89%** (8/9)	
Total (n)			**26**	**13**	**39**			**96%** (25/26)

* Sup, supernatant fluids; E, CHAPS extracts from the pellets.
❶, ❷, ❸, ❹: Significantly different from each other (P <0.05).

Table 2. The correlation of either PSA value (A) or Gleason Score (B) with telomerase activity in prostatic fluid specimens from a hospital-based patient population.

			Telomerase Activity: Positive	Negative	Total(n)	Sensitivity	Specificity	Positive Predictive Value
A	PSA Value *	>4	21 ❶ ❸	4 ❶	25	84% (21/25)		
		≤4	4 ❷ ❸	10 ❷	14		71% (10/14)	
		Total (n)	25	14	39			84% (21/25)
B	Gleason Score	>4	22 ❹ ❺	4 ❹	26	85% (22/26)		
		≤4	2 ❺	2	4		50% (2/4)	
		Total (n)	24	6	30			92% (22/24)

* The normal range of serum PSA value is equal to or less than 4 ng/ml.
❶, ❷, ❸, ❹, ❺: Significantly different from each other (P <0.05).

FIGURE LEGENDS

Fig. 1. Telomerase activity in PC-3 cells, a human prostate cancer cell line. Lanes 1-4, telomerase activity in serial dilutions of CHAPS extract, 1000, 100, 10, and 1 cell equivalents, respectively; lane 5, lysis buffer; lane 6, CHAPS extract, 1000 cell equivalents, pretreated with heat.

Fig. 2. Telomerase activity in prostatic fluid specimens from two PCa patients (A, B) with the addition of protease inhibitors. Lanes 1-4, specimen A; lanes 5-8, specimen B; lane 9, lysis buffer; lanes 10, 11, CHAPS extract of PC-3 cells (6 μg protein), without or with heat pretreatment, respectively. Supernatant fluid (1 μl), lanes 1, 2, 5, 6; CHAPS extract of the pellet (6 μg protein), lanes 3, 4, 7, 8. Heat pretreatment, lanes 1, 3, 5, 7; no heat pretreatment, lanes 2, 4, 6, 8.

Fig. 3. Effect of varying durations of heat pretreatment on telomerase activity in the CHAPS extract of a specimen pellet. Lane 1, an aliquot (6 μg protein) preheated at 85 °C for 15 min followed by RNase A pretreatment at 37 °C for 30 min; lanes 2, 3, 4, aliquots (6 μg protein each) preheated at 85 °C for 60 min, 15 min, and 5 min, respectively; lane 5, an aliquot (6 μg protein) without heat pretreatment; lane 6, lysis buffer; lanes 7, 8, CHAPS extract of PC-3 cells (6 μg protein), without or with heat pretreatment, respectively.

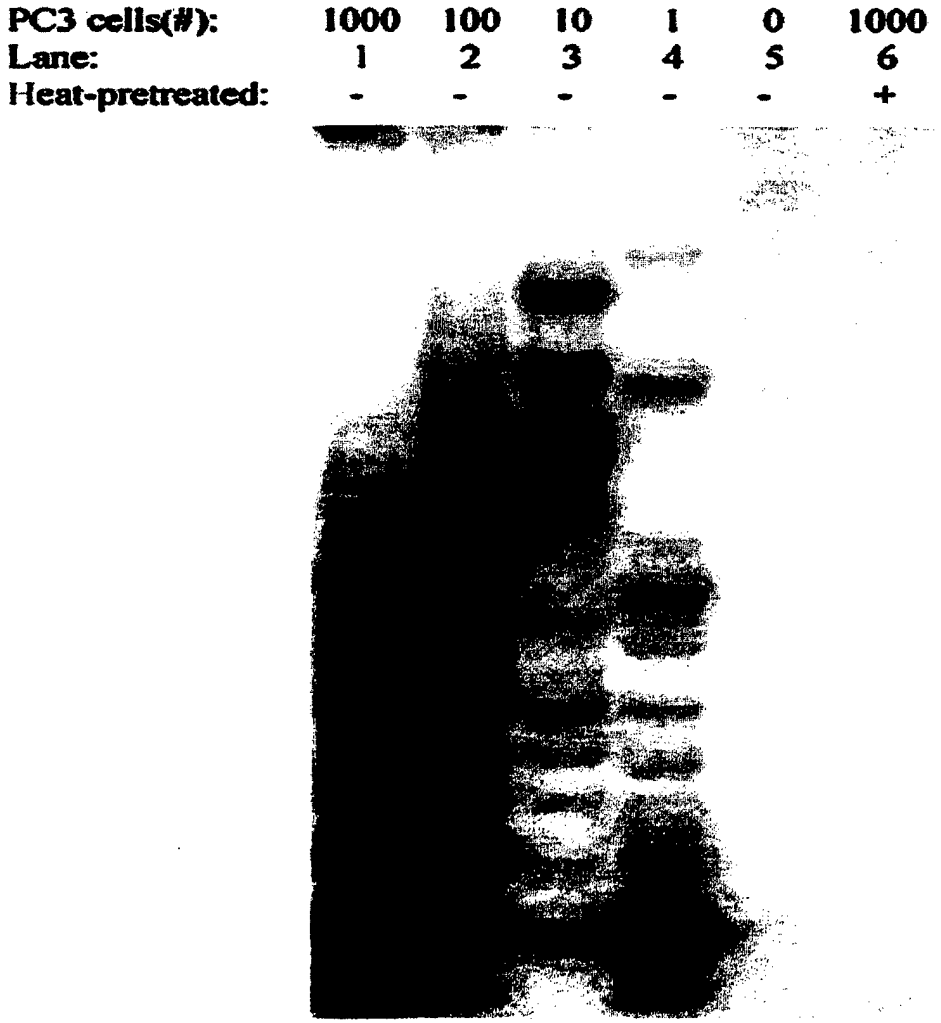
PC3 cells(#): 1000 100 10 1 0 1000
Lane: 1 2 3 4 5 6
Heat-pretreated: - - - - - +

Case (#):	1				2					PC-3 (ug)	
Aliq. of PF (ul):	1	1	6(ug)	6(ug)	1	1	6(ug)	6(ug)		6	6
Heat-pretreated:	+	-	+	-	+	-	+	-	-	-	+
Lanes:	1	2	3	4	5	6	7	8	9	10	11

Case (#):	2						PC-3	
Heat-pretreated:	+	+	+	+	-	-	-	+
RNase-pretreated:	+	-	-	-	-	-	-	-
Lanes:	1	2	3	4	5	6	7	8

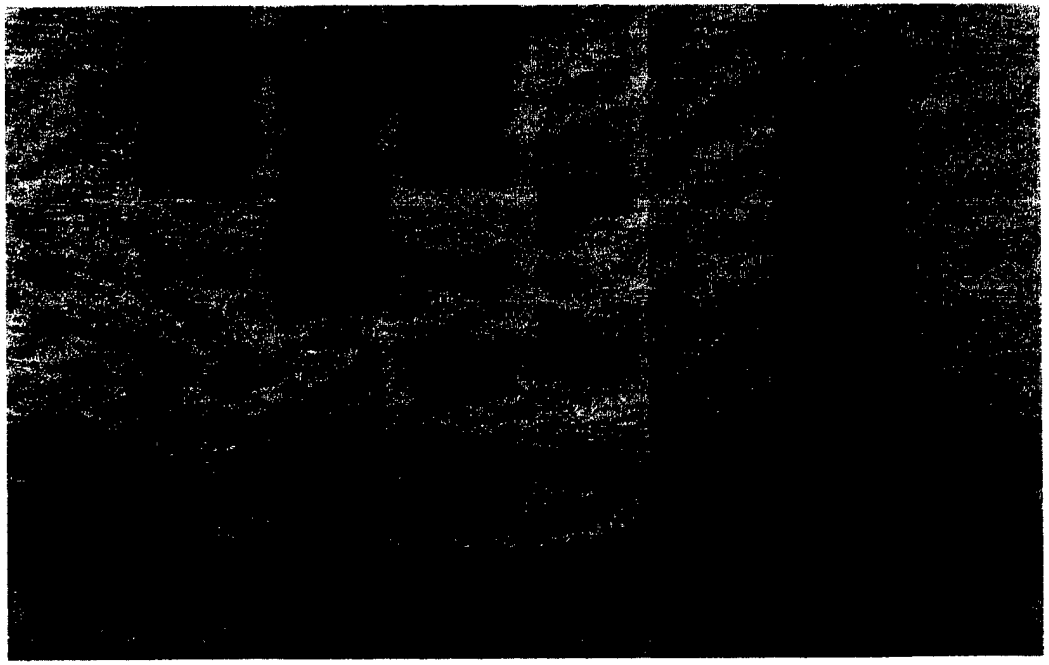

Evaluation of the telomerase PCR ELISA in examining prostate needle biopsy and prostatic fluid specimens for cancer

INTRODUCTION

Based on the knowledge in cancer biology, progression to a cancerous state in a cell does require the accumulation of a series of genetic alterations or mutations. In the development of some kinds of human cancer, alternative gene mutations cause a clone of normal somatic cells to lose the ability to respond to growth inhibitory signals, allowing cell division without the specific growth stimulatory signals. Over-proliferation can speed up telomere shortening in the cells. Telomerase could be therefore activated in a clone of the cells to elongate the shortened telomeric sequences and to stabilize chromosome ends if additional mutations occur according to the telomere hypothesis of cell aging and immortalization (Harley, 1991; Harley et al., 1992; Holt et al., 1996). The cell containing telomerase activity reflects its potentially immortal state, but implies very little about malignancy. Cell immortality does not mean unregulated rates of cell proliferation or metastasis, but only gives the cells the proliferative capacity to accumulate the necessary mutations to become malignant. Therefore, more mutations must be required for those immortal cells to progress to invasive and then metastatic states. However, in the development of other kinds of human cancer, the pre-cancerous cells may need far fewer mutations in order to become malignant and may not exhaust the normal limits of proliferation before they cause disease. These types of cancer would be expected to be both mortal and negative for telomerase activity.

Since the highly sensitive PCR-based telomerase assay, Telomeric Repeat Amplification Protocol (TRAP), was created in 1994 (Kim et al., 1994), telomerase activity in normal or cancer cells in human beings has been widely investigated. Numerous published data have shown that telomerase is active in about 85% of human cancers tested, including prostate cancer, but the activity is absent in most human somatic cells and tissues (Kim et al., 1994; Shay and Wright, 1996; Shay and Bacchetti, 1997), suggesting that telomerase activity is a promising molecular marker for the diagnosis of human cancer and the TRAP assay for the detection of telomerase activity is sensitive and specific enough to be involved in this process. However, this conventional TRAP assay is methodologically radioisotope-involved, visualized by autoradiography after gel electrophoresis, and the results are of limited linearity. These methods are hazardous, time consuming, and affect the accurate evaluation of the activity in different cancers. These disadvantages may limit further clinical applications. In recent years, several modifications of the conventional TRAP assay have been made to overcome these disadvantages. The changes include the use of modified primers to improve the specificity of PCR amplification (Tatematsu et al., 1996; Kim and Wu, 1997), the introduction of an internal standard in the assay to increase the reliability and linearity (Wright et al., 1995; Kim and Wu, 1997), the use of fluorescent or biotinylated primers or probes in the assay instead of the use of the ^{32}P radioisotope (Ohyashiki et al., 1996; Savoisky et al., 1996; Aldous and Grabil, 1997; Gelmini et al., 1998; Uehara et al., 1999), and the application of other biotechniques to save testing time and to simplify the procedures (Fujita et al., 1998; Hirose et al., 1998; Sun et al., 1998; Cheng et al., 1999). All of these trials have provided an interesting evolution of the assay although some disadvantages still exist in each modified assay.

The telomerase PCR ELISA, developed by Boehringer Mannheim, is an expansion of the conventional TRAP assay (Kim et al., 1994). It allows highly specific amplification of telomerase-mediated extension products combined with nonradioactive detection following an ELISA protocol. Compared to the conventional assay, this new PCR ELISA contains all compounds required for the

telomerase reaction and PCR in a ready-to-use reaction mixture for combining both reactions in a one-step/one-tube-reaction. Furthermore, the use of optimized primer sequences in the new assay eliminates the need for separation of the primers by a wax barrier and avoids amplification artifacts, such as primer dimers.

To evaluate the possible clinical application in the diagnosis or other aspects of prostate cancer, we selected the telomerase PCR ELISA to determine telomerase activity in both sextant needle biopsy specimens and prostatic fluid specimens clinically collected. In the process, the radioisotope-requiring TRAP assay was necessarily performed for comparison with this new PCR ELISA.

MATERIALS AND METHODS

Cell Culture and CHAPS Protein Extraction

A human prostate cancer cell line derived from a bone metastasis, PC-3, with a doubling time of 2.7 days in tissue culture (Kaighn et al., 1979) and obtained from the ATCC (Rockville, MD), was grown in RPMI 1640 medium supplemented with 10% new-born calf serum. The cells were harvested when 90% confluent using trypsin. After the cells were collected by centrifugation, the cell pellet was washed twice with cold phosphate-buffered saline, resuspended in ice-cold Buffer A [10 mM HEPES-KOH (pH 7.5), 1.5 mM $MgCl_2$, 10 mM KCl, 1 mM dithiothreitol], and recentrifuged. The pellet was lysed in Buffer B (Lysis Buffer) [0.5% 3-(3-cholamidopropyl-dimethylammonio)-1-propanesulfonate (CHAPS), 5 mM β-mercaptoethanol, 0.1 mM phenylmethanesulfonyl fluoride (PMSF), 10% glycerol, 10 mM Tris-HCl (pH 7.5), 1 mM $MgCl_2$] for 30 min on ice. Then, the lysate was centrifuged at 16,000 x g for 20 min at 4 °C. Aliquots of the supernatant fluid were immediately stored at -80 °C. The protein concentration was determined by ultraviolet spectrophotometry (Robyt and White, 1990).

Collection of Sextant Needle Biopsies from Radical Retropubic Prostatectomy (RRP)

A total of 48 sextant needle biopsy specimens from the prostates of 7 PCa patients were collected in the Operating Room. In the process, needle cores, using 18-gauge cutting needles (C.R. Bard, Inc., Covington, GA) from a Biopty gun, were mainly obtained from six regions and the possible nodule of the posterior prostate once the prostate was removed by RRP (Fig. 1). For further pathological examination, dye (Bradley Products, Inc., Bloomington, MN), colored green, red or yellow, was applied to mark the areas where the needle cores were taken. Two needle cores mixed with a little dye, one for testing telomerase activity while the other for the possible pathohistological examination, were obtained from the same area at the same time. The needle cores were kept on ice until they could be frozen at -80 °C, usually within 30 minutes after collection. For the CHAPS protein extraction, the frozen biopsied needle core was soaked in a 5X volume/weight of lysis buffer and homogenized on ice in a Kontes tube, using a matching pestle, and then extracted for protein as described for the PC3 cells. The protein concentration was determined by ultraviolet spectrophotometry (Robyt and White, 1990). Aliquots were frozen at -80 °C until assayed.

Collection of Prostatic Fluid with protease inhibitors added (PF)

A total of 18 specimens with protease inhibitors added (PF), with half of them from PCa patients and the other half from the patients clinically confirmed as cancer-free, were collected clinically. In brief, siliconized microcentrifuge tubes were prepared in advance to contain 1.18 ml of a mix of protease

inhibitors. A few minutes prior to specimen collection, 20 µl of an ethanol solution of PMSF was added to each microcentrifuge tube. The prostatic fluid was obtained by prostatic massage performed on patients about to undergo radical prostatectomy. Approximately 300 µl of prostatic fluid from each patient was collected by palpating the prostate and milking the fluid through the urethra, pipetting the specimen immediately into the microtube, and mixing it with the protease inhibitors by inversion three times. The final concentrations of the protease inhibitors were 10 mM disodium EDTA, 5 mM BZA, 20 mM sodium caproate, and 0.2 mM PMSF. The microtube was then centrifuged 5 min in an Eppendorf table-top centrifuge at 4 °C. The supernatant fluid was divided into aliquots, which together with the pellet were placed on dry ice and transferred to the laboratory. The aliquots of the supernatant fluid were stored at -80 °C for the coming assay, while the pellet was further treated by the CHAPS protein extraction as described above. This extract was also divided into aliquots for freezing and storage at -80 °C. The protein concentrations of the CHAPS extracts were determined by ultraviolet spectrophotometry.

Telomerase PCR ELISA Method

For the needle cores, two aliquots (0.6 µg protein each) of the CHAPS extract with or without an RNase pretreatment, in which the sample was incubated with RNase A at the concentration of 0.2 µg/µl at 37 °C for 30 min, were applied in the assay. For each PF specimen, three aliquots of both the supernatant (1 µl) and the CHAPS extract of the pellet (0.6 µg protein)] with or without a pre-heating (85 °C for 15 min) or an RNase pretreatment were used for the assay. To set up a semi-log standard curve for a semi-quantitative analysis, aliquots of PC-3 cell extracts corresponding to 3,000, 300, 30, 3 cells were also assayed.

For each reaction, 25 µl of ready-to-use reaction mixture was transferred into a 0.5 ml tube (thin-wall) on ice. It was mixed with an aliquot (1µl) of the clinical specimen described above and an extra 24 µl of DEPC-treated dH_2O. The tube was then transferred to a PCR thermal cycler to perform a combined primer extension or elongation/amplification reaction wherein telomerase added telomeric repeats (TTAGGG) to the 3' end of the biotin-labeled synthetic P1-TS-Primer, and elongated products were further amplified by PCR using the primers P1-TS and P2, generating PCR products with the telomerase-specific 6 nucleotide increments. The protocol was 30 min at 25 °C for primer elongation, 5 min at 94 °C for telomerase inactivation, and 30 PCR cycles consisting of 94 °C for 30 s, 50 °C for 30 s, and 72 °C for 90 s followed by 10 min at 72 °C.

The next step was the detection of products by ELISA. Briefly, 5 µl of the PCR product was mixed with 20 µl of denaturation reagent and incubated at room temperature. The mixture was further mixed with 225 µl of hybridization buffer containing a digoxigenin-(DIG)-labeled, telomeric repeat-specific detection probe. The resulting product (100 µl) was transferred into a well of the microtiter plate, sealed and incubated at 37 °C on a shaker (200 rpm) for a few hours for immobilization via the biotin labeled primer to a streptavidin-coated microtiter plate. The immobilized PCR product was then detected with 100 µl of anti-DIG-POD working solution, which contains an antibody against digoxigenin that is conjugated to peroxidase, after the well was washed by washing buffer several times. After a period of incubation at room temperature on a shaker (200 rpm) and further rinsing with washing buffer for a few times, 100 µl of TMB substrate solution was added to the well and incubated for color development, in which the probe is visualized by virtue of peroxidase metabolizing TMB to form a colored reaction product. The color development could be stopped by adding 100 µl of stop reagent. The difference between the absorbances at 450 nm and 655 nm (A_{450} - A_{655} or ΔA) was measured with a Microtiter plate (ELISA) reader. In general, telomerase activity in the needle core specimens is positive

if the difference in absorbance is higher than 0.2, whereas the activity in prostatic secretion specimens is considered to be positive if the difference in absorbance is higher than 0.1. For a semi-quantitative analysis, the activity in 0.6 μg protein of CHAPS extract of PC-3 cells, equivalent to the CHAPS extract from 300 PC-3 cells, was defined as 100 units. A relative activity (Unit) in a specimen could be expressed after the difference in absorbance (ΔA) from this specimen was normalized to PC-3 standard curve (Fig. 2). To minimize the result deviation, the semi-log standard curve was also set up for each experiment.

The Radioisotope-requiring TRAP assay

As a parallel test, the conventional TRAP assay was also performed to confirm the activity in each specimen tested by the PCR ELISA method. For a semi-quantitative analysis, a semi-log PC-3 standard curve should be set up for each experiment. The TRAP assay for telomerase activity was performed as described (Kim et al., 1994) with minor modifications. In brief, an appropriate aliquot of either a prostatic specimen, including tissue and secretion, or the CHAPS extract of PC-3 cells was assayed in 50 μl of reaction mixture containing 50 μM dNTPs, 0.1 μg of TS primer (5'-AATCCGTCGAGCAGAGTT-3'), 2 Units of *Taq* polymerase, 1 μl of [α-^{32}P]dCTP (10 mCi/ml, 3,000 Ci/mmol), 20 mM Tris-HCl (pH 8.3), 1.5 mM $MgCl_2$, 63 mM KCl, 1 mM EGTA, 0.005% Tween-20, and an aliquot of the supernatant or the CHAPS extract, including the extract from either the needle core, or the pellet of prostatic fluid, or PC-3 cells, in a 0.5 ml tube that contained 0.1 μg of CX primer (5'-CCCTTACCCTTACCCTTACCCTAA-3') sequestered at the bottom of the 0.5 ml tube by a wax barrier (Ampliwax, Perkin Elmer, Foster city, CA). After a period (30 min in testing needle core specimens and 45 min in testing prostatic secretion specimens) of incubation at room temperature, the reaction mixture was subjected to 30 PCR cycles for the needle cores or 34 PCR cycles for PF specimens, consisting of 94 °C for 30 s, 50 °C for 30 s, and 72 °C for 90 s. The PCR product was then subjected to electrophoresis on a 10% nondenaturing polyacrylamide gel, dried, and exposed to X-ray film, or developed in a Bio-Rad Molecular Imager in conjunction with the Molecular Analyst software (Bio-Rad Laboratories, Hercules, CA). Typical products of telomerase activity were shown by the 6-bp ladder bands starting from 40 bp. The following standards were used to judge a sample telomerase positive: (1) the presence in a sample lane of more than four bands of the 6-bp telomerase repeat, which could be eliminated by either RNase A or heat, and (2) repetition of the result with two or more repeat samplings. For a semi-quantitative assay, the lane was scanned by using a Bio-Rad Molecular Imager in conjunction with the Molecular Analyst software, and all of peaks found were summed to yield a net incorporation per assay, which minus its own background created a mean density per assay. If the activity in 0.6 μg protein of PC-3 cell extract equivalent to 300 cells was defined as 100 units, a relative activity (Unit) in a specimen could be expressed after its mean density from the assay was normalized to PC-3 standard curve.

Statistical Analysis

Differences were evaluated by means of the chi-square test (χ^2 test). *P* values less than or equal to 0.05 were considered statistically significant.

RESULTS

Examining Telomerase Activity in Prostate Needle Biopsy Specimens Using the PCR ELISA Method.

With a suggestion from the kit, the sample could be considered to be positive if ΔA is higher than 0.2, but the relative activity in units corresponding to 0.2 ΔA in each experiment was varied a little from 5.8 to 7.5 units because of a deviation of the slopes of the standard curves. The mean activity for the positive cutoff point was 6.9 ± 0.7 units (mean ± SD). At the same time, we also confirmed the activity in these specimens using the radioisotope-requiring TRAP assay. The activity in units for the positive cutoff point could be set up when the mean density was equal to zero, which was also varied because of a deviation of the slopes of the standard curves, and the mean activity at this point was 7.6 ± 3.2 units.

For the PCR ELISA, of 32 prostate needle cores with pathohistologically confirmed cancer, 29 (91%) showed positive telomerase activity, whereas 11 of 16 (69%) needle cores without histologically confirmed cancer had no activity, the other five specimens still showed weak activity. Positive predictive value (PPV) and negative predictive value (NPV) were 85% and 79%, respectively. The mean activity per needle core containing cancer cells was 24.5 ± 28.4 units, which is significantly higher than that without cancer cells (7.2 ± 2.2 unit) (Table 1). After the radioisotope-requiring TRAP assay was performed to test telomerase activity in these specimens at the same time, a similar data could be obtained. For this assay, telomerase activity was positive in 88% or 28 of 32 specimens containing pathohistologically confirmed cancer cells, while only 3 of 16 needle cores without histologically confirmed cancer cells had weak telomerase activity, the specificity was up to 81%. Compared with the data in the PCR ELISA group, the higher PPV and NPV were also consistently obtained, which were 90% and 76%, respectively. Contrary to a relatively lower average activity (7.3 ± 1.8 units) in the specimens without cancer cells, the average activity per specimen containing cancer cells (25.6 ± 27.8 units) was significantly higher and close to that (24.5 ± 28.4 units) in the PCR ELISA group (Table 1). Telomerase activity tested by two methods in these sextant needle cores could be also summarized in a pair comparison individually. As expected, telomerase activity in the cores tested by one method was usually and excellently matching with the activity tested by the other (Fig. 3). The data above suggest that the telomerase PCR ELISA is methodologically sensitive enough to detect telomerase activity in a small quantity of needle biopsy tissue by showing a perfect parallel to the activity confirmed by the radioisotope-requiring TRAP assay.

Examining Telomerase Activity in Prostatic Fluid Specimens Using the PCR ELISA Method.

Based on previous results in our laboratory (data not shown), the signals from the CHAPS extracts of the pellets of prostatic fluid with protease inhibitors added were stronger than those from the supernatants, and in some specimens the telomerase activity was increased after a pre-heating at 85 °C for 15 min. Therefore, we designed experiments where telomerase activity was determined in the aliquots of both the supernatant (1 μl) and the CHAPS extract of the pellet (0.6 μg protein)] with or without a pre-heating, while aliquots with an RNase pretreatment from both the supernatant and the CHAPS extract of the pellet were also tested as a specific negative control for each specimen. The specimen from a patient was considered to have positive telomerase activity if at least one sample from the specimen showed positive activity. In the process, both the PCR ELISA and the radioisotope-requiring TRAP assay were performed to determine the activity in the specimens at the same time. Because of the relatively lower activity in the specimens compared with that in those tissue specimens, we changed the positive cutoff point from 0.2 ΔA to 0.1 ΔA, which increased the sensitivity from 44%

(data not shown) to 78% without an affecting the specificity in testing the clinical specimens. For a further semi-quantitative analysis, the semi-log standard curve from a serial dilution study of PC-3 cell extract was set up for each experiment. The mean activity at the positive cutoff point from several standard curves was 7.6 ± 0.5 units. While the positive cutoff point for the radioisotope-requiring TRAP assay was 7.0 ± 0.2 units in average.

Using both the PCR ELISA and the radioisotope-requiring TRAP assay, telomerase activity was detected in 7 of 9 specimens (78%) from PCa patients, whereas only 1 of 9 specimens (11%) from the patients with cancer-free showed weak activity. PPV and NPV could be further determined to be 88% and 80%, respectively. Interestingly, the mean activity for each specimen from cancer patient was only 7.1 ± 1.5 units for the PCR ELISA and 7.2 ± 1.8 units for the radioisotope-requiring TRAP assay. Both values of telomerase activity were just slightly higher than the values, 6.2 ± 0.4 and 5.7 ± 0.9 units, respectively, from the cancer-free patients (Table 2), suggesting that weak telomerase activity was usually detected in these prostatic fluid specimens. Nevertheless, the data above indicate that the PCR ELISA kit could be practically used to detect telomerase activity in prostatic fluid specimens by showing a comparable result with the radioisotope-requiring TRAP assay.

DISCUSSION

With the previous data from our laboratory, telomerase activity has been proven to be a specific marker in the diagnosis and the prognosis of prostate cancer. However, the methodological disadvantages of the conventional TRAP assay limit its further clinical expansion. Here we selected the telomerase PCR ELISA, which is more conveniently handled and gives faster results, to evaluate its possible clinical use in the diagnosis of prostate cancer. In the process, the radioisotope-requiring TRAP assay was necessarily performed for comparison with this new PCR ELISA. Testing different protein amounts of PC-3 cell extract as the positive controls in both assays allows not only a semi-quantitative analysis by setting up the standard curve but also makes the paired results from a specimen quantitatively comparable. All standard curves had good linearity from 10 units (0.06 μg PC-3 cell extract) to 1000 units (6 μg PC-3 cell extract), indicating a good relationship with the quantities of DNA synthesized after PCR amplification, while significant deviations appeared on the spots beyond that range (Fig. 2). Similar results could be seen based on the standard curves from the radioisotope-requiring TRAP assay.

For prostate needle biopsy specimens, telomerase activity detected in the PCR ELISA matched well with that in the conventional TRAP assay generally. However, the results showing lower or weak telomerase activity from both assays were occasionally not parallel due to possible methodological reasons, resulting in a relatively lower specificity (69%) in the PCR ELISA group. Statistical analysis also confirmed the results above, and suggesting that the PCR ELISA kits could be clinically used to detect telomerase activity in prostate needle cores, which usually contain a very small amount of prostate tissue, instead of the conventional TRAP assay. In other words, the PCR ELISA could be practically applied not only for the detection of telomerase activity in sextant needle biopsy specimens but also for a further indication of the possible cancer regions in the prostate.

For prostatic fluid specimens with protease inhibitors added, we initially realized that a relatively higher percentage of the specimens from PCa patients shows a lower or weak telomerase activity in the radioisotope-requiring TRAP assay because this kind of specimen usually contains a very limited number of cancerous cells, and in some cases telomerase activity could be increased after a heat-pretreatment of the original specimens, which may contributes to a satisfactory sensitivity in statistical analysis. Therefore, to evaluate if telomerase PCR ELISA could be used to determine the activity in

prostatic fluid specimens with protease added, we tested the activity in multiple samples of a specimen, termed multi-sample testing, including both original and a pre-heating samples of both the CHAPS extract of the pellet and the supernatant from a specimen. The way we did that provides more chances to have positive activity in these testing samples of a specimen, and greatly increases the positive probability or decreases the false-negative probability for a cancer patient. For example, only 9 of 36 testing samples from 9 cancer patients had positive telomerase activity using the PCR ELISA, which indicates a lower positive rate (25%) for the testing samples (data not shown). However, these 9 positive samples were from 7 cancer patients. If we regard the results in a patient's view, the positive rate or sensitivity was dramatically increased to 78% (Table 2). At the same time, 1 of 36 testing samples (specificity 97%) from 9 patients who were cancer-free showed weak activity (data not shown), the specificity was only reduced to 89% (8 of 9 patients with no activity) from the patient's view. A similar phenomenon was also present in the data from the conventional TRAP assay. It seems that the activity and statistical results in the PCR ELISA matched well with those in the conventional TRAP assay, even though the lower activities in the samples from both assays were not parallel due to possible methodological reasons.

We also tried to analyze the data to look for a better sample source for testing in the PCR ELISA. Interestingly, 8 of 10 samples with positive activity, including the samples from the patients with or without prostate cancer, were the aliquots of CHAPS extracts of the pellets with heat pretreatment, suggesting that CHAPS extract of the pellet from pure prostatic fluid with protease inhibitors added contains more telomerase molecules, while heat pretreatment appears to be inactivating the inhibitor of telomerase, such as the protease inhibitors, rather than inactivating the telomerase.

In summary, the PCR ELISA is methodologically capable of determining telomerase activity in prostate needle cores and prostatic fluid specimens, and could be therefore involved in the diagnosis of prostate cancer although multi-sample testing and a proper reduction of the company-suggested positive cutoff point in testing prostatic fluid specimens are recommended.

CONCLUSIONS

The conventional TRAP assay has been proven to be very powerful for determining telomerase activity in the specimens from tissue or other sources. However, the methodological disadvantages limit its further clinical expansion. To set up a practical system for the measurements of telomerase activity in the detection or early detection of prostate cancer (PCa), we target and evaluate the application of a modified TRAP assay, the telomerase PCR ELISA developed by Boehringer Mannheim Co. On the way, we examined telomerase activity in 48 sextant needle biopsy specimens from pathologically confirmed cancer or cancer-free regions of the prostate of 7 PCa patients and 18 prostatic fluid specimens clinically collected from the patients with PCa or that were cancer-free using the PCR ELISA. The conventional TRAP assay was also performed for comparison. With excellent matching of the results by the two methods individually in sextant needle biopsy specimens, both higher sensitivity (91%) and specificity (69%) in the PCR ELISA were consistent with those, 88% and 81%, respectively, in the conventional TRAP assay. Quantitatively, the mean activity per needle core containing cancer cells (24.5 ± 28.4 units) was significantly higher than that without cancer cells (7.2 ± 2.2 unit) in the PCR ELISA, which were also parallel well to those, 25.6 ± 27.8 units and 7.3 ± 1.8 units, respectively, in the conventional TRAP assay. In prostatic fluid specimens, with a lower mean activity for each specimen from cancer patients (7.1 ± 1.5 units in the PCR ELISA, 7.2 ± 1.8 units in the conventional TRAP assay), statistical analysis showed a good match between the results from two methods overall although the results from two methods did not always pair with each other in some individuals. In

conclusion, the PCR ELISA is methodologically able to be a qualified candidate for the clinical use in the diagnosis of prostate cancer although multi-sample testing and a proper reduction of the company-suggested positive cutoff point in testing prostatic fluid specimens are recommended.

REFERENCES

Aldous, W. K., and Grabil, N. R. A fluorescent method for detection of telomerase activity. Diagn. Mol. Pathol., *6:* 102-110, 1997.

Cheng, A. J., Tang, R., Wang, J. Y., Chang, J. T. Wang, T. C. Polymerase chain reaction-based enzyme immunoassay for quantitation of telomerase activity: application to colorectal cancers. Jpn. J. Cancer Res., *90:* 280-285, 1999.

Fujita, M., Tomita, S., Ueda, Y., and Fujimori, T. Gel staining methods for detection of telomerase activity with the telomeric repeat amplification protocol (TRAP) assay. Mol. Pathol., *51:* 342, 1998.

Gelmini, S., Caldini, A., Becherini, L., Capaccioli, S., Pazzagli, M., and Orlando, C. Rapid, quantitative nonisotopic assay for telomerase activity in human tumors. Clin. Chem., *44:* 2133-2138, 1998.

Harley, C. B. Telomere loss: mitotic clock or genetic time bomb? Mutat. Res., *256:* 271-282, 1991.

Harley, C. B., Vaziri, H., Counter, C. M., and Allsopp, R. C. The telomere hypothesis of cellular aging. Exp. Gerontol., *27:* 375-382, 1992.

Hirose, M., Abe-Hashimoto, J., Tahara, H., Ide, T., and Yoshimura, T. New method to measure telomerase activity by transcription-mediated amplification and hybridization protection assay. Clin. Chem., *44:* 2446-2452, 1998.

Holt, S. E., Shay, J. W., and Wright, W. E. Refining the telomere-telomerase hypothesis of aging and cancer. Nature Biotechnol., *14:* 836-839, 1996.

Kaighn, M. E., Narayan, K. S., Ohnuki, Y., Lechner, J. F., and Jones, L. W. Establishment and characterization of a human prostatic carcinoma cell line (PC-3). Invest. Urol., *17:* 16-23, 1979.

Kim, N. W., Piatyszek, M. A., Prowse, K. R., Harkey, C. B., West, M. D., Ho, P. L., Coviello, G. M., Wright , W. E., Weinrich, S. L., and Shay, J. W. Specific association of human telomerase activity with immortal cells and cancer. Science, *266:* 2011-2015, 1994.

Kim, N. M., and Wu, F. Advances in quantification and characterization of telomerase activity by the telomeric repeat amplification protocol (TRAP). Nucleic Acids Res., *25:* 2595-2597, 1997.

Ohyashiki, J. H., Ohjashiki, K., Sano, T., and Toyama, K. Non-radioisotopic and semi-quantitative procedure for terminal repeat amplification protocol. Jpn. J. Cancer Res., *87:* 329-331, 1996.

Robyt, J. F., and White, B. J. Biochemical Techniques: Theory and Practice, pp. 232-236. U.S.A.:

Waveland Press, Inc., 1990.

Savoisky, E., Akamatsu, K., Tsuchiya, M., and Yamazaki, T. Detection of telomerase activity by combination of TRAP method and scintillation proximity assay (SPA). Nucleic Acids Res., *24:* 1175-1176, 1996.

Shay, J. W., and Bacchetti, S. A survey of telomerase activity in human cancer. Eur. J. Cancer, *33:* 787-791, 1997.

Shay, J. W., and Wright , W. E. Telomerase activity in human cancer. Curr. Opin. Oncol., *8:* 66-71, 1996.

Sun, D., Hurley, L. H., and Von Hoff, D. D. Telomerase assay using biotinylated-primer extension and magnetic separation of the products. BioTechniques, *25:* 1046-1051, 1998.

Tatematsu, K., Nakayama, J., Danbara, M., Shionoya, S., Sato, H., Omine, M., and Ishikawa, F. A novel quantitative "stretch PCR assay" that detects a dramatic increase in telomerase activity during the progression of myeloid leukemias. Oncogene, *13:* 2265-2274, 1996.

Uehara, H., Nardone, G., Nazarenko, I., and Hohman, R. J. Detection of telomerase activity utilizing energy transfer primers: comparison with gel- and ELISA-based detection. BioTechniques, *26:* 552-558, 1999.

Wright, W. E., Shay, J. W., and Piatyszek, M. A. Modifications of a telomeric repeat amplification protocol (TRAP) result in increased reliability, linearity and sensitivity. Nucleic Acids Res., *23:* 3794-3795, 1995.

TABLES

Table 1. Telomerase activity tested by two methods in needle biopsy specimens

Method		the PCR ELISA				the Radioisotope-requiring TRAP Assay			
Telomerase Activity		Pos [2]	Neg [2]	Total (n)	Unit/Speci. [4]	Pos [3]	Neg [3]	Total (n)	Unit/Speci. [4]
Pca [1]	Present	29 ❶	3 ❷	32	24.5 ± 28.4 ❸	28 ❹	4 ❺	32	25.6 ± 27.8 ❻
	Absent	5 ❶	11 ❷	16	7.2 ± 2.2 ❸	3 ❹	13 ❺	16	7.3 ± 1.8 ❻
	Total (n)	34	14	48		31	17	48	
Sensitivity		91% (29/32)				88% (28/32)			
Specificity			69% (11/16)				81% (13/16)		
Positive Predictive Value (PPV)		85% (29/34)				90% (28/31)			
Negative Predictive Value (NPV)			79% (11/14)				76% (13/17)		

[1] needle core specimens were further confirmed by the pathohistological examination.
[2] Pos (positive): ΔA: ≥0.2 or the mean activity: 6.9 ± 0.7 units; Neg, negative;
[3] Pos (positive): the activity: 7.6 ± 3.2 units; Neg, negative;
[4] the mean activity per specimen (Unit/Specimen)
❶, ❷, ❸, ❹, ❺, ❻: significantly different from each other (P <0.001).

Table 2. Telomerase activity tested by two methods in prostatic secretion specimens

Method		the PCR ELISA				the Radioisotope-requiring TRAP Assay			
Telomerase Activity		Pos [2]	Neg [2]	Total (n)	Unit/patient [4]	Pos [3]	Neg [3]	Total (n)	Unit/patient [4]
Pca [1]	Present	7 ❶	2 ❷	9	7.1 ± 1.5 ❺	7 ❸	2 ❹	9	7.2 ± 1.8 ❻
	Absent	1 ❶	8 ❷	9	6.2 ± 0.4 ❺	1 ❸	8 ❹	9	5.7 ± 0.9 ❻
	Total (n)	8	10	18		8	10	18	
Sensitivity		78% (7/9)				78% (7/9)			
Specificity			89% (8/9)				89% (8/9)		
Positive Predictive Value (PPV)		88% (7/8)				88% (7/8)			
Negative Predictive Value (NPV)			80% (8/10)				80% (8/10)		

[1] patients were clinically and pathologically diagnosed;
[2] Pos (positive): ΔA: ≥0.1 or the mean activity: 7.6 ± 0.5 units; Neg, negative;
[3] Pos (positive): the mean activity: 7.0 ± 0.2 units; Neg, negative;
[4] the mean activity per patient (Unit/patient);
❶, ❷, ❸, ❹: significantly different from each other (P <0.001);
❺, ❻: not significantly different from each other (P >0.05).

FIGURE LEGENDS

Fig. 1. Six regions of the prostate in posterior coronal plane. Needle cores were basically obtained from these six regions for the detection of telomerase activity. RB = right base; RM = right mid-section; RA = right apex; LB = left base; LM = left mid-section; LA = left apex.

Fig. 2. Standard Curve of Telomerase Activity in the PCR ELISA method. The X axis is a logarithmic scale of the relative telomerase activity (Unit), which is originated from a definition that 100 units represents the activity in 0.6 μg protein of PC-3 cell extract equivalent to 300 cells. The Y axis is the difference between the absorbances at 450 nm and 655 nm. The standard curve was set up by a serial dilution study on the CHAPS extract of PC-3 cells (60, 30, 6, 3, 0.6, 0.3, 0.06, 0.006 μg protein) for a semi-quantitative analysis, in which the absorbances of 10,000 units (60 μg protein), 5,000 units (30 μg protein), and1 unit (0.006 μg protein) of PC-3 should be given up due to the significant deviations. Therefore, a relative activity (Unit) in a specimen could be expressed after the difference in absorbance (A_{450} - A_{655}) from the assay was normalized to the standard curve.

Fig. 3. Comparison of telomerase activity tested by two methods in needle biopsy specimens from a PCa patient. Sextant needle cores from the prostate with cancer were examined by two methods, the radioisotope-requiring TRAP assay and the telomerase PCR ELISA, at the same time. Telomerase activity in each core was quantitated, normalized to the standard curve from PC-3 cells, and given in units relative to the control. The results suggest a good parallel for two methods, and also indicate the possible sites of cancer occurred or the volume of cancer.

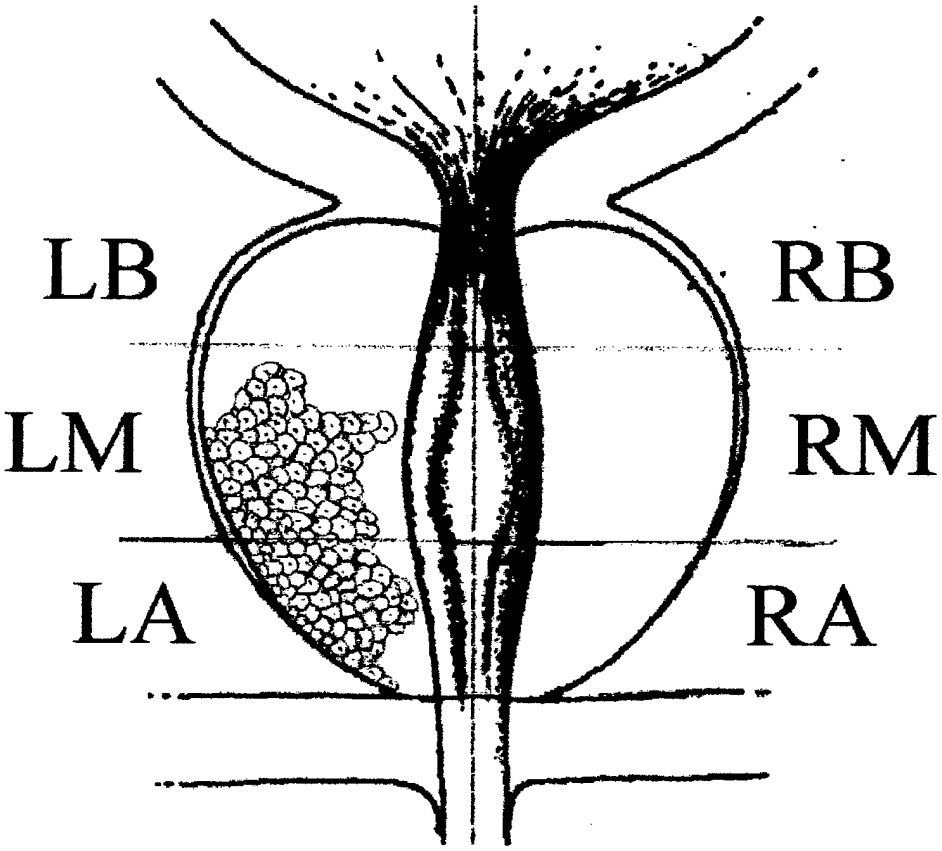
LB
RB
LM
RM
LA
RA

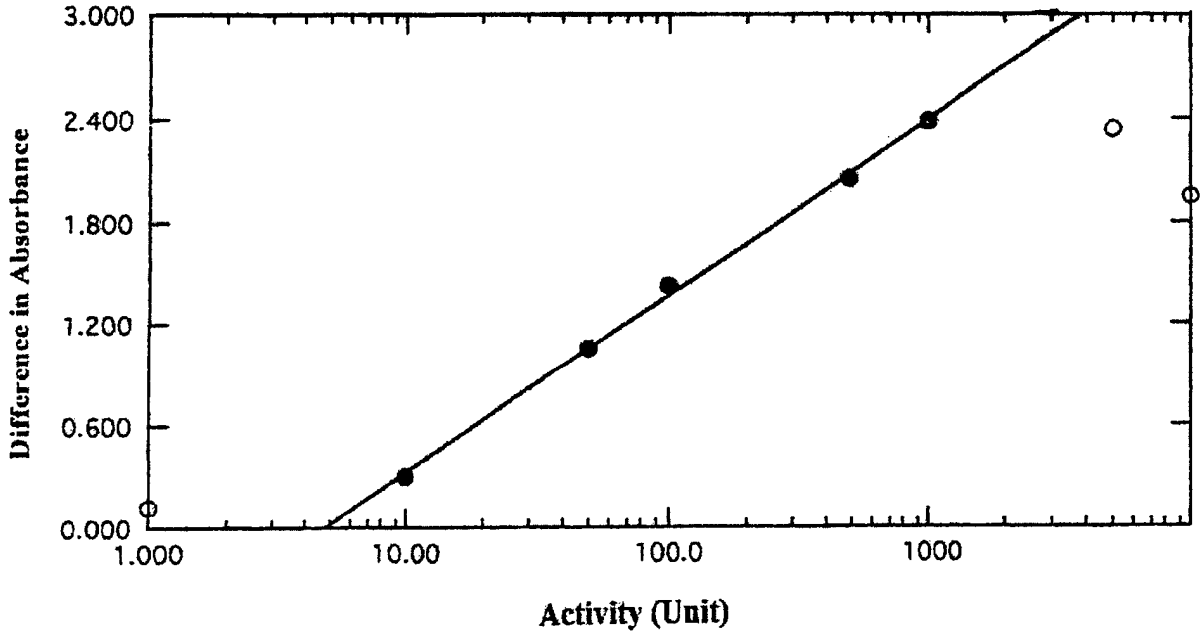
3.000
2.400
1.800
1.200
0.600
0.000
Difference in Absorbance
1.000
10.00
100.0
1000
Activity (Unit)

Comparison of Telomerase Activities Tested by Two Methods in needle biopsy specimens from a PCa patient

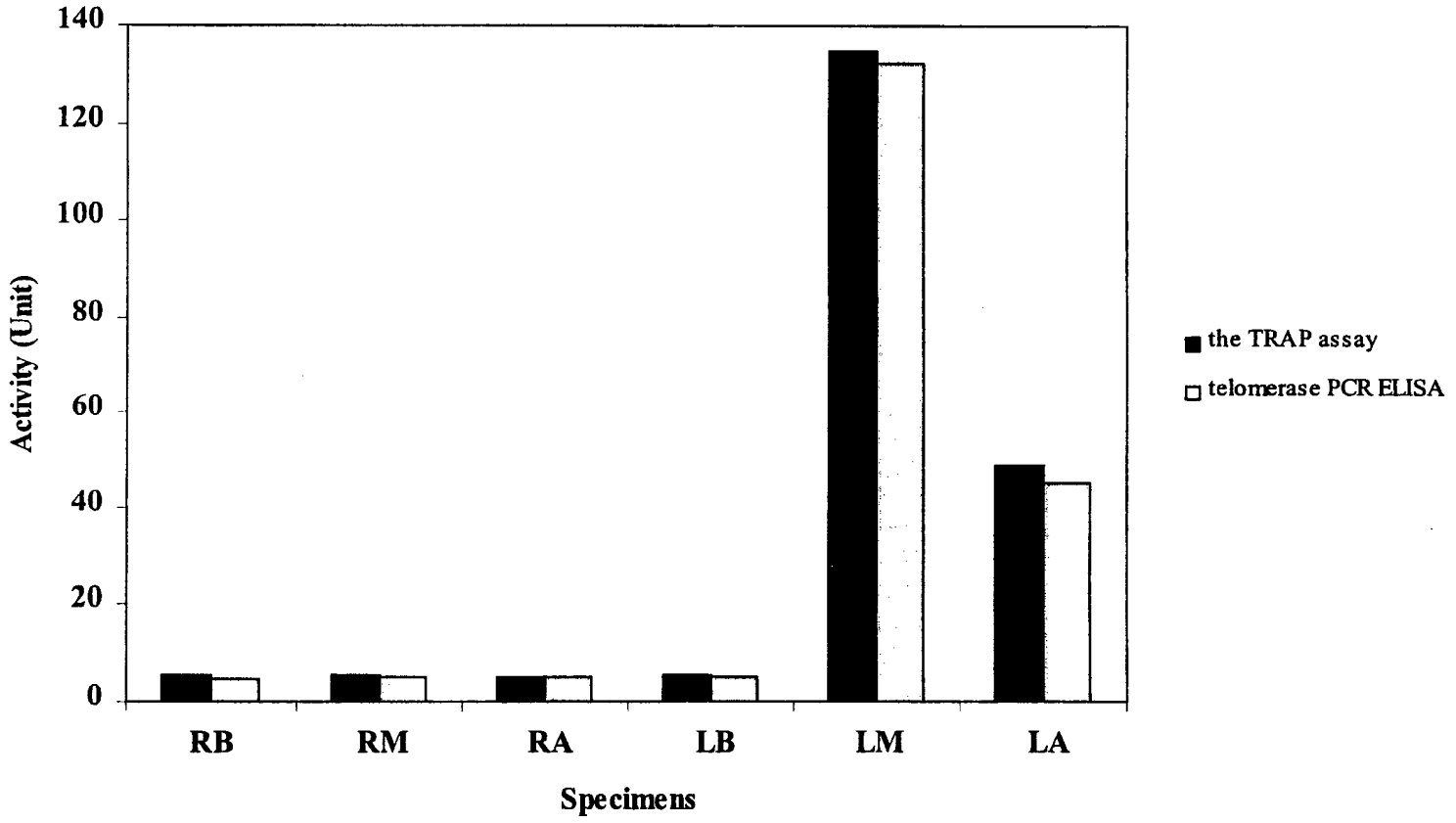

APPENDIX

1. Manuscript submitted to *Urologic Oncology* on 1/18/2000. "Detection of Telomerase Activity in Prostatic Fluid Specimens" by Z. Wang, S.A. Ramin, C. Tsai, P. Lui, P.J. Herbert, E. Kyeyune-Nyombi, H. Ruckle, R.E. Beltz and J.F. Sands.

2. Manuscript submitted to *Urologic Oncology* on 2/11/2000. "Application of the Telomeric Repeat Amplification Protocol for Detection of Cancer in Prostate Needle Biopsy Speciments" by Z. Wang, S.A. Ramin, C. Tsai, P. Lui, H.C. Ruckle, R.E. Beltz and J.F. Sands.

3. Manuscript in preparation. "Evaluation of the Telomerase PCR ELISA in Examining Prostate Needle Biopsy and Prostatic Fluid Specimens for Cancer" by Z. Wang, S.A. Ramin, C. Tsai, P. Lui, H.C. Ruckle, R.E. Beltz and J.F. Sands.

FILE COPY

NM TB

NATIONAL MEDICAL TECHNOLOGY TESTBED

August 4, 1999

John F. Sands, Ph.D.
Assistant Professor of Biochemistry
Department of Biochemistry
School of Medicine
Loma Linda University
Loma Linda, CA 92350

Subject: Approval of Proposed Publication Abstracts and Manuscripts

Dear Dr. Sands:

This is to inform you that National Medical Technology Testbed, Inc. (NMTB) approved your request to publish two papers. The first one is entitled "Detection of Telomerase Activity in Prostatic Secretion Specimens" and the second one is entitled "A Novel Approach for Detecting Prostate Cancer: Telomerase Activity in Prostatic Fluids is Indicative of Prostate Cancer." Please provide us with a copy of the journal, publication, or seminar brochure that contains your papers once they are published.

Please feel free to call Lydia Pearson, our Contracts Administrator, at (909) 558.6184 with any questions. We are pleased with the progress you are making on your research and look forward to seeing your papers in print.

Sincerely,

Thomas J. Callanan
Administrative Director
TJC:lmp

c J. Patrick Yhip

11354 Mountain View Avenue, Suite D, Loma Linda, California 92354, Voice: 909/558-6184 Fax: 909/558-6200

Detection of Telomerase Activity in Prostatic Fluid Specimens[1]

Zhilian Wang, BM, Soroush A. Ramin, MD, Christopher Tsai, MD, Paul Lui, MD, Percy J. Herbert, MS, Eru Kyeyune-Nyombi, PhD, Herbert C. Ruckle, MD, Richard E. Beltz, PhD[2], John F. Sands, PhD

Department of Biochemistry, School of Medicine, Loma Linda University *[Z. W., P. J. H., E. K.-N., R. E. B, J. F. S.]*, Division of Urology, Department of Surgery, School of Medicine Loma Linda University Medical Center *[S. A. R., C. T., P. L., H. C. R.]*

RUNNING TITLE

TELOMERASE ACTIVITY IN PROSTATIC FLUID

KEY WORDS

telomerase, telomeric repeat amplification protocol, prostate cancer, prostatic fluid, protease inhibitors

FOOTNOTES

[1] This study was supported by the U.S. Department of the Army and the National Medical Technology Testbed, Inc. The views, opinions and/or findings contained in this report are those of the author(s) and should not be construed as a position, policy, decision or endorsement of the federal Government or the National Medical Technology Testbed, Inc.

[2] To whom requests for reprints should be addressed: Department of Biochemistry, School of Medicine, Loma Linda University, Loma Linda, CA 92354. Phone: 909-558-4527; Fax: 909-558-4887; E-mail: rbeltz@som.llu.edu.

ABSTRACT

We report here the extended use of the Telomeric Repeat Amplification Protocol (TRAP) assay for the detection of telomerase activity in freshly collected prostatic fluid. Out of 30 prostatic fluid specimens from patients with confirmed prostate cancer (PCa), 25 had positive telomerase activity (sensitivity 83%), while only 1 of 9 samples from patients with benign prostatic hyperplasia or prostate-normal subjects tested negative (specificity 89%). The positive predictive value (PPV) of the TRAP assay for prostate cancer was 96%. We found a strong correlation between telomerase activity in prostatic fluid specimens and serum prostate specific antigen (PSA) values. Telomerase activity was found in 79% of specimens from patients with PSA values >4 ng/ml, while in specimens from patients with PSA values ≤4 ng/ml only 29% tested positive for telomerase activity. In patients with PSA values above the standard 0-4 ng/ml reference range, the PPV of the TRAP assay was 84%. Furthermore, telomerase activity could be detected in 85% of the specimens from PCa patients with Gleason scores >4. In prostatic fluid from PCa patients with Gleason scores of ≤4, telomerase activity was detected 50% of the time. The PPV was 92% when a Gleason score of 4 was used as the lower limit. The use of the TRAP assay to detect telomerase activity in prostatic fluid is a novel approach to diagnosing prostate cancer and should become an effective tool for the diagnosis of prostate cancer.

INTRODUCTION

Telomeres, the specialized protein-DNA structures at the ends of eukaryotic chromosomes, function in the protection, positioning, and replication of chromosomes (1-3). Human telomeres consist of tandem arrays of the G-rich, highly conserved DNA sequence TTAGGG and the proteins which bind to them (4). During DNA replication, synthesis of the leading strand of the replication fork proceeds in a continuous manner, while synthesis of the lagging strand is discontinuous, consisting of Okazaki fragments which initiate with a labile RNA primer. After Okazaki fragment extension and RNA primer removal, the most 5' Okazaki fragment will remain incomplete since the removed RNA primer cannot be replaced with DNA. If the 5'-terminal Okazaki fragment does not initiate directly opposite the 3' end of the template DNA, there will be additional complementary bases unreplicated. This replication strategy predicts the progressive shortening of chromosomal DNA at the 3' ends over multiple cycles of replication in normal somatic cells (5-7). The telomere hypothesis of cell aging and immortalization suggests that telomere shortening in the absence of telomerase is the mitotic clock for replicative senescence in normal somatic cells (8,9). Immortalized cells, on the other hand, restore and maintain their telomeres by expressing telomerase and possess unlimited proliferative potential as well, which is one of the characteristics of malignant tumor cells.

Telomerase is a ribonucleoprotein enzyme whose activity depends on both its RNA and protein components, as shown by loss of activity following treatment with either RNase or heat (10,11). The basic function of telomerase is to extend the 3' end of

telomeres by *de novo* synthesis of the G-rich telomeric repeat strand (12,13). Telomerase can be considered a RNA dependent DNA polymerase, or reverse transcriptase, that possesses its own RNA template. Telomerase activity was first identified in *Tetrahymena* (14) and later in several other eukaryotes, including *Oxytricha*, yeast, mice, and humans (11,15,16). Initially, the presence of human telomerase activity was found only in HeLa cells (11) and in ovarian carcinoma (17) until a highly sensitive polymerase chain reaction (PCR)-based telomerase assay, the Telomeric Repeat Amplification Protocol (TRAP), was developed (18). Telomerase activity can be detected in 85-90% of tumors and in 14% of benign or early-stage tumors, but it is not detectable in most human somatic cells (18,19). The level of telomerase activity correlates with the clinical outcome of many cancers (20, 21). The high correlation between telomerase activity and the presence of cancer suggests that telomerase activity could be a valuable diagnostic and prognostic cancer marker.

Prostate cancer is the most common noncutaneous malignancy in men and is second only to lung cancer in causing cancer-related deaths of males in the United States (22). It is believed by most urologists that the early detection of prostate cancer increases the probability of successful treatment (22). Diagnostic techniques, including the serum prostate specific antigen (PSA) test and transrectal ultrasound, have a low incidence of complications and have increased the sensitivity of cancer detection over digital rectal examination, thus benefitting many patients (23). Telomerase activity has been detected in tissue specimens from prostate cancer patients (18,19,24-27), raising the possibility that telomerase activity in tissue may be an independent marker for prostate cancer. However, an even more significant clinical use of detecting telomerase activity would be in the

detection of prostate cancer through the analysis of readily accessible body fluids such as urine, semen, or prostatic secretions. Collection of such fluid specimens has the advantage of avoiding surgical invasion of the prostate gland. In this study, we have used the TRAP assay to measure telomerase activity in freshly collected prostatic fluid specimens with the goal of developing the TRAP assay into a reliable diagnostic tool for prostate cancer detection.

MATERIALS AND METHODS

Cell Culture and CHAPS Protein Extraction

PC-3, a human prostate cancer cell line derived from a bone metastasis with a doubling time of 2.7 days in tissue culture (28) and obtained from the ATCC (Rockville, MD), was grown in RPMI 1640 medium supplemented with 10% new-born calf serum. The cells were harvested when 90% confluent using trypsin. After the cells were collected by centrifugation, the cell pellet was washed twice with cold phosphate-buffered saline, resuspended in ice-cold Buffer A [10 mM HEPES-KOH (pH 7.5), 1.5 mM $MgCl_2$, 10 mM KCl, 1 mM dithiothreitol] and recentrifuged. The pellet was lysed in Buffer B (Lysis Buffer) [0.5% 3-(3-cholamidopropyl-dimethylammonio)-1-propanesulfonate (CHAPS), 5 mM β-mercaptoethanol, 0.1 mM phenylmethanesulfonyl fluoride (PMSF), 10% glycerol, 10 mM Tris-HCl (pH 7.5), 1 mM $MgCl_2$] for 30 min on ice. Then, the lysate was centrifuged at 16,000 x g for 20 min at 4 °C. Aliquots of the supernatant fluid were

immediately stored at -80 °C. The protein concentration was determined by ultraviolet spectrophotometry (29).

Collection of Prostatic Fluid

Prostatic fluid specimens were collected from 30 PCa patients and from 9 patients clinically confirmed as cancer-free, including 6 benign prostatic hyperplasia (BPH) patients. In brief, siliconized microcentrifuge tubes were prepared in advance to contain 1.18 ml of a master mix of protease inhibitors (see below). A few minutes prior to specimen collection, 20 µl of an ethanol solution of PMSF was added to each microcentrifuge tube. Prostatic fluid was collected from each patient by palpating the prostate and milking the fluid through the urethra. Approximately 300 µl of the extruded specimen was transferred immediately into the microtube, mixing the specimen with protease inhibitors by inversion three times. The final concentrations of the added protease inhibitors were 10 mM disodium EDTA, 5 mM benzamidine-HCl, 20 mM sodium caproate, and 0.2 mM PMSF. The microtube was then centrifuged 5 min in an Eppendorf table-top centrifuge at 4 °C. The supernatant fluid was divided into aliquots, which together with the pellet were placed on dry ice and transferred to the laboratory. The aliquots of the supernatant fluid were stored at -80 °C, while the pellet was further treated by the CHAPS protein extraction method as described above. This extract was also divided into aliquots for freezing and storage at -80 °C. The protein concentrations of the CHAPS extracts were determined by ultraviolet spectrophotometry (29). Specimen

collection procedures were approved by the Loma Linda University School of Medicine Internal Review Board.

TRAP Assay

Each specimen was assayed for telomerase activity using supernatant fluid samples (1 µl) and aliquots of the CHAPS protein extract of the pellet that contained 6 µg protein. An aliquot of CHAPS protein extract of PC-3 cells, containing 6 µg of protein corresponding to approximately 3,000 PC-3 cells, was assayed along with specimen samples as a positive control. An identical aliquot inactivated by heat (85 °C for 15 min) or by exposure to RNase A (0.2 µg/µl at 37 °C for 30 min) was assayed as a negative control. CHAPS lysis buffer was also used as a negative control. Aliquots of PC-3 cell extracts corresponding to 1,000, 100, 10, and 1 cells were assayed to standardize the telomerase activity and estimate how much telomerase was present in each specimen.

The TRAP assay for telomerase activity was performed as described by Kim et al. (18) with minor modifications. In brief, an appropriate aliquot of either a prostatic specimen or a protein extract of PC-3 cells was assayed in 50 µl of reaction mixture containing 50 µM deoxynucleotide triphosphates, 0.1 µg of TS primer (5'-AATCCGTCGAGCAGAGTT-3'), 2 Units of *Taq* polymerase, 1 µl of [α-^{32}P]dCTP (10 mCi/ml, 3,000 Ci/mmol), 20 mM Tris-HCl (pH 8.3), 1.5 mM $MgCl_2$, 63 mM KCl, 1 mM EGTA, 0.005% Tween-20 in a 0.5 ml tube that contained 0.1 µg of CX primer (5'-CCCTTACCCTTACCCTTACCCTAA-3') sequestered at the bottom of the 0.5 ml tube by

a wax barrier (Ampliwax, Perkin Elmer, Foster City, CA). After 45 min of incubation at room temperature, the reaction mixture was subjected to 34 PCR cycles consisting of 94 °C for 30 s, 50 °C for 30 s, and 72 °C for 90 s. The PCR product was then subjected to electrophoresis on a 10% nondenaturing polyacrylamide gel, dried, and exposed to X-ray film, or developed in a Bio-Rad Molecular Imager in conjunction with the Molecular Analyst software (Bio-Rad Laboratories, Hercules, CA). Typical products of telomerase activity were shown by the 6-bp ladder bands starting from 40 bp. Telomerase activity was graded on a scale of 0 to 3 (0, no activity; 3, highest activity). The following standards were used to judge a sample telomerase positive: (1) the presence in a sample lane of more than four bands of the 6-bp telomerase repeat, which could be eliminated by either RNase A or heat, and (2) repetition of the result with two or more repeat samplings.

Statistical analysis

Statistically significant differences were evaluated by means of the chi-square test. *P* values less than or equal to 0.05 were considered statistically significant.

RESULTS

In agreement with previously reported data (24), substantial telomerase activity was observed in lysates of the PC-3 human prostate cancer cell line. In a serial dilution study of the PC-3 CHAPS lysate, telomerase activity could be detected in a protein extract

corresponding to as little as one PC-3 cell when using a 34-PCR cycle (Fig. 1), confirming the high sensitivity of this assay system to detect telomerase activity in immortal cells.

Telomerase activity was detected in supernatant fluid and/or pellet extract of specimens obtained from 25 of 30 PCa patients (83%), whereas no activity was similarly detectable in specimens taken from 8 of 9 patients (89%) with either a normal prostate gland or BPH (Table 1). The telomerase signals from the CHAPS protein extracts of the pellets were stronger than those from the supernatant fluids (Fig. 2). The telomerase ladder obtained from most of the prostate fluid specimens suggested that each assayed aliquot contained the telomerase equivalent of approximately 10 PC-3 cancer cells (Fig. 1 and Fig. 2). The positive rate (80%) from the CHAPS extracts of the pellets was significantly higher than that (53%) from the supernatant fluids (Table 1). Furthermore, in some specimens the telomerase activity was increased after heating at 85 °C for 15 min (Fig. 2, lanes 3, 7), while in other specimens the telomerase activity was diminished but could not be abolished by such heating (Fig. 2, lane 1). This is in contrast to the effect of heating a CHAPS extract of PC-3 cells to 85 °C for 15 min, which essentially eliminates telomerase activity (Fig. 2, lane 11). This phenomenon was further investigated by heating the aliquots of protein extract from a prostate cancer patient specimen to 85 °C for 60, 15, and 5 min and then determining the amount of telomerase activity that remained after the heat treatment (Fig. 3, lanes 2, 3, 4). Telomerase activity was still detectable after an hour at 85 °C. A double pretreatment was performed which involved heating at 85 °C for 15 min followed by exposure to RNase A (0.2 μg/μl) for 30 min at 37 °C (Fig. 3, lane 1). No telomerase activity was detectable in the specimens pretreated with both heat and

RNase A. Our results suggest that a heat-pretreatment is not always an appropriate negative control for telomerase activity in prostatic fluid specimens. On the contrary, heat-pretreatment of some of the specimens improves the ability to detect telomerase activity.

We also analyzed the relationship between telomerase activity in the prostatic fluid specimens and the PSA values of patients, and found that telomerase activity had a strong correlation with the PSA levels (Table 2A). Patients with PSA values >4 ng/ml had telomerase activity in their prostatic fluid specimens 84% of the time, while only 29% of the patients with PSA values ≤4 ng/ml had telomerase activity in their prostatic secretions. Using this comparison, the positive predictive value (PPV) of the TRAP assay for an elevated PSA was 84%.

Telomerase activity was also correlated with the Gleason scores of PCa patients (Table 2B). Telomerase activity could be detected in 85% of prostatic fluid specimens from PCa patients with Gleason scores >4, and half of PCa patients with Gleason scores ≤4 also had telomerase activity in their prostatic fluid specimens. Using the Gleason score of 4 as the dividing point for these two groups produced a PPV of 92% for the higher group.

DISCUSSION

Since the development of the TRAP assay by Kim et al. (18), telomerase activity has been detected in a wide variety of malignant tumors, including prostate cancer (18,19).

Therefore, telomerase shows promise as a cancer marker. Telomerase activity is detectable in surgically collected tissue specimens from PCa patients, indicating that the TRAP assay can be used as a diagnostic tool for PCa (24-27). However, telomerase detection in nonsurgically obtained body fluids, such as prostatic fluid, would likely be more practical for the diagnosis of prostate cancer because of easier patient compliance and lower expense.

Clinically, prostatic adenocarcinoma arises in the acinar and proximal ductal epithelium of the prostate gland and accounts for over 95% of prostatic cancers (30). Prostatic fluid contains proteases, lipids, metal ions and amines secreted daily from acinar cells of the prostate gland (31). Furthermore, a few exfoliated cells from the prostate and telomerase from those cancer cells might be in prostatic fluid. Telomerase activity has been detected in exfoliated cells present in urine from bladder carcinoma patients (32,33), as well as in colonic luminal washings from colon carcinoma patients (34).

The present study focuses on determining the diagnostic value of the TRAP assay applied to prostatic fluid specimens. More than 80% of 30 PCa patients showed positive telomerase activity in their specimens. The PPV for prostate cancer was 96%. Almost 90% of the normal and BPH patients were negative for telomerase activity. These results indicate that telomerase activity in prostatic fluid is a useful diagnostic marker for prostate cancer. The pellets from centrifuged fresh prostatic fluid specimens, which probably contain exfoliated cancer cells, were shown to be better for detecting telomerase activity than supernatant fluids.

Telomerase is a ribonucleoprotein enzyme whose activity depends on both its RNA

and protein components. Numerous data have shown that its activity can be eliminated by a pretreatment with either RNase A or heat (10,11). However, the results from some specimens showed that the telomerase activity could be increased after heat-pretreatment. In other specimens, the telomerase signals became weakened, but could not be totally abolished by pre-heating. This hints that inhibitors of telomerase are present in pure prostatic fluid specimens which bind tightly to the telomerase enzyme. Heat pretreatment appears to be inactivating the inhibitors rather than inactivating telomerase.

Serum PSA is commonly used as a marker for prostate cancer. In general, the higher the PSA level, the greater is the likelihood of an advanced pathologic stage (35). Serum PSA level has been found to correlate with tumor volume and is an important predictor of tumor progression and prognosis (36). In this study, we demonstrated that telomerase activity is highly correlated with PSA levels. In addition, we showed that a strong correlation exists between the presence of telomerase and a Gleason score greater than 4. Therefore, the detection of telomerase in prostatic fluid appears to serve as a prognostic marker as well as a diagnostic marker for prostate cancer. In our study, 96% of patients who showed positive telomerase activity in their prostatic fluid specimens also had prostate cancer. In contrast, only about 35% of males with serum PSA levels above 4 ng/ml are found to have prostate cancer (37). Therefore, the presence of telomerase in prostatic fluid is a more specific marker than serum PSA for diagnosing prostate cancer.

In conclusion, the PCR-based TRAP assay was sensitive enough to detect telomerase activity in prostatic fluid. Telomerase activity was detectable in more than 80% of prostatic fluid specimens obtained from prostate cancer patients, but it was not

detectable in close to 90% of specimens taken from prostate-normal or BPH patients. The prostatic fluid specimens can be collected easily and with minimal discomfort or risk to patients. The ability to detect telomerase activity in those specimens strongly suggests that the TRAP assay of prostatic fluid has the potential of playing a key role in the clinical diagnosis of prostate cancer.

REFERENCES

1. Muller HJ (1938): The remaking of chromosomes. The collecting net. Woods Hole 13:181-198.
2. McClintock B (1941): The stability of broken ends of chromosomes in *Zea mays.* Genetics 41:234-282.
3. Blackburn EH (1994): Telomeres: no end in sight. Cell 77:621-623.
4. Blackburn EH (1991): Structure and function of telomeres. Nature 350:569-573.
5. Olovnikov AM (1973): A theory of marginotomy: The incomplete copying of template margin in enzymic synthesis of polynucleotides and biological significance of the phenomenon. J Theor Biol 41:181-190.
6. Watson JD (1972): Origin of concatemeric T7 DNA. Nat. New Biol. 239:197-201.
7. Levy MZ, Allsopp RC, Futcher AB, Greider CW, Harley CB (1992): Telomere end-replication problem and cell aging. J Mol Biol 225:951-960.
8. Harley CB (1991): Telomere loss: mitotic clock or genetic time bomb? Mutat Res 256:271-282.
9. Harley CB, Vaziri H, Counter CM, Allsopp RC (1992): The telomere hypothesis of cellular aging. Exp Gerontol 27:375-382.
10. Greider CW, Blackburn EH (1987): The telomere terminal transferase of *Tetrahymena* is a ribonucleoprotein enzyme with two kinds of primer specificity. Cell 51:887-898.
11. Morin GB (1989): The human telomere terminal transferase enzyme is a

ribonucleoprotein that synthesizes TTAGGG repeats. Cell 59:521-529.

12. Greider CW, Blackburn EH (1989): A telomeric sequence in the RNA of *Tetrahymena* telomerase required for telomere repeat synthesis. Nature 337:331-337.

13. Shippen-Lentz D, Blackburn EH (1990): Functional evidence for an RNA template in telomerase. Science 247:546-552.

14. Greider CW, Blackburn EH (1985): Identification of a specific telomere terminal transferase activity in *Tetrahymena* extracts. Cell 43:405-413.

15. Greider CW (1996): Telomere length regulation. Annu Rev Biochem. 65:337-365.

16. Cohn M, Blackburn EH (1995): Telomerase in yeast. Science 269:396-400.

17. Counter CM, Hirte HW, Bacchetti S, Harley CB (1994): Telomerase activity in human ovarian carcinoma. Proc Natl Acad Sci USA 91:2900-2904.

18. Kim NW, Piatyszek MA, Prowse KR, *et al* (1994): Specific association of human telomerase activity with immortal cells and cancer. Science 266:2011-2015.

19. Shay JW, Wright WE (1996): Telomerase activity in human cancer. Curr Opin Oncol 8:66-71.

20. Tahara E, Semba S, Tahara H (1996): Molecular biological observations in gastric cancer. Semin Oncol 23:307-315.

21. Hiyama E, Hiyama K, Yokoyama T, Matsuura Y, Piatyszek MA, Shay JW (1995): Correlating telomerase activity levels with human neuroblastoma outcomes. Nat Med 1:249-255.

22. Naitoh J, Zeiner RL, Dekernion JB (1998): Diagnosis and treatment of prostate

cancer. Am Fam Physician 57:1531-1547.

23. Gohagen JK, Prorok PC, Kramer BS, Cornett JE (1994): Prostate cancer screening in the prostate, lung, colorectal and ovarian cancer screening trial of the National Cancer Institute. J Urol 152:1905-1909.

24. Sommerfeld H-J, Meeker AK, Piatyszek MA, Bova GS, Shay JW, Coffey DS (1996): Telomerase activity: a prevalent marker of malignant human prostate tissue. Cancer Res 56:218-222.

25. Lin Y, Uemura H, Fujinami K, Hosaka M, Harada M, Kubota Y (1997): Telomerase activity in primary prostate cancer. J Urol 157:1161-1165.

26. Takahashi C, Miyagawa I, Kumano S, Oshimura M (1997): Detection of telomerase activity in prostate cancer by needle biopsy. Eur Urol 32:494-498.

27. Lin Y, Uemura H, Fujinami K, *et al* (1998): Detection of telomerase activity in prostate needle-biopsy samples. Prostate 36:121-128.

28. Kaighn ME, Narayan KS, Ohnuki Y, Lechner JF, Jones LW (1979): Establishment and characterization of a human prostatic carcinoma cell line (PC-3). Invest Urol 17:16-23.

29. Robyt JF, White BJ: Biochemical Techniques: Theory and Practice. Prospect Heights, IL, Waveland Press, 1990.

30. Trump DL, Shipley WU, Dillioglugil O, Scardino PT: Neoplasms of the Prostate. In Holland JF, Frei III E, Bast, Jr. RC, Kufe DW, Morton DL, Weichselbaum RR (eds): Cancer Medicine 1997. Philadelphia, PA, Lippincott Williams & Wilkins, 1997.

31. Grover PK, Resnick MI (1995): Analysis of prostatic fluid: Evidence for the presence of a prospective marker for prostatic cancer. Prostate 26:12-18.

32. Yoshida K, Sugino T, Tahara H, *et al* (1997): Telomerase activity in bladder carcinoma and its implication for noninvasive diagnosis by detection of exfoliated cancer cells in urine. Cancer 79:362-369.

33. Kinoshita H, Ogawa O, Kakehi Y, *et al* (1997): Detection of telomerase activity in exfoliated cells in urine from patients with bladder cancer. J Natl Cancer Inst 89:724-730.

34. Yoshida K, Sugino T, Goodison S, *et al* (1997): Detection of telomerase activity in exfoliated cancer cells in colonic luminal washings and its related clinical implications. Br J Cancer 75:548-553.

35. Stamey TA, Kabalin JN (1989): Prostate-specific antigen in the diagnosis and treatment of adenocarcinoma of the prostate. I. Untreated patients. J Urol 141:1070-1075.

36. Ohori M, Wheeler TM, Dunn JK, Stamey TA, Scardino PT (1994): The pathological features and prognosis of prostate cancers detectable with current diagnostic tests. J Urol 152:1714-1720.

37. Catalona WJ, Smith DS (1994): Comparison of different serum prostate specific antigen measures for early prostate cancer detection. Cancer 74:1516-1518.

Table 1. Diagnostic significance of telomerase activity in prostatic fluid specimens from a hospital-based patient population.

	Carcinoma	Sample Source *	Telomerase Activity: Positive	Negative	Total (n)	Sensitivity	Specificity	Positive Predictive Value
PF	Present	Sup	16	14	30	53% (16/30) ❶		
		E	24	6	30	80% (24/30) ❶		
	Total (n)		**25 ❷ ❹**	**5 ❷**	**30**	**83%** (25/30)		
	Absent	Sup	0	9	9			
		E	1	8	9			
	Total (n)		**1 ❸ ❹**	**8 ❸**	**9**		**89%** (8/9)	
Total (n)			**26**	**13**	**39**			**96%** (25/26)

* Sup, supernatant fluids; E, CHAPS extracts from the pellets.
❶, ❷, ❸, ❹: Significantly different from each other (P <0.05).

Table 2. The correlation of either PSA value (A) or Gleason score (B) with telomerase activity in prostatic fluid specimens from a hospital-based patient population.

			Telomerase Activity					Positive Predictive Value
			Positive	Negative	Total (n)	Sensitivity	Specificity	
A	PSA Value *	>4	21 ❶ ❸	4 ❶	25	84% (21/25)		
		≤4	4 ❷ ❸	10 ❷	14		71% (10/14)	
		Total (n)	25	14	39			84% (21/25)
B	Gleason Score	>4	22 ❹ ❺	4 ❹	26	85% (22/26)		
		≤4	2 ❺	2	4		50% (2/4)	
		Total (n)	24	6	30			92% (22/24)

* The normal range of serum PSA value is equal to or less than 4 ng/ml.
❶, ❷, ❸, ❹, ❺: Significantly different from each other ($P < 0.05$).

Figure Legends

Fig. 1. Telomerase activity in PC-3 cells, a human prostate cancer cell line. Lanes 1-4, telomerase activity in serial dilutions of CHAPS extract, 1000, 100, 10, and 1 cell equivalents, respectively; lane 5, lysis buffer; lane 6, CHAPS extract, 1000 cell equivalents, pretreated with heat.

Fig. 2. Telomerase activity in prostatic fluid specimens from two PCa patients (A, B) with the addition of protease inhibitors. Lanes 1-4, specimen A; lanes 5-8, specimen B; lane 9, lysis buffer; lanes 10, 11, CHAPS extract of PC-3 cells (6 μg protein), without or with heat pretreatment, respectively. Supernatant fluid (1 μl), lanes 1, 2, 5, 6; CHAPS extract of the pellet (6 μg protein), lanes 3, 4, 7, 8. Heat pretreatment, lanes 1, 3, 5, 7; no heat pretreatment, lanes 2, 4, 6, 8.

Fig. 3. Effect of varying durations of heat pretreatment on telomerase activity in the CHAPS extract of a specimen pellet. Lane 1, an aliquot (6 μg protein) preheated at 85 °C for 15 min followed by RNase A pretreatment at 37 °C for 30 min; lanes 2, 3, 4, aliquots (6 μg protein each) preheated at 85 °C for 60 min, 15 min, and 5 min, respectively; lane 5, an aliquot (6 μg protein) without heat pretreatment; lane 6, lysis buffer; lanes 7, 8, CHAPS extract of PC-3 cells (6 μg protein), without or with heat pretreatment, respectively.

FIGURE 1

FIGURE 2

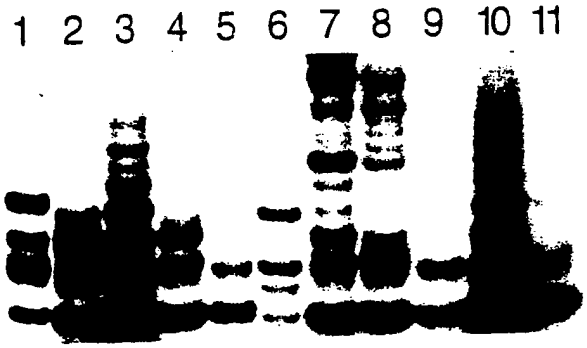

FIGURE 3

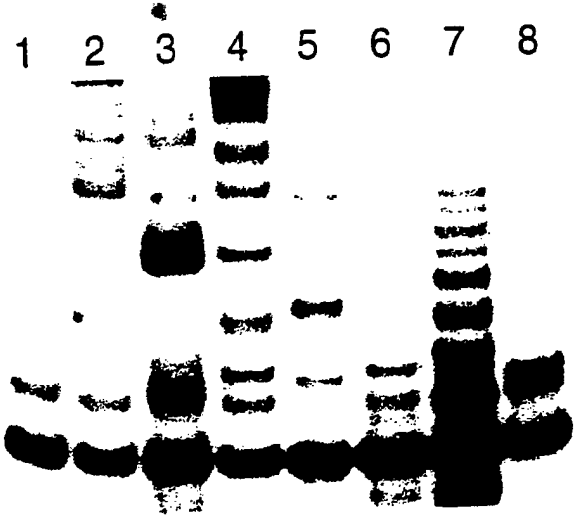

APPLICATION OF THE TELOMERIC REPEAT AMPLIFICATION PROTOCOL FOR DETECTION OF CANCER IN PROSTATE NEEDLE BIOPSY SPECIMENS[1]

Zhilian Wang, MD, Soroush A. Ramin, MD, Christopher Tsai, MD, Paul Lui, MD, Herbert C. Ruckle, MD, Richard E. Beltz[2], PhD, John F. Sands, PhD

Department of Biochemistry, School of Medicine, Loma Linda University *[Z. W., E. K.-N., R. E. B, J. F. S.]*, Division of Urology, Department of Surgery, School of Medicine, Loma Linda University Medical Center *[S. A. R., C. T., P. L., H. C. R.]*

RUNNING TITLE

TELOMERASE ACTIVITY IN PROSTATE NEEDLE CORES

KEY WORDS

telomerase, telomeric repeat amplification protocol, prostate cancer, sextant needle biopsy specimens

FOOTNOTES

[1] This study was supported by the U.S. Department of the Army and the National Medical Technology Testbed, Inc. The views, opinions and/or findings contained in this report are those of the author(s) and should not be construed as a position, policy, decision or endorsement of the federal Government or the National Medical Technology Testbed, Inc.

[2] To whom requests for reprints should be addressed: Department of Biochemistry, School of Medicine, Loma Linda University, Loma Linda, CA 92354. Phone: 909-558-4527; Fax: 909-558-4887; E-mail:rbeltz@som.llu.edu

ABSTRACT

Human telomerase acts to maintain functioning telomeres, which are required for cellular immortality and very likely for cancer progression. Telomerase activity is present in about 85% of human cancers tested, but it has not been found in most normal human somatic cells and tissues. We report here the use of the Telomeric Repeat Amplification Protocol for detection of telomerase activity in sextant needle biopsy specimens collected clinically from human prostate glands. Telomerase activity was found in one or more specimens from 41 of 45 prostate cancer patients (91%), but was absent in all specimens from 7 of 8 cancer-free patients (88%). Further analysis showed that poorly differentiated cancers with higher Gleason scores were always associated with a higher rate of telomerase detection and stronger telomerase activity. Moreover, comparison of telomerase activity with the volume of cancer in the needle cores showed that stronger activity was positively correlated with a higher cancer volume. Thus, the progression of prostate cancer and the expression of telomerase appear to be linked, indicating that telomerase activity can be considered a prognostic marker as well as a diagnostic marker for prostate cancer.

INTRODUCTION

Telomeres are specialized DNA-protein structures at the ends of eukaryotic chromosomes that normally function in the protection, positioning, and replication of chromosomes (1-3). The "end replication problem" causes telomere shortening in normal human somatic cells after each

cell division. However, the telomere hypothesis of cell aging and immortalization (4-6) suggests that mutations of tumor suppressor genes or other genes may in time induce the formation of a cell clone that has escaped from cell crisis by activating telomerase and/or other mechanisms to maintain telomere integrity and thereby become immortal.

Telomerase as an RNA-dependent DNA polymerase, or reverse transcriptase, is a ribonucleoprotein complex capable of synthesizing the telomeric repeat sequence using its own RNA subunit as a template (7, 8). Telomerase activity is detectable in approximately 85% of human cancers, but is not found in most human somatic cells and tissues (9-11). This suggests that telomerase activity should be assayed as a marker for the diagnosis of human cancer. Furthermore, the presence of telomerase activity in some tumors is correlated with clinical outcome, suggesting that telomerase activity could be useful as a prognostic indicator (12-15).

Prostate needle core biopsy has been well developed and is one of the most favored methods for obtaining diagnostic material from the prostate gland (16). In the present study, sextant needle biopsies from radical retropubic prostatectomy (RRP) specimens were collected and assayed by the PCR-based TRAP to determine telomerase activity with the objective of evaluating the assay as a mini-invasive diagnostic tool for prostate cancer detection.

MATERIALS AND METHODS

Cell Culture and CHAPS Protein Extraction

The human prostate cancer cell line PC-3 was obtained from the ATCC (Rockville, MD)

and grown in RPMI 1640 medium supplemented with 10% new-born calf serum. The cells were harvested when 90% confluent using trypsin. After the cells were collected by centrifugation, the cell pellet was washed twice with cold phosphate-buffered saline, resuspended in ice-cold Buffer A [10 mM HEPES-KOH (pH 7.5), 1.5 mM $MgCl_2$, 10 mM KCl, 1 mM dithiothreitol], and recentrifuged. The pellet was lysed in Buffer B (Lysis Buffer) [0.5% 3-(3-cholamidopropyl-dimethylammonio)-1-propanesulfonate (CHAPS), 5 mM β-mercaptoethanol, 0.1 mM phenylmethanesulfonyl fluoride (PMSF), 10% glycerol, 10 mM Tris-HCl (pH 7.5), 1 mM $MgCl_2$] for 30 min on ice. The lysate was centrifuged at 16,000 x g for 20 min at 4 °C. Aliquots of the supernatant fluid were immediately stored at -80 °C. The protein concentration was determined by ultraviolet spectrophotometry (17).

Collection of Sextant Needle Biopsies from Radical Retropubic Prostatectomy Specimens

Prostate tissue specimens were collected from the prostates of patients undergoing RRP or transurethral resection of the prostate (TURP). These included 291 needle biopsy specimens from 45 prostate cancer (PCa) patients, as well as 12 sextant needle biopsy and 6 TURP specimens from 8 patients with no evidence of PCa or other kinds of cancer. Using a Biopty gun with an 18-gauge cutting needle (C.R. Bard, Inc., Covington, GA), needle cores were obtained from 6 regions and from an occasional nodule of the posterior prostate once the prostate was removed by RRP. The needle cores were kept on ice approximately 30 min until they could be frozen at -80 °C. The frozen biopsied needle core was soaked in a 5X volume/weight of CHAPS lysis buffer, homogenized on ice in a Kontes tube, and then extracted for protein as described

above. The protein concentration was determined by ultraviolet spectrophotometry (17). Aliquots were kept frozen at -80 °C until assayed. Specimen collection was approved by the Loma Linda University School of Medicine Internal Review Board.

TRAP Assay

Two aliquots of the CHAPS extract (0.6 μg protein each) from each specimen were used in the TRAP assay. One of them was pretreated with RNase A (0.2 μg/μl at 37 °C for 30 min) to serve as a telomerase-specific negative control. Aliquots of the PC-3 CHAPS extract, corresponding to approximately 3,000 cells and containing 6 μg protein, were assayed as a positive control, or as a negative control by inactivating the extract with RNase A (0.2 μg/μl at 37 °C for 30 min). CHAPS lysis buffer was also used as a negative control. To standardize the telomerase activity and estimate how much telomerase was present in each specimen, aliquots of PC-3 cell extracts corresponding to 3,000, 300, 30, and 3 cells were assayed.

The TRAP assay was performed as described (9) with minor modifications. In brief, an appropriate aliquot of the CHAPS extract of either a prostate needle core or PC-3 cells was assayed in 50 μl of reaction mixture containing 50 μM dNTPs, 0.1 μg of TS primer (5'-AATCCGTCGAGCAGAGTT-3'), 2 Units of *Taq* polymerase, 1 μl of [α-^{32}P]dCTP (10 mCi/ml, 3,000 Ci/mmol), 20 mM Tris-HCl (pH 8.3), 1.5 mM $MgCl_2$, 63 mM KCl, 1 mM EGTA, 0.005% Tween-20, and an aliquot of the CHAPS extract in a 0.5 ml tube that contained 0.1 μg of CX primer (5'-CCCTTACCCTTACCCTTACCCTAA-3') sequestered at the bottom of the 0.5 ml tube by a wax barrier (Ampliwax, Perkin Elmer, Foster City, CA). After 30 min of incubation at room temperature, the reaction mixture was subjected to 30 PCR cycles consisting of 94 °C for

30 s, 50 °C for 30 s, and 72 °C for 90 s. The PCR product was then subjected to electrophoresis on a 10% nondenaturing polyacrylamide gel, dried, and exposed to X-ray film, or developed in a Bio-Rad Molecular Imager in conjunction with the Molecular Analyst software (Bio-Rad Laboratories, Hercules, CA). Typical products of telomerase activity were shown by the 6-bp ladder bands starting from 40 bp. Telomerase activity was graded on a scale of (-) to (+++) [(-), negative; (+++), strongly positive]. The following standards were used to judge a sample telomerase positive: (1) the presence in a sample lane of more than four bands of the 6-bp telomerase repeat, which could be eliminated by either RNase A or heat, and (2) repetition of the result with two or more repeat samplings.

Statistical Analysis

Statistically significant differences and associations were evaluated by means of the chi-square test. *P* values less than or equal to 0.05 were considered statistically significant.

RESULTS

In agreement with previously reported data (18), substantial telomerase activity was observed in lysates from PC-3 cells. In a serial dilution study of the PC-3 CHAPS extract, telomerase activity could be detected in a protein extract corresponding to as few as three PC-3 cells when using a regular 30-PCR cycle (Fig. 2, lanes 14-17), confirming the high sensitivity of the assay system to detect telomerase activity in immortal cells. The results from this dilution

study were employed as a standard of comparison to evaluate the relative telomerase activity in the clinical specimens.

Telomerase assay was performed on sextant needle biopsy specimens from each excised prostate gland. The results not only showed which needle core had positive telomerase activity, but also indicated the presence and location of cancer cells in the prostate gland (Fig. 1). As seen in Figure 1A, lanes 10 and 12, the prostate cancer is localized to the left mid section (LM) and left apex (LA) of this particular patient's prostate. The cancerous region is further illustrated in Figure 1B.

Telomerase activity was detected in at least one needle biopsy specimen from 41 of 45 PCa patients (91%) (P <0.001), but was absent in specimens from 7 of 8 noncancerous patients (88%) (P <0.001) (Table 1). In the patient group, the positive predicative value (PPV) for prostate cancer was 98%, while the negative predictive value (NPV) for the absence of prostate cancer was 64%. In the specimen group, 88 of 98 specimens (90%) containing cancer cells, confirmed by histopathological examination, showed positive telomerase activity (P <0.001), whereas 102 of 130 specimens (78%) with histopathologically confirmed absence of cancer cells were telomerase negative (P <0.001) (Table 1). The PPV was 76%, while the NPV was 91%.

For histopathological examination, 24 sextant needle cores from 4 PCa patients were subjected to extra multiple slide-cutting for each specimen. The volumes of cancerous tissue on 80 slides were estimated. These volumes were compared with telomerase activity in needle cores from the same area (Table 2). Low cancer volumes on the slides from the needle cores were statistically associated with relatively weak telomerase activity, while stronger activity was usually found in the needle cores with high cancer volume. The statistically significant

correlation between telomerase activity and a given volume of cancer (P <0.05) suggests that relative telomerase activity indicates the volume of prostate carcinoma.

The relationship between telomerase activity and Gleason score (Gs) was also examined. Telomerase activity was present in 12 of 36 needle core specimens (33%) from patients with well differentiated PCa (Gs 2 to 4), 116 of 210 specimens (55%) from moderately differentiated cancers (Gs 5 to 7), and 19 of 24 specimens (79%) from poorly differentiated cancers (Gs 8 to 10) (Table 3). Telomerase activity in needle cores was statistically correlated with the Gs (P <0.01). The average telomerase-positive needle cores per patient in different Gs groups were calculated for 270 needle cores from 45 PCa patients. One needle core, on average, showed telomerase-positive activity in the Gs 2 group, 2.2 in the Gs 4 group, 2.7 in the Gs 5 group, 3.4 in the Gs 6 group, 3.6 in the Gs 7 group, 4 in the Gs 8 group, and 5 in Gs groups 9 and 10. Furthermore, average needle cores that showed telomerase-positive activity in low-grade tumors were 2 (Gs 2-4), 3.3 in intermediate-grade tumors (Gs 5-7), and 4.8 in high-grade tumors (Gs 8-10) (Fig. 2). Thus, the number of needle cores with telomerase activity increased with higher Gleason scores.

DISCUSSION

The high percentages of sensitivity and specificity found in the data from the patient group or the specimen group (Table 1) indicates that telomerase activity is a promising diagnostic marker for prostate cancer. A patient was scored as positive for telomerase if at least one of the sextant needle biopsy specimens was telomerase-positive. This definition may

contribute to the finding that PPV was relatively higher than NPV in the patient group compared to the specimen group. It could further imply that collecting multiple needle biopsy specimens from six regions of the prostate gland increased the probability of obtaining tumor tissue positive for telomerase activity, which would signal the presence of cancer in a patient. One of the sextant needle cores from a high PIN patient among 8 noncancerous patients showed weak positive telomerase activity, suggesting that this prostate contained a localized and pathologically undetected cancer (19). This result was consistent with data previously published, showing that telomerase activity can be detected in a low percentage (14%) of premalignant tumor tissues (10, 11).

We found that 10% of histopathologically confirmed cancerous specimens were telomerase negative, whereas 22% of confirmed noncancerous specimens showed positive activity. The lack of telomerase activity in a region of a prostate gland that was histopathologically diagnosed as containing cancer cells could be explained by sampling target error in obtaining a needle core. On the other hand, the presence of telomerase activity in a region of a prostate gland that was histopathologically diagnosed as being cancer-free could be explained by the fact that some premalignant lesions, i.e. PINs, do have telomerase activity (19). Another possibility is that a small number of undetected infiltrating cancerous cells in some needle biopsy specimens with normal phenotypes may have been responsible for weak positive telomerase activity, since the TRAP assay is sensitive enough to detect telomerase activity in only a few cancerous cells. Finally, inhibitors of *Taq* polymerase may exist in some specimens, causing false-negative results.

Based on Gleason scores, prostate cancer can be classified into three groups: well

differentiated (Gs 2 to 4), moderately differentiated (Gs 5 to 7), and poorly differentiated (Gs 8 to 10) (20). Previous studies revealed that the Gs is tightly correlated with the prognosis of prostate cancer and with the cancer volume in the patient (21). Our results indicated that relative telomerase activity is statistically associated with the volume of histopathologically-confirmed prostate cancer, suggesting that a prostate gland with a large cancer volume also has a greater level of telomerase activity (Table 2). However, low telomerase activity was often seen in the specimens with relatively high cancer volume. The explanation could be that the lower telomerase activity may reflect cancers that are more differentiated (22). Telomerase activity in the needle cores was also found to be correlated with the Gs and pathological differentiation (Table 3), in agreement with data previously published (23). The higher the incidence of cores with positive telomerase activity, the higher was the Gs (Fig. 2). These results confirm the relationship between the Gs and the volume of cancer (21). Our results suggest that telomerase has an important role in the progression of prostate carcinoma. The level of telomerase activity appears to be a good prognostic marker of prostate cancer.

Clinically, it is helpful for a pathological diagnosis to collect multiple needle biopsy specimens, such as sextant needle cores, from the prostate gland. Although we procured the needle cores for our study from excised prostates, the results obtained provide a basis for clinical use. We conclude that testing telomerase activity in needle biopsy specimens may not only play an important role in the diagnosis of prostate cancer, but may also provide added pathological information for therapeutic evaluation.

REFERENCES

1. Muller HJ (1938): The remaking of chromosomes. The collecting net. Woods Hole 13:181-198.
2. McClintock B (1941): The stability of broken ends of chromosomes in *Zea mays*. Genetics 41:234-282.
3. Blackburn EH (1994): Telomeres: no end in sight. Cell 77:621-623.
4. Harley CB (1991): Telomere loss: mitotic clock or genetic time bomb? Mutat. Res. 256:271-282.
5. Harley CB, Vaziri H, Counter CM, Allsopp RC (1992): The telomere hypothesis of cellular aging. Exp. Gerontol. 27:375-382.
6. Holt SE, Shay JW, Wright WE (1996): Refining the telomere-telomerase hypothesis of aging and cancer. Nature Biotechnol. 14:836-839.
7. Greider CW, Blackburn EH (1989): A telomeric sequence in the RNA of *Tetrahymena* telomerase required for telomere repeat synthesis. Nature 337:331-337.
8. Shippen-Lentz D, Blackburn EH (1990): Functional evidence for an RNA template in telomerase. Science 247:546-552.
9. Kim NW, Piatyszek MA, Prowse KR, *et al* (1994): Specific association of human telomerase activity with immortal cells and cancer. Science 266:2011-2015.
10. Shay JW, Wright WE (1996): Telomerase activity in human cancer. Curr. Opin. Oncol. 8:66-71.
11. Shay JW, Bacchetti S (1997): A survey of telomerase activity in human cancer. Eur. J.

Cancer 33:787-791.

12. Norrback KF, Dahlenborg K, Carlsson R, Roos G (1996): Telomerase activation in normal B lymphocytes and non-Hodgkin's lymphomas. Blood 88:222-229.

13. Tahara E, Semba S, Tahara H (1996): Molecular biological observations in gastric cancer. Semin. Oncol. 23:307-315.

14. Langford LA, Piatyszek MA, Xu R, Schold SC Jr, Wright WE, Shay JW (1997): Telomerase activity in ordinary meningiomas predicts poor outcome. Hum. Pathol. 28:416-420.

15. Hoos A, Hepp HH, Kaul S, Ahlert T, Bastert G, Wallwiener D (1998): Telomerase activity correlates with tumor aggressiveness and reflects therapy effect in breast cancer. Int. J. Cancer 79:8-12.

16. Renshaw AA, Corless CL: Prognostic features in the pathology of prostatic carcinoma. In Kantoff PW, Wishnow KI, Loughlin KR (eds): Prostate Cancer 1997. Malden, Massachusetts, Blackwell Science, 1997.

17. Robyt JF, White BJ: Biochemical Techniques: Theory and Practice. U.S.A., Waveland Press, 1990.

18. Sommerfeld H-J, Meeker AK, Piatyszek MA, Bova GS, Shay JW, Coffey DS (1996): Telomerase activity: a prevalent marker of malignant human prostate tissue. Cancer Res. 56:218-222.

19. Zhang W, Kapusta LR, Slingerland JM, Klotz LH (1998): Telomerase activity in prostate cancer, prostatic intraepithelial neoplasia, and benign prostatic epithelium. Cancer Res. 58:619-621.

20. Deshmukh N, Foster CS: Grading prostate cancer. In Foster CS, Bostwick DG (eds): Pathology of the prostate 1998. Philadelphia, W.B. Saudners, 1998.

21. McNeal JE (1992): Cancer volume and site of origin of adenocarcinoma in the prostate: relationship to local and distant spread. Hum. Pathol. 23:258-266.

22. Sharma HW, Sokoloski JA, Perez JR, *et al* (1995): Differentiation of immortal cells inhibits telomerase activity. Proc. Natl. Acad. Sci. USA 92:12343-12346.

23. Lin Y, Uemura H, Fujinami K, *et al* (1998): Detection of telomerase activity in prostate needle-biopsy samples. Prostate 36:121-128.

Tables

Table 1. Telomerase activity in prostate needle core tissues

		Patient group [1]			Specimen group [3]		
Prostate Carcinoma		Present	Absent	Total (n)	Present	Absent	Total (n)
Telomerase Activity	Positive	41 ❶	1 ❷	42	88 ❸	28 ❹	116
	Negative	4 ❶	7 ❷	11	10 ❸	102 ❹	112
	Total (n)	45	8	53	98	130	228 [2]
Sensitivity (%)		91 (41/45)			90 (88/98)		
Specificity (%)			88 (7/8)			78 (102/130)	
Positive Predictive Value (PPV) (%)		98 (41/42)			76 (88/116)		
Negative Predictive Value (NPV) (%)			64 (7/11)			91 (102/112)	

[1] Patients were clinically and pathologically diagnosed.
[2] 210 sextant needle cores from 35 PCa patients and 18 needle cores from patients without PCa or other cancer-invasions were examined.
[3] Presence or absence of cancer was determined by histopathological examination.
❶, ❷, ❸, ❹: significantly different from each other (P <0.001).

Table 2. Comparison of telomerase activity with histopathologically determined volume of cancer in prostate needle cores ❶

Relative Telomerase Activity in Needle core	Volume Distribution of Cancer on the Slide [1]				
	No Cancer Seen	<25%	25% - 50%	>50%	Total (n)
Negative (-)	10 (50%)	12 (38%)	4 (25%)	0 (0%)	26
Weak Positive (+)	6 (30%)	13 (41%)	7 (44%)	5 (42%)	31
Positive (++)	4 (20%)	5 (16%)	3 (19%)	2 (17%)	14
Strong Positive (+++)	0 (0%)	2 (6%)	2 (13%)	5 (42%)	9
Total (n)	20	32	16	12	80

[1] The number of slides exhibiting a given volume of cancer (% of total slides for each given volume); ❶: high correlation shown between the relative telomerase activity and a given volume of cancer (χ^2 test, P <0.05).

Table 3. Correlation of Gleason score with telomerase activity in needle core specimens from PCa patients

	Gleason Scores	Telomerase Activity		
		Positive	Negative	Total (n)
No. of Specimens (Patients)	2 - 4 [1]	12 ❶ (5)	24 (1)	36 (6)
	5 - 7 [2]	116 ❶ (32)	94 (3)	210 (35)
	8 - 10 [3]	19 ❶ (4)	5 (0)	24 (4)
	Total (n)	147 (41)	123 (4)	270 (45) [4]

[1] well differentiated adenocarcinoma;
[2] moderately differentiated adenocarcinoma;
[3] poorly differentiated adenocarcinoma;
[4] 270 needle cores from 45 PCa patients were analyzed.
❶: high correlation shown between telomerase activity and Gleason scores based on information from needle core specimens (χ^2 test, P <0.01).

Figure Legends

Fig. 1. A. Telomerase activity in sextant needle core specimens from a PCa patient. Lanes 1 and 2, 3 and 4, 5 and 6, 7 and 8, 9 and 10, 11 and 12, CHAPS extract of needle cores (0.6 μg protein) from RB (right base), RM (right mid-section), RA (right apex), LB (left base), LM (left mid-section), LA (left apex) regions of prostate, respectively; lanes 1, 3, 5, 7, 9, 11, CHAPS extract (0.6 μg protein) with RNase pretreatment; lane 13, lysis buffer; lanes 14, 15, 16, 17, serial dilutions of CHAPS extract of PC-3 cells, 3000, 300, 30, and 3 cell equivalents, respectively; lane 18, CHAPS extract of PC-3 cells, 3000 cell equivalent, pre-treated with RNase A. B. Outline of the six regions of the posterior prostate with possible cancerous regions. Prostate cancer mainly occurred in LM and LA based on the results above.

Fig. 2. Association of Gleason score (Gs) with number of needle cores with positive telomerase activity in PCa patients. Average positive needle cores per patient in different Gs groups were calculated for 270 needle cores from 45 PCa patients. An average of 1.0 needle core shows positive telomerase activity in the Gs 2 group, 2.2 in the Gs 4 group, 2.7 in the Gs 5 group, 3.4 in the Gs 6 group, 3.6 in the Gs 7 group, 4 in the Gs 8 group, and 5 in the Gs 9 group. Furthermore, 2 needle cores show positive activity in the well differentiated cancer group (Gs 2-4), 3.3 in the moderately differentiated cancer group (Gs 5-7), and 4.8 in the poorly differentiated cancer group (Gs 8-10).

A. 1 2 3 4 5 6 7 8 9 10 11 12 13 14 15 16 17 18

B.

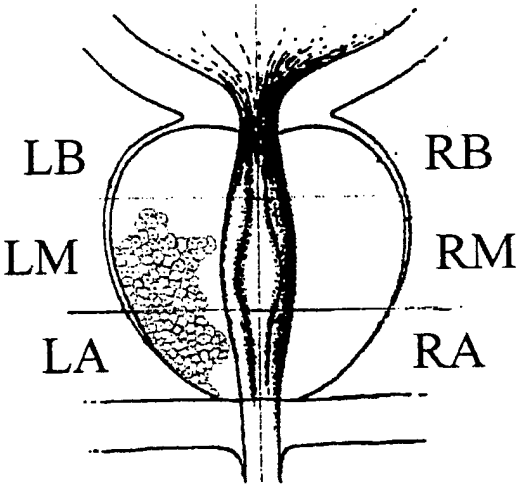

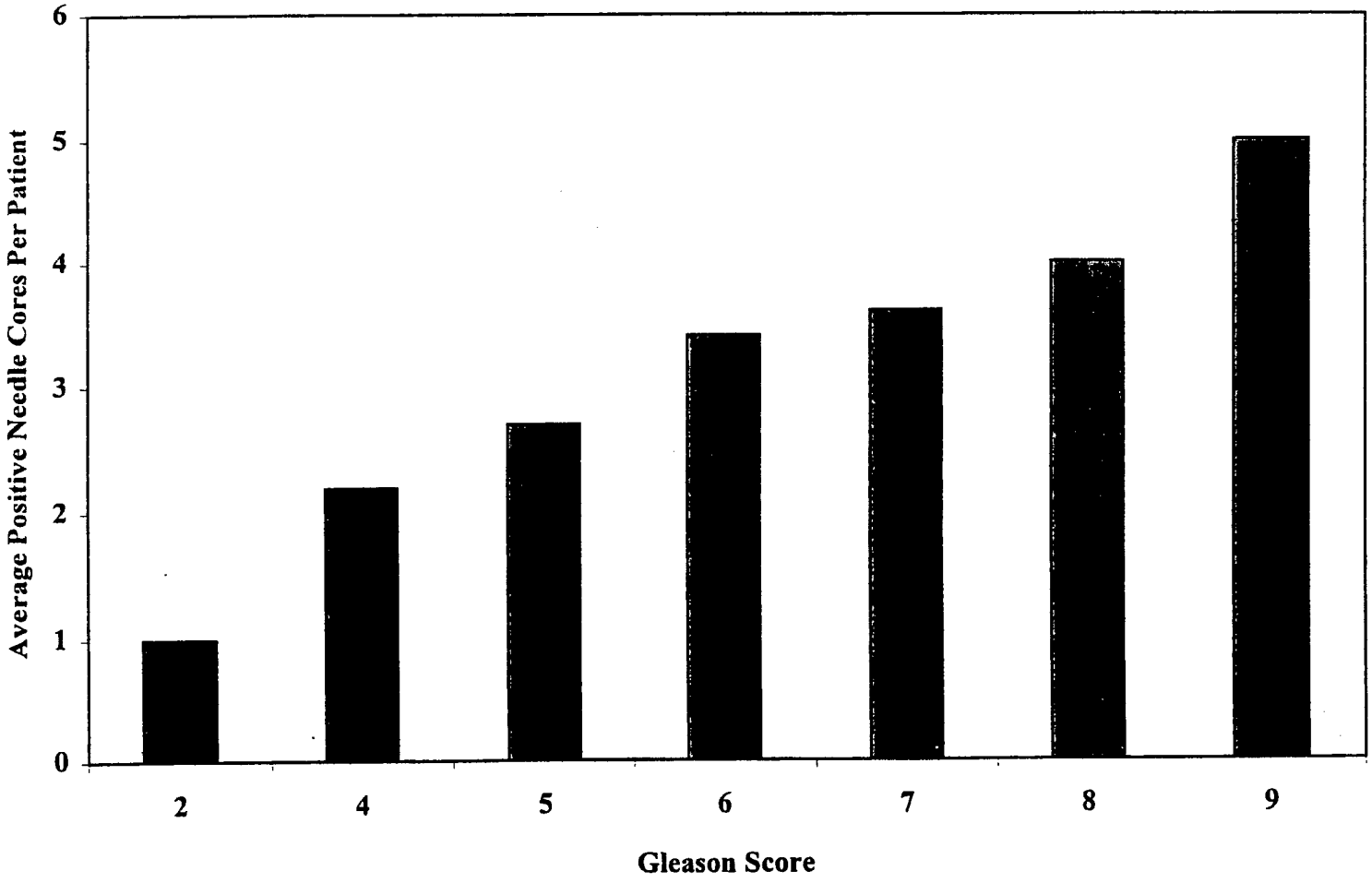
Average Positive Needle Cores Per Patient
0
1
2
3
4
5
6
2
4
5
6
7
8
9
Gleason Score

Name of Project Director: Schu

DESCRIPTION: State the goal of the project, including how it relates to improving health care. Use succinct language to describe how the project goals will be achieved. Do not exceed the space provided.

The investigators propose the development of an advanced experimental technique, called nanodosimetry, which will permit, for the first time, the measurement of the statistics of ionization clusters in small, wall-less gas samples of nanometer-equivalent dimensions. The proposed method is based on single ion counting. The project will be shared by three institutions with complementary expertise in the fields of radiation detector physics, biophysical modeling, and molecular biology: the Radiation Detector Group at the Weizmann Institute of Science in Israel, the Department of Radiation Medicine at Loma Linda University Medical Center (LLUMC), and the Division of Radiobiology at the University of California, San Diego (UCSD). Preliminary experimental studies in propane, performed at the Weizmann Institute of Science have demonstrated that the resolution of the new technique is in fact better than 1 nm equivalent length in condensed matter. Biophysical modeling based on Monte Carlo track structure data, performed at LLUMC, will support the design of the first nanodosimeter. During a later phase of the project experimental nanodosimetric data will help to test and to improve biophysical models of radiation action. New assays of DNA repair will be developed at UCSD, which will be needed to link nanodosimetric data to DNA damage. At the end of the initial funding period (one year), we will provide an experimental set-up that satisfies the requirements of nanodosimetry for biomedical applications It is anticipated that nanodosimetric radiation quality detectors will have wide applications in basic radiobiology, radiation protection, and radiation medicine. Nanodosimeters may be used to monitor the biological quality of unknown or unexpected radiation fields on earth or in space, the latter being important for extended space missions. Nanodosimeter may also prove to be useful in defining and optimizing therapeutic and diagnostic radiation fields in medicine.

PROJECT SITE(S) (organization, city, state):

Loma Linda University Medical Center
Loma Linda, CA

Weizmann Institute of Science
Rehovot, Israel (Contractual arrangement)

University of California, San Diego
San Diego, CA (Contractual arrangement)

COPY

DEVELOPMENT OF NANODOSIMETRY FOR BIOMEDICAL APPLICATIONS

FINAL REPORT FOR YEAR 2

DECEMBER 21, 1998 – JANUARY 31, 2000

Reinhard W. M. Schulte[1], M.D., M.S., George Coutrakon[1], Ph.D., Daniel Miller[1], Ph.D. Vladimir Bashkirov, Ph.D.[1],

Amos Breskin[2], Ph.D., Rachel Chechik[2], Ph.D., Sergei Shchemelinin[2], Ph.D., Guy Garty, M.S.

Jamie R. Milligan[3], Ph.D., John F. Ward[3], Ph.D.

[1]Loma Linda University Medical Center
Department of Radiation Medicine
11234 Anderson Street
Post Office Box 2000
Loma Linda, CA 92354, USA

[2]Weizmann Institute of Science
Department of Particle Physics
76100 Rehovot
Israel

[3]Radiation Biology Division
Radiology Department 0610
University of California San Diego
La Jolla, CA 92093, USA

Reinhard W. Schulte

Reinhard W. Schulte, Prinicipal Investigator March 7, 2000

Table of Contents

1. Introduction 3
2. Experimental Methods 3
    2.1 Detector Design and Experimental Characterization 3
    2.2 Data Acquisition System 4
    2.3 Biological Assays 5
3. Results and Discussion 7
    3.1 Sensitive Volume Mapping 7
    3.2 Preliminary Experience with the Nanodosimeter 7
    3.3 Biological Assays 8
4. Conclusion 10
5. References 10
6. Tables 12
7. List of Figures 13

1. Introduction

During irradiation energetic charged particles, e.g., protons, penetrate living tissues and lose their energy to the atoms and molecules, leaving them in an excited or ionized state. Based on fundamental physics principles, it has long been known that this energy loss is discontinuous. In particular, energy transfer points are not distributed uniformly along the particle track but are clustered on the nanometer scale. The initial distribution of energy transfers immediately after the irradiation is believed to be very important for the subsequent radiation-induced chemical and biological effects, and if one wants to understand the mechanisms of the biological action of radiation, the initial conditions of this complex and multistage process must be known. At present, the only tool for studying distributions of energy transfers at the nanometer level is purely theoretical and consists of full simulation of particle slowing by the Monte Carlo method. Due to the very large number of interactions, the processing time for an event-by-event Monte Carlo code that would yield results such as energy deposited in nanometer volumes with reasonable accuracy for complex radiation fields is prohibitive. Therefore, it is necessary to develop suitable experimental techniques that permit the study of energy transfer statistics in nanometer volumes. Our research project is a multidisciplinary effort, which aims at developing such an experimental technique by measuring ionizations in nanometer-equivalent gas volumes with single-event resolution. We call such a detector a *nanodosimeter*. The major goal of our project is to develop and optimize nanodosimetry in order to make it suitable for biomedical research as well as many applications in medicine, radiation protection, and space travel. The research is conducted by the Department of Radiation Medicine at Loma Linda University in close collaboration with one of the world's leading radiation detector group at the Weizmann Institute of Science (WIS) in Israel and the Division of Radiobiology at the University of California, San Diego (UCSD). In December of 1998, the National Medical Testbed approved the second year continuation funding of our project. This report details research and development work accomplished during the second project year from December 1998 to December 1999.

2. Experimental Methods

2.1 Detector Design and Experimental Characterization

The new nanodosimeter is based on the ion-counting nanodosimetric technique in low-pressure gases, originally suggested by Dr. Shchemelinin from the Weizmann Institute of Science [1,2]. Figure 1 shows the conceptual design of the detector. Ions induced by ionizing radiation in a gas of very low pressure (approximately 1 Torr) are extracted through a small aperture and then accelerated into a vacuum-operated multiplier. Experimental results obtained during the first project year, using a provisional experimental set-up, proved the feasibility of the ion counting technique with a vacuum-operated multiplier and demonstrated the possibility of nanometer spatial resolution [3,4].

It is important to know the equivalent size of the sensitive volume formed inside the nanodosimeter. In general, the volume in which ionization statistics is measured should correspond to the structures of biological relevance. It is generally accepted that the DNA and its associated water molecules are the most critical radiobiological targets. This means that the sensitive volume of the detector must have a diameter of a few nanometers. Furthermore, model calculations performed by us, which were based on Monte Carlo track structure data, showed

that energy deposition statistics in a cylinder of 2nm diameter and 16 nm length, corresponding to a 47 base-pair segment of the DNA molecule, provides the biologically most relevant information with respect to radiation-induced cell death in mammalian cells [5].

In our nanodosimeter, the sensitive volume is defined as the gas region from which electric-field extraction of the positive ions produced by ionizing radiation is possible through a small aperture. The selected ions are accelerated, detected and counted in vacuum. It should be noted that the formation of the sensitive volume in this way avoids the use of solid walls, which are known to distort the track structure [6,7]. The arrival time of the ions enables localization of the Z coordinate of the ionization event, whereas the X, Y coordinates are determined by the aperture location. The effective lateral size of the sensitive volume is determined by the aperture size, the charge diffusion properties of the gas, and electric field parameters. Due to the complex dependence of the volume size and shape on these parameters, a technique is required can determine the three-dimensional spatial distribution of the ion collection efficiency with submillimeter precision.

To date, we have developed two independent methods to map out the sensitive nanodosimetric volume. The first method is based on measured ion transport parameters and a known model of ion diffusion under an electric field. The second method, originally proposed by our collaborators at the Weizmann Institute, is based on direct scanning of the nanodosimeter ionization cell using a low-energy proton beam (10 keV). For testing of this method the Weizmann physicists designed and built a special version of the nanodosimeter, the so-called "scanning nanodosimeter", in which the sensitive volume can be displaced in two orthogonal directions perpendicular to a narrow low-energy proton beam [8].

The first version of the nanodosimeter for beam experiments was built during project year 2 at the Weizmann Institute of Science. Figure 2 shows a photograph of the detector, which is now installed on the research beam line of the Loma Linda proton accelerator. A detailed technical design drawing of the detector is presented in Figure 3. Its main components are a low-pressure gas-filled ionization chamber equipped with a scintillator photo-multiplier tube (PMT) combination, a vacuum-operated ion counter, and a built-in α source. A differential pumping system, consisting of two turbo pumps, generates the pressure gradient between the gas-filled ionization chamber and the ion counter. The nanodosimeter can measure ionization spectra from two principal sources: (1) The built-in collimated americium source, which produces high-LET alpha particles that directly traverse the sensitive volume. (2) External particle beams, in our case protons produced by the Loma Linda University proton accelerator, which enter the detector through a broad entrance window and traverse most of the gas-filled detector volume, including the sensitive volume. The latter set-up simulates the broad beam configuration typical for biological experiments.

2.2 Data Acquisition System

The data acquisition (DAQ) system is a central component of the electronics associated with the nanodosimeter (see Fig. 4). We have designed and built the first version of the DAQ system, and have implemented the required front-end electronics for triggering the DAQ system. The DAQ system provides three time-to-digit conversion real-time data streams, which are synchronized to the time structure of the LLU proton beam. An additional amplitude-to-digit conversion data stream will be implemented in a future version of the DAQ system during project year 3.

The first data stream is formed by the start signals from the Loma Linda proton accelerator, which mark the beginning of each 300-ms proton spill and are used for synchronizing the DAQ process to the 2.2 +/- 0.02 s accelerator cycle. The signals from this data stream also serve as a reference time tag (t = 0). The second data stream provides a time mark for the arrival of primary protons during a proton spill, as well as information on the time structure of individual proton spills. It should be noted that due to the oscillating spill structure of the LLU proton synchrotron (peak-to-valley beam intensity ratio up to 10) the primary particle distribution is very non-uniform. The third data stream is derived from the signals provided by the vacuum-operated ion counter after appropriate front-end electronic conditioning. This data stream is used to evaluate the ion drift time, the spacing of individual ionizations, and the number of ionizations per event.

We chose the PCI 6602 and PCI6023E boards from the National Instruments for our DAQ system. The PCI 6602, a timing and digital I/O module, is used with the PCI bus of a PC-compatible computer. It offers eight 32-bit counter channels and up to 32 lines of individually configurable TTL/CMOS-compatible digital I/O. With the 6602 module, the DAQ computer acts as a system timing controller and event-time measurement instrument.

The fast signals from the front-end electronics of the nanodosimeter are fed into the DAQ boards through an interface board providing fast NIM signal conversion to TTL/CMOS signals. An additional function of the interface board is to prevent a false signal (e.g., noise or cosmic/background events) transmission during the accelerator duty cycles. These unwanted background signals would distort the data stream timing sequences and lead to data corruption.

We have written application software for the DAQ system in the Visual Basic programming language. It utilizes the NI-DAQ function library developed by National Instruments for their DAQ products. For the large amount of data produced by the nanodosimeter, a fast and efficient data storage algorithms was required, which manages the data stream transfer to the DAQ computer hard disk as well as storage of all collected data in an appropriate format on large capacity external storage media (tape or CD).

2.3 Biological Assays

It is generally accepted that the induction and reparability of DNA damage by ionizing radiation is related to the amount of local energy deposition in DNA and surrounding water [9,10]. For example, double strand breaks (DSBs), which result when at least two individual DNA strand breaks are located within a short distance (~10 nm) on opposite strands, require at least two ionizations within or adjacent to the DNA molecule. Non- or misrepaired DSBs are considered a major source for mutations and lethal lesions. Factors that may influence the reparability of DSBs are the number and spacing of breaks per site and the number and spacing of additional base damages adjacent to the breaks. Once the structure of irreparably damaged sites is known, it should be possible, in principle, to predict the yield of such lesions from nanodosimetric measurements by analyzing the number and spacing of ionizations in small volumes simulating DNA and its surrounding water molecules.

To establish a relationship between ionization clusters measured with the nanodosimeter and the frequency and reparability of DNA lesions, we have utilized a model system in which DNA from supercoiled plasmids is irradiated in aqueous solution in the presence of radical scavengers (0.1 mol dm^{-3} DMSO). Plasmids with at least one single strand break (SSB) are transformed into an "open circle" form, whereas those with one or more DSBs become linear. The yield of SSBs

and DSBs is determined by separating the open-circle and linear plasmid fractions from the residual supercoiled fraction after employing agarose gel electrophoresis and measuring the amount of DNA in each fraction [11].

A first approach to establish a relationship between certain DNA damages and ionization clusters in DNA-equivalent volumes is to compare the *yield of plasmid DSBs* and its dependence on particle energy with that of ionization clusters larger than a specified size. Similar absolute yields of DSBs and ionization clusters and a similar dependence on particle energy would indicate that a correlation exists. Thus far, we have measured the DSB yields at three different points of the proton Bragg peak curve corresponding to mean proton energies of 30 MeV, 3 MeV, and 1 MeV. Since reliable experimental nanodosimetric spectra are not available at this time, we have compared these results to Monte Carlo simulations of energy deposition events larger than 40 eV in cylinders of 2 nm diameter and 16 nm length [12].

In repair-competent mammalian cells, most DSBs can be repaired error-free and are thus not critical for cell survival and cancer induction. It may therefore be more valuable to to use nanodosimetric measurements to predict the yield of DNA lesions, which cannot be repaired by any of the intracellular repair mechanisms. A prerequisite for the study of the relationship between large ionization clusters and *irreparable DNA lesions* is the capability to identify these lesions with the help of biological assays.

It has been hypothesized that irreparable DSBs cannot be re-ligated by repair enzymes. To test this hypothesis, we have employed a *plasmid-rejoining assay*. Irradiated DNA is incubated with cellular extract derived from *Xenopus laevis* frog eggs for up to two hours. After incubation, the remaining fraction of linear plasmids is determined as a function of incubation time. The fraction of linear plasmids remaining after 2 hours of incubation is then defined as the fraction of irreparable DSBs. From previous experience with this assay it has been known that the *Xenopus* frog cellular extract rejoins the majority of DSBs induced by low-LET irradiation within two hours.

More recently, we have begun to develop a *plasmid mutation assay* in order to measure the frequency of *misrepaired* DSBs and to study the quality of the resulting mutations. The main motivation behind this approach is the possibility that plasmids containing irreparable damage may still undergo rejoining although by an error-prone mechanism that results in mutations. Our assay employs the pHAZE plasmid, which contains an ampicillin resistance gene, a β-galactosidase gene, and an origin of replication. After irradiation, plasmids rejoined by the repair extract are used to transform *E. coli* bacterial host cells. The ampicillin gene is employed to identify bacteria that have been transformed successfully. Bacteria containing a plasmid with an intact ampicillin gene when incubated on an appropriate medium will grow into visible colonies. Bacterial colonies characterized by the absence of a functioning β-galactosidase gene identify plasmids that carry a mutation of this gene. The quality of the mutations can then be further analyzed by using restriction-fragment analysis.

3. Results and Discussion

3.1 Sensitive Volume Mapping

Figure 5 shows an example of two efficiency maps which were calculated based on experimental measurements of diffusion parameters maps for two different electric drift field conditions and a gas pressure of 1 Torr. The two maps were obtained under the assumption of a homogeneous electric field throughout the sensitive volume. Due to the different field strength they differ with respect to the efficiency along the longitudinal axis of the sensitive volume. These results demonstrate that a closed wall-less sensitive volume in the order of 2 nm across and 10 to 20 nm length can be formed in the ion-counting nanodosimeter. Based on model calculations, we have predicted that such a volume would be most useful for correlating spectra with biological effectiveness.

The assumption of a homogeneous electric field throughout the sensitive volume is only adequate to a first approximation. Ions drifting through the aperture are further accelerated towards the ion counter by a strong electric field. This electric field partially extends through the aperture into the ionization cell, and may distort the homogeneous field in the cell and affect the ion extraction process. To study this effect, we performed Monte Carlo (MC) simulations of the ion drift in the ionization cell. First, it was verified that the MC method and the integral method used to obtain the maps shown in Figure 5 give equivalent results under homogeneous field conditions. The MC method was then applied to obtain efficiency maps under realistic (inhomogeneous) field conditions. Results of these calculations are shown in Figure 6. By comparing the maps of Figure 5 and 6, it can be seen that the distortion of the drift trajectories near the aperture significantly affects the entire efficiency distribution producing a narrower and significantly longer sensitive volume.

Figure 7 shows results obtained with the scanning version of the nanodosimeter at the Weizmann Institute of Science. It must be acknowledged that the efficiency values obtained have relatively large error margins, which is due to a large noise component caused by background ionizations. Based on a semiquantitive comparison, these data were found to be consistent with the maps obtained with the first method. The scanning experiments had to be discontinued since the turbo pumping systems were needed for the nanodosimetric experiments in Loma Linda. It is planned, however, to resume scanning experiments during our third project year. Furthermore, an alternative scanning method using high-energy protons will become available once the position-sensitive capability of the nanodosimeter is implemented.

3.2 Preliminary Experience with the Nanodosimeter

Since the fabrication of the first nanodosimeter was completed in October and the detector was installed on the Loma Linda proton beam line, we have obtained first nanodosimetric ionization cluster size spectra produced in propane by the built-in alpha source as well as high- and low-energy protons from the Loma Linda accelerator. Figure 8 shows a cluster size spectrum and ion-arrival-time spectrum for alpha particles for the electric drift field conditions displayed in Figure 6 and a gas pressure of 1 Torr. These spectra are the first ever-recorded ionization event spectra in gas volumes equivalent to segments of DNA. It can be seen that for alpha

particles directly crossing the sensitive volume the most common events are ion clusters containing 6-10 ions, in addition, considerably larger clusters are seen albeit with much lower frequencies.

Figure 9 shows a comparison of ionization cluster size spectra obtained with high-LET alpha particles and intermediate-LET protons of about 3-4 MeV average energy. Compared to alpha particles, the average number of ions formed per proton passing through the sensitive volume is rather small (~0.19), and in fact more than 90% of the measured protons did not induce any ionizations within the sensitive volume. One should note, however, that the two spectra are not directly comparable because the alpha spectra were produced only by particles directly passing *trough* the sensitive volume whereas the proton spectra contain events from both particles traversing trough and passing outside of the sensitive volume.

These first spectra show that the nanodosimeter is able to produce meaningful results for different radiation qualities. On the other hand, the operations of the last two months have made it clear that the detector in its current form needs to be further improved. In particular, the following points have to be addressed in the next project year:

- *Signal-to-noise ratio*: Currently there is a relatively large background noise level. Some reasons for this noise have already been identified. Possible solutions to improve the signal-to-noise ratio include improved shielding and a lower operational voltage of the ion counter.
- *Read-out-stability*: Formation of oxidative layers on metal surfaces inside the nanodosimeter may cause detector electrodes to charge up. Charging of the electrodes will result in instabilities due to changes in ion collection efficiency. Such instabilities have been observed during first detector operations. It is planned to replace the current electrodes by gold-plated electrodes.
- *Ion-counting efficiency*: The electron multiplier presently used as the ion counter requires a very good vacuum for efficient and stable operation. The vacuum that can be achieved in the current detector is ~10^{-4} Torr, which is at the upper limit of the working range. This may cause variations in the ion-counting efficiency. Two possible solutions have been suggested: First, the aperture confining the accelerated ions may be narrowed, thus, allowing the current differential pumping system to work more efficiently. Second, a different type of ion counter, e.g., a micro-sphere counter, may be employed that operates under less stringent vacuum conditions.

3.3 Biological Assays

Double Strand Break Yields

Figure 10 shows the results of experiments in which plasmid DNA was irradiated with protons of 30 MeV, 3 MeV, and 1 MeV average energies. The results are complemented by additional data for low-LET gamma rays. The figure shows the number of DSBs per plasmid as a function of dose. Individual data are shown together with least squares straight-line fits. As the dose increases, the number of DSBs increases linearly in accordance with a single hit mechanism. Table 1 summarizes the DSB yields (in units of Gy^{-1} $dalton^{-1}$), which were calculated assuming a length of 10327 base pairs for pHAZE and relative molecular mass of 650

Daltons per base pair. Included in the table are standard deviations and 95% confidence limits of the break yields.

The data demonstrate that the DSB yields of protons with 3 MeV average energy exceeds that of protons with 30 MeV and 1 MeV average energy by a factor of about 1.5. The DSB yield of protons of 1 MeV and 30 MeV average energy is not significantly different from that of low-LET gamma rays. It is of interest to compare these DSB yields with the induction frequencies of energy deposition events larger than 40 eV in cylindrical segments of 2 nm diameter and 16 nm length (corresponding to a DNA segment of 47 base pairs). The energy deposition threshold of 40 eV was chosen because it is believed to correspond to the threshold of DSB induction in DNA. Monte-Carlo calculated absolute frequencies of energy deposition events per unit dose have been published for low energy protons (0.3 – 4 MeV) and low-LET electrons (100 keV electrons). The absolute yields of energy deposition events are 6.1×10^{-11} Gy^{-1} $dalton^{-1}$ for low-LET electrons and 8.1×10^{-11} Gy^{-1} $dalton^{-1}$ for 4 MeV protons. A comparison of these frequencies with the yields shown in Table 1 indicates that about 20% of the energy deposition events > 40 eV leads to a double strand break.

Figure 11 shows the LET dependence of the relative yield of energy deposition events > 40 eV in DNA segments of 47 bp using low-LET electrons as reference irradiation (relative yield = 1). It can be seen that low energy protons produce energy deposition events larger than 40 eV about 1.3 - 1.5 more efficiently than low-LET electrons, which agrees with the experimental findings of the efficiency for DSB induction of 3 MeV protons relative to 30 MeV protons and gamma rays. However, the experimentally observed decrease of DSB yields for protons of 1 MeV and lower is at variance with the further increase in the relative yield of energy deposition events for this proton energy range (see Figure 11). There are several explanations for this discrepancy. One possibility is that plasmids may be intersected by the same particle track more than one time, and with higher ionization density (LET) the induction of more than one DSB per intersection becomes likely. Since fragmented plasmids are lost during the gel electrophoresis process, these multi-DSBs are not counted as double strands breaks, thereby the DSB yield is reduced. Another possibility is that a certain fraction of DSBs is induced indirectly by OH radicals, which are generated by water ionization within 4 nm from the DNA molecule. With the higher ionization densities produced by low energy protons, these OH radicals have a greater likelihood to recombine before they react with DNA. Thus, although the total number of energy deposition events > 40 eV is increased, their efficiency of producing DSBs may be reduced. This points to the fact that sophisticated models of DSB induction are needed, which take into account the spacing of ionizations and the location of ionizations with respect to the DNA molecule and the surrounding water.

Plasmid Rejoining Assay

Table 2 shows the result of plasmid rejoining studies with protons of 30 MeV and 3 MeV average energy. The table also shows rejoining data after irradiation with gamma rays (low LET) and alpha particles (high LET). One should note that no attempt was made to separate the three different plasmid fractions (supercoiled, open circles, and linear) before incubating them with the *Xenopus* frog extract. The data in Table 2 give the overall fractions of linearized plasmids in the samples incubated with the frog extract for zero and two hours, as well as the ratio between the fraction of linearized plasmids after two hours and at zero hours.

After two hours of incubation the fraction of remaining unrejoined plasmids varied between 35% and 50%. Furthermore, the values show no clear LET dependence. This demonstrates that the efficiency of the extract to rejoin linearized plasmids *does not strongly depend* on the radiation quality. It is likely, however, that many of the linearized plasmids generated by high-LET irradiation are not rejoined correctly.

Plasmid Mutation Assay

The new mutation assay is still under development and requires optimization. No conclusive data can be presented at this time.

4. Conclusion

During the second project year, we have made substantial progress in the development of nanodosimetry for biomedical applications. The first version of the nanodosimeter has been fabricated and installed on the research beam line of the Loma Linda proton accelerator. It was demonstrated that the detector is sensitive to different ionization patterns produced by protons and alpha particle, thus, supporting our original hypothesis. During the first two months of operation a few shortcomings of the detector became apparent that will be addressed during the next project year. Initial scanning experiments to map the sensitive volume of the detector were performed, and the results were consistent with those obtained using a semi-analytical method. It is acknowledged that the scanning method needs to be further refined and more reliable data need to be obtained. Biological assays have been developed, which will permit direct comparison between DNA damage quantity or quality and ionization cluster quantity or quality measured with the nanodosimeter. More emphasis will be placed on the quality of DNA lesions and their reparability since rejoining efficiency of strand breaks does not appear to be a good indicator for different break qualities. Thus far, a direct comparison of biological data, such as yields of DSBs and its dependence on particle energy has only been possible with theoretical data of energy deposition in DNA volumes. This comparison indicates that the relationship between energy deposition (or ionization) events in nanometer volumes and the induction of DNA damages is quite complex. Biophysical models need to be developed or refined that translate nanodosimetric data into the induction of double strand breaks and more complex forms of DNA damage.

5. References

1. Shchemelinin S., Breskin A., Chechik R., Pansky A., Colauti P., Conte V., De Nardo L., and G. Tornielli. Ionization measurements in small gas samples by single ion counting. *Nucl. Instr. & Meth.* A368, 895-861, 1996.
2. Shchemelinin S., Breskin A., Chechik R., Pansky A., and P. Colautti. A nanodosimeter based on single ion counting. In: *Microdosimetry - An interdisciplinary approach.* Goodhead D., O'Neel P. & Menzel H. (Eds.), The Royal Society of Chemistry (Cambridge), pp 375-378 , 1997.
3. Schulte R.W.M. "Development of nanodosimetry for biomedical applications" *Project progress report* Nov. 1997-Aug. 1998.
4. Schemelinin S., Breskin A., Chechik R., Colautti P., and R. Schulte. First ionization cluster measurements on the DNA scale in a wall-less sensitive volume. *Radiat. Prot. Dosim*, 82 43-50, 1999.

5. Schulte, R.W.M. Prediction of cellular effects of high- and low-LET radiation based on the energy deposition pattern at the nanometer level. In: *Microdosimetry - An interdisciplinary approach*. Goodhead D., O'Neel P. & Menzel H. (Eds.), The Royal Society of Chemistry (Cambridge), pp – 1997.
6. Kellerer A.M. An assessment of wall effects in microdosimetric measurements. *Radiation Research* 47, 377-386, 1971.
7. Kellerer A.M. Event simultaneity in cavities: theory of the distortions of energy deposition in proportional counters. *Radiation Research* 48, 216-233, 1971.
8. Schulte R.W.M. "Development of nanodosimetry for biomedical applications" *Project progress report*. Dec. 1998-Sep. 1999.
9. Ward J.F. The complexity of DNA damage: relevance to biological consequences. *Int. J. Radiat. Biol.* 66, 427-32, 1994.
10. Brenner D.J. and J.F. Ward. Constraints on energy deposition and target size of multiply damaged sites associated with DNA double-strand breaks. *Int. J. Radiat. Biol.* 61, 737-48, 1992.
11. Milligan J.R., Aguilera J.A., and J.F. Ward. Variation of single-strand break yield with scavenger concentration for plasmid DNA irradiated in aqueous solution. *Radiat. Res.* 133, 151-7, 1993.
12. MRC Monographs. http://www.ragsu.har.mrc.ac.uk/nikjoo/mono/mono.htm

6. Tables

Table 1

Radiation Quality	Mean LET (kev/μm)	G_{DSB} (Gy^{-1} Da^{-1})± S.E.	95% C.I.
Gamma rays	0.3	$1.2 \times 10^{-11} \pm 1.1 \times 10^{-12}$	1.0×10^{-12} - 1.4×10^{-11}
30 MeV protons	2	$1.3 \times 10^{-11} \pm 0.8 \times 10^{-12}$	1.2×10^{-12} - 1.5×10^{-11}
4 MeV protons	10	$2.0 \times 10^{-11} \pm 0.5 \times 10^{-12}$	$1.9 \times 10^{-12} - 2.1 \times 10^{-11}$
1 MeV protons	20	$1.3 \times 10^{-11} \pm 0.9 \times 10^{-12}$	1.1×10^{-12} - 1.4×10^{-11}

Table 2

Radiation Quality	Mean LET (keV/μm)	% rejoined		Ratio (%)
		0 hours	2 hours	2 hours : 0 hours
Gamma rays	0.3	22.5	11.2	50
Alpha (Cu-241)	100	18.5	8.1	44
30 MeV protons	2	17.6	6.1	35
4 MeV protons	10	15.4	5.9	38

List of Figures

Fig 1.: A schematic diagram of the nanodosimeter based on single-ion counting. Only ions formed in the sensitive volume (shaded) are extracted into the vacuum and detected in the ion counter.

Fig 2.: Photograph of the nanodosimeter as seen from the external beam entry side. The G10 entrance window has been removed permitting a view of the ionization cell.

Fig 3.: Detailed design drawing of the nanodosimeter showing its main components.

Fig 4.: Diagram of the nandosimeter with accessory power supplies, triggering system, and data accquisition electronics.

Fig 5.: Ion collection efficiency maps calculated under the assumption of a homogeneous field of (a) 60 V/cm and (b) 100 V/cm inside the ionization cell.

Fig 6.: Same as Fig. 5, however, the maps are based on Monte Carlo studies of individual ion trajectories and take into account electric field inhomogeneities.

Fig 7.: Measured integral ion collection efficiencies along (a) the transverse axis and (b) the longitudinal axis of the sensitive volume.

Fig 8.: First nanodosimetric spectra obtained with propane using the built-in alpha source that emits alpha particles across the sensitive volume. The two sets of data were measured under two different extraction field conditions: (a) 60 V/cm and (b) 100 V/cm. The upper panels show the distribution of ion cluster sizes and the lower panels the distribution of ion-arrival times.

Fig 9.: First ionization cluster size spectra of protons and alpha particles in a tissue-equivalent sensitive volume of nanometer extensions measured in 1 Torr propane. One can clearly see the difference between high-LET alpha-particle and intermediate-LET proton spectra (~ 10 keV/μm).

Fig 10.: Experimental results of plasmid experiments at LLU. Shown are the average number of DSBs per plasmid as a function of dose for protons of 30 MeV (■), 3 MeV (◆), and 1 MeV (▲) average energy. For comparison, results obtained low-LET gamma rays (×) are also shown. The lines correspond to least squares straight-line fits.

Fig 11.: LET dependence of the relative yield of energy deposition events > 40 eV in DNA segments of 47 bp as a function of proton energy. Low-LET electrons of 100 keV energy were used as reference irradiation (relative yield = 1). The curve is based on Monte Carlo simulation of low-energy proton track segments [12].

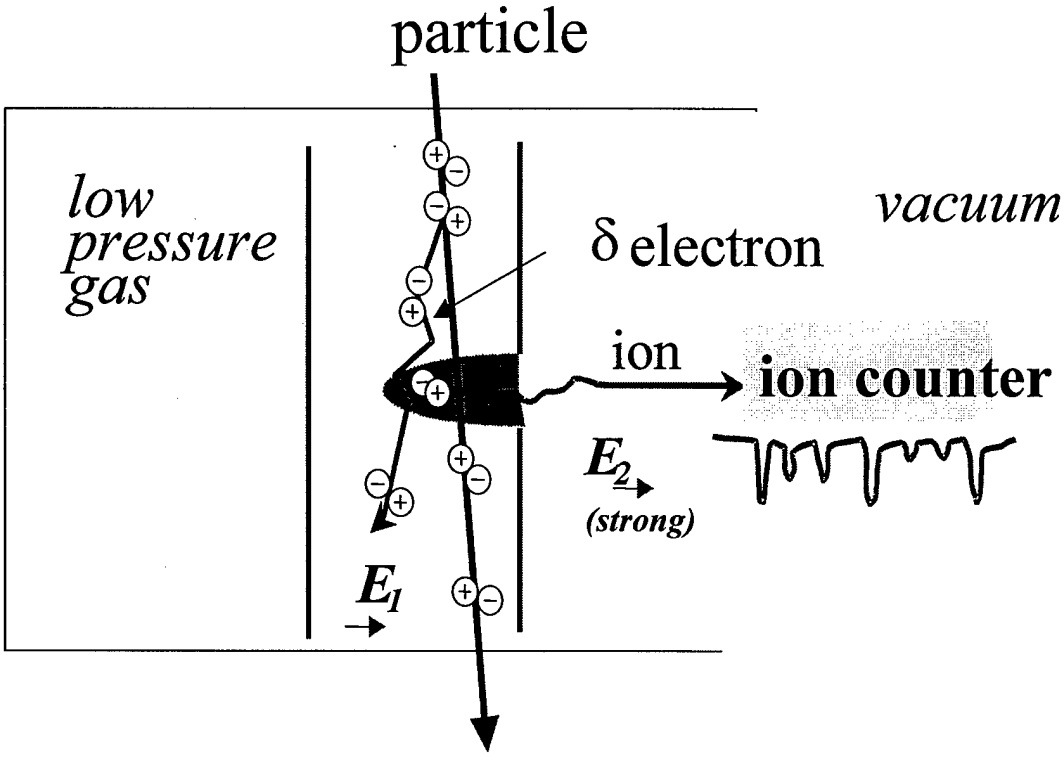
particle
low pressure gas
vacuum
δ electron
ion
ion counter
E_2
(strong)
E_1

Figure 1

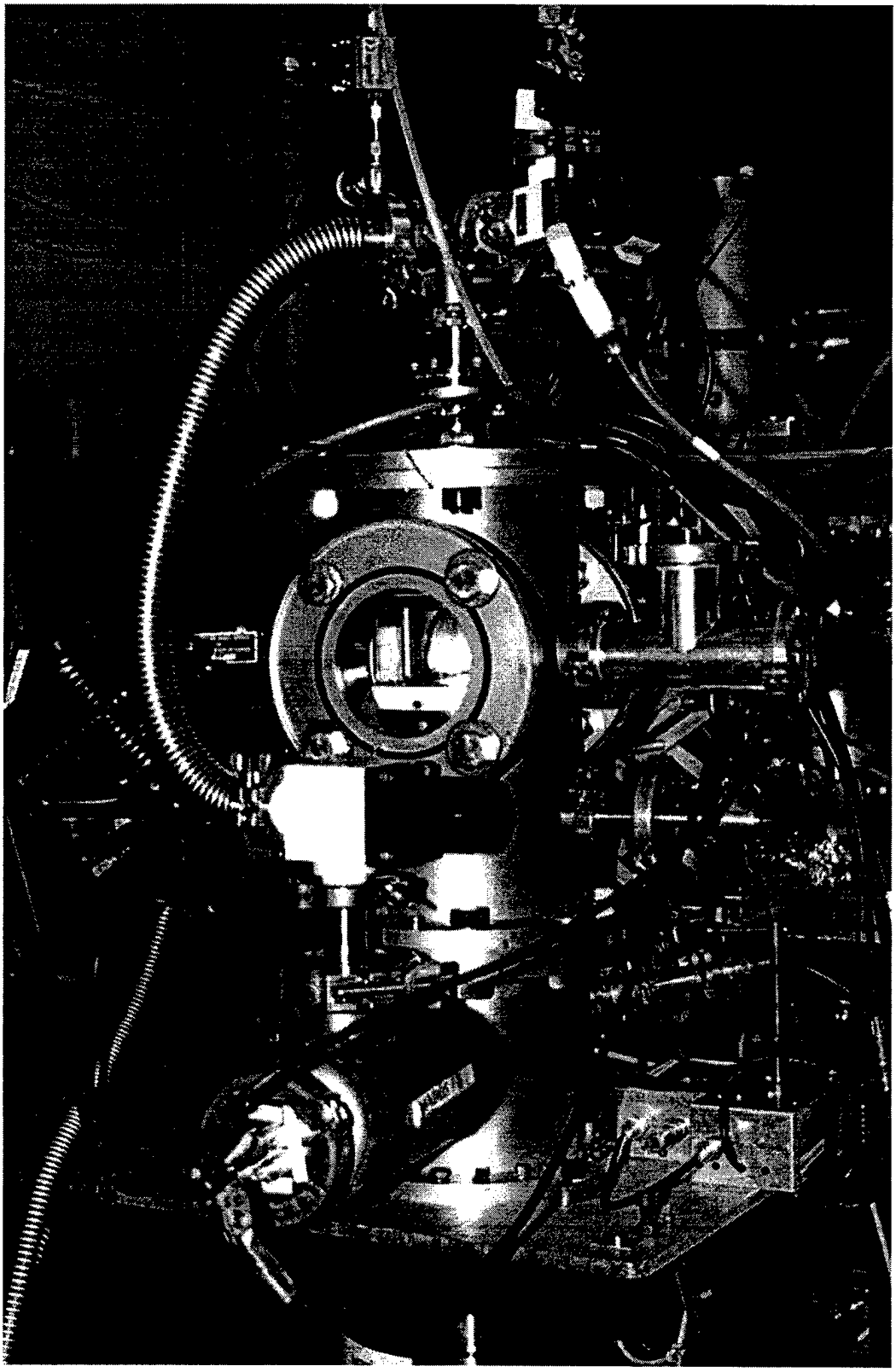

Figure 2

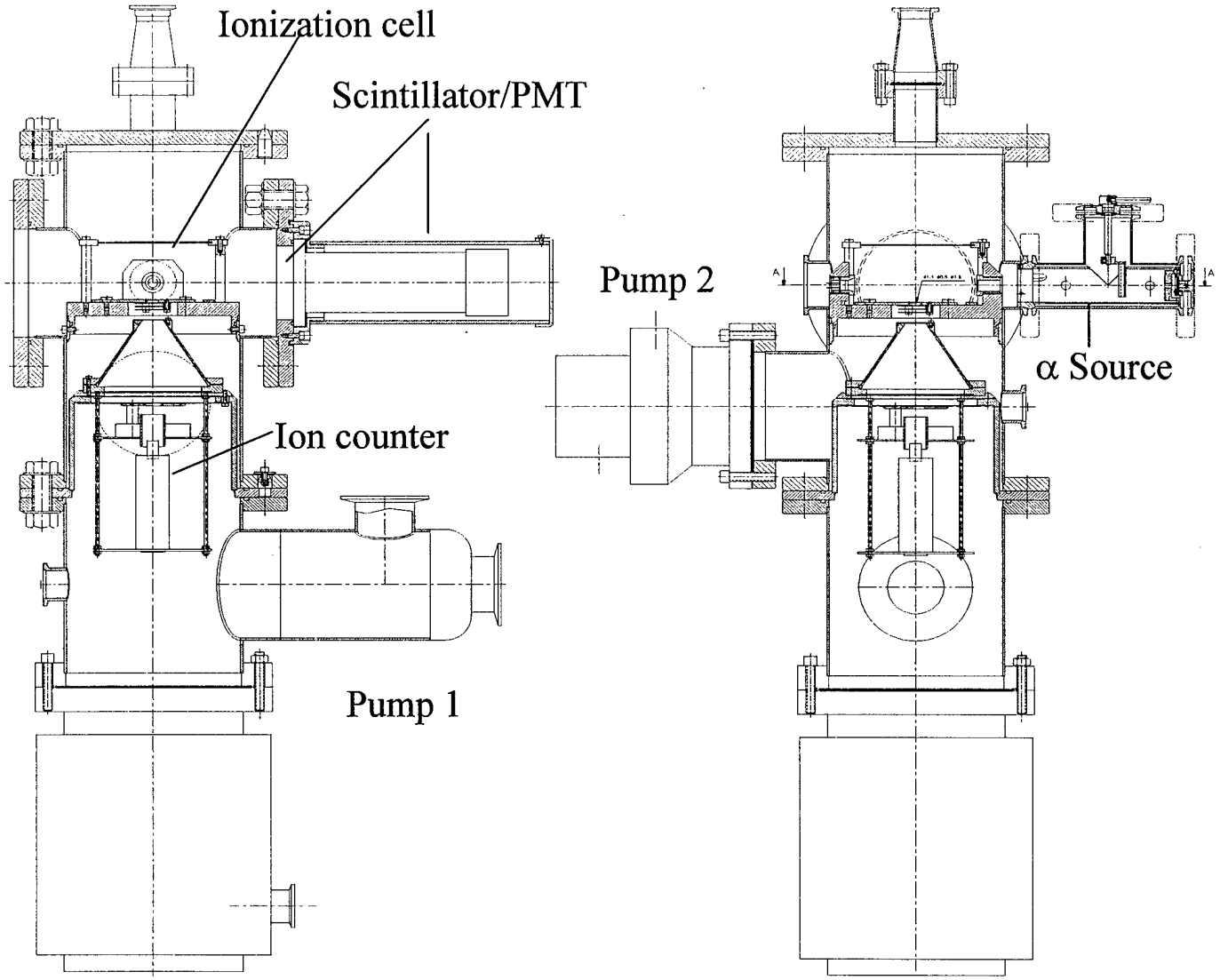
Ionization cell
Scintillator/PMT
Ion counter
Pump 1
Pump 2
α Source

Figure 3

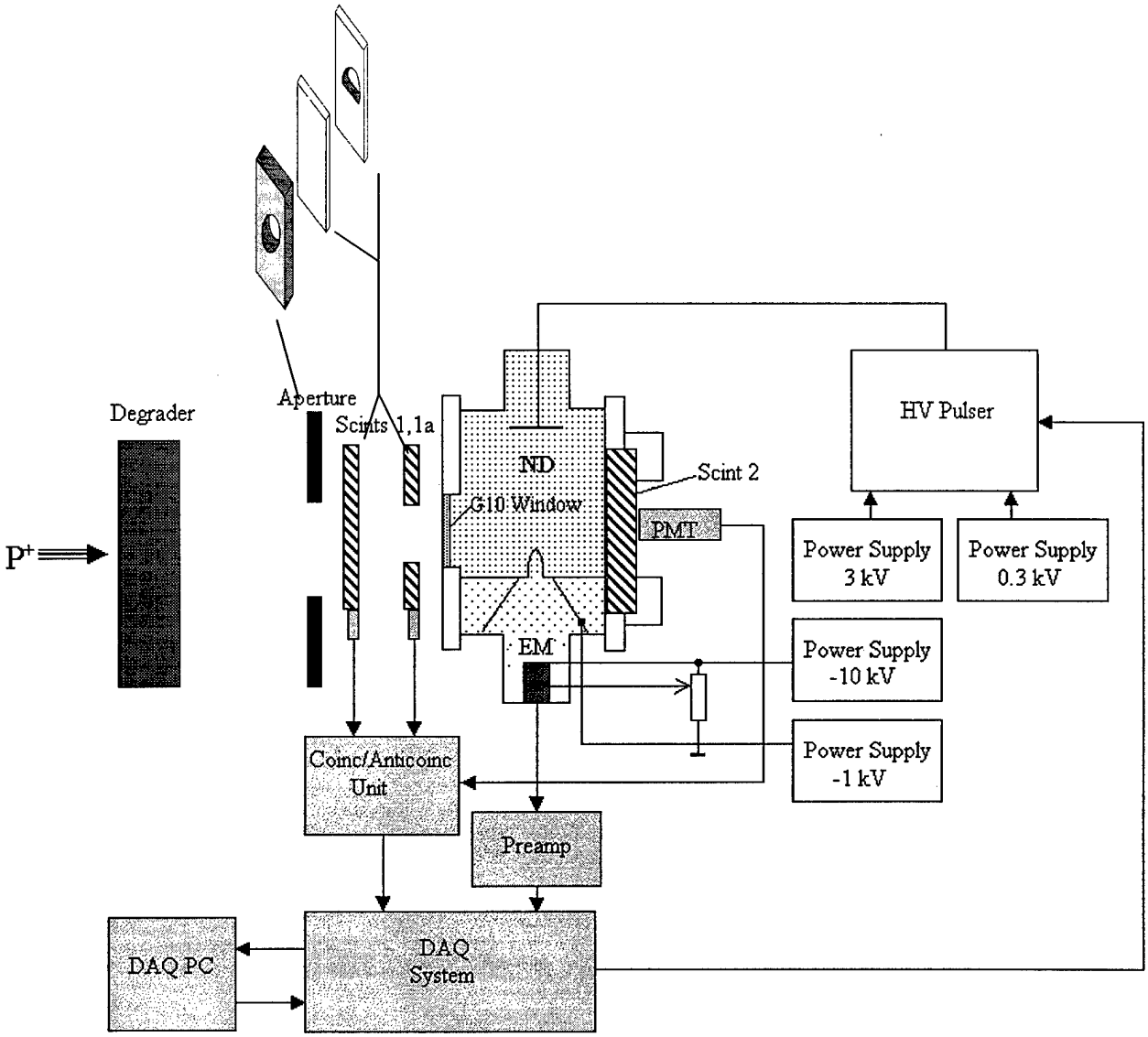
Degrader
Aperture
Scints 1, 1a
ND
G10 Window
Scint 2
PMT
EM
HV Pulser
Power Supply 3 kV
Power Supply 0.3 kV
Power Supply -10 kV
Power Supply -1 kV
P+
Coinc/Anticoinc Unit
Preamp
DAQ PC
DAQ System

Figure 4

PROPANE 1 Torr 100 V/cm

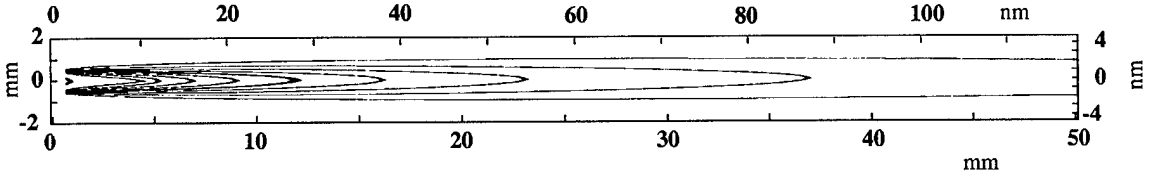

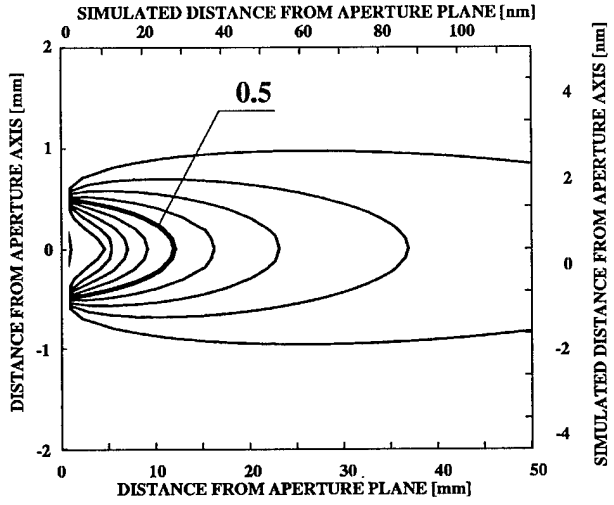

The ion collection efficiency shown by contours:

0.99, 0.9, 0.8, 0.7, 0.6, **0.5,** 0.4, 0.3, 0.2, 0.1

a

PROPANE 1 Torr 60 V/cm

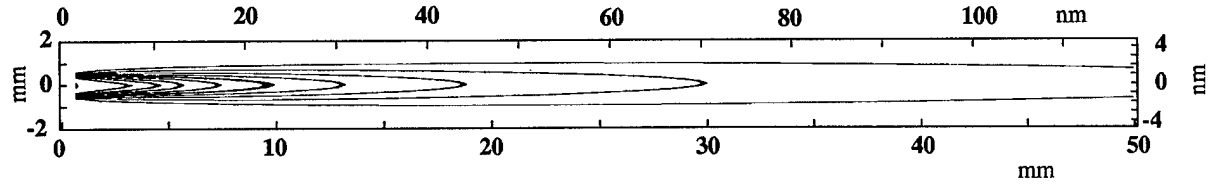

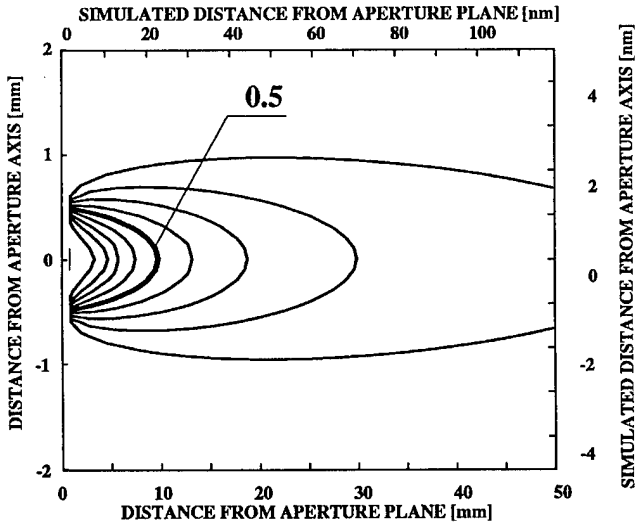

The ion collection efficiency shown by contours:

0.9, 0.8, 0.7, 0.60**.5,** 0.4, 0.3, 0.2, 0.1

b

Figure 5

MC SIMULATION

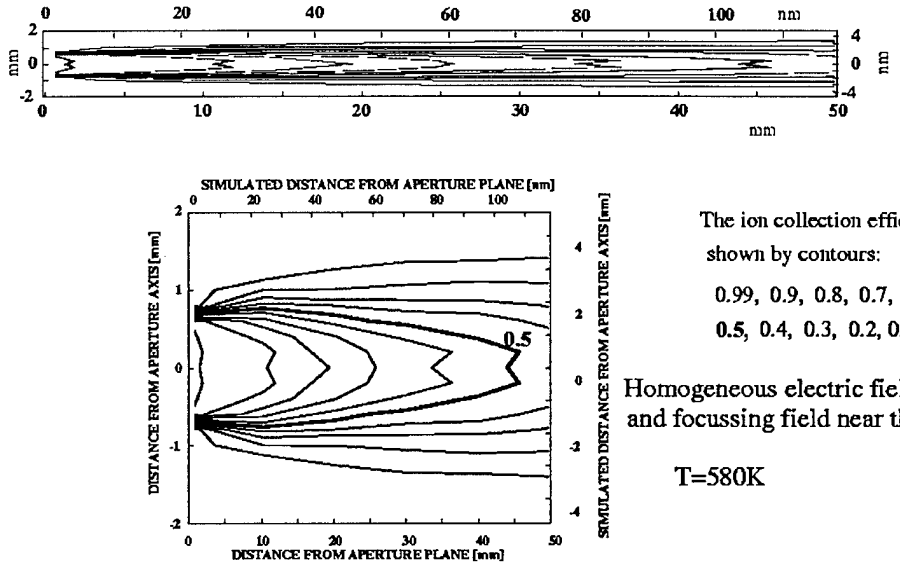

The ion collection efficiency shown by contours:

0.99, 0.9, 0.8, 0.7, 0.6, **0.5**, 0.4, 0.3, 0.2, 0.1

Homogeneous electric field 100 V/cm and focussing field near the aperture

T=580K

a

MC SIMULATION

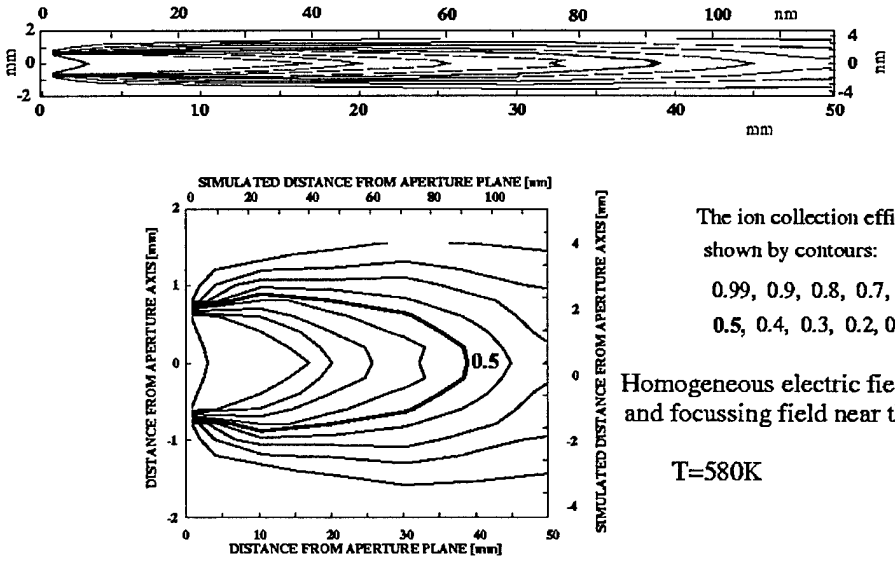

The ion collection efficiency shown by contours:

0.99, 0.9, 0.8, 0.7, 0.6, **0.5**, 0.4, 0.3, 0.2, 0.1

Homogeneous electric field 60 V/cm and focussing field near the aperture

T=580K

b

Figure 6

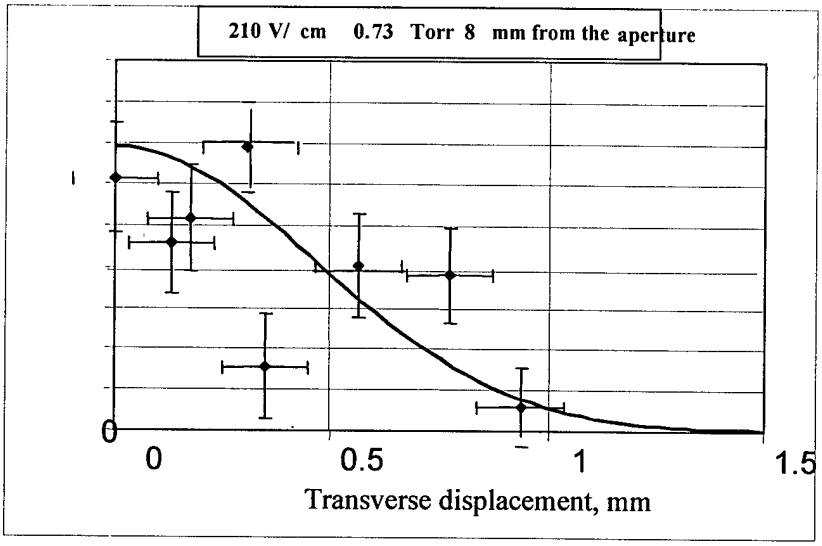
210 V/ cm 0.73 Torr 8 mm from the aperture
I
0
0
0.5
1
1.5
Transverse displacement, mm

a

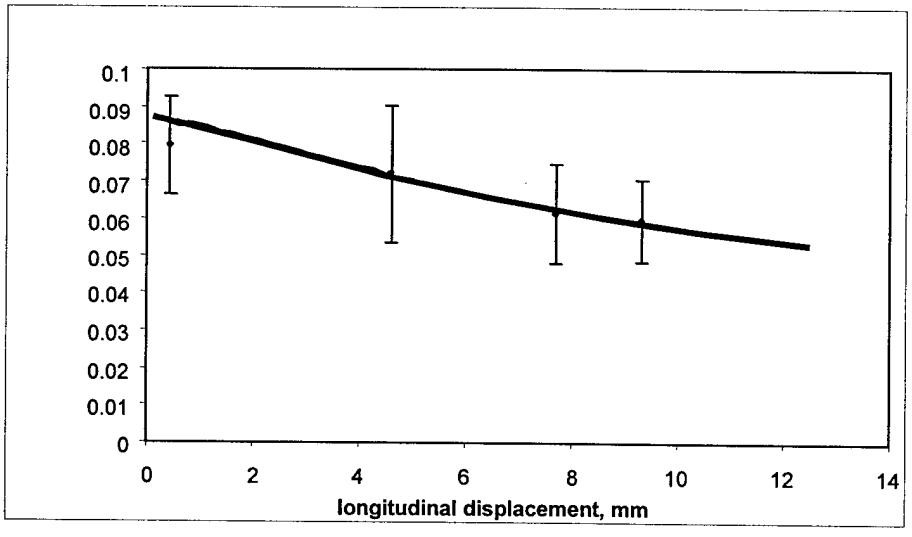
0.1
0.09
0.08
0.07
0.06
0.05
0.04
0.03
0.02
0.01
0
0
2
4
6
8
10
12
14
longitudinal displacement, mm

b

Figure 7

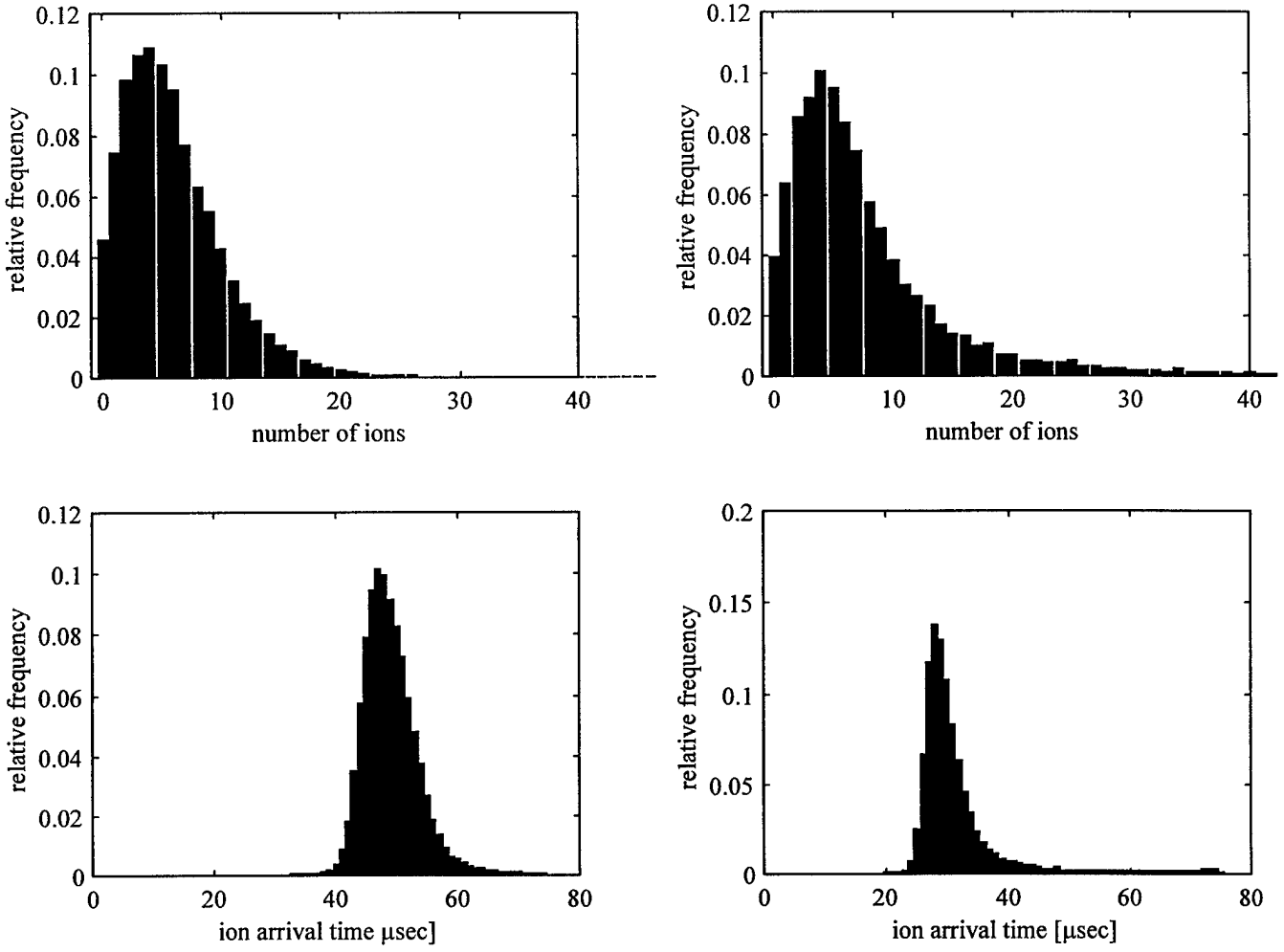
0.12
0.1
0.08
0.06
0.04
0.02
0
relative frequency
0
10
20
30
40
number of ions
0.12
0.1
0.08
0.06
0.04
0.02
0
relative frequency
0
10
20
30
40
number of ions
0.12
0.1
0.08
0.06
0.04
0.02
0
relative frequency
0
20
40
60
80
ion arrival time µsec]
0.2
0.15
0.1
0.05
0
relative frequency
0
20
40
60
80
ion arrival time [µsec]

a **b**

Figure 8

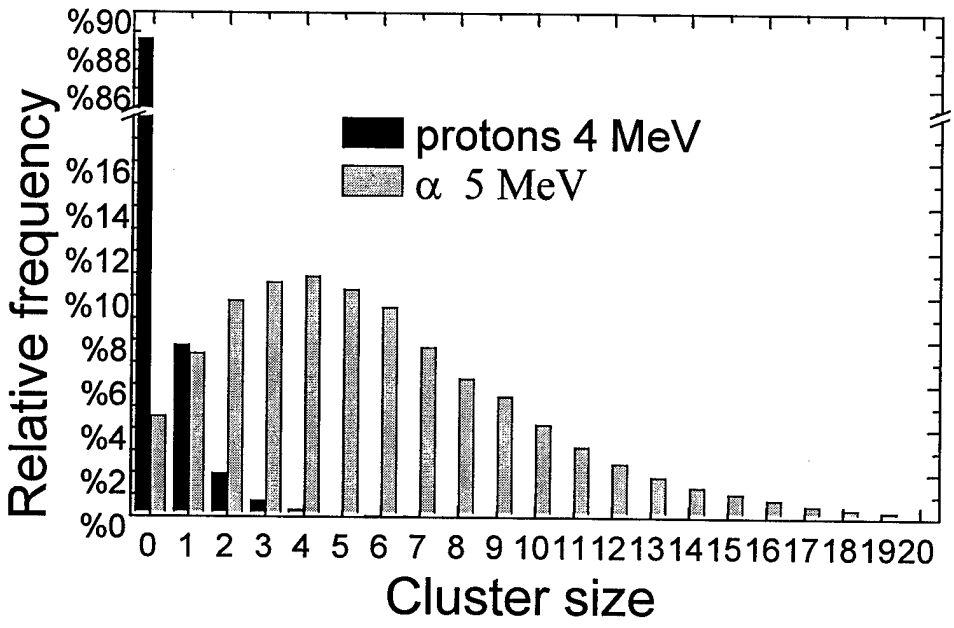
%90
%88
%86
%16
%14
%12
%10
%8
%6
%4
%2
%0
Relative frequency
protons 4 MeV
α 5 MeV
0 1 2 3 4 5 6 7 8 9 10 11 12 13 14 15 16 17 18 19 20
Cluster size

Figure 9

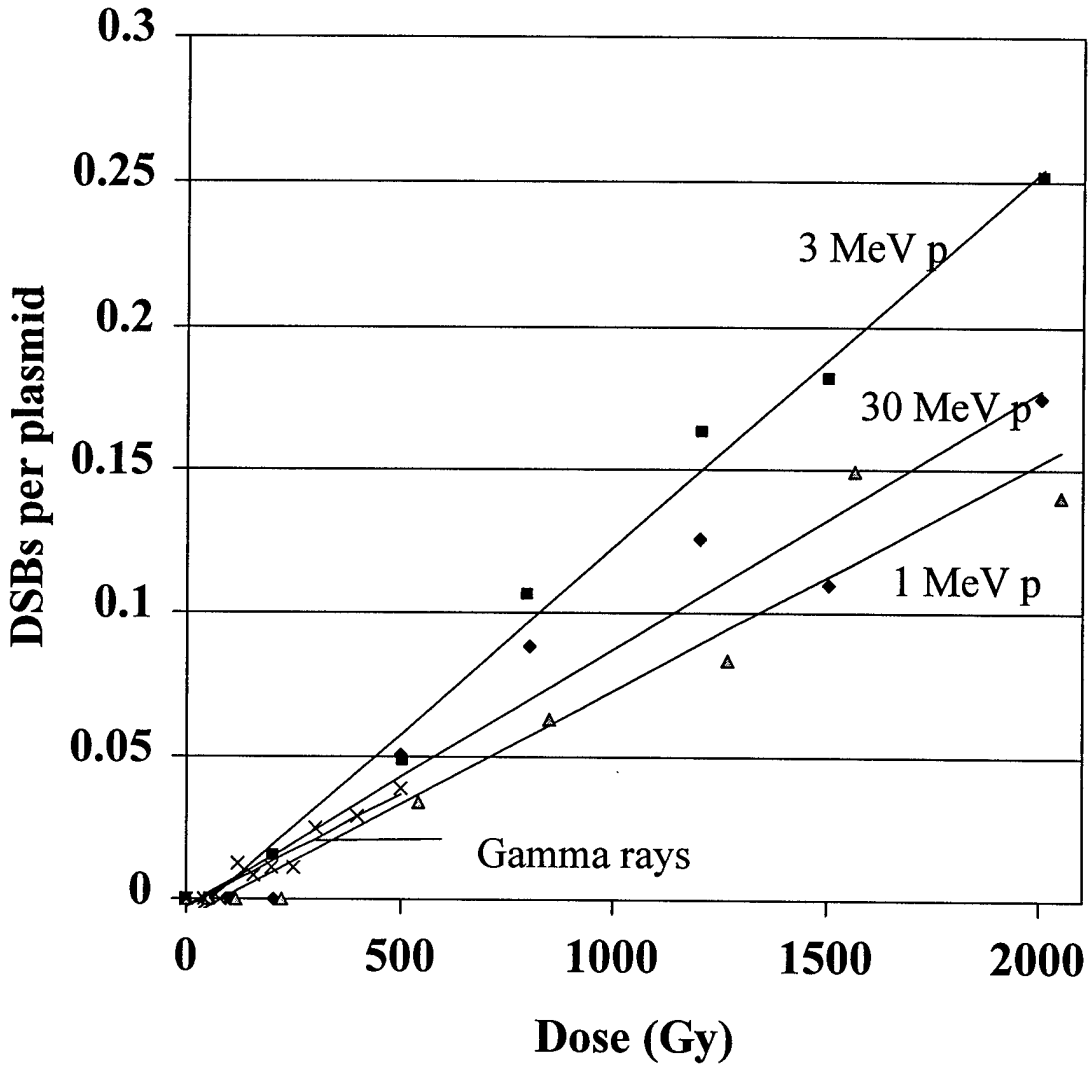
0.3
0.25
0.2
0.15
0.1
0.05
0
DSBs per plasmid
3 MeV p
30 MeV p
1 MeV p
Gamma rays
0
500
1000
1500
2000
Dose (Gy)

Figure 10

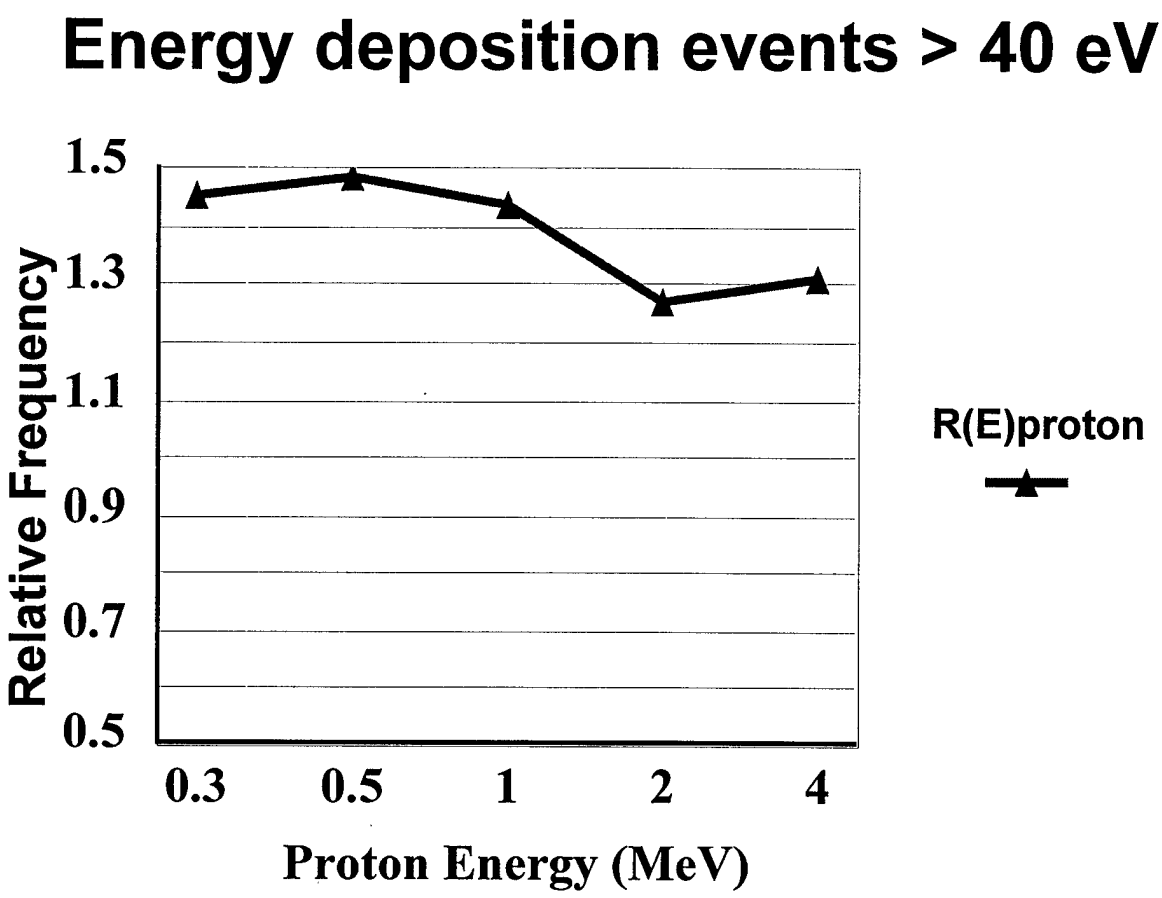
Energy deposition events > 40 eV
1.5
1.3
1.1
0.9
0.7
0.5
Relative Frequency
0.3
0.5
1
2
4
Proton Energy (MeV)
R(E)proton

Figure 11

DESCRIPTION: State the goal of the project, including how it relates to improving health care. Use succinct language to describe how the project goals will be achieved. **Do not exceed the space provided.**

Since Roentgen's discovery of the x-ray in 1896 and the subsequent use of radiation for medical treatment, the field of radiation research has been vigorous, attracting physicists, biologists, and clinicians and spawning a diverse mixture of clinical and basic research. The one constant in radiation research in the past century has been the fundamental goal of the radiation oncologist: maximizing dose to cancerous tissue while minimizing dose to normal tissue. The establishment of proton therapy at Loma Linda and elsewhere has been a significant step towards that goal.

Proton therapy exploits the dose distribution characteristics of protons. Unlike the photons employed in conventional radiotherapy, which deposit their maximal dose near the skin surface, protons deposit minimal dose when entering the body and maximal dose within the body at a sharp spike known as the Bragg peak. At the Proton Treatment Center the Bragg peak is modulated, that is, the Bragg peak is spread out to match the depth of the tumor volume. Along the beam axis, the normal tissue beyond the tumor receives virtually no dose, and the normal tissue in front of the tumor receives a lower dose than does the tumor.

Just as the Bragg peak is used to shape the maximal dose to the depth of the tumor (along the beam axis), an aperture is used to shape the maximal dose to the proper height and width dimensions of the tumor. The aperture is a block made of lead alloy that has a hole in the middle. The precise shape of the treatment area for the patient's tumor is cast into the aperture, which shields all areas except the tumor.

Presently, custom apertures must be made for each treatment angle used to treat each patient. The apertures are expensive to make and dispose of – production and disposal costs now approach $1.5 million per year. In addition, the weighty, bulky apertures must be changed manually by the radiation therapist before each treatment, slowing treatment times.

We propose to investigate the possibility of replacing the existing aperture system with a multi-leaf collimator. A multi-leaf collimator is an automated, three-dimensional, variable aperture device. Multi-leaf collimators have been employed successfully in photon therapy, and experimental work in proton multi-leaf collimation has been conducted at Berkeley. A multi-leaf collimator would not only dramatically reduce costs but also permit more precise dose localization along the beam line.

The research and development project would include: 1) development of design parameters and constraints; 2) development of Roman jaw, coarse resolution, and fine resolution concepts; 3) writing of design report for each design; 4) conceptual design review; 5) selection of winning design by review committee; and 6) preparation of detailed specifications for chosen multi-leaf collimator design.

PROJECT SITE(S) (organization, city, state):

Proton Treatment Center/Department of Radiation Medicine, Loma Linda University Medical Center
Loma Linda, California

FINAL REPORT TO THE NATIONAL MEDICAL TECHNOLOGY TESTBED

PROJECT: MULTILEAF COLLIMATOR

Subcontract #: #025-FY97-LLU-Slater

Period covered by report: November 1997 – November 1999

Date of report: 3/15/2000

Principal Investigator: Dr. James M. Slater

Signature: FILE COPY

Phone #: (909) 558-4644
Fax #: (909) 558-4824

I. TABLE OF CONTENTS

	Page Number
I. Table of Contents	2
II. Introduction	3
III. Body	4
IV. Conclusion	6
V. References	7
VI. Appendices	9

A. Electro-Mechanical Requirements Specification
B. Software Requirements Specification
C. Treatment Planning Simulation Tests
D. 3-D Conceptual Design Drawings

II. INTRODUCTION

Figure 1 demonstrates a proton beam as it passes through the treatment nozzle to the target. Scatterers disperse the protons, transforming the pencil-thin beam into a cone. Fixed apertures block stray radiation after the scatterers. The precise shape of the treatment area is cast into a lead alloy aperture, which shields all areas except the tumor.

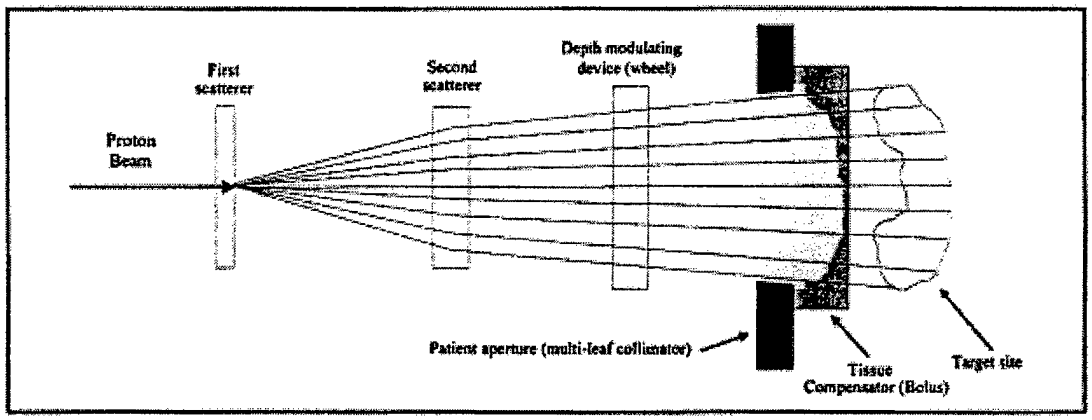

Figure 1 Passive beam spreading configuration for proton treatments.

Presently, custom apertures must be made for each treatment angle (portal) used to treat each patient with proton radiation therapy. The apertures are expensive to make and dispose of. The weighty, bulky apertures must be changed manually by the radiation therapist before each treatment. This time-consuming step impedes treatment efficiency in a facility that often treats over 100 patients per 16-hour operating day. In addition, large-field apertures that may be developed for future treatments of breast cancer and other diseases could exceed 200 pounds, rendering manual installation and removal impractical. Finally, a single aperture per-portal configuration may preclude intensity modulation, a precision dose delivery technique that has come into use only recently in radiation therapy. For these reasons, considerable interest has grown in the development of an adjustable collimator, a device that can be automatically manipulated to conform to any required two-dimensional shape. The multileaf collimators that have recently become common in conventional radiation therapy are inadequate for use with protons (proton collimation will requires different collimator materials, collimation as close as possible to the skin, and other design considerations).

The initial goal of this project was to determine the optimal overall solution, develop specific design parameters and constraints which would lead to a successful design, and prepare detailed design specifications that could be used to build multi-leaf collimators for the LLUMC facility and elsewhere. Because the project was funded significantly below the requested amount, the project scope was reduced to preparing requirement specifications as opposed to design specifications. Specifically, the goal of the project was to: A) analyze clinical requirements; B) develop design parameters and constraints; C) write requirements specifications; D) conduct a requirements review; E) prepare final requirements specifications.

III. BODY

The project results are described in detail in the requirements specifications attached as Appendix A and Appendix B. Below is a description of the research process.

A. Clinical Requirements

The first task of the project was to establish clinical requirements. Clinical staff and medical physicists met regularly with Optivus engineers to help define requirements. Several of the broad issues investigated are described below

1. Categories of tumors and disease sites for which a multileaf collimator would be appropriate
2. Optimal leaf width and end shape, and the potential effect of these parameters on accuracy, penumbra, range, and dose distribution
3. Quality assurance issues relating to inter-leaf leakage and calibration.
4. Treatment efficiency issues (maintain high rate of patient throughput)

The primary concern regarding the first of these issues, that is, which tumors can be treated using a multileaf collimator, was whether replacing custom-made smooth apertures with stepped collimator leaves would decrease dose delivery precision significantly. To assess the efficacy of a multileaf in comparison to cast apertures, the treatment planning system software was modified to permit simulation of the effects of multileaf collimation on radiation dose to the target, normal tissue and critical structures. Simulations were performed comparing smooth apertures to stepped, multileaf apertures for a wide range of regular, geometric shapes and irregularly-shaped tumors.

Appendix C displays screen captures and dose-volume histograms from treatment planning simulations of dose delivery using multi-leaf collimators with varying leaf spacing. Simulations were completed for a variety of geometric shapes tumor targets at several leaf spacings. Comparisons with cast apertures were also made.

The clinical staff on the project team analyzed the results of the simulation and determined that for leaf widths of 1 cm, with a rectangular end shape, the multileaf collimator provided sufficient accuracy for most tumor types treated at the Proton Treatment Center.

The other clinical requirements issues listed above--leaf parameters, inter-leaf leakage, calibration, and treatment efficiency—were referred to the engineering team, and were addressed in the *Design Parameters and Constraints* portion of the project.

B. Design Parameters and Constraints

Optivus engineers used the requirements specified by the clinical and medical physics staff to begin establishing engineering requirements. Gantry geometry, nozzle geometry, and control system integration were studied extensively. Existing multileaf collimators used in conventional radiation therapy were also analyzed.

After a preliminary analysis, the engineers generated an initial conceptual design (several of the design drawings are attached in Appendix D).

After further study, the engineering team developed a list of requirements to be specified. The requirements were:

1. Dimensional/Physical Characteristics
2. Field Size and Resolution
3. Leaf Location Parameters
4. Leaf Movement
5. Cast Aperture
6. Bolus Mounting Requirement
7. System Deflection
8. Leaf Projection Past CAX
9. Leaf End Shape
10. Leaf Material
11. Rotation Around CAX
12. Leaf Leakage and Penumbra

The remainder of the project period was spent establishing these specifications and developing a requirements specification.

C. Requirements Specification

Electro-mechanical and software requirements specifications are attached in Appendix A and Appendix B.

D. Prototype testing

The project was essentially complete after the initial 12-month period, at which time a prototype heavy-ion MLC that had been developed at UC Berkeley in the 1980's became available. The project team requested and received an extension of the project period in order to build a test stand for the prototype MLC to permit leak testing of the device.

The test stand was completed in late 1999, and the MLC was mounted in the beam for testing. Leaf patterns were set to simulate a prostate treatment. Tests using radiographic film in the beam line showed no beam leakage.

In addition, the film data validated the conclusions reached during the treatment planning simulations that the multileaf is suitable for prostate treatments.

IV. CONCLUSION

The results of the treatment planning simulations, electrical and mechanical engineering analyses, and leak tests indicate that building a proton multi-leaf collimator in a gantry is technically and clinically feasible. The project team achieved its objectives by developing a requirements specification which can serve as the foundation for the design and construction of a multileaf collimator.

V. SELECTED REFERENCES

1. Brahme A, Svensson H. Methods of improving dose uniformity in high energy photon and electron beams. Digest Fourth ICMP Phys. 1976(28.3)
2. Brahme A. Design principles and clinical possibilities with a new generation of radiation therapy equipment. Acta Oncologic 1987; 26:403.
3. Coutrakon G, Bauman M, Lesyna D, et al. A prototype beam delivery system for the proton medical accelerator at Loma Linda. Medical Physics 18(6):1093-1099; November/December 1991.
4. Daftari I, Petti PL, Collier JM, Castro JR, Pitluck S. Evaluation of fixed- versus variable-modulation treatment modes for charged-particle irradiation of the gastrointestinal tract. Medical Physics 1993; 20(5):1387.
5. Flickinger JC, Lunsford LD, Wu A, Maitz AH, Kalend AM. Treatment planning for gamma knife radiosurgery with multiple isocenters. Int. J. Radiation Oncology Biology Physics 1990; 16(6):1495.
6. Kaanai T, Kawachi K, Matsuzawa H, Inada T. Broad beam three-dimensional irradiation for proton radiotherapy. Medical Physics 1983; 10(3):344.
7. Kjellberg RN, Hanamura T, Davis KR, Lyons SL, Adams RD. Bragg-peak proton-beam therapy for arterio-venous malformation of the brain. New England Journal of Medicine 1983; 309:269.
8. Kurup RG, Hogstrom KR, Otte VA, Moyers MF, Tung S, Shiu AS. Dosimetric evaluation of a two-dimensional, arc electron, pencil-beam algorithm in water and PMMA. Physics in Medicine and Biology 1992; 37(1):127.
9. Larsson B, Sarby B. Equipment for radiation surgery using narrow 185 MeV proton beams. Acta Oncologica 1987; 26:143.
10. Leavitt DD, Gibbs FA, Heilbrun MP, Moeller JH. Dynamic field shaping to optimize stereotactic radiosurgery. Int. J. Radiation Oncology Biology Physics 1990; 19(S1):133.
11. Loeffler JS, Larson DA. Subspecialization in radiation oncology: impact of stereotactic radiosurgery. Int. J. Radiation Oncology Biology Physics 1992; 24(5):885.
12. Moyers MF. Generation and characterization of a proton microbeam. Medical Physics 1993; 20(3):867.
13. Moyers M, Siebers JV, Blair M, Thomas R, Miller DW. A continuously variable thickness scatterer for proton beams using self-compensating dual linear wedges. Medical Physics 1993; 20(3):173.
14. Podgorsak EB, Pike GB, Olivier A, Pla M, Souhami L. Radiosurgery with high energy photon beams: a comparison among techniques. Int. J. Radiation Oncology Biology Physics 1989; 16(3):857.
15. Rassow. . Strahlentherapie 1970; 139:116.
16. Schlegl W, Pastyr O, Bortfield T, et al. Computer systems and mechanical tools for stereotactically guided conformation therapy with linear accelerators. Int. J. Radiation Oncology Biology Physics 1992; 24(4):781.

17. Slater JM, Miller DW, Slater JW. Developing a clinical proton accelerator facility: consortium-assisted technology transfer. IEEE 1991:532-536.
18. Slater JM, Archambeau JO, Miller D, Notarus M, Preston W, Slater JD. The proton treatment center at Loma Linda University Medical Center: Rationale for and description of its development. Int J Radiat Oncol Biol Phys 22:383-389, Oct. 1991. 1991.
19. Urie M. Comparison of variable and fixed modulation proton beam dose distributions in the cranium. Physics in Medicine and Biology 1988; 33(S1):131.
20. Yonemoto LT, Slater JD, Rossi CT, et al. Combined proton and photon conformal radiation therapy for locally advanced carcinoma of the prostate: preliminary results of a phase I/II study. International Journal of Radiation Oncology Biology Physics; June 1995 1995.
21. Yonemoto LT, Slater JD, Friedrichsen EJ, et al. Phase I/II study of proton beam irradiation for the treatment of subfoveal choroidal neovascularization in age-related macular degeneration: treatment techniques and preliminary results. Int. J. Radiation Oncology Biol. Phys. 1996; 36(4):867-871.

IV. APPENDICES

Attached:

Treatment Planning Simulation Tests
3-D Conceptual Design Drawings
Electro-Mechanical Multileaf Collimator Requirements Specification
Multileaf Collimator System Software Requirements Specification

APPENDIX A: ELECTRO-MECHANICAL REQUIREMENTS SPECIFICATION

ELECTRO-

MECHANICAL

MULTILEAF

COLLIMATOR

REQUIREMENTS

SPECIFICATION

Revision History

DESCRIPTION	AUTHOR	DATE	REVISION
Initial Draft	R. Summers	May 4, 1998	XA
Preliminary Release-for File-Not for Production	R. Summers	March 19, 1999	A

TABLE OF CONTENTS

I. INTRODUCTION ____ *1*

A. PURPOSE ____ 1

B. SCOPE ____ 1

C. DEFINITIONS, ABBREVIATIONS, ACRONYMS ____ 1
1. Definitions ____ 1
2. Acronyms ____ 2

D. REFERENCES ____ 2
1. Design Control Policy ____ 2
2. Multileaf Collimator System Software Requirements Specification ____ 2

II. REQUIREMENTS ____ *2*

A. GENERAL REQUIREMENTS ____ 3
1. 510K ____ 3
2. OTI SOP's ____ 3
3. Product Life ____ 3
4. Training ____ 3
5. Gantry Installation ____ 3

B. SPECIFIC PERFORMANCE AND CONFIGURATION REQUIREMENTS ____ 3
1. Dimensional/Physical Characteristics ____ 3
2. Field Size and Resolution ____ 3
3. Leaf Location Parameters ____ 3
4. Leaf movement ____ 4
5. Cast Aperture ____ 5
6. Bolus mounting requirement ____ 5
7. System deflection ____ 5
8. Leaf projection Past CAX ____ 5
9. Leaf end shape ____ 5
10. Leaf Material ____ 5
11. Rotation around CAX ____ 6
12. Leaf Leakage and Penumbra ____ 7

C. RELIABILITY REQUIREMENTS ____ 7
1. MTBF ____ 7

D. REPAIR AND REPLACEMENT REQUIREMENTS ____ 7
1. MTTR ____ 7

E. MAINTENANCE REQUIREMENTS ____ 7
1. System is to be re-furbished annually ____ 7
2. Deflection Validation ____ 8
3. Manuals ____ 8
4. Finite Lifetime Components ____ 8

III. TESTING AND EVALUATION ____ *8*

A. SCATTER-VS-RESOLUTION ____ 8
B. LEAF MATERIAL AND GEOMETRY ____ 8
IV. DELIVERABLES ____ *8*
A. DESIGN ____ 8
B. MANUFACTURING AND INSTALLATION ____ 9

Optivus Technology, Inc.

MULTILEAF COLLIMATOR REQUIREMENTS SPECIFICATION

I. INTRODUCTION

A. PURPOSE

An NMTB Grant has been secured by LLUMC to prepare a Requirements Specification for a proton therapy Multileaf collimator. From these specifications a collimator that will reduce the cost and increase the therapeutic ratio of proton therapy can be detailed and built. The Purpose of this specification is to identify and establish formal written, agreed upon, specifications for a Multileaf Collimator that will establish the requirements to meet the above objectives.

This document will provide the means to communicate the requirements to potential users, physicists, facility personnel, as well as standard PBTC safety operations and requirements. This document will serve as the design input for the development team.

B. SCOPE

This document specifies specific requirements for the LLUMC facility and assumes only minor modifications to the existing nozzle assembly. This specification is intended to integrate into a proton treatment system. This document is also limited to a design for Gantry use only and is not intended to provide specifications for a fixed beam room. This document is intended to provide a baseline for total MLC requirements, design, and implementation costs and schedules. Although released as Revision "A", the final requirements for the Multileaf Collimator are to be determined based on a final decision to proceed with a full project. **This document lists a number of requirements that reflect the consensus of the development team, however, will need to be finalized and approved by LLUMC when approval for further project steps is obtained. Review and Revise this document before proceeding to detailed requirements. There are a number of derived detailed requirements that will need to be removed and transferred to a detailed requirements specification when appropriate.**

C. DEFINITIONS, ABBREVIATIONS, ACRONYMS

1. Definitions

Multileaf Collimator	A MultiLeaf collimator is collimating device that is comprised of more than one collimating leaf, which will provide coarse and/or fine collimating resolution.
Gantry	A rotating support structure that allows, in this case, Proton Beam transportation to a specific central target location.
Over-run Distance	The distance past beam center that a leaf will extend.
Dosimetric Penumbra	The dose that exists at a lesser degree immediately adjacent to a collimated region.
Leaf Side Focussing	The dosimetric penumbra resolution generated from leaf edges

Attenuation	Beam intensity reduction. Refereed in this document as attenuation length.
Attenuation length	The length (Or thickness) of material required to block a specified charged proton.
Envelope dimensions	The outer most dimensions of a configuration.

2. Acronyms

MLC	Multileaf Collimator
NMTB	National Medical Technology Test Bed
LLUMC	Loma Linda University Medical Center
OTI	Optivus Technology, Inc.
PBTC	Proton Beam Treatment Center
PBTS	Proton Beam Transport System
CAX	Central Axis
MTBF	Mean Time Between Failure
MTTR	Mean Time To Repair
IAW	In Accordance With
SOP	Standard Operating Procedures

D. REFERENCES

1. Design Control Policy
   a) OTI Operating Procedure: 4-1, Revision F

   This document is to provide for a system and instructions, and to assign responsibilities for product design and design verification activities in compliance with United States Food and Drug Administration (FDA) Quality System Regulation (QSR) 21 C.F.R. 820.

2. Multileaf Collimator System Software Requirements Specification
   a) OTI Document number 3000260, Revision 1.0, Initial Versions

   This document is to define software system requirement specifications for a proton therapy Multileaf collimator.

II. REQUIREMENTS

A. GENERAL REQUIREMENTS

1. 510K
   a) LLUMC's 510K will need to be reviewed and if necessary revised for inclusion of this device

2. OTI SOPs
   a) All Design and Manufacturing are to be IAW OTI SOPs

3. Product Life
   a) Product Life > 20 years

4. Training
   a) A training program is to be approved prior to release of final design

5. Gantry Installation
   a) MLC is to be designed for LLUMC Gantry 2 or Gantry 3

B. SPECIFIC PERFORMANCE AND CONFIGURATION REQUIREMENTS

1. Dimensional/Physical Characteristics
   a) The Distance to iso-center-from exit of MLC
      (1) Fully extended <=25.4cm(10")
      (2) Fully Retracted =>63.5cm(25").

   b) Overlap on optionally mounted aperture
      (1) Overlap between the inside shape of the MLC and the outside shape of an inserted aperture =>6mm (.25 inches)

   c) Envelope Dimensions
      (1) Maximum Length from CAX <=105cm(41.3 inches)
      (2) Overall Length <=210cm(82.6 inches) maximum outside length
      (3) Width-50.8cm(20 inches)

   d) Weight
      (1) Maximum Mounted Weight <=1360KG(3000lbs).

2. Field Size and Resolution
   a) Field Size
      (1) Fully Open => 40cm square as projected to Isocenter
      (2) Closed-0.00cm(0.000 inches)
      (3) Leaf resolution
         (a) Leaf width-1cm

3. Leaf Location Parameters
   a) Leaf positioning:
      (1) Leaf Location -20cm to +20cm from CAX
      (2) Leaf location command resolution capability <=.1mm as projected to Isocenter.
      (3) Location tolerance <=.5mm as projected to Isocenter.

b) Leaf position monitoring
   (1) Leaves shall be electrically driven.
   (2) Drive device location tolerance<=.25mm(1/2 half the leaf positioning tolerance)

c) Acceptable drives
   (1) Servo motor
   (2) Stepper motor
   (3) Other-Must meet above requirements
   (4) The feed back loop attached directly to the drive motor will provide positional accuracy to the drive motor.
   (5) Location resolution <=.1mm(.1 Rev. for 1mm pitch drive screw)
   (6) Locational Tolerance<=.25mm(.25 Rev. for 1mm pitch drive screw)

d) Primary Position Monitor
   (1) Drive device will provide primary position location and feedback
   (2) Acceptable Feed back sources
      (a) Resolver
      (b) Encoder
      (c) Other-Must meet above requirements

e) Secondary Position Monitor
   (1) A secondary position monitor will provide independent feed back to the software controls to assure that the leave position matches the drive device position indication.
      (a) Acceptable secondary feedback devices
         (i) Optical Sensor
         (ii) Linear resolver
         (iii) Incremental encoder
         (iv) Other-Must meet above requirements
      (b) Feed back device tolerance
      (c) Feedback resolution <=.1mm
      (d) Feedback Tolerance<= ±1mm.
   (2) Visual Position Verification
      (a) The leaves will additionally provide for not less than 3 visual verification locations that will allow manual verification of device accuracy across the available field.

4. Leaf movement
   a) Leaf velocity position verification => 5cm/s

b) The MLC is to be able to reconfigure itself within (1) spill cycle time. The reconfiguration would be a maximum 5cm movement and position verification in 1 second.

5. Cast Aperture
   a) The MLC is to have the capability of accepting a cast aperture.
      (1) Cast aperture field size => 18cm.

   b) The cast aperture mounting system is to be basically the same as is utilized in Gantry 2, with the cone extension upgrade scheduled for completion in 1999. The system is to be able to accept the following Aperture field sizes:
      (1) 3cm
      (2) 8cm
      (3) 13cm
      (4) 18cm
      (5) If deemed acceptable at the time of funding, and alternate aperture arrangement may be made to locate apertures directly in the leaves of the MultiLeaf.

6. Bolus mounting requirement
   a) The MLC is to have the capability to accept a wax bolus.
      (1) Wax bolus field size => 18cm.
      (2) The Bolus mounting system is to be basically the same as is utilized in Gantry 2, with the cone extension upgrade scheduled for completion in 1999. The system is to be able to accept the following Bolus field sizes:
         (a) 3cm
         (b) 8cm
         (c) 13cm
         (d) 18cm

7. System deflection
   a) As installed system deflection to iso-center <= 4mm (.16 inches) at any nozzle extension and/or angle.
   b) As software corrected system deflection to iso-center <= 1mm(.04") at any nozzle extension and/or angle.

8. Leaf projection Past CAX
   a) Over-run Distance => 20cm

9. Leaf end shape
   a) Flat end without overlap or interlock
   b) End Finish <= 30µi.
   c) Leaf leakage at 0.00 opening will be accomplished by moving leaf abutting away from CAX

10. Leaf Material

a) Suitable materials for leaves are listed in Table 1. Although all of these materials are deemed acceptable for collimating, the following items are to be evaluated at the time of detailed design and test to ensure optimum performance and safety.
   (1) Activation <= existing Brass Pre-collimators.
   (2) Material Machining Tolerance Capability<=.005"/foot
   (3) Material Finish Capability < 30μi finish.

b) Wear
   (1) Material Wear < .005" wear over an 8.00 square inch surface area with a weight of not more than 15 lbs. Wear requirement is based on 1.2 million inches of travel(Or 365 days of 200 full 40cm strokes/day).
   (2) Wear is based on running on hard steel, 62 Rc or greater, channels finished to 25μi.
   (3) If it is identified that the selected material is not capable meeting the above wear requirement, rollers are to be designed into the leaf runner system to assure goal is met.
   (4) Radiation lubricant may be applied to achieve wear requirements.
   (5) Friction-The selected material when mated with hard steel 62 Rc is to have a coefficient of friction >.4 static and >.2 sliding. Radiation lubricant may be applied to achieve friction requirements.

c) Attenuation length
   (1) The material thickness required for the MLC, capable of blocking 275MeV protons, is as listed in Table 1.
   (2) Leaf thickness described in Table 1 will be increased, sufficient to adjust for leakage due to leaf geometry and/or assembly.
   (3) Total leakage is not to exceed 1% of delivered dose at 275MeV dose.

Material	Material Thickness (mm)	Material Thickness (Inches)	Material Density (lbs/cu. in.)	Lbs/sq.in.
Tungsten	43.9	1.73	.630	1.09
Brass	78.1	3.08	.310	.96
Copper	62.6	2.47	.295	.73
Iron	80.0	3.15	.260	.82
Stainless Steel	79.6	3.14	.283	.89

Table 1

11. Rotation around CAX
   a) The Multileaf will not be capable of rotation around center axis.
   b) Software considerations for MLC rotation are not included as a current requirement.
      (1) Any future consideration for rotation will be made in software and the individual leaves would be adjusted accordingly.

12. Leaf Leakage and Penumbra
    a) Penumbra
        (1) Leaf is to be designed to limit Interleaf leakage
        (2) Penumbra Height < .75mm around leaf

    b) Inter-leaf leakage
        (1) Total leakage <= 1% of delivered dose at 275MeV dose.

    c) Staggered leaves under dosage and/or over dosage-TBD

    d) Abutting-leaf leakage (Totally closed)
        (1) When leaves are required to be totally closed for complete proton beam blockage, the leaves will be moved to an "Off Center" abutting location. "Off Center" locations will be tested and determined at the time of detail design.
        (2) Total leakage <= 1% % of delivered dose at 275MeV dose.

C. RELIABILITY REQUIREMENTS

1. MTBF
    a) Leaves > 2 years
    b) Drives/Primary Feedback Devices > 2 years
    c) Secondary Feedback Devices > 2 years
    d) System => 1 year

D. REPAIR AND REPLACEMENT REQUIREMENTS

1. MTTR
    a) Leaves < 1 hour
    b) Ball Screw and Nut < 2 hour
    c) Drives/Primary Feed Back Devices < 4 hours
    d) Secondary Feedback Devices < 4 hours
    e) System < 4 hours

E. MAINTENANCE REQUIREMENTS

1. System is to be re-furbished annually
    a) Leaves
        (1) To be inspected and replaced as required => annually
        (2) To be replaced => 3 years
    b) Ball Screw and Nut
        (1) To be inspected and replaced as required => annually
        (2) To be replaced => 3 years
    c) Electronic Components internal to MLC
        (1) To be inspected and replaced as required => annually
        (2) To be replaced => 2 years

    d) Electronic Components External to MLC
        (1) To be inspected and replaced as required <= 2 years
        (2) To be replaced <= 20 years

2. Deflection Validation
   a) Weekly for first 3 months
   b) Monthly or as determined to maintain reliability

3. Manuals
   a) Maintenance
   b) Users

4. Finite Lifetime Components
   a) Components with an expected life of less than 20 years are to be identified prior to fabrication
   b) A maintenance plan is to be developed to address spare parts for 20 year life

III. TESTING AND EVALUATION

A. SCATTER-VS-RESOLUTION

1. In model analysis, it has been found that a 1cm leaf thickness provides optimum resolution without major degradation of resolution. A leaf thickness less than 1cm does not appear to dramatically improve collimating resolution in most cases and the overall scattered resolution does not show any significant improvement with leaves under 1cm thick.
2. Actual Scatter-vs-Resolution tests are to be conducted and completed prior to final design release of a MultiLeaf collimator.

B. LEAF MATERIAL AND GEOMETRY

1. Leaf material is to be tested for wear IAW 2.2.14.5 to assure final materials will meet and or exceed requirements prior to release of final designs
2. Prototype leaves are to be tested to assure the interlocking geometry/pattern meets and or exceed Leakage requirements IAW 2.2.16.2 prior to release of final designs
3. Prototype leaves are to be tested to assure the interlocking geometry/pattern meets and or exceed Penumbra requirements IAW 2.2.16.1 prior to release of final designs

IV. DELIVERABLES

A. DESIGN

1. Complete Mechanical Designs and Documentation for a MLC, which meets or exceed the specification in this document
2. Complete Electrical Designs and Documentation for a MLC, which meets or exceed the specification in this document

3. Complete Software Designs and Documentation for a MLC, which meets or exceed the specification in this document and Multileaf Collimator System Software Requirements Specification OTI Document number 3000260, Revision 1.0

B. MANUFACTURING AND INSTALLATION

1. A complete MLC Manufactured, Installed, Verified, and Validated meeting or exceeding the specification in this document and Multileaf Collimator System Software Requirements Specification OTI Document number 3000260, Revision 1.0
2. Complete Software Integration, Verification, and Validation meeting or exceeding the specification in this document and Multileaf Collimator System Software Requirements Specification OTI Document number 3000260, Revision 1.0

APPENDIX B: SYSTEM SOFTWARE REQUIREMENTS SPECIFICATION

Optivus Technology, Inc.

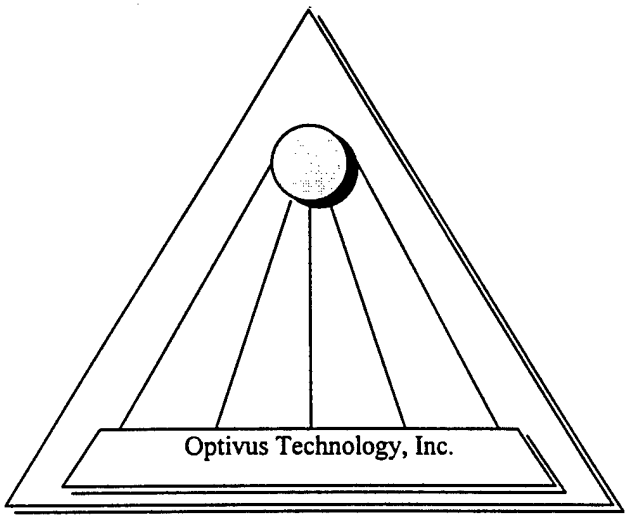

Multi-Leaf Collimator
System Software Requirements Specification

Document No.: 3000260

© 1998 Optivus Technology, Inc.

Proprietary

Revision History

Date	Revision	Description	Author
10/15/98	1.0	Initial Version	Ken Rice
mm/dd/yy			

Table of Contents

1. INTRODUCTION ..... 1—1

1.1. PURPOSE ..... 1—1
1.2. SCOPE ..... 1—1
1.3. DEFINITIONS, ACRONYMS, ABBREVIATIONS ..... 1—1
1.3.1. Definitions ..... 1—1
1.3.2. Acronyms ..... 1—2
1.4. REFERENCES ..... 1—2
1.4.1. Configuration File Format Specification ..... 1—2
1.4.2. PBTS Logging and Monitoring, Field Service Support Software Requirements Specification 1—3
1.4.3. Graphical User Interface Standard ..... 1—3
1.4.4. Multi-Leaf Requirements Specification ..... 1—3

2. OVERALL DESCRIPTION ..... 2—1

2.1. PRODUCT PERSPECTIVE ..... 2—1
2.1.1. Hardware Interfaces ..... 2—1
2.1.2. Data Interface ..... 2—1
2.1.3. Communications Interfaces ..... 2—1
2.2. PRODUCT FUNCTIONS ..... 2—1

3. SPECIFIC REQUIREMENTS ..... 3—1

3.1. EXTERNAL INTERFACE REQUIREMENTS ..... 3—1
3.1.1. Treatment Planning System (TPS) ..... 3—1
3.1.2. Configuration File Format ..... 3—1
3.1.3. Hardware Interface ..... 3—1
3.1.4. Calibration System ..... 3—1
3.1.5. Treatment Control System Software Interfaces ..... 3—2
3.1.6. Digital Imaging System Interfaces ..... 3—2
3.1.7. User Interfaces ..... 3—2
3.2. FUNCTIONAL REQUIREMENTS ..... 3—4
3.2.1. Initialization ..... 3—4
3.2.2. Configuration Parameters ..... 3—4
3.2.3. Monitoring Leaf Position ..... 3—4
3.2.4. Leaf Position Correction Factors ..... 3—4
3.2.5. Leaf Collision Avoidance ..... 3—4
3.2.6. Calibration System ..... 3—5
3.2.7. Treatment Control System Software ..... 3—5
3.2.8. Error Messages ..... 3—5
3.2.9. Message logger interface ..... 3—6
3.2.10. Application information ..... 3—6
3.3. PERFORMANCE REQUIREMENTS ..... 3—6
3.3.1. Timing Requirements ..... 3—6
3.3.2. Multiple instances ..... 3—6
3.4. SOFTWARE SYSTEM ATTRIBUTES ..... 3—6
3.4.1. Reliability ..... 3—6
3.4.2. Security ..... 3—6
3.4.3. On-Line Help ..... 3—6
3.5. OTHER REQUIREMENTS ..... 3—7
3.6. PORTABILITY ..... 3—7

1. Introduction

1.1. Purpose

The goal of the Multi-Leaf Collimator (MLC) project is to produce requirement specifications for a proton therapy multi-leaf collimator. A multi-leaf collimator i.e. variable aperture, would minimize or eliminate the production and disposal costs associated with custom apertures that are currently being used. A multi-leaf collimator would also decrease patient treatment times by eliminating the need for a radiation therapist to manually change the heavy apertures before each treatment.

1.2. Scope

This document shall provide the system level software requirements for treatment planning interfaces, configuration, calibration and diagnostic systems, software interfaces, monitoring systems and graphic user interface requirements for the MLC project.

1.3. Definitions, Acronyms, Abbreviations

1.3.1. Definitions

1.3.1.1. Beam Off

The end of the flat top region on the dipole ramp (**event 88**)

1.3.1.2. Host computer

A networked computer the application is running on. The host computer possesses a name to identify it on the network.

1.3.1.3. Multi-Leaf Collimator

Multiple collimators stacked to produce a three-dimensional variable aperture device. The Multi-Leaf collimator is typically automated to provide the variability feature.

1.3.1.4. Network connection

A connection of one computer to a network of computers via network protocol.

1.3.1.5. Network protocol

A set of coded commands for computers to communicate on a network.

1.3.1.6. Requirement

Any information (textual or graphic) that represents important information to the user.

1.3.1.7. User

The person, or persons who operate or interact directly with this product.

1.3.2. Acronyms

1.3.2.1. DICOM

Digital Imaging and Communications in Medicine

1.3.2.2. GUI

Graphical User Interface

1.3.2.3. LLUMC

Loma Linda University Medical Center

1.3.2.4. MLC

Multi-Leaf Collimator

1.3.2.5. NMTB

National Medical Technology Test Bed

1.3.2.6. TCP/IP

Transfer Control Protocol/Internet Protocol

1.3.2.7. TPS

Treatment Planning System

1.3.2.8. UDP/IP

User Datagram Protocol/Internet Protocol

1.4. References

1.4.1. Configuration File Format Specification

This document describes the syntax and file format of configuration files that may be used by the ConfigParam class.

Document No.: *3000155*

Rev. A

Released: 1997

By Optivus Technology, Inc.

1.4.2. PBTS Logging and Monitoring, Field Service Support Software Requirements Specification

This document describes the monitoring requirements that support system diagnostics and preventive maintenance.

Document No.: *3000XXX*

Rev. XA

Released:

By Optivus Technology, Inc.

1.4.3. Graphical User Interface Standard

This document describes the graphical user interface standards for Optivus Technology, Inc software applications.

Document No.: *3000150*

Rev. A

Released: 1997

By Optivus Technology, Inc.

1.4.4. Multi-Leaf Requirements Specification

This document details the mechanical specifications for the Multi-Leaf Collimator project.

Document No.: 5000052

Rev. XA

Released:

By Optivus Technology, Inc.

2. Overall Description

2.1. Product Perspective

The Multi-Leaf Collimator (MLC) planned for this project will contain a total of 80 leaves. The leaves are precision machined corrugated sheets of metal that are stacked and individually positioned by servo motors. The leaves will be assembled with 40 leaves on each side of the center of axis. Each leaf will be aligned with the opposing leaf such that their zero position will be at the center of axis. The MLC software control system will provide control and monitoring capability of each leaf position. The software control system will also include leaf position calibration tools and will retrieve the treatment leaf positions from a treatment planning interface.

2.1.1. Hardware Interfaces

In order to provide position motion control of each leaf a software system will be necessary at the hardware level. Potentially 80 drive motors may be necessary to provide the rapid motion control of each leaf. The drive motors will be specified in a Mechanical Requirements Specification document. The drive motors may have on board controllers that will provide monitoring capability of the motor position. Software drivers will be used to interface with these motors and take advantage of on board motor controls.

2.1.2. Data Interface

The LLUMC proton facility treatment planning information must be transferred to the Proton Beam Treatment System (PBTS) control system. Figure 2-1 provides an overview of the data flow that is anticipated between the various systems involved in the coordination of MLC treatments. The actual design may incorporate the Prescription storage and the Patient Treatment Data Storage into one storage location.

2.1.3. Communications Interfaces

All communication will be based on Berkeley sockets and use either Transfer Control Protocol/Internet Protocol (TCP/IP) or User Datagram Protocol/Internet Protocol (UDP/IP).

2.2. Product Functions

In order to successfully provide Multi-Leaf Collimator patient treatments, numerous systems must be integrated. The treatment planning functionality must provide the treatment plan to the PBTS treatment control and patient setup/calibration systems. Other systems, such as the Digital Imaging system, may take advantage of a centrally located patient data storage design.

With an integrated treatment planning and PBTS control system, a more efficient and responsive treatment capability will result. Patient setup and calibration activities will be streamlined and capable of accepting patient calibration factors created in the treatment planning phase or performing those calculations in the patient calibration phase, depending on the needs of the treatment. The patient prescription will contain the MLC positions which will be retrieved by the PBTS treatment control system.

Once the PBTS treatment control system has retrieved the patient specific treatment parameters, the information will be directed to the PBTS accelerator control system, the Digital Imaging system and the MLC system. The PBTS treatment control system will prepare for patient treatment by monitoring the patient preparation process, verifying the MLC system is ready for treatment via predetermined leaf position exercises and retrieving the pre-calculated patient calibration factors.

During patient treatment the MLC leaf positions will be monitored to verify the prescribed positions, as well as other prescribed parameters, are maintained. If the patient prescription dictates new MLC leaf positions, the beam delivery may be delayed, (for leaf positions greater than 5 centimeters), while the system automatically repositions, without the need of the treatment technologist entering the treatment room. Data captured during the patient treatment will be stored as a historical record of the treatment.

The PBTS treatment control system or MLC control software system will not compensate for rotations in the leaf collimator positions. If rotations of the projected field are necessary, it will be accomplished with patient rotation.

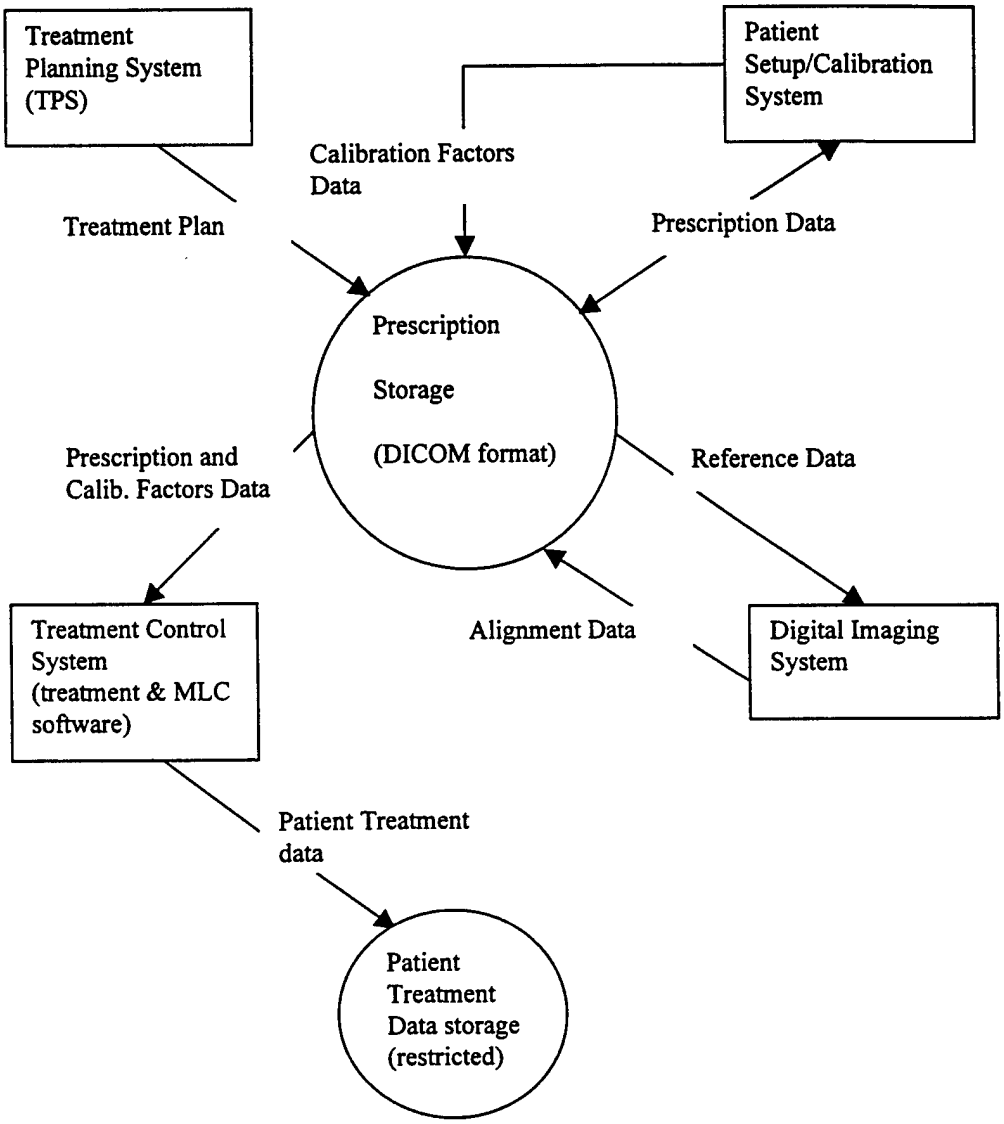

Figure 2-1. Data flow from Treatment Planning System to Proton Beam Treatment System.

3. Specific Requirements

3.1. External Interface Requirements

The incorporation of the Multi-Leaf Collimator (MLC) capability into the PBTS shall require modification to several existing systems. The following paragraphs detail the systems that are impacted by the addition of the MLC treatment capability.

3.1.1. Treatment Planning System (TPS)

The Treatment Planning System shall provide the patient treatment prescriptions to a storage location that is accessible via the PBTS Radiation Medicine local network. The prescription data format shall be DICOM.

3.1.2. Configuration File Format

The MLC software control system shall follow the Optivus Technology Inc. configuration file format standard detailed in reference 1.4.1. When configuration parameters are applicable, all user interface applications shall follow the configuration file format.

3.1.3. Hardware Interface

The MLC software control system shall have the capability to issue commands and receive readback information from the motors used for leaf motion control. Detailed hardware interface requirements shall be documented based on the motors described in the MLC Mechanical Specifications reference 1.4.4.

3.1.4. Calibration System

A calibration system is required for the MLC project to determine calibration factors based on the dose per monitor unit. A Patient Calibration Model application is presently used to perform calibration factor calculations for non-MLC treatments. Although the patient calibration functionality must exist, incorporation of the MLC calibration functionality into the current Patient Calibration Model is not a requirement.

3.1.4.1. Patient Calibration System

The patient calibration system shall include the capability to retrieve the necessary parameters contained in the treatment planning system output.

The patient calibration system shall have the capability to recognize prescriptions that detail MLC patient calibrations. The patient calibration system shall perform the calibration factor calculations for each segment and

store those factors in the appropriate patient directory. The calibration factor calculations shall be stored in a standard data format that can be interpreted by the treatment control system software.

3.1.5. Treatment Control System Software Interfaces

The current LLUMC PBTS treatment software shall be modified to retrieve patient prescription information contained in the treatment planning files. The treatment control system software shall be modified to retrieve the patient calibration factors for each segment in a MLC treatment from the centrally located prescription storage.

The treatment control system shall provide each segment's leaf positions, from the treatment planning files, to the MLC control system.

The treatment control system shall provide the user MLC system status information.

The treatment control software system shall record each leaf position for each segment that beam delivery occurs. This data shall be stored into the appropriate patient data file.

3.1.6. Digital Imaging System Interfaces

The Digital Imaging systems that are installed in the PBTS shall have access to the reference images, which are part of the treatment plan, for the appropriate patient. The Digital Imaging systems shall be capable of interpreting the data format of the treatment plans. The Digital Imaging systems shall have the capability to write any alignment data collected to the centrally located storage of patient information.

3.1.7. User Interfaces

In order to verify correct multi-leaf motion control, leaf position calibration and system diagnostic user interface functionality shall be provided.

3.1.7.1. Leaf Position Calibration

The MLC leaf position calibration system shall permit the user to load and command predetermined leaf positions. The user shall be provided a method of initiating the leaf position command sequence. The system shall provide the user the capability to display a position readback and the commanded position for each leaf. The user shall have the capability to issue a command to terminate motion of all leaves.

The MLC leaf position calibration system shall provide the user indicators of the leaf status i.e. in motion, halted, leaf collision, motor stalled, OK/Not OK to treat patients.

The MLC leaf position calibration system shall notify the user if the commanded leaf position is not achieved within the tolerance. The system shall provide a method to identify leaves that are out of tolerance.

If an out of tolerance failure occurs the system shall identify the system as faulted and inhibit beam delivery. The fault shall be removed upon successful completion of a leaf position calibration test.

3.1.7.2. Leaf Position Motion Control Diagnostics

The MLC leaf position motion control diagnostic system shall provide an interface that permits the user to save, load and command leaf positions. The user interface shall provide motor acceleration and deceleration measured rates, motor status information, measured motor velocity, resolver turns, and measured motor position.

The MLC system shall provide the user with the capability to display the data collected during motion control testing. The system shall provide the user the capability to print or save the data collected at the completion of a motion sequence command.

The user shall be notified when an out of tolerance condition results during motion control testing.

The user shall be provided a method of initiating the leaf position command sequence. The system shall provide the user the capability to display a position readback and the commanded position for each leaf. The user shall have the capability to issue a command to terminate motion of all leaves.

The system shall provide the user indicators of the leaf status i.e. in motion, halted, leaf collision, motor stalled, OK/Not OK to treat patients.

The system shall notify the user if the commanded leaf position is not achieved within the tolerance. The system shall provide a method to identify leaves that are out of tolerance.

If an out of tolerance failure occurs the system shall identify the system as faulted and inhibit beam delivery. The fault shall be removed upon successful completion of a leaf position motion control test.

3.1.7.3. Patient Setup/Calibration System

The patient setup/calibration system shall provide the user the functionality to create and store patient prescriptions to the appropriate patient directory. The capability to setup and calibrate multi-leaf collimator treatments shall be provided for the user.

The patient setup/calibration system shall provide the user a method of viewing the patient treatment prescription parameters (all segments).

The patient setup/calibration system shall contain the same user functionality that currently exists.

The patient setup/calibration system shall provide the user an indication of a potential leaf collision during the patient setup functionality.

The user shall be provided the indication of a failed patient calibration attempt and the reason of the failure.

3.2. Functional Requirements

3.2.1. Initialization

The MLC control system shall command each leaf to return to a default position prior to the next patient's treatment. The default position for each leaf shall be configurable. The permit to continue patient treatment shall be disabled until the initialization sequence is satisfied.

3.2.2. Configuration Parameters

The MLC system shall take advantage of configuration parameters to define those system parameters that may change throughout the life cycle of the system. The configuration files shall be text files that do not require a software system be re-compiled when a parameter is modified. The configuration parameter files shall have file write restrictions as appropriate depending the context of the file. For example, LLUMC medical physics users would have file write access to patient calibration configurable parameters.

The MLC system treatment configuration parameters and tolerances shall be used for all motion control tests in the treatment room.

3.2.3. Monitoring Leaf Position

The system shall verify each leaf is correctly positioned with respect to the commanded position prior to beam delivery. The system shall monitor each leaf position during patient treatment to verify the leaf position is accurately maintained within the tolerance. If a leaf position is not achieved or maintained the monitor shall initiate a signal to terminate beam delivery. The positioning tolerance for each leaf shall be configurable.

The system shall provide a stall detection function to recognize when a leaf's motion has prematurely halted. In the event a motor stall does occur, the status indicators shall be updated to reflect the stalled condition.

3.2.4. Leaf Position Correction Factors

The weight of the MLC may result in nozzle superstructure deflection dependant on the angle of the nozzle (gantry angle). The system shall permit configurable leaf position correction factors based on the gantry angle.

3.2.5. Leaf Collision Avoidance

The MLC system shall provide a verification that the desired position of the opposing leaves do not result in a collision. The leaf collision avoidance check shall be performed before any leaf motion toward MLC isocenter. If a potential leaf collision is detected, leaf motion shall be inhibited.

3.2.6. Calibration System

Two types of calibration systems are required for the MLC project i.e. a calibration factor to determine the dose per monitor unit and a physical calibration of the motion control of each leaf.

3.2.6.1. Patient Setup/Calibration System

The patient setup/calibration system shall include the capability to retrieve the necessary parameters from the treatment planning system output for all patient treatments. The patient setup/calibration system shall have the capability to setup the patient prescription files in preparation for patient calibrations. The patient setup/calibration system shall have the capability of performing the necessary calculations to determine the patient calibration factors for nominal patient prescriptions.

On those prescriptions that detail MLC treatments, patient calibration factor calculations shall be performed for each segment and stored in the appropriate patient directory.

The system shall perform a leaf collision avoidance check as part of the patient setup functionality. The patient calibration functionality shall not be successful if a potential leaf collision exists.

3.2.6.2. Leaf Position/Motion Control Calibration

The system shall be capable of containing sets of predetermined leaf positions. The predetermined leaf positions shall be configurable. Modification of the predetermined leaf positions shall be restricted to LLUMC Medical Physics personnel.

The system shall have the capability to provide an automatic leaf positioning sequence. The MLC software control system shall command each leaf through its entire range of motion. If the commanded position is not achieved within 8.0 seconds a failure report shall be generated which inhibits beam delivery.

3.2.7. Treatment Control System Software

The treatment control system software shall be capable of permitting the requested dose delivered from each MLC segment. Once the current dose has been delivered for the segment, the treatment software shall cause the beam delivery to pause if the leaf position change exceeds 5 centimeters. If the leaf position is less than 5 centimeters, the beam delivery shall not be paused. The treatment software shall provide the next segment leaf positions and command the MLC system to reposition. The treatment software shall continue this process until the entire dose has been delivered for the portal.

3.2.8. Error Messages

The MLC system shall provide error and warning messages to the user. The messages shall provide the user detailed information to identify the problem or faulted component

and the symptoms of the failure. The MLC system shall follow the Optivus Technology, Inc. accepted error numbering scheme.

3.2.9. Message logger interface

The MLC system shall follow the PBTS logging specifications in reference 1.4.2.

3.2.10. Application information

Each MLC application shall provide information about the application. The following minimum information shall be provided: application name, version number, part number, and release date.

3.3. Performance Requirements

3.3.1. Timing Requirements

The application shall process all its MLC leaf position monitoring verification every beam cycle after each Beam Off event. Leaf position monitoring shall be completed and reported to the safety system such that the next beam spill may be rejected.

3.3.2. Multiple instances

Multiple instances of the MLC control software shall not be permitted within each treatment room.

3.4. Software System Attributes

3.4.1. Reliability

The annual MLC software control system uptime shall be greater than 96 percent.

3.4.2. Security

Access to the MLC system shall be authorized by the established PBTS access system. Access to the patient treatment plans and data shall be restricted to the appropriate personnel.

3.4.3. On-Line Help

The MLC system shall provide an on-line help facility with all graphical user interfaces for this project. The on-line help shall be accessible to each graphical user interface. The on-line help facility shall provide descriptions of the GUI application's functionality, tips on usage and general operating instructions.

3.5. Other Requirements

The MLC system Graphical User Interfaces shall follow the Optivus Technology, Inc standard guidelines provided in reference 1.4.3.

3.6. Portability

The MLC system portability requirements shall be addressed within the detailed requirements.

APPENDIX C: TREATMENT PLANNING SIMULATION TESTS

STATEMENT OF WORK

The Contractor shall simulate the multi-leaf collimator (MLC) system using the treatment planning computer application (TPN). The contractor shall perform a series of test cases using proton beam radiation fields projected as shaped by the MLC. The resulting dose distributions will be computed in three dimensions. A variety of clinical disease sites will be simulated, and a range of design parameters will be varied for each disease site.

The following MLC design parameters will be varied in the simulation study:

1. maximum opening
2. leaf width
3. over-run distance
4. MLC to skin distance

The contractor shall be provided with a list of disease sites to test, and a range for each design parameter for the given disease site. The contractor shall perform the tests, collect dose distribution data, and prepare a detailed report of the study results for the Principal Investigator.

The clinical staff will assess each test based on the target volume coverage and the ability to spare nearby normal tissue organs. In this way an envelope of acceptable parameters can be established.

The contractor shall perform the described tasks between June 1, 1998 and August 1, 1998.

prescribed dose = 50gy
normal critical dose = 45gy
gantry 1
no bolus
slow calc
xy spacing .2
inout = .5

target radius in z direction = 2cm
normal radius in z direction = 4cm

depth to back of target = 11.5

ntacd auto ap = .204

spacing = .2
ntacd = .206
spacing = .4
ntacd = .217
spacing = .8
ntacd = .241

depth to back of target = 17.5

ntacd auto ap = .201

spacing = .2
ntacd = .222
spacing = .4
ntacd = .225
spacing = .8
ntacd = .238

depth to back of target = 27.5

ntacd auto ap = .196

spacing = .2
ntacd = .210
spacing = .4
ntacd = .225
spacing = .8
ntacd = .222

target radius in z direction = 4cm
normal radius in z direction = 6cm

depth to back of target = 11.5

ntacd auto ap = .375

spacing = .2
ntacd = .416
spacing = .4
ntacd = .423
spacing = .8
ntacd = .511

depth to back of target = 17.5

ntacd auto ap = .387

spacing = .2
ntacd = .382
spacing = .4
ntacd = .390
spacing = .8
ntacd = .469

depth to back of target = 27.5

ntacd auto ap = .459

spacing = .2
ntacd = .458
spacing = .4
ntacd = .469
spacing = .8
ntacd = .517

target radius in z direction = 6cm
normal radius in z direction = 8cm

depth to back of target = 15.5

ntacd = .500

spacing = .2
ntacd = .507
spacing = .4
ntacd = .513
spacing = .8
ntacd = .573

Prostate FEOI

Kets projected stem
out aperture

spacing = .25

DOSE VOLUME HISTOGRAM

Patient: JB test, patient

Tissue Region: prostate + sv

spacig = .25

auto ap

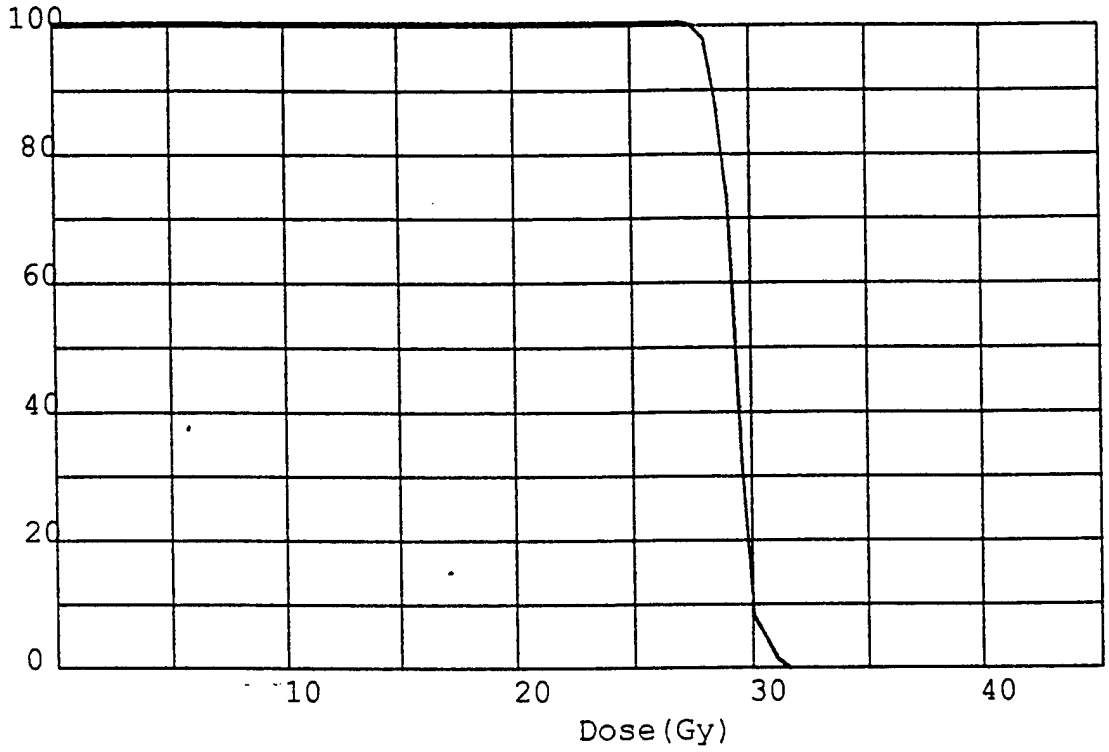

DOSE VOLUME HISTOGRAM

Patient: JB test, patient

Tissue Region: bladder

spacy = .25

auto ap

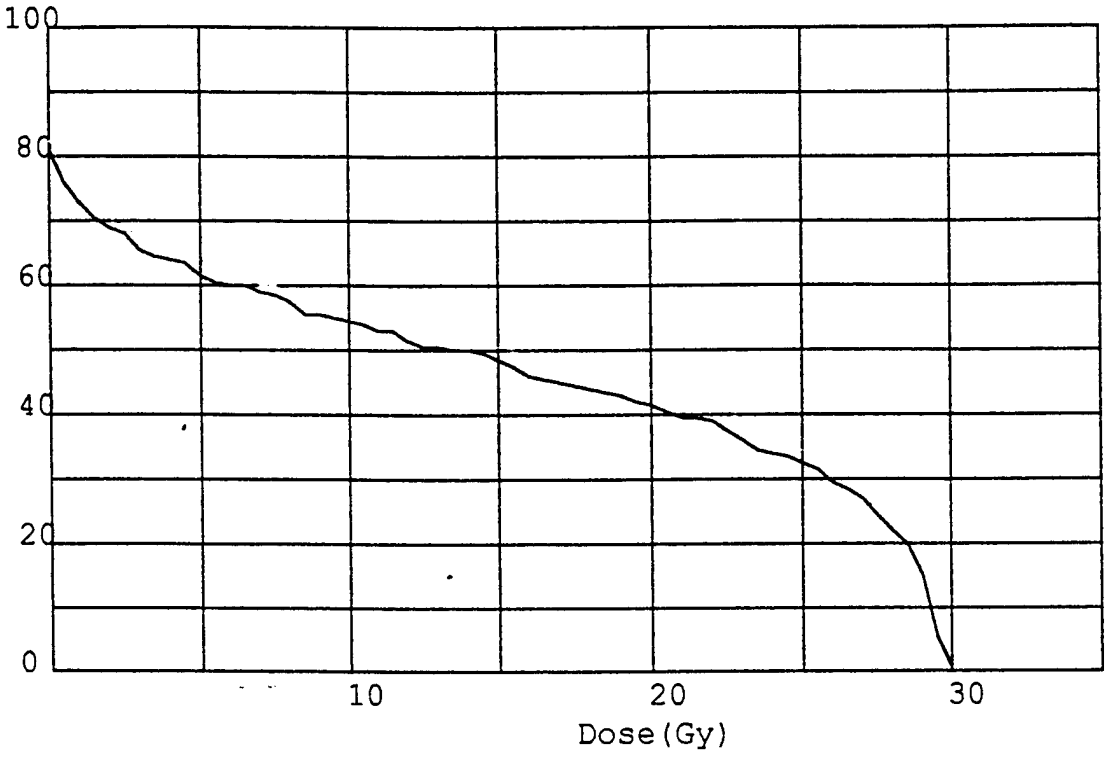

DOSE VOLUME HISTOGRAM

Patient: JB test, patient

Tissue Region: rectum

spacy = .25

auto ap

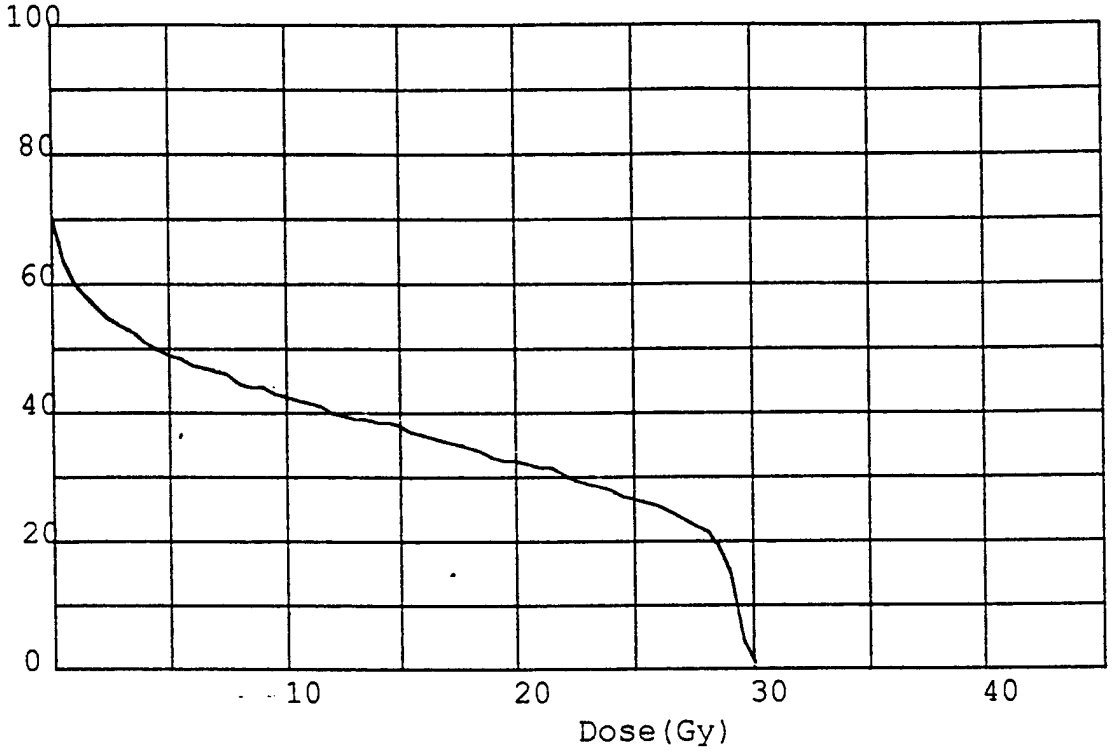

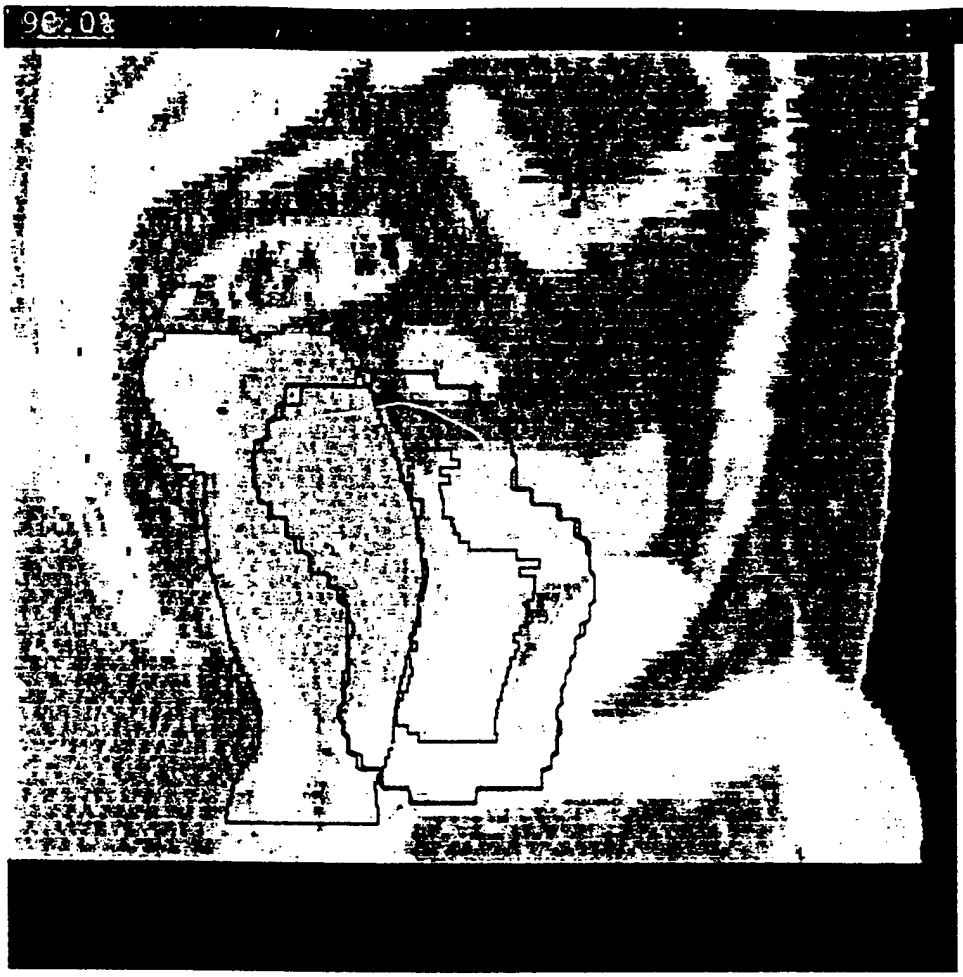

spacing = .4 cm

DOSE VOLUME HISTOGRAM

Patient: JB test, patient

Tissue Region: prostate + sv

spacing = .4cm

auto ap

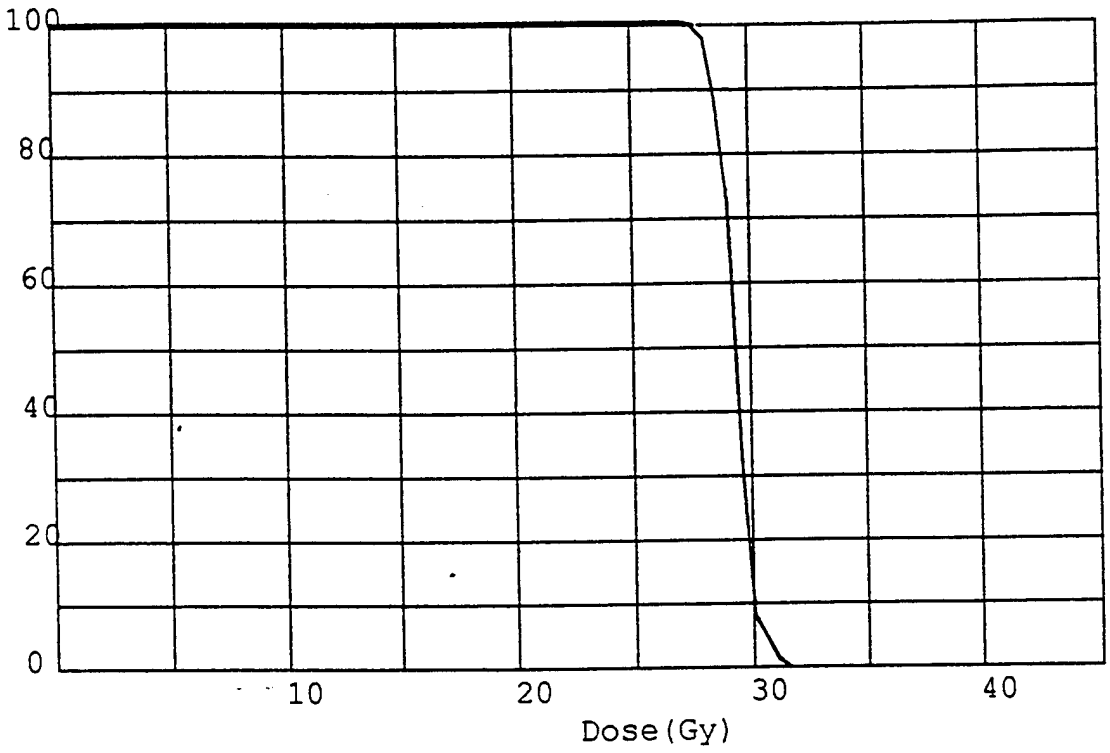

DOSE VOLUME HISTOGRAM

Patient: JB test, patient

Tissue Region: bladder

spacing = .4cm

auto ap

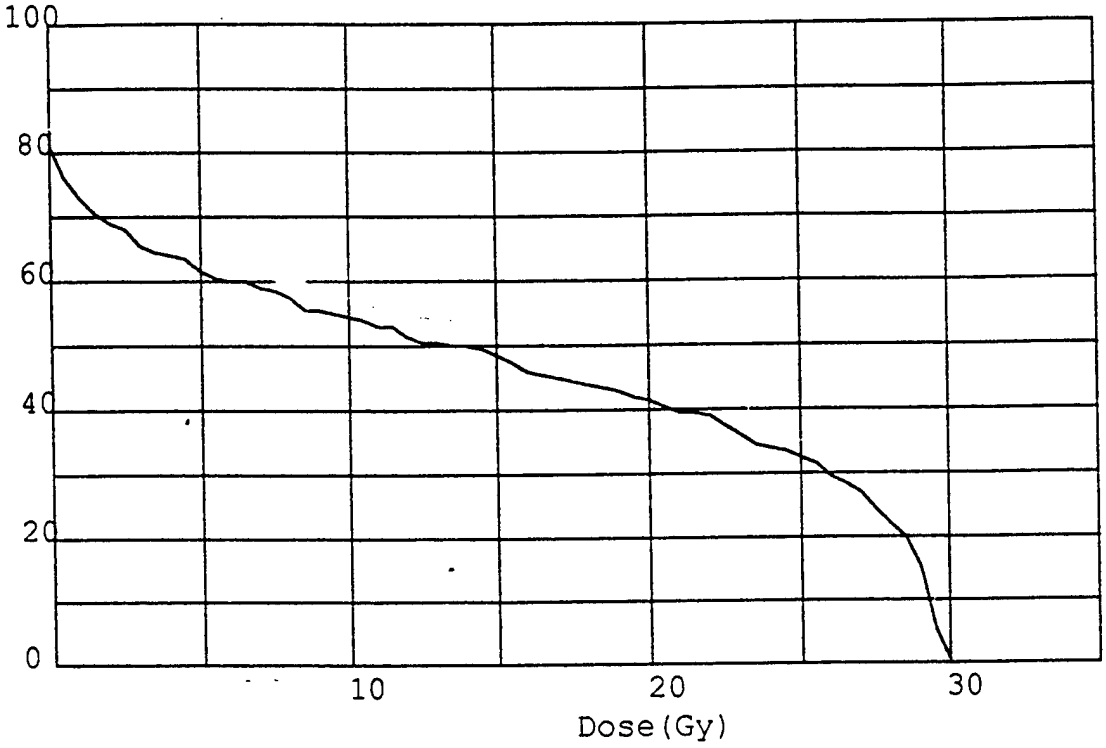

DOSE VOLUME HISTOGRAM

Patient: JB test, patient

Tissue Region: rectum

Spacy = .4

auto ap

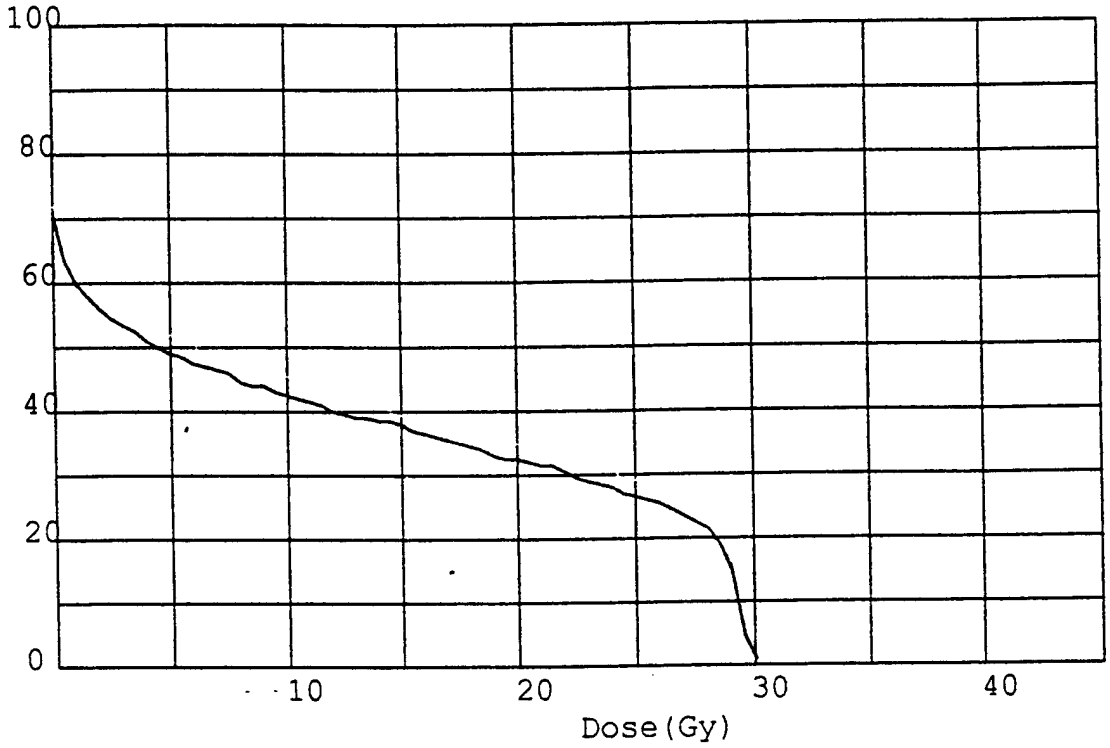

spacing = .5

DOSE VOLUME HISTOGRAM

Spacing = .5

Patient: JB test, patient

Tissue Region: prostate + sv

auto ap

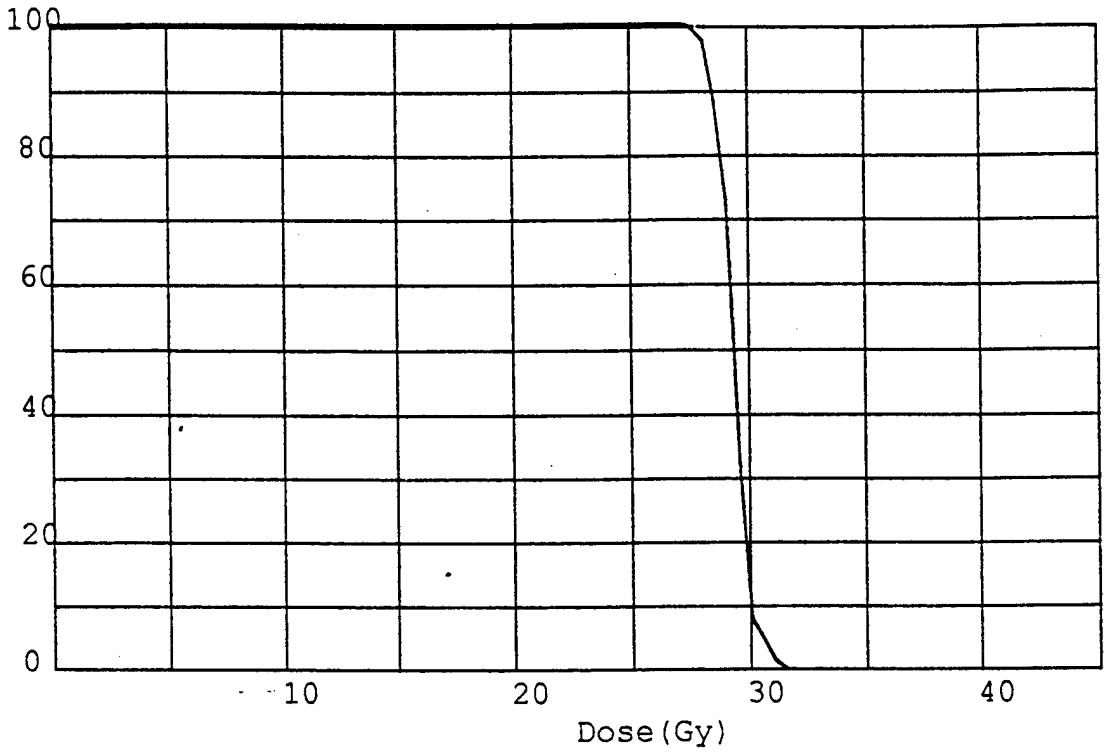

DOSE VOLUME HISTOGRAM

Spacing = .5 cm

Patient: JB test, patient

Tissue Region: bladder

auto ap

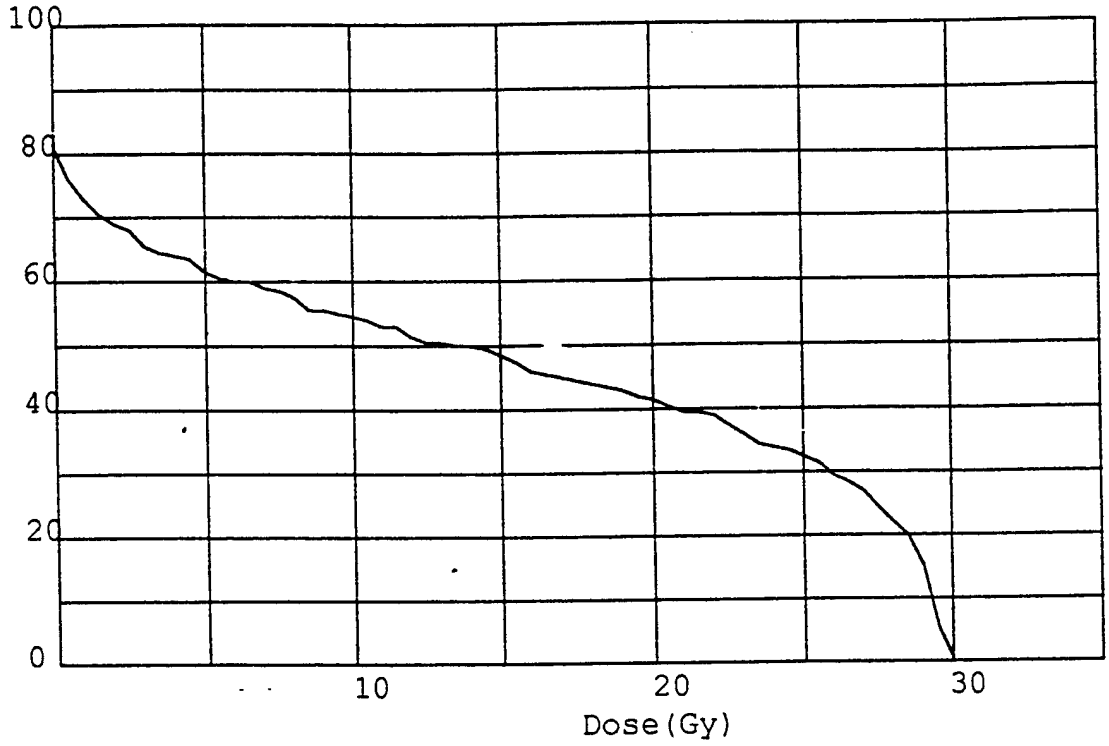

DOSE VOLUME HISTOGRAM

Spacing = .5

Patient: JB test, patient

Tissue Region: rectum

auto ap

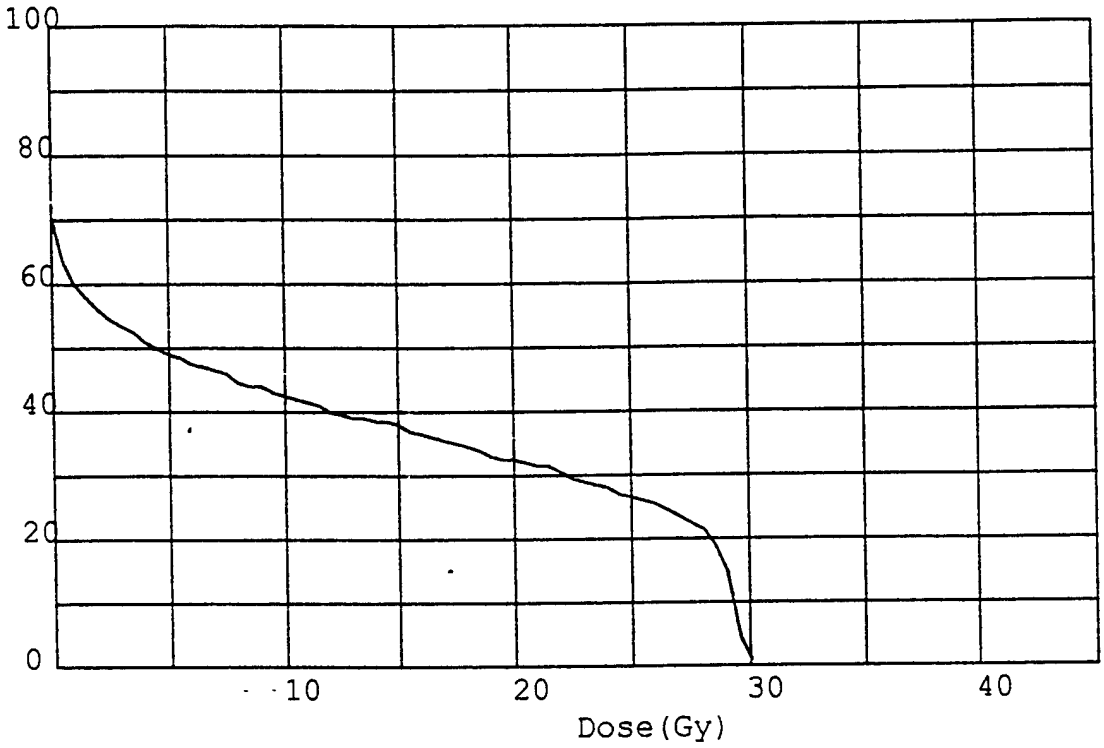

APPENDIX D: 3-D CONCEPTUAL DESIGN DRAWINGS

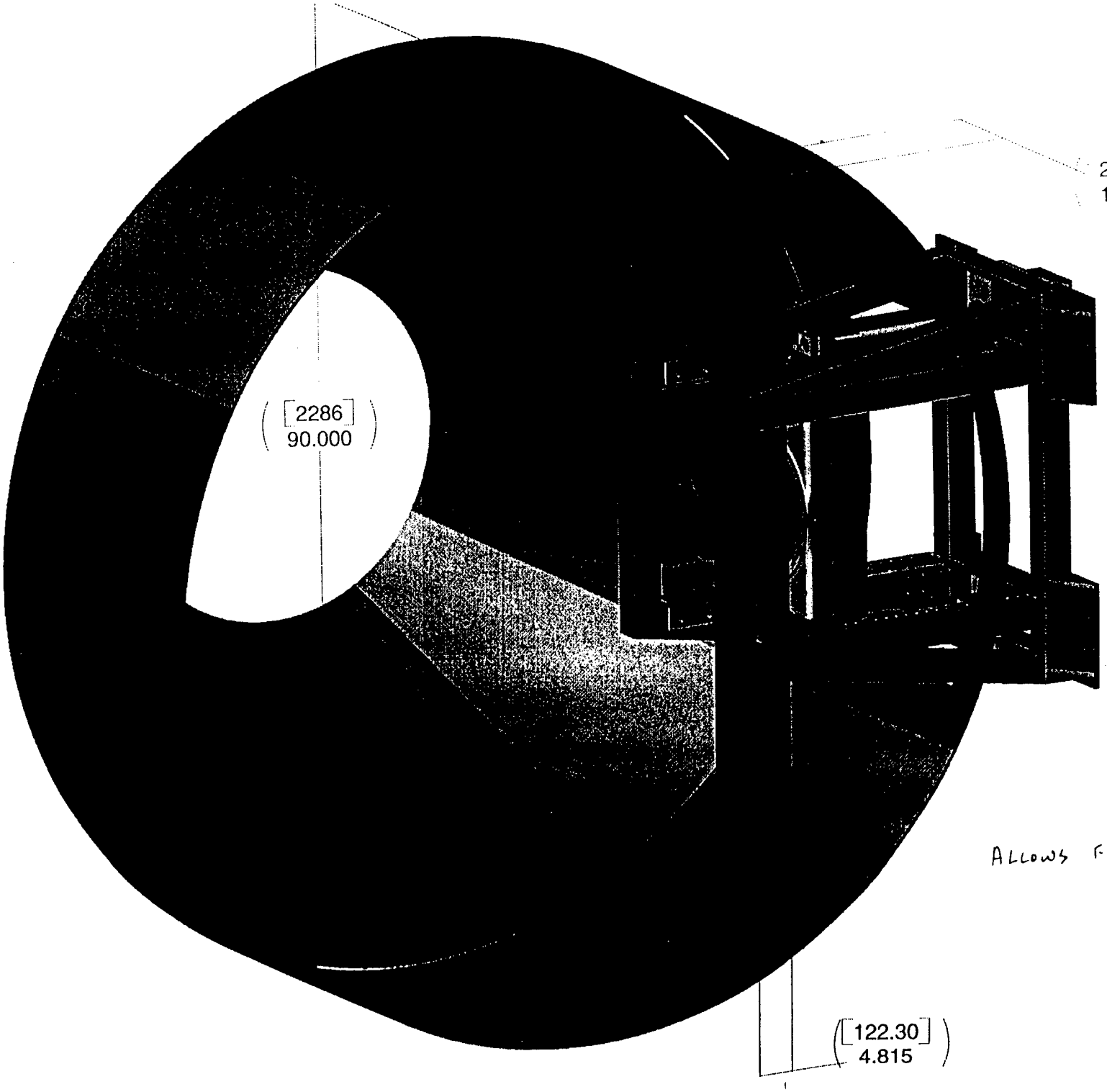

ALLOWS FOR ±10° ROTATIONAL

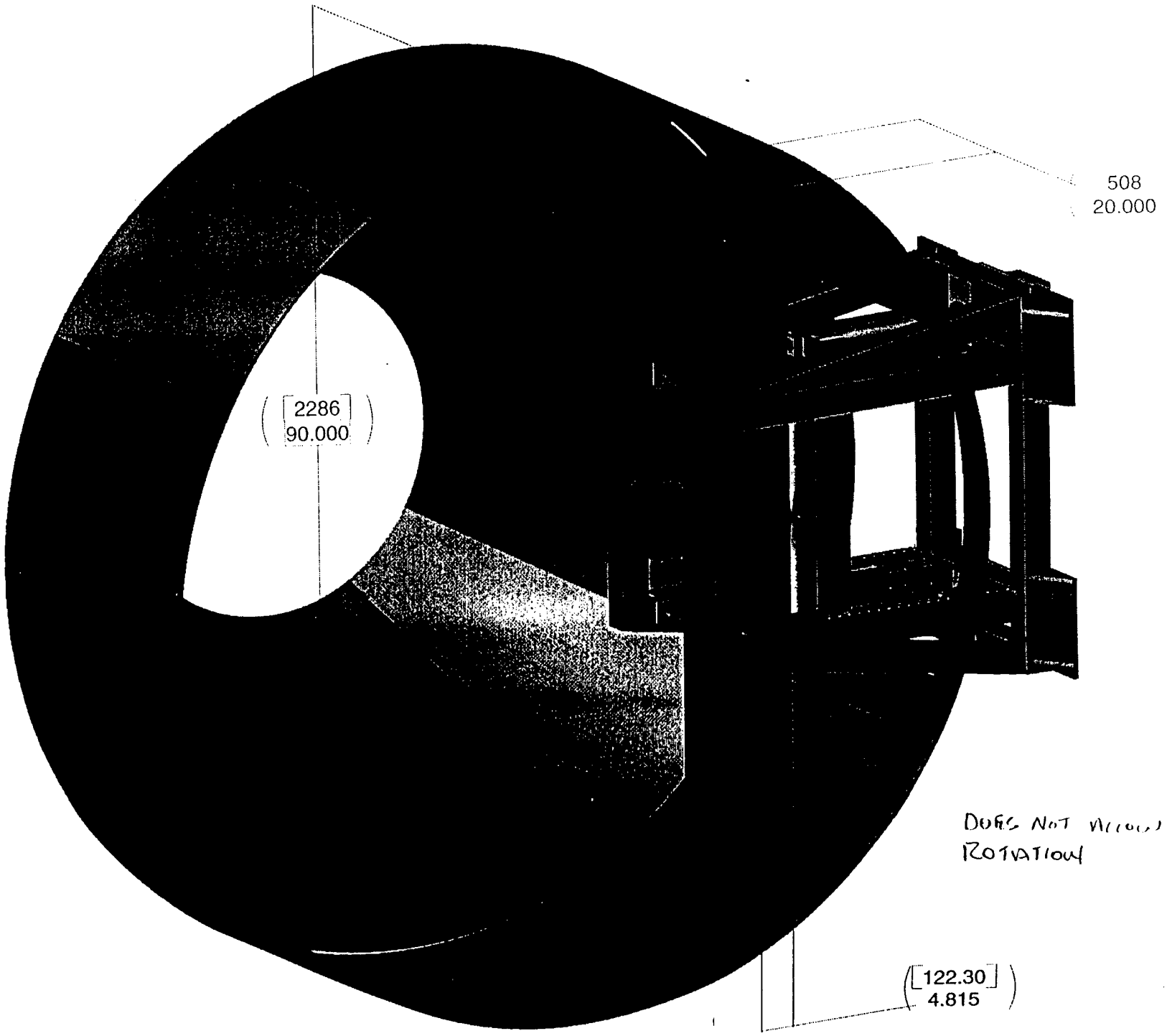
508
20.000
2286
90.000
122.30
4.815
DOES NOT ALLOW
ROTATION

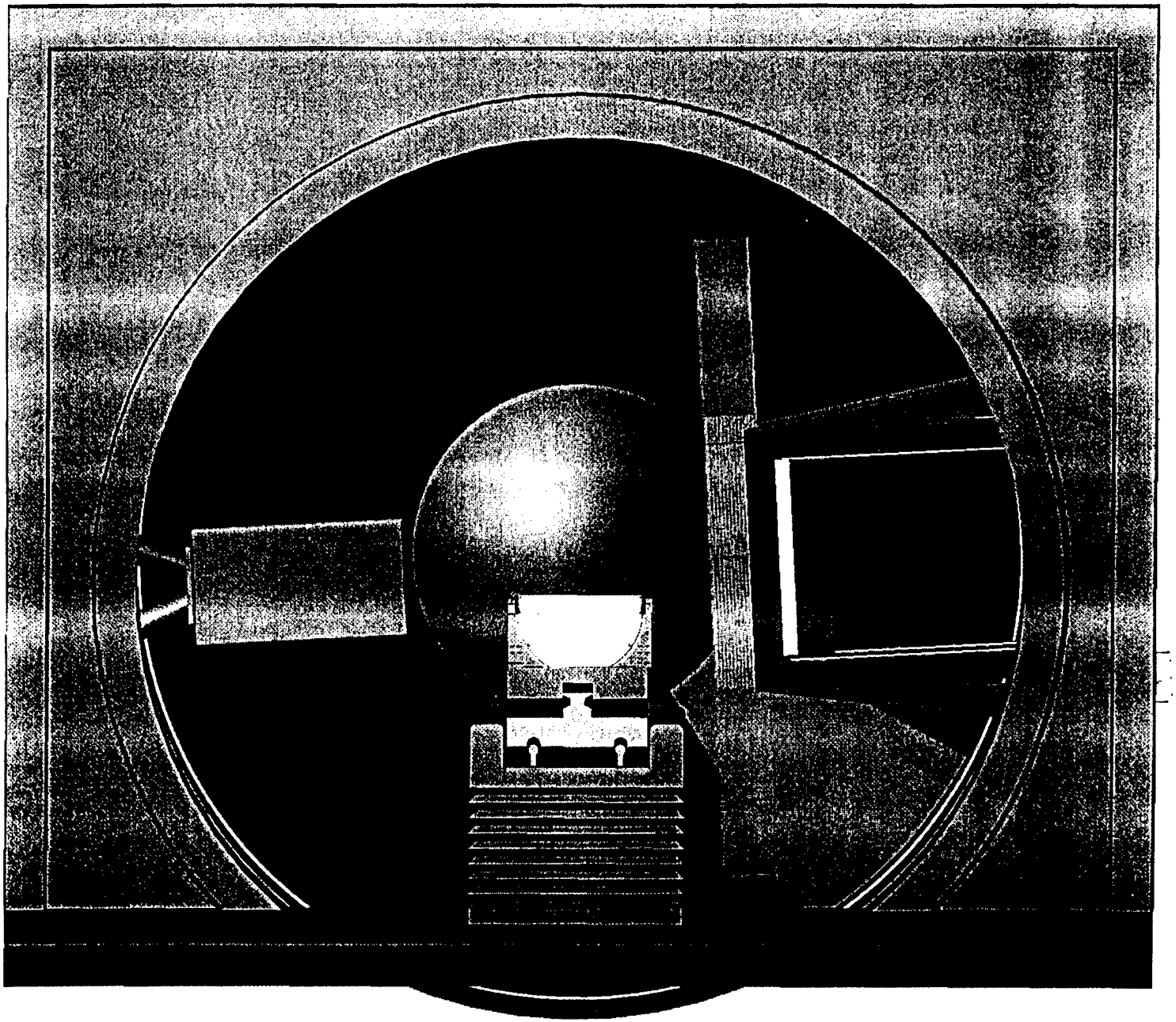

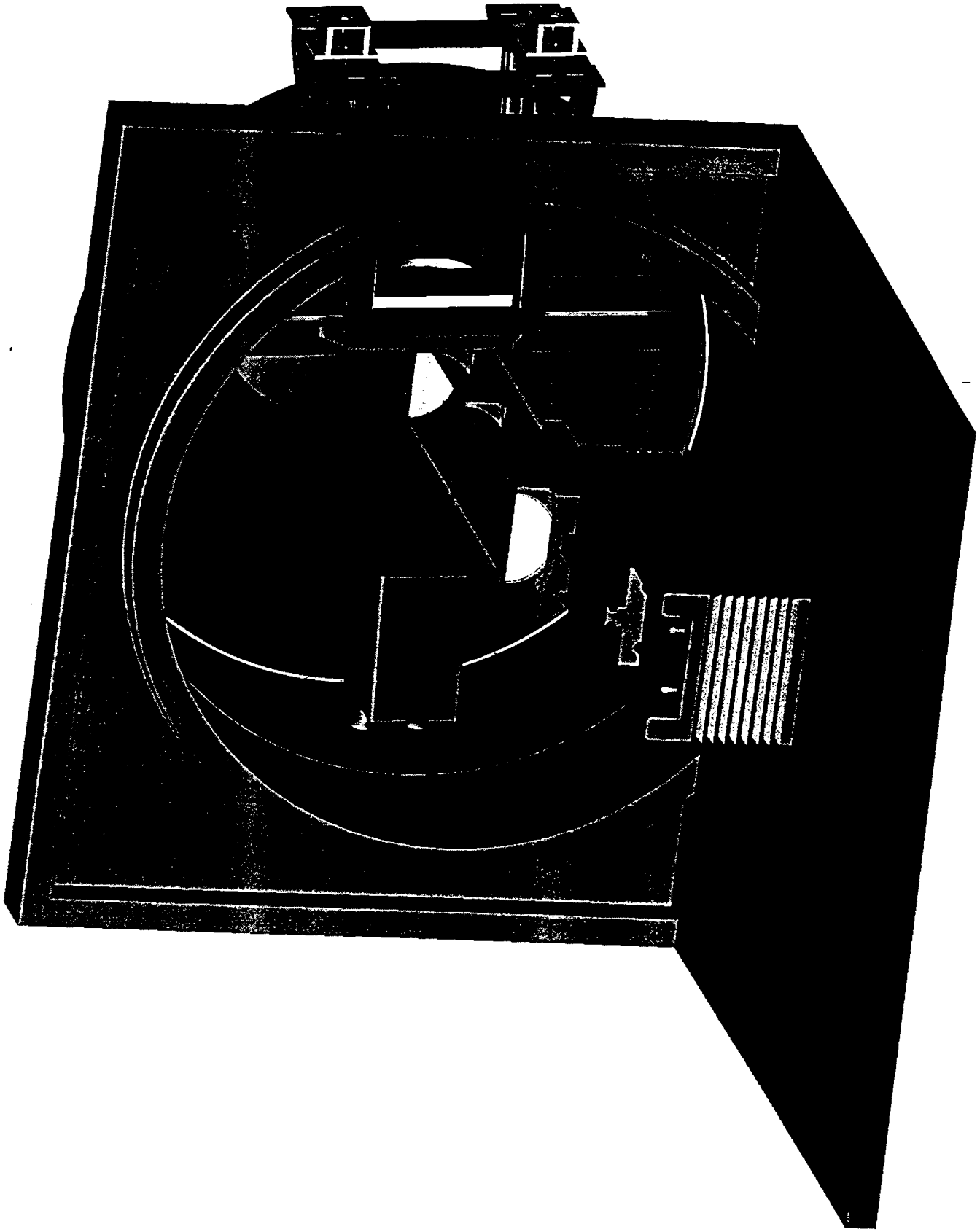

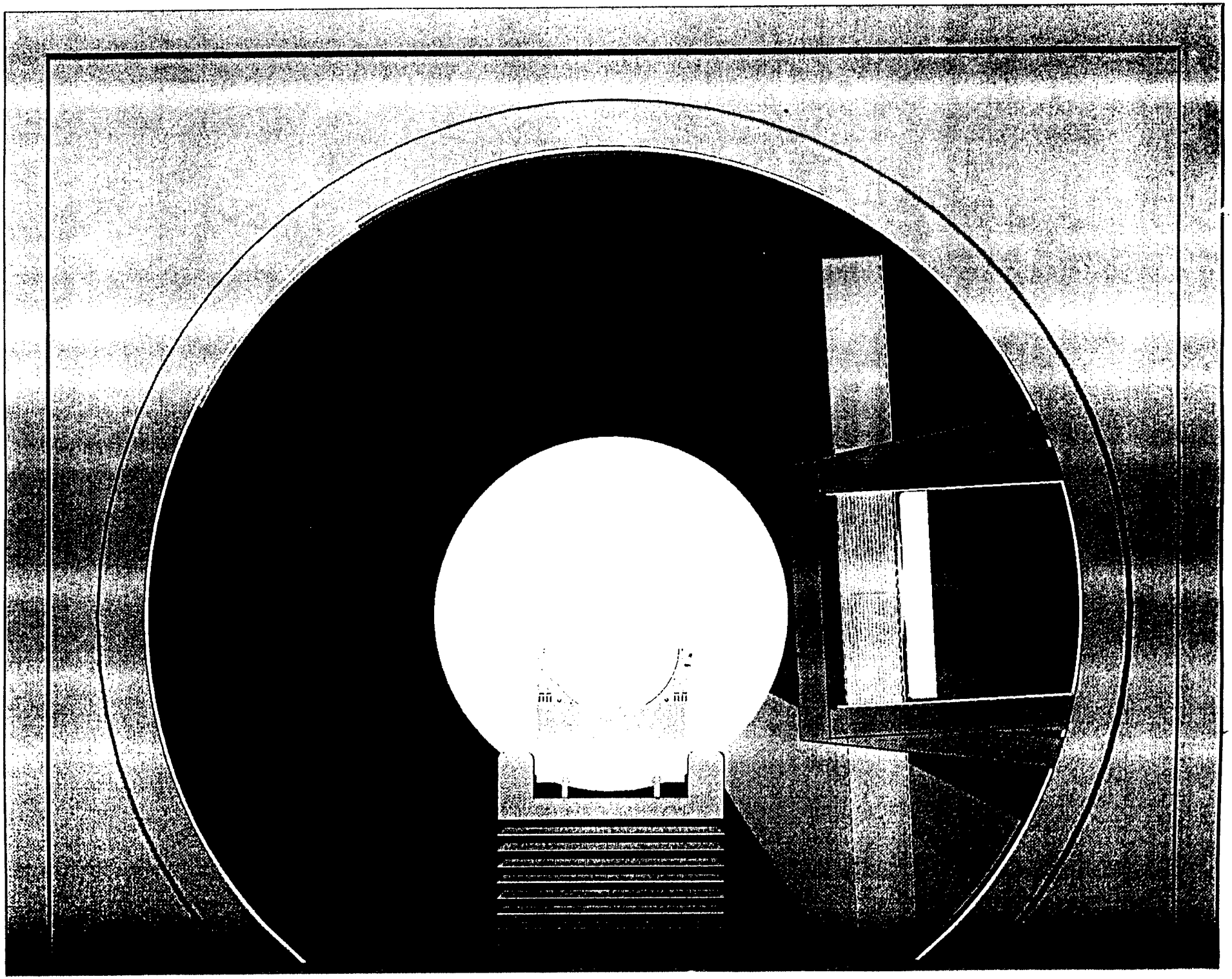

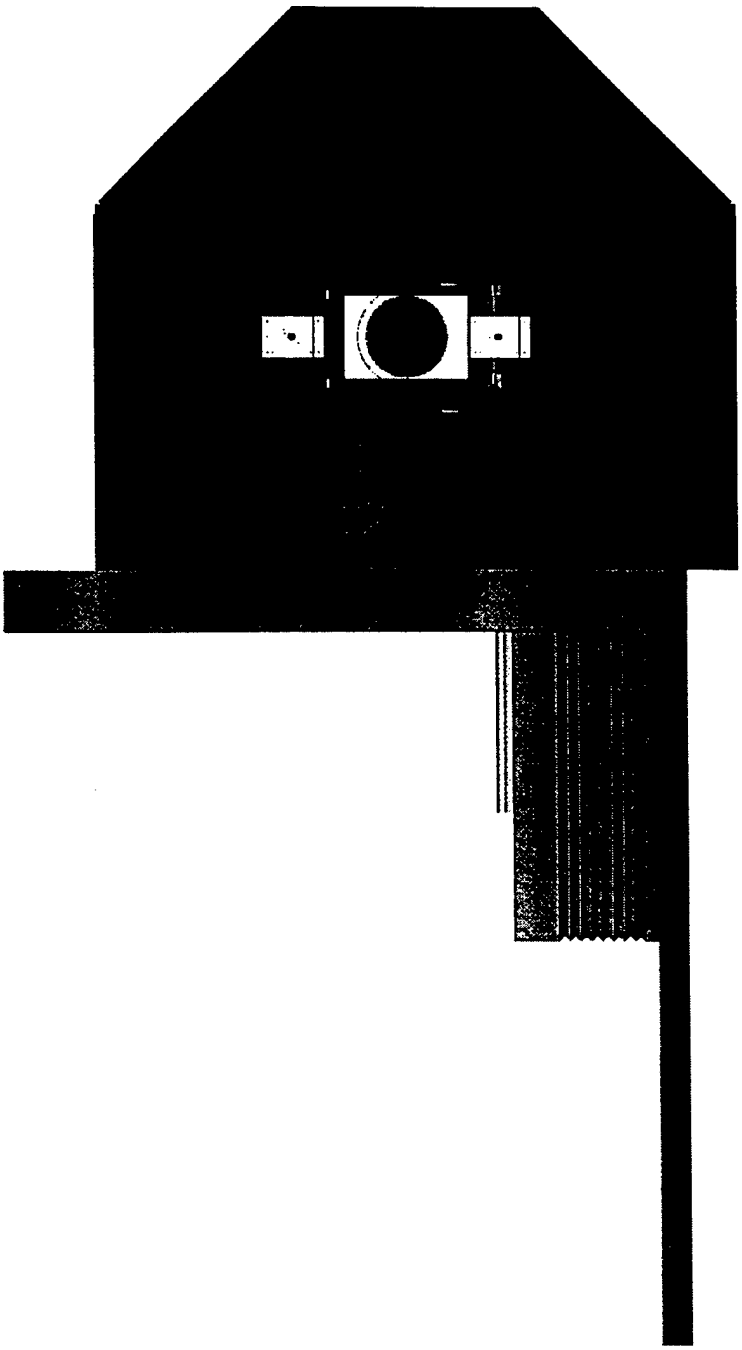

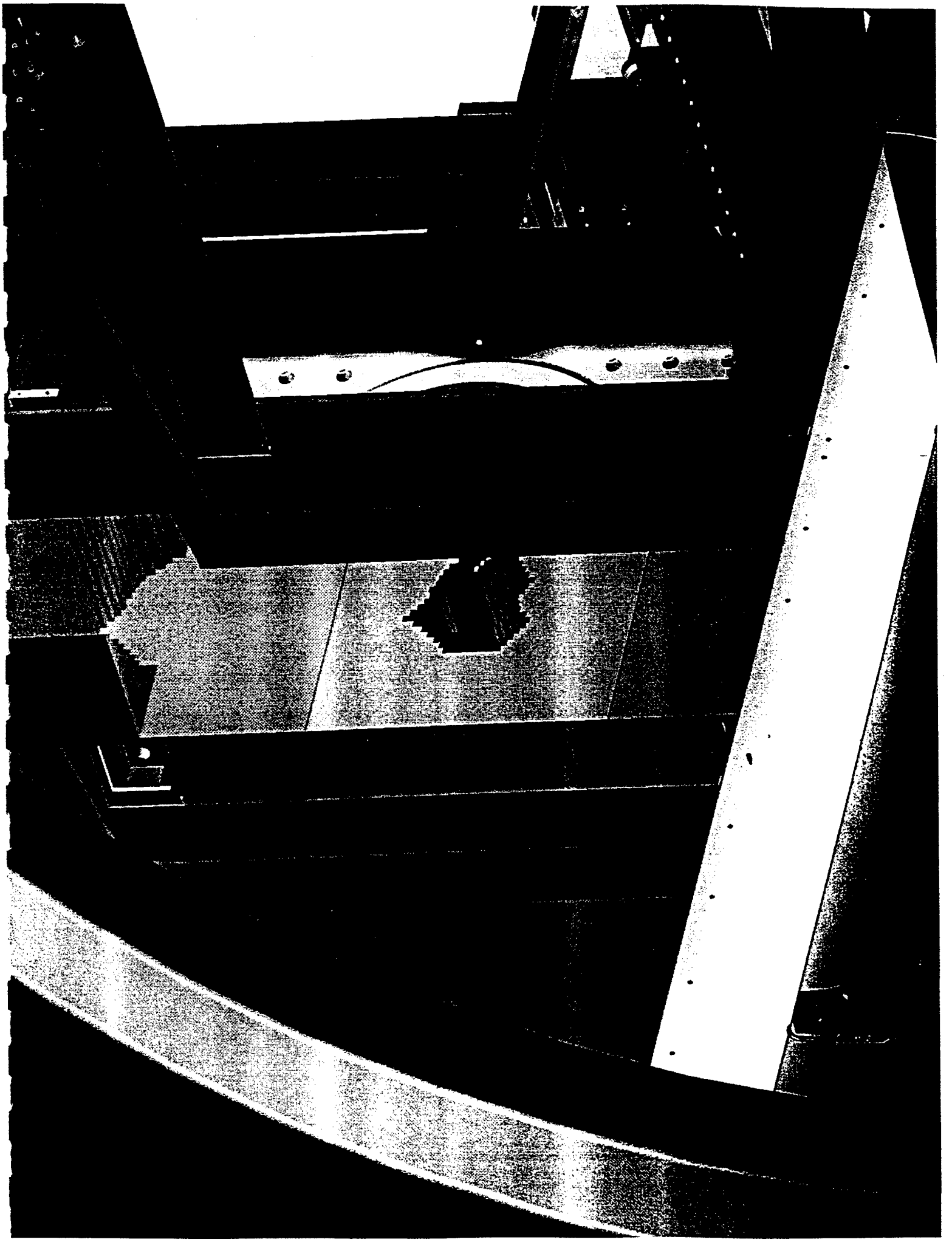

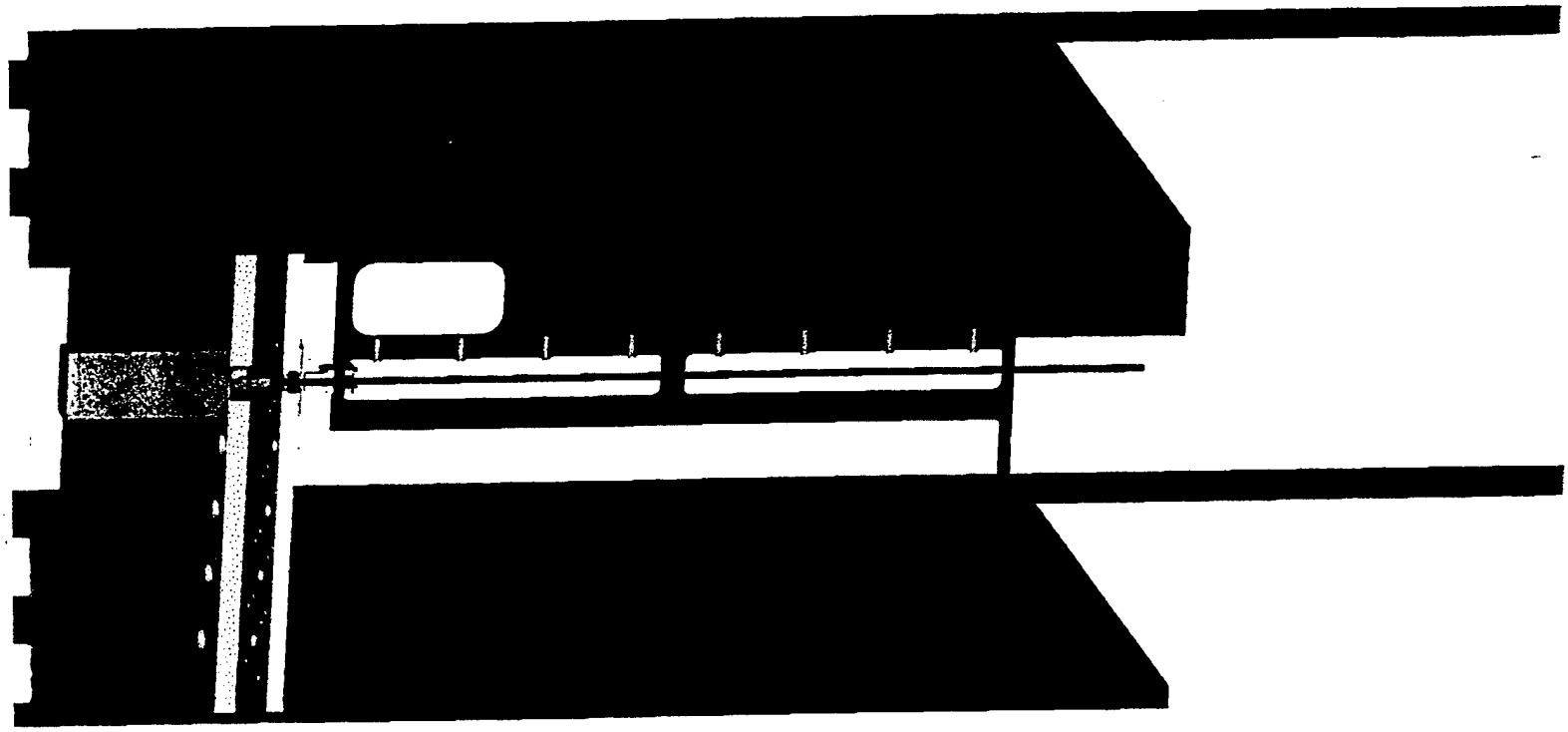

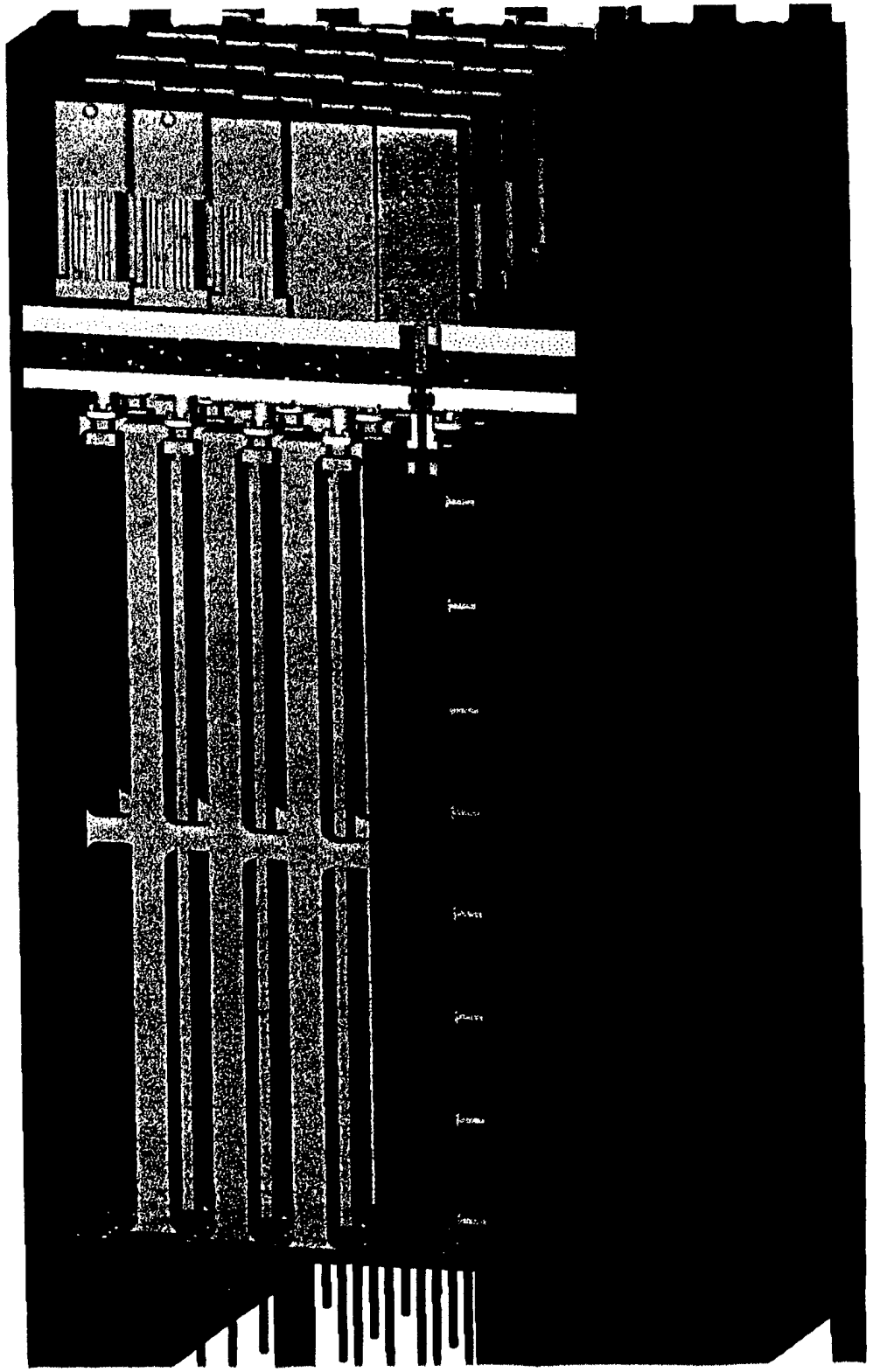

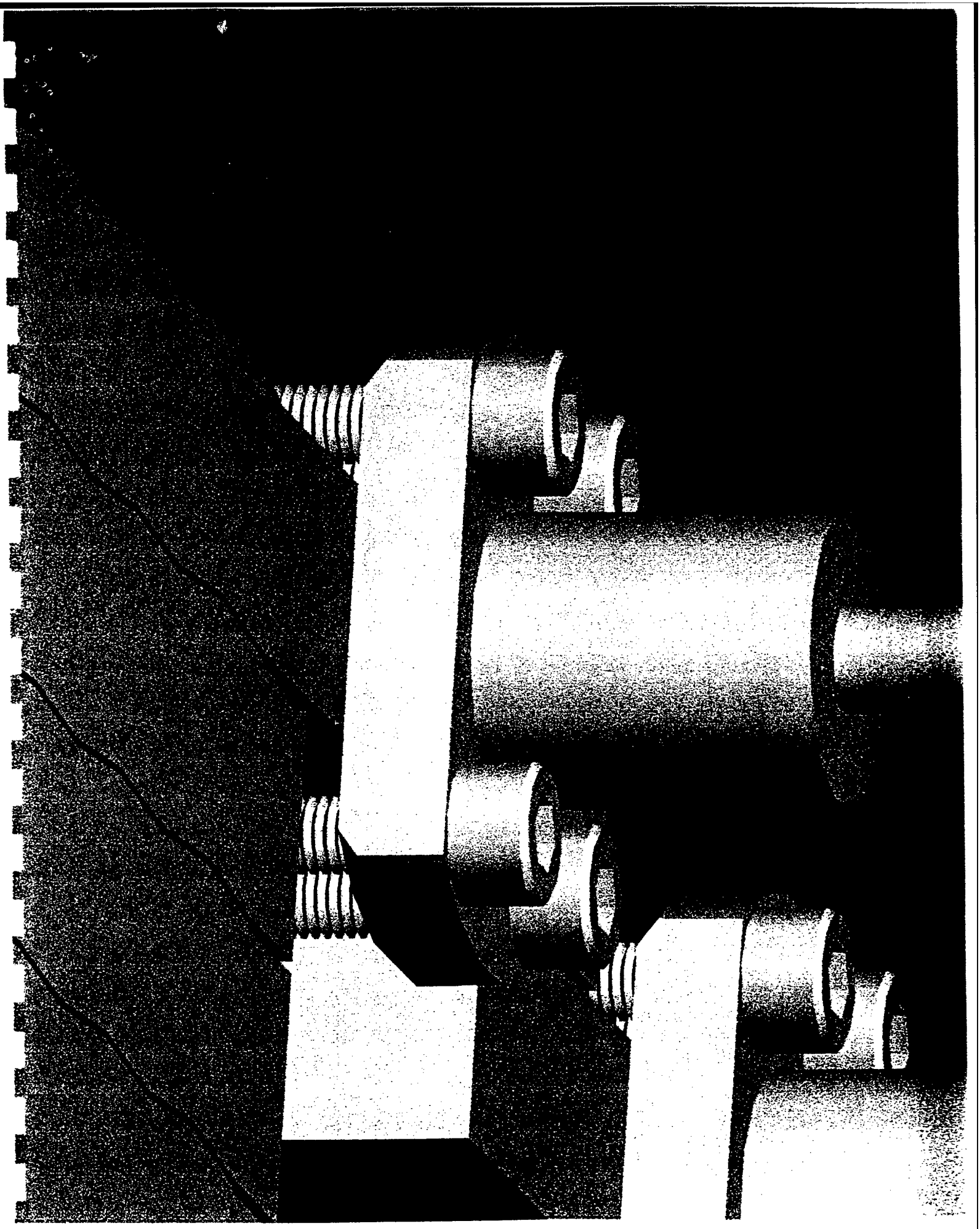

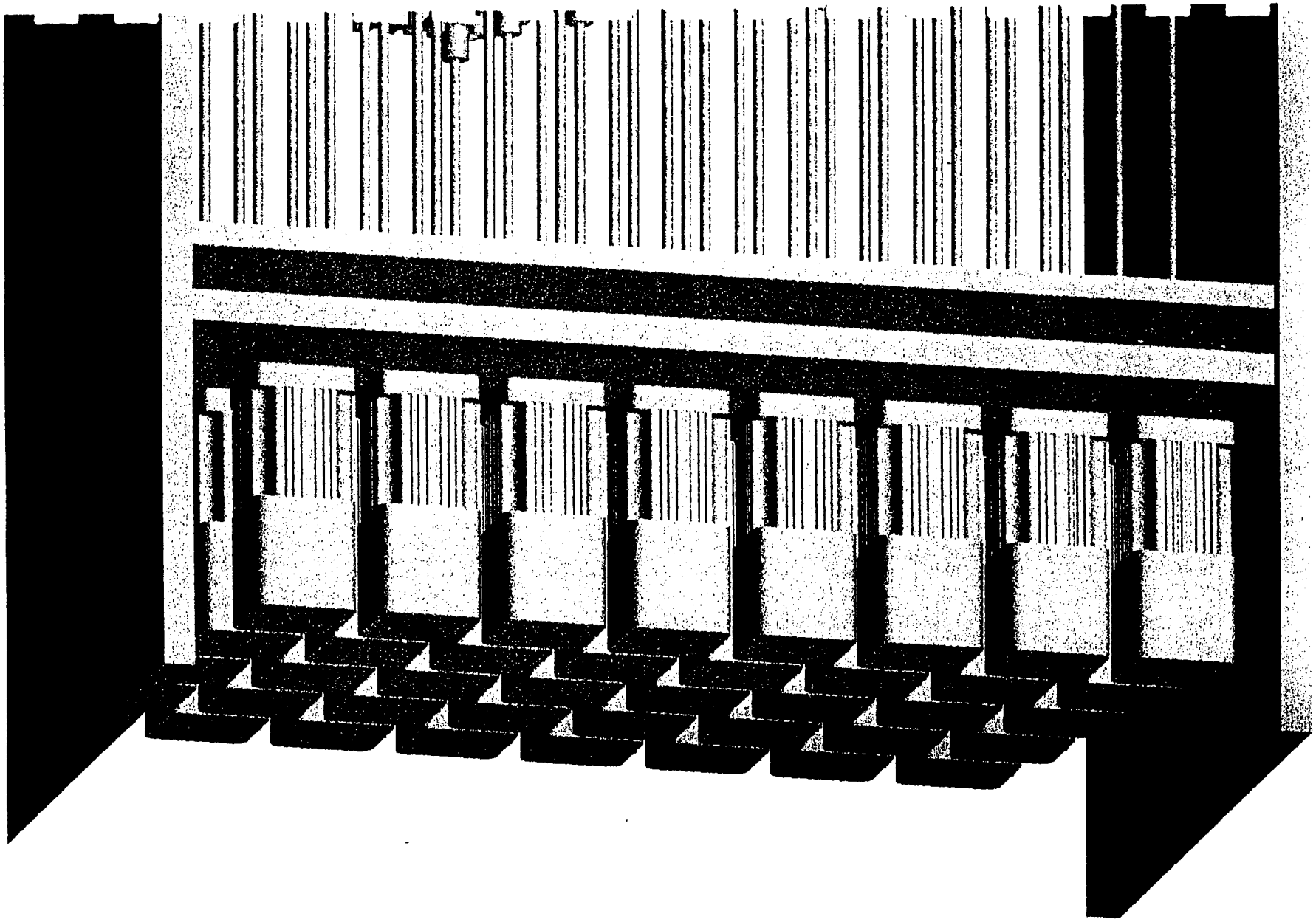

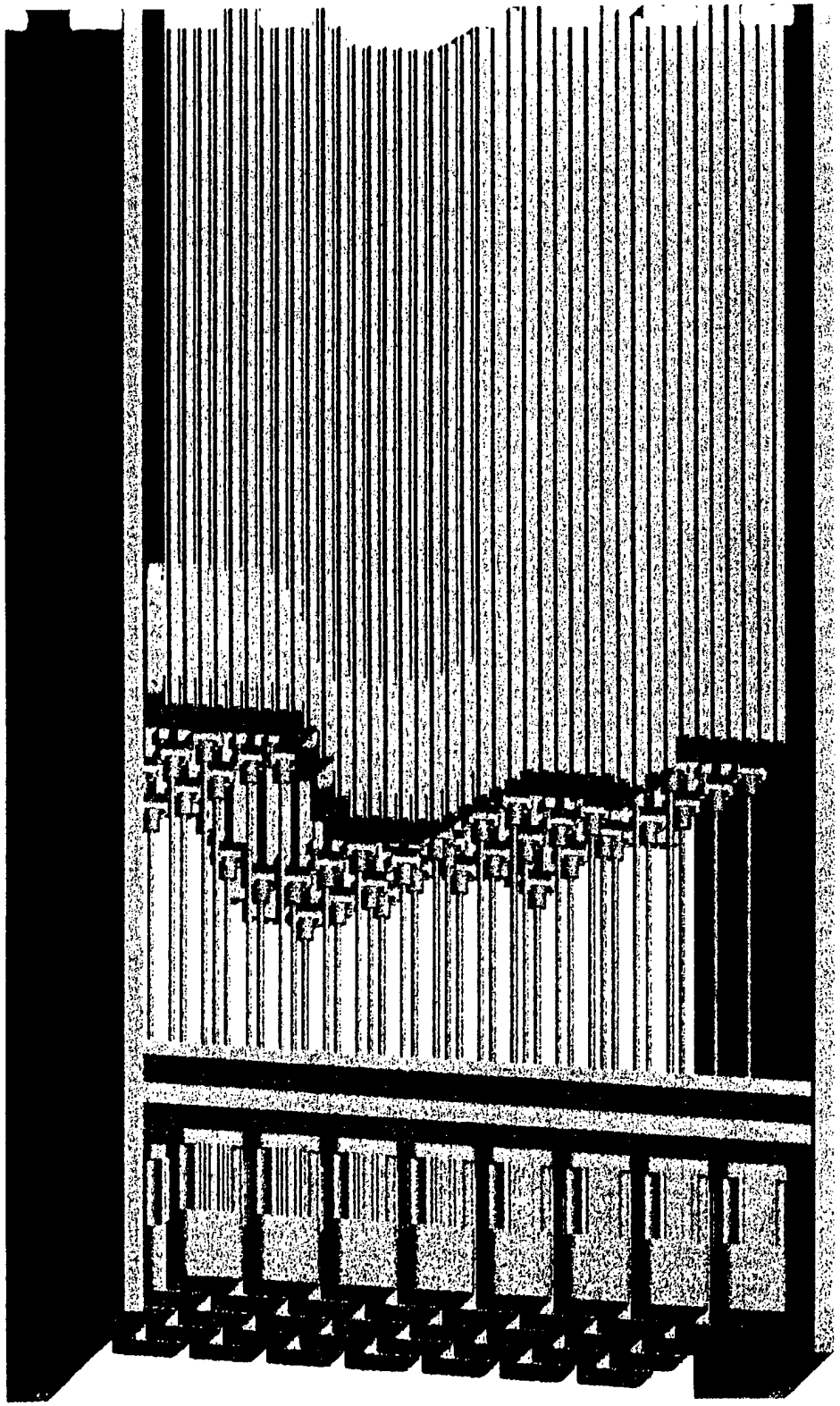

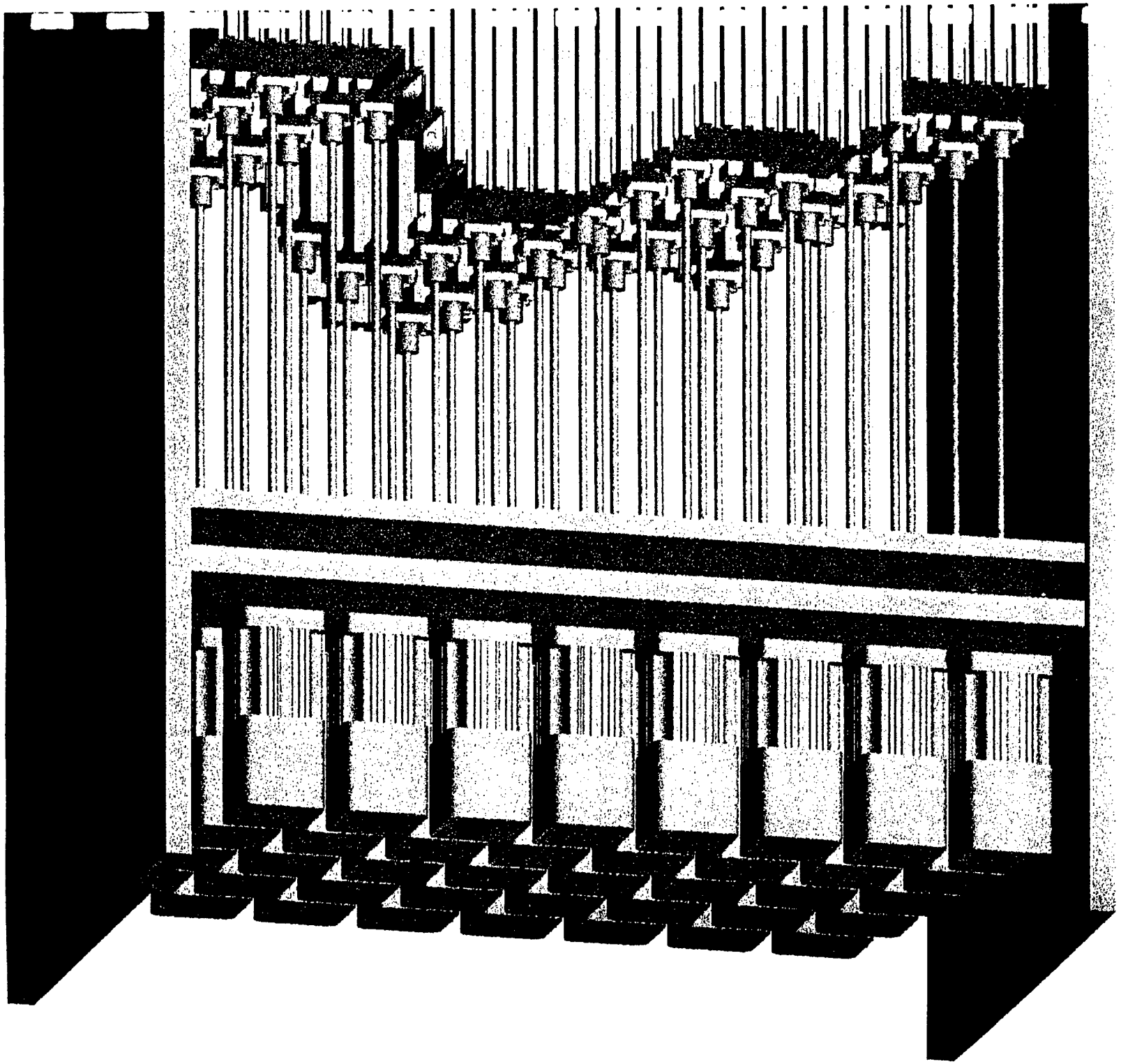

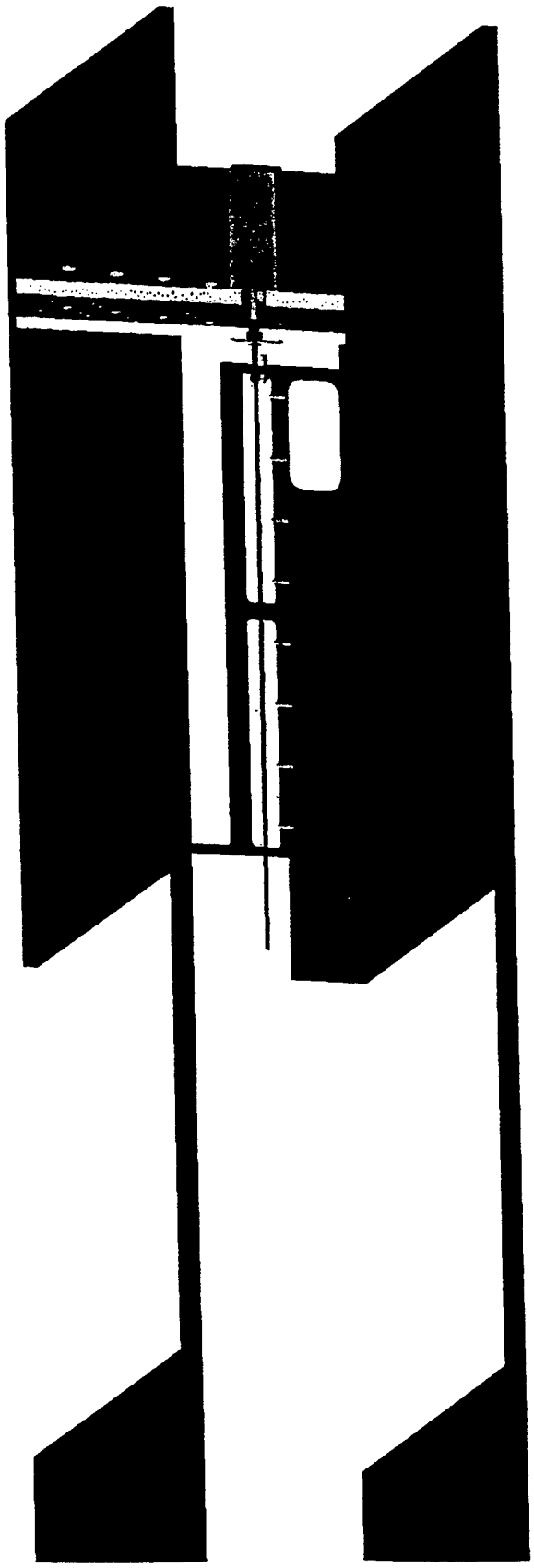

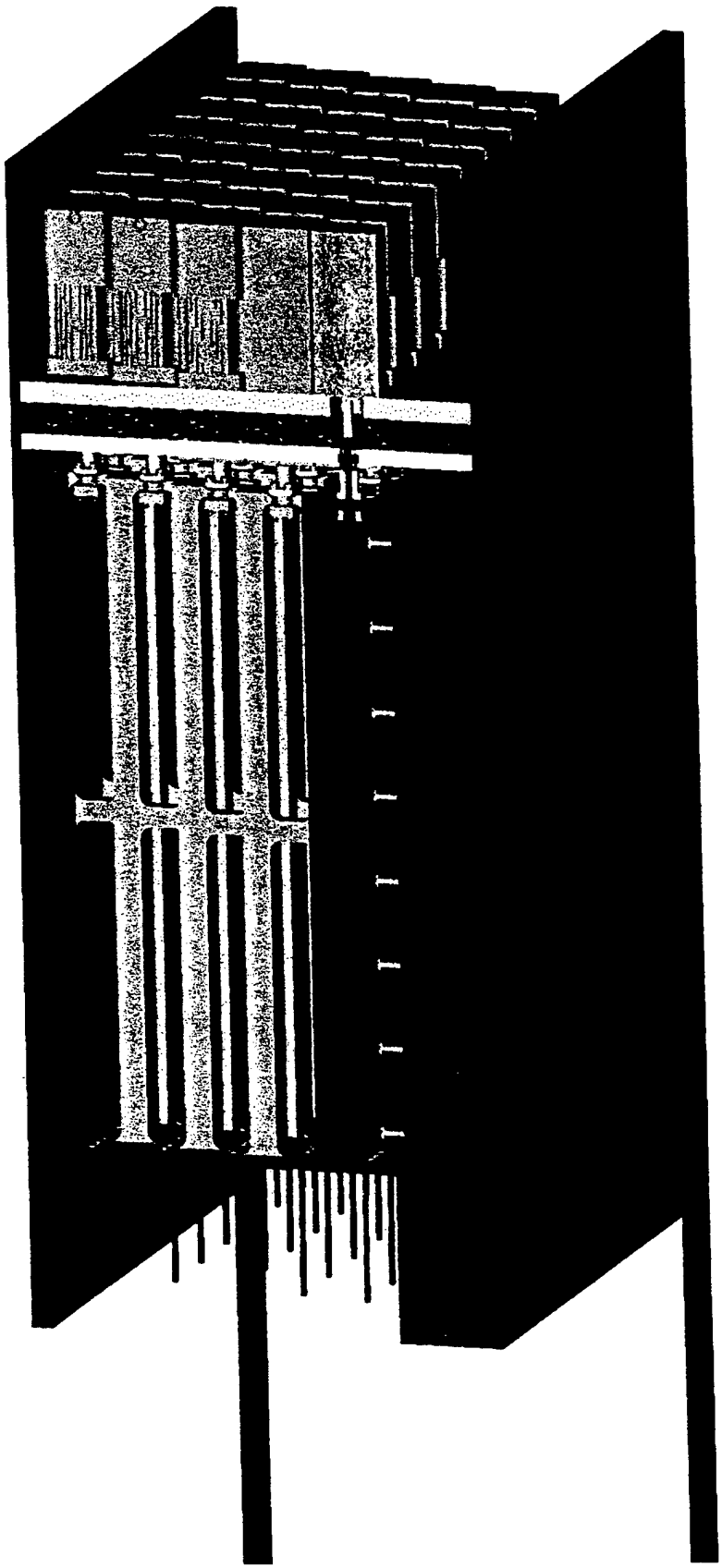

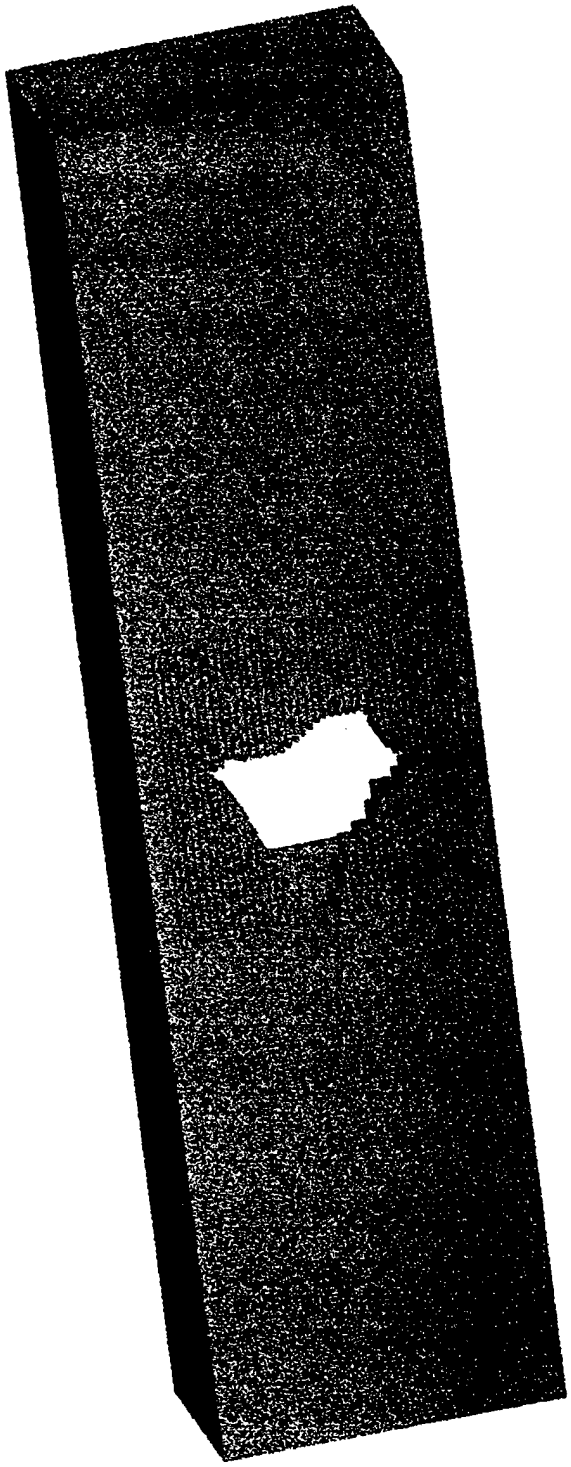

.me of Project Director: BAY

DESCRIPTION: State the goal of the project, including how it relates to improving health care and noting the advanced technology that will be developed or tested. Use succinct language to describe how the project goals will be achieved. **Do not exceed the space provided.**

The long-term goal of this project is to apply state-of-the-art technologies in gene therapy to increase the repair rate of all types of skeletal lesions, including the healing of uncomplicated fractures and also non-union fractures, the filling in of large bony defects due to trauma, the regeneration of bone in sites of avascular necrosis, the promotion of spinal fusion in degenerative disc disease, and the repair of bone density at specific local sites, such as the hip, in patients with generalized osteoporosis. We propose to use genes that code for growth factors, since growth factors are known to participate in the normal repair process of bony tissue. The growth factor genes that we have selected are bone morphogenetic protein-4 (BMP-4) and basic fibroblast growth factor (bFGF). These two genes were selected for several reasons, including the fact that they are the two most potent bone formation stimuli that have been discovered. Moreover, these two growth factor proteins have different mechanisms of action and, as such, could act synergistically to increase bone formation. The feasibility of the proposed work has been documented by our work and that of others with peptide growth factors. If the growth factors are effective, it is quite tenable that the corresponding gene therapy would also be effective, because in the proposed work we will use gene therapy as a sophisticated growth factor delivery system. Gene therapy has several advantages over inoculating growth factor proteins themselves, including the fact that one inoculation of growth factor genes into an osseous lesion could result in growth factor being present for a much longer period of time than might be achieved by direct administration of the growth factor peptide. While we have good evidence that gene therapy is feasible for skeletal repair, what we do not know is the experimental conditions which would allow us to employ gene therapy to stimulate deposition of a large amount of bone in a short period of time, which is a requirement for many skeletal lesions. This is the basis of the proposed work, namely to optimize gene therapy for skeletal repair. More specifically we propose to 1) inject the BMP-4, bFGF and combinations of the non-viral expression vectors driven with the viral CMV promoter directly into the rat tibial proximal metaphyseal marrow space test site and 2) inject the same therapeutic genes in a non-viral expression vector that is driven by a bone cell specific promoter developed from the bone sialoprotein (BSP) gene. These experiments will provide us with the information to optimize gene therapy for the repair of skeletal lesions. If our results are promising (as we anticipate from our preliminary data), this would warrant a strong effort towards developing gene therapy techniques in larger test animals and eventually humans.

PROJECT SITE(S) (organization, city, state):

Jerry L. Pettis VA Medical Center
Musculoskeletal Disease Center (151)
11201 Benton Street
Loma Linda, CA 92357

SEMI-ANNUAL PROGRESS REPORT
FY 1999 AWARD

ORIGINAL

Cooperative Agreement No.: DAMD17-97-2-7016

Subagreement No.: 50-FY99-LLVARE-Baylink

Project Title: Gene Therapy for Skeletal Repair

Principal Investigator: David J. Baylink, M.D.

Performance Period: December 1, 1999 through June 1, 2000

Signed: 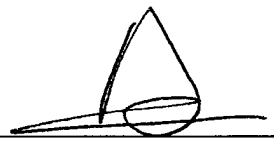 6-22-00

David J. Baylink, M.D. Date
David.Baylink@med.va.gov
Phone: 909-422-3101
Fax: 909-796-1680

Gene Therapy of Skeletal Repair

Project Director: David J. Baylink
Semi-annual Progress Report 12/1/1999 to 6/1/2000

I. Introduction

The long-term goal of this project is to apply state of the art gene therapy to increase the healing rate of all types of bone defects. Such therapy would be applicable to all types of skeletal lesions, such as the healing of fractures, including non-union fractures, the promotion of spinal fusion in degenerative disk disease, and the building up of bone density at specific sites, such as the hip, in patients with generalized osteoporosis. The genes we have chosen are growth factor genes that are known to participate in the normal repair process of skeletal tissues. Specifically, we have selected basic fibroblast growth factor (bFGF) and bone morphogenetic protein-4 (BMP-4), two of the most potent bone formation stimuli discovered to date. These two growth factor proteins have different mechanisms of action and may act synergistically to increase bone formation. It is our hypothesis that both growth factors applied in combination will lead to formation of bone with better mechanical properties than the application of each factor alone. In order to test this hypothesis during our three year program, we proposed to: 1) develop BMP-4 and bFGF expression vectors and optimize transfection of cells for growth factor production; 2) demonstrate that the growth factor produced by transfected cells is biologically active; 3) establish stable cell lines (stromal, fibroblast or osteoblast) from cells transfected with optimized plasmid vectors producing BMP-4 and bFGF to produce the appropriate concentration of growth factor to form bone when inoculated into the marrow space of the proximal rat tibia; 4) determine the optimal dose and the optimal exposure time for producing bone in our test site; 5) determine if there is a synergism between BMP-4 gene expression and bFGF gene expression to increase bone formation. These experiments will provide us with the information to optimize gene therapy for the repair of skeletal lesions.

II. Objectives for Period (12/1/1999-11/30/2000)

The first goal for this period was to:

- Determine if cells expressing both of the growth factors, bFGF and BMP-4, stimulate bone formation in the rat tibial marrow cavity more than each growth factor separately.

The steps required to complete this aim include:

- Inject cells producing bFGF and BMP-4 into the test site and determine levels of growth factors expressed and amount of bone formation.
- Inject plasmid DNA alone and complexed with carrier reagents and determine the amount of bone formation in the test site.
- Develop histological methods to detect bFGF and BMP-4 by immunohistochemistry in the test site.
- Optimize, by location and sample site selection, the use of pQCT for the measurement of bone formation.

The second goal for this period was to:

- Develop a natural promoter from the bone specific human Bone Sialoprotein (BSP) gene to replace the viral promoter in an enhanced plasmid vector which will express therapeutic levels of BMP-4 and bFGF when injected into the test site.

The steps required to complete this goal include:

- Preparation of the BSP promoter region from genomic DNA
- Insertion of the BSP promoter into a plasmid vector so that promoter specificity could be evaluated.
- Insertion of the BSP promoter into the VR1012 vector in place of a viral promoter to express marker genes and therapeutic genes.
- Prepare osteoblasts which express the bFGF and BMP-4 under the control of the BSP promoter.
- Inject the osteoblasts which express the growth factors into the test site and measure bone formation.

III. Progress Report for Period from 12/1/1999-6/1/2000

A. Preparation of a BMP-4 plasmid expression vector which produces therapeutic levels of biologically active BMP-4.

1. Development of the BMP-4 Bioassay

We have already reported that 10^6 Cos-7 cells produce up to 100 ng/ml of BMP-4-HA in the CM as determined by western blot analysis with an anti-HA antibody within 24 hours. It then became important to verify that HA-tagged BMP-4 was biologically active. To this end, a differentiation assay was developed based on the ability of BMPs to

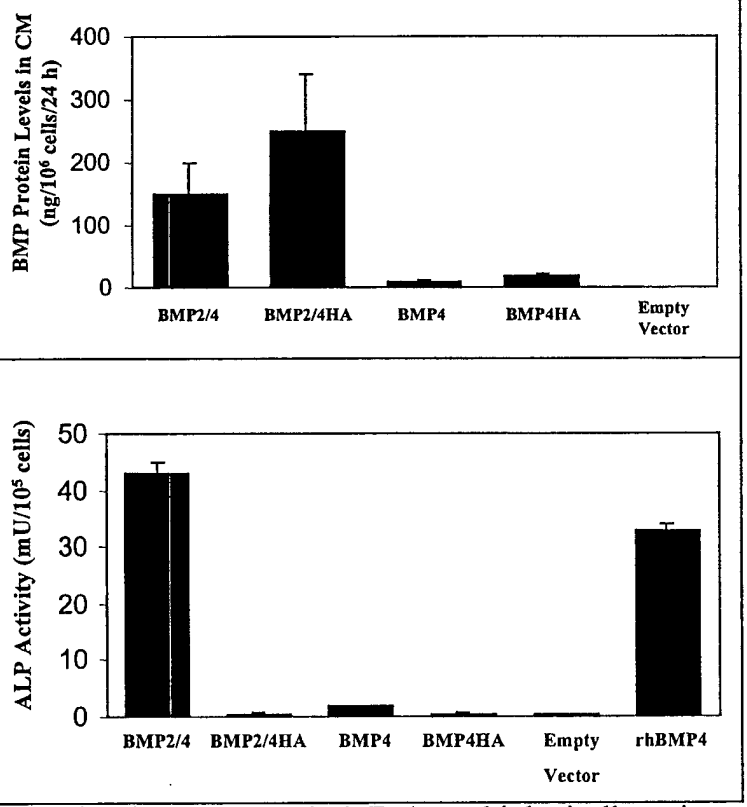

Figure 1. Analysis of BMP-4 expression products and bioactivity from various MLV BMP cDNA expression vectors. Upper panel. BMP4 and BMP-2/4 protein with or without the HA epitope tag was secreted from HT1080 cells after transduction with MLV vectors. More BMP was secreted when cells were transduced with BMP2/4 than with BMP4. The HA tag did not reduce protein expression.
Lower panel. The CM from HT1080 cells after transduction with various MLV vectors was collected and used to condition C2C12 cells. Only CM from HT1080 cells transduced with MLV based BMP2/4 vectors showed significant biological activity (stimulation of ALP activity). 80 ng/ml of rhBMP4 was added to the CM to stimulate ALP activity.

increase alkaline phosphatase (ALP) activity (a marker of osteoblast differentiation) in C2C12 mouse myoblasts to evaluate BMP-4 HA activity. To perform an ALP activity assay, C2C12 cells were plated at 1-5 x 10^4 cells per 24 well plate overnight in 500 ul of DMEM/10% fetal bovine serum. The medium was replaced with conditioned media (CM) for 24 hours by HT1080 cells transfected with a BMP-4 viral vector. ALP activity was determined 24 hours after media replacement.

ALP activity can be visualized in cell populations using the Sigma ALP staining kit. ALP activity can also be quantitated as previously described (Anh, et al. 1998).

2. Evaluation of the bioactivity of the BMP-4HA protein.

Protein production and bioactivity from the constructs, BMP-4 HA, BMP-4, BMP-2/4, BMP-2/4-HA in a murine leukemia virus (MLV) viral vector, were compared after transduction of HT1080 cells. Serum free media from transduced cells was collected after 48 hours of conditioning and assayed by western blot or was applied to C2C12 cells to assay for bioactivity. Figure 1(upper panel) indicates that from 10-100 fold higher levels of BMP2/4 was secreted from HT1080 cells transduced with a BMP2/4 expression vector compared to cells transduced with a BMP-4 expression vector. This was consistent with previous studies (Hammonds, et al. 1990) indicating that cells transfected with a BMP2/4 hybrid vector secreted more BMP-4 than did cells transduced with the wild type BMP-4 vector.

In addition, and more importantly, the BMP2/4HA and the BMP-4HA polypeptides were not biologically active while the BMP2/4 and BMP-4 polypeptides were biologically active. Figure 1 (lower panel) indicates changes in ALP activity observed after conditioning C2C12 cells with media from transduced cells. CM from cells transduced with the BMP-2/4 hybrid vector contains more biologically active BMP-4 than cells transduced with other vectors. From these results, the decision to use the BMP-2/4 hybrid cDNA for VR1012 plasmid vector development was initiated.

3. Preparation of a VR1012 with a hygromycin resistance gene for growth factor gene insertion and stable clone selection.

Because only 1/500 cells expressed β-gal after transient transfection with two separate plasmid vectors (pcDNA3.1 with a neomycin resistance gene and the enhanced expression VR1012 vector with β-gal), selection of stable clones expressing high bFGF or BMP-4 protein would be difficult and expensive if thousands of clones had to be screened as was required to select a high β-gal expressing stable clone for marking and in vivo test studies. Therefore, a 1.5 kb hygromycin resistance cassette was isolated from the pUC19-TK-hyg vector after digestion with BamHI/HindIII and was introduced into the Bal I site of VR1012 after blunt end ligation. This cassette was inserted into VR1012 in 2 orientations and selected with a negative orientation relative to the CMV promoter driven cassette to create hyg-VR1012. This was also selected in this way to reduce transcriptional interference between the adjacent transcription units to increase overall expression from this vector.

4. Development of a hybrid BMP-2/4 cDNA for insertion into the hygVR1012 vector

Hammonds, et al (1991) found that the Bone Morphogenetic Protein (BMP)4 was expressed in mammalian cells at very low levels and that related BMP2 was expressed at

much higher levels. A hybrid BMP2/BMP4 cDNA comparable to that described by Hammonds was prepared to improve BMP4 expression in fibroblasts and marrow stromal cells by Dr. Peng of the MDC Viral Core facility. To prepare this hybrid BMP, full length BMP2 and BMP4 cDNAs were prepared by PCR. *Bal* I restriction fragments were prepared from each BMP which divided them into prepro and mature BMP fragments. Hybrid BMP2/4 contained prepro BMP2 and mature BMP4 and was housed in the pBS plasmid vector (Stratagene).

To prepare the hygromycin selectable BMP2/BMP4 hybrid VR1012 vector, several steps were required: 1) the BMP2/BMP4 cDNA was removed from the pBS vector with *Not* I and *Cla* I; 2) the 5' overhangs were removed with mung bean nuclease to form blunt ends for ligation; 3) the hygVR1012 vector (see section B.2. below) was digested with EcoRV to create blunt ends for subsequent ligation; 4) the BMP2/BMP4 cDNA fragment was combined with the linear VR1012 vector in a 1:1 molar ratio and ligated at 12 °C overnight; and 5) the ligation products were introduced into competent INVαF' (Invitrogen) cells and several clones were tested by PCR for the BMP insert. Insert orientation was determined by restriction enzyme analysis.

One clone which contained the full length BMP2/4 cDNA insert in the forward orientation relative to the CMV promoter was sequenced. A full length cDNA in the correct orientation is ready for transfection into Cos-7 cells for assessment of protein production levels and amount of biologically active protein produced before preparation of stable fibroblast clonal cell populations.

5. Development of a BMP2/4 protein expression assay.

a. RIA: The core assay laboratory of the MDC attempted to establish an RIA for BMP4 or the BMP2/4 hybrid using several of the best commercial antibodies available. The assays were not sensitive below the 50 ng range and therefore were not adequate for our experiments.

b. Development of a BMP-4 Western blot procedure that can be used for BMP-2/4 and BMP-4 determination.

The MDC Core Assay Lab have developed and optimized the BMP4 Western blot procedure for analysis of BMP4 expression after retroviral transductions. This assay will be used to follow BMP-4 production from cells transfected with the hygVR1012-BMP2/4 vector. To conduct this assay the hygVR1012 BMP2/4 vector will be transiently transfected into 10^5 HT1080 cells and the CM will be collected 48 h after transfection and stored at –20 °C. The cells will then be lysed and the lysate stored at –20 °C. Cell lysates and CM will then be run on a 12% polyacrylamide gel and blotted onto PVDF membranes. BMP4 is detected by ECL (Enhanced Chemiluminescence, Pierce) after incubation with an anti-human BMP4 monoclonal antibody (R & D Systems) at a concentration of 0.5 ug/ml of purified IgG. Human recombinant BMP-4 (Research Diagnostics Inc, Flanders, NJ) is used as the standard.

B. Development of other hygVR1012 expression vectors.

1. Concentrations of hygromycin required to select stable cell lines. In order to determine the selection conditions for various cell populations with hygromycin, cultures of rat stromal cells, osteoblasts and fibroblasts were exposed to a range of toxin concentrations

from 50-250 ug/ml. The concentrations that we found effective in killing untransfected cells were 50 ug/ml for stromal cells and osteoblasts and 100 ug/ml for fibroblasts, respectively.

2. Development of the hygVR1012-bFGF expression vector.

bFGF was inserted into the hygVR1012 vector and was used to transfect Cos-7 cells. The bFGF ELISA of the CM indicates that the new hygVR1012 vector expressed bFGF at levels similar to the original VR1012 vector (88% + 19% of control, n=6). The insertion of the hygromycin cassette immediately adjacent to the CMV promoter did not impair expression of bFGF. It is anticipated that preparation of this vector will provide more positive clones for stable stromal, fibroblast and osteoblast cell line preparation compared to the dual plasmid vector transfection scheme utilized previously. No adherent stable stromal clones expressing β-gal or bFGF were generated using the dual plasmid vector transfection scheme.

3. Development of β-gal hygVR1012 vector.

The β-gal cDNA was removed from the pcDNA3.1 vector (Invitrogen) with *Not* I. The cDNA insert was inserted into the *Not* I site of VR1012. This vector will be used for marking studies to follow cell populations in vivo.

4. Development of the VR1012 SEAP vector and SEAP assay protocols. Because the results obtained with β-gal in the past could frequently not be carried over to our growth factor constructs, we wanted an alternative reporter construct to provide a marker gene control of a secreted protein. A good candidate is the secreted human placental alkaline phosphatase (SEAP) system, which has been recently used as a model to study the kinetics and regulation of expression of secreted proteins. Vical has provided the SEAP-VR1012 plasmid vector (called VR3301).

The assay for the heat resistant secreted enzyme is extremely sensitive and inexpensive. Methods for tissue staining of alkaline phosphatase (ALP) activity and for analysis of this activity in the serum have been established in our laboratory. We determined that all endogenous enzymes are inactivated by the heat inactivation step (30 min at 65 °C) both in the conditioned medium and in the cell lysates. On a per cell basis, osteoblasts secrete the highest amount of SEAP into the medium, while secreted levels from stromal cells and fibroblasts were 73% and 25% respectively of the osteoblast value. The lower level in fibroblasts was due to the lower transfection efficiency.

Heat-resistant ALP activity in the cell lysates was remarkably low, indicating that osteoblasts secreted 97% and stromal cells 91% of the total enzyme activity (cell lysates in fibroblasts were below the detection limit of the assay). From these results we can conclude that the stromal cells which in our experience have not secreted growth factors very well, have the capability of secreting SEAP very efficiently. This may therefore warrant a closer look at the SEAP signal sequence, which is the unmodified 22 amino acid signal of human placental ALP. The only modification of this construct was to truncate the C-terminal of the protein coding region, thereby eliminating the membrane anchor domain of the native enzyme.

C. Preparation of stable cell lines expressing marker genes or growth factors.

1. Use of alternative transfection methods to create cells for selection of stable clones producing growth factors.

In order to increase the chance to get stable genomic integration of the plasmid and strong expression, we tried different transfection methods.

Effectene (Qiagen) was superior in the number of stable clones produced to the calcium phosphate precipitation method, superfect (Qiagen) or electroporation with linear VR1012 plasmid. Effectene was used to prepare the hygVR1012-β-gal and hygVR1012-bFGF clonal cell populations described below.

We found that marrow stromal cells and osteoblasts stopped growing during or soon after the selection process was complete and could not be used to provide the stable clonal cell lines that expressed marker genes or growth factors. We have therefore focused our efforts on the production of stable fibroblast cell lines because 1) Dr. Qin, an MDC investigator, was able to maintain the adult skin fibroblasts under selection for more than 6 months after transduction with an MLV vector expressing PTH and 2) in fibroblasts, we have maintained β-gal expression from the hygVR1012-β-gal vector under hygromycin selection for 6 weeks, which is longer than demonstrated by stromal cells and osteoblasts.

2.Establishment of stable rat fibroblast cell lines expressing growth factor or marking genes for in vivo studies.

a. General transfection and stable clone isolation protocol.

Effectene transfection was used to prepare stable fibroblasts. On the day prior to transfection, 5 X 10^5 cells were plated per 10 cm dish in DMEM with 10% calf serum (CS). The transfection mixture was prepared according to the manufacturers instructions and contained, per dish, 15 ug of plasmid DNA solubilized in 500 ul of EC buffer, 45 ul of Enhancer, 35 ul Effectene, and 4 ml of DMEM with 10% CS. The cells were washed with serum-free DMEM and then incubated with the transfection mixture for 5 h at 37 C. After washing with DMEM, the cells were again cultured in DMEM with 10% CS. Hygromycin B (100 ug/ml) was added 48 h after transfection and the medium was changed every 3-4 days. Resistant colonies were isolated with cloning rings after 2-3 weeks, and transferred to 6- well plates.

b. Preparation of stable rat fibroblasts with hygVR1012-β-gal.

Normal rat skin fibroblasts from adult rats were transfected with linear plasmid DNA. Cells were grown in a selection medium and clonal populations were selected, frozen or expanded. Clonal cell lines expressing β-gal have been obtained.

c. Preparation of stable rat fibroblasts with hygVR1012-bFGF.

Normal skin fibroblasts from adult rats were transfected and selected as described above. Selection is on-going and has been conducted as described in the previous section. Sixty individual clones are now being followed for stability and level of growth factor production. The lines have been stable for 6 weeks.

d. Preparation of stable rat fibroblasts with hygVR1012-BMP2/4

Stable cell lines will be produced as described above as soon as protein expression levels and biological activity can be assessed in Cos-7 cells that are transiently transfected with the hygVR1012-BMP2/4 vector.

3. Use of the photochemical transfection method to prepare large numbers of transiently transfected cells.

In order to increase the number of transfected cells that can be used for selection of stable transfectants with hygromycin, or to prepare a large number of transiently transfected cells that could be used directly for in vivo gene therapy experiments if stable lines cannot be maintained, we will test the recently described photochemical transfection method (Hogset, et al, 2000). The authors have described transfection efficiencies with various cell lines between 40-60%. We expect that this will greatly increase the number of positive clones, since our optimal transfection efficiencies using the Effectene reagent are 2-4% for normal rat fibroblasts.

To conduct photochemical transfection, cells are incubated with aluminum phthalocyanine photosensitizer ALPcS2a (Porphyrin Products, Logan UT) for 18 h. Plasmids are complexed with poly-L lysine at a charge ratio of 1.7 and the cells are transfected with 25 ug of DNA per 10 cm petri dish. The cultures are then exposed for 4 minutes to a light source through a long-pass filter with 550-600 nm cutoff in order to activate the photosensitizer. This light activation leads to rupture of endosomal and lysosomal membranes, releasing the endocytosed plasmid DNA into the cytosol. Subsequent selection for transfected cells in hygromycin and testing of individual clones for growth factor expression will then be carried out according to standard procedures.

D. Development of the rat tibia model for gene therapy.

1. In vivo testing of β-galactosidase marked marrow stromal cells for engraftment.

Normal rat marrow stromal cells were transduced with an MLV virus which expressed β-gal to mark the cells so that the fate of cells could be followed in vivo.

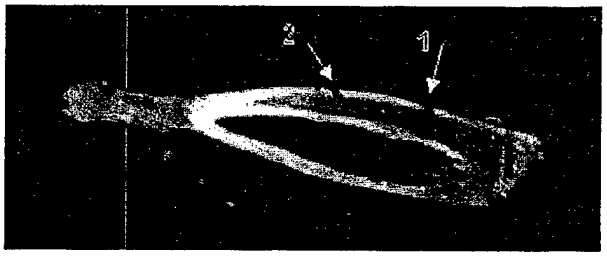

Figure 2. Genetically altered rat marrow stromal cells (MSCs) do not effectively engraft in the rat tibial marrow space after injection. Upper panel. Longitudinal section of tibia with arrows showing position of drill holes used for cell injection. 50 ul of MSCs (2×10^6) transduced with MLV-β-gal virus and expressing β-gal were injected into the site 2 drill hole. Maintenance of β-gal expressing MSCs in this site was evaluated at 1 h, 24 h and 6 days after injection by histology. Lower panel. Histologic staining of β-gal expressing MSCs in the marrow 1 h after injection. A few β-gal expressing cells (blue stained cells) were found in the marrow 1 day after injection but no cells were observed 6 days after injection (data not shown).

These cells were used to study the expression patterns, location and lifetime of these marrow stromal cells after being injected into the tibial site. When 2 x 10^6 of these cells were injected in 50 ul of PBS into the marrow cavity, many blue cells were found in the marrow cavity after histological staining 1h after injection (Figure 2). A few cells remained after 24 h but after 6 days no β-gal producing cells were found in the rat bone marrow (data not shown). In contrast, when the same β-gal producing marrow stromal cells were attached to Cytodex beads (collagen coated dextran beads), β-gal stained cells were observed up to day 6 (Figure 3). These results indicate that to retain cells in this test

Figure 3. Survival of genetically modified rat marrow stromal cells (MSCs) attached to cytodex beads in the tibia marrow space.
Upper panel. MSCs attached to Cytodex beads (170 μm average diameter) were stained for β-gal activity. Blue staining indicates that MSCs attached to the bead surface continued to express β-gal activity.
Middle panel. A cross-section of the tibia was examined for the presence of Cytodex beads after injection into the marrow cavity through the site 2 drill hole (Fig. 2). Backlighting of the sample was used to show the location of the Cytodex beads (center) in the metaphyseal marrow cavity. Cortical bone appears as a dark outline surrounding the marrow cavity.
Lower panels. Sections prepared from the tibia 6 days after injection of cytodex beads with β-gal MSCs were stained for β-gal activity. Two views of the same section show a cluster of beads with very strong β-gal staining (left), and beads with fewer blue β-gal positive cells (right). This indicates that significant numbers of genetically altered β-gal expressing cells remained at the tibial test site when a carrier material such as cytodex beads is present

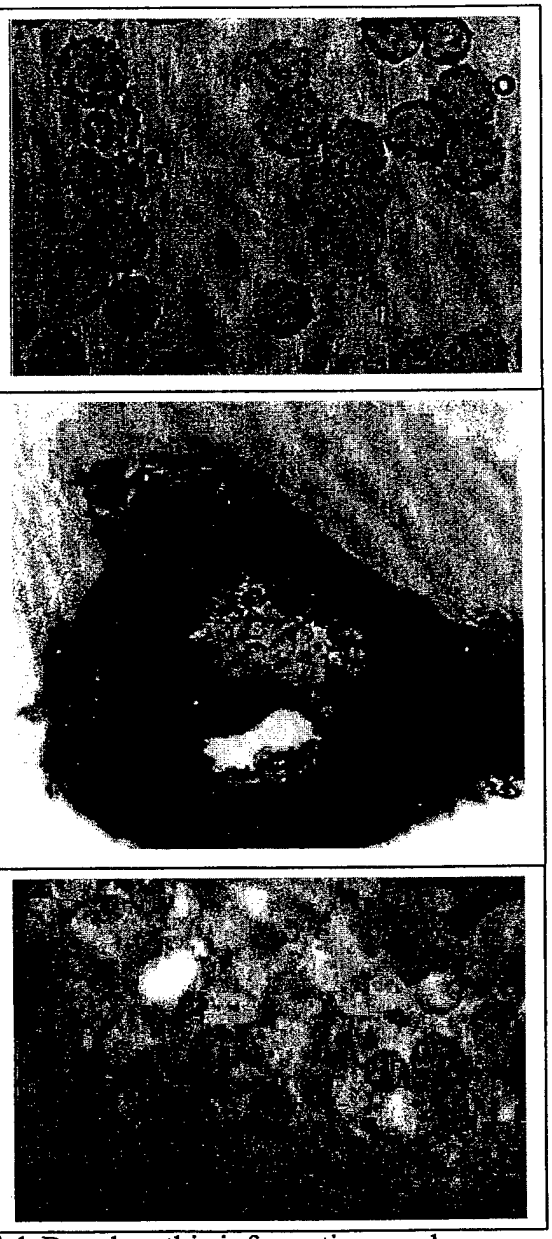

site, they must be attached to a carrier material. Based on this information, we have begun to test collagen based matrix materials for effects on cell viability that could be used to maintain our genetically engineered cells in the tibial test site.

2. Use of a collagen matrix to imbed cells for in vivo implantation.

Several publications describe the use of acid soluble collagen either from the rat tail or from bovine skin for the preparation of embedded cells for in vivo implants. While cells are not dividing in this matrix, they remain viable and retain the ability to secrete proteins. An injectable or implantable collagen matrix has been used by others as a delivery and depot vehicle for plasmids or *ex vivo* modified cells. Using acid soluble bovine skin collagen from Sigma and procedures described in the literature, we have been able to get consistent gel formation after the neutralized collagen solution is warmed to 37 °C. We have embedded β-gal expressing fibroblasts in this matrix and found that the cells are viable in culture for at least two weeks.

A recent publication by Krebsbach, et al. (2000) has shown that fibroblasts expressing BMP-7 when incorporated into collagen based gelfoam led to bone formation in a critical size defect in the calvaria of rats.

Based on these studies and our results, we will inject plasmid DNA in the semi-solid collagen gel with and without non-toxic lipid transfection reagents. We will also inject the semi-solid gel containing the stably producing fibroblast cell lines and fluorescent beads into the tibial test site. The fluorescence from the beads will provide a mechanism to determine if the cells and collagen gel remain at the test site for the duration of the in vivo experiment. An amendment to include non-toxic biomaterials (collagen, beads and lipids) with cell injections into the tibial test site will be submitted to our animal committee for its July meeting for consideration of this minor change in animal protocol.

E. Development of immunohistochemical staining of bFGF for in vivo localization.

Dr. Wergedal and Dr. Shen in the MDC Histology Core Laboratory have developed the immunohistochemical method to locate bFGF protein expression at sites of bone formation (Figure 4). To conduct this assay, bone samples were sectioned (5μm/section). These sections were deparaffinized, rehydrated to H_2O and incubated in 3% H_2O_2 in 70% methanol/PBS for 15 minutes. The samples were blocked with 15% normal goat serum for 30 minutes at room temperature. The following immunostaining procedures were carried out at 37 ° to 40 °C with an automatic immunostainer (Ventana, AZ). The specimens were first digested for 12 minutes in 0.2% hyaluronidase in 0.1 M sodium acetate buffer for antibody penetration. The sections were rinsed with TBS and the sections were incubated for 32 minutes with diluted monoclonal anti-human bFGF antibodies (Upstate Biotechnologies, New York), rinsed with TBS and then incubated for 8 minutes in a biotinylated goat anti-mouse IgG antibody (Ventana, AZ). Human bFGF on the specimens was visualized by incubation of these specimens with streptavidin-horseradish peroxidase (HRP), DAB and hydrogen peroxide. The sections were then counter-stained with hematoxyline and mounted in permount. The specificity of immunostaining was determined by incubating sections in the absence of the primary antibody. The slides were prepared from bone samples that were obtained from a critical defect model where gelfoam (an absorbable gelatin matrix, Pharmacia & Upjohn Co., Kalamazoo, MI) was filled with recombinant bFGF protein. Figure 4 demonstrates that bFGF protein is located along the bone forming surface and on the surface of osteoblasts. This assay is thus ready to use to verify expression of the bFGF in fibroblasts that will be embedded in collagen gel in our tibial test site.

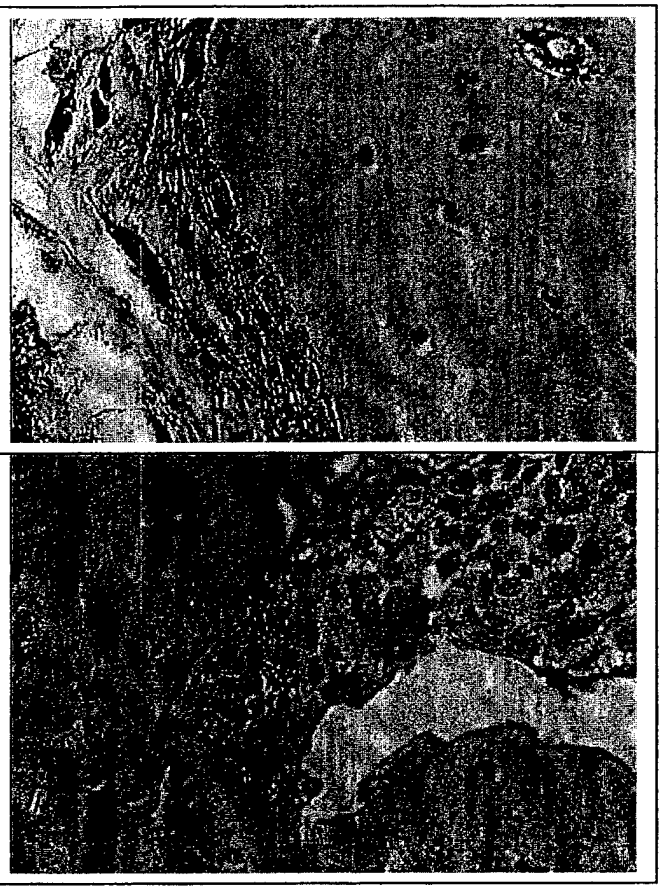

Figure 4. Immunohistochemical localization of bFGF on osteoblasts at the bone forming surfaces. To develop a bFGF immunohistochemical staining method, residual histological sections of rat calvarial bone were taken from a critical size defect model experiment where the defect had been filled with bFGF protein in collagen based gelfoam to increase the healing rate. The upper and lower panels show that in two separate samples, bFGF protein can be detected with anti-bFGF at the bone forming surface on osteoblasts. The primary anti-bFGF antibody was detected with a secondary antibody conjugated to horseradish peroxidase (HRP). HRP activity appears as a brown stain.

F. Conclusions.

Summary of Results:

- We have developed hygromycin selectable enhanced plasmid vectors which express β-gal, bFGF, and BMP-2/4. We are in the process of preparing stable fibroblast cell lines which express therapeutic levels of the growth factor proteins. Many more stable clones are produced with this vector than with our previous dual vector system.
- We have prepared a BMP-4 hybrid molecule and have inserted it into the hygVR1012 vector which is capable of being secreted and is biologically active after it is secreted.
- We have developed an *in vivo* injection model using cytodex beads which will retain our genetically engineered cells expressing the test gene in the test site for at least 6 days.
- We have constructed the hBSP promoter from genomic DNA and found it to be expressed more in osteoblasts than other cell types, however expression is very low compared to typical expression from the viral promoters after transient transfection.

For the final six months of study funding to complete the first specific aim, we will introduce fibroblast cells expressing bFGF, BMP2/4 or fibroblast cells expressing both growth factors attached to cytodex beads into the tibial marrow test site and evaluate bone formation at weekly intervals. We will introduce the plasmids expressing BMP-4 and bFGF in a collagen gel into the marrow of the tibia and evaluate bone formation by pQCT analysis. Completion of these experiments depends on the ability of the collagen

gel to maintain fibroblasts or plasmid DNA in the site for at least one week and also on our ability to prepare stable fibroblast cell lines that continually produce therapeutic levels of each growth factor.

In its present form, the BSP promoter provides only low levels of expression in osteoblasts and would not be able to express therapeutic levels of growth factor protein from the enhanced VR1012 plasmid vector. The BSP promoter is large and it is possible that inhibitory sequences exist in the full length promoter region which reduce expression. It might be possible to remove these putative inhibitory sequences by preparing a smaller core promoter and it would then be possible to complete the second aim of the proposed studies. This BSP core promoter would consist of the proximal promoter sequence that is conserved across species. The promoter would be inserted into the pGL3 vector and would be used to transiently transfect osteoblasts and fibroblasts to determine if the remaining sequence directs high levels of osteoblast specific expression. Experiments to test this hypothesis will be conducted during the last 6 months of the proposed studies. A full deletion analysis of the 2.3 kb BSP promoter, however, is beyond the scope of the proposed studies with the current staff.

References:

1. Anh DJ, Dimai HP, Hall SL, Farley J 1998 Skeletal ALP activity is primarily released from human osteoblasts in an insoluble form and the net release is inhibited by calcium and skeletal growth factors. Calcified Tissue Int 62:332-340.
2. Hammonds RG, Schwall R, Dudley A, Berkemeier L, Lai C, Lee J, Cunningham N, Reddi AH, Wood WI, Mason AJ 1990 Bone-inducing activity of mature BMP-2b produced from a hybrid BMP-2a/2b precursor. Molecular Endo 4:149-155.
3. Hogset A, Prasmickaite L, Tjelle TE, Berg K 2000 Photochemical transfection: A new technology for light-induced, site-directed gene delivery. Human Gene Therapy 11:869-880.
4. Krebsbach PH, Gu K, Granceschi RT, Rutherfold RB 2000 Gene therapy-directed osteogenesis: BMP-7-transduced human fibroblasts form bone in vivo. Human gene therapy 11:1201-1210.

Gene Therapy of Skeletal Repair

Project Director: David J. Baylink

Semi-annual Progress Report 12/1/1999 to 6/1/200

Appendices

There have been no additional abstracts, or other items to include in the appendices at this time.

Patents

There are no patent applications pending, submitted or approved related to the ongoing studies.

Commercialization

The research proposed in this application is entirely in the basic research phase of technology development. It is possible, if experiments are successful during the last period of funding, that a proof of principle describing that the combination of growth factors that we have chosen is better at forming bone than the individual components, will be established. At that point, it is possible that intellectual properties could be patented.

APPENDIX 1

1. MANUSCRIPT: Postnatal and Pubertal Skeletal Changes Contribute Predominantly to the Differences in Peak Bone Density Between C3H/HeJ and C57BL/6J Mice, C. Richman, S. Kutilek, N. Miyakoshi, A.K. Srivastava, W. Beamer, L.R. Donahue, C. Rosen, J.E. Wergedal, D.J. Baylink and S. Mohan. (Submitted to *JBMR*).

2. ABSTRACT: Postnatal and Pubertal Skeletal Changes Predominantly Contribute to the Differences in Peak Bone Density Between C3H/HeJ and C57BL/6J Mice, C. Richman, S. Kutilek, N. Miyakoshi, A.K. Srivastava, W. Beamer, L.R. Donahue, C. Rosen, J.E. Wergedal, D.J. Baylink and S. Mohan. (Submitted to the Endocrine Society).

POSTNATAL AND PUBERTAL SKELETAL CHANGES CONTRIBUTE PREDOMINANTLY TO THE DIFFERENCES IN PEAK BONE DENSITY BETWEEN C3H/HEJ AND C57BL/6J MICE*

(submitted to JBMR)

C. RICHMAN[1], S. KUTILEK[1], N. MIYAKOSHI[1], A.K. SRIVASTAVA[1], W. BEAMER[2], L.R. DONAHUE[2], C. ROSEN[3], J. WERGEDAL[1], D.J. BAYLINK[1] and S. MOHAN[1].
[1]JL Pettis VA Medical Center and Loma Linda University, Loma Linda, CA, [2]Jackson Laboratories, Bar Harbor, ME. and [3]St. Joseph Hospital, Bangor, ME.

Running title: Skeletal changes in mice during puberty

*The view, opinions and/or findings contained in this report are those of the author(s) and should not be construed as a position, policy, decision or endorsement of the Federal Government or the National Medical Technology Testbed, Inc.

A. Abstract

Previous studies have shown that 60-70% of peak bone density is genetically determined. The higher the peak bone density, the less likely an individual is to eventually develop osteoporosis. Therefore, the amount of bone accrued during postnatal and pubertal growth is an important determining factor in the development of osteoporosis. We evaluated the contribution of skeletal changes before, during and after puberty to the development of peak bone density in C3H/HeJ (C3H) and C57BL/6J (B6) mice. Volumetric bone density and geometric parameters at the middiaphysis of femora were measured by pQCT from day 7 through 56. Additionally, biochemical markers of bone turnover in serum and bone extracts were quantified. Both B6 and C3H mice showed similar body and femoral weights. B6 mice had greater middiaphysial total bone area and thinner cortices than did C3H mice. Within strains, males had thicker cortices than did females. C3H mice accumulated more mineral throughout the study, with the most rapid accumulation occurring postnatally (day 7-23) and during pubertal maturation (day 23-31). C3H mice had higher volumetric bone density as early as day 7, with males tending to have a higher volumetric bone density than did females. Higher serum IGF-I was present in C3H mice postnatally until day 23. Until day 35, B6 mice had significantly higher serum osteocalcin. Alkaline phosphatase was found to be significantly higher in the bone extract of C3H mice until day 23. These data are consistent with and support the hypothesis that the greater amount of bone accrued during postnatal and pubertal growth in C3H mice compared to B6 mice may be due to increased cortical thickness caused by increased endosteal bone formation and decreased endosteal bone resorption.

Key words: bone density, puberty, IGF-I, osteocalcin, C3H/HeJ and C57BL/6J mice

POSTNATAL AND PUBERTAL SKELETAL CHANGES PREDOMINANTLY CONTRIBUTE TO THE DIFFERENCES IN PEAK BONE DENSITY BETWEEN C3H/HEJ AND C57BL/6J MICE.* C. Richman, D.J. Baylink, S. Kutilek, N. Miyakoshi, A.K. Srivastava, W. Beamer, L.R. Donahue, C. Rosen, J. Wergedal and S. Mohan. JL Pettis VA Medical Center and Loma Linda University, Loma Linda, CA; Jackson Laboratories, Bar Harbor, ME; and St. Joseph Hospital, Bangor, ME.

Previous studies have shown that 60-70% of peak bone density is genetically determined. The higher the peak bone density, the less likely an individual is to eventually develop osteoporosis. Therefore, the amount of bone accrued during postnatal and pubertal growth is an important determining factor in the development of osteoporosis. We evaluated the contribution of skeletal changes before, during and after puberty to the development of peak bone density in C3H/HeJ (C3H) and C57BL/6J (B6) mice. Volumetric bone density and geometric parameters at the mid-diaphysis of femora were measured by pQCT in both males and females from day 7 through 56 at weekly intervals. Both B6 and C3H mice showed similar body and femoral weights. B6 mice had greater mid-diaphysial total bone area and thinner cortices than did C3H mice. Within strains, males had thicker cortices than did females. C3H mice accumulated more mineral throughout the study, with the most rapid accumulation occurring postnatally (day 7-23) and during pubertal maturation (day 23-31). C3H mice had higher volumetric bone density than B6 mice as early as day 7. The rate of bone density gain in C3H mice during postnatal and pubertal growth was twice that of B6 mice, though it was not different after puberty. To evaluate if the greater accumulation of bone during postnatal and pubertal periods in C3H mice compared to B6 mice is due to increased bone formation, we measured ALP activity in bone extracts. C3H mice exhibited significantly greater ALP activity in the femoral bone extract than did B6 mice at the time when maximal differences in bone density between the two strains occur. In addition, bone extract ALP showed significant positive correlation with bone density during postnatal periods. Because IGF-I is an important growth factor regulating bone formation, we evaluated the relationship between IGF-I level in serum and changes in bone accretion between C3H and B6 mice. We found serum IGF-I levels increased dramatically during postnatal growth in both strains and that C3H mice had significantly higher serum IGF-I levels compared to B6 mice. Serum IGF-I levels also showed significant positive correlation with bone density and bone extract ALP activity during postnatal period. [underline]Conclusions:[/underline] 1) The greater amount of bone accrued during postnatal and pubertal growth in C3H mice compared to B6 mice led to increased cortical thickness caused by increased endosteal bone formation and decreased bone resorption. 2) Two growth periods, namely postnatal and pubertal, are critical to the development of peak bone density between C3H and B6 mice. 3) The genes that are differentially expressed in the skeleton of C3H and B6 mice during postnatal and pubertal growth may provide clues regarding genes that contribute to the differences in bone density between these two strains.

*The view, opinions and/or findings contained in this report are those of the author(s) and should not be construed as a position, policy, decision or endorsement of the Federal Government or the National Medical Technology Testbed, Inc. This project was sponsored with funds by the U.S. Department of the Army and the National Medical Technology Testbed, Inc.

DESCRIPTION: State the goal of the project, including how it relates to improving health care and noting the advanced technology that will be developed or tested . Use succinct language to describe how the project goals will be achieved. **Do not exceed the space provided.**

The long-term goal of this project is to identify the mechanisms responsible for the accelerated bone formation (BF), seen during puberty, that culminates in the acquisition of peak bone density (BD) at the end of puberty. The higher the peak BD the less likely an individual is to develop senile osteoporosis. Hence, the amount of bone formed during puberty i.e., peak BD attained, is a very important determining factor in the development of osteoporosis later in life. Therefore, identifying the molecular mechanisms involved in the BF occurring during puberty is extremely important to our understanding of the cause, potential prevention and treatment of osteoporosis. This project will focus on the role of the growth hormone (GH)/insulin-like growth factor (IGF) axis, an important growth factor system in bone, which has previously been shown to be upregulated during puberty. In our studies on the role of GH/IGF-I axis in regulating peak BD, we propose to use mouse models for a number of reasons, including the recent development of transgenic mice deficient in GH and/or IGF-I. As a means of testing the hypothesis that skeletal changes that occur during puberty are mediated in part by upregulation of IGF system components followed by corresponding increase in BF, we will first determine the serum levels of the stimulatory IGF system components as a function of time during puberty in normal mice and then correlate these measurements with BF parameters obtained during the same time period. We anticipate an increase in GH first, followed by IGF-I, BF markers, and finally BD, in that order. To extend these correlative data, we will seek cause and effect relationship by determining if the increase in BF during puberty is caused by the preceding increase in the production of IGF system components by comparing changes in BF in mice deficient in GH or IGF-I action with those of control mice during puberty. If our hypothesis that GH/IGF-I axis plays a major role in regulating peak BD is correct, we should be able to rescue the BF deficit in GH deficient mice by daily treatment of mice deficient in GH action with GH and/or IGF-I during puberty. We will therefore treat GH deficient mice with various doses of GH or IGF-I daily throughout puberty to evaluate the changes in BF parameters and BD. We believe that comparison of skeletal phenotype changes that occur during puberty using transgenic mice deficient in GH/IGF-I action and control mice will help unravel not only the physiological role of these growth regulatory peptides but also their mechanism of action. The clinical significance of this study is as follows. The GH/IGF-I axis is an important determinant of peak BD and may have important ramifications for identifying individuals at risk for developing osteoporosis. We anticipate that the impending findings of this study will provide important information regarding 1) strategies to treat GH deficient children with GH and/or IGF-I to increase peak bone mass during puberty, and 2) future development of novel therapies to increase peak BD by upregulating the GH/IGF-I axis during puberty. The attainment of peak BD to a higher level could lead to a decrease in the incidence of osteoporosis and its associated health care costs.

PROJECT SITE(S) (organization, city, state):

Jerry L. Pettis VA Medical Center
Musculoskeletal Disease Center (151)
11201 Benton Street
Loma Linda, CA 92357

National Medical Test Bed
Final Progress Report

APR 12 2000

"Role of Growth Hormone/Insulin-like Growth Factor Axis" (Subcontract ID 3398)

Period: March 1, 1999 to February 29, 2000

Signature of P.I.: SMohan Date Prepared: March 23, 2000

TEL: 825-7084, ext. 2932; FAX: 796-1680; E-MAIL: subburaman.mohan@med.va.gov

INTRODUCTION

The long-term goal of this project is to identify the mechanisms responsible for the accelerated bone formation seen during puberty that culminates in the acquisition of peak bone density at the end of puberty. The higher the peak bone density the less likely an individual is to develop senile osteoporosis. Hence, the amount of bone formed during puberty (i.e., peak bone density attained) is a very important determining factor in the development of osteoporosis later in life. Therefore, identifying the molecular mechanisms involved in the bone formation occurring during puberty is extremely important to our understanding of the cause, potential prevention, and treatment of osteoporosis. In this regard, the objective of this proposal is to determine the role of growth hormone/insulin-like growth factor (GH/IGF) axis in the regulation of bone formation that occurs during puberty. In our studies on the role of GH/IGF-I axis in regulating peak bone density, we have used mouse models for a number of reasons, including the recent development of transgenic mice deficient in growth hormone and IGF-I. Our goal of the proposed studies in year 1 was to evaluate serum levels of IGF stimulatory system components in a temporal manner during sexual development in mice and correlate these measurements with biochemical measurements of bone formation, bone resorption, and bone density. Our hypothesis in this study is that there is an increase in IGF-I, followed by changes in bone formation, ultimately resulting in an increase in bone density.

DETAILED PROGRESS REPORT

We performed two studies during the first year. In the first study, we evaluated the skeletal changes that occur during pre-pubertal, pubertal, and post-pubertal periods in two strains of mice, a strain with low bone density and a strain with high bone density. In the second study, we evaluated the temporal changes in IGF system components and biochemical markers of bone formation during puberty. Our results in these two studies are summarized below.

STUDY 1: Skeletal Changes During Pre-pubertal, Pubertal, and Post-pubertal Periods in C57BL/6J and C3H/HeJ Mice.

1. Experimental Design & Methods.

We used C3H/HeJ (C3H) and C57BL/6J (B6) for our puberty studies because C57BL and C3H exhibit lowest and highest peak bone density among various inbred strains of mice. To evaluate the relative contribution of skeletal changes occurring during puberty, to peak bone density difference between the two strains, we compared skeletal changes during puberty in C57BL and C3H mice. Breeder C57BL and C3H mice were obtained from The Jackson Laboratory and used to generate offspring belonging to various age groups. At days 23, 31, 35, 42, 49, and 56, the mice were sacrificed and blood was collected and used for biochemical measurements of bone formation and bone resorption. Bones were collected and used for bone density measurements, as well as for biochemical measurements of bone formation. Serum was also used for measurements of IGF system components. Nine animals were used for each time point. Both males and females were studied. Offspring from several litters were included in each time point to rule out artifacts due to litter size. The precision of pQCT measurements was less than 6%, while that of biochemical measurements was less than 15%.

2. Results.

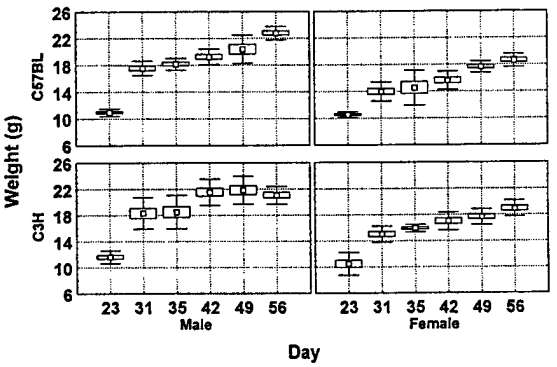

Figure 1: Body weight changes in males & females of C57BL/6J & C3H/HeJ mice during & after puberty. Boxes represent SEM & bars represent SD.

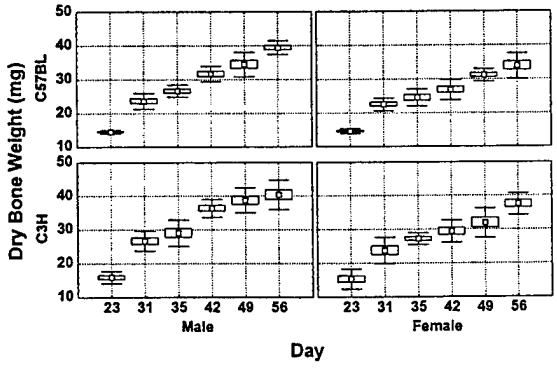

Figure 2: Dry bone weight changes in males and females of C57BL/6J & C3H/HeJ mice during & after puberty. Boxes represent SEM & bars represent SD.

a. Body Weight. Body weight increased by 60% and 33%, respectively, during puberty in female and male C57BL mice. In C3H mice, the puberty-induced gain in body weight represented an increase of 58% and 43%, respectively, in females and males (**Figure 1**). There was no significant difference in body weight gain between C3H and C57BL strains during puberty. The rate of gain in body weight during puberty (0.4 – 0.8 gm/day) was much greater than the rate of gain in body weight after puberty (0.1 – 0.2 gm/day). Our studies also showed that the body weight gained during puberty was significantly higher in males than in females in both strains (0.8 gm/day in males vs. 0.5 gm/day in females). During Year 2, the role of growth hormone (GH)/IGF-I axis in mediating the changes in somatic growth during puberty will be studied using transgenic mice deficient in GH and IGF-I action.

b. Bone Weight. Consistent with our earlier studies in humans, we found evidence for rapid gain in bone mass during puberty in mice. Between days 23 – 31, dry bone weight increased by 63% and 61%, respectively, in male and female C57BL mice (**Figure 2**). Similar increases

in bone weight (68% and 55%, respectively) were also seen in males and females of C3H mice. The rate of increase in bone weight per day (1.14 vs. 1.0 mg/day) during puberty was 10-20% higher in C3H mice than in C57BL mice, despite no differences in body weight gain during the same period. We also found that the gain in bone weight was about 2 – 3 times higher during puberty than after puberty in both strains of mice. This rapid increase in bone weight of 55 – 65% during the period of sexual maturation (i.e., 23 – 31 days) suggests that this period is critical in the acquisition of peak bone mass. Thus, puberty provides a unique window in time to evaluate the potential mechanisms responsible for changes in bone mass, as large increases in bone mass occur during the period of sexual maturation.

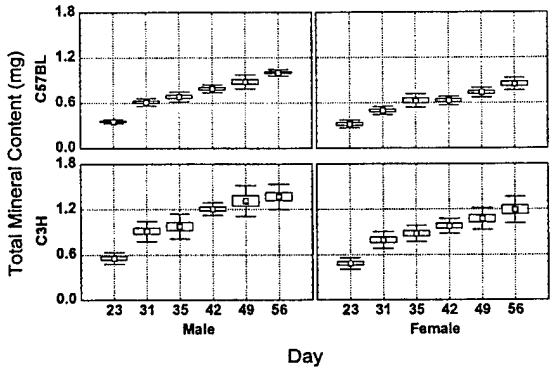

Figure 3: Total mineral content at femoral mid-diaphysis in male & female C57BL/6J & C3H/HeJ mice during & after puberty. Boxes represent SEM & bars represent SD.

c. Total Mineral Content. The total mineral content (mg/slice) was evaluated at the mid-diaphysis using pQCT. The total mineral content was increased by 74% and 50%, respectively, during puberty in males and females of C57BL mice. The increase in total mineral content was 65% in both sexes during puberty in C3H mice (**Figure 3**). The mineral accumulation per day at mid-diaphysis was 2 – 2.5-fold greater during puberty compared to post-pubertal period. In addition, this study also shows that the increase in total mineral content was 40% and 50% greater during puberty in male and female C3H mice than in C57BL mice. These data suggest that an accumulation of minerals occurs at a much more rapid pace in the C3H mice during puberty than in the C57BL mice. Therefore, studies on the molecular mechanisms that contribute to the differences in mineral accumulation between the two strains during this critical period may provide important clues on the genes that control bone growth during puberty.

The increase in total mineral content during puberty (23 – 31 days) was about 20-30% higher in males than in females of C57BL and C3H strains. The question of whether sex-steroid hormones play an important role in mediating the differences in the bone mineral content gained between the two different sexes in C3H and C57BL strains of mice requires further studies.

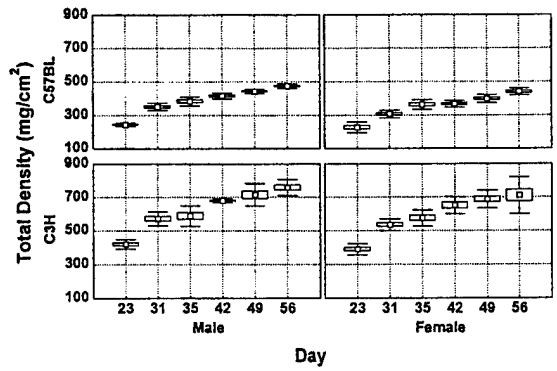

Figure 4: Total bone density at femoral mid-diaphysis in male & female C57BL/6J & C3H/HeJ mice during & after puberty. Boxes represent SEM & bars represent SD.

d. Total Bone Density. As bone density is one of the main determinants of fracture risk, maximizing bone density at skeletal maturity (peak bone mass) is a logical strategy to protect against osteoporosis. In our studies to use the mouse as a model to understand the molecular mechanisms that contribute to the rapid changes in bone density that occur during puberty, we found that bone density increases between 35% and 45% in the males and females of C57BL mice. The bone density also increases between 35% and 40% in the males and females of C3H mice (**Figure 4**). Our studies also show that the gain in bone density was much greater during puberty (2.5 – 3-fold) compared to post-pubertal period in both C57BL and C3H strains of mice.

Therefore, studies on the molecular mechanisms that contribute to the rapid increase in bone density during this critical period of sexual maturation are important to identify treatment strategies to increase peak bone density.

Comparison of bone densities in the C3H and C57BL strains of mice show that the bone densities were about 72% higher in both males and females of the C3H strain compared to the C57BL strain at day 23 (i.e., before puberty). Furthermore, the gain in bone density during puberty was greater in C3H mice than in C57BL mice (152 mg/cm^2 vs. 107 mg/cm^2). These data demonstrate that changes occurring during pre-pubertal and pubertal periods contribute predominantly to the observed differences in peak bone density between C3H and C57BL strains.

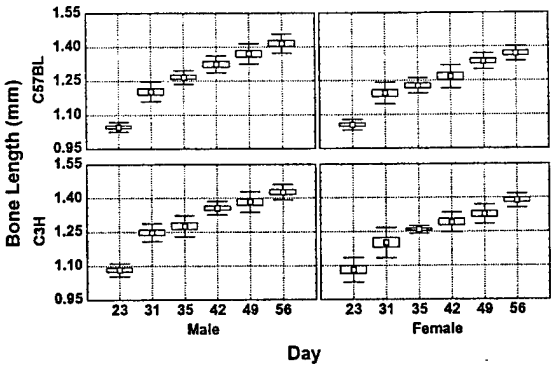

Figure 5: Femoral bone length in male & female C57BL/6J & C3H/HeJ mice during & after puberty. Boxes represent SEM & bars represent SD.

e. Bone Length. In previous studies we found that metacarpal length increased significantly in girls during the period of sexual maturation. In order to determine if a similar increase in bone length occurs during the period of sexual maturation in mice, we measured changes in bone length during puberty. Our data show that femur bone length increased by about 15% in males and females of both C3H and C57BL strains (**Figure 5**). The rate of increase in bone length is about 3 to 5 times greater during puberty compared to post-pubertal period. For example, in C3H males, bone length increased by 0.021 mm/day between 23 and 31 days compared to the rate of increase of 0.004 mm/day between days 35 and 42. Thus, our data in mice demonstrating rapid skeletal changes during the period of sexual maturation provides experimental evidence for usefulness of the mouse model for mechanistic studies.

Because of the importance of GH/IGF axis in regulating skeletal growth, and because the GH/IGF axis is up-regulated during puberty in both humans and in mice (see section III.C.10.), our subsequent studies will be focused on the role of the GH/IGF axis in mediating the rapid increase in bone length that occurs during puberty. The issue of how sex steroid hormones interact with the GH/IGF axis in mediating this rapid increase in bone length will also be a subject of future study.

f. Periosteal and Endosteal Circumference. The rapid increase in bone density during the period of sexual maturation could be due to an increase in bone formation and/or a decrease in bone resorption at the periosteum and/or endosteum. We, therefore, evaluated the changes in periosteal and endosteal circumferences in C57BL and C3H strains of mice before, during, and after puberty. Our data show that periosteal circumference increased by 10% in the males of both C57BL and C3H strains of mice during the period of puberty (i.e., between days 23 to 31). The increase in periosteal circumference in the females was about 7% (**Figure 6**). Based on the previous findings that an increase in GH expression in the erythroid cells using the β-globin promoter causes an increase in the periosteal bone formation, we speculate that the increase in periosteal circumference during puberty may, in part, be caused by GH/IGF axis. We have, therefore, proposed studies in Year 2 to use mice deficient in GH and/or IGF-I to evaluate the role of the GH/IGF axis in mediating the increase in periosteal circumference during the period of sexual maturation in mice.

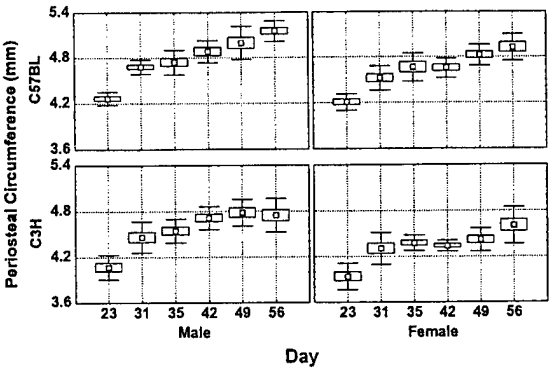

Figure 6: Femoral periosteal circumference in male & female C57BL/6J & C3H/HeJ mice during & after puberty. Boxes represent SEM & bars represent SD.

Comparison of periosteal circumference in the C57BL and C3H strains of mice revealed that the periosteal circumference was 5% greater in the C57BL mice than in the C3H mice at 23 days of age. At day 56, the C57BL mice had 8% greater periosteal circumference than the C3H mice. These data suggest that the higher bone density in the C3H mice than the C57BL mice was probably not due to higher periosteal bone formation and/or lower periosteal bone resorption in the C3H mice. Comparison of the endosteal circumference in the C57BL and C3H strains of mice revealed that the endosteal circumference was 20% greater in the C57BL mice than in the C3H mice at day 23. At day 56, C57BL mice exhibited a 30% greater endosteal circumference than the C3H mice. These data are consistent with the possibility that the higher bone density in C3H mice compared to C57BL mice may, in part, be determined by the differences in the endosteal bone formation and/or resorption.

Measurement of endosteal circumference in C57BL mice and C3H strains of mice before, during and after puberty revealed that the endosteal circumference did not change significantly during puberty in either sexes of C3H and C57BL strains of mice. While the endosteal circumference remained unchanged during the post-pubertal growth in the C3H mice, the endosteal circumference increased by 7% and 10%, respectively, in the females and males of C57BL mice. The cortical thickness increased by 31% and 29%, respectively, in the females and males of C3H mice during puberty. Similarly, the cortical thickness also increased by 25% and 22%, respectively, in the males and females of C57BL mice. Based on the findings that the periosteal circumference increased during puberty and that the endosteal circumference did not show significant change, it can be concluded that the increase in cortical thickness during puberty is mainly due to an increase in periosteal bone formation and/or decrease in periosteal bone resorption. The role of the GH/IGF axis and sex steroid hormones in mediating this rapid increase in cortical thickness will be the subject of studies proposed in Year 2.

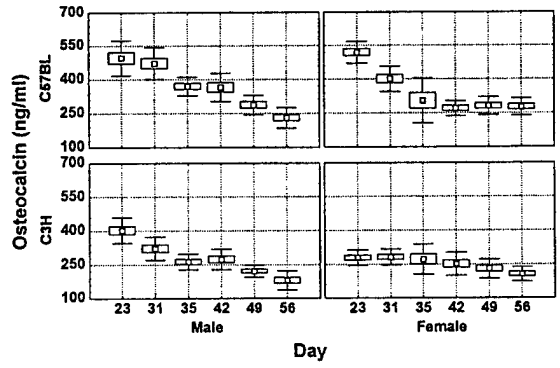

Figure 7: Serum osteocalcin levels in male & female C57BL/6J & C3H/HeJ mice during & after puberty. Boxes represent SEM & bars represent SD.

g. Serum Level of Osteocalcin. In order to determine if the rapid increase in bone density during puberty is associated with changes in bone turnover, we measured serum levels of bone formation and bone resorption markers in the mice during the period of sexual maturation, as well as during the post-pubertal period. The serum osteocalcin level was not significantly different between 23 and 31 days in C57BL male mice. Although serum osteocalcin level were slightly lower at day 31 in the female C57BL mice, this decrease was not statistically significant compared to day 23 (**Figure 7**). Serum osteocalcin levels did not change during puberty either in male or female C3H mice. Serum

osteocalcin levels declined significantly during post-pubertal period in both male and female C57BL mice. A similar decline in serum osteocalcin levels during post-pubertal period was also seen in C3H mice. Comparison of serum levels of osteocalcin in C57BL and C3H strains of mice reveal that the serum osteocalcin levels were significantly higher in the C57BL mice compared to the C3H mice in both sexes. These data suggest that C3H mice, with higher bone density, exhibit lower bone turnover compared to C57BL mice, with lower bone density. The differences in bone turnover between C3H and C57BL mice are consistent with previous studies by Slemenda, et al., who have shown that Black children accumulate a 10% greater bone mass than White children and have significantly reduced bone turnover, as measured by serum levels of osteocalcin and tartrate-resistant acid phosphatase compared to White children during pubertal growth. The role of GH/IGF axis and sex steroid hormones in regulating bone turnover differently in the C3H and C57BL mice will be studied during Year 2 of the proposed studies.

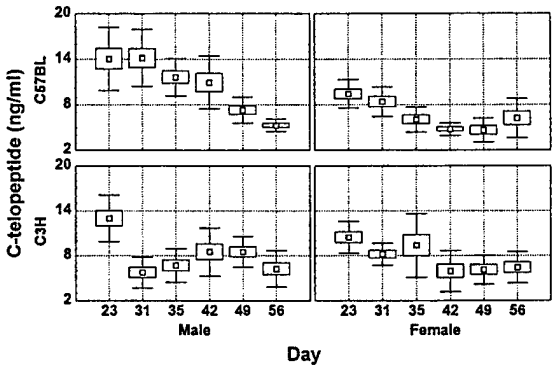

Figure 8: Serum c-telopeptide levels in male & female C57BL/6J & C3H/HeJ mice during & after puberty. Boxes represent SEM & bars represent SD.

h. Serum Level of C-telopeptide Levels. Carboxy-terminal cross-linked c-telopeptide of type I collagen (c-telopeptide) is a well-established marker of bone resorption. We, therefore, measured serum levels of c-telopeptide in mice before, during and after puberty to monitor changes in bone resorption. Serum c-telopeptide levels were significantly lower in male C3H mice at day 31 compared to day 23 (**Figure 8**). Although c-telopeptide levels in female C3H mice were decreased during puberty, this decrease was not statistically significant. Similar to serum osteocalcin, c-telopeptide levels also declined during the post-pubertal period in the C57BL males and females. The question of whether changes in testosterone levels play a role in the reduction of serum c-telopeptide in male C3H mice requires further study.

i. The Relationship Between Changes in BMD and Femoral Bone Indices vs. Markers of Bone Turnover in Mice. In general, bone turnover markers showed significant negative correlation with bone density, total bone mineral content, cortical thickness, and periosteal circumference in both strains of mice. These data suggest that bone turnover decreases during puberty in mice, as in the case of girls. The molecular cues that are responsible for the acute reduction in bone turnover during sexual maturation remain unknown. Based on the findings that cytokines are important regulators of osteoclast formation and activity and that IGFs regulate cytokine production, it is likely that GH/IGF axis plays an important role in mediating changes in bone turnover via modulating cytokine production. This hypothesis would be tested by evaluating changes in serum levels of cytokines during puberty in mice deficient in GH/IGF action.

j. Serum Levels of IGF-I. According to our hypothesis, up-regulation of GH/IGF axis plays an important role in the attainment of peak bone mass during puberty. We, therefore, measured serum levels of IGF-I in mice during puberty. Our studies show that serum levels of IGF-I increased by 43% and 87%, respectively, in the male and female C3H mice (**Figure 9**). The increase in serum IGF-I level during puberty is greater in C3H mice than in C57BL mice. Based on the findings that GH/IGF-I is an important regulator of bone formation, we proposed that that the differences in bone gain during puberty between C3H and C57BL mice may in part be

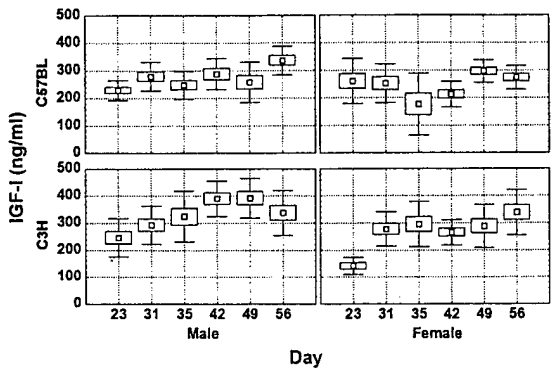

Figure 9: Serum IGF-I levels in male & female C57BL/6J & C3H/HeJ mice during & after puberty. Boxes represent SEM & bars represent SD.

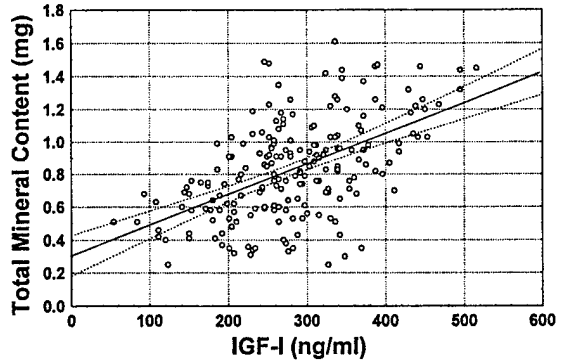

Figure 10: Relationship between serum IGF-I levels & total bone mineral content in the pooled data of male & female C3H/HeJ & C57BL/6J mice during pubertal & post-pubertal periods (r=0.49, p<0.001).

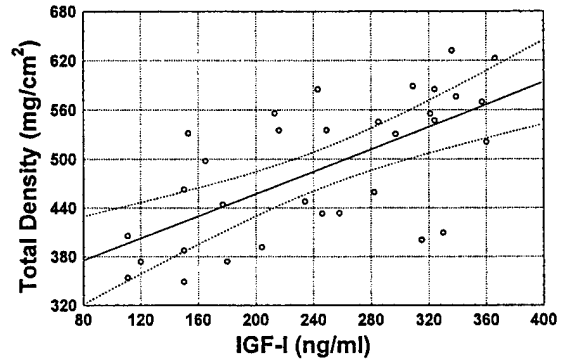

Figure 11: Relationship between serum IGF-I levels & total bone density in C3H/HeJ mice during puberty (i.e., pooled data from 23 & 31 days) (r=0.65, p<0.001).

mediated by differences in puberty-induced GH/IGF levels between these two strains. We therefore evaluated the relationship between serum IGF-I levels and skeletal changes during puberty (see below).

k. Relationship Between Serum IGF-I and Skeletal Changes During Puberty. In order to determine if the changes in serum levels of IGF-I are associated with the corresponding skeletal changes, we determined the relationship between serum IGF-I vs. femoral bone indices in mice. In the pooled data from males and females of 23- and 31-day old C3H mice, we found serum levels of IGF-I showed significant positive correlation with bone length, total mineral content, total density, cortical thickness and periosteal circumference (**Figures 10-13**). These highly significant correlations between serum levels of IGF-I and femoral bone indices are consistent with the premise that IGF-I plays an important role in mediating the rapid changes that occur during puberty. The importance of IGF-I in mediating the skeletal changes will be investigated further using mice deficient in IGF-I and GH action in the second year of this proposal.

l. Relationship Between Serum Levels of IGF-I and Biochemical Markers of Bone Turnover in Mice. In order to determine if changes in serum levels of IGF-I is associated with the corresponding changes in biochemical markers of turnover, we determined the relationship between serum levels of IGF-I and biochemical markers of bone formation and bone resorption. In the pooled data from males and females of 23- and 31-day old C3H mice, we found serum levels of IGF-I to correlate positively with serum levels of osteocalcin ($r = 0.35$, $p<0.01$). In contrast, serum levels of IGF-I showed significant negative correlation with serum levels of c-telopeptide ($r = -0.45$, $p<0.01$) in the same mice. We will, therefore, examine the puberty-induced changes in bone turnover markers in mice deficient in GH and IGF-I action. The findings that the puberty causes a reduction in bone turnover in mice with intact IGF-I gene but not in mice lacking functional IGF-I gene would provide strong evidence that IGF-I plays an important role in mediating the decreased bone turnover seen during puberty in mice.

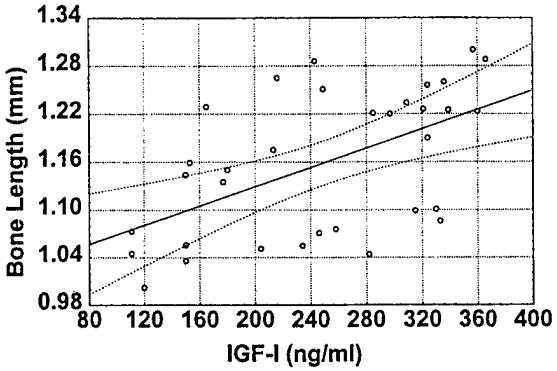

Figure 12: Relationship between serum IGF-I levels & femoral bone length in C3H/HeJ mice during puberty ($r=0.63$, $p<0.001$).

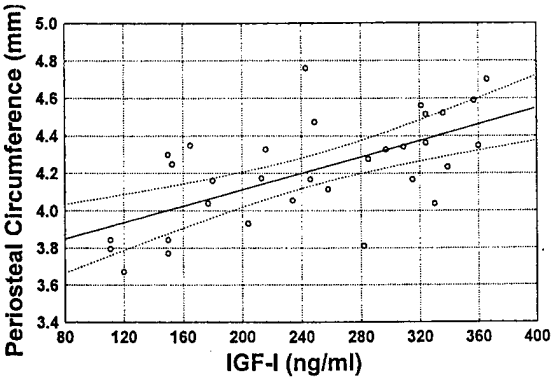

Figure 13: Relationship between serum IGF-I levels & periosteal circumference in the femur of C3H/HeJ mice during puberty ($r=0.71$, $p<0.001$).

3. Conclusion.

In conclusion, there is rapid accumulation of bone within a short period of one week during the period of sexual maturation in mice. The gain in bone weight, total mineral content, total density and cortical thickness in C3H mice during puberty is 20-50% more than that acquired in the C57BL mice at the same period. **INSERT 1**

STUDY 2: Temporal Changes in Serum Level of IGF-I and Bone Formation Markers During Puberty in C57BL/6J Mice.

1. Experimental Design & Methods.

To determine if changes in serum levels of IGF-I correlate positively with skeletal changes during sexual maturation, we measured serum levels of IGF-I and skeletal changes at different times during puberty in male and female mice. Breeder C57BL mice were obtained from The Jackson Laboratory and used to generate offspring belonging to various age groups. At days 23, 24, 25, 26, 27, 28, 29, 30, and 31, the mice were sacrificed and blood was collected and used for biochemical measurements of bone formation and bone resorption. Bones were collected and used for bone density measurements, as well as for biochemical measurements of bone formation. Serum was also used for measurements of IGF system components. Seven to nine animals were used for each timepoint. Both males and females were studied. Offspring from several litters were included in each timepoint to rule out artifacts due to litter size. Our findings are summarized below.

2. Results.

a. Body Weight. The body weight almost doubled in the male C57BL mice between days 23 and 31. In females, the body weight increased by 60% between day 23 and 31. A dramatic increase in body weight was seen between days 24 to 29 in both males and females. The increase in body weight during this period was approximately 40-50%. Although both males and females gained significant body weight during puberty, it appears that the males gained body weight at a faster rate compared to females during the period of sexual maturation (**Figure 1**).

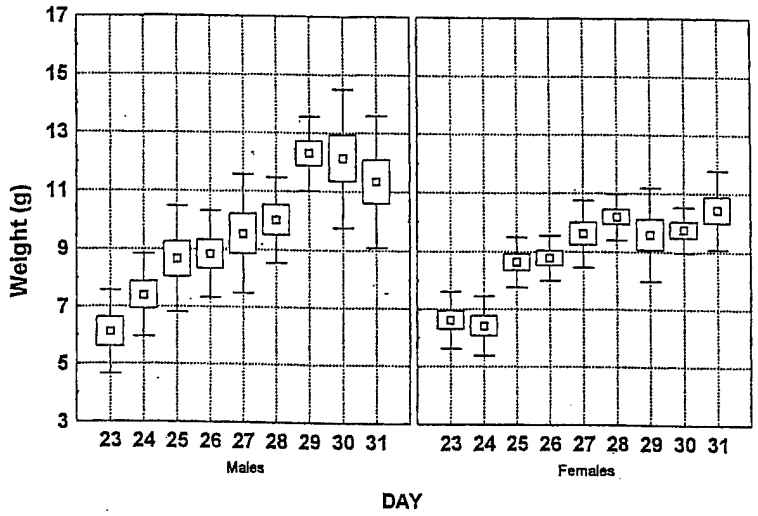

FIGURE 1: Body weight changes in males and females of C57BL/6J mice during puberty. Boxes represent SEM and bars represent SD.

b. Bone Weight. Consistent with our earlier studies in humans, we found evidence for rapid gain in bone mass during puberty in mice. Between days 23 to 31, dry bone weight increased by 60-80% in male and female C57BL mice (**Figure 2**). The rate of increase in bone weight corresponded with changes in body weight seen during the same period. This rapid increase in bone weight during the period of sexual maturation (that is, days 23 to 31) suggest that this period is critical in the acquisition of peak bone mass. Thus, puberty provides a unique window in time to evaluate the potential mechanism responsible for changes in bone mass, as large increases in bone mass occurs during the period of sexual maturation.

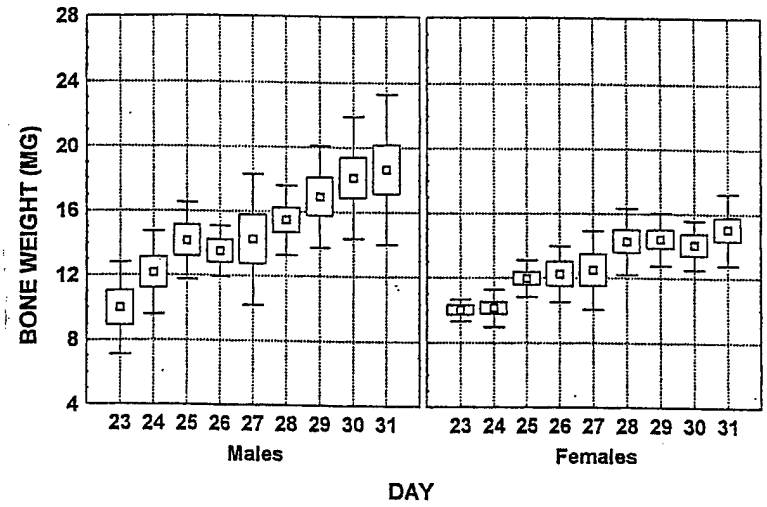

FIGURE 2: Dry femoral bone weight changes in males and females of C57BL/6J mice during puberty. Boxes represent SEM and bars represent SD.

c. Bone Length. In previous studies we found that metacarpal length increased significantly in girls during the sexual maturation. In order to determine if a similar increase in bone length occurred during the period of sexual maturation in mice, we measured changes in bone length during puberty. Our data show that femur bone length increased by about 15% in males and females of C57BL strain (**Figure 3**). Consistent with the changes in bone weight and body weight, the most dramatic increase in femur length was seen between days 24 to 29. So this period appears to be critical for future studies on the molecular cues that are responsible for mediating the rapid skeletal changes that occur during the period of sexual maturation in mice.

d. Serum Levels of Osteocalcin. In order to determine if the rapid increase in bone weight during puberty is associated with changes in bone turnover, we measured serum levels of bone formation marker, serum osteocalcin, in mice during the period of sexual maturation. Serum levels of osteocalcin increased significantly by 50-80% between days 23 to 27 in both males and females of C57BL mice. However, serum osteocalcin levels started to decline after day 27 and, as such, at day 31 serum osteocalcin levels were only slightly elevated compared to day 23

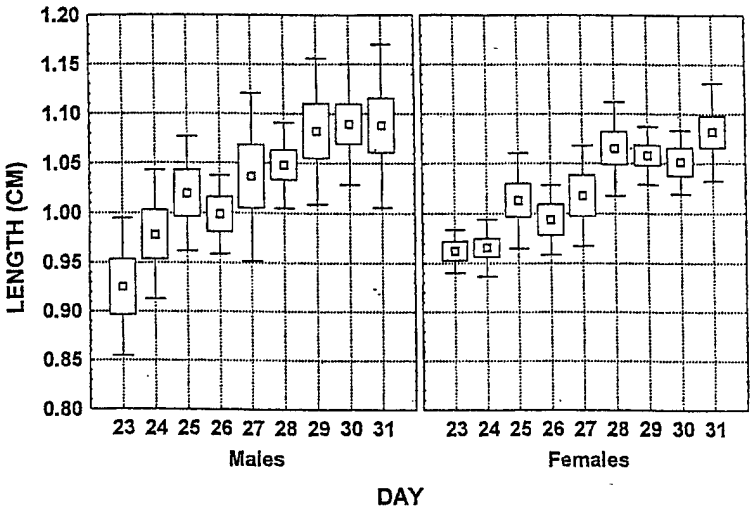

FIGURE 3: Femoral bone length changes in males and females of C57BL/6J mice during puberty. Boxes represent SEM and bars represent SD.

(**Figure 4**). Thus, serum levels of osteocalcin showed a biphasic response, that is, increase during the early period of sexual maturation and then decrease during the latter part of the sexual maturation. The increase in serum osteocalcin may reflect an increase in bone formation that happens during the early period of sexual maturation, and the corresponding decline in serum level of osteocalcin during the later period of sexual maturation may correspond with the decrease in bone turnover, which could occur as a consequence of increase in sex steroid hormone resulting in a decrease in bone resorption. Since complex changes, including longitudinal growth, periosteal expansion, modeling and remodeling, and sex hormone dependent reduction and remodeling of trabecular bone, are occurring at the skeleton during puberty, the changes in serum level of osteocalcin during different periods of sexual maturation may depend on the extent to which changes in these different metabolic processes are occurring at any given time during puberty.

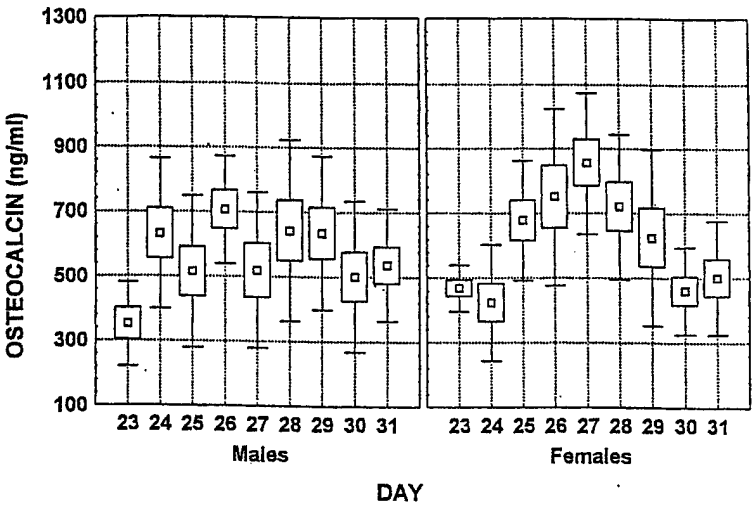

FIGURE 4: Serum osteocalcin level changes in males and feamles of C57BL/6J mice during puberty. Boxes represent SEM and bars represent SD.

e. Bone Alkaline Phosphatase. Consistent with the serum osteocalcin data, measurement of alkaline phosphatase activity in skeletal extracts showed that the alkaline phosphatase activity increased by nearly two-fold between days 23 and day 28 (**Figure 5**). Bone alkaline phosphatase activity did not change significantly during the later period of sexual maturation. These data are consistent with the possibility that the increase in bone length, as well as rapid changes in bone weight, may, in part, be mediated by an increase in bone formation.

f. Changes in Serum Level of IGF-I During Puberty. According to our hypothesis, up-regulation of growth hormone/IGF axis play an important role in the attainment of peak bone mass during puberty. We, therefore, measured serum levels of IGF-I in mice during puberty. Our studies show that serum levels of IGF-I increased by 70-90% between days 23 to day 29 in

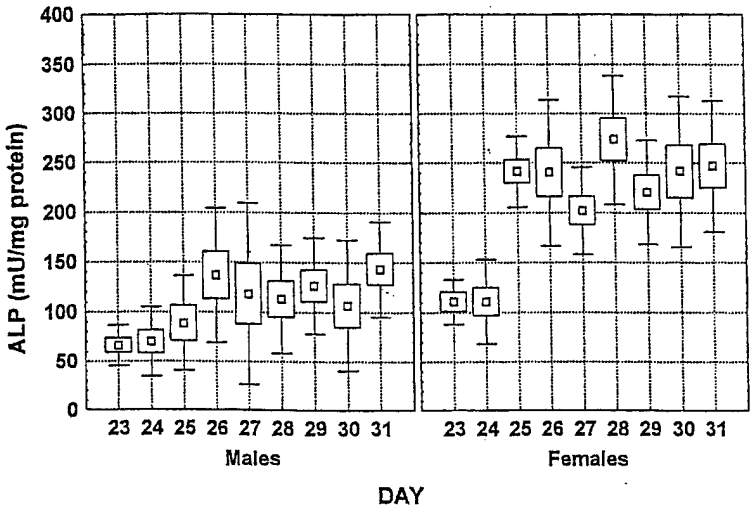

FIGURE 5: Alkaline phosphatase activity changes in femoral bone extracts of males and females of C57BL/6J mice during puberty. Boxes represent SEM and bars represent SD.

both male and female C57BL mice (**Figure 6**). Based on the findings that growth hormone/IGF-I is an important regulator of bone formation and based on the findings that both body weight and bone weight are severely decreased in IGF-I knockout mice, we propose that the skeletal changes that occur during puberty is, in part, mediated by changes in IGF-I production. We, therefore, evaluated the relationship between serum IGF-I levels and skeletal changes during puberty (see below).

g. Relationship between Serum IGF-I and Skeletal Changes During Puberty. In order to determine if the changes in serum levels of IGF-I are associated to corresponding skeletal changes, we determined the relationship between serum IGF-I versus femoral bone indices in mice. In the pooled data from males and females of 23 to 31-day old C57BL mice, we found serum levels of IGF-I showed significant positive correlation with dry weight of femur (**Figure 7**). In addition, serum levels of IGF-I also showed significant positive correlation with femur length and body weight. These data are consistent with our hypothesis that IGF-I plays an important role in regulating skeletal changes that occur during puberty and as such we will investigate the role of IGF-I in mediating skeletal changes by using mice deficient in IGF-I action in the second year of this proposal.

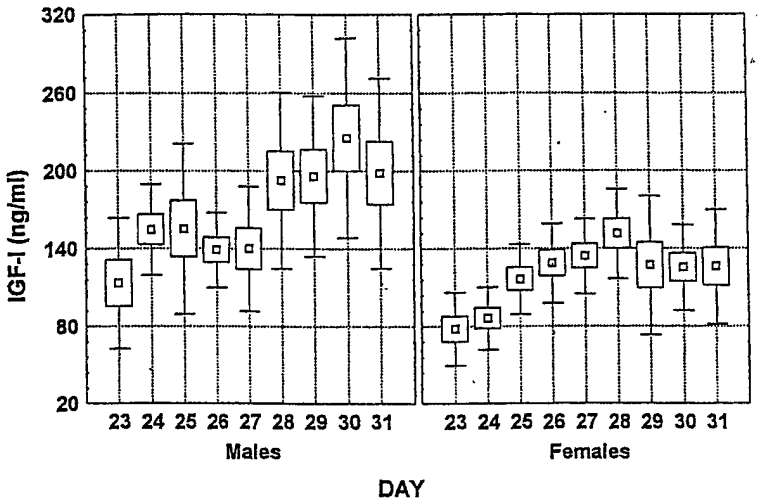

FIGURE 6: Serum IGF-I levels in males and females of C57BL/6J mice during puberty. Boxes represent SEM and bars represent SD.

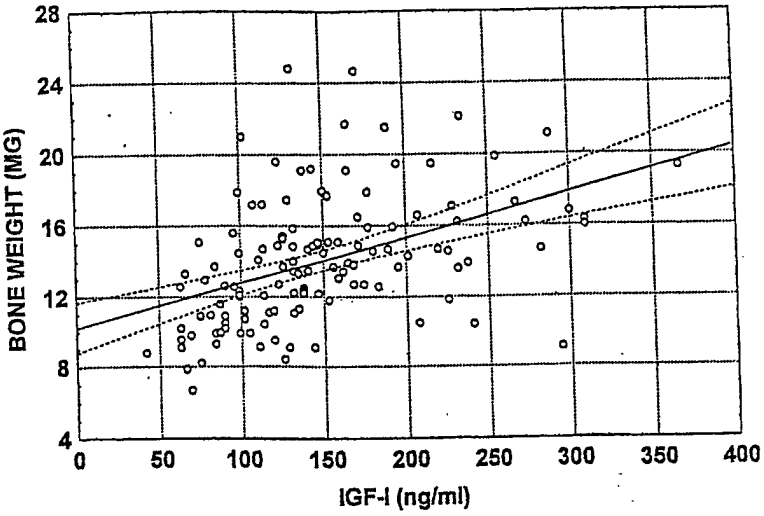

FIGURE 7: Relationship between serum IGF-I levels and femoral bone dry weight in the pooled data from males and females of 23-31 day C57BL/6J mice.

3. Conclusion.

In summary, there is rapid accumulation of bone within a short period of 4 to 5 days during the period of sexual maturation in mice. This rapid gain in bone weight appears to be mediated, in part, due to a rapid increase in bone formation seen during the early period of sexual maturation. In addition, the changes in bone weight also showed significant positive correlation with the serum level of IGF-I, suggest that GH/IGF axis play an important role in mediating pubertal skeletal changes that occur in mice. The potential role of GH/IGF axis in regulating skeletal changes during puberty is evaluated in the continuation studies using mice deficient in GH/IGF-I action.

REFERENCES

None.

APPENDICES

See attached manuscript submitted to *The Journal of Bone and Mineral Research* and an abstract submitted to the Endocrine Society.

PATENTS

None.

APPENDIX 1

1. MANUSCRIPT: Postnatal and Pubertal Skeletal Changes Contribute Predominantly to the Differences in Peak Bone Density Between C3H/HeJ and C57BL/6J Mice, C. Richman, S. Kutilek, N. Miyakoshi, A.K. Srivastava, W. Beamer, L.R. Donahue, C. Rosen, J.E. Wergedal, D.J. Baylink and S. Mohan. (Submitted to *JBMR*).

2. ABSTRACT: Postnatal and Pubertal Skeletal Changes Predominantly Contribute to the Differences in Peak Bone Density Between C3H/HeJ and C57BL/6J Mice, C. Richman, S. Kutilek, N. Miyakoshi, A.K. Srivastava, W. Beamer, L.R. Donahue, C. Rosen, J.E. Wergedal, D.J. Baylink and S. Mohan. (Submitted to the Endocrine Society).

POSTNATAL AND PUBERTAL SKELETAL CHANGES CONTRIBUTE PREDOMINANTLY TO THE DIFFERENCES IN PEAK BONE DENSITY BETWEEN C3H/HEJ AND C57BL/6J MICE*

(submitted to JBMR)

C. RICHMAN[1], S. KUTILEK[1], N. MIYAKOSHI[1], A.K. SRIVASTAVA[1], W. BEAMER[2], L.R. DONAHUE[2], C. ROSEN[3], J. WERGEDAL[1], D.J. BAYLINK[1] and S. MOHAN[1].
[1]JL Pettis VA Medical Center and Loma Linda University, Loma Linda, CA, [2]Jackson Laboratories, Bar Harbor, ME. and [3]St. Joseph Hospital, Bangor, ME.

Running title: Skeletal changes in mice during puberty

*The view, opinions and/or findings contained in this report are those of the author(s) and should not be construed as a position, policy, decision or endorsement of the Federal Government or the National Medical Technology Testbed, Inc.

A. Abstract

Previous studies have shown that 60-70% of peak bone density is genetically determined. The higher the peak bone density, the less likely an individual is to eventually develop osteoporosis. Therefore, the amount of bone accrued during postnatal and pubertal growth is an important determining factor in the development of osteoporosis. We evaluated the contribution of skeletal changes before, during and after puberty to the development of peak bone density in C3H/HeJ (C3H) and C57BL/6J (B6) mice. Volumetric bone density and geometric parameters at the middiaphysis of femora were measured by pQCT from day 7 through 56. Additionally, biochemical markers of bone turnover in serum and bone extracts were quantified. Both B6 and C3H mice showed similar body and femoral weights. B6 mice had greater middiaphysial total bone area and thinner cortices than did C3H mice. Within strains, males had thicker cortices than did females. C3H mice accumulated more mineral throughout the study, with the most rapid accumulation occurring postnatally (day 7-23) and during pubertal maturation (day 23-31). C3H mice had higher volumetric bone density as early as day 7, with males tending to have a higher volumetric bone density than did females. Higher serum IGF-I was present in C3H mice postnatally until day 23. Until day 35, B6 mice had significantly higher serum osteocalcin. Alkaline phosphatase was found to be significantly higher in the bone extract of C3H mice until day 23. These data are consistent with and support the hypothesis that the greater amount of bone accrued during postnatal and pubertal growth in C3H mice compared to B6 mice may be due to increased cortical thickness caused by increased endosteal bone formation and decreased endosteal bone resorption.

Key words: bone density, puberty, IGF-I, osteocalcin, C3H/HeJ and C57BL/6J mice

POSTNATAL AND PUBERTAL SKELETAL CHANGES PREDOMINANTLY CONTRIBUTE TO THE DIFFERENCES IN PEAK BONE DENSITY BETWEEN C3H/HEJ AND C57BL/6J MICE.* C. Richman, D.J. Baylink, S. Kutilek, N. Miyakoshi, A.K. Srivastava, W. Beamer, L.R. Donahue, C. Rosen, J. Wergedal and S. Mohan. JL Pettis VA Medical Center and Loma Linda University, Loma Linda, CA; Jackson Laboratories, Bar Harbor, ME; and St. Joseph Hospital, Bangor, ME.

Previous studies have shown that 60-70% of peak bone density is genetically determined. The higher the peak bone density, the less likely an individual is to eventually develop osteoporosis. Therefore, the amount of bone accrued during postnatal and pubertal growth is an important determining factor in the development of osteoporosis. We evaluated the contribution of skeletal changes before, during and after puberty to the development of peak bone density in C3H/HeJ (C3H) and C57BL/6J (B6) mice. Volumetric bone density and geometric parameters at the mid-diaphysis of femora were measured by pQCT in both males and females from day 7 through 56 at weekly intervals. Both B6 and C3H mice showed similar body and femoral weights. B6 mice had greater mid-diaphysial total bone area and thinner cortices than did C3H mice. Within strains, males had thicker cortices than did females. C3H mice accumulated more mineral throughout the study, with the most rapid accumulation occurring postnatally (day 7-23) and during pubertal maturation (day 23-31). C3H mice had higher volumetric bone density than B6 mice as early as day 7. The rate of bone density gain in C3H mice during postnatal and pubertal growth was twice that of B6 mice, though it was not different after puberty. To evaluate if the greater accumulation of bone during postnatal and pubertal periods in C3H mice compared to B6 mice is due to increased bone formation, we measured ALP activity in bone extracts. C3H mice exhibited significantly greater ALP activity in the femoral bone extract than did B6 mice at the time when maximal differences in bone density between the two strains occur. In addition, bone extract ALP showed significant positive correlation with bone density during postnatal periods. Because IGF-I is an important growth factor regulating bone formation, we evaluated the relationship between IGF-I level in serum and changes in bone accretion between C3H and B6 mice. We found serum IGF-I levels increased dramatically during postnatal growth in both strains and that C3H mice had significantly higher serum IGF-I levels compared to B6 mice. Serum IGF-I levels also showed significant positive correlation with bone density and bone extract ALP activity during postnatal period. [underline]Conclusions:[/underline] 1) The greater amount of bone accrued during postnatal and pubertal growth in C3H mice compared to B6 mice led to increased cortical thickness caused by increased endosteal bone formation and decreased bone resorption. 2) Two growth periods, namely postnatal and pubertal, are critical to the development of peak bone density between C3H and B6 mice. 3) The genes that are differentially expressed in the skeleton of C3H and B6 mice during postnatal and pubertal growth may provide clues regarding genes that contribute to the differences in bone density between these two strains.

*The view, opinions and/or findings contained in this report are those of the author(s) and should not be construed as a position, policy, decision or endorsement of the Federal Government or the National Medical Technology Testbed, Inc. This project was sponsored with funds by the U.S. Department of the Army and the National Medical Technology Testbed, Inc.

DESCRIPTION: State the goal of the project including how it relates to improving health care. Use succinct language to describe how the project goals will be achieved. Do not exceed the space provided.

(No change)

The major goal of this study is to find reliable noninvasive means of evaluating the left ventricular (LV) relaxation process and end-diastolic stiffness, abnormalities of which are the earliest signs of myocardial disease independent of etiology. Myocardial function, especially the LV diastolic function, plays a central or pivotal role in the genesis of symptoms and is major determinant of prognosis in a variety of disease processes including coronary artery disease, valvular heart disease, heart failure and hypertension. Detection and quantification of myocardial dysfunction in these disorders plays an important role in making therapeutic decisions. Reliable detection of abnormal relaxation as an early sign of myocardial disease may help to intervene at an earlier stage of myocardial disease before irreversible damage occurs to myocardial function.

It has been shown that mitral E wave propagation is related to LV relaxation and the A wave to late diastolic stiffness, but the precise mechanism behind their transmission has not been understood. Their relation to regional geometry and function of the myocardium along which its transmission occurs, and LV loading conditions in different pathological states has not been investigated.

This study is aimed at gaining deeper insights into the precise mechanism of E and A wave transmission, such that its various determinants may be factored in the interpretation of their relation to LV relaxation process and late diastolic stiffness respectively. An attempt will be made to develop multivariate equations to derive Tau and indices of LV diastolic stiffness with a high level of accuracy independent of physiological and pathological states.

PROJECT SITES (Organization, city, state): No change

1.Cardiology Section (111C)
Jerry L Pettis VA Medical Center,
Loma Linda, CA 92357

2.Cardiovascular Fluid Dynamics Laboratory,
Georgia Institute of Technology,
Atlanta, GA.

NO. 34

LLVARE/Pai

Assessment of Left Ventricular Relaxation and Elastic Properties from Analysis of Mitral E and A Wave Propagation

This project has been tabled as the principal investigator has taken a leave of absence to work in the mid-east

No report at this time

Name of Project Director: Lawr

DESCRIPTION: State the goal of the project, including how it relates to improving health care and noting the advanced technology that will be developed or tested . Use succinct language to describe how the project goals will be achieved. **Do not exceed the space provided.**

Beginning with an existing immunologically-inert biomaterial, *Placopecten* abductin, we propose to develop a prosthetic bioelastomer material (PBM) for the repair of articular cartilage in weight bearing joints. The biomechanical properties of this natural biomaterial, unprecedented compressional stability and resilience, will offer significant advantages over existing treatments for orthopedic injury and osteoarthritis (OA), including enhanced prosthetic longevity. The proposed breakthroughs in the design and synthesis of biomaterials call for a multi-disciplinary research approach. This proposal brings together the necessary biosynthetic (VA) and rational material design expertise (Caltech). Military and civilian populations that will benefit by development of a PBM treatment include a) veterans; b) paratroopers, recruits in training, and active duty personnel; c) athletes; d) automobile accident victims; 3) children and the elderly suffering degenerative joint diseases such as chondromalacia and OA, respectively.

Patients with damaged articular cartilage in weight-bearing joints experience a quality of life characterized by long-term pain and disability. Traditional medical treatments offer inconsistent results and only short-term relief. Musculoskeletal soft-tissue injuries in military personnel totaled 34% and 27% in the Persian Gulf War (Truax 1997) and Operation Joint Guard in Bosnia (McKee 1998), respectively. Injuries to weight-bearing joints of the knees and ankles are common during military training. At Fort Bragg alone, a total of 1,840 injuries occurred from parachute landings between May 1993 and December 1994 (Craig 1997). Untreated, such injuries result in OA 15 years after trauma (Roos 1995). OA is the most prevalent form of arthritis and the leading cause of disability in the US, affecting an estimated 20.7 million Americans, with special implications for our nation's 25.6 million aging veteran population.

PROJECT SITE(S) (organization, city, state):

1. Jerry L. Pettis Memorial Veterans Medical Center, Loma Linda, CA
2. California Institute of Technology, Pasadena, California (no consortium/contractual arrangement is involved)

COPY

JUN - 1 2000

ORIGINAL

National Medical Technology Testbed, Inc. Final Scientific Report

March 1999-May 2000

Cooperative Agreement DAMD17-97-2-7016

Subagreement 012-FY98-LLVARE-SANDBERG

5/31/00

Date

Lawrence B. Sandberg M.D., Ph.D.
Jerry L. Pettis Memorial Veterans Med. Center
Research 151
11201 Benton Street
Loma Linda, CA. 92357
Voice: (909) 825-7084 ext. 1536
Fax: (909) 478-5043

A. Introduction

Our goal was to study and characterize the abductin protein derived from *Placopecten magellanicus* at the molecular and biophysical level. Specifically, the nucleotide/amino acid sequence of *Placopecten* abductin will be determined. Of upmost importance, the cross-links between the abductin monomers will be confirmed and ultimately, the three-dimensional structural conformation of the abductin monomer will be ascertained. This structural information will prove most useful in designing a biopolymer which resembles abductin at the structural and functional level such that it may be used primarily to replace articular cartilage in patients undergoing arthroplasty.

B. Objectives

- Nucleotide/amino acid sequence of *Placopecten* abductin
- Cross-link types in *Placopecten* abductin
- Three-dimensional structure of *Placopecten* abductin

C. Experimental Data.

C.1. Nucleotide/amino acid sequence of *Placopecten* abductin

Peptide sequencing of abductin peptides generated via proteolytic digestion of *Placopecten* abductin revealed a repeating pentapeptide, FGGMG. This pentapeptide is found to occur six times in the amino acid sequence for abductin in the non-swimming *Argopecten irradians* scallop, or 23% of the molecule's mass (1) (Fig. 1). In addition, these segments are spatially arranged so that there are five residues between most of the repeating pentapeptides. This spatial arrangement may serve to position the very hydrophobic phenylalanine residues toward the interior of the molecule to shield them from the surrounding water. The region of the molecule containing this spatial arrangement of pentapeptides will most surely prove to be the functional domain of abductin, which governs its ability to compress. Furthermore, we hypothesized that the high frequency of FGGMG occurring in both *Placopecten* and *Argopecten* abductin indicates that this conserved trait between swimming and non-swimming scallops is essential for preserving the tertiary structure governing abductin's ability to compress. Initial proof for the

function of this domain will be discussed later in conjunction with molecular dynamics modeling of repeating abductin peptides.

Fig. 1. Protein sequence alignment of sequenced *Placopecten* abductin peptides with the published amino acid sequence for *Argopecten* abductin. (-) indicates sequence homology while a one-letter amino acid designation corresponds to sequence non-homology.

```
            1234567890 1234567890 1234567890 1234567890 1234567890
Argopecten  MNAYICLAAC LIAAVSAAGY GGGAGSMGGT GGMGGGMNAG GFGGMGGMGG
Placopecten   .                                          - -----
Argopecten  GKGGFGGIGG FGGGMGGGPG GFGGMGGFGG MAAKGGFGGM GSGMGGFGGM
Placopecten  Q----- -- ---      - ---------- -  Q------ -G--------
Argopecten  GGGNAGFGGM GGGNAGFGGM GGQGGFGGKG Y
Placopecten ---   ---- ---   ---N ---------
```

Further peptide sequencing of *Placopecten* abductin in our lab revealed evolutionary amino acid substitutions when compared to the *Argopecten* abductin sequence. It appears that lysine 52 and lysine 84 are converted, via a point mutation to the first codon base, to glutamine in both cases. This observation may provide a clue for the existence of another cross-link in abductin, resembling the cross-link responsible for blood clotting in humans. The suspected cross-link is ε(γ-glutamyl) lysine, which is an isopeptide bond formed between the side chains of glutamine and lysine. Peptide sequencing also revealed that glutamine 123 and lysine 129 are conserved in both *Placopecten* and *Argopecten*. In Placopecten, it is quite possible for lysine 129 to cross-link with glutamine 52, glutamine 84, and glutamine 123 in another abductin monomer.

In addition, a full cDNA sequence determination of *Placopecten* abductin was attempted with little success. Forward and reverse primers were made based on peptide sequences of *Placopecten* abductin and the cDNA sequence for *Argopecten* abductin. Freshly isolated mRNAs from mantle cells were subjected to rtPCR (reverse transcription polymerase chain reaction) for 26 cycles in the presence of the previously mentioned primers. A ~134bp band was observed upon electrophoresis of the PCR mix on a 1% high melt agarose gel stained with ethidium bromide (Fig. 2).

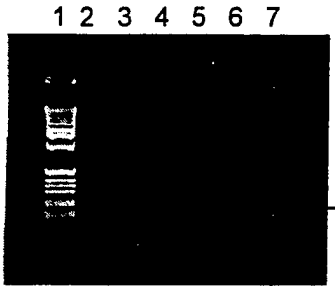

Fig. 2. High melt agarose gel stained with ethidium bromide. Arrow points to ~134bp PCR product.

Subsequent attempts at recreating this experiment were unsuccessful. Analysis of the mRNA isolated from the scallop mantle cells on a formaldehyde agarose gel indicated that little to no mRNA was present. A literature search indicated that this is a common problem in isolating mRNA from invertebrate sea creatures due to high concentrations of carbohydrate surrounding the organ tissues. It is apparent that carbohydrates must be enzymatically removed prior to isolating mRNA from the mantle cells. In the interest of progress, we decided to move forward with the project using only the information obtained through peptide mapping.

C.2. Cross-link types in *Placopecten* abductin

Disulfide bonds have been identified thus far as the cross-links in abductin. However, the disulfide cross-links are found both in the form of cystine and homocystine. These intact cross-links were identified via fluorescence amino acid analysis of abductor ligaments exhaustively digested with two proteolytic enzymes (Fig. 3). The free amino acids and intact cross-links were derivatized with o-phthaldialdehyde and separated on a C8 reverse phase column with a methanol gradient. This analytical method, was described by Griffin and Wilson (1984) to identify ε(γ-glutamyl) lysine in amino acid analyses of blood clots in animals (2). As yet, we cannot confirm the presence or absence of ε(γ-glutamyl) lysine in *Placopecten* abductin.

In order to create a 3D network of peptides to form PBM, the spatial density of disulfide cross-links must be determined in *Placopecten* abductin. It is not known as yet how many cysteine and homocysteine residues occur in *Placopecten* abductin nor their respective positioning, due to the lack of cDNA sequence data. The amount of cysteine and homocysteine can be readily determined via analytical amino acid analysis by oxidizing them first to the stable cysteic and homocysteic acids. The positions of cysteine residues can be determined from cDNA

sequencing, and the positioning of homocysteine residues by sequencing their carboxy-methylated derivatives in intact peptides via classic Edman chemistry.

The number of cross-links between peptide chains is directly related to the stiffness, or Young modulus, of the resultant 3D protein network. The more cross-links present, the higher the Young modulus (3) (4). This correlation will be extremely useful when designing an abductin-based bioelastomer because it will allow us to tailor the elastic modulus of the abductin-based bioelastomer to approximate the elastic modulus of normal hyaline cartilage.

Fig. 3. Identification of intact cystine and homocystine via fluorescence amino acid analysis of *Placopecten* abductin exhaustively digested with Pronase and Aminopeptidase M.

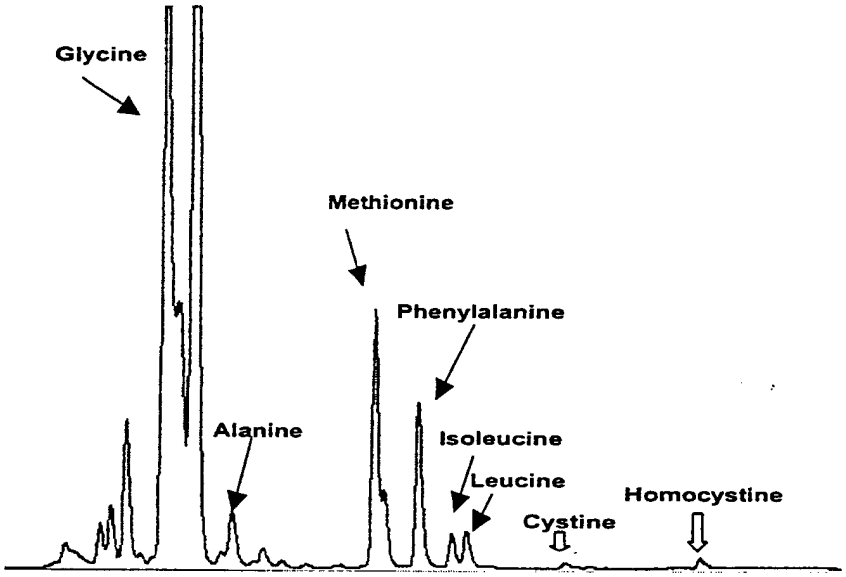

C.3. Three-dimensional structure of abductin

CD spectra for the abductin decapeptide, FGGMGGGNAG, were obtained in water and trifluoroethanol (TFE), respectively, at three different temperatures. The dominant features in both solvents (one positive band at 216-218 nm and one negative band at 200 nm) are those typical of quasi-extended polyproline II structure, together with an undefined amount of random flexible conformations (Fig. 4). In water the reduced intensity of the positive band and the

appearance of one negative band around 230 –235 nm could possibly suggest a minor population of β-turn conformers, most probably of type II.

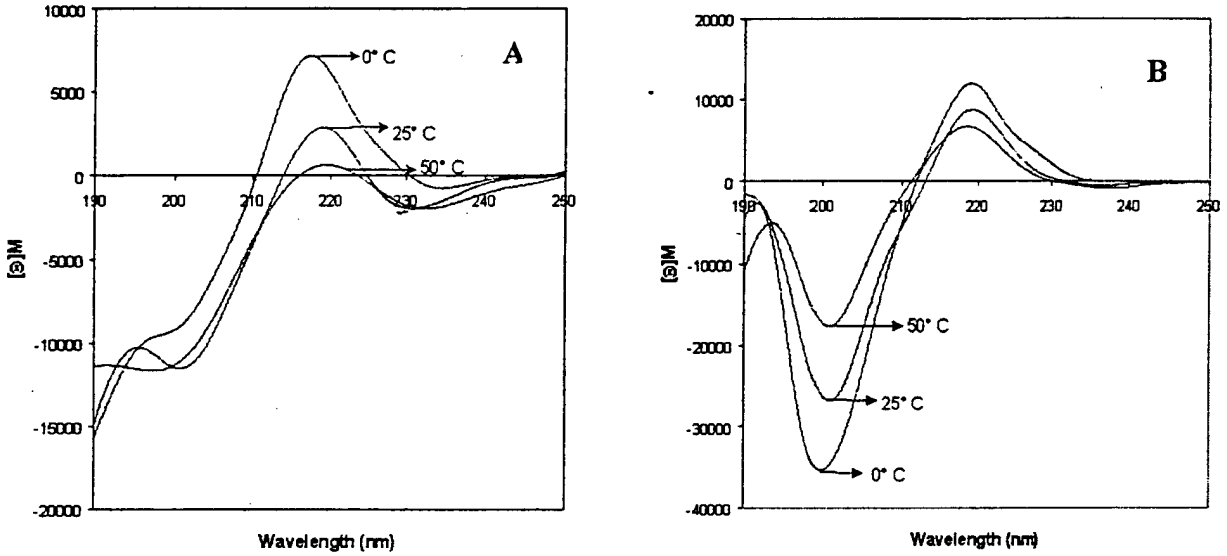

Fig. 4(A) CD spectra of FGGMGGGNAG in water and **(B)** TFE at 0°C, 25°C and 50°C. CD spectra at all three temperatures gave a positive band at 216-218 nm and a negative band at 200 nm.

The polyproline II structure has been shown to be present in the solid state of polyglycine (5) (polyglycine II structure (6)) and therefore is not unexpected for the abductin decapeptide containing six glycyl residues and a stretch of three consecutive glycines to adopt a polyproline II structure. Moreover, the polyproline II structure is characteristic of the collagen triple helix which further makes a case for the importance of the decapeptide in abductin secondary and tertiary structure.

To further elucidate the structural role of the decapeptide in abductin, various sequences from *Argopecten* abductin containing the repetitive FGGMG and FGGMGGGNAG motif were selected for tertiary structure prediction using Molecular Dynamics (MD) calculations.

Due to the insoluble nature of the abductor ligament, when exposed to conventional denaturing agents such as DTT, beta mercaptoethanol, urea, and guanidine hydrochloride, it has proven difficult to obtain the intact abductin monomer for subsequent structural analysis. The high Gly

content points to a globular coiled protein for which large crystals for x-ray crystallographic data analysis may not be attainable. In the absence of full sequence NMR data, Molecular Dynamics (MD) modeling was performed using MPSIM (7) as a means to obtain tertiary structure information for (1) *Argopecten* abductin (*A119NSP*) without the 17 aminoacid signal peptide lead sequence as predicted using the neural network approach of Nielsen (8), (2) abductin's core 48 aminoacid sequence (*A48CS*), (3) the 47 aminoacid Abductin mimetic peptide with Factor XIII flanking sequences (*A47MP*), (4) an 11 aminoacid Abductin structural motif sequence GGMGGGNAGFG (*A11SMS*). The generalized Born solvation model (9) as implemented by Frisner (10) was used to predict the tertiary structure of *A119NSP, A48CS, and A47MP* in the presence of implicit water solvent. A newly developed solvent accessible surface model (SASM) was employed to predict the structural stability of *A11SMS* and its dimerized versions.

Constant temperature-volume (NVT) dynamics at 330 °K were carried out for 585 picoseconds on *A119NSP*. This temperature is required to anneal the sample and allow a broad region of torsional space (ϕ,ψ) to be sampled by each of the residues present. At the end of the annealing process, *A119NSP* was quenched to milder temperatures (310 °K) for an additional 50 picoseconds. The torsions of all residues were monitored as a function of time. Only ocassional deviations of at most one torsion from the expected occupied regions in a Ramachandran plot were observed. This process was repeated three times using random velocity initializations. As a direct results of the high Gly content all three predicted *A119NSP* tertiary structures were distinct, globular proteins consisting mostly of random coils lacking clearly defined secondary structures.

This predicted overall globular structure of abductin, unlike the more ordered secondary and tertiary structures of elastin and collagen respectively, may prove suitable for providing compressional stability. Having a globular shape may be more fitting for isotropic properties, meaning that an external force will illicit an equal compressional response regardless of where that force is applied to the molecule.

Unlike *A119NSP, A48CS* showed significant secondary structure at the end of the molecular dynamics simulations. Figure 5 shows selected residues to illustrate that the tertiary structure of

A48CS peptide had converged to a final equilibrium state in less than 100 picoseconds. Quite possibly the shorter size of *A48CS* facilitates the appearance of secondary structural motifs during the finite simulation times.

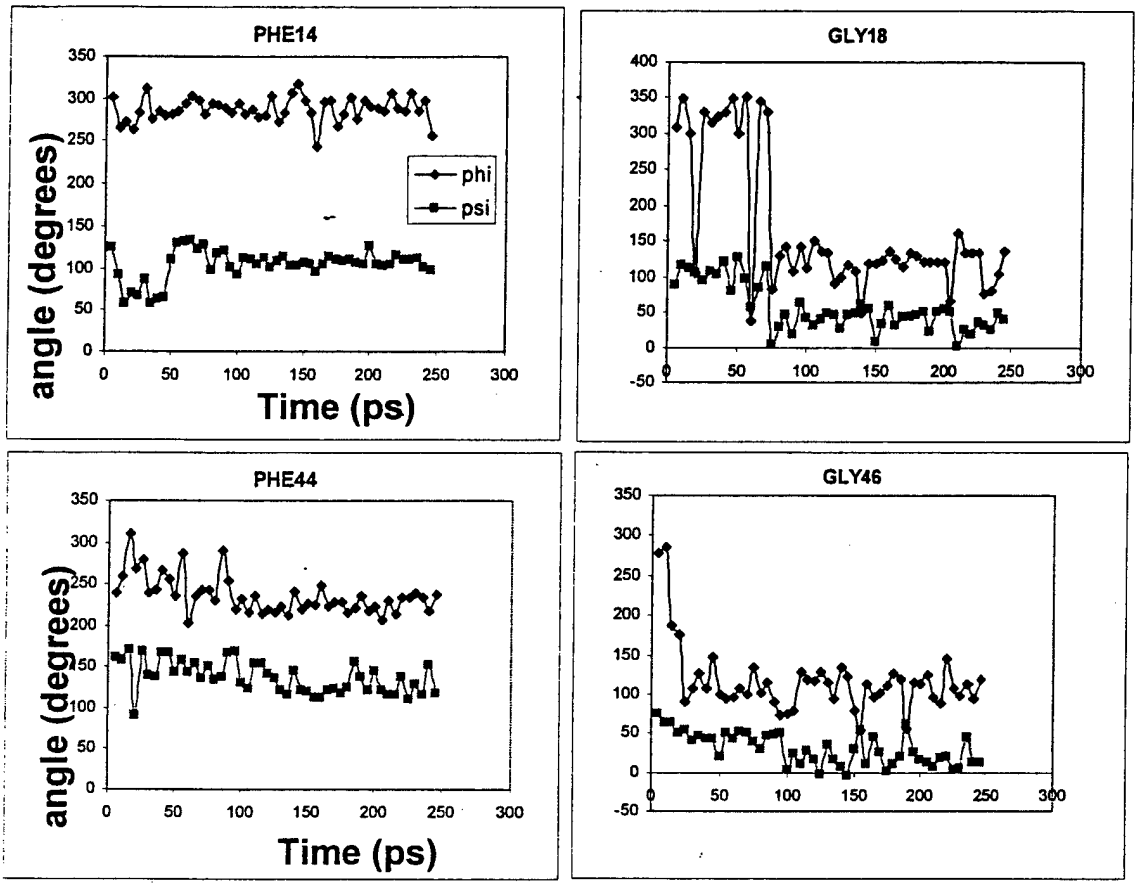

Fig. 5: Shown are the time evolution for *A48CS* torsion angles versus time. The ϕ angle for Gly 18 appears to fluctuate greatly before adopting a more stable conformation near 100ps in contrast to the ϕ angle of Gly 46 that stabilizes after ~35ps.

Figure 6 shows the equilibrated *A48CS* after 250 picoseconds. Unexpectedly, the methionine residues are completely exposed to the surrounding medium. Three central phenylalanine groups are positioned partly inside the globular protein inside a local loop created by nine sequential aminoacids, GGMGGGNAG. Repeated simulations of *A48CS* indicate the presence of this tertiary structure motif, three times in each modeled structure. Two other Phe residues remain fully exposed to the surrounding solvent. These may serve to form intermolecular associations via hydrophobic interactions with other similar protein segments.

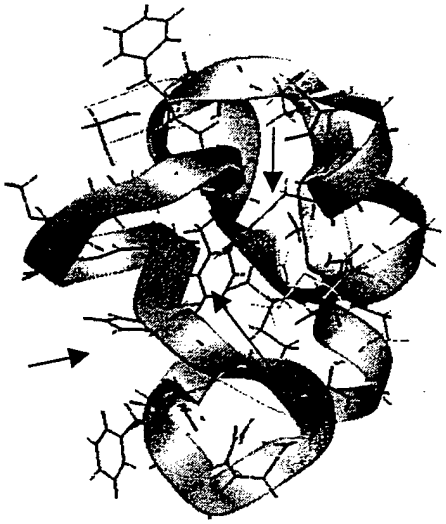

Fig. 6: Equilibrated tertiary structure of *A48CS* after 250 picoseconds of molecular dynamics. Arrows indicate the locations of three partially buried phenylalanine hydrophobic groups. Two more remain fully exposed.

We propose that these hydrophobic motifs, in conjunction with putative covalent cross-linking, are responsible for the stabilization of the abductin protein aggregate (abductor ligament). To test this hypothesis we used solid peptide synthesis to synthesize 0.25 millimoles of *A47MP, or* approximately 800 mg dry weight.

D. Additional Experimental Data

D.1. Abductin peptide mimetic

Based on these previous results, we designed a 47 aminoacid abductin mimetic peptide *A47MP* that incorporates a 25 amino acid stretch of *Argopecten* Abductin. In addition, we incorporated partial Factor XIII substrate sequences (11) both on the n-terminus and c-terminus of *A47MP*. Figure 7 illustrates the abductin mimetic peptide design. The partial Factor XIII substrate sequences were incorporated into the design in order to enzymatically cross-link the abductin mimetic peptides into a 3D matrix or aggregate using Factor XIII in the presence of thrombin (11) at a later stage. The Factor XIII substrate sequences are the cross-linking domains which flank the abductin functional domain. Partial Factor XIII substrate sequences were used because the full sequences, which contain highly hydrophobic amino acids on their n-termini, may increase the overall hydrophobicity of the mimetic peptide disrupting hydrogel formation.

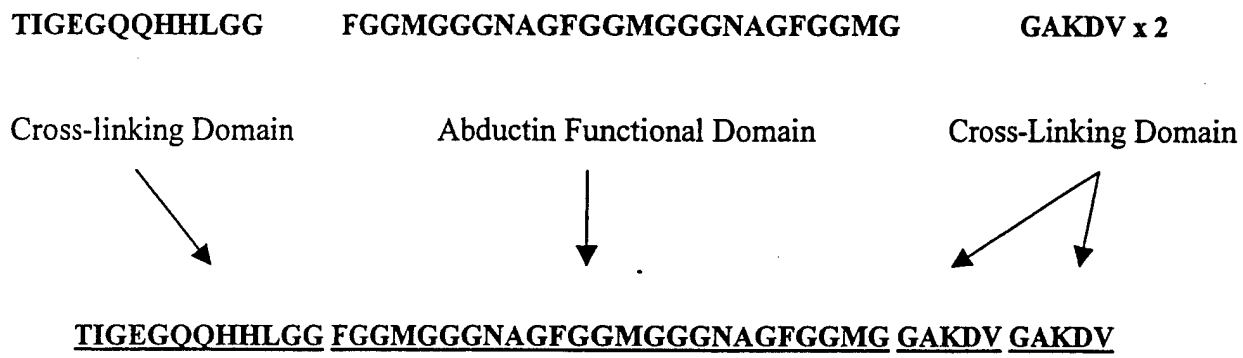

Fig. 7. A47MP abductin mimetic peptide design. (Patent Pending)

The A47MP design incorporates three hydrophobic groups, the minimum number required to generate a three dimensional network of hydrophobic "crosslinks". A47MP's tertiary structure was modeled with molecular dynamics. Three independent runs, each a minimum of 100 ps long, produced similar looking tertiary structures. A representative structure is shown in Fig.8. The most stable PHE loops were used as starting geometries for later studies of a shorter 11 aminoacid structural motif sequence GGMGGGNAGFG , A11SMS.

Fig. 8. A47MP abductin mimetic molecular dynamics tertiary structure. The structure contains three loops around each of the three PHE hydrophobic residues.

The abductin mimetic peptide was synthesized via standard solid phase FMOC chemistry on a preloaded resin. After synthesis, 100 mg of peptide resin were cleaved using a standard TFA cleavage protocol and the peptide was immediately precipitated in ether to remove the hydrophobic protecting groups. The precipitated peptide was then spun down and dryed under a gentle stream of nitrogen overnight. Surprisingly, the dry un-crosslinked peptide formed a gel-like, nearly translucent, yellowish pellet that was rubbery to the touch (Figure 9). The abductin

peptide mimetic polymer (A47MP aggregate) pellet gave some fluorescence upon exposure to UV light and is only marginally soluble in water due to its hydrophobic Phe and Met residues.

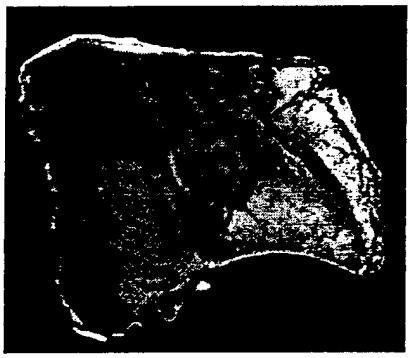

Fig. 9: Photograph of un-crosslinked A47MP aggregate. Notice the gel-like nearly translucent properties of A47MP aggregate.

What is remarkable about A47MP aggregate is that it exhibits rubber-like material properties even though it is not covalently cross-linked. We believe that this initial aggregate is held together by a combination of peptide monomer "entanglement" and intermolecular hydrophobic interactions or "hydrophobic cross-links". Peptide monomer "entanglement" probably occured between the amorphous regions of the peptide when exposed to ether. In addition, the biphasic (protein + water) properties of this aggregate suggest that there is some water sequestered within that most likely contributes to the elastic properties.

This preliminary peptide aggregate strongly suggests that the repeating peptide sequences in abductin do indeed play a role in molecular self-assembly and elasticity. It is quite remarkable that hydrophobic cross-linking alone can catalyze self-assembly of a three-dimensional network or matrix of peptides in the absence of covalent cross-linking. In addition, hydrophobic cross-linking provided enough structural stability to perform mechanical property measurements on the uncross-linked A47MP aggregate shaped like a flat cylinder (Fig. 10).

D.2. Mechanical Properties of A47MP aggregate

The average data (n=6 per group) are reported in Table 1 for the dry abductin mimetic polymer. An average modulus of 4.25 ± 1.71 MPa was calculated for a polyurethane elastomer as a comparison to the calculated Young's modulus for the un-cross-linked A47MP aggregate shown in figure 10. Saline immersion led to a degradation of the abductin mimetic polymer which caused instant fracture under loading after 30 minutes of immersion, and complete disintegration

after 60 minutes. Therefore, no compression modulus could be calculated for these two groups. The modulus of the abductin mimetic polymer calculated by Finkin's method was significantly lower than that of the polyurethane elastomer used by others in tribological studies for cartilage replacement (student "t" tests (α= 0.05)) (12).

Elastomer	Parameters	Nomenclature	Values
A47MP aggregate	Thickness	d	1 mm
(dry)	Applied load	P	17.4 ± 9.13 grams
	Deformation	H	53.0 ± 1.6 μm
	Calculated Modulus	E	79.36 ± 41.4 kPa

Table 1. Mean ± Standard Deviation of Original Specimen Thickness, Deformation and Calculated Elastic Modulus Using Finkin's Equation for the dry A47MP aggregate [Finkin, 1972].

The calculated Young's modulus for the abductin mimetic polymer was approximately 0.08 MPa. Although this compressive modulus is two orders of magnitude lower than the compressive modulus for the polyurethane elastomer, this data proves that hydrophobic interactions alone can account for at least partial elastomeric stability.

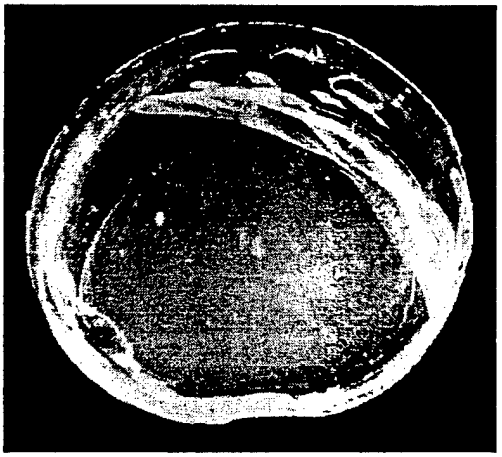

Fig. 10: Abductin mimetic polymer shaped in the form of a nickel for mechanical testing and calculation of compressive modulus.

D.3. Quaternary Structure of A47MP Aggregate

Molecular dynamics modeling was employed to visualize the way in which A47MP might form a three-dimensional network. Figure 11A shows the most stable predicted quaternary structure that A47MP might adopt. Notice that the A47MP monomers are held together via hydrophobic interactions between the partially solvent-exposed hydrophobic side-chains of phenylalanine residues. Figure 11B shows the quaternary structure of A47MP with a Connolly water accessible surface. Interestingly, there appears to be a water channel through the center of the A47MP 3D network. This may explain why the A47MP aggregate is able to retain water to form a biphasic material. Figure 11C shows an electron micrograph at high power of an abductor ligament fiber. We propose that abductin forms a similar 3D network as that shown in Figure 11A, possibly corresponding to the small dark clusters that make up the individual abductor ligament fibers (Fig. 11C).

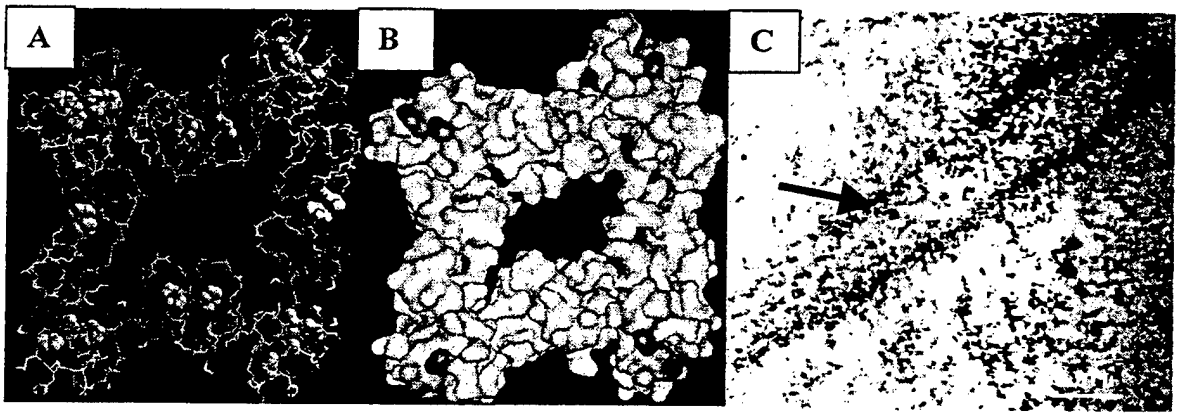

Fig. 11A. Predicted model for the quaternary structure of A47MP. **B** The predicted model for the quaternary structure of A47MP with a Connolly water accessible surface. **C** High power electron micrograph of an individual abductor ligament fiber.

D.4. Preliminary In-vitro Toxicology/Immunology of Soluble *Placopecten* Abductin

Two tests were performed to determine whether the presence of exogenously aqueous solubilized abductin interfered with immune functional properties. An in-vitro natural killer (NK) activity assay was conducted, wherein, freshly isolated whole blood (human) lymphocytes mixed at various ratios (100:1; 50:1; 25:1; and 12.5:1) with NK target cells. The assay was incubated for 4 hours at 37°C after which the supernatant was removed and mixed with 100μL of lactate dehydrogenase (LDH) reaction mix which measures reductase activity released as a function of

cell death. A quantitative colored product was formed and read at 490 nm wavelength (13). The same lymphocyte preparation was tested with and without solubilized abductin to determine if the presence of abductin altered NK activity (Figure 12A).

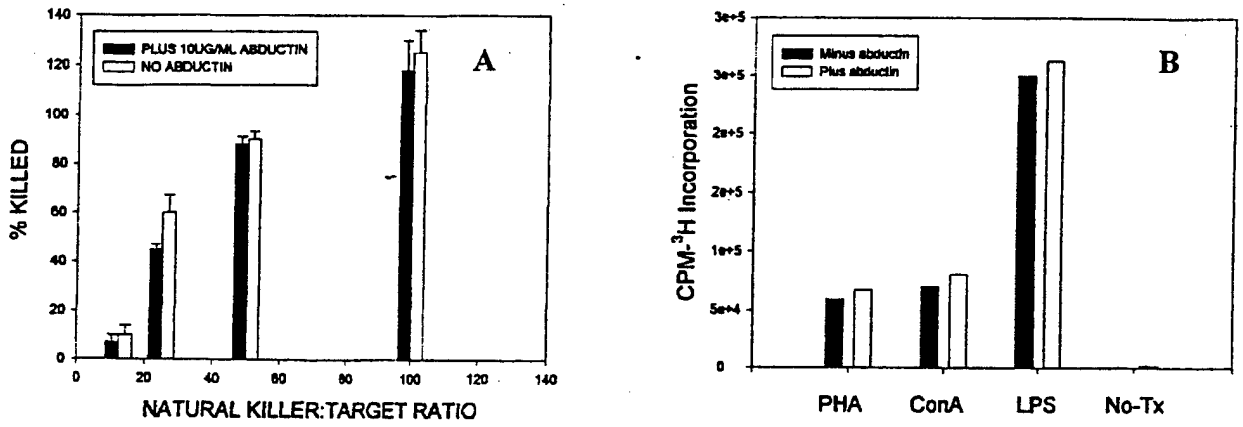

Fig. 12. A Effect of exogenously added abductin on natural Killer (NK) activity. **B** Effect of exogenously added abductin on the mitogenic induction of lymphocyte proliferation in-vitro.

A second test of immune function was mitogen induced lymphocyte proliferation as measured by ^{3}H-thymidine incorporation into newly synthesized DNA. The ability to respond to immune challenge requires that the immune competent cells divide rapidly when stimulated. Agents or substances that dampen or cause an anergic state in immune function reflected by their reduced-induced proliferation would be extremely dangerous. To test whether abductin had any such effect, we divided a sample of freshly isolated human lymphocytes into 2 fractions. One fraction received no abductin and the other was incubated with 10μg/mL solubilized abductin. In a 96 well plate format, $2x10^{5}$ cells per well were dispensed into triplicate sets (phytohemagglutinin-A (PHA), concanavalin A (ConA), lipopolysaccharide (LPS) and no mitogen). The cells were incubated at 37°C for 48 hours after which time they were washed and counted for the amount of radioactive tritium they had incorporated (Figure 12B).

The results of these two initial experiments indicate that the exogenous addition of solubilized abductin does not interfere with NK activity (Figure 12A) or induction of blastogenesis (Figure 12B). The graphs show that there is little to no statistical difference in the percent NK target cells killed or the induction of human lymphocyte growth in the presence or absence of abductin. This

data is extremely important to the potential human use of the proposed abductin-based bioelastomer, because it suggests that implantation of an abductin-based bioelastomer will not, as suggested in these initial tests, alter immune function.

E. Proposed Theory(s)

E.1. Hydroelasticity Model

The molecular basis for the elasticity of non-biological elastomers (14-18), point to a retractive force largely of entropic origin, the positive gain in free energy upon deformation arising from the loss in polymer chain entropy. For protein based elastomers such as elastin (19) and abductin, elasticity is highly dependent on the presence of water. The water content in abductin can be as high as 50%. Dessicated samples are brittle and exhibit little recovery and resilience. Proposed models should explain the interplay between peptide structure, water solvation, and the elastic recovery properties of these bioelastomers. We begin by writing an approximate expression for the change in free energy for a system consisting of a peptide chain made up of partly buried hydrophobic groups.

$$\Delta G_{solv} = \Sigma\ \delta A_i\ \sigma_i \qquad (4)$$

An externally applied strain or pressure changes the state of amino acid groups from partly buried to exposed. δA_i is the change in the water exposed surface area for the i-th atom in the protein upon application of an external pressure or strain, σ_i is the surface tension contributed by each solvent accessible atom. We use the Connolly algorithm (20) to calculate the solvent accessible surface with the probe solvent molecule radius set at 1.53 Å.

Experimental free energy solvation data on a set of 322 compounds (21) were used to evaluate the atomic surface tension parameteres σ_i. Atom types were defined according to the definitions of the Dreiding force field. The values, in Kcal/mole-A^2, are σ_{H_A} =-0.222 for hydrogen bonded to oxygen or nitrogen, $\sigma_{H_}$ =0.01143 for hydrogen bonded to carbon, σ_{C_3} =-0.008 for sp3 carbon, σ_{C_R} =-0.026 for carbon in a resonance structure, σ_{N_R} =-0.171 for nitrogen in a peptide bond, σ_{O_2} =-0.126 for carbonyl oxygen, σ_{O_R} =-0.142 for C-terminal oxygens, and σ_{S_3} =-0.016

for sulfur. Model predictions compare well with the experimental solvation free energies as shown in Fig. 13.

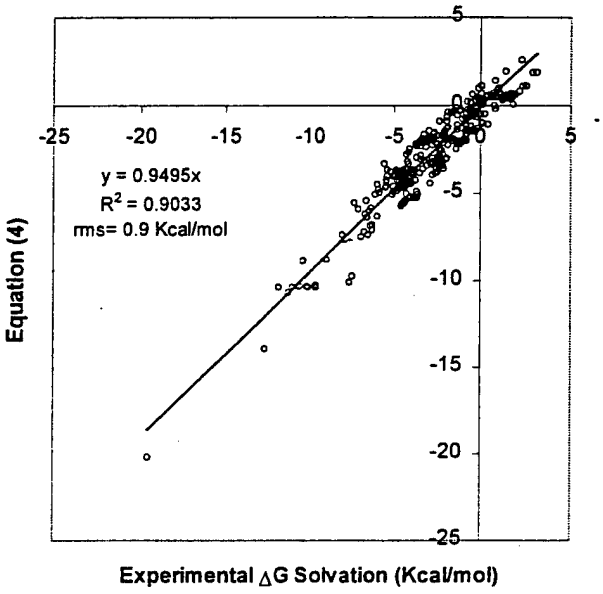

Fig. 13: Calculated (Kcal/mol) vs experimental (Kcal/mol) solvation free energies for 322 organic compounds. The rms deviation is 0.9 Kcal/mol.

The *A47MP* MD simulations indicate that hydrophobic residues are partially protected from the surrounding aqueous environment. An externally applied compressional stress may deform the network in *A47MP* exposing a greater hydrophobic surface area (Fig. 14A). The additional hydrophobic contributions come nearly exclusively from phenylalanine. We use Equation (4) to calculate the change in solvation free energy of the *A11SMS* phenylalanine loop region as a function of changes in the phenylalanine C_α backbone ϕ angle. The results are shown in Fig. 14B. Complete water exposure of phenylalanine (ϕ = 120°) leads to a net increase in free energy of 4 Kcal/mol suggesting that applied mechanical work might be stored as a positive change in solvation free energy for subsequent release as elastic recoil. The jump in free energy may be seen as caused by the increased disruption of the hydrogen bond water network surrounding a hydrophobic group. The restorative angular force, 3.7 x 10-2 Kcal/mol-degree, is approximately constant. Estimates of the entropic change, from the power spectrum of the dipole autocorrelation function around hydrophobic groups indicate that ΔS is negative (22), i.e., the first water coordination shell has a higher level of organization around phenylalanine than the bulk liquid. Consequently, enthalpic and entropic factors work in the same direction to yield a positive ΔG when hydrophobic groups are exposed to water. Because elastic work is stored in

the surrounding water medium as a state of higher free energy we referred to this as a hydroelasticity model.

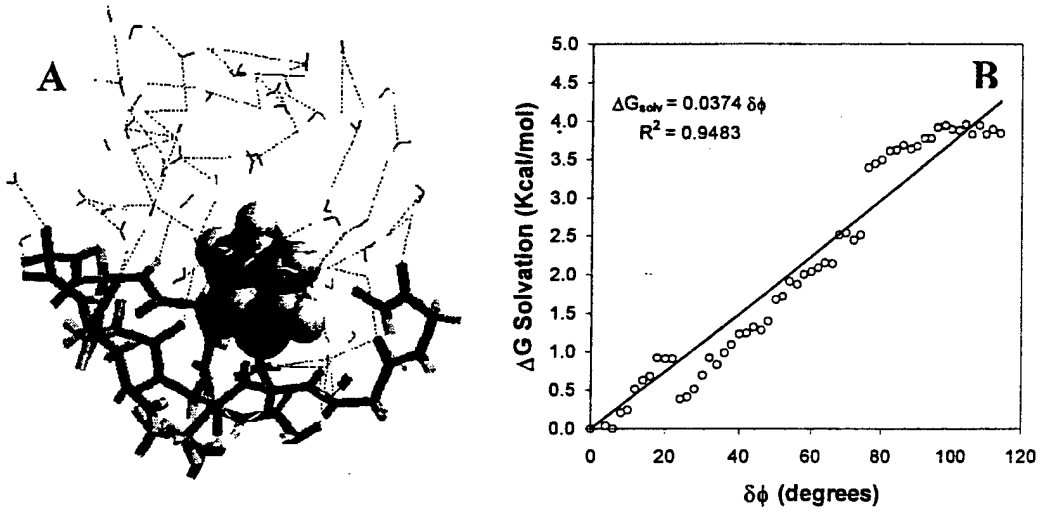

Fig. 14: **(A)** A network of hydrogen bonded water molecules covers the exposed side of each of three phenylalanines in *A47MP*. **(B)** The solvation free energy (Kcal/mol) increases with increased torsional (phi angle) displacement (degrees) of the phenylalanine side chain from partially to fully exposed to the surrounding medium.

E.2. Hydrophobic cross-links and elastic recoil

The *A11SMS* loop sequence, the phenylalanine loop region, constitutes a simple structural model for the estimation of the elastic force developed by abductin upon an applied external deformation. Two *A11SMS* loop sequences were placed in close contact and energy minimized after 10 picoseconds of anneal dynamics. The dimer was then pulled apart from its closest point of approach in increments of 0.2 Å. Equation (4) was employed to calculate the change in solvation free energy as a function of the separation distance (Fig. 15A). This procedure resulted in the plot shown in Fig. 15B. One phenylalanine captures both loop sequences leaving the other available for "crosslinking" to a separate loop, a geometry reminiscent of a leucine zipper. This dimeric form, which we termed *snapped*, has an equilibrium distance R_o in water 3.4 Å away from the point of closest contact. The depth of the free energy solvation well, the energy required to break the hydrophobic cross-link, is approximately 5.3 Kcal/mole. The restorative

force can be estimated by fitting the bottom of the well section of the hydrophobic free energy potential analytically and evaluating the second derivative at R_o.

$$\Delta G_{solv(snapped)} = 19.2\ (R\text{-}R_o)^2 + 1.6\ (R\text{-}R_o) - 78.1 \quad (5)$$

This gives a value of 38.4 Kcal/mol-Å. This is the predicted value for the elastic force responsible for bringing the abductin mimetic back to its native globular state, either in compression or elongation according to the hydroelasticity model (4).

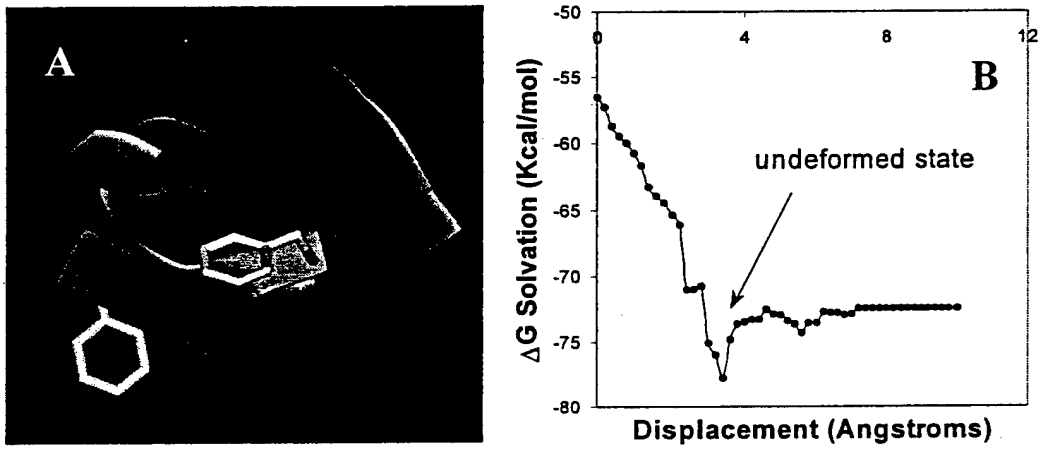

Fig. 15(A) Typical structure of a hydrophobic cross-link configuration. The hydrophobic cross-links was displaced from its position of closest approach in 0.2 Å steps and the solvation free energy (ΔG Kcal/mol) evaluated with Equation (4). **(B)** The change in solvation free energy against displacement (angstroms) leads to a elastic restorative force upon positive and negative deformations from the stable (well bottom) position.

F. Conclusions

F.1. Scientific Conclusions

The globular abductin protein has evolved to optimize recoil under compression. Abductin is shown to contain long repeat sequences of hydrophobic groups flanked by glycine. Using these

repeat sequences along with partial Factor XIII substrate sequences, a mimetic peptide of abductin was designed, modeled, synthesized and tested. The mimetic peptide forms a stable rubbery hydrogel capable of sustaining a load under compression even in the absence of covalent cross-links. These results suggest that self-assembly of functional biomaterials can be achieved through a network of non-covalent "hydrophobic" cross-links. The magnitude of the recoil force can be quantitatively predicted using structural information and a "hydroelasticity" model based on the changes in solvation free energy of the various molecular surface areas exposed to water. In contrast to classical theory of rubber elasticity, enthalpic contributions are important. The disruption of the hydrogen bond network around additional non-polar groups exposed during the deformation process leads to a higher enthalpy state. Entropic contributions are present and just as in the case of synthetic elastomers the entropy of the deformed state is lower, owing the higher water organization of the first coordination solvation shell.

F.2. Significance/Innovation

The research data described above is a significant contribution to both biology and the elastomer industry having potential ramifications in medicine (see section F.3. Medical Importance/Application(s)). The contribution to biology includes a unique "hydroelasticity model" that sheds light on the contribution of hydrophobic amino acid side chains to the production of compressive elasticity. We have also obtained preliminary data that indicates that hydrophobicity alone can drive molecular self-assembly of three-dimensional protein matrices. In general, the data described in this report also elucidates the mechanism by which abductin monomers might assemble to form the compressible abductor ligament found in scallops.

The contribution of this project to the elastomer industry is far reaching. It is quite possible that this project has shown the feasibility for making bioelastomer materials from rationally designed peptides. One might say that this project marks the beginning of the "bioelastomer industry". One very important feature of bioelastomers is that they may be mass produced in an environmentally safe manner using expression systems such as plants as opposed to the environmentally detrimental production processes for the production of conventional rubber elastomers and analogues such as fluoroelastomers.

F.3. Medical Importance/Application(s)

F.3.1 Chondrocyte Seeded Molecular Scaffold for Cartilage Replacement

In the United States there are over 500,000 *surgical* procedures each year relating to cartilage repair, resulting in an estimated market potential of $600 million. State of the art procedures include cartilage grafts from the patient, and marrow cell stimulating techniques, such as abrasion arthroplasty, drilling, and microfracture, that populate damaged portions of articular cartilage with pluripotential stem cells (23). However, these cells produce fibrocartilage repair tissue that lacks the compressibility of naturally occurring hyaline cartilage (articular cartilage) and surgical intervention only delay cartilage degeneration. Because there is currently no approved biomaterial for the treatment of articular cartilage defects, and since a significant backlog of patients exists, it is difficult to exactly quantify this market. A worldwide market potential for a developed product could conservatively be estimated at $1.2 billion/year.

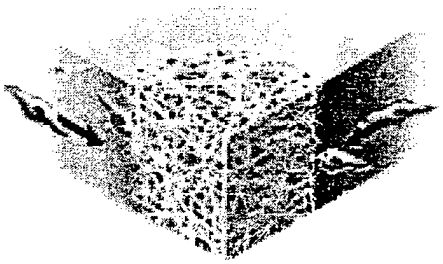

Current treatment methods for damaged cartilage involve the use of cultured autologous chondrocytes that are cells of a committed pathway to develop hyaline-like cartilage. These chondrocyte cells can be seeded into collagen gels (24), collagen matrices (25) or hydroxyapatite (26) then implanted into damaged areas of full-thickness articular cartilage. These current methods of treatment have experienced some success thus far in animal models.

We envision that an abductin-based bioelastomer will be a better resorbable molecular scaffold for autologous chondrocytes due to its elastic and gel-like attributes. Because the rationally designed abductin-based bioelastomer resembles abductin and can be modified to have a Young modulus similar to that of hyaline cartilage, the new abductin-based bioelastomer is predicted to be suitable to withstand the shear forces endured by weight bearing joints.

F.3.2 A Vertebroplastic Biomaterial for the Treatment of Osteoporosis

Osteoporosis, or porous bone, is a disease characterized by low bone mass and structural deterioration of bone tissue, leading to bone fragility and an increased susceptibility to fractures of the hip, spine, and wrist. Osteoporosis is a major public health threat for more than 28 million Americans, 80% of whom are women. In the U.S. today, 10 million individuals already have the disease and 18 million more have low bone mass, placing them at increased risk for osteoporosis. The estimated national direct expenditures (hospitals and nursing homes) for osteoporotic and associated fractures was $13.8 billion in 1995 alone ($38 million each day) with costs rising (National Osteoporosis Foundation).

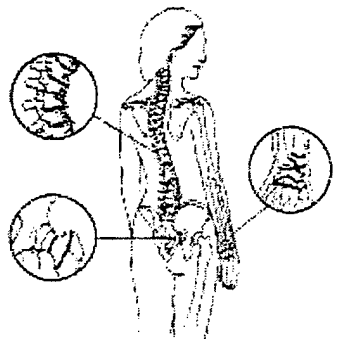

Fractures resulting from osteoporosis can be debilitating, causing chronic pain and disability. Biomaterials such as the rationally designed abductin-based bioelastomer, offer the chance to stabilize the fractures and give time for the natural healing process to take its course. Specifically, the abductin-based bioelastomer can be used as a means to stabilize or temporarily immobilize the spine so that it does not collapse and cause **compression** to the spinal cord. Current materials include injectable polymethyl methacrylate (PMMA also known as Plexiglass™) to stabilize vertebral bodies. This material is widely used in orthopedic surgery in a procedure called vertebroplasty to fill spaces in the spine that have been compressed and fractured due to bone loss. Although PMMA has good properties for this application, it forms a permanent bone cement, irreversibly immobilizing the spine. Since people outlive the procedure by 10 or more years (not withstanding young osteoporosis patients), this "cement" treatment is less than optimal. A resorbable biomaterial that will allow bone to stabilize is needed to provide a permanent *biological* solution (David B. Cohen, Assistant Professor of spine surgery at Johns Hopkins University School of Medicine).

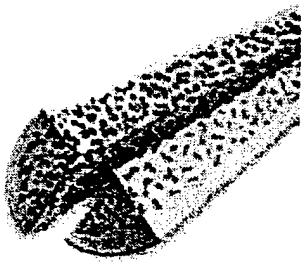

G. References

1. Q. Cao, Y. Wang, H. Bayley, *Curr Biol* **7**, R677-8 (1997).
2. M. Griffin, J. Wilson, *Mol Cell Biochem* **58**, 37-49 (1984).
3. R. D. Ashby, A. M. Cromwick, T. A. Foglia, *Int J Biol Macromol* **23**, 61-72 (1998).
4. C. S. Osborne, J. C. Barbenel, D. Smith, M. Savakis, M. H. Grant, *Med Biol Eng Comput* **36**, 129-34 (1998).
5. V. Lalitha, E. Subramanian, R. Parthasarathy, *Int J Pept Protein Res* **27**, 223-8 (1986).
6. G. N. Ramachandran, V. Sasisekharan, C. Ramakrishnan, *Biochim Biophys Acta* **112**, 168-70 (1966).
7. K.T. Lim, thesis, California Institute of Technology (1995).
8. H. Nielsen, J. Engelbrecht, S. Brunak, G. von Heijne, *Protein Eng* **10**, 1-6 (1997).
9. W.C. Still, A. Tempczyk, R.C. Hawley, T. Hendrickson, *JACS.* **112**, 6127 (1990).
10. S.R. Edinger, C. Cortis, P.S. Shenkin, R.A. Friesner, *J Phys Chem.* **101**, 1190 (1997).
11. J. C. Schense, J. A. Hubbell, *Bioconjug Chem* **10**, 75-81 (1999).
12. B.F. Finkin, *Wear.* **19**, 277 (1972).
13. J. A. Cook, J. B. Mitchell, *Anal Biochem* **179**, 1-7 (1989).
14. H.M. James, J Chem Phys. 15, 651 (1947).
15. H. M. James, E. Guth, J Chem Phys. 15, 669 (1947).
16. P.J. Flory, Polymer Journal. 17, 1-12 (1985).
17. S.F. Edwards, Polymer Journal. 17, 271-276 (1985).
18. S.F. Edwards, T. A. Vilgis, Rep Prog Phys. 51, 243-295 (1988).
19. L. Debelle, A.M. Tamburro, *Int J Biochem Cell Biol.* **31**, 261 (1999).
20. M.L. Connolly, *J Appl Crystallogr.* **16**, 548-558 (1983).
21. S. Cabani, G. Conti, V. Mollica, L. Bernazzani, *J Chem Soc Faraday Trans.* **87**, 2433-2442 (1991).
22. M. Blanco, F. Jimenez, W. A. Goddard III, under preparation.
23. S.D. Gillogly et al., *J Orthop Sports Phys Ther.* **28**, 241-251 (1998).
24. S. Wakitani et al., *Tisuue Eng.* **4**, 429-44 (1998).
25. Nehrer et al., *Biomaterials.* **19**, 2312-28 (1998).
26. Van Susante et al., *Biomaterials.* **19**, 2367-74 (1998).

H. Appendix

N/A

I. Patents

A provisional patent (serial # 60/184,590) was filed on February 24, 2000 entitled, "Peptide Based on Scallop Abductin Primary Structure" by Loma Linda University. The Veterans Administration (VA) has declined any such right over this invention and therefore the provisional patent has been assigned to Loma Linda University. A foreign filing license was granted as of April 28, 2000. Loma Linda University is actively preparing for the filing of a full patent application with regard to this invention.

J. Commercialization

Loma Linda University is currently involved in potential commercialization of this invention through exclusive or non-exclusive licensing. We envision having a product ready for exclusive or non-exclusive licensing at the end of our second year NMTB funding period.

K. Abstracts and Manuscripts

K.1. Manuscripts

1. Jimenez-Oronoz, F.; Blanco, M.; Tamburro, AM.; Laberge, M.; Goddard III, WA.; Sandberg, LB.; Scallop Abductin Translates Hydrophobicity to Elasticity. *In preparation.* (2000)
2. Blanco, M.; Jimenez-Oronoz, F.; Goddard III, WA.; Thermodynamic Contributions of Aromatic Amino Acids in Elastic Recoil. *In preparation.* (2000)

K.2. Abstracts

1. Jimenez-Oronoz F, Blanco M, Sandberg LB. Design and Synthesis of a Ligament Peptide Mimetic. 219th Annual National American Chemical Society Meeting, San Francisco CA. March 2000.

2. Jimenez-Oronoz F, Blanco M, Sandberg LB. Design and Synthesis of a Ligament Peptide Mimetic. MSC 2000 Conference, California Institute of Technology, Pasadena CA.

p. 12. March 2000.

3. Jimenez-Oronoz F, Roos PJ, Sandberg LB. A New Biopolymer for Replacement of Cartilage. 2nd Annual CORE21 Technology Transfer Symposium, Riverside CA. March 1999.

DESCRIPTION: State the goal of the project, including how it relates to improving health care. Use succinct language to describe how the project goals will be achieved. Do not exceed the space provided.

Stroke is the third most common cause of death and the leading cause of disability among adults in the U.S. One of the prominent risk factors for stroke is the degree of carotid artery stenosis. At present there is no appropriate instrument for screening for this disorder at a reasonable cost. We propose to develop such an instrument, the Vector Doppler Ultrasonic Velocimeter (VDUV), to measure blood velocity in the carotid artery (directly related to the degree of stenosis). Our overall goal is to develop the VDUV into an easy-to-use instrument that automatically displays an image of carotid blood flows. We have two goals for FY98:

- modification of our existing single-gate system into a multi-gate VDUV and processing of the data collected into color images representing carotid blood velocity,
- testing the VDUV with both laboratory tests and clinical tests in three human volunteers (one normal and two with carotid stenoses).

PROJECT SITE(S) (organization, city, state):

1. NorthWest Research Associates, Inc.
   14508 NE 20th Street
   Bellevue, WA 98007-3713

2. Department of Vascular Surgery
   University of Washington
   Seattle, WA 98195-6410

No. 36
Northwest Research Corp/Fraser

COP

NorthWest Research Associates, Inc.
P.O. Box 3027 • Bellevue, WA 98009-3027

NWRA-CR-99-R209

9 February 2000

FINAL REPORT
Contract #016-NWRA-Fraser
For the period of March 6, 1998 through February 8, 2000

A Vector-Doppler Ultrasonic Velocimeter for Assessing Carotid Stenosis

by

Dr. Robert Fraser

Submitted to:

Lydia Pearson
Contracts Administrator
National Medical Testbed, Inc.
11165 Mt. View Ave., Suite 121
Loma Linda, CA 92354

14508 N.E. 20th Street • Bellevue, WA 98007-3713 • (425) 644-9660 • FAX (425) 644-8422

NWRA-CR-99-R209 9 February 2000

FINAL REPORT
Contract #016-NWRA-Fraser
For the period of March 6, 1998 through February 8, 2000

A Vector-Doppler Ultrasonic Velocimeter for Assessing Carotid Stenosis

by

Dr. Robert Fraser

Submitted to:

Lydia Pearson
Contracts Administrator
National Medical Testbed, Inc.
11165 Mt. View Ave., Suite 121
Loma Linda, CA 92354

COPY

Table of Contents

Introduction 1
Development 2
Tests and Results 3
Production Prototype and Commercial Prospects 5
Discussion 6
References 7
Figures
Appendices

Final Report for #016-NWRA-FRASER
FY97 and FY98

A Vector-Doppler Ultrasound Velocimeter for Assessing Carotid Stenosis

Introduction

The main task proposed and carried out during the entire period of our subcontract (FY97 and FY98) was the development of a prototype Vector-Doppler Ultrasound Velocimeter (VDUV) for the measurement of the degree of stenosis in carotid arteries by measuring the blood velocity in the carotid arteries using ultrasound signals. Development of this prototype included both (1) hardware design and fabrication for the acquisition, processing, and storage of data and (2) software design and implementation for the processing and display of the appropriate signals. The prototype was tested using both non-patient data and patient data from normal and diseased arteries. We also assessed the market for the commercial application of the VDUV.

Design and Development

Hardware Development

Figure 1 shows the electronic block diagram for the prototype VDUV and Figure 2 shows the compact ultrasound scanhead (the central transducer is the transmitter and the other two are receivers all focused at a depth of about 1.5 cm). The Doppler-receiver and transmitter boards and digital signal processing (DSP) boards were custom-made for a previous project and only needed to be modified for our carrier frequency (5 MHz) and pulse repetition frequency (PRF of 10 and 15 kHz). The Compuscope 1250 signal acquisition and transfer boards were obtained "off-the-shelf" from Gage Applied Sciences, although considerable software modifications were required by our consultant to get them to perform properly (their development had just been completed at Gage). Final processing, storage, and display were carried out in a Pentium II 440BX2 PC using both Gage software for data transfer and Matlab software for post-processing. The scanhead was designed by us and fabricated at a local ultrasound company.

Figure 3 shows the how the tasks for the data acquisition board are divided up for one pulse. The DRT boards provide a RF input for the transmitter and a RF output for each of the two receivers. The pulse repetition frequency (PRF) can be selected at either 10 or 15 kHz. At a given delay (8.8 μsec) after each pulse is sent (corresponding to one-cm depth below the surface of the neck) the signals at the two receivers and one transmitter are sampled with 12-bit accuracy at 5 megasamples/sec for 38.4 μsec (i.e., 3x64=192 samples). This sampling rate corresponds to a spatial resolution of 0.6 mm. The rate at which these pulses are sent out, the PRF, is fast enough to ensure that the velocity of the blood has not changed substantially between pulses, but slow enough to ensure that the reflected signals have been seen by the receivers. Three seconds of data (about three cardiac cycles) are collected at each site.

Software Development

The goal of having an operator-independent instrument for measuring carotid blood flow velocities requires an algorithm that will automatically calculate the velocity from the stored data described above. The algorithm has gone through an extensive evolution since we started on this project two years ago. I will describe the state of the algorithm as it exists currently (i.e., where blood velocities less than 200 cm/sec can be automatically calculated – discussed further in the results and discussion sections). There are three modules in the VDUV software: data-acquisition, data transfer, and post-processing. The first two modules are covered by the Gage software (and its modification by us). The third module is the post-processing software and is composed of several steps. First, the data must be sorted from its serial form into arrays for each of the two receivers with rows corresponding to depths and columns to time. This task was done at the University of Washington (part of the work carried out under our subcontract to them). Then the software is required to create a spectrogram from the data for each receiver and automatically find the optimal depth, optimal systolic peak, and peak systolic velocity. This development task was carried out here at Northwest Research Associates (NWRA) over the last two years. The resulting Matlab program (read_calcdoptpsv_NWRA2.m) appears in Appendix A (and on the enclosed floppy disk) and is documented fairly extensively. A brief summary of its components follows.

- The quadrature components (i and q) are combined to created one time series each for the two receivers (named the red and yellow transducers for their color code).
- Spectrograms are created from the time series with the Matlab FFT algorithm and the frequencies of +- lowf1 (set in initial conditions – usually 300 to 500 Hz) are filtered out to eliminate the reflections from the moving walls of the artery.
- For each depth (each row in the matrix) a rectangular window (wB) in time-frequency space is calculated across the entire space and the maximum such window (labeled p) is selected at each depth. Then the maximum of the function p(d) is found, which identifies the optimal depth.
- The spectrograms for the red and yellow transducers are selected at the optimal depth, the background intensity is calculated, the point at which the spectral intensity is four times the background intensity is selected as the spectral envelope, and the optimal sign of the Doppler frequency (either positive or negative) is also selected. The optimal systolic peak is then selected from the envelope.
- The peak Doppler frequencies are then calculated from these systolic peaks in the time-frequency domain and the vector-Doppler formula (see Appendix B) is used to calculate the vector velocity.
- The color-intensity spectrograms are then plotted for both the red and yellow transducers.

Tests and Results

Both the hardware and software were tested at various points in their development. These tests will be described in roughly chronological order; laboratory tests first then tests with human volunteers.

1. Flow through an orifice

For this test an apparatus was used that modeled the human carotid artery. The device consisted of a pump and tubing system designed to deliver a steady flow at physiological flow rates. The tube was 16 mm in inside diameter and had a 40% orifice to simulate a carotid stenosis. The VDUV probe was operated in single-gate mode; i.e., it received pulses at one depth only. The two transducers of the probe were set at 30° to the left and right of the perpendicular to the flow. The probe was moved with a micrometer device in the radial direction in 0.5 mm increments from 0 (at the wall) to 12 mm across the tube at 10 axial positions: at 5 cm upstream of the orifice and at 1 through 9 cm downstream of the orifice.

Two key aspects of data processing and display were demonstrated with this apparatus:

a) The binary data was unpacked as quadrature pairs for each of the two transducers over a one-second period (15,000 pulses). This step showed us that we could unpack, parse, process, and display the data, which appeared in a form similar to the clinical case.
b) Then similar data points were collected over the entire flow field and saved in a matrix. The resulting matrix is displayed in Figure 4 where the key for velocity appears on the color bar at the right. From this step we learned how to display a flow cross-section like we might see in the region around a carotid stenosis. A physician would immediately see flows exceeding 120 cm/sec as yellow (a possible limit for healthy carotid flows) and the more clinically dangerous velocities as red. Of course, the velocities assigned to each color could be modified. As one would expect, the highest velocities are just downstream of the orifice and approximately in the middle of the tube.

2. String moving at constant velocity and multi-gate data

For this test the data was taken on a string moving at constant velocity of 105 cm/sec in a tray of water. This time the VDUV was operated in multi-gate mode and the data was parsed so that the Doppler signal at a given depth could be obtained over one second of data and used to create a power spectrum at that depth. Specifically, the received Doppler signal was divided into 100 depths (gates) for each of the 15,000 pulses/sec. A program was written to search through the power spectra at each depth to find the optimal depth associated with the actual depth of the string. The power spectrum at the optimal gate-depth of 11 (about 1.1 cm) which corresponds to the actual string depth is shown for a single transducer in Figure 5. The modal velocity calculated from this power spectrum was 111 cm/sec and was within 6% of the actual velocity.

3. Flow through a normal femoral artery

Our first data from a human subject were taken from a single scan through the femoral artery (in the leg). The processing techniques developed for the multi-gate string data were applicable to this data. The spectrograms were taken over one-and-a-half cardiac cycles for the left and right transducers separately. The left transducer (also known as the red transducer because of its color code) is looking into the flow, so its signal is positive. The right (or yellow) transducer signal is negative because it is looking in the opposite direction. The total vector spectrogram was derived from combining the left and right signals into a single spectrogram.

The modal velocity was derived from this spectrogram and is shown in Figure 6. The modal velocity at the systolic peak derived from this curve was 50.25 cm/sec, within expected physiological limits for normal flow in the femoral artery. These results suggested that our study of carotid arteries would produce good results as well.

4. Flow through a normal carotid artery – UW system/NWRA software

In the human study descriptions that follow, the VDUV transducer head was combined with the UW custom Vector-Doppler system to utilize the multi-gate capability of the commercial instrument. These tests were carried out before we had our own Vector-Doppler electronics. With this first study of the carotid artery we developed and tested an optimum depth and optimum systolic peak search routine. Figure 6 shows the peak systolic velocity at the points measured along the common carotid artery of the subject. These velocities are within 10% of the velocities calculated with the UW routines.

5. Flow through a diseased carotid artery – UW system/NWRA software

As with the normal carotid, data was obtained for a stenotic carotid artery (80% closed) using the UW custom Vector-Doppler system (this patient was already being seen as part of a routine exam before carotid surgery). The scanhead used, however, was one we designed at NWRA and had fabricated at a local ultrasound company (Figure 2). The data was run through our algorithm to automatically select the optimal depth and optimal point of peak systole and to calculate peak systolic velocity. The results are shown in Figure 7. The algorithm correctly selected one of the systolic peaks (the second one) and found peak Doppler frequencies for the red and yellow transducers of 4395 Hz and –5830 Hz respectively. This in turn led to a vector velocity of 303 cm/sec, within 10% agreement with the UW calculations and within the expected velocity at the stenosis for an 80% closure. Note that there is considerable noise in the background signal around the spectrograms. We will see in the next section that with the new electronics designed by us the noise is virtually imperceptible.

6. Flow through one normal and two diseased carotid arteries – NWRA system and software

One normal subject and two patients with carotid stenoses (one at 60% and one at 80% stenosis) were examined using the new NWRA Vector-Doppler multi-gate electronics (the VDUV) and the NWRA scanhead. Measurements with the VDUV were compared to the measurements made by one of the standard duplex ultrasound instruments used in the clinical ultrasound labs at UW (typically a Hewlett-Packard duplex imager). For the normal subject the VDUV measured a velocity in the common carotid of 110 cm/sec, within 20% of the duplex instrument. For the case of the 60% stenosis, our algorithm found the optimal depth and peak systolic velocity at several sites along the carotid artery, specifically, in the common carotid, bulb, stenosis, and internal carotid. Figure 8 shows the spectrograms for both transducers of the VDUV at a point within the stenosis. The peak frequencies were 3457 Hz and –4287 Hz (shown on the figure) and the velocity was 229 cm/sec. A measurement at a point within about one millimeter from this one gave a velocity of 180 cm/sec (the velocity gradients are severe within a significant stenosis like this). The average of the two, 204.5 cm/sec, is within 3% of the velocity measured by the duplex instrument at 200 cm/sec, and well within measurement error in carotid stenoses (10% to 20%). At the other points in the carotid the VDUV read about 20% below the

duplex instrument. This difference could simply be due to operator variance and measurement error or could be a real difference. More data would have to be taken to decide whether or not we were reading consistently below the duplex instrument. As mentioned above, the noise around the spectrograms is nearly imperceptible.

In the patient with the 80% stenosis the velocities in the stenosis exceeded 300 cm/sec (as measured with the duplex instrument). The spectrograms with the VDUV were clear and allowed us to calculate velocities also exceeding 300 cm/sec. However, the automatic algorithm did not give the correct answer here because the Doppler frequency in the yellow transducer exceeded 7500 Hz (PRF/2). Clearly, more work must be done to improve the algorithm to read Doppler frequencies up to 15,000 Hz (the PRF). The problem was being able to find a way to consistently identify the peak systolic frequency at these velocities, the way a trained vascular technologist does. We have ideas on how to approach this (e.g., looking at the relative maxima and minima of spectral intensities during systole), but there was not time to complete the work before the end of the contract period.

Production Prototype and Commercial Prospects

We made some preliminary designs of a production prototype for the VDUV. Figures 9 and 10 show a possible physical layout and the corresponding electronic block diagram for a production prototype. In this design what now requires two large chassis would be reduced to a chassis of about one cubic foot. The PC we now use would be replaced by an embedded microprocessor and an LCD display. A sketch of a possible 2D scanner is shown in Figure 11. Scanning takes place in two perpendicular directions allowing the area of interest around the carotid bifurcation to be scanned from one position (the multi-gate feature of the VDUV gives the 3rd dimension in the direction of depth). The gimbal shown holding the stepper motor for scanning in the x direction is driven in the y direction by a second stepper motor. The entire gimbal assembly is surrounded by electrically non-conductive fluid to ensure a proper ultrasonic connection to the subject's skin.

After a year of searching, we found no interest in commercializing the VDUV. There are at least two reasons for this. First is the lack of corporate interest. Of the two ultrasound firms we know about, ATL in Bothell, WA has recently created their own program for developing a vector-Doppler instrument and it will not be used for carotid scanning (apparently its proposed use is proprietary). The other company, Diagnostic Ultrasound in Redmond, WA, already has as many projects as they can handle. Secondly, a search on the web revealed that there is little interest in carotid screening of the general public, as it is not perceived to be cost effective. This apparently rapid change in attitude (compared with three years ago when we first proposed this project) has arisen because of several studies (e.g., Longstreth *et al*, 1998, Hill 1998, and Lewis *et al*, 1997) showing that significant asymptomatic carotid stenosis (now considered as >80%) is extremely rare. As a result, major health-care organizations like Kaiser in California claim that general screening for carotid stenosis is unwarranted (Lee, 1997). The most convincing of these new studies appeared at the end of 1998 (Longstreth *et al*, 1998) (although we didn't see it until May of 1999) and reported on the screening of a cross-section of the general population over the age of 65. They found that the prevalence of asymptomatic carotid stenosis warranting surgery (>=80% stenosis) is only 0.25% of the population as compared to the 6% reported by Branas *et al* (1994), a factor of 24 different. Longstreth confirmed (private conversation, 1999) that after

the results of the ACAS study came out (NINDS, 1994), it was thought that one only had to set up screening sites around the country and send all the patients found with stenoses > 80% for carotid endarterectomy. As it turns out, the occurrence of asymptomatic stenoses of this magnitude are far too rare to warrant the cost of screening. The money would be better spent in educating people on the dangers of their risky life styles (overweight, poor diet, lack of exercise, smoking, etc.). We attempted to find out in the last several months if there was any sentiment to the contrary in the commercial sector, but these conclusions were only confirmed. We did feel, however, that it was worth completing the project, since it has generally gone very well and our results with clinical data looked good. There are other uses for a Vector -Doppler instrument and some of these are being explored at the Division of Vascular Surgery at the University of Washington by a team I have been working with over the last five years (including Dr. Kirk Beach and engineer, Barbrina Dunmire). For example, they are looking at the relationship between hemodynamics and vascular remodeling in vein grafts in the leg. They hope to determine hemodynamic parameters that indicate future stenosis or occlusion in these grafts and, thus, be able to use the VDUV to guide the revision of the grafts to prevent occlusion. This research could lead to a product used by physicians to guide them in the period after vascular surgery. The UW team is considering submitting a proposal to NMTB to continue the development of the VDUV.

Discussion

The development and testing of the VDUV has gone very well. At each stage the results of tests show that the VDUV and the associated software have performed within the limits expected. In fact, the low noise level in the new electronics was an unexpected bonus. There is the problem of getting the software that finds systole and calculates peak systolic velocity to perform correctly at velocities over 300 cm/sec. There are some approaches that might resolve the difficulty, as mentioned in the last section. However, any subject with a carotid blood velocity exceeding 200 cm/sec (60% stenosis) would be sent for a full duplex exam. So the instrument still works effectively as a screening device.

The lack of commercial prospects for the VDUV as a carotid-stenosis screening device is discouraging. However, as mentioned above, the applications being explored at the University of Washington have some promise of commercialization.

References

Branas, C.C., M.S. Weingarten, M. Czeredarczuk, and P.F. Schafer, Examination of carotid arteries with quantitative color Doppler flow imaging, *Ultras. Med., 13*, 121-127, 1994.

Hill, A.B., Should patients be screened for asymptomatic carotid artery stenosis?, *Ca. J. Surg., 41(3)*, 208-213, 1998.

Lee, T.T., N.A. Solomon, P.A. Heidenreich, J. Oehlert, and A.M. Garber, Cost-effectiveness of screening for carotid stenosis in asymptomatic persons., *Ann. Intern. Med., Mar. 1, 126(5)*, 337-346, 1997.

Lewis, R.F., M. Abrahamowicz, R. Cote, and R.N. Battista, Predictive power of duplex ultrasonography in asymptomatic carotid disease, *Ann. Intern. Med., Jul. 1, 127(1)*, 13-20, 1997.

Longstreth, W.T., L. Shemanski, D. Lefkowitz, D.H. O'Leary, J.F. Polak, and J. S.K. Wolfson, Asymptomatic internal carotid artery stenosis defined by ultrasound and the risk of subsequent stroke in the elderly, *Stroke, Nov. 29(11)*, 2371-2376, 1998.

NINDS, Clinical advisory: Carotid endarterectomy for patients with asymptomatic internal carotid artery stenosis., *NINDS/NIH/DHHS Special Report, 2523*, 1994.

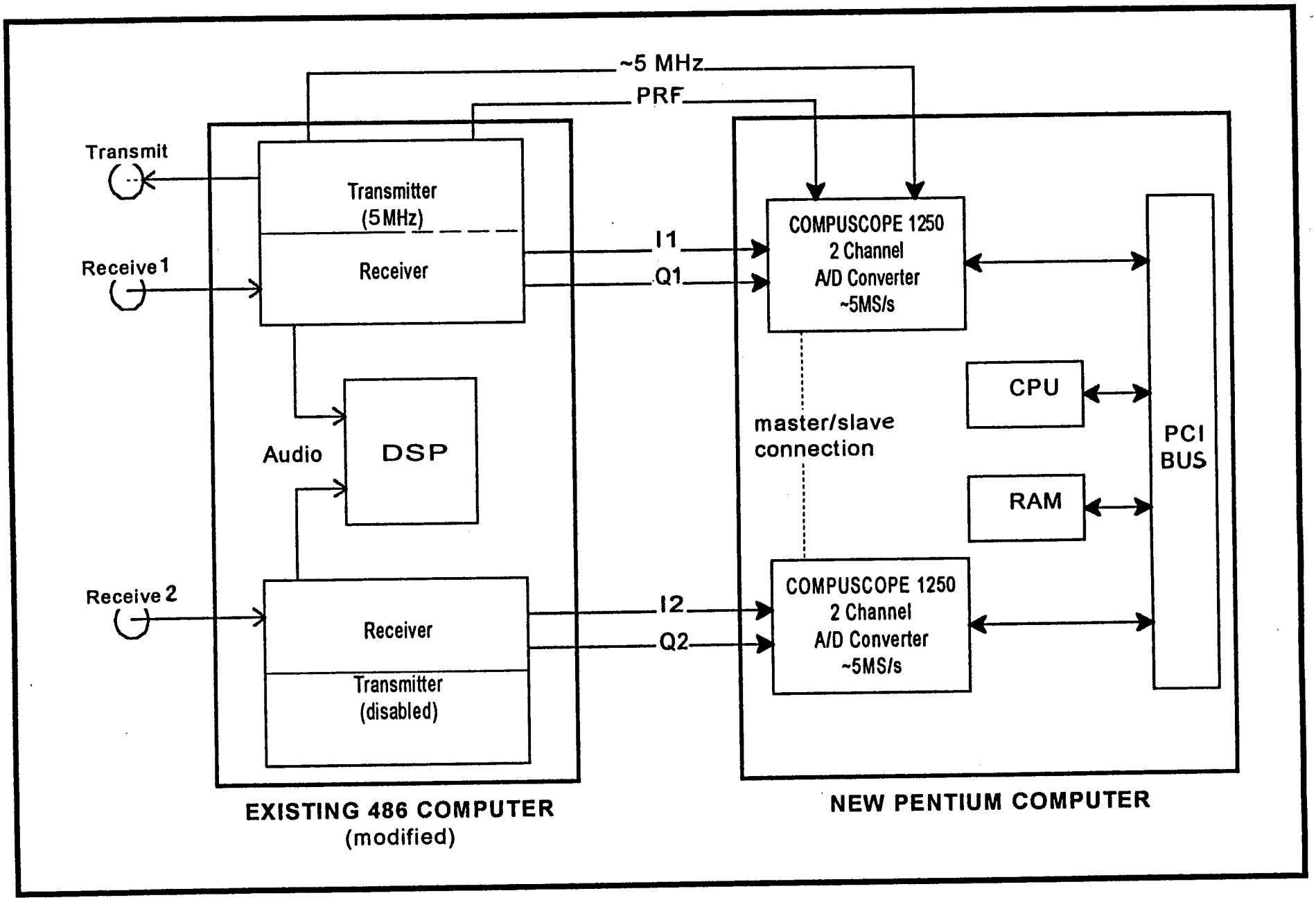

Figure 1. Block diagram of the VDUV system.

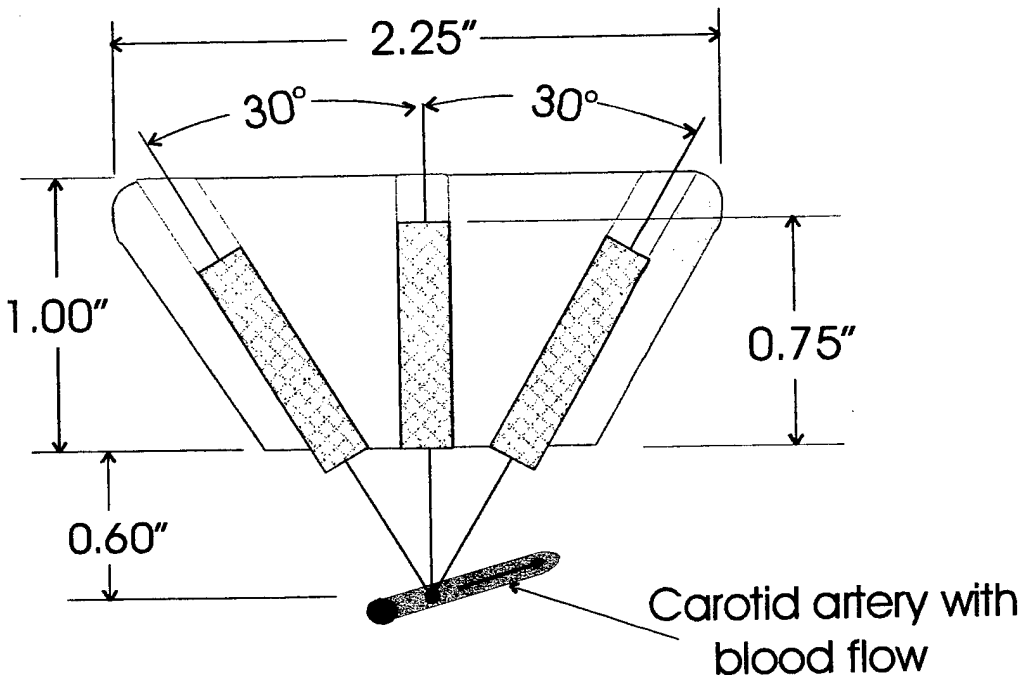

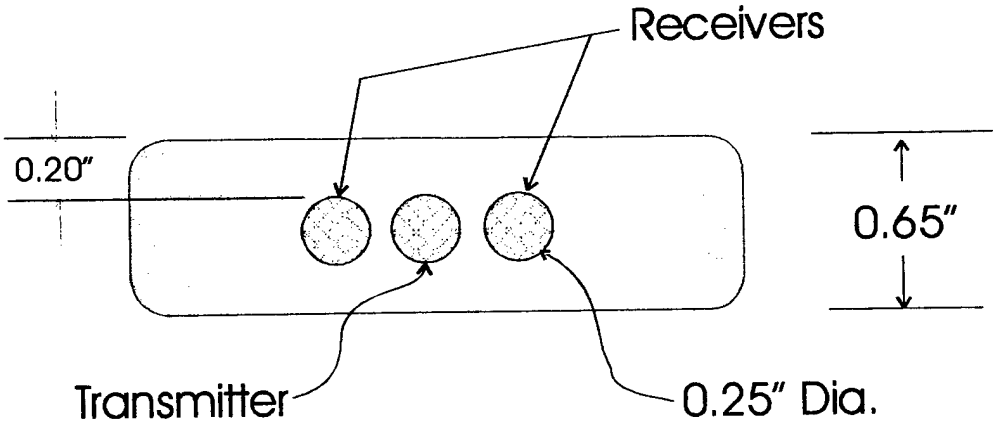

Figure 2. The VDUV scan head showing the transmitter and two receivers.

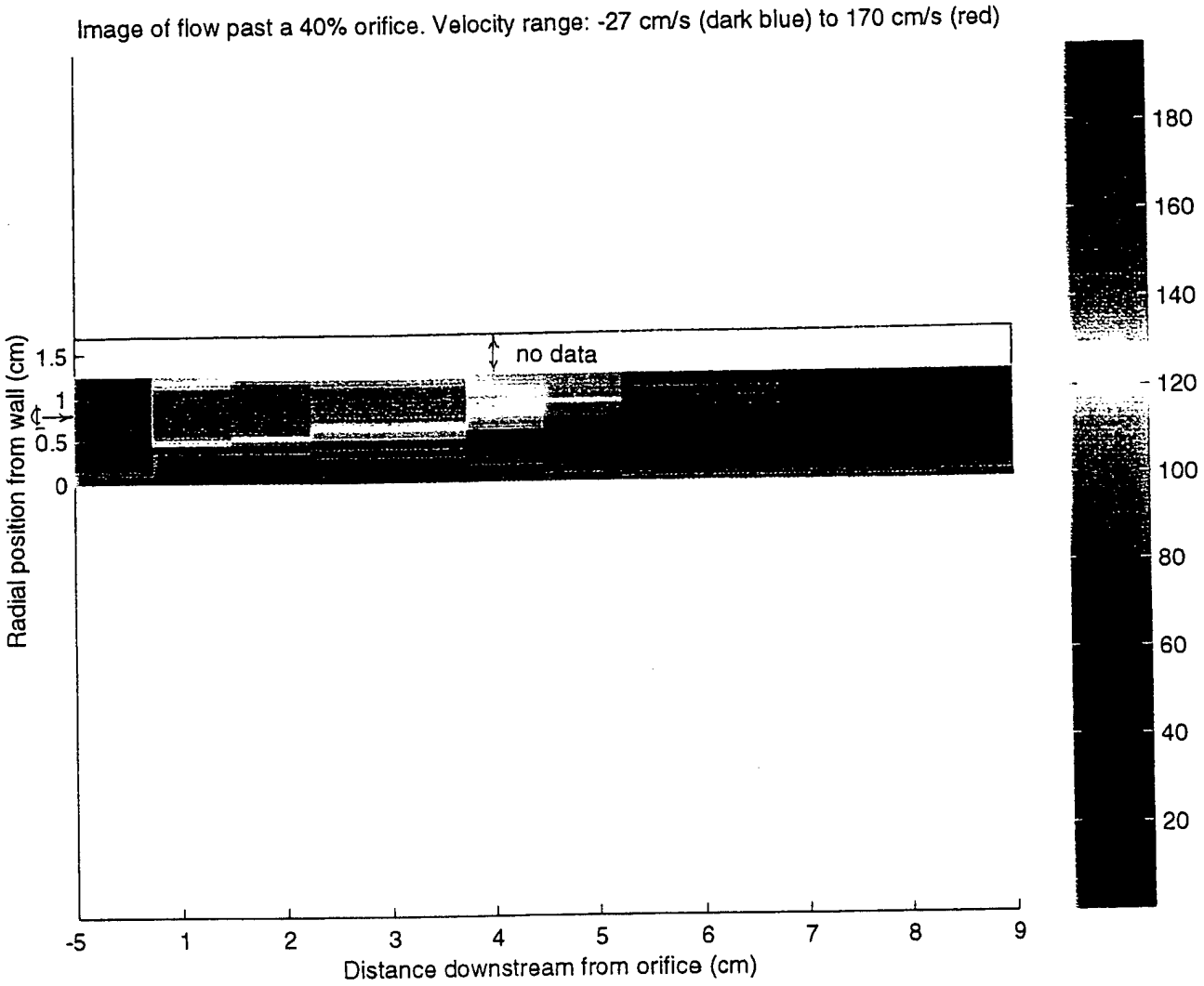

Figure 4. Two-dimensional color-coded image of modal Doppler velocities in a plane parallel to the tube axis for flow through a 16-mm tube with a 40% orifice. This view shows the velocity (from blue to red) at each point in the flow from 5 cm before the orifice to 9 cm downstream of the orifice. The measurements were made every 0.5 mm in the radial direction and every 1.0 cm in the axial direction downstream of the orifice and at 5 cm upstream of the orifice.

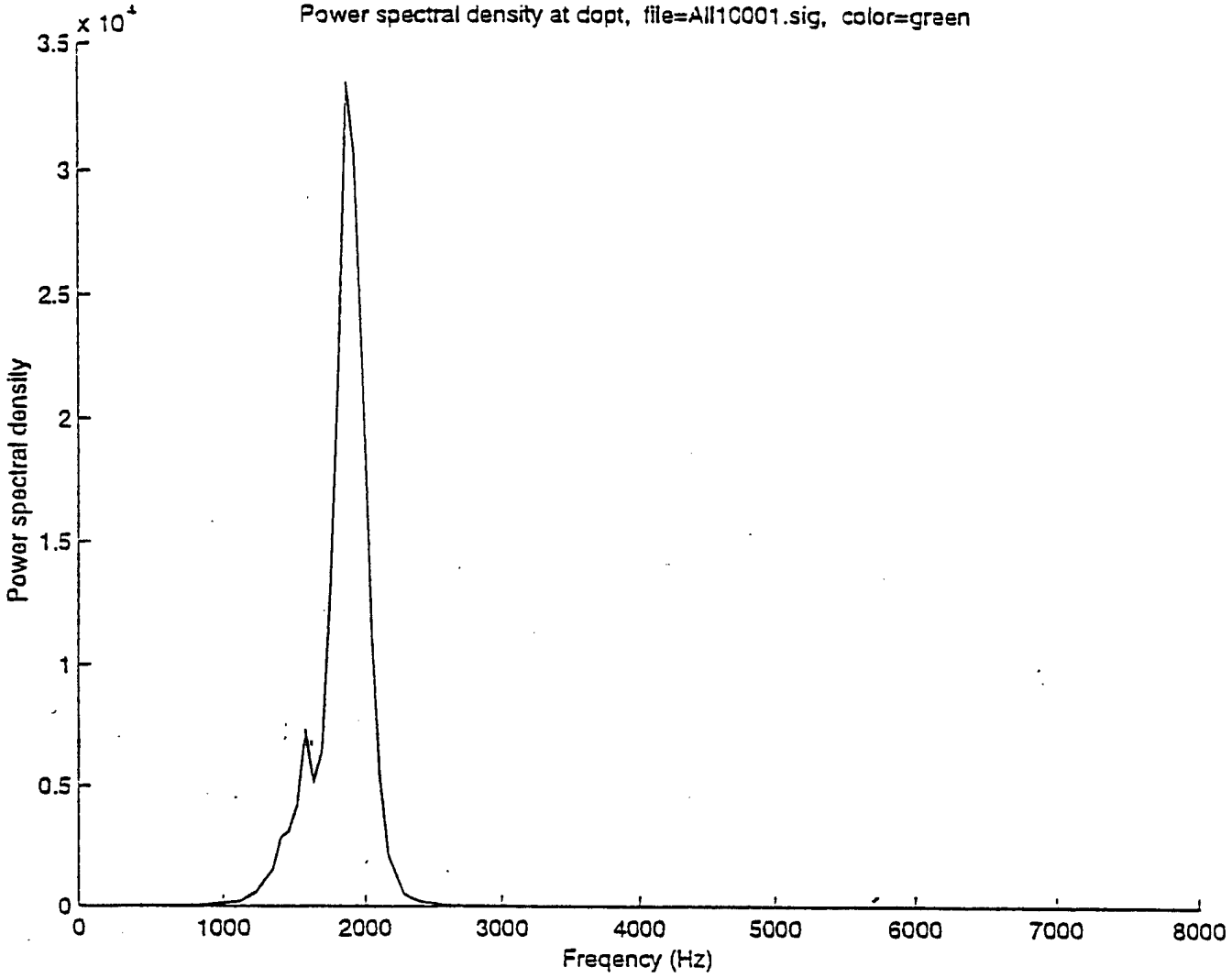

dopt = depth of maximum string velocity = 11
number of points in fft = 256
low freqency cutoff = 292.9688 Hz
Doppler frequency at max power = 1875 Hz
corresponding string velocity = 111 cm/sec

Figure 5. Power spectral density of the Doppler signal from a string moving at a constant velocity of 105 cm/sec in a tray of water. The received Doppler signal was divided into 100 depths (gates) for each of the 15,000 pulses/sec. This is the power spectrum at the optimal gate-depth of 11 (about 1.1 cm) which corresponds to the actual string depth. The modal velocity (corresponds to the frequency with the greatest power density) calculated from this power spectrum was 111 cm/sec.

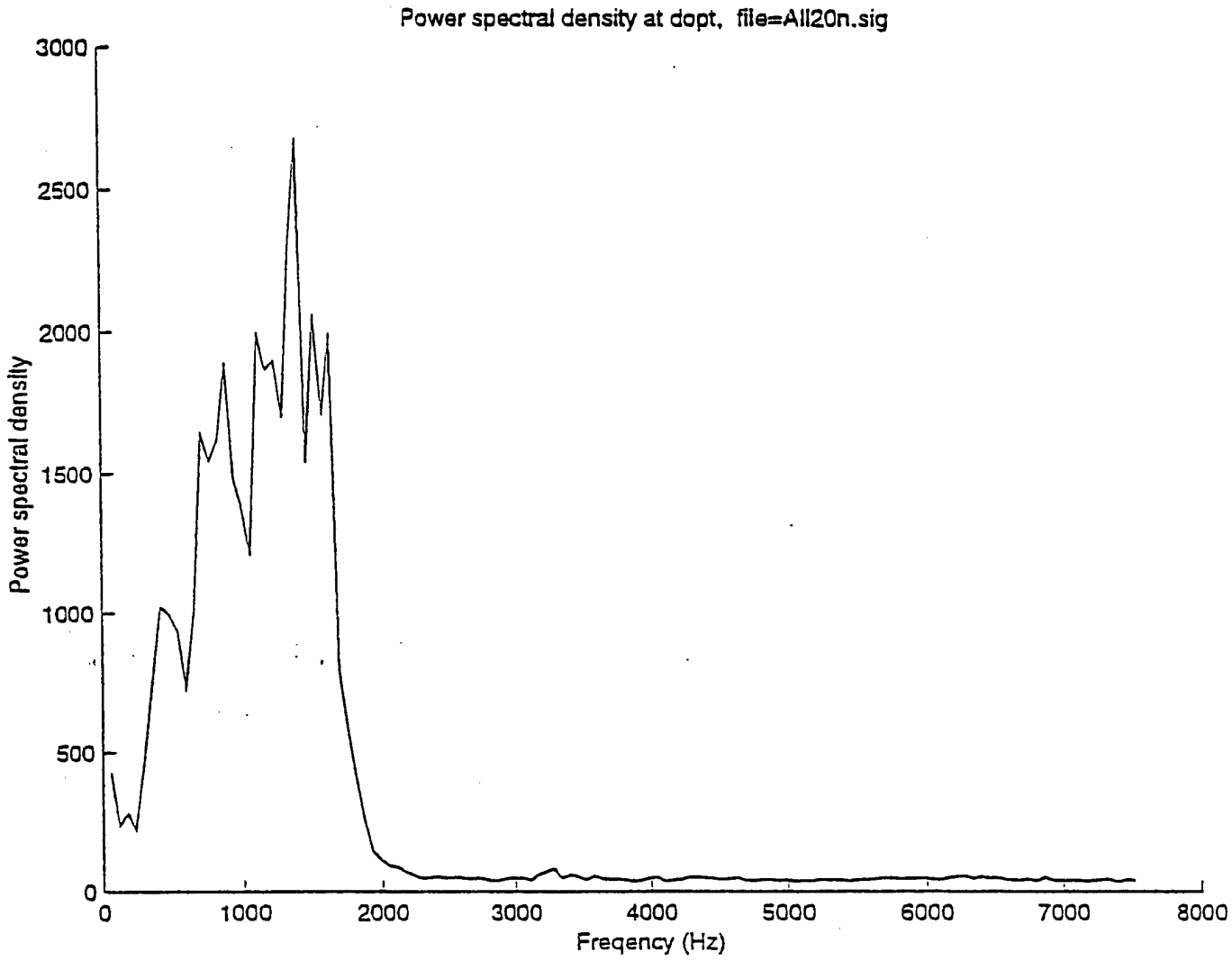

dopt = depth of maximum velocity = 10
number of points in fft = 256
low freqency cutoff on data = 100 Hz
number of poles for filter = 5
Doppler frequency at max power = 1697.7809 Hz
corresponding blood velocity = 50.2543 cm/sec

Figure 6. Average power spectral density for the combined left and right transducer signals for blood flow in the femoral artery of a normal volunteer.

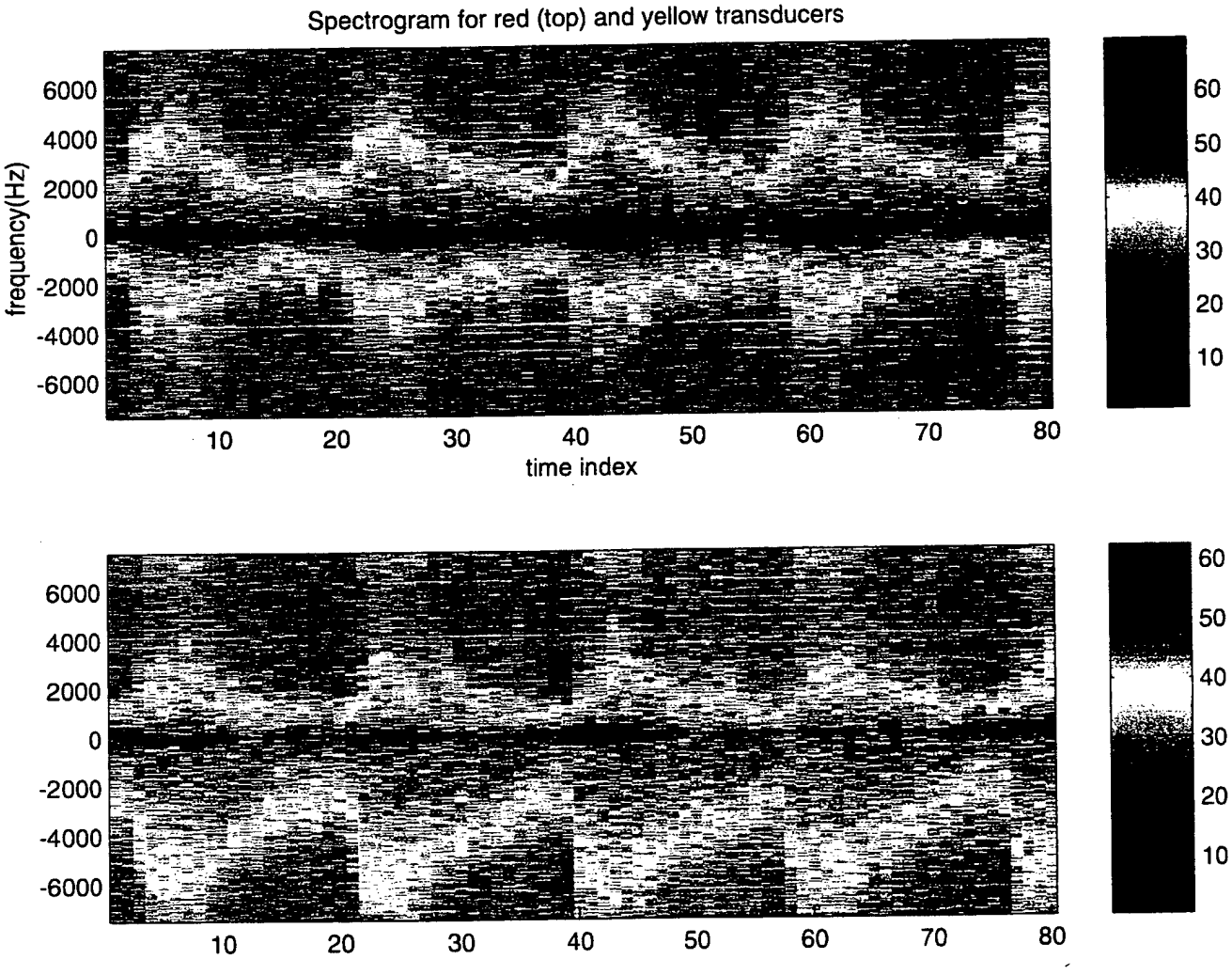

program = read-calcry-NWRA1.m (updated 8/20/99), data file = ALs5d10q.sig in carotid-ptAL
depth Pout1 Pout2 lowf harmf flag = 8 0.3 0.1 300 100 2
fpsr fpsy fmodr fmody zmax = 4395 -5830 308 293 24
vector Doppler frequency = 10232 Hz vector Doppler velocity = 303 cm/sec

Figure 7. Spectrograms of the Doppler signals at depth = 8

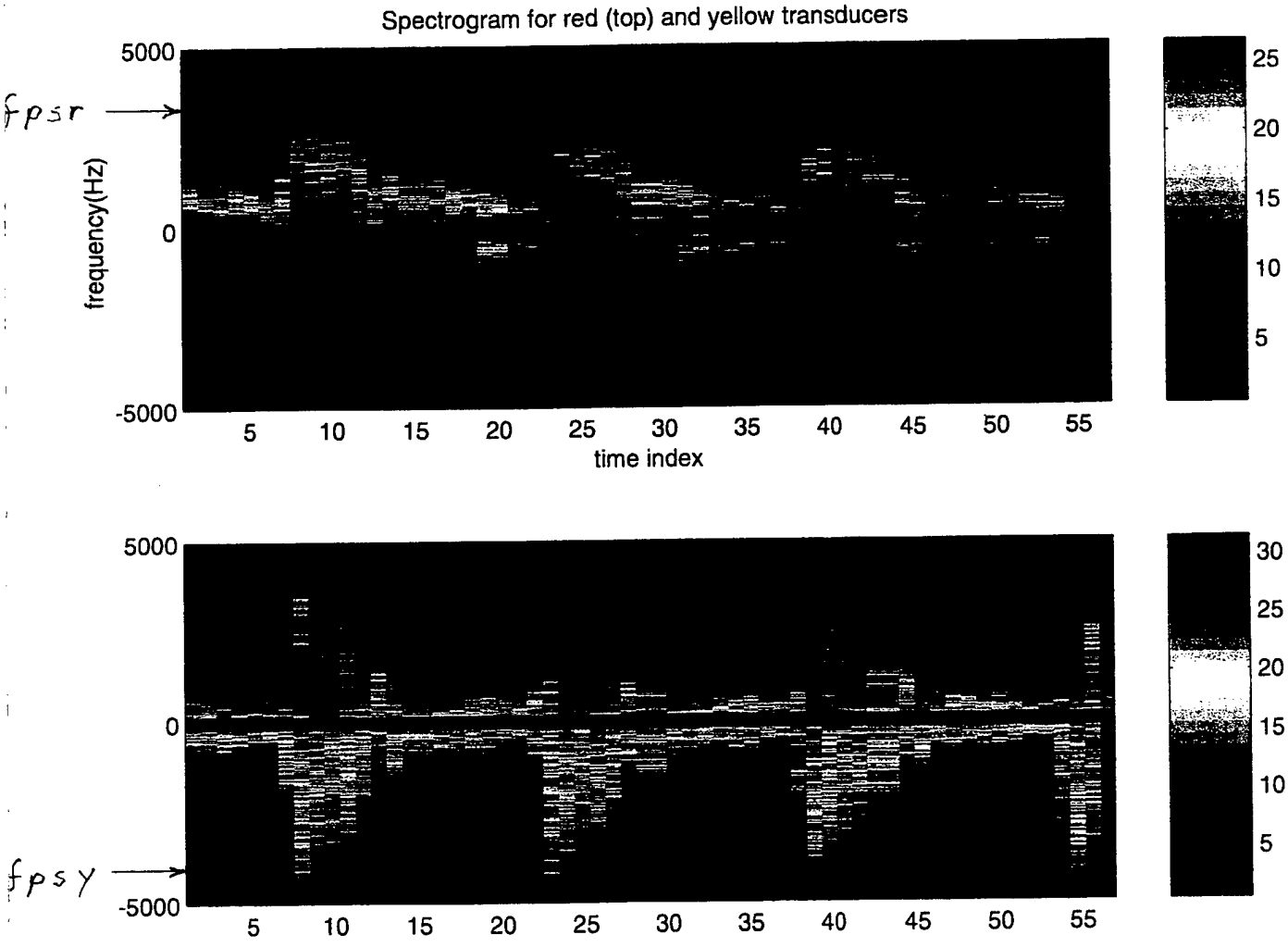

program = read-calcdoptpsv-NWRA2.m (updated 2/3/00), data file = carotid-stenosisD-Fds4d2
optimal depth lowf2 mave = 111 300 20
fpsr fpsy fmodr fmody zmaxr zmaxy = 3457 -4287 2100 -3027 8 8
vector Doppler frequency = 7747 Hz vector Doppler velocity = 229 cm/sec

Figure 8. Spectrograms of the Doppler signals at depth = 111

VDUV Production Prototype

Physical Layout

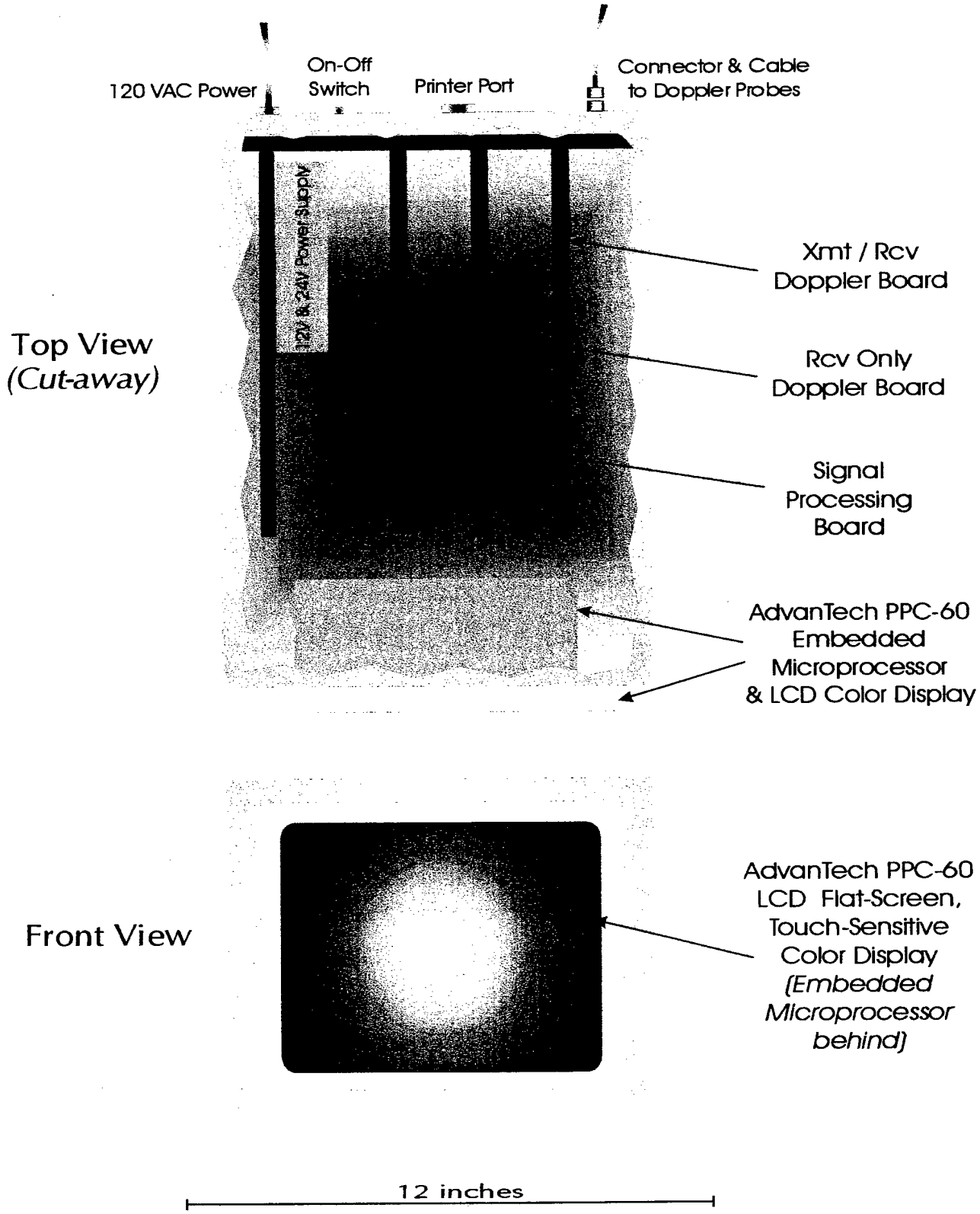

Figure 9. Physical Layout.

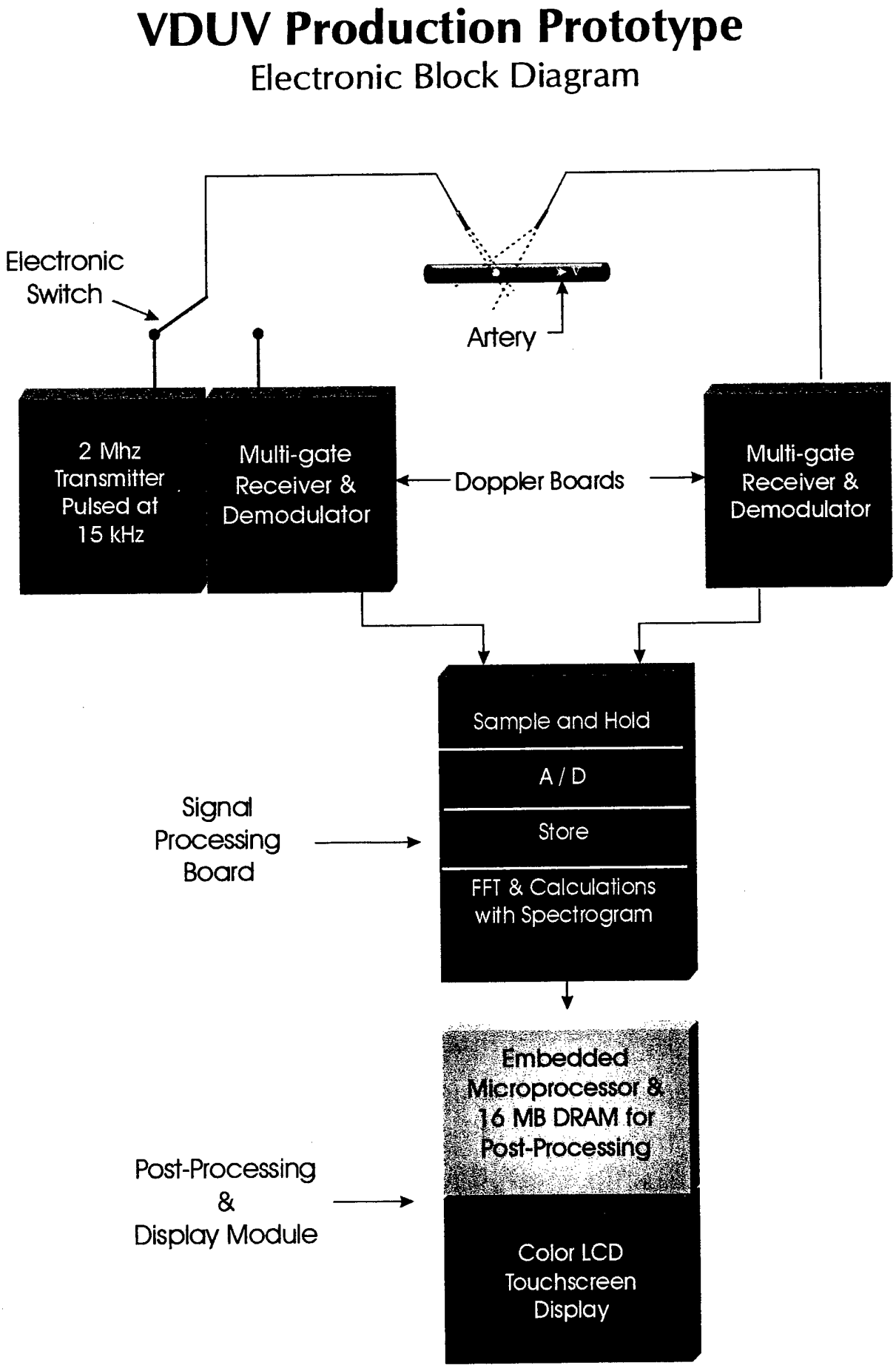

Figure 10. Electronic Block Diagram.

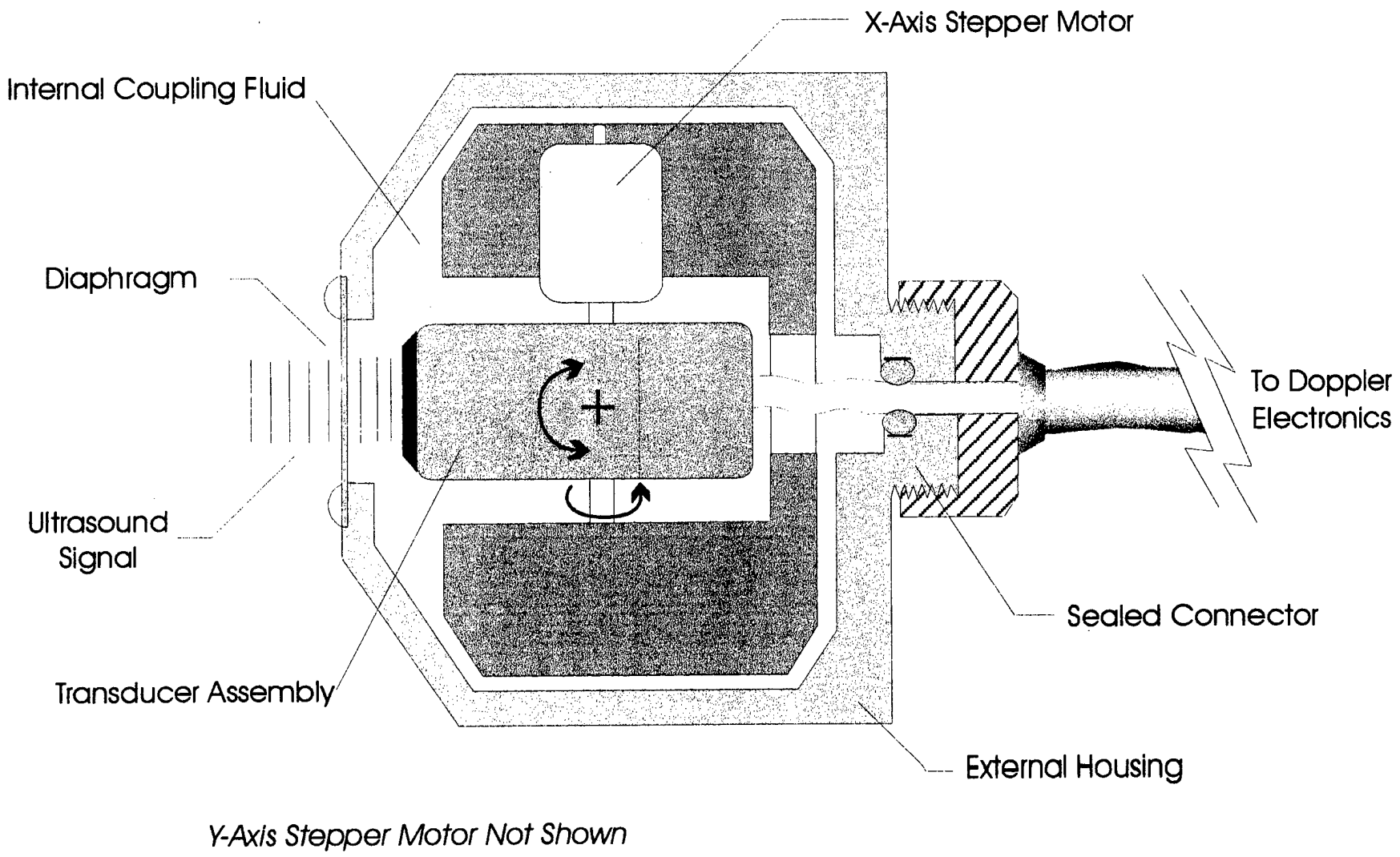

Figure 11. A possible 2-D scanhead for use with the VDUV. It would scan laterally and axially along the carotid artery. The multi-gate feature of the VDUV allows data to be obtained in the 3rd dimension, in the direction of depth.

Appendix A

Matlab program for finding the optimal depth in the carotid artery and for finding the optimal systolic peak and peak velocity at that depth

```
% read_calcdoptpsv_NWRA2.m     updated 2/3/00

% This is a combination of read_calcdopt_NWRA2.m and read_calcpsv_NWRA2.m

% The 7 parts of read_calcdoptpsv_NWRA2.m are as follows:

% 1. Data is read in from with read_new_file.m and saved as ir, qr, iy, qy.
% 2. The quadrature components (i and q) are combined to created one time series each
%    for the two receivers (named the red and yellow transducers for their color code).
% 3. Spectrograms are created from the time series with the specgm algorithm. The
%    frequencies of +- lowf1 are filtered out to eliminate the reflections from the
%    moving walls of the artery.
% 4. For each depth (each row in the matrix) a rectangular window (wB) in
%    time-frequency space is calculated across the entire space and the maximum such
%    window (labeled p) is selected at each depth.  Then the maximum of the function
%    p(d) is found, which identifies the optimal depth.
% 5. The spectrograms for the red and yellow transducers are selected at the optimal
%    depth, the background intensity is calculated, the point at which the spectral
%    intensity is 4 times the background intensity is selected as the spectral
%    envelope, and the optimal sign of the Doppler frequency (either positive or
%    negative) is also selected.  The optimal systolic peak is then selected from
%    the envelope.
% 6. The peak Doppler frequencies are then calculated from these systolic peaks in
%    the time-frequency domain and the vector-Doppler formula is used to calculate
%    the vector velocity.
% 7. The color-intensity spectrograms are then plotted for both the red and yellow
%    transducers.

% Run time ~= 20 min

% Initial conditions (set data file in read_new_file.m):
clear all
filename='read-calcdoptpsv-NWRA2.m';
update='2/3/00';
datafile='carotid-stenosis-1-P1s4d1';
d1=110          % beginning depth to search for dopt
d2=130          % final depth to search for dopt
PRF=15000       % PRF=pulse repetition frequency
nfft=256;       % nfft=number of points in fft
fdel=60;        % size of sliding window in freq units(1024/15kHz) for calc dopt
tdel=10;        % size of sliding window in time units(30/sec) for calc dopt
mave=20         % size of moving average in freq units(1024/15kHz) for smoothing B2h
lowf1=500       % low freq cut off in Hz to calc dopt.
lowf2=300       % Note that lowf2->500 will lead to unrealistically high values for
                % peak sys vel, so must recalc B2h with lowf2 for psv calc in part 3.
fmax=PRF/2;     % maximum frequency used to set y-limits in Figure 1 below
c=1.48*10^5;    % sound speed in water
f0=5*10^6;      % insonating frequency
A=pi/6;         % A=angle between rcvr and trnsmtr

% 1.  Read in the data (must set initial conditions and file name in read_new_file)
read_new_file

% 2. Find optimal depth
for d=d1:d2
   ir=ired(d,:);
   qr=qred(d,:);
   r=ir+i*qr;
   iy=iyellow(d,:);
   qy=qyellow(d,:);
   y=iy+i*qy;

   % Calculate the spectrogram of r
   [B,f,t]=specgram(r,1024,PRF,1024,512);
   B=abs(B);
   [m,n]=size(B);
   for z=1:n
```

```
      B2(:,z)=fftshift(B(:,z));
   end

   % Create a filtered spectrogram B2h for r.
   lowfi=round(lowf1/(PRF/m));
   B2h=zeros(m,n)+0.1;    % filled matrix with 0.1 instead of 1 because of low sig intens.
   B2h(1:512-lowfi,:)=B2(1:512-lowfi,:);    % filters out band of +-lowf1 around f=0
   B2h(512+lowfi:1024,:)=B2(512+lowfi:1024,:);

   % Calculate window (fdel in freq axis=x and tdel along time axis=z) for r.
   for z=1:n
      for x=1:1024-(fdel-1)
%         mB(x,z)=mean(B2h(x:x+fdel-1,z));  % power in sliding window in x direction
        mB(x,z)=(x+fdel/2)^2*mean(B2h(x:x+fdel-1,z));  % 2nd moment of power in sliding
window in x direction
      end
   end
   [mmB,xB]=max(mB);     % mmB(z)=max of mB and xB(z)=bottom of window in x-dir.
   for z=1:n-(tdel-1)
      wBr(z)=mean(mmB(z:z+tdel-1));  % mean power in sliding win in z direction for r
   end
   [mwBr,Bwzr]=max(wBr);  % mwB=max of wB and Bwz=left side of B-window in z-dir

   % Calculate the spectrogram of y
   [B,f,t]=specgram(y,1024,PRF,1024,512);
   B=abs(B);
   [m,n]=size(B);
   for z=1:n
      B2(:,z)=fftshift(B(:,z));
   end

   % Create a filtered spectrogram B2h for y.
   lowfi=round(lowf1/(PRF/m));
   B2h=zeros(m,n)+0.1;    % filled matrix with 0.1 instead of 1 because of low sig intens.
   B2h(1:512-lowfi,:)=B2(1:512-lowfi,:);    % filters out band of +-lowf1 around f=0
   B2h(512+lowfi:1024,:)=B2(512+lowfi:1024,:);

   % Calculate window (fdel in freq axis=x and tdel along time axis=z) for y.
   for z=1:n
      for x=1:1024-(fdel-1)
%         mB(x,z)=mean(B2h(x:x+fdel-1,z));  % power in sliding window in x direction
        mB(x,z)=(x+fdel/2)^2*mean(B2h(x:x+fdel-1,z));  % 2nd moment of power in sliding
window in x direction
      end
   end
   [mmB,xB]=max(mB);     % mmB(z)=max of mB and xB(z)=bottom of window in x-dir.
   for z=1:n-(tdel-1)
      wBy(z)=mean(mmB(z:z+tdel-1));  % mean power in sliding win in z direction for y.
   end
   [mwBy,Bwzy]=max(wBy);  % mwB=max of wB and Bwz=left side of B-window in z-dir
   if mwBr>=mwBy   % finds out if max xz window in r or y spectr.
      p(d)=mwBr;
   else
      p(d)=mwBy;
   end
end   % end of "for loop" for optimal depth calculation

[mp,dp]=max(p);     % finds the max of p (mp) and depth of mp (dp)
dopt=dp;
dopt_d1_d2_fdel_tdel_lowf1 = [dopt d1 d2 fdel tdel lowf1]

% plot p
clear str
figure(1)
xlabel('Depth index')
ylabel('p(max power in fdelxtdel window at each depth)')
title(['Parameter p used for selecting the optimal depth (dopt) of the Doppler signal.'])
hold on
```

```
set(gca,'ylim',[0 inf])   % insures that we only look at maxp>0
set(gca,'xlim',[d1 d2])
plot(p)
T1=['Program = ',filename,' (updated ',update,'),   data file = ',datafile];
T2=['p = optimization parameter = max power in a rectang window (fdel x tdel) in specgm
space for each depth.'];
T3=['Calculated from the red signal specgm with frequencies in the band +/-
',num2str(lowf1),'Hz removed.'];
T4=['dopt d1 d2 fdel tdel lowf1 = ',num2str(dopt_d1_d2_fdel_tdel_lowf1)];
T5=['Figure 1.  Plot of the optimization parameter, p.'];
str(1)={T1};
str(2)={T2};
str(3)={T3};
str(4)={T4};
str(5)={''};
str(6)={''};
str(7)={T5};
h=axes('position',[0 0 1 1],'Visible','off');
set(gcf,'currentaxes',h)
text(.1,-.1,str,'FontSize',11)
hold off

% 3. Find the max of the spectral envelope (envrmax & envymax) for each transducer.
% Get r and y at dopt.
d=dopt;
iy=iyellow(d,:);  % colors of 1st and 2nd transducers for i and q
ir=ired(d,:);
qy=qyellow(d,:);
qr=qred(d,:);
y=iy+i*qy;
r=ir+i*qr;

% Calculate the spectrogram of r (the red complex signal)
[B,f,t]=specgram(r,1024,PRF,1024,512);
B=abs(B);
[m,n]=size(B);
for z=1:n
   B2(:,z)=fftshift(B(:,z));
end

% Create a filtered spectrogram B2hr.
lowfi=round(lowf2/(PRF/m));
B2h=zeros(m,n)+0.1;   % filled matrix with 0.1 instead of 1 because of low sig intens.
B2h(1:512-lowfi,:)=B2(1:512-lowfi,:);    % filters out band of +-lowf2 around f=0
B2h(512+lowfi:1024,:)=B2(512+lowfi:1024,:);
B2hr=B2h;
[mb,mbj]=max(B2hr);          % calc mbj = modal freq index as fnc of time
mbjmr=mbj-m/2;              % shifts 1 to 1024 range to -512 to 512 range

% Find specgm envelope for red signal
B2hudr=flipud(B2hr);
BGr=mean(mean(B2hr));
for z=1:n
   if mean(mean(B2hr(1:m/2,:)))>=mean(mean(B2hr(m/2:m,:)))  % true => Dopp freq < 0
      clear Bave
      Bave(1:mave/2)=mean(B2hr(1:mave/2,z));
      for j=mave/2+1:m/2-mave/2,Bave(j)=mean(B2hr(j-mave/2:j+mave/2,z));,end
      if Bave(1)<=BGr,Benvr(z)=Bave(1);,else,Benvr(z)=BGr;,end   % picks the lesser of
Bave(1) or BGr to create envelope
      if find(Bave>=4*Benvr(z)); % tests if there is a Bave>4*Benvr(z); if not env=0
         envr2(z)=m/2-min(find(Bave>=4*Benvr(z))); %finds where specgm emerges from bckgrd
      else
         envr2(z)=0;
      end
      if Bave(1)<10*BGr,envr(z)=envr2(z);,else,envr(z)=m/2-mave/2;,end  %need to have this
cond if Dop freq at max (e.g.,5kHz)
      flagr=-1;
   else                          % true => Doppler freq is primarily > 0
```

```
      clear Bave
      Bave(1:mave/2)=mean(B2hudr(1:mave/2,z));
      for j=mave/2+1:m/2-mave/2,Bave(j)=mean(B2hudr(j-mave/2:j+mave/2,z));,end
      if Bave(1)<=BGr,Benvr(z)=Bave(1);,else,Benvr(z)=BGr;,end   % picks the lesser of
Bave(1) or BGr to create envelope
      if find(Bave>=4*Benvr(z)); % tests if there is a Bave>4*Benvr(z); if not env=0
         envudr2(z)=m/2-min(find(Bave>=4*Benvr(z))); %finds where specgm emerges from
bckgrd
      else
         envudr2(z)=0;
      end
     if Bave(1)<10*BGr,envr(z)=envudr2(z);,else,envr(z)=m/2-mave/2;,end  %need to have
this cond if Dop freq at max (e.g.,5kHz)
      flagr=1;
   end
end

% Calculate the spectrogram of y (the yellow complex signal)
% with +-lowf2 removed.
[B,f,t]=specgram(y,1024,PRF,1024,512);
B=abs(B);
[m,n]=size(B);
for z=1:n
   B2(:,z)=fftshift(B(:,z));
end
lowfi=round(lowf2/(PRF/m));
B2h=zeros(m,n)+0.1;
B2h(1:512-lowfi,:)=B2(1:512-lowfi,:);    % filters out band of +-lowf2 around f=0
B2h(512+lowfi:1024,:)=B2(512+lowfi:1024,:);
B2hy=B2h;
[mb,mbj]=max(B2h);          % calc mbj = modal freq index as fnc of time
mbjmy=mbj-m/2;              % shifts 1 to 1024 range to -512 to 512 range

% Find specgm envelope for yellow signal
B2hudy=flipud(B2hy);
BGy=mean(mean(B2hy));
for z=1:n
   if mean(mean(B2hy(1:m/2,:)))>=mean(mean(B2hy(m/2:m,:)))  % true => Doppler freq is
primarily < 0
      clear Bave
      Bave(1:mave/2)=mean(B2hy(1:mave/2,z));
      for j=mave/2+1:m/2-mave/2,Bave(j)=mean(B2hy(j-mave/2:j+mave/2,z));,end
      if Bave(1)<=BGy,Benvy(z)=Bave(1);,else,Benvy(z)=BGy;,end   % picks the lesser of
Bave(1) or BGy to create envelope
      if find(Bave>=4*Benvy(z)); % tests if there is a Bave>4*Benvy(z)(z); if not env=0
         envy2(z)=m/2-min(find(Bave>=4*Benvy(z))); %finds where specgm emerges from bckgrd
      else
         envy2(z)=0;
      end
      if Bave(1)<10*BGy,envy(z)=envy2(z);,else,envy(z)=m/2-mave/2;,end  %need to have this
cond if Dop freq at max=PRF/2
      flagy=-1;
   else                              % true => Doppler freq is primarily > 0
      clear Bave
      Bave(1:mave/2)=mean(B2hudy(1:mave/2,z));
      for j=mave/2+1:m/2-mave/2,Bave(j)=mean(B2hudy(j-mave/2:j+mave/2,z));,end
      if Bave(1)<=BGy,Benvy(z)=Bave(1);,else,Benvy(z)=BGy;,end   % picks the lesser of
Bave(1) or BGy to create envelope
      if find(Bave>=4*Benvy(z)); % tests if there is a Bave>4*Benvy(z); if not env=0
         envudy2(z)=m/2-min(find(Bave>=4*Benvy(z))); %finds where specgm emerges from
bckgrd
      else
         envudy2(z)=0;
      end
      if Bave(1)<10*BGy,envy(z)=envudy2(z);,else,envy(z)=m/2-mave/2;,end  %need to have
this cond if Dop freq at max (e.g.,5kHz)
      flagy=1;
   end
```

```
end

% 4. Find the optimal systolic peak (found from transducer with the highest envave).
[envrmax,zmaxr]=max(envr);  % zmaxr=time of peak systole for red xducer
[envymax,zmaxy]=max(envy);  % zmaxy=time of peak systole for yellow xducer
if flagr==-1                % true => Doppler freq is primarily < 0
   Tr=mean(mean(B2hr(1:m/2,:)))   % mean specgm intensity in neg half of red xducer
else                        % true => Doppler freq is primarily > 0
   Tr=mean(mean(B2hr(m/2:m,:)))   % mean specgm intensity in pos half of red xducer
end
if flagy==-1                % true => Doppler freq is primarily < 0
   Ty=mean(mean(B2hy(1:m/2,:)))     % mean specgm intensity in neg half of yellow xducer
else                        % true => Doppler freq is primarily > 0
   Ty=mean(mean(B2hy(m/2:m,:)))   % mean specgm intensity in pos half of yellow xducer
end
if Tr>=Ty&abs(zmaxr-zmaxy)>2       % condition to choose time of systolic peak
   zmaxy=zmaxr
elseif Ty>Tr&abs(zmaxr-zmaxy)>2
   zmaxr=zmaxy
end
fmodr=(PRF/m)*mbjmr(zmaxr);  % modal freq of at systolic peak
fmody=(PRF/m)*mbjmy(zmaxy);  % modal freq of at systolic peak
if flagr==-1                % true => Doppler freq is primarily < 0
    fpsr=-PRF/m*envr(zmaxr);  % freq at peak systole
elseif flagr==1                     % true => Doppler freq is primarily > 0
    fpsr=PRF/m*envr(zmaxr);  % freq at peak systole
end
if flagy==-1                % true => Doppler freq is primarily < 0
   fpsy=-PRF/m*envy(zmaxy);  % freq at peak systole
elseif flagy==1                     % true => Doppler freq is primarily > 0
   fpsy=PRF/m*envy(zmaxy);   % freq at peak systole
end

% 5. Calculate vector velocity
fp=fpsr+fpsy;
fn=fpsr-fpsy;
fps=((fn/(2*sin(A)))^2+(fp/(2+2*cos(A)))^2)^0.5;
ups=c*fps/f0;
format bank
dopt_lowf2_mave = [dopt lowf2 mave]
fpsr_fpsy_fmodr_fmody_zmaxr_zmaxy=round([fpsr fpsy fmodr fmody zmaxr zmaxy])
fps_ups=round([fps ups])

% 6. Plot spectrograms as subplots
% Plot the spectrogram for r without filters
hold on
figure(2)
f2=linspace(-PRF/2,PRF/2,1024);
ti=[1:n]';
maxB2hr=20*log10(max(max(10*B2hr))); %finds max of B2hr so color map will cover correct
range
subplot(2,1,1);
image(ti,f2,20*log10(10*B2hr));
axis([1 n -fmax fmax]);
axis xy;
colormap(jet(maxB2hr));  % plots vs ti .  Factor of 10 before B2hr is to insure that the
signal is >> 1 => log(10*B2hr) > 0.
colorbar

% Plot the spectrogram for y without filters
xlabel('time index')
ylabel('frequency(Hz)')
title(['Spectrogram for red (top) and yellow transducers'])
f2=linspace(-PRF/2,PRF/2,1024);
ti=[1:n]';
maxB2hy=20*log10(max(max(10*B2hy))); %finds max of B2h so color map will cover correct
range.
subplot(2,1,2);
```

```
image(ti,f2,20*log10(10*B2hy));
axis([1 n -fmax fmax]);
axis xy;
colormap(jet(maxB2hy));  % plot vs ti.  Factor of 10 before B2hy is to insure that the
signal is >> 1 => log(10*B2hy) > 0.
colorbar
T1=['program = ',filename,' (updated ',update,'),   data file = ',datafile];
T2=['optimal depth  lowf2  mave  = ',num2str(dopt_lowf2_mave)];
T3=['fpsr  fpsy  fmodr  fmody  zmaxr  zmaxy =
',num2str(fpsr_fpsy_fmodr_fmody_zmaxr_zmaxy)];
T4=['vector Doppler frequency = ',num2str(round(fps)),' Hz           vector Doppler
velocity = ',num2str(round(ups)),' cm/sec'];
T5=['Figure 2.  Spectrograms of the Doppler signals at depth = ',num2str(d)];
str(1)={T1};
str(2)={T2};
str(3)={T3};
str(4)={T4};
str(5)={''};
str(6)={''};
str(7)={T5};
h=axes('position',[0 0 1 1],'Visible','off');
set(gcf,'currentaxes',h)
text(.1,-.11,str,'FontSize',10)
hold off
```

Appendix B

Doppler equation for the UW scanhead

The Doppler frequencies seen at the r and y receivers are as follows:

Eq. (1) $f_r = kV\left[\cos\theta + \cos(\theta - \alpha)\right]$

Eq. (2) $f_y = kV\left[\cos\theta + \cos(\theta + \alpha)\right]$

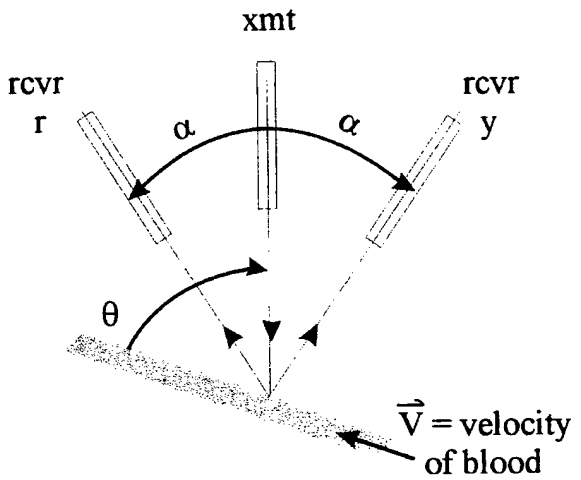

where $k = f_0/c$, f_0 = carrier frequency, and c = speed of sound in tissue.

Eq. (3) $f_n = f_r - f_y = kV\left[\cos(\theta - \alpha) - \cos(\theta + \alpha)\right] = 2kV\sin\theta \bullet \sin\alpha$

Eq. (4) $f_p = f_r + f_y = kV\left[\cos(\theta - \alpha) + \cos(\theta + \alpha) + 2\cos\theta\right] = 2kV\cos\theta(1 + \cos\alpha)$

(Ref: CRC Standard Math Tables, p. 409.)

Then dividing Eq. (3) by Eq. (4), we have:

$$\tan\theta = \frac{f_n}{f_p K_\alpha} \quad \text{where } K_\alpha = \frac{\sin\alpha}{1 + \cos\alpha}$$

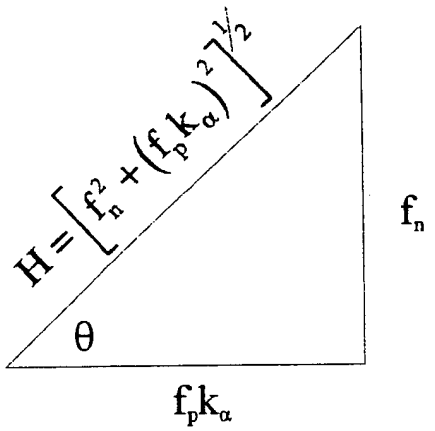

From the figure, we see that:

$$\sin\theta = \frac{f_n}{H} \quad \text{where } H = \left[f_n^2 + \left(f_p k_\alpha\right)^2\right]^{1/2}$$

using Eq. (3):

$$f_n = 2kV\frac{f_n}{H}\sin\alpha \quad \text{or} \quad V = \frac{H}{2k\sin\alpha} = c\frac{f_D}{f_0}$$

where f_D = effective Doppler frequency $= \left[\left(\frac{f_n}{2\sin\alpha}\right)^2 + \left(\frac{f_p}{2 + 2\cos\alpha}\right)^2\right]^{1/2}$

DESCRIPTION AND PERFORMANCE SITES (FORM B)

DESCRIPTION: State the goal of the research project and how it relates to improving the health care of the nation's people. Use succinct language to describe how the project goals will be achieved. Do not exceed the space provided on this page.

The long-term objective of SRI International is to address the problem of human performance limitations in microsurgery. Current microsurgery techniques are used with good success rates in a variety of applications ranging from surgeries of the reproductive organs, urinary tract, eyes and ears to reconstructive procedures for the treatment of traumatic injuries and corrective surgeries to treat congenital abnormalities. However, because of surgeon hand tremor and the fundamental limits of human fine coordination and positioning ability, it is generally quite difficult to successfully manipulate and repair blood vessels or other tissue structures that are smaller than about 1 mm in diameter. This problem is perhaps most evident in microvascular tissue transplantation and digit reattachment in children, where the small size of vessels and nerves (<0.5 mm dia.) often makes surgical replantation or repair impossible. Similar limitations arise in surgeries of the eye and ear, as well as in urological and neurosurgical procedures.

Telepresence-based microsurgery has the potential to overcome these limitations by providing surgeons with a magnified workspace in which they can comfortably work with their hands on conventional instrument handles, using normal hand motions and experiencing the feel they would expect from the magnified tissues being viewed. With telepresence technology, microsurgeons will potentially be able to manipulate very small tissue structures with relative ease, enabling them to successfully perform a variety of vascular, urologic, and neurosurgical procedures that are not currently possible.

To achieve our objective, we propose to undertake a three-year research program in which we will apply and successively refine telepresence surgery technology, previously developed at SRI International, for an advanced Telepresence Microsurgery System (TMS) that will enhance human capabilities in microsurgery. Specifically, we propose to

- assemble of a panel of expert microsurgeons to advise and work closely with the SRI technical staff
- with the expert panel, determine the motion access, force levels, and force limits necessary to successfully manipulate the tissues and place sutures in microsurgical procedures as the size of the target tissues diminishes
- develop micromanipulator components with sufficient sensitivity, dexterity, and accuracy to successfully perform microsurgical procedures on tissue structures much smaller than is possible with conventional techniques
- develop an *orthostereoscopic* imaging system that preserves human spatial perception and provides a sharp image over the surgical depth of field
- integrate the micromanipulator and imaging system into an advanced telepresence microsurgery system (TMS)
- develop microsurgical techniques for joining 0.5- and 0.25-mm vessels through a series of experiments using training models and animal tissues

Once this work has been completed, we will develop design rules for extending microsurgery to smaller scales and for developing cost-effective telepresence systems for enhanced human microsurgical applications.

PROJECT SITE(s) *(organization, city, state):*

SRI International, 333 Ravenswood Ave. Menlo Park, CA 94025

SRI International

APR 20 2000

COPY

Semiannual Report • April 2000
Covering the period 18 October 1999 to 17 April 2000

OPEN MICROSURGERY SYSTEM

ITAD-10523-SR-00-043
Cooperative Agreement DAMD17-97-2-7016
Subagreement 25-FY98-SRI-JENSEN

Submitted by

Subramanian V. Shastri, Program Manager
Principal Investigator
Advanced Automation Technology Center
venkat@erg.sri.com
Phone: (650) 859-5835; Fax: (650) 859-5510

P. Garcia for V.S.

Pablo Garcia, Research Engineer
Co-principal Investigator
Innovative Product Engineering & Technologies
garcia@erg.sri.com
Phone: (650) 859-5419; Fax: (650) 859-4812

Prepared for

National Medical Technology Testbed
11354 Mountain View Avenue, Suite D
Loma Linda, California 92354
Attention: Thomas J. Callanan, Administrative Director

Approved by

Michael S. Frankel, Vice President and Director
Information, Telecommunications, and Automation Division

1 INTRODUCTION

SRI International (SRI) is pleased to submit this semiannual report, ITAD-10523-SR-00-043, to the National Medical Technology Testbed (NMTB). During a 3-year research project SRI is applying and refining telepresence surgery technology, previously developed at SRI, for an advanced Telepresence Microsurgery System (TMS) that will enhance human capabilities in microsurgery. SRI's telepresence microsurgery technology was developed under internal funding and was based on telepresence technology developed under a contract with the Defense Advanced Research Projects Agency. We expect to generate intellectual property in the form of novel technologies and designs in several areas, including sensor-based instrument concepts that maintain control of tissue without damage, and methods for the magnification of force reflection to the surgeon's hand. This system also will have the potential to be used in telemedicine for remote microsurgery, because the slave system can be operated in a remote location.

2 MICROSURGERY SYSTEM DEVELOPMENT

2.1 OVERVIEW

As part of the initial work on this project, SRI conducted interviews with doctors and potential commercial partners to determine the areas where telerobotic microsurgery could have greater impact. The doctors interviewed included hand surgeons, pediatric heart surgeons, and pediatric surgeons practicing minimally invasive techniques. Three main areas were identified, some of which expand the scope of this project beyond what was initially identified by SRI:

1. Reduce the minimum size of vessels that can be worked on, and increase the sensing capabilities of microsurgeons operating on small amounts of tissue (this area was identified in the initial proposal to NMTB).
2. Allow regular vascular surgeons to perform surgeries currently limited to specialized microsurgeons.
3. Open up the possibility of performing complex, minimally invasive surgeries to correct conditions ranging from heart defects to digestive system problems in small children.

The system development approach outlined in the original proposal to NMTB addresses primarily the first area. The plan was to enhance the current microsurgery system by improving its accuracy, implementing force feedback, and adding two slow-moving degrees of freedom (DOF) to the base of the slave manipulator. Adding two slow-moving degrees of freedom to reposition the 4-DOF manipulator was considered the most feasible way of enhancing the dexterity of the system. Since then it has transpired that it is also feasible to add two active degrees of freedom to the distal end of the manipulator by using some recently commercialized actuators [RMB 2000], effectively addressing the second and third areas outlined above. The original 4-DOF manipulator is shown in Figure 1.

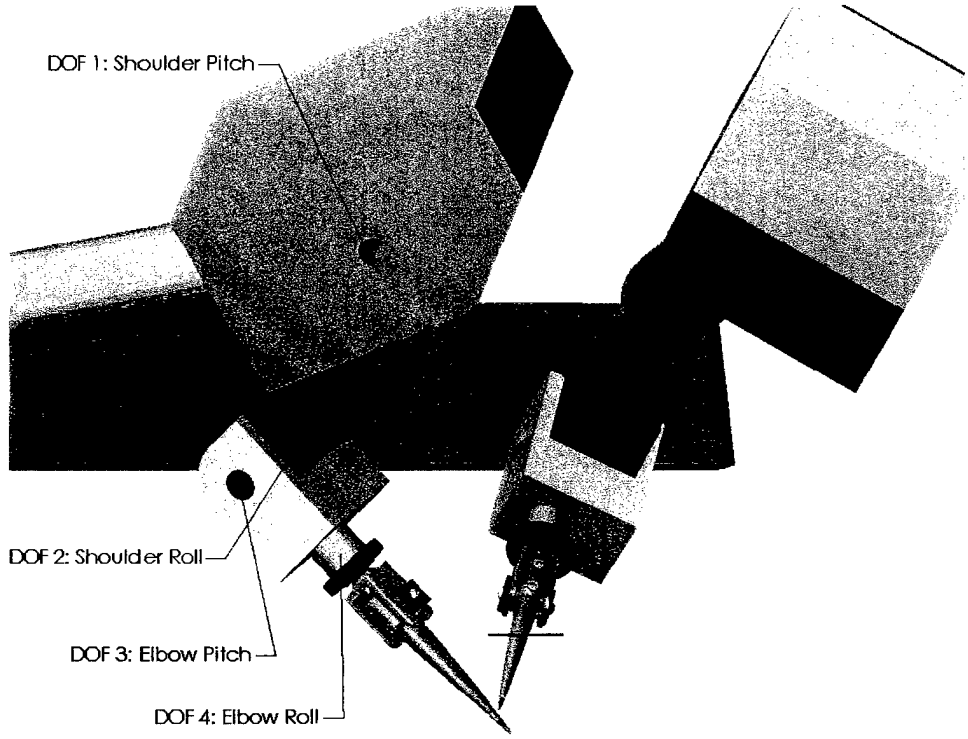

Figure 1. 4-DOF Manipulator

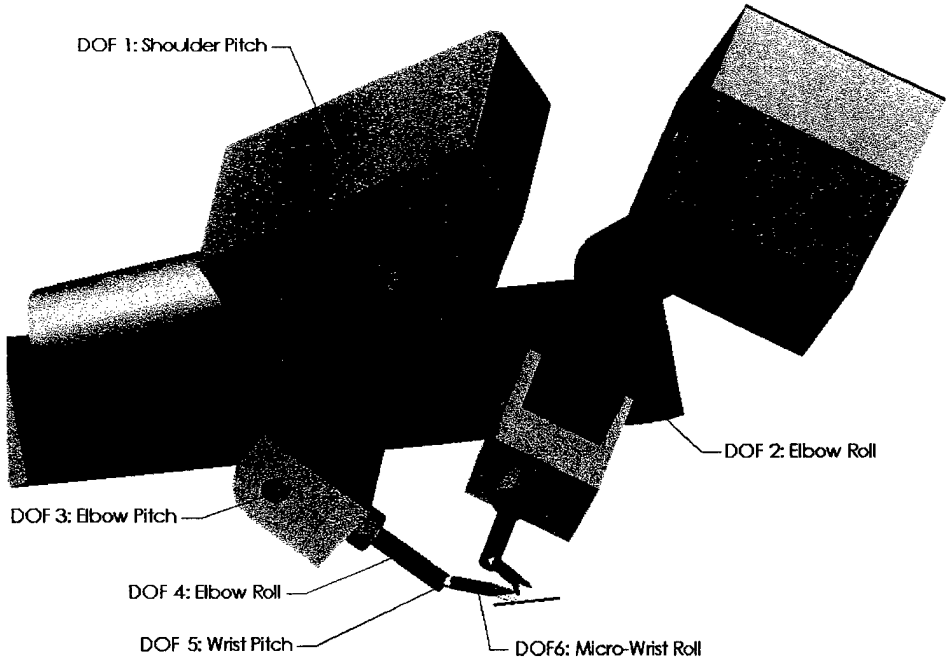

Figure 2. New 6-DOF Manipulator

A microsurgery system with two active degrees of freedom and a capability to scale the surgeon's movements could perform the standard 6-DOF movements made in regular vascular surgery, enabling vascular surgeons to perform microsurgery procedures without specialized training. In addition, the distal degrees of freedom will incorporate unique components that can enable the development of new tools for minimally invasive microsurgery on small children. Minimally invasive robotic surgery is currently limited to adults and a limited number of procedures, mainly because of the lack of small high-dexterity tools. The new components designed by SRI for the TMS would enable the development of such tools, expanding the applicability of minimally invasive robotic surgery. One of these components, an electrically powered microwrist, has been presented to potential commercial partners including Intuitive Surgical, Inc.,* and was received very positively. According to Intuitive Surgical, the microwrist would enable current minimally invasive robotic surgery systems to reduce the size of their tools by 50%, and therefore would enable the systems to be used for microsurgery.

As a result of these findings, during the rest of Year 1 we will place more emphasis on developing an enhanced slave system with two additional motorized distal degrees of freedom that incorporate some of these components. A similar task was initially proposed [Jensen 1999] for Year 2 in Task 9: motorizing the slow-moving degrees of freedom at the base of the robot. Because of the increased complexity of the new design, during Year 1 we will place less emphasis on enhancing force feedback and increasing the resolution of the current system. These areas will be addressed during Year 2.

Following are descriptions of each of the tasks described in the statement of work of the original proposal [ibid.], with a summary of the progress to date.

2.2 TASKS AND PROGRESS

2.2.1 Task 1: Determine Microsurgery System Requirements

Task 1, as originally proposed, was as follows: "SRI will determine the motion access and levels of force necessary to manipulate the tissues and sutures required to carry out microprocedures, as well as to determine force thresholds for damage to tissue and suture materials" [ibid.].

This task has been performed by consultation with doctors in the field and ex-vivo tissue experiments.

The instruments used for the experiments are described below:

- Instrumented tweezers with strain gages placed axially to measure the bending of each arm
- Instrumented needle holders to measure the force required to hold the needles in place
- A precision scale with a fixture to hold different types of tissue and measure the load in one direction.

*All product and company names mentioned in this document are the trademarks of their respective holders.

Most of the tissue used in the experiments was extracted from dissected pork hearts and included samples of valves, muscles, arteries, and inner heart walls. The size of the needles used ranged from 5-0 to 10-0.

The results of the force experiments are summarized in Table 1. Although the design being developed is intended mainly for smaller needles, from the results obtained, it will also accommodate the forces required by larger needles. This versatility is useful since some procedures, such as pediatric heart surgery to correct atrial septum defects (ASDs), combine the use of small (8-0) and large (5-0) needles. In addition, the process of dissection to prepare the site for microsurgery often involves larger forces than the ones required for suturing with small needles.

Table 1. Needle Forces

PROCEDURE	10-0 NEEDLE (g)	9-0 NEEDLE (g)	7-0 NEEDLE (g)	5-0 NEEDLE (g)
Pierce Vessel	5–15	15–30	10–30	25–35
Pierce Muscle	5–10		10–30	
Pierce Valve	5–15	10–15	15–25	30–40
Pierce Inner Heart Wall	5–10	5–8		40–100
Tear Vessel				
Tear Muscle	(Needle bends)	(Needle bends)	100	60–120
Tear Valve				250–300
Bend Needle	12	55	150	300
Break Suture	5	20	50	800
Tie Knot	2	5	10	80
Hold Needle	500	500	750	1500

Table 2. Tissue Grasping Forces

ACTIVITY	MAXIMUM FORCE (g)
Grab 1 mm Vessel	5
Grab Outer Vessel Wall	20
Pull 1 mm Vessel	100
Pull Muscle	100
Pull Valve	300

2.2.2 Task 2: Upgrade Microsurgery Manipulators of Prototype TMS

Task 2, as originally proposed, was as follows: "We will improve the existing SRI microsurgery manipulator system for use in the proposed research program. We will focus on improved force feedback and increased motion scaling (demagnification) to improve both the manipulation capabilities and human interface for microsurgery" [ibid.].

The following work was accomplished:

- The current manipulator was modified to reduce backlash and increase precision, by preloading all the bearings in the critical joints and tightening the tolerances of the

precision parts. It is estimated that the backlash has been reduced by 80% from that of the initial prototype. The resolution at the tip of the tool is 7.5 μm. The backlash is less than 0.5 μm.

- Some new quick-disconnect tools were designed and built. These include forceps, scissors, and needle holders that can handle needles ranging in size from 8-0 to 12-0 (Figure 3). The grip-activating mechanism described in Section 9 of the original proposal [ibid.] has not been modified yet because the needle gripping forces do not make it suitable for a lightweight actuator.
- The motion demagnification currently is being developed to 8X and 16X.

As explained in Subsection 2.1, work on the force feedback based on force sensors, and experiments with force-limiting controls has been set aside until the new Slave Manipulator specified under Task 5 has been completed.

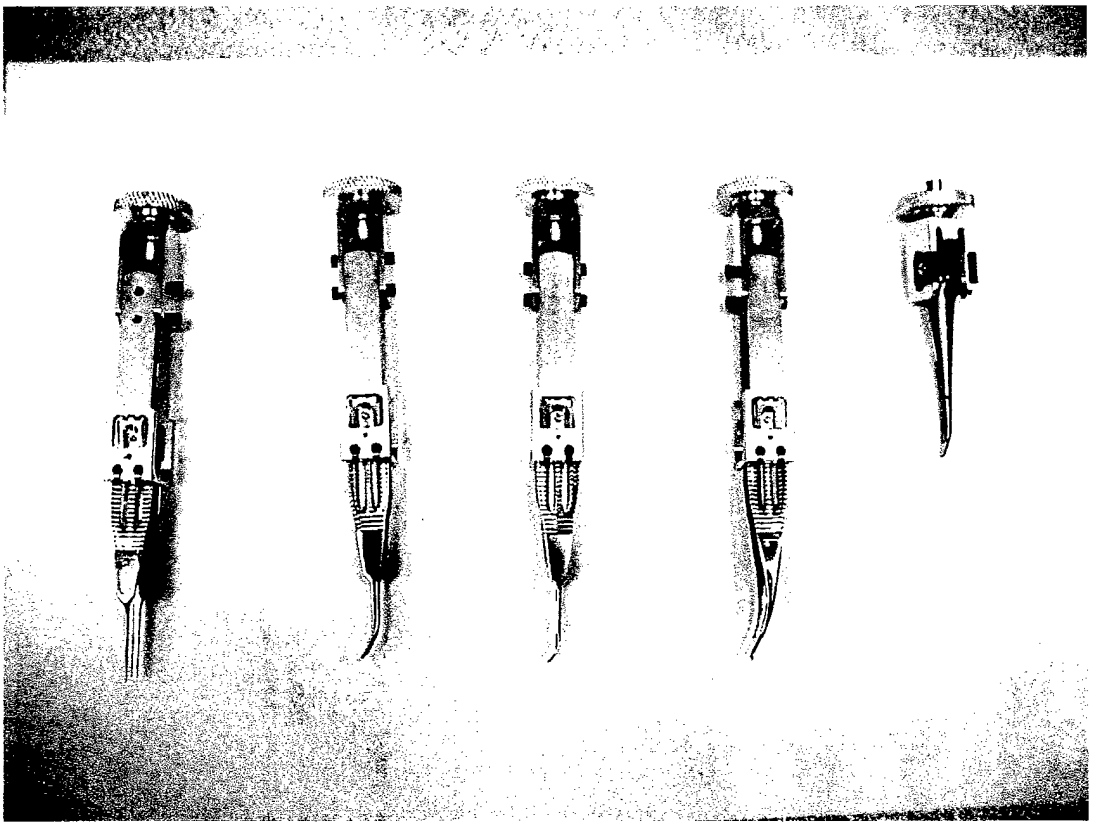

Figure 3. New Tools for Microsurgery System

2.2.3 Task 3: Upgrade Imaging System of Prototype

As proposed, Task 3 was as follows: "We will improve the existing SRI microsurgery stereo vision system for use in the proposed research program. We propose to implement and test several different prototype imaging approaches during year 1, so that we can compare their performance and select the best approach for further development in Year 2" [ibid.].

The following work is underway:

- Installing and testing a microscope (acquired from Carl Zeiss) with automatic zooming capabilities. The microscope contains a powerful light source and increased depth of field. The system is being borrowed for evaluation and will be tested on a set of controlled experiments by a surgeon.
- Installing a stereo viewer with independent optical channels, so that no shuttering glasses are required. The viewer, donated by Intuitive Surgical, Inc., is expected to increase the image sharpness and the comfort level of the surgeon.

2.2.4 Task 4: Conduct Performance Experiments

As proposed, Task 4 was as follows: "We will conduct a wide range of performance experiments with the upgraded TMS to learn as much as possible about the principles of telepresence microsurgery before embarking on the new design" [ibid.].

No experiments have been performed to date, as the hardware is still being updated. The first set of experiments is scheduled to start at the end of April 2000. This set of experiments will be performed with the upgraded microsurgery manipulator system from Task 2, and the new imaging system implemented in Task 3. The experiments with the upgraded TMS system will take place in parallel with the development of the new design. The reason this approach has been taken is that the features of the new design, as described in Subsection 2.2.5 (Task 5), provide advantages that have already been identified. At the same time, some of the results of the experiments conducted with the upgraded TMS system can still be used to improve the final design.

2.2.5 Task 5: Develop Slave Microvascular Manipulator

As proposed, Task 5 was as follows: "Based on the findings of Tasks 1 through 4, we will develop a new pair of slave manipulators specifically designed for use in vascular microsurgery" [ibid.].

As described above in Subsection 2.1, it has been determined that developing a 6-DOF manipulator with two additional distal degrees of freedom has more potential for commercialization than increasing the resolution and force feedback of the current system. The key component to achieve this is a microwrist at the distal end of the manipulator; this microwrist (shown in Figure 4) has been designed and is being prototyped. This wrist contains an internal micromotor 3 mm in diameter and 12 mm in length (See Figure 5) that provides a roll motion to the surgical tool. The final surgical tool will have an outside diameter of 5 mm, a gripping force up to 10 N, and a torque that can drive a needle through tissue with 100 g of force. The design of this actuator represents a breakthrough in the development of robotic surgical tools, because it will allow the development of very small, minimally invasive surgical tools with high dexterity. Currently, the smallest surgical tool with 6 DOF, developed by Intuitive Surgical, Inc., has a diameter of 9 mm, which makes it unsuitable for pediatric applications. Other efforts to activate distal joints by hydraulic power have resulted in larger actuators with poor performance [Cavasoglu et al. 1998].

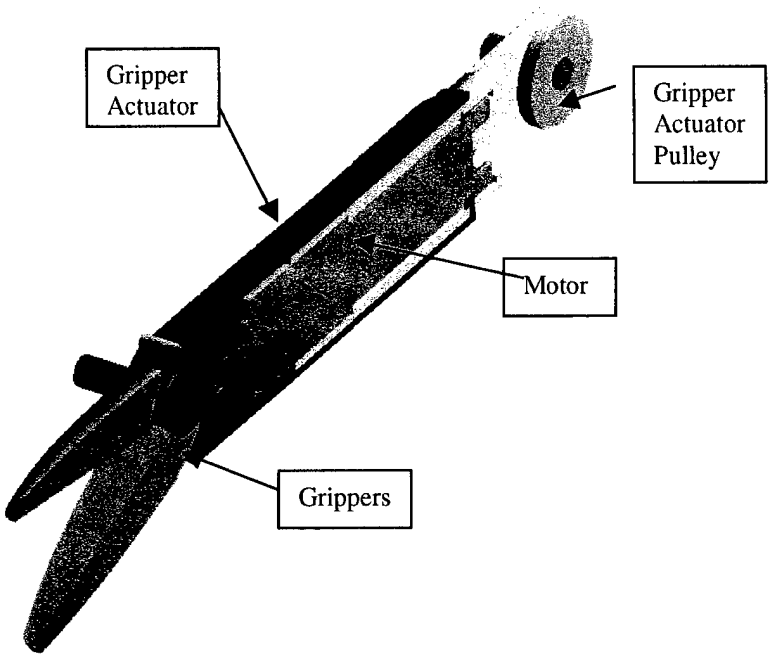

Figure 4. An Axial Section of the Microwrist

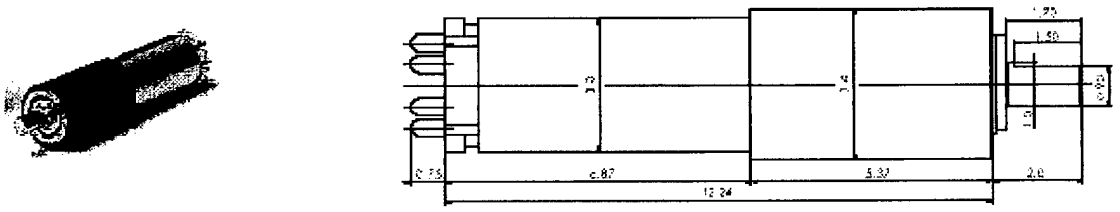

Figure 5. 3-mm Geared Motor Used in Microwrist

The second distal degree of freedom, which provides pitch to the microwrist, is currently being designed. A mock-up of the two additional degrees of freedom has been incorporated into the manipulator (Figure 6) in order to study the kinematics of the whole system for performing anastomosis. The dynamics of the system are being analyzed with the simulation package Working Model 3D.

The minimum workspace for the robot, determined in consultation with surgeons, is 60 mm × 60 mm × 60 mm (width × length × height). The space where the precision surgery work is performed is limited to 20 mm × 20 mm × 10 mm.

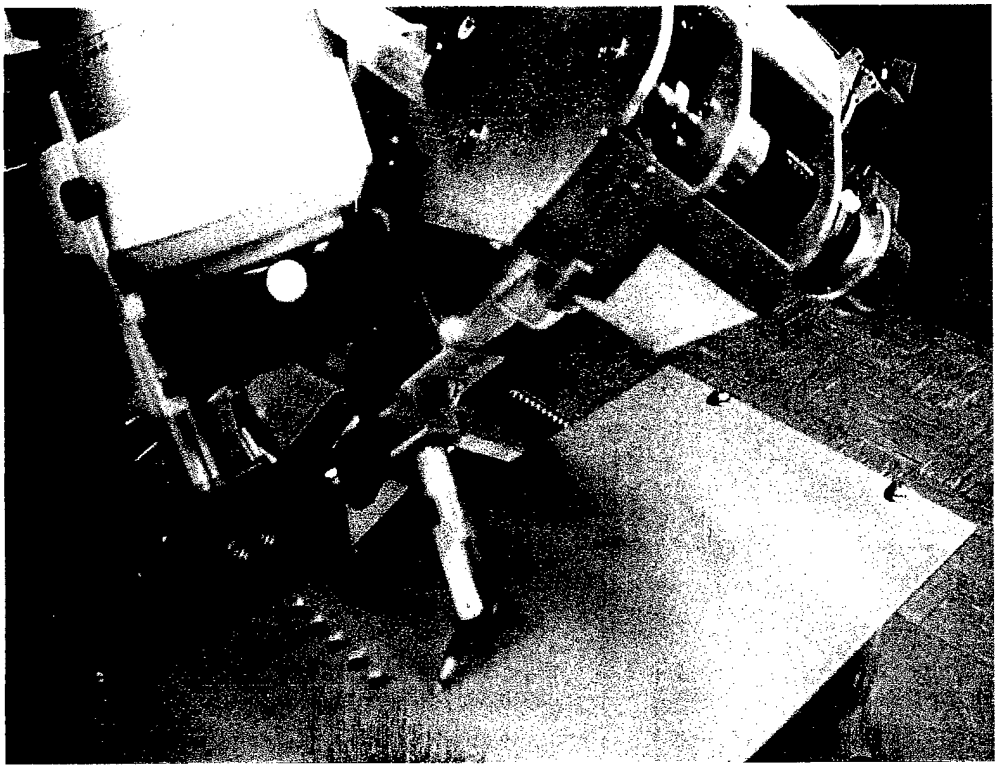

Figure 6. 6-DOF Mockup of Microsurgery System

The system specifications for each of the distal degrees of freedom, based on the results of the Task 1 measurements, are summarized in Table 3; the overall system loads are summarized in Table 4.

Table 3. Specifications for Distal Degrees of Freedom

Distal Pitch	**Target**
Maximum Torque	0.3 Nm
Displacement Range	-45° to +45°
Resolution	10 μm on tip of tool
Torque Sensitivity	0.0003 Nm
Time Constant	180° in 0.5 s
Bandwidth	10 Hz
Distal Roll (Microwrist)	**Target**
Maximum Torque	0.003 (100 g over 4 mm)
Displacement Range	360°
Resolution	0.5°, or 15 μm at tip of needle
Force Sensitivity	Nonbackdriveable
Time Constant	360° in 0.5 s
Bandwidth	10 Hz
Grip	**Target**
Maximum Force	10 N
Displacement Range	+/-30° or 6 μm at tip
Resolution	10 μm
Force Sensitivity	0.01 N
Time Constant	60° in 0.5 s
Bandwidth	10 Hz

Table 4. Maximum Loads on System

LOAD	TARGET
Perpendicular to Gripper X	10 N
Perpendicular to Gripper Y	10 N
Pull Along Gripper	10 N
Push Along Gripper	10 N
Torsional Torque	0.2 Nm

3 CONCLUSIONS

In the area of minimally invasive microsurgery we have identified new applications and commercial opportunities that can be addressed within the scope of the current TMS development. We have designed an innovative microwrist for the current system; this microwrist will increase the active degrees of freedom of the manipulator from 4 to 6 DOF. This will greatly enhance the performance of current systems and open new paths in the development of surgical tools for minimally invasive surgery in microsurgery applications such as pediatric surgery.

Because of the complexity of the new design, which is greater than that of the design initially proposed, we will perform the development of force feedback algorithms and force limiting controls in Year 2 of the project. We can do so because some of the design improvements initially planned for Year 2, such as those specified in Task 9, will be addressed during Year 1.

The current system has been partially enhanced and experiments at the end of this April are intended to provide a measure of the improvements in tools, in the accuracy of the TMS system, and in its vision system.

4 REFERENCES

Cavusoglu, M.C., M.B Cogn, F. Tendick, and S.S. Sastry. 1998. "Laparoscopic Telesurgical Workstation," presented at SPIE Conference 3262 on Surgical-Assist Systems, San Jose, California (January).

Jensen, J. 1999. *Open Microsurgery System: National Medical Technology Testbed, Inc. Application (Form A)*, ATU 98-722R2, SRI International, Menlo Park, California (7 October).

RMB. 2000. "High Precision Motor . . . SYH390001," RMB S.A., http://www.smoovy.com/products/syh39001.htm.

DESCRIPTION AND PERFORMANCE SITES (FORM B)

DESCRIPTION: State the goal of the research project including how it relates to improving health care for the nation's people. Use succinct language to describe how the project goals will be achieved. Do Not exceed the space provided on this page.

The aims of this project are 1) to develop an in vitro model of mechanical force induced neurodegeneration which is appropriate for the use in studying traumatic head injury and 2) to identify new therapeutic strategies to reduce the neurological damage associated with traumatic head injury. An in vitro model of mechanical force induced neurodegeneration would greatly facilitate the study of the effects of traumatic brain injury and the elucidation of the cellular mechanism of neurodegeneration. Screening and assessment of new compounds with the potential for reducing the severity of injury would also be facilitated. An understanding of the cellular mechanism of neurodegeneration that occurs following traumatic brain injury will enable us and others to design new strategies to block events central to neurodegeneration, thus reducing/preventing the neurological deficits which accompany traumatic brain injury.

The in vitro model we propose to develop uses a differentiated neuroblastoma cell line and exposes it to shear and strain, the forces believed to be important during head injury. We will use a variety of pharmacological and biochemical techniques to examine the mechanism of cell death. Based on the steps in the mechanism elucidated, strategies will be designed to prevent mechanical force induced neurodegeneration.

PROJECT SITE(s) (*Organization, City, State*):

Texas Engineering Experiment Station
Bioscience Engineering Laboratory
College Station, Texas 77843-3122

ORIGINAL

MAY 12 2000

Development of In vitro models of head injury and glaucoma:

Examining the effects of shear stress and strain on cells of the central nervous system

Theresa Good, Michael Edwards, Dina Triyoso

and Sheng-Shih Wang

Sponsored by the U.S. Department of the Army, the National Medical Technology Testbed, Inc. and a National Glaucoma Research Grant from the American Health Assistance Foundation

The view, opinions and/or findings contained in this talk are those of the authors and should not be construed as a position, policy, decision, or endorsement of the federal Government or the National Medical Technology Testbed, inc.

Glaucoma significance

- Population burden
  - 1% of population ≥ age 40
  - 67 million affected worldwide by year 2000
  - 7 million experience complete vision loss

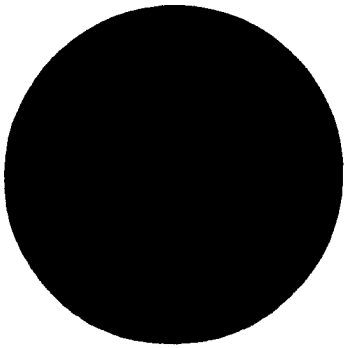

- Economic burden
  - $3 B annually in USA
    - $1.2 B to physicians
    - $600 M for surgery
    - $400 M for drugs
    - $800 M for indirect costs

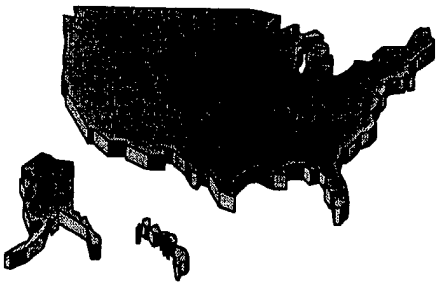

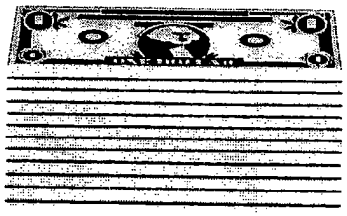

Glaucoma overview

- Group of diseases generally characterized by elevated IOP resulting in localized RGC damage and optic nerve degeneration.
- Generally, as IOP increases, vision loss increases.
- Relationship between IOP and vision loss is not understood.

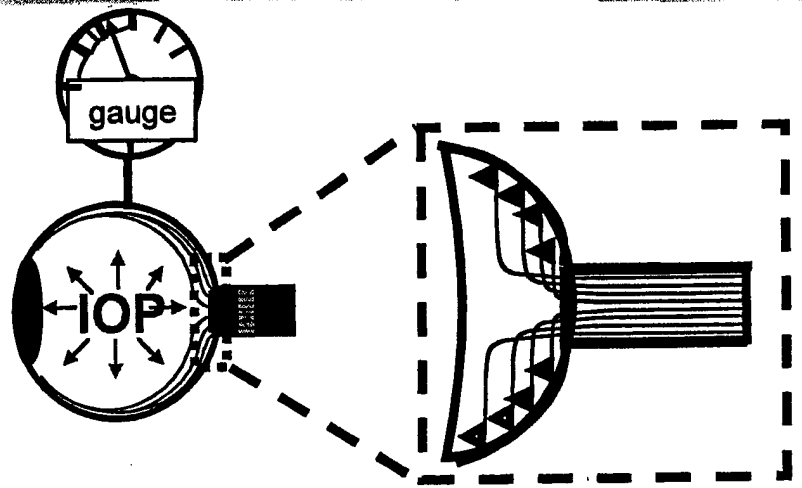

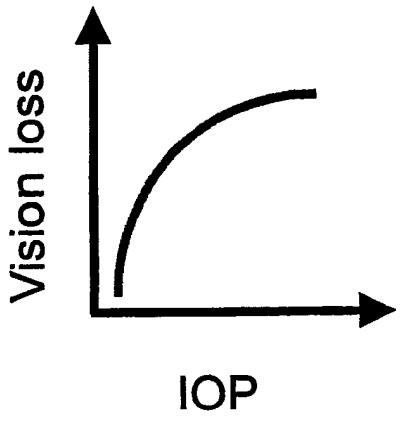

Head Injury

- 500,000 people, 4 billion dollars/year
- increase in intracranial pressure, high shear stress regions correspond to patterns of injury
- mechanism is not well understood

Research objectives

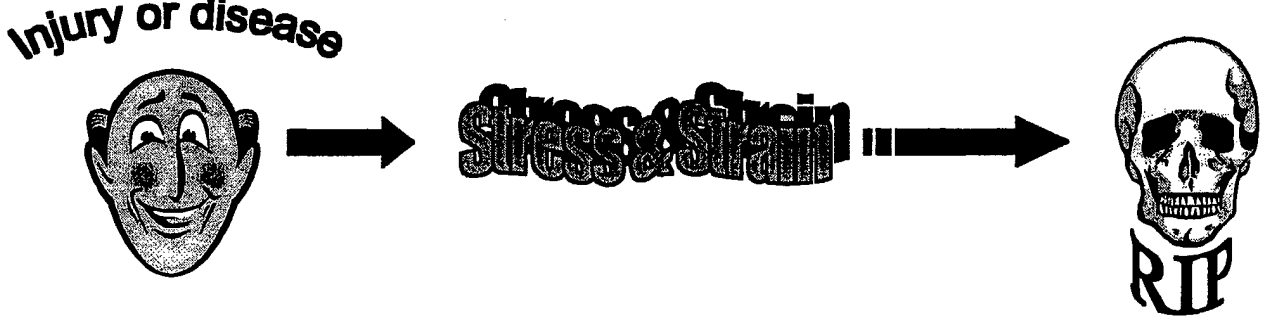

- Develop an *in vitro* model which can be used to determine:
  - the effect of stress and strain to neurons .
  - the mechanism of neuronal injury.
  - potential sites for therapeutic intervention.
  - Screen new drugs for treatment of injury or disease.

Cell deformation analysis - principle strain

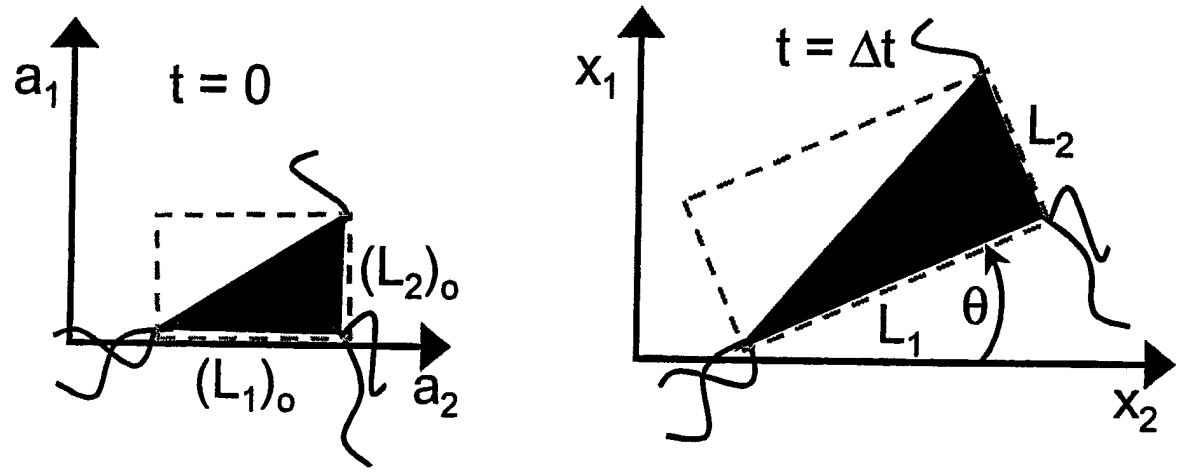

$$\lambda_{1\,cell} = \frac{L_1}{(L_1)_o} \quad \Rightarrow \quad E_1 = \frac{1}{2}\left(\lambda_{1cell}{}^2 - 1\right)$$

Long axis stretch ratio — Maximum principle strain

$$\lambda_{2\,cell} = \frac{L_2}{(L_2)_o} \quad \Rightarrow \quad E_2 = \frac{1}{2}\left(\lambda_{2cell}{}^2 - 1\right)$$

Short axis stretch ratio — Minimum principle strain

θ = direction of maximum elongation

Cell deformation analysis - system

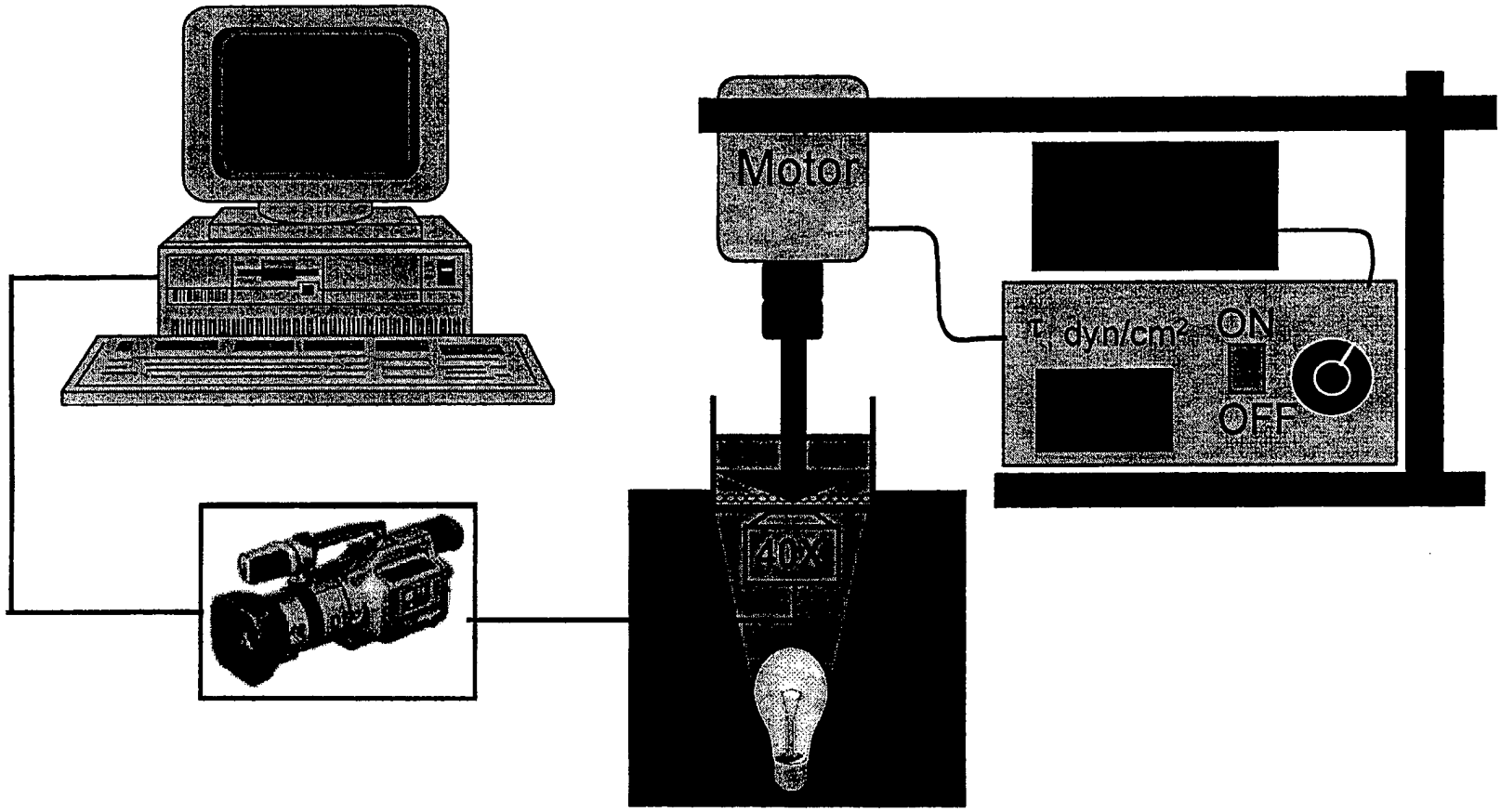

Increasing duration of strain does not increase extent of injury

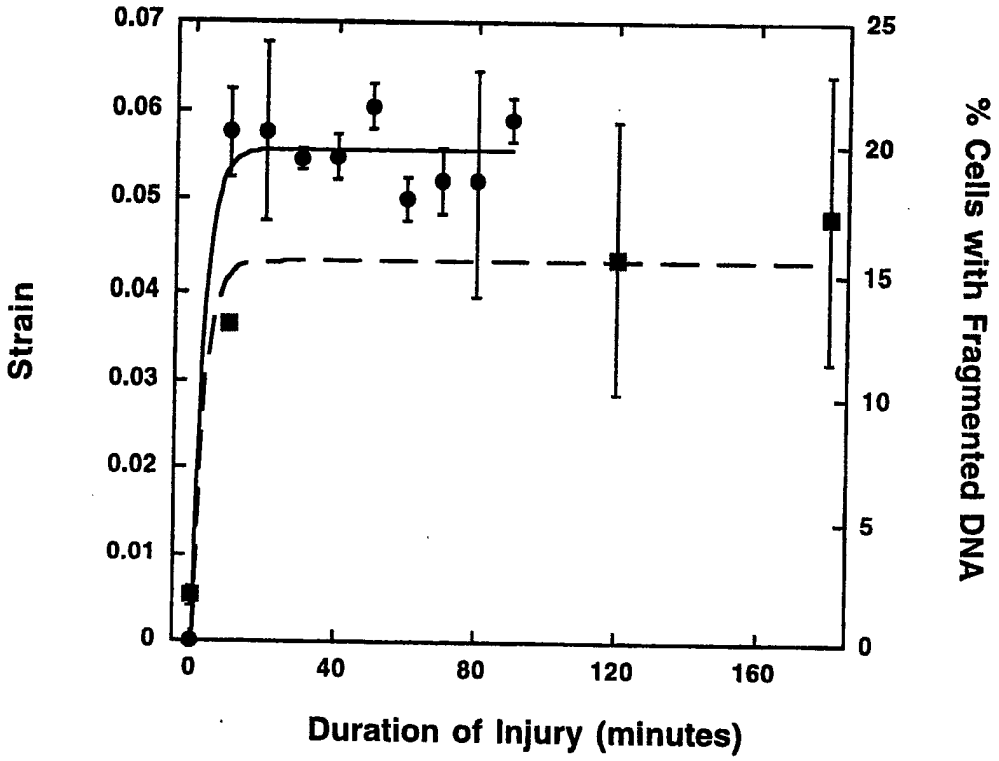

Increasing magnitude and periodicity of stress/strain increases extent of injury.

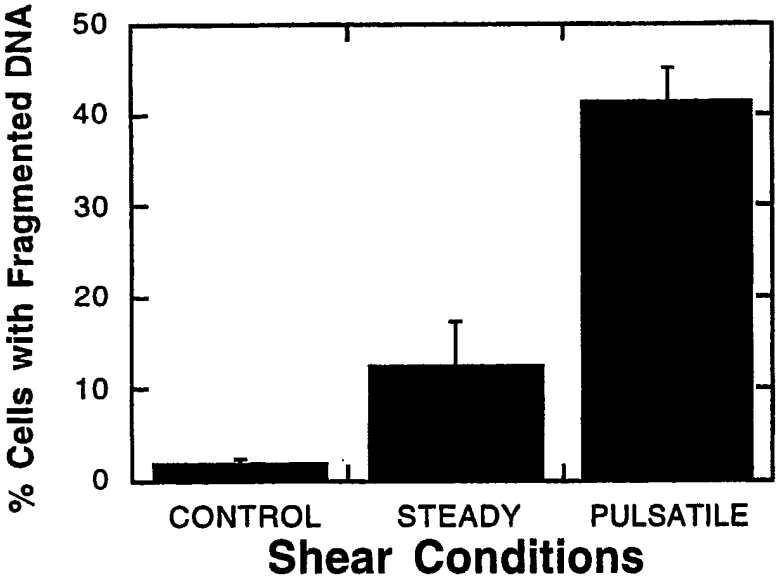

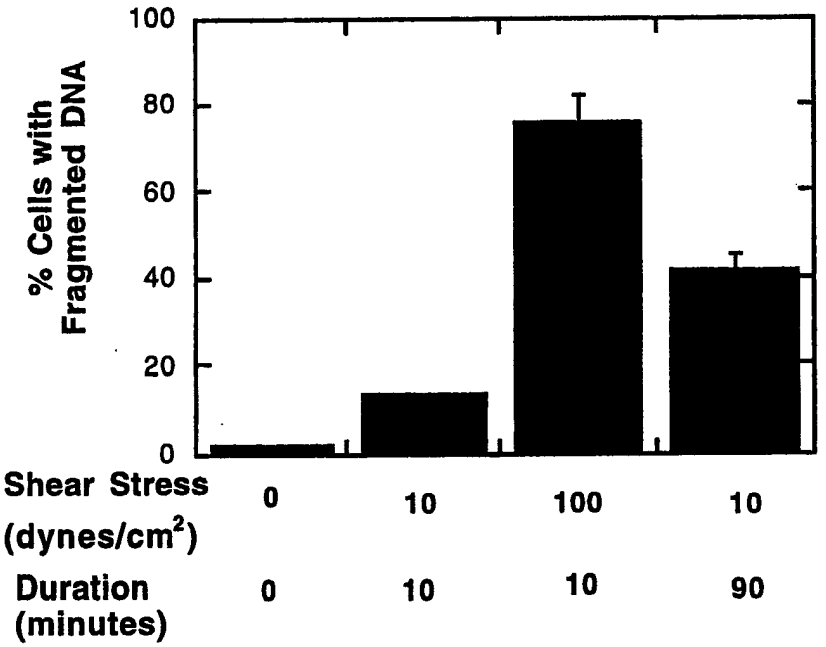

- Pulsatile shear is more damaging than steady shear.
- High shear, short duration is comparable to moderate shear, long duration.

G protein and IP_3 pathway may be involved mechanism of cell injury.

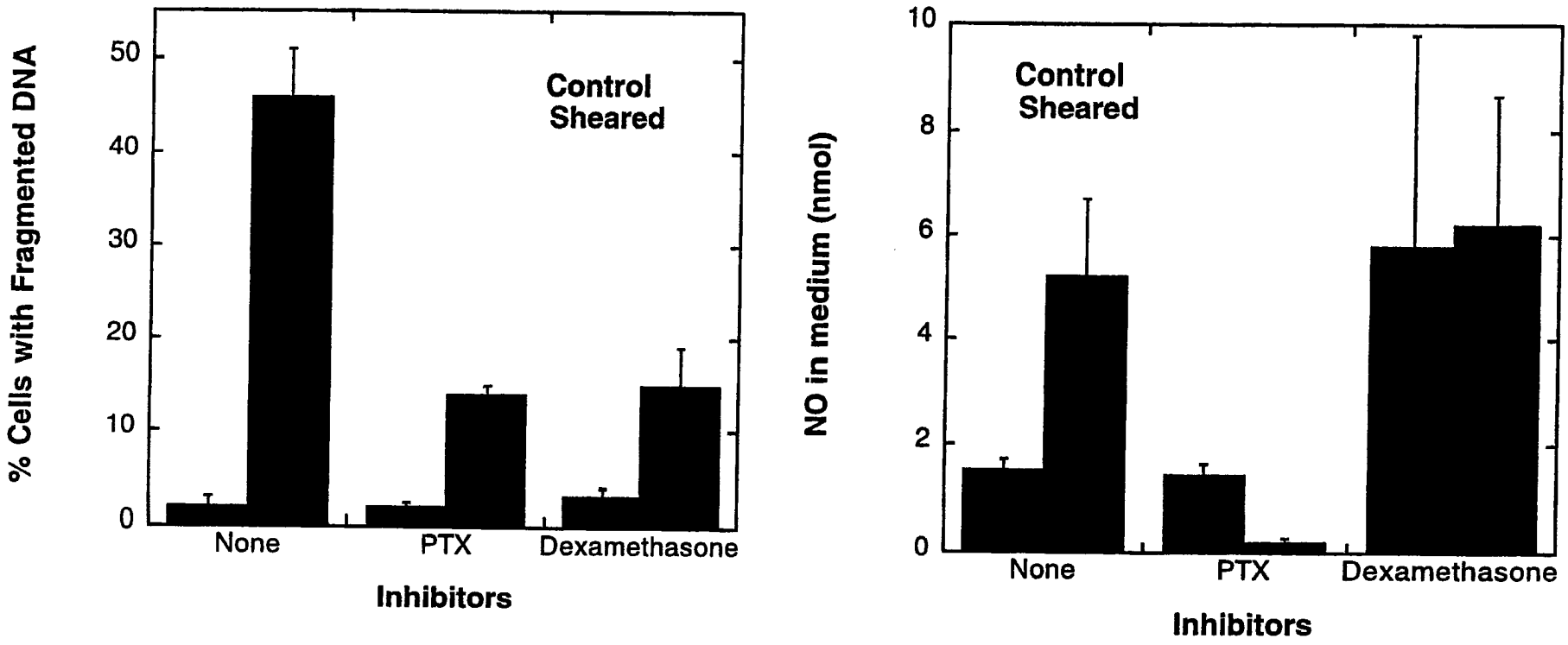

Pertussis toxin and dexamethasone, inhibitors of Gi/o and PLC (among others), respectively, attenuated shear stress induced injury.

Cells respond to repetitive injury via loss of tubulin cytoskeleton.

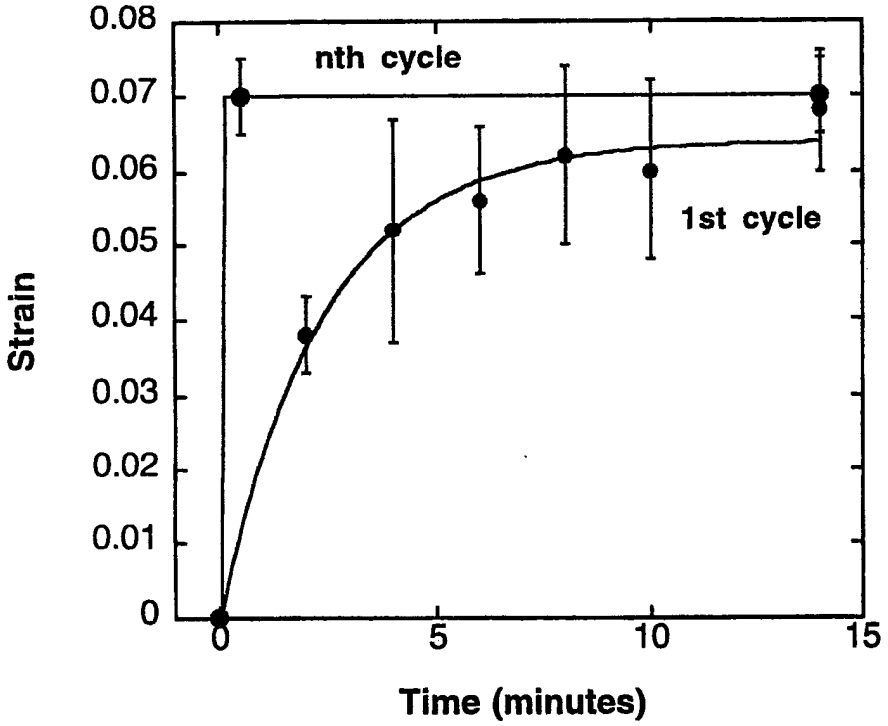

Sheared Control Control Sheared
Polymerized Tubulin Total Tubulin

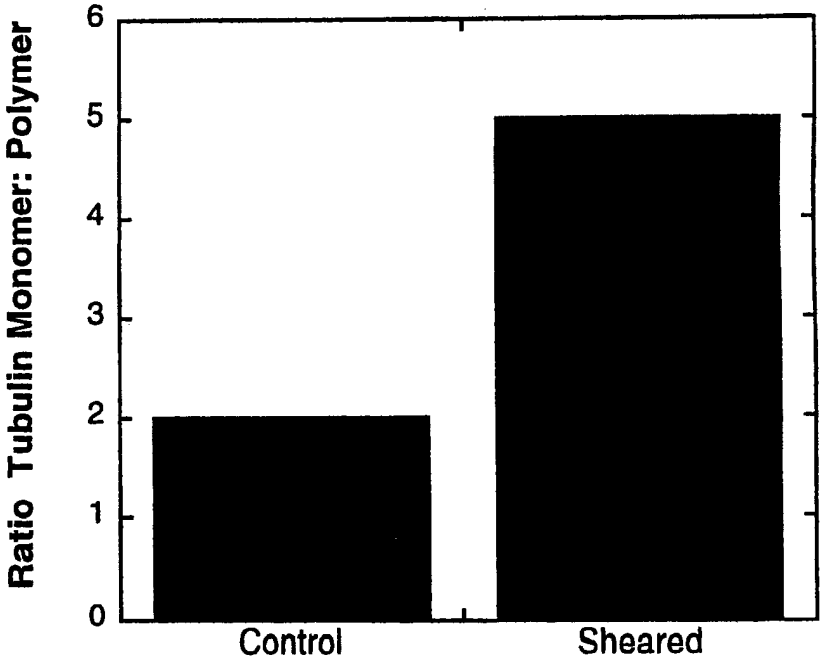

Antioxidants and NOS inhibitors attenuate cell injury.

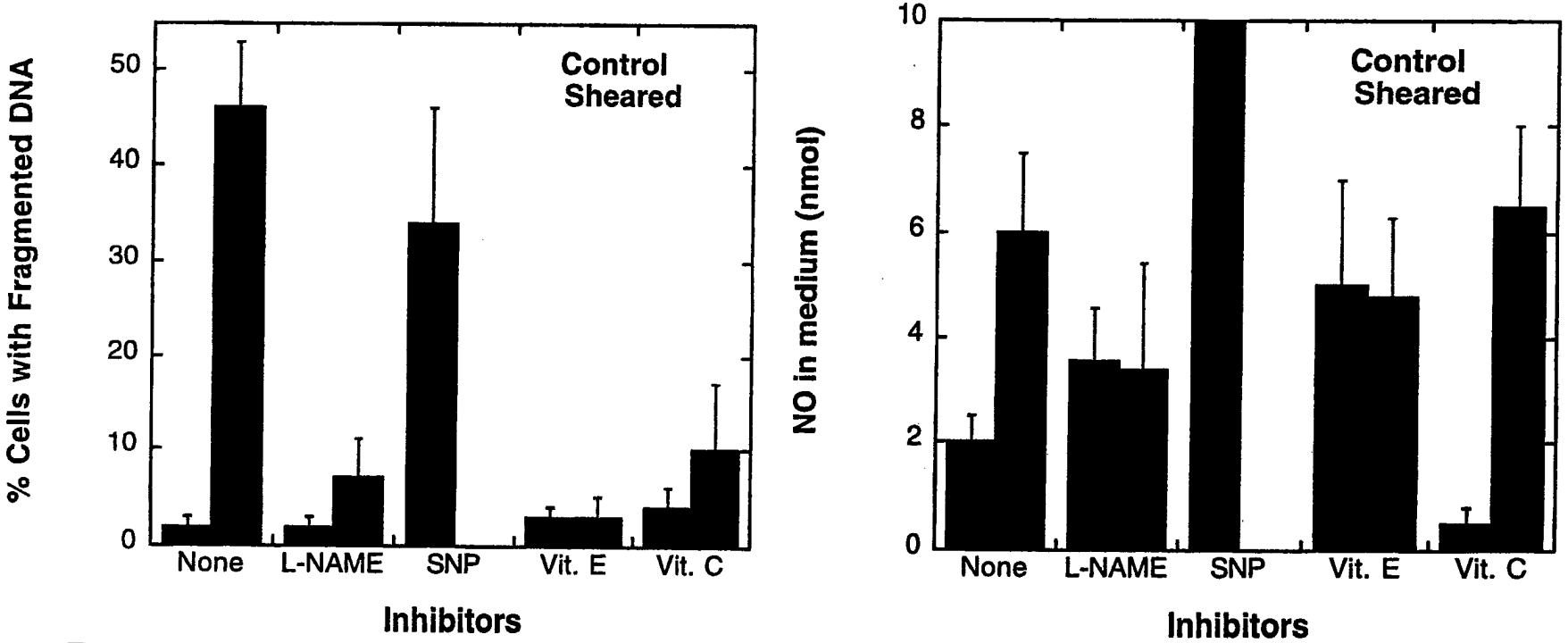

Peroxynitrites may be important in cell injury mechanism.

NMDA channel and intracellular stores antagonists protect cells from injury.

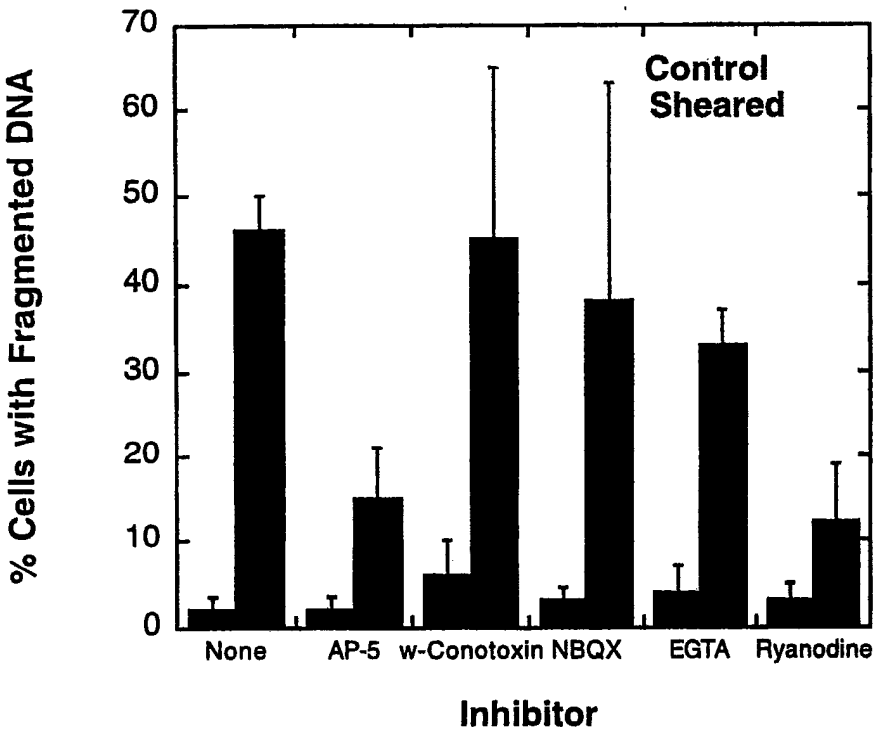

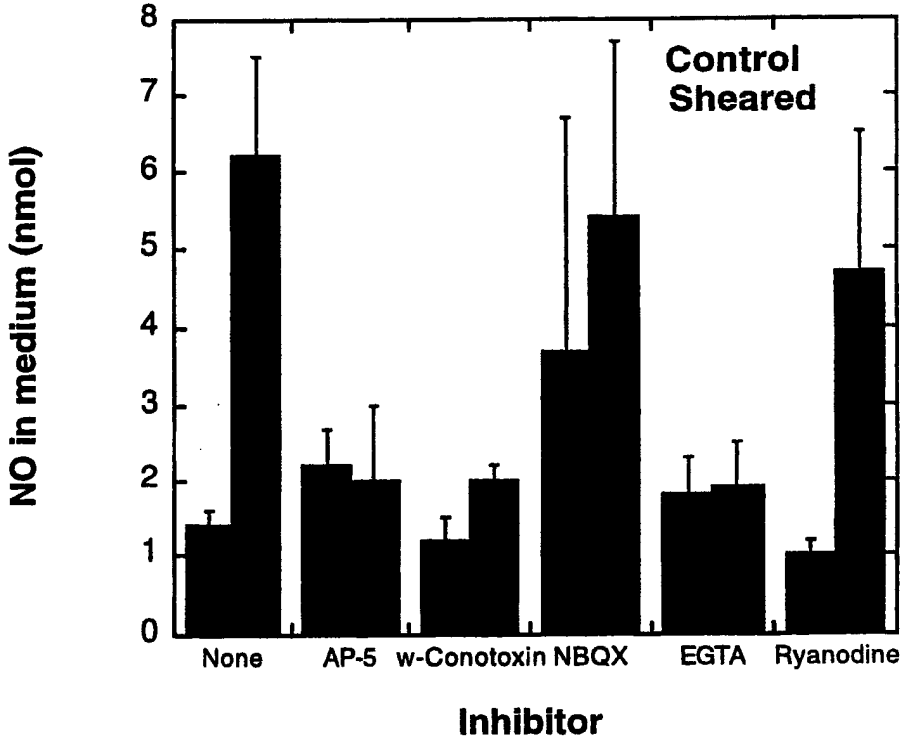

Relationship between intracellular calcium and NO production is not obvious.
Roles of NO and Ca^{2+} in mechanism are probably independent.

Autoradiogram of SDS PAGE electrophoresis gel shows distinct bands of protein in sheared cells.

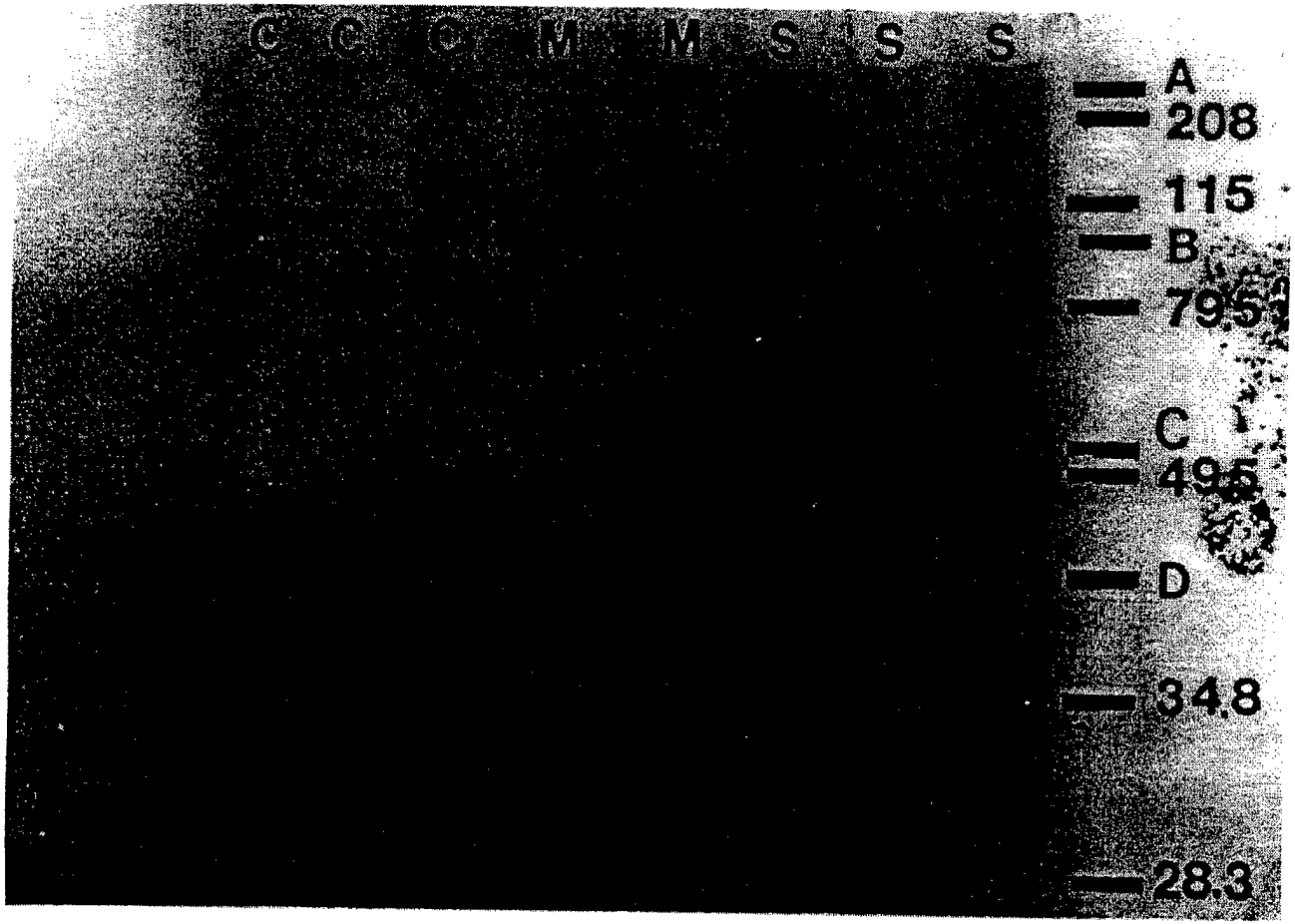

A >210 kDa

B 100 kDa

C 50 kDa

D 40 kDa

Mechanism of injury differs when cells are streched vs exposed to shear stress.

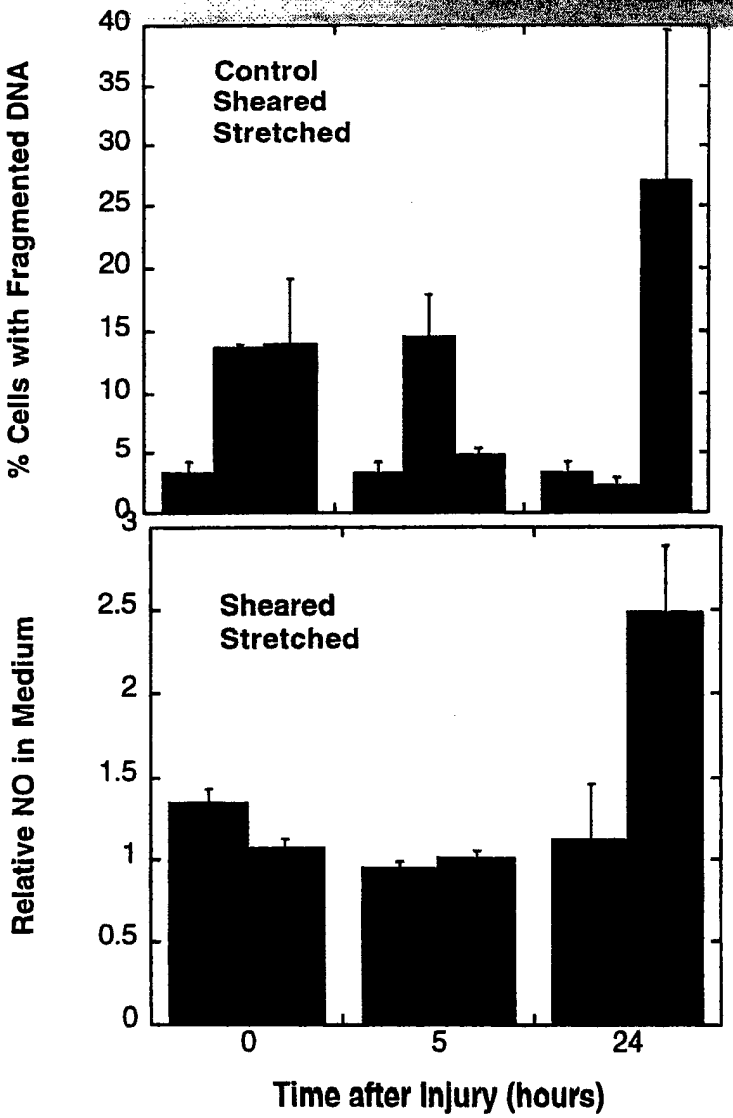

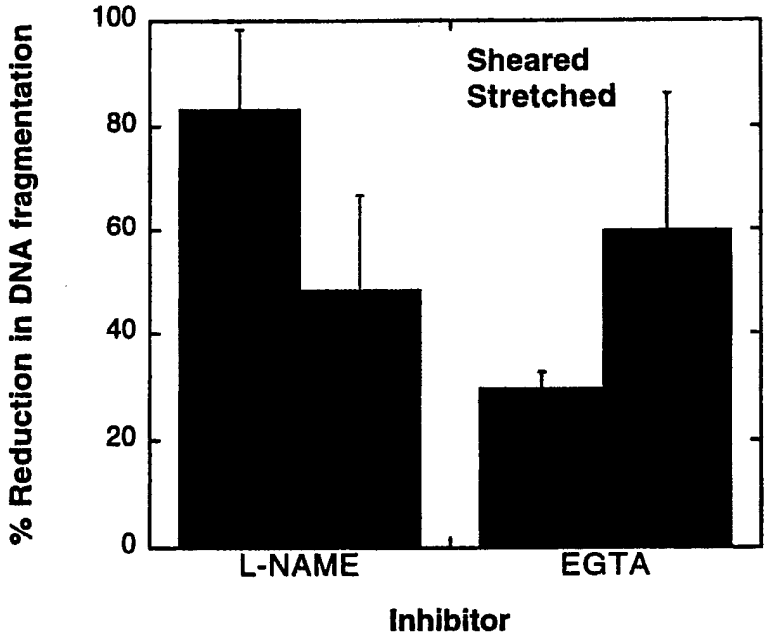

Summary

- Shear stress *in vivo* greatly exceeds shear stress *in vitro* needed for cell injury.
- Strain estimated *in vivo* is comparable to strain *in vitro* needed for cell injury.
- Stress/strain leads to DNA fragmentation, caspase activation, w/o membrane damage indicative of apoptosis.
- Cyclic stress is more damaging than steady stress. Loss of polymeric tubulin may be a factor.
- G protein activation, NO production, Ca^{2+}entry through NMDA channel, Ca^{2+}release from stores, and new protein synthesis are implicated in injury mechanism.
- All methods of deforming a cell are not equal.
- The model developed may be appropriate for both glaucoma and head injury (under different strain rate conditions) and may be a useful tool in drug discovery.

Low Strain Rate Leads to Cellular Injury Consistent with Apoptosis in Differentiated SH-SY5Y Cells

Dina H. Triyoso, MS, Michael E. Edwards, Ph.D., and Theresa A. Good, Ph.D.

Department of Chemical Engineering

Texas A&M University

College Station, TX 77843-3122 USA

Running Title: Low strain rate injury leads to apoptosis

Table of Contents Title: Low strain rate injury leads to apoptosis in differentiated SH-SY5Y cells

Corresponding Author:
Theresa Good
Department of Chemical Engineering
337 Zachry
Texas A&M University
College Station, TX 77843-3122
Phone (409) 845-3413
Fax (409) 845-6446
tgood@tamu.edu

Disclaimer: The view, opinions and /or findings contained in this report are those of the authors and should not be construed as a position, policy, decision, or endorsement of the federal Government or the National Medical Technology Testbed, Inc.

ABSTRACT: The potential damage to cortical tissue by deformation at a low strain rate is currently not well understood. An *in vitro* model of shear stress induced cell deformation was used in order to illuminate the mechanism of cell injury associated with low strain rate. We show that a low strain rate of less than 0.03 min^{-1} is achieved in our shear apparatus. Application of a low strain rate injury to differentiated SH-SY5Y cells, a human neuroblastoma line, led to phosphatidylserine accumulation on the external membrane surface, DNA fragmentation, and loss of cellular redox potential. Lactate dehydrogenase (LDH) release by injured cells did not differ significantly from LDH release from untreated cells, indicating that the low strain rate injured cells maintained the integrity of their plasma membranes. These results demonstrated that low strain rate deformation applied to SH-SY5Y cells leads to cell injury consistent with apoptosis. Understanding the relationship between strain rate and cell injury may lead to improved management of injuries, both traumatic and mild, to central nervous tissue.

Key Words: apoptosis, head injury, neuroblastoma, shear stress, strain

INTRODUCTION

Traumatic head injury (TBI) is associated with the generation of stress and strain within the cerebral cortex. During TBI, the primary injury is typically diffuse axonal injury. Diffuse axonal injury is associated with high shear and stress rates (Margulies et al., 1990; Ueno et al., 1995; and Chu et al., 1994). Shear stresses predicted during head injury are on the order of 4 x 10^5 dynes cm^{-2}. Tissue strain is predicted to reach a maximum of 0.1 to 0.2 within approximately 10 ms of impact (Margulies et al., 1990). Strain is predicted to be periodic and dampen with time. A 10% strain is predicted to be the critical strain above which injury occurs during diffuse axonal injury (Margulies and Thibault, 1992). The primary injury during TBI is not likely to be preventable.

A number of *in vitro* models have been developed to investigate the effects of high strain rate injury on neurons and neuron-like cells (Cargill and Thibault, 1996; LaPlaca et al., 1997; Ellis et al., 1995; Rzigalinski et al., 1997; and Maxwell et al., 1994). In these models, the duration of shear or strain applied was on the order of 50 ms to 200 ms, with an associated strain rate of greater than 1 s^{-1} (LaPlaca et al., 1997, LaPlaca and Thibault, 1997). Acute injury results in lactate dehydrogenase (LDH) release (LaPlaca et al., 1997), uptake of propidium iodine (PI) (Ellis et al., 1995 and Rzigalinski et al., 1997), and an increase in intracellular Ca^{2+} (Cargill and Thibault, 1996; LaPlaca et al., 1997; Ellis et al., 1995; and Rzigalinski et al., 1997). Only when the onset of

injury was very rapid, did significant and sustained injury occur as determined by LDH release after 24 hours.

The effects of low strain rate injury on neurons and neuron-like cells have not been as well studied as the effects of high strain rate injury. Low strain rate injury may be important during secondary brain damage following traumatic injury or during milder injuries. We report the development of an *in vitro* model of cell injury in which differentiated SH-SY5Y cells are subjected to strain at a low strain rate to induce cellular damage. We show that low strain rate applied to differentiated SH-SY5Y cells is not harmless, but leads to cellular injury consistent with apoptosis. Exposure to strain at a low strain rate for 10 minutes leads to changes in the cell membrane properties and patterns of DNA fragmentation indicative of apoptosis. These results could contribute to the understanding of the mechanism of neurodegeneration during mild or low strain rate injuries to the central nervous system (CNS).

MATERIALS AND METHODS

Materials

Tissue culture reagents were obtained from GibcoBRL (Grand Island, NY). Merocyanine 540 was from Molecular Probes (Eugene, OR). Methanol free formaldehyde was obtained from Poly Sciences Inc.(Warrington, PA). Dulbecco phosphate buffered saline (PBS) was obtained from Pierce Chemical Co. (Rockford, IL). Apoptosis Detection System, Fluorescein was obtained from Promega (Madison, WI). Annexin V Apoptosis Detection Kit was obtained from R&D Systems (Minneapolis, MN). The lactate dehydrogenase (LDH) diagnostic kit and all other chemicals were purchased from Sigma (St. Louis, MO).

Cell Culture

The human neuroblastoma cell line, SH-SY5Y, a kind gift from Dr. Evelyn Tiffany-Castiglioni (College of Veterinary Medicine, Texas A&M University, College Station, TX), was used for all experiments. The cells were cultured in a humidified 5% (v/v) CO_2/air environment at 37°C and grown in Eagles' minimum essential medium with 10% fetal bovine serum, 100U ml^{-1} penicillin, 100 $\mu g\ ml^{-1}$ streptomycin, and 3 mM L-glutamine using standard techniques. For experiments in which cells were exposed to shear stress and viability was measured, cells were plated at a density of 4 million cells per 60 mm tissue culture dish. Cells were differentiated in the dish for 6 - 9 days by adding 8 ng ml^{-1} of human β-nerve growth factor (β-NGF) directly to the culture dish. For experiments where strain and strain rate were measured, 10,000 cells were

plated per 35 mm tissue and differentiated with 8 ng ml^{-1} human β-NGF for 6-15 days prior to conducting experiments.

Shear Stress Application

The shear stress apparatus was a modification of a cone and plate viscometer previously described in detail (Triyoso and Good, 1999). It consisted of a GlasCol stirrer and motor controller (Terre Haute, IN), and a stainless steel or plexiglass cone (Texas A&M Chemical Engineering machine shop, College Station, TX). The cone had a 5° angle relative to a stationary tissue culture dish containing a layer of SH-SY5Y cells and outside dimensions such that it had 1 mm clearance from the dish edge. The monolayer of cells adherent to the culture dish was exposed to fluid flow by rotating the cone, whose tip contacted the plate, over the surface of the plate. Culture medium fills the space between the cone and the layer of cells. Only those cells within a 1.5 mm radius of the center of the culture dish (less than 1% of the cells) were displaced by the placement of the cone.

The motor controller was used to precisely control the cone angular velocity, Ω. The flow generated by the rotation of the cone is characterized by the Reynolds number, N_{RE}

$$N_{RE} = \frac{\rho \Omega R^2}{\mu} \qquad (1)$$

where ρ and μ are the density and viscosity of culture medium, respectively (approximated by ρ and μ for water at system temperature), and R is the characteristic length, which in this case is

the radius of the plate. For conditions used during this study, Reynolds numbers ranged from 22 to 202, which would indicate that flow could be assumed to be laminar. Using the laminar flow assumption, the shear stress generated on the cell surface, $\tau_{\phi\theta}$, can be approximated by:

$$\tau_{\phi\theta} = \frac{2\mu\Omega}{\left[\frac{\cos\theta_1}{\sin^2\theta_1} + \ln(\csc\theta_1 - \cot\theta_1)\right]\frac{1}{\sin^2\theta}} \qquad (2)$$

For all experiments, a culture dish containing cells was positioned beneath the cone, the motor and controller were turned on, and shear stress of a prescribed magnitude was applied for a fixed length of time. For viability experiments, the entire apparatus was placed in a 37 C incubator. Culture medium was replaced with fresh warm medium immediately prior to shear stress application. The control plate was treated exactly the same as the sheared plate except for the application of shear. For strain measurements, the entire apparatus was mounted on the stage of a Zeiss Axiovert 135 florescent microscope at ambient temperature.

Strain and Strain Rate Measurement

Strain measurements were made by staining cells with merocyanine 540 (MC540), a fluorescent dye, and using video microscopy and image processing to capture and analyze cell deformation upon exposure to shear stress using our apparatus.

Stock solutions (1 mg/ml) of MC 540 were prepared by dissolving in absolute ethanol and diluting 1:1 with water. MC 540 stock was stored in the dark at 4°C until needed. To stain cells, human NGF-β differentiated SH-SY5Y cells attached to the dish surface were washed 3 times

with 2 ml of a 5 mM Tris-HCL buffered isotonic saline solution to remove culture medium. The cells were exposed to 18 μM MC 540 diluted in the wash buffer for 10 min at ambient temperature prior to being washed 3 times with 2 ml of Ringer's buffer. SH-SY5Y cells were sheared in the presence of Ringer's buffer.

Fluorescently stained cells were observed with a Zeiss Axiovert 135 fluorescent microscope (Thornwood, NJ) equipped with an HBO 50W short arc mercury lamp. Excitation and emission wavelengths were 540 nm and 605 nm, repectively. Images were captured with the Zeiss continuous image capture 128 system. Zeiss Scientific Image Analysis Software was used to analyze the captured images.

Cell Deformation Analysis

Cell deformation (strain) was estimated from the shear induced shape changes in the cell. A whole cell stretch ratio, λ_i was defined as the ratio of the shear induced characteristic length, L_i, to the unstressed length, $(L_i)_0$, both measured in the ith direction (Eq. 3) (16).

$$\lambda_i = \frac{L_i}{(L_i)_0} \qquad (3)$$

Cell lengths for SY5Y cells were determined by measuring the lengths of a rectangle enclosing the cells (Figure 1). The cell boundaries were determined using the auto tracing feature of the Zeiss Image 3.0 imaging software package. The principle axis was chosen to be the axis of maximum elongation. The maximum strain in the ith direction, E_i, was calculated from the relation

$$E_i = \frac{1}{2}\left(\lambda_i^{\,2} - 1\right) \tag{4}$$

A nonlinear least squares regression was used to estimate cell deformation time constants for the strain data as a function of time using an equation of the form seen in Equation 5.

$$E = E_{\max}\left(1 - e^{-\frac{t}{\tau}}\right) \tag{5}$$

where E is the cell strain, E_{max} is the maximum strain observed, t is time, and τ is the deformation time constant. We assumed that the deformation time constant was not a function of stress level.

Strain rate was determined by taking the time derivative of Equation 5. The average strain rate was determined by taking the integral of the strain rate over the duration of the strain injury divided by the duration of the injury.

Loss of Viability

DNA fragmentation was measured using a TdT-mediated dUTP nick end translation (TUNEL) assay kit from Promega (Fitchburg, WI). Cells were permeablilzed, the 3' OH termini were labeled with fluorescein-12-dUTP, and whole DNA 3'ends were labeled with propidium iodide (PI) according to the procedure outlined for cell suspension with flow cytometry given by the manufacturer with minor modifications. For each measurement, 2-3 million cells (one plate) were used. To prepare cells for the TUNEL assay, the culture medium was removed from the culture dish and trypsin/EDTA was added to gently detach the cell monolayer from the dish.

The cell suspension was then centrifuged and washed with phosphate buffer saline (PBS). Afterwards, cells were fixed with methanol free formaldehyde for 20 minutes. Another wash with PBS was performed after fixing the cells. Finally, the cells were permeabilized by adding ethanol. The cells were then stored in –20°C freezer for at least four hours before carrying out the rest of the procedure outlined by the manufacturer.

Results were analyzed on a FACS Caliber flow cytometer (Becton Dickinson) using a 15 mW argon laser at 488 nm excitation wavelength. Emission filters of 530 nm bandpass for green fluorescence (fluorescein labeled dUTP in this case) and 585 nm for red (PI) were used. Electronic compensation was used to prevent bleed through fluorescence. Forward and side light scatter, green fluorescence, FL1, and red fluorescence, FL2, were collected and analyzed on 30,000 cells/sample with Cellquest software (Becton Dickinson). The two parameter histogram of FL2 area versus FL2 width was used to gate on single cells. A positive apoptotic region on the FL1 versus FL2 histogram was set so that <2% of the non sheared cells (control) were positive for apoptosis. The fraction of cells with fragmented DNA was determined by counting cells with green (fluorescein) fluorescence whose intensity was above a threshold determined from control cells.

The accumulation of phosphatidyl serine (PS) on the external surface of the cell is one of the changes that occur in the cell membrane early in apoptosis (Van Engeland et al., 1997). The amount of PS expression was probed using fluorescently labeled annexin and flow cytometry.

Annexin is known to bind preferentially to PS in membranes. The amount of annexin binding to cells, an indication of the relative PS present in the membrane, was determined using the Annexin V Apoptosis Detection kit (R&D Systems, Minneapolis, MN) according to manufacturer's direction. Cells were counter-stained with PI to indicate the relative permeability of the membrane. Cells were detached gently from dish and pelleted by centrifugation at 500g for 10 minutes. Cells were then washed in PBS and pelleted by centrifugation. Afterwards, 100μL of Annexin V Incubation Reagent (containing 0.25μg/mL annexin and 5μg/mL PI) was added for every 500,000 cells. The cell suspension was incubated in the dark at 24°C. Samples were analyzed using flow cytometry within 1 hour of preparation for maximal signal. The x axis of the plot is the log of Annexin-V-FITC fluorescence while the y axis is the log of propidium iodide fluorescence. Results were analyzed on the FACS Caliber flow cytometer as described for the TUNEL assay. Threshold levels for annexin positive and PI positive staining were determined from staining of the control cells and are indicated by the vertical and horizontal lines, respectively, on the plot of flow cytometry results. Cells were considered annexin or PI positive if the fluorescence intensity for the marker exceed the preset threshold.

The ability of cells to reduce 3-(4,5-dimethylthiazol-2-yl)-2,5-dipenyltetrazolium bromide (MTT) to blue formazan crystals was taken as an indicator of cellular redox potential and viability (Pollack et al., 1995). MTT was added to the culture medium at a concentration of 5 mg ml^{-1} and a volume of 10% of the total volume of medium in the culture dish. Cells were then

incubated for 4 hours in the humidified 37°C incubator with 5% CO_2, during which time metabolically active cells reduced MTT. A 50% dimethylformamide (DMF), 30% water and 20% sodium laurel (SDS) solution at pH 4.7 of equal volume to the volume of medium in the culture dish was added to stop the reaction and dissolve the formazan crystals. Cells were incubated with the DMF/SDS solution overnight, after which time the absorbance was read at 580 nm using an Emax Precision Microplate Reader (Molecular Devices, Sunnyvale, CA). Percent MTT reduction, a measure of viability, was taken as the ratio of the absorbance measured from treated cells relative to the absorbance measured from untreated control cells.

The LDH release from cells was measured using a prepackaged assay (Sigma, St. Louis, MO) according to the manufacturer's directions. The assay was performed using the procedure given by the manufacturer with slight modifications. 1 ml of sodium pyruvate solution was added into each NADH vial. The vials were incubated for several minutes in the 37°C water bath. 100μL of pyruvate/NADH solution was then pipetted into each of 10 eppendorf microcentrifuge tubes. Ten μL of culture medium was added to each tube. After precisely 30 minutes incubation at room temperature, 100 μL of Sigma color reagent was added to the mixture to stop reaction. Twenty minutes later, 1 ml of 0.4 M NAOH is added. The solution was then transferred to a 96 well plate and absorbance was read at 405 nm using Emax microplate reader (Molecular Devices). The percentage LDH release was determined from the ratio of the enzymatic activity (LDH release) in the supernatant of cells exposed to shear stress injury relative to the enzymatic

activity in the supernatant of untreated control cells. A percentage LDH release below 100 % indicates that the LDH activity measured in the supernatant of injured cells was less than the LDH activity measured in the supernatant of control cells. The maximum LDH release (that obtained if cells are lysed with detergent or osmotic swelling) was approximately 300% of the untreated control cells.

Data analysis

Data presented are expressed as the mean ± the standard error of the mean of n independent determinations. Every independent determination was a unique culture dish exposed to shear for the specified amount of time. The value of n for each data set is reported in the figure captions. To determine whether a given data set was significantly different than a control data set, the student's t test with unequal variance was used. A criteria for significance of $p<0.05$ was employed unless otherwise noted.

RESULTS

We examined the relationship between fluid shear stress and strain in differentiated SH-SY5Y cells exposed to increasing levels of shear ranging from 5 to 45 dynes/cm^2 for 10 min using our modified cone and plate viscometer apparatus. As seen in Figure 2, the principle strain observed in cells upon their first exposure to fluid shear stress reached a maximum strain level within ten minutes of stress application at both 5 and 15 dynes/cm^2 stress levels. The maximum observed cell strain increased with increased stress level. We calculated a time constant for cell deformation of 3±1 min from the data shown in Figure 2. The maximum and average strain rate for the experimental conditions used in this study were calculated. The maximum strain rates used ranged from 0.013±0.005 min^{-1} to 0.03±0.01 min^{-1}, for shear stresses ranging from 5 dynes/cm^2 to 15 dynes/cm^2 , respectively. Average strain rates were 0.004±0.0007 min^{-1} to 0.008±0.001 min^{-1} during 10 minute shear stress application and approximately order of magnitude lower when shear stress was applied for periods of two to three hours.

Cells were exposed to shear stress (low strain rate injury) and at various times after shear stress application a number of markers of cellular injury were examined in order to determine the nature of the cellular injury. The percentage of cells with DNA fragmentation in negative controls (no stress), positive controls (cells treated with sodium nitroprusside (SNP)), and low strain rate injury (shear stress for 10 minutes) was determined using the TUNEL assay. Representative histograms are shown in Figure 3. DNA fragmentation was measured

immediately after cell injury was terminated. Low strain rate injury resulted in TUNEL positive staining (high fluorescein-12-dUTP and low PI staining) in 13% of cells. Approximately 35% of cells were TUNEL positive after treatment with SNP. Both SNP and low strain rate lead to a significant increase in the percentage of cells with fragmented DNA relative to uninjured controls ($p<0.05$).

The presence of phosphatidyl serine in the outer membrane of the cell as an early marker for cell injury (apoptosis) was probed using fluorescently labeled annexin. As seen in Figure 4, after 10 minutes of shear stress application, approximately nineteen percent of cells stained positive for phosphatidyl serine as compared to only half percent in unsheared controls, while no significant increase in PI staining was observed ($p>0.2$). After longer injuries, the same trend was observed. When sodium nitroprusside was added to cells (positive control), both an increase in phosphatidyl serine staining and an increase in PI staining was observed relative to untreated controls.

As seen in Figure 5, cells subjected to low strain rate injury (constant shear stress application) for times ranging from 10 minutes to 3 hours show no significant increase in the percentage of cells with fragmented DNA ($p<0.05$). Cell strain did not increase during this time period.

Indicators of cell injury, LDH release, loss of MTT reduction, and DNA fragmentation, were measured as a function of time folloiwing low strain rate injury (Figure 6). LDH release, a

measure of membrane permeability, did not increase relative to controls at any time within 24 hours after the injury (Figure 6A). Even at 48 hours after injury, no significant LDH release was observed (data not shown). MTT reduction by cells, a measure of the redox potential of the cell, decreased significantly between zero and three hours after injury to a level of 71±5 percent of MTT reduction measured in unsheared control cells ($p<0.01$, Figure 6B). MTT reduction did not decrease further or return to near control levels at times measured after 3 hours after injury. Even as long as 48 hours after injury, MTT reduction was still reduced relative to untreated controls (63±12 percent). The percentage of cells with fragmented DNA increased to a maximum level of 18±5 percent approximately 3 hours after injury (Figure 6B). The measured percentage of cells with fragmented DNA then decreased during the next 21 hours. At all times 3 hours and longer after injury, the measured percentage of cells with fragmented DNA was significantly greater than that measured in unsheared control cells (1.5±0.5%, $p<0.05$). When SNP was added to cells, our positive control for apoptotic death, the percentage of TUNEL positive cells varied with time from thirty five percent five hours after injury, to fifteen percent 24 hours after injury.

These results are significantly different than those obtained from cells exposed to high shear stress (and presumably a higher strain rate injury). When cells were subjected to shear stress at 100 dynes/cm^2 for 10 minutes, LDH measured in the culture medium of cells was 220±20% greater than the concentration of LDH measured in medium taken from control cells immediately after the injury. This represents release of approximately one half of the total LDH

contained in cells. During similar experiments (100 dynes/cm^2 for 10 minutes, MTT and TUNEL assay performed immediately after injury), 75±6% of cells were TUNEL positive and MTT reduction by injured cells was 44±6% of that reduced by control cells and immediately after injury. The difference in results for LDH, MTT and TUNEL assays between high shear stress/strain rate and low strain rate injury were significant with $p<0.05$ or less (n=3 to 6).

DISCUSSION

A number of *in vitro* models have been developed to examine the effects of high shear stress and strain rate on neurons (Cargill and Thibault, 1996; LaPlaca et al., 1997; Ellis et al., 1995; Rzigalinski et al., 1997; and Maxwell et al., 1994). In these models LDH release and PI staining have been observed, indicative of transient membrane permeability, or if LDH release and PI staining persist, necrotic cell death resulting from injury. To our knowledge, however, there has not been a study of the effects of low strain rate injury to neurons or neuron-like cells. Low strain rate injury may also contribute to the cellular damage observed during traumatic brain injury or during milder injuries to the CNS. Thus, we examined the feasibility of using an *in vitro* model similar to those developed previously to examine the effects of low strain rate injury on neuron-like cells.

Apoptosis has been observed during development and in the mature brain during neurodegenerative disease and injury (Rink et al, 1995, Chang et al, 1996, Edwards et al, 1997 for example). In experimental head injury and in postmortem studies following TBI, regions of apoptosis in the brain have been observed (Pohl et al, 1999, Xu et al, 1998, Conti et al, 1998, Shah et al, 1997, Kotapka et al., 1993). Previous *in vitro* models of high strain rate injury have not demonstrated that cell death occurred via apoptosis, suggesting that perhaps the apoptosis observed *in vivo* originates from something other than a high strain rate injury. We were

therefore interested in determining if a low strain rate injury could lead to cell death via apoptosis.

Differentiated SH-SY5Y cells were chosen as a model cell because they express G proteins, have neuron-like ion channels such as L-type Ca^{2+} channels, express a number of glutamate receptors such as the NMDA receptor, and, when differentiated, have long processes similar to those observed in neurons (Prince and Oreland, 1997; Hong, 1997; Nikonorov et al., 1998; and Yoshioka et al., 1996)

We used shear stress to apply strain to cells. It has been shown by others using a similar device that fluid shear stress leads to cell strain (LaPlaca et al., 1997). In the device designed by LaPlaca and coworkers a rotating disk is used instead of a cone, leading to variation in the stress field across the culture dish. However, the distance between the disk and the cells was very small, which resulted in much higher strain rates produced, ranging from less than 1 s^{-1} to approximately 9 s^{-1}. We show in Figure 2 that in our device, cells reach their final deformation within 10 minutes, resulting in a maximum strain rate of 0.03 min^{-1}, which is considerably lower that rates of strain applied by others.

Using our low strain rate model of cell injury, between 5 and 25 percent of cells subjected to low strain rate injury for times ranging from 10 minutes up to 3 hours had DNA that stained positively with fluorescein-12-dUTP, while less than 2% of unsheared control cells stained with fluorescein-12-dUTP (Figures 3 and 5). An increase in cell staining for annexin without the same

level of increase in staining with PI with injury (Figure 4) was also observed. The high degree of end labeling of DNA from sheared cells, and indicator of DNA fragmentation, along with the increase annexin staining , an indicator of increased phosphtidylserine present on the outer membrane surface are both indicators of cell or membrane injury (Van Engeland, 1997). TUNEL staining and annexin staining without membrane permeability (as indicated by the absence of PI staining) are indicators of apoptosis, while PI staining and annexin staining together would indicate necrosis or late apoptosis. The lack of LDH release at anytime after shear induced injury (Figure 6A) would suggest that no increase in membrane permeability occurred, again, consistent with apoptotic cell death. If injury had resulted in transient membrane permeability, which would have enabled annexin to bind to phosphatidyl serine regardless of its location in the membrane, both PI staining and LDH release (at least transient release) would have been observed. The loss of ability to reduce MTT, seen 3 hours after injury, has been associated with loss of mitochondrial function and is consistent with an apoptotic cell death mechanism (Pollack et al., 1995). A similar pattern of injury, TUNEL postive staining and annexin positive staining without LDH release was observed when cells were treated with SNP. SNP as well as other NO donors have been shown to lead to apoptosis in cultured cells (Maruyama et al., 1998).

Approximately the same percentage of sheared cells show evidence of high annexin staining (and high phosphatidylserine content in their outer membrane) as eventually have significant DNA fragmentation and lose their ability to reduce MTT (19% compared to 18±5%

and 29±5%, respectively). Slightly more cells (but not significantly more, $p=0.2$) lose their ability to reduce MTT than are detected by the other two methods, possibly because the cells processed for flow cytometry are harvested, stained, washed, and then sampled and counted, while during the MTT assay, cells are unharvested and undisturbed. We interpret these results to indicate that the three assays used (annexin, TUNEL, and MTT), all detect the same population of injured cells.

At three hours after shear injury, significant loss in ability to reduce MTT by cells and the maximum percentage of cells with fragmented DNA were observed (Figure 6B). The ability of cells to reduce MTT did not change significantly after 3 hours, indicating that the damage sustained by cells was permanent. The percentage of sheared cells with fragmented DNA decreased significantly from about 18% at 3 hours to about 5% at 24 hours ($p<0.05$). The decrease in measurement of cells with fragmented DNA could indicate that DNA was repaired in most cells after the original injury, or that, due to the method of harvesting and counting cells, cells in later stages of apoptosis could not effectively be counted. The former interpretation of results is consistent our interpretation of the MTT data. The time lag between shear injury and loss of cellular redox potential and DNA fragmentation could be due to the time necessary to upregulate proteins necessary in the apoptotic death pathway. When SNP was used to induce apoptosis, the number of TUNEL positive cells detected decreased from 35% detected 5 hours after SNP addition to 15% 24 hours after SNP addition, which supports our interpretation that

DNA is not being repaired after injury, but that cells are not being counted effectively because of the processing method. The time required for apoptosis to begin has been reported to be between 5 minutes and 4 days, depending on the model (Russel et al., 1972, Matter et al., 1979, and Oberhammer et al., 1991). Thus, the 3 hour delay we observed is not out of the ordinary.

As seen in Figure 5, application of low shear stress (10 dynes/cm^2) for longer than 10 minutes, the time required to reach a maximum cell deformation, does not further deform the cell or further increase the extent of injury. That duration of time cells were deformed is unimportant in determining the extent of injury would suggest another variable, most likely strain rate, is the key variable in determining the extent, and possibly the characteristics of cell injury. In our model, high shear stress (and presumably high strain rate) led to injury characterized by a high degree of TUNEL staining, loss of ability to reduce MTT, and an increase in membrane permeability as indicated by LDH release, which is significantly different than the nature of injury observed at low strain rate. While our results do not conclusively demonstrate the role of strain rate in determining extent or nature of injury, other researchers have also found strain rate to be important in determining the characteristics of cellular injury (LaPlaca and Thibault, 1997, LaPlaca et al., 1997, Cargill and Thibault, 1996). Both LaPlaca and coworkers (1997) and Cargill and Thibault (1996) found significant differences in changes in intracellular calcium concentration (LaPlaca et al., 1997 and Cargill and Thibault, 1996) and in LDH release (LaPlaca et al., 1997) during low and high strain rate injury. In addition, Cargill and Thibault (1996) found that even

during low strain rate injury, intracellular calcium concentration increased significantly, but in a strain independent fashion. Therefore there is prior evidence to support the role of strain rate in determining the extent of injury, and evidence that neuron-like cells respond (via increase in intracellular calcium) to low strain rate injuries.

In conclusion, we show that differentiated SH-SY5Y cells, a human neuroblastoma cell line, respond to low strain rate via a mechanism of injury consistent with apoptosis. Our work, together with the work of others, will contribute the understanding of the role of strain rate in injury to neurons and neuron-like cells and may lead to development of new treatments for injuries to the CNS resulting from elevated shear stress and strain.

REFERENCES

CARGILL, R. S. 2ND and THIBAULT, L. (1996). Acute alterations in $[Ca^{2+}]_i$ in NG108-15 cells subjected to high strain rate deformation and chemical hypoxia: an in vitro model for neural trauma. Journal of Neurotrauma **13,** 395-407.

CHANG, C. J., LAI, W. W., EDWARD, D. P., AND TSO, M. O. (1995). Apoptotic photoreceptor cell death after traumatic retinal detachment in humans. Archives of Ophthalmology. **113,** 880-6.

CHU, C., LIN, M., HUANG, H., and LEE, M. (1994). Finite element analysis of cerebral contusion. Journal of Biomechanics. **27,** 187-194.

CONTI A. C., RAGHUPATHI R., TROJANOWSKI J. Q, and MCINTOSH T. K. (1998) Experimental brain injury induces regionally distinct apoptosis during the acute and delayed post-traumatic period. Journal of Neuroscience. **18**:5663-72

EDWARDS, A. D., YUE, X., COX, P., HOPE, P. L., AZZOPARDI, D. V., SQUIER, M.V., and MEHMET H. (1997). Apoptosis in the brains of infants suffering intrauterine cerebral injury. Pediatric Research. **426,** 684-689.

EHRICH, M. and CORRELL, L. (1998). Inhibition of carboxylesterases in SH-SY5Y human and NB41A3 mouse neuroblastoma cells by organophosphorus esters Journal of Toxicology and Environmental Health. **53,** 385-399.

ELLIS, E., MCKINNEY, J., WILLOUGHBY, K., LIANG, S., and POVLISHOCK, J. (1995). A new model for rapid stretch-induced injury of cells in culture: characterization of the model using astrocytes. Journal of Neurotrauma. **12**, 325-339.

HONG, M. S. (1997). Bioremediation and Neurotoxicological Characterization of Organophosphorus Compounds. Ph.D. Dissertation, Texas A&M University.

KOTAPKA, M. J., GRAHAM, D. I., ADAMS, J. H., DOYLE, D. and GENNARELLI, T. A. (1993). Hippocampal damage in fatal pediatric head injury. Neuropathology and Applied Neurobiology. **19**, 128-133.

LAPLACA, M. and THIBAULT, L. E. (1997). An in vitro traumatic injury model to examine the response of neurons to a hydrodynamically-induced deformation. Annals of Biomedical Engineering. **25**, 665-677.

LAPLACA, M., LEE, V. Y. and THIBAULT, L. E. (1997). An in vitro model of traumatic neural injury: loading rate-dependent changes in acute cytosolic calcium and lactate dehydrogenase release. Journal of Neurotrauma. **14**, 355-368.

MACKRILL, J. J., CHALLISS, R. A., O'CONNEL, D. A., LAI, F., A., and NAHORSKI, S. R. (1997). Differential expression and regulation of ryanodine receptor and myo-inositol 1,4,5-triphosphate receptor Ca^{2+} release channels in mammalian tissues and cell lines. Biochemical Journal, **327**, 251-258.

MARGUILES, S., THIBAULT, L., and GENNARELLI, T. (1990) Physical Model Simulations of Brain Injury in the Primate. Journal of Biomechanics. **23**, 823-836.

MARGULIES, S. and THIBAULT, L. (1992). A proposed tolerance criterion for diffuse axonal injury in man. Journal of Biomechanics. **25**, 917-923.

MATTER, A. (1979). Microcinematographic and electron microscopic analysis of target cell lysis induced by cytotoxic T lymphocytes. Immunology. **36**, 179-190.

MAXWELL, W., ISLAM, M., GRAHAM, D., and GENNARELLI, T. (1994). A qualitative and quantitative analysis of the response of the retinal ganglion cell soma after stretch injury to the adult guinea-pig optic nerve. Journal of Neurocytology. **23**, 379-392.

MILLER, S. W., TRIMMER, P. A., PARKER, W. D., and DAVIS, R. E. (1996). Creation and characterization of mitochondrial DNA-depleted cell lines with "neuronal-like" properties. Journal of Neurochemistry. **67**, 1897-1907.

NIKONOROV, I. M., BLANCK, T. J., and RECIO-PINTO, E. (1998). The effect of halothane on single human neuronal L-type calcium channels. Anesthesia & Analgesia. **86**, 885-895.

OBERHAMMER, F., BURSCH, W., PARZEFALL, W., BREIT, P., ERBER, E., STADLER, M., and SCHULTE-HERMANN, R. (1991). Effect of transforming growth factor beta on cell death of cultured rat hepatocytes. Cancer Research. **51**, 2478-2485.

POHL, D., BITTIGAU, P, ISHIMARU M. J., STADTHAUS, D, HUBNER, C, OLNEY J. W., TURSKI, L, and IKONOMIDOU, C. (1999). N-Methyl-D-aspartate antagonists and apoptotic

cell death triggered by head trauma in developing rat brain. Proceedings of the National Academy of Sciences of the United States of America. **96**, 2508-13

POLLACK, S., SADLER, I., HAWTIN, S., TAILOR, V. and SHEARMAN, M. (1995). Sulfated glycosaminoglycans and dyes attenuate the neurotoxic effects of β-amyloid in rat PC12 cells. Neuroscience Letters. **184**, 113-116.

PRINCE, J. A. and ORELAND, L. (1997). Staurosporine differentiated human SH-SY5Y neuroblastoma cultures exhibit transient apoptosis and trophic factor independence. Brain Research Bulletin. **43**, 515-23.

RINK, A., FUNG, K. M., TROJANOWSKI, J. Q., LEE, V. M., NEUGEBAUER, E. and MCINTOSH, T. K. (1995). Evidence of apoptotic cell death after experimental traumatic brain injury in the rat. American Journal of Pathology. **147**, 1575-83.

RZIGALINSKI, B., LIANG, S., MCKINNEY, J., WILLOUGHBY, K., and ELLIS, E. (1997). Intracellular free calcium dynamics in stretch-injured astrocytes. Journal of Neurochemistry. **68**, 289-296.

SHAH, P. T., YOON, K. W., XU, X. M, and BRODER, L. D. (1997). Apoptosis mediates cell death following traumatic injury in rat hippocampal neurons. Neuroscience. **79**, 999-1004.

TRIYOSO, D. H., and GOOD, T. A. (1999). Pulsatile shear stress leads to DNA fragmentation in human SH-SY5Y neuroblastoma cell line. Journal of Physiology. **515**, 355-365..

UENO, K., MELVIN, J. W., LI, L. and LIGHTHALL, J. W. (1995). Development of tissue level brain injury criteria by finite element analysis. Journal of Neurotrauma. **12**, 695-706.

VAN ENGELAND, M., KUIJPERS, H., RAMAEKERS, F., REUTELINGSPERGER, C., and SCHUTTE, B. (1997). Plasma membrane alterations and cytoskeletal changes in apoptosis. Experimental Cell Research. **235**, 421-430.

XU, R. X., NAKAMURA, T., NAGAO, S, MIYAMOTO, O, JIN, L, TOYOSHIMA, T, and ITANO, T. (1998). Specific inhibition of apoptosis after cold-induced brain injury by moderate postinjury hypothermia. Neurosurgery. **43,** 107-114.

WHITE, B., and KRAUSE, G. (1993). Brain injury and repair mechanisms: the potential for pharmacologic therapy in closed head trauma. *Annals of Emergency Medicine.* 22, 970-979.

YOSHIOKA, A., IKEGAKI, N., WILLIAMS, M., and PLEASURE, D. (1996). Expression of N-methyl-D-aspartate (NMDA) and non-NMDA glutamate receptor genes in neuroblastoma, medulloblastoma, and other cells lines. *Journal of Neuroscience Research.* 46, 164-178.

ACKNOWLEDGEMENTS

This work was supported by a grant from the U.S. Department of the Army and National Medical Technology Testbed, Inc.

Figure Legends

Figure 1. Schematic diagram of neuroblastoma cell in unstrained and strained configuration. The stretch ratio in direction i, (for i = 1, 2) is define as ratio of the strained length, L_i to the original unstrained length $(L_i)_0$.

Figure 2. Time dependence of strain for differentiated SH-SY5Y clusters of 4 or more cells. Cells were exposed to constant shear for 10 min. Shear stress levels were 5 dynes/cm^2 (filled circles), 15 dynes/cm^2 (open circles), and 45 dynes/cm^2 (filled squares). Data represent mean ± standard error of the mean for n = 4 cells for each shear level.

Figure 3. Representative flow cytograms of TUNEL stained cells. The cells were unsheared (**a**), treated with 10mM sodium nitroprusside (SNP) and assayed for DNA fragmentation four hours after treatment (**b**), or sheared for ten minutes at 10 dynes/cm^2 and assayed for DNA fragmentation three hour after injury (**c**). The y-axis (FL1-Height) indicates the intensity of fluorescein-12-dUTP staining and represents the amount of fragmented DNA. The x-axis (FL2-Area) indicates the intensity of PI staining and represents the length of DNA in the cell. Very few unsheared cells are observed to be undergoing apoptosis (low FL-1 Height), however, upon application of shear, there is an increase in fraction of cells with short (low FL2-Area) fragmented (high FL1-Height) DNA. Treatment with SNP resulted in a large number of cells with

fragmented DNA (high FL1-Height) with a distribution of DNA lengths. 30,000 cells were counted per sample.

Figure 4. Representative flow cytograms of Annexin stained cells. The cells were unsheared (**a**), treated with 10mM sodium nitroprusside (SNP) and assayed for annexin binding four hours after treatment (**b**), or sheared for 10 minutes at 10 dynes/cm^2 and assayed for annexin binding immediately after injury (**c**). The y-axis (FL2-Height) indicates the intensity of PI staining and represents the relative permeability of the membrane. The x-axis (FL1-Height) indicates the intensity of fluorescein labeled annexin staining and represents the amount of phosphatidyl serine (PS) on the outer membrane surface. In unsheared cells, the majority of the signal appears in the lower and upper left quadrants, indicating two populations of cells, one with some membrane permeability and one without membrane permeability, but both with low PS. Upon application of shear, there is a significant increase in signal in the lower right quadrant indicating an increase in PS on the outer membrane without membrane permeability (characteristic of early apoptosis). There is staining in the upper right quadrant as well, indicating a population of cells with both PS staining and membrane permeability. In the SNP treated cells, there is an increase in staining in the upper and lower right quadrants indicating an increase in PS in both permeable and impermeable cells. 30,000 cells were counted per sample.

Figure 5. Cell strain and DNA fragmentation as a function of duration of shear stress application. Cells were subjected to shear stress of magnitude between 7.5 and 15 dynes/cm^2 for times from 10 minutes to 3 hours. Cell strain (filled circles) was measured continuously on the

same group of cells during shear stress period (n=3). DNA fragmentation (filled squares) was determined independently for each time point where data are presented (n=3 to 6). The maximum DNA fragmentation measured at any time after injury as determined by the TUNEL assay is reported. The error bars represent the standard error of the mean.

Figure 6. Effect of shear on cell viability as a function of time after injury. Cells were sheared for either two or three hours at 7.5 to 10 dynes/cm^2 and 37°C. No significant difference in results was observed at these shear levels or durations. After injury, cells were returned to a humidified CO_2 incubator until viability measurement at times indicated. **(a)** The percentage of LDH released from the sheared cells relative to the control cells is reported. (n=11 at time=0, n=3-5 for others). **(b)** Percent MTT reduction by sheared cells relative to unsheared controls (open squares), percent cells with fragmented DNA, sheared (closed circles), and unsheared (open circles). (n=5-9). The error bars represent the standard error of the mean. * indicates result is significantly different than unsheared control ($p<0.05$).

Initial unstrained state at
t = 0

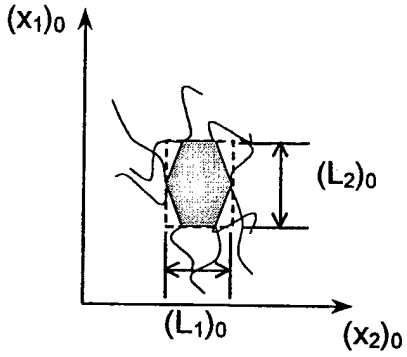

Final strained state at
t > 0

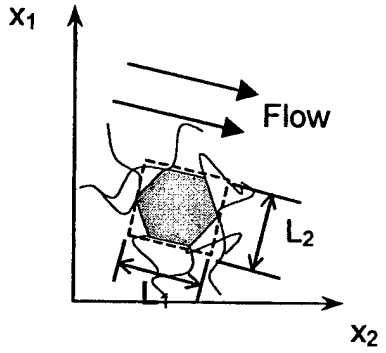

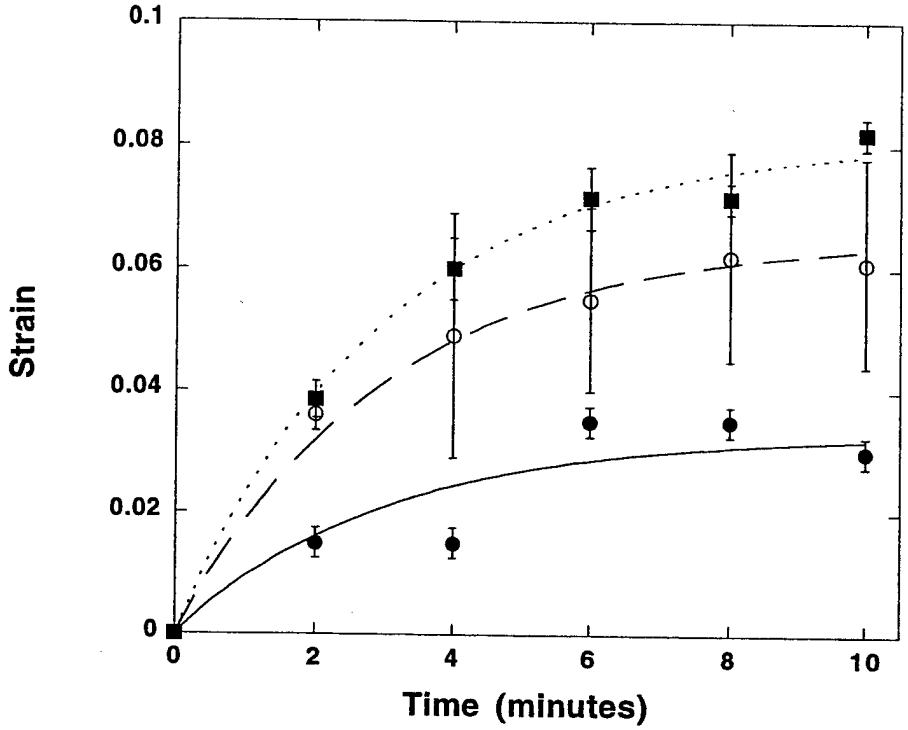
0.1
0.08
0.06
0.04
0.02
0
Strain
0
2
4
6
8
10
Time (minutes)

a

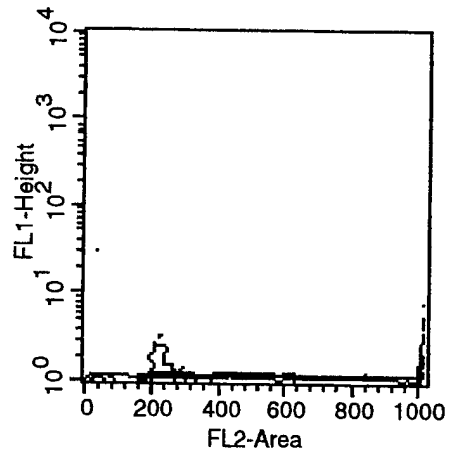
FL1-Height
10^0
10^1
10^2
10^3
10^4
0
200
400
600
800
1000
FL2-Area

b

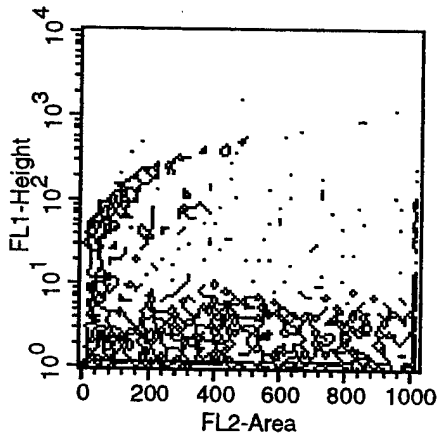
FL1-Height
10^0
10^1
10^2
10^3
10^4
0
200
400
600
800
1000
FL2-Area

c

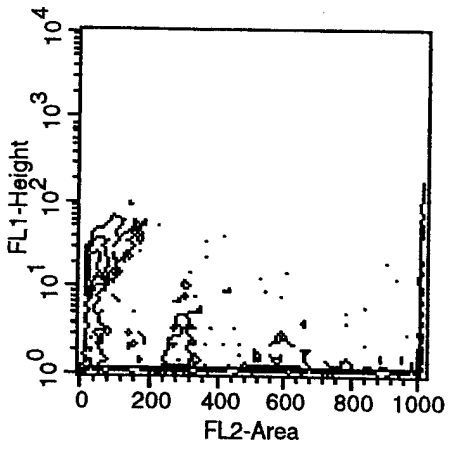
FL1-Height
10^0
10^1
10^2
10^3
10^4
0
200
400
600
800
1000
FL2-Area

a

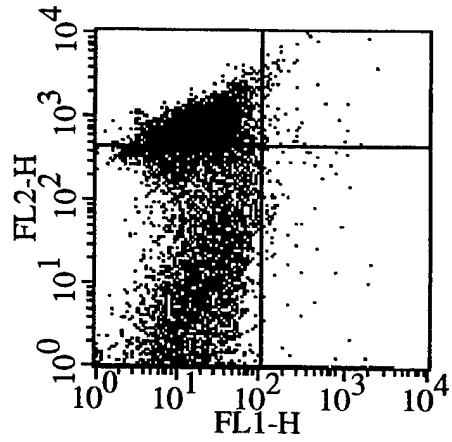
FL2-H
FL1-H
10^0 10^1 10^2 10^3 10^4

b

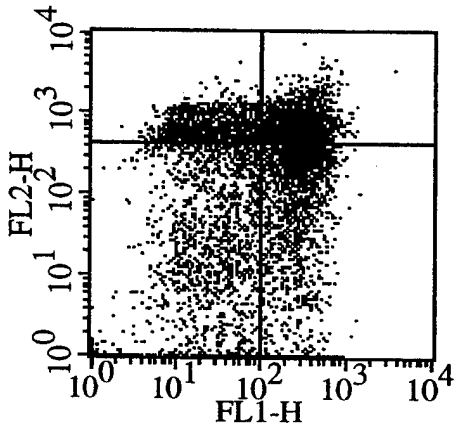
FL2-H
FL1-H
10^0 10^1 10^2 10^3 10^4

c

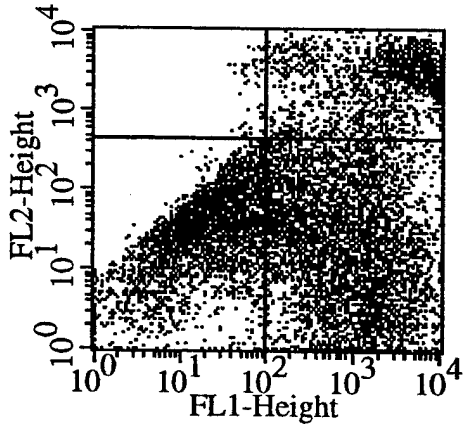
FL2-Height
FL1-Height
10^0 10^1 10^2 10^3 10^4

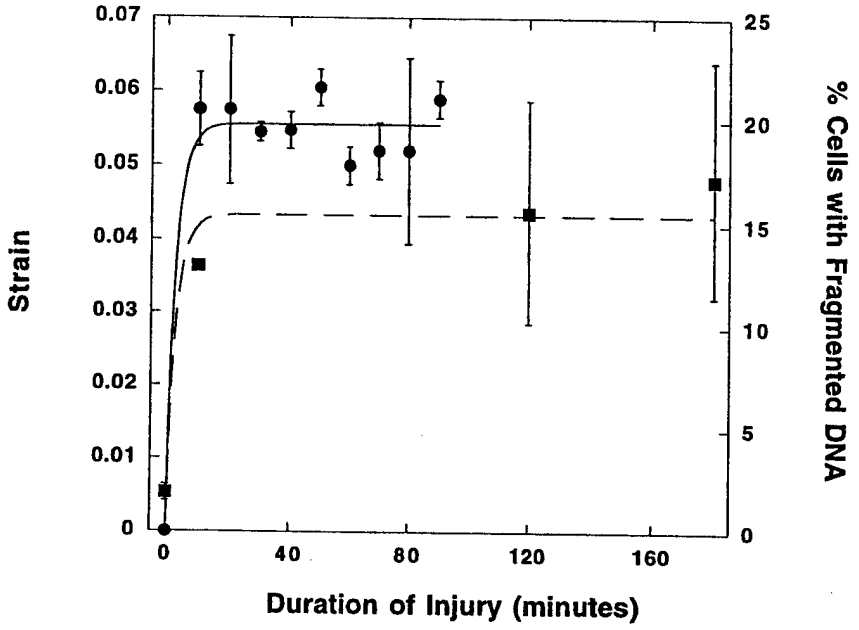
0.07
0.06
0.05
0.04
0.03
0.02
0.01
0
Strain
25
20
15
10
5
0
% Cells with Fragmented DNA
0
40
80
120
160
Duration of Injury (minutes)

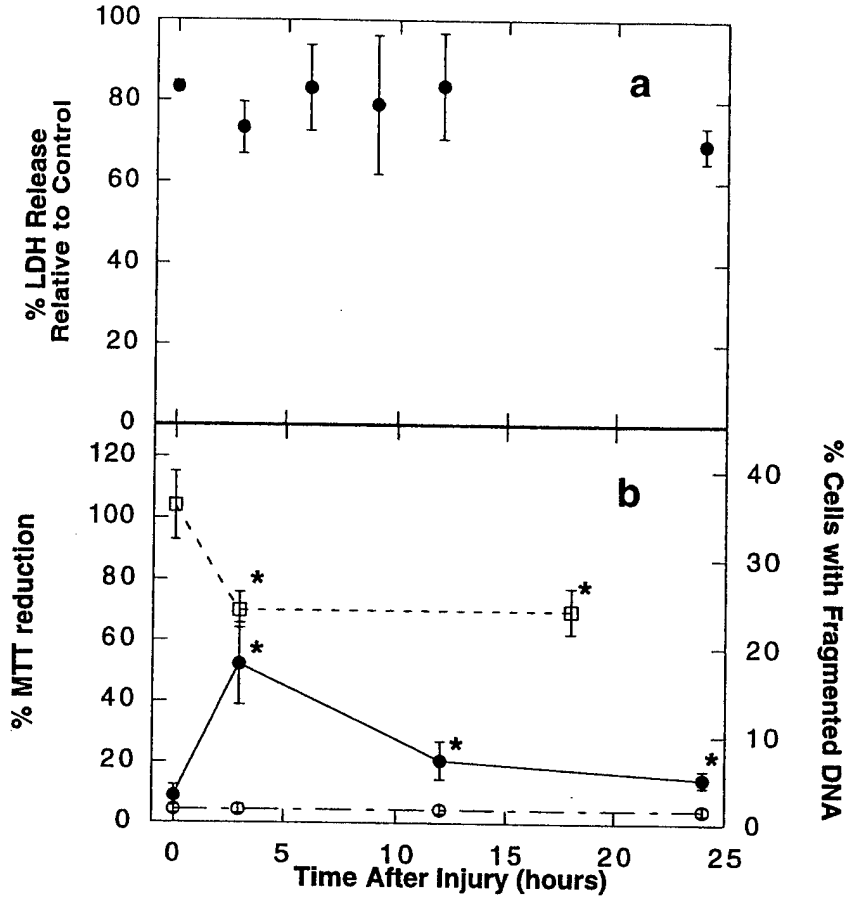
a
b
% LDH Release
Relative to Control
% MTT reduction
% Cells with Fragmented DNA
Time After Injury (hours)
100
80
60
40
20
0
120
100
80
60
40
20
0
40
30
20
10
0
0
5
10
15
20
25
*

CASPASE 1 AND 3 ARE ACTIVATED IN SHEAR STRESS-INDUCED INJURY TO DIFFERENTIATED SH-SY5Y CELLS

Dina H. Triyoso and Theresa A. Good

Department of Chemical Engineering

Texas A&M University

College Station, TX 77843-3122 USA

Running Title: Caspases are activated in shear stress induced injury

Corresponding Author:
Theresa Good
Department of Chemical Engineering
337 Zachry
Texas A&M University
College Station, TX 77843-3122
Phone (409) 845-3413
Fax (409) 845-6446
tgood@tamu.edu

Disclaimer: The view, opinions and /or findings contained in this report are those of the authors and should not be construed as a position, policy, decision, or endorsement of the federal Government or the National Medical Technology Testbed, Inc.

Abstract

We investigated the role of caspases in shear stress-induced injury using the differentiated human neuroblastoma cell line, SH-SY5Y. It is generally believed that exposure of neurons to shear stress and strain, such as occurs during traumatic injury, leads to neurodegeneration. We have previously established that shear stress leads to DNA fragmentation in differentiated SH-SY5Y cells. In the present study, differentiated SH-SY5Y cells are exposed to fluid shear stress using a cone and plate viscometer. After shear stress-induced injury, caspase activity and the extent of DNA fragmentation are assessed. Our results indicate that a significant increase in caspase 1 and caspase 3 enzymatic activity is observed within 24 hours after injury. Inhibition of caspase activation attenuates shear stress-induced DNA fragmentation. These results suggest that caspase activation is important in the mechanism of shear stress-induced injury.

Key Words: shear stress, strain, apoptosis, caspase 1, caspase 3, neuroblastoma, head injury

Exposure of the central nervous system to mechanical forces is deleterious. Shear stress and strain are believed to contribute to neuronal loss observed following head injury. We have demonstrated, *in vitro,* that neuron-like cells respond to pulsatile shear stress by nitric oxide production and DNA fragmentation, and that DNA fragmentation is attenuted by inhibition of nitric oxide synthase, calcium release from ryanodine sensitive stores and calcium entry through NMDA receptor gated channels [18-20]. *In vivo*, it has been determined that cells in select regions of the brain undergo apoptotic cell death associated with experimental head injury [3]. Apoptosis during head injury appears to be associated with caspase activation [2].

We report here that increased enzymatic activity of caspase 1 and caspase 3 were observed upon shear stress application to differentiated SH-SY5Y cells, a human neuroblastoma cell line. Inhibition of caspase activation significantly reduced the extent of shear stress-induced cell injury as seen by the reduction in the percentage cells with fragmented DNA when caspase inhibitors were administered relative to that observed when no inhibitors were present. To the best of our knowledge, this work establishes, for the first time, the role of caspase activation in shear stress-induced neuron-like cell injury.

In all experiments, human SH-SY5Y neuroblastoma cell lines were used. This cell line was cultured using standard techniques in a humidified 5% CO_2/air incubator at 37°C. Prior to shear stress experiments, the cells were differentiated for 5-7 days in culture medium containing 10 ng/ml of human-β-NGF (Nerve Growth Factor, Sigma, St. Louis, MO). Fluid shear stress was used to induce strain in the SH-SY5Y cells using a modified cone and plate viscometer as previously described in detail [18]. For shear stress applications of 30 to 90 minutes, stress was applied in six cycles. For the 90 minute-long experiment, cells were sheared for 13 minutes and

allowed to rested for two minutes. For 60 and 30 minute-long experiments, cells were sheared for nine and five minutes, respectively, followed by a one minute rest period. For five minute shear stress application, continuous fluid shear stress was applied to cells. After the application of fluid shear stress, the enzymatic activities of caspase 1 and caspase 3 were determined by first lysing the cells to extract their cellular contents. Caspase 1 and 3 specific peptides, WEHD and DEVD, respectively, that were conjugated to the color reporter molecule p-nitroanilline (pNA, R&D Systems, Minneapolis, MN), were added to cell lysates. In the presence of caspases in the cell lysate, the peptide would be cleaved, releasing pNA, which was measured using an Emax microplate reader (Molecular Probes, Sunnyvale, CA). The extent of DNA fragmentation in cells following shear stress application was assessed using a TUNEL assay (Promega, Fitchburg, WI) [18]. In brief, 3' OH termini were labeled with fluorescein terminal deoxynucleotide transferase (TdT) and whole DNA 3'ends were labeled with propidium iodide (PI) according to the procedure outlined for cell suspension with flow cytometry given by the manufacturer. Results were analyzed on a FACS Caliber flow cytometer (Becton Dickinson, San Jose, CA). The fraction of cells with fragmented DNA was determined by counting cells labeled with fluorescein-TdT whose fluorescence intensity was above a threshold determined from control cells. In order to assess the role of caspase 1 and 3 in shear stress-induced DNA fragmentation, 100μM of Z-VAD-FMK, a general caspase inhibitor, Z-WEHD-FMK a caspase 1 specific inhibitor, or Z-DEVD-FMK, a caspase 3 specific inhibitor (R&D Systems, Minneapolis, MN) were added to cells 1.5 hours prior to shear stress application. Immediately after shear stress application, the extent of DNA fragmentation was determined.

As seen in Figures 1 and 2, the activity of both caspase 1 and 3 was increased by about 30% after 30 minutes or more of shear stress application. Caspase 1 activity increased after as little as 5 minutes of shear stress application (Figure 1). The increase in activity was marginally significant relative to activity seen in the unsheared control cells ($p=0.06$). Caspase 1 activity remained elevated for at least 24 hours after 90 minutes shear stress application. No significant change in activity was observed from 0 hours to 24 hours ($p>0.1$).

As shown in Figure 2, the level of caspase 3 activity was significantly elevated after 5, 30 and 90 minutes of shear application relative to unsheared control ($p<0.06$). The level of caspase 3 activity did not increase significantly with time of shear stress application ($p>0.15$), nor did it return to control levels 24 hours after shear stress application.

To determine if caspases play a role in the mechanism of shear stress induced DNA fragmentation, cells were sheared in the presence of general and specific caspase inhibitors, after which DNA fragmentation was measured using the TUNEL assay. The general, caspase 1 and caspase 3 inhibitors led to the reduction in the percentage of cells with fragmented DNA after shear application from 45±4% for untreated sheared cells to 12±6%, 5±2% and 6±2.5 % respectively, for the treated cells (Figure 3). All caspase inhibitors led to a significant reduction in the fraction of cells with fragmented DNA relative to unsheared controls ($p<0.005$). These results indicate that activation of caspase 1 and 3 is involved in shear stress-induced DNA fragmentation of differentiated SH-SY5Y cells.

A number of investigators have used shear stress injury to neuron-like cells as an *in vitro* model of head injury [7]. Caspase activation has been observed in a number of *in vivo* models of head injury [2, 9,12]. The development of *in vitro* models of injury which capture the salient

features of the injury *in vivo* will be important in both the elucidation of the mechanism and the development and screening of new drugs to treat injury or disease in which neurons and neuron-like cells are exposed to shear stress and strain.

We have previously established that shear stress leads to nitric oxide production and DNA fragmentation in a differentiated human neuroblastoma cell line [18]. We also showed that shear stress induced cell injury led to the accumulation of phosphatidyl serine of the outer membrane surface, characteristic of apoptosis [19]. Our finding that caspases are involved in shear induced injury is important in that it confirms that shear stress leads to apoptotic death in SH-SY5Y cells. Caspases are only activated in cells undergoing apoptosis and not necrosis [15]. Apoptosis is preventable, while necrosis is not. Our findings therefore suggest that shear stress induced cell death is preventable.

Caspase 1 and 3 activation have been shown to be associated with apoptosis in SH-SY5Y cells [6, 13, 16]. Caspase 1 is associated with inflammation which is responsible for the conversion of interleukin 1β (IL-1β) into its active form. IL-1β has been implicated in head injury [9]. Inhibition of IL-1 β reduces brain damage associated with injury [14, 17]

Of the various members of the caspase family, caspase 3 is considered to be the 'essential caspase'. Caspase 3 activates the protein responsible for DNA laddering. The involvement of caspase 3 in apoptosis induced by microtubule instability, serum deprivation, and glutamate toxicity has been reported [1, 5, 6]. In addtion, caspase 3 activation has been associated with nitric oxide induced or peroxynitrite induced DNA fragmentation in SH-SY5Y cells and rat hippocampal neurons [8, 11], which is consistent with our findings that shear stress leads to apoptotic cell death via a pathway involving nitric oxide production and caspase activation.

In recent postmortem studies, cleavage of caspase 1 and upregulation and cleavage of caspase 3 was observed in the brain tissue samples indicating that apoptosis occurs in humans after head injury [2]. Inhibition of caspase 1 attenuated cold-injury induced brain trauma and DNA fragmentation *in vivo* [10]. These studies support our findings that caspase 1 and 3 activity increase by 30 to 40% during shear stress induced cell injury (Figures 1 and 2) and that their activation affects DNA fragmentation (Figure 3). In addition, caspase activation reaches a maximum within 30 minutes of shear stress and remains elevated for at least 24 hours after shear stress is terminated. This suggests that once caspases are activated, they remain active and mediate cell disassembly long after the initiating insult has ceased. We have also seen that inhibition of protein synthesis with cylcloheximide blocks any significant increase in shear stress-induced caspase 3 activation (data not shown), which is consistent with observations of caspase 3 upregulation during head injury reported by others [2].

Our results indicate, for the first time, that shear stress induced cell injury to neuron-like cells involves the activation of caspase 1 and caspase 3. We further confirm that injury following shear stress is via an apoptotic mechanism. These results have implications for treatment of disorders or injuries of the nervous system where neurons are exposed to abnormal shear stress and strain.

This work was supported by a grant from the U.S. Department of the Army and National Medical Technology.

REFERENCES

[1]. Armstrong, R. C., Aja, T. J., Hoang, K. D., Gaur, S., Bai, X., Alnemri, E. S., Litwack, G., Karanewsky, D. S., Fritz, L. C., and Tomaselli, K. J., Activation of the CED3/ICE-related protease CPP32 in cerebellar granule neurons undergoing apoptosis but not necrosis, Journal of Neuroscience, 17 (1997) 553-562.

[2]. Clark, R. S., Kochanek, P. M., Chen, M., Watkins, S. C., Marion, D. W., Chen, J., Hamilton, R. L., Loeffert, J. E., and Graham, S. H., Increases in Bcl-2 and cleavage of caspase-1 and caspase-3 in human brain after head injury, FASEB Journal, 13 (1999) 813-821.

[3]. Conti, A. C., Raghupathi, R., Trojanowski, J. Q., and McIntosh, T. K., Experimental brain injury induces regionally distinct apoptosis during the acute and delayed post-traumatic period, Journal of Neuroscience, 18 (1998) 5663-5672.

[4]. Coxon, F. P., Benford, H. L., Russell, R. G., and Rogers, M. J., Protein synthesis is required for caspase activation and induction of apoptosis by bisphosphonate drugs, Molecular Pharmacology, 54 (1998) 631-638.

[5]. Du, Y., Bales, K. R., Dodel, R. C., Hamilton-Byrd, E., Horn, J. W., Czilli, D. L., Simmons, L. K., Ni, B., and Paul, S. M, Activation of a caspase 3-related cysteine protease is required for glutamate-mediated apoptosis of cultured cerebellar granule neurons, Proceedings of the National Academy of Sciences of the United States of America, 94 (1997) 11657-11662.

[6]. Gorman, A. M., Orrenius, S., and Ceccatelli, S., Apoptosis in neuronal cells: role of caspases, NeuroReport, 9 (1998) R49-R55.

[7]. LaPlaca, M. C. and Thibault, L. E., An in vitro traumatic injury model to examine the response of neurons to a hydrodynamically-induced deformation, Annals of Biomedical Engineering, 25 (1997) 665-677.

[8]. Maiese K., and Vincent, A. M., Group I metabotropic receptors down-regulate nitric oxide induced caspase-3 activity in rat hippocampal neurons, Neuroscience Letters, 264 (1999) 17-20.

[9]. Minami, M., Kuraishi, Y., Yabuuchi, K., Yamazaki, A., and Satoh, M, Induction of interleukin-1 beta mRNA in rat brain after transient forebrain ischemia, Journal of Neurochemistry. 58 (1992) 390-392.

[10]. Morita-Fujimura, Y., Fujimura, M., Kawase, M., Murakami, K., Kim, G. W., and Chan, P. H., Inhibition of interleukin-1beta converting enzyme family proteases (caspases) reduces cold injury-induced brain trauma and DNA fragmentation in mice, Journal of Cerebral Blood Flow and Metabolism, 19 (1999) 634-42.

[11]. Oh-hashi, K., Maruyama, W., Yi, H., Takahashi, T., Naoi, M., and Isobe, K, Mitogen-activated protein kinase pathway mediates peroxynitrite-induced apoptosis in human dopaminergic neuroblastoma SH-SY5Y cells, Biochemical & Biophysical Research Communications, 263 (1999) 504-9.

[12]. Pike, B. R., Zhao, X., Newcomb, J. K., Posmantur, R. M., Wang, K. K., and Hayes, R. L., Regional calpain and caspase-3 proteolysis of alpha-spectrin after traumatic brain injury, Neuroreport, 9 (1998) 2437-2442.

[13]. Posmantur, R., McGinnis, K., Nadimpalli, R., Gilbertsen, R. B., and Wang, K. K., Characterization of CPP32-like protease activity following apoptotic challenge in SH-SY5Y neuroblastoma cells, Journal of Neurochemistry, 68 (1994) 2328-2337.

[14]. Relton, J. K. and Rothwell, N. J., Interleukin-1 receptor antagonist inhibits ischaemic and excitotoxic neuronal damage in the rat, Brain Research Bulletin, 29 (1992) 243-246.

[15]. Ruemmele, F. M., Dionne, S., Levy, E., and Seidman, E. G., TNF-alpha-induced IEC-6 cell apoptosis requires activation of ICE caspases whereas complete inhibition of the caspase cascade leads to necrotic cell death, Biochemical and Biophysical Research Communications, 260 (1999) 159-166.

[16]. Takadera, T. and Ohyashiki, T., Apoptotic cell death and CPP32-like activation induced by thapsigargin and their prevention by nerve growth factor in PC12 cells, Biochimica et Biophysica Acta, 1401 (1998) 63-71.

[17]. Toulmond, S. and Rothwell, N. J., Interleukin-1 receptor antagonist inhibits neuronal damage caused by fluid percussion injury in the rat, Brain Research, 671 (1995) 261-266.

[18]. Triyoso, D. H. and Good, T. A., Pulsatile shear stress leads to DNA fragmentation in human SH-SY5Y neuroblastoma cell line, Journal of Physiology, 515 (1999a) 355-365.

[19]. Triyoso, D. H. and Good, T. A., The role of nitric oxide and calcium in shear induced DNA fragmentation in human SH-SY5Y neuroblastoma cell line, Annals of Biomedical Engineering, (1999b) (submitted).

[20]. Triyoso, D. H., Edwards, M. E., and Good, T. A, Low strain rate leads to cellular injury consistent with apoptosis in differentiated SH-SY5Y cells, Journal of Neurotrauma, (1999) (submitted).

Figure captions

Fig 1. The increase in enzymatic activity of caspase 1 in sheared cells as a function of shear duration. Results are reported as a percentage of activity measured relative to unsheared control cells. Cells were sheared from 5 minutes to 90 minutes at 10 dynes·cm^{-2}. Enzymatic activity of caspase 1 was assayed immediately after shear application for all shear duration and also 24 hours after shear application for the 90 minute shear duration. For all data, n =3-5. * indicates result is significant relative to unsheared control cells ($p<0.05$).

Fig 2. The increase in enzymatic activity of caspase 3 in sheared cells as a function of shear duration. Results are reported as a percentage of activity measured relative to unsheared control cells. Cells were sheared from 5 minutes to 90 minutes at 10 dynes·cm^{-2}. Enzymatic activity of caspase 3 was assayed immediately after shear application for all shear duration and also 24 hours after shear application for the 90 minute shear duration. For all data, n =3-5. * indicates result is significant relative to unsheared control cells ($p<0.05$).

Fig 3. Percentage of TUNEL positive cells (with fragmented DNA) in the presence of caspase inhibitors. Cells are exposed to no shear (hatched bars) or pulsatile shear (solid bar) for 90 minutes at 10 dynes·cm^{-2} in the presence of no inhibitor (None), Z-VAD-FMK (Gen. Casp), Z-WEHD-FMK (Casp 1), or Z-DEVD-FMK (Casp 3). For all data, n=3-4. *** indicates result is significant relative to untreated control cells ($p<0.001$).

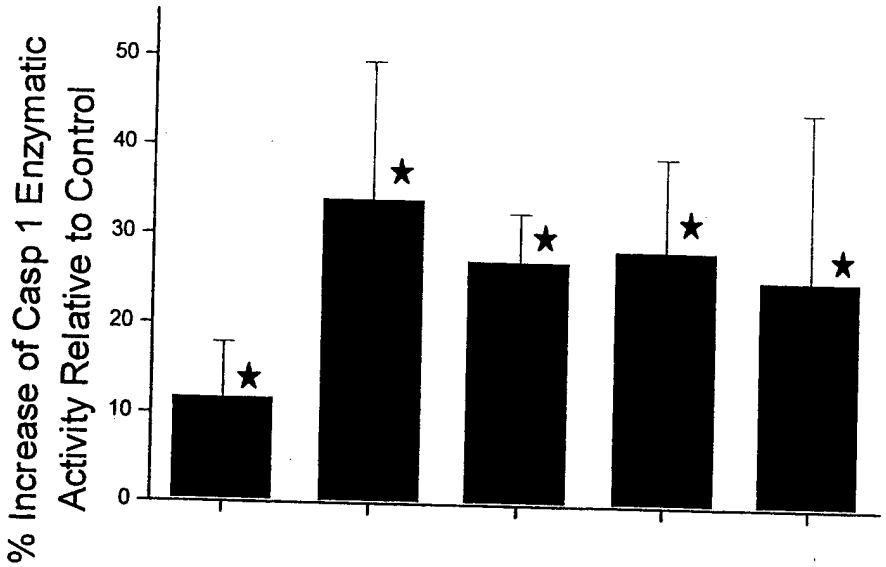

Shear duration (min)	5	30	60	90	90
Time after shear (hrs)	0	0	0	0	24

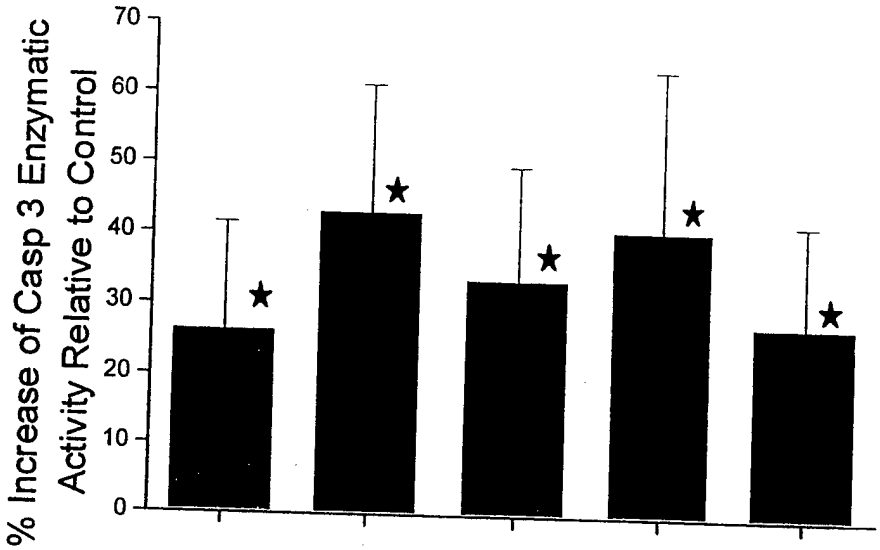

Shear duration (min)	5	30	60	90	90
Time after shear (hrs)	0	0	0	0	24

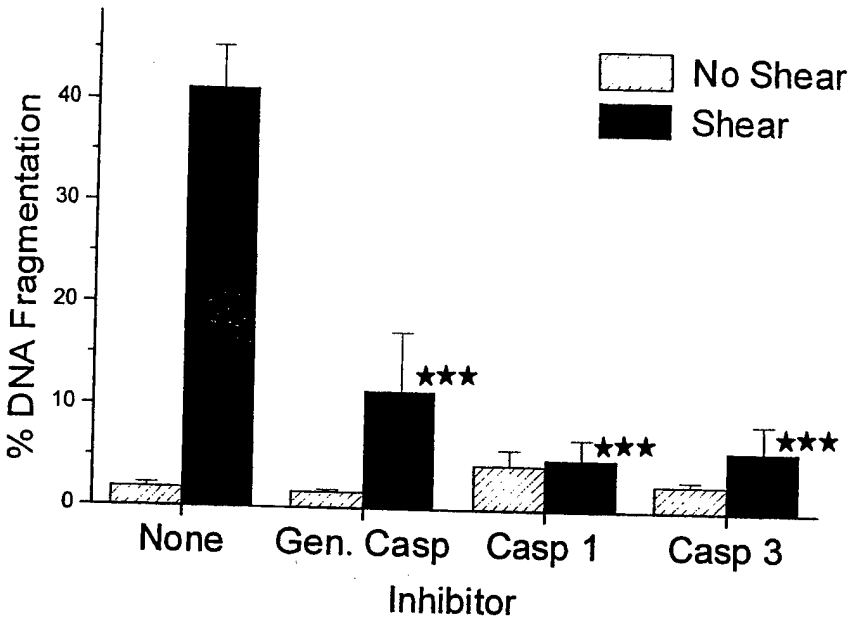
No Shear
Shear
% DNA Fragmentation
40
30
20
10
0
***
***
***
None
Gen. Casp
Casp 1
Casp 3
Inhibitor

The Role of Viscoelastic Properties of Differentiated Human Neuroblastoma Cells in Shear Stress Induced Cell Injury

*Michael E. Edwards, Sheng-Shih Wang, and Theresa A. Good

Department of Chemical Engineering, Texas A&M University, College Station, TX 77843-3122
*Current address is The Proctor and Gamble Company, 8700 Mason Montgomery Road, Mason, OH 45040

Running title: Role of viscoelastic behavior in shear stress induced cell injury

Corresponding Author:

Theresa Good
337 Zachry
Texas A&M university
College Station, TX 77843-3122
Phone (409) 845-3413
Fax (409) 845-6446
tgood@tamu.edu

draft
5/10/00

ABSTRACT

Shear stress and strain lead to neurodegeneration *in vivo* during head injury and possibly during glaucoma. *In vitro*, shear stress and strain have been shown to lead to cell injury in a number of models using neurons and neuron-like cells. In the present study we examined the relationship between shear stress, strain and the extent of cell injury in a shear stress induced model of cell injury using differentiated SH-SY5Y (human neuroblastoma) cells. Shear stress led to cell strain that increased with increasing stress, and diminished upon cessation of shear. Strain rate during cyclic application of shear stress increased by over an order of magnitude from the first to all subsequent cycles. From an analysis of the viscoelastic properties of the cells we concluded that the cell and/or its polymer network became more elastic upon cyclic shear stress application. To support this conclusion we measured the degree of cytoskeletal polymerization before and after exposure of cells to cyclic shear stress and found that the fraction of polymerized tubulin in the cell relative to total tubulin decreased from 0.33 before application of shear stress to 0.17 after six cycles of shear stress. The extent of injury, as indicated by the fraction of cells with fragmented DNA, was three times higher for cyclic shear stress than for steady shear stress and may be related to strain rate. We believe the change in rheological properties of the cell may be important in determining susceptibility of injury. These findings may aid in elucidating the mechanism by which neurons and neuron-like cells respond to shear stress and strain, and lead to new treatments for disease or injury arising from the exposure of neurons to abnormal stress and strain.

INTRODUCTION

Cells of the central nervous system experience elevated shear stress and strain during a variety of pathological states including head injury, hydrocephalus, and glaucoma. Head injury is known to be associated with the generation of stress and strain within the cerebral cortex (1-3). Shear stresses predicted during head injury are on the order of 4×10^5 dynes cm^{-2}. Tissue strain is predicted to reach a maximum of 0.1 to 0.2 within approximately 10 ms of impact (1). Hydrocelphalus and glaucoma are associated with elevated intracranial and intraocular pressure, respectively, and that elevated pressure is speculated to lead to tissue deformation and associated elevated shear stress and strain (4-6). Strain rate associated with glaucoma is expected to be much lower than that associated with head injury.

There is some evidence that cyclical or repetitive compression or stress and strain acting on cells of both the central and peripheral nervous system is particularly damaging ([redacted]). During glaucoma, intraocular pressure varies throughout the day and these diurnal variations give rise to cyclic variations in stress and strain in the cells in the optic disk ([redacted]). Individuals with large diurnal variations in IOP are more likely to experience greater vision loss than individuals with constant elevated IOP (ref). In addition, there are a variety of repetitive motion disorders including carpel tunnel syndrome and cubital tunnel syndrome where the frequency of the strain/compression of the nerve is known to be correlated with the extent of injury ([redacted]).

A number of *in vitro* models have been developed to investigate the effects of high shear stress and strain rate on neurons and neuron-like cells (7-10). In these models, the duration of shear or strain applied was on the order of 50 ms to 200 ms. Acute injury results in lactate dehydrogenase (LDH) release (8), uptake of propidium iodine (PI) (9), and an increase in

intracellular Ca^{2+} (7-9). Only when the onset of injury was very rapid, did significant and sustained injury occur as determined by LDH release after 24 hours.

In results reported here, we use an *in vitro* model that utilizes fluid shear stress to produce cell strain in differentiated SH-SY5Y neuroblastoma cells. We measured cell strain, strain rate, the degree of tubulin polymerization, and cell viability as a function of shear stress in order to assess the relationship of the viscoelastic properties of the cell on the extent of cell injury. Cell strain increased at high shear stress, and returned to near normal dimension after the cessation of shear. During cyclical shear stress, which might mimic cell exposure conditions associated with diurnal variations in IOP or repetitive strain injury, the strain rate increased significantly from the first cycle to all subsequent cycles, with the relaxation constant for the cell increasing by over an order of magnitude. The fraction of polymerized tubulin within the cell decreased by a factor of two after application of cyclic shear stress. Cyclical shear stress produced far greater injury in cells than steady shear stress. We believe the change in viscoelastic properties of the cell may be related to the change in extent of injury in response to shear stress. These results will contribute to the understanding of the mechanism of shear stress and strain induced neurodegeneration.

MATERIALS AND METHODS

MATERIALS

Minimal Essential Media (MEM) with Earle's salts, non-essential amino acids, fetal bovine serum (FBS), L-glutamine, penicillin G-streptomycin, and Fungizone were obtained from GibcoBRL (Grand Island, NY). Merocyanine 540 (MC540) was from Molecular Probes (Eugene, OR). Glycerol, sodium dodecylsulfate (SDS), and bovine serum albumin (BSA), were obtained from Fisher Scientific (Houston, TX). Mini EDTA-free protease inhibitor cocktail tablet was obtained from Boehringer Mannheim (GmbH, Germany). Pre-cast SDS polyacrylamide electrophoresis gels were from Owl Separation System (Portsmouth, NH). Nitrocellulose membranes were from Pierce (Milwaukee, WI). Biotinylated anti-rabbit Ig G secondary antibody and VECTASTAIN ABC reagent were obtained from Vector Laboratories (Burlingame, CA). A TUNEL assay kit was obtained from Promega (Madison, WI). All other chemicals were obtained from Sigma (St. Louis, MO).

METHODS

Cell Culture

Human neuroblastoma SH-SY5Y cells (a kind gift of Dr. Evelyn Tiffany-Castiglioni) were cultured in a humidified 5% (v/v) CO_2/air environment at 37°C in MEM supplemented with 10% (v/v) FBS, 3 mM L-glutamine, 100 U/ml penicilin, 100 µg/ml streptomycin and 2.5 µg/ml amphotericin B (Fungizone), henceforth referred to as complete MEM (cMEM). Cells (passage 89-92) were replated at density of 5,000 cells/ml or 500,000 cells/ml in 35mm tissue culture

dishes and differentiated with 10 ng/ml recombinant human nerve growth factor-β (NGF-β) for 6-15 days prior to conducting strain measurements or viability experiments, respectively.

Shear Stress Apparatus

Shear stress was applied to differentiated SH-SY5Y cells using a modification of a standard cone and plate viscometer mounted on a Zeiss Axiovert 135 florescent microscope. The apparatus consists of a stainless steel cone with a 5° angle relative to a stationary polystyrene tissue culture dish, a Glas-Col variable speed precision stirrer (Terre Haute, IN) to precisely control the cone angular velocity, and a 7 day 6 on/6 off controller (Radio Shack, College Station, TX) to automatically control shear cycles ([redacted]). The shear stress profile used in cyclic shear experiments consisted of 6 cycles of alternating shear (13 min) and static (2 min) conditions (90 min total). A monolayer of cells adherent to the culture dish was exposed to laminar flow by rotating the cone, whose tip contacted the plate, over the surface of the plate. Only those cells within a 1.5 mm radius of the center of the 35 mm plate (less than 1% of the cells) were displaced by the placement of the cone.

Strain Measurement

Stock solutions (1 mg/ml) of MC 540 were prepared by dissolving in absolute ethanol and diluting 1:1 with water. MC 540 stock was stored in the dark at 4°C until needed. Human NGF-β differentiated SH-SY5Y cells attached to the dish surface were washed 3 times with 2 ml of a 5 mM Tris-HCL buffered isotonic saline solution to remove cMEM. The cells were exposed to 18 μM MC 540 diluted in the wash buffer for 10 min at ambient temperature prior to being washed 3 times with 2 ml of Ringer's buffer. SH-SY5Y cells were sheared in the presence of Ringer's buffer.

Fluorescently stained cells were observed with a Zeiss Axiovert 135 fluorescent microscope (Thornwood, NJ) equipped with an HBO 50W short arc mercury lamp. Excitation and emission wavelengths were 540 nm and 605 nm, repectively. Images were captured with the Zeiss continuous image capture 128 system. Zeiss Scientific Image Analysis Software was used to analyze the captured images.

Cell deformation (strain) was estimated from the shear induced shape changes in the cell. A whole cell stretch ratio, λ_i was defined as the ratio of the shear induced characteristic length, L_i, to the unstressed length, $(L_i)_0$, both measured in the ith direction (Eq. 1) (16).

$$\lambda_i = \frac{L_i}{(L_i)_0} \tag{1}$$

Cell lengths for SY5Y cells were determined by measuring the lengths of a rectangle enclosing the cells (Figure 1). The cell boundaries were determined using the auto tracing feature of the Zeiss Image 3.0 imaging software package. The principle axis was chosen to be the axis of maximum elongation. The maximum strain in the ith direction, E_i, was calculated from the relation

$$E_i = \frac{1}{2}\left(\lambda_i{}^2 - 1\right) \tag{2}$$

Estimation of Strain Time Constant

A nonlinear least squares regression was used to estimate a strain or deformation time constant from strain data as a function of time using an equation of the form seen in Equation 3.

$$E = E_{\max}\left(1 - e^{-\frac{t}{\tau}}\right) \tag{3}$$

where E is the cell strain, E_{max} is the maximum strain observed, t is time, and τ is the strain time constant. The first derivative of Equation 3 with respect to time yields the strain rate of the cells.

Cytoskeleton Polymerization

Microtubule (polymerized) and total tubulin extracts from cultured SH-SY5Y cells were obtained by an adaptation of a published procedures (Caron et al., 1985; Dennerll et al., 1988; Putnam et al., 1998). To isolate the polymeric cytoskeletal fraction, cells were washed gently in a microtubule stabilization buffer (MTSB) which contains 0.1 M Pipes, pH 6.75, 1 mM EGTA, 1 mM MgSO4, 2 M glycerol, and a complete, Mini EDTA-free protease inhibitor cocktail tablet, and incubated at 37°C for 10 minutes with MTSB plus 0.1% Triton X-100 to remove unassembled tubulin. The remaining Triton-extracted cytoskeletal ghosts were then solubilized from the dish by adding 300ul of lysis buffer (25 mL Tris-HCl pH 7.4, 0.4 M NaCl, and 0.5% SDS) and scrapping with a rubber policeman. After 5 minutes at 37°C, cell lysates were transferred to 1.5 ml microcentrifuge tubes. The samples were boiled for 3 minutes and either kept on ice for immediate analysis or stored at -80°C freezer. Total tubulin was extracted by addition of lysis buffer directly to intact cells. All extraction steps were performed at 37°C. Polymerized and total tubulin fractions were analyzed using standard western blotting techniques.

The protein concentrations of samples were determined by BCA assay (Smith et al., 1985). Equivalent volumes of protein samples were electrophoresed in 12.5% pre-cast SDS PAGE page-one gels, and then transferred onto a 0.20 micron nitrocellulose membrane using a Bio-Rad Miniblot apparatus (Bio-Rad) at 85 V for 4.5 hours. The nitrocellulose blot was subsequently blocked overnight with 3% fish gelatin, 2% BSA and 8% FBS in phosphate buffered saline solution (PBS). After rinsing briefly in PBS containing 0.04% Tween 20 (PBST),

the membrane was incubated with shaking at 4°C overnight with a monoclonal anti-β-tubulin antibody diluted 1:800. The membrane was washed using at least 4 changes of PBST over 10 minutes with gentle agitation and then transferred to a diluted biotinylated anti-rabbit Ig G secondary antibody in PBST. After rinsing the blot at least 4 times with PBST for 10 minutes with shaking, the membrane was incubated in the VECTASTAIN ABC reagent for 45 minutes with gentle agitation. Before adding the substrate solution, the membrane was rinsed 4 times with PBST for 10 minutes each with shaking. 50 µl 30% H_2O_2, 30 mg diaminobenzidine dissolved in 45 ml of 50 mM Tris buffer, and 5 ml of 0.3% $NiCl_2$ were added to the membrane and the reaction allowed to proceed for 5 minutes. The blot was rinsed in 2 changes of distilled water over 10 minutes and dried for analysis.

Total tubulin and polymerized tubulin lanes on the western blots were analyzed via densitometry. Cell extracted tubulin and tubulin standards were treated identically. The denisty of bands was assumed to be proportional to the total amount of protein present. The ratio of soluble tubulin to polymerized tubulin was taken as the ratio of the quantity, the density of the total tubulin band minus the density of the polymerized tubulin band, to the density of the polymerized tubulin band.

TUNEL Assay

DNA fragmentation was measured using a TUNEL assay. Cells were permeablilzed, the 3' OH termini were labeled with fluorescein-12-dUTP, and whole DNA 3'ends were labeled with propidium iodide (PI) according to the procedure outlined for cell suspension with flow cytometry given by the manufacturer with minor modifications. For each measurement, 2-3 million cells (one plate) were used. To prepare cells for the TUNEL assay, the culture medium was removed from the culture dish and trypsin/EDTA was added to gently detach the cell monolayer from the

dish. The cell suspension was then centrifuged and washed with PBS. Afterwards, cells were fixed with methanol free formaldehyde for 20 minutes. Another wash with PBS was performed after fixing the cells. Finally, the cells were permeabilized by adding ethanol. The cells were then stored in –20°C freezer for at least four hours before carrying out the rest of the procedure outlined by the manufacturer.

Results were analyzed on a FACS Caliber flow cytometer (Becton Dickinson) using a 15 mW argon laser at 488 nm excitation wavelength. Emission filters of 530 nm bandpass for green fluorescence (fluorescein labeled dUTP in this case) and 585 nm for red (PI) were used. Electronic compensation was used to prevent bleed through fluorescence. Forward and side light scatter, green fluorescence, FL1, and red fluorescence, FL2, were collected and analyzed on 30,000 cells/sample with Cellquest software (Becton Dickinson). The two parameter histogram of FL2 area versus FL2 width was used to gate on single cells. A positive apoptotic region on the FL1 versus FL2 histogram was set so that <2% of the non sheared cells (control) were positive for apoptosis. The fraction of cells with fragmented DNA was determined by counting cells with green (fluorescein) fluorescence whose intensity was above a threshold determined from control cells.

MTT Assay

Cell viability was measured using the 3, (4, 5-dimethylthiazol-2-yl) 2, 5-diphenyl-tetrazolium bromide (MTT) reduction assay (Pollack, 1995). Cells were plated in dishes at uniform density, treated, then MTT reduction was assessed. MTT was added to a final concentration of 0.5 mg/mL in the culture dish. Culture dishes were then incubated at 37°C in a 5% (v/v) CO_2 environment for 4 h to allow metabolically active cells time to reduce MTT. The reaction was stopped and formazan crystals were dissolved by the addition of a 5:2:3

DMF:SDS:H_2O solution at pH 4.7 in an amount equal to the volume of the culture medium. The plates were incubated for at least 12 h in a 5% (v/v) CO_2 environment at 37°C prior to reading the absorbance at 585 nm (Emax microplate reader, Molecular Probes). Particulate scatters were accounted for by subtracting the absorbance at measured 650 nm from the absorbance measured at 585 nm. Controls (cells not subjected to shear stress) were normalized to 100% viability. Viability was reported as a percentage of the absorbance (MTT reduction) measurement of the treated cells relative to the absorbance measurement from the untreated controls.

Data Analysis

All data represent means ± S.E.M. for n independent determinations. Specific n values are given in figure legends. The significance of results was determined by one tailed Student's t test assuming unequal variances. For all results, a p value of 0.05 was used for the level of significance, although for individual data sets, a more stringent significance level may have been employed as indicated in figure legends.

RESULTS

We examined the relationship between fluid stress and strain for differentiated SH-SY5Y cells exposed to increasing levels of shear ranging from 5 to 45 dynes/cm^2 for 10 min. As seen in Figure 2, the principle strain observed in cells not previously exposed to fluid shear stress reached a maximum strain level within ten minutes of stress application at both 5 and 15 dynes/ cm^2 stress levels. Longer durations of shear stress (up to 90 minutes) did not result in further cell strain (data not shown). At a stress level of 45 dynes/cm^2, the maximum cell strain may not have been reached within 10 minutes. The maximum observed cell strain increased with increased stress level. The difference in strain observed at 5 and 45 dynes/cm^2 was significant.

To simulate the oscillatory nature of pressure, stress and strain *in vivo*, SH-SY5Y cells were sheared under cyclic flow conditions. We examined the extent of cell injury for both steady and pulsatile flow conditions using a TUNEL assay. Differentiated SH-SY5Y cells were exposed to 10 dynes/cm^2 steady shear stress (one cycle) for 10 minutes, steady shear stress for 90 minutes, or cyclic shear stress (six cycles) for 1.5 h. The percentage of cells with fragmented DNA increased from 13 $\pm$ 0.2 % to 45 $\pm$ 4 % when the number of cycles of shear stress increased from one to six. Changing the duration of steady shear stress from 10 minutes to 90 minutes did not significantly affect the percentage of cells with fragmented DNA, however, changing the relative amounts of time that cells were exposed to shear stress relative to the times where shear stress was off did appear to affect the level of injury. In general, if shear stress times were greater than rest/recovery times, injury was high, while if rest/recovery times were of equal magnitude to shear stress times, injury was low. A summary of results of the effects of cyclic shear stress on cell injury can be seen in Figure 3.

Figure 4A shows the SH-SY5Y strain profile for cells sheared at a frequency of 6 cycles of pulsatile flow (on for 13 minutes then off for 2 minutes) at 15 dynes/cm^2 for at total time of 1.5 h. These are the conditions under which we observed the greatest cell injury as measured by DNA fragmentation. Figure 4B (inset) shows the average strains at the end of the shear cycle, at the midpoint of the static cycle, and within 13 ± 1 s of the beginning of the subsequent cycle. During the 2 min static period, there was a 3.5 fold decrease in cell strain to nearly the original cell dimension compared to the strain during flow conditions. There was no significant difference between the level of strain at the beginning of a cycle and that at the end of a cycle for all but the first cycle.

We also measured the strain rate for both steady shear to cyclic shear to explore the relationship between strain rate, cycles of shear stress, and extent of cellular injury. Figure 5 shows the strain as a function of time during the first cycle of shear stress compared to the strain observed during all other cycles (designated the nth cycle). During the first cycle (t = 0 – 13 min), 4 min of shear is required to reach maximum strain. However, for every additional nth cycle, maximum strain is reached seconds following the initiation of shear.

We fit the strain rate data to a viscoelastic model in order to examine the role of changes in the cell polymer network in the extent of cellular injury during shear stress application. We found the deformation time constant of the cell for the first cycle and the nth cycle to be 3 ± 1 min and 0.17 ± 0.08 min, respectively. This corresponds to a strain rate of 4 ± 1 *10^{-4} s^{-1} and 7 ± 3 *10^{-3} s^{-1} for the first and nth shear stress cycle, respectively. The decrease in time constant for deformation from the first to nth shear cycle is consistent with the cell response to shear stress becoming more elastic after the first shear stress cycle.

We examined directly the effect of shear stress on the cell cytoskeleton. We measured the amount of polymerized tubulin and total tubulin in cells before and after six cycles of shear stress. As seen in Figure 6, shear stress causes a large decrease in the amount of polymerized tubulin in cells compared to untreated controls. Immunoblots of total and polymerized tubulin for sheared and control cellsare shown in Figure 6A. The fraction of polymerized tubulin relative to total tubulin, as measured from densitometric analysis of immunoblots is shown in Figure 6B.

DISCUSSION

Shear stress and strain have long been know to affect cell physiology. Shear stress has been implicated in the mechanism of neurodegeneration associated with head injury (ref). During glaucoma, elevated IOP leads to regions of high shear stress in the region of the eye where the optic nerve tranverses the globe (ref). Cell death via apoptosis is seen following elevated IOP in the retinal ganglion cells that make up the optic nerve (ref). There are a variety of other disorders and injuries where compression, stress or strain may be involved in nerve/neuro-degeneration. Hydrocephalus, carpel tunnel syndrome, and other repetitive strain injuries are some examples (ref).

The strain rate associated with cell injury may be important in determining the mechanism of cell injury. During head injury, strain rates are predicted to be high (on the order of 10 s^{-1}) (ref). During glaucoma, deformation and changes in deformation may occur at a rate closer to 10^{-4} s^{-1}(ref).

A number of investigators have also demonstrated the importance of shear stress and strain in models of neuronal cell injury (7-10). Shear stress in these models resulted in propidium dye uptake, lactate dehydrogenase release, phophatidyl choline biosynthesis, and calcium ion influx (ref). Cell injury was associated with high strain rate. We have recently shown that shear stress induces G protein activation, nitric oxide synthase activation, new protein synthesis, and DNA fragmentation without lactate dehydrogenase release in differentiated human SH-SY5Y neuroblastoma cells (12, ref). The mechanism of injury in our model appears to be significantly different than that reported for high strain rate models. Because of the presumed importance of strain rate in injury, both *in vivo* and *in vitro*, we were interested in examining

how the viscoelastic properties of cells were related to the extent of cell injury in our *in vitro* model.

We measured cell body mechanical deformation (strain) for cells. The maximum strain observed for a shear stress level of 15 dynes/cm^2 was 0.084 ± 0.004 (Figure 2). This result compares favorably with those of Laplaca and Thibault, who reported shear stress (20 dynes/cm^2) induced strains of 0.12 ± 0.05 for clusters of retanoic acid differentiated NT2-N cells sheared with a parallel plate viscometer (13).

Based on observations from *in vivo* injuries and diseases, we believe that repetitive or cyclic shear stress may be more harmful to neurons than constant steady injury. Two examples are the increased progression of vision loss in glaucoma that is associated with individuals with large diurnal variations in IOP (ref) and the increased severity of carpel tunnel syndrome associated with high frequency of motion (ref). *In vitro*, in non-neuronal cells, a number of investigators have reported that cyclical (or pulsatile) shear stress leads to greater cellular response than constant shear stress in endothelial cells (14-16). We examined if the same was true for neuron-like cells. We had previously shown that pulsatile shear stress led to DNA fragmentation in differentiated SH-SY5Y neuroblastoma cells (ref). In the present study, we compared the effect of cyclic shear stress and steady shear stress on differentiated SH-SY5Y cells and examined the role of cycle frequency on the level of injury (Figure 3). Cyclic shear stress leads to three times more cells with fragmented DNA than steady shear stress of the same magnitude and duration under our experimental conditions (Figure 3A). In addition, when shear stress/ no stress cycle times were varied, only cycles in which the rest or recovery period was less than the shear stress time resulted in significant loss of viability in cells (Figure 3B). We speculate that there is some change in cell property during shear stress associated with the cell's

ability to resist mechanical deformation, which is given sufficient time between insults, can recover to normal values. However, if recovery time between cycles of shear stress is too short, cell properties do not return to normal and increased loss of viability will result.

To investigate the role of cell rheological properties in cyclic shear stress induced injury, we measured cell strain during a typical cyclic stress protocol. When the profile of the applied shear stress is cyclical, the resulting strain is also cyclical (Figure 4) indicating the deformation experienced by the cells is at least partially elastic. Because the resulting strain remains finite during the static periods, we speculate a residual plastic deformation component also exists or that insufficient time was allowed for complete strain relaxation.

We examined the strain rate associated with one cycle or steady shear stress and that associated with all subsequent cycles of shear stress. As seen in Figure 5, strain rate increased dramatically from the first cycle to all subsequent cycles. When viscoelastic models were fit to the strain rate data, the deformation time constant for the first cycle was over an order of magnitude higher than the deformation time constant for the subsequent cycles. This decrease in time constant is indicative of an increase in elasticity of the cell or of the polymer network forming the cell cytoskeleton. Such an increase in elasticity could be due to increased crosslinking or a higher degree of polymerization of the network. Alternatively, the change in elasticity could be due to loss of the viscous element (one of the cytoskeletal components) from the cell. Thus the cell would deform to some maximum (probably defined by the membrane, matrix adhesion molecules, and the remaining cytoskeletal filaments) at a rate that is not dampened by the stretching and/or reorganization of the polymer network inside the cell.

We investigated cytoskeletal changes upon application of cyclic shear stress. As seen in Figure 6, cyclic shear stress under conditions which result in significant DNA fragmentation,

also lead to significant loss of polymerized tubulin within the cell. Therefore, it appears that the increase in elasticity of the cell under shear stress is due to the loss of microtubules which resist, in a viscoelastic manner, the deformation of the cell. The role of the length of the recovery period between shear stress periods may be related to the time it takes for the tubulin cytoskeleton to reassemble to resist subsequent deformation. It is believed that injury occurs more readily at high strain rate, therefore the ability of the cytoskeleton to resist cell deformation may play an important role in modulating strain rate of cells exposed to shear stress and protecting cells from injury.

Cytoskeletal involvement in shear stress induced cell injury is not unexpected. A number of experimenters have seen decreased tissue levels of microtubule associated proteins even in mild head injury (Saatman, Hielis). Large (1000 fold) increases in tau, another microtubule binding protein, have been seen in cerebral spinal fluid (Zemlan). Decrease in tissue level microtubule associated proteins and increases in tau in cerebral spinal fluid are consistent with a loss of microtubules associated with head injury. *In vitro*, large changes in cytoskeletal organization after optic nerve stretch experiments are seen (ref). Loss of microtubules are seen even in mild injuries (ref).

In summary, we have examined the relationship between cyclic shear stress, cell strain, cytoskeletal polymerization, and loss of viability in an *in vitro* model of cell injury. We believe the changes in strain rate associated with cyclic shear stress are due to loss of microtubules during shear stress and that the increased strain rate after the first cycle of shear stress may be an important in determining the extent of cell injury with each subsequent cycle of shear stress. Our work should contribute to a better understanding of the mechanism of shear stress and strain

induced neurodegeneration, especially in cases where the stress to the nerve or neuron is cyclical or repetitive.

REFERENCES

1. Margulies, S.S., Thibault, L.E., and Gennarelli, T.A. (1990) J.Biomech. **23**, 823-836.

2. Shauquillo, J., Vilalta, J., Lamarca, J., Rubio, E., Rodriguez-Pazos, M., and Salva, J.A. (1989) Acta Neurochir (Wein) **101**, 149-158.

3. White, B. and Krause, G. (1993) Ann.Emer.Med. **22**, 970-979.

4. Moss, S., Marchbanks, R., Reid, A., Burge, D., and Martin, A. (1989) Zeitschrift fur Kinderchirurgie **44**, 29-31.

5. Urlesberger, B., Muller, W., Ritschl, E., and Reiterer, F. (1991) Child's Nerv.Sys. **7**, 85-87.

6. Yan, D.B., Coloma, F.M., Metheetrairut, A., Trope, G.E., Heathcoat, J.G., and Ethier, C.R. (1994) Br.J.Ophthalmol. **78**, 643-648.

7. Zeimer, R.C. and Chen, K. (1987) Invest.Ophthalmol.Vis.Sci. **28**, 1735-1739.

8. LaPlaca, M.C., Lee, V.M.Y., and Thibault, L.E. (1997) J.Neurotrauma **14**, 355-368.

9. LaPlaca, M.C. and Thibault, L.E. (1997) Ann.Biomed.Eng. **25**, 665-677.

10. Shepard, S.R., Ghajar, J.B.G., Giannuzzi, R., Kufferman, S., and Hariri, R.J. (1991) J.Surg.Res. **51**, 417-424.

11. Murphy, E.J. and Horrocks, L.A. (1993) J.Neurotrauma **10**, 431-444.

12. Gross, G.W., Lucas, J.H., and Higgins, M.L. (1993) J.Neurosci. **3**, 1979-1993.

13. Ellis, E.F., McKinney, J.S., Willoughby, K.A., Liang, S., and Povishock, J.T. (1995) J.Neurotrauma **12**, 325-339.

14. Regan, R.F. and Choi, D.W. (1994) Brain Res. **633**, 236-242.

15. Bird, R.B., Stewart, W.E., and Lightfoot, E.N. (1960) Transport Phenomena, John Wiley & Sons, New York.

16. Simon, S.I. and Schmid-Schönbein, G.W. (1990) Biophys.J. **58**, 319-332.

17. Edwards, M.E. and Good, T.A. (1998) Neurophysiology(in press)

18. Edwards, M.E. and Good, T.A. (1998) Br.J.Ophthalmol.(in press)

19. Triyoso, D.H. and Good, T.A. (1998) Biochem.Biophys.Res.Comm.(in press)

20. Cargill, R.S., II and Thibault, L.E. (1996) J.Neurotrauma **13**, 395-407.

21. Lamb, R.G., Harper, C.C., McKinney, J.S., Rzigalinski, B.A., and Ellis, E.F. (1997) J.Neurochem. **68**, 1904-1910.

22. Edwards, M.E. and Good, T.A. (1998) Ann.Biomed.Eng.(in press)

23. Lagerberg, J.W.M., Kallen, K.-J., Haest, C.W.M., VanStevenick, J., and Dubbleman, T.M.A.R. (1995) Biochim.Biophys.Acta **1235**, 428-436.

24. Onganer, Y. and Quitevis, E.L. (1994) Biochim.Biophys.Acta **1192**, 27-34.

25. Berthiaume, F. and Frangos, J.A. (1994) Biochim.Biophys.Acta **1191**, 209-218.

26. Frangos, J.A., Huang, T.Y., and Clark, C.B. (1996) Biochem.Biophys.Res.Comm. **224**, 660-665.

27. Noris, M., Morigi, M., Donadelli, R., Aiello, S., Foppolo, M., Todeschini, M., Orisio, S., Remuzzi, G., and Remuzzi, A. (1995) Circ.Res. **76**, 536-543.

28. Hsieh, H.J., Li, N.Q., and Frangos, J.A. (1993) J.Cell.Physiol. **154**, 143-151.

29. Triyoso, D.H. and Good, T.A. (1998) J.Physiol.(in press)

30. Levesque, M.J., Nerem, R.M., and Sprague, E.A. (1990) Biomaterials **11**, 702-707.

31. Papadaki, M. and Eskin, S.G. (1997) Biotechnol.Prog. **13**, 209-221.

32. Davies, P.F. (1995) Physiol.Rev. **75**, 519-560.

FIGURE LEGENDS

Figure 1. Schematic diagram of neuroblastoma cell in unstrained and strained configuration. The stretch ratio in direction i, (for i = 1, 2) is define as ratio of the strained length, L_i to the original unstrained length $(L_i)_0$.

Figure 2. Time dependence of strain for differentiated SH-SY5Y clusters of 3 or more cells. Cells were exposed to constant shear for 10 min. Data represent mean ± S.E.M. for n = 4 cells for each shear level. * indicates strains are different with a significance of $p < 0.05$.

Figure 3. Effect of cyclic shear stress on SH-SY5Y cell viability. (A) Cells were exposed to no shear stress (Control), steady shear stress for 90 minutes (1 Cycle), or cyclic shear stress for 90 minutes (6 Cycles) at 10 dynes/cm^2. Extent of cell injury is reported as the percentage of cells with fragmented DNA as measured by the TUNEL assay (solid bars) and as percentage of MTT reduction relative to untreated cells (open bars). In our hands, the MTT assay underreports the extent of cell injury as compared to the TUNEL assay, however comparable trends are observed using either measurement. * indicates result is significantly different from untreated controls $p<0.05$, ** indicates result is significantly different from steady shear stress/1 cycle data $p<0.01$. (B) Cells were exposed to 6 cycles of shear stress at 5 dynes/cm^2 with shear stress times (On) followed by recovery times (Off) as indicated making up each cycle. Cell viability after shear stress is reported as the percent reduction of MTT relative to untreated cells. * indicates result is significantly different from untreated controls $p<0.05$. Data represent means ± S.E.M. for n = 6 – 8 measurements. Significance was determined by Student's t test.

Figure 4. Strain for differentiated SH-SY5Y cells subjected to pulsatile shear profile. Cells were exposed to 15 dyn/cm^2 shear stress for 13 min followed by 2 min of no shear. This cycle was repeated 6 times for a total of 90 min. Grey bars symbolize the beginning of a new 13 min shear period. Open bars designate the 2 min no shear period. Solid (black) bars represent the end of a 13 min shear period. The solid line beneath the time scale indicates periods when shear is applied. Data represent mean ± S.E.M. for n = 10 cells. Inset: Average strain at end, no shear, and beginning of shear cycle. Data represents mean ± S.E.M. for n = 60, 50, and 50 measurements for end of cycle, no shear, and beginning of cycle, respectively. * indicates that strain at beginning and end of cycle are significantly different than strain during no shear period with $p < 0.05$.

Figure 5. Strain as a function of time and cycle number for differentiated SH-SY5Y cells exposed to cyclic shear stress. Circles indicate cell strain during first cycle. Squares indicate strain during all other cycles. Data represent mean ± S.E.M. for $n \geq 4$ cells.

Figure 6. Extent of tubulin polymerization before and after cyclic shear stress. (A) Immunoblot of polymerized tubulin from sheared cells (lane 1), polymerized tubulin from control cells (lane 2), total tubulin from control cells (lane 3), and total tubulin from sheared cells (lane 4). (B) Fraction of polymerized tubulin relative to total tubulin in control and sheared cells as estimated from densitometry of immunoblots.

Initial unstrained state at t = 0

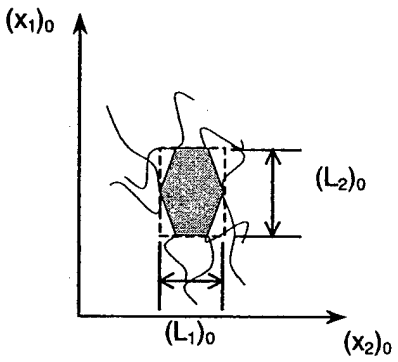

Final strained state at t > 0

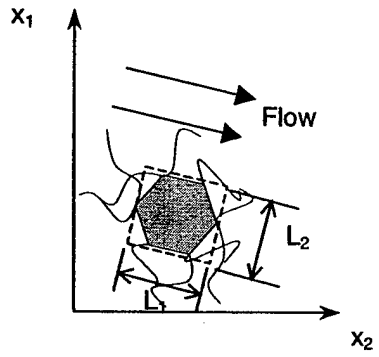

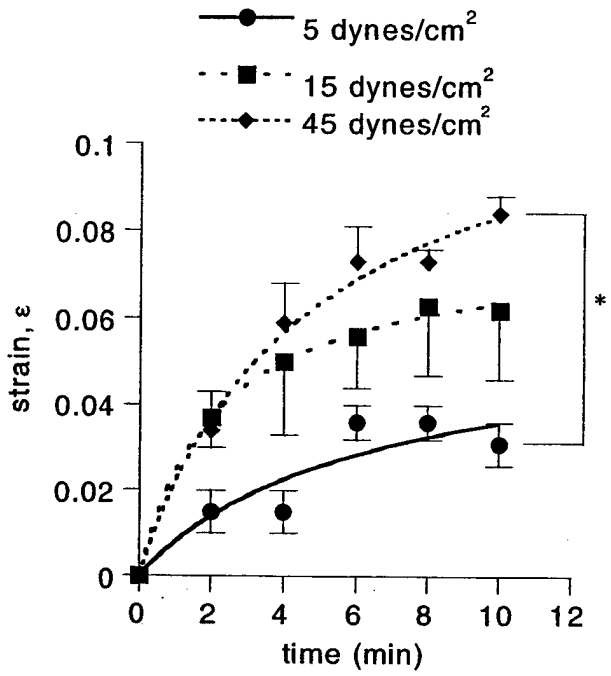
5 dynes/cm2
15 dynes/cm2
45 dynes/cm2
0.1
0.08
0.06
0.04
0.02
0
strain, ε
0
2
4
6
8
10
12
time (min)
*

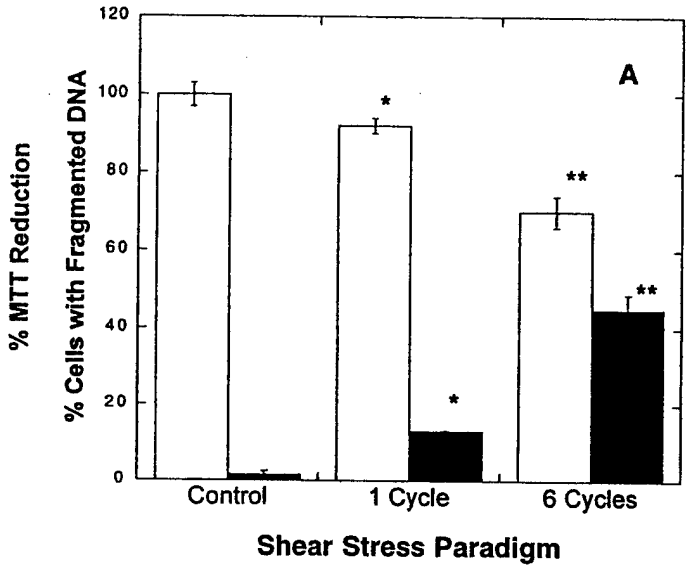
A
% MTT Reduction
% Cells with Fragmented DNA
120
100
80
60
40
20
0
*
*
**
**
Control
1 Cycle
6 Cycles
Shear Stress Paradigm

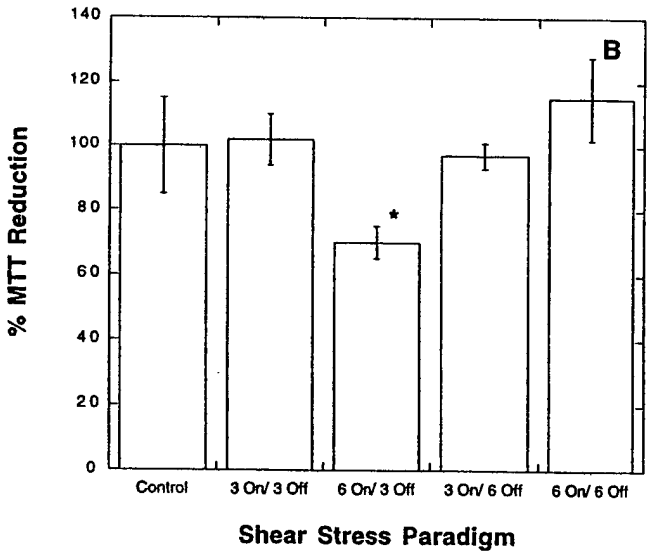
B
% MTT Reduction
140
120
100
80
60
40
20
0
*
Control
3 On/ 3 Off
6 On/ 3 Off
3 On/ 6 Off
6 On/ 6 Off
Shear Stress Paradigm

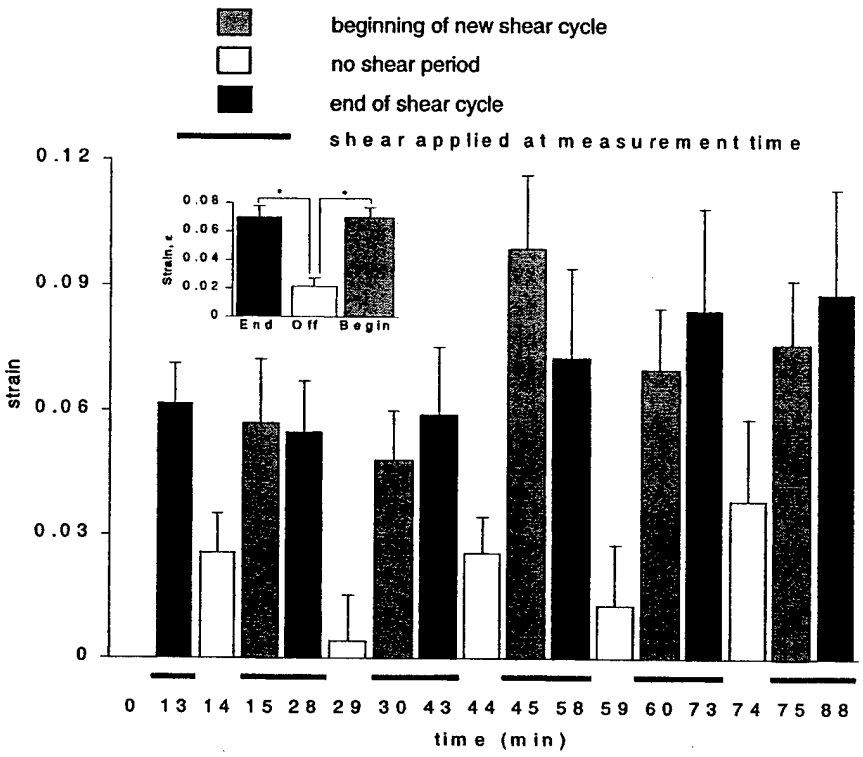
beginning of new shear cycle
no shear period
end of shear cycle
shear applied at measurement time
strain
0.12
0.09
0.06
0.03
0
0 13 14 15 28 29 30 43 44 45 58 59 60 73 74 75 88
time (min)
Strain, ε
0.08
0.06
0.04
0.02
0
End
Off
Begin

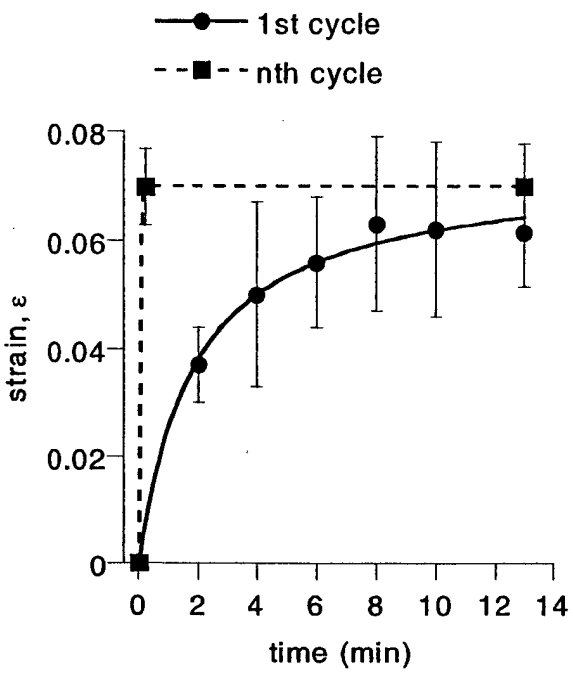
1st cycle
nth cycle
0.08
0.06
0.04
0.02
0
strain, ε
0
2
4
6
8
10
12
14
time (min)

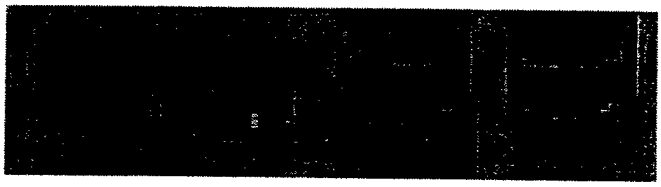

1 2 3 4

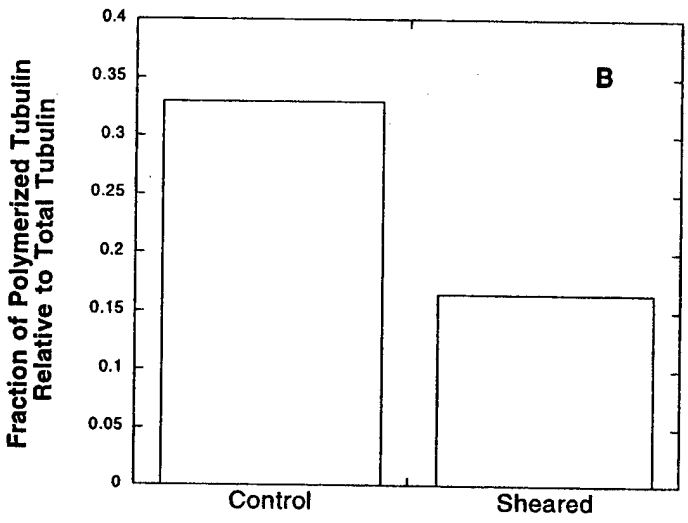
Fraction of Polymerized Tubulin
Relative to Total Tubulin
0.4
0.35
0.3
0.25
0.2
0.15
0.1
0.05
0
B
Control
Sheared

The Role of Nitric Oxide and Calcium in Shear Induced DNA Fragmentation in Human SH-SY5Y Neuroblastoma Cell Line

Dina H. Triyoso and Theresa A. Good

Department of Chemical Engineering

Texas A&M University

College Station, TX 77843-3122 USA

Running Title: NO and calcium in shear induced DNA fragmentation

Corresponding Author:
Theresa Good
Department of Chemical Engineering
337 Zachry
Texas A&M University
College Station, TX 77843-3122
Phone (409) 845-3413
Fax (409) 845-6446
tgood@tamu.edu

Work sponsored by the U.S. Department of the Army and the National Medical Technology Testbed, Inc.

Disclaimer: The view, opinions and /or findings contained in this report are those of the authors and should not be construed as a position, policy, decision, or endorsement of the federal Government or the National Medical Technology Testbed, Inc.

Abstract

Abnormal shear stress and strain, when applied to the central nervous system as during traumatic injury or disease, results in cell death via apoptosis. We have previously shown that shear stress application to neuron-like cells *in vitro* leads to elevated nitric oxide (NO) production and DNA fragmentation. Here we report that antioxidants, an inhibitor of phospholipase C, an NMDA receptor antagonist, and an inhibitor of calcium release from intracellular stores attenuated shear stress induced DNA fragmentation. We show the relationship between NO production and other steps in the apoptotic pathway. This work will contribute to the elucidation of the mechanism of shear stress-induced cell injury and should be relevant to the development of treatments for traumatic injury and disease where the central nervous system is exposed to abnormal stress and strain.

Key Words: shear stress, strain, apoptosis, head injury, glaucoma, *in vitro* model

Introduction

Shear stress and strain are known to be deleterious to central nervous tissue. *In vivo*, high levels of shear stress and high strain rates are associated with traumatic head injury.[17] During glaucoma, the lamina cribrosa deforms with elevated intraocular pressure, producing shear stress and strain on cells in the retina.[36] In both glaucoma and head injury, cell death via apoptosis has been observed.[11,23]

In vitro, shear stress and/or strain applied to neurons and neuron-like cells have been shown to lead to increased intracellular Ca^{2+} concentration, uptake of propidium iodide, and lactate dehydrogenase release.[9,13,14,24,25,30] We have shown, using an *in vitro* model of shear-induced cell injury, that shear stress and strain, applied to differentiated neuroblastoma cells, lead to G protein activation (unpublished results), increased nitric oxide (NO) production, and DNA fragmentation.[30] Here we further examine the mechanism of shear stress and strain induced injury in differentiated SH-SY5Y neuroblastoma cells.

We show that NO and Ca^{2+} play a role in shear stress induced cell injury. We provide evidence that implicates free radical production, the inositol triphosphate pathway, and calcium entry into cells through the N-methyl-d- aspartate (NMDA) channel in the mechanism of shear stress induced DNA fragmentation. Addition of antioxidants and the inhibition of NO production, phospholipase C activation, calcium release from stores, and calcium entry through the NMDA channel all attenuate shear stress induced DNA fragmentation. These results contribute to the development of *in vitro* models of shear stress-induced neuron-like cell injury

and could aid in the design of new therapeutic strategies for the treatment of injury or disease in which the cells of the nervous system are exposed to abnormal stress and strain.

Materials and Methods

Materials

Tissue culture reagents were obtained from GibcoBRL (Grand Island, NY). Methanol free formaldehyde was obtained from Poly Sciences Inc.(Warrington, PA). Dulbecco phosphate buffered saline (PBS) was obtained from Pierce Chemical Co. (Rockford, IL). Apoptosis Detection System, Fluorescein was obtained from Promega (Madison, WI). Annexin V Apoptosis Detection Kit was obtained from R&D Systems (Minneapolis, MN). The lactate dehydrogenase (LDH) diagnostic kit and all other chemicals were purchased from Sigma (St. Louis, MO).

Cell Culture

The human neuroblastoma cell line, SH-SY5Y, a kind gift from Dr. Evelyn Tiffany-Castiglioni, was used for all experiments. The SH-SY5Y cell line is the neuronal subclone derived from SK-N-SH cell line. The cells were cultured in a humidified 5%(v/v) CO_2 air environment at 37°C using minimum essential media supplemented with antibiotics as previously described.[30] Prior to shear experiments cells are plated at a density of 400,000 cells/ml and differentiated in the 60 mm tissue culture dish for 5-7 days by directly adding 10 ng mL^{-1} of NGF-β.

Shear Stress Application

The shear stress apparatus was a modification of a cone and plate viscometer previously described in detail.[30] It consisted of a GlasCol stirrer and motor controller (Terre Haute, IN), and a stainless steel or plexiglass cone (Texas A&M Chemical Engineering machine shop, College Station, TX). The cone had a 5° angle relative to a stationary tissue culture dish containing a layer of SH-SY5Y cells and outside dimensions such that it had 1 mm clearance from the dish edge. The monolayer of cells adherent to the culture dish was exposed to fluid flow by rotating the cone, whose tip contacted the plate, over the surface of the plate. Culture medium filled the space between the cone and the layer of cells. The angular velocity of the cone was directly proportional to the shear stress applied to the fluid above the cell layer. The shear flow of the fluid above the cell layer resulted in a slow or low strain rate deformation of cells.[31] For an applied shear stress of 10 dynes cm^{-2}, a cell strain of approximately 0.06 was achieved within 10 minutes of commencement of rotation of cone.

To generate pulsatile shear stress, the rotating cone was started and stopped automatically such that the cone was rotating for 13 minutes, then stopped for two minutes, repeatedly for a period of 90 minutes. During the 13 minutes "on" period, the cone was rotated at a constant angular velocity. For a shear stress of 10 dynes cm^{-2}, the angular velocity of the cone was controlled at 90 revolutions per minute. Except for the treated and untreated control cells, all cells were exposed to pulsatile shear for 90 minutes at 10 dynes cm^{-2}. The sheared cells were either untreated or treated with various pharmacological agents.

Inhibition of shear induced cell injury

The cell culture medium was changed prior to exposure of cells to shear stress. At times prior to application of shear stress, various pharmacological agents were added to cells to examine their effect on the extent of shear stress induced injury. Agent concentration and time of incubation prior to shear stress application are listed in Table 1.

Cells were subjected to pulsatile shear at 10 dynes cm^{-2} for 90 minutes. Immediately after shear stress application, samples of culture medium were taken for nitric oxide (NO) analysis and cells were prepared for measurement of DNA fragmentation via the TUNEL assay. Control cells were treated identically except for the application of shear.

Nitric oxide measurement

NO formed by cells is rapidly converted to nitrite in cell culture medium. Nitrite present in the culture medium was measured chemiluminescently using a Sievers Nitric Oxide Analyzer 270B (Boulder, CO). 100 μL of sample was injected into the NOA. In an acidic environment, nitrite was reduced by potassium iodide to NO and then transferred to a reaction cell to react with ozone. The light produced by this reaction was detected via a photomultiplier tube. The signal from photomultiplier tube was calibrated against nitrite standards. NO measurements were taken immediately after shear application.

Apoptosis determination

DNA fragmentation was measured using a TdT-mediated dUTP nick end translation (TUNEL) assay kit from Promega (Fitchburg, WI). Cells were permeablilzed, the 3' OH termini

were labeled with fluorescein-12-dUTP, and whole DNA 3'ends were labeled with propidium iodide (PI) according to the procedure outlined for cell suspension with flow cytometry given by the manufacturer with minor modifications. For each measurement, 2-3 million cells (one plate) were used. To prepare cells for the TUNEL assay, the culture medium was removed from the culture dish and trypsin/EDTA was added to gently detach the cell monolayer from the dish. The cell suspension was then centrifuged and washed with phosphate buffer saline (PBS). Afterwards, cells were fixed with methanol free formaldehyde for 20 minutes. Another wash with PBS was performed after fixing the cells. Finally, the cells were permeabilized by adding ethanol. The cells were then stored in –20°C freezer for at least four hours before carrying out the rest of the procedure outlined by the manufacturer.

Results were analyzed on a FACS Caliber flow cytometer (Becton Dickinson) using a 15 mW argon laser at 488 nm excitation wavelength. Emission filters of 530 nm bandpass for green fluorescence (fluorescein labeled dUTP in this case) and 585 nm for red (PI) were used. Electronic compensation was used to prevent bleed through fluorescence. Forward and side light scatter, green fluorescence, and red fluorescence, were collected and analyzed on 30,000 cells/sample with Cellquest software (Becton Dickinson). A positive apoptotic region on the fluorescein-dUTP versus PI histogram was set so that <2% of the non sheared cells (control) were positive for apoptosis. The fraction of cells with fragmented DNA was determined by counting cells with green (fluorescein) fluorescence whose intensity was above a threshold determined from control cells.

The accumulation of phosphatidyl serine (PS) on the external surface of the cell is one of the changes that occur in the cell membrane early in apoptosis. The amount of PS expression

was probed using fluorescently labeled annexin and flow cytometry. Annexin is known to bind preferentially to PS in membranes. The amount of annexin binding to cells, an indication of the relative PS present in the membrane, was determined using the Annexin V Apoptosis Detection kit (R&D Systems, Minneapolis, MN) according to manufacturer's direction. Cells were counter-stained with PI to indicate the relative permeability of the membrane. Cells were detached gently from dish and pelleted by centrifugation at 500g for 10 minutes. Cells were then washed in PBS and pelleted by centrifugation. Afterwards, 100μL of Annexin V Incubation Reagent (containing 0.25μg mL^{-1} annexin and 5μg mL^{-1} PI) was added for every 500,000 cells. The cell suspension was incubated in the dark at 24°C. Samples were analyzed using flow cytometry within 1 hour of preparation for maximal signal. Results were analyzed on the FACS Caliber flow cytometer as described for the TUNEL assay. Threshold levels for annexin positive and PI positive staining were determined from staining of the control cells and are indicated by the vertical and horizontal lines, respectively, on the plot of flow cytometry results. Cells were considered annexin or PI positive if the fluorescence intensity for the marker exceed the preset threshold determined from control cells.

Data analysis

All data presented are expressed as the mean ± the standard error of the mean of n independent determinations. Every independent determination was a unique culture dish exposed to shear and/or pharmacological agent for the specified amount of time. The value of n for each data set is reported in the figure captions. To determine whether two sets of data were significantly different, the student's t test with unequal variance was used. For comparison of multiple data set relative to each other, Duncan's test for multiple comparison was performed

using SAS Statistical Package (Cary, NC). Unless otherwise noted a criteria of $p<0.05$ was employed to determine whether the two sets of data were different.

Results

We have previously reported that shear stress application to differentiated SH-SY5Y cells led to DNA fragmentation that was accompanied by increased G protein and nitric oxide synthase activity.[30] Pertussis toxin, an inhibitor of $G_{o/i}$, attenuated both shear stress induced DNA fragmentation and NO production, indicating a relationship between G protein activation and NO production. In the current work, we examine more closely the role of NO and Ca^{2+} in shear stress induced DNA fragmentation.

As seen in Figure 1, DNA fragmentation in cells (Figure 1A), induced either through shear stress application or addition of sodium nitroprusside (SNP) into the culture medium, is correlated with elevated NO levels measured in the culture medium (Figure 1B). The percentage of cells with fragmented DNA after shear stress application (45±4%) and after SNP addition (36±14%) was significantly greater than that observed in untreated cells (1.9±1.0%) ($p<0.05$). Addition of L-NAME, a NO synthase inhibitor, to cells prior to shear stress application led to a significant reduction in the percentage of cells undergoing DNA fragmentation (7.3±0.4%) relative to sheared cells untreated with the inhibitor ($p<0.05$). NO levels measured in the culture medium of cells that were exposed to shear stress or SNP were significantly greater than NO levels measured in the culture medium of untreated cells ($p<0.03$), while the difference between NO levels of control cells and cells exposed to shear stress in the presence of L-NAME was not significant ($p>0.1$).

Free radicals are known to react with NO to form peroxynitrites, which are harmful to cells.[15] To examine the role of free radical generation in the mechanism of shear induced cell injury, we tested the ability of two antioxidants to protect cells from shear stress induced DNA fragmentation and injury (Figures 2 and 3). Vitamin E (tocopherol) and vitamin C (ascorbic acid) both significantly reduced the fraction of cells with DNA fragmentation relative to untreated sheared cells ($p<0.002$) without significantly reducing the NO level measured in the medium after shear stress application ($p>0.7$) (Figure 2). As seen in Figure 3, representative flow cytometry results from an Annexin assay, cells that were untreated (no shear, no antioxidants) did not uptake propidium iodide nor stain significantly with annexin indicating cell membranes were not permeable and did not express phosphatidylserine on the outer surface, respectively. Cells sheared without pretreatment with an antioxidant stained positively for annexin, but did not uptake propidium iodide indicating that membranes were not permeable but did express phosphatidylserine on their outer surface. The combination of no membrane permeability and phosphatidylserine on the membrane outer surface is typically seen in early apoptosis.[4] Cells sheared in the presence of vitamin E did not uptake propidium iodide and did not stain with annexin. Similar results were obtained when cells are sheared in the presence of vitamin C (data not shown).

G protein activation can lead to increased intracellular calcium concentration, a known mediator of apoptosis in neurons,[37] through phospholipase C (PLC) activation, inositol triphosphate production, and Ca^{2+} release from stores. To examine the role of the inositol phospholipid pathway in shear stress induced cell injury, we blocked PLC activation and Ca^{2+} release from stores using dexamethasone and ryanodine, respectively. As seen in Figure 4A,

incubating cells with dexamethasone and ryanodine significantly reduced the extent of shear stress induced cell injury ($p<0.0001$). As expected, neither compound significantly altered NO production by sheared cells ($p>0.8$) (Figure 4B). Thapsigargin, which affects IP_3 mediated Ca^{2+} release from the endoplasmic reticulum, did not protect cells from shear stress induced injury (data not shown).

The protective effects of blocking calcium entry into the cell are shown in Figure 5A. Shear stress induced DNA fragmentation was significantly reduced in the presence of AP-5 ($p<0.0001$), an NMDA channel antagonist, but not significantly altered in the presence of ω-conotoxin, an L-type voltage gated calcium channel blocker, nifedipine, an N-type channel blocker, or NBQX, an AMPA channel antagonist ($p>0.1$). EGTA, an extracellular calcium chelator, was somewhat protective against shear stress induced DNA fragmentation (31±4 % compared to 45±4% for controls, $p=0.06$). The effect of calcium channel blockers on shear stress induced NO production can be seen in Figure 5B. In contrast to what was observed for modulators of the inositol phospholipid pathway, several agents that reduced calcium entry into cells (AP-5, ω-conotoxin, and EGTA) significantly reduced the level of NO measured in the medium after shear stress application ($p<0.02$).

Discussion

Stress and strain, when applied to cells of the nervous system, are associated with neurodegeneration as occurs during traumatic head injury and glaucoma. Traumatic head injury results in the generation of regions of high shear stress and strain in the cortex. Areas of high

shear stress correspond to areas in the cortex where injury is observed.[17] Apoptosis has been observed in experimental head injury models as well as in postmortem studies of head injury victims.[11,22,27]

During glaucoma, elevated intraocular pressure, associated with vision loss, leads to the compression and displacement of the optic nerve head.[36] Cell injury is greatest at the optic nerve head in regions predicted to have the highest levels of shear stress and strain.[3] Apoptosis has been observed in retinal ganglion cells during experimental glaucoma.[23]

We have shown that shear stress-induced strain applied to differentiated human neuroblastoma cells, SH-SY5Y, leads to cell injury characteristic of apoptosis, consistent with *in vivo* findings.[30] We now endeavor to use the same *in vitro* model to examine the mechanism of shear stress and strain induced apoptosis. These findings may help in elucidating the role of different cell populations (such as neuronal or endothelial cells) in pathology associated with mechanical injury to the nervous system.

There is ample evidence of the importance of NO and calcium in head injury and glaucoma.[2,5,13,14,26] Within seconds after traumatic head injury, extracellular calcium concentrations have been observed to decrease 100 fold, indicating a dramatic rise in intracellular calcium.[20,29] The region of decreased extracellular calcium (and associated increased intracellular calcium) includes the region of high shear stress generated by the injury.[20] Blockade of specific calcium channels, particularly N-type and NMDA receptor channels, has been shown to be neuroprotective in experimental traumatic brain injury.[35]

Nitric oxide has also been implicated in the pathophysiology of traumatic brain injury. As early as 5 minutes after injury, constitutive NO synthase (NOS) activity, localized to

neurons, is elevated in some experimental injury models.[32] Specific inhibition of neuronal NOS has been shown to reduce the injury volume. At 6 hours after injury, tissue NO levels are significantly elevated in the cerebral cortex and brain stem in a diffuse injury model.[28] At 30 to 42 hours after injury, nitrite and nitrate levels, reaction products of NO, are elevated in cerebral spinal fluid (CSF) in human victims of traumatic brain injury.[6] Death after injury is positively correlated with significant CSF increases in nitrite/nitrate levels. At 3 days after experimental injury, inducible NOS activity, localized to astrocytes, is significantly elevated.[33] It appears that NO plays a role in both primary and secondary phases of head injury.

During glaucoma, elevated NO levels in the aqueous humor of patients have been reported.[5] Upregulation of NOS in astrocytes in the vicinity of the lamina cribrosa has been observed, along with evidence of NO toxicity.[18] In addition, there is a variety of evidence that glutamate excitotoxicity, which affects calcium homeostasis, plays a role in glaucoma.[26]

Based on studies *in vivo*, it is clear that in both head injury and glaucoma, NO and calcium play a role in neurodegeneration associated with injury or disease, however, the mechanism by which these signaling molecules lead to pathology has not been elucidated. Through the use of *in vitro* models in which neurons and neuron-like cells are exposed to shear stress and strain analogous to that occurring during injury or disease, a simplified experimental system is available that provides a vehicle with which to examine the mechanism of injury and to screen agents for the treatment of neurodegeneration associated with shear stress and strain.

In other *in vitro* models of shear stress and strain induced injury to neurons, astrocytes, and neuron-like cells, the role of calcium in injury has been implicated. After acute shear stress or stretch induced injury, an increase in intracellular Ca^{2+} has been observed.[13,14,25] Elevated calcium

currents through the NMDA channel contributed to the rise in intracellular calcium .[13,38] In addition, phospholipase activation, free radical formation and mitochondria damage have also been observed.[24,34]

We have shown that differentiated SH-SY5Y cells, a human neuroblastoma cell line, respond to shear stress via increases in nitric oxide level accompanied with DNA fragmentation.[30] We have evidence that pertussis toxin sensitive G protein activation is an early step in the mechanism of shear stress induced injury (unpublished results). Other investigators have discovered that G protein activation is a common early event in the apoptotic pathway.[16] G protein activation can lead to a cascade of intracellular reactions including phospholipase C activation and NO synthase activation. We were interested in establishing the importance of these G protein mediated pathways in shear stress induced DNA fragmentation and cell injury.

Inhibition of NO synthase using L-NAME attenuated shear stress induced DNA fragmentation.[30] This result suggested that high levels of nitric oxide induce cell injury. To confirm that elevated NO could lead to DNA fragmentation in differentiated SH-SY5Y cells, SNP, a nitric oxide donor, was added to SH-SY5Y cells that were not subjected to shear stress. As seen in Figure 1, SNP induced a comparable level of DNA fragmentation as untreated sheared cell, 36±14 versus 45±4%, respectively. In unrelated studies, nitric oxide has been shown to induce apoptosis in cerebellar granule cultures.[15] It should be noted that upon treatment with SNP, cells were subjected to much higher levels of NO extracellularly than was measured in the culture medium from sheared cells. During shear stress induced cell injury, local NO levels may

be much higher than the levels measured in the culture medium, or, more likely, NO production is just one of the many affects of shear stress on SH-SY5Y cells that leads to cell death.

It is known that oxidative stress can induce apoptosis by generation of peroxynitrite resulting from reaction between free radical or reactive oxidative species with NO.[10] We show that the antioxidants vitamin E and vitamin C protect cells from shear stress-induced DNA fragmentation (Figure 2A), and prevent phosphatidyl serine expression on the cell outer membrane surface (Figure 3), two markers of apoptosis. Figure 2B shows that the mechanism by which vitamin E and vitamin C lower DNA fragmentation is independent of nitric oxide formation. We conclude that shear stress leads to oxidative stress in differentiated SH-SY5Y cells. These findings are consistent with other reports that antioxidants are neuroprotective during apoptosis induced by oxidative stress.[8,12]

The level of shear stress-induced DNA fragmentation was lowered in the presence of dexamethasone, a nonspecific phospholipase C (PLC) inhibitor, suggesting that PLC activation participates in the apoptotic mechanism (Figure 4). This is consistent with findings by Wei and coworkers who reported elevated phospholipase C activity during experimental head injury.[34] Phospholipase C causes the breakdown of phosphatidylinositol triphosphate into inositol triphosphate (IP_3) and diacylglycerol. IP_3 induces the release of calcium from intracellular stores. Thapsigargin, which acts on the IP_3 sensitive calcium stores, did not prevent shear stress induced apoptosis (data not shown), however, ryanodine, which inhibits release from calcium sensitive intracellular stores, significantly attenuated shear stress induced cell injury (Figure 4). Ryanodine and dexamethasone had no effect on shear stress-induced NO production, indicating the protective effects of these agents were independent of an NO pathway.

In a number of experimental brain injury models, elevated intracellular calcium concentrations are seen in injured neurons and glia.[13,14,19,24] Loss of calcium homeostasis has been repeatedly linked to neuronal apoptosis. We investigated the source of calcium entry into cells that led to shear stress-induced DNA fragmentation and the source of calcium entry that modulated NO production. Only AP-5 and EGTA significantly reduced shear stress-induced DNA fragmentation (Figure 5A) while most calcium channel antagonists tested inhibited shear stress-induced NO production (Figure 5B). Our results suggest that calcium entry through NMDA channels is involved in shear stress-induced DNA fragmentation while calcium entry through a number of voltage and ligand gated calcium channels modulated NOS activity. Glutamate release and extracellular glutamate accumulation are known to accompany traumatic head injury[21,38] and glutamate receptor antagonists, particularly NMDA receptor antagonists, have been effective at preventing injury in *in vivo* models.[1] In an *in vitro* model similar to ours, blocking the NMDA receptor channel prevented both the intracellular calcium concentration increase and lactate dehydrogenase release that accompanied high strain rate injury.[13] Thus, the protective effect of AP-5, an NMDA receptor antagonist, in shear stress-induced DNA fragmentation, is consistent with the observed role of glutamate in head injury. In addition, increases in NO production seen in shear stress-induced cell injury may be related to glutamate toxicity as NOS inhibitors have been shown to be effective at preventing glutamate toxicity.[7]

We postulate that the shear stress leads to neuron-like cell injury via the mechanism depicted in Figure 6. Shear stress leads to pertussis toxin sensitive G protein activation, which then leads to activation of NOS and phospholipase C. NO produced reacts with other oxidative species in the cell to yield reactive species which lead to DNA fragmentation. Calcium enters the

cell through both voltage and glutamate gated ion channels. Elevated intracellular calcium concentrations further modulate NOS activity and may also lead to calcium induced calcium release from intracellular stores. Calcium entry through NMDA receptor gated channels and release from ryanodine sensitive stores result in DNA fragmentation.

The development of *in vitro* models of injury which capture the salient features of the injury *in vivo* will be important in both the elucidation of the mechanism and the development and screening of new drugs to treat injury or disease in which neurons and neuron-like cells are exposed to shear stress and strain. We believe this work contributes to the development of an *in vitro* model of shear stress-induced cell injury and demonstrates the importance of both NO and calcium in cell injury.

Acknowledgements

This work was supported by a grant from the U.S. Department of the Army and National Medical Technology Testbed, Inc.

References

1. Bemert, H. and Turski, L. Traumatic brain damage prevented by the non-N-methyl-D-aspartate antagonist 2,3-dihydroxy-6-nitro-7-sulfamoylbenzo[f] quinoxaline. PNAS. 93: 5235-5240, 1996.

2. Carriedo, S. G., H. Z Yin, S. L. Sensi, J. H. Weiss. Rapid Ca^{2+} entry through Ca^{2+}-permeable AMPA/Kainate channels triggers marked intracellular Ca2+ rises and consequent oxygen radical production. *J. Neurosci.* 18:7727-7738, 1998

3. Cartwright, M. J. and D. R. Anderson. Correlation of asymmetric damage with asymmetric intraocular pressure in normal tension glaucoma (low tension glaucoma). *Arch. Ophthalmol.* 106:898-900, 1988.

4. Chan A, R. Reiter, S. Wiese, G. Fertig, and R Gold. Plasma membrane phospholipid asymmetry precedes DNA fragmentation in different apoptotic cell models. *Histochemistry & Cell Biology.* 110:553-8, 1998.

5. Chiou, S. H., C. J.Chang, C. K. Chou, W. M. Hsu, J. H. Liu, and C. H. Chiang. Increased nitric oxide levels in aqueous humor of diabetic patients with neovascular glaucoma [letter]. *Diabetes Care.* 22:861-2, 1999.

6. Clark, R., Kochanek, P., Obrist, W., Wong, H., Billiar, T., Wisniewski, S. and Marion, D. Cerebrospinal fluid and plasma nitrite and nitrate concentrations after head injury in humans. *Critical Care Medicine.* 24: 1243-1251, 1996.

7. Dawson, T., Dawson, V., and Snyder, S. Molecular mechanisms of nitric oxide actions in the brain. *Annals of the New York Academy of Sciences.* 738:76-85, 1994.

8. Desole, M. S., L. Sciola, M. R. Delogu, S. Sircana, R. Migheli, and E. Miele. Role of oxidative stress in the manganese and 1-methyl-4-(2'-ethylphenyl)-1,2,3,6-tetrahydropyridine-induced apoptosis in PC12 cells. *Neurochemistry International.* 31:169-176, 1997.

9. Ellis, E., McKinney, J., Willoughby, K., Liang, S., and Povlishock, J. A new model for rapid stretch-induced injury of cells in culture: characterization of the model using astrocytes. *Journal of Neurotrauma.* 12, 325-339, 1995.

10. Ischiropoulos, H., L Zhu, J. Chen, H. M. Tsai, J. C. Martin, C. D. Smith, and J. S. Beckman. Peroxynitrite-mediated tyrosine nitration catalyzed by superoxide dismutase. *Archives of Biochemistry and Biophysics.* 298:431-437, 1992.

11. Kotapka, M. J., D. I. Graham, J. H. Adams, D. Doyle, and T. A. Gennarelli. Hippocampal damage in fatal pediatric head injury. *Neuropathology and Applied Neurobiology.* 19:128-133, 1993.

12. Kruman, I., A. J. Bruce-Keller, D. Bredesen, G. Waeg, and M. P. Mattson. Evidence that 4-hydroxynonenal mediates oxidative stress-induced neuronal apoptosis. *Journal of Neuroscience.* 17:5089-5100, 1997.

13. LaPlaca, M. and L. E. Thibault. Dynamic mechanical deformation of neurons triggers an acute calcium response and cell injury involving the N-methyl-D-aspartate glutamate receptor. *Journal of Neuroscience Research.* 52:220-229, 1998.

14. LaPlaca, M., V. Y. Lee, and L. E. Thibault. An *in vitro* model of traumatic neural injury: loading rate-dependent changes in acute cytosolic calcium and lactate dehydrogenase release. *Journal of Neurotrauma.* 14:355-368, 1997.

15. Leist, M, E. Fava, C. Montecucco, and P. Nicotera. Peroxynitrite and nitric oxide donors induce neuronal apoptosis by eliciting autocrine excitotoxicity. *European Journal of Neuroscience.* 9:1488-1498, 1998.

16. Lin , S Z, G. M.Yan, K. E. Koch, S. M. Paul, and R. P. Irwin Mastoparan-induced apoptosis of cultured cerebellar granule neurons is initiated by calcium release from intracellular stores. *Brain Research.* 771:184-95, 1997.

17. Margulies, S., L. Thibault, and T. Gennarelli. Physical model simulations of brain injury in the primate. *Journal of Biomechanics.* 23, 823-836, 1990.

18. Neurfeld, A. Nitric Oxide: A potential mediator of retinal cell damage in glaucoma. *Survey of Ophthalmology.* 43:S129-S135, 1999.

19. Nilsson, P., L. Hillered, Y. Olsson, M. J. Sheardown, and A. J. Hansen. Regional changes in interstitial K^+ and Ca^{2+} levels following cortical compression contusion trauma in rats. *Journal of Cerebral Blood Flow & Metabolism.* 13:183-1992.

20. Nilsson, P., Laursen, H., Hillered, L., and Hansen, A. Calcium movements in traumatic brain injury: the role of glutamate receptor-operated ion channels. *Journal of Cerebral Blood Flow and Metabolism.* 16: 262-270, 1996.

21. Palmer, A., Marion, D., Botscheller, M., Swedlow, P., Styren, S., and DeKosky, S. Traumatic brain injury-induced excitotoxicity assessed in a controlled cortical impact model. *Journal of Neurochemistry*. 61: 2015-2024, 1993.

22. Pohl, D., P. Bittigau, M. J. Ishimaru, D. Stadthaus, C. Hubner, J. W. Olney, L. Turski, and C. Ikonomidou. N-Methyl-D-aspartate antagonists and apoptotic cell death triggered by head trauma in developing rat brain. *Proceedings of the National Academy of Sciences of the United States of America*. 96, 2508-13, 1999.

23. Quigley, H. A., R. W. Nickells, L. A. Kerrigan, M. E. Pease, D. J. Thibault, & D. J. Zack. Retinal ganglion cell death in experimental glaucoma and after axotomy occurs by apoptosis. *Investigative Opthalmology & Visual Science*. 36:774-786, 1995.

24. Rzigalinski, B. A., J. T. Weber, K. A. Willoughby, and E. F. Ellis. Intracellular free calcium dynamics in stretch-injured astrocytes. *Journal of Neurochemistry*. 70:2377-2385, 1998.

25. Rzigalinski, B., S. Liang, J. McKinney, K. Willoughby, and E. Ellis. Effect of Ca^{2+} on in vitro astrocyte injury. 68, 289-296, 1997.

26. Schumer, R. A., S. M. Podos. The nerve of glaucoma. *Archives of Ophthalmology*. 112:37-44, 1994

27. Shah, P. T., Yoon, K. W., Xu, X. M, and Broder, L. D. Apoptosis mediates cell death following traumatic injury in rat hippocampal neurons. *Neuroscience*. 79: 999-1004, 1996.

28. Sharma, A., Misra, M., Prat, R., Alden, K., Sam, A., Markiv, V., Dujovny, M., and Ferguson, J. A differential response of diffuse brain Injury on the concentrations of

endothelins and nitric oxide in the plasma and brain regions of rats. Neurological Research. 20: 632-636, 1998.

29. Stokes, B. T., P. Fox, and G. Hollinden. Extracellular calcium activity in the injured spinal cord. *Exp. Neurology.* 80:561-572,1983

30. Triyoso, D H, and T. A. Good. Pulsatile shear stress leads to DNA fragmentation in human SH-SY5Y neuroblastoma cell line. *Journal of Physiology.* 515: 355-365, 1999.

31. Triyoso, D H, M. E. Edwards, and T. A. Good. Low Strain Rate Leads to Cellular Injury Consistent with Apoptosis in Differentiated SH-SY5Y Cells. *Journal of Neurotrauma.* (submitted).

32. Wada, K., Chatzipanteli, K., Busto, R., and Dietrich, W. Role of nitric oxide in traumatic brain injury in the rat. *Journal of Neurosurgery.* 89: 807-818, 1998.

33. Wada, K., Chatzipanteli, K., Kraydieh, S., Busto, R., and Dietrich, W. Inducible Nitric Oxide Synthase Expression after Traumatic Brain Injury and Neuroprotection with Aminoguanidine Treatment in Rats. *Neurosurgery.* 43: 1427-1436, 1998.

34. Wei, E. P., R. G. Lamb, and H. A. Kontos. Increased phospholipase C activity after experimental brain injury. *J. of Neurosurg.* 56:695-698, 1982.

35. Xiong, Y., Peterson, P., Verweij, B., Vinas, F., Muizelaar, J., and Lee, C. Mitochondrial dysfunction after experimental traumatic brain injury: combined efficacy of SNX-111 and U-101033E. *Journal of Neurotrauma.* 1: 531-544, 1998.

36. Yan, D., Coloma, F., Metheetrairut, A., Trope, G., Heathcoat, J., & Ethier, C. Deformation of the lamina cribrosa by elevated intraocular pressure. *British Journal of Ophthalmology.* 78, 643-648, 1994.

37. Yan, G. M., S. Z. Lin, R. P. Irwin, and S. M. Paul. Activation of G proteins bidirectionally affects apoptosis of cultured cerebellar granule neurons. *Journal of Neurochemistry.* 65:2425-2431, 1995..

38. Zhang, L, Rzigalinski, B., Ellis, E., and Satin, L. Reduction of voltage-dependent Mg2+ blockade of NMDA current in mechanically injured neurons. *Science.* 274: 1921-1923, 1996.

Table 1. Pharmacological Agents Used

Agent (abbreviation)	**Concentration**	**Incubation Time** (hours)
D-(-)-2-amino-5-phosphonovaleric acid (AP-5)	50 μM	0
Ascorbic Acid (Vit C)	3 mM	0.025
Dexamethasone (Dex)	1 μM	16
Ethylene x glycol-bis(beta-aminoethyl ether)-N, N,N',N'-tetraacetic acid (EGTA)	1 mM	1.5
L $N^{(G)}$-nitro-L-arginine-methyl ester (L-NAME)	1 mM	1.5
1,2,3,4-tetrahydro-6-nitro-2,3-dioxo-benzo(f)quinoxaline-7-sulfonamide (NBQX)	10 μM	0
Nifedipine	1 μM	0.25
Ryanodine	200μM	0.25
Sodium Nitroprusside (SNP)	10 mM	5
Thapsigargin (TG)	25nM	0.25
Tocopherol (Vit E)	1 mM	1.5
ω-Conotoxin	0.4 μM	0

Figure Legends

Figure 1a. NO induced DNA fragmentation. Cells were exposed to no shear, no shear but in the presence of SNP, shear stress in the absence of any inhibitors or additives, and shear stress in the presence of L-NAME. The percentage of cells with fragmented DNA was measured immediately after shear stress application or, in the case of no shear, 5 hours after SNP addition to the culture medium. Data are presented as the mean ± the standard error of the mean of n independent determinations, where the error bars represent the standard error of the mean. n equals 9 for unsheared untreated control, 3 for unsheared treated with SNP, 7 for sheared cells without inhibitor, and 5 for sheared cells treated with L-NAME. ** refers to the significance of the result relative to unsheared untreated control cells ($p<0.001$).

Figure 1b. NO level in the presence and absence of NO inhibitors. NO concentrations reported were obtained from nitrite concentrations measured in the culture medium immediately after shear stress application or immediately after SNP addition to the culture medium. n equals 11 for unsheared untreated control, 3 for unsheared treated with SNP, 12 for sheared cells without inhibitor, and 5 for sheared cells treated with L-NAME. *** and * refer to the significance of the result relative to unsheared untreated control cells ($p<0.0001$ and $p<0.05$, respectively).

Figure 2a. Effect of antioxidants on shear stress induced DNA fragmentation. Cells were either untreated (None), preincubated with vitamin E (Vit E) or preincubated with vitamin C (Vit C). Solid bars represent cells exposed to shear stress. Hatched bars represent cells treated identically except for the application of shear stress. The percentage of cells with fragmented DNA was measured immediately after shear stress application. n equals 9 for unsheared untreated control, 9 for sheared cells without inhibitor, and 3 for all others. ** refers to the significance of the result relative to sheared untreated control cells ($p<0.001$).

Figure 2b. Effect of antioxidants on shear stress induced NO accumulation in culture medium. NO concentrations reported were obtained from nitrite concentrations measured in the culture medium immediately after shear stress application. n equals 11 for unsheared untreated control, 12 for sheared untreated control, and 3 for all others.

Figure 3. Representative flow cytometry results of assay for phosphatidylserine on cell surface. X axis represents fluorescence intensity of fluorescein labeled annexin and indicates the relative amount of phosphatidylserine in the membrane available for binding. Y axis represents fluorescence intensity of propidium iodine and indicates the relative permeability of the membrane. (a) unsheared control cells, (b) sheared cells untreated with an antioxidant, (c) sheared cells treated with vitamin E.

Figure 4a. Effect of inhibitors of the inositol phospholipid pathway on shear stress induced DNA fragmentation. Solid bars represent cells exposed to shear stress. Hatched bars represent cells treated identically except for the application of shear stress. n equals 9 for unsheared untreated control, 7 for sheared untreated control, and 3-4 for all others. * refers to the significance of the result relative to untreated sheared control cells ($p<0.05$).

Figure 4b. Effect of inhibitors of the inositol phospholipid pathway on shear stress induced NO accumulation in culture medium. n equals 11 for unsheared untreated control, 12 for sheared untreated control, and 3-4 for all others

Figure 5a. Effect of inhibition of calcium entry from extracellular space on shear stress-induced DNA fragmentation. n equals 9 for unsheared untreated control, 7 for sheared untreated control, and 3-4 for all others. *** and * refer to the significance of the result relative to untreated sheared control cells ($p<0.0001$ and $p<0.06$, respectively).

Figure 5b. Effect of inhibition of calcium entry from extracellular space on shear stress-induced NO accumulation in culture medium. n equals 11 for unsheared untreated control, 12 for sheared untreated control, and 3-4 for all others. * refers to the significance of the result relative to untreated sheared control cells ($p<0.05$).

Figure 6. Proposed mechanism of the role of nitric oxide and calcium in shear stress-induced DNA fragmentation.

a

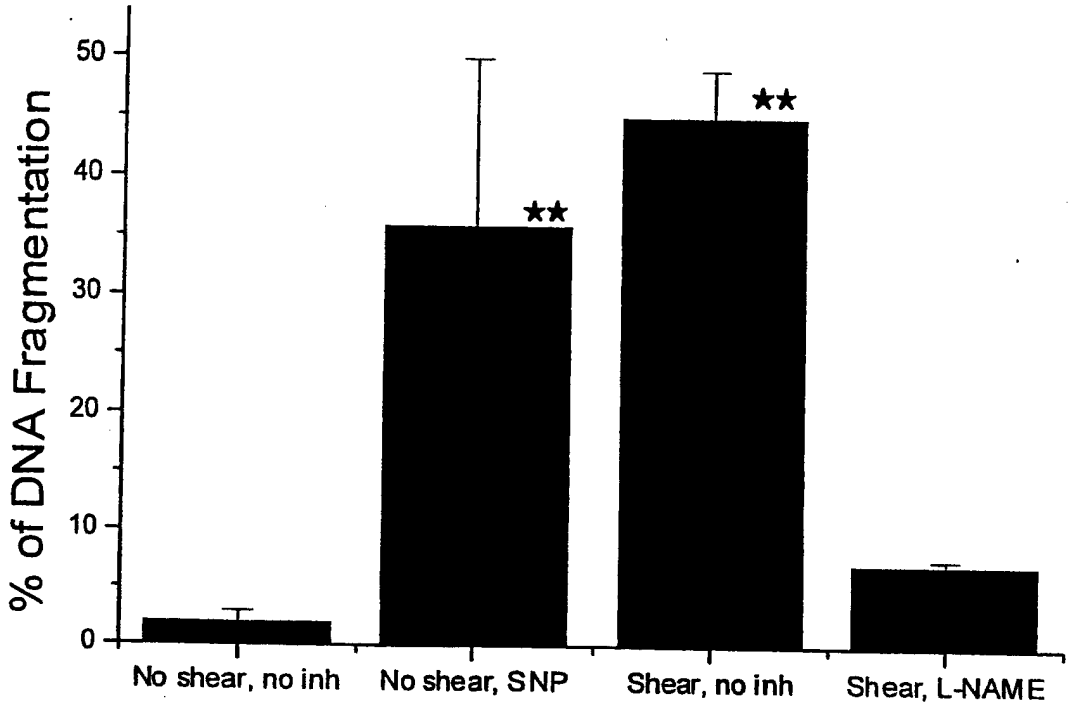
% of DNA Fragmentation
50
40
30
20
10
0
**
**
No shear, no inh
No shear, SNP
Shear, no inh
Shear, L-NAME

b

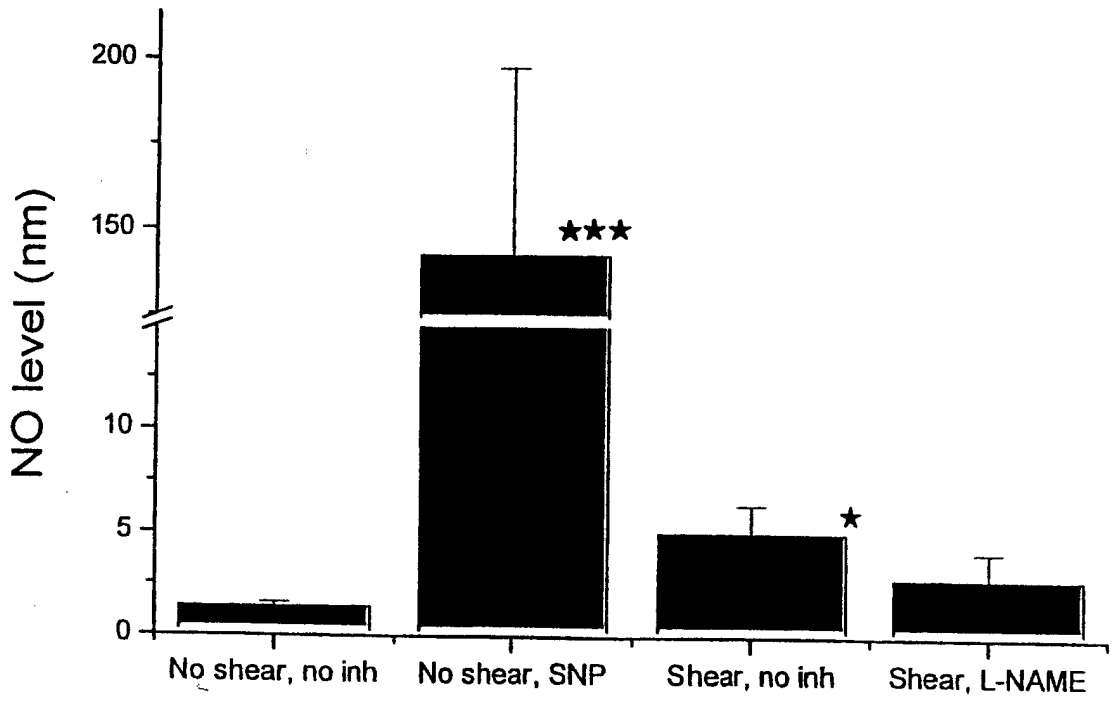
NO level (nm)
200
150
10
5
0
***
*
No shear, no inh
No shear, SNP
Shear, no inh
Shear, L-NAME

a

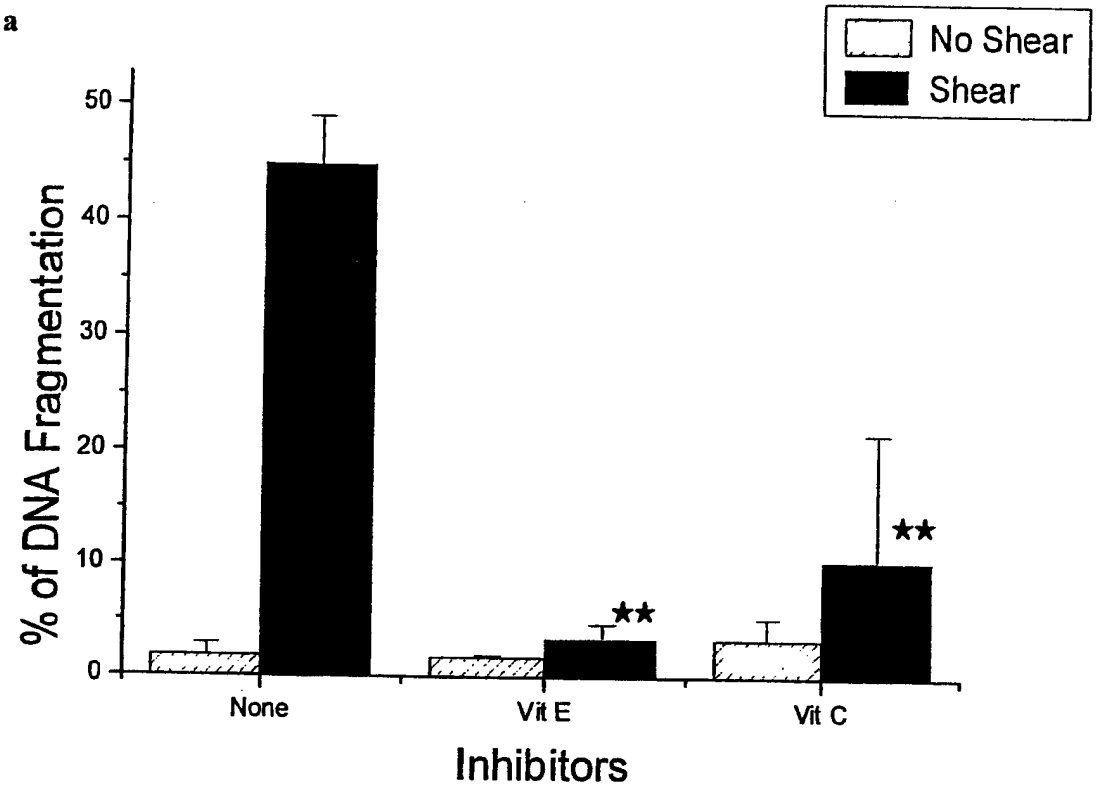
No Shear
Shear
% of DNA Fragmentation
50
40
30
20
10
0
**
**
None
Vit E
Vit C
Inhibitors

b

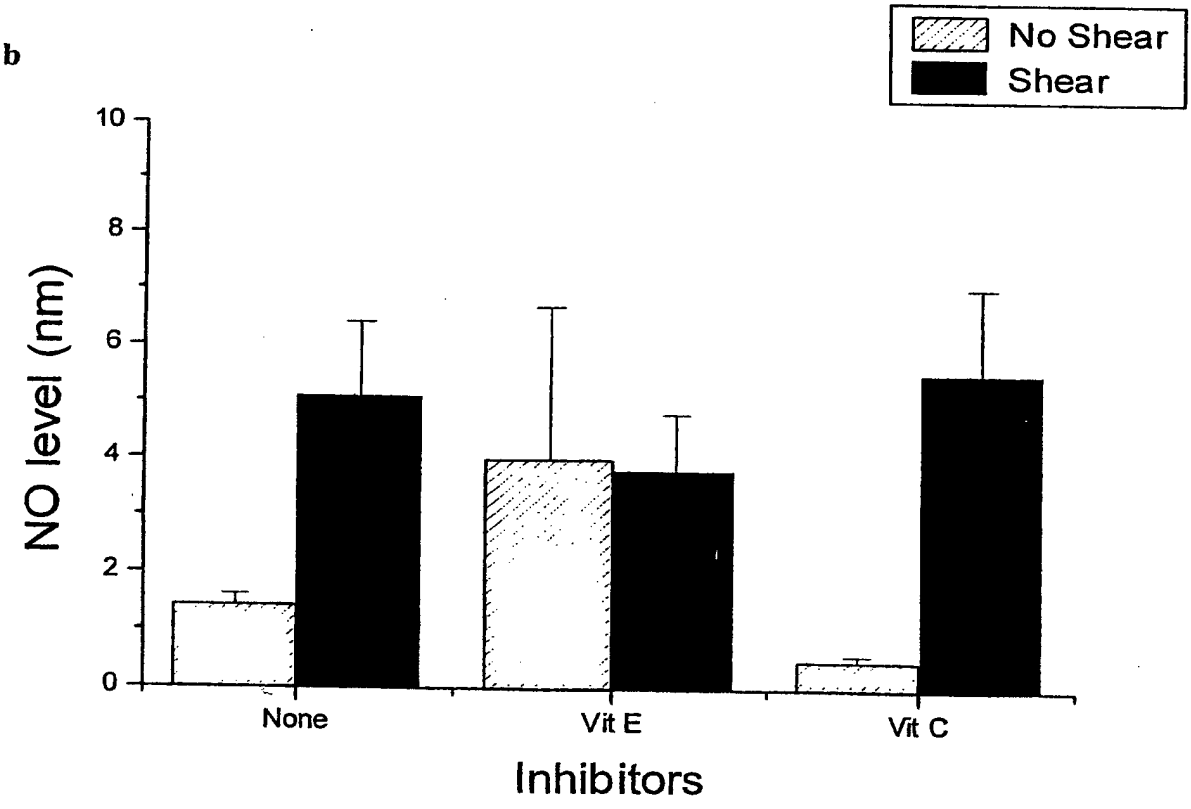
No Shear
Shear
NO level (nm)
10
8
6
4
2
0
None
Vit E
Vit C
Inhibitors

a

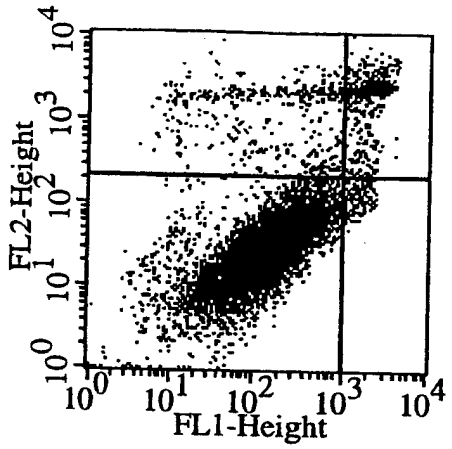
FL2-Height
FL1-Height
10^0
10^1
10^2
10^3
10^4

b

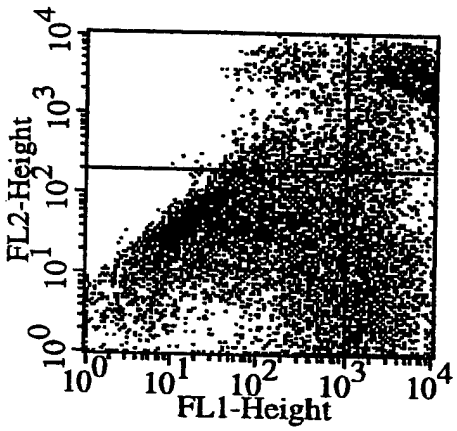
FL2-Height
FL1-Height
10^0
10^1
10^2
10^3
10^4

c

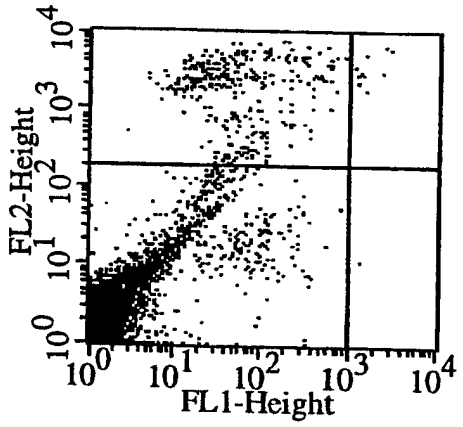
FL2-Height
FL1-Height
10^0
10^1
10^2
10^3
10^4

a

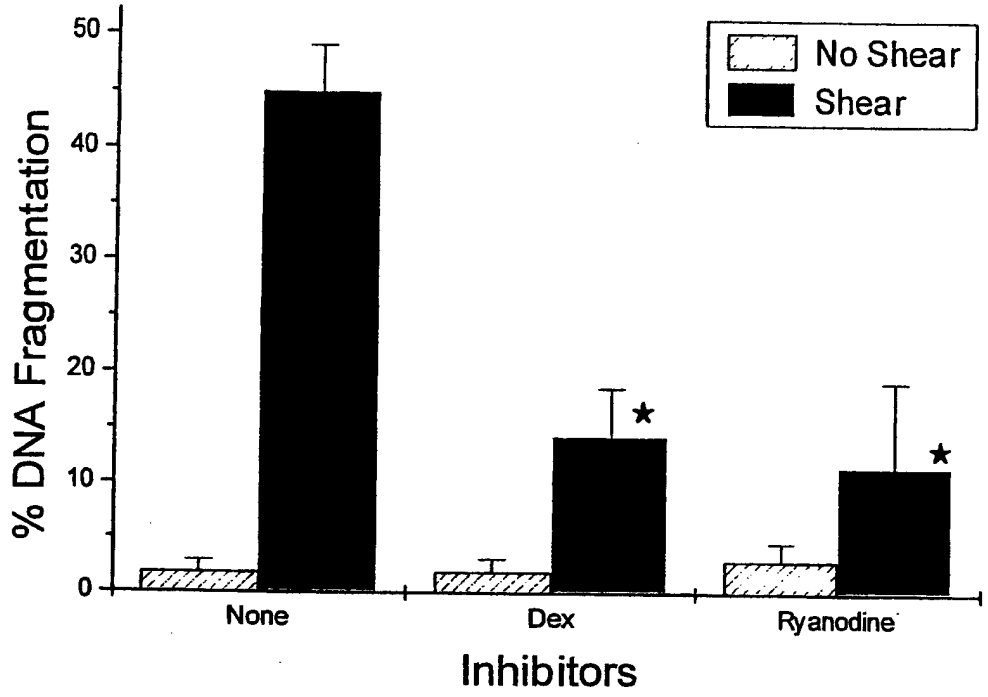
50
40
30
20
10
0
% DNA Fragmentation
No Shear
Shear
★
★
None
Dex
Ryanodine
Inhibitors

b

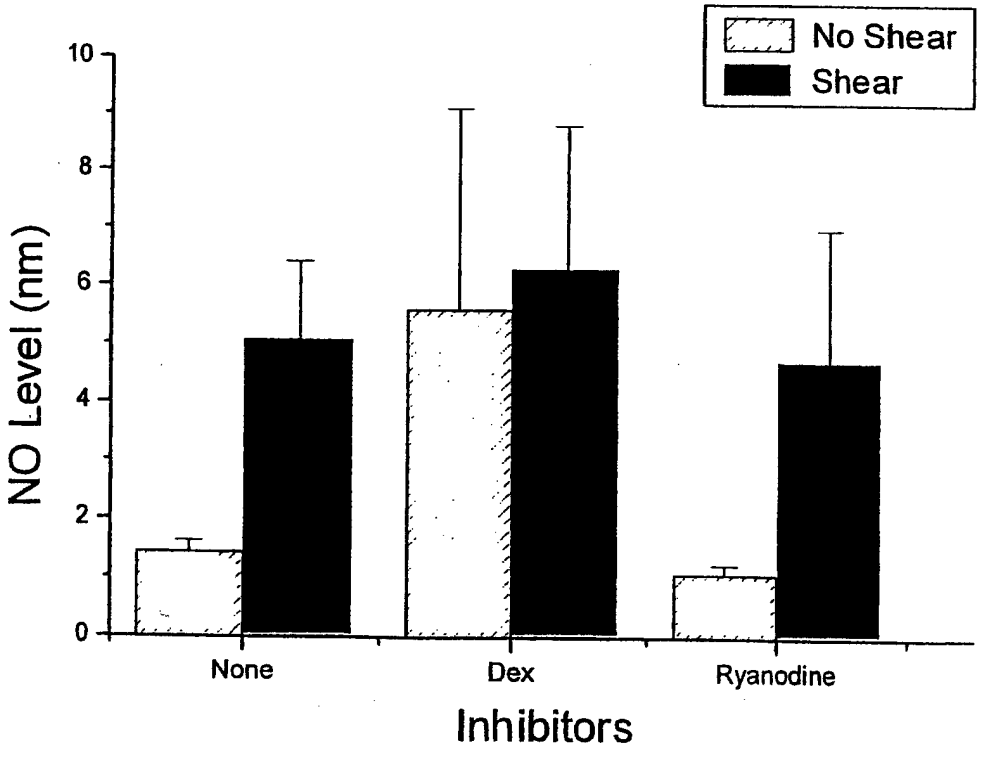
10
8
6
4
2
0
NO Level (nm)
No Shear
Shear
None
Dex
Ryanodine
Inhibitors

a

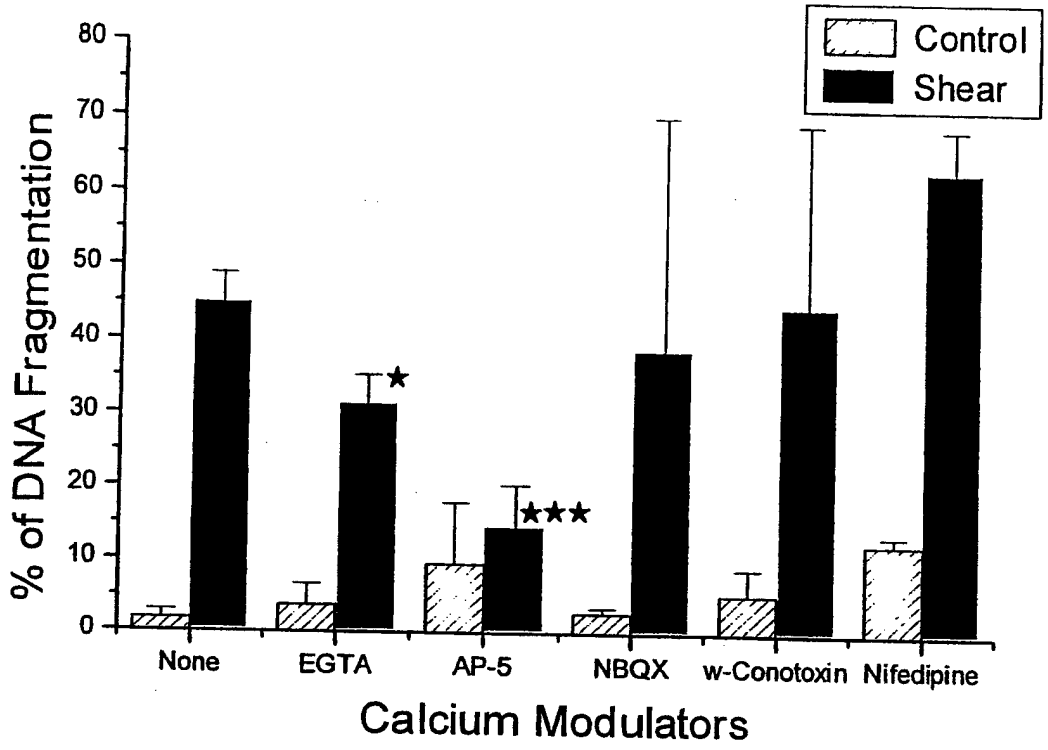
Control
Shear
% of DNA Fragmentation
80
70
60
50
40
30
20
10
0
★
★★★
None
EGTA
AP-5
NBQX
w-Conotoxin
Nifedipine
Calcium Modulators

b

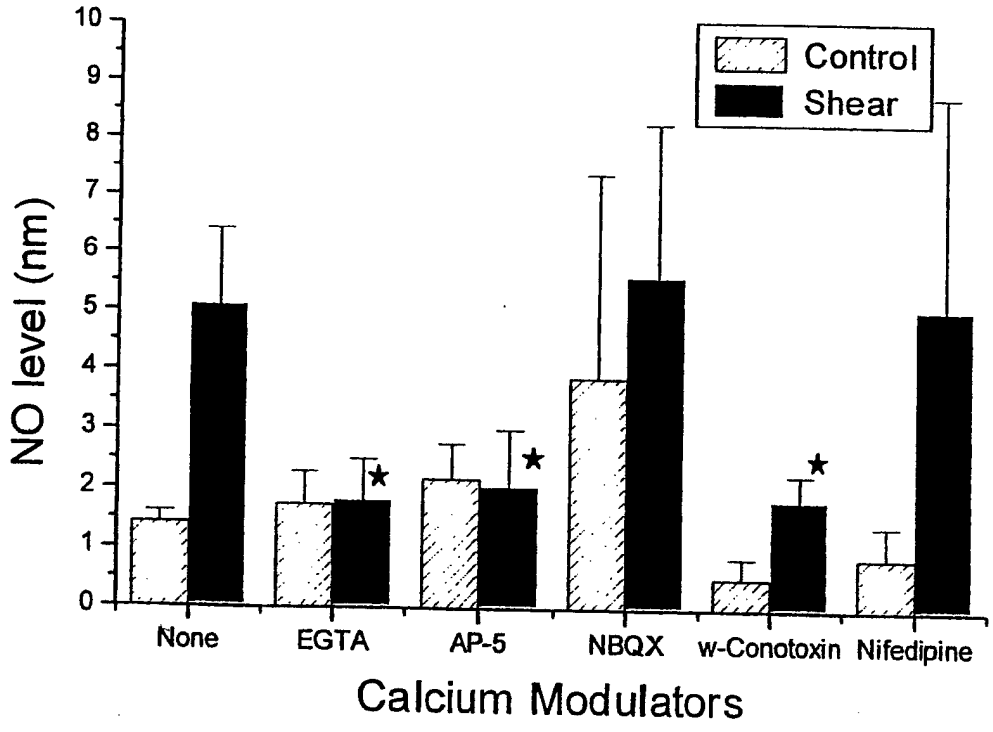
Control
Shear
NO level (nm)
10
9
8
7
6
5
4
3
2
1
0
★
★
★
None
EGTA
AP-5
NBQX
w-Conotoxin
Nifedipine
Calcium Modulators

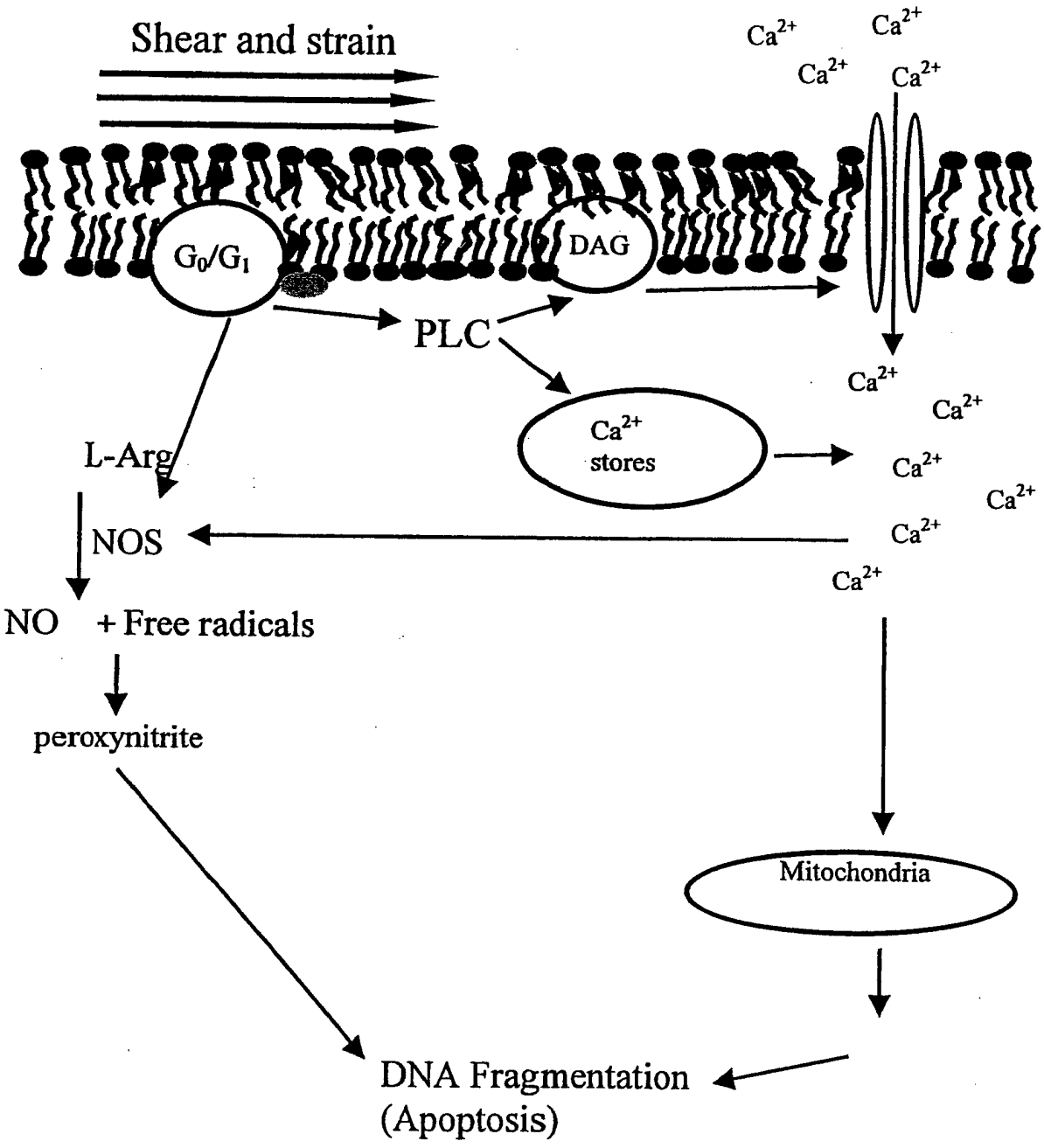
Shear and strain
Ca^{2+}
Ca^{2+}
Ca^{2+}
Ca^{2+}
G_0/G_1
DAG
PLC
Ca^{2+}
Ca^{2+}
Ca^{2+}
stores
Ca^{2+}
Ca^{2+}
L-Arg
NOS
Ca^{2+}
Ca^{2+}
NO + Free radicals
peroxynitrite
Mitochondria
DNA Fragmentation
(Apoptosis)

To: Lydia Pearson, Contracts Administrator

From: Theresa Good
(979) 845-3413 (phone)
(979) 854-6446 (fax)
tgood@tamu.edu

5/10/00

MAY 12 2000

ORIGINAL

Subject: Final Progress Report, Year 1
Cooperative Agreement # DAMD17-97-2-7016
Subagreement #027-FY98-TEES-GOOD
In Vitro Model of Mechanical Force Induced Neurodegeneration

Date: May 10, 2000

Period of Report: 4/1/99-4/1/00

Introduction

Head injury occurs at an incidence of about 200/100,000 population (1). In 1992, over 5000 individuals in the US military system were treated for head injuries with a cost of about $43 million (2). Life long costs of support services, lost wages, and continued medical treatment can easily exceed $1,000,000 per person (3). We proposed to develop an *in vitro* model of mechanical force induced neurodegeneration which could be used to examine the mechanism of neurodegeneration associated with head injury and screen drugs for the treatment of head injury. The development of an early intervention or treatment after injury, which would result in the reduction of neurological deficits, could present a great savings both to the military and the population at large.

Summary of Project Objectives for Year 1 (4/99-4/00):

We had proposed: **1)** to develop an **in vitro model of mechanical force induced neurodegeneration** which is appropriate for the use in studying traumatic head injury. We proposed to modify an existing shear stress apparatus and examine the relationship between shear stress, strain, strain rate and cellular injury. We also proposed to design, construct, and test a novel apparatus which would apply a controlled strain to cells without the application of fluid shear stress. **2)** to begin to investigate **the mechanism of shear and/or strain induced neuronal apoptosis** and **identify inhibitors of mechanical force induced apoptosis.** We proposed to use a variety of pharmacological agents to examine the role of calcium, glutamate, and nitric oxide in strain induced cell injury. We proposed to examine the effects of strain on protein synthesis and cytoskeletal rearrangements. We also proposed to examine the ability of compounds to attenuate injury, especially when delivered after the injury as such compounds would have greater clinical relevance.

Progress Towards Specific Aims of NMTB Project Awarded 4/99:

We have made substantial progress towards achieving a number of the aims of the project. **Towards completion of specific aim 1,** we have examined the stress-strain relationship in a differentiated neuroblastoma cell line (SH-SY5Y) using a modified cone and plate viscometer and begun to relate strain and strain rate to cellular injury using the device. Understanding and controlling the strain and strain rate of cells in the *in vitro* model developed will be essential if the model is to be useful in examining the mechanism of and finding new treatments for traumatic injury. In the current apparatus (Figure 1), a uniform shear field is generated in a culture dish via rotation of a precision machined cone above a cell monolayer. Tissue culture medium filled the space between the cone and cell layer. Viscous flow of the tissue culture medium generated the shear stress on the surface of the cells.

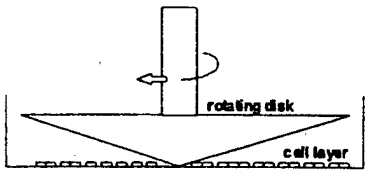

Figure 1. Controlled Shear Apparatus. The design is a modification of a standard cone and plate viscometer. The bottom plate is a polystyrene tissue culture dish upon which an adherent cell layer

is grown. The cone is made of stainless steal and has an angle of 5 degrees from the bottom plate. Culture medium fills the space between the cone and plate. The rate of rotation of the cone is controlled via a precision motor controller. The tip of the cone touches the plate and displaces approximately 1% of the cells in the plate.

Strain, rather than shear stress, may be the more significant determinant of cell injury. Based on mathematical models of traumatic brain injury, shear stresses in cortical tissue are estimated to be on the order of 10^5 dynes/cm^2. Cell strains, on the other hand, are estimated to be closer to 10% of the original cell size. We therefore measured, using fluorescence video microscopy, the cell strain resulting from shear stress applied in our device. We found that the shear stress resulted in a controlled and reproducible strain being applied to cells. We were then able to manipulate the strain applied to cells via a relatively simple device. The relationship between shear stress and observed cell strain can be seen in Figure 2.

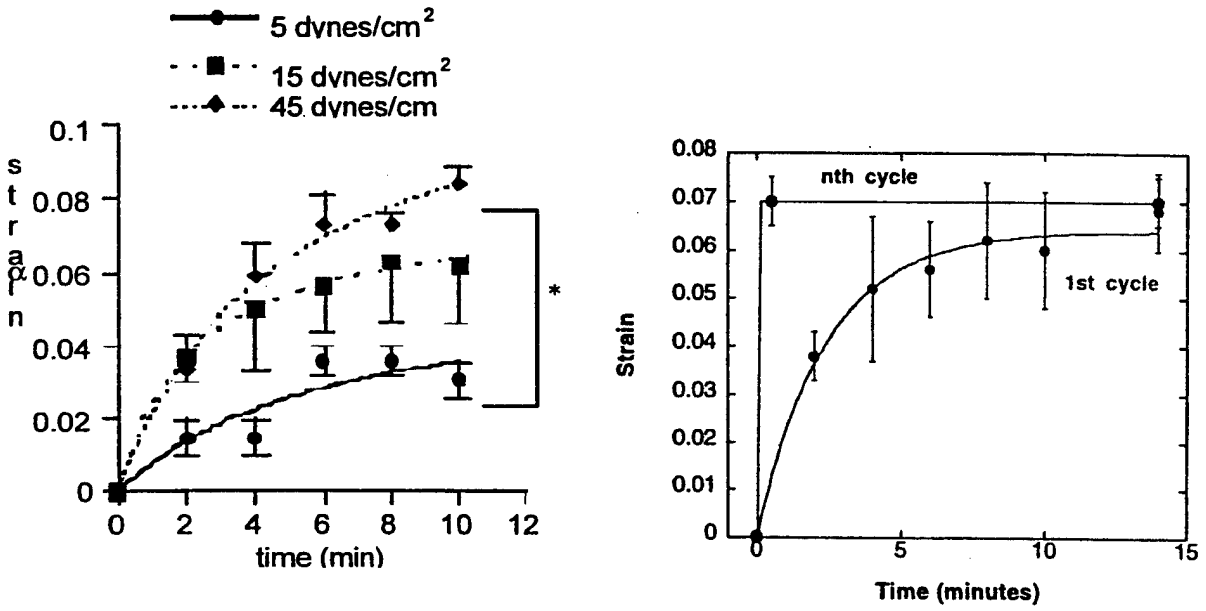

Figure 2 (right). Cell strain as a function of time at different shear stress levels. Experiments were performed in differentiated human neuroblastoma (SH-SY5Y) cells. Strain was measured by staining cells with a fluorescent dye (MC540) which preferentially binds to membranes. The cells were imaged on a Zeiss Axovert 135 fluorescent microscope. The cone and plate viscometer was mounted above the stage of the microscope and images of the cells were captured automatically during application of shear stress. The maximum strain observed for a given shear stress occurred within the first 10 minutes of shear stress application. After shear stress is stopped, cells return to original unstrained dimensions within 2 minutes. * indicates that strains are significantly different $p<0.05$, $n=4$ for each point, error bars represent standard error of the mean.

Figure 3 (left). Strain memory for first and nth shear stress cycle. Cell were exposed to 15 dyn/cm^2 shear stress cyclically. Cell strain was measured as a function of time for each cycle. Circles indicate cell strain during first cycle. Squares indicate strain during all other cycles. Data represent mean ± S.E.M. for $n \geq 4$ cells.

We observed that cells returned to close to their original dimension upon termination of shear stress. The return to original dimension occurred within the two minute "off" period of the shear stress apparatus. During the first application of shear stress to cells, maximum cell strain was observed after 10 minutes of shear stress application. However, as seen in Figure 3, during subsequent shear stress application, maximum strain was observed within the first minute of shear stress application. The viscoelastic behavior of the cell observed in Figure 3 resemble the viscoelastic behavior of a polymer. The retardation time of the polymer would describe the relationship between strain and time seen in Figure 2. The reduction in retardation time from the first cycle to the nth cycle, seen in Figure 3, is characteristic of an increase in the fluid nature of the polymer, possibly due to a loss in crosslinking or orientation of the polymer (cytoskeleton?) network within the cell.

In order to test the hypothesis that shear stress leads to changes in the cell cytoskeleton, we performed experiments in which we examined the degree of tubulin polymerization before and after application of shear stress. As seen in Figure 4, about half of the polymerized tubulin within the cell was lost after application of shear stress.

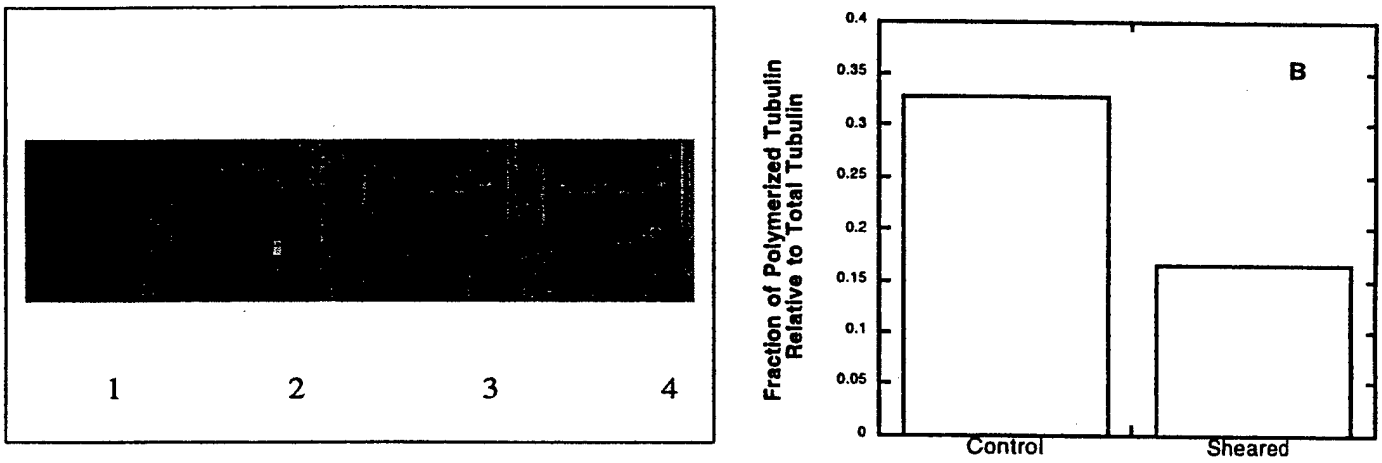

Figure 4. Extent of tubulin polymerization before and after cyclic shear stress. (A) Immunoblot of polymerized tubulin from sheared cells (lane 1), polymerized tubulin from control cells (lane 2), total tubulin from control cells (lane 3), and total tubulin from sheared cells (lane 4). (B) Fraction of polymerized tubulin relative to total tubulin in control and sheared cells as estimated from densitometry of immunoblots.

We found that cyclic injury was significantly more damaging to cells than steady injury of the same magnitude and duration. Using differentiated SH-SY5Y cells, we have shown that 46±8% of cells exposed to 90 minutes of cyclic shear stress (6 cycles) have fragmented DNA indicative of apoptosis immediately after shear stress application. Only 18±5 % of cells exposed to constant shear stress (1 cycle) had fragmented DNA. Less that 2% of unsheared control cells had similar evidence of DNA fragmentation and apoptosis. Cell survival decreased as the number of cycles of applied stress/strain was increased. Thus, not only is stress, strain, and strain rate important to consider in cell injury, but also the periodicity of the injury may be very important. This could have

implications, not only for head injury, but also for repetitive trauma to the peripheral nervous system.

We have modified the proposed design of a strain apparatus which could be used to deform cells at a controlled strain rate. The device, depicted in Figure 5, consists of Flexcell elastic culture dishes which are deformed using a high performance vacuum pump. The extent and rate of deformation of the elastic substrate are controlled by a pressure transducer/controller, and software from the control manufacturer. The components of the system have been purchased and a prototype has been assembled. We are beginning to test the system performance, both in terms of ability to culture cells on the elastic culture dish, which is somewhat problematic, and measuring strain rate obtained in the device.

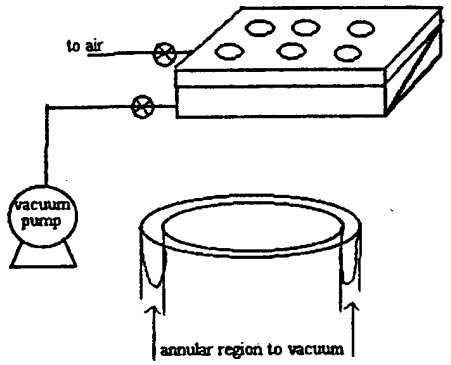

Figure 5. Strain Apparatus. A vacuum pump is used to deform the bottom surface of elastic culture dishes (as seen in detail of one well). Annular region is deformed, creating a surface inside the annular region where cells are exposed to uniform biaxial strain. By controlling rate of evacuation of gases in the volume beneath the culture surface (pressure), the rate of strain can be controlled. A control loop will be set up using a pressure controller, control valves (to vacuum and to atmosphere), and control software provided by the manufacturer.

We have compared the mechanism of cell injury in the shear stress apparatus and the cell strain apparatus. Differentiated SH-SY5Y cells, a human neuroblastoma cell line, were used in both devices. In both devices, significant DNA fragmentation, indicative of cell injury was observed, however the characteristics of injury were different in the two models.

In both devices, the final cell strain was between 7 and 14%. Strain in the equibiaxial strain apparatus was slightly higher than that in the shear stress apparatus during preliminary experiments. As seen in Figure 6, mechanical loading in both devices (via shear stress or stretching of the underlying matrix) resulted in a significant fraction of cells with fragmented DNA relative to that of undeformed controls ($p<0.05$). The same level of DNA fragmentation is observed immediately after strain application, 14±5.3% for stretched cells versus 14±0.2% for sheared cells. 20 hours after cell deformation, greater numbers of cells with fragmented DNA were detected relative to the numbers of cells detected immediately after injury when cells were stretched, while no increase was seen in the sheared cells.

Figure 7 shows that cells that are stretched release about 1.6 times the amount of LDH as that released by unstretched cells. Whereas sheared cells did not release a significant level of LDH relative to unsheared cells at all time ($p>0.1$). The maximum possible LDH release (when all cells

are lysed) is 3.2±0.2 times that of unstretched cells. Assuming unstretched cells are completely intact, 22 % of cells might have lysed upon stretching. Alternatively, since LDH release appears to be transient during stretch injury (LDH release 24 hours later is less than that measured immediately after injury), transient membrane permeability in stretched cells was observed sufficient to release 20 % of the total possible LDH release. The level of LDH release of stretched cells at time zero is significantly different from the sheared cells as shown in Figure 2 ($p<0.05$). DNA fragmentation in stretched cells is accompanied with significant LDH release. This is not the case in sheared cells. The level of LDH release in stretched cells, however, is still significantly lower that the level expected when all cells are lysed (die via necrosis). Furthermore, within 20 hours, the level of LDH release decreases relative to LDH release measured immediately after injury suggesting that the increased in membrane permeability is not permanent, as it would be in the case of necrosis.

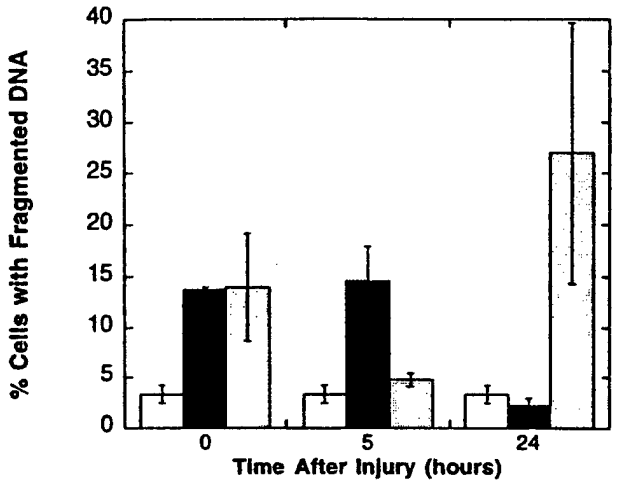

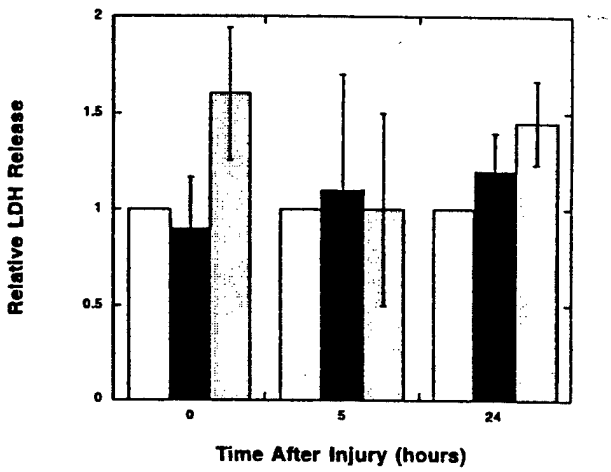

Figure 6. (left) The percentage of TUNEL positive cells (with fragmented DNA) as a function of time and mode of strain. Cells were exposed to no strain (open bar), shear stress (solid bar) or stretch (dotted bar) for 10 minutes. DNA fragmentation was assayed immediately, 5 hours or 20 hours after strain application. For all data n = 3-5 except for no strain data where n=14. * refers to the significance of the result relative to unstrained cells with $p<0.05$.

Figure 7. (right) The level of LDH release as a function of time and mode of strain. Cells were exposed to no strain (open bar), shear stress (solid bar) or stretch (dotted bar) for 10 minutes. LDH release was immediately, 5 hours or 20 hours after strain application. For all data, the ratio of LDH release from strained cells relative to the unstrained controls is reported. N equals 9 for 10 minute stretch data, for all others, n = 3-5. * refers to the significance of the result relative to unstrained control cells with $p<0.05$.

Figure 8 depicts that nitric oxide production occurs with different patterns for different mode of strain. Nitric oxide production is only slightly elevated immediately after stretch application but is significantly elevated 20 hours after stretch ($p<0.05$). The level of nitric oxide released into culture medium by cells increased 35 to 248% within 24 hours for injured cells. Stretched cells increase production of NO only after a significant delay after injury, while sheared cells increase production

of NO immediately after injury. After an initial burst in NO production in sheared cells, the level drops relative to unsheared control for the 24 hour period of time.

Figure 9 gives a comparison of the effect of treatment of strained cells using NOS inhibitor, L NAME and extracellular calcium chelator, EGTA. Both agents are neuroprotective to different degrees depending on the mode of strain. Sheared cells responded more to L-NAME than EGTA treatment whereas stretched cells responded slightly better to EGTA than L-NAME. Based on our results, we hypothesize that stretch application leads to an indirect increase in nitric oxide production, possibly through increases in calcium influx. During shear, nitric oxide synthase is most likely activated very early during shear stress application, possibly through a G protein dependent mechanism.

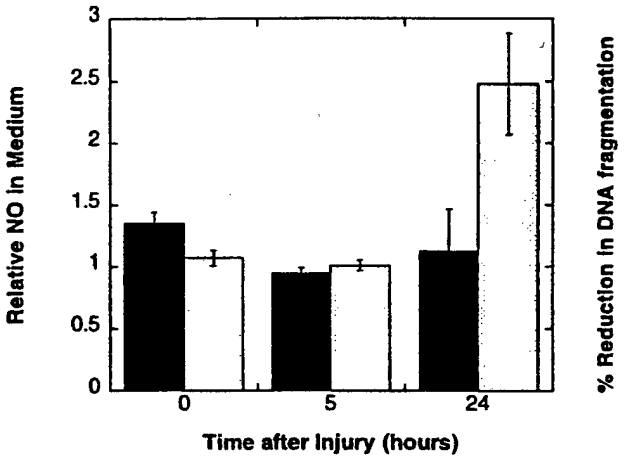

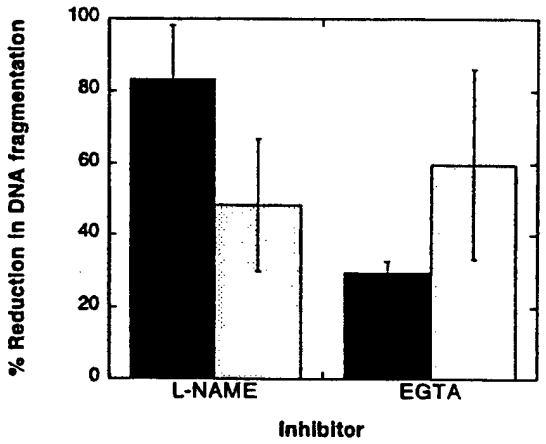

Figure 8. (left) Comparison of the level of NO production of stretched and sheared cells. Cells were exposed to shear (solid bar) or stretch (dotted bar) for 10 minutes. NO level was measured immediately after, 5 hours or 20 hours after strain application. For all data, the ratio of NO release relative to unstrained cells are reported. For all data, n=3-6. * refers to the significance of the result relative to unstrained control cells with $p<0.05$.

Figure 9. (right) The percent reduction in TUNEL positive cells (with fragmented DNA) in strained cells treated with L-NAME or EGTA. Cells were incubated with L-NAME or EGTA prior to exposure to shear (solid bar) or stretch (dotted bar). DNA fragmentation was assayed immediately after strain application. The percent reduction in the amount of TUNEL positive cells relative to untreated strained cells is reported. For all data, n=3-6. * and *** refer to the significance of the result relative to untreated strained cells with $p<0.05$ and $p<0.0001$ respectively.

The data presented indicate that a different pattern of injury occurs when cells are exposed to shear stress versus when they are deformed via stretch of the underlying matrix. There are a variety of factors which could account for the difference including: differences in cell strain, differences in strain rate, equibiaxial strain versus uniaxial strain, or that the strain induced in the cell was the result of a shear stress acting on the top surface of the cell versus a tensile stress pulling at the cell through cytoskeleton-matrix connections. If the differences observed in cell response to load were simply differences in magnitude of response, we might conclude that we were observing a "dosage" effect that was due to differences in strain rate and/or final strain of cell. However, because the

dynamics of the response are quite different in the two models, we are inclined to believe that there is a fundamental difference in the mechanism by which the cells respond to shear stress versus tensile stress.

We are currently improving the design of the of the strain apparatus such that we have better control of rate of strain of cells and a wider range of strain rates that we can utilize with the instrument. The better instrumentation and control should also simplify some of the measurement of cell strain during experimentation. We are also building more devices such that we can carry out experiments with better efficiency.

Towards the completion of specific aim 2, we the role of caspases in the cell injury observed upon application of shear stress to differentiated SH-SY5Y cells. We found that both caspase 1 and 3 were activated during shear stress application and that acitivty increased by 30-40% over unsheared controls. Futhermore, inhibition of caspases attenuated shear stress induced DNA fragmentation indicating their role in cellular injury (Figure 10).

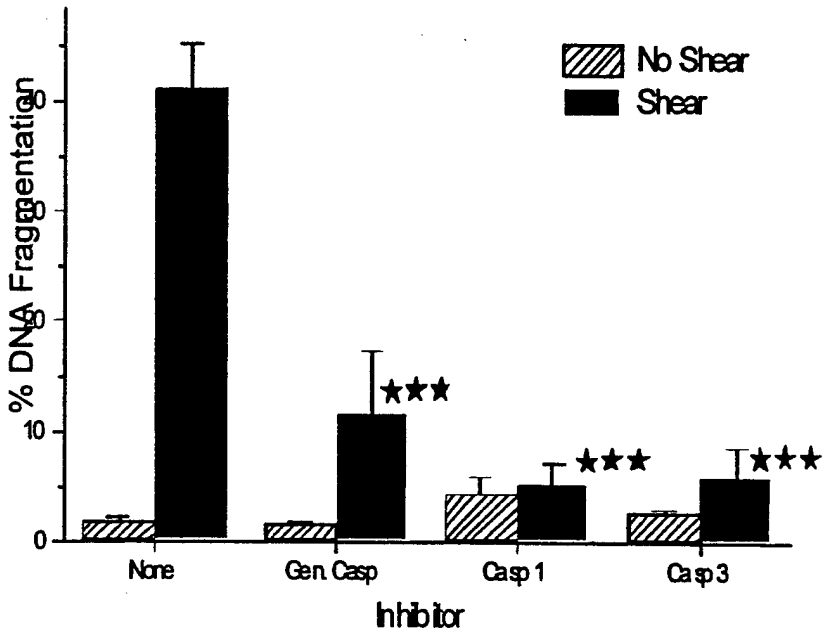

Figure 10. Percentage of TUNEL positive cells (with fragmented DNA) as a function of inhibitors of caspases. Cells are exposed to no shear (hatched bars) or pulsatile shear (solid bar) for 90 minutes at 10 dynes·cm^{-2} in the presence of inhibitors.

We examined the ability of a number of pharmacological agents to protect cells from shear stress/strain induced injury. As seen in Figures 11 and 12, shear induced DNA fragmentation in SH-SY5Y cells was attenuated by inhibition of NO production using L-NAME, and incubation of cells with the free radical scavengers ascorbic acid and vitamin E. We suggest that NO production is an important step in the mechanism of shear stress induced apoptosis in differentiated SH-SY5Y cells, possibly through a pathway involving the reaction of NO with superoxide to form peroxynitrite. The peroxynitrite may then react with regulatory proteins, altering their activities and signaling apoptosis.

G protein activation can lead to increased intracellular calcium concentration, a known mediator of apoptosis in neurons, through phospholipase C (PLC) activation, inositol triphosphate production, and Ca^{2+} release from stores. To examine the role of the inositol phospholipid pathway in shear stress induced cell injury, we blocked PLC activation and Ca^{2+} release from stores using dexamethasone and ryanodine, respectively. As seen in Figure 13, incubating cells with dexamethasone and ryanodine significantly reduced the extent of shear stress induced cell injury ($p<0.0001$). Thapsigargin, which affects IP_3 mediated Ca^{2+} release from the endoplasmic reticulum, did not protect cells from shear stress induced injury (data not shown).

The protective effects of blocking calcium entry into the cell are shown in Figure 14. Shear stress induced DNA fragmentation was significantly reduced in the presence of AP-5 ($p<0.0001$), an NMDA channel antagonist, but not significantly altered in the presence of ω-conotoxin, an L-type voltage gated calcium channel blocker, nifedipine, an N-type channel blocker, or NBQX, an AMPA channel antagonist ($p>0.1$). EGTA, an extracellular calcium chelator, was somewhat protective against shear stress induced DNA fragmentation (31±4 % compared to 45±4% for controls, $p=0.06$).

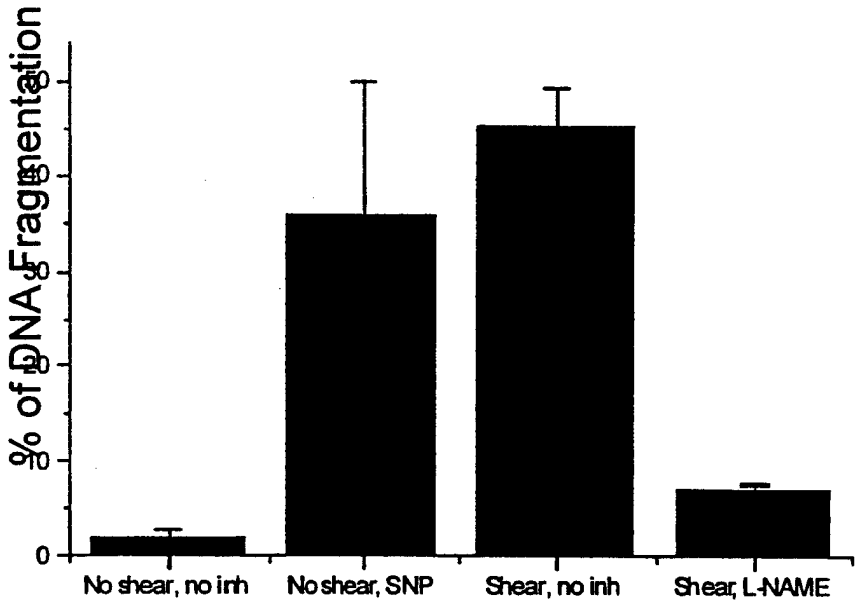

Figure 11. NO induced DNA fragmentation. Cells were exposed to no shear, no shear but in the presence of SNP, shear stress in the absence of any inhibitors or additives, and shear stress in the presence of L-NAME. The percentage of cells with fragmented DNA was measured immediately after shear stress application or, in the case of no shear, 5 hours after SNP addition to the culture medium. Data are presented as the mean ± the standard error of the mean of n independent determinations, where the error bars represent the standard error of the mean. n equals 9 for unsheared untreated control, 3 for unsheared treated with SNP, 7 for sheared cells without inhibitor, and 5 for sheared cells treated with L-NAME. ** refers to the significance of the result relative to unsheared untreated control cells ($p<0.001$).

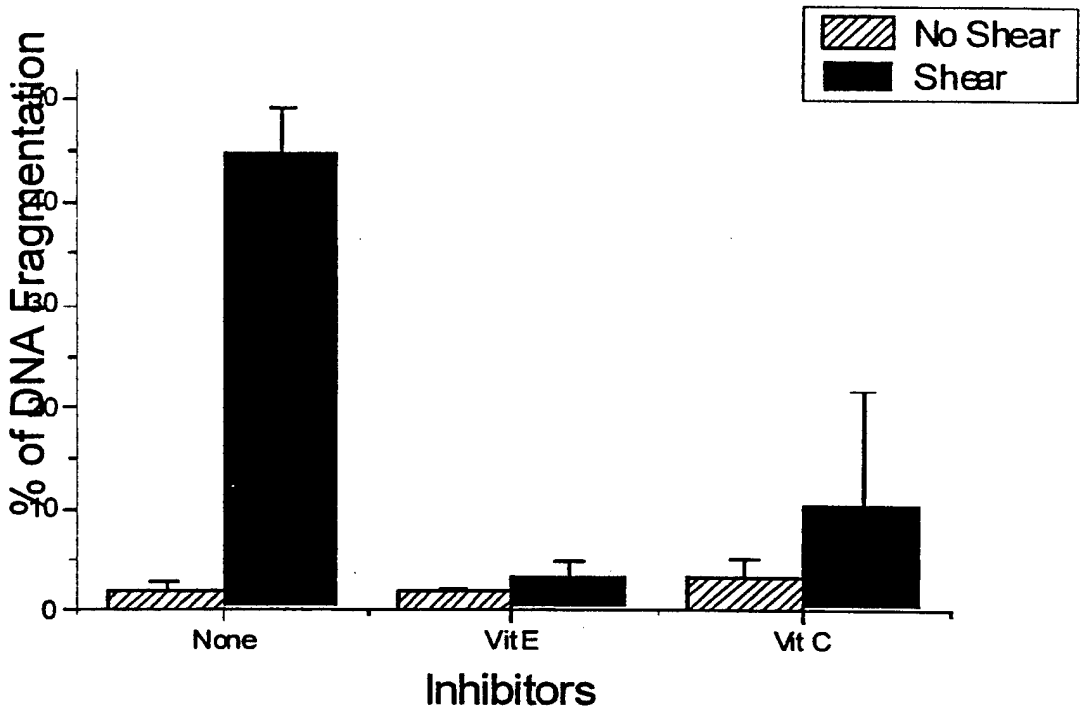

Figure 12. Effect of antioxidants on shear stress induced DNA fragmentation. Cells were either untreated (None), preincubated with vitamin E (Vit E) or preincubated with vitamin C (Vit C). Solid bars represent cells exposed to shear stress. Hatched bars represent cells treated identically except for the application of shear stress. The percentage of cells with fragmented DNA was measured immediately after shear stress application. n equals 9 for unsheared untreated control, 9 for sheared cells without inhibitor, and 3 for all others. ** refers to the significance of the result relative to sheared untreated control cells ($p<0.001$).

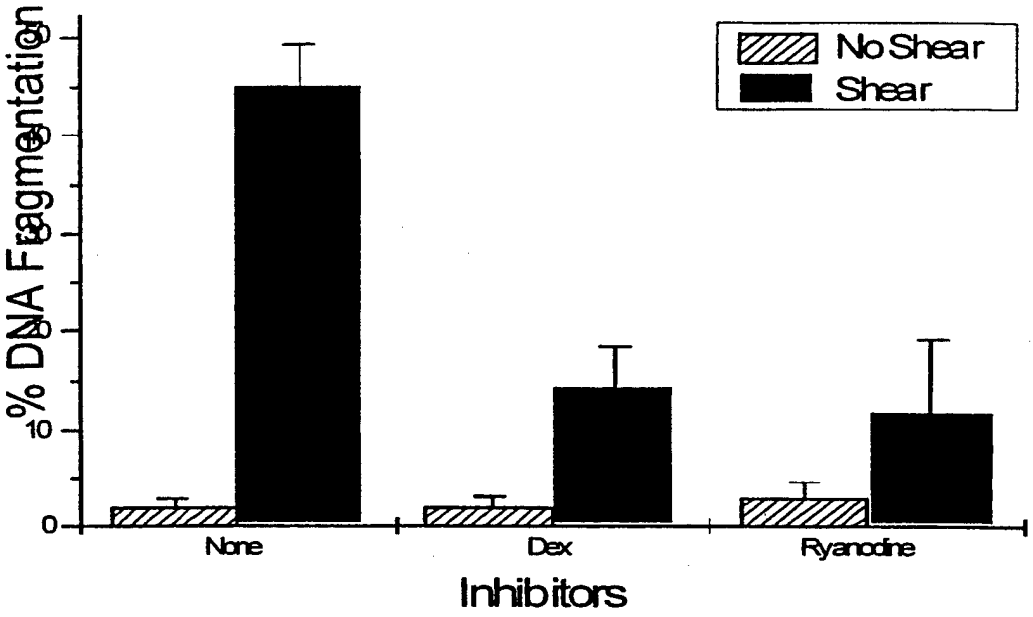

Figure 13. Effect of inhibitors of the inositol phospholipid pathway on shear stress induced DNA fragmentation. Solid bars represent cells exposed to shear stress. Hatched bars represent cells treated identically except for the application of shear stress. n equals 9 for unsheared untreated control, 7 for sheared untreated control, and 3-4 for all others. * refers to the significance of the result relative to untreated sheared control cells ($p<0.05$).

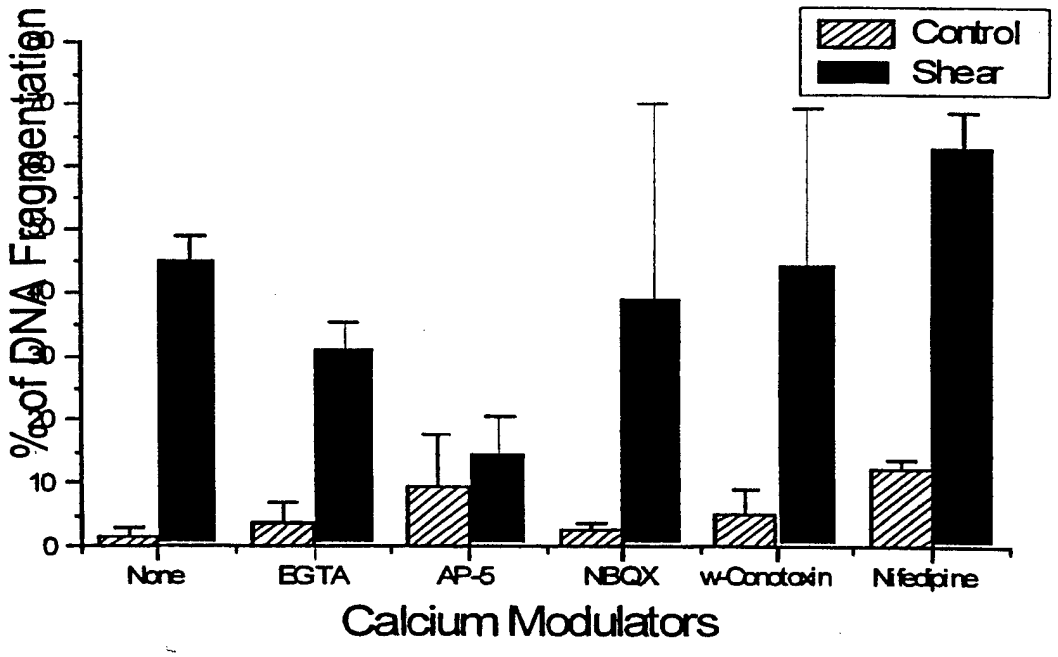

Figure 14. Effect of inhibition of calcium entry from extracellular space on shear stress-induced DNA fragmentation. n equals 9 for unsheared untreated control, 7 for sheared untreated control, and 3-4 for all others. *** and * refer to the significance of the result relative to untreated sheared control cells ($p<0.0001$ and $p<0.06$, respectively).

We have measured new protein synthesis during injury using radiochemical techniques and have seen almost a ten fold increase in new protein synthesis associated with injury. We are currently performing a number of experiments to elucidate the identity and importance of the new proteins being synthesized. We have identified, using radiochemical techniques, the molecular weights of 4 proteins that are synthesized during injury. We will examine, using immunoblotting, the identity of the proteins. This process may be somewhat arduous, therefore we are examining the feasibility to use 2D electrophoresis followed by mass spectroscopy to more efficiently identify the proteins associated with injury. Based on these results we can design inhibitors of proteins involved early in the process of injury (or gene therapy/antisense vectors) that may be useful in treatment of injury.

In the second year of funding, we will focus on what we believe will be novel targets for preventing injury. Those targets include agents which will alter the structural properties of the membrane and cytoskeleton and may therefore make cells more resistant to structural damage. This may be especially appropriate if we try to prevent a nerve injury induced by repetitive motion/vibration.

In addition, we will begin examining the timing needed for an intervention such that we can prevent neurodegeneration following the initial shear or stretch insult. Besides examining the effectiveness of using molecules already identified in preventing neurodegeneration when applied after the insult, we will examine molecules such as IL-1, which is known to be important in the caspase 1 pathway, and other proteins which we believe may interfere downstream in the neurodegenerative pathway.

Conclusions

We believe these results demonstrate significant progress towards achieving the aims of the proposed work. Our results support our original hypothesis that mechanical force induced apoptosis proceeds via a mechanism involving G protein activation, NO production, calcium entry into cells, and protein synthesis. We have evidence that calcium entry into cells is through glutamate gated channels, making the role of glutamate release/metabolism potentially very important. In addition, given the importance of strain rate in cell injury, structural feature of the cell such as the cytoskeleton, are potentially very important in early steps in injury. We have unique data that demonstrates that the mode by which cells are deformed affects the nature of injury the cells experience. Because the dynamics associated with different modes of injury are different, we believe that cell injury via stretching of the underlying matrix may be far more easy to prevent relative to injury caused by shear stress.

Development of models of head injury and other neurodegenerative diseases associated with mechanical loading of cells provides new and cheaper ways to investigate mechanisms of disease and screen drugs for treatment of disease. Understanding the mechanism of injury and how the injury relates to the forces which caused it will be essential in designing new treatments for traumatic injury. All of our findings clearly reflect the potential of developing new treatments for traumatic injury to the CNS and possibly repetitive injury to the peripheral nervous system. In addition, we believe that the model developed, when application of stress is at a low strain rate, has relevance to glaucoma.

Publications and Reports

T. Good. Development of In vitro models of head injury and glaucoma: examining the effects of shear stress and strain on cells of the central nervous system. *Cell Culture 7.* Sante Fe, NN, February 2000.

D. Triyoso and T. Good. Role of Nitric Oxide and Calcium in Stress Induced Injury to Differentiated SH-SY5Y Cells. *Annals of Biomedical Engineering* (submitted)

D. Triyoso, M. Edwards and T. Good. Low Strain Rate Leads to Cellular Injury Consistent with Apoptosis in Differentiated SH-SY5Y Cell Line Leads . *J. Neurotrauma* (submitted).

D. Triyoso and T. Good. Caspase 1 and 3 are activated in shear stress-induced injury to differentiated SH-SY5Y cells. *Neuroscience Letters.* (submitted).

M. Edwards, D. Triyoso and T Good. Development of an In vitro model of glaucoma. *Biotechnology Progress* (in preparation).

M. Edwards, S. Wang, and T. Good. The Role of Viscoelastic Properties of Differentiated Human Neuroblastoma Cells in Shear Stress Induced Cell Injury. *Biotechnology Progress* (in preparation).

D. Triyoso, I-H Yang, and T. Good. Comparison of Injury induced by Shear Stress and Equibiaxial Strain in Differentiated Human Neuroblastoma Cells. (work still in progress).

Patents and Commercialization.

No patent applications are currently being prepared nor are any pending or approved. Currently, there are no plans for commercialization of the product of this research.

References

1. McGregor, K. and Pentland, B. 1997. *Social Science and Medicine.* 45: 295-303.
2. Ommaya, A., Dannenberg, A. L. & Salazar, A. M. (1996). Causation, incidence, and costs of traumatic brain injury in the U.S. military medical systems. *Journal of Trauma.* **40**, 211-217.
3. Berkowitz, M. 1993. *J. Emergency Medicine.* 11 Suppl 1: 63-67.

[Prepared for publication as an article in *Analytical Chemistry* -- ~4100 words w/o figures, captions or references]

Principal Component Analysis as a Tool for Fault Detection in Amperometric Biosensor Arrays

Kaushik Sirkar and Michael V. Pishko*

Department of Chemical Engineering

Texas A&M University

College Station, TX 77843-3122

Email: pishko@tamu.edu

Phone: (979) 847-9395

Fax: (979) 845-6446

*Author to whom correspondence should be addressed

Submitted: April 25, 2000

Abstract

Principal component analysis (PCA) has been used to examine simulated data from redundant biosensor arrays operating properly or experiencing malfunction. Initial cases focus on specific mechanisms of sensor failure and the ability of PCA to identify the failed sensors in these cases. Effective discrimination of faulty sensors from those functioning properly was demonstrated for individual cases of completely failed, noisy, biased and drifting sensors, and sensors experiencing transient errors. Further cases were generated to simulate failure via multiple mechanisms in one sensor array. Although PCA on the complete data set was capable of identifying faulty sensors in this case, the specific cause or type of failure could not be identified. To identify the exact problem, a time-based examination of sensor function was implemented in the form of PCA on a time-variant data set. This permitted not only the identification of faulty sensors within the array, but also the determination of the exact mode of sensor failure.

Introduction

Redundancy in sensor systems is frequently used for critical safety applications such as chemical process monitoring.[1-3] Many clinical applications that can be addressed by biosensors could also benefit from the introduction of redundancy, particularly those in which a patient's well-being is at stake. In the case of an *in vivo* glucose sensor, both short-term inaccurate readings and long-term sensor drift may lead to improper insulin administration by a patient, potentially leading to extended periods of hyperglycemia or life threatening hypoglycemia. The use of a multi-sensor array, however, introduces sensor redundancy, permitting some individual sensing elements to fail without compromising the overall measurement.

There have recently been numerous studies exploring the development of biosensor arrays, including those based on the photolithography of photodeprotectable biotin derivatives[4], functional antibodies on silane monolayers[5], electrochemically deposited enzymes on individually addressable array members[6], micropatterning of electrostatically complexed multilayers[7], and redox polymer hydrogels patterned via photolithography.[8] The implementation of biosensor arrays requires that two very distinct problems be addressed. First is the development of sensor fabrication chemistries and techniques amenable towards the rapid and reproducible generation of arrays using methods such as those described above. Second is the development of statistical techniques and/or signal processing algorithms capable of analyzing data produced by the sensor array and eliminating measurements generated from faulty sensors. Here we report on the development of such algorithms based on principal component analysis (PCA).

Many numerical techniques are available for developing signal processing algorithms with applications in biosensor arrays. These are typically divided into two categories; univariate statistical techniques and multivariate methods such as neural networks (NN), partial least squares (PLS) and principal component analysis (PCA). Univariate statistical methods take advantage of upper and lower bounds; if the data do not conform to these bounds, the sensor is considered faulty. Unfortunately, this type of analysis often results in numerous indicators for the root cause of failure, making identification of the primary problem difficult. In addition, all types of failure cannot be diagnosed with univariate methods, for example, consider the case of a sensor functioning improperly, yet displaying measurements within the predetermined upper and lower bound limits.[9, 10] A univariate method would not be able to identify this failed sensor and thus more sophisticated multivariate techniques become necessary.

PLS, NN and PCA are frequently employed multivariate statistical techniques for analyzing large data sets. PLS, like PCA, is a dimension reduction method with the goal of maximizing the correlation between input and output matrices. This permits focusing fault detection efforts on the variables that most specifically influence another set of variables.[11] Neural networks are the most sophisticated of the three multivariate techniques mentioned above. They have been employed in numerous studies, including the determination of blood glucose by near-infrared spectroscopy,[12] the calibration of an array of voltammetric microelectrodes[13] and for on-line monitoring with an electronic nose.[13] Despite the sophistication of the neural networks employed in these and other studies, various drawbacks exist with respect to their application for *in vivo* biosensing. The necessity for training sets, which may be quite large in some instances, is a

considerable complication associated with neural networks. The generation of such training sets *in vivo* may be difficult or impractical. This drawback is not inherent with PCA, as a PCA model may be applied to analyze a large data set without prior training, minimizing the requirements for *a priori* model development. Because of these advantages, PCA has been used for many applications, albeit unrelated to biosensor arrays, including the analysis of data generated by an electronic tongue[14] and disturbance detection in wastewater treatment plants.[11] PCA will be described briefly in the following section.

Based upon its advantages and relative simplicity, this work explores the use of PCA for fault detection in biosensor arrays. As a model system, simulated data from an *in vivo* glucose sensor array was used. This simulated data will contain numerous "test cases" depicting various types of sensor failure and/or error, and ascertain the ability of PCA to distinguish these faulty sensors from those sensors functioning properly. Finally, a simulated time-variant data set consisting of sensor failure via multiple mechanisms will be analyzed with a time-based PCA algorithm.

Theory

Principal Component Analysis. A fault detection and identification scheme is desired for application with redundant biosensor arrays. PCA is one such technique that is capable of reducing a complex data set, with numerous dimensions, to a simpler one with fewer dimensions by projecting the data on a new coordinate system. Specifically, PCA is a mathematical transform that may be applied to a data matrix, **X**, in this case the data acquired from a sensor array, to assess variance in the data set. **X** is typically

composed of n sensors (rows) and m measurements (columns). For **X** with a set of k rank 1 matrices where k is less than or equal to the smaller of (m,n), PCA breaks **X** into k rank 1 matrices (X). These matrices are then arranged in order of decreasing eigenvalue, plus a residual matrix **E**. Thus we have

$$\mathbf{X} = X + \mathbf{E} \quad \text{or} \qquad \text{Equation (1)}$$

$$\mathbf{X} = q_1 p_1^T + q_2 p_2^T + \ldots + q_k p_k^T + \mathrm{E} = Q_k P_k^T + \mathbf{E} \qquad \text{Equation (2)}$$

where X represents the relevant data in the principal component subspace and **E** represents noise or irrelevant information present in the residual subspace.[10, 15]

These expressions may be further simplified to yield the following relationships

$$X = QP^T \text{ and } \mathbf{E} = Q_e P_e^T \qquad \text{Equation (3)}$$

where Q and P are referred to as the score and loading matrices, respectively. A PCA factorization is therefore able to take a data matrix **X** and break it down into the latent variables X and **E**. These variables describe as much of the variance as possible under the limits imposed by the scores (Q) and loading (P) vectors. Score plots, essentially the Q of the 1st principal component against the Q of the 2nd principal component, may then be generated to assess the relationship between data sets, permitting grouping of the data. Loading plots, where P of the 1st principal component is plotted against P of the 2nd principal component, may also be used to assess the relative influence of an individual variable on the system. Results from these plots are similar to those obtained from a PLS

analysis. Thus a vector, the first principal component, is calculated and describes the direction of largest variance in the data. Subsequently, further principal components may be calculated, each orthogonal to the previous one, the sum of which describes nearly 100 % of the observations in the data set.

Experimental Section

All PCA calculations were performed in MATLAB 5.3 (The MathWorks, Inc., Natick, MA). An experimental data set from a subcutaneously implanted glucose sensor initially published by Quinn et al.,[16] shown in Figure 1, is used as the basis for the development of simulated data from a sensor array containing both properly functioning and malfunctioning glucose sensors.

This data was originally reported in the form of a sensor current as a function of time. However, to better illustrate the significance of sensor errors to diabetes management, we transformed the data to glucose concentration as a function of time using the following equation (4).

$$\text{Glucose (mg/dL)} = m * i \qquad \text{Equation (4)}$$

In this equation, i is the sensor current in nA and m is the calibration factor in (mg/dL)/nA. The calibration factor was determined by a one-point calibration method using a blood glucose measurement and a sensor current measurement from the baseline region prior to glucose injection (Figure 1). As a part of this one-point calibration, a glucose concentration of zero was assumed to produce zero current.

Abnormal variations in sensor performance were subsequently introduced into the data set, corresponding to the following types of failure an *in vivo* glucose sensor may experience: complete failure, increased noise, bias, drift, and transient errors (temporary bias). Data from these cases typically consisting of ten sensors with 141 data points each {(m,n) equal to (141,10)} was analyzed by PCA. The results for individual cases of failure, as well as for an example containing multiple fault types within a given array, are examined using score plots.

Results and Discussion

Actual *in vivo* glucose monitoring data was used as a basis for the generation of a simulated data set for a glucose sensor array. The data from a single subcutaneously implanted glucose sensor (Figure 1) was taken and reproduced, with ± 15 % variability, for a total of ten sensors, simulating an array. Failure by various mechanisms was subsequently introduced to individual sensors in the array and the resultant data sets analyzed graphically with PCA generated score plots. This was followed by introducing multiple failures within a ten sensor array and determining the ability of PCA to not only identify which sensors have failed, but distinguish the mechanisms of failure between failed sensors. Finally, an initial example of a time-based PCA algorithm was implemented capable of identifying more effectively not only failed sensors, but also the specific mode of failure.

Complete Sensor Failure. This mode of failure is the case where a member of the sensor array produces zero current, or a current that does not change with variations in local glucose concentration.[17-19] In this case, failure may be caused by a number of

factors, including complete enzyme deactivation, a failure in the leads/wiring leading to the device[17] or an extremely strong chronic inflammatory response by the body that walls off the sensor and prevents its adequate contact with interstitial fluid.[18] Figure 2a shows eight sensors operating properly with ± 15 % variation in the signal. However, two other sensors in the array are not responsive to glucose. One failed sensor displays a glucose measurement partially within the bounds of correct operation (~ 70 mg/dL), as dictated by the other eight sensors, while the other failed sensor displays a zero current response. A score plot based upon PCA of this data set is shown in Figure 2b. The eight sensors working properly are grouped together very closely, while the failed sensors are deviant from this group. The failed sensor constantly reading 0 mg/dL glucose is a large outlier along the 1st principal component axis. The sensor erroneously reading ~ 70 mg/dL glucose and unresponsive to glucose is also a large outlier, but is deviant along both principal component axes, with variance primarily in the 2nd principal component axis.

Increase in Noise. Signal to noise ratio (SNR) is an important concern for glucose sensors to be implanted *in vivo*. Increased noise in glucose sensors may be induced by numerous factors, including electromagnetic radiation from power lines[19], electronic article surveillance (EAS) systems[20-22], or movement of the patient.[23] In this simulated case, eight sensors are operating properly with ± 15 % variability in signal and two are operating incorrectly with ± 25 % variability (Figure 3a). It is not readily apparent visually which sensors, if any, are deviant from those functioning properly. A score plot based on PCA of this data set is presented in Figure 3b. Here, the eight sensors operating at ± 15 % variability are grouped together, while two other noisy sensors are

separated. However, these two failed sensors do not differ from the eight properly functioning sensors in the same manner. In the score plot, the magnitude by which they differ from the set of correctly operating sensors is approximately the same. However, the directional contributions to their respective variations are quite different. This is a reasonable result, as both failed sensors increase in noise by the same amount, yielding magnitude shifts that are similar. However, due to the very nature of noise, the directional component of this variation is random in both positive and negative directions.

Bias. Bias in glucose sensors can be induced by a change in the working potential of the electrode[24] leading to a precise response by the sensor at a consistently inaccurate value. An erroneously low or high measurement by a glucose meter can lead to improper insulin administration by a patient, potentially leading to death. Figure 4a shows seven sensors operating properly at ± 15 % variability. However, sensor eight is biased positively by 50 mg/dL glucose, sensor nine is biased negatively by 50 mg/dL glucose, and sensor ten is biased positively by 200 mg/dL glucose. PCA of this data, presented in Figure 4b, permits visual identification of the biased sensors from those working properly. The sensors operating effectively are all aligned along the same 1st principal component with only minor variations along the 2nd principal component. The biased sensors, however, vary greatly along the 1st principal component. The sensors biased to erroneously high glucose readings shift positively along the 1st principal component while the sensors biased erroneously low shift negatively along the same axis. The magnitude of the bias also is apparent as the sensor corresponding to + 200 mg/dL sensor is shifted further than that corresponding to + 50 mg/dL sensor. Thus, bias has both magnitude and directional components, providing a means for distinguishing bias from noise, which only

has a magnitude component as described earlier. These differences between bias and noise modes of failure will be discussed in greater detail later when multiple modes of failure are imparted within one sensor array.

Transients. Transients in the signal from the biosensor are often caused by shorts where the sensor signal is temporarily biased or zero, as may be induced by the breakdown of vital electronic sensor components.[25] The longer these transients persist, the greater the risk of the patient interpreting the transient as a correct glucose measurement. Figure 5a shows this scenario with seven sensors working appropriately with a noise of ± 15 %. However, sensors eight, nine and ten experienced transients, corresponding to shifts of + 100 mg/dL, - 100 mg/dL and + 200 mg/dL glucose, respectively. A score plot based on this data is shown in Figure 5b, and demonstrates the ability to identify, by both direction and magnitude, differences from normal data. The + 200 mg/dL transient is further to the left, along the 1st principal component, as opposed to the + 100 mg/dL sensor. The – 100 mg/dL transient is shifted in the opposite direction along the 1st principal component by a magnitude approximately equal to that of the + 100 mg/dL transient. The case of transients is similar to that of bias. However, for similar values, due to smaller time duration of a transient as opposed to bias, the magnitude of the variation is smaller, with a similar directional component.

Sensor Drift. The final case potentially leading to sensor failure deals with the drift of the sensor signal. This may be caused by enzyme deactivation[17, 26, 27], degradation of sensor materials[18] or remodeling of the implant site by a chronic inflammatory response.[18] Figure 6a shows seven sensors that are functioning effectively, however, sensor eight is biased positively by an arbitrary function, sensor nine positively

by a similar function with an increased slope, and sensor ten drifting negatively. In Figure 6b, we see that a score plot based on PCA is able to group the seven sensors working effectively, as compared to the drifting sensors. Sensor eight is shifted negatively along the 1st principal component axis. Sensor nine, larger in magnitude than eight with respect to its deviation, is shifted further to the left, also along the 1st principal component axis. Finally, sensor 10, drifting in the opposite direction from the other two failed sensors, is shifted positively along the 1st principal component axis. As in the case of bias, both magnitude and directional effects are apparent. However, difficulties may arise when attempting to distinguish biased sensors from drifting sensors. This will be further described in the following discussion of arrays experiencing multiple modes of failure.

Multiple Failures. The previous examples demonstrate the potential of PCA to identify faulty sensors under cases of specific failure. In the earlier discussion two general types of failure have been identified; those related to drift, bias or transients where magnitude and directional (positive or negative) components are present, and noise related failure where, despite the presence of a magnitude change, direction is random. Under actual *in vivo* conditions, however, the mechanism of failure will not be known *a priori* and multiple types of failure are possible. Determination of the specific mode of failure may help identify what kinds of problems are present and how they may be remedied. The case in Figure 7a depicts failure of an *in vivo* glucose sensor array. To determine the capabilities of PCA when faced with a potential worst case scenario, this data set has an extremely high failure rate of 60 % (i.e. six out of ten sensors have failed). Four sensors are operating correctly with noise of ± 5 %. However, sensor five is biased

by + 20 mg/dL glucose, sensor six is functioning with noise of ± 50 %, sensor seven is biased by + 200 mg/dL glucose, sensor eight undergoes a temporary step corresponding to – 100 mg/dL glucose, sensor nine is drifting by some positive function and sensor ten is completely failed reading 0 mg/dL glucose.

A PCA score plot of this data set is shown in Figure 7b. As compared to the group of properly functioning sensors (sensors 1-4) there are significant deviations from this group in the score plot, specifically for sensors seven, nine, and ten along the 1st principal component axis, and sensors five, six and eight to smaller degrees along both principal component axes. A sensor failing in the positive direction may be distinguished against one failing negatively, if the deviation from the group operating correctly is of a large enough magnitude. Sensors seven and nine deviate positively and ten negatively, indicating these sensors are not failing by noise related mechanisms. However, distinguishing drift from bias or transients is not possible with these sensors (specifically sensors five, six and eight) based upon the analysis that has been performed. A possible solution is the implementation of a time-based monitoring scheme that quantifies relative changes in the principal components.

PCA on a time variable data set may result in a complete identification of the types of failures undergone by sensors in an array. To perform this analysis, the data set shown in Figure 7a was separated into seven ten minute segments (total experiment time ~ 70 minutes). Thus, each data subset consisted of 10 sensors with approximately 20 data points, or $(m,n) \sim (20,10)$. PCA analyses were performed on data from each of the time segments, and the relevant 1st and 2nd principal components were recorded for these sets and plotted against time as is shown in Figures 8a and 8b.

Figure 8a shows the 1st principal component as a function of time for the four sensors operating properly at a ± 5 % variation level and six malfunctioning sensors. A sensor biased by + 20 mg/dL can be observed as slightly positive of those working properly. Sensor eight with a temporary negative step may be identified by its temporary deviation along the 1st principal component before returning to values matching that of the effective sensors. Sensor nine, drifting positively, displays a steady increase along the 1st principal component axis. Sensor ten, at 0 mg/dL, and sensor seven, biased by + 200 mg/dL, are shifted positively and negatively, respectively, along the 1st principal component. Sensors seven and ten indicate a consistent 1st principal component until they shift at approximately the time of a glucose bolus, due to the change in their relative errors as the correct glucose sensor readings increase with increasing blood glucose. The failed sensor displaying 0 mg/dL glucose is shifted further away from the sensors operating effectively, as is expected considering the magnitude of the error increases. The sensor biased by a reading of + 200 mg/dL shifts closer to the sensors operating effectively, which is expected as the relative importance of a 200 mg/dL error decreases during the glucose spike.

The one sensor that cannot necessarily be identified by the 1st principal component is sensor six, displaying a large variation in signal of ± 50 %. The error in this sensor can be seen in a plot of the 2nd principal component against time, Figure 8b, through variations that are both positive and negative, from those sensors operating effectively. As per earlier results shown in Figures 4a and b for failure induced by increased noise, there appears to be no directional component for the noisy sensor in this data set, thus random noise imparts only a magnitude component. Figure 8b also

demonstrates temporary negative shifts for the failed sensors reading + 200 mg/dL and 0 mg/dL at the time of the glucose bolus, analogous to the shifts that we see along the 1st principal component.

The majority of sensors failing by a drift or bias related mechanism may be identified simply by plotting the 1st principal component against time, as was shown in Figure 8a. Biased sensors are permanently offset from those sensors working properly, while sensors experiencing transients undergo only a temporary deviation. Drifting sensors undergo a slow yet steady digression from those operating effectively. This may be identified by PCA of a time-variant data set, whereas a static analysis misinterprets a drifting sensor for one that is biased or undergoing a transient. The simplest category of failed sensor to identify consists of those having undergone complete failure as the relative error of these sensors changes significantly with changes in glucose concentration. The mechanism of failure is not readily apparent in a plot of the 1st principal component against time is that of increased noise. This is because random noise has only a magnitude component and, unlike all other mechanisms of failure, has a random directional component. Noise may only be identified as having a magnitude shift along the 2nd principal component, indicating that noise does not contribute as significantly to sensor error as does a bias related failure. However, this is only true for this data set and will not necessarily apply to other groups of sensors.

Conclusions

PCA was used as a signal processing technique for the analysis of data from biosensor arrays such as the simulated implantable glucose sensor array that was used

here as a model system. Individual cases of sensor failure, including noisy, drifting, biased, completely failed and sensors experiencing transients were assessed and a score plot based on a principal component analysis used to visually identify a sensor failed by any of these mechanisms. Specifically, sensor failure fell into two categories: noise and drift/bias effects. Failure due to drift/bias displayed deviation with both magnitude and directional components along the 1st principal component axis. Noise related effects were typically identified by shifts along both principal component axes. However directional effects were minimal, as noise is typically equally distributed in both positive and negative directions. PCA was finally performed on a time variable data set containing failed sensors via multiple mechanisms for the purpose of identifying not only faulty sensors, but also their mechanism of failure. Though *in vivo* glucose sensor arrays were used here as a model system, this technique could potentially be applied to other redundant biosensor arrays for both *in vitro* and *in vivo* applications.

Acknowledgements

We would like to thank the following funding sources: the Whitaker Foundation, Juvenile Diabetes Foundation International (1-1998-298), United States Department of the Army and the National Medical Technology Testbed, Inc.(DAMD17-97-2-7016). "The view, opinions and/or findings contained in this report are those of the author(s) and should not be construed as a position, policy, decision or endorsement of the Federal Government or the National Medical Technology Testbed, Inc." MVP also wishes to thank the Alfred P. Sloan Foundation for its support through a research fellowship.

References

(1) Puers, R.; Bruyker, D. D.; Cozma, A. ; *Sensors and Actuators A* **1997,** *60*, 68-71.

(2) Stork, C. L.; Kowalski, B. R. ; *Chem. Int. Lab. Sys.* **1999,** *46*, 117-131.

(3) Yaqoob, A.; Shankar, N. ; *AIChE Journal* **1995,** *4*, 2237-2249.

(4) Sundberg, S.; Barrett, R.; Pirrung, M.; Lu, A.; Kiangsoontra, B.; Holmes, C. ; *J. Am. Chem. Soc.* **1995,** *117*, 12050-12057.

(5) Mooney, J.; Hunt, A.; McIntosh, J.; Liberko, C.; Walba, D.; Rogers, C. ; *Proc. Natl. Acad. Sci. USA* **1996,** *93*, 12287-12291.

(6) Sangodkar, H.; Sukeerthi, S.; Srinivasa, R. S.; Lal, R.; Contractor, A. Q. ; *Anal. Chem.* **1996,** *68*, 779-783.

(7) Sirkar, K.; Revzin, A.; Pishko, M. V. ; *Anal Chem.* **2000**, in press.

(8) Sirkar, K.; Pishko, M. ; *Anal. Chem.* **1998,** *70*, 2888-2894.

(9) Dunia, R.; Qin, S. J. ; *Control Engineering Practice* **1998,** *6*, 457-469.

(10) Dunia, R.; Qin, S. J. ; *Computers Chem. Engng.* **1998,** *22*, 927-943.

(11) Rosen, C.; Olsson, G. ; *Wat. Sci. Tech.* **1998,** *37*, 197-205.

(12) Jagemann, K.-U.; Fischbacher, C.; Danzer, K.; Muller, U. A.; Mertes, B. ; *Zeitschrift fur Physikalische Chemie* **1995,** *191*, 179-190.

(13) Wehrens, R.; van der Linden, W. E. ; *Analytica Chimica Acta* **1996,** *334*, 93-101.

(14) Winquist, F.; Wide, P.; Lundstrom, I. ; *Analytica Chimica Acta* **1997,** *357*, 21-31.

(15) Stork, C. L.; Veltkamp, D. J.; Kowalski, B. R. ; *Anal. Chem.* **1997,** *69*, 5031-5036.

(16) Quinn, C. P.; Pishko, M. V.; Schmidtke, D. W.; Ishikawa, M.; Wagner, J. G.; Raskin, P.; Hubbell, J. A.; Heller, A. ; *American Journal of Physiology* **1995,** E155.

(17) Moussy, F.; Jakeway, S.; Harrison, D.; Rajotte, R. ; *Anal. Chem.* **1994,** *66,* 3882-3888.

(18) Pickup, J.; Claremont, D.; Shaw, G. ; *Acta Diabetol.* **1993,** *30,* 143-148.

(19) Wood, D. E.; Ewins, D. J.; Balachandran, W. ; *Medical & Biological Engineering & Computing* **1995,** *33,* 63-68.

(20) Harris, C.; Boivin, W.; Boyd, S.; Coletta, J.; Kerr, L.; Kempa, K.; Aronow, S. ; *Health Physics* **2000,** *78,* 21-27.

(21) McIvor, M. E.; Reddinger, J.; Floden, E.; Sheppard, R. C. ; *PACE - Pacing and Clinical Electrophysiology* **1998,** *21,* 1847-1861.

(22) Zuckerwar, A. J.; Pretlow, R. A.; Stoughton, J. W.; Baker, D. A. ; *IEEE Transactions on Biomedical Engineering* **1993,** *40,* 963-969.

(23) Pickup, J. C.; Shaw, G. S.; Claremont, D. J. ; *Diabetologia* **1989,** *32,* 213-7.

(24) Velho, G.; Froguel, P.; Sternberg, R.; Thevenot, D.; Reach, G. ; *Diabetes* **1989,** *38,* 164-171.

(25) Hediger, S.; Sayah, A.; Gijs, M. A. M. ; *Sensors and Actuators B* **1999,** *56,* 175-180.

(26) Pickup, J. C.; Shaw, G. W.; Claremont, D. J. ; *Biosensors* **1989,** *4,* 109-119.

(27) Sternberg, F.; Meyerhoff, C.; Mennel, F.; Hoss, U.; Mayer, H.; Bischof, F.; Pfeiffer, E. ; *Horm. Metab. Res.* **1994,** *26,* 523-525.

Figure Captions

Figure 1. *In vivo* glucose sensor data from Quinn et al.[16] For this work the data from the subcutaneous sensor was used to generate a simulated data set for a redundant glucose sensor array.

Figure 2. Complete sensor failure where the sensor is displaying either no response or a completely inaccurate response. a) Simulated glucose sensor array data consisting of eight sensors operating effectively with a variability of ~ 15 % and two failed sensors displaying constant values of 0 and 70 mg/dL glucose. b) Score plot showing PCA of this data resulting in the eight sensors operating correctly grouped together while the failed sensors are deviant along both axes.

Figure 3. The effect of noise on a sensor. a) Simulated glucose sensor array depicting two failed sensors with 25 % noise against eight sensors operating correctly with 15 % noise. b) Score plot showing PCA of this data where the eight sensors operating correctly are grouped together whereas the two equally noisy sensors are deviant by similar magnitudes but in random directions.

Figure 4. Sensors temporarily biased are compared to those operating correctly. a) Simulated glucose sensor array data consisting of seven sensors operating effectively with a variability of ~ 15 % and three biased sensors (+ 50, - 50, and + 200 mg/dL

readings). b) Score plot showing PCA of biased sensors where both magnitude and directional components are evident. A sensor biased by + 200 mg/dL instead of + 50 mg/dL is shifted further from those sensors functioning properly. However a sensor biased negatively is shifted in the opposite direction along the 1st principal component.

Figure 5. Sensors undergoing transients ("shorts"). a) Simulated glucose sensor array data consisting of seven sensors operating effectively with a variability of ~ 15 % and three sensors undergoing steps (+ 100, - 100, + 200 mg/dL readings). b) Score plot showing PCA distinguishing the sensors undergoing a step change from those operating correctly. Both magnitude and direction deviations are present. The sensor experiencing a + 200 mg/dL transient undergoes a larger magnitude shift along the 1st principal component than the + 100 mg/dL sensor. The – 100 mg/dL transient is shifted in the opposite direction by a magnitude approximately equal to the + 100 mg/dL sensor.

Figure 6. Sensors that are steadily drifting. a) Simulated glucose sensor array data consisting of seven sensors operating effectively with a variability of ~ 15 % and three sensors drifting, two positively and one negatively. b) Score plot showing PCA of this data indicating the presence of both magnitude and directional deviations. The sensors experiencing drift in the positive direction are shifted in the same direction along the 1st principal component. The sensor subjected to a greater drift function is shifted further along the 1st principal component. The sensor experiencing a negative drift is shifted in the opposite direction along the 1st principal component.

Figure 7. This case examines the identification of failure in an array when the mechanism of failure is not predetermined (multiple root causes are possible). a) Simulated glucose sensor array data consisting of four sensors operating effectively with a variability of ~ 5 %, one sensor biased by + 20 mg/dL, another by + 200 mg/dL, one experiencing a transient of – 100 mg/dL, one sensor operating at a noise of 50 %, one sensor drifting positively and the last sensor at a 0 mg/dL reading. b) Score plot showing PCA distinguishing the failed sensors from those operating correctly. The sensors operating improperly undergo numerous shifts both in magnitude and direction along both principal components. However, the specific type of failure is not readily apparent for all cases based upon this analysis.

Figure 8. Dynamic analysis of a time-variant data set from Figure 8 using PCA to generate plots of a) 1^{st} principal component and b) 2^{nd} principal component versus time.

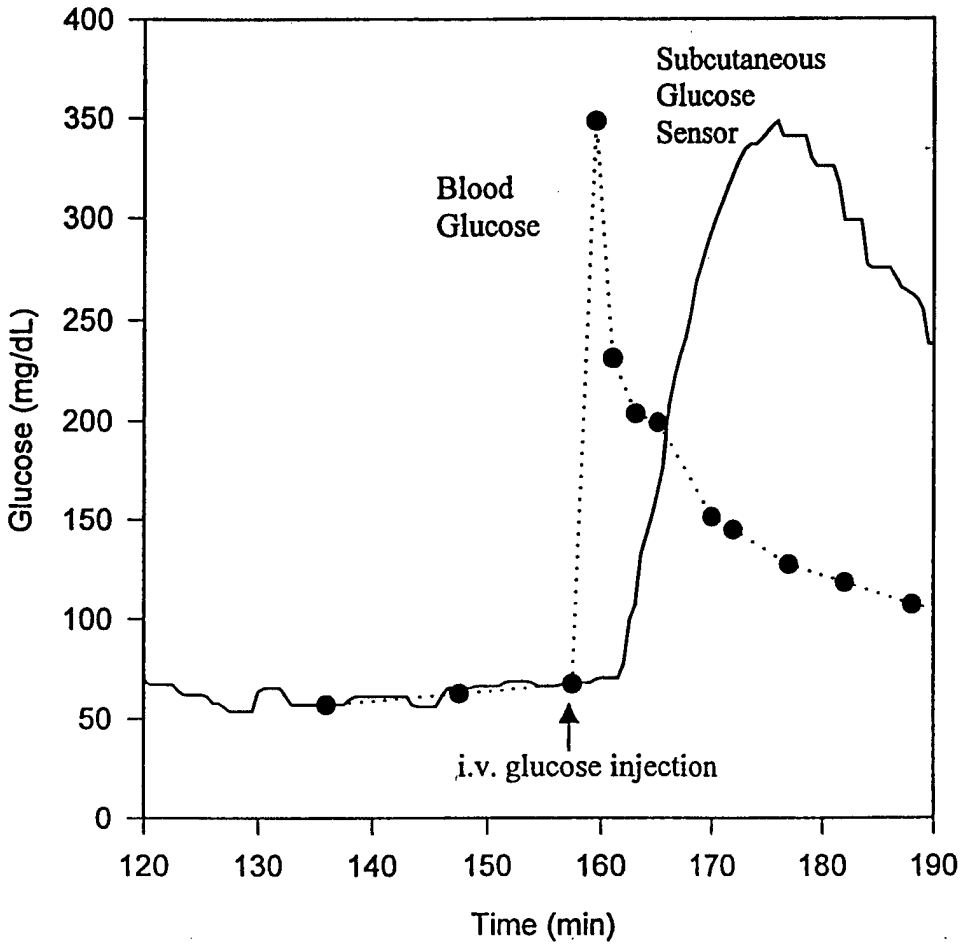
400
350
300
250
200
150
100
50
0
Glucose (mg/dL)
120
130
140
150
160
170
180
190
Time (min)
Subcutaneous
Glucose
Sensor
Blood
Glucose
i.v. glucose injection

Figure 1

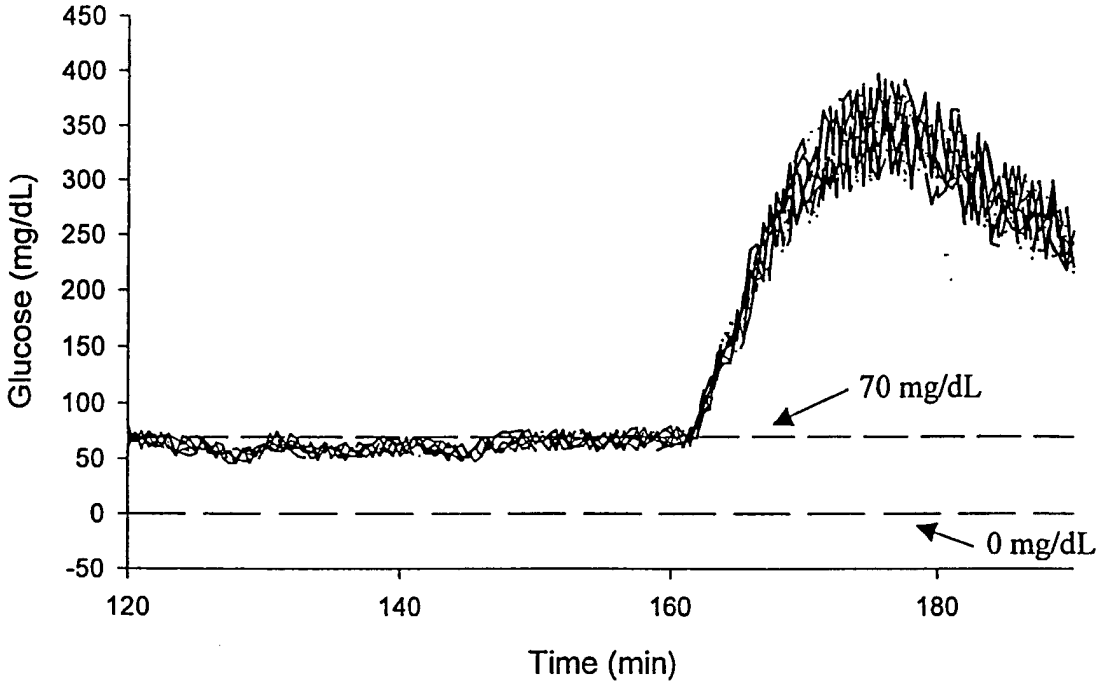
Glucose (mg/dL)
450
400
350
300
250
200
150
100
50
0
-50
120
140
160
180
Time (min)
70 mg/dL
0 mg/dL

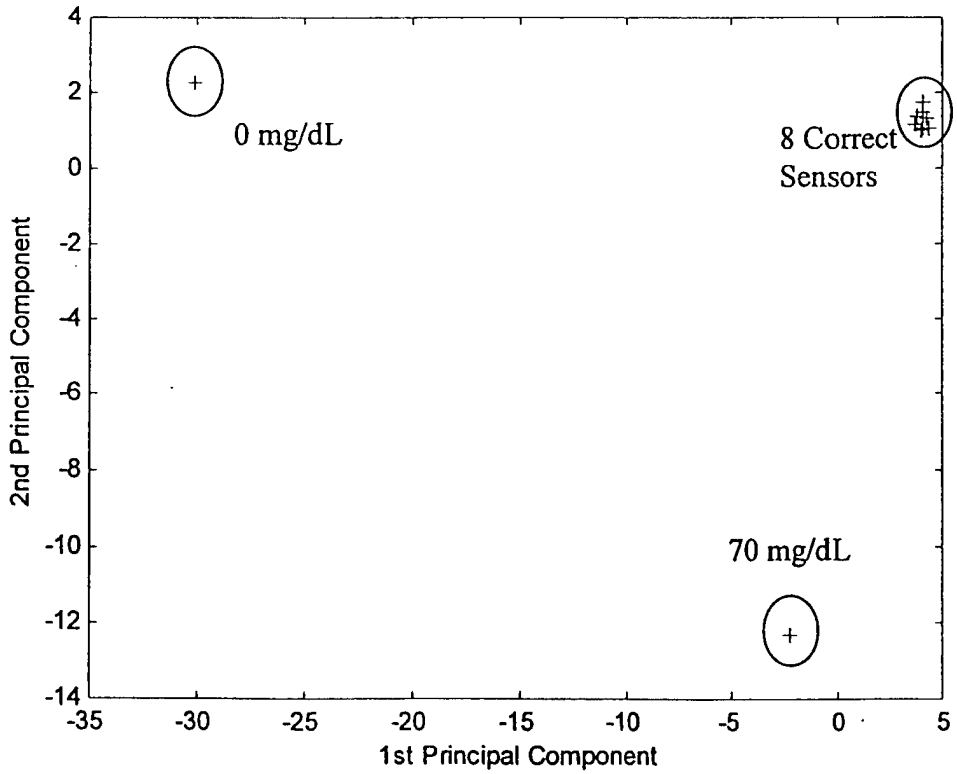
2nd Principal Component
4
2
0
-2
-4
-6
-8
-10
-12
-14
-35
-30
-25
-20
-15
-10
-5
0
5
1st Principal Component
0 mg/dL
8 Correct
Sensors
70 mg/dL

Figure 2

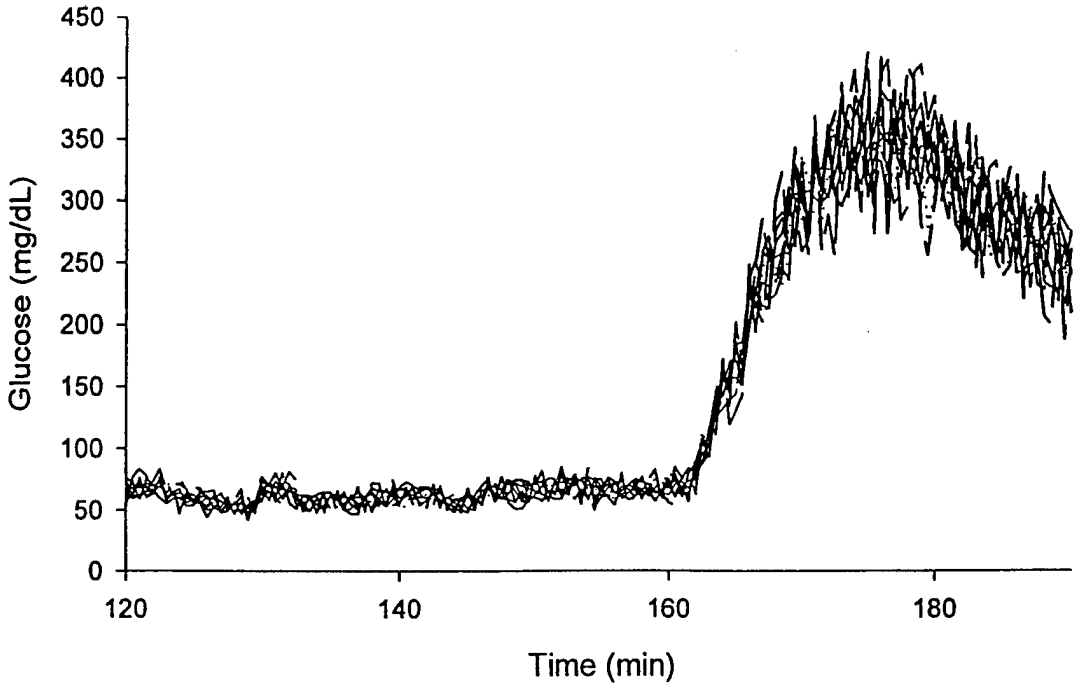
Glucose (mg/dL)
450
400
350
300
250
200
150
100
50
0
120
140
160
180
Time (min)

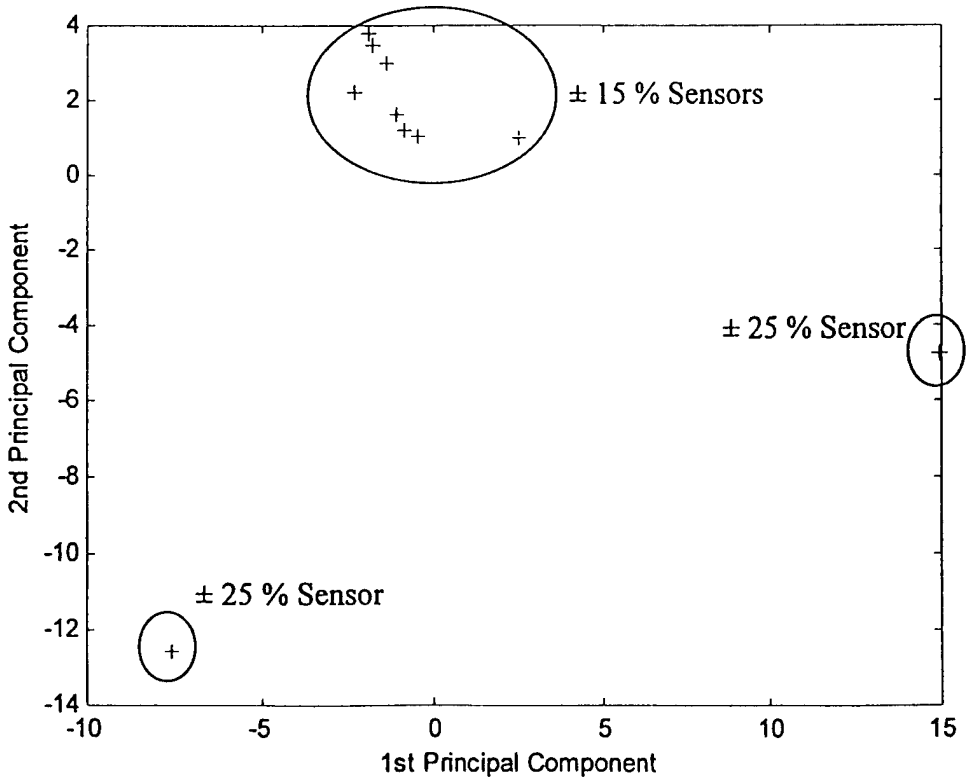
± 15 % Sensors
± 25 % Sensor
± 25 % Sensor
2nd Principal Component
1st Principal Component
4
2
0
-2
-4
-6
-8
-10
-12
-14
-10
-5
0
5
10
15

Figure 3

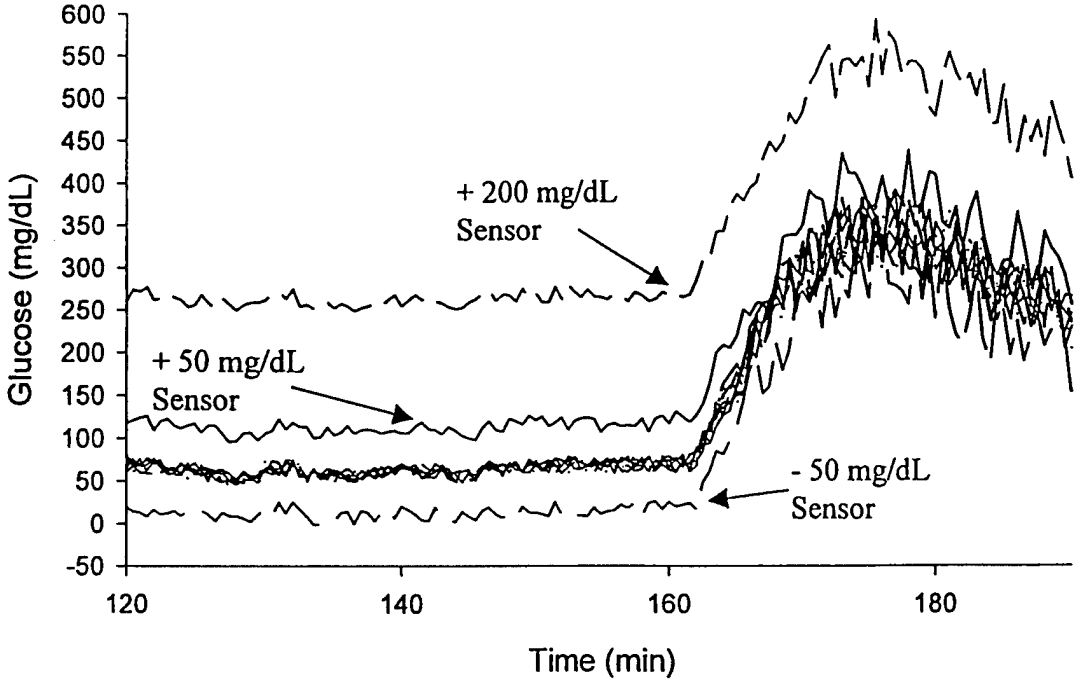
Glucose (mg/dL)
600
550
500
450
400
350
300
250
200
150
100
50
0
-50
120
140
160
180
Time (min)
+ 200 mg/dL
Sensor
+ 50 mg/dL
Sensor
- 50 mg/dL
Sensor

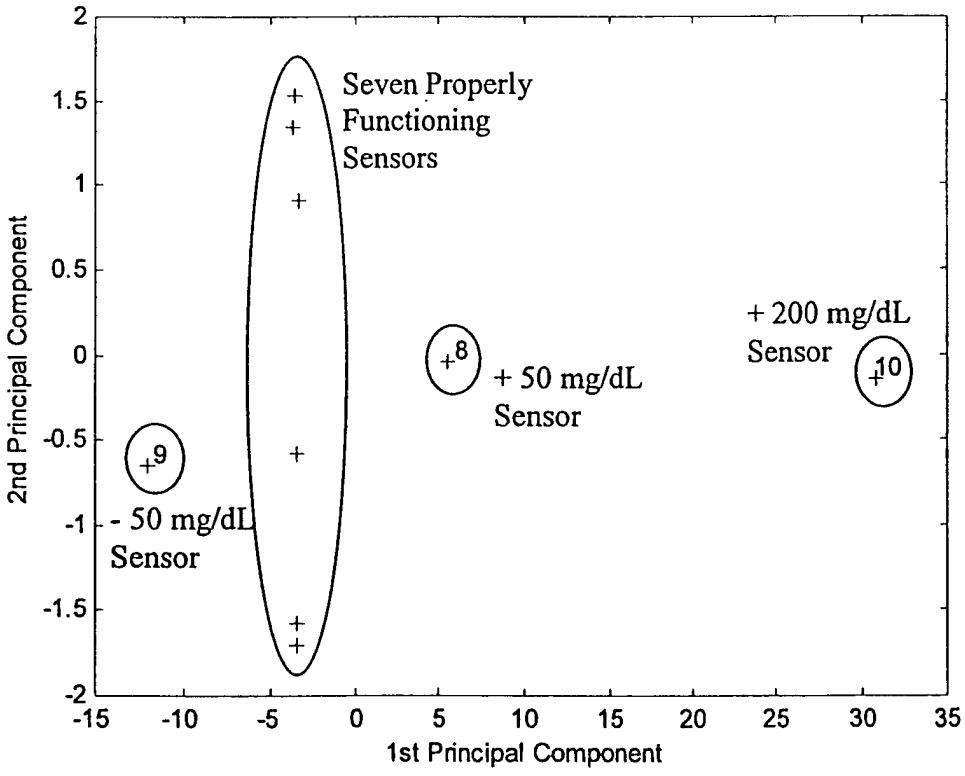
2nd Principal Component
2
1.5
1
0.5
0
-0.5
-1
-1.5
-2
-15
-10
-5
0
5
10
15
20
25
30
35
1st Principal Component
Seven Properly
Functioning
Sensors
+ 200 mg/dL
Sensor
+ 50 mg/dL
Sensor
- 50 mg/dL
Sensor
8
9
10

Figure 4

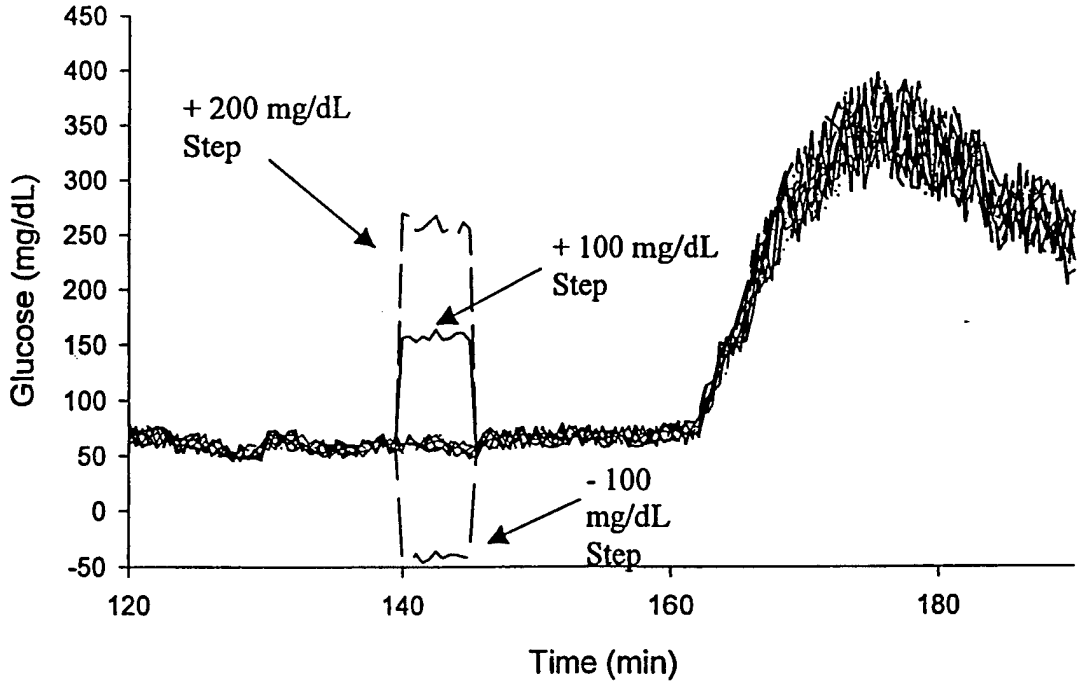
450
400
350
300
250
200
150
100
50
0
-50
Glucose (mg/dL)
+ 200 mg/dL
Step
+ 100 mg/dL
Step
- 100
mg/dL
Step
120
140
160
180
Time (min)

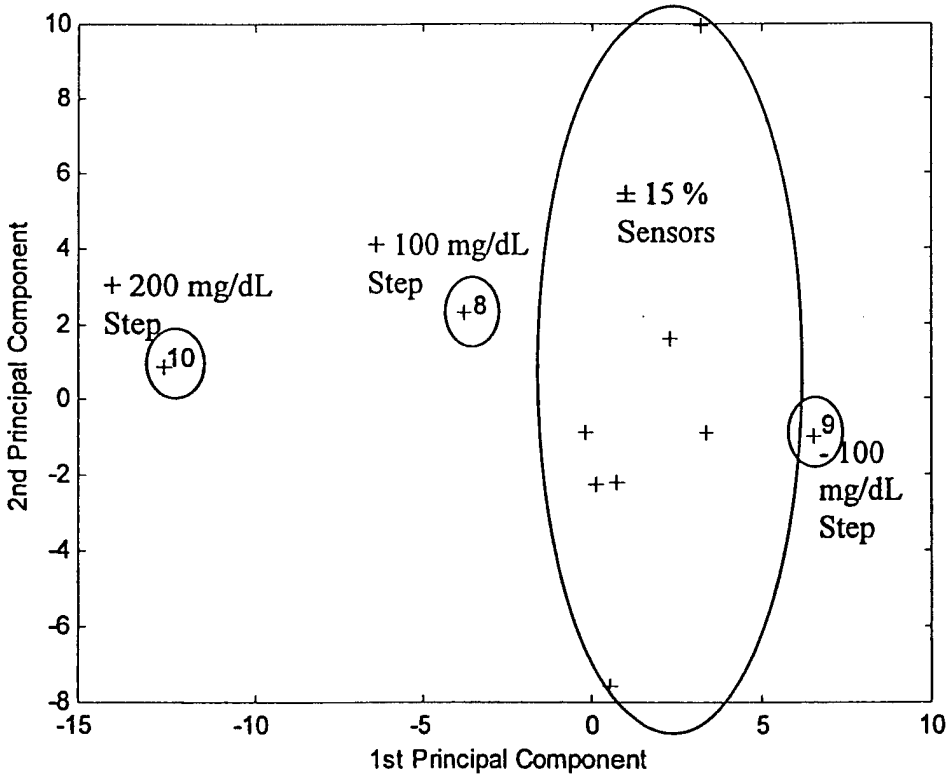
10
8
6
4
2
0
-2
-4
-6
-8
2nd Principal Component
+ 200 mg/dL
Step
+10
+ 100 mg/dL
Step
+8
± 15 %
Sensors
+9
-100
mg/dL
Step
-15
-10
-5
0
5
10
1st Principal Component

Figure 5

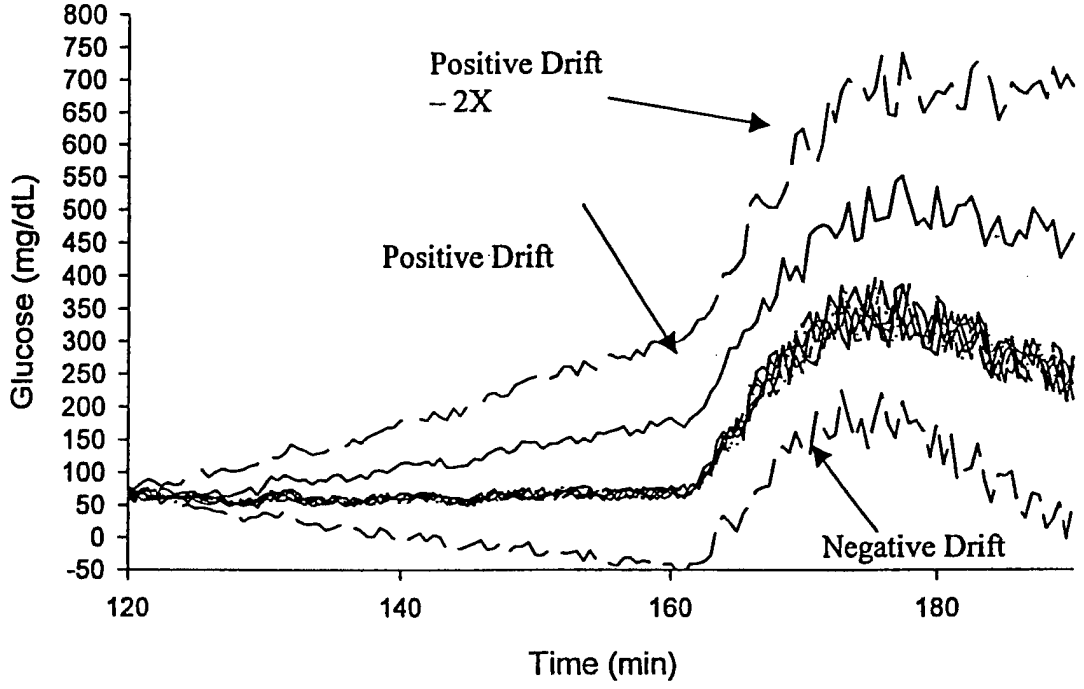
Positive Drift
– 2X
Positive Drift
Negative Drift
Glucose (mg/dL)
Time (min)
800
750
700
650
600
550
500
450
400
350
300
250
200
150
100
50
0
-50
120
140
160
180

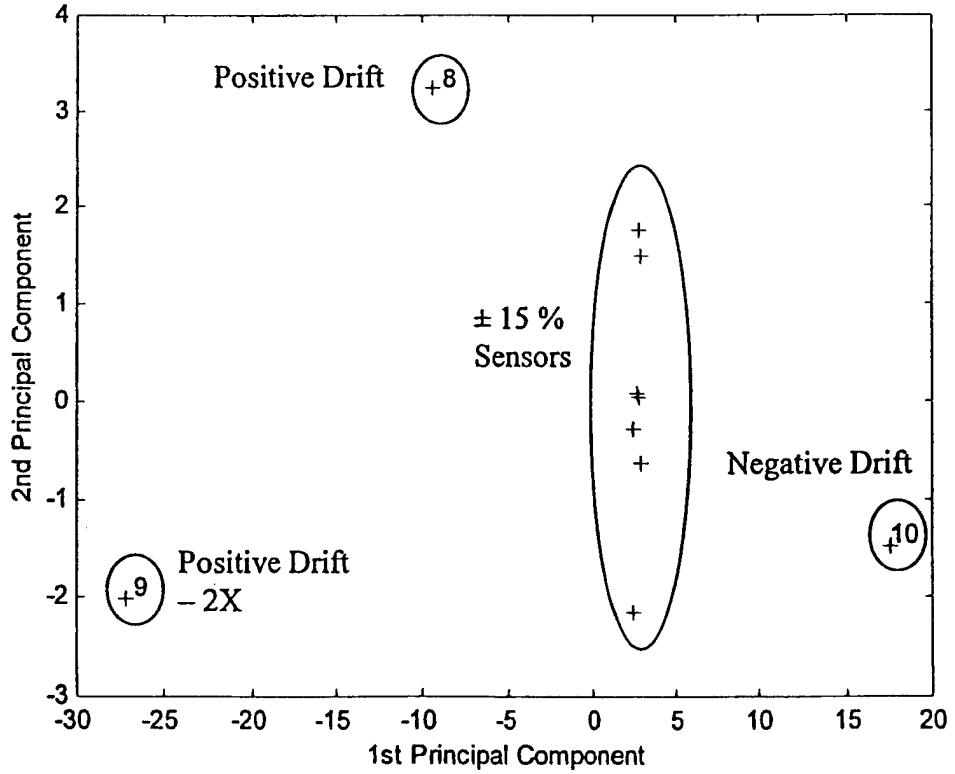
Positive Drift
+8
± 15 %
Sensors
Negative Drift
+10
Positive Drift
– 2X
+9
2nd Principal Component
1st Principal Component
4
3
2
1
0
-1
-2
-3
-30
-25
-20
-15
-10
-5
0
5
10
15
20

Figure 6

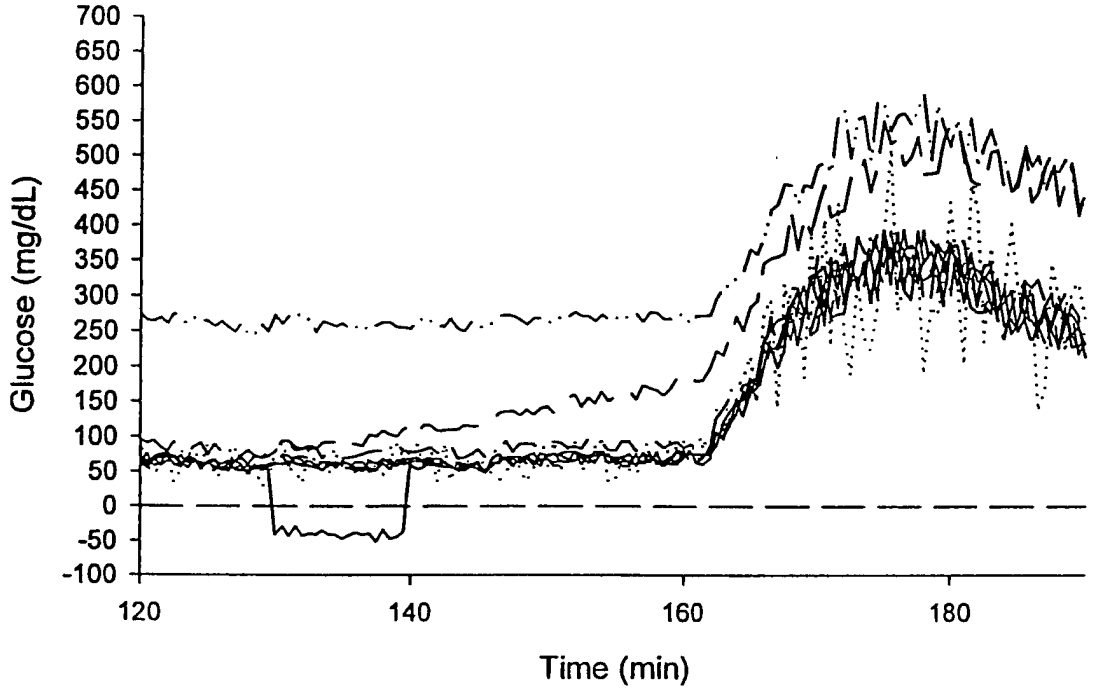
Glucose (mg/dL)
700
650
600
550
500
450
400
350
300
250
200
150
100
50
0
-50
-100
120
140
160
180
Time (min)

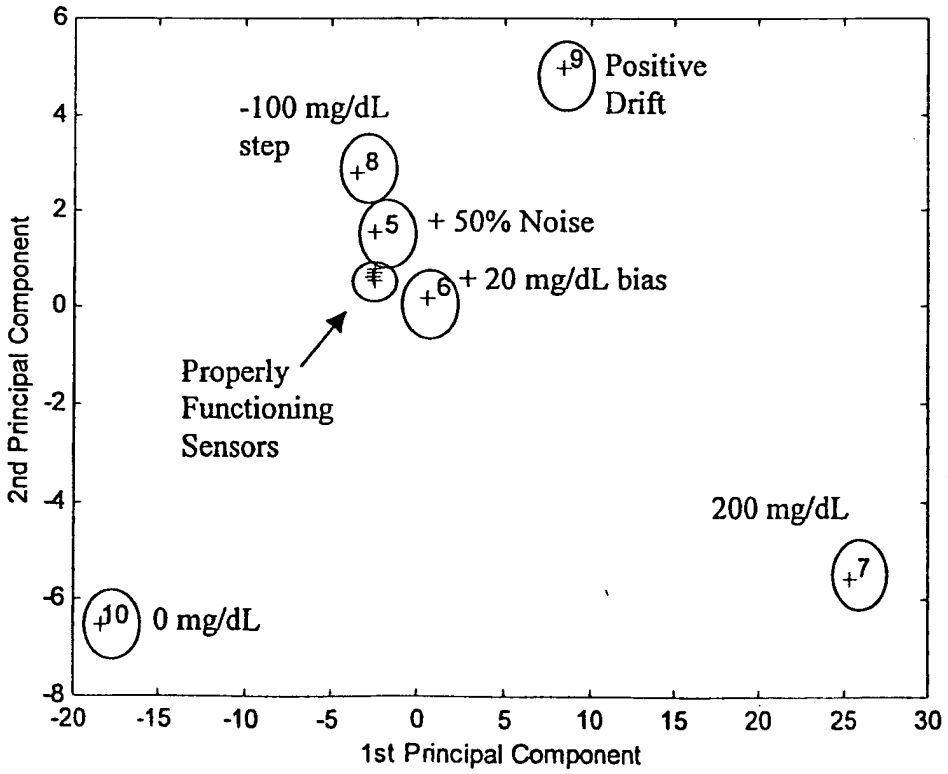
2nd Principal Component
1st Principal Component
+9 Positive Drift
-100 mg/dL step
+8
+5 + 50% Noise
+6 + 20 mg/dL bias
Properly Functioning Sensors
200 mg/dL
+7
+10 0 mg/dL

Figure 7

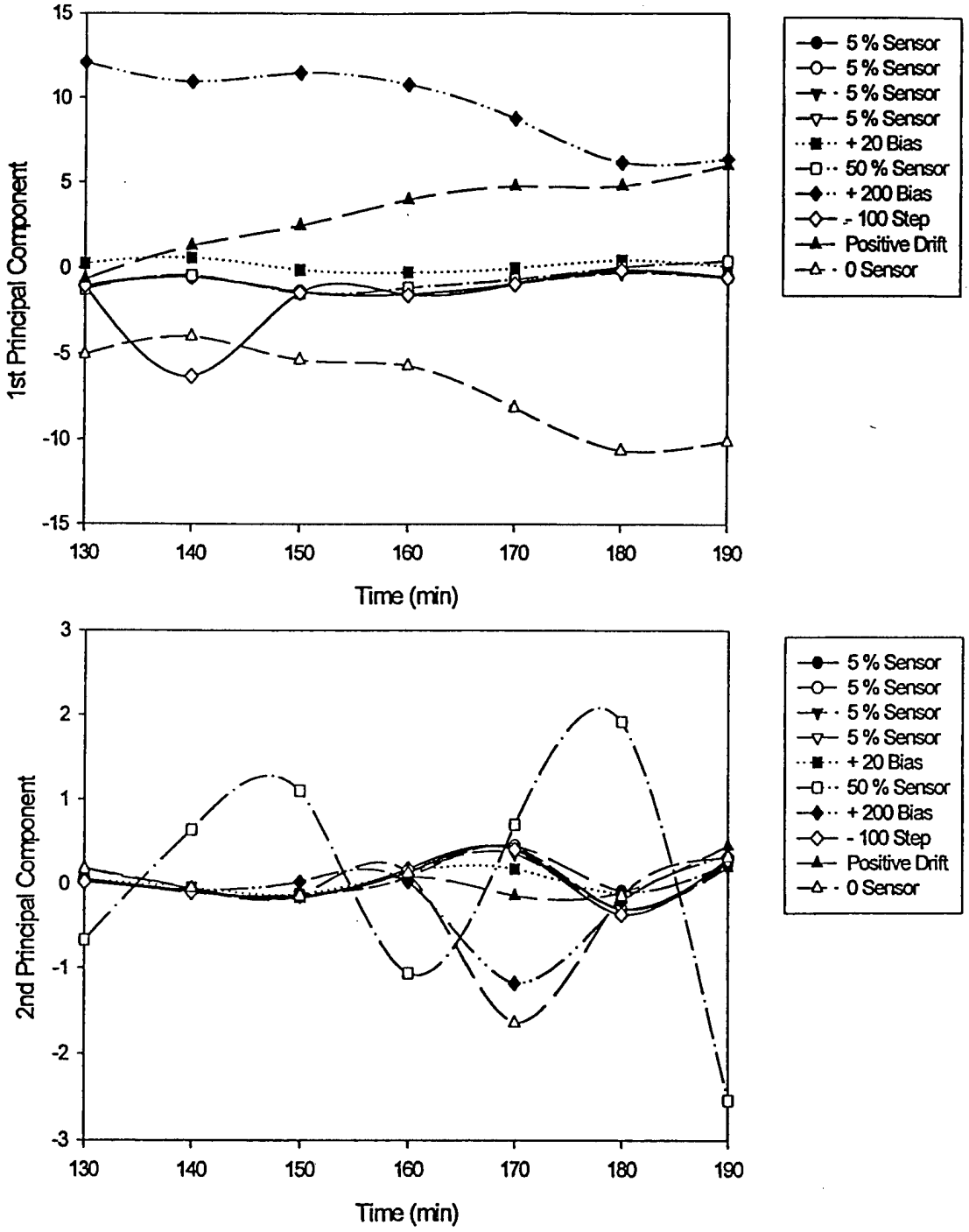
15
10
5
0
-5
-10
-15
1st Principal Component
130
140
150
160
170
180
190
Time (min)
5 % Sensor
5 % Sensor
5 % Sensor
5 % Sensor
+ 20 Bias
50 % Sensor
+ 200 Bias
- 100 Step
Positive Drift
0 Sensor
3
2
1
0
-1
-2
-3
2nd Principal Component
130
140
150
160
170
180
190
Time (min)
5 % Sensor
5 % Sensor
5 % Sensor
5 % Sensor
+ 20 Bias
50 % Sensor
+ 200 Bias
- 100 Step
Positive Drift
0 Sensor

Figure 8

I: ac6a34 USER: rjb69 DIV: @xyv04/data1/CLS_pj/GRP_ac/JOB_i11/DIV_ac991041k DATE: April 7, 2000

SEE AUTHOR
QUERIES IN
MANUSCRIP

Glucose and Lactate Biosensors Based on Redox Polymer/Oxidoreductase Nanocomposite Thin Films

Kaushik Sirkar, Alexander Revzin, and Michael V. Pishko*

Department of Chemical Engineering, Texas A&M University, College Station, Texas 77843-3122

Glucose and lactate enzyme electrodes have been fabricated through the deposition of an anionic self-assembled monolayer and subsequent redox polymer/enzyme electrostatic complexation on gold substrates. These surfaces were functionalized with a negative charge using 11-mercaptoundecanoic acid (MUA), followed by alternating immersions in cationic redox polymer solutions and anionic glucose oxidase (GOX) or lactate oxidase (LAX) solutions to build the nanocomposite structure. The presence of the multilayer structure was verified by ellipsometry and sensor function characterized electrochemically. Reproducible analyte response curves from 2 to 20 mM (GOX) and 2–10 mM (LAX) were generated with the standard deviation between multiple sensors between 12 and 17%, a direct result of the reproducibility of the fabrication technique. In the case of glucose enzyme electrodes, the multilayer structure was further stabilized through the introduction of covalent bonds within and between the layers. Chemical cross-linking was accomplished by exposing the thin film to glutaraldehyde vapors, inducing linkage formation between lysine and arginine residues present on the enzyme periphery with amine groups present on a novel redox polymer, poly[vinylpyridine Os(bisbipyridine)$_2$Cl]-*co*-allylamine. Finally, an initial demonstration of thin-film patterning was performed as a precursor to the development of redundant sensor arrays. Microcontact printing was used to functionalize portions of a gold surface with a blocking agent, typically 1-hexadecanethiol. This was followed by immersion in MUA to functionalize the remaining portions of gold with negative charges. The multilayer deposition process was then followed, resulting in growth only on the regions containing MUA, resulting in a "positive"-type pattern. This technique may be used for fabrication of thin-film redundant sensor arrays, with thickness under 100 Å and lateral dimensions on a micrometer scale.

The need for effective enzyme-based amperometric biosensors is present for many clinically relevant applications, with glucose and lactate sensing two of the most commercially important. Numerous types of amperometric devices for both substrates have been reported in the literature that take advantage of the enzymatic properties of glucose oxidase (GOX) and lactate oxidase (LAX). These electrodes include those based upon the electrochemical oxidation of H_2O_2 generated during the reaction between glucose or lactate and oxygen catalyzed by the corresponding oxidoreductase[1,2] and those that use charge mediators to transfer electrons between the redox center of the enzyme and the electrode surface.[3–7] The actual commercial application of biosensor technology, however, has been somewhat limited, typically to home glucose test meters and blood-gas instruments designed to detect glucose and lactate. Technically demanding applications such as the detection of multiple analytes in vivo require a high density of individual analyte-sensing electrodes, required for miniaturization, which themselves contain a large concentration of enzyme molecules necessary to provide high signal levels. In addition, these sensors must be fabricated easily, reproducibly, and at spatially distinct, readily addressable regions on a discrete portion of a surface. Biosensor development with a priority on spatial orientation and assembly on the nanoscale has thus become an important issue. Examples of such research include thin-film biosensors that use biotin/avidin linkages to immobilize enzymes in an ordered fashion[8,9] and assembled GOX/pyrroloquinoline (PQQ) multilayers using techniques including carbodiimide coupling of PQQ to surface polyamines.[10–12] Array or pattern development has also begun to receive attention for thin-film biosensing applications. Various macromolecules, including antibodies and proteins, have been deposited into discrete patterns using photolithography[13,14] and microcontact printing.[15,16]

(1) Tatsuma, T.; Saito, K.-I.; Oyama, N. *Anal. Chem.* **1994**, *66*, 1002–1006.
(2) Shram, N. F.; Netchiporouk, L. I.; Martelet, C.; Jaffrezic-Renault, N.; Bonnet, C.; Cespuglio, R. *Anal. Chem.* **1998**, *70*, 2618–2622.
(3) Hale, P. D.; Boguslavsky, L. I.; Inagaki, T.; Karan, H. I.; Lee, H. S.; Skotheim, T. A.; Okamoto, Y. *Anal. Chem.* **1991**, *63*, 677–682.
(4) Pishko, M. V.; Michael, A. C.; Heller, A. *Anal. Chem.* **1991**, *63*, 2268–2272.
(5) Kenausis, G.; Chen, Q.; Heller, A. *Anal. Chem.* **1997**, *69*, 1054–1060.
(6) Sirkar, K.; Pishko, M. *Anal. Chem.* **1998**, *70*, 2888–2894.
(7) Osborne, P. G.; Niwa, O.; Yamamoto, K. *Anal. Chem.* **1998**, *70*, 1701–1706.
(8) Dontha, N.; Nowall, W.; Kuhr, W. *Anal. Chem.* **1997**, *69*, 2619–2625.
(9) Anzai, J.; Kobayashi, Y.; Nakamura, N.; Nishimura, M.; Hoshi, T. *Langmuir* **1999**, *15*, 221–226.
(10) Willner, I.; Heleg-Shabtai, V.; Blonder, R.; Katz, E.; Tao, G. *J. Am. Chem. Soc.* **1996**, *118*, 10321–10322.
(11) Willner, I.; Katz, E.; Willner, B. *Electroanalysis* **1997**, *9*, 965–977.
(12) Moore, A. N. J.; Katz, E.; Willner, I. *Electroanalysis* **1996**, *8*, 1092.
(13) Mooney, J.; Hunt, A.; McIntosh, J.; Liberko, C.; Walba, D.; Rogers, C. *Proc. Natl. Acad. Sci. U.S.A.* **1996**, *93*, 12287–12291.

One technique that has received a great deal of attention recently involves the building of individual monolayers on surfaces based upon the attraction between oppositely charged species. Hammond et al. have addressed many issues in the development of patterned polyion multilayers.[17-19] Typically, these systems utilized sulfonated polystyrene as the anionic component and compounds such as poly(allylamine hydrochloride) as the cationic component. These polyion multilayers were grown in distinct patterns through the use of microcontact printing (μCP) and blocking agents anchored to a gold substrate. The effects of solution ionic strength[20,21] as well as the attachment of redox-active osmium complexes have been addressed in similar studies.[22]

Electrostatic complexation of the redox polymer and enzyme may be utilized to generate amperometric biosensors with high current densities, despite physical limitations on the total amount of sensor materials. This type of electrostatic complexation was demonstrated earlier with the complexation of polycationic poly(vinylpyridine) complexes of $[Os(bpy)_2Cl]^{2+}$ and polyanionic glucose oxidase at graphite electrodes.[23] Complexations of this type have been utilized in recent layer-by-layer deposition approaches for the development of glucose sensors. Chen et al. utilized alternating GOX and charge mediator layers for the fabrication of glucose enzyme electrodes.[24,25] Other groups also performed similar work utilizing ferrocene derivatives as their polycationic charge mediator.[26] Although these studies have demonstrated the fabrication of amperometric glucose sensors using the electrostatic layer-by-layer approach, no mention was made of the thickness of the sensing layers, attempts to improve sensor stability, patterning, or oxidoreductases other than GOX.

The present work expands on the concepts of electrostatic complexation between redox polymers and oxidoreductases. We describe glucose and lactate sensors that use a multilayer deposition approach based upon attraction between oppositely charged species, namely, a novel cationic redox polymer and anionic GOX or LAX. The thickness of the individual monolayers was determined via ellipsometry with the number of redox sites within a given monolayer established through cyclic voltammetry. The sensor function of the polyion multilayer was compared to that of multilayers stabilized via chemical cross-linking. Finally, a demonstration of patterning was performed through the utilization of microcontact printing of MUA and blocking agents such as 1-hexadecanethiol (C16-SH). This is a necessary precursor to the development of a single-analyte redundant sensor array or multianalyte sensor arrays.

EXPERIMENTAL SECTION

Reagents. Glucose oxidase (EC 1.1.3.4, type X-S, 128 units/mg of solid from *Aspergillus niger*), lactate oxidase (35 units/mg of solid, from *Pediococcus* species), and lactic acid (60% w/w in H_2O) were obtained from Sigma Chemical Co. (St. Louis, MO). Ammonium hexachloroosmate(IV), 1-hexadecanethiol, 11-mercaptoundecanoic acid (MUA), 2,2′-azobisisobutyronitrile (AIBN), poly(4-vinylpyridine), and 2,2′-dipyridyl (bpy) were obtained from the Aldrich Chemical Co. (Milwaukee, WI). Dextrose, methanol, ethyl alcohol, glutaraldehyde, ethylene glycol, hydrochloric acid (11 N), and acetonitrile were obtained from Fisher Scientific Co. (Pittsburgh, PA). An α-acryloyl, ω-*N*-hydroxysuccinimidyl ester of poly(ethylene glycol)propionic acid (PEG-NHS, MW 3400) was purchased from Shearwater Polymers (Huntsville, AL). All reagents, unless otherwise stated, were used as received. Phosphate-buffered saline (PBS) solution was composed of 1.1 mM potassium phosphate monobasic, 3 mM sodium phosphate dibasic heptahydrate, and 0.15 M NaCl in 18 MΩ·cm deionized water (E-pure, Barnstead).

Equipment. The equipment for electrochemical analysis included a CV-50W voltammetric analyzer (Bioanalytical Systems, West Lafayette, IN), a C2 cell stand, a Ag/AgCl reference electrode, and a platinum counter electrode. The electrochemical apparatus was controlled and data were acquired using a Toshiba Pentium PC. Ellipsometry was performed using a Gaertner L2W26D ellipsometer (Gaertner Scientific Corp., Chicago, IL). Film thickness and refractive indexes were calculated using Gaertner software, utilizing a film model that assumed a refractive index (n_f) of 1.46. All measurements were made using a He/Ne (633.8 nm) laser and a 70.00 ± 0.02° angle of incidence. Micrographs of multilayer patterns were acquired using a Meiji optical microscope (Meiji Techno America, San Jose, CA) and a Kodak DC240 digital camera (Eastman Kodak Co., Rochester, NY).

Electrodes. Gold electrodes with diameters of 1.6 mm each were purchased from Bioanalytical Systems. Prior to deposition of the multilayers, the electrodes were polished with 1-μm diamond polishing slurry on nylon polishing pads and then with 0.05-μm alumina on microcloth pads followed by sonication along with water and methanol rinses. Gold-coated silicon wafers (200 Å Cr, 1000 Å Au on polished Si(111), Lance Goddard Associates, Foster City, CA) were fabricated into electrodes (6.45 cm^2) by soldering a conducting wire to the substrate surface. Gold-coated wafers were rinsed with ethanol, cleaned in an ozone cleaner (Boekel Industries, Inc., model 135500) for 10 min, and rinsed with ethanol again before use.

Polymer Synthesis. Osmium-based polycationic redox polymers were synthesized using modifications of established protocols. $Os(bpy)_2Cl_2$ was synthesized according to a standard procedure.[27] In brief, 2 equiv of bipyridine (720 mg) was mixed with 1 equiv of ammonium hexachloroosmate(IV) (1000 mg) in 50 mL of ethylene glycol. This mixture was heated to reflux for 45 min, precipitated with supersaturated sodium dithionite, and

(15) Kratzmuller, T.; Appelhans, D.; Braun, H.-G. *Adv. Mater.* **1999**, *11*, 555–558.
(16) James, C. D.; Davis, R. C.; Kam, L.; Craighead, H. G.; Isaacson, M.; Turner, J. N.; Shain, W. *Langmuir* **1998**, *14*, 741–744.
(17) Hammond, P. T.; Whitesides, G. M. *Macromolecules* **1995**, *28*, 7569–7571.
(18) Clark, S. L.; Hammond, P. T. *Adv. Mater.* **1998**, *10*, 1515–1519.
(19) Gregoriou, V. G.; Hapanowicz, R.; Clark, S. L.; Hammond, P. T. *Appl. Spectrosc.* **1997**, *51*, 470–476.
(20) Clark, S. L.; Montague, M. F.; Hammond, P. T. *Macromolecules* **1997**, *30*, 7237–7244.
(21) Sukhorukov, G. B.; Schmitt, J.; Decher, G. *Ber. Bunsen-Ges. Phys. Chem.* **1996**, *6*, 948–953.
(22) Bretz, R. L.; Abruna, H. D. *J. Electroanal. Chem.* **1996**, *408*, 199–211.
(23) Pishko, M. V.; Katakis, I.; Lindquist, S.-E.; Ye, L.; Gregg, B. A.; Heller, A. *Angew. Chem., Intl. Ed. Engl.* **1990**, *29*, 82.
(24) Hou, S.-F.; Fang, H.-Q.; Chen, H.-Y. *Anal. Lett.* **1997**, *30*, 1631–1641.
(25) Hou, S.-F.; Yang, K.-S.; Fang, H.-Q.; Chen, H.-Y. *Talanta* **1998**, *47*, 561–567.
(26) Hodak, J.; Etchenique, R.; Calvo, E. J.; Singhal, K.; Bartlett, P. N. *Langmuir* **1997**, *13*, 2708–2716.
(27) Kober, E. M.; Caspar, J. V.; Sullivan, B. P.; Meyer, T. J. *Inorg. Chem.* **1988** *27*, 4587–4598.

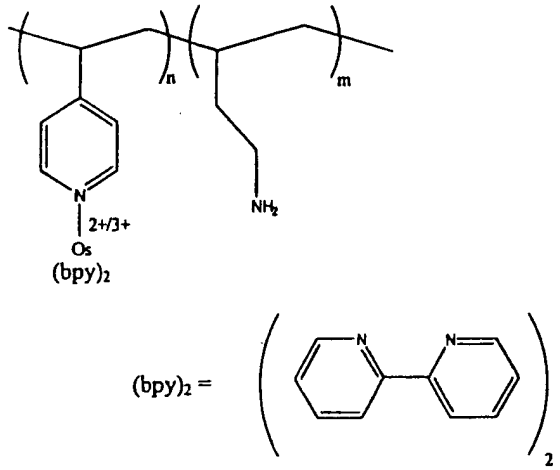

Figure 1. Structure of cross-linkable, organometallic osmium redox polymer used in development of electrostatic multilayers: poly[4-vinylpyridine Os(bisbipyridine)$_2$Cl]-*co*-allylamine (PVP–Os–AA).

repeatedly washed with water and ether. The $Os(bpy)_2(Cl)_2$ precursor was used in the synthesis of cross-linkable redox polymers used in these studies.

Poly[vinylpyridine Os(bis-bipyridine)$_2$Cl]-*co*-allylamine (PVP–Os–AA), was synthesized as follows: 1.0 g of 4-vinylpyridine, 1.0 g of allylamine, 0.2 g of AIBN, and 200 μL of HCl were mixed in 50 mL of acetonitrile. This solution was refluxed for 2 h and then concentrated using rotary evaporation for the removal of acetonitrile. The resulting polymer was dissolved in 1 mL of methanol and precipitated in 50 mL of ethyl ether. A 100-mg sample of $Os(bpy)_2Cl_2$ was then added to 100 mg of PVP-*co*-allylamine in 50 mL of ethylene glycol and refluxed under N_2 for 1.5 h. Ethylene glycol was removed and the product dissolved in a minimal amount of methanol followed by precipitation in 70 mL of diethyl ether. The ether was then decanted off and PVP–Os–AA was dried and collected. Figure 1 depicts the structure of PVP–Os–AA.

Multilayer Fabrication. Gold substrates were initially functionalized by immersing in 1 mM MUA in ethanol for ~20 min. The substrates were removed, washed, sonicated, and dried under N_2. The substrates were then alternately placed first in a polycationic 10 mg/mL solution of PVP–Os–AA for ~20 min and a polyanionic solution of GOX (10 mg/mL in PBS) or LAX (0.7 mg/mL in PBS) for ~40 min. Between immersions, the substrates were rinsed with 0.1 M PBS, sonicated for ~20 s, and dried under flowing N_2. A depiction of the final multilayer structure is presented in Figure 2.

Multilayer Cross-Linking. To chemically stabilize the multilayer structures, the cationic and anionic layers were chemically cross-linked using glutaraldehyde.[28] This was accomplished by exposing the coated substrates to glutaraldehyde vapors for ~15 min and then removing to room air prior to electrochemical testing.

Multilayer Patterning. Stamps for microcontact printing structures were made via replica molding, using a slightly modified version of a published protocol.[29] In brief, Shipley STR1045

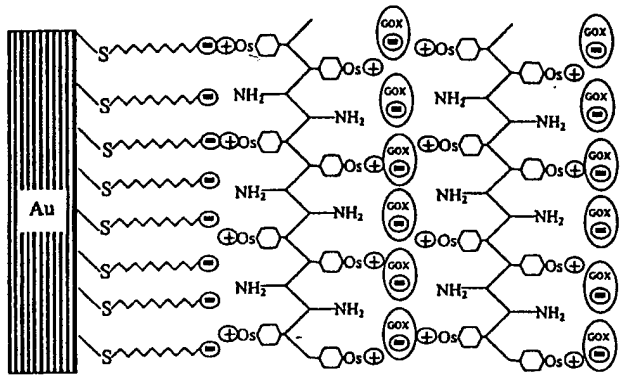

Figure 2. Depiction of the multilayer structure. Positive charges on redox polymer are electrostatically attracted to negative charges on enzyme and substrate surface.

photoresist (MicroChem Corp., MA) was deposited in a thin layer via spin coating at ~5000 rpm on a clean Si wafer. This photoresist was exposed to 365-nm, 20 W/cm^2 UV light through an optical test mask (USAF resolution chrome test target, Melles Griot). After photoresist development, poly(dimethylsiloxane) (PDMS) (Sylgard 184 silicone elastomer and curing agent in a 10:1 ratio, Dow Corning Corp.) was deposited over the patterned photoresist. The uncured PDMS was confined with a small cylinder pressed down on the substrate with a slight weight. This prestamp was then placed in a vacuum oven to be degassed and cured for ~24 h. Upon curing, the PDMS was lifted off the substrate resulting in the patterned stamp.

Application of the stamp to form a patterned substrate was performed as follows. Initially, the stamp was dipped in 1 mM C16-SH solution (ethanol) for ~20 s. It was then dried, and pressed on a cleaned gold surface for ~20 s. The stamp was then removed, the substrate exposed to 1 mM MUA for ~20 min, and the multilayer deposition procedure followed as described earlier.

Electrochemical Characterization. Electrodes were tested in a cell containing Pt counter and Ag/AgCl reference electrodes as well as 0.1 M PBS degassed with N_2 (15 min prior to start of experiment and for the duration of experiment). Bubbling with N_2 was used to agitate the solution rather than a stir bar. Either of two experiments was conducted to characterize sensor response: cyclic voltammetry or constant-potential amperometry. For cyclic voltammetry, the applied potential was cycled linearly from 0 to 500 mV at a scan rate of 20 mV/s. The anodic peaks of individual scans were integrated to determine the surface coverage or the total amount of charge mediator present in any one layer. Constant-potential amperometry required the preconditioning (~50 s) and operation of the electrode at a constant applied potential of 300 mV. When the current reached a baseline in the absence of substrate, aliquots of substrate were added and steady changes in current monitored with time. Unless otherwise stated $n = 3$ for all substrate response curves.

RESULTS AND DISCUSSION

The development of reliable and robust amperometric biosensor arrays is dependent upon the miniaturization of sensor features to increase both the density of sensing elements in a spatially distinct region and the density of biorecognition molecules within

(28) Wiseman, A. In *Ellis Horwood Series in Biochemistry and Biotechnology incorporating Molecular Biology*; Wiseman, A., Ed.; Ellis Horwood: London, 1995; p 738.

(29) Xia, Y.; Whitesides, G. M. *Angew. Chem., Intl. Ed.* 1998, *37*, 550–575.

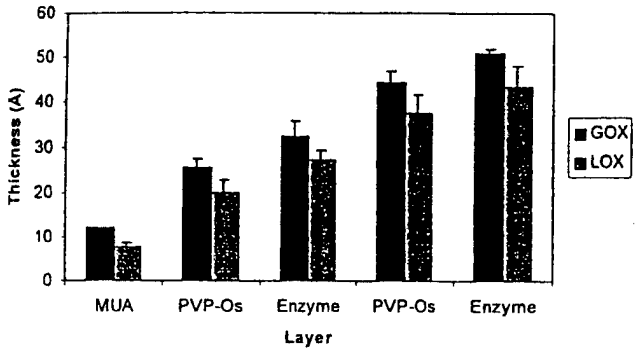

Figure 3. Increase in thickness as measured by ellipsometry upon attachment of each subsequent layer.

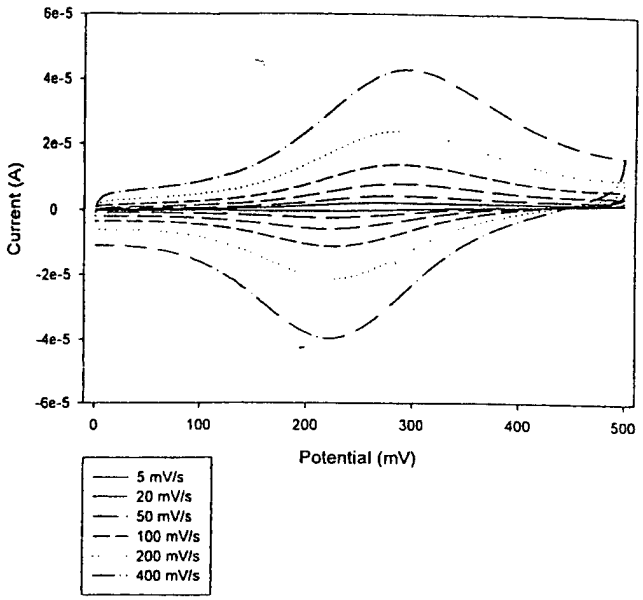

Figure 4. Cyclic voltammograms as a function of increasing scan rate (5–400 mV/s) for a GOX/PVP–Os–AA nanocomposite thin film. A formal potential of 250 mV was found with a peak separation of ~60 mV.

an individual sensor. Miniaturization, however, may result in low current densities and inadequate signal-to-noise ratios. To overcome this problem, we have formed redox polymer and enzyme complexes through an electrostatic layer by layer deposition scheme, a technique that has been shown to increase current densities in the resulting biosensors.[23] This scheme for sensor development minimizes the use of such components as retaining membranes or thick polymer matrixes, resulting in an increased density of the primary sensing components, namely, the enzyme and redox polymer. This permits rapid and efficient sensor performance, which may be further improved by chemically cross-linking the multilayer structure by exposure to glutaraldehyde. The goal of minimizing sensor dimensions was achieved by keeping the thickness of the sensing layers well under 100 Å through repeated attachment of single redox polymer/enzyme monolayers. The feasibility of depositing these layers in micrometer-scale patterns was then demonstrated using μCP techniques. This may eventually permit rapid generation of multilayer sensor arrays.

Multilayer Formation. The first step in the fabrication of these nanocomposite structures was the functionalization of a gold substrate for subsequent layer-by-layer deposition. As an adhesion layer, a monolayer of MUA[30] with a pK_a of ~6.5 was adsorbed to the gold substrate via its thiol end group. At the buffer pH of ~7.4, MUA presents the electrode–solution interface with an initial negative surface charge, via its partially deprotonated carboxyl acid groups, with which to begin the layer-by-layer deposition process. Poly(4-vinylpyridine) complexes of $Os(bpy)_2Cl_2$ are highly cationic[23] and will electrostatically adsorb to the negatively functionalized surface. GOX has an isoelectric point[31] of ~3 and LAX has a pI of ~4.6; thus, at pH 7.4, both enzymes possess a net negative charge, permitting their adsorption to the cationic redox polymer. Alternating deposition of positively charged redox polymers and negatively charged enzymes permitted the buildup, layer-by-layer, of a nanocomposite structure.

One of the requisite features for the formation of well-ordered and defined biosensors is the ability to tailor the organization of the sensor components as close to the molecular level as possible. With this goal in mind, ellipsometric data were obtained after adsorption of subsequent layers to verify that very thin layers were being deposited after each adsorption step. Figure 3 shows the increase in film thickness upon addition of each layer during the alternate immersions in polycation/polyanion solutions. For glucose enzyme electrodes, the increase in thickness was linear with each addition, with an $R^2 > 0.98$. The average thickness of the cationic multilayer, PVP–Os–AA, was larger, ~12.5 Å, than the average anionic multilayer (GOX), ~6.7 Å. GOX from *A. niger* in its native state is a globular glycoprotein with an elliptical shape and a maximum diameter as determined by X-ray crystallography of ~45 Å along its primary axis.[32] However, perpendicular to this axis, the diameter is smaller, in the range from 15 to 20 Å. On the basis of the ~6.7-Å increase in thickness after GOX adsorption, the enzyme is likely buried and intercalated within the redox polymer thin film. This is expected due to the nature of the electrostatic interactions between the polyions where very strong multipoint contacts are prevalent. The thickness determined for LAX multilayers is almost identical to those determined for GOX. The average thicknesses of LAX-containing films were ~11 Å for the redox polymer layers and 6.5 Å for the enzyme layers, with a linear increase in film thickness upon the addition of each layer ($R^2 > 0.98$). The thicknesses of these multilayered nanocomposites are comparable with the few reported values for nonbiosensor applications.[17,20] Controls were performed on gold substrates that were not functionalized with MUA, and it was found that there was a negligible change in thickness as measured via ellipsometry when an attempt was made to deposit both enzyme and/or redox polymer layers.

Electrochemical Characterization. Cyclic voltammetry, shown in Figure 4 for scan rates ranging from 5 to 400 mV/s, indicated a formal potential of ~250 mV with a difference in peak potential of ~60 mV. This indicated that the system is reversible, as the peak potential is independent of the scan rate and the peak current changes linearly with scan rate raised to the one-half power (not

(30) Jordan, C. E.; Corn, R. M. *Anal. Chem.* **1997**, *69*, 1449–1456.
(31) Schumann, W.; Ohara, T. J.; Schmidt, H.-L.; Heller, A. *J. Am. Chem. Soc.* **1991**, *113*, 1394–1397.
(32) Franchina, J. G.; Lackowski, W. M.; Dermody, D. L.; Crooks, R. M.; Bergbreiter, D. E.; Sirkar, K.; Russell, R. J.; Pishko, M. V. *Anal. Chem.* **1999**, *71*, 3133–3139.

shown). Repeated cyclic voltammetry without the presence of glucose produced scans whose peaks did not degrade appreciably over time, demonstrating that the electroactive components were not free to diffuse away from the electrode surface. Subsequently, cyclic voltammograms at a scan rate of 20 mV/s were used to characterize the number of electroactive osmium redox sites present in each layer, an important criterion for the assessment of the sensor's electrochemical function. This number was determined based upon the cyclic voltammogram of a wafer with only a single redox polymer layer adsorbed (MUA/PVP–Os–AA). The area under the anodic peak was integrated from the voltammogram and used to determine the surface coverage of osmium redox sites present per adsorbed layer. This value, ~4.1 × 10^{-11} mol cm^{-2}, compares favorably with the values of (4–5) × 10^{-11} mol cm^{-2} reported for ferrocene monolayers[26] and 3 × 10^{-11} mol cm^{-2} reported for $Os(bpy)_3^{2+}$ layers.[33] On the basis of the redox polymer film thickness reported earlier and the surface coverage, the concentration of redox sites per monolayer is ~3.2 × 10^{-4} mol cm^{-3}.

Substrate Response. The multilayer scheme has distinct advantages over other types of sensor fabrication methods reported in the literature. Consider specifically the sensing mechanism for enzymatic catalysis and electron transfer between polycationic osmium redox polymers and polyanionic glucose oxidase.

$$\beta\text{-D-glucose} + \text{GOX(FAD)} \rightarrow \text{gluconolactone} + \text{GOX(FADH}_2\text{)}$$

$$\text{GOX(FADH}_2\text{)} + 2\text{Os(bpy)}_2\text{(vp)}^{2+} \rightarrow \text{GOX(FAD)} + 2\text{Os(bpy)}_2\text{(vp)}^{1+}$$

$$\text{Os(bpy)}_2\text{(vp)}^{2+} + \text{Os(bpy)}_2\text{(vp)}^{1+} \rightarrow \text{Os(bpy)}_2\text{(vp)}^{1+} + \text{Os(bpy)}_2\text{(vp)}^{2+}$$

$$2\text{Os(bpy)}_2\text{(vp)}^{1+} \rightarrow 2e^- + 2H^+ + 2\text{Os(bpy)}_2\text{(vp)}^{2+}$$

Qualitatively, sensor response times should be minimized due to increased proximity between the enzyme and charge mediator in an ordered structure where enzymes are in direct contact with the redox polymer. Distances much larger than 10 Å result in very low rates of electron transfer;[34] the multilayer structure places redox sites well within 10 Å of each other and of enzymes.

The response of the enzyme electrodes to the addition of substrate was characterized using both constant-potential amperometry and cyclic voltammetry. Current response values for nanocomposite films consisting of native LAX and PVP–Os–AA are depicted in Figure 5. We see a linear response for a multilayer structure consisting MUA/PVP–Os–AA/LAX with a sensitivity of 0.027 μA cm^{-2} mM^{-1}, an R^2 value of ~0.98, and a standard deviation of ~12% between electrodes.

For a GOX multilayer, we see a relatively linear calibration curve from 2 to 20 mM substrate with a sensitivity of 0.015 μA cm^{-2} mM^{-1} and an R^2 value of ~0.98 (Figure 6). The error bars indicate a standard deviation of ~17% between electrodes. This

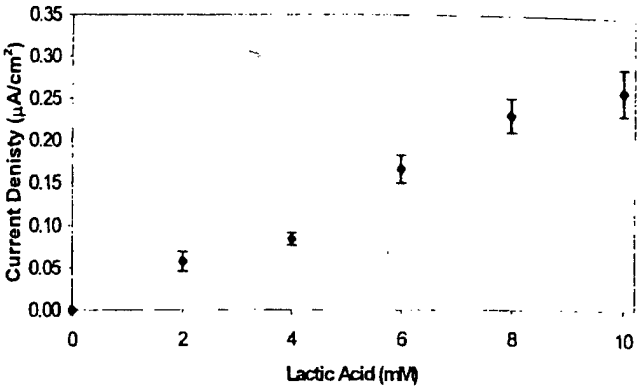

Figure 5. Increase in current density with substrate concentration for lactate enzyme electrode using multilayer scheme consisting of LAX and PVP–Os–AA (MUA/Os/LAX).

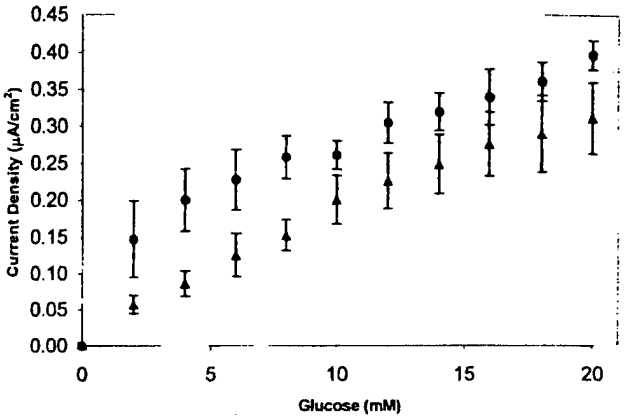

Figure 6. Response of glucose enzyme electrodes to substrate addition: (▲) electrostatically assembled multilayer structure; (●) chemically cross-linked multilayer structure.

compares favorably with the American Diabetes Association acceptable standard deviation of 15%.[35] The response in the absence of oxygen indicates electron transfer between GOX and osmium sites along with charge propagation through the redox polymer to the electrode surface. In the presence of oxygen, the response is reduced by ~50%. This indicates, as expected, that oxygen does compete with osmium sites in the multilayer structure. The signal-to-noise ratio (SNR) was determined from the electrode response, under N_2, at 6 mM glucose and was calculated as the steady-state current at that substrate concentration divided by the standard deviation of the current (i.e., the noise). At 6 mM, the SNR was ~100, indicating a relatively sensitive electrode at physiological glucose levels. As expected by the thickness of the nanocomposite thin film, the response times are quite rapid for both glucose and lactate enzyme electrodes, with times to reach 95% of the final response under 4 s for step changes in substrate concentration in the physiological range.

The lactate enzyme electrodes demonstrate a higher response as compared to a glucose enzyme electrode. The opposite might be expected since the glucose oxidase solution used for enzyme deposition was ~2 orders of magnitude greater in activity than that of lactate oxidase. However, one must consider the size o

(33) Kuhn, A.; Anson, F. C. *Langmuir* **1996**, *12*, 5481–5488.
(34) Marcus, R. A.; Sutin, N. *Biochim. Biophys. Acta* **1985**, *811*, 265.
(35) Association, A. D. *Diabetes Care* **1987**, *10*, 95–99.

each of these macromolecules. GOX is a dimer of large molecular weight, ~180 000, more than twice the size of LOX, ~80 000. Considering enzyme intercalation in a highly charged redox polymer layer, it is possible that a larger amount of LOX was electrostatically incorporated into each layer. This may be true from a physical standpoint, as a larger number of smaller spheres (both GOX and LOX are globular) will pack into a given space than will larger spheres. This may also be true from an electrostatic standpoint, as the negative or anionic portions of LOX are potentially more accessible for electrostatic complexation, as the enzyme is smaller and these residues will more likely reside near the surface of the protein. This type of phenomenon has been observed in the past where Heller and colleagues[36] demonstrated higher current densities (~25–50%) for lactate enzyme electrodes as compared to glucose enzyme electrodes under analogous conditions.

The current densities determined in these experiments for both lactate and glucose enzyme electrodes, as expected, are relatively low due to the size of the electrodes used. As ellipsometry necessitated the use of larger Au substrates (6.45-cm^2 electrodes), the obtained current densities do not compare favorably to those present in the literature, including studies reporting 10–20 μA cm^{-2} mM^{-1} for polymer film-based sensors.[37,38] However, when these nanocomposite films were fabricated on gold microelectrodes ($d \sim 250$ μm), current densities approached 10 μA cm^{-2} mM^{-1}.

Multilayer Cross-Linking. Further covalent stabilization of the resultant nanocomposite thin films was desired not only to physically strengthen the film structure but also to eliminate potential desorption due to changes in pH, ionic strength, or high oxidation potentials. We have demonstrated that extreme changes in pH are capable of releasing biomolecules that are entrapped through electrostatic interactions.[32] Other studies have demonstrated the destruction or desorption of SAMs at negative applied potentials.[39,40] In addition, covalent bonds between the layers are likely to improve charge-transfer rates and, hence, sensor response. In redox polymers, electron transfer is believed to occur by two primary mechanisms: electron hopping between redox sites and routing along polymer chains. Although imparting covalent cross-links may suggest a decrease in redox polymer flexibility and subsequently reduced conductivity, cross-linking of the multilayer structure likely decreases the distance between enzyme active sites and redox sites while providing additional direct routes of charge transfer, both from the enzyme to redox sites and between redox sites via self-exchange.[41]

To further stabilize the structure, previously tested GOX enzyme electrodes were chemically cross-linked by exposure to glutaraldehyde vapors where it is anticipated that arginine and lysine residues of the enzyme will react with amines present on the redox polymer. Figure 6 also shows that there is an increase

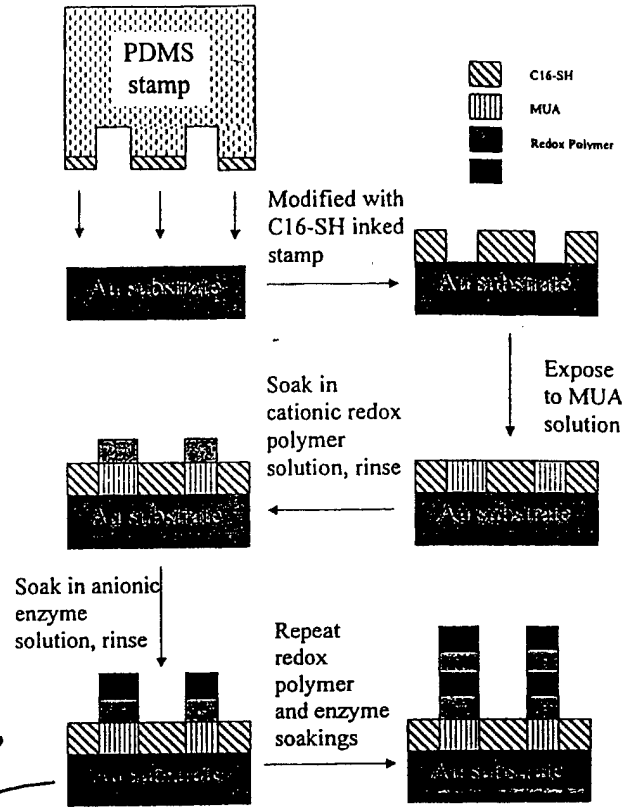

Figure 7. Schematic for buildup of multilayer films; repeated t generate the desired number of layers and sonicated between eac step.

in current density upon cross-linking with glutaraldehyde a opposed to non-cross-linked films, with an average increase ~60%. The standard deviation for electrodes based on cross-linke multilayer structures was ~13% between electrodes. With an I ~ 88%, the response is not as linear as that for the non-cros linked films. This appears to indicate that the Michaelis–Mente enzyme kinetics of the enzyme become rate limiting in th electrode reactions when the nanocomposite film is cross-linke possibly due to improved electron transfer between the redc polymer and enzyme. These cross-linked films were able to reta nearly 100% of their activity for a minimum of three weeks whe refrigerated (tested up to four weeks of retained activity), opposed to a maximum of two weeks for non-cross-linke nanocomposites.

Patterning. With the goal of achieving spatially distinct ar individually addressable biosensor array members, patterns of t multilayers were generated using the microcontact printi technology developed by Xia and Whitesides.[29] Stamps for μC were fabricated by depositing and curing PDMS on a photolith graphically generated master—a USAF test grid, consisting rectangles and numbers of varying size. The scheme for patterni is depicted in Figure 7, with a resultant pattern shown in Figu 8. The bars shown here have the critical lateral dimensions ~280 and 150 μm. This is true for both of the distinctly visit regions—those containing the multilayer structure and the ba blocked with C16-SH. Features as small as 10 μm have be identified, and 1–2-μm features are feasible using this technique Analogous to typical optical lithography techniques, the resulti film would be a "positive" pattern, as the regions stamped do r

(36) Delumleywoodyear, T.; Rocca, P.; Lindsay, J.; Dror, Y.; Freeman, A.; Heller, A. *Anal. Chem.* **1995**, *67*, 1332–1338.
(37) Malitesta, C.; Palmisano, F.; Torsi, L.; Zambonin, P. G. *Anal. Chem.* **1990**, *62*, 2735–2740.
(38) Ryan, M. R.; Lowry, J. P.; O'Neill, R. D. *Analyst* **1997**, *122*, 1419–1424.
(39) Garrell, R. L.; Chadwick, J. E. *Colloids Surf. A: Physicochem. Eng. Aspects* **1994**, *93*, 59–72.
(40) Widrig, C. A.; Chung, C.; Porter, M. D. *J. Electroanal. Chem.* **1991**, *310*, 335–359.
(41) Aoki, A.; Heller, A. *J. Phys. Chem.* **1993**, *97*, 11014–11018.

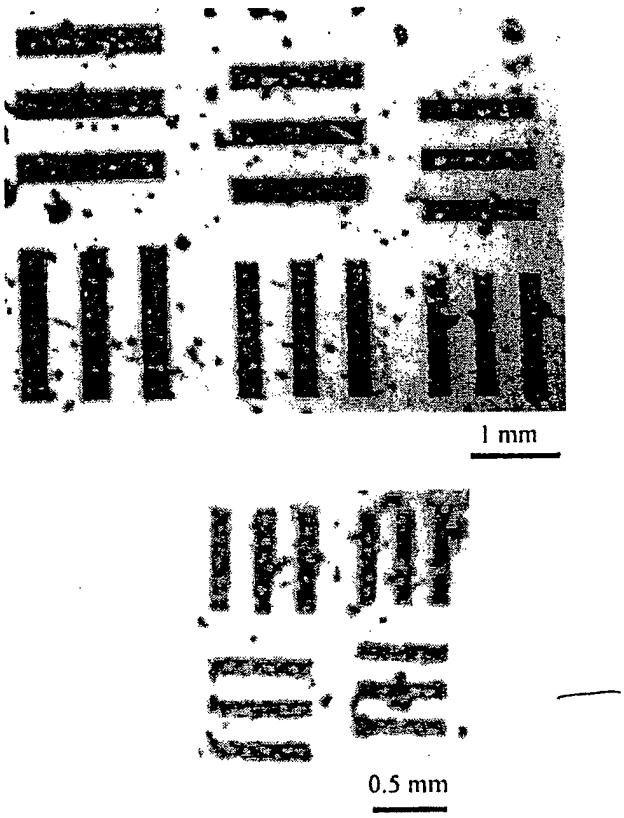

Figure 8. Patterns generated by μCP and subsequent multilayer buildup (dark regions on micrograph). Bars from pattern (top) have the critical lateral dimension of ~280 μm. Smaller features below have the critical lateral dimension of ~150 μm in width.

contain the multilayer sensing nanocomposite. If MUA or some other surface functionalizing agent were stamped instead of the blocking agent, or if an inverted stamp were fabricated, a "negative" pattern could be generated. This type of patterning may be utilized for the generation of redundant sensor arrays based upon nanocomposite electrostatic multilayers in the future.

CONCLUSIONS

We have developed robust glucose and lactate sensors using techniques of self-assembly and polyion adsorption. A gold surface was functionalized with a negative charge through reaction with MUA. Subsequently, cationic redox polymers were adsorbed followed by attachment of anionic GOX or LAX. This process was repeated as desired for the development of highly reproducible enzyme electrodes with standard deviations of ~12−17% between multiple electrodes. Sensor function was further improved through interlayer chemical cross-linking that stabilized the structure. Finally, a preliminary demonstration of patterning using the techniques of μCP was performed as a precursor to the development of a redundant glucose sensor array.

ACKNOWLEDGMENT

We thank the Whitaker Foundation, Juvenile Diabetes Foundation International (1-1998-298), United States Department of the Army, and the National Medical Technology Testbed, Inc. (DAMD17-97-2-7016) for support. M.P. thanks the Alfred P. Sloan Foundation for its support through a research fellowship. We also thank Prof. Richard M. Crooks of the Department of Chemistry at Texas A&M University for the use of his ellipsometer and his graduate students for numerous fruitful discussions. The view, opinions, and/or findings contained in this report are those of the author(s) and should not be construed as a position, policy, decision, or endorsement of the Federal Government or the National Medical Technology Testbed, Inc.

Received for review September 8, 1999. Accepted March 10, 2000.

AC991041K

DESCRIPTION AND PERFORMANCE SITES (FORM B)

DESCRIPTION: State the goal of the research project including how it relates to improving health care for the nation's people. Use succinct language to describe how the project goals will be achieved. Do Not exceed the space provided on this page.

The need for more sensitive, rapid, and reliable chemical diagnostic tests is becoming very apparent in a number of different segments in society, such as at home, at work, in hospitals and on the battlefield. Applications include home blood glucose measurements for diabetes management, testing food for the presence of pathogenic microorganisms such as *Salmonella* and *E. coli*, and sensing chemical and biological warfare agents in times of war. Many of these applications require the specific detection of one or more analytes in a complex chemical environment and possibly with a limited sample size. Sensors based on biorecognition molecules (e.g. enzymes, antibodies, receptors, oligonucleotides) coupled to microelectronic or optical transducers, commonly called biosensors, have great potential to address the above applications. However, the application of biosensors has been primarily limited to home glucose test meters and blood-gas instruments containing sensors for glucose and lactate. Applications such as the simultaneous detection of multiple complex biomolecules in biological media (blood, serum, cerebrospinal fluid, tissue culture media) require a high density of individual sensing elements. Thus individual biomolecules must be immobilized in spatial distinct, addressable regions on a surface. If biosensors are to see more wide spread application, sensor fabrication technologies must be developed that allow the development of stable, easily manufactured multisensor arrays.

In brief, we propose to develop a widely-applicable technique using mid-UV photolithography to polymerize and pattern on a micrometer scale three-dimensional polymer films containing biological recognition molecules and fabricate both single and multianalyte sensor arrays based on these films. Specifically we will apply this technology to the fabrication of redundant glucose microsensors arrays for use in diabetes management and multianalyte sensor arrays for analytes important to critical care medicine such as lactate, pyruvate, and glucose. Our preliminary experiments have shown that redox enzymes such as glucose oxidase and lactate oxidase can be covalently immobilized in photopolymerized poly(ethylene glycol) hydrogels with little loss in activity. These hydrogels showed rapid mass transfer for the analytes of interest and were shown to be biocompatible in previous studies. These hydrogels were also patterned into arrays using standard mid-UV photolithography. With continued progress in the areas of photopolymer chemistry, biomolecule stabilization, and hydrogel patterning, the development of multianalyte hydrogel arrays fabricated using existing processing methods will be feasible.

PROJECT SITE(s) (*Organization, City, State*):

Texas Engineering Experiment Station, Texas A&M University
College Station, TX 77843

NMTB FINAL PROGRESS REPORT

Sub-agreement #026-FY98-TEES-PISHKO

MAY 24 2000

Electrochemical Microsensor Arrays

Period: April 1, 1999 – March 31,2000

Principal Investigator: Michael Pishko

Department of Chemical Engineering
Texas A&M University
3122 TAMU
College Station, TX 77843-3122

TEL 979-847-9395
FAX 979-845-6446

Email: pishko@tamu.edu

Michael Pishko

April 28, 2000

INTRODUCTION **3**
OBJECTIVES AND SPECIFIC AIMS 3
PROGRESS REPORT **3**
POLYMER/OXIDOREDUCTASE NANOCOMPOSITE THIN FILMS 3
Experimental Methods *4*
Results and Discussion *6*
DEVELOPMENT OF REDUNDANT GLUCOSE AND LACTATE SENSOR ARRAYS 10
Experimental Methods *10*
Results and Discussion *12*
SIGNAL PROCESSING ALGORITHMS 15
Theory *15*
Experimental Methods *16*
Results and Discussion *16*
OPTICAL MICROSENSOR ARRAYS 20
Experimental Section *21*
Results and Discussion *23*
INTEGRATION OF DRUG DELIVERY ELEMENTS INTO SENSOR PLATFORMS 27
STUDIES TO BE COMPLETED 28
CONCLUSIONS 28
DEVIATIONS FROM ORIGINAL RESEARCH PLAN 29
PAPERS AND ABSTRACTS RESULTING FROM THIS CONTRACT 29
Refereed Journal Publications *29*
Presentations *29*
Manuscripts under review or in preparation *30*
REFERENCES **30**

INTRODUCTION

OBJECTIVES AND SPECIFIC AIMS

As stated in the original proposal, we proposed to develop both single and multianalyte implantable sensor arrays using mid-UV photolithography to polymerize and pattern on a micrometer scale three-dimensional polymer hydrogels containing biological recognition molecules. In specific we have been working to:

- Develop chemistries that permit the rapid immobilization of functioning biorecognition molecules (initially oxidoreductases) within photochemically polymerized redox hydrogels.
- Develop methods of patterning biosensor films on surfaces using mid-UV photolithography. Specifically we will seek to optimize the resolution of the pattern and adhesion of the polymer/biomolecule network to the substrate.
- Fabricate implantable single and multianalyte micro-biosensor arrays on metallized silicon substrates and flexible polyimide substrates. Using mid-UV photolithography, we will fabricate an array of redundant glucose sensors and a multianalyte array for lactate, glucose, and pyruvate. These devices will be tested both *in vitro* and *in vivo* by implantation in rats.

Silicon microsensor fabrication technologies have several inherent features, including high volume production capabilities, low manufacturing cost, high reliability, high reproducibility and small size. We ultimately wish to take advantage of these benefits by developing photolithography as technology for incorporating biosensor elements into microelectronic devices.

PROGRESS REPORT

Below we will describe our efforts to complete all three specific aims. In specific, we will describe the development of redox polymer/oxidoreductase thin films for amperometric sensing, the development of redundant sensor arrays based on these materials, and the development of algorithms for fault detection in these arrays. We will also describe the development of microfabricated drug delivery systems and microfabricated optical microsensors. Both of the technologies were derived from the proposed research, yet unforeseen at the time of the original proposal.

POLYMER/OXIDOREDUCTASE NANOCOMPOSITE THIN FILMS

Glucose and lactate enzyme electrodes have been fabricated through the deposition of an anionic self-assembled monolayer and subsequent redox polymer/enzyme electrostatic complexation on gold substrates. These surfaces were functionalized with a negative charge using 11-mercaptoundecanoic acid (MUA), followed by alternating immersions in cationic redox polymer solutions and anionic glucose oxidase (GOX) or lactate oxidase (LAX) solutions to build the nanocomposite structure. The presence of the multilayer structure was verified by ellipsometry and sensor function characterized electrochemically. Reproducible analyte response curves from 2 – 20 mM (GOX) and 2 – 10 mM (LAX) were

generated with the standard deviation between multiple sensors between 12 and 17 %, a direct result of the reproducibility of the fabrication technique. In the case of glucose enzyme electrodes, the multilayer structure was further stabilized through the introduction of covalent bonds within and between the layers. Chemical crosslinking was accomplished by exposing the thin film to glutaraldehyde vapors, inducing linkage formation between lysine and arginine residues present on the enzyme periphery with amine groups present on a novel redox polymer, poly[vinylpyridine Os(*bis*-bipyridine)$_2$Cl]-co-allylamine (PVP-Os-AA). Finally, an initial demonstration of thin film patterning was performed as a precursor to the development of redundant sensor arrays. Microcontact printing (μCP) was used to functionalize portions of a gold surface with a blocking agent, typically 1-hexadecanethiol (C16-SH). This was followed by immersion in MUA to functionalize the remaining portions of gold with negative charges. The multilayer deposition process was then followed, resulting in growth only on the regions containing MUA, resulting in a "positive" type pattern. This technique may be used for fabrication of thin film redundant sensor arrays, with thickness under 100 Å and lateral dimensions on a micron scale.

EXPERIMENTAL METHODS

Glucose oxidase (GOX, EC 1.1.3.4, Type X-S, 128 units/mg solid from *Aspergillus niger*), lactate oxidase (LAX, 35 units/mg solid, from *Pediococcus* species) and lactic acid (60 % w/w in H_2O) were obtained from Sigma Chemical Co. (St. Louis, MO). Ammonium hexachloroosmate(IV), 1-hexadecanethiol (C16-SH), 11-mercaptoundecanoic acid (MUA), 2,2'-azobisisobutyronitrile (AIBN), poly(4-vinylpyridine), and 2,2'-dipyridyl (bpy) were obtained from the Aldrich Chemical Co. (Milwaukee, WI). Dextrose, methanol, ethyl alcohol, glutaraldehyde, ethylene glycol, hydrochloric acid (11 N), and acetonitrile were obtained from Fisher Scientific Co. (Pittsburgh, PA). An α-acryloyl, ω-N-hydroxysuccinimidyl ester of poly(ethylene glycol)-propionic acid (PEG-NHS, MW 3,400) was purchased from Shearwater Polymers (Huntsville, Al). All reagents, unless otherwise stated, were used as received. Phosphate buffered saline (PBS) solution was composed of 1.1 mM potassium phosphate monobasic, 3 mM sodium phosphate dibasic heptahydrate and 0.15 M NaCl in 18 MΩ•cm deionized water (E-pure, Barnstead).

The equipment for electrochemical analysis included a CV-50W Voltammetric Analyzer (Bioanalytical Systems), a C2 Cell Stand, a Ag/AgCl reference electrode and a platinum counter electrode. The electrochemical apparatus was controlled and data acquired using a Toshiba Pentium PC. Ellipsometry was performed using a Gaertner L2W26D ellipsometer (Gaertner Scientific Corp., Chicago, IL). Film thickness and refractive indices were calculated using Gaertner software, utilizing a film model that assumed a refractive index (n_f) of 1.46. All measurements were made using a He/Ne (633.8 nm) laser and a 70.00 +/- 0.02° angle of incidence. Micrographs of multilayer patterns were acquired using a Meiji optical microscope (Meiji Techno America, San Jose, CA) and a Kodak DC240 Digital Camera (Eastman Kodak Company, Rochester, NY).

Gold electrodes with diameters of 1.6 mm each were purchased from Bioanalytical Systems (West Lafayette, IN). Prior to deposition of the multilayers, the electrodes were polished with 1 μM diamond polishing slurry on nylon polishing pads, then polished with

0.05 μm alumina on microcloth pads followed by sonication along with water and methanol rinses. Gold-coated silicon wafers (200 Å Cr, 1000 Å Au on polished Si(111), Lance Goddard Associates, Foster City, CA) were fabricated into electrodes (6.45 cm^2) by soldering a conducting wire to the substrate surface. Gold-coated wafers were rinsed with ethanol, cleaned in an ozone cleaner (Boekel Industries, Inc., model 135500) for 10 minutes, and rinsed with ethanol again before use.

Osmium based polycationic redox polymers were synthesized using modifications of established protocols. $Os(bpy)_2Cl_2$, was synthesized according to a standard procedure.[1] In brief, two equivalents of bipyridine (720 mg) were mixed with one equivalent ammonium hexachloroosmate(IV) (1000 mg) in 50 mL ethylene glycol. This mixture was heated to reflux for 45 minutes, precipitated with supersaturated sodium dithionite, and repeatedly washed with water and ether. The $Os(bpy)_2(Cl)_2$ precursor was used in the synthesis of crosslinkable redox polymers used in these studies.

Poly[vinylpyridine Os(*bis*-bipyridine)$_2$Cl]-co-allylamine (PVP-Os-AA), was synthesized as follows: 1.0 g of 4-vinylpyridine, 1.0 g allylamine, 0.2 g AIBN and 200 μL HCl were mixed in 50 mL acetonitrile. This solution was refluxed for 2 hours and then concentrated using rotary evaporation for the removal of acetonitrile. The resulting polymer was dissolved in 1 mL of methanol and precipitated in 50 mL of ethyl ether. 100 mg of $Os(bpy)_2Cl_2$ was then added to 100 mg of (PVP)-co-allylamine in 50 mL ethylene glycol and refluxed under N_2 for 1.5 hours. Ethylene glycol was removed, and the product dissolved in a minimal amount of methanol followed by precipitation in 70 mL of diethyl ether. The ether was then decanted off and poly(vinylpyridine Os(*bis*-bipyridine)$_2$Cl)-co-allylamine was dried and collected. Figure 1 depicts the structure of PVP-Os-AA.

Gold substrates were initially functionalized by immersing in 1 mM MUA in ethanol for ~ 20 min. The substrates were removed, washed, sonicated and dried under N_2. The substrates were then alternately placed first in a polycationic 10 mg/mL solution of PVP-Os-AA for ~ 20 min and a polyanionic solution of GOX (10 mg/mL in PBS) or LAX (0.7 mg/mL in PBS) for ~ 40 min. In between immersions, the substrates were rinsed with 0.1 M PBS, sonicated for ~ 20s and dried under flowing N_2. A depiction of the final multilayer structure is presented in Figure 2.

To chemically stabilize the multilayer structures, the cationic and anionic layers were chemically crosslinked using glutaraldehyde. This was accomplished by exposing the coated substrates to glutaraldehyde vapors for ~ 15 minutes then removing to room air prior to electrochemical testing.

Stamps for microcontact printing structures were made via replica molding, using a slightly modified version of a published protocol.[2] In brief, Shipley STR1045 photoresist (MicroChem Corp., MA) was deposited in a thin layer via spin coating at ~ 5000 rpm on a clean Si wafer. This photoresist was exposed to 365 nm, 20 W/cm^2 UV light through an optical test mask (USAF resolution chrome test target, Melles Griot). After photoresist development, poly(dimethylsiloxane) (PDMS) (Sylgard 184 silicone elastomer and curing agent in a 10:1 ratio, Dow Corning Corp.) was deposited over the patterned photoresist.

The uncured PDMS was confined with a small cylinder pressed down on the substrate with a slight weight. This pre-stamp was then placed in a vacuum oven to be degassed and cured for ~ 24 hrs. Upon curing, the PDMS was lifted off the substrate resulting in the patterned stamp.

Application of the stamp to form a patterned substrate was performed as follows. Initially, the stamp was dipped in 1 mM C16-SH solution (ethanol) for ~ 20 s. It was then dried, and pressed on a cleaned gold surface for ~ 20 s. The stamp was then removed, the substrate exposed to 1 mM MUA for ~ 20 min, and the multilayer deposition procedure followed as described earlier.

Electrodes were tested in a cell containing Pt counter and Ag/AgCl references electrodes as well as 0.1 M PBS degassed with N_2 (15 min prior to start of experiment and for the duration of experiment). Bubbling with N_2 was used to agitate the solution rather than a stir bar. Either of two experiments was conducted to characterize sensor response; cyclic voltammetry or constant potential amperometry. For cyclic voltammetry, the applied potential was cycled linearly from 0 to 500 mV at a scan rate of 20 mV/s. The anodic peaks of individual scans were integrated to determine the surface coverage or the total amount of charge mediator present in any one layer. Constant potential amperometry required the preconditioning (~ 50 s) and operation of the electrode at a constant applied potential of 300 mV. When the current reached a baseline in the absence of substrate, aliquots of substrate were added and step changes in current monitored with time. Unless otherwise stated, n = 3 for all substrate response curves.

RESULTS AND DISCUSSION

The development of reliable and robust amperometric biosensor arrays is dependent upon the miniaturization of sensor features to increase both the density of sensing elements in a spatially distinct region and the density of biorecognition molecules within an individual sensor. Miniaturization, however, may result in low current densities and inadequate signal to noise ratios. To overcome this problem, we have formed redox polymer and enzyme complexes through an electrostatic layer by layer deposition scheme, a technique that has been shown to increase current densities in the resulting biosensors.[3] This scheme for sensor development minimizes the use of such components as retaining membranes or thick polymer matrices, resulting in an increased density of the primary sensing components, namely the enzyme and redox polymer. This permits rapid and efficient sensor performance, which may be further improved by chemically crosslinking the multilayer structure by exposure to glutaraldehyde. The goal of minimizing sensor dimensions was achieved by keeping the thickness of the sensing layers well under 100 Å through repeated attachment of single redox polymer/enzyme monolayers. The feasibility of depositing these layers in micron scale patterns was then demonstrated using μCP techniques. This may eventually permit rapid generation of multilayer sensor arrays.

The first step in the fabrication of these nanocomposite structures was the functionalization of a gold substrate for subsequent layer by layer deposition. As an adhesion layer, a monolayer of MUA with a pKa of approximately 6.5 was adsorbed to the

gold substrate via its thiol end group. At the buffer pH of ~ 7.4, MUA presents the electrode-solution interface with an initial negative surface charge, via its partially deprotonated carboxyl acid groups, with which to begin the layer by layer deposition process. Poly(4-vinylpyridine) complexes of $Os(bpy)_2Cl_2$ are highly cationic[3] and will electrostatically adsorb to the negatively functionalized surface. GOX has an isoelectric point[4] of ~ 3 and LAX has a pI of ~ 4.6, thus at pH 7.4, both enzymes possess a net negative charge, permitting their adsorption to the cationic redox polymer. Alternating deposition of positively charged redox polymers and negatively charged enzymes permitted the buildup, layer by layer, of a nanocomposite structure.

One of the requisite features for the formation of well ordered and defined biosensors is ability to tailor the organization of the sensor components as close to the molecular level as possible. With this goal in mind, ellipsometric data was obtained after adsorption of subsequent layers to verify that very thin layers were being deposited after each adsorption step. Figure 3 shows the increase in film thickness upon addition of each layer during the alternate immersions in polycation/polyanion solutions. For glucose enzyme electrodes, the increase in thickness was linear with each addition, with an $R^2 > 0.98$. The average thickness of the cationic multilayer, PVP-Os-AA, was larger, ~ 12.5 Å, than the average anionic multilayer (GOX), ~ 6.7 Å. GOX from *Aspergillus niger* in its native state is a globular glycoprotein with an elliptical shape and a maximum diameter as determined by x-ray crystallography of ~ 45 Å along its primary axis.[5] However, perpendicular to this axis, the diameter is smaller, in the range from 15 – 20 Å. Based on the ~ 6.7 Å increase in thickness after GOX adsorption, the enzyme is likely buried and intercalated within the redox polymer thin film. This is expected due to the nature of the electrostatic interactions between the polyions where very strong multipoint contacts are prevalent. The thickness determined for LAX multilayers are almost identical to those determined for GOX. The average thickness of LAX containing films were ~ 11 Å for the redox polymer layers and 6.5 Å for the enzyme layers, with a linear increase in film thickness upon the addition of each layer ($R^2 > 0.98$). Controls were performed on gold substrates that were not functionalized with MUA, and it was found that there was a negligible change in thickness as measured via ellipsometry when attempting to deposit both enzyme and/or redox polymer layers.

Cyclic voltammetry, shown in Figure 4 for scan rates ranging from 5 to 400 mV/s, indicated a formal potential of ~250 mV with a difference in peak potential of ~ 60 mV. This indicated that the system is reversible, as the peak potential is independent of the scan rate and the peak current changes linearly with scan rate raised to the one-half power (not shown). Repeated cyclic voltammetry without the presence of glucose produced scans whose peaks did not degrade appreciably over time, demonstrating that the electroactive components were not free to diffuse away from the electrode surface. Subsequently, cyclic voltammograms at a scan rate of 20 mV/s were used to characterize the number of electroactive osmium redox sites present in each layer, an important criteria for the assessment of the sensor's electrochemical function. This number was determined based upon the cyclic voltammogram of a wafer with only a single redox polymer layer adsorbed (MUA/PVP-Os-AA). The area under the anodic peak was integrated from the voltammogram, and used to determine the surface coverage of osmium redox sites present per adsorbed layer. This value, ~ 4.1×10^{-11} mol cm^{-2}, compares favorably with the values of (4 to 5) $\times 10^{-11}$

mol cm^{-2} reported for ferrocene monolayers[6] and 3 x 10^{-11} mol cm^{-2} reported for $Os(bpy)_3^{2+}$ layers.[7] Based on the redox polymer film thickness reported earlier and the surface coverage, the concentration of redox sites per monolayer is ~ 3.2 x 10^{-4} mol cm^{-3}.

The multilayer scheme has distinct advantages over other types of sensor fabrication methods reported in the literature. Consider specifically the sensing mechanism for enzymatic catalysis and electron transfer between polycationic osmium redox polymers and polyanionic glucose oxidase (below).

$$\beta\text{-D-glucose} + GOX(FAD) \rightarrow \text{Gluconolactone} + GOX(FADH_2)$$

$$GOX(FADH_2) + 2Os(bpy)_2(vp)^{+2} \rightarrow GOX(FAD) + 2\,Os(bpy)_2(vp)^{+1}$$

$$Os(bpy)_2(vp)^{+2} + Os(bpy)_2(vp)^{+1} \rightarrow Os(bpy)_2(vp)^{+1} + Os(bpy)_2(vp)^{+2}$$

$$2\,Os(bpy)_2(vp)^{+1} \rightarrow 2e^- + 2H^+ + 2\,Os(bpy)_2(vp)^{+2}$$

Qualitatively, sensor response times should be minimized due to increased proximity between the enzyme and charge mediator in an ordered structure where enzymes are in direct contact with the redox polymer. Distances much larger than 10 Å result in very low rates of electron transfer[8]; the multilayer structure places redox sites well within 10 Å of each other and of enzymes.

The response of the enzyme electrodes to the addition of substrate was characterized using both constant potential amperometry and cyclic voltammetry. Current response values for nanocomposite films consisting of native LAX and PVP-Os-AA are depicted in Figure 5. We see a linear response for a multilayer structure consisting MUA/PVP-Os-AA/LAX with a sensitivity of 0.027 μA cm^{-2} mM^{-1}, an R^2 value of ~ 0.98 and a standard deviation of ~ 12 % between electrodes.

For a GOX multilayer, we see a relatively linear calibration curve from 2 – 20 mM substrate with a sensitivity of 0.015 μA cm^{-2} mM^{-1} and an R^2 value of ~ 0.98 (Figure 6). The error bars indicate a standard deviation of ~ 17 % between electrodes. This compares favorably with the American Diabetes Association acceptable standard deviation of 15 %.[9] The response in the absence of oxygen indicates electron transfer between GOX and osmium sites along with charge propagation through the redox polymer to the electrode surface. In the presence of oxygen, the response is reduced by ~ 50 %. This indicates, as expected, that oxygen does compete with osmium sites in the multilayer structure. The signal to noise ratio (SNR) was determined from the electrode response, under N_2, at 6 mM glucose and was calculated as the steady state current at that substrate concentration divided by the standard deviation of the current (i.e. the noise). At 6mM, the SNR was ~ 100, indicating a relatively sensitive electrode at physiological glucose levels. As expected by the thickness of the nanocomposite thin film, the response times are quite rapid for both glucose and lactate enzyme electrodes, with times to reach 95 % of the final response under 4 s for step changes in substrate concentration in the physiological range.

The lactate enzyme electrodes demonstrate a higher response as

compared to a glucose enzyme electrode. The opposite might be expected since the glucose oxidase solution used for enzyme deposition was approximately 2 orders of magnitude greater in activity than that of lactate oxidase. However, one must consider the size of each of these macromolecules. GOX is a dimer of large molecular weight, ~ 180,000, more than twice the size of LOX, ~ 80,000. Considering enzyme intercalation in a highly charged redox polymer layer, it is possible that a larger amount of LOX was electrostatically incorporated into each layer. This may be true from a physical standpoint, as a larger number of smaller spheres (both GOX and LOX are globular) will pack into a given space than will larger spheres. This may also be true from an electrostatic standpoint, as the negative or anionic portions of LOX are potentially more accessible for electrostatic complexation, as the enzyme is smaller and these residues will more likely reside near the surface of the protein. This type of phenomena has been observed in the past where Heller and colleagues[10] demonstrated higher current densities (~ 25 – 50 %) for lactate enzyme electrodes as compared to glucose enzyme electrodes under analogous conditions.

The current densities determined in these experiments for both lactate and glucose enzyme electrodes, as expected, are relatively low due to the size of the electrodes used. As ellipsometry necessitated the use of larger Au substrates (6.45 cm^2 electrodes), the obtained current densities do not compare favorably to those present in the literature, including studies reporting 10 – 20 $\mu A\ cm^{-2}\ mM^{-1}$ for polymer film based sensors.[11, 12] However, when these nanocomposite films were fabricated on gold microelectrodes (d ~ 250 μm) current densities approached 10 $\mu A\ cm^{-2}\ mM^{-1}$.

Further covalent stabilization of the resultant nanocomposite thin films was desired not only to physically strengthen the film structure, but also to eliminate potential desorption due to changes in pH, ionic strength or high oxidation potentials. We have demonstrated that extreme changes in pH are capable of releasing biomolecules that are entrapped through electrostatic interactions.[5] Other studies have demonstrated the destruction or desorption of SAM's at negative applied potentials.[13, 14] In addition, covalent bonds between the layers are likely to improve charge transfer rates, and hence, sensor response. In redox polymers, electron transfer is believed to occur by two primary mechanisms; electron hopping between redox sites and routing along polymer chains. Although imparting covalent crosslinks may suggest a decrease in redox polymer flexibility and subsequently reduced conductivity, crosslinking of the multilayer structure likely decreases the distance between enzyme active sites and redox sites while providing additional direct routes of charge transfer, both from the enzyme to redox sites, and between redox sites via self-exchange. [15]

To further stabilize the structure, previously tested GOX enzyme electrodes were chemically crosslinked by exposure to glutaraldehyde vapors where it is anticipated that arginine and lysine residues of the enzyme will react with amines present on the redox polymer. Figure 6 also shows that there is an increase in current density upon crosslinking with glutaraldehyde as opposed to non-crosslinked films, with an average increase of ~ 60 %. The standard deviation for electrodes based on crosslinked multilayer structures was ~ 13 % between electrodes. With an R^2 ~ 88 %, the response is not as linear as that for the non-crosslinked films. This appears to indicate that the Michaelis-Menten enzyme kinetics of the enzyme become rate limiting in the electrode reactions when the nanocomposite film is

crosslinked, possibly due to improved electron transfer between the redox polymer and enzyme. These crosslinked films were able to retain nearly 100 % of their activity for a minimum of three weeks when refrigerated (tested up to four weeks of retained activity), as opposed to a maximum of two weeks for non-crosslinked nanocomposites.

With the goal of achieving spatially distinct and individually addressable biosensor array members, patterns of the multilayers were generated using the microcontact printing technology developed by Whitesides et al.[2] Stamps for μCP were fabricated by depositing and curing PDMS on a photolithographically generated master -- a USAF test grid, consisting of rectangles and numbers of varying size. The scheme for patterning is depicted in Figure 7, with a resultant pattern shown in Figure 8. The bars shown here have the critical lateral dimensions of ~ 280 and 150 μm. This is true for both of the distinctly visible regions – those containing the multilayer structure and the bars blocked with C16-SH. Features as small as 10 μm have been identified, and 1 – 2 μm features are feasible using this technique.[2] Analogous to typical optical lithography techniques, the resulting film would be a "positive" pattern, as the regions stamped do not contain the multilayer sensing nanocomposite. If MUA or some other surface functionalizing agent were stamped instead of the blocking agent, or if an inverted stamp were fabricated, a "negative" pattern could be generated. This type of patterning may be utilized for the generation of redundant sensor arrays based upon nanocomposite electrostatic multilayers in the future.

DEVELOPMENT OF REDUNDANT GLUCOSE AND LACTATE SENSOR ARRAYS

Glucose and lactate sensor arrays have been fabricated by depositing electrostatically complexed monolayers on lithographically patterned gold electrodes. Initially, standard photolithographic techniques combined with metal deposition were used to fabricate gold arrays. These arrays were first functionalized with a negative surface charge through chemisorption of 11-mercaptoundecanoic acid (MUA) followed by electrostatic attachment of a cationic osmium redox polymer and anionic enzymes, either glucose oxidase (GOX) or lactate oxidase (LAX). Sensor function was characterized with cyclic voltammetry for both glucose and lactate enzyme electrodes. Standard deviations of ~ 18 % (glucose) and 20 % (lactate) were determined for the enzyme electrodes with n =5 array members in all cases. Furthermore, the potential problem of crosstalk was addressed by subsequently testing one array member and then that array member in conjunction with an adjacent sensor. The two sensors gave a value nearly two times (1.95 X) that of the individual array member. This result not only eliminated crosstalk, but also further demonstrated the reproducibility inherent with this scheme of sensor array development.

EXPERIMENTAL METHODS

Glucose oxidase (GOX, EC 1.1.3.4, Type X-S, 128 units/mg solid from *Aspergillus niger*), was obtained from the Sigma Chemical Co. (St. Louis, MO). Ammonium hexachloroosmate(IV), 1-hexadecanethiol (C16-SH), 11-mercaptoundecanoic acid (MUA), 2,2'-azobisisobutyronitrile (AIBN), poly(4-vinylpyridine), and 2,2'-dipyridyl (bpy) were obtained from the Aldrich Chemical Co. (Milwaukee, WI). Dextrose, methanol, ethyl alcohol, ethylene glycol and acetonitrile were obtained from Fisher Scientific Co.

(Pittsburgh, PA). All reagents, unless otherwise stated, were used as received. Phosphate buffered saline (PBS) solution was composed of 1.1 mM potassium phosphate monobasic, 3 mM sodium phosphate dibasic heptahydrate and 0.15 M NaCl in 18 MΩ•cm deionized water (E-pure, Barnstead). Shipley Microposit STR1045 positive photoresist (G line), Microposit 452 Developer and Microposit Remover were purchased from MicroChem Corp.(Newton, MA).

The equipment for electrochemical analysis included a CV-50W Voltammetric Analyzer (Bioanalytical Systems), a C2 Cell Stand, a Ag/AgCl reference electrode and a platinum counter electrode. The electrochemical apparatus was controlled and data acquired using a Toshiba Pentium PC. Ellipsometry was performed using a Gaertner LSE Stokes Ellipsometer (Gaertner Scientific Corp., Chicago, IL). Film thickness and refractive indices were calculated using Gaertner software, utilizing a film model that assumed a refractive index (n_f) of 1.46. All measurements were made using a He/Ne (633.8 nm) laser and a 70.00 +/- 0.02° angle of incidence. Scanning electron microscopy (SEM) was performed with a JEOL T330A electron microscope with a magnification range of 15-20000x and a resolution of 4.5 nm. Spin coating was performed using a P-6000 spin coater (Integrated Technologies, Inc., Acushnet, MA). Softbake was performed on a Thermolyne 1900 hot plate (Barnstead/Thermolyne, Dubuque, IA). Photomasks were obtained from Advance Reproductions (North Andover, MA).

Si wafers (2 in diameter, (111), n-doped, 500 μm thick) were purchased from Wafer World, Inc. (St. Petersburg, Fl). The wafers were treated with a Buffered Oxide Etch (BOE) to remove any residual native oxides or organics from the surface. They were then washed with deionized water and dried under flowing nitrogen. Subsequently, the wafers were placed in a quartz boat and put in a N_2 purged oxidation furnace. Initially, ~ 500 Å of dry oxide was grown through oxidation at 1100 °C for thirteen minutes. The oxygen flow was then diverted through a bubbler resulting in a water-saturated O_2 stream. The wafers were exposed to this new stream for 34 minutes reasulting in 5000 Å of wet oxide. Lastly, 100 Å of additional dry oxide were grown to cap off the wet oxide. In effect, this resulted in a high quality insulating layer by alternating between wet and dry modes of oxidation.

After growth of the oxide layers, the lithographic patterning of gold was performed. As a first step, hexamethyldisilazane (HMDS) was spun onto the substrate to improve photoresist adhesion. Next, a positive photoresist (Shipley Microposit STR1045) was deposited onto the substrate surface at a coverage of approximately 1 ml/in and subsequently spun down. The Si substrate was then softbaked on a hotplate for approximately two minutes at a temperature of 100 °C to drive off as much remaining solvent as possible. Upon cooling to room temperature, a photomask was placed in contact with the hardened photoresist in preparation for pattern generation via contact printing. The mask was then exposed to 365 nm, 20 W/cm^2 UV light for ~ 0.5 s and subsequently placed in a developer solution (Microposit 452) for 3 – 4 minutes to remove portions of the photoresist that were exposed to UV light resulting in a distinct pattern of photoresist on the Si surface. Chrome (200 Å) was then deposited as an adhesion layer, followed by deposition of gold (1000 Å) via sputter coating (Lance Goddard Associates, Foster City, CA) over the entire substrate. The photoresist was subsequently stripped (Shipley Microposit Remover) leading to the

lift-off of gold from all non-patterned areas. This results in a spatially distinct pattern of gold with two primary functions; gold array members that serve as electrodes and thin gold lines serving as leads to contact pads. Finally, wires were attached to contact pads by soldering for connections during electrochemical experiments. A schematic depicting this lithographic process is present in Figure 9, along with a corresponding schematic in Figure 10.

The scheme employed for the synthesis of the polycationic redox polymer, poly[vinylpyridine Os(*bis*-bipyridine)$_2$Cl]-co-allylamine (PVP-Os-AA), has been outlined previously.[16]

Electrode arrays were functionalized with a negative surface charge by immersing in 1 mM MUA (ethanol) for 20 min. The substrates were washed with ethanol and dried under N_2. The arrays were then alternately exposed to a polycationic 10 mg/mL solution of PVP-Os-AA for ~ 20 min and a polyanionic solution of GOX (10 mg/mL in PBS) or LAX (0.7 mg/mL in PBS) for ~ 40 min. In between immersions, the substrates were rinsed with 0.1 M PBS and dried under flowing N_2. This process is depicted in Figure 11.

Array members were tested in a cell of volume approximately 1 ml containing 0.1 M PBS degassed with N_2 (15 min prior to start of experiment, for duration of experiment) and also containing Pt counter and Ag/AgCl reference electrodes. Rather than use a stir bir, degassing with N_2 agitated the solution and provided convection. Cyclic voltammetry, from 0 to 500 mV (vs. Ag/AgCl) was performed to characterize sensor response at a scan rate of 20 mV/s.

RESULTS AND DISCUSSION

In vivo biosensing applications require sensors that may be fabricated in a reproducible manner and function with a high degree of accuracy. This work explores the lithographic fabrication of gold electrode arrays for use as redundant glucose and lactate sensors. Upon establishment of reproducible fabrication, the electrodes were functionalized, first with a negative surface charge, and subsequently with a cationic redox polymer and an anionic enzyme. The response of array members within one array is compared to assess a standard deviation for the operating range of array members. In addition, responses of multiple array members linked together are compared to that of a single array member to demonstrate that the array members do not suffer from signal crosstalk.

An SEM of a representative electrode array is depicted in Figure 12. Each of the five individually addressable array members of the electrode arrays was 500 μm in diameter while each lead was 10 μm wide. The array members appeared to be smooth with well-defined edges. No discontinuities were visible between the leads and array members nor was there overlapping between leads evident. This proved to be a very reproducible process as numerous defect-free electrode arrays of the same geometry were fabricated.

Placement of the array members is an important issue. They must not be so close together that the individual electrodes improperly mimic one larger electrode. Specifically the rules indicated in Equations 1 and 2[17]

$d >> 2r_o$ Equation (1)

$d = 2r_o$ Equation (2)

serve as excellent preliminary guidelines when designing a sensor array. In these equations, *d* refers to the distance between array members and r_o refers to the radius of the electrode. The electrode arrays generated in this work have electrodes with an r_o of 250 μm and a *d* of 1000 μm. The inter-electrode distance is therefore placed at an adequate value, as it is two times greater than $2r_o$. Therefore it is likely that the electrodes will function independently with no cross-talk present.

The scheme used for fabrication of these sensors is based upon electrostatic attraction of an osmium redox polymer and GOX or LAX. First, the electrode surface was functionalized with MUA where the –thiol end group was chemisorbed to gold. The carboxylic acid end group of MUA presented the solution-electrode interface with a net negative charge, assuming that with a pKa of 6.5[18] the acid group is at least partially deprotonated at a pH of 7.4. Polycationic osmium derivatives are known to be cationic[3] at neutral pH and have been electrostatically adsorbed to the negatively functionalized surface. Subsequent deposition of anionic GOX[4] with an isoelectric point of ~ 3.0 or LAX with isoelectric point ~ 4.6 was then possible to the positively charged surface. This process was then repeated as desired to deposit multiple layers. The resultant electrostatic attraction was found to be strong as sonication was incapable of detaching individual or multiple layers from the multilayer structure. The presence of these layers has been characterized with ellipsometry in earlier, more detailed studies on larger gold substrates.[16] As a brief synopsis, the MUA layer thickness averaged ~ 12 Å, the redox polymer layer ~ 12 Å, and the enzyme layer ~ 7 Å.

Cyclic voltammetry constituted the majority of electrochemical experiments performed in this work. Aside from verifying the presence of the redox polymer layers, cyclic voltammetry served two primary functions; 1) to quantify sensor response and 2) determine if there is any cross-talk phenomena present. With these goals, a set of representative cyclic voltammograms, taken from a single array member, is shown in Figure 13 for scan rates ranging from 20 to 100 mV/s. A formal potential of ~ 280 mV with difference in peak potential of ~ 60 mV was obtained, suggesting a very stable system as peak potential was independent of scan rate. In addition, these cyclic voltammograms did not change appreciably over time (tested up to six weeks) indicating that the electrostatically attached redox polymer was not free to diffuse.

The GOX catalyzed reaction scheme may be represented where Os sites serve as electron relays between the enzyme and electrode surface may be expressed as follows:

$$\beta\text{-D-glucose} + \text{GOX(FAD)} \rightarrow \text{Gluconolactone} + \text{GOX}(FADH_2)$$

$$\text{GOX}(FADH_2) + 2(\text{PVP-Os-AA})^{+2} \rightarrow \text{GOX(FAD)} + 2(\text{PVP-Os-AA})^{+1}$$

$$(\text{PVP-Os-AA})^{+2} + (\text{PVP-Os-AA})^{+1} \rightarrow (\text{PVP-} \qquad \text{Os-AA})^{+1} + (\text{PVP-Os-AA})^{+2}$$

$$2(\text{PVP-Os-AA})^{+1} \rightarrow 2e^- + 2H^+ + 2(\text{PVP-Os-AA})^{+2}$$

GOX(FAD) and GOX ($FADH_2$) represent the oxidized and reduced forms, respectively, of the enzymatic active site – flavin adenine dinucleotide. The +2 and +1 net charges show the redox states the mediator complex as a whole is at. Os itself would exist at +3 when the site was at +2 or +2 when the moeity was at + 1. Sensing chemistries incorporating charge mediators have numerous advantages over those based on hydrogen peroxide oxidation.[19] For *in vivo* applications, oxygen, whose concentration is variable, may act as a co-substrate. In addition, just as easily as hydrogen peroxide may diffuse towards the electrode and become oxidized, it may diffuse away from the electrode resulting in a decreased signal-to-noise ratio.

As stated earlier, cyclic voltammetry was used to quantify the response of the sensors in an array and to determine the reproducibility between array members. Figure 14 depicts the average response from one glucose sensor array (n =5). The response is linear with an R^2 value of ~ 0.98 and a sensitivity of 0.26 $\mu A\ cm^{-2}\ mM^{-1}$. The standard deviation between array members averages approximately 18 %. This value compares reasonably well with the American Diabetes Association's recommended value of 15 % variability between sensors.[9] In addition, these sensors operated effectively when degassed with N_2 suggesting mediated electron transfer from the enzyme, through the redox polymer, to the electrode surface. Earlier studies with electrostatically complexed multilayer sensors have demonstrated that when degassed with air, competition with molecular oxygen does decrease resultant current densities, typically by ~ 50 %.[16] Lactate sensor arrays, fabricated in the same manner as the glucose arrays, were also characterized with cyclic voltammetry. The response was linear with an R^2 of ~ 0.96 and a sensitivity of ~ 0.24 $\mu A\ cm^{-2}\ mM^{-1}$(n=5). The standard deviation between sensors was slightly higher at approximately 20 %.

In the electrode fabrication section, the placement of the array members has been addressed to minimize potential crosstalk problems between array members. Cyclic voltammetry was once again used to verify whether these array members were actually capable of functioning independently. Substrate response experiments, under identical conditions, were performed with first only one array member and repeated with two array members simultaneously connected as the working electrode to the potentiostat. Calibration curves resulting from these experiments are depicted in Figure 15 for lactate enzyme electrodes. The result was an increase by a factor of ~ 1.95 in response when two array members placed next to each other were connected simultaneously as opposed to either array member individually. This indicates that the array members are capable of functioning independently and at relatively consistent values further validating our earlier assertions regarding reproducibility.

In the future, it is likely that the scale of the arrays will be reduced by over one order of magnitude to increase resultant current densities. In addition, deposition of the sensing layers will become much more precise by taking advantage of mask alignment techniques.[20]

SIGNAL PROCESSING ALGORITHMS

Principal component analysis (PCA) has been used to examine simulated data from redundant biosensor arrays operating properly or experiencing malfunction. Initial cases focus on specific mechanisms of sensor failure and the ability of PCA to identify the failed sensors in these cases. Effective discrimination of faulty sensors from those functioning properly was demonstrated for individual cases of completely failed, noisy, biased and drifting sensors, and sensors experiencing transient errors. Further cases were generated to simulate failure via multiple mechanisms in one sensor array. Although PCA on the complete data set was capable of identifying faulty sensors in this case, the specific cause or type of failure could not be identified. To identify the exact problem, a time-based examination of sensor function was implemented in the form of PCA on a time-variant data set. This permitted not only the identification of faulty sensors within the array, but also the determination of the exact mode of sensor failure.

THEORY

A fault detection and identification scheme is desired for application with redundant biosensor arrays. PCA is one such technique that is capable of reducing a complex data set, with numerous dimensions, to a simpler one with fewer dimensions by projecting the data on a new coordinate system. Specifically, PCA is a mathematical transform that may be applied to a data matrix, **X**, in this case the data acquired from a sensor array, to assess variance in the data set. **X** is typically composed of n sensors (rows) and m measurements (columns). For **X** with a set of k rank 1 matrices where k is less than or equal to the smaller of (m,n), PCA breaks **X** into k rank 1 matrices (X). These matrices are then arranged in order of decreasing eigenvalue, plus a residual matrix **E**. Thus we have

$$\mathbf{X} = X + \mathbf{E} \quad \text{or} \qquad \text{Equation (3)}$$

$$\mathbf{X} = q_1 p_1^T + q_2 p_2^T + \ldots + q_k p_k^T + E = Q_k P_k^T + \mathbf{E} \qquad \text{Equation (4)}$$

where X represents the relevant data in the principal component subspace and **E** represents noise or irrelevant information present in the residual subspace.[21, 22]

These expressions may be further simplified to yield the following relationships

$$X = QP^T \text{ and } \mathbf{E} = Q_e P_e^T \qquad \text{Equation (5)}$$

where Q and P are referred to as the score and loading matrices, respectively. A PCA factorization is therefore able to take a data matrix **X** and break it down into the latent variables X and **E**. These variables describe as much of the variance as possible under the limits imposed by the scores (Q) and loading (P) vectors. Score plots, essentially the Q of the 1st principal component against the Q of the 2nd principal component, may then be generated to assess the relationship between data sets, permitting grouping of the data. Loading plots, where P of the 1st principal component is plotted against P of the 2nd principal component, may also be used to assess the relative influence of an individual variable

on the system. Results from these plots are similar to those obtained from a PLS analysis. Thus a vector, the first principal component, is calculated and describes the direction of largest variance in the data. Subsequently, further principal components may be calculated, each orthogonal to the previous one, the sum of which describes nearly 100 % of the observations in the data set.

EXPERIMENTAL METHODS

All PCA calculations were performed in MATLAB 5.3 (The MathWorks, Inc., Natick, MA). An experimental data set from a subcutaneously implanted glucose sensor initially published by Quinn et al.,[23] shown in Figure 16, is used as the basis for the development of simulated data from a sensor array containing both properly functioning and malfunctioning glucose sensors.

This data was originally reported in the form of a sensor current as a function of time. However, to better illustrate the significance of sensor errors to diabetes management, we transformed the data to glucose concentration as a function of time using the following equation (6).

$$\text{Glucose (mg/dL)} = m * i \qquad \text{Equation (6)}$$

In this equation, i is the sensor current in nA and m is the calibration factor in (mg/dL)/nA. The calibration factor was determined by a one-point calibration method using a blood glucose measurement and a sensor current measurement from the baseline region prior to glucose injection (Figure 16). As a part of this one-point calibration, a glucose concentration of zero was assumed to produce zero current.

Abnormal variations in sensor performance were subsequently introduced into the data set, corresponding to the following types of failure an *in vivo* glucose sensor may experience: complete failure, increased noise, bias, drift, and transient errors (temporary bias). Data from these cases typically consisting of ten sensors with 141 data points each $\{(m,n)$ equal to $(141,10)\}$ was analyzed by PCA. The results for individual cases of failure, as well as for an example containing multiple fault types within a given array, are examined using score plots.

RESULTS AND DISCUSSION

Actual *in vivo* glucose monitoring data was used as a basis for the generation of a simulated data set for a glucose sensor array. The data from a single subcutaneously implanted glucose sensor (Figure 16) was taken and reproduced, with ± 15 % variability, for a total of ten sensors, simulating an array. Failure by various mechanisms was subsequently introduced to individual sensors in the array and the resultant data sets analyzed graphically with PCA generated score plots. This was followed by introducing multiple failures within a ten sensor array and determining the ability of PCA to not only identify which sensors have failed, but distinguish the mechanisms of failure between failed sensors. Finally, an initial example of a time-based PCA algorithm was implemented capable of identifying more effectively not only failed sensors, but also the specific mode of failure.

Complete Sensor Failure

This mode of failure is the case where a member of the sensor array produces zero current, or a current that does not change with variations in local glucose concentration.[24-26] In this case, failure may be caused by a number of factors, including complete enzyme deactivation, a failure in the leads/wiring leading to the device[27] or an extremely strong chronic inflammatory response by the body that walls off the sensor and prevents its adequate contact with interstitial fluid.[28] Figure 17a shows eight sensors operating properly with ± 15 % variation in the signal. However, two other sensors in the array are not responsive to glucose. One failed sensor displays a glucose measurement partially within the bounds of correct operation (~ 70 mg/dL), as dictated by the other eight sensors, while the other failed sensor displays a zero current response. A score plot based upon PCA of this data set is shown in Figure 17b. The eight sensors working properly are grouped together very closely, while the failed sensors are deviant from this group. The failed sensor constantly reading 0 mg/dL glucose is a large outlier along the 1st principal component axis. The sensor erroneously reading ~ 70 mg/dL glucose and unresponsive to glucose is also a large outlier, but is deviant along both principal component axes, with variance primarily in the 2nd principal component axis.

Increase in Noise

Signal to noise ratio (SNR) is an important concern for glucose sensors to be implanted *in vivo*. Increased noise in glucose sensors may be induced by numerous factors, including electromagnetic radiation from power lines[29], electronic article surveillance (EAS) systems[24-26], or movement of the patient.[30, 31] In this simulated case, eight sensors are operating properly with ± 15 % variability in signal and two are operating incorrectly with ± 25 % variability (Figure 18a). It is not readily apparent visually which sensors, if any, are deviant from those functioning properly. A score plot based on PCA of this data set is presented in Figure 18b. Here, the eight sensors operating at ± 15 % variability are grouped together, while two other noisy sensors are separated. However, these two failed sensors do not differ from the eight properly functioning sensors in the same manner. In the score plot, the magnitude by which they differ from the set of correctly operating sensors is approximately the same. However, the directional contributions to their respective variations are quite different. This is a reasonable result, as both failed sensors increase in noise by the same amount, yielding magnitude shifts that are similar. However, due to the very nature of noise, the directional component of this variation is random in both positive and negative directions.

Bias

Bias in glucose sensors can be induced by a change in the working potential of the electrode[32] leading to a precise response by the sensor at a consistently inaccurate value. An erroneously low or high measurement by a glucose meter can lead to improper insulin administration by a patient, potentially leading to death. Figure 19a shows seven sensors operating properly at ± 15 % variability. However, sensor eight is biased positively by

50 mg/dL glucose, sensor nine is biased negatively by 50 mg/dL glucose, and sensor ten is biased positively by 200 mg/dL glucose. PCA of this data, presented in Figure 19b, permits visual identification of the biased sensors from those working properly. The sensors operating effectively are all aligned along the same 1st principal component with only minor variations along the 2nd principal component. The biased sensors, however, vary greatly along the 1st principal component. The sensors biased to erroneously high glucose readings shift positively along the 1st principal component while the sensors biased erroneously low shift negatively along the same axis. The magnitude of the bias also is apparent as the sensor corresponding to + 200 mg/dL sensor is shifted further than that corresponding to + 50 mg/dL sensor. Thus, bias has both magnitude and directional components, providing a means for distinguishing bias from noise, which only has a magnitude component as described earlier. These differences between bias and noise modes of failure will be discussed in greater detail later when multiple modes of failure are imparted within one sensor array.

Transients

Transients in the signal from the biosensor are often caused by shorts where the sensor signal is temporarily biased or zero, as may be induced by the breakdown of vital electronic sensor components.[33] The longer these transients persist, the greater the risk of the patient interpreting the transient as a correct glucose measurement. Figure 20a shows this scenario with seven sensors working appropriately with a noise of ± 15 %. However, sensors eight, nine and ten experienced transients, corresponding to shifts of + 100 mg/dL, - 100 mg/dL and + 200 mg/dL glucose, respectively. A score plot based on this data is shown in Figure 20b, and demonstrates the ability to identify, by both direction and magnitude, differences from normal data. The + 200 mg/dL transient is further to the left, along the 1st principal component, as opposed to the + 100 mg/dL sensor. The – 100 mg/dL transient is shifted in the opposite direction along the 1st principal component by a magnitude approximately equal to that of the + 100 mg/dL transient. The case of transients is similar to that of bias. However, for similar values, due to smaller time duration of a transient as opposed to bias, the magnitude of the variation is smaller, with a similar directional component.

Sensor Drift

The final case potentially leading to sensor failure deals with the drift of the sensor signal. This may be caused by enzyme deactivation[27, 30, 31, 34], degradation of sensor materials[28] or remodeling of the implant site by a chronic inflammatory response.[28] Figure 21a shows seven sensors that are functioning effectively, however, sensor eight is biased positively by an arbitrary function, sensor nine positively by a similar function with an increased slope, and sensor ten drifting negatively. In Figure 21b, we see that a score plot based on PCA is able to group the seven sensors working effectively, as compared to the drifting sensors. Sensor eight is shifted negatively along the 1st principal component axis. Sensor nine, larger in magnitude than eight with respect to its deviation, is shifted further to the left, also along the 1st principal component axis. Finally, sensor 10, drifting in the

opposite direction from the other two failed sensors, is shifted positively along the 1st principal component axis. As in the case of bias, both magnitude and directional effects are apparent. However, difficulties may arise when attempting to distinguish biased sensors from drifting sensors. This will be further described in the following discussion of arrays experiencing multiple modes of failure.

Multiple Failures

The previous examples demonstrate the potential of PCA to identify faulty sensors under cases of specific failure. In the earlier discussion two general types of failure have been identified; those related to drift, bias or transients where magnitude and directional (positive or negative) components are present, and noise related failure where, despite the presence of a magnitude change, direction is random. Under actual *in vivo* conditions, however, the mechanism of failure will not be known *a priori* and multiple types of failure are possible. Determination of the specific mode of failure may help identify what kinds of problems are present and how they may be remedied. The case in Figure 22a depicts failure of an *in vivo* glucose sensor array. To determine the capabilities of PCA when faced with a potential worst case scenario, this data set has an extremely high failure rate of 60 % (i.e. six out of ten sensors have failed). Four sensors are operating correctly with noise of ± 5 %. However, sensor five is biased by + 20 mg/dL glucose, sensor six is functioning with noise of ± 50 %, sensor seven is biased by + 200 mg/dL glucose, sensor eight undergoes a temporary step corresponding to – 100 mg/dL glucose, sensor nine is drifting by some positive function and sensor ten is completely failed reading 0 mg/dL glucose.

A PCA score plot of this data set is shown in Figure 22b. As compared to the group of properly functioning sensors (sensors 1-4) there are significant deviations from this group in the score plot, specifically for sensors seven, nine, and ten along the 1st principal component axis, and sensors five, six and eight to smaller degrees along both principal component axes. A sensor failing in the positive direction may be distinguished against one failing negatively, if the deviation from the group operating correctly is of a large enough magnitude. Sensors seven and nine deviate positively and ten negatively, indicating these sensors are not failing by noise related mechanisms. However, distinguishing drift from bias or transients is not possible with these sensors (specifically sensors five, six and eight) based upon the analysis that has been performed. A possible solution is the implementation of a time-based monitoring scheme that quantifies relative changes in the principal components.

PCA on a time variable data set may result in a complete identification of the types of failures undergone by sensors in an array. To perform this analysis, the data set shown in Figure 22a was separated into seven ten minute segments (total experiment time ~ 70 minutes). Thus, each data subset consisted of 10 sensors with approximately 20 data points, or $(m,n) \sim (20,10)$. PCA analyses were performed on data from each of the time segments, and the relevant 1st and 2nd principal components were recorded for these sets and plotted against time as is shown in Figures 23a and 23b.

Figure 23a shows the 1st principal component as a function of time for

the four sensors operating properly at a ± 5 % variation level and six malfunctioning sensors. A sensor biased by + 20 mg/dL can be observed as slightly positive of those working properly. Sensor eight with a temporary negative step may be identified by its temporary deviation along the 1st principal component before returning to values matching that of the effective sensors. Sensor nine, drifting positively, displays a steady increase along the 1st principal component axis. Sensor ten, at 0 mg/dL, and sensor seven, biased by + 200 mg/dL, are shifted positively and negatively, respectively, along the 1st principal component. Sensors seven and ten indicate a consistent 1st principal component until they shift at approximately the time of a glucose bolus, due to the change in their relative errors as the correct glucose sensor readings increase with increasing blood glucose. The failed sensor displaying 0 mg/dL glucose is shifted further away from the sensors operating effectively, as is expected considering the magnitude of the error increases. The sensor biased by a reading of + 200 mg/dL shifts closer to the sensors operating effectively, which is expected as the relative importance of a 200 mg/dL error decreases during the glucose spike.

The one sensor that cannot necessarily be identified by the 1st principal component is sensor six, displaying a large variation in signal of ± 50 %. The error in this sensor can be seen in a plot of the 2nd principal component against time, Figure 23b, through variations that are both positive and negative, from those sensors operating effectively. As per earlier results shown in Figures 19a and b for failure induced by increased noise, there appears to be no directional component for the noisy sensor in this data set, thus random noise imparts only a magnitude component. Figure 23b also demonstrates temporary negative shifts for the failed sensors reading + 200 mg/dL and 0 mg/dL at the time of the glucose bolus, analogous to the shifts that we see along the 1st principal component.

The majority of sensors failing by a drift or bias related mechanism may be identified simply by plotting the 1st principal component against time, as was shown in Figure 23a. Biased sensors are permanently offset from those sensors working properly, while sensors experiencing transients undergo only a temporary deviation. Drifting sensors undergo a slow yet steady digression from those operating effectively. This may be identified by PCA of a time-variant data set, whereas a static analysis misinterprets a drifting sensor for one that is biased or undergoing a transient. The simplest category of failed sensor to identify consists of those having undergone complete failure as the relative error of these sensors changes significantly with changes in glucose concentration. The mechanism of failure is not readily apparent in a plot of the 1st principal component against time is that of increased noise. This is because random noise has only a magnitude component and, unlike all other mechanisms of failure, has a random directional component. Noise may only be identified as having a magnitude shift along the 2nd principal component, indicating that noise does not contribute as significantly to sensor error as does a bias related failure. However, this is only true for this data set and will not necessarily apply to other groups of sensors.

OPTICAL MICROSENSOR ARRAYS

We present a new approach for microfabrication of biosensor arrays based upon poly(ethylene glycol) diacrylate (PEG) hydrogels patterned photolithographically on silicon substrates. An oxidized silicon surface was treated with 3-(trichlorosilyl)propyl methacrylate

to form a self assembled monolayer (SAM) with pendant acrylate groups. SAM presence on the silicon wafer was verified using ellipsometry and Time-of-Flight secondary ion mass spectrometry (TOF SIMS). A solution containing PEG and a photoinitiator 2,2-dimethoxy-2-phenyl-acetophenone (DMPA) was spin-coated onto the acrylated silicon wafer. The polymer layer was then covered with a photo mask and exposed to 365 nm ultraviolet (UV) light. Areas exposed to the UV light cross-linked via free radical polymerization; the resulting hydrogel network was insoluble in the developer solution. Arrays were then developed with toluene and water, or supercritical CO_2. In both cases, the result was immobilization of three-dimensional, cross-linked PEG array elements on a silicon surface. Individual array member sizes were varied from 600 μm to 5 μm by use of different masks; in the latter case as many as 400 elements were generated in a 1 mm^2 square pattern. The resultant hydrogel patterns were hydrated for as long as three weeks without considerable delamination or deformation of the elements.

To examine possible sensing applications, patterns containing disks with immobilized SNAFL-modified glucose oxidase were prepared. Film pH sensitivity was verified by immersing the SNAFL-containing hydrogel elements into acidic and basic buffer solutions. The maximum fluorescent emission wavelength shifted as a result of the microenvironment pH changes.

EXPERIMENTAL SECTION

Poly(ethylene glycol) diacrylate (PEG-DA, MW 575), 2,2'- dimethoxy-2-phenyl-acetophenone (DMPA), anhydrous carbon tetrachloride, anhydrous toluene, and n-heptane were purchased from Aldrich Chemical Co.(Milwaukee, WI). 3-(trichlorosilyl)propyl methacrylate (TPM) was obtained from Fluka Chemicals (Milwaukee, WI). Hydrogen peroxide was purchased from EM Science (Gibbstown, NJ). Sulfuric acid was obtained from Fisher Scientific (Fair Lawn, NJ). Glucose Oxidase, potassium phosphate monobasic, sodium phosphate dibasic heptahydrate, and sodium chloride were purchased from Sigma Chemical Company (St. Louis, MO). Carbon dioxide of 97.7% purity was purchased from Botco (Bryan, TX). The succinimidyl ester varient of 5-(and-6)-carboxy SNAFL-1 was purchased from Molecular Probes (Eugene, OR). All reagents were used as received. Four inch diameter, (111), n-doped silicon wafers with thickness of approximately 500 μm, were purchased from Wafer World, Inc. (West Palm Beach, FL). One-tenth molar phosphate buffered saline (PBS) consisted of 1.1 mM potassium phosphate monobasic, 3 mM sodium phosphate dibasic heptahydrate, and 0.15 M NaCl in 18 MΩ•cm deionized water (E-pure, Barnstead, Dubuque, IW).

Photopolymerization was performed using 365 nm, 20 W/cm^2 light source (EFOS Ultracure 100ss Plus, UV spot lamp, Mississauga, Ontario). Scanning electron microscopy (SEM) was performed with a JEOL T330A at 15 kV (JEOL ,Ltd., Peabody, MA). Before SEM characterization, substrates were attached to aluminum mounts with carbon tape and coated with gold to a thickness of 200Å. A Veeco Dektak3 (Veeco Instruments, Plainview, NY) profilometer was employed to obtain height of individual array members. A Zeiss Axiovert 135 microscope equipped with an integrated CCD camera and fluorescent optical

package (Carl Zeiss Inc., Thosrnwood, NY) was used to determine lateral dimensions of individual array elements and examine element fluorescence. FITC and TRITC microscope fluorescence filters with excitation and emission wavelengths of 480 ± 30 nm / 535 ± 40 (FITC) and 540 ± 25 nm / 605 ± 50 nm (TRITC) were used when observing the fluorescent nature of the dye-encapsulated spheres. Fluorescent spectra of the SNAFL-Glucose Oxidase conjugates were recorded using a fluorescence spectrometer (QM-1, Photon Technology International, Monmouth Junction, NJ). The supercritical CO_2 (SC-CO_2) apparatus was assembled in-house. A Gaertner L2W26D ellipsometer (Gaetner Scientific Corp., Chicago, IL) was used for thickness measurements. Film thickness was calculated using Gaertner software assuming a refractive index (n_f) of 1.46. Measurements were made using a He/Ne (633.8) red laser at a 70.00 ±0.02° angle of incidence. Attenuated total reflectance/Fourier transform infrared (ATR/FTIR) spectroscopy was performed using a Mattson 5020 spectrophotometer with a ZnSe crystal (Spectra-Tech Inc., Shelton, CT). Time-of-Flight Mass Spectroscopy (TOF SIMS) was achieved by bombarding silicon wafers with ^{252}Cf fission fragments. Both negative and positive secondary ion (SI) species were analyzed under the same experimental conditions. Bias voltage for SI species was ± 4 kv. The chrome sodalime photomasks used for patterning of the arrays was obtained from Advance Reproductions (Andover, MA). USAF negative target mask was purchased from Melles Griot (Irvine, CA)

Surface functionalization

Silicon wafers were cut into 0.5 in. or 1in. squares and washed in ethanol to remove silicon dust from the surface. Wafers were then exposed to 365 nm UV radiation for 15 min. to remove organic residues. After washing with distilled water and drying under N_2, the samples were immersed in "piranha" solution consisting of 3:1 ratio of 30% w/v aqueous solutions of H_2SO_4 and H_2O_2 (*caution: this mixture reacts violently with organic materials and must be handled with extreme care*). Wafers were again washed with distilled water and dried under N_2 after the completion of the "piranha" step. Substrates were then reacted for 5 minutes at room temperature in a 1 mM solution of TPM in 4:1 ratio of heptane:carbon tetrachloride. Both solution preparation and reaction were conducted under a N_2 atmosphere in a glovebag, to prevent the highly hygroscopic trichlorosilane compound from reacting with atmospheric moisture. After the reaction, funtionalized wafers were washed with heptane and distilled water.

Preparation of SNAFL-GOX

SNAFL-conjugated glucose oxidase was prepared by reacting the succinimidyl ester activated version of SNAFL-1 (1 mg of dye dissolved in 100 µl of DMSO) with the lysine residues present on Glucose Oxidase dissolved in 100 mM PBS (adjusted with NaOH to pH 8.2). Unreacted dye was separated overnight by dialysis. Final enzyme concentration was approximately 2 mg/mL.

Fabrication of elements

Fluorescent PEG-DA elements were prepared from a precursor solution of 10 mg DMPA dissolved per mL of PEG-DA. This precursor solution was spin coated at 4000 rpm onto a surface of an acrylated wafer, forming a uniform polymer layer. This layer was covered with a photo mask and exposed to 365 nm UV light for 0.6 sec. The mask was aligned as close to the substrate surface as possible without coming in contact with the polymer layer. Areas exposed to UV light underwent free radical polymerization and subsequent cross-linking, thus becoming insoluble in the developer. Finally, patterns were developed by washing away uncrosslinked PEG-DA with anhydrous toluene and distilled water.

Supercritical CO_2 development of patterns

Alternatively, development of array elements was performed using SC-CO_2 to remove unpolymerized PEG-DA from the surface (see Figure 24). A similar fabrication procedure was followed as described in the previous section up to the development step. After UV-exposure, the wafers were placed into a 316-stainless steel pressure cell constructed from a 2-in. by 2-in. long cylinder with a 1.125-in. bore. The pressure cell was pressurized to 80 bar with CO_2 by a miniPump metering pump, (model number 870046, from Thermo Separation products, Riviera Beach, Fl). The temperature of the pressure cell was maintained at 35°C by a heating mantle (Rope Heater FGR-030, from Omega, Stamford, CT) equipped with a temperature controller (model CN 76000, from Omega. Stamford, CT). Once the pressure of 80 bar was achieved, isobaric conditions were maintained by a back-pressure regulator (model number 26-1722-24-161, obtained from Tescom Corporation, Elk River, MN). A CO_2 flow rate of 150 ml/hr was maintained for 2 h. by a LC-5000 Syringe Pump (Isco, Lincoln, NE). Wafers were washed with distilled water upon completion of the development process.

Fluorescence Detection

Fluorescent PEG-DA elements were prepared from a precursor solution of 10 mg DMPA and 50 µl of SNAFL-GOX per mL of PEG, following the procedure outlined previously. Fluorescence of SNAFL-GOX containing elements was examined using FITC and TRITC-filtered light on the fluorescence microscope. The silicon wafer containing the array elements was placed on a glass slide coverslip, and examined for fluorescence. Wafer elements were exposed to solutions of 0.1 M PBS, adjusted to pH 12.5 and 5.5 with NaOH and HCl, for approximately five minutes to alter array element pH. Elements were first examined in a dehydrated state after the toluene wash; they were then hydrated in 0.1M PBS and exposed to the acidic and basic solutions.

RESULTS AND DISCUSSION

We are presenting novel, microfabricated PEG-DA hydrogel patterns grafted onto planar surfaces. While some efforts have been directed toward grafting of PEG onto planar surfaces, we propose to combine grafting with photolithographic patterning of the graft polymer in a single step procedure.

Surface functionalization

In the initial experiments PEG-DA patterns were generated on silicon surfaces treated with piranha only. While patterns could be developed, surface attachment was very poor and array elements easily delaminated upon hydration. As a solution to this problem, the principle of self-assembly of alkyltrichlorosilanes on SiO_2/Si surfaces was used. This technique is a fast and effective way to form dense, self-assembled monolayers (SAM) on silicon surfaces. Self-assembly is believed to occur at the hydrated silicon surfaces via reaction between chlorosilane functionalities and hydroxy groups as shown in Eq. 8:

$$Cl\text{-}SiR + H\text{-}O\text{-}Si \rightarrow Si\text{-}O\text{-}SiR + HCl \qquad (8)$$

Result of the reaction is formation of a dense monolayer containing strong Si-O-Si bonds in both perpendicular and horizontal directions with respect to the surface, as illustrated by Figure 25. Presence of a thin, 10-15 Å, water layer at the silicon surface has been reported to be very important for the creation of the two-dimensional bond structure of the monolayer. "Piranha" pretreatment is used to ensure that such a layer is present after irradiation with UV light. Upon hydration, surfaces were exposed to a solution of TPM in heptane and carbon tetrachloride. Carbon tetrachloride serves to stabilize polar $SiCl_3$ groups of the coupling agent, while heptane length matches well with an allyl chain of trichlorosilanes, making it a good solvent for TPM.

Treated surfaces were found to be highly hydrophobic which indicated that surface modification took place, since untreated surfaces were hydrophilic. Ellipsometry measurements yielded thickness measurements of 14 ± 3Å, pointing to the presence of a single monolayer on the silicon surface.

Composition of the monolayer was further characterized with TOF SIMS. The plasma desorption mass spectroscopy (PDMS) technique was employed for analysis of functionalized silicon surfaces. This technique allows fragmentation and release of large pieces of a parent molecule from the substrate surface. Acrylated and clean silicon wafers were bombarded by ^{252}Cf fission fragments after which mass spectra of positive and negative SI species were collected and analyzed by means of TOF mass spectrometry (see Figure 26). Analysis of the mass spectra showed that in general functionalized surfaces contained hydrocarbon peaks of greater intensity. Moreover, we were able to observe distinct fragmentation patterns. Acrylated trichlorosilane molecules contain carbonyl functionalities which are sites of a characteristic α cleavage (see Figure 26). Spectra of functionalized surfaces distinctly showed masses 41 and 69, which are associated with such cleavage. Emission intensities of these masses were 20 and 30 fold less, respectively, in the control (uncoated) wafers (data not shown). Another very distinct peak collected in the positive spectrum is mass 85 which corresponds to $C_4H_5O_2$. Emission intensity of this mass is extremely low in case of bare silicon control sample. Hence, evidence collected by mass spectroscopy points to presence of acrylated trichlorosilane molecules on the silicon substrates. Altogether, TOF SIMS and ellipsometry indicate that successful surface modification occurred resulting in formation of an allyltrichlorosilane monolayer on the silicon substrate.

Fabrication of micropatterned PEG hydrogels

Formation of array elements from PEG-DA is based upon principles of free-radical polymerization. DMPA, a photoinitiator, dissociates upon exposure to UV radiation creating a highly reactive methyl radical which then attacks unsaturated carbon-carbon double bonds (C=C), producing unstable active sites which can react with other active sites created in the process. Thus, polymerization occurs. Since, two active centers per monomer are created, propagation results in formation of a highly cross-linked PEG-DA network. This network represents a three-dimensional, insoluble structure, capable of entrapping sensing agents.

Conversion of C=C bonds was monitored using ATR/FTIR spectroscopy. Thin films of PEG-DA were placed on the ZnSe ATR crystal and an IR spectrum was obtained before and after exposure to 365 nm UV light. Maximum conversion was achieved within a few seconds of illumination. Thus, highly cross-linked network was created almost immediately upon exposure to UV radiation.

The acrylated surface of the silicon substrate should also take part in the free-radical polymerization reaction since it also contains unsaturated C=C functionalities. Acrylate groups on the surface of the substrate reacted with C=C bonds present in the polymer to effectively anchor the polymer to the surface of the silicon (see Figure 25). Thus, delamination or detachment of PEG networks from the substrate should be less likely to occur.

The property of PEG-DA to become insoluble upon exposure to UV light was employed to create negative patters using photolithography techniques. Such patterns were created by spin-coating polymer onto the silicon substrate and then exposing coated surface with UV light through carefully aligned shadow mask placed on top of the polymer layer. Light was projected through the photo mask creating polymerized regions which corresponded to the pattern of the photo mask. Unpolymerized PEG-DA dissolved in toluene or SC-CO_2 so that only insoluble, cross-linked patterns remained on the surface. Chrome-coated sodalime photomask employed for patterning contained circles with diameters of 600 μm, 50 μm and 5 μm arranged into three squares, 20x20 elements in each square. These patterns were reproduced on the silicon surface as cylinders with height of 13 ± 0.1 μm. Height of the individual array members was determined by using Veeco Dektak3 profilemeter. Proximity printing was used for patterning 600 μm elements, whereas, contact printing was employed to create smaller patterns. Minimum resolution is directly proportional to the square root of the gap between a photomask and polymer layer, which means that the gap had to be minimized in order to obtain highest resolution.

Morphology of the generated patterns was studied with SEM. Figure 27 shows SEM micrographs of an array of 600 μm elements, with 500 μm distance between the elements, as well as a single element. Clearly defined pattern areas with no residual polymer (precursor solution) remaining on the substrate are observed. Inspection of an individual array member at higher magnification reveals a very smooth surfaces, normally associated with poly(ethylene glycol),[35] without visible defects in the polymer network. Figure 28 depicts hydrogel patterns with 50 μm diameter elements and 50 μm distance between the

elements. A high density and quality of the pattern is indicated by Figure 28(a) which shows as many as 300 elements. Side-view of the elements presented in Figure 28(b,c) emphasizes three-dimensional nature of the pattern. Smallest microfabricated arrays consisting of 5 μm diameter elements separated by a distance of 50 μm are depicted in Figure 29a. Inspection of a single array element (Figure 29b) shows a difference in geometry brought forth by the dramatic increase in the aspect ratio when compared to two previous patterns.

Potential of imaging of PEG was further explored by patterning of USAF test target mask. Negative image of this mask obtained by contact printing shown in Figure 30, indicates a minimum feature size of 25 μm. This image accentuates high quality and versatility of photolithographic patterning of PEG. Thus, our photolithography technique allows fabrication of PEG arrays of high quality, structural integrity, spatial density and provides an opportunity for creation of much more complex images.

Supercritical development

While organic solvent based development discussed in the previous section yielded satisfactory results, it was felt that exposure of the PEG arrays to possibly toxic chemicals i.e. toluene may be detrimental to *in vivo* compatibility of the elements and activity of the proteins entrapped in them. Studies have shown that proteins tend to lose some of the biological activity when in contact with anhydrous organic solvents due to denaturing or loss of the secondary structure. Therefore, an alternative route for development of the drug delivery arrays was explored.

CO_2 is an environmentally benign, non-toxic compound which is being used in the pharmaceutical industry as a reaction medium for synthesis of drug compounds. In addition, SC-CO_2 is being investigated as a possible medium for photoresist image development. Motivating factor for the latter studies is potential of this solvent in achieving high feature resolution, as well as, ability to control solvating power by varying temperature or pressure. Therefore, use of SC-CO_2 for development of patterned biosensor elements may be advantageous from the biocompatibility, protein activity, as well as, photolithography considerations.

Main concern for the supercritical development of polymer images is solubility of a given polymer in the supercritical fluid (SCF). In our work, limited solubility of the polymer in the SCF was overcome due to continuos supply of CO_2 (150ml/h) and the fact that only small amount of uncross-linked polymer (less than 1ml) needed to be removed from the surface.

Elements with diameters of 600 μm, 50 μm and 5 μm were patterned on silicon surface by the method described in the previous section. SEM micrographs of the hydrogel arrays developed in supercritical media, presented in Figure 31, compare very favorably to patterns developed in organic solvents. In fact, no differences in morphology of individual array elements of different diameters developed with the two techniques were observed.

Solubility problems can potentially be addressed by increasing the flow

rate or pressure of CO_2 in the chamber. Increase in pressure makes this SCF more liquid-like thus increasing its solvating power while increased flow rate means larger amount of polymer can be removed on per time basis. In addition, surfactants may be added to further improve solubility of the polymer in the SC-CO_2.

Fluorescence Sensing

Fluorescent array elements were fabricated by incorporating SNAFL-1 into the precursor spin solution to verify potential usage of PEG-crafted microarrays in optical sensors. SNAFL-1 is a pH-sensitive dye which exhibits both intensity and emission wavelength changes with changing pH. Dye pKa is approximately 7.8. In an acidic environment, free dye is optimally excited at 510 nm, with an emission maximum at 545 nm. In a basic environment, the optimum excitation/emission values red shift to 542/645 nm. Glucose oxidase-conjugated dye (MW 180,000) was incorporated into the thin films to hinder dye diffusion out of the disks. The conjugated dye had acidic and basic emission maximums of 538 and 620 nm, respectively.

Figure 32 shows the fluorescent nature of a 500 μm array element with encapsulated dye. Figure 32a shows an element, which has undergone the deionized water/toluene wash development step. Our prior research efforts have shown a slightly acidic environment inside PEG hydrogels with weak buffering.[36] When observed on the fluorescence microscope, both 500 and 50 μm array elements initially showed a slightly acidic spectrum, with strong emission through the FITC filter and weak emission through the TRITC filter. As shown in Figure 32b, after exposure to a buffered solution with a basic pH, element fluorescence underwent a strong redshift. Emission when excited through the FITC filter was weak, while the TRITC filter provided an intense red fluorescence. The fluorescent response was reversed by soaking the wafer in a small solution of buffered solution with an acidic pH, as shown in Figure 32c.

Array elements of similar quality to those shown earlier were fabricated without difficulty from the SNAFL-GOX containing solution, although the decrease in precursor spin solution viscosity did limit the amount of PBS solution containing the SNAFL-GOX which could be added. While PEG-NHS has previously been used to covalently encapsulate fluorophore-protein conjugates without significant decrease in fluorescent intensities, physical encapsulation of SNAFL-GOX inside the PEG hydrogel network was sufficient to retard dye diffusion out of the gel. This work only utilized one fluorophore and a single spin step as an initial test of array suitability for optical sensing. Multianalyte fluorescence sensor arrays should prove simple to fabricate, however, by repeatedly aligning the wafer and spin coating additional elements from precursor solutions containing alternate fluorophores.

INTEGRATION OF DRUG DELIVERY ELEMENTS INTO SENSOR PLATFORMS

We are also developing novel approach for the fabrication of drug delivery elements on sensor platforms as a method of delivering angiogenic factors to promote vessel growth and mass transfer around sensors. This work came about when we noticed the slow leakage

of enzyme from redox hydrogels in which the protein was physically entrapped but not covalently immobilized. To take advantage of this phenomena for drug delivery, microfabricated drug delivery elements consisting of poly(ethylene glycol) hydrogels containing the drug of interest are fabricated using photolithography techniques. Such methods allow the incorporation of drug delivery elements on the same planar surface with microfabricated amperometric biosensors. These biosensor/drug delivery devices may then be implanted in vivo with the delivery elements releasing basic fibroblast growth factor (bFGF), vascular endothelial growth factor (VEGF), and other proteins which promote neovascularization and decrease fibrosis in the immediate vicinity of the implant.

To fabricate these devices, the surface of silicon wafer is etched with piranha which produces a layer of silicon oxide on top of silicon and rendered the surface hydrophilic. The oxidized surface is then treated with 3-(trichlorosilyl)propyl methacrylate to form a self assembled monolayer (SAM) with pendent acrylate groups . A solution containing PEG-DA, a photoinitiator (2,2-dimethoxy-2-phenyl-acetophenone) (DMPA) and protein dissolved in phosphate buffered saline (PBS) is prepared and spin-coated onto acrylated silicon wafer. The polymer layer is then covered with a photomask and exposed to 365 nm UV light source. Areas exposed to the UV light undergo free radical polymerization and subsequent crosslinking, becoming insoluble in the developer solution. In addition, PEG-DA react with free acrylate groups of the wafer surface to anchor the gel to the silicon surface. Finally, arrays are developed by washing away uncrosslinked PEG-DA with a developer such as toluene, water, SC-CO_2. The result is the creation of cross-linked hydrogels fixed on the silicon surface. Release studies are currently underway and have thus far we have demonstrated the release of an angiogenic factor, basic fibroblast growth factor (bFGF) as shown in Figure 33.

STUDIES TO BE COMPLETED

The following studies are underway and will be reported to NMTB upon completion:

- Implant studies of redundant glucose sensor arrays
- Fabrication of multianalyte sensor arrays

Though these studies were not completed at the end of the contract, NMTB will receive acknowledgement as specified in the research contract.

CONCLUSIONS

Based on the results of this study, we have come to the following conclusions:

1. Nanocomposite thin films of redox polymers and oxidoreductases can be used to fabricate amperometric biosensors that exhibit a high degree of structural and operation reproducibility.

2. Using these nanocomposite films, redundant amperometric sensor arrays for glucose and lactate can be fabricated on thin film gold microelectrode arrays.

3. Principal component analysis can be used for fault detection and identification in amperometric sensor arrays.

4. Using photopolymerized hydrogels, fluorescent optical microsensor arrays can be fabricated with micron scale resolution.

5. Drug delivery elements can be microfabricated on sensor materials using photolithography and these arrays can release angiogenic factors such as bFGF.

DEVIATIONS FROM ORIGINAL RESEARCH PLAN

The addition of nanometer-scaled redox polymer/enzyme films represents a small deviation from the original proposal where we discussed using spin coating to form sensor layers on electrodes. However, layer by layer construction of sensors on a nanometer scale may produce sensors that are more reproducible than those produced by spin coating and thus should continue to be investigated for use in electrochemical sensor arrays.

The fabrication of optical microsensor arrays using this technology represents an unexpected side product of the original proposal. For lab-on-a-chip and bioMEMS applications, optical sensing may produce higher sensitivity. While we basically demonstrated pH detection here, other work by our group has previously demonstrated sensing based on enzyme catalysis[36] and macromolecular recognition[37] in these materials.

The integration of drug delivery elements into the sensor platforms represents an unexpected side product of the original proposed research. We believe that the integration of biosensing and drug delivery will yield more biocompatible sensors and eventually lead to closed-loop drug delivery systems.

PAPERS AND ABSTRACTS RESULTING FROM THIS CONTRACT

REFEREED JOURNAL PUBLICATIONS

1. Sirkar, K.; Revzin, A.; Pishko, M. "Glucose and Lactate Biosensors Based on Redox Polymer/Oxidoreductase Nanocomposite Thin Films" *Anal Chem.* **2000**, in press.

PRESENTATIONS

1. Sirkar, K.; Revzin, A.; Pishko, M. "Glucose and Lactate Biosensors Based on Redox Polymer/Oxidoreductase Nanocomposite Thin Films" presented at IEEE-EMBS, Oct. 12, 1999. Atlanta, GA. (Abstract submitted prior to NMTB contract).
2. Revzin, A.; Mellott, M.; Pishko, M. "Microfabricated Poly(ethylene glycol) Hydrogels for Drug Delivery from Sensor Platforms" to be presented at the 6th World Biomaterials Congress in Honolulu, HW, May 2000. (Abstract submitted prior to NMTB contract).
3. Sirkar, K.; Revzin, A.; Pishko, M. "Glucose and Lactate Biosensors Based on Redox Polymer/Oxidoreductase Nanocomposite Thin Films" to be presented at the spring annual meeting of Electrochemical Society Meeting in Toronto, Canada, May 2000. (Abstract

submitted prior to NMTB contract).

MANUSCRIPTS UNDER REVIEW OR IN PREPARATION

1. Sirkar, K.; Pishko, M. "Application of Principal Component Analysis to Glucose Sensor Arrays", submitted to NMTB for review.
2. Revzin, A.; Sirkar, K.; Pishko, M. "Lactate and Pyruvate Sensor Based upon Electrostatically Complexed Redox Polymers and Oxidoreductases", manuscript in preparation.
3. Revzin, A.; Russell, R.; Mellott, M.; Hile, D.; Pishko, M. "Fabrication of Optical Microsensor Arrays Based on Patterned Poly(ethylene glycol) Hydrogels", manuscript in preparation.

REFERENCES

1. Kober, E.M., *et al.*, *Synthetic Routes to New Polypyridyl Complexes of Osmium (II).* Inorg. Chem., 1988. **27**: p. 4587-4598.

2. Xia, Y. and G. Whitesides, *Soft Lithography.* Angew. Chem. Int. Ed., 1998. **37**: p. 550-575.

3. Pishko, M.V., *et al.*, *Direct Electrical Communication between Graphite Electrodes and Surface Adsorbed Glucose Oxidase/Redox Polymer Complexes.* Angewandte Chemie Intl. Ed., 1990. **29**: p. 82.

4. Schuhmann, W., *et al.*, *Electron Transfer Between Glucose Oxidase and Electrodes via Redox Mediators Bound with Flexible Chains to the Enzyme Surface.* J. Am. Chem. Soc., 1991. **113**: p. 1394-1397.

5. Franchina, J., *et al.*, *Entrapment of a biorecognition molecule in a weak-acid, polyelectrolyte hyperbranched thin film on gold.* Anal. Chem., 1999. **71**(15): p. 3133-3139.

6. Hodak, J., *et al.*, *Layer-by-Layer Self-Assembly of Glucose Oxidase with a Poly(allylamine)ferrocene Redox Mediator.* Langmuir, 1997. **13**: p. 2708-2716.

7. Kuhn, A. and F.C. Anson, *Adsorption of Monolayers of P2Mo18O626- and Deposition of Multiple Layers of Os(bpy)32+-P2Mo18O626- on Electrode Surfaces.* Langmuir, 1996. **12**: p. 5481-5488.

8. Marcus, R.A. and N. Sutin, *Electron Transfers in Chemistry and Biology.* Biochim. Biophys. Acta, 1985. **811**: p. 265-322.

9. American Diabetes Association, *Consensus statement on self-monitoring of blood glucose.* Diabetes Care, 1987. **10**(1): p. 95-99.

10. DeLumley-Woodyear, T., *et al.*, *Polyacrylamide-Based Redox Polymer for*

Connecting Redox Centers of Enzymes to Electrodes. Anal. Chem., 1995. **67**(8): p. 1332-1338.

11. Malitesta, C., *et al.*, *Glucose Fast-Response Amperometric Sensor Based on Glucose Oxidase Immobilized in an Electropolymerized Poly(o-phenylenediamine) Film.* Anal. Chem., 1990. **62**: p. 2735-2740.

12. Ryan, M.R., J.P. Lowry, and R.D. O'Neill, *Biosensor for Neurotransmitter L-Glutamic Acid Designed for Efficient Use of L-Glutamate Oxidase and Effective Rejection of Interference.* Analyst, 1997. **122**: p. 1419-1424.

13. Garrell, R.L. and J.E. Chadwick, *Structure, Reactivity and Microrheology in Self-Assembled Monolayers.* Colloids and Surfaces A-Physicochemical and Engineering Aspects, 1994. **93**: p. 59-72.

14. Widrig, C.A., C. Chung, and M.D. Porter, *The Electrochemical Desorption of N-Alkanethiol Monolayers from Polycrystalline Au and Ag Electrodes.* J. Electroanal. Chem., 1991. **310**(1-2): p. 335-359.

15. Aoki, A. and A. Heller, *Electron Diffusion Coefficients in Hydrogels formed of Crosslinked Redox Polymers.* J. Phys. Chem., 1993. **97**: p. 11014-11019.

16. Sirkar, K., A. Revzin, and M. Pishko, *Glucose and lactate biosensors based on redox polymer/oxidoreductase nanocomposite thin films.* Anal. Chem., 2000. **in press**.

17. Morf, W.E. and N.F. de Rooij, *Performance of amperometric sensors based on multiple microelectrode arrays.* Sensors and Actuators B, 1997. **44**: p. 538-541.

18. Jordan, C.E. and R.M. Corn, *Surface Plasmon Resonance Imaging Measurements of Electrostatic Biopolymer Adsorption onto Chemically Modified Gold Surfaces.* Anal. Chem., 1997. **69**: p. 1449-1456.

19. Tatsuma, T., K.-I. Saito, and N. Oyama, *Enzyme Electrodes Mediated by a Thermoshrinking Redox Polymer.* Anal. Chem., 1994. **66**: p. 1002-1006.

20. James, C., *et al.*, *Aligned microcontract printing of micrometer-scale poly-L-lysine structures for controlled growth of cultured neurons on planar microelectrode arrays.* IEEE Trans. Biomed. Eng., 2000. **47**(1): p. 17-21.

21. Dunia, R., *et al.*, *Identification of faulty sensors using prinicipal component analysis.* AIChE Journal, 1996. **42**(10): p. 2797-2812.

22. Stork, C., D. Veltkamp, and B. Kowalski, *Identification of multiple sensor disturbances during process monitoring.* Anal. Chem., 1997. **69**: p. 5031-5036.

23. Quinn, C.P., *et al.*, *Kinetics of Glucose Delivery to Subcutaneous Tissue in Rats: A*

Study Utilizing Amperometric Biosensors. Am. J. Physiol., 1995. **269**(32): p. E155.

24. Harris, C., *et al.*, *Electromagnetic field strength levels surrounding electronic article surveillance (EAS) systems.* Health Physics, 2000. **78**(1): p. 21-27.

25. McIvor, M.E., *et al.*, *Study of Pacemaker and Implantable Cardioverter Defibrillator Triggering by Electronic Article Surveillance Devices (SPICED TEAS).* PACE - Pacing and Clinical Electrophysiology, 1998. **21**(10): p. 1847-1861.

26. Zuckerwar, A.J., *et al.*, *Development of a Piezopolymer Pressure Sensor for a Portable Fetal Heart Rate Monitor.* IEEE Transactioons on Biomedical Engineering, 1993. **40**(9): p. 963-969.

27. Moussy, F., *et al.*, *In vitro and in vivo performance and lifetime of perfluorinated ionomer-coated glucose sensors after high temperature curing.* Anal. Chem., 1994. **66**: p. 3882-3888.

28. Pickup, J., D. Claremont, and G. Shaw, *Responses and calibration of amperometric glucose sensors implanted in the subcutaneous tissue of man.* Acta Diabetol., 1993. **30**: p. 143-148.

29. Wood, D.E., D.J. Ewins, and W. Balachandran, *Comparative analysis of power-line interference between two- or three-electrode bipotential amplifiers.* Medical & Biological Engineering & Computing, 1995. **33**(1): p. 63-68.

30. Pickup, J.C., G.W. Shaw, and D.J. Claremont, *Potentially-Implantable Amperometric Glucose Sensors with Mediated Electron Transfer: Improving the Operating Stability.* Biosensors, 1989. **4**: p. 109-119.

31. Pickup, J.C., G.S. Shaw, and D.J. Claremont, *In Vivo Molecular Sensing in Diabetes Mellitus: An Implantable Glucose Sensor with Direct Electron Transfer.* Diabetologia, 1989. **32**: p. 213-7.

32. Velho, G., P. Froguel, and G. Reach, *Determination of Peritoneal Glucose Kinetics in Rats: Implications for the Peritoneal Implantation of Closed-Loop Insulin Delivery Systems.* Diabetologia, 1989. **32**: p. 331-336.

33. Hediger, S., A. Sayah, and M.A.M. Gijs, *Fabrication of a novel microsystem for the electrtical characterisation of cell arrays.* Sensors and Actuators B, 1999. **56**: p. 175-180.

34. Sternberg, F., *et al.*, *Calibration problems of subcutaneous glucosensors when applied in situ in man.* Horm. Metab. Res., 1994. **26**: p. 523-525.

35. Lackowski, W., *et al.*, *An atomic force microscopy study of the surface morphology of hyperbranched poly(acrylic acid) thin films.* Adv. Mater., 1999. **in press**.

36. Russell, R., *et al.*, *Poly(ethylene glycol) Hydrogel Encapsulated Fluorophore-Enzyme Conjugates for Direct Detection of Organophosphorus Neurotoxins.* Anal. Chem., 1999. **71**(21): p. 4909-4912.

37. Russell, R., *et al.*, *A fluorescence-based glucose biosensor using concanavalin A and dextran encapsulated in a poly(ethylene glycol) hydrogel.* Anal. Chem., 1999. **71**: p. 3126-3132.

Figure 1. Structure of poly[(vinylpyridine Os(bpy)$_2$Cl)-co-allyl amine].

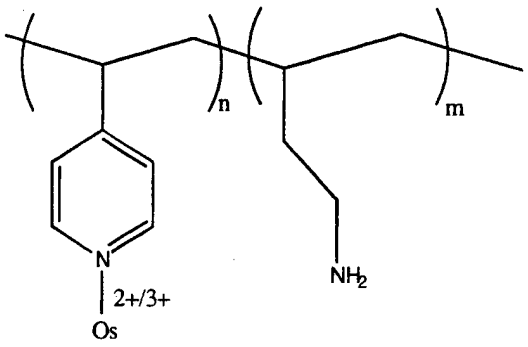

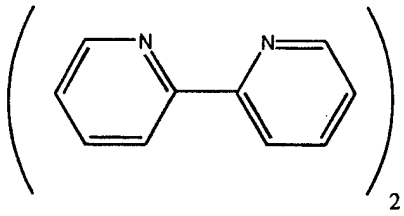

Figure 2. Schematic of the multilayer redox polymer/glucose oxidase nanocomposite film structure.

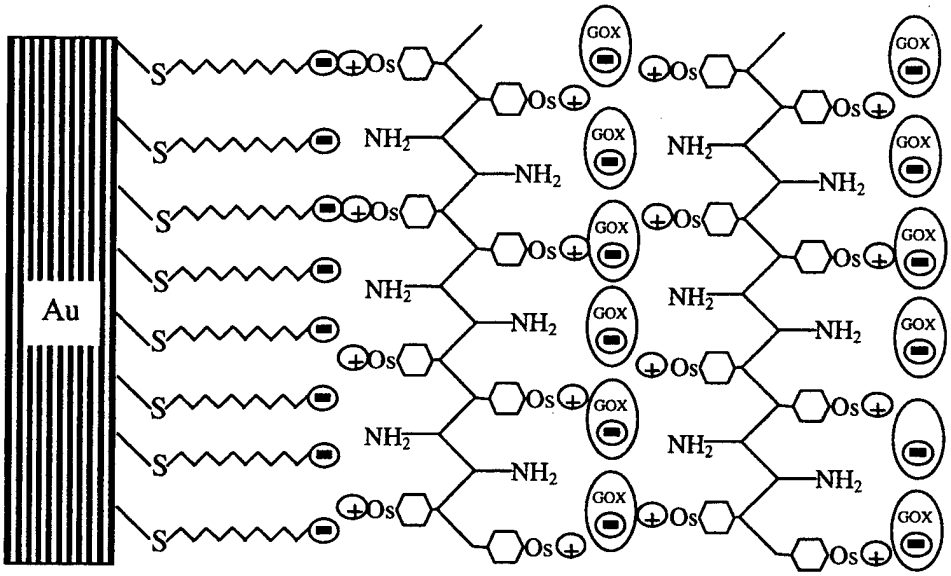

Figure 3. Ellipsometric measurements of film thickness during the fabrication of the nanocomposite thin film. Results are shown for both glucose oxidase and lactate oxidase containing films.

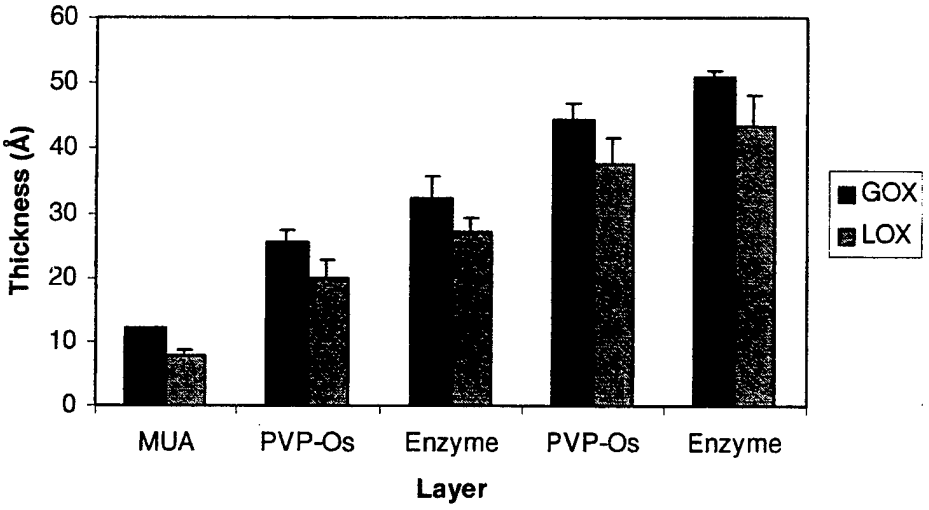

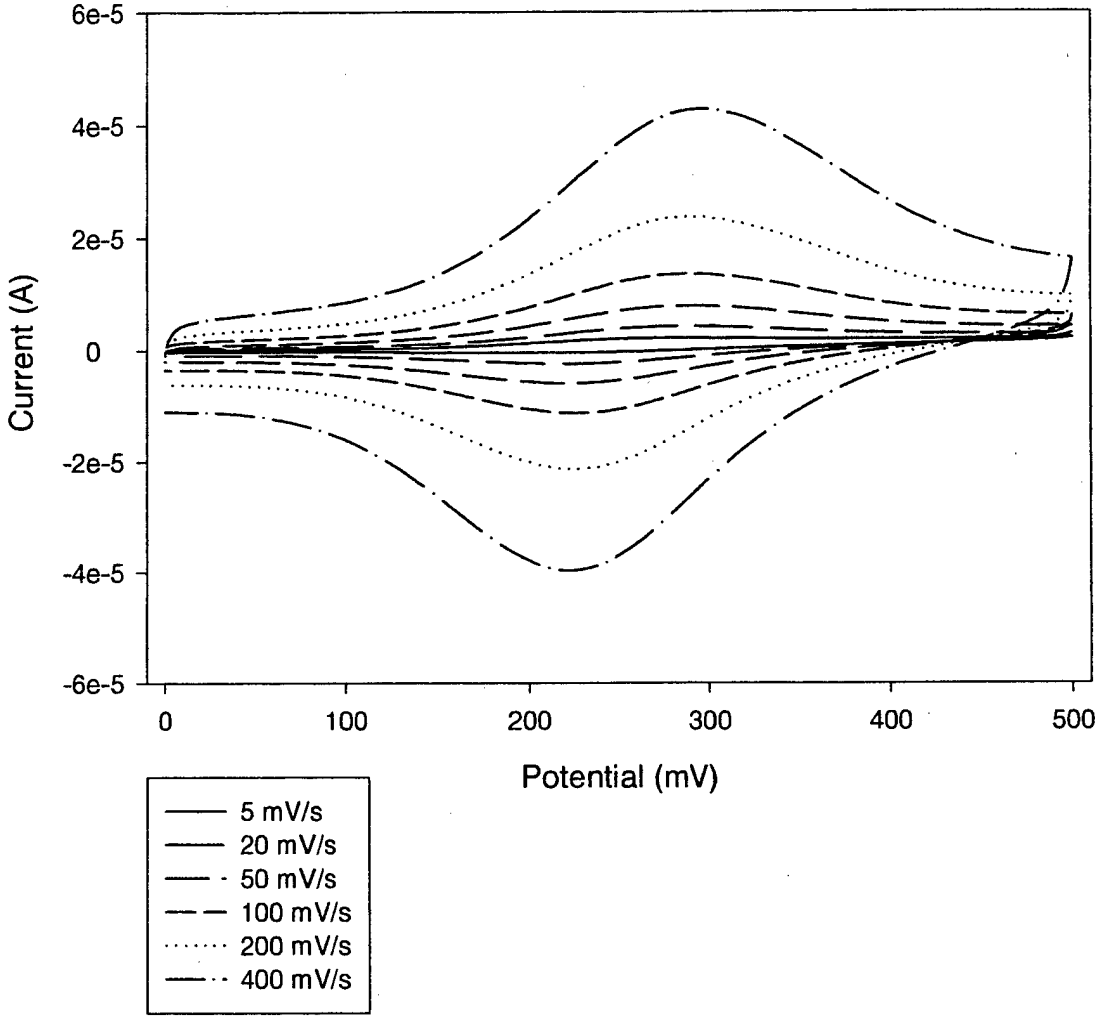

Figure 4. Cyclic voltammetry of a nanocomposite thin film consisting of MUA/PVPOS/GOX/PVPOS/GOX.

Figure 5. Concentration dependence of the current density for a lactate sensor based on a redox polymer/lactate oxidase nanocomposite thin film.

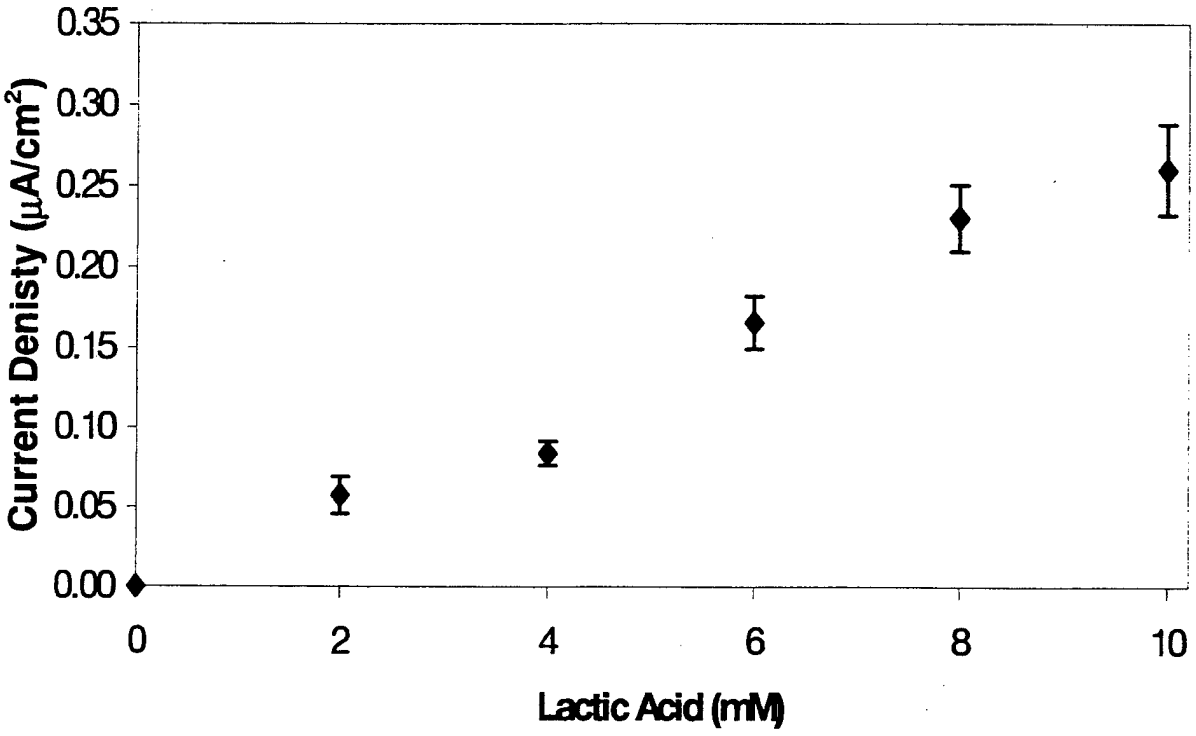

Figure 6. Concentration dependence of the current density for a glucose sensor based on a nanocomposite thin film of redox polymer/glucose oxidase. ●: Film crosslinked with glutaraldehyde; triangle: uncrosslinked film.

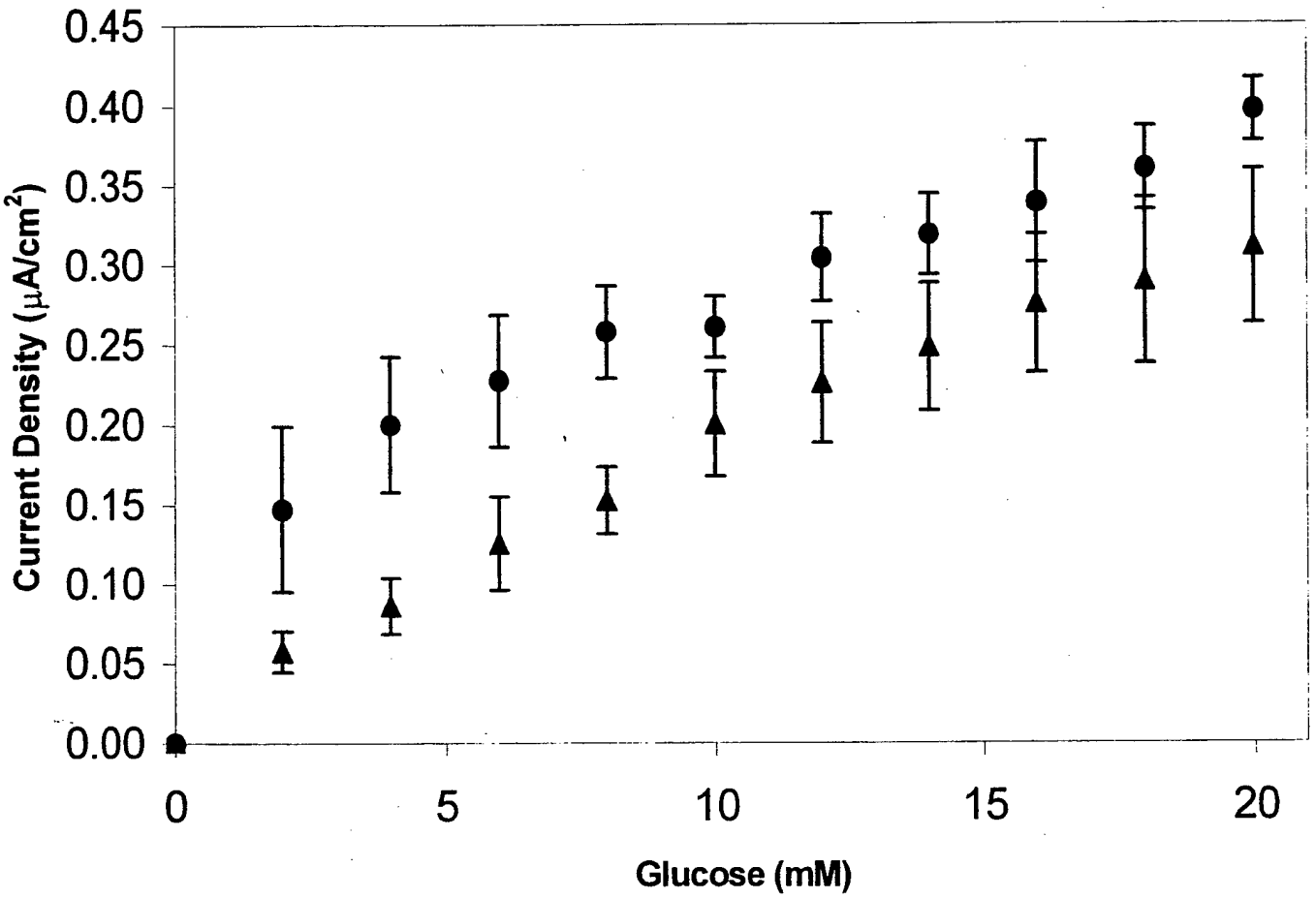

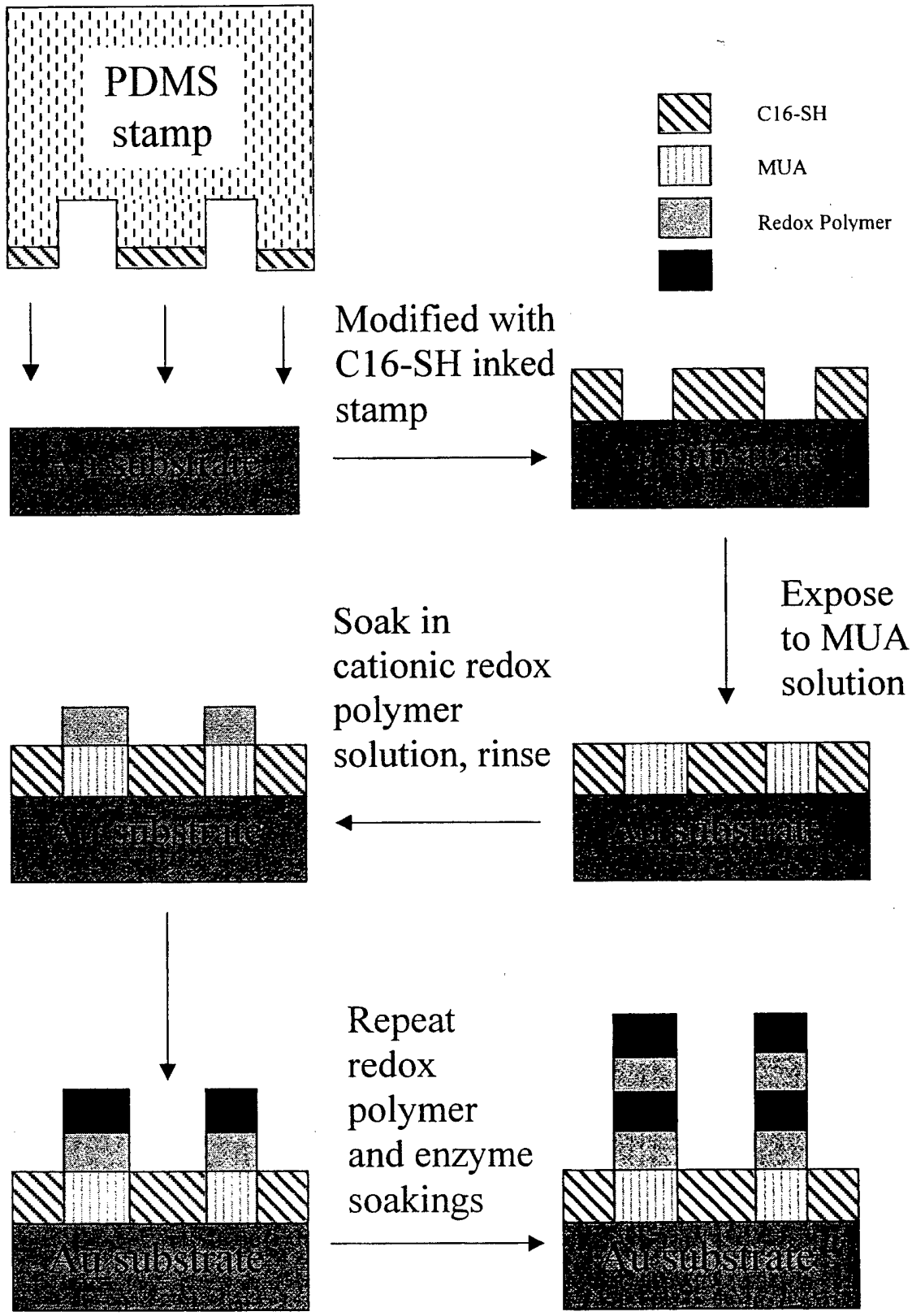

Figure 7. Schematic of nanocomposite thin film patterning using microcontact printing.

Figure 8. Optical micrographs of nanocomposite thin film patterns.

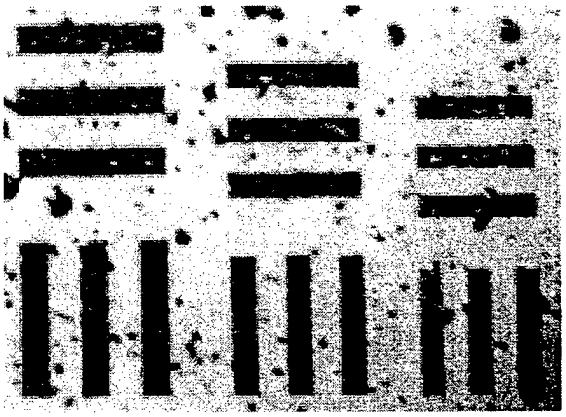

Figure 9. Fabrication process for thin film microelectrode arrays.

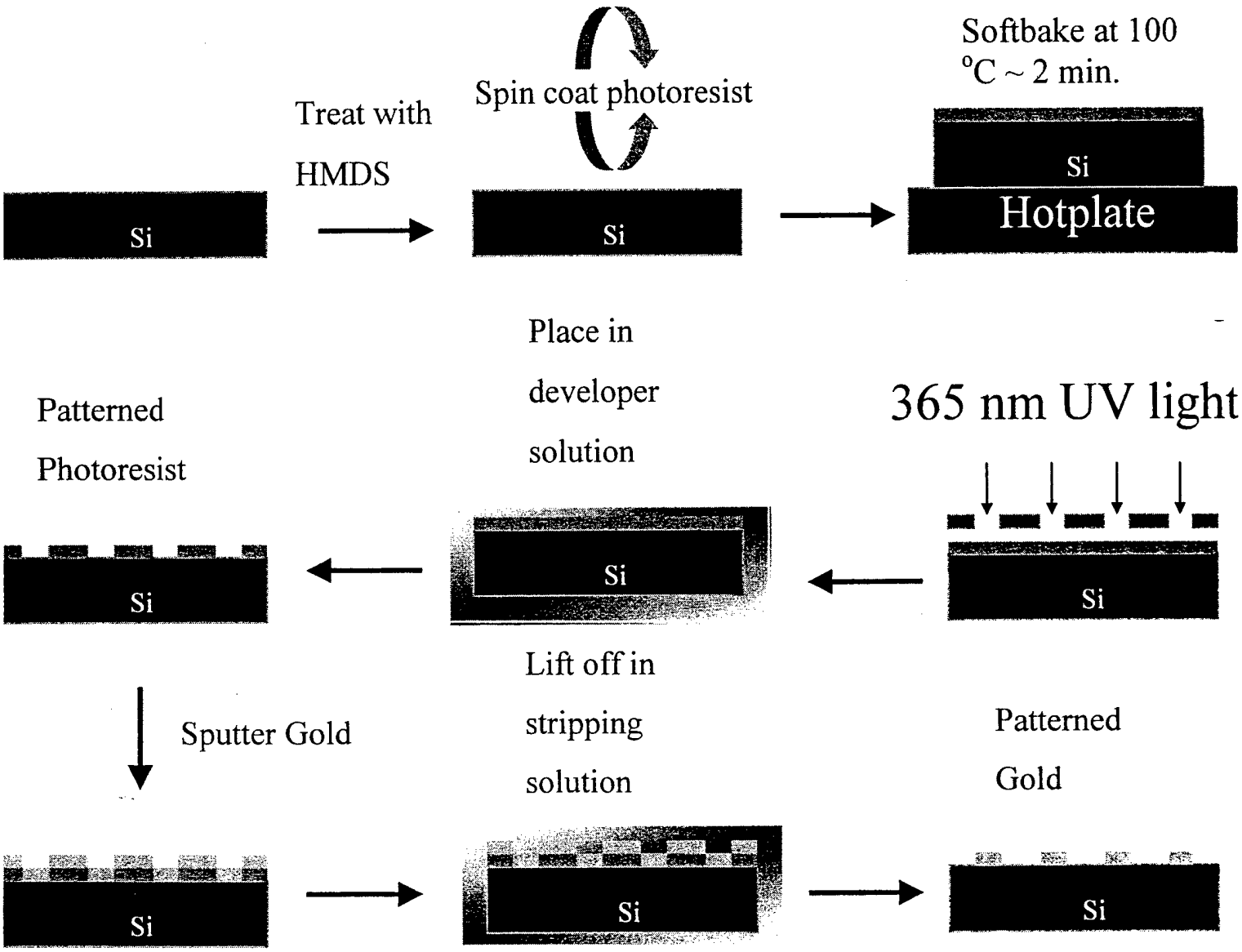

Figure 10. Design for a five electrode array.

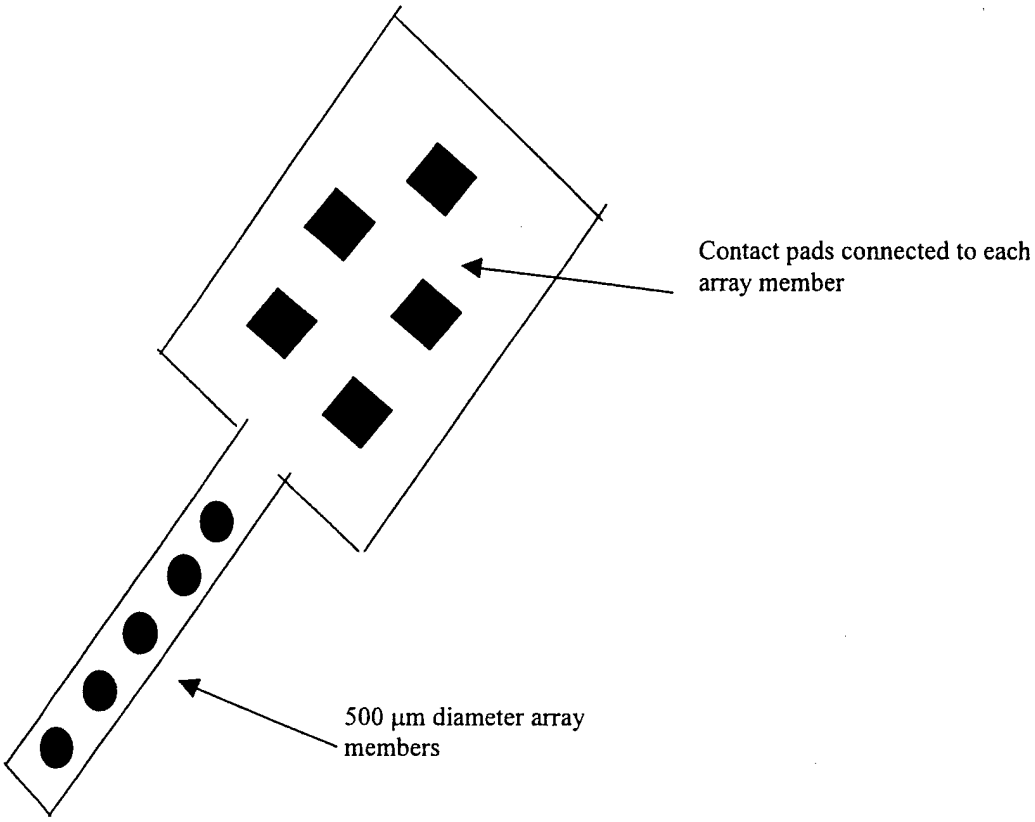

Figure 11. Fabrication process for forming nanocomposite thin films on microelectrode arrays.

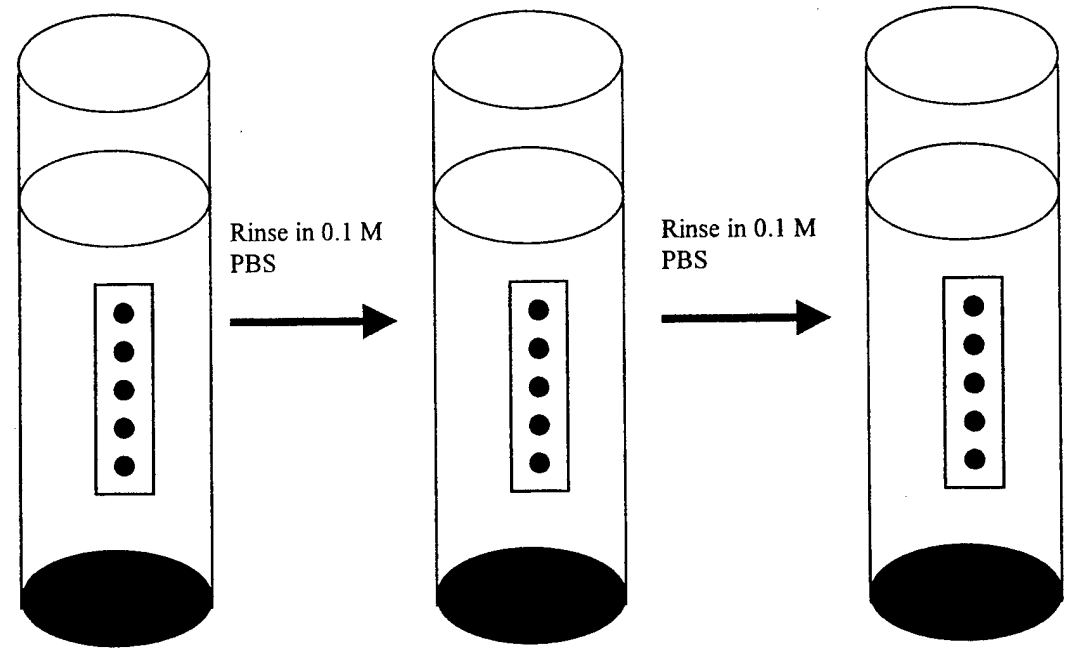

Figure 12. Electron micrograph of a five Au electrode array fabricated on Si.

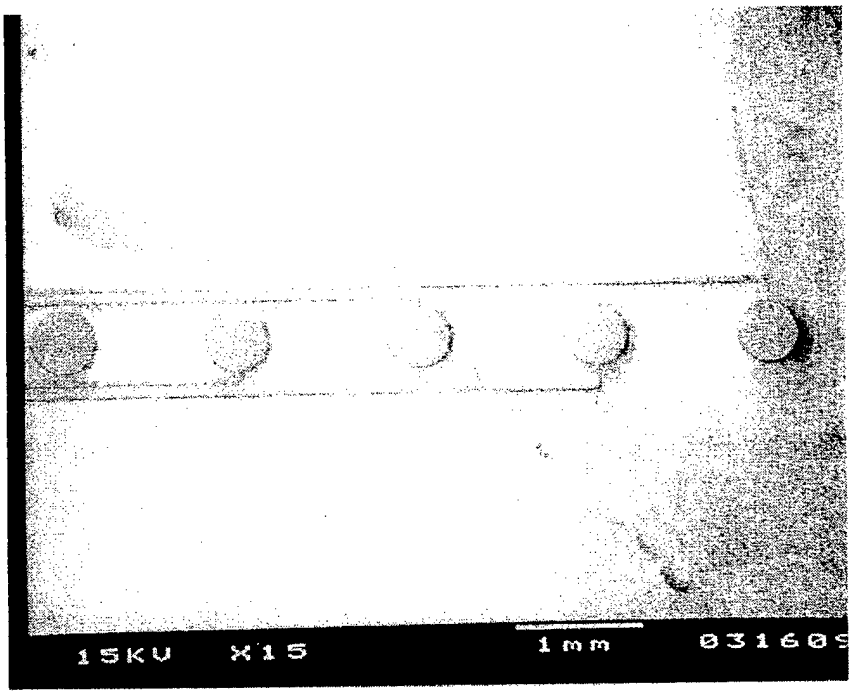

Figure 13. Cyclic voltammetry of a redox polymer/glucose oxidase nanocomposite thin film on a five electrode array.

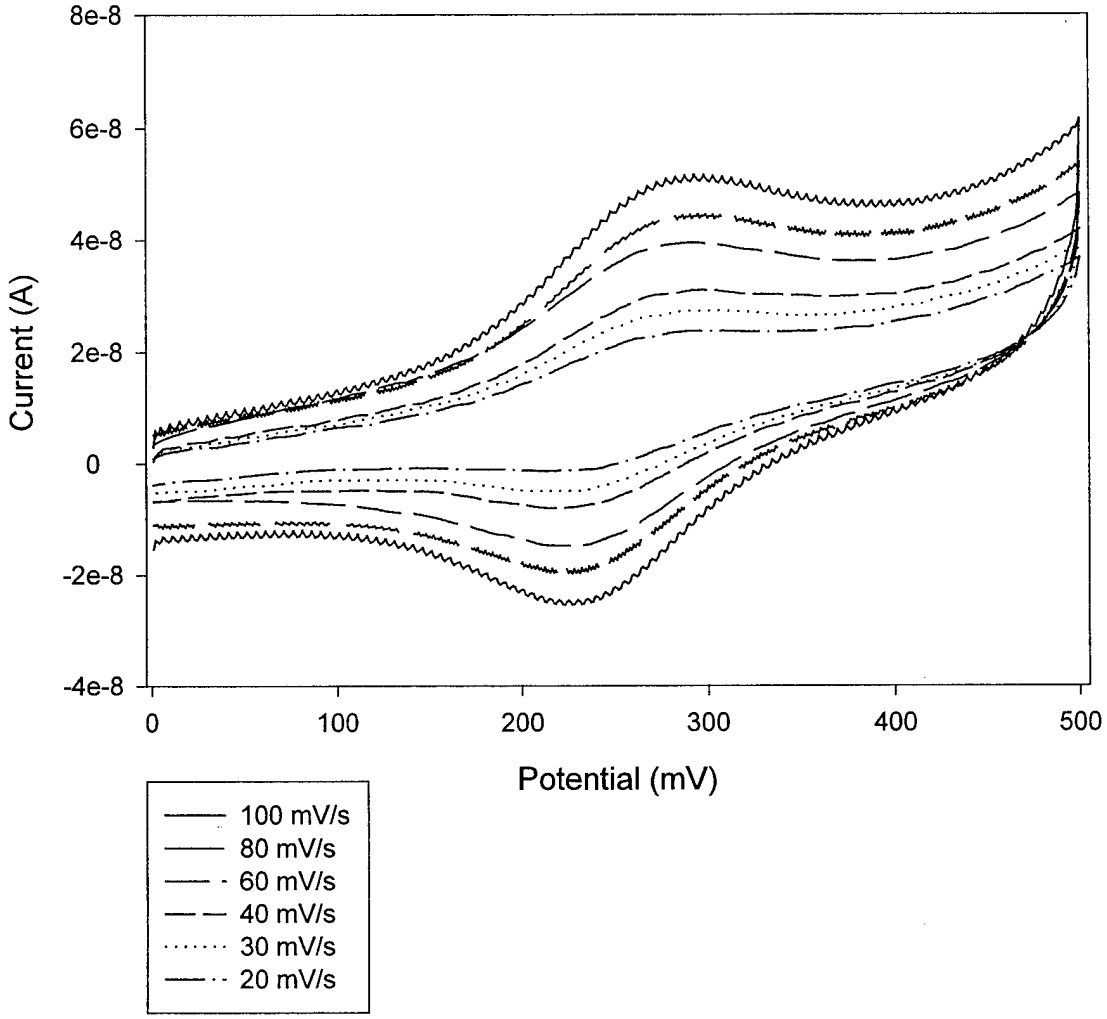

Figure 14. Concentration dependence of the current for a nanocomposite redox polymer/glucose oxidase thin film microelectrode. n = 5.

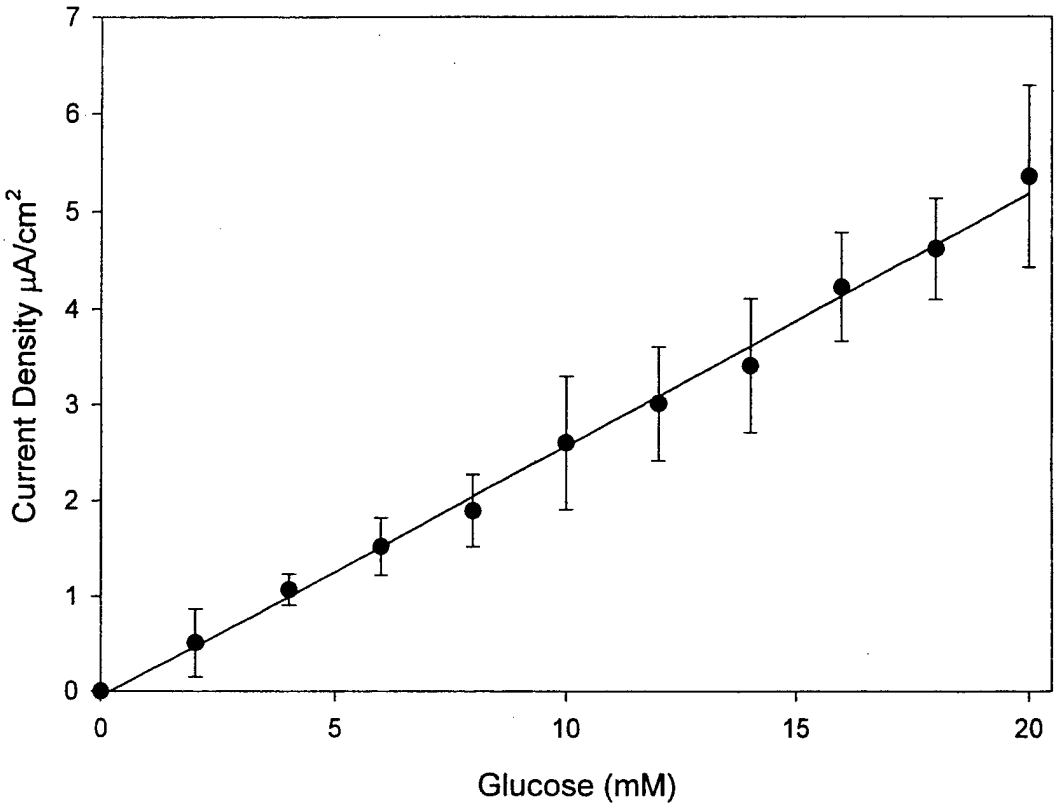

Figure 15. Concentration dependence of the current for a lactate electrode array sensor based on a nanocomposite thin film of redox polymer and lactate oxidase. Triangle: current response of a single electrode in the array. Circle: current response of the array operating with two electrodes.

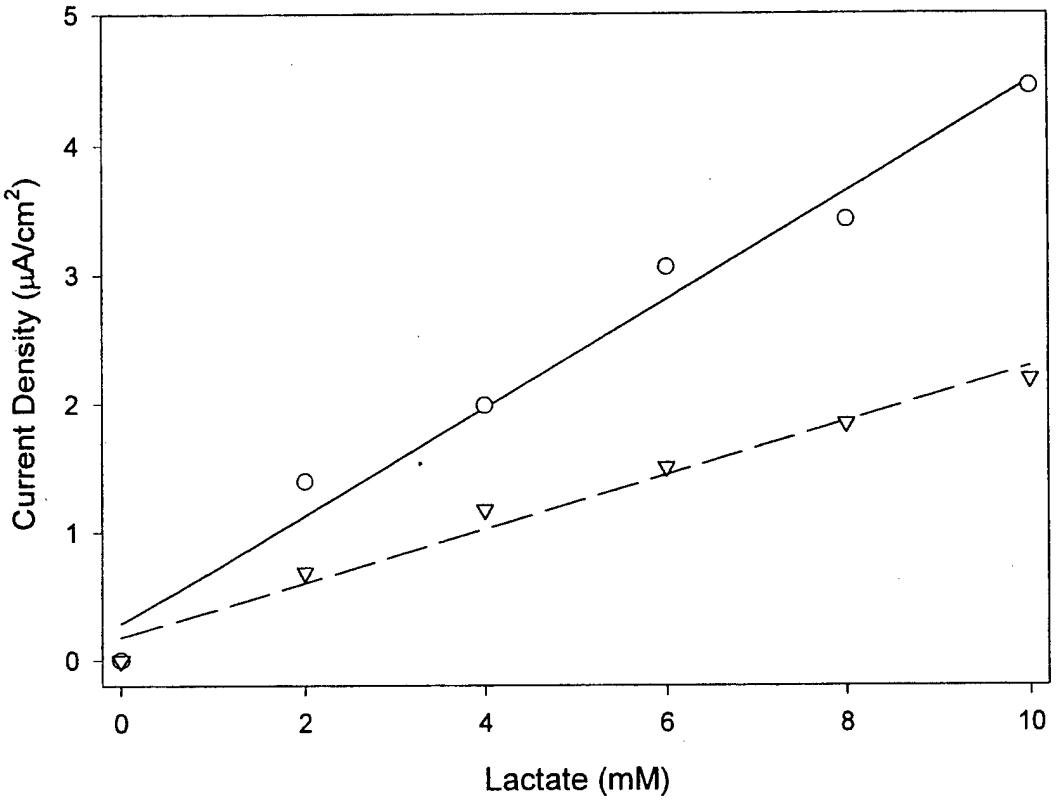

Figure 16. Subcutaneously implanted glucose sensor used to generate simulated array data for principal component analysis.

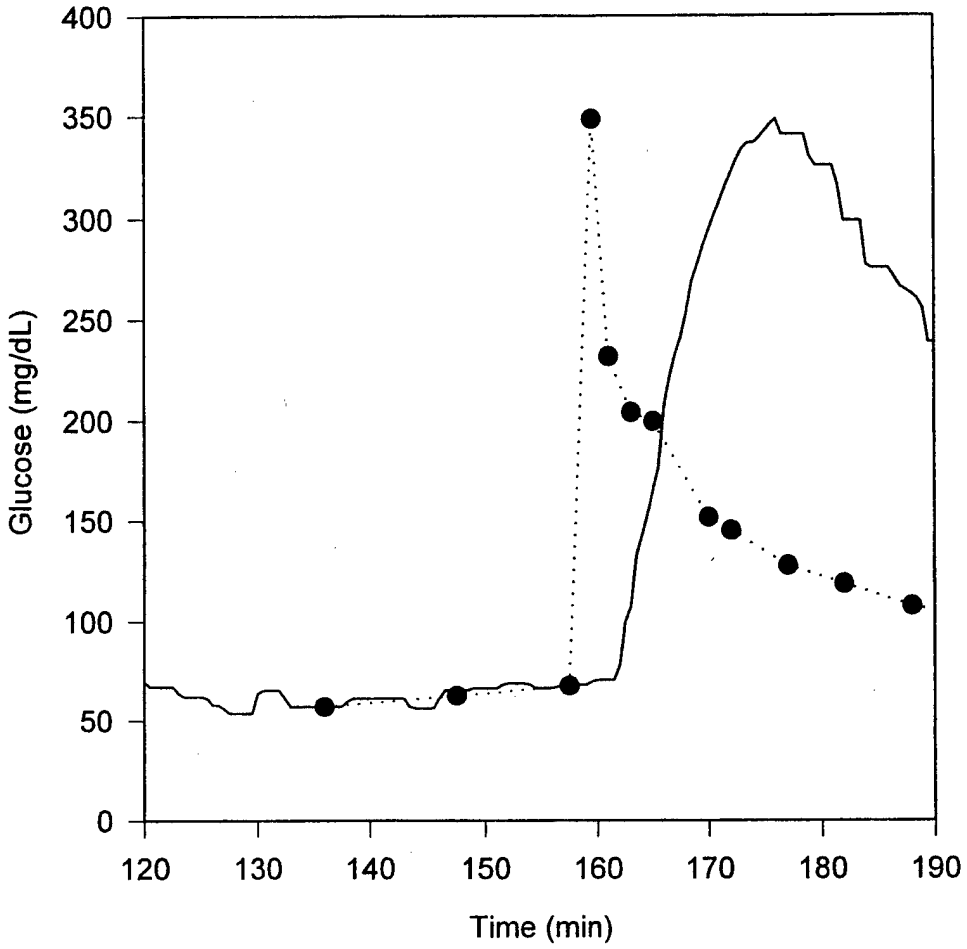

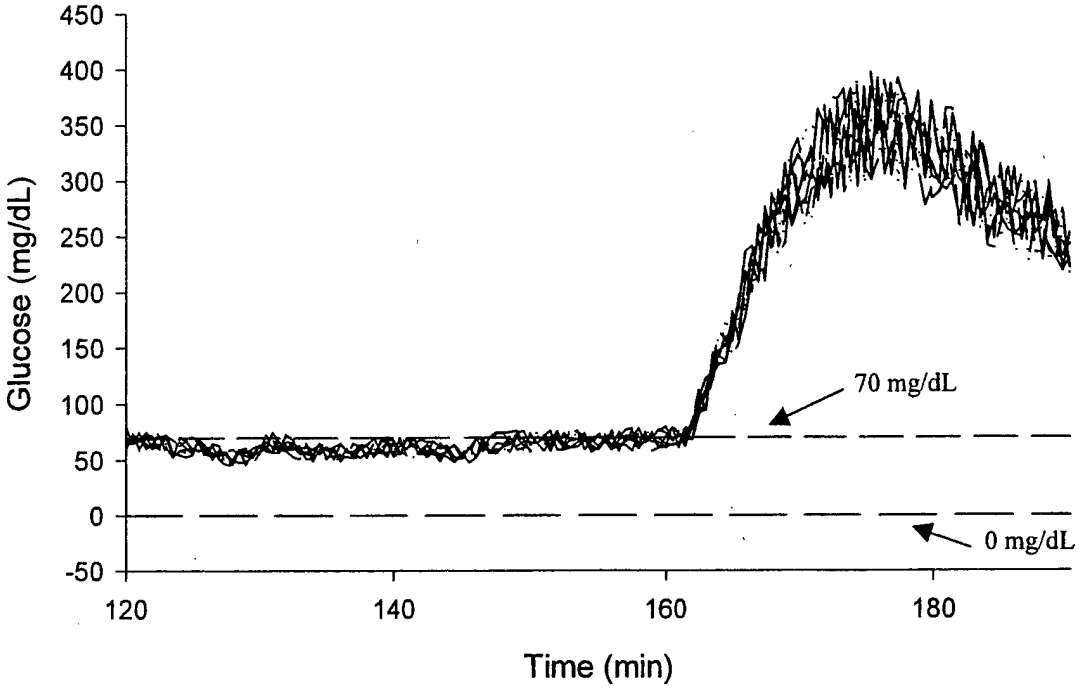

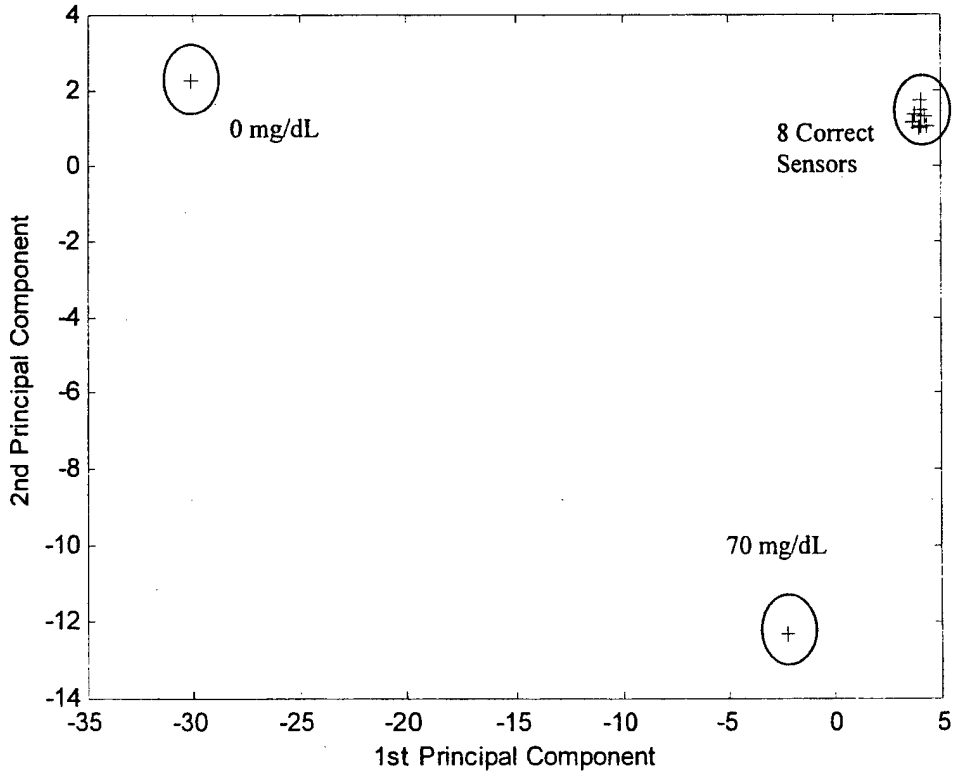

Figure 17. Fault detection in a 10 sensor array where two sensors have completely failed.

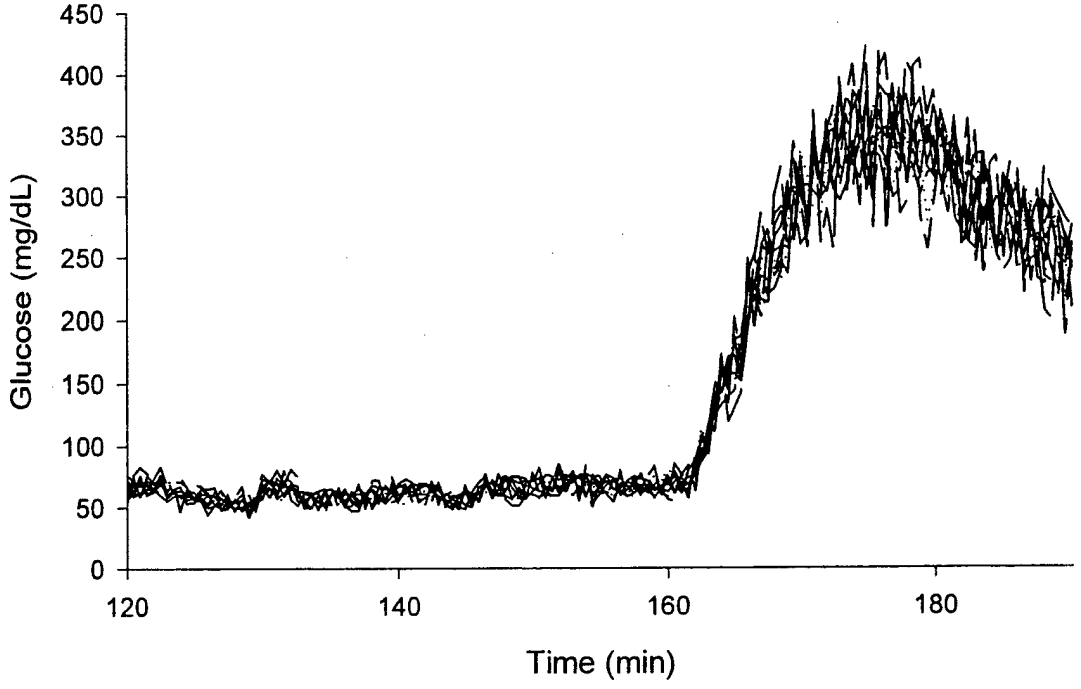

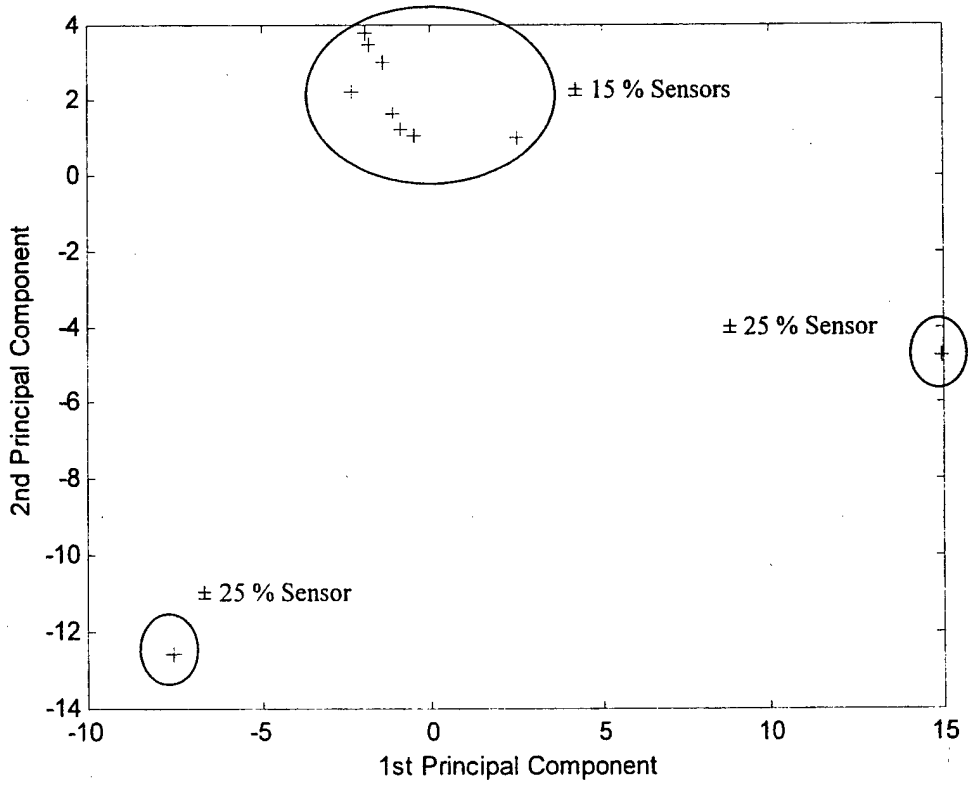

Figure 18. Fault detection in a 10 electrode sensor array where two electrodes are experiencing excessive noise.

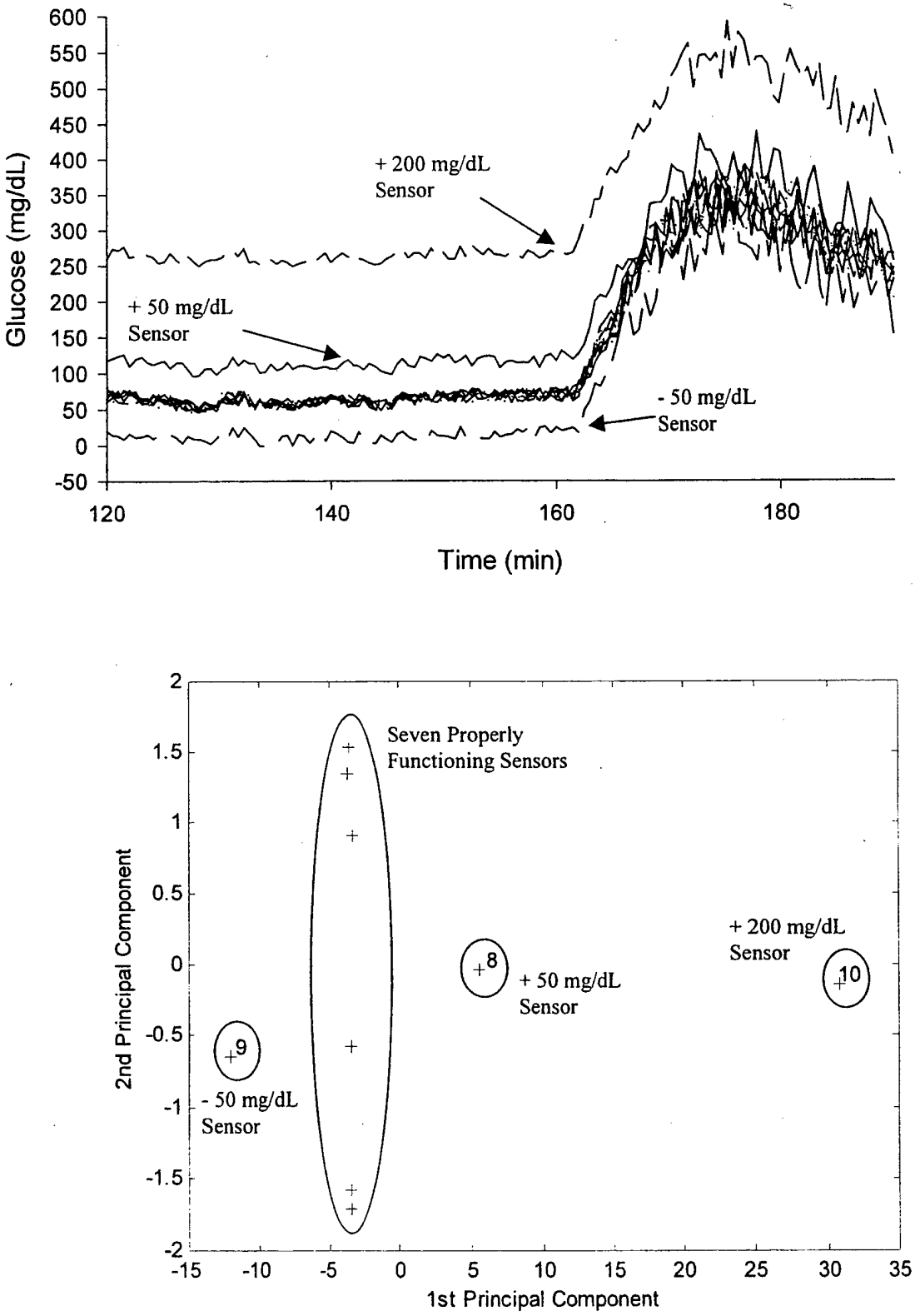

Figure 19. Fault detection in a 10 electrode sensor array where three of the electrodes are incorrectly biased.

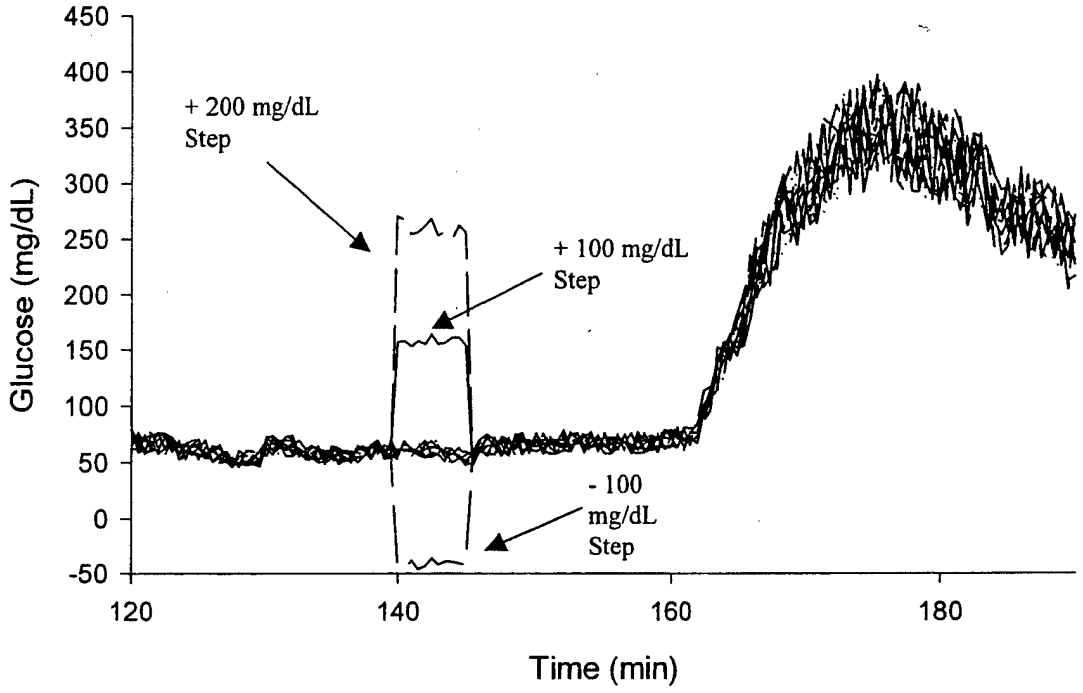

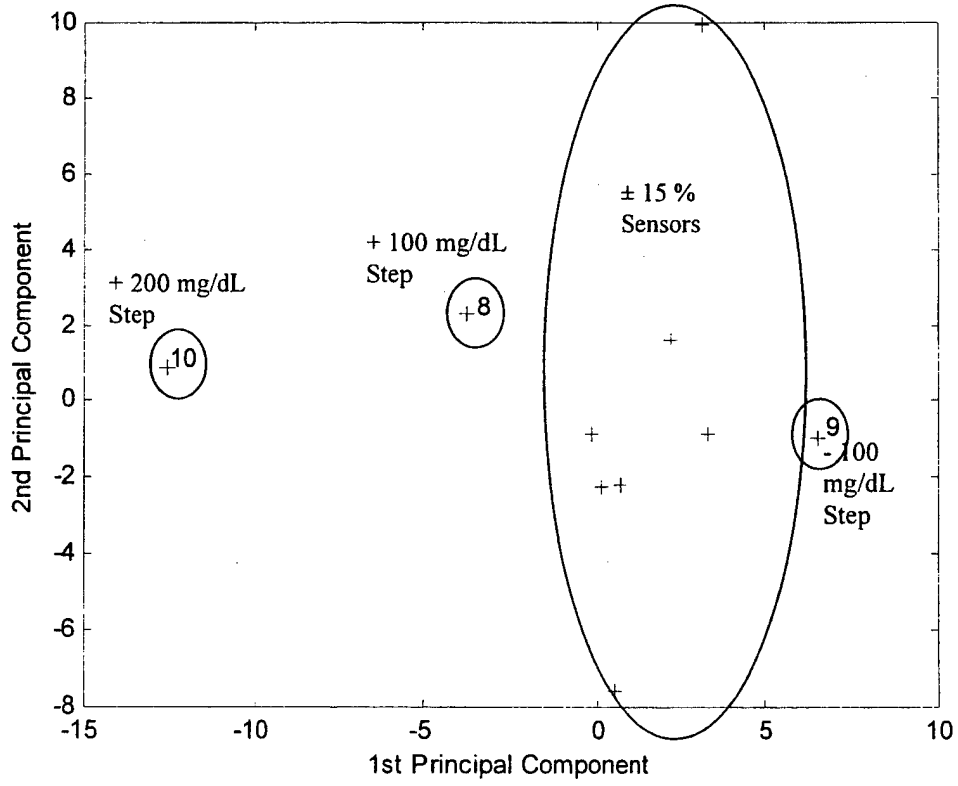

Figure 20. Fault detection in a 10 electrode sensor array where three electrodes are experiencing transient errors.

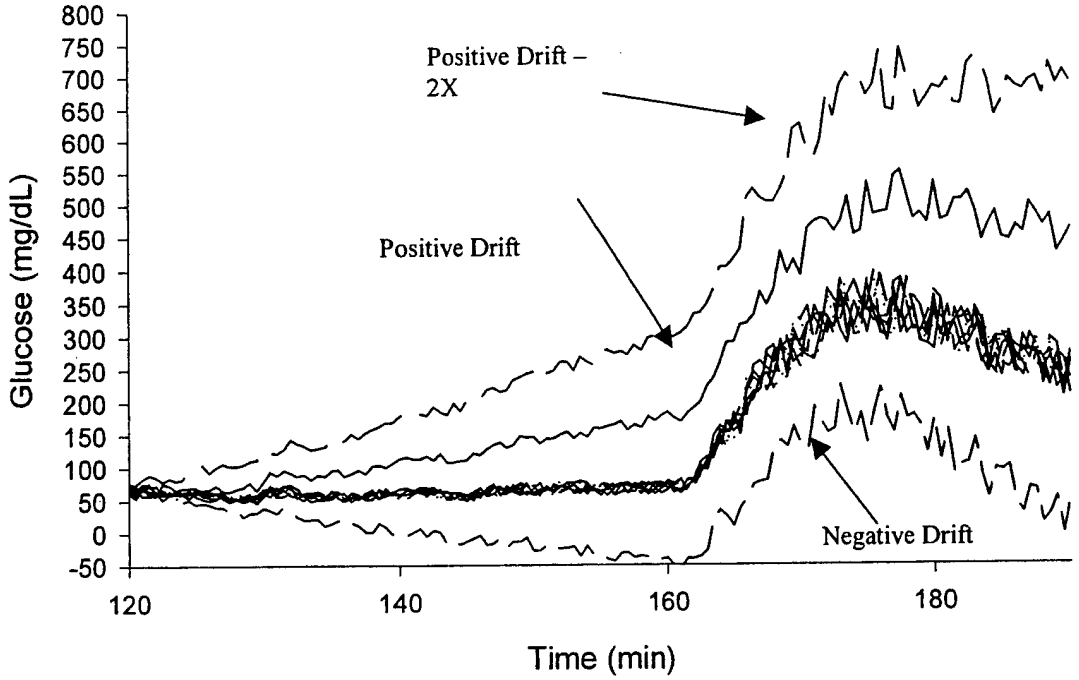

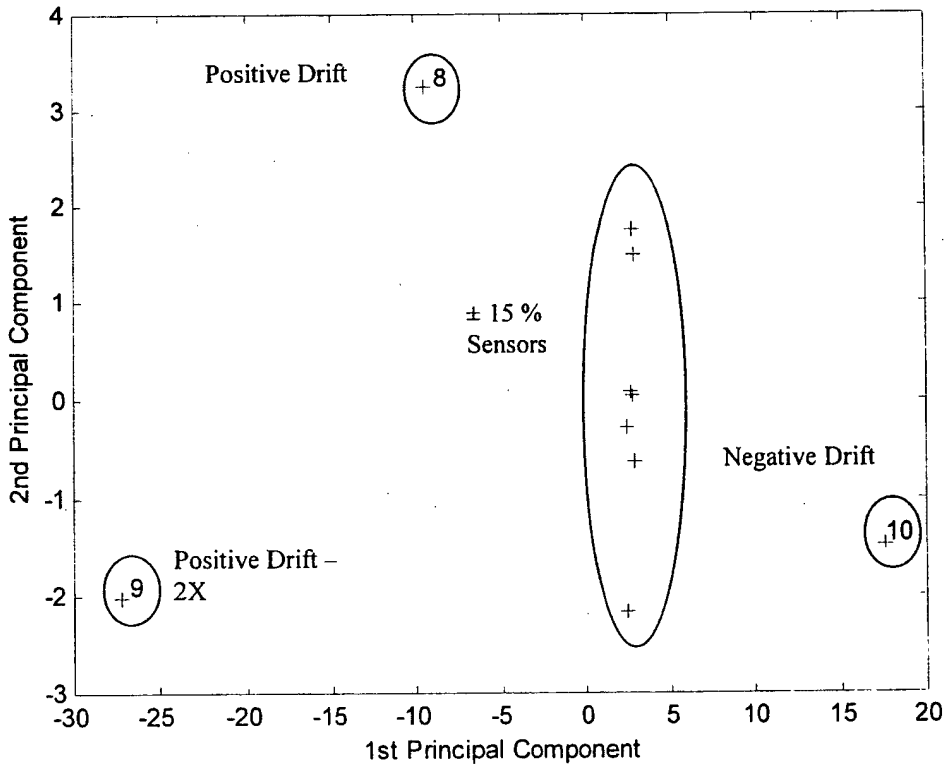

Figure 21. Fault detection in a 10 electrode sensor array where three of the electrodes are drifting.

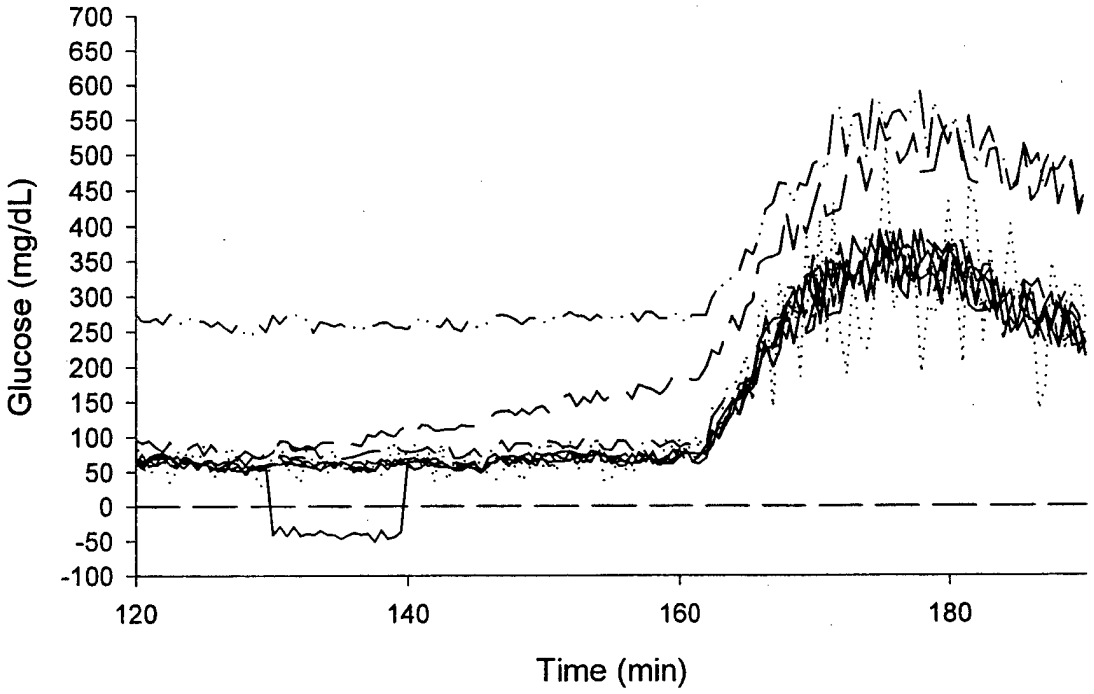

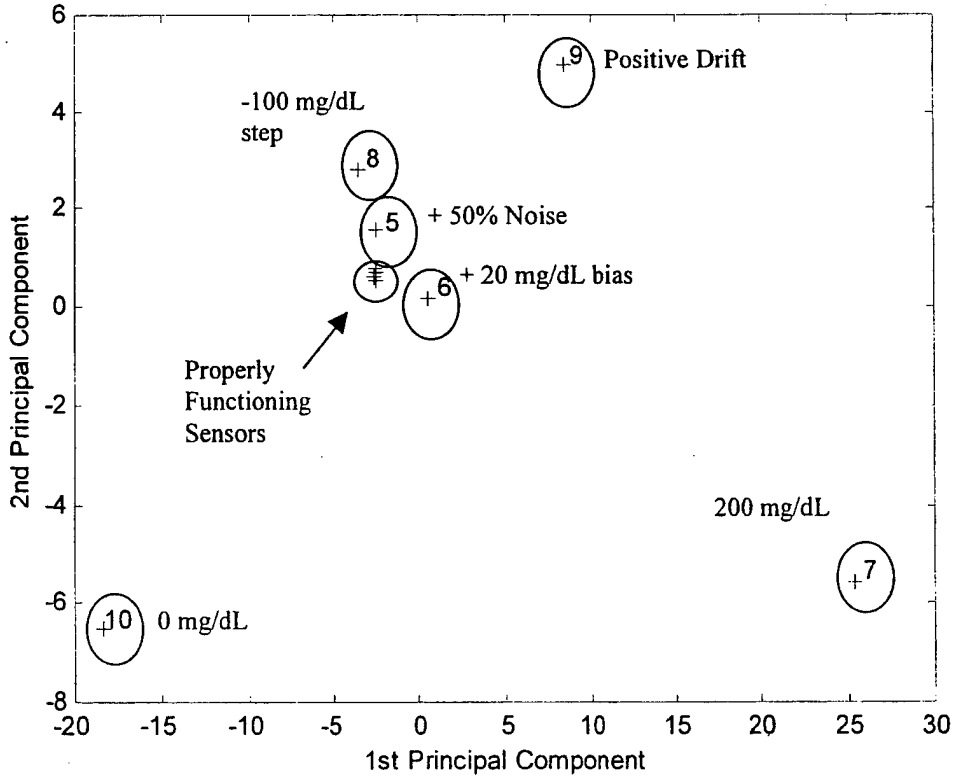

Figure 22. Fault detection in a 10 electrode array experiencing failure by multiple mechanisms.

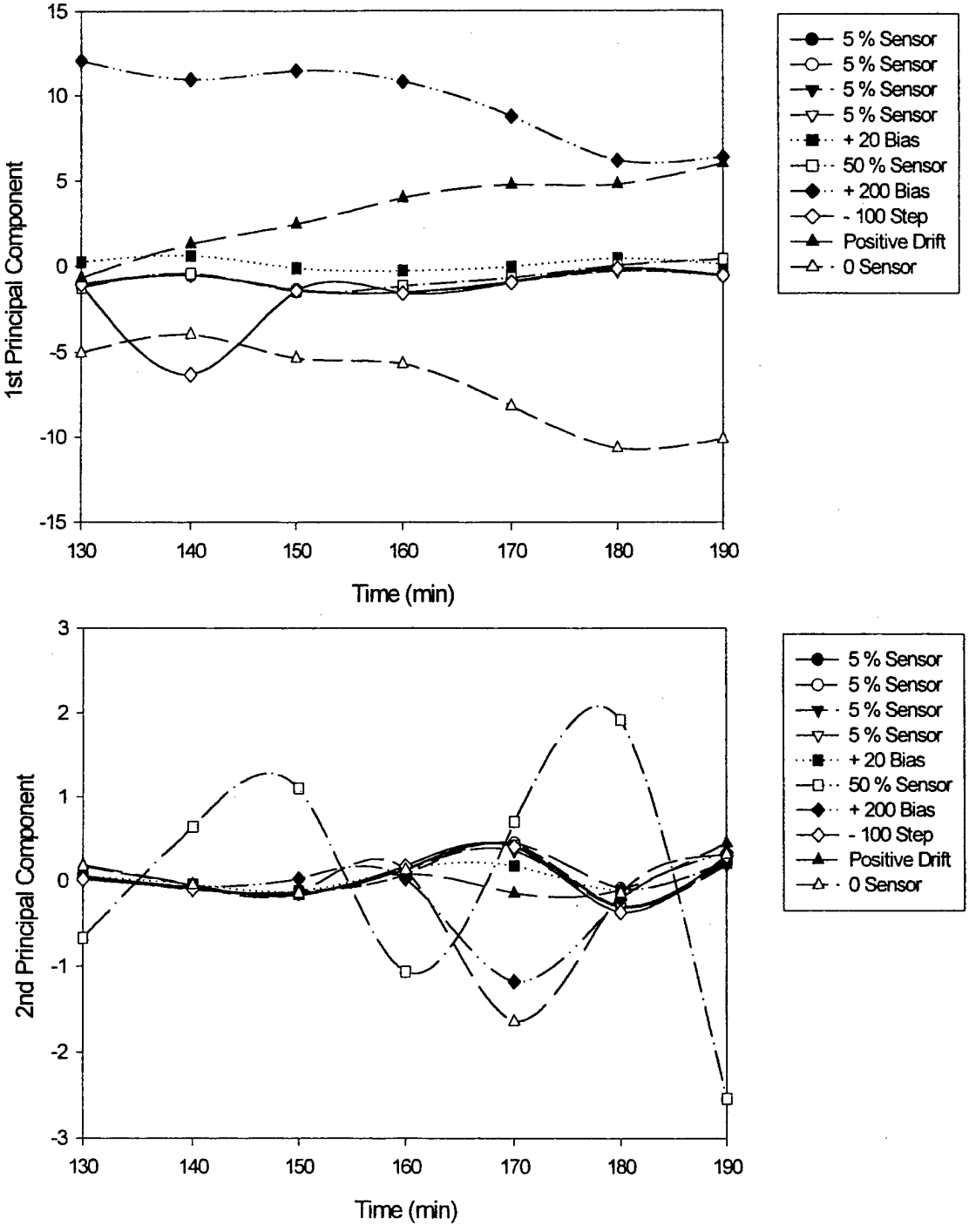

Figure 23. Fault detection and identification in a 10 electrode sensor array experiencing multiple modes of failure.

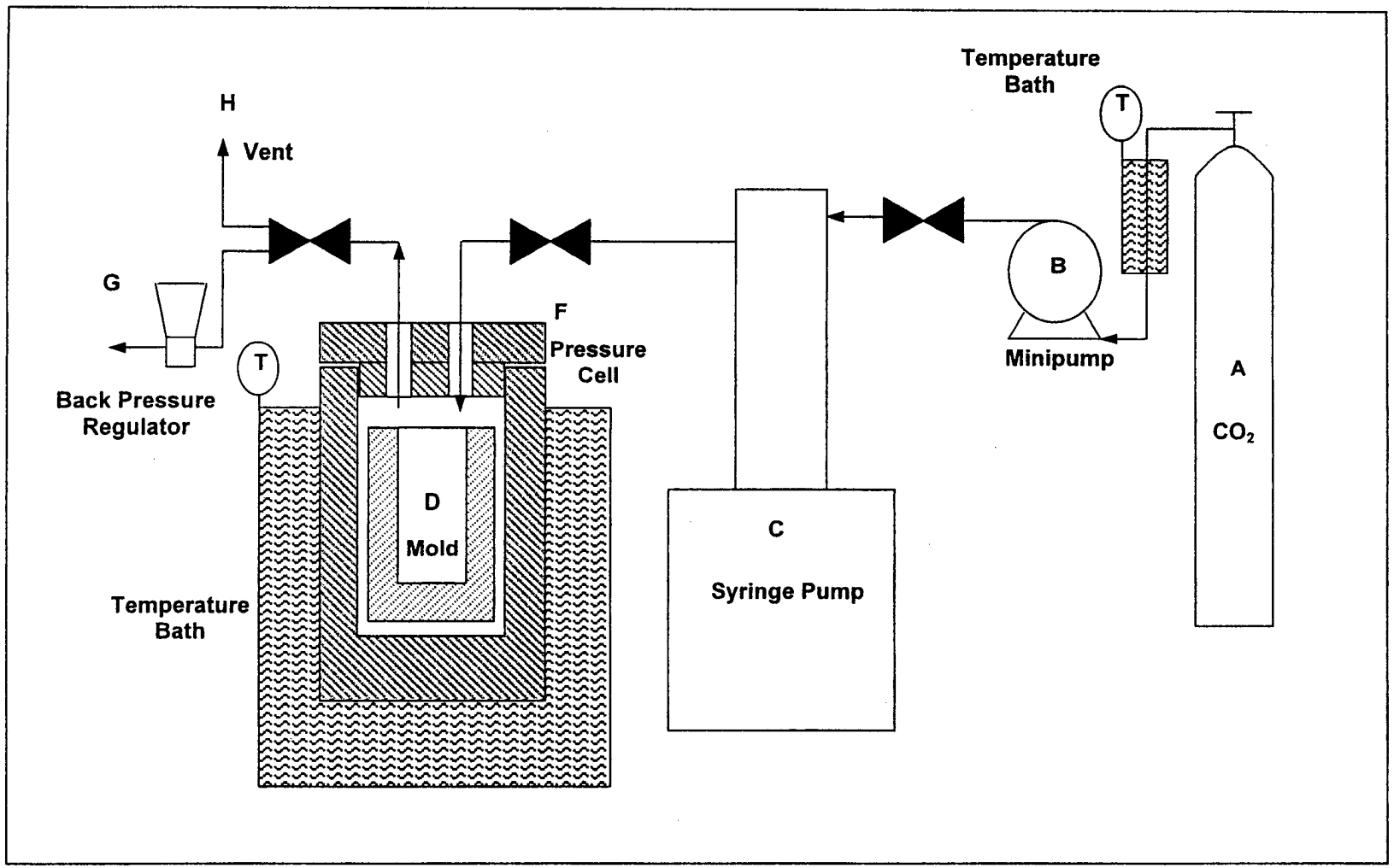

Figure 24. Schematic of super-critical carbon dioxide system of developing photolithographically patterned sensor arrays.

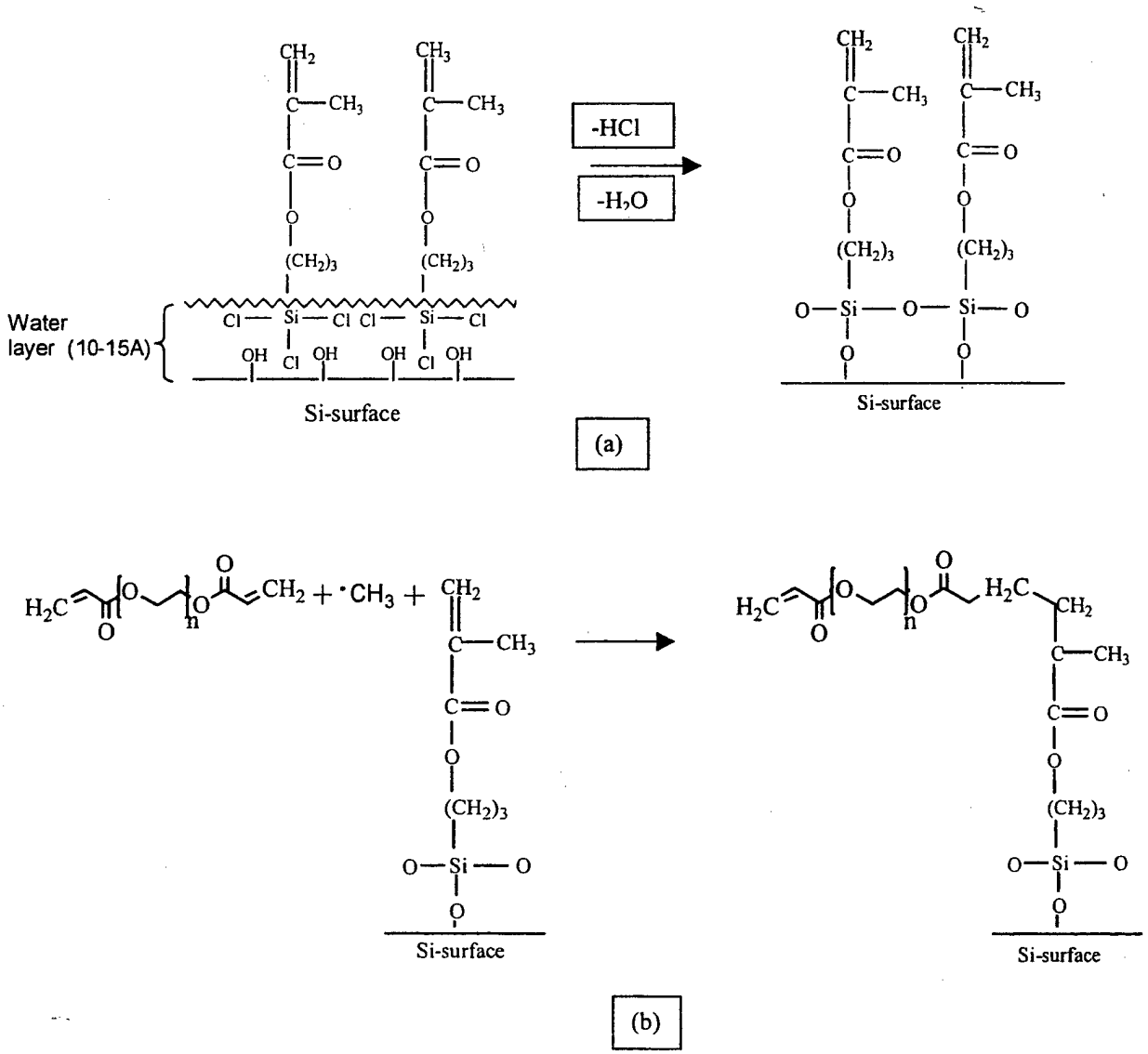

Figure 25. Surface modification of silicon substrate with a methacrylated chlorosilane and the subsequently reaction of the functionalized surface with poly(ethylene glycol) diacrylate).

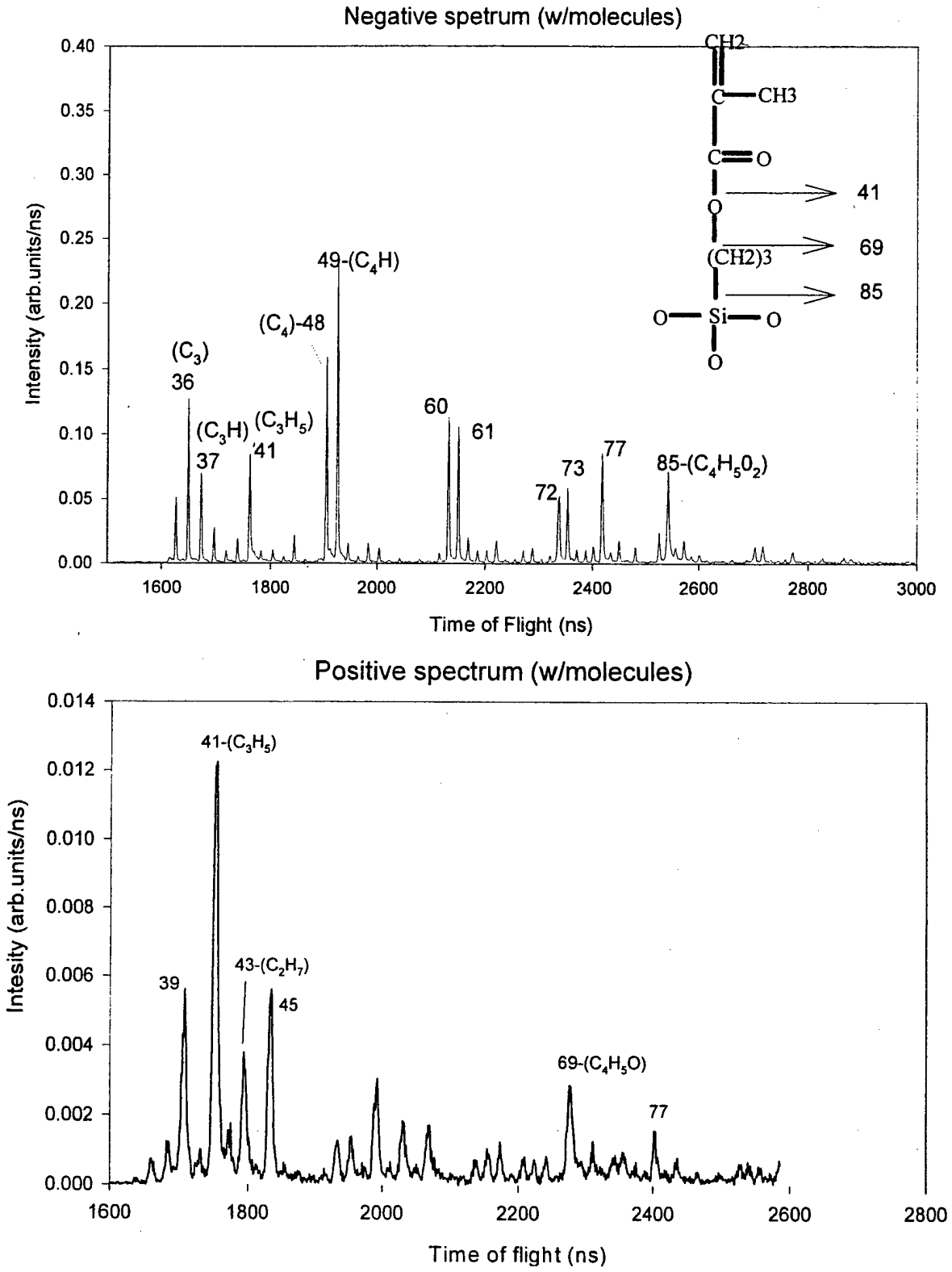

Figure 26. Time-of-flight secondary ion mass spectroscopy of a silicon surface modified with a methacrylated chlorosilane.

Figure 27. Electron micrograph of a 600 μm poly(ethylene glycol) hydrogel array.

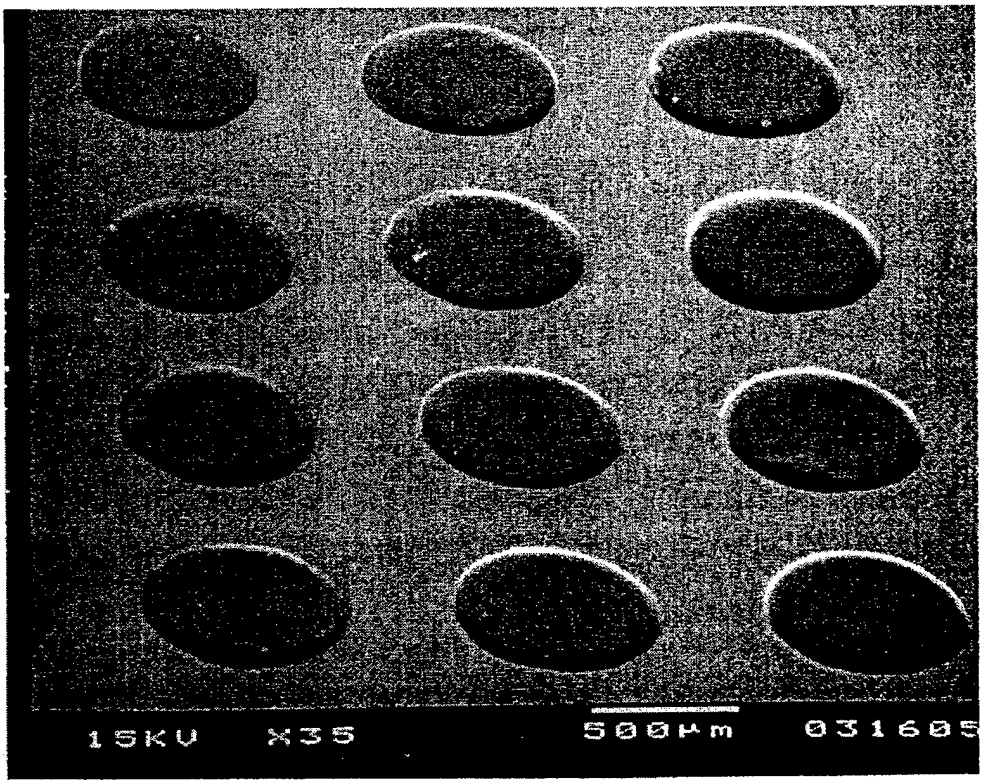

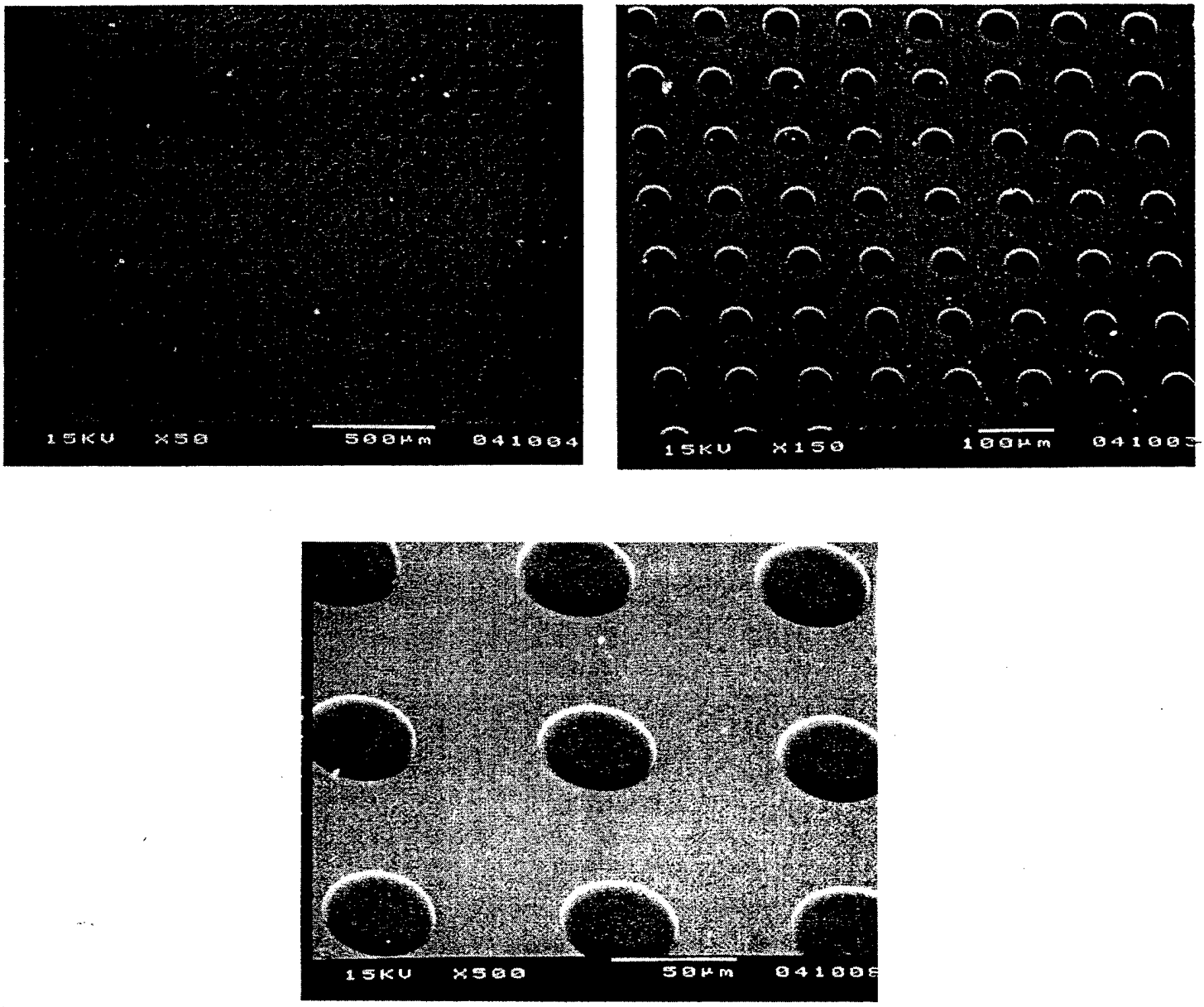

Figure 28. Electron micrographs of a 50 µm poly(ethylene glycol) hydrogel array.

Figure 29. Electron micrographs of a 5 μm poly(ethylene glycol) hydrogel array.

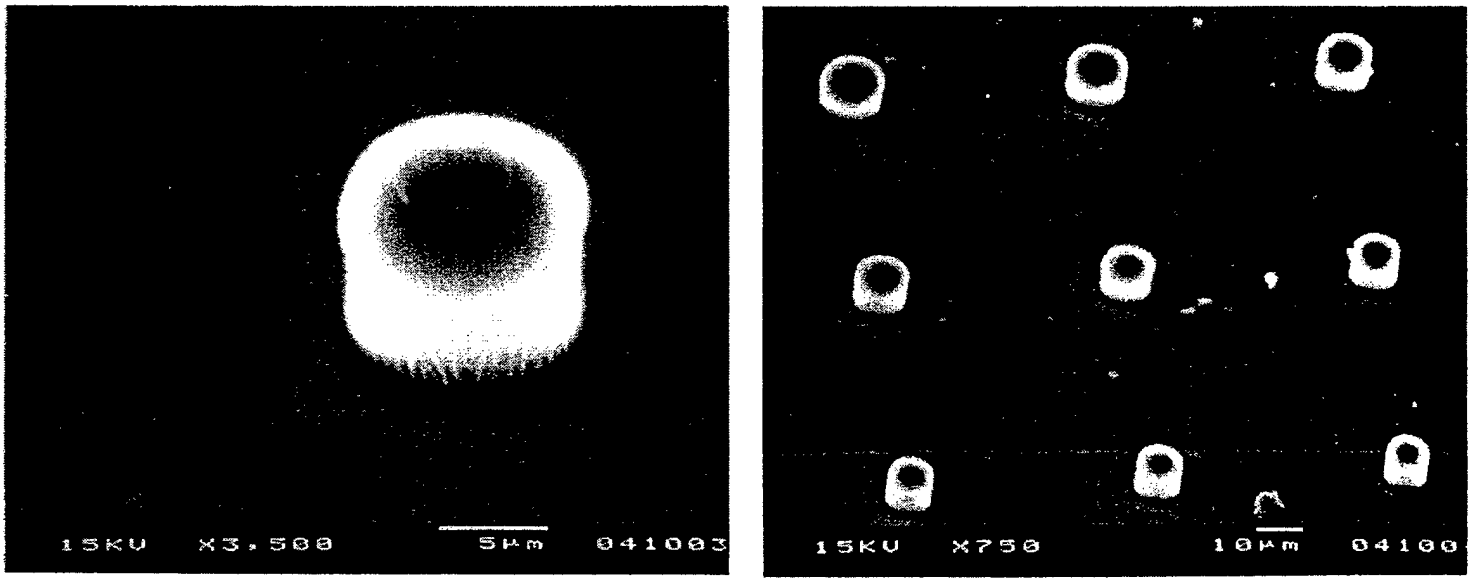

Figure 30. Electron micrograph of a patterned hydrogel of poly(ethylene glycol) fabricated using a USAF test mask.

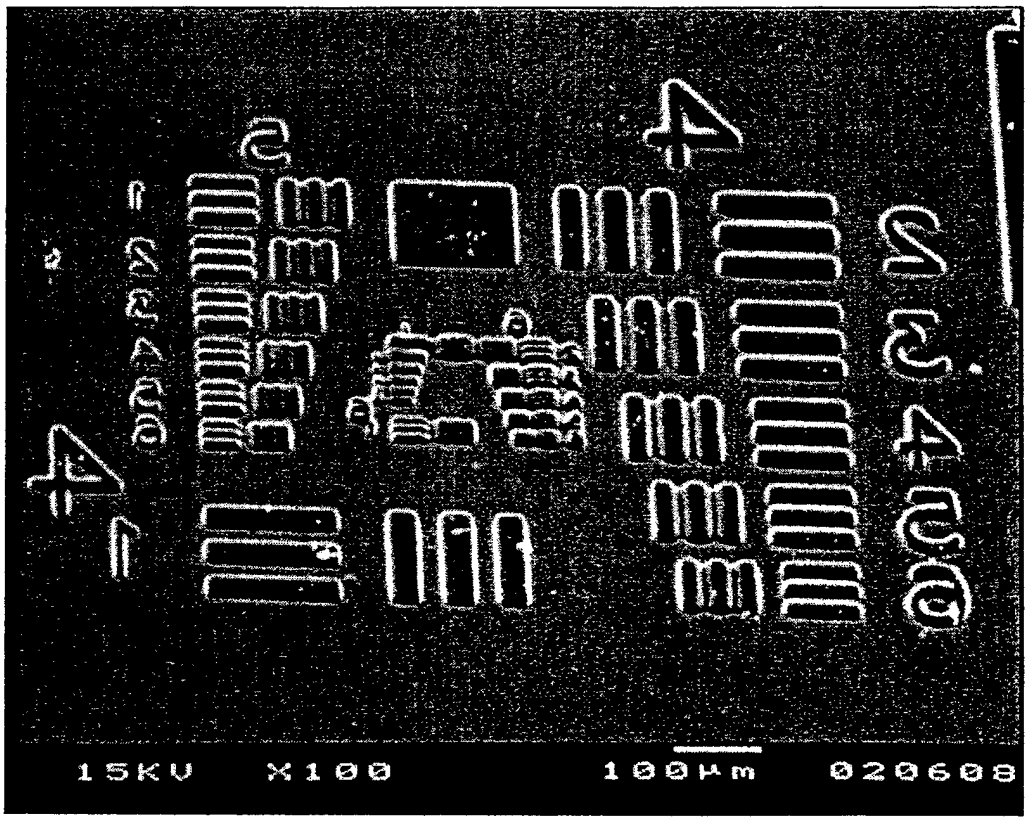

Figure 31. Electron micrograph of a poly(ethylene glycol) hydrogel array developed in super-critical carbon dioxide.

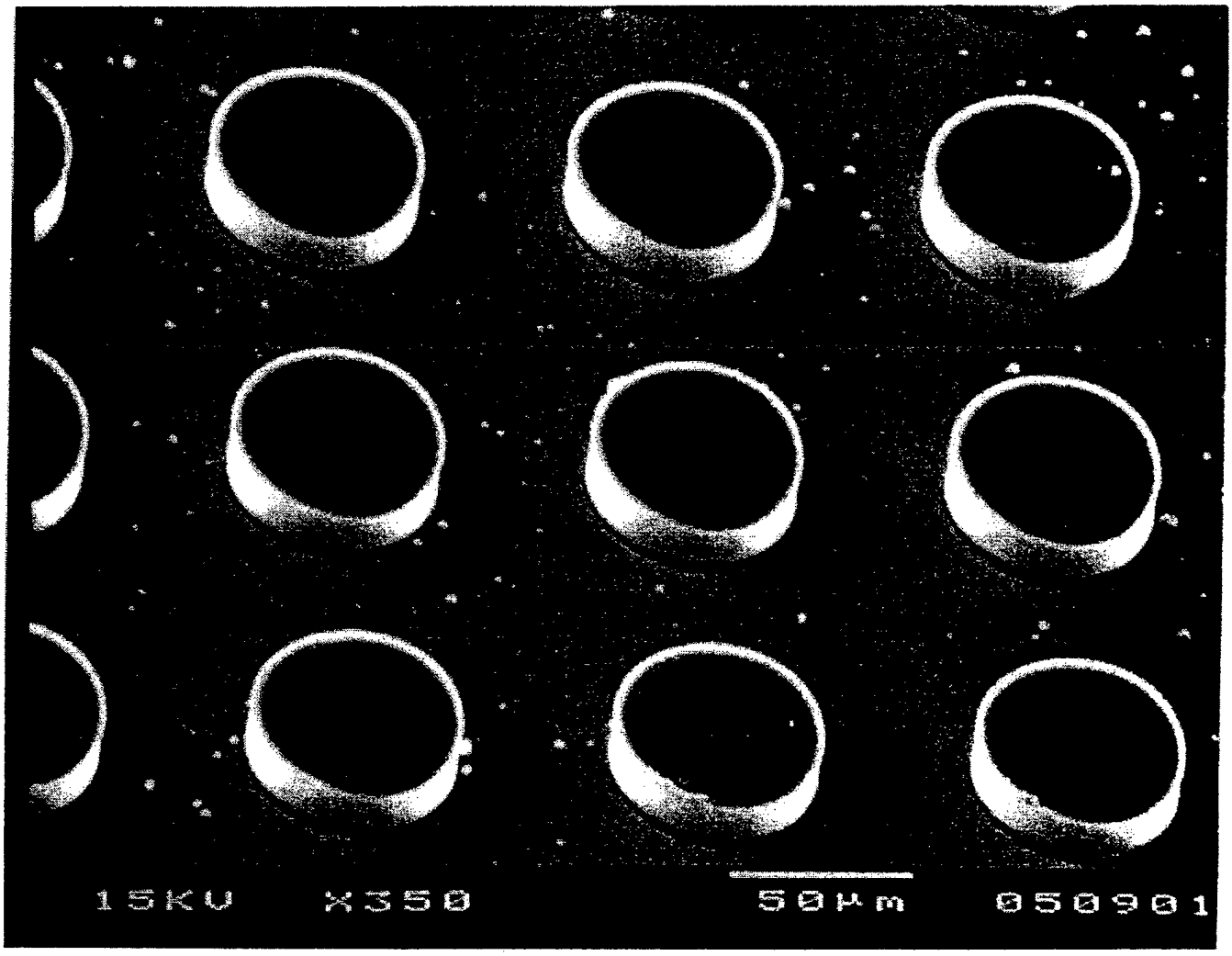

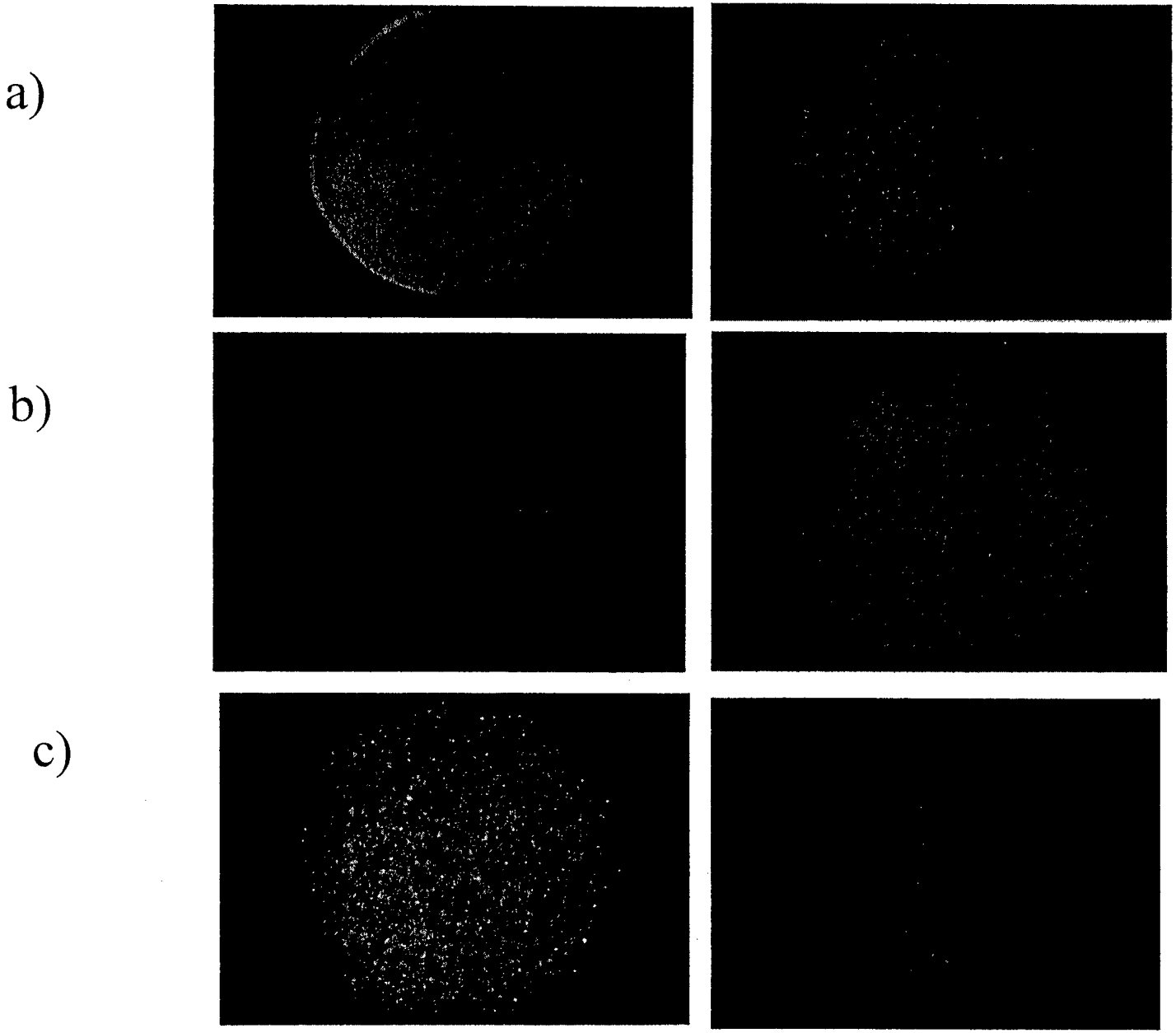

Figure 32. Fluorescent micrographs of a SNAFL-Glucose oxidase containing microfabricated hydrogel. A) gel exposed to water. B) Gel exposed to a basic solution. C) Gel exposed to an acidic solution.

Figure 33. Controlled release of active bFGF from a poly(ethylene glycol) hydrogel array. Array elements were 50 microns in diameter and 7 micron thick. bFGF activity was measured using a cell-based bioassay.

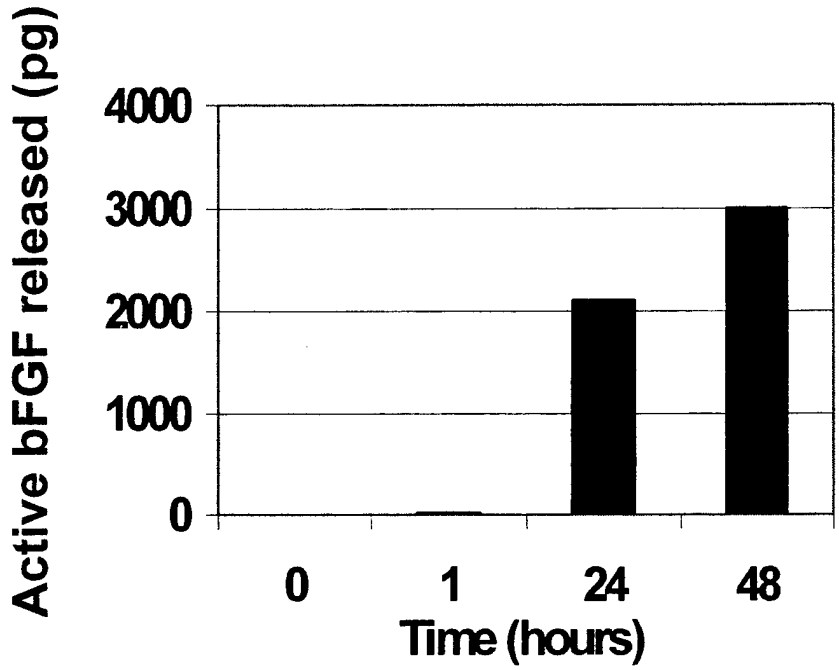

DESCRIPTION AND PERFORMANCE SITES (FORM B)

DESCRIPTION: State the goal of the research project including how it relates to improving health care for the nation's people. Use succinct language to describe how the project goals will be achieved. Do Not exceed the space provided on this page.

Absorber Assisted Laser Surgery provides a significant improvement over conventional methods used in laser surgery. In conventional laser applications the most influential factors governing the process are the optical properties (absorption and scattering coefficients) of the tissue. Unfortunately there is strong location- and subject-specific dependence on optical properties which obviates the ability to exactly predict the effect a laser irradiation dose would have on a target tissue. Furthermore, one of the key chromphores of laser energy for many medical lasers is water but the amount of water at the target tissue is highly variable. As a means to overcome this uncertainty due to optical properties we propose a techniques involving the use of a highly precise microjet device that allows deposition on the target tissue controlled minute amounts of absorber materials of known absorption property. The system will then be tested for development of laser based handpiece for application in preparation of hard dental tissues. Dr. Charles Arcoria of Baylor College of Dentistry will be a consultant collaborator. The laser may help dispel the pain, fear, and noise related to the high speed drill. The system has the potential to perform many procedures without anesthesia because of the highly localized, short duration of each laser pulse. The laser's fine control and accuracy combined with MircoFab's highly precise deposition of absorbers provides a unique combination. The non-contact treatment could decrease replacement cost and possibly reduce cross contamination from patient to patient, patient to physician, or physician to patient. The laser has potential to remove dental hard more accurately and without the negative stimuli associated with conventional dental handpiece.

PROJECT SITE(s) (*Organization, City, State*):

Texas A&M University
Texas Engineering Experiment Station
College Station, Texas

COPY

Technical Progress Report
October 1999

SPONSOR: National Medical Technology Testbed
TITLE: Absorber Assisted Laser Ablation of Hard Dental Tissue using Precise Microjet Technology
PI: Sohi Rastegar

Texas A&M University, Texas Engineering Experiment Station, 301 WERC, College Station, TX 77843

I. Task Objectives:

The specific objectives of this one-year research project were modified from the Specific Aims 2 and 3 of the original proposal as modified by our later dated 12 November 1998.

Specific Aim #1: To determine optimal parameters for efficient ablation of enamel and dentin using Er:YAG Laser and water as absorber.

Specific Aim #2: To determine quality of laser-absorber prepared cavities as compared to conventional handpiece using microleakage study.

II. Description of Results to Date

Majority of effort for the first phase of the project was focused on Specific Aim #1 and preparing for performance of Aim #2.

Specific Aim #1: To determine optimal parameters for efficient ablation of enamel and dentin using Er:YAG Laser and water as absorber.

Over these first 5 months the ablation rate for samples of enamel of two different thickness values were measured for varying number of water volumes between laser pulses. Each water pulse was 200 pico-liters. The results are shown in Figures 1 and 2. Note that in both samples there is an optimal number of water pulses. For the 1-mm thick samples the optimal was 10 water pulses and for the thicker sample (2.3 mm thick) the optimal water volume was 20 water pulses (or 4 nano-liters). This suggests that for removing a larger volume of tooth a relatively larger volume of water should be used but that there is an optimal water volume to consider. One explanation is that as the water volume is increased beyond a certain point more of the energy would be consumed in vaporizing the water rather than inducing a recoil momentum on the tooth.

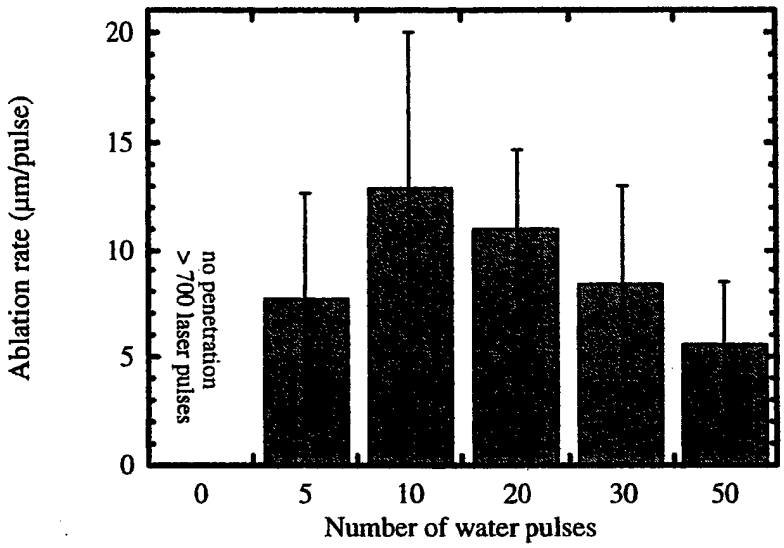

Figure 1. Ablation rate versus number of water pulses on enamel. The volume of one water pulse was 200 pl. The thickness of the slice was 1 mm. The energy of laser was 48 mJ.

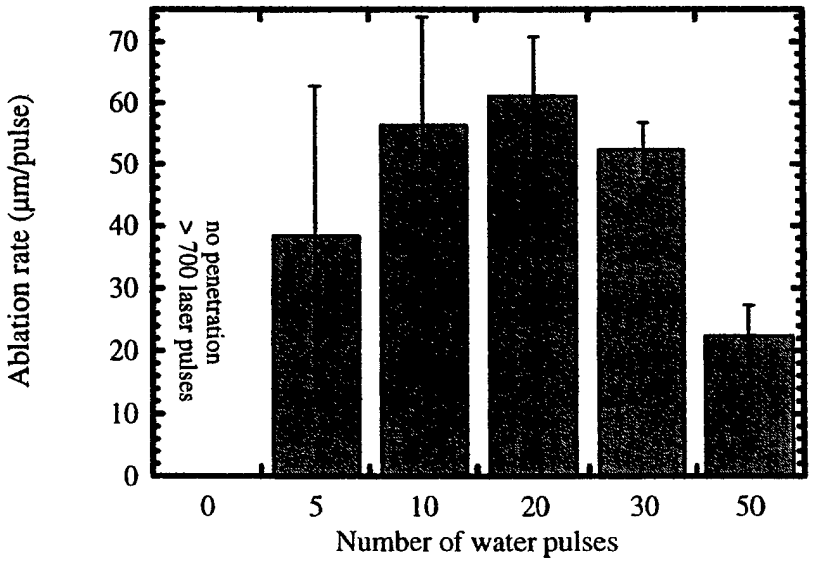

Figure 2. Ablation rate versus number of water pulses on enamel. The volume of one water pulse was 200 pl. The thickness of the slice was 2.3 mm. The energy of laser was 145 mJ.

A typical Scanning Electron Micrograph (SEM) of laser induced hole in enamel is shown in Figure 3. The inner surface of the ablated enamel appeared to have raised and rolled. A small bead-like recrystalized enamel was more common on the wall of the crater at lower laser energy. However, the recrystalized enamel was more visible on the surface and at the entrance of the hole at higher energy. At higher energy, it is believed that the molten enamel was more strongly expelled out of the hole and then recrystalized. Similar studies will be done on dentin and results will be reported in the next phase.

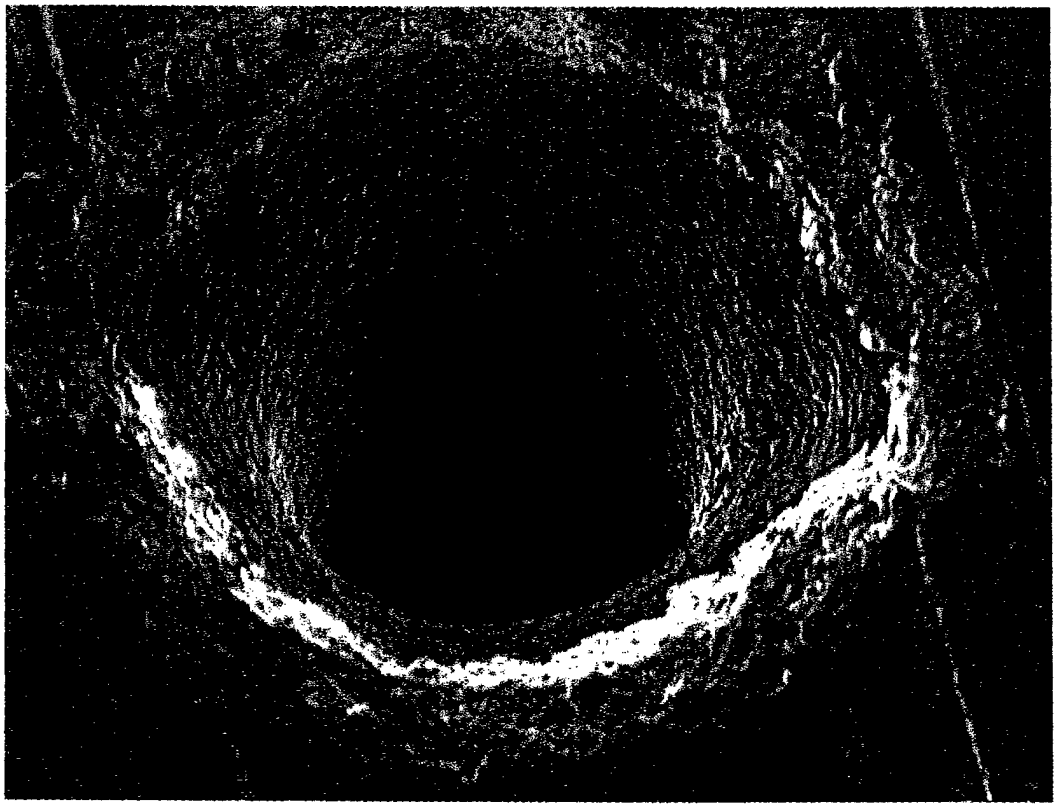

Figure 3. Scanning Electron Micrograph (SEM) of tooth ablated by water-assisted Er:YAG laser method using microjet technology.

The temperature rise in the pulp cavity caused by repeatedly irradiated laser pulses and exogenous water drops on the whole tooth surface is shown in Fig. 4. The temperature rise in the pulp cavity with and without an exogenous water drop was 1.6°C and 4°C respectively. From this result it is clear that a repeatedly dispensed water drop, even with a small volume, could significantly lower the temperature rise in the pulp cavity to a safe level.

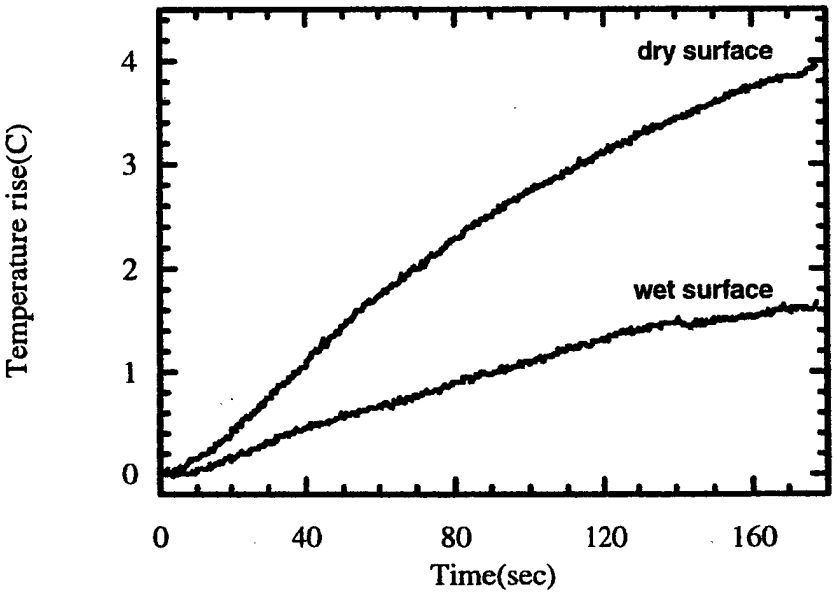

Figure 4. Temperature rise in the pulp cavity during laser irradiation with and without an exogenous water jet. The volume of one water drop was 400 pl. Water was dispensed every two seconds. The laser was irradiated every second with 100 J/cm^2 rate.

Based on the early positive results, we are prepared to work of Aim # 2 to characterize the quality of cavity preparations in laser prepared cavities.

Specific Aim #2: To determine quality of laser-absorber prepared cavities as compared to conventional handpiece using microleakage study.

Experimental protocol has been designed. Ten teeth will be used for this study. On the same tooth both conventional handpiece cavities preparations as well as laser induced ones will be applied. Each tooth will be subjected to thermal cycles described in the proposal and microleakage study will be performed to assess the quality of preparations.

Characterization of Birefringence in a Rabbit Cornea

Bhavana Satheesan (bhavana@tamu.edu), Gerard L. Coté
Biomedical Engineering Program, Texas A&M University, College Station, TX.

***Abstract*-The aim of this project is to develop an optical system to characterize the variations in corneal birefringence in a rabbit model, both qualitatively and quantitatively, via the use of Mueller matrix theory. The system was characterized with a known birefriagent material, namely a ¼ wave plate, followed by *in vitro* studies on an excised rabbit eye.**

Keywords: birefringence, cornea, glucose sensing, polarimetry.

I. INTRODUCTION

The anterior chamber of the eye is the principle site under investigation for the development of a noninvasive *in vivo* optical polarimetric glucose sensor [1,2]. However, it is well known that the cornea of the eye is birefringent and the birefringence is negligible at the center and increases towards the periphery [1]. Even small amounts of birefringence are known to confound the overall signal due to glucose in the anterior chamber of the eye and hence the sensitivity of the system. This is of particular concern when the light beam is to be propagated through the base of the cornea [1]. Thus, a detailed qualitative and quantitative characterization of the corneal birefringence is essential for the development of the noninvasive glucose sensor.

II. METHODS

The optical setup used to characterize birefringence is shown in Fig 1. The light source consists of a uniform intensity beam obtained from a tungsten halogen lamp whose intensity is reduced via a neutral density filter. Various input polarization states are obtained through different orientations of polarization optics which consist of a sheet polarizer and ¼ wave plate. This beam is then directed onto a sample. After passing through the sample, the beam is imaged through polarization analyzer optics (similar to the input stage) using a 16-bit CCD camera.

Two sets of experiments were performed using this setup. The first set of experiments utilized a ¼ wave plate with its fast axis at 0° and 45°, respectively. The second set of experiments were conducted on a excised rabbit eye. The eye was placed on a specially made mount, with care being taken to ensure that the cornea was completely covered with saline solution. This was done in order to overcome the index of refraction mismatch between the cornea and air, thus allowing the light beam to be propagated straight through the anterior chamber [3].

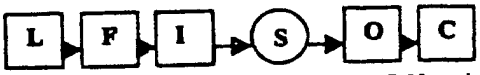

Fig 1: Optical Setup .L: Tungsten Halogen lamp, F: Neutral density filter, I: Input Polarizer and ¼ wave plate, S: sample, O: output polarizer and ¼ wave plate, C: CCD camera

III. RESULTS

In the first experiment, in order to verify the operation of the experimental system, two different alignments (fast axis +45° and 0°) of a ¼ wave plate sample were investigated. The change in intensity of the output beam, for the crossed input and output polarization state for each orientation of the sample was calculated theoretically and subtracted resulting in a normalized value of 0.25. This is equivalent to the change in the intensity obtained experimentally. Further, a single Mueller element (S_{23}) was calculated for the sample ¼ wave plate with its fast axis at +45°(Fig 2). This was compared and shown to be similar to the theoretical Mueller element.

Fig 2. Comparison between the theoretical and experimental S_{23}=[(hh+vv)-(hv+vh)] element of the Mueller matrix for a ¼ plate at 45 degrees.

In the final experiment, images were obtained of a rabbit cornea for the case of no polarization optics and compared with the image for the crossed polarization state. As expected, the image for the crossed state showed varying intensity (birefringence) along the edges of the cornea and almost zero intensity at the apex (Fig 3).

Fig 3: Images of the rabbit cornea obtained for the 'Open' state and 'Crossed' state of polarizers.

IV. DISCUSSION AND CONCLUSION

An optical polarization setup for monitoring the birefringence of a sample was built and tested. The system was first calibrated with a known birefringent material (1/4 wave plate) and compared to the theoretical output expected from this element showing a good correlation of image intensities. Lastly the change in birefringence across the rabbit cornea was observed and compared to the case with no polarizers. The image was found to have higher intensities at the edges, as expected, thus indicating increased birefringence.

ACKNOWLEDGEMENTS

We are grateful to the National Medical Technology Testbed (NMTB) for the funding of this project.

REFERENCES

[1] B.D. Cameron et. al.,."The use of Polarized Laser Light Through the Eye for Noninvasive Glucose Monitoring", *Diabetes Technology & Therapeutics*, vol.1, no. 2, 1999.

[2] C. Chou et. al., "Noninvasive glucose monitoring in vivo with an optical heterodyne polarimeter", *Applied Optics* , vol. 37, pp. 3553-3557, 1998.

[3] B.D Cameron et. al.," Measurement and Calculation of the two-dimensional back scattering Mueller matrix of a turbid medium", *Optics Letters*, vol. 23, no.7, pp. 485-487, 1998.

JUN 19 2000

No. 41
Texas Engineering/Cote

Investigation of pH and Temperature on Optical Rotatory Dispersion for Glucose Monitoring

Justin S. Baba and Gerard L. Coté

Biomedical Engineering Program, Texas A&M University, College Station, TX 77840-3120

ABSTRACT

The application of optical polarimetry, using the anterior chamber of the eye as the sensing site, is being investigated as a potential method to develop a noninvasive physiological glucose monitor. One mechanism proposed for removing the rotation in our system due to the optically rotatory elements other than glucose (albumin, ascorbic acid, etc.) in the anterior chamber is to use a multi-wavelength polarimetric approach commonly referred to as optical rotatory dispersion. In our efforts to obtain the wavelengths of interest for characterizing glucose in the presence of other components in the aqueous humor that rotate light, we present results characterizing the optical rotatory dispersion as a function of the pH and temperature. In addition, we present *in vivo* results using New Zealand White rabbits that indicate the average time delay between blood and aqueous humor glucose levels is below five minutes and we discuss the main issue that needs to be overcome for the measurement of glucose with this approach, namely corneal birefringence in the presence of motion artifact.

Acknowledgement & Disclaimer:
This work was supported by a grant from the National Medical Technology Testbed (NMTB): a subcontract under the U.S. Army Medical Research Acquisition Activity (Grant No. DAMD17-97-2-7016). The view, opinions and/or findings contained in this report are those of the authors and should not be construed as a position, policy, decision or endorsement of the federal Government or the National Medical Technology Testbed, Inc.

Keywords: polarimetry, glucose, diabetes, optical rotatory dispersion

Development of an Optical Polarimeter for *in vivo* Glucose Monitoring

Brent D. Cameron, Harshal Gorde, and Gerard L. Coté

Biomedical Engineering Program, Texas A&M University, College Station, TX 77840-3120

ABSTRACT

In our investigation, we present both multi-spectral *in vitro* and preliminary single wavelength *in vivo* results supporting the use of optical polarimetry as a potential non-invasive method for glucose sensing. The site utilized for our *in vivo* measurements is the anterior chamber of the eye in a rabbit model. The anterior chamber of the eye contains a relatively clear and minimal scattering fluid known as the aqueous humor. The glucose levels of the aqueous humor are correlated to those of blood, therefore providing a mechanism to indirectly estimate blood glucose levels. A device to effectively couple light through the anterior chamber is also presented. As for the *in vitro* experiments, a multi-spectral approach is demonstrated as a method to minimize prediction error when glucose is not the only optically active component that varies in concentration.

Keywords: polarimetry, glucose sensing, diabetes mellitus, multi-spectral, optical activity

1. INTRODUCTION

A method to non-invasively monitor glucose levels within the body would have a significant impact on millions of diabetic patients worldwide. Currently, all commercially available techniques require the invasive extraction of blood or other bodily fluids for glucose analysis. Thus, diabetic patients often have to extract multiple samples of blood daily, which is usually obtained by the lancing of a finger. This procedure requires the use of relatively expensive enzymatic test reagents, in addition to, subjecting the user to possible infection risks and nerve damage at the testing site. Therefore, recently, several optical approaches have been proposed as possible mechanisms to overcome the invasiveness of current monitoring techniques.[1-15] In our investigation, we utilize a polarimetric approach that incorporates a Faraday rotation of linear polarized light for both modulation and closed-loop feedback.[10-13]

Chiral molecules, such as glucose, are known as optically active. The asymmetrical structural plane of a chiral molecule results in the rotation of linear polarized light. The amount of observed rotation is directly proportional to the specific rotation, optical path length, and concentration of the sample. The specific rotation of a compound describes the extent to which it can rotate linearly polarized light. This quantity itself is a function of wavelength, pH, and temperature. If the path length, pH, and temperature of a sample remains constant and the amount of rotation of a linearly polarized light beam is measured after it propagates through the sample, the concentration of the optically active compound can be estimated. The device used to measure this rotation is known as a polarimeter.

In order for polarimetry to be used as a potential non-invasive method for blood glucose monitoring, the polarized light beam must propagate through the test medium without total depolarization of the beam. Since the majority of available *in vivo* test sites possess high scattering coefficients (i.e. skin/blood), a polarized light beam passing through a path length of suitable size (approximately 1 cm)[13] would result in almost complete depolarization of the test beam. However, an alternative test site exists that has a relatively low scattering coefficient, suitable path length, and glucose levels proportional to those of blood. This site is the anterior chamber of the eye that contains a relatively clear and minimal scattering fluid known as the aqueous humor. Therefore, this is testing site we chose for our *in vivo* studies.

The use of the eye as a potential sensing site for optical polarimetry to monitor glucose levels in the body was initially described by March et. al..[1,2] In their study, it was shown that glucose levels in the aqueous humor were correlated to those in blood with a slight time delay (on the order of minutes) in a rabbit model. Coté et. al. later developed an open loop phase based method that was able to achieve millidegree rotational sensitivity.[8] This work was followed by King et. al., who

Part of the SPIE Conference on Optical Diagnostics of Biological Fluids IV
San Jose, California • January 1999
SPIE Vol. 3599 • 0277-786X/99/$10.00

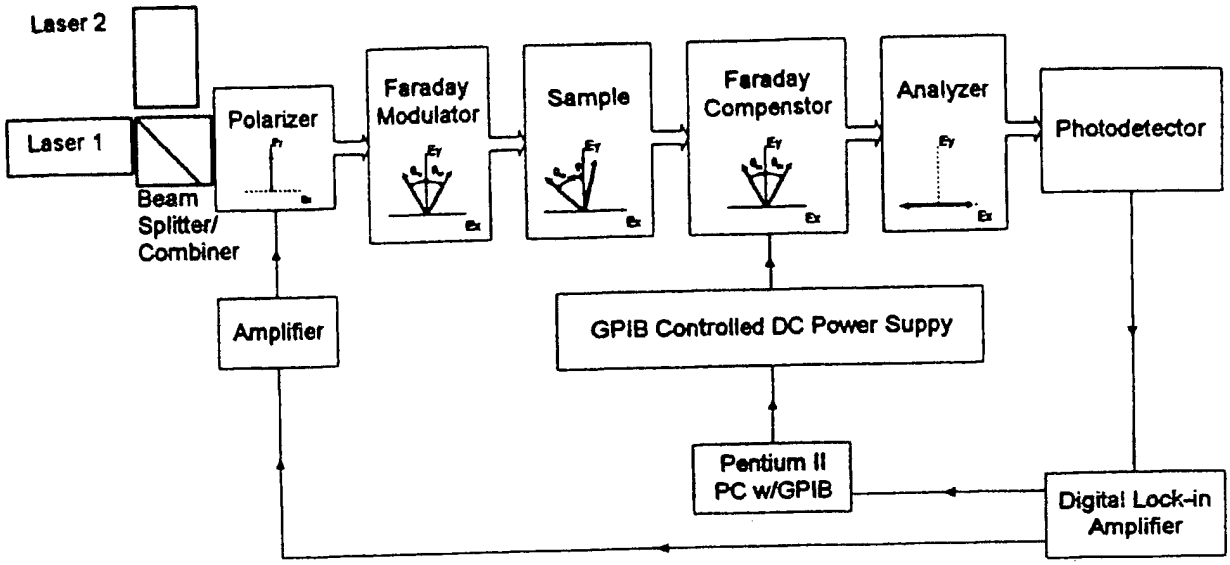

Figure 1. Polarimeter block diagram

developed a multi-spectral closed-loop polarimeter utilizing a Pockels cell for both modulation and feedback using 5 cm path length test cell.[9] In their study, it was demonstrated *in vitro* how a multi-spectral approach could compensate for interference due to the presence of multiple optically active components in a sample. Recently, Cameron and Coté have developed a single wavelength polarimeter incorporating a digital closed-loop controller based on a Faraday modulation and feedback approach.[10-13] In their system, sub-millidegree sensitivity has been demonstrated *in vitro* for a range test media including water, bovine cell culture medium (a complex growth media containing many optically active components), and aqueous humor. This system is very robust and demonstrates a high degree of stability and reproducibility, which has been an issue for past polarimetric studies. Overall prediction errors in both calibration and validation have been shown to be on the order of home-based glucose sensors in all media. Most recently, Chou et. al. using an optical heterodyne polarimetric approach have reported similar errors for their *in vitro* studies and have illustrated the use of polarimetry for glucose detection through the eye of a rabbit.[14,15]

In this study, we report on a few issues that are of concern in using optical polarimetry for *in vivo* glucose monitoring. These include the application of a multi-spectral approach to minimize glucose prediction error when multiple optically active substances vary in concentration and a mechanism to effectively couple light through the anterior chamber of the eye. In addition, some preliminary *in vivo* results will be presented illustrating that a polarimetric signal can be obtained through the anterior chamber of a rabbit eye.

2. MATERIALS AND METHODS

2.1 Instrumentation

A block diagram of the experimental apparatus designed and constructed for this investigation is illustrated in Figure 1. For the multi-spectral experiment, Laser 1 and 2 are laser diodes (Merideth Instruments, Glendale, AZ) emitting 5mW of power at the wavelengths 670 nm and 820 nm, respectively. For the *in vivo* experiment, only laser 1 is used emitting 5mW of power at 635 nm (LaserMax Inc., Rochester, NY). A Glan-Thompson 100,000:1 polarizer initially polarizes the light beam. A Faraday rotator (Deltronic Crystal Inc., Dover, NJ) is then used to modulate the polarization vector. It is driven by a

sinusoidal source at a frequency of 1.09 kHz. This modulated signal then propagates either through a rectangular sample cell (Starna Cells Inc.) constructed of optical grade glass with a path length of 1 cm for the *in vitro* experiments or through the anterior chamber of the eye via a coupling mechanism for the *in vivo* experiment. Following the sample is another Faraday rotator that provides feedback compensation. The purpose of this Faraday rotator is to eliminate any rotation of the polarization vector due to the glucose sample. The next component is another Glan-Thompson polarizer, known as the analyzer, with its transmission axis oriented perpendicular to that of the initial polarizer. The analyzer transforms the polarization modulation into intensity modulation according to Malus' law that can be sensed by the light detector (Thorlabs Inc., Newton, NJ). The output of the light detector is a voltage proportional to the detected light intensity.

A digital lock-in amplifier (DLIA) (Stanford Research Systems –SR830) provides the input into the digital controller. The DLIA is the used to measure the relative amplitude of the signal present at the modulation frequency. This allows the precise measurement of the signal of interest at 1.09 kHz while rejecting low and high frequency electromagnetic noise. The signal amplitude information is then sent to a Pentium II PC via an IEEE 488 general-purpose interface bus (GPIB) into a control algorithm implemented using LabView 5.01 (National Instruments, Austin TX).

Upon receiving the amplitude information of the detected signal present at the modulation frequency, the digital controller decides the course of action to take in order to compensate for any rotation due to the sample.[13] The output of the control is then sent to a GPIB controlled DC power supply that outputs a voltage to the compensation Faraday rotator.

Through the use of Jones matrices, the electric field for a single laser through the optical train can be modeled as:

$$\mathbf{E} = -\sin\left(\theta_m \sin(\omega_m t) + \phi\right), \tag{1}$$

where θ_m is the modulation depth, ω_m is the modulation frequency, t is time, and $\phi = \phi_g - \phi_f$ where ϕ_g and ϕ_f are the rotations in polarization due the glucose sample and compensation Faraday, respectively.[13] The intensity of the signal that impinges on the light detector is proportional to the square of the electric field and can be modeled as:

$$I \propto E^2 = \left(\phi^2 + \frac{\theta_m^2}{2}\right) + 2\phi\theta_m \sin(\omega_m t) - \frac{\theta_m^2}{2}\cos(2\omega_m t), \tag{2}$$

which assumes a small angle approximation where that $\sin(x) \equiv x$ for $x \ll 1$. As can be seen from equation 2, the relative amplitude of the sinusoidal term at the modulation frequency is proportional to the rotation due to the glucose sample assuming no compensation ($\phi_f = 0$). This is used as the input into the digital control which forces the net rotation in polarization (ϕ) to zero via the compensation Faraday rotator. Upon completion, the output voltage of the digital controller is proportional to the glucose concentration of the sample.

2.2 Multi-spectral confounding component experiment

A set of *in vitro* experiments were performed to assess the glucose predictive capability of our polarimeter in the presence of an optical confounder. Sample solutions were prepared by mixing appropriate amounts of glucose and albumin over a physiological concentration range. Thirty seperate samples of 10 ml each were prepared. The span covered a range from 0 mg/dl to 400 mg/dl for glucose and 0 to 100 mg/dl for albumin in 100 mg/dl and 20 mg/dl, respectively. Normal concentrations of albumin in the eye are below 10 mg/dl, however, we chose to use a larger range of albumin concentrations in order to better illustrate how a multiple wavelength approach can help reduce glucose prediction errors with the application of a multiple linear regression calibration model.

Three separate models were computed for the two data sets collected at different wavelengths in order to assess their predictive capablility. The first two models were based on a standard least-squares linear regresion model using information from a single wavelength. For example, the 670nm model predicts glucose concentrations merely by using the feedback voltage obtained for a given mixture of glucose and albumin. The third model was computed using a multiple linear regression technique. For example, both feedback voltages for 670 nm and 820 nm needed to null the system for a given mixture of glucose and albumin were considered during the computation of the calibration model.

The multiple linear regression calibration model takes the form of :

$$\begin{bmatrix} V_{\lambda 1} \\ V_{\lambda 2} \end{bmatrix} = \begin{bmatrix} a_1 & b_1 \\ a_2 & b_2 \end{bmatrix} \begin{bmatrix} Glucose \\ Albumin \end{bmatrix} + \begin{bmatrix} c_1 \\ c_2 \end{bmatrix} \quad (3)$$

where $V_{\lambda 1}$ and $V_{\lambda 2}$ are the feedback voltages for each wavelength, a_1, a_2, b_1,b_2 are the components of the slope coefficent matrix, [Glucose] and [Albumin] are the respective concentrations within each sample, and c_1 and c_2 are the corresponding intercepts. This model is then rearraged for in the form of :

$$\begin{bmatrix} Glucose \\ Albumin \end{bmatrix} = \begin{bmatrix} a_1 & b_1 \\ a_2 & b_2 \end{bmatrix}^{-1} \left(\begin{bmatrix} V_{\lambda 1} \\ V_{\lambda 2} \end{bmatrix} - \begin{bmatrix} c_1 \\ c_2 \end{bmatrix} \right) \quad (4)$$

to predict unknown the sample concentrations for a given set of feedback voltages at each corresponding wavelength.

2.3 *In vivo* experiment

In order to demonstrate that a useful polarimetry signal can be obtained for *in vivo* measuremenis, an experimental setup similar to that shown in Figure 1 was used. However, only a single diode laser was used which emitted 5mW of power at 635nm. In place of the sample, the eye of a 3.6 kg New Zealand White (NZW) rabbit was used. The modulated polarized light beam is coupled through the anterior chamber of the eye using an eye-coupling device we constructed. This device is depicted in Figure 2. The coupling mechanism consists of an open ended cylindrical glass shaft that is placed over the cornea. The shaft has two ports, one port allows saline to be injected into the cylinder and the other port acts as a vent to equalize the inside pressure to that of the atmosphere. The saline acts as an index matching fluid allowing light to propagate in a straight path through the anterior chamber. The input laser beam is coupled through the eye by first reflecting off a 45° mirror mounted on the device. This beam then enters a right angle prism at the base of the device. The prism acts as a flat optical window into the inner chamber of the shaft. The beam then propagates through the anterior chamber of the eye and exits the device via another right angle prism. The exit beam is then reflected upward to a second 45° mirror that reflects the light toward the analyzer/detector.

The anesthesia protocol used consists of the intra-muscular injection of 35mg/kg of ketamine, 5 mg/kg of xylazine and 1 mg/kg of acepromazine. The rabbit is then placed on an adjustable platform underneath the eye coupling mechanism. The coupling mechanism is then lowered into place over the rabbit's eye. Once contact with the eye is made, a saline based index-matching fluid is then injected into the eye-coupling device. Leakage of the fluid is minimal due to the contact seal made with the eye at the base of the device.

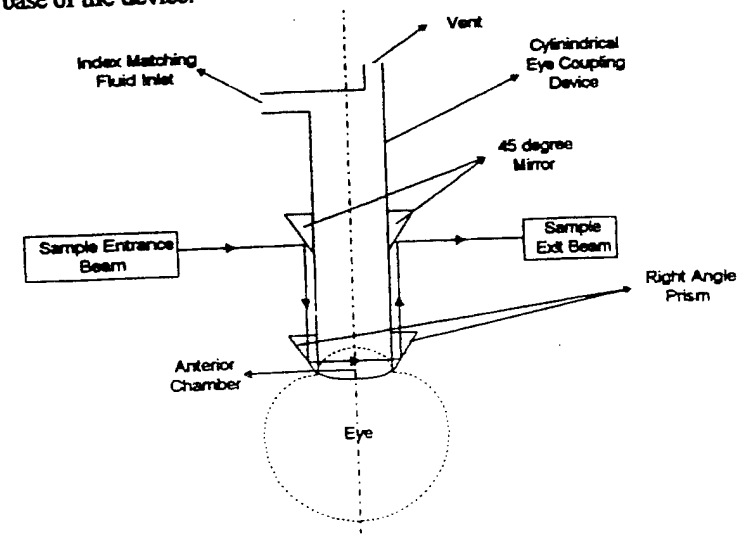

Figure 2. Device to couple light through the anterior chamber of the eye

3. RESULTS AND DISCUSSION

3.1 Multi-spectral polarimetric sensing approach

Presented in Figure 3 are the results of the glucose and albumin multi-spectral experiment. The purpose of this experiment was to demonstrate how other chiral components, such as, albumin that are present in the aqueous humor in addition to glucose could be compensated for if their concentrations were not constant. Figure 3a and 3b illustrate glucose prediction in the presence of different albumin concentrations varying between 0 to 100 mg/dl using a single wavelength regression model for 670 and 820 nm light, respectively. The calibration errors for the 670 and 820 nm experiments are 38.92 and 42.67 mg/dl, respectively. As can be seen, for each concentration of glucose, there are distinct errors resulting due to the varying concentrations of albumin. However, if a multiple linear regression technique is applied, the model takes the form seen in equations 3 and 4. The calibration prediction results for the multi-spectral case are shown in Figure 3c. As can be seen, the prediction results for glucose are grouped much closer the theoretical line than in the single wavelength cases. The overall calibration error for the multi-spectral model is 21.69 mg/dl, which is significantly lower than the single wavelength regression models.

It should be noted that the effects of other optically active components present in the aqueous humor are expected to be minimal.[16] Glucose levels in the eye are considerably higher in concentration than other optically active components, such as, albumin. Also, the specific rotation of glucose at 635 nm is considerably higher than the specific rotations of the several other various amino acids that are also present in the aqueous humor. Thus, the observed rotation due to glucose will be considerably larger than those rotations due to the other confounding components.

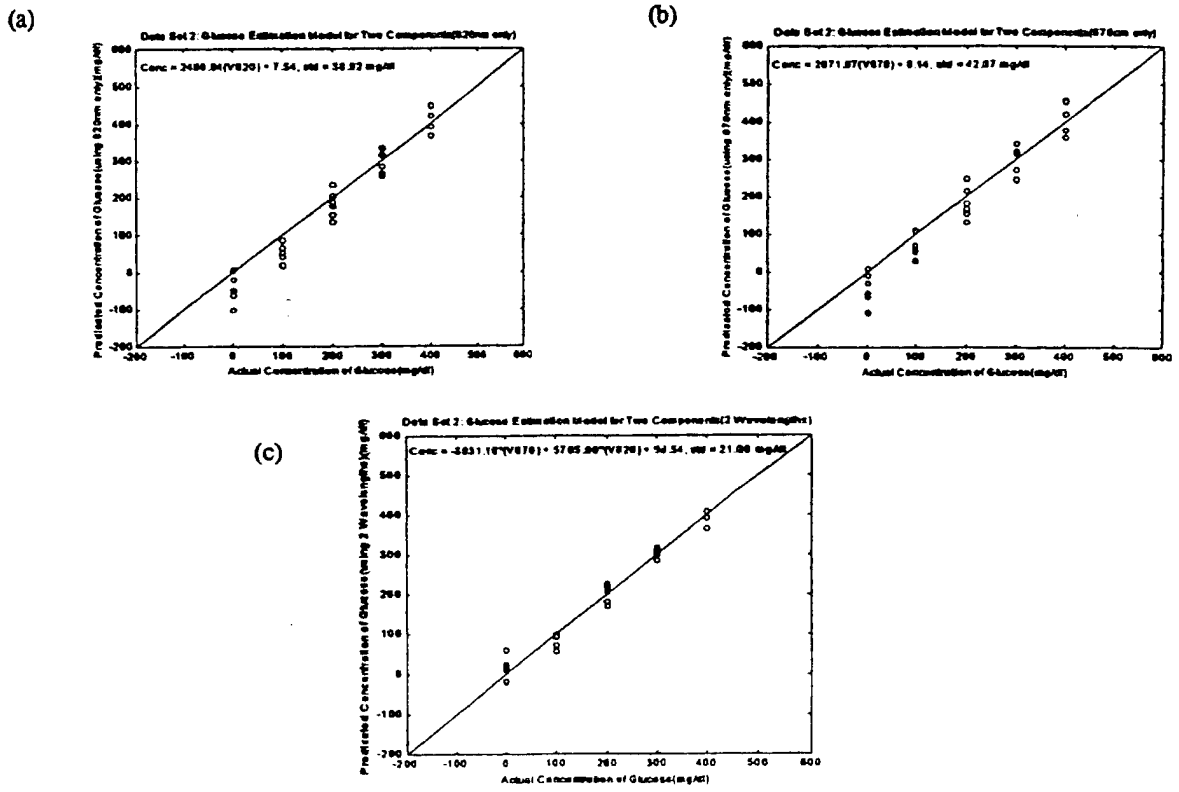

Figure 3. Multi-spectral glucose prediction results (a) 670 nm single wavelength prediction (b) 820 nm single wavelength and (c) 670/820 nm multi-spectral prediction results

3.2 *In vivo* polarimetry experiment

Through the use of the eye-coupling device developed for this experiment, the collimated modulated polarized laser beam of the polarimeter was effectively coupled in and out of the anterior chamber of a rabbit eye. Minimal effects due to the scattering and bending of light caused by variations in the refractive index mismatch were observed. Shown in Figure 4 is a scope trace of the detected *in vivo* signal (top) and modulation reference signal (bottom). As modeled by equation 4, the detected *in vivo* signal is comprised of a sinusoid at twice the modulation frequency in addition to another sinusoid at the modulation frequency. The component at the modulation frequency, which is proportional to the optical rotation, causes the slight differences between the peaks of the detected signal. The DC-component was removed via ac-coupling.

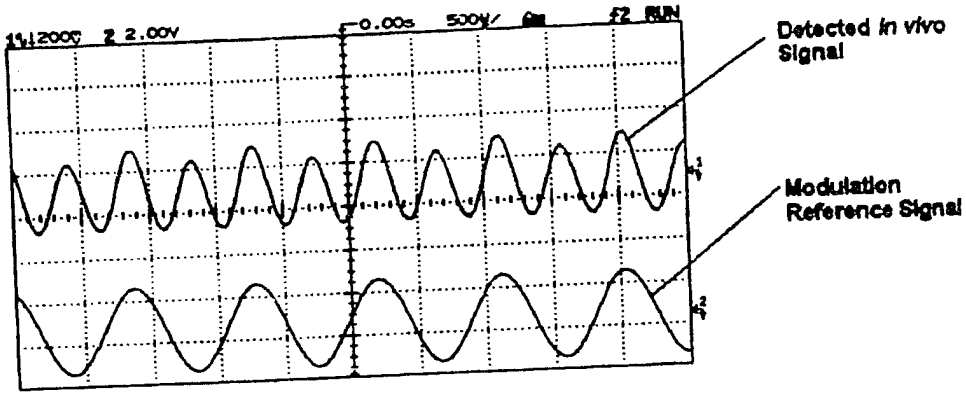

Figure 4. *In vivo* detected polarimetry signal

4. CONCLUSION

In summary, it has been shown *in vitro* that a multi-spectral polarimetric approach could be utilized to minimize glucose prediction errors in solutions comprised of more than one optically active component varying in concentration. It has also been shown that a polarimetric signal can be effectively coupled and detected *in vivo* through the anterior chamber of a rabbit eye. The next phase of this research will be comprised of verifying the transport time delay between the diffusion of glucose between the blood/aqueous humor barrier along with developing methods to characterize and compensate for variations in corneal birefringence.

ACKNOWLEDGMENTS

This work was supported in part by grants from the National Aeronautics and Space Administration (Grant No. NAG9-821) and the National Medical Technology Testbed (NMTB): a subcontract under the U.S. Army Medical Research Acquisition Activity (Grant No. DAMD17-97-2-7016).

REFERENCES

[1] March, W.F., Rabinovitch, B. and Adams, R.L. (1982), Noninvasive Glucose Monitoring of the Aqueous Humor of the Eye: Part II. Animal Studies and the Scleral Lens, *Diabetes Care*, 5(3), pp. 259-265, 1982.

[2] Rabinovitch, B., March, W.F., and Adams, R.L. (1982), Noninvasive Glucose Monitoring of the Aqueous Humor of the Eye: Part I. Measurement of Very Small Optical Rotations, *Diabetes Care*, 5(3), pp.254-258, 1982.

[3] Goetz, M.J. Coté, G. L., March, W.F., Erckens, R. And Motamedi, M., "Application of a multivariate technique to Raman spectra for quantification of body chemicals," *IEEE Transactions on Biomedical Engineering, 42*(7), pp.728-731, 1995.

[4] Wicksted, J.P., Erkens, R.J., Motamedi, M. And March, W.F., "Monitoring of Aqueous Humor Metabolites Using Raman Spectroscopy," SPIE Proceedings, V2135, pp. 264-274, 1994.

[5] Pan, S., Chung, H., Arnold, M.A., and Small, G.W., "Near-Infrared Spectroscopic Measurement of Physiological Glucose Levels in Variable Matrices of Protein and Triglycerides," *Anal. Chem.*, 68, pp. 1124-1135, 1996.

[6] McShane, M., Rastegar, S., and Coté, G.L., "Fluorescence-based implantable biosensors: Monte Carlo modeling for Optical probe design", Proceedings of the 20th International Conference of the IEEE EMBS, Hong Kong, Oct 29 - Nov 1, 1998.

[7] Russell, R., Pishko, M., Gefrides, C., and Coté, G.L., "A fluorescent glucose assay using poly-l-lysine and calcium alginate microencapsulated tritc-succinyl-concanavalin A and FITC-Dextran", Proceedings of the 20th International Conference of the IEEE EMBS, Hong Kong, Oct 29 - Nov 1, 1998.

[8] Coté, G.L., Fox, M.D., and Northrop, R.B. (1992), Noninvasive Optical Polarimetric Glucose Sensing Using a True Phase Measurement Technique, *IEEE Transactions on Biomedical Engineering*, 39(7):752-756, 1992.

[9] King, T.W., Coté, G.L, McNichols, R. and Goetz, Jr., M.J. (1994), Multispectral Polarimetric Glucose Detection Using a Single Pockels Cell, *Optical Engineering*, 33(8):2746-2753.

[10] Cameron, B.D. and Coté, G.L., "Polarimetric Glucose Sensing in Aqueous Humor Utilizing Digital Closed-Loop Control," 18th Annual International Conference Proceedings of IEEE-EMBS, Amsterdam, The Netherlands, October 31-November 3, 1996.

[11] Cameron, B.D., and Coté, G.L., "Polarimetric Detection of Chiral Chemicals in Biological Fluids", SPIE International Biomedical Optics Conference, San Jose, CA., SPIE V2982; pp 308-313: Feb. 8-14, 1997.

[12] Coté, G.L. and Cameron, B.D., "Noninvasive Polarimetric Measurement of Glucose in Cell Culture Media," *Journal of Biomedical Optics*, 2(3), pp. 275-281, July 1997.

[13] Cameron, B.D., and Coté, G.L., "Noninvasive Glucose Sensing Utilizing a Digital Closed-Loop Polarimetric Approach", *IEEE Transactions on Biomedical Engineering*, 44(12), pp. 1221-27: December 1997.

[14] Chou, C., Huang, Y.C., Feng C.M., and Chang M., "Amplitude sensitive optical heterodyne and phase lock-in technique on small optical rotation angle detection of chiral liquid," *J. Appl. Phys.*, 36, pp. 356-359, 1997.

[15] Chou, C., Han C.Y., Kno, W.C., Huang, Y.C., Feng C.M., and Shyu J.C., "Noninvasive glucose monitoring *in vivo* with an optical heterodyne polarimeter," *Applied Optics*, 37(16), pp. 3553-3557, June 1998.

[16] Gough, D.A., "The composition and optical rotatory dispersion of bovine aqueous humor," *Diabetes Care*, 5, pp.266-270, 1982.

DESCRIPTION

The end goal of this research is the development of a unique, forward reaching, advanced optical technology based on multispectral polarimetry to be used for noninvasive monitoring of glucose levels *in vivo*. A robust single wavelength system has been developed in part for the NASA space program to monitor glucose *in vitro* in cell culture media. The optical polarimetric sensing technique is based on the fact that the polarization vector of light rotates when it interacts with an optically active material such as glucose. The amount of rotation of polarization is directly proportional to the glucose concentration and to the sample path length. Since the polarization rotation of a given substance is a function of the wavelength of light, in this proposal a multispectral approach will be tested to both distinguish potential rotatory confounding components found in the anterior chamber of the eye from that of glucose and compensate for eye motion artifact. The sensitivity and specificity of the system to glucose will first be tested *in vitro* using glucose doped bovine aqueous humor solution in the presence of varying rotatory components such as amino acids, ascorbic acid, and albumin. Fresh post-mortem rabbit, bovine, and human eyes will then be used to assess the ability of the system to compensate for any corneal birefringence, eye motion artifact, variable eye pathlength, and variable corneal curvatures. Lastly, *in vivo* tests will be performed on New Zealand White rabbits to evaluate the repeatability, accuracy, and specificity of the noninvasive optical polarization technique to changes in blood glucose. If a second year of support is granted further animal and human studies will be performed.

The primary application of the system focuses on noninvasive glucose monitoring through the anterior chamber of the eye for the diagnosis and management of diabetes mellitus. This disease currently afflicts over 100 million people worldwide and nearly 14 million in the United States. In the U.S. this disorder, along with its associated complications, is ranked as the seventh leading cause of death. The design and development of this novel polarimetric glucose sensing technology would provide a means for indirect noninvasive measurement of blood glucose, thereby facilitating increased frequency of the measurement, tighter control, and fewer secondary complications from diabetes mellitus.

PROJECT SITE

Texas Engineering Experiment Station
Optical Biosensing Laboratory
145 Wisenbaker Engineering Research Center
College Station, TX 77843

ORIGINAL

Final Technical Progress Report

for the

APR 18 2000

National Medical Technology TestBed (NMTB)

Report Period Covered: August 6, 1998 – February 28, 2000

Cooperative Agreement No: DAMD17-97-2-7016

Subagreement No: 023-FY97-TEXAS A&M-COTE

Title: Noninvasive Glucose Sensing Using a Novel Optical Technique

PI: Gerard L. Coté, Ph.D., P.E.
Associate Professor of Biomedical Engineering
Texas A&M University, Texas Engineering Experiment Station, 301 WERC, College Station, TX 77843
Phone: 979-845-4196
Fax: 979-847-9005
e-mail: cote@tamu.edu

Gerard L. Coté 3/22/00

Signature of PI Date

I. Introduction

Research in the field of optical polarimetry offers several fascinating possibilities in the fields of analytical chemistry and biosensing. In this study, we proposed to develop a unique, forward reaching, advanced optical technology based on polarimetry to be used for noninvasive monitoring of glucose levels *in vivo*. The long term goal is to develop this technology to ultimately monitor glucose noninvasively through the anterior chamber of the eye as an indirect measure of blood glucose concentrations. The approach was developed in part for the NASA space program to monitor glucose *in vitro* in cell culture media. If successful, the obvious benefit of our approach is that it would be noninvasive which, for diabetic patients for whom it is recommended to monitor their blood glucose levels up to five times a day, is a significant advantage. In the original proposal the following three specific aims were given.

Specific Aim #1: To minimize corneal birefringence artifacts due to eye motion and elucidate glucose concentration in the presence of other optically active molecules that vary in concentration.

Specific Aim #2: To design, implement and test a sensitive polarimeter that allows for coupling in and out of the eye.

Specific Aim #3: To measure the in vivo aqueous humor glucose levels and quantify blood glucose levels accounting for the equilibration time delay.

II. Body- Description of Methods & Results broken down by aim

Specific Aim #1:

A modified version of the original polarimetric system was discussed in the 5th quarterly report (see Appendix 1-report 5 and Appendix 2 – paper 1). This system was an extension of the original system in that it provides two simultaneous measurements of optical rotation by using a red (635 nm) laser in a closed-loop configuration and a green (532 nm) laser in an open loop configuration. The block diagram of the designed and constructed system is shown in Figure 1. The motivation behind this system was two fold. First, such a multi-wavelength system has the potential to minimize glucose prediction error in multiple optically active component samples. Secondly, this type of system can potentially be used to minimize the effects of corneal birefringence due to motion artifacts.

To test the ability of the system to reduce glucose prediction error in a sample containing more than one optically active component that varies in concentration, a set of *in vitro* experiments were performed in triplicate. Albumin was chosen as the confounder because it is one more abundent optically active components in the eye with a relatively significant specfic rotation as shown in the fourth quarter report. In this experiment, glucose was varied between the physiological hyperglycemic range of 0 to 600 mg/dl in 50 mg/dl increments and albumin was varied from 0 to 100 mg/dl in 25 mg/dl increments. These albumin values are 5-10 times above normal levels found in the aqueous humor of the eye.

D-glucose and rabbit albumin were purchased in dry form from Sigma Chemical (St. Louis, MO). Stock solutions for each chemical were prepared in deionized water and individual 5 ml samples at each respective sample concentration were prepared by combining appropriate amounts of each stock solution with deionized water.

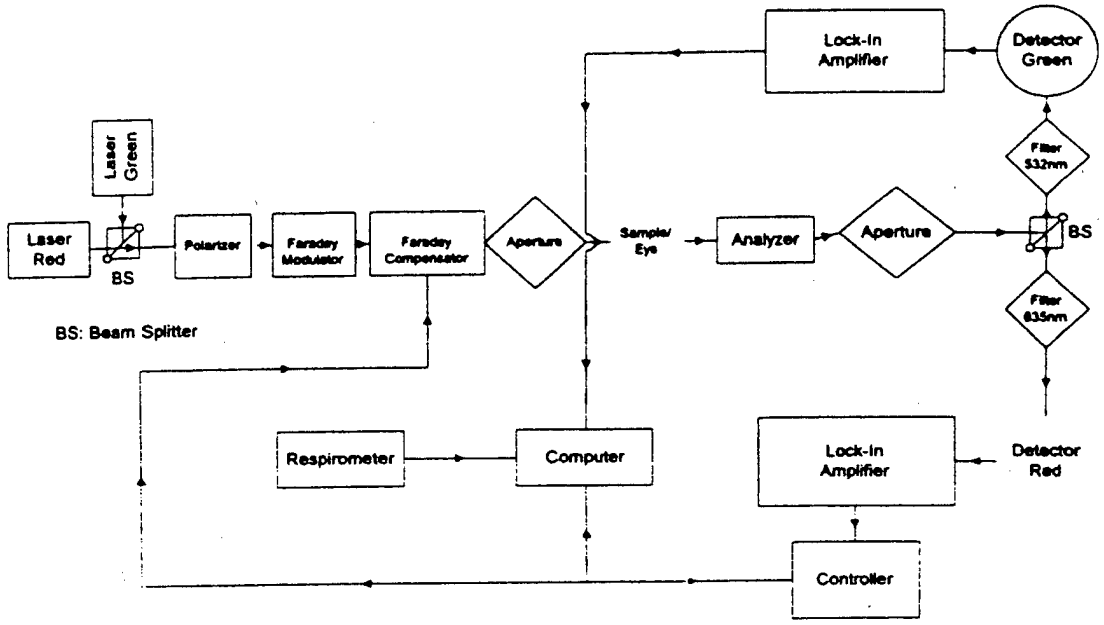

Figure 1: Block diagram of the designed polarimeter

For each set of experiments, three separate calibration models were computed in order to demonstrate the benefit of a multiple wavelength system in reducing glucose prediction error compared to a single wavelength system. The first two models computed are based on a standard least-squares linear regresion model using information only from a single wavelength. For example, the first model predicted glucose concentrations by using the closed-loop feedback voltage obtained for nulling the 635 nm wavelength for a given mixture of glucose and albumin. The second model used the open-loop 532 nm signal to predict glucose concentration. Lastly, the third model was computed using a multiple linear regression technique. Both the closed-loop feedback voltage (635 nm) and the open-loop (532 nm) signal were used to compute a single calibration model. The multiple linear regression calibration model takes the form of :

$$\begin{bmatrix} V_{\lambda 1} \\ V_{\lambda 2} \end{bmatrix} = \begin{bmatrix} a_1 & b_1 \\ a_2 & b_2 \end{bmatrix} \begin{bmatrix} \text{Glucose} \\ \text{Albumin} \end{bmatrix} + \begin{bmatrix} c_1 \\ c_2 \end{bmatrix} \quad (1)$$

where $V_{\lambda 1}$ and $V_{\lambda 2}$ are the feedback voltages for each wavelength, a_1, a_2, b_1,b_2 are the components of the slope coefficent matrix, [Glucose] and [Albumin] are the respective concentrations within each sample, and c_1 and c_2 are the corresponding intercepts. This model is then rearraged for in the form of :

$$\begin{bmatrix} \text{Glucose} \\ \text{Albumin} \end{bmatrix} = \begin{bmatrix} a_1 & b_1 \\ a_2 & b_2 \end{bmatrix}^{-1} \left(\begin{bmatrix} V_{\lambda 1} \\ V_{\lambda 2} \end{bmatrix} - \begin{bmatrix} c_1 \\ c_2 \end{bmatrix} \right) \quad (2)$$

to predict unknown the sample concentrations for a given set of feedback voltages at each corresponding wavelength.

The average standard errors of calibration (SEC) for the closed and open-loop experiments were 40.3 and 143.5 mg/dl, respectively. These errors are based on the use of a single dependent variable linear regression model. However, when a multiple linear regression model of the form of equation 2 is computed using both the open-loop and closed-loop signals, the average SEC is dramatically reduced to 22.6 mg/dl, thus demonstrating the advantage of such a system. The glucose prediction results for one of the multi-spectral experiments are shown in Figure 2.

The next experiment was conducted to test the *in vivo* sensitivity of the designed polarimetric system in presence of motion artifact. This experiment utilized the newly designed dual wavelength polarimeter and actual glucose samples were used. Glucose samples were varied between a concentration range of 0 to 600 mg/dl in 100 mg/dl increments and placed in a 1 cm sample cell before the polarized beam entered the eye of a live rabbit. The analog controller was used to keep the system nulled in the presence of motion artifact and the open-loop signal was recorded as a measure of glucose. Each sample was placed individually in the sample cell and the open-loop single frequency component of the green laser was recorded for two seconds at a sample rate of 10 Hz. Least-squares linear regression was used to compute a linear model. This model was then used to predict glucose concentration. The results from this experiment are shown in Figure 3. There is a linear trend (R=0.95) in predicted versus actual glucose concentrations. This indicates that the current system is sensitive enough to measure the small rotations due to the physiological glucose concentrations in the presence of motion artifact. Although the current system does to some degree compensate for motion artifact in the short-term, long-term gross changes in corneal birefringence due to motion artifact still remain a problem.

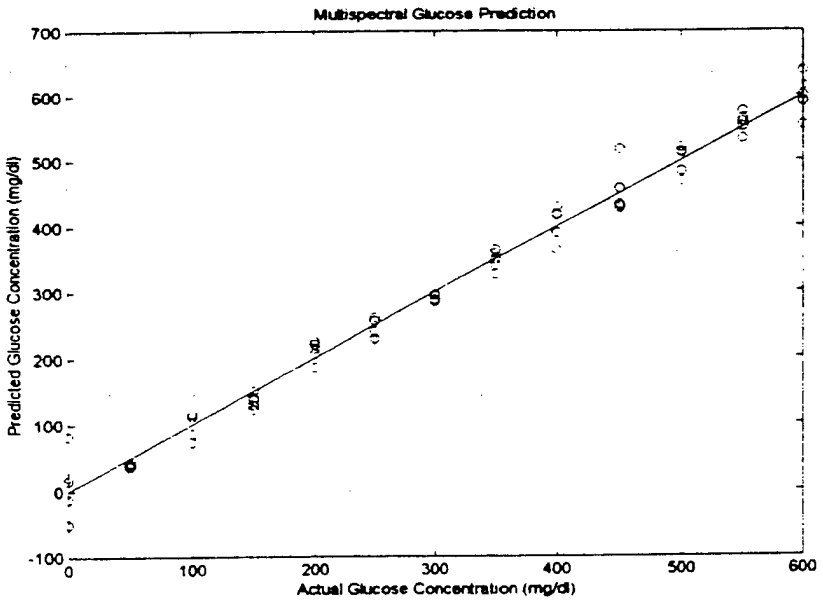

Figure 2: Glucose prediction in the presence of albumin using a multi-spectral model

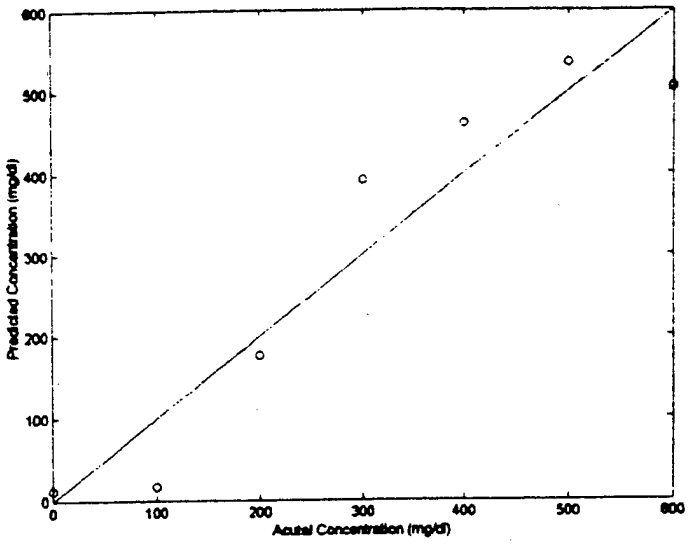

Figure 3: *In vivo* sensitivity experiment

As detailed in the second year proposal plan, we will fully characterize the wavelength dependency of the corneal birefringence and will investigate multi-spectral and post-processing techniques to further remove or compensate for its effects in the detected signal.

Specific Aim #2:

A coupling device was designed and used quite successfully to overcome index of refraction changes as described in detail in the second quarter report (See appendix 1 – report 2 and Appendix 2 – paper 1). The sensitive dual wavelength polarimetric system has been previously described above (Also see appendix 2 – paper 1).

Specific Aim #3:

A preliminary experiment was previously performed in an effort to characterize the blood glucose response for NZW rabbits over time for the current anesthesia protocol (described in Appendix 1 – report 5). In addition to the anesthesia effects of this protocol, an elevation in the blood glucose levels is also initiated in the animal. As a recap from the previous quarter, the following information was concluded:

- The rising trend in blood glucose levels in response to the anesthesia protocol is similar between rabbits.
- Blood glucose levels can be expected to rise from 100 mg/dl (basal levels) to approximately 220 mg/dl throughout the course of the experiment
- Blood glucose levels should peak approximately 80 minutes after the initial administration of the anesthesia, at which point the will begin to decline

- A sampling interval of 10 minutes should be sufficient during the first 65 minutes of the experimental procedure, after which the time between samples should be reduced to 3-5 minutes (in order to increase the response resolution) as the peak in the blood glucose response is approached.

Using this information, an experiment was devised and conducted to physically measure the time delay between the blood and aqueous humor levels. These experiments were conducted over a series of weeks, in which the blood glucose levels of five New Zealand White rabbits were elevated. As previously mentioned, the method of glucose concentration elevation is due to a side effect of the anesthesia protocol used. The resulting effect is that xylazine causes a significant but temporary rise in blood glucose levels and thus also in the aqueous humor of the eye. This effect is desirable in our investigation because the blood glucose levels are similar to those seen in diabetic patients without having to permanently induce diabetes or give a bolus injection of glucose. Because the aqueous humor sampling during this investigation was invasive, requiring the puncturing of the cornea, the experiments were conducted over a five-week period. Glucose measurements were collected over a localized forty-minute time interval centered about the blood glucose peak. During each week, at different times, a single 0.3 ml blood sample and a 0.1 ml sample of the aqueous humor of the eye from each rabbit were passively extracted using a 27 gauge needle. All samples were withdrawn in five-minute increments at a given instance in time in reference to the time the rabbit was anesthetized.

The reasoning behind conducting the experiment over a period of weeks was to insure the integrity of the blood-aqueous barrier, such that it was not affected due to the corneal penetration. Once the cornea is punctured, there is a change in intraocular pressure and fluid can leak out at the puncture site leading to an alteration in glucose transport, an influx of proteins, and other molecules that normally would not be present in the eye. Therefore, in this investigation only a single measurement was acquired per rabbit per week and sufficient time (two weeks) was provided for the eye to heal and glucose transport within the eye to normalize.

The collected samples were analyzed using a One-Touch Basic (Lifescan, Milpitas, CA) hand-held glucose meter, a Glucometer Elite (Bayer Diagnostics, Tarrytown NY) hand-held glucose meter, and a YSI (YSI, Yellow Springs, OH) 2300 glucose analyzer. Since the samples analyzed with the YSI meter were performed at a different location, the samples were placed in vacutainers (Becton-Dickinson, Franklin Lakes, NJ) containing sodium fluoride and potassium oxalate. The purpose of the sodium fluoride and potassium oxalate is to prevent blood coagulation and to quench any further glucose metabolism.

To aid in the determination of the time delay between blood and aqueous humor glucose levels, a second order polynomial curve was fitted around the peak responses for both the blood and aqueous humor glucose response curves in each rabbit. The time peak occurred was determined from the fitted data. The time delay between the blood and aqueous humor glucose levels was defined as the differences in time between the peaks of the aqueous humor and blood glucose peak, as shown in the following equation:

$$T_{delay} = T_{peak_aqueous} - T_{peak_blood} \tag{3}$$

The results of the time delay experiment for a single rabbit are shown in Figure 4. For this plot, all the measurements presented are the glucose levels predicted via the YSI glucose analyzer. The YSI values were chosen instead of those obtained by the other meters due to its superior sensitivity and accuracy. It should be noted that since all samples analyzed by the YSI were combined with sodium fluoride and potassium oxalate, the predicted glucose levels were slightly lower than actual. This was due to a slight confounding effect, however, this was not of a concern because the time delay measurements are based on the time of the peak locations, not the actual glucose levels.

Using the fitted curves, the peak locations in time for both the blood and aqueous humor glucose levels were identified. The time delay was then computed according to equation 3. The estimated average time delay for the five rabbits is 3.44 minutes with a standard deviation of 4.9 minutes. The importance of these results is due to the fact that if the aqueous humor of the eye is to be used as an indirect measure of blood glucose, the time delay must be small enough to provide useful information to the diabetic in regards to their blood glucose levels. This is extremely important for type I diabetics who do not produce insulin and can have significant variations in their blood glucose levels over a very short period of time. Therefore, the time delays measured in this investigation show that the anterior chamber of the eye can be used as an eventual sensing site for the development of a noninvasive blood glucose monitor.

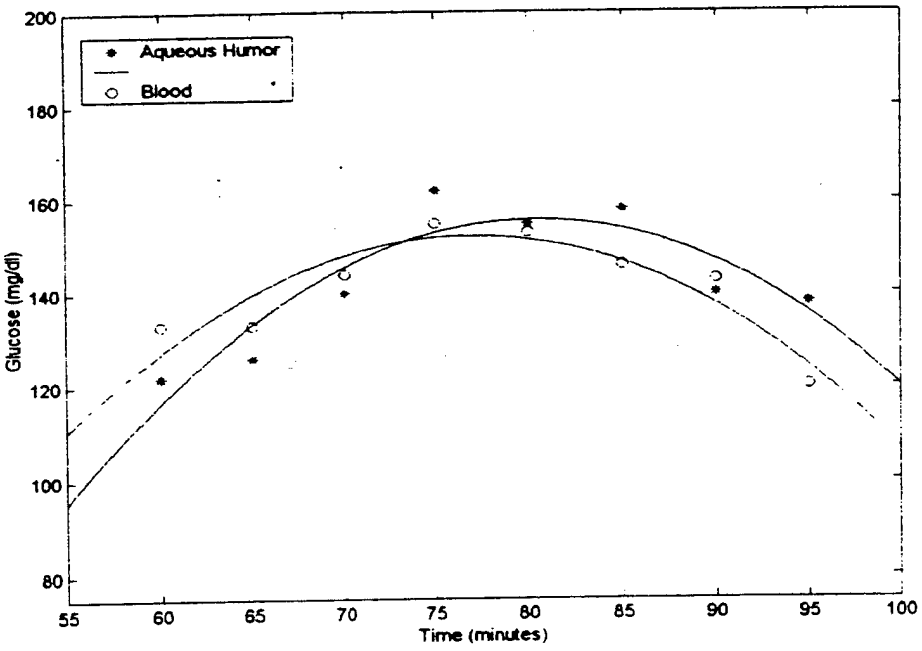

Figure 4: Time-delay results for a single NZW rabbit

III. Conclusions

Overall, in the first year and one half, which includes the no-cost six month extension, all aims have now been completed. The conclusions drawn from this work are the following:

1. Corneal birefringence can be minimized with a good choice of input polarization. This birefringence is problematic, however, in the presence of motion artifact (i.e. breathing and heart beat) but has been reduced using a simultaneous two wavelength system, one wavelength monitored using an open loop configuration and one using a closed loop configuration. In year two, the focus needs to be on utilization of a multispectral system and more sophisticated post-processing using first and second order harmonic information to further overcome this motion induce birefringence.

2. The presence of other optically active components in the aqueous humor solution are minimal and the small rotations that do occur were effectively eliminated with the use of a multispectral approach.

3. An effective coupling device has been designed and utilized to overcome index of refraction mismatch between the air-cornea interface and the two wavelength polarimeter shows the required sensitivity for glucose monitoring at physiologic levels.

4. The time delay between blood and aqueous humor glucose concentration has been effectively measured across five rabbits and was found to be within 5 minutes on average. This delay is comparable to reported interstitial fluid delays and is sufficiently small for the device to be useful even for type I diabetics.

IV. Patents and Commercialization

To date there have been no patents or patent disclosures filed. It is anticipated that disclosures will be filed through the Texas A&M University System in the upcoming second year of this research. If the *in vivo* animal studies are successful in year two, then a rigorous effort will be made to secure additional outside funds for diabetic animal studies and pre-clinical studies. An industrial partner will be solicited in order to develop this bench-top technology into a working prototype and perform pre-clinical studies and eventually clinical trials.

Appendix 1

Previous quarterly reports

(The five previous quarterly reports have been appended here for your reference.)

NM TB

NATIONAL MEDICAL TECHNOLOGY TESTBED

December 28, 1998

Gerald L.Cote, Ph.D.
Texas A&M
Biomedical Engineering Program
332 Wisenbaker Rd.
College Station, TX. 77843-3000

Sent via US Mail

Re: **Subcontract:** #023-FY97-Texas A&M-Cote
Project: Non Invasive Glucose Sensing Using a Novel Optical Technique
Principal Investigator: Gerald L. Cote, Ph.D.
Quarterly Report: #1 Performance Period: 8/6/98-11/16/98

Dear Dr. Cote:

This letter will serve to inform you that Dr. Cote's Quarterly Report #1 for the performance period 8/6/98 to 11/16/98 was approved on December 18, 1998, by National Medical Technology Testbed, Inc's Scientific Director.

Please be advised that your next quarterly report will be due on February 16, 1999, and will cover the period 11/6/98 to 2/6/99. Please call Lydia Pearson, our Contracts Administrator, at (909) 558.3244 if you have any questions regarding this letter. Thank you for your assistance.

Sincerely,

Thomas J. Callanan
Administrative Director
TJC:mc

11165 Mountain View Avenue, Suite 121, Loma Linda, California 92354, Voice: 909/478-3244 Fax: 909/478-3254

Technical Progress Report – 1st Quarter

SPONSOR: National Medical Technology Testbed
PROGRAM: Subcontract USAMC
GRANT NUMBER: #023-FY97-TEXAS A&M-COTE
TITLE: Noninvasive Glucose Sensing Using a Novel Optical Technique
Quarter: August 6, 1998 – November 16, 1998
PI: Gerard L. Coté

Texas A&M University, Texas Engineering Experiment Station, 301 WERC, College Station, TX 77843

I. Task Objectives:

The specific objectives of this one-year research project, as listed in the original proposal, are as follows:

Specific Aim #1: To minimize corneal birefringence artifacts due to eye motion and elucidate glucose concentration in the presence of other optically active molecules that vary in concentration.

Specific Aim #2: To design, implement and test a sensitive polarimeter that allows for coupling in and out of the eye.

Specific Aim #3: To measure the time delay between aqueous humor and blood glucose levels.

II. Description of Results from the first quarter

Specific Aim #1: Overcoming motion artifact and other chirally confounding chemicals

Over these first 3 months a real time two laser system (wavelengths of 670 nm and 830 nm), similar to the non-real time system reported previously by our group, was built (Figure 1) and tested for both motion artifacts as well as the ability to measure glucose in the presence of albumin. The sensitivity was compared to our previous single laser system and found to be less than 10 mg/dL for glucose in water alone. The sensitivity of the system was then estimated using glucose in the presence of the optical chiral confounder albumin in doped water solutions. Sample solutions were prepared by mixing appropriate amounts of glucose and albumin to cover their respective normal and abnormal physiologic ranges in the eye (0-400 mg/dL glucose and 0-100 mg/dL albumin). Although the actual concentration of albumin in the eye is only 5mg/dl, one of the intentions behind the system designed is to confirm the usefulness of dual wavelengths to account for the optical confounders rotations comparable to those of glucose. Thus, the concentrations of albumin were chosen on the higher side than normal physiologic levels. Figure 2 shows the plot of the actual glucose concentration versus predicted glucose concentration in the presence of varying albumin obtained using the two wavelength system and a multiple linear regression approach. As depicted, the plot is very linear with a standard error in the glucose concentration of 20 mg/dL. This error, although comparable to current hand held glucose meters, was due in part to the wavelengths used and should be overcome with the three laser system. Motion artifact data was taken *in vitro* with the two wavelength system by moving the test cell. The results are plotted in Figure 3. As depicted, the motion artifact is not a function of wavelength and is correlated for each wavelength, indicating the capability for it to be subtracted or otherwise cancelled out within the system. Since the rotation of the light due to changes in the concentration of glucose are wavelength dependent they would not be cancelled. After creating the motion artifact, the light beams did not pass through the same path within the test cell, as was

indicated by a different feedback voltage required to null the same concentration. The plots thus show that although the feedback voltage to achieve the null state changed due to motion artifacts, the relative difference between them was maintained constant. This was remarkable, as the feedback voltage required to null the same sample was different in both cases, indicating a signal tracking relationship between the nulling and feedback wavelength.

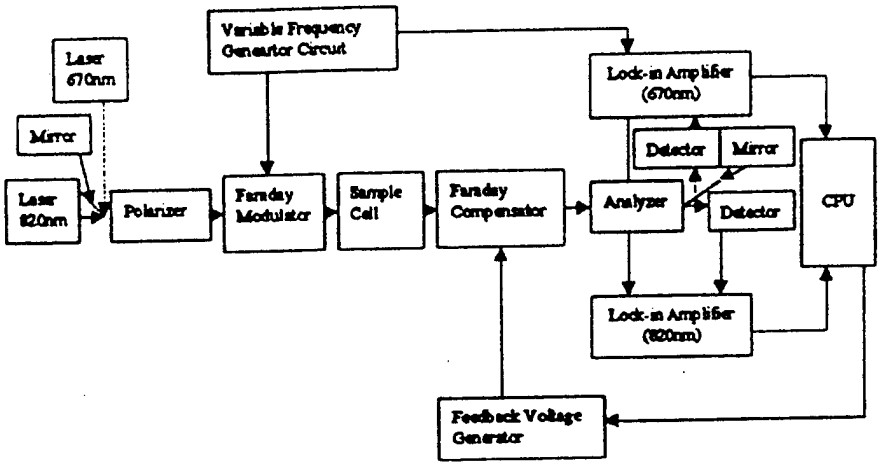

Figure 1: Block diagram of the two laser polarimetric system used to monitor glucose and test motion artifact.

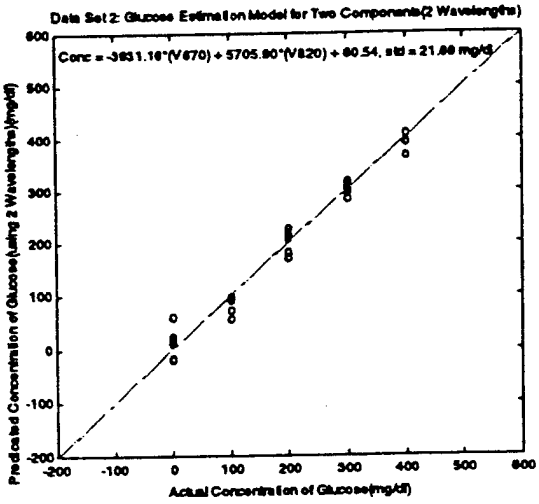

Figure 2: Glucose estimation model using the two wavelength (670nm & 820nm) polarimetric system.

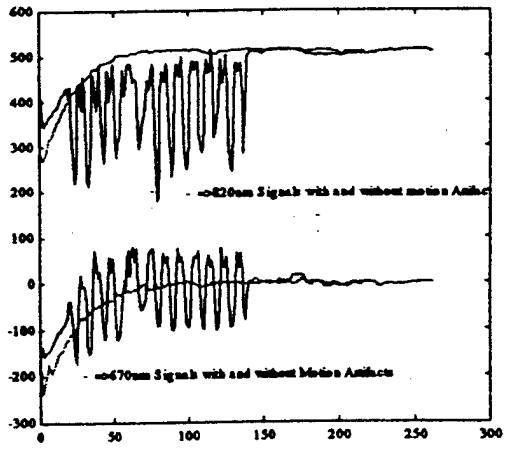

Figure 3: Motion artifact plot showing the correlation between the 670 and 820 nm signals.

Given the early positive results of the two laser system, a three laser system has been designed and is in the process of being built for use in *in vivo* rabbit studies as described in the original proposal.

Specific Aim #2: Development of a sensitive polarimeter and an eye coupling device.

Simultaneously with the two laser system, over this first month an initial eye coupling device was built and tested on two New Zealand White rabbits. Using the first NZW rabbit the results were positive, in that we were able to couple light through the aqueous humor *in vivo* as shown in Figure 4a. We were also able to measure the double frequency signal as shown in the close-up digital photograph the oscilloscope screen in Figure 4b. In order to assess repeatability

in coupling with this device we tried the same experiment on the second NZW rabbit which was considerably smaller than the first. We were able to weakly couple light through the anterior chamber but were not able to obtain a double frequency component. This was primarily a result of the inability of the coupling lens to accommodate for the smaller size of the rabbits eye. Based on these results a more flexible water filled coupling device is being designed and built.

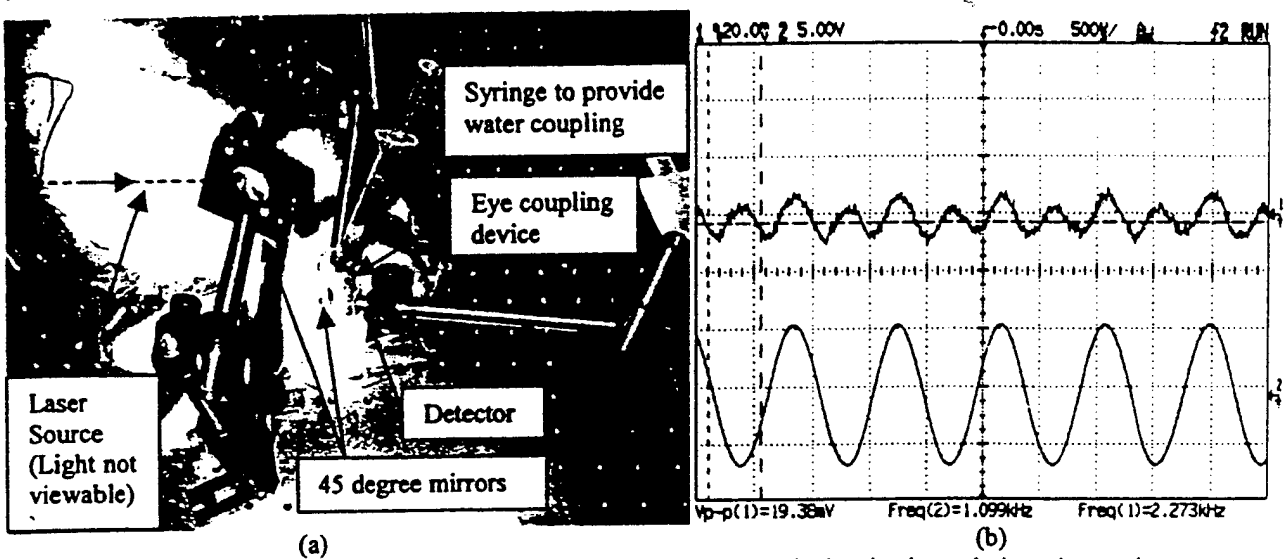

Figure 4: (a) Photograph of the rabbit with the initial eye coupling device in the polarimetric sensing system and (b) double sinusoidal frequency depicted on the oscilloscope indicating a functional nulled system along with the single frequency reference signal.

Specific Aim #3: Test the time lag between blood and aqueous humor glucose.

Over the next few months the tasks to accomplish this aim will begin. We will test the eye coupling design and re-design if required. Once the coupling device is working across several different sized rabbits and the three laser system is working *in vitro*, we will integrate the optical system with the coupling device and quantify the time lag *in vivo* (Previous work has indicated this to be on the order of minutes). Lastly, at the end of the first year and beginning in the second year with the time lag known we will test the sensitivity of the device to the accurate quantification of glucose *in vivo* in rabbits. As discussed below, throughout the second year the major aims are to perform studies on a small number of rabbits and redesign the system as required to get quantifiable results.

NM TB

NATIONAL MEDICAL TECHNOLOGY TESTBED

March 29, 1999

Gerald L Cote, Ph.D.
Texas A&M
Biomedical Engineering Program
332 Wisenbaker Rd.
College Station, TX 77843-3000

Re: Subagreement: #023-FY97-Texas A&M-Cote Second Quarterly Report

Dear Dr. Cote:

This letter will serve to inform you that your second quarterly report was approved on March 25, 1999, by National Medical Technology Testbed, Inc.'s Scientific Director.

Your next quarterly report will be due on May 6, 1999. Please contact Lydia Pearson, Contracts Administrator, at (909) 558.3244, with any questions you may have. Thank you for your assistance.

Sincerely,

Thomas J. Callanan
Administrative Director
TJC:mc

c Russell Brewer, Director
File

11165 Mountain View Avenue, Suite 121, Loma Linda, California 92354, Voice: 909/478-3244 Fax: 909/478-3254

Technical Progress Report – 2nd Quarter

SPONSOR:	National Medical Technology Testbed
PROGRAM:	Subcontract USAMC
GRANT NUMBER:	#023-FY97-TEXAS A&M-COTE
TITLE:	Noninvasive Glucose Sensing Using a Novel Optical Technique
Quarter:	November 6, 1998 – February 6, 1999
PI:	Gerard L. Coté

Texas A&M University, Texas Engineering Experiment Station, 301 WERC, College Station, TX 77843

I. Task Objectives:

The specific objectives of this one-year research project, as listed in the original proposal, are as follows:

Specific Aim #1: To minimize corneal birefringence artifacts due to eye motion and elucidate glucose concentration in the presence of other optically active molecules that vary in concentration.

Specific Aim #2: To design, implement and test a sensitive polarimeter that allows for coupling in and out of the eye.

Specific Aim #3: To measure the time delay between aqueous humor and blood glucose levels.

II. Description of Results from the second quarter

Specific Aim #1:

The first quarter for this aim were spent on developing a two laser system for elucidating glucose concentration in the presence of other optically chiral molecules while the focus of the three months in the second quarter under this aim was spent toward development of a laser system for characterization of the corneal birefringence. The aim of the study is to characterize the birefringence of a rabbit cornea *in vitro* and *in vivo,* in order to obtain qualitative as well as quantitative information of the birefringent properties of the cornea. The results from this study are also essential to better develop the mechanism to help compensate for variations in the corneal birefringence in the experiments performed for the *in vivo* detection of glucose in the aqueous humor of the rabbit cornea. The basic setup of this study is as shown in Figure 1. In order to fully characterize the birefringence and polarization of the light passing through the eye, we will be the first group to attempt to obtain all 16 elements of the 4×4 Mueller Matrix via 49 images acquired using various input and output polarization optics. These 49 images consist of combinations of Open (no optics), Linear(Horizontal / Vertical), +/- 45°, Right and Left Circular polarized light, at the input and output stage.

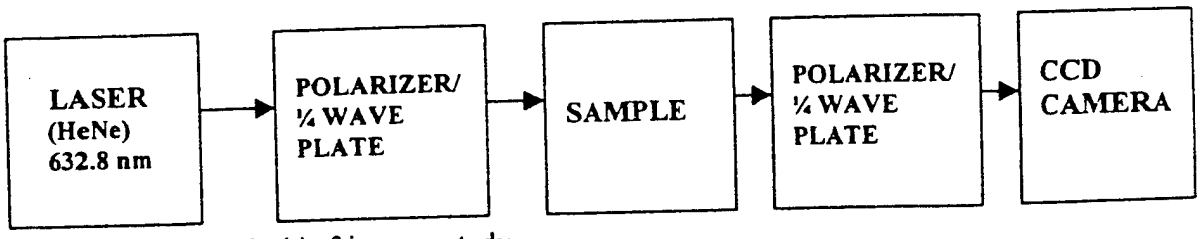

Figure 1: Basic setup for the birefringence study

As depicted, a Helium Neon laser (632.8nm wavelength and 6.5 mW output power), was used to provide a collimated input laser beam. As mentioned, the laser beam was polarized via various polarization optics, such as the polarizer (Polaroid), a ¼ wave plate and a cylindrical lens, to obtain the desired input polarization. The beam was then directed onto the sample. After passing through the sample, the beam is imaged through polarization analyzer optics (similar to the input polarizer and ¼ wave plate). A CCD Camera (16-bit, TE cooled) was then used at the final output stage to convert the optical images into electronic signals. The CCD array size was 338×244 and the pixel size was $10\times10\mu m^2$. The exposure time for the camera was set at .06sec.

Recently, we began our first set of experiments, in which the sample used was water, which is known to have zero birefringence. This was done in order to obtain a set of reference images. The results from these initial experiments showed that since the power of the laser source was high (6.5mW), the camera would become saturated and thus affect the quality of the images. The saturation of the camera was greatly reduced by using a Neutral Density Filter (1% transmission) at the input stage. However, this has not completely eliminated the problem. Hence the optimal neutral density filter and exposure time of the camera for improving the image quality are currently being determined.

Once the saturation problem is overcome an image of a material with known birefringence (¼ wave plate) will be acquired in the next quarter. These images will be taken in order to draw a comparison between the birefringent and non-birefringent samples. In the third set of experiments, excised rabbit eyes will be used as the sample. The eye coupling device described under specific aim 2 below will be used to hold the cornea in proper position. A cylindrical lens will placed after the laser, in order to pass a laser beam with a horizontal profile through the cornea. This will enable us to study the birefringence at different points along the same plane or level in the cornea. We expect to see a variation in the birefringence pattern, as we move from the center of the cornea to the periphery. It is already known that the birefringence at the center of the cornea is approximately zero and increases at the edges. Therefore, this information will be used to qualitatively verify proper functioning of our system *in vivo*.

Specific Aim #2:

Over the first quarter an initial eye coupling device was built and tested on two New Zealand White (NZW) rabbits. Using the first NZW rabbit the results were positive, in that we were able to couple light through the aqueous humor *in vivo*. In order to assess repeatability in coupling with this device we tried the same experiment on the second NZW rabbit which was considerably smaller than the first. We were able to weakly couple light through the anterior chamber but were not able to obtain a double frequency component. This was primarily a result of the inability of the coupling lens to accommodate for the smaller size of the rabbits eye. The eye coupling mechanism also had several other inherent problems. For instance, excessive negative pressure was needed to bring the eye up into the device resulting in eye trauma. In addition, the eye would often become tilted in the device making the coupling of light through the anterior chamber difficult. Lastly, the plastic lens used in the original design was extremely birefringent. In order to address these issues, the eye coupling mechanism was redesigned to eliminate these inherent problems. The newly designed device is shown in Figure 2.

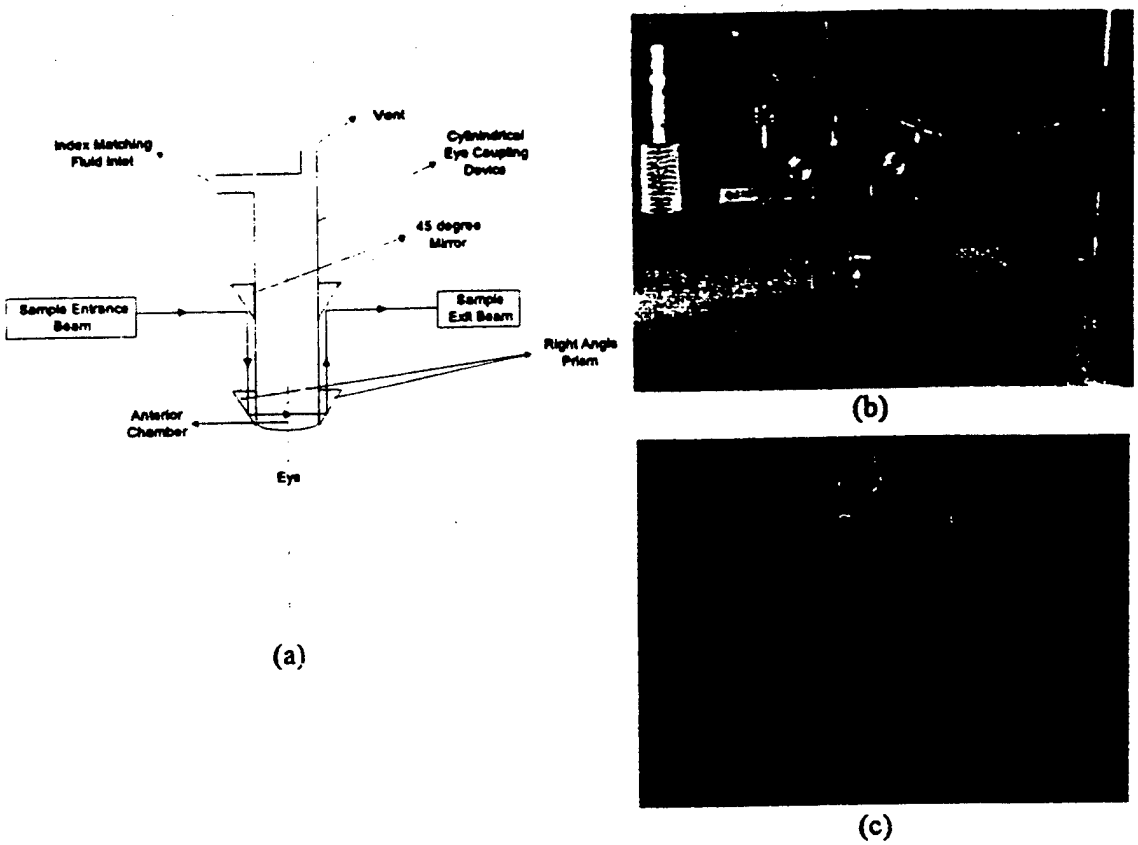

Figure 2: (a) Block diagram of the newly designed rabbit eye coupling device. (b) Image of the eye coupling device. (c) Eye coupling device used with a rabbit showing the laser passing through the aqueous humor.

This coupling mechanism consists of an open ended cylindrical glass shaft that is placed over the cornea. The shaft has two ports, one port allows saline to be injected into the cylinder and the other port acts as a vent to equalize the inside pressure to that of the atmosphere. The saline acts as an index matching fluid allowing light to propagate in a straight path through the anterior chamber. The input laser beam is coupled through the eye by first reflecting off a 45° mirror mounted on the device. This beam then enters a right angle prism at the base of the device. The prism acts as a flat optical window into the inner chamber of the shaft. The beam then propagates through the anterior chamber of the eye and exits the device via another right angle prism. The exit beam is then reflected upward to a second 45° mirror that reflects the light toward the analyzer/detector.

The newly designed device was tested on 4 rabbits across 6 days with two rabbits tested twice, and has yielded a more repeatable and stronger signal (depicted in Figure 3) than the previous apparatus. There was some long term drift detected which appeared to be a result of the large beam diameter which manifests itself as birefringence due to motion artifact of the sample and fluctuations across the face of the detector. This was minimized by aperturing the input beam to a pinpoint collimated beam.

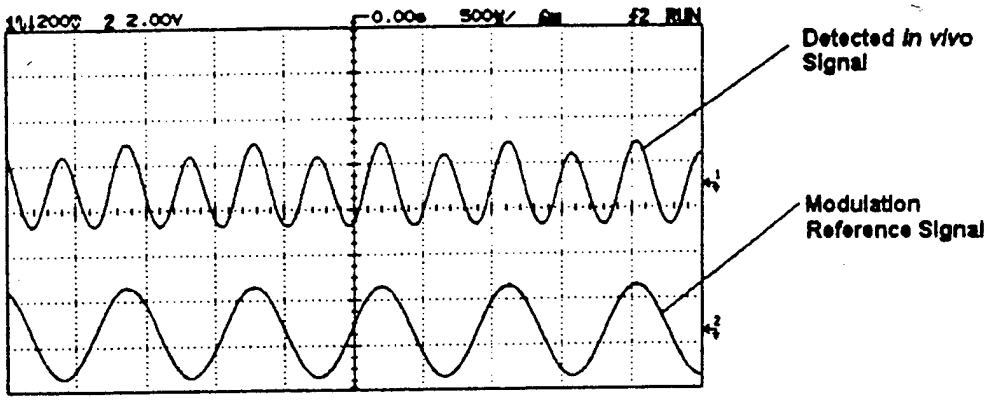

Figure 3. *In vivo* detected polarimetry signal

Specific Aim #3:

Given the new eye coupling design and pinpoint collimation developed in this quarter preliminary testing to characterize the time delay between blood and aqueous humor glucose levels has recently begun. In order to characterize the time delay, initially a concentrated bolus injection of glucose was given through the stomach. However, this often resulted in a gross movement artifact upon administering the injection, interrupting the course of the experiment. Thus, an intravenous infusion of a 5% solution of dextrose was investigated. Within the first 5 minutes of infusion, a blood glucose reading was obtained. It was observed that within this time blood glucose levels were already greater than 300 mg/dl and over the course of 40 minutes raised to just over 400 mg/dL. This problem has been tracked down to the drug Xylazine, which is part of our anesthesia protocol and was found to elevate glucose by over 200 mg/dL over a one hour period. This property of Xylazine, is thus being investigated as a mechanism to bypass glucose injections in normal rabbits. It will be administered after the eye coupling device has been placed on the rabbit and may provide a convenient method of raising blood glucose to considerably elevated levels in a short period of time.

We will use the new eye coupling design and protocol over the next six months to quantify the time lag *in vivo* by varying the glucose concentration and monitoring the blood glucose with standard meter technology. These measurements will be compared to the reading of the aqueous humor glucose level utilizing the single laser system. Beginning in the second year, with the time lag known, we can then combine the multi-wavelength system with the eye coupling device to demonstrate the sensitivity of the device to the accurate quantification of glucose *in vivo* in rabbits.

NM TB

NATIONAL MEDICAL TECHNOLOGY TESTBED

June 9, 1999

Gerald L Cote, Ph.D.
Texas A & M University
Biomedical Engineering Program
233 Zachry Building
College Station, TX 77843-3120

Re: Approval of Quarterly Report

Dear Dr. Cote:

This letter will serve to inform you that your third quarterly report under Subcontract #023-FY97-Texas A&M-Cote was approved on June 3, 1999, by National Medical Technology Testbed, Inc.'s Scientific Director. We would like to remind you that your fourth report is due on August 16, 1999.

Please contact Lydia Pearson, our Contracts Administrator, at (909) 558.3244, if you have any questions regarding this letter.

Sincerely,

Thomas J. Callanan
Administrative Director
TJC:lmp

c: Russell Brewer

11165 Mountain View Avenue, Suite 121, Loma Linda, California 92354, Voice: 909/478-3244 Fax: 909/478-3254

Technical Progress Report – 3rd Quarter

SPONSOR:	National Medical Technology Testbed
PROGRAM:	Subcontract USAMC
GRANT NUMBER:	#023-FY97-TEXAS A&M-COTE
TITLE:	Noninvasive Glucose Sensing Using a Novel Optical Technique
Quarter:	February 7, 1999 – May 5, 1999
PI:	Gerard L. Coté

Texas A&M University, Texas Engineering Experiment Station, 301 WERC, College Station, TX 77843

I. Task Objectives:

The specific objectives of this one-year research project, as listed in the original proposal, are as follows:

Specific Aim #1: To minimize corneal birefringence artifacts due to eye motion and elucidate glucose concentration in the presence of other optically active molecules that vary in concentration.

Specific Aim #2: To design, implement and test a sensitive polarimeter that allows for coupling in and out of the eye.

Specific Aim #3: To measure the time delay between aqueous humor and blood glucose levels.

II. Description of Results from the third quarter

Specific Aim #1:

The first quarter for this aim were spent on developing a two laser system for elucidating glucose concentration in the presence of other optically chiral molecules while the focus of the in the second quarter under this aim was spent toward design and initial development of a laser system for characterization of the corneal birefringence. In the third quarter results were obtained with the designed system and compared to the theory for a known birefringent material (quarter waveplate). To re-iterate from the last report, the aim of the study is to characterize the birefringence of a rabbit cornea *in vitro* and *in vivo,* in order to obtain qualitative as well as quantitative information of the birefringent properties of the cornea. The results from this study are essential to better develop the mechanism to help compensate for variations in the corneal birefringence in the experiments performed for the *in vivo* detection of glucose in the aqueous humor of the rabbit cornea. The basic setup of this study is as shown in Figure 1. In order to fully characterize the birefringence and polarization of the light passing through the eye, we will be the first group to attempt to obtain all 16 elements of the 4x4 Mueller Matrix via 49 images acquired using various input and output polarization optics. These 49 images consist of combinations of Open (no optics), Linear(Horizontal / Vertical), +/- 45°, Right and Left Circular polarized light, at the input and output stage. The optical setup used to characterize birefringence is shown in Figure 1. The light source was a uniform intensity beam obtained from a tungsten halogen lamp whose intensity was reduced using a neutral density filter (1% Transmission). Various input polarization states were obtained through different orientations of polarization optics which included either a sheet polarizer, a ¼ wave plate, or both. This beam was then directed onto the sample. After passing through the sample, the beam was imaged through

polarization analyzer optics (similar to the input stage) using a 16-bit, TE cooled CCD camera. The CCD array size was 338×244 and the pixel size was $10\times10\mu m^2$.

In the experiments performed in the second quarter the images were saturated, requiring the selection of an optimal neutral density filter and exposure time. In this third quarter, our first set of experiments used an exposure time of 0.01 seconds and neutral density filter of 1% transmission for the quarter waveplate sample which eliminated the saturation problem. The quarter waveplate was selected as the sample because it has known birefringence properties which could be used as a reference in order to obtain a set of 16 Mueller matrix images and then be compared to simulated theoretical image set. The results from these experiments are shown in Figure 2.

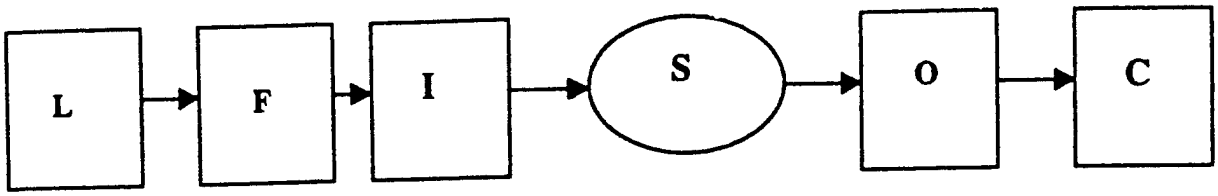

Figure 1: Optical Setup- L: Tungsten Halogen lamp, F: Neutral Density Filter, I: Input Polarizing Optics, S: Sample, O: Output Polarizing Optics, C: CCD camera.

In order to verify the operation of the experimental system, two of the Mueller elements (no polarization optics, s11, and a combination of horizontal and vertically aligned input and output optics s22, $[hh_{in}+vv_{out}]-[hv_{in}+vh_{out}]$) were calculated theoretically and obtained experimentally for the sample quarter waveplate rotated to +45°. Figure 2 shows the theoretical and experimental images obtained for each of the two elements of the Mueller Matrix. The experimental images have been cropped to remove the mounting apparatus and show the uniform intensity in the center of the quarter waveplate. As expected, the element s11 shows a higher intensity due to the absence of input and output polarization optics. The element s22 shows a lower intensity in the experimental setup, due to the presence of the input and output polarization optics. All 16 elements of the Mueller matrix were calculated theoretically, and the 49 images required for recreating the Mueller matrix from the experimental data are still being collected.

We are now beginning a new set of experiments using excised rabbit eyes as the sample. Initially the excised rabbit eye was placed in a simple holder, which in turn was placed in a glass (non birefringent) cuvette with parallel sides. However, many problems were encountered while collecting the images, due to the tilting of the eye and floating of the eye in the saline solution. This hindered the process of focussing at the same region for different orientations of the input and output polarization optics, which in turn provided incorrect analysis. Thus, an eye coupling device was designed, as depicted in Figure 3, in order to hold the cornea in proper position. In this setup being used to mount the rabbit eye, the holder is screwed firmly on to the glass cuvette, preventing it from floating in the saline solution. Also, in order to hold the eye in place, negative pressure is applied via a tiagon tubing, one end of which is connected to the bottom of the holder and the other to a syringe.

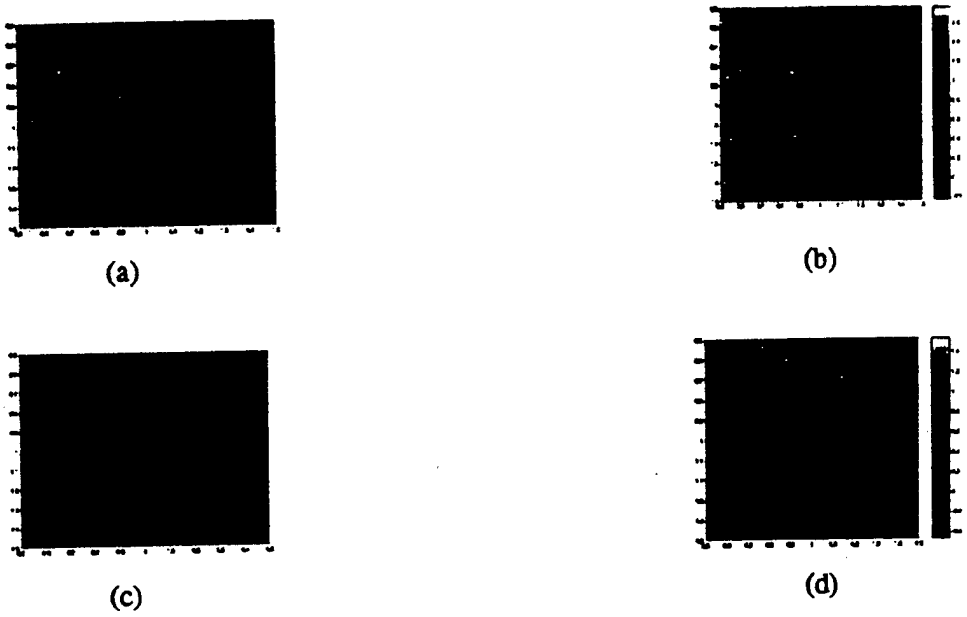

Figure 2: (a) and (b) show the theoretical and experimental images obtained for the Mueller element s11 (no polarization optics). In (b) the dark background is seen due to the imaging of the background (1/4 wave plate mount) as well. (c) and (d) show the theoretical and experimental images obtained for the element s22([hh+vv]-[hv+vh]). As can be seen from the color bar the intensity is almost zero.

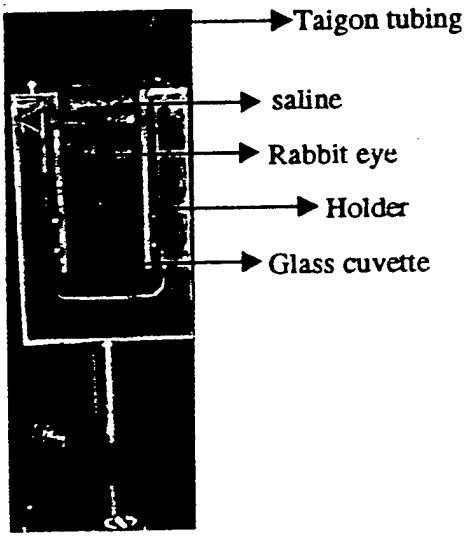

Figure 3: Rabbit eye holder for in vitro experiments on corneal birefringence characterization.

In the second set of experiments, images were obtained of a rabbit cornea for the case of no polarization optics and compared with the image for the crossed polarization state. As expected, the image for the crossed state showed varying intensity (birefringence) along the edges of the cornea and almost zero intensity at the apex (Figure 4).

(a) (b)

Figure 4 : (a) Image of rabbit cornea with no input and output polarizers. (b) Image of the rabbit cornea for the crossed state of input and output polarizers.

The in depth analysis of the birefringence in the rabbit cornea is in the initial stage. The results obtained from the first set of experiments on the rabbit cornea were promising and enables us to direct the research towards obtaining the 49 images of the rabbit cornea for different orientations of the input and output polarization optics. These 49 images will then be used to calculate the 16 Mueller elements, which will provide the required quantitative characterization of the corneal birefringence.

Specific Aim #2:

Over the first quarter an initial eye coupling device was built and tested on two New Zealand White (NZW) rabbits. Using the first NZW rabbit the results were positive, in that we were able to couple light through the aqueous humor *in vivo*. In order to assess repeatability in coupling with this device we tried the same experiment on the second NZW rabbit which was considerably smaller than the first. We were able to weakly couple light through the anterior chamber but were not able to obtain a double frequency component. This was primarily a result of the inability of the coupling lens to accommodate for the smaller size of the rabbits eye. The eye coupling mechanism also had several other inherent problems. For instance, excessive negative pressure was needed to bring the eye up into the device resulting in eye trauma. In addition, the eye would often become tilted in the device making the coupling of light through the anterior chamber difficult. Lastly, the plastic lens used in the original design was extremely birefringent. In order to address these issues, in the second quarter the eye coupling mechanism was redesigned to eliminate these inherent problems. The newly designed device was a main focus of the second quarter report. It was tested on 4 rabbits across 6 days with two rabbits tested twice, and yielded a more repeatable and stronger signal than the previous apparatus. There was some long term drift detected which appeared to be a result of the large beam diameter which manifests itself as birefringence due to motion artifact of the sample and fluctuations across the face of the detector. This was reduced by aperturing the input beam to a pinpoint collimated beam. However, there is still some motion artifact during the polarimetric measurement of glucose, in which spatial variations in birefringence of the cornea mask the small rotations due to physiologic glucose levels. Therefore, one task specific to this quarter was to identify the main source of the motion artifact and to develop a mechanism to eliminate or reduce its effect.

To achieve this task we chose to continuously monitor the double frequency component of the detected polarimetric signal during the course of two rabbit experiments. The overall detected signal is modeled by the following equation:

$$I \propto E^2 = \left(\phi^2 + \frac{\theta_m^2}{2} \right) + 2\phi\theta_m \sin(\omega_m t) - \frac{\theta_m^2}{2}\cos(2\omega_m t).$$

The nomenclature is as follows: the net rotation (ϕ) is equal to ϕ_s- ϕ_f where ϕ_f is the rotation in polarization due to the compensation Faraday rotator, ϕ_s is rotation due to the optically active sample, θ_m is the modulation depth, ω_m is the modulation frequency, and t is time. As can be seen, the double frequency component is not a function of glucose rotation and this is the reasoning behind it not being used as part of the controller input. However, any motion artifact resulting in variations of birefringence will be directly superimposed on this term. Therefore, the overall amplitude this term is especially suited for directly monitoring motion artifact.

Through the use of a digital lock-in amplifier, the amplitude of the double frequency term (2nd harmonic) was continuously monitored during the course of two rabbit experiments. A partial time series of the amplitude of the 2nd harmonic term during the course of an *in vivo* polarimetric experiment is presented below:

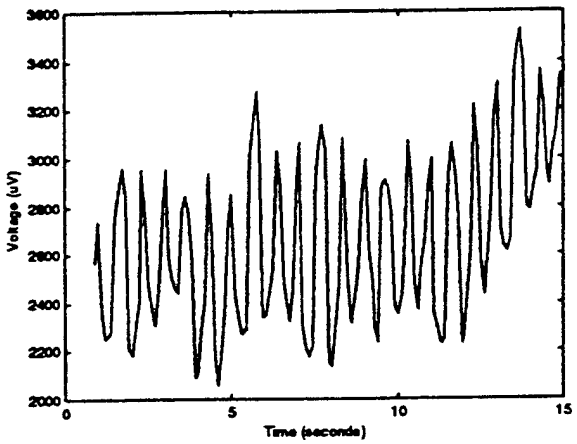

In ideal circumstances (i.e no motion artifact), the overall amplitude of the 2nd harmonic term should be constant. Therefore, in the ideal case, the above plot should merely consist of a horizontal line since the lock-in amplifier outputs a DC value proportional to the amplitude of the signal of interest. However, as can be seen, the overall amplitude of the 2nd harmonic term varies periodically as a function of time. The motion artifact is specifically the cause of these variations. Therefore, we wanted to determine the specific frequencies present in the oscillations of the discrete time series in order to isolate the main sources of the motion artifact. To achieve this task, spectral analysis utilizing the fast Fourier transform was performed on the full discrete time series to determine the relative energy present as a function of frequency. The following is the corresponding energy spectral analysis plot:

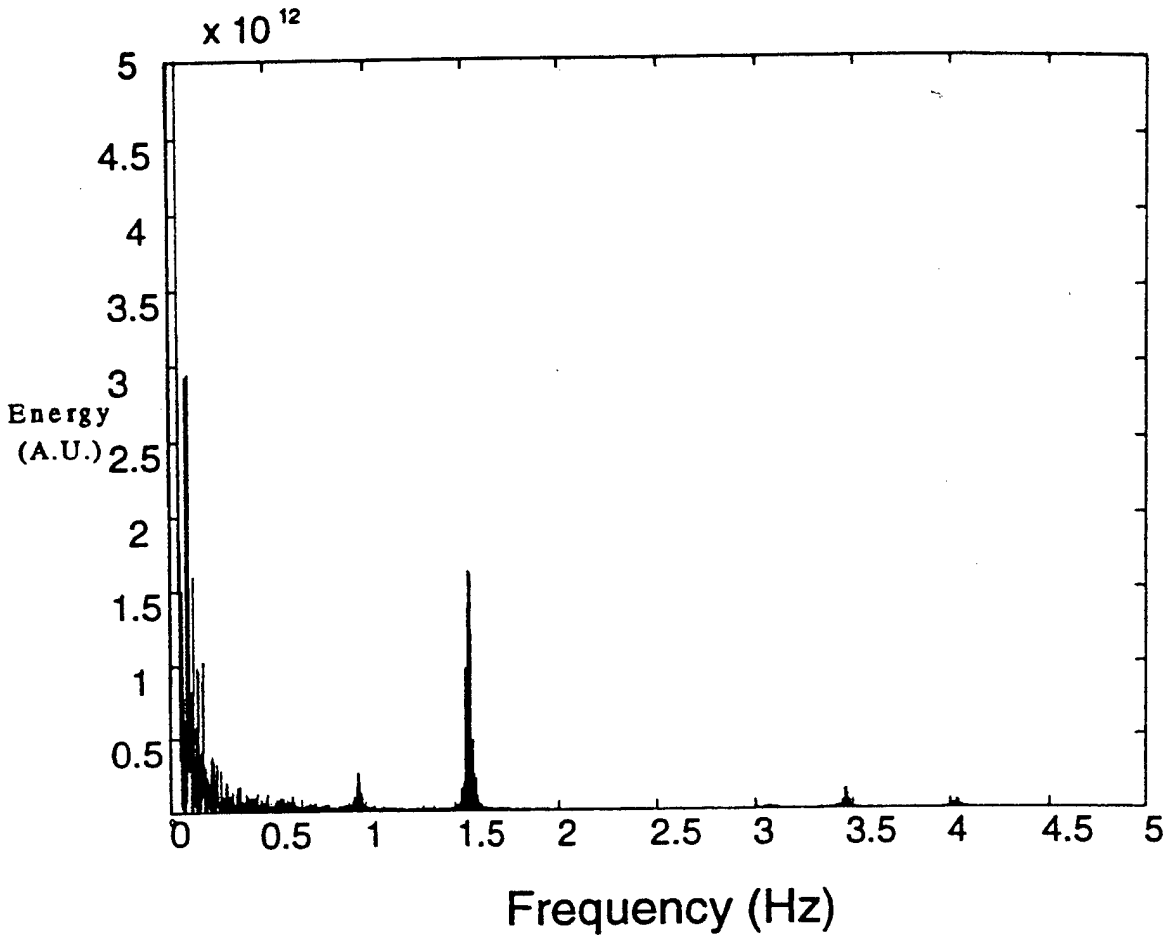

Ideally in an anesthetized rabbit model in which the rabbit is lying on its side, possible motion sources include breathing and the cardiac cycle. In a human patient, presumably monitoring upright, these artifacts should be less than in the rabbit model. These artifacts occur at approximately 60-100 breaths/min and 200-300 beats per minute, respectively. In terms of cycles per second (Hz), these correspond to 1 to 1.7 Hz (breathing) and 3.3 to 5 Hz (cardiac). As can be seen in above spectral analysis plot, the largest peak occurs at roughly 1.6 Hz, corresponding to breathing. Other high frequency peaks also occur past 3.4 Hz which probably are due to the cardiac cycle. In addition, the peak near 0 Hz is due to the average value of the 2nd harmonic signal that manifests itself as a DC component, as mentioned previously.

Therefore, confirming the major motion sources, we are currently in the process of constructing a mechanism to help reduce the transmission of motion due to respiratory and the cardiac cycle to the eye (the site of polarimetric testing). This device consists of a form fitting body cast to help reduce overall body movements, as well as a head fixation device. Specifically, the head fixation device consists of a plate positioned over the head of the rabbit. This plate holds numerous adjustable fixation pins that come in contact with the head to hold it in place. We are currently in the process of testing the effectiveness of this device.

Specific Aim #3:

As described previously, preliminary testing to characterize the time delay between blood and aqueous humor glucose levels has begun but with no quantifiable results to date. As reported, we did find that a bolus infusion in the stomach produced to much motion artifact to obtain a good measurement and that the anesthetic drug inhibits glucose uptake artificially elevating the glucose level as high as 450 mg/dL. This property of Xylazine, is thus being investigated as a mechanism to be used in conjunction with glucose injections in normal rabbits. It will be administered after the eye coupling device has been placed on the rabbit and may provide a convenient method of raising blood glucose to considerably elevated levels in a short period of time. With these results, in addition to the new eye coupling device and the new fixation device, the focus this quarter will be to quantify this time delay.

NATIONAL MEDICAL TECHNOLOGY TESTBED

September 28, 1999

Gerald L Cote, Ph.D.
Texas A & M University
Biomedical Engineering Program
233 Zachry Building
College Station, TX 77843-3120

Subject: Approval of Quarterly Report for Subcontract No. 023-FY97-TEES-Cote

Dear Dr. Cote:

This letter will serve to inform you that your fourth quarterly report has been approved by National Medical Technology Testbed, Inc.'s Scientific Director. We would like to remind you that your next report is due November 16, 1999 and should cover the first three months of your extension period.

Please contact Lydia Pearson, our Contracts Administrator, at (909) 558.6184, if you have any questions regarding this letter.

Sincerely,

Thomas J. Callanan
Administrative Director
TJC:lmp

c Russell Brewer, Contracting

11354 Mountain View Avenue, Suite D, Loma Linda, California 92354, Voice: 909/558-6184 Fax: 909/558-6200

Technical Progress Report – 4th Quarter

SPONSOR:	National Medical Technology Testbed
PROGRAM:	Subcontract USAMC
GRANT NUMBER:	#023-FY97-TEXAS A&M-COTE
TITLE:	Noninvasive Glucose Sensing Using a Novel Optical Technique
Quarter:	May 6, 1999 – August 6, 1999
PI:	Gerard L. Coté

Texas A&M University, Texas Engineering Experiment Station, 301 WERC, College Station, TX 77843

I. Task Objectives:

The specific objectives of this one-year research project, as listed in the original proposal, are as follows:

Specific Aim #1: To minimize corneal birefringence artifacts due to eye motion and elucidate glucose concentration in the presence of other optically active molecules that vary in concentration.

Specific Aim #2: To design, implement and test a sensitive polarimeter that allows for coupling in and out of the eye.

Specific Aim #3: To measure the time delay between aqueous humor and blood glucose levels.

II. Description of Results from the fourth quarter

Specific Aim #1:

The fourth quarter for this aim was concentrated on developing a sensitive multi-spectral polarimeter capable of experimentally measuring the optical rotatory dispersion (ORD) spectra (i.e. specific rotation versus wavelength) of common optically active components present in the aqueous humor that are not available in literature. This step is needed to further characterize the specific wavelengths that would be required to make a long-term polarimetric *in vivo* glucose sensor feasible (i.e. a sensor that can predict glucose concentration in the presence of other optically rotatory components that fluctuate in concentration over long-periods of time).

The basic instrumentation setup designed and constructed to measure the ORD spectra is depicted in Figure 1. This system utilizes a white light source in conjunction with a monochromator to provide a multi-spectral light source. The input wavelength into the polarimetric system is determined via computer control of the orientation of the diffraction grating present in the monochromator. The input beam is polarized via a linear polarizer and modulated sinusoidally by a Faraday rotator. The beam passes through a 5 cm optical sample cell and the modulation of the polarization vector is converted to intensity modulation via the analyzer (simply another polarizer with its transmission axis normal to the initial polarizer). A lock-in amplifier measures the component of the detected signal at the modulation frequency, which is proportional to the optical rotation due to the sample. A program was written in LabVIEW 5.1 to automate the procedure of collecting ORD spectra, involving serial control of the input

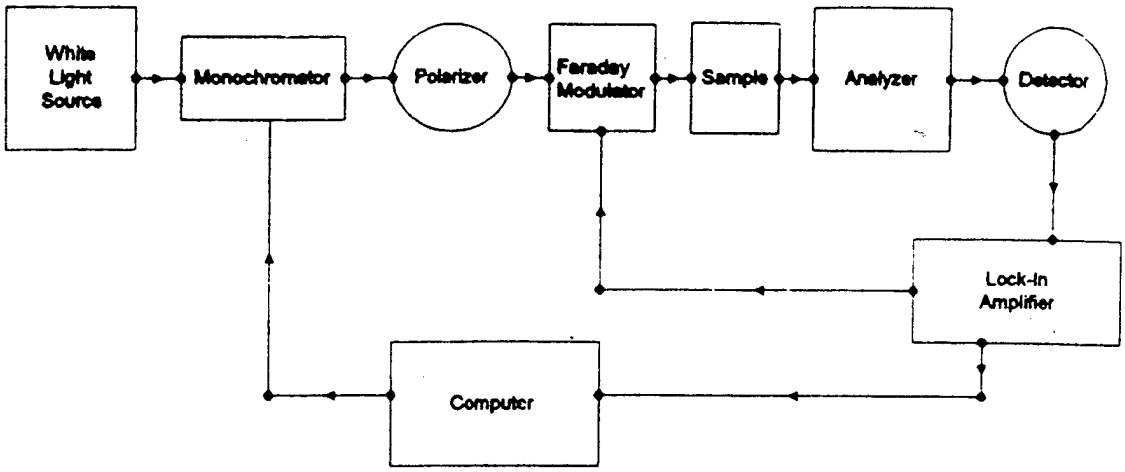

Figure 1: Optical rotatory dispersion measurement setup

wavelength and acquisition of the signal component at the modulation frequency via a general purpose interface bus. In order to compute the ORD curves, the overall system response is measured with a water reference and divided out to obtain the ORD spectrum. All rotation spectra are calibrated to the known specific rotation of glucose at the sodium D-line (589 nm). Specific rotation for a given sample is then computed via the equation:

$$[\alpha] = \frac{\alpha}{LC} = \frac{kV}{LC}$$

Where $[\alpha]$ is the specific rotation, α is the observed rotation, k is a factor to convert the detected voltage (V) into the observed optical rotation, L is path length, and C is the concentration of the sample. At present, glucose and the main optically active confounder present in aqueous humor, albumin, were measured. The respective ORD curves are shown in Figure 2a. As can be seen, albumin rotates light opposite to glucose. When the actual rotation due to the normal physiological concentrations of glucose and albumin are considered, 100 mg/dl and 6 mg/dl, respectively, for the approximate 1 cm path length of the eye, the rotation due to albumin is negligible in comparison to glucose, as shown in Figure 2b. We are currently in the progress of characterizing the ORD curves of the other optically active components found in the aqueous humor and utilizing statistical methods to determine the optimal and minimal set of wavelengths needed for accurate *in vivo* glucose prediction.

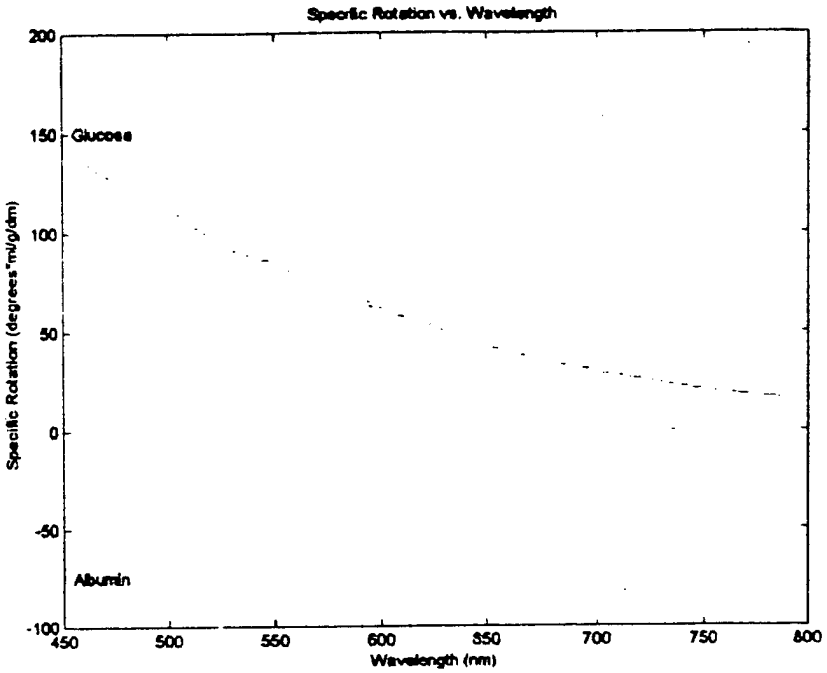

Figure 2a: ORD spectra for glucose and albumin

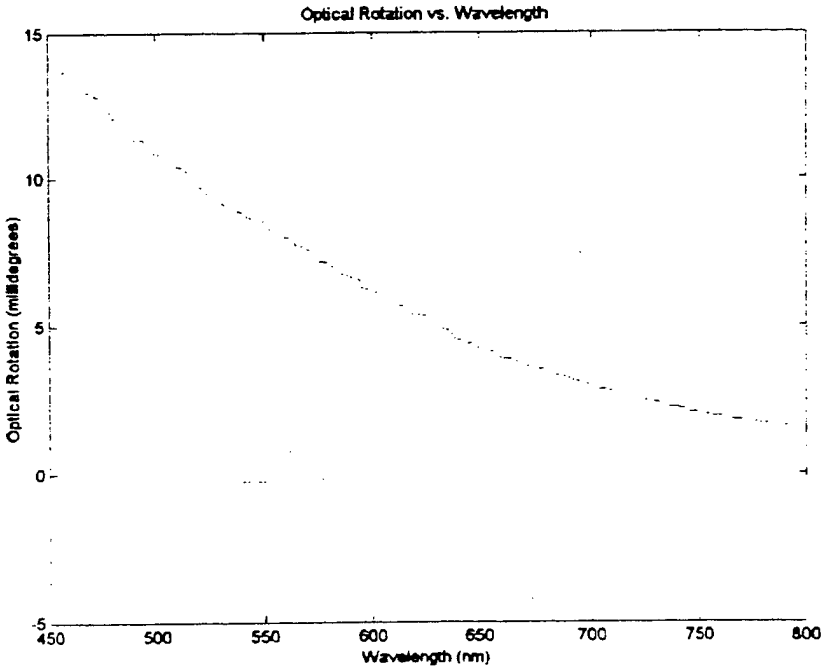

Figure 2b: Optical rotation of glucose and albumin at physiological aqueous humor concentration (Red-Glucose) (Green – Albumin)

Specific Aim #2:

As reported in the third quarter report, spectral analysis of the acquired time-based *in vivo* polarimetric signal at the modulation frequency revealed possible sources of motion artifact (including respiratory and cardiac cycles) resulting in a masking of the glucose signature. Therefore, the goal of this quarter was to specifically identify the sources of motion artifact and minimize their effects. To achieve this goal, a real-time spectral analyzer was created utilizing LabVIEW 5.1 and an A/D board to compute the spectral response during the course of the animal studies. This allowed online monitoring of the performance of modifications made during the course of the *in vivo* experiment for motion artifact reduction. These studies consisted of five *in vivo* experiments.

As indicated in the third quarter report, motion artifact due to the respiratory cycle was singled out as the most probable source. Therefore, the goal of this quarter was to confirm that respiration was the major source of motion artifact and to investigate various means to minimize its effects. The first three experiments performed this quarter were concentrated on developing a mechanism to reduce these effects. It was originally thought that motion from the lower body due to breathing was resulting in slight head movements, leading to the observed variations in the detected signal. Initially, the lower body was placed in a form fitting half-body cast and a belt-type system was fixated to the optics table and placed over the upper chest area of the rabbit. The belt was tightened to a point such that normal breathing was not affected. In the spectral analyses, no noticeable differences were observed. In the second experiment, a shoulder fixation plate was tested. The plate did reduce the transmittance of motion from the lower body to the head, however, significant motion artifact corresponding to the respiratory cycle was still observed. In the third experiment, in addition to the previous fixation methods, a rod and pin fixation device was utilized. No noticeable differences in the detected signal were observed, and the device caused slight stretching of the facial skin resulting in movements in the eye/coupling device. This led to leaking of the index matching fluid used to couple the light through the anterior chamber of the eye and beam alignment problems. Upon further investigation, the majority of the motion artifact due to respiration seems to be caused by slight eye movements resulting from the eye being located anterior to the nasal passage.

The last experiment performed investigated the use of a two-detector system, as depicted in the Figure 3. Such a system could possibly compensate for polarimetric measurements in the presence of motion artifact via a differencing technique. In conjunction with monitoring the single frequency terms present on both detectors, a bladder type respirometer was constructed to monitor breathing. As can be seen in Figure 4, motion artifact due to respiration is shown as the red trace. The artifact in the polarization signal due to breathing is clearly superimposed on both detected signals (blue and green traces). Other higher frequency motion artifact, possibly due to the cardiac cycle, is also observed in the detected signals. One possible mechanism to reduce the effects of respiration, as well as other motion artifacts, could be accomplished via a differencing technique, in which the difference between the two detectors is utilized or via real-time filtering techniques to remove the breathing artifact. These are currently under evaluation.

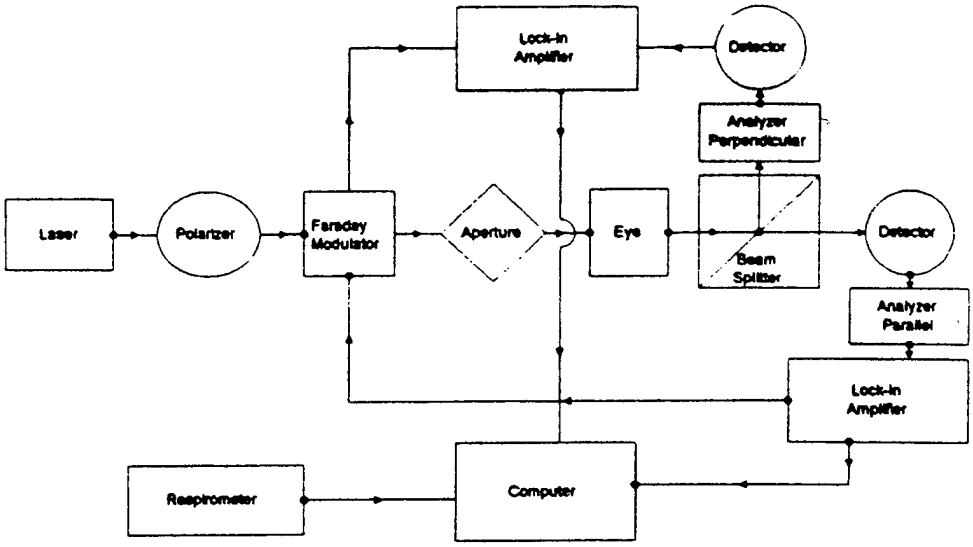

Figure 3: Block Diagram of a the two-detector system

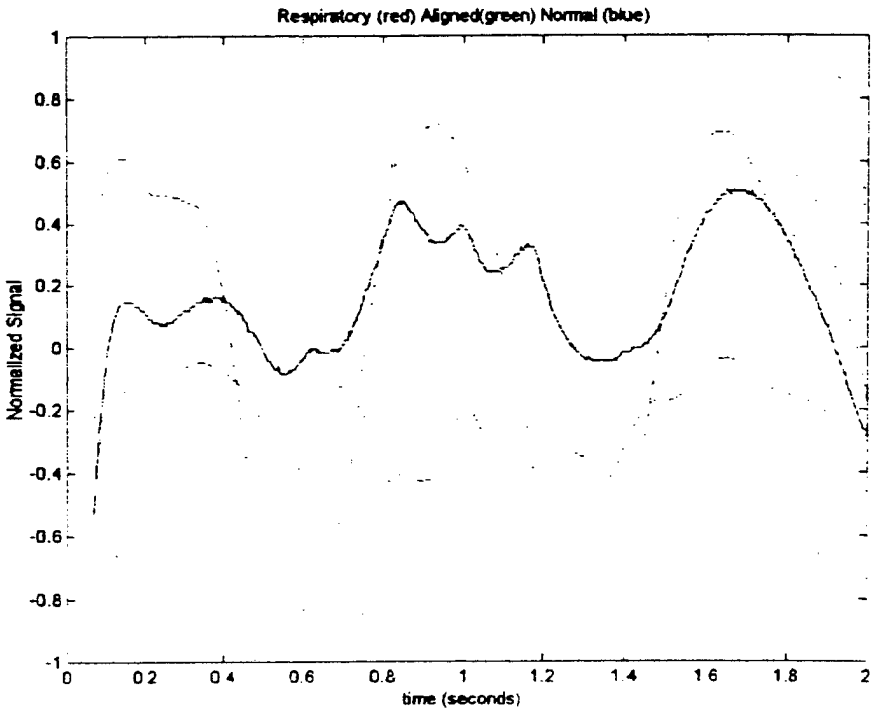

Figure 4: *In vivo* detected signals using the two detector system.
Red – respiratory signal
Blue – Normal Analyzer
Green – Parallel Analyzer

Specific Aim #3:

In an effort to reach this objective, we are investigating alternative methods to eliminate motion artifact in addition to the modifications discussed as part of specific aim #2. The ability to intubate the lungs to bypass the nasal passage has been requested as an amendment to the current animal protocol. In addition, the investigators have scheduled training sessions for this procedure. Upon approval, this method will be investigated as a means to reduce the observed motion artifact. Although this is a somewhat invasive procedure, it potentially has the ability to eliminate the majority of the motion artifact due to breathing. This potentially will enable the successful completion of this aim and aid in the proof of concept. Work on the polarimetric measurement of glucose in the presence of motion artifact will also continue to make an *in vivo* sensor more feasible.

NMTB

February 22, 2000

Gerald L Cote, Ph.D.
Texas A & M University
Biomedical Engineering Program
233 Zachry Building
College Station, TX 77843-3120

Subject: Approval of Quarterly Report for Subcontract No. 023-FY97-TEES-Cote

Dear Dr. Cote:

This letter will serve to inform you that your fifth quarterly report has been approved by National Medical Technology Testbed, Inc.'s Scientific Director. We would like to remind you that your final report is due March 28, 2000.

Please contact Lydia Pearson, our Contracts Administrator, at (909) 558.6184, if you have any questions regarding this letter.

Sincerely,

Thomas J. Callanan
Administrative Director
TJC:lmp

c Russell Brewer, Contracting

National Medical Technology TestBed
11554 MOUNTAIN VIEW AVE., SUITE D, LOMA LINDA, CA 92354 • TELEPHONE (909) 558-6184 FACSIMILE (909) 558-6200

Technical Progress Report – 5th Quarter

SPONSOR:	National Medical Technology Testbed
PROGRAM:	Subcontract USAMC
GRANT NUMBER:	#023-FY97-TEXAS A&M-COTE
TITLE:	Noninvasive Glucose Sensing Using a Novel Optical Technique
Quarter:	August 6, 1999 – November 6, 1999
PI:	Gerard L. Coté

Texas A&M University, Texas Engineering Experiment Station, 301 WERC, College Station, TX 77843

I. Task Objectives:

The specific objectives of this one-year research project, as listed in the original proposal, are as follows:

Specific Aim #1: To minimize corneal birefringence artifacts due to eye motion and elucidate glucose concentration in the presence of other optically active molecules that vary in concentration.

Specific Aim #2: To design, implement and test a sensitive polarimeter that allows for coupling in and out of the eye.

Specific Aim #3: To measure the time delay between aqueous humor and blood glucose levels.

II. Description of Results from the fifth quarter

Specific Aim #1:

The optical system, originally discussed in the second quarterly report, designed to characterize corneal birefringence involved the manual adjustment of the polarization optics. These optical components had to be adjusted in 49 different combinations throughout the experiment in order to compute the Mueller matrix of the sample. As a result, the entire process of collecting the 49 images, for any given sample, took approximately 3-5 hours. In addition, with so many degrees of freedom in the experimental setup, such as rotating the optics through different angular orientations, it was extremely difficult to replicate measurements for a given sample, especially, when trying to characterize the variations in birefringence expected for the cornea. Therefore, a portion of this quarter was spent designing and constructing a new experimental setup that employs electro-optic polarization components to reduce the previously mentioned difficulties, primarily the collection time.

The automated system designed and implemented is depicted in the block diagram below:

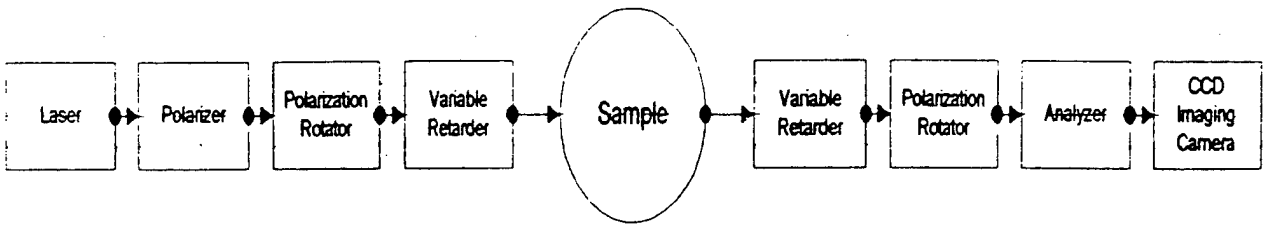

The polarizer and the analyzer are fixed with their transmission axes oriented vertically throughout the experiment. Both polarization rotators and variable retarders are controlled electrically by changing the applied voltage to the device. This allows for very precise control of all the combinations of input and output polarizations needed to reconstruct the Mueller matrix of the sample. It takes approximately 20 ms to adjust the electro-optic components versus the manual case in which it takes several minutes to adjust the polarization components for each of the 49 combinations. Therefore, in the final automated system, the Mueller matrix of the sample can be measured in a matter of seconds versus the 3-5 hours needed for the manual system. In addition, such an automated imaging system could allow for the extraction of optical rotation due to glucose, regardless of the variations in corneal birefringence due to motion artifact. Currently, we are in the final implementation/calibration stages of this device and will finalize the investigation of the birefringent structure of the cornea within the final quarter.

Specific Aim #2:

The fifth quarter for this aim was concentrated on verifying the sensitivity of the current polarimeter for *in vivo* physiologic glucose detection and on furthering the reduction of the effects caused by motion artifact. In order to test the *in vivo* sensitivity of the current polarimetric system, we employed a Faraday based electro-optic polarization rotator driven in DC mode. This device is used to impose an optical rotation on the order of that expected for physiological glucose levels during the course of an *in vivo* experiment. This makes it possible to control the rotational variations, thus providing an "artificial" glucose signal or "pseudo-glucose" signal, in which we can now manually control the "concentration" of the pseudo-glucose signal at our discretion during the presence of eye motion artifact. Throughout the extensive *in vitro* experiments we have conducted, for 635 nm laser light, it has been shown that a 40 mV DC-voltage applied to the Faraday rotator corresponds to the rotation caused by a 100 mg/dl glucose sample through a 1 cm path length. For example, the application of 40 mV to the Faraday rotator corresponds to 100 mg/dl, 80 mV → 200 mg/dl, 120 mV → 300 mg/dl, and 160 mV → 400 mg/dl. The results of the one of these *in vivo* experiments are shown below.

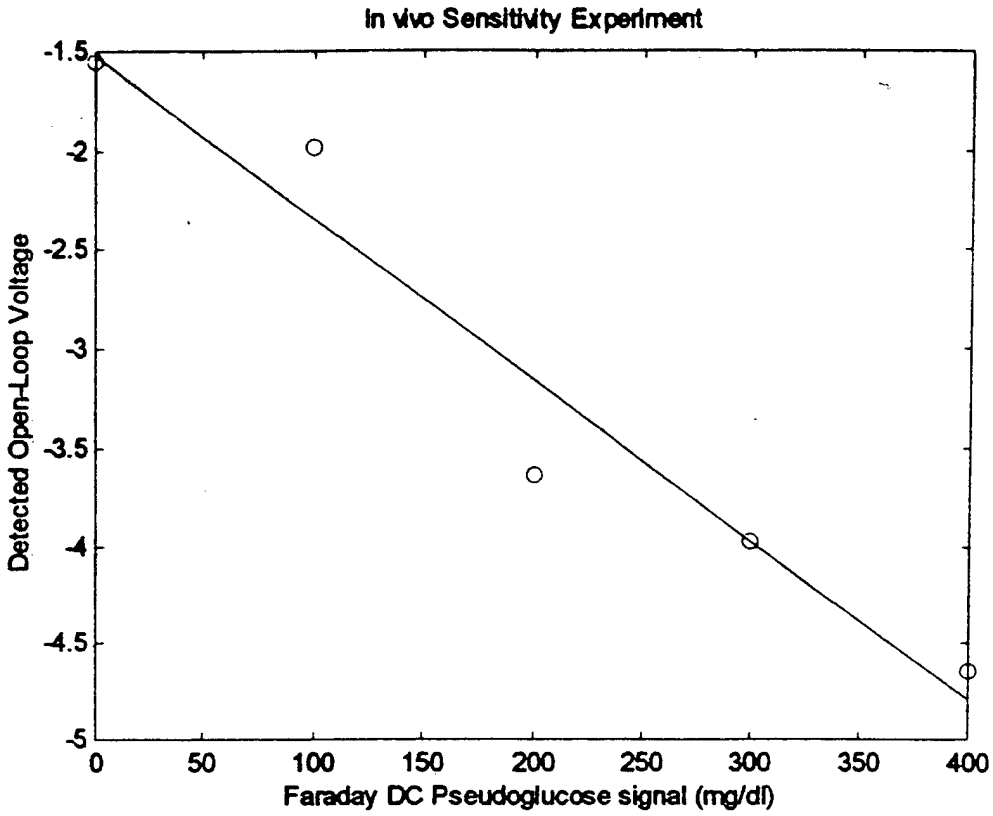

As can be seen from the following figure, there are distinct variations in the detected signal as the pseudo-glucose signal is varied during the course of the *in vivo* experiment. Specifically, the data has a correlation coefficient of -0.97. Although the error is still considable due to the presence of motion artifact, the main importance of this experiment is that the collected data confirms that the current *in vivo* polarimetric sensor has a sensitivity within the range needed to detect the physiologic glucose levels commonly seen in diabetic patients.

With the *in vivo* sensitivity of the current polarimetric system known, the next step was to make appropriate modifications to the system, such that the effects due to the motion artifact could be minimized. Although, the intubation procedure, as indicated in the previous quarterly report, helped to reduce the effects due to motion artifact considerably, the small amount of motion still present causes problems with the experimental measurements. If a reference measurement could be made, the effects of motion artifact would be significantly minimized. However, unlike the *in vitro* experiments in which the sample can be easily replaced with a 'blank' for the reference measurement, in the case of the *in vivo* experiments the aqueous humor within the anterior chamber of the eye cannot be replaced with a 'blank'. Therefore, we are in the process of developing a system that could possibly provide some type of reference measurement. The system we are currently investigating employs a two-wavelength laser system, in which one of the wavelengths is used for control feedback (as in the original system) and the other wavelength provides an open-loop measurement. The block diagram of this system is shown below:

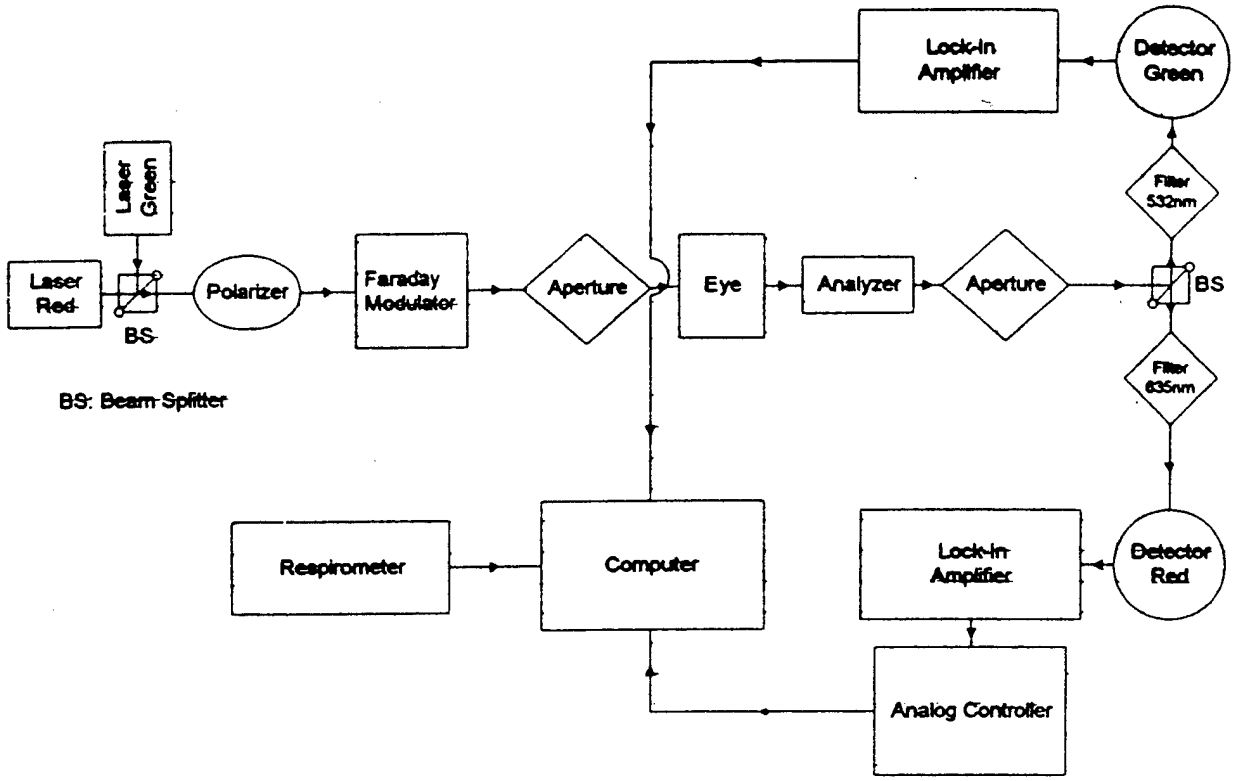

The system above incorporates both green (532 nm) and red (635 nm) laser modules, in which the red laser is used for closed-loop feedback control and the green laser provides an open-loop signal measurement. The digital controller of the previous system was replaced with an analog controller to speed up the system response. Since the rotation in polarized light caused by the sample is significantly greater for green versus red light, when the system is nulled for the red light, there will still be a net rotation present for the green light. This rotation is thus proportional to the glucose concentration of the sample. Therefore, this system may be able to cancel out the variations seen previously in the detected signal due to changes in corneal birefringence caused by motion artifact while providing a measurement that is proportional to glucose. We are currently in the process of evaluating the performance of this system.

Specific Aim #3:

In an effort to achieve this aim in conjunction with the previous aims, the blood glucose response for NZW rabbits over time needed to be characterized. Specifically, the purpose of this experiment is to provide the necessary experimental parameters needed for the polarimetric experiments (e.g. experimental duration, sampling intervals, and general trends to expect). Currently, the mixture of Ketamine/Xylazine that is used for anesthesia also results in an elevation of glucose levels in the blood. In these experiments, two different NZW rabbits were used. After the administration of the anesthesia, 1 ml blood glucose samples were withdrawn from the central artery of the rabbit's ear over a duration of approximately two hours. Each blood sample was analyzed for glucose concentration. The results of these experiments are shown in the plot below.

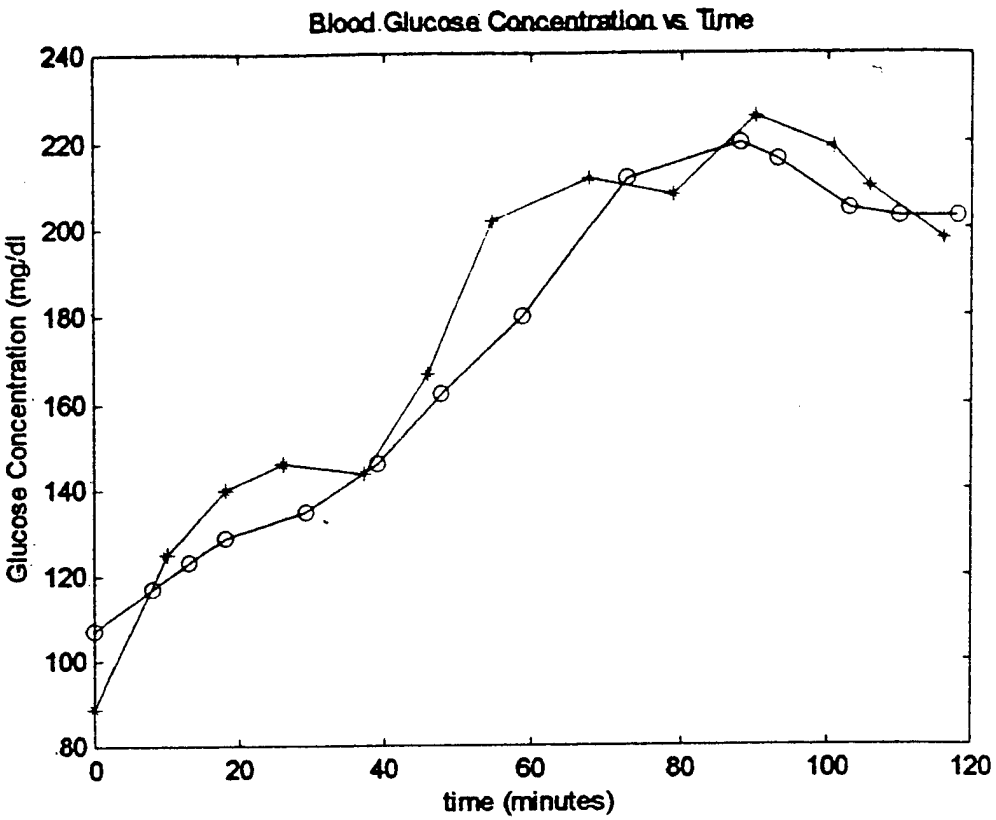

As can be seen, both rabbits exhibit the same general trend in blood glucose concentrations after the administration of the anesthesia. The glucose levels continue to rise to over twice the initial levels within approximately 80 minutes at which point the levels begin to fall as the effects of the anesthesia begin to dissipate. These experiments provided several pieces of useful information. The following information can be concluded from the above experiments:

- The trend in blood glucose levels in response to the anesthesia protocol is similar between rabbits.
- Blood glucose levels can be expected to rise from 100 mg/dl (basal levels) to approximately 220 mg/dl from just the anesthesia injection throughout the course experiment
- Blood glucose levels should peak approximately 80 minute after the initial administration of the anesthesia, at which point the will begin to decline
- A sampling interval of 10 minutes should be sufficient during the first 65 minutes of the experimental procedure, after which the time between samples should be reduced to 3-5 minutes (in order to increase the response resolution) as the peak in the blood glucose response is approached. The time delay between the blood and aqueous humor glucose levels can then be measured as the time between the peaks in the respective glucose response curves.

Optical Polarimetry Applied to the Development of a Noninvasive *in vivo* Glucose Monitor

Brent D. Cameron, Justin S. Baba, and Gerard L. Coté

Biomedical Engineering Program, Texas A&M University, College Station, TX 77840-3120

ABSTRACT

The application of optical polarimetry, using the anterior chamber of the eye as the sensing site, is being investigated as a potential method to develop a noninvasive physiological glucose monitor. Common questions currently associated with the use of polarimetry for noninvasive glucose detection include: "is polarimetry specific enough to elucidate glucose concentration in the presence of other optically active components?," "if the eye is proposed as the sensing site, is the time delay between blood and aqueous humor glucose concentrations small enough to make the development of such a sensor feasible (i.e. useful to a diabetic)?," and lastly "what are the issues currently hindering *in vivo* polarimetric glucose measurements?." In our investigation, we attempt to address these questions. First, we present results characterizing the optical rotatory dispersion of the main optically active analytes found within the aqueous humor of the eye including, glucose, albumin, and ascorbic acid. This information is used conjunction with multiple linear regression to demonstrate how multispectral polarimetry can be used to minimize glucose prediction error in samples containing varying physiological concentrations of glucose and albumin. For this multispectral study, a novel dual wavelength (532 nm and 635 nm) polarimeter was designed and constructed. This sensor is novel in that it provides simultaneous measurements using a 532 nm laser in an open-loop configuration and a 635 nm laser in a closed-loop configuration. In addition, we present *in vivo* results using New Zealand White rabbits that indicate the time delay between blood and aqueous humor glucose levels is below ten minutes. Lastly, we provide preliminary *in vivo* polarimetric results and discuss the main issues currently hindering the measurement of glucose.

Keywords: polarimetry, glucose, diabetes, multispectral, optical activity, ORD

1. INTRODUCTION

A method to noninvasively monitor glucose levels within the body would have a significant impact on millions of diabetic patients worldwide. Currently, all commercially available techniques require the invasive extraction of blood or other bodily fluids for glucose analysis. Thus, diabetic patients often have to extract multiple samples of blood daily, which is usually obtained by the lancing of a finger. This procedure requires the use of relatively expensive enzymatic test reagents, in addition to, subjecting the user to possible infection risks and nerve damage at the testing site. Therefore, recently, several optical approaches have been proposed as possible mechanisms to overcome the invasiveness of current monitoring techniques.[1-15]

In this study, we propose the use of optical polarimetry in conjunction with using the anterior chamber of the eye as the sensing site as a potential method to develop a noninvasive physiological glucose monitor. Specifically, in this paper we attempt to address some of the common questions currently associated with the use of polarimetry for noninvasive glucose detection, such as "is polarimetry specific enough to elucidate glucose concentration in the presence of other optically active components?," "if the eye is proposed as the sensing site, is the time delay between blood and aqueous humor glucose concentrations low enough to make the development of such a sensor feasible (i.e. useful to a diabetic)?," and lastly "what are the issues currently hindering *in vivo* polarimetric glucose measurements?."

2. MATERIALS AND METHODS

2.1 Optical Rotatory Dispersion Measurements

A SPEX FLUOROLOG fluorimeter (Edison, NJ) was modified to allow for the polarimetric measurement of optical rotatory dispersion (ORD). A generalized block diagram of the experimental setup is depicted in Figure 1. A Xenon arc lamp is used as the input white light source. The purpose of the first polarizer is to linearly polarize the input light that then propagates through a 5 cm rectangular sample cell (Starna Cells Inc., Atascadero CA) containing the optically active sample under investigation. The beam is then transmitted through the analyzer, which is merely another polarizer oriented perpendicular to the initial polarizer. The purpose of the analyzer is the convert the rotation in the polarization plane, due to the optically active sample, into a proportional intensity. At this point, an optical fiber is used to collect the light and route it into a monochromator/photo-multiplier tube (PMT) configuration. Since the input white light is composed of several wavelengths, the monochromator is employed after the fiber to separate the individual intensities present at each wavelength. These intensities are proportional to the individual optical rotations in polarization. A PMT is then used to measure the light intensities as the monochromator sweeps across the wavelength range of interest. For each optically active sample, a water reference was used to divide out the system response. The system was then calibrated for optical rotation using the well-known glucose ORD curve.

D-glucose, L-ascorbic acid, and rabbit albumin were purchased in dry form from Sigma Chemical (St. Louis, MO). For each chemical, stock solutions were prepared at a concentration of 10,000 mg/dl. The ORD characteristics were then measured for each chemical between the wavelengths of 475 to 800 nm in 1 nm increments.

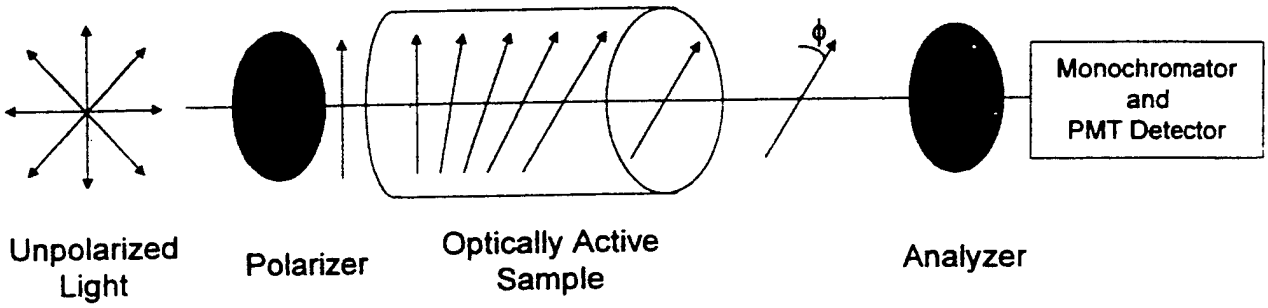

Figure 1: Generalized Block Diagram of an ORD Measurement System

2.2 Instrumentation for Multispectral *In Vitro and In Vivo* Polarimetric Studies

A block diagram of the experimental apparatus designed and constructed for both the *in vitro* and *in vivo* multispectral polarimetric studies is illustrated in Figure 2. The input light sources are a green (532 nm) laser diode module (Oriel Instruments, Stratford, CT) emitting 20 mW of power and a red (635 nm) laser diode (Lasermax, Inc.) emitting 5 mW of power. A beam splitter (Newport Inc., Irvine CA) is used to combine each beam into a single ray. A Glan-Thompson (Newport Inc, Irvine CA) polarizer is then used to linearly polarize the combined beam. At this point it should be noted for the purpose of eye safety that after the green laser passes through the beam splitter and the initial polarizer, its power level is well below 2 mW. This is due, in part, to the fact that the green laser emits a somewhat linear polarized beam and its plane of polarization is not aligned with the initial polarizer. The red diode power level is also considerably lower than 2 mW after the initial polarizer.

A Faraday rotator (Deltronic Crystal Inc., Dover, NJ) is then used to modulate the polarization vector of each laser. It is driven by a sinusoidal source at a frequency of 1.09 kHz. Following the modulator is another Faraday rotator that provides feedback compensation. The purpose of this Faraday rotator is to eliminate any rotation of the polarization vector due to the glucose sample at the wavelength of 635 nm. An aperture is then used to reduce the beam diameter to below 1 mm. This modulated signal then propagates either through a rectangular sample cell (Starna Cells Inc., Atascadero CA) constructed of optical grade glass with a path length of 1 cm for the *in vitro* experiments or through the anterior chamber of the eye via a coupling mechanism for the *in vivo* experiment. The designed coupling mechanism for the *in vivo* experiments has been described previously.[16,17] The next component is another Glan-Thompson polarizer, known as the analyzer, with its

transmission axis oriented perpendicular to that of the initial polarizer. The analyzer transforms the polarization modulation into intensity modulation according to Malus' law. Another aperture is present to prevent any scattered light from being directed toward the detector. The combined beam is then separated via a 50/50 beamsplitter (Newport Inc., Irvine CA) and directed toward one of two detectors. The silicon detectors (Thorlabs Inc., Newton, NJ) each have an interference filter window, 532 nm or 635 nm respectively. The output of the light detector is a voltage proportional to the detected light intensity.

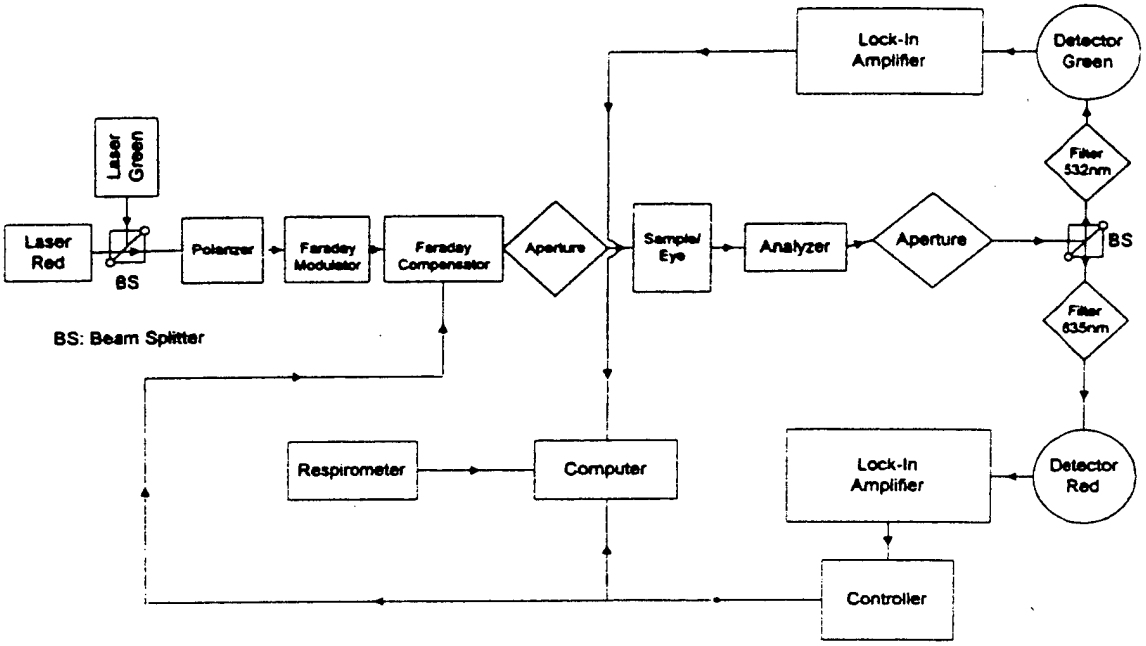

Figure 2: Block diagram of the experimental polarimeter

Digital lock-in amplifiers (DLIA) (Stanford Research Systems, CA) are used to detect the signal of each wavelength at the modulation frequency. This allows the precise measurement of the signal of interest at 1.09 kHz while rejecting low and high frequency electromagnetic noise. The measured signal corresponding to the 635 nm laser is used as the input into an analog controller and the 532 nm signal is measured by the other DLIA as an open-loop measure of rotation. It should be noted that the measured open-loop signal is proportional to the difference in optical rotation between the 635 nm and 532 nm lasers. The signal amplitude information from the open-loop DLIA and the controller voltage are then sent to a Pentium II PC via an IEEE 488 general-purpose interface bus (GPIB) and recorded to a file using LabView 5.1 (National Instruments, Austin TX).

Through the use of Jones matrices, the electric field for a single laser through the optical train can be modeled as:

$$\mathbf{E} = -\sin\left(\theta_m \sin(\omega_m t) + \phi\right), \tag{1}$$

where θ_m is the modulation depth, ω_m is the modulation frequency, t is time, and $\phi = \phi_g - \phi_f$ where ϕ_g and ϕ_f are the rotations in polarization due the glucose sample and compensation Faraday, respectively.[13] The intensity of the signal that impinges on the light detector is proportional to the square of the electric field and can be modeled as:

$$I \propto E^2 = \left(\phi^2 + \frac{\theta_m^2}{2}\right) + 2\phi\theta_m \sin(\omega_m t) - \frac{\theta_m^2}{2}\cos(2\omega_m t), \tag{2}$$

which assumes a small angle approximation where that $\sin(x) \cong x$ for $x<<1$. As can be seen from equation 2, the relative amplitude of the sinusoidal term at the modulation frequency is proportional to the rotation due to the glucose sample assuming no compensation ($\phi_f=0$). This is used as the input into the controller, which forces the net rotation in polarization (ϕ), for the 635 nm laser, to zero via the compensation Faraday rotator. Upon completion, the output voltage of the controller is proportional to the glucose concentration of the sample. Since the plane of polarization for the 532 nm beam is rotated to a different degree than the 635 nm beam (due to differences in the specific rotation for each wavelength), the open-loop signal detected for 532 nm laser will be proportional to the difference in rotation between the two wavelengths upon complete closed-loop compensation. Lastly, the respirometer in Figure 2 is used to monitor respiration during the *in vivo* experiments.

2.3 *In Vitro* Multispectral Experiment

An *in vitro* experiment was performed to assess the glucose predictive capability of the designed polarimeter in the presence of an optically active confounder that varies in concentration. Albumin was chosen as the confounder due to it being one of the more abundent optically active components in the eye.[18] Sample solutions were prepared by mixing appropriate amounts of glucose and albumin over a physiological concentration range. Sixty-five separate 5 ml samples were prepared. The span covered a range from 0 mg/dl to 600 mg/dl of glucose and 0 to 100 mg/dl of albumin in 50 mg/dl and 25 mg/dl increments, respectively. Although, normal concentrations of albumin in the eye are below 10 mg/dl, we chose to use a larger range in order to better illustrate how a multiple wavelength approach can help reduce glucose predictive errors through the use of a multiple linear regression calibration model.

Three separate calibration models were computed in order to demonstrate the benefit of a multiple wavelength system in reducing glucose prediction error compared to a single wavelength system. The first two models computed are based on a standard least-squares linear regresion model using information only from a single wavelength. For example, the first model predicted glucose concentrations by using the closed-loop feedback voltage obtained for nulling the 635 nm wavelength for a given mixture of glucose and albumin. The second model used the open-loop 532 nm signal to predict glucose concentration. Lastly, the third model was computed using a multiple linear regression technique. Both the closed-loop feedback voltage (635 nm) and the open-loop (532 nm) signal were used to compute a single calibration model. The multiple linear regression calibration model takes the form of :

$$\begin{bmatrix} V_{\lambda 1} \\ V_{\lambda 2} \end{bmatrix} = \begin{bmatrix} a_1 & b_1 \\ a_2 & b_2 \end{bmatrix} \begin{bmatrix} \text{Glucose} \\ \text{Albumin} \end{bmatrix} + \begin{bmatrix} c_1 \\ c_2 \end{bmatrix} \tag{3}$$

where $V_{\lambda 1}$ and $V_{\lambda 2}$ are the feedback voltages for each wavelength, a_1, a_2, b_1,b_2 are the components of the slope coefficent matrix, [Glucose] and [Albumin] are the respective concentrations within each sample, and c_1 and c_2 are the corresponding intercepts. This model is then rearraged for in the form of :

$$\begin{bmatrix} \text{Glucose} \\ \text{Albumin} \end{bmatrix} = \begin{bmatrix} a_1 & b_1 \\ a_2 & b_2 \end{bmatrix}^{-1} \left(\begin{bmatrix} V_{\lambda 1} \\ V_{\lambda 2} \end{bmatrix} - \begin{bmatrix} c_1 \\ c_2 \end{bmatrix} \right) \tag{4}$$

to predict unknown the sample concentrations for a given set of feedback voltages at each corresponding wavelength.

2.4 *In Vivo* Glucose Time Delay Experiments

In order to address the time delay between the blood and aqueous humor glucose levels, a set of invasive experiments were performed. These experiments were conducted over a series of weeks, in which the blood glucose of five New Zealand White rabbits were elevated. The method of glucose concentration elevation is due to a side effect of the anesthesia protocol used. The anesthesia administered consisted of the intramuscular injection of 35 mg/kg of ketamine, 5 mg/kg of xylazine and 1 mg/kg of acepromazine. Xylazine is known to have a strong hyperglycemic effect due to its blocking of the pancreatic insulin release via stimulation of parasympathetic (α_2-adrenergic) receptors.[19,20] The resulting effect is that xylazine causes a significant but temporary rise in blood glucose levels and thus also in the aqueous humor of the eye. This effect is desirable in our investigation because the blood glucose levels are similar to those seen in diabetic patients without having to permanently induce diabetes or giving a bolus injection of glucose.

During each week at different times, a single 0.3 ml blood sample and a 0.1 ml sample of the aqueous humor of the eye from each rabbit were passively extracted using a 27 gauge needle. The samples were then analyzed using both a One-Touch hand held glucose meter and a YSI 2300 glucose analyzer. In order to determine the time delay between blood and aqueous humor glucose levels, a second order polynomial curve was fitted around the peak response of both the blood and aqueous humor glucose response curves. The time at which each peak occurred was identified. The time delay between the blood and aqueous humor glucose levels was defined as the differences in time between the peaks of the aqueous humor and blood glucose peak. (see Equation 5)

$$T_{delay}=T_{peak_aqeuous}-T_{peak_blood} \quad (5)$$

2.5 *In vivo* Polarimetric Studies

In order to identify noise sources during the *in vivo* polarimetric measurement of glucose, polarimetric studies were performed on multiple rabbits using the experimental apparatus previously described in Figure 2. For these experiments, the 635 nm laser and closed-loop controller were turned off and only the open-loop portion was used. In place of the sample, the eye of a New Zealand White (NZW) rabbit was used. The modulated polarized light beam is coupled through the anterior chamber of the eye using an eye-coupling device we constructed.[16,17] The rabbits were anesthetized via an intramuscular injection of a combination of ketamine, xylazine, and acepromazine at the following dosages 35 mg/kg, 5 mg/kg, and 1 mg/kg, respectively. The specimen was then placed on an adjustable platform underneath the eye coupling mechanism. The coupling mechanism is then precisely lowered into place over the rabbit's eye. Once contact with the eye is made, a saline-based index-matching fluid is then injected into the eye-coupling device. Leakage of the fluid is minimal due to the contact seal made with the eye at the base of the device. In addition, breathing activity was monitored and recorded via a lab-built respirometer.

3 RESULTS AND DISCUSSION

3.1 Optical Rotatory Dispersion Experiments

It is well known that the specific rotation for a given optically active molecule varies as a function of wavelength. This phenomenon is known as optical rotatory dispersion (ORD). When more than one optically active component is present in solution, a single wavelength is inadequate to distinguish the amount of rotation that each analyte contributes to the overall rotation. Thus, when this information in used to predict the concentration of one of the analytes, there will be an error associated with the measurement due to the presence of the other component. If it is desired to distinguish the optical rotation solely due to glucose in the presence of the other optically active component, additional information is required.

Since each molecule has its own unique ORD curve, the use of multiple wavelengths can be used to reduce the prediction error associated with single wavelength polarimetric measurements.[9,16,17] It is therefore desirable to know exactly how the wavelength dependencies in specific rotation for given optically active molecules behave, such that the most optimum and minimal number of wavelengths can be chosen in order to minimize prediction error. For example, suppose one wishes to measure glucose rotation in the presence of albumin, ideally, it would be preferable to chose at least one wavelength that is more sensitive to glucose rotation and less sensitive to albumin.

The blood-aqueous humor barrier within the eye is a very selective membrane that acts as a filter. Specifically, it will not let particulate matter, such as large globular proteins, pass into the aqueous humor of the eye. In addition, the barrier is also very selectively permeable to certain molecules, such as glucose that can easily traverse the membrane. In terms of optically active molecules, the aqueous humor of the eye contains several. However, the majority of these optically active components are either present in very minute concentrations (such as amino acids) and/or have negligible specific rotations (i.e. lactic acid).[18] The three main optically active components present in the aqueous humor of the eye are glucose, ascorbic acid, and albumin.

Although previous investigations have measured the specific rotation for many chiral molecules found in the aqueous humor of the eye, this information is usually limited to the sodium D-line at 589.3 nm. In our work, we extend this analysis to include most of the visible spectrum for the previously mentioned major optically active analytes in the aqueous humor. In

the multispectral experiments, presented later in section 3.2, this information is applied and it is demonstrated how it may be used to reduce glucose prediction error in solutions containing varying concentrations of both glucose and albumin.

Shown in Figure 3a are the ORD curves for D-glucose, L-ascorbic acid, and rabbit albumin. The curves were measured with the experimental apparatus and methods described in section 2.1. As can be seen, compared to ascorbic acid and albumin, glucose has the largest specific rotation. The specific rotation of glucose is positive due to its dextrorotatory nature and that of albumin is negative due to its levorotatory nature. As for L-ascorbic acid, one would expect that its specific rotation would be negative since in dry form it is levorotatory, however, it is transformed into a dextrorotatory configuration when dissolved in water. As seen in Figure 3a, for the visible region of light, the specific rotation of each analyte approaches zero as wavelength increases. Shown in Figure 3b are the actual observed rotations in polarized light for each analyte. This is computed based on the previously measured specific rotations and assuming a path length of 1 cm (average path length of a human eye) and normal physiological concentrations. The normal physiological concentrations within the aqueous humor are 100 mg/dl for glucose, 20 mg/dl for ascorbic acid, and 6 mg/dl for albumin. As can be seen, when the overall contribution to observed rotation is considered, the majority of rotation is due to glucose, specifically 94 to 97 % depending on the wavelength. Therefore, the error contribution due to ascorbic acid and albumin would be at most 6%. Even though the rotations due to these substances are much less than that of glucose, it can be shown that glucose prediction error can be minimized through the use of multiple wavelengths as shown in the next section.

(a)

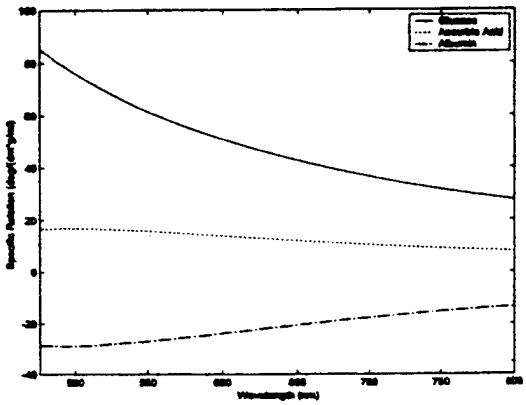

(b)

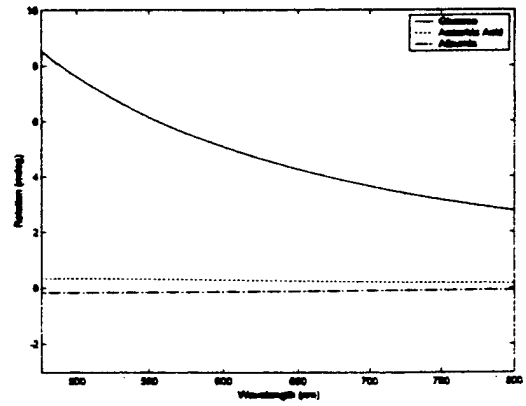

Figure 3: (a) ORD Curves for glucose, ascorbic acid and albumin
(b) actual observed rotation within the aqueous humor at for normal physiological concentrations.

3.2 *In Vitro* Multispectral Experiment

Using the experimental apparatus described in section 2.2 and the methods described in 2.3, an experiment was performed to illustrate the usefulness of a multispectral approach in minimizing glucose prediction error when there is an additional optically active component that varies in concentration. Presented in Figure 4 are the results of the glucose and albumin multi-spectral experiment. Figure 4a and 4b illustrate glucose prediction, in the range of 0 to 600 mg/dl, using only a single wavelength in the presence of albumin that varies in concentration between 0 to 100 mg/dl. Each symbol in the plots corresponds to a certain concentration of albumin. For the open-loop 532 nm experiment, the standard error of calibration in glucose prediction is 142 mg/dl (Figure 4a) and for the closed-loop 635 nm experiment the error is 40 mg/dl (Figure 4b). The correlation coefficients are 0.659 and 0.977 respectively. However, when the data sets of both previous models are used to compute a multiple linear regression calibration model of the form of equations 3 and 4, the error in glucose prediction drops dramatically to 20.0 mg/dl (see Figure 4c). As seen in figure 4c, there is a much tighter grouping (R=0.994) of the predicted to actual glucose concentrations compared to the single wavelength experiments. Although the concentration of albumin used in this experiment was 10 times higher than normally seen in the eye, this concept still should help minimize the glucose prediction error even at the concentrations of albumin found within the eye.

(a)

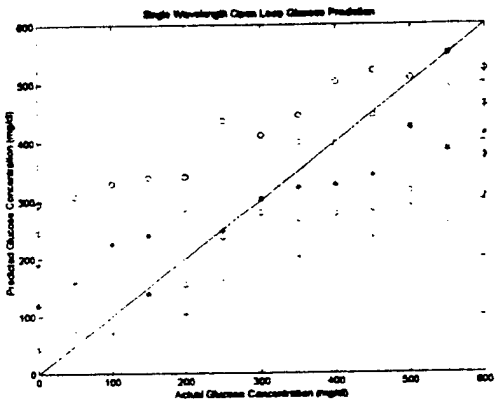

(b)

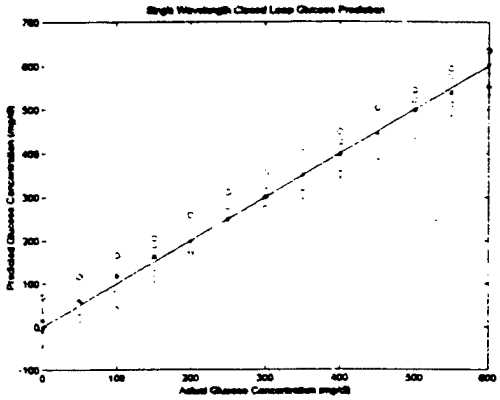

(c)

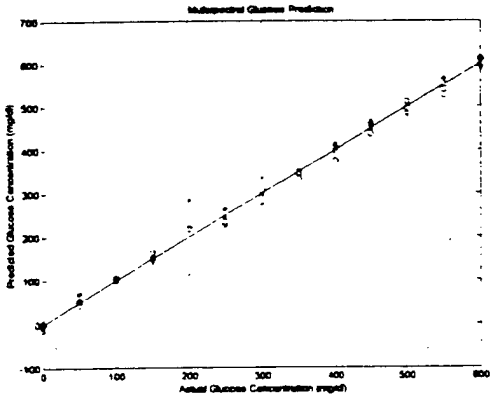

Figure 4: Multi-spectral glucose prediction results
(a) 532 nm open-loop prediction (b) 635 nm closed-loop prediction
(c) 532/635 nm dual wavelength multiple linear regression prediction

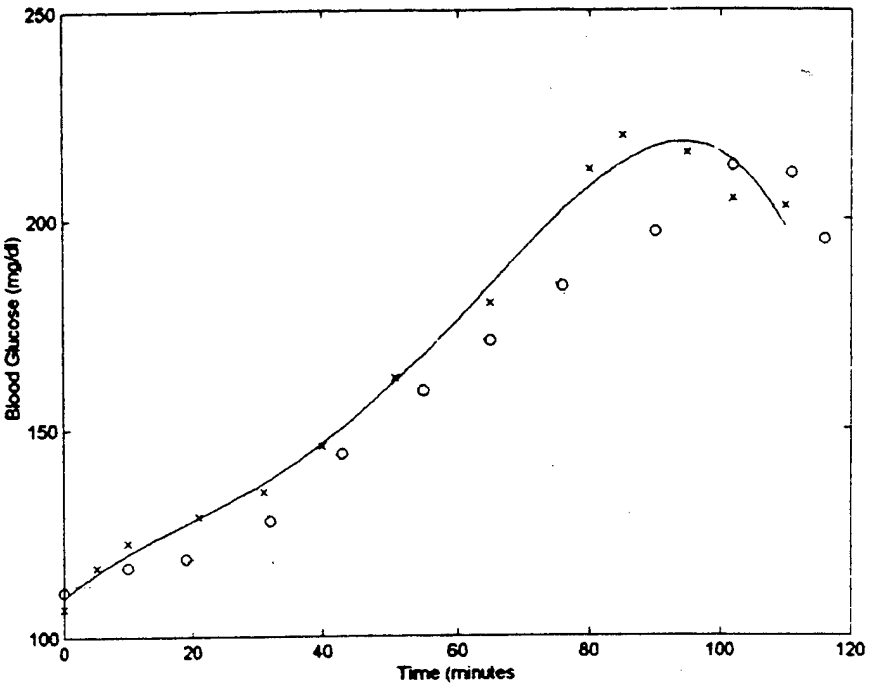

Figure 5: Blood Glucose Response for NZW rabbits

3.3 *In Vivo* Glucose Time Delay Experiments

According to the methods described in section 2.4, the time-delay between the blood and aqueous humor glucose levels was measured in five NZW rabbits. Initially, in order to gain a better feel for how the anesthesia affects the blood glucose response as a function of time in a rabbit, the response was recorded for two different NZW rabbits as a function of time (see Figure 5). A blood sample was acquired from the central ear artery every 5 to 10 minutes for up to 140 minutes after the initial anesthesia dosage. The glucose concentration was measured with a One-Touch Basic handheld blood glucose meter.

As can be seen, both rabbits exhibit the same general trend in blood glucose concentrations after the administration of the anesthesia. The glucose levels continue to rise to over twice the initial levels within approximately 80 to 100 minutes at which point the levels begin to fall as the effects of the anesthesia begin to dissipate. These experiments provided several pieces of useful information. The following information can be concluded from the above experiments:

- The trend in blood glucose levels in response to the anesthesia protocol is similar between rabbits.
- Blood glucose levels can be expected to rise from 100 mg/dl (basal levels) to approximately 220 mg/dl throughout the course experiment
- Blood glucose levels should peak approximately 80-100 minutes after the initial administration of the anesthesia, at which point they will begin to decline

Using this information, we chose to localize our time delay analysis to the area around the peak of the blood glucose response (see section 2.4). Shown in Figure 6, is the time delay results for a single rabbit. Because the aqueous humor sampling method was invasive, requiring the puncturing of the cornea, the experiments were conducted over a five-week period. During each week, a blood and aqueous humor sample were withdrawn at a given instance in time in reference to the time the rabbit was anesthetized. The reasoning behind this is to insure the integrity of the blood-aqueous barrier such that it is not affected due to the corneal penetration. Once the cornea is punctured, there is a change in intraocular pressure and fluid can leak out at the puncture site leading to an alteration in glucose transport, an influx of proteins, and other molecules

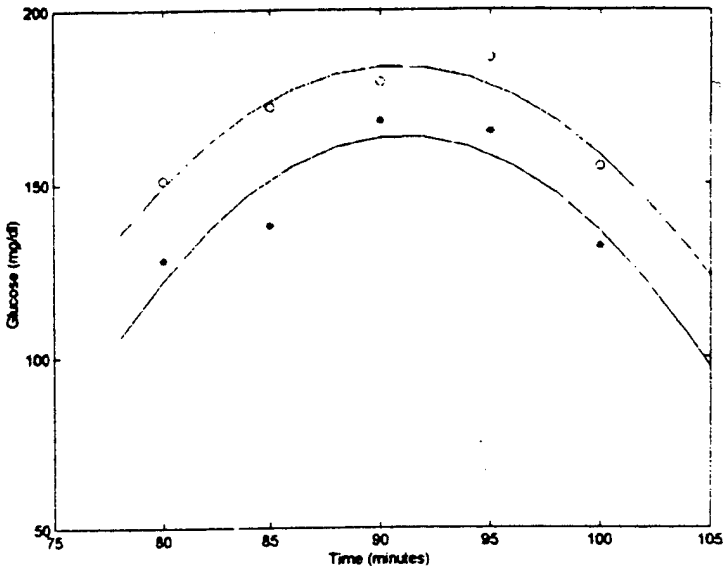

Figure 6: Blood and Aqueous Humor Glucose Time Delay Results
(*: aqueous humor; o: blood)

that normally would not be present in the eye. Therefore, we acquire only a single measurement and provide sufficient time for the eye to heal and the glucose transport rate to normalize.

In order to reconstruct the glucose response, second order polynomial curves are fitted to both the blood and aqueous humor glucose responses. The time delay is then determined as the time between the aqueous humor and blood glucose peaks (see equation 5). For the results presented in Figure 6, the time delay was approximately two minutes. In the remaining rabbits, similar trends were seen and all delays were below 10 minutes. The importance of these results is due to the fact that if the aqueous humor of the eye is to be used as an indirect measure of blood glucose, the time delay must be small enough to provide useful information to the diabetic in regards to their blood glucose levels. This is extremely important for type I diabetics who do not produce insulin and can have significant variations in their blood glucose levels over a very short period of time. The order of the time delays measured in our study show considerable potential for using the eye as an eventual sensing site for the development of a noninvasive blood glucose monitor.

3.4 *In vivo* polarimetry experiments

Using the system described in section 2.2 and the methods described in section 2.5, *in vivo* polarimetric signals were acquired through the eye in several NZW rabbits. Blood glucose levels are increased throughout the experiments as previously described in section 2.4. At present, polarimetric signals can be obtained through the eye, however, noise sources are too great to extract a useful glucose signal. Therefore, in this study a set of experiments was performed to identify the noise sources.

If the first experiment, a digital lock-in amplifier was used to continuously monitor the amplitude of the double frequency term (2^{nd} harmonic) of the detected polarimetry signal during the course of a rabbit experiment (see equation 2). In an ideal situation, the amplitude of the 2^{nd} harmonic term should remain constant, however, if there is noise present, such as motion artifact, it will appear in this term. A partial time series of the amplitude of the 2^{nd} harmonic term during the course of an *in vivo* polarimetric experiment is shown in Figure 7a. As stated previously, in the ideal circumstance (i.e no motion artifact), the overall amplitude of the 2^{nd} harmonic term should remain constant. Therefore, the plot in Figure 7a should merely consist of a horizontal line since the lock-in amplifier outputs a DC value proportional to the amplitude of the signal of interest. However, as can be seen, the overall amplitude of the 2^{nd} harmonic term varies periodically as a function of time. The presence of motion artifact is specifically the cause of these variations. More specifically, since the cornea is birefringent, as the cornea moves relative to the input polarized beam, the variations in the corneal birefringence affect the polarization of light beam in addition to the rotation in linear polarization due to glucose. In order to determine the specific frequencies present in the time based polarimetric signal shown in Figure 7a, FFT spectral analysis of this signal was performed to identify the possible sources of motion artifact (see Figure 7b).

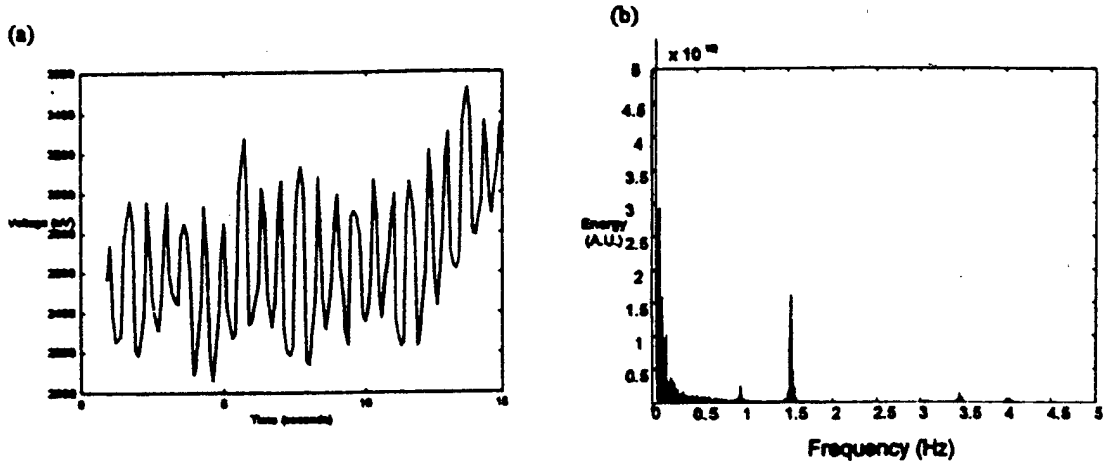

Figure 7: (a) detected *in vivo* polarimetric signal (2nd harmonic); (b) spectral analysis of the time-based polarimetric signal

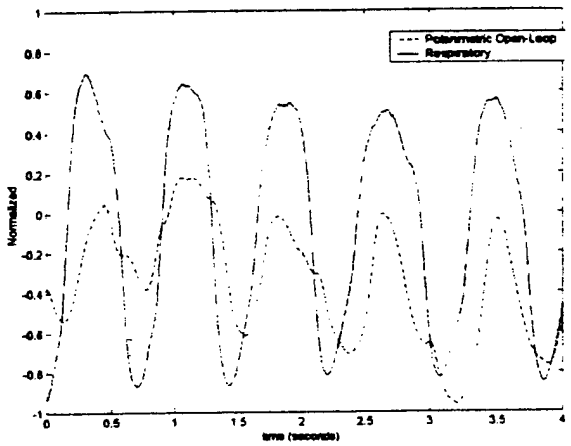

Figure 8: *In Vivo* Open-Loop Polarimetric and Respiratory Signals

Ideally, in an anesthetized rabbit, the possible sources of motion include breathing, the cardiac cycle, and saccadic eye movements. Respiration and the cardiac cycle occur at approximately 60-100 breaths/min and 200-300 beats per minute, respectively, or in terms of frequency, 1 to 1.7 Hz (breathing) and 3.3 to 5 Hz (cardiac). As can be seen in Figure 7b, the largest peak occurs at roughly 1.6 Hz, which possibly corresponds to respiration. Other high frequency peaks also occur past 3.4 Hz which probably are due to the cardiac cycle. In addition, the peak near 0 Hz is due to the average value of the 2nd harmonic signal that manifests itself as a DC component, as mentioned previously.

In order to verify that respiration was the major source of motion artifact, a lab-built respirometer was used during a *in vivo* polarimetric experiment. Both the respiratory and the single frequency polarimetric signal were acquired. The results from this experiment are shown in Figure 8. The signals seen are ac-coupled and normalized in order to plot both signals on a single figure. As can be seen, there is a direct correlation between respiration and the detected polarimetric signal. As stated previously, breathing was suspected of slightly moving the cornea, inducing slight variations in the polarization signal leading to a masking of the glucose signature. In later experiments, various lower body and head fixation devices were employed to reduce this motion artifact with minor success. The reason why the fixation devices were believed to have little improvement is due to the fact that the eye is directly anterior to the nasal passage. As the air moves through the passage during respiration, the eye moves slightly up and down due to the variations in pressure within the nasal passage. An

intubation procedure was later performed and dramatically reduced the effect of the motion artifact due to breathing. However, the amount of motion present, all be it minor, still masks the signal due to glucose. In terms of a practical polarimetric glucose sensor, it would not be feasible to completely eliminate motion artifact, therefore we are currently in the process of investigating several methods to compensate for the variations in polarimetric signal due to motion artifact and corneal birefringence.

ACKNOWLEDGMENTS

This work was supported by a grant from the National Medical Technology Testbed (NMTB): a subcontract under the U.S. Army Medical Research Acquisition Activity (Grant No. DAMD17-97-2-7016). In addition, we would like to thank BioTex, Incorporated (Bryan, TX) for the use of their YSI glucose analyzer.

REFERENCES

[1] March, W.F., Rabinovitch, B. and Adams, R.L. (1982), Noninvasive Glucose Monitoring of the Aqueous Humor of the Eye: Part II. Animal Studies and the Scleral Lens, *Diabetes Care,* 5(3), pp. 259-265, 1982.

[2] Rabinovitch, B., March, W.F., and Adams, R.L. (1982), Noninvasive Glucose Monitoring of the Aqueous Humor of the Eye: Part I. Measurement of Very Small Optical Rotations, *Diabetes Care,* 5(3), pp.254-258, 1982.

[3] Goetz, M.J. Coté, G. L., March, W.F., Erckens, R. And Motamedi, M., "Application of a multivariate technique to Raman spectra for quantification of body chemicals," *IEEE Transactions on Biomedical Engineering, 42*(7), pp.728-731, 1995.

[4] Wicksted, J.P., Erkens, R.J., Motamedi, M. And March, W.F., "Monitoring of Aqueous Humor Metabolites Using Raman Spectroscopy," SPIE Proceedings, V2135, pp. 264-274, 1994.

[5] Pan, S., Chung, H., Arnold, M.A., and Small, G.W., "Near-Infrared Spectroscopic Measurement of Physiological Glucose Levels in Variable Matrices of Protein and Triglycerides," *Anal. Chem.*, 68, pp. 1124-1135, 1996.

[6] McShane, M., Rastegar, S., and Coté, G.L., "Fluorescence-based implantable biosensors: Monte Carlo modeling for Optical probe design", Proceedings of the 20th International Conference of the IEEE EMBS, Hong Kong, Oct 29 - Nov 1, 1998.

[7] Russell, R., Pishko, M., Gefrides, C., and Coté, G.L., "A fluorescent glucose assay using poly-l-lysine and calcium alginate microencapsulated tritc-succinyl-concanavalin A and FITC-Dextran", Proceedings of the 20th International Conference of the IEEE EMBS, Hong Kong, Oct 29 - Nov 1, 1998.

[8] Coté, G.L., Fox, M.D., and Northrop, R.B. (1992), Noninvasive Optical Polarimetric Glucose Sensing Using a True Phase Measurement Technique, *IEEE Transactions on Biomedical Engineering,* 39(7):752-756, 1992.

[9] King, T.W., Coté, G.L, McNichols, R. and Goetz, Jr., M.J. (1994), Multispectral Polarimetric Glucose Detection Using a Single Pockels Cell, *Optical Engineering,* 33(8):2746-2753.

[10] Cameron, B.D. and Cote, G.L., "Polarimetric Glucose Sensing in Aqueous Humor Utilizing Digital Closed-Loop Control," 18th Annual International Conference Proceedings of IEEE-EMBS, Amsterdam, The Netherlands, October 31-November 3, 1996.

[11] Cameron, B.D., and Coté, G.L., "Polarimetric Detection of Chiral Chemicals in Biological Fluids", SPIE International Biomedical Optics Conference, San Jose, CA., SPIE V2982; pp 308-313: Feb. 8-14, 1997.

[12] Coté, G.L. and Cameron, B.D., "Noninvasive Polarimetric Measurement of Glucose in Cell Culture Media," *Journal of Biomedical Optics,* 2(3), pp. 275-281, July 1997.

[13] Cameron, B.D., and Coté, G.L., "Noninvasive Glucose Sensing Utilizing a Digital Closed-Loop Polarimetric Approach", *IEEE Transactions on Biomedical Engineering*, 44(12), pp. 1221-27: December 1997.

[14] Chou, C., Huang, Y.C., Feng C.M., and Chang M., "Amplitude sensitive optical heterodyne and phase lock-in technique on small optical rotation angle detection of chiral liquid," *J. Appl. Phys.*, 36, pp. 356-359, 1997.

[15] Chou, C., Han C.Y., Kuo, W.C., Huang, Y.C., Feng C.M., and Shyu J.C., "Noninvasive glucose monitoring *in vivo* with an optical heterodyne polarimeter," *Applied Optics*, 37(16), pp. 3553-3557, June 1998.

[16] Cameron, B.D., Gorde, H.W., Satheesan, B., and Coté, "The Use of Polarized Laser Light Through the Eye for Noninvasive Glucose Monitoring," *Diabetes Technology and Therapeutics*, 1(2), pp. 135-143, 1999.

[17] Cameron, B.D., Gorde, H.W., and Coté, "Development of an Optical Polarimeter for *in vivo* Glucose Monitoring," Proceedings of SPIE International Biomedical Optics Conference, vol. 3599, pp.43-49, San Jose, CA., 1999.

[18] Gough, D.A., "The composition and optical rotatory dispersion of bovine aqueous humor," *Diabetes Care*, 5, pp.266-270, 1982.

[19] Arnbjerg J. and Eriksen T., "Increased Glucose Content in the Aqueous Humour Caused by the Use of Xylazine," *Ophth. Res.*, 22, 265-268, 1990.

[20] Chalabi K., Schutte M., and Reim M., "Alterations of Glucose Levels in the Blood and the Anterior Eye Segment of Rabbits Exposed to Ketamine-Xylazine Anaesthesia," *Ophth. Res.*, 19, 289-291, 1987.

Appendix 3

Photocopy of Animal Use Report form filed in January 2000.

Texas Engineering Experiment Station
Gerard L. Cote'
Biomedical Engineering Program
Optical Biosensing Laboratory
145 WERC
College Station, TX 77843

NIMAL USE REPORTING

is: TEES - Gerard L. Coté

Contract number:

023-FY97-Texas A&M-Cote'
Cooperative agreement
#DAMD17-97-2-7016

Animal Type Genus/Species	Animals Purchased or Bred	Animals Used	USDA Pain Column C	USDA Pain Column D	USDA Pain Column E	AAALAC Accreditation
NZW male Rabbit	0	10	10	10	0	ULACC-AUP #8-367 #7-288

USAMRAA FORM 52-R (NOVEMBER 1994)

DAMD17-97-2-7016

Texas Engineering Experiment Station
Gerard L. Cote'
Biomedical Engineering Program
Optical Biosensing Laboratory
145 WERC
College Station, TX 77843

ANIMAL USE REPORTING

is: TEES - Gerard L. Coté

Contract number: 023-FY97-Texas A&M-Cote'
Cooperative agreement
#DAMD17-97-2-7016

Animal Type Genus/Species	Animals Purchased or Bred	Animals Used	USDA Pain Column C	USDA Pain Column D	USDA Pain Column E	AAALAC Accreditation
NZW male Rabbit	0	10	10	10	0	ULACC-AUP #8-367 #7-288

USAMRAA FORM 52-R (NOVEMBER 1994)

DAMD17-97-2-7016

ANIMAL AND PLANT HEALTH INSPECTION SERVICE

ANIMAL CARE INSPECTION REPORT

74-R-012 #1 — 1 OF 2

☒ Routine ☐ Reinspection ☐ Pre-license ☐ Attempted ☐ Other

2. DATE OF INSPECTION: 4.9.97 — 4. TIME: 10:30

5. DATE OF LAST INSPECTION: 4-16-96 — 6. TIME: 11:15

7. NAME AND MAILING ADDRESS OF LICENSEE OR REGISTRANT
TEXAS A+M University
4C LARR Agronomy Rd
College Station, TX. 77843

8. ADDRESS OF PREMISES AT TIME OF INSPECTION (If different than Item 7)
LARR Bldg 972

STANDARDS AND REGULATIONS	DOGS A	CATS A	GUINEA PIGS A	HAMSTERS B	RABBITS C	PRIMATES D	MARINE MAMMALS E	OTHER MAMMALS F			
9. NO. OF ANIMALS INSPECTED	0	8	253	0	11	0	0	0			

"X" if in compliance; CIRCLE Non-compliant Items (explain on APHIS FORM 7108, Continuation Sheet); NA if not applicable; NS if not seen.

FACILITIES	GENERAL	10. Structure and Construction	3.1	3.1	3.25	3.25	3.50	3.75	3.101	3.125			
		11. Condition and Site	3.1	X				3.75	3.101				
		12. Surfaces & Cleaning	3.1	X				3.75	3.101				
		13. Utilities/Washrooms/Storage	3.1	X	X	3.25	X	3.75	3.101	3.125			
		14. Drainage and Waste Disposal	3.1	X	X	3.25	X	3.75	3.101	3.125			
	INDOOR	15. Temperature/Ventilation/Lighting	3.2	X	X	3.26	X	3.76	3.102	3.126			
		16. Interior Surfaces	3.2	X	X	3.26	X		3.101				
		17. Drainage							3.101	3.126			
	SHELTERED	18. Temperature/Ventilation/Lighting	3.3	N/A				3.77					
		19. Shelter from elements	3.3	X				3.77					
		20. Surfaces	3.3	X									
		21. Capacity/Perimeter fence/Barrier						3.77					
	OUTDOOR	22. Restrictions or Acclimation	3.4	X	N/A	3.27		3.78	3.103				
		23. Shelter from elements	3.4	X	X		N/A	3.78	3.103	3.127			
		24. Drainage			X		N/A			3.127			
		25. Construction	3.4	X	X			3.78	3.101				
		26. Capacity/Perimeter fence/Barrier						3.78	3.101	3.125			
	MOBILE	27. Temperature/Ventilation/ Lighting	3.5	N/A				3.79					
		28. Public Barrier						3.79					
PRIMARY ENCLOSURE		29. General Requirements	3.6	X	X	3.28	X	3.80	3.104	3.125			
		30. Space & Additional Requirements	3.6	X	X	3.28	X	3.80	3.104	3.128			
		31. Protection from Predators	3.6	X	X	3.25	X	3.80	3.101	3.125			
ANIMAL HEALTH AND HUSBANDRY		32. Exercise and Socialization	3.8										
		33. Environment Enhancement						3.81					
		34. Feeding	3.9	X	X	3.29	X	3.82	3.105	3.129			
		35. Watering	3.10	X	X	3.30	X	3.83	3.106	3.130			
		36. Cleaning and Sanitation	3.11	X	X	3.31	X	3.84	3.107	3.131			
		37. Housekeeping and Pest Control	3.11	X	X	3.31	X	3.84	3.107	3.131			
		38. Employees	3.12	X	X	3.32	X	3.85	3.108	3.132			
		39. Social Grouping and Separation	3.7	X	X	3.33	X		3.109	3.133			
TRANSPORTATION		40. Primary Enclosure	3.14	X	X	3.36	X	3.87	3.113	3.137			
		41. Primary Conveyance	3.15	X	X	3.37	X	3.88	3.114	3.138			
		42. Food and Water	3.16	X	X	3.38	X	3.89	3.115	3.139			
		43. Care in Transit	3.17	X	X	3.39	X	3.90	3.116	3.140			
		44. Handling during Transportation	3.19	X	X	3.41	X	3.92	3.118	3.142			

45. Identification - 2.38 & 2.50

46. Records & Holding Period - 2.35, .38, .75-.78, .101, .132 & .133

47. Handling - 2.38 & 2.131

48. Veterinary Care - 2.33, 2.40, & 3.110

49. IACUC - 2.31 1-16-97

50. Personnel Qualifications - 2.32

51. Other Items? YES (If yes, see continuation sheet) NO

52. PREPARED BY (Signature and title) 4019
Elizabeth Pannill DVM — 53. DATE 4/9/97

54. COPY RECEIVED BY (Signature and title)
Jennifer Brown Vet Med — 55. DATE 4/9/97

56. REVIEWED BY (Signature and title) — 57. DATE

APHIS FORM 7006 (FEB 93) (Previous edition may be used.) *U.S.GPO:1994518-421/80282 PART 2 - FACILITY

ANIMAL AND PLANT HEALTH INSPECTION SERVICE

CONTINUATION SHEET FOR ANIMAL CARE INSPECTION REPORT (S)

(APHIS FORMS 7004 and 7008)

1. LICENSEE OR REGISTRANT AND NUMBER	2. LIC. OR REG. NO.	3. DATE	4. PAGE
TEXAS A+M University	74-R-012 #1	4-9-97	2 OF 2

5. LOCATION OR SITE	6. WAYBILL NUMBER AND DATE (If Applicable)
LARR Bldg 972	

7. NARRATIVE: I. Non-compliant item(s) previously identified that have been corrected; II. Non-compliant item(s) previously identified for which time remains for correction; III. Non-compliant item(s) identified this inspection; IV. Non-compliant item(s) previously identified that have not been corrected

Inspection was conducted with Dr. KAZACOS, LARR

III Newly identified non compliant items on 4-9-97

10 Structure & Construction 3.1a, 3.25a, 3.50
Facility shall be kept in good repair.
Ceiling in clean side cage wash area near the wall on the right side of room has an area where the paint is beginning to WARP & CRACK. The ceiling is also cracked area in Procedure Room 452.
These areas need repair to maintain husbandry correct by 5-9-97

45 Identification 2.38 g Cats shall be identified by tag or tatoo 2 cats on Flea Project have NO tag or tattoo
these Animals need to have proper Identification
* corrected during inspection correct by 5-9-97

8. PREPARED BY (Signature)	9. TITLE	10. DATE
Elizabeth Parrill DVM	VMO	4-9-97
11. COPY RECEIVED BY (Signature)	12. TITLE	13. DATE
Kurt A Brown DVM MS	Assoc Dir	4-9-97
14. REVIEWED BY (Signature)	15. TITLE	16. DATE

APHIS FORM 7100
(AUG 91)

PART 2 - FACILITY

*U.S. GPO: 1992-321-398/60358

"27. USE OF LABORATORY ANIMALS

a. ANIMAL WELFARE (NOV 1996) (USAMRAA)

(1) The recipient shall register its research facility with the Secretary of Agriculture in accordance with 7 U.S.C. 2316 and 9 CFR, Subchapter A, Part 2, Subpart C, and Section 2.30, and furnish evidence of such registration to the Contracting Officer before beginning work under this cooperative agreement.

(2) The recipient shall acquire animals only from dealers licensed by the Secretary of Agriculture under 7 U.S.C. 2133 and 9 CFR, Subchapter A, Part 2, Subpart A, Sections 2.1 through 2.11, or from sources that are exempt from licensing under those sections.

(3) The recipient agrees that the care and use of animals will conform with the pertinent laws of the United States and regulations of the Department of Agriculture. (See 7 U.S.C. 2131 et. seq. and 9 CFR Subchapter A, Parts 1 through 4.)

(4) The Contracting Officer may immediately suspend, in whole or in part, work and further payments under this cooperative agreement for failure to comply with the requirements of paragraphs (a) through (c) of this clause.

(a) The suspension will stay in effect until the recipient complies with the requirements.

(b) Failure to complete corrective action within the time specified by the Contracting Officer may result in termination of this cooperative agreement and removal of the recipient's name from the list of contractors with approved Public Health Service Welfare Assurances.

(5) The recipient may request registration of its facility and a current listing of licensed dealers from the Regional Office of the Animal and Plant Health Inspection Service (APHIS), United States Department of Agriculture (USDA), for the region in which its research facility is located. The location of the appropriate APHIS regional office, as well as information concerning this program may be obtained by contacting the Senior Staff Officer, Animal Care Staff, USDA/APHIS, Animal Care, 4700 River Road, Unit 84, Riverdale, MD 20737-1234 (Phone Number 301-734-7833).

(6) The recipient shall include this clause, including this paragraph (6), in all subcontracts/subgrants involving research of live vertebrate animals.

a. USE OF LABORATORY ANIMALS (OCONUS) (JAN 1992) (USAMRAA)

All laws, customs, and practices of the country in which the research is to be conducted shall be complied with insofar as use of laboratory animals is concerned. In those instances where the local laws and regulations are in conflict with the laws and regulations of the United States and the Department of Agriculture, the more humane and stringent will be followed. The following U.S. standards and regulations for the protection, treatment, and use of animals should be adhered to where practicable: 7 U.S. Code 2131 et. seq. and 9 Code of Federal Regulations, Subchapter A, Parts 1 - 4.

b. POST-AWARD OVERSIGHT OF THE USE OF LABORATORY ANIMALS (AUG 1993) (USAMRAA)

Cooperative agreement post-award oversight of the use of laboratory animals shall be the responsibility of the recipient's Animal Care and Use Committee (ACUC). The principal investigator will notify the Contracting Officer in writing of any significant changes to the proposed use of animals which was the basis for award. These changes must be approved by the recipient's ACUC and the USAMRMC. In addition, the ACUC shall immediately notify the Contracting Officer of any violations of law, regulation, or publication for animal care.

c. ANIMAL USE REPORTING (NOV 1996) (USAMRAA)

(1) The recipient shall prepare and submit the "U.S. Army Medical Research and Material Command Animal Use Report" (Attachment) annually detailing the use of animals in the research, development, test and evaluation sponsored by the Army. The reporting period shall be each Federal Fiscal Year, i.e., 1 October thru 30 September, each year. Additionally, the recipient shall furnish a copy of the most recent USDA Inspection Report (APHIS Form 7008 and Continuation Sheets APHIS Form(s) 7100). The recipient is responsible for ensuring that a separate U.S. Army Medical Research and Materiel Command Animal Use Report and USDA Inspection Report (APHIS Form 7008 and Continuation Sheets APHIS Form(s) 7100) are submitted for any subcontract/subgrant facility using animals.

(2) The following definitions shall apply to the U.S. Army Medical Research and Materiel Command Animal Use Report.

(a) Column A. Animal. List all animal types by common name used for the particular work unit or protocol. For the purposes of this reporting requirement, an animal is defined as any live nonhuman vertebrate, used for research, development, test, and evaluation (RDT&E), clinical investigations, diagnostic procedures, and/or instructional programs. Only animals that are on hand in the facility or acquired during the reporting fiscal year should be reported. Animal organs, tissues, cells, fluid components, and/or by-products purchased or acquired as such animal/biological components should not be reported.

(b) Column B. Number of Animals Purchased, Bred or Housed but not yet used. The term "animals purchased or bred" refers to the purchase, breeding, or other acquisition of individual animals in the reporting fiscal year for assignment to a particular work unit or protocol. Animals carried over from the previous fiscal year and not yet used in any procedures or studies, must be included in this number for the work unit or protocol to which they are assigned.

(c) Columns C-F. Number of Animals Used. A single animal must be counted only once in determining the number of animals used during the fiscal year for a particular work unit or protocol. The term "animals used" does not refer to the number of times an individual animal is injected, manipulated, handled, or administered medication and/or experimental compounds within a given work unit, protocol, or program. Animals on hand during the reporting fiscal year, but not actually used during the fiscal year, must not be included in this column.

(i) Column C. Number of Animals Used Involving No Pain or Distress. The number of animals placed in this column must have been used in procedures which did not cause more than slight or momentary pain or distress, as defined by the institution's ACUC and 9 CFR, Subchapter A, Part 1.

(ii) Column D. Number of Animals Used in which appropriate anesthetic, analgesic, or tranquilizing drugs were used to Alleviate Pain. The number of animals placed in this column must have received appropriate pharmacological agents to relieve pain or distress, as defined by the institution's ACUC and 9 CFR, Subchapter A, Part 1.

(iii) Column E. Number of Animals Used in which Pain or Distress was not Alleviated. Animals counted in this column were not given pharmacologic agents to relieve pain or distress, as defined by the institution's ACUC and 9 CFR, Subchapter A, Part 1.

(3) Animal Use Reports

(a) The recipient shall submit the U.S. Army Medical Research and Materiel Command Animal Use Report and a copy of the most recent USDA Inspection Report (APHIS Form 7008 and Continuation Sheets APHIS Form(s) 7100) each year, no later than 1 December.

(b) These reports shall be submitted to:

National Medical Technology Testbed
11354 Mountain View Avenue
Suite D
Loma Linda, CA 92354

DESCRIPTION AND PERFORMANCE SITES (FORM B)

DESCRIPTION: State the goal of the research project including how it relates to improving health care for the nation's people. Use succinct language to describe how the project goals will be achieved. Do Not exceed the space provided on this page.

The overall goal of this research is to establish a novel gene delivery strategy for sustained modulation of gene expression in retinal vascular cells. Long-term complications of diabetes such as diabetic retinopathy develop over several years and involve altered gene expression. Thickening of retinal capillary basement membrane (BM) is a well-documented, early feature of diabetic microangiopathy that has been widely observed in diabetic humans and animals. Studies in our laboratory and by other investigators suggest that the process of BM thickening is linked to increased gene expression of BM components such as fibronectin (FN) and collagen type IV, found increased in retinal capillaries of diabetic individuals. We have applied antisense oligonucleotides by intravitreal injection and reduced the FN overexpression in rat retinal cells. However, for prolonged antisense effect a different strategy is necessary because intravitreal injection is a risky procedure and unsuitable for repeated use. The proposed study investigates three strategies for prolonged modification of retinal gene expression. (1) We will develop plasmid constructs to reduce FN and collagen IV expression based on the oligonucleotide sequence we currently use against the 5' translation initiation site of the two transcripts. Delivery of such plasmid constructs should provide long-term gene modulation and require only a single intravitreal injection. (2) A noninvasive means to deliver antisense oligonucleotides into retinal cells will be developed; we will examine the topical delivery route and optimize it for repeated oligonucleotide delivery. (3) Improve delivery of oligonucleotides into retinal cells by varying the length of the oligos. In addition, we will determine the duration of inhibition of fibronectin expression using the antisense oligos we designed and found effective in studies of short-term gene downregulation. The proposed work will provide information on long-term modulation of gene expression in the retinal vascular cells, and clarify if the devastating lesions of diabetic retinopathy are linked to abnormally expressed ECM genes in the retina.

PROJECT SITE(s) (*Organization, City, State*):

All experiments proposed in this application will be performed at the Schepens Eye Research Institute research building located at 20 Staniford Street, Boston, MA 02114. The PI occupies a 500 sq ft laboratory in the Schepens Eye Research Institute. The laboratory is fully equipped for studies involving tissue culture, biochemistry, and molecular biology.

NO. 42

Trustees Boston U/Roy

Gene Delivery and Regulation of Abnormal Gene Expression in Diabetes—A Novel Approach

This is a recently begun project with first report due October 2000.

No report at this time

NOV 29 1999

only one Month

FINAL REPORT FOR FY98 INTERIM CONTINUATION PERIOD
(June 16, 1999 – October 31, 1999) 9/99 - 10/99

This report describes the progress made during the interim continuation period between June–October 1999, based on a funding amount of $35,000. As stated in our proposal, the specific research aims for this interim continuation period of funding consisted of: (1) Investigation of the effect of hemofiltration on patient heart rate and patient blood pressure; (2) Design of the cardiovascular component of a fuzzy logic supervisory algorithm for adjustment of desired ultrafiltration rate. In addition to the above two aims we were also able to perform some initial testing and evaluation of the designed supervisory controller. Overall, we have achieved our research goals for this funding period and we are slightly ahead of schedule on our long-term plans for this research program.

A. Effect of Hemofiltration on Patient Heart Rate and Blood Pressure (AIM 1)

One of the key objectives of our research project is to develop a feedback loop between the patient and the hemofiltration device. This will allow information on the current condition of the patient to be used for adjustment (and, ultimately, optimization) of the ultrafiltration rate performed by the hemofiltration machine. The most relevant information on the patient's condition, from a hemofiltration perspective, are the patient heart rate and blood pressure. It is important to note that so far there exist no dialysis-type of devices that provide automated procedures for responding to changes in the cardiovascular state of the patient. Therefore, we had to start from some basic research in understanding the inherent relationship between ultrafiltration rate and the patient cardiovascular condition. This investigation helped us in the derivation of suitable rules for implementing the supervisory controller.

Cardiac output is the volume of blood pumped by the left ventricle into the aorta per unit time; likewise, venous return is the volume of blood flowing from the veins into the right atrium per unit of time. The Frank-Starling law is based on the observation that the heart will pump whatever amount of blood enters the right atrium without a significant buildup of back pressure in the right atrium [1, 2]. This pumping is a function of the blood entering the chamber (preload), the pressure head against which the blood is pumped (afterload), and the intrinsic ability of the muscle to contract (contractility). If the quantity of blood in the circulation is too little to adequately fill the system, blood will flow poorly from the periphery to the heart. Therefore, the degree of filling of the circulation, preload, which is measured by the mean systemic filling pressure, is one of the most important factors determining the cardiac output [3].

Ultrafiltration of critically ill patients directly impacts cardiac output. The ultrafiltration volume is the net intravascular fluid that is removed from a patient during the hemofiltration process. This volume loss due to an excessively high ultrafiltration rate could lead to a decreased intravascular volume, or hypovolemia, which decreases the mean systemic filling pressure and therefore decreases the cardiac output [4]. If filtration continues unchecked and the cardiac output falls below normal, then the body will mount an intense vasoconstrictive response to attempt to maintain pressure. This intense vasoconstriction and potential drop in blood pressure are symptoms of inadequate blood flow through the body. The rate of intravascular volume reduction is also important. Faster reductions lead to much more

rapid symptoms, whereas a similar volume loss that is done much more slowly may be well tolerated.

The adaptive process to decrease cardiac output is aimed at maintaining blood pressure and occurs through increasing the peripheral vascular resistance as well as increasing the heart rate. This is caused by powerful sympathetic reflexes initiated mainly by baroreceptors that stimulate vasoconstriction throughout the body resulting in three important effects.

1. Arterioles constrict and thereby increase the total peripheral resistance causing an increase in the arterial pressure.

2. The veins and venous reservoirs constrict, thereby helping maintain adequate venous return despite diminished blood volume.

3. The sympathetic output increases the heart rate from a normal value of approximately 72 beats per minute (bpm) for an adult to as much as 200 bpm.

The adaptive sympathetic reflexes to hypovolemia have a greater effect on maintaining arterial pressure than on maintaining cardiac output. The importance of arterial pressure even in the face of decreasing cardiac output is to protect blood flow through the coronary and cerebral circulatory systems. Sympathetic tone does not cause significant vasoconstriction in either the cerebral or cardiac vessels; both these vascular beds exhibit extensive local autoregulation which prevents moderate changes in arterial pressure from significantly affecting blood delivery to these critical organs. Therefore, blood flow through the heart and brain is maintained essentially at normal levels as long as the arterial pressure does not fall below 70 mmHg for an adult, despite the fact that blood flow in many other areas of the body might be decreased almost to zero because of intense vasospasm.

Because of the long duration of hemofiltration routines and the precarious conditions of the patient, health care personnel must frequently monitor the procedure and, based on the condition of the patient, adjust some of the procedure parameters, such as the ultrafiltration and blood flow rate. The basic objective of the adjustment is to maintain an appropriately high ultrafiltration rate while the patient remains in safe condition [5]. Based on the above description of the relation between ultrafiltration rate and patient heart rate and blood pressure, we developed some basic supervisory rules, which constitute the expert knowledge utilized in the construction of the cardiovascular supervisory controller.

Supervisor Rule 1: If the patient heart rate (R_h) is high and the patient blood pressure (P_b) is normal or low, then decrease ultrafiltration. Wait 10 minutes.
The patient cardiovascular state is deteriorating. Lowering the ultrafiltration rate will increase tissue perfusion and should ameliorate the patient's condition.

Supervisor Rule 2: If P_b is low and R_h is normal or high, then decrease ultrafiltration. Wait 10 minutes.
The reason for a decrease in ultrafiltration here is the same as for Rule 1.

Supervisor Rule 3: If both P_b and R_h are low, then provide the user with a choice between a decrease or increase of the ultrafiltration rate. Wait 5 minutes.
The patient may have a type of cardiac conduction abnormality or be responding to pharmaceutical intervention such as narcotic administration. In any case, the information needed to decide between a decrease or an increase of the ultrafiltration rate is unavailable to the

hemofiltrator. Even though the hemofiltrator does not have all information to make a decision about the sign of the adjustment, it can calculate its magnitude.

Supervisor Rule 4: If both P_b and R_h are high for 30 consecutive minutes, then provide the user with a choice between a decrease or increase of the ultrafiltration rate.
Again the sign of the ultrafiltration rate change is determined by the user and the algorithm calculates its magnitude. The supervisor waits 30 minutes before making an adjustment because transiently high parameters can be caused by pain, moving of the patient, and administration of drugs, which are situations that are transient and do not require adjustments.

Supervisor Rule 5: If P_b is high and R_h is low for 60 consecutive minutes, then increase ultrafiltration.
The patient cardiovascular state is getting better and can tolerate faster bodily fluid shifts. The larger the ultrafiltration rate, without sacrificing tissue perfusion, the more beneficial hemofiltration is to the patient.

B. Design of Cardiovascular Supervisory Controller (AIM 2)

Monitoring the patient's vital signs and hemofiltration parameters and making appropriate hemofiltration adjustments are vital for the patients safety during the hemofiltration process. In order to reduce the burden on human operators, and increase the safety of an autonomous system, the main objective of the cardiovascular supervisory controller is to emulate some of the decisions and actions of an expert nephrologist. Fuzzy logic methods facilitate the synthesis of a mapping between observation and action, and therefore provides a framework for incorporating expert knowledge into an automated system.

The basic structure of fuzzy control systems has been described in earlier reports. Basically, it is composed of four components: *a rule-base* (a set of If-Then rules), *an inference mechanism*, *a fuzzification interface*, and *a defuzzification interface*. The selection of input and output variables for the fuzzy logic controller is a crucial step in the design procedure. The patient heart rate and systolic blood pressure are good indicators of the patient's condition and provide suitable parameters for a nephrologist making adjustments. Therefore, based on the supervisor rules described above, we choose the patient heart rate and patient blood pressure as the inputs to the controller, while the output of the fuzzy logic controller is the adjustment to the ultrafiltration rate $\Delta(n)$. The change is implemented by keeping the replacement fluid flows constant and adding $\Delta(n)$ to the drain flow rate. That is, once a change in ultrafiltration $\Delta(n)$ is calculated at sample time n, it is applied as follows:

$$q^*_{\text{repl}}(n+1) = q^*_{\text{repl}}(n) \tag{1}$$
$$q^*_{\text{rep2}}(n+1) = q^*_{\text{rep2}}(n) \tag{2}$$
$$q^*_{\text{dra}}(n+1) = q^*_{\text{dra}}(n) + \Delta(n) \tag{3}$$
$$q^*_{\text{ult}}(n+1) = q^*_{\text{dra}}(n+1) - q^*_{\text{repl}}(n+1) - q^*_{\text{rep2}}(n+1)\ , \tag{4}$$

resulting in an ultrafiltration rate changed by $\Delta(n)$ from sample time n to $n+1$. In the above equations, q^* denotes desired fluid flow.

It can be seen from the monitoring protocol that formulating a supervisory rule base as a single fuzzy system is difficult if time is not included as one of the inputs. However, including time as an input results in a large rule base that may be cumbersome to understand, defeating

one of the purposes of utilizing fuzzy logic. Instead, the part of the algorithm supervising ultrafiltration flow is decomposed into four separate fuzzy systems. Fuzzy system FSI deals with the case of high patient heart rate and/or low blood pressure (Supervisor Rules 1 and 2). Fuzzy system FSII corresponds to the case that both the patient heart rate and systolic blood pressure are low (Supervisor Rule 3), while fuzzy stem FSIII is activated when both variables are high (Supervisor Rule 4). Finally, fuzzy system FSIV calculates increases in ultrafiltration rate as a consequence of improvement in the patient's condition.

A switch logic resides at the highest level and determines, based on the heart rate R_h and blood pressure P_b, which fuzzy system is active. It is noted that the instructions to wait in Supervisor Rules 1-5 are local to each rule: if the ultrafiltration is decreased because of Supervisor Rule 1, it cannot be changed again *because of Supervisor Rule 1* until 10 minutes have passed. Therefore, only one of the fuzzy systems is turned on at a given time, and the switch logic at this level also performs the operation of waiting the required amount of time before or after a supervisory adjustment to the ultrafiltration rate as required by the supervisor rules.

Another important feature of the cardiovascular supervisory controller is that it should be robust to some of the typical type of disturbances and noises that are present in the cardiovascular state of a patient during the hemofiltration process. More specifically, the following three types of noise have been considered:

1. Due to pain or patient movement, the heart rate rises to some high value temporarily (typically less than five minutes), while the patient blood pressure remains normal. This situation corresponds to Supervisor Rule 1.

2. If the patient is subjected to pain drugs, the heart rate and blood pressure may both decrease for a short time period (less than two minutes for the heart rate, and five to ten minutes for the blood pressure). In this case, the conditions of Supervisor Rules 2 or 3 could be activated.

3. As a result of patient movement, the blood pressure decreases to some low value for less than two minutes. This case is not included in any of the cardiovascular supervisory rules described above, and therefore supervisor is immune to this type of noise.

In the presence of such disturbance/noise situations the cardiovascular supervisory controller should be able to recognize that its a noise situation and not make any unnecessary adjustments to the desired ultrafiltration rate. For example, in the case of noise due to pain drugs, neither Supervisory Rule 2 nor Rule 3 should be activated. We have incorporated these situations in our design by developing a waiting mechanism. More specifically, the Supervisory Rules 1–3 are not activated immediately after their conditions are satisfied. Instead, only if the conditions remain true for a sufficiently long time (specified by each noise situation given above), the corresponding fuzzy control subsystem is activated, and the ultrafiltration rate is adjusted.

In order to achieve the desired supervision, the design of each fuzzy subsystem (FSI, FSII, FSIII, FSIV) needs to be customized to the corresponding supervisory rules. To illustrate the design methodology and provide intuition for the issues that need to be addressed in each case, we describe in more detail below the design of the first fuzzy subsystem FSI. The details of the design for the other three fuzzy subsystems are omitted in this report.

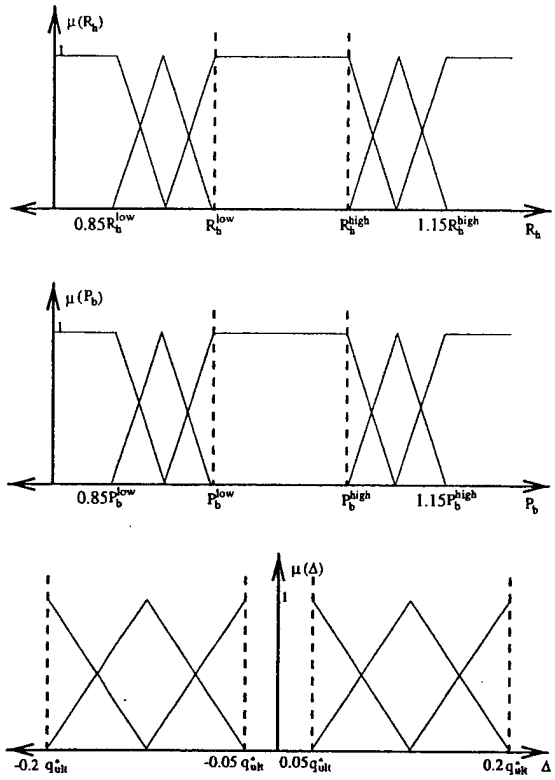

Figure 1: Fuzzy membership functions for patient heart rate and blood pressure, and for change in ultrafiltration.

The design of Fuzzy System FSI is as follows. The nephrologist chooses high and low thresholds of the heart rate (R_h^{high}, R_h^{low}) and the systolic blood pressure (P_b^{high}, P_b^{low}), based on the size and cardiovascular state of the patient. These thresholds are used in the characterization of the magnitudes of the patient heart rate (R_h) and systolic blood pressure (P_b). For example, if the patient heart rate satisfies $R_h^{\text{low}} < R_h < R_h^{\text{high}}$, then the heart rate is called "normal"; if $R_h^{\text{low}} \geq R_h$ then the heart rate is characterized as being "low", and if $R_h \geq R_h^{\text{high}}$ then the heart rate is "high" (similarly for the patient's blood pressure). Since the patient's cardiovascular state may be changing during hemofiltration, the thresholds may be manually changed during the procedure.

In order to specify the fuzzy systems proposed, we define the following universes of discourse in $\mathbb{R}$ for the patient heart rate ($\mathbb{U}_i$), blood pressure ($\mathbb{V}_i$), and change in ultrafiltration ($\mathbb{Y}_i$):

$$\begin{aligned}
\mathbb{U}_1 &= (-\infty, R_h^{\text{low}}] & \mathbb{U}_2 &= (R_h^{\text{low}}, R_h^{\text{high}}) & \mathbb{U}_3 &= [R_h^{\text{high}}, +\infty) \\
\mathbb{V}_1 &= (-\infty, P_b^{\text{low}}] & \mathbb{V}_2 &= (P_b^{\text{low}}, P_b^{\text{high}}) & \mathbb{V}_3 &= [P_b^{\text{high}}, +\infty) \\
\mathbb{Y}_1 &= [-0.2q^*_{\text{ult}}, -0.05q^*_{\text{ult}}] & & & \mathbb{Y}_2 &= [+0.05q^*_{\text{ult}}, +0.2q^*_{\text{ult}}]
\end{aligned}$$

where $q^*_{\text{ult}}(n) = q^*_{\text{dra}}(n) - q^*_{\text{repl}}(n) - q^*_{\text{rep2}}(n)$ is the desired ultrafiltration rate at the time the supervisor is activated. Figure 1 shows the fuzzy memberships used for this subsystem.

Fuzzy system FSI corresponds to Supervisor Rules 1 and 2, and hence it supervises the decrease of ultrafiltration because of a high patient heart rate and/or low patient systolic blood pressure. In this case, the output of FSI is a negative number to be added to the current drain flow rate. FSI is further divided into three fuzzy subsystems (FSIA-FSIC). The switch logic activates FSI if ($R_h \in \mathbb{U}_3$ and $P_b \notin \mathbb{V}_3$) or ($P_b \in \mathbb{V}_1$ and $R_h \notin \mathbb{U}_1$). The switch also tags FSI as a system that cannot be activated again for another 10 minutes, and it chooses which subsystem will perform the calculation of the drain flow rate decrease.

Subsystem FSIA is activated if $R_h \in \mathbb{U}_3$ and $P_b \in \mathbb{V}_2$. This means that the patient blood pressure is normal, and thus the correction to the ultrafiltration is due only to the heart rate. The corresponding fuzzy rule base for FSIA is given as:

- *FSIA Rule (1):* "If R_h is μ^u_{31} then Δ is μ^y_{13}."
- *FSIA Rule (2):* "If R_h is μ^u_{32} then Δ is μ^y_{12}."
- *FSIA Rule (3):* "If R_h is μ^u_{33} then Δ is μ^y_{11}."

The fuzzy system resulting from applying fuzzy logic concepts to this rule base is

$$\Delta_{\text{IA}} = \frac{\sum_{i=1}^{3} \mu^u_{3i}(R_h) c_i^{IA}}{\sum_{i=1}^{3} \mu^u_{3i}(R_h)} , \tag{5}$$

where c_i^{IA} is the center of the output fuzzy set, as defined in $\mathbb{Y}_1$, from the i^{th} rule of system FSIA. It is noted that all fuzzy systems used in this design are derived by combining the singleton fuzzifier, the product inference engine, and the center average defuzzifier.

Fuzzy subsystem FSIB is activated if $R_h \in \mathbb{U}_2$ and $P_b \in \mathbb{V}_1$. This subsystem decreases the ultrafiltration rate when the patient heart rate is normal and the systolic blood pressure is low. The corresponding fuzzy rule base for FSIB is given as

- *FSIB Rule (1):* "If P_b is μ^v_{11} then Δ is μ^y_{11}."
- *FSIB Rule (2):* "If P_b is μ^v_{22} then Δ is μ^y_{12}."
- *FSIB Rule (3):* "If P_b is μ^v_{33} then Δ is μ^y_{13}."

and the resulting fuzzy system is

$$\Delta_{\text{IB}} = \frac{\sum_{i=1}^{3} \mu^u_{1i}(P_b) c_i^{IB}}{\sum_{i=1}^{3} \mu^u_{1i}(P_b)} . \tag{6}$$

The switch logic turns on subsystem FSIC when $R_h \in \mathbb{U}_3$ and $P_b \in \mathbb{V}_1$. In this situation, both patient parameters are outside their normal regions, so using a two dimensional fuzzy system is reasonable. The rule base for FSIC consists of nine rules, which are similar in structure to those of FSIA and FSIB.

C. Initial Simulation Testing of Cardiovascular Supervisory System

In addition to the tasks itemized in the proposal, we conducted some preliminary simulations to test the safety and robustness of the designed fuzzy supervisory system. In these simulations, the hemofiltration system was operated by simulating a patient with a container

Method for Hypothesis 1:

A laboratory simulation will test this hypothesis as follows:
Two stroke specialists will each score the neurological examination of two different patient cases. The neurological examination will be viewed by each stroke specialist using two different formats: 1) by desktop TeleBAT system, and 2) by videotape on a TV/VCR. For patient 1, stroke specialist 1 will grade the neurological exam (by the NIHSS) using her desktop computer, which is connected to the TeleBAT system, thus simulating a patient en-route to the hospital in a Maryland ExpressCare ambulance. For patient 1, stroke specialist 2 will view the videotaped version (on a TV/VCR) of the same patient examination and grade it (by the NIHSS). The process will be repeated for patient 2. To reduce bias, stroke specialist 1 is blinded to the exam and scoring performed by stroke specialist 2 (and vice versa) for each patient.

Statistical Analysis for Hypothesis 1:

The scores will be tabulated and an item-by-item analysis performed between stroke specialists for each case. Interrater reliability will be analyzed using the κ statistic (The measurement of interrater agreement, in Fleiss JL: Statistical Methods for Rates and Proportions. New York, John Wiley & Sons, Inc., 1981). A κ statistic of > 0.5 will indicate good interrater reliability and will be considered successful. This was used as the test for reliability for the NIHSS. (Brott TG, Adams HP, Olinger CP, et. al. Measurement of acute cerebral infarction: A clinical examination scale. Stroke 1989; 20:864-870).

Hypothesis 1: Lab Simulation (2 cases)

Stroke Specialist	Viewing Format Patient Number **Exam Assignment**	Viewing Format **Patient Number** **Exam Assignment**
Stroke Specialist 1	Desktop TeleBAT Patient 1 $NIHSSS_{TB}$ 1*	Videotape Patient 2 $NIHSSS_{VT}$ 2*
Stroke Specialist 2	Videotape Patient 1 $NIHSSS_{VT}$ 1*	Desktop TeleBAT Patient 2 $NIHSSS_{TB}$ 2*

* $NIHSSS_{TB}$ 1 compared to $NIHSSS_{VT}$ 1, and $NIHSSS_{VT}$ 2 compared to $NIHSSS_{TB}$ 2. If κ>0.5, then TeleBAT has interrater reliability.

Hypothesis 2: A neurologist will be able to make the same neurological assessment through the mobile telemedicine system as that made in face-to-face contact with the patient.

Methods for Hypothesis 2:

This hypothesis will be tested using actor patients. An actor will simulate a patient with a predefined stroke deficit with a predefined NIHSS score. The actor patient (AP) will be transported in the moving ambulance to simulate an actual patient transport. The stroke specialist viewing the AP by TeleBAT will perform the NIHSS score twice. First, during the transport, and second, using the videotape (the face-to-face examination) of the AP's transport. The videotaped examination from the transport must be used as a proxy to the actual face-to-face examination. That is because the patient's condition might deteriorate or improve from the time of NIHSSS determination by TeleBAT during transport.

Statistical Analysis for Hypothesis 2:

The two scores will be tabulated and an item-by-item analysis will be performed. Reliability will be analyzed using the κ statistic. We will compare NIHSSS1 vs NIHSSS2 ; if r> 0.5 then TeleBAT is valid. (See figure below)

Hypothesis 2: Laboratory Simulation (2 cases)

Stroke Specialist	Viewing Format Model Patient Number Examination Assignment	Viewing Format Model Patient Number Examination Assignment
Stroke Specialist 1	TeleBAT Model Patient 1 $NIHSSS_{TB}$ 1*	Videotape Model Patient 1 $NIHSSS_{VT}$ 1*
Stroke Specialist 2	TeleBAT Model Patient 2 $NIHSSS_{VT}$ 2*	Videotape Model Patient 2 $NIHSSS_{TB}$ 2*

* $NIHSSS_{TB}$ 1 compared to $NIHSSS_{VT}$ 1, and $NIHSSS_{VT}$ 2 compared to $NIHSSS_{TB}$ 2. If >0.5, then TeleBAT is valid.

Hypothesis 3: The mean time to complete evaluation* will be shortened for the patient group using the TeleBAT system as compared to that for an historical group not using TeleBAT.

The Brain Attack Team has maintained a prospective continuous data bank since August 1996 for all patients evaluated who meet inclusion and not exclusion criteria above and data has been recorded including:

1. Time of symptom onset;
2. Time to referring hospital;
3. Time to UMM
4. Time to completed evaluation

Our prospective data bank enters patients identified by a unique data bank number, which is not associated with the patients' name or medical record number. All information entered is blinded to patient identifiers.

*Time to complete evaluation for time sensitive therapy. The patient must have both general medical and neurological examinations, have a completed and analyzed brain CT scan, and must have laboratories returned and assessed by the treating stroke specialist.

Methods for Hypothesis 3
Historical control patients' data:
From August 1996, a total of 15 patients were transferred to UMM from another hospital and received time sensitive therapy (t-PA). The average time for a complete evaluation from arrival in the emergency department to initiation of time sensitive therapy was 33 minutes. The same data collection will be used for patients that are transported using TeleBAT, and the average time to complete evaluation for time sensitive therapy will be calculated for the TeleBAT patients (n=8).

Statistical Analysis for Hypothesis 3
We will use a 2-sample t-test to analyze this hypothesis. With 15 historical control patients having a mean time to complete evaluation of 33 minutes (SD ± 17 minutes), and 8 TeleBAT patients, we will have 80% power for the detection of a 60% reduction in time to complete evaluation with a 2 tailed t-test at the 0.05 significance level.

Above Section from Modified Protocol Version 02/25/00

However, on February 28, 2000, we received preliminary comments from the army's Louise Pascal about the revisions we had submitted on February 25, 2000. The army requested that we make the following changes: 1) to delete all references to medical monitor and 2) to delete all references to a volunteer registry database. Louise Pascal informed us that they no longer considered the protocol to be a high-risk study and that it was now considered as a no greater than minimal risk study.

The Army's HSRRB met on March 8, 2000 and teleconferenced Dr. LaMonte for questions and comments. On March 14th, we received a draft of the unofficial minutes from that meeting stating that more changes were required before the protocol could be approved. We started work on these right away.

Please note our Principal Investigator, Dr. Marian LaMonte, was out on maternity leave during much of this time. Despite being out of the office from January 10, 2000 to April 17, 2000 and adjusting to the demands of a young child, Dr. LaMonte made substantial changes to the protocol and submitted all the revisions to the army in a timely manner.

F. **Conclusions:** No publications have resulted from this work. **Major work during this period has been the rewriting revisions and requests for additions and revisions to the research plan and consent forms at the specific request of the HSRRB. The major effort during this time was spent making every effort to**

accommodate the army's wishes to get the protocol approved. . During this quarterly report period, numerous phone calls went back and forth, between Dr. LaMonte and the army's Colonel Zadinsky and between Lee Bromberger and the army's Louise Pascal. Every effort was made to comply with the army's wishes. We continued to work on revising the protocol.

On March 18, 2000, Dr. LaMonte emailed Colonel Zadinsky our latest version of revised protocol and simulated patient consent form. On March 20, 2000, we received the official minutes from the Army's HSRRB March 8, 2000 meeting confirming the remarks made in the unofficial draft. On April 1, 2000, Colonel Zadinsky emailed Dr. LaMonte with her comments regarding the March 18, 2000 protocol revisions. She said "she recognizes that there have now been substantial changes to the protocol since the initial submission. Once you make these requested changes, they should have no problem giving approval now that all human subjects protection issues have been addressed." We are in the process of making these latest requested changes.

On March 24, 27, 28, testing of the TeleBAT system using a simulated patient occurred. On April 4, Dr. LaMonte and the army's Colonel Zadinsky held a teleconference during which time, Colonel Zadinsky had a demonstration of the TeleBAT system in action, including the viewing of a simulated patient on the dedicated, secure, TeleBAT website.

G: **References:** There are no references.

H: **Appendices:** There are no appendices.

I: **Patents:** No patents are pending or planned. No publications have resulted from the work performed within this time period.

J: **Publication of Abstracts, Manuscripts, Brochures, etc.** None.

K. **Commercialization:** None expected.

University of Cincinnati

Department of Electrical & Computer Engineering and Computer Science
University of Cincinnati
PO Box 210030
Cincinnati OH 45221-0030

814 Rhodes Hall
Fax (513) 556-7326

November 24, 1999

Ms. Lydia Pearson
National Medical Technology Testbed (NMTB), Inc.
11354 Mountain View Avenue, Suite D
Loma Linda, CA 92354

Dear Ms. Pearson:

Enclosed is the final report for the interim continuation funding period of the project entitled *Intelligent Control of Hemofiltration Systems.*

If you have any questions please don't hesitate to contact me. Thanks for your help.

Sincerely,

Marios M. Polycarpou
Principal Investigator
Associate Professor

An affirmative action/equal opportunity institution

DESCRIPTION: State the goal of the project, including how it relates to improving health care and noting the advanced technology that will be developed or tested . Use succinct language to describe how the project goals will be achieved. **Do not exceed the space provided.**

The ultimate long-term goal of this research is to reduce health care costs while improving the quality of patient care. This proposal advances this goal by developing a novel intelligent control architecture for hemofiltration systems. Hemofiltration is a lifesaving renal replacement therapy used in an intensive care setting. Patients with life threatening illness often develop renal failure, and hemofiltration replaces the blood filtering process while the kidney recovers. When done correctly, this procedure is very labor intensive in terms of monitoring and control of equipment, for nephrologist and nurse alike. Our plan is to use intelligent control and a newly developed filtration system to facilitate the procedure so that the computerized hemofiltration machine will respond to patient needs based on moment to moment monitoring and thereby result in more accurate hemofiltration with reduced human intervention. The intelligent hemofiltration control algorithm will initially emulate the operation of an expert nephrologist and then improve in accuracy and reliability by learning with experience. We will test the hypothesis that the intelligent hemofiltration machine can learn to monitor and control the filtration procedure and respond to patient changes more smoothly than can intermittent human intervention. The computerization and application of intelligent control to hemofiltration will improve patient comfort and therefore increase patient compliance. The intelligent control algorithm will be designed to adapt on a short-term basis to accommodate specific patient needs and on a long-term basis for specific classes of patients. In addition to its immediate importance, this technology also can be applied to the automation of hemodialysis, to reduce the number of care-givers required per dialysis patient thereby realizing significant savings.

PROJECT SITE(S) (organization, city, state):

This research will be performed at the University of Cincinnati. Dr. Polycarpou's laboratory is in the College of Engineering, while Drs. Bissler and Benzing are with the Children's Hospital Medical Center (the two locations are within walking distance from each other).

DESCRIPTION: State the goal of the project, including how it relates to improving health care and nothing the advanced technology that will be developed or tested. Use succinct languageto describe how the project goals will be achieved. **Do not exceed the space provided.**

Monitoring cerebral oxygenation offers great promise in the management of acute, life-threatening neurologic illnesses, including severe traumatic brain injury. To date, the two primary methods used to monitor brain oxygenation are invasive - one requires percutaneous insertion of a catheter into the jugular bulb to continuously measure cerebral venous oxygenation and the other requires insertion of a probe through the skull into the brain parenchyma to measure tissue PO_2. Jugular venous monitoring provides a global assessment of brain oxygenation, but requires frequent recalibration. Brain tissue PO_2 provides a precise regional measurement of tissue oxygenation but cannot indicate inadequate tissue oxygenation in remote sites. Both jugular venous desaturation and low brain tissue PO_2 have been associated with poorer neurologic outcome and many clinicians use treatment protocols that initiate interventions when either or both of these values deteriorate. Near-infrared spectroscopy, a third, noninvasive method of monitoring cerebral blood oxygenation, is promising, but has yet to be satisfactorily calibrated to provide quantitative measurement. Therefore, at present there is no system for accurate, non-invasive, and continuous monitoring of cerebral blood oxygenation. We propose a novel technique that will utilize well-established differences in optical absorption coefficients of oxy- and deoxyhemoglobin in the near-infrared spectral range to accurately monitor blood oxygenation.
The objective of this project is to build and test a novel optoacoustic system to measure the absolute value of cerebral venous oxygenation directly from the superior sagittal sinus (SSS), a structure that can be localized due to the high resolution of the optoacoustic technique. The optoacoustic technique is based on generation of ultrasonic waves by laser pulses and detection of these waves by a sensitive acoustic transducer. Our preliminary studies demonsrate that (1) the amplitude and temporal profile of the ultrasonic waves are linearly dependent on blood oxygenation; (2) the use of specially designed transducers allows sensitive detection despite optical and acoustic attenuation by thick bone; and (3) this technique will measure blood oxygenation with high accuracy. The specific aims of the project are: (1) to build the optoacoustic system; (2) to validate the concept *in vitro* using human skulls with blood circulating through a model SSS; and (3) to test the system *in vivo* in sheep. Performance will be evaluated in normal sheep and in experimental models in sheep that replicate conditions typical of severe clinical traumatic brain injury. By the end of the first year of the project the system will be modified in preparation for preliminary clinical trials. In addition to brain monitoring, the proposed system can potentially be used for local non-invasive measurement of blood oxygenation in other organs.

PROJECT SITE(S) (organization, city, state):

University of Texas Medical Branch
Center for Biomedical Engineering
301 University Boulevard
Galveston, Texas 77555-0456

COP

SEMI-ANNUAL TECHNICAL REPORT

Period: 03/01/2000 - 08/31/2000

Cooperative Agreement # DAMD17-97-2-7016

Subagreement No: 71-FY99-UofTexas-Esenaliev

Principal Investigator: Dr. Rinat Esenaliev

Date: 09/07/2000

Address:

Rinat O. Esenaliev, Ph. D.
Assistant Professor,
Director of Laboratory for Optical Sensing and Monitoring,
Biomedical Engineering Center, MS 0456
Department of Physiology and Biophysics
and Department of Anesthesiology
301 University Boulevard
Rm. 621 Jennie Sealy Hospital
The University of Texas Medical Branch at Galveston,
Galveston, Texas 77555-0456
Phone: (409)-772-8144
Fax: (409)-772-0751
E-mail: riesenal@utmb.edu

1. Introduction

The long-term objective of this project is to develop and test a novel optoacoustic system for non-invasive, real-time, accurate, continuous monitoring of cerebral venous oxygenation. Low cost and portability of the system will permit wide application in the field (as in military or mass-casualty settings), in emergency care vehicles, and in hospitals. The objective of the first year of the project is to build and test a novel optoacoustic system to measure the absolute value of cerebral venous oxygenation directly from the superior sagittal sinus (SSS), a structure that can be localized due to the high resolution of the optoacoustic technique. Our specific aims for the first year are: (1) to develop and build a compact laser optoacoustic system for continuous monitoring of cerebral venous oxygenation; (2) to evaluate the system performance in human cranium; (3) to evaluate the system performance in animal model. The first six months of the project are devoted to full implementation of Aim 1 and partial implementation of Aim 2.

2. Body of the Report

During the period from the grant application submission and the start day of the project we continued our efforts in the development of the optoacoustic system for non-invasive continuous monitoring of cerebral blood oxygenation. This report includes data obtained during this period and the first six months of the funded period.

2.1. Optoacoustic System for Blood Oxygenation Monitoring

We developed and built the compact system with the following components : (1) a compact nanosecond Nd:YAG laser, (2) a fiber-optic light delivery system combined with a sensitive acoustic transducer in an optoacoustic probe, and (3) a computer for signal registration and processing. The compact Nd:YAG laser (Ultra CFR, $\lambda = 1064$ nm) was purchased from Big Sky Technologies Inc. This laser does not need external water cooling and provides pulse energy of up to 55 mJ at stability of 0.3%. The laser head was coupled with one end of a fiber-optic bundle. The other end of bundle was incorporated into the optoacoustic probe.

The optoacoustic probe combines a sensitive PVDF piezoelement with the diameter of 8 mm and optical fibers around the transducer with the diameter of 0.2 mm. The fibers are mounted around the transducer. Axial resolution of the optoacoustic probe is 0.3 mm.

The optoacoustic signals are recorded and processed by using a portable digital scope and computer (Dell Inc., Processor: Pentium III, 550 MHz). Recently, the Department of Anesthesiology (UTMB) purchased a laptop computer (Dell Inc., Inspiron 3800, Processor: Pentium III, 650 MHz) for the project that substantially decreases size and weight of the monitoring system. We also developed an algorithm for processing of optoacoustic signals.

2.2. In vitro tests of the system (major results)

We evaluated the performance of our system in vitro with the use of a blood oxygenator and in phantoms simulating blood with different oxygenation.

The oxygenator consists of a reservoir in which blood accumulates, a supply of gases (oxygen, carbon dioxide, and nitrogen), a membrane oxygenator, an "arterial" line (which in patients would be inserted into the aorta), a rotary pump, and a "venous" line (which in patients would return blood from the great veins in the chest) (Fig. 1). In this model, the arterial and venous lines are simply connected through a monitoring phantom (which replicates features of tissue through which a vessel courses) to form a complete ex vivo circuit. By changing the gas supply into the membrane oxygenator and permitting time for equilibration, the oxyhemoglobin saturation can be adjusted over a broad range and also can be changed in random order. For instance, changing the gas supply to 95% oxygen results in nearly complete oxyhemoglobin saturation; changing the gas supply to 5% oxygen results in oxyhemoglobin saturation of approximately 50%. Changing the gas supply below 5% provides oxyhemoglobin saturation below 50%.

Fig. 2 shows optoacoustic signals recorded from blood circulating through a 5-mm latex tube simulating a blood vessel. The tube was embedded in a phantom simulating tissue between the optoacoustic probe and the vessel. The signals were recorded through a 5-mm turbid gelatin slab (50 cm x 50 cm) with optical properties typical for tissues in the near IR spectral range (absorption coefficient = 0.11 cm^{-1}, reduced scattering coefficient = 2.9 cm^{-1}, effective attenuation coefficient = 1.0 cm^{-1}) and a plastic cuvette with 7-mm walls. The figure shows optoacoustic pressure signals recorded from the phantom at different blood oxygenation: 100%, 44%, 27%, and 10%. Fresh sheep blood was used in these experiments. Blood samples (1 mL) were taken simultaneously with the optoacoustic data acquisition and blood oxygenation was measured with a standard CO-Oxymeter (IL 813 Instrumentation Laboratories, USA).

The first sharp peak was produced by generation of optoacoustic waves directly on the surface of the optoacoustic probe. The long signal with the wide maximum at 2.4 μs was due to optoacoustic wave generation in the turbid gelatin. The signal between 5 and 8 μs was generated in blood circulating in the tube. It is clearly seen that the parameters of the signal are dependent on blood oxygenation. The amplitude and slope of the signal increase with the increase of blood oxygenation due to higher absorption coefficient of oxyhemoglobin compared with that of deoxyhemoglobin. These experiments demonstrate capability of the optoacoustic technique to detect changes in blood oxygenation continuously, non-invasively, and in real time through a tissue-like turbid medium by with the optoacoustic probe in the forward mode.

Our tests in thick gelatin phantoms simulating thick human skull and blood circulating in the SSS confirmed the capability of the system to detect optoacoustic signals from SSS phantom. Fig. 3 shows optoacoustic signal recorded from a gelatin slab with the thickness of 15 mm and optical properties typical for tissues such as skull and skin in the near IR spectral range (absorption coefficient = 0.11 cm^{-1}, reduced scattering coefficient = 2.9 cm^{-1}, effective attenuation coefficient = 1.0 cm^{-1}). The first sharp peak was produced by optoacoustic wave generation on the surface of the probe. The second (wide) peak with the following negative part was detected from the turbid gelatin. This optoacoustic signal is typical for uniform media.

To simulate blood circulating in the SSS under human skull, a layered tissue phantom was used. The first 9-mm layer was made of the same turbid gelatin. The second layer was made of gelatin with higher absorption coefficient (5 cm^{-1}) typical for venous blood in the near IR spectral range. The optoacoustic probe was placed on the surface of the turbid gelatin. The

signal recorded from the layered phantom (Fig. 4) has one more peak. This peak was produced in the absorbing gelatin.

These experiments demonstrate that the optoacoustic probe is capable of detection of optoacoustic waves in the forward mode (irradiation and detection of optoacoustic waves from the same side) from absorbing objects through thick turbid media simulating human skull.

The in vitro tests of the optoacoustic system in human cranium obtained from the Anatomy Department at the University of Texas Medical Branch demonstrated high acoustic attenuation of optoacoustic waves in the human skull. It is due to the air pockets that are produced in bone tissues because of desiccation of water in in vitro conditions. Such a high attenuation is not typical for bones in vivo and fresh bones isolated from air immediately after extraction from a body. We decided to test our system in freshly excised sheep skulls (see below) while trying to remove the air trapped in the human skulls using different techniques.

Our results of the development and tests of the optoacoustic monitoring system indicate that there are two possible designs of the optoacoustic probe. One of them is the design described above and proposed in the NMTB grant applications, where an acoustic transducer is surrounded by optical fibers. There is also another probe configuration that we have envisioned after we submitted the grant application to NMTB. The design uses so-called ring transducer and optical fibers inserted in the center of the transducer. This design offers the potential to significantly improve the signal-to-noise ratio of the optoacoustic waves induced in the superior sagittal sinus. While the original design for the probe is simpler and may have higher integral (over a wide angle of acceptance) sensitivity, it may have significant background (noise) signal from the scalp and skull due to the wide angle of acceptance. On the other hand, the use of the ring optoacoustic probe is expected to significantly improve lateral resolution and reduce unwanted background optoacoustic signal from the scalp and skull. The ring transducer has narrow angle of acceptance that may result in higher sensitivity of optoacoustic wave detection from the superior sagittal sinus with minimal lateral signal from the other tissues.

We performed preliminary feasibility tests with the ring optoacoustic probe. Figure 5 shows typical optoacoustic signals recorded from absorbing solutions through a 10-mm turbid tissue phantom. The solutions had different absorption coefficients and simulated blood with different oxygenation. Naphthol green, a stable dye with absorption in the near infra-red spectral range, was used as an absorber in these solutions. The range of absorption coefficient was from 1 to 12 cm^{-1} that covers the entire range of venous blood absorption coefficient at different oxygenation and hemoglobin concentration (2 to 10 cm^{-1}). The tissue phantom was a milk solution with optical properties similar to that of bone tissue in the near infra-red spectral range. The thickness of the tissue phantom is close to that of human skull above the SSS (8 - 10 mm). Thin polymer film was used to separate these two solutions. The parameters of the signals (slope and amplitude) are dependent on the absorption coefficient of the solution. The results of the first tests with the ring optoacoustic probe are encouraging and we believe that the ring probe configuration should be further developed.

In vitro experiments were performed with freshly excised sheep skull (thickness = 5 mm). A small slab of 10%-gelatin colored with naphthol green was placed under the skull. It simulated blood in the SSS. Standard ultrasonic gel was used to provide acoustic contact between the optoacoustic probe and the skull and between the skull and the slab. The optoacoustic system was capable of detection of the signals from the slab (Fig. 6). Slabs with different absorption coefficients (4 and 20 cm^{-1}) induced different optoacoustic signals. The in

vitro experiments with sheep skulls are in progress and should be done by the 8th month of the project when we planned to start in vivo tests in sheep.

Absorption coefficient of blood is dependent not only on oxygenation but on total hemoglobin concentration too. This can decrease accuracy of oxygenation measurements, in particular, in the situations when saline or drug infusions are used for treatment of patients. These injections change total hemoglobin concentration (and, hence, the optoacoustic signals from the SSS) even if the hemoglobin saturation is constant. In order to improve accuracy of oxygenation measurements, one can use one more pulsed laser operating in the near infra-red spectral range but at a different wavelength. Such a two-wavelength approach is being applied in conventional near-infrared oximeters and provide sufficient accuracy in some organs. Typically, one wavelength of the oxymeters is longer while the other one is shorter than the isobestic point of oxy- and deoxyhemoglobin (805 nm). The absorption spectrum of oxy- and deoxyhemoglobin is well-known (see [1, 2] and Fig. 7). Currently, there is one pulsed near-infrared laser available in the market with the wavelength shorter than 805 nm: Alexandrite laser operating at 750 nm. Alexandrite laser can generate short (nanosecond) laser pulses that are needed to produce optoacoustic waves in tissues.

The use of the two laser sources will improve the accuracy optoacoustic monitoring of oxygen saturation measurements in the superior sagittal sinus (SSS), because we will have two equations for venous blood circulating in the SSS:

$$\mu a\,(1064) = C[oxy] \times K\,[oxy, 1064] + C[deoxy] \times K\,[deoxy, 1064]$$

and

$$\mu a\,(750) = C[oxy] \times K\,[oxy, 750] + C[deoxy] \times K\,[deoxy, 750]$$

where μa (1064) and μa (750) are absorption coefficients of blood measured by the two-wavelength optoacoustic system at 1064 and 750 nm, respectively; C[oxy] and C[deoxy] are concentrations of oxy- and deoxy- hemoglobin in blood; and K [oxy, 1064], K [deoxy, 1064], K [oxy, 750] and K [deoxy, 750] are known values of extinction coefficients of oxy- and deoxyhemoglobin at these two wavelengths. Having the two equations and the two unknowns C[oxy] and C[deoxy], one can calculate C[oxy] and C[deoxy] and, hence, hemoglobin saturation of the venous blood circulating in the SSS which is determined as the ratio: C[oxy] / (C[oxy] + C[deoxy]). Therefore, variation of the total hemoglobin concentration will not influence the accuracy of oxygenation measurements.

FIGURES

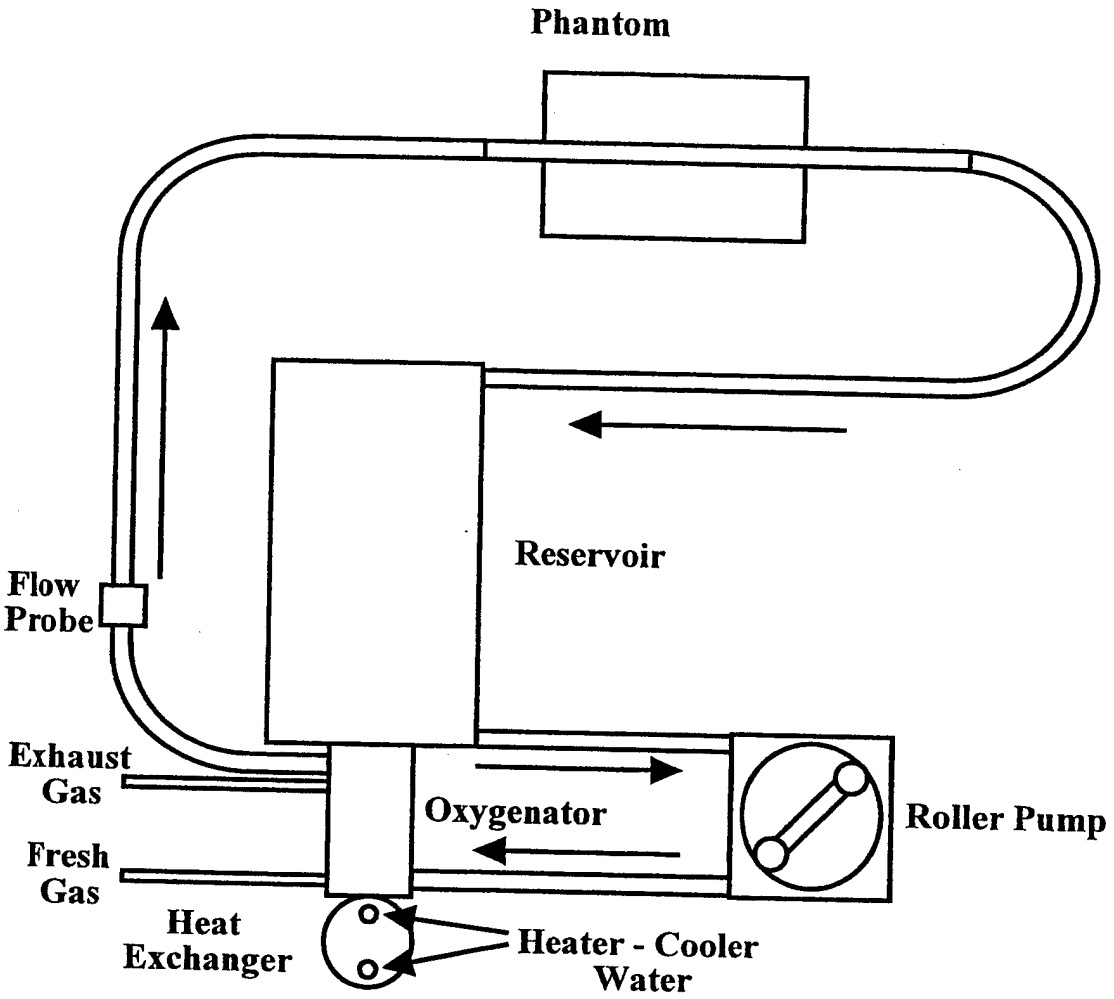

Figure 1. Schematics of blood oxygenator for in vitro tests of the optoaocustic system for cerebral blood oxygenation monitoring.

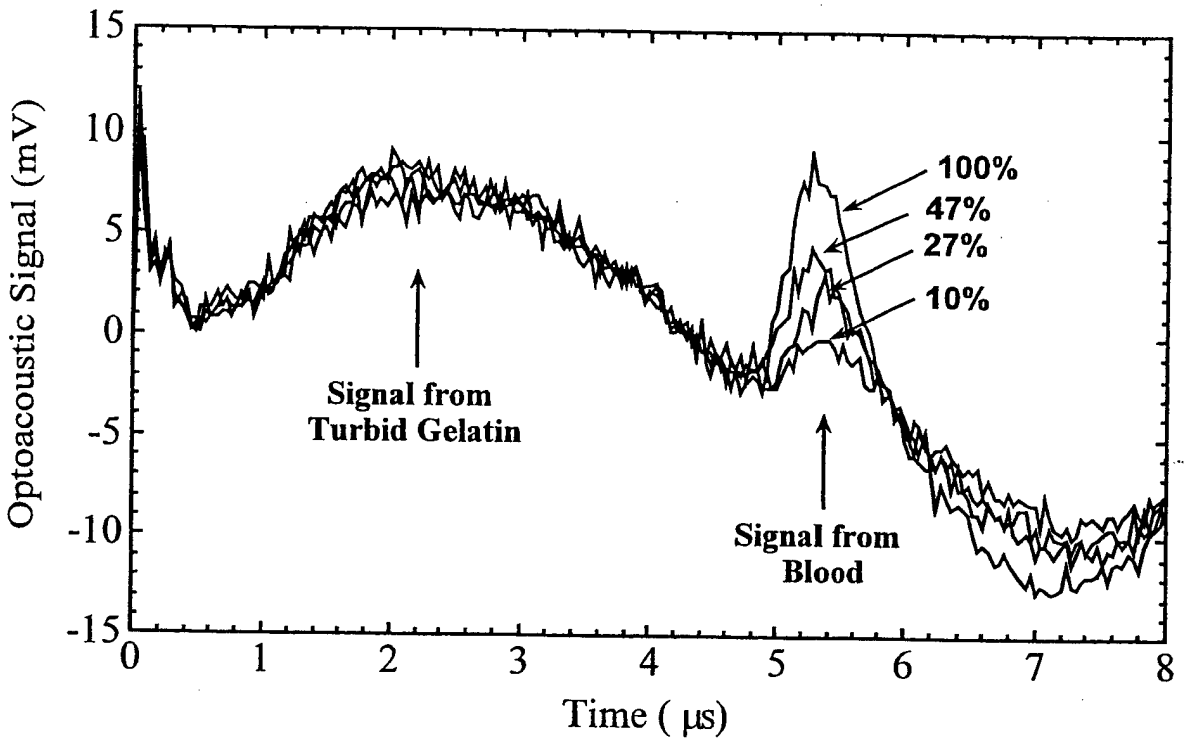

Figure 2. Optoacoustic signals recorded with the optoacoustic probe from a turbid tissue phantom with blood at different oxygenation (100, 47, 27, and 10%) circulating in a 5-mm tube.

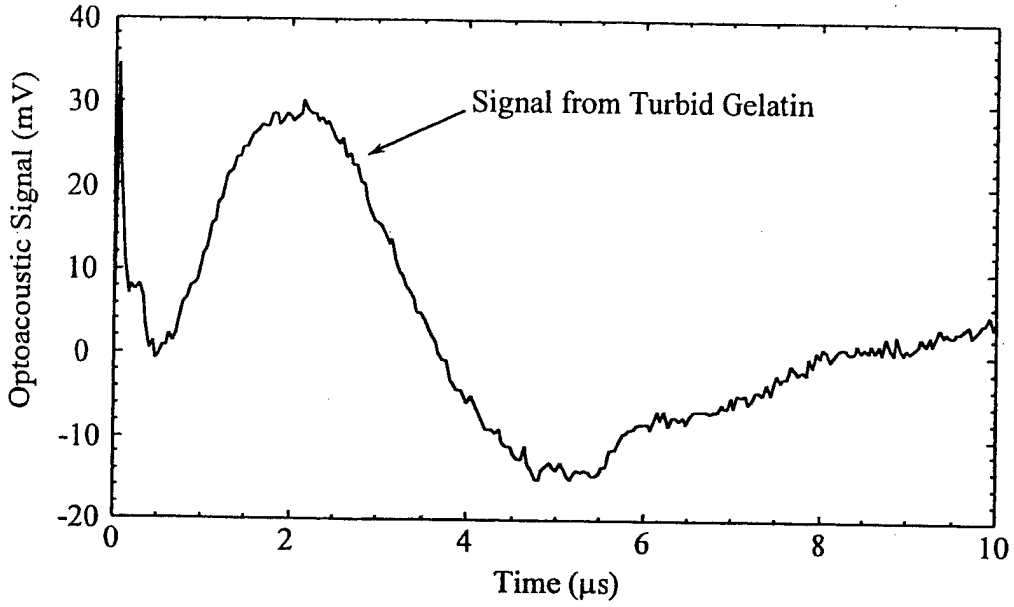

Figure 3. Optoacoustic signal recorded with the optoacoustic probe from 15-mm turbid uniform gelatin simulating thick tissue.

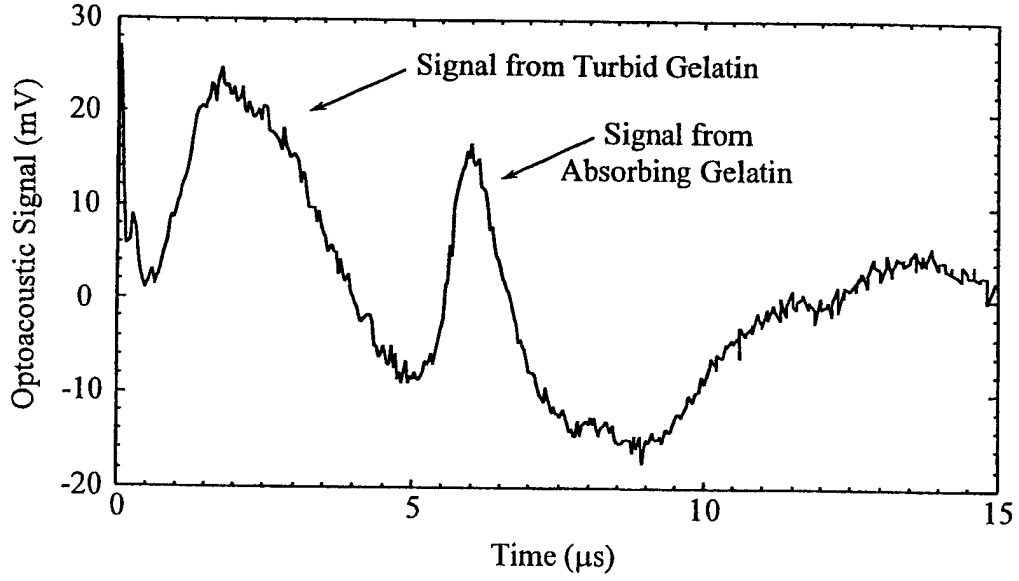

Figure 4. Optoacoustic signal recorded with the optoacoustic probe from a layered tissue phantom (9-mm turbid gelatin slab and a slab of absorbing gelatin simulating blood under thick tissue).

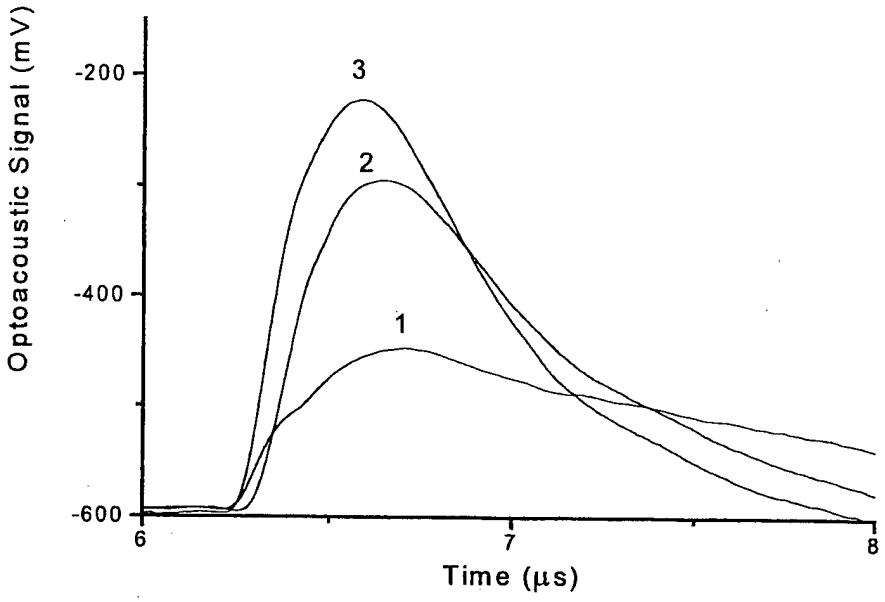

Figure 5. Optoacoustic signals recorded from absorbing solutions with different absorption coefficients (3 cm^{-1} , 8 cm^{-1} , and 12 cm^{-1} : 1, 2, 3, respectively) through 10-mm turbid tissue phantom.

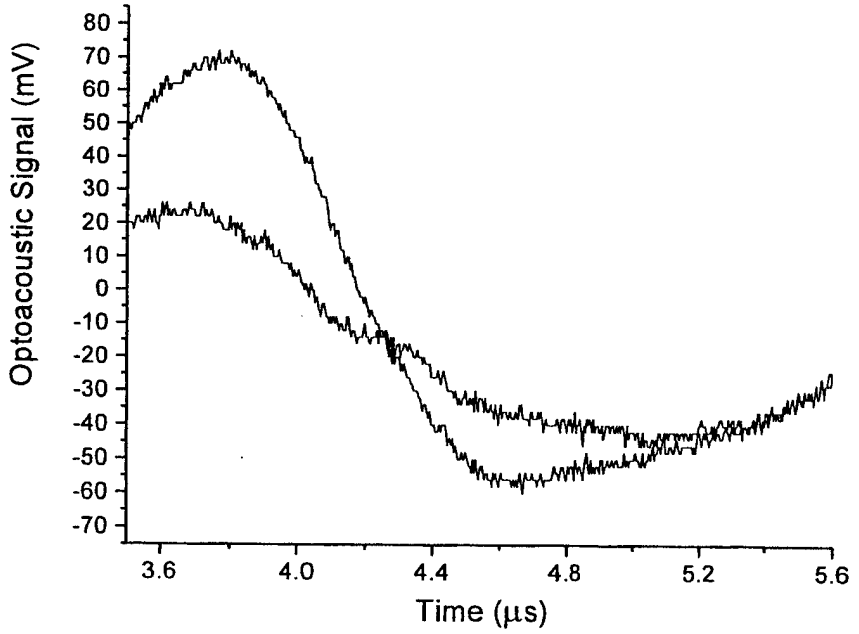

Figure 6. Optoacoustic signals recorded from gelatin slabs with different absorption coefficient (4 cm^{-1} and 20 cm^{-1} : 1, 2, respectively) through 5-mm sheep skull.

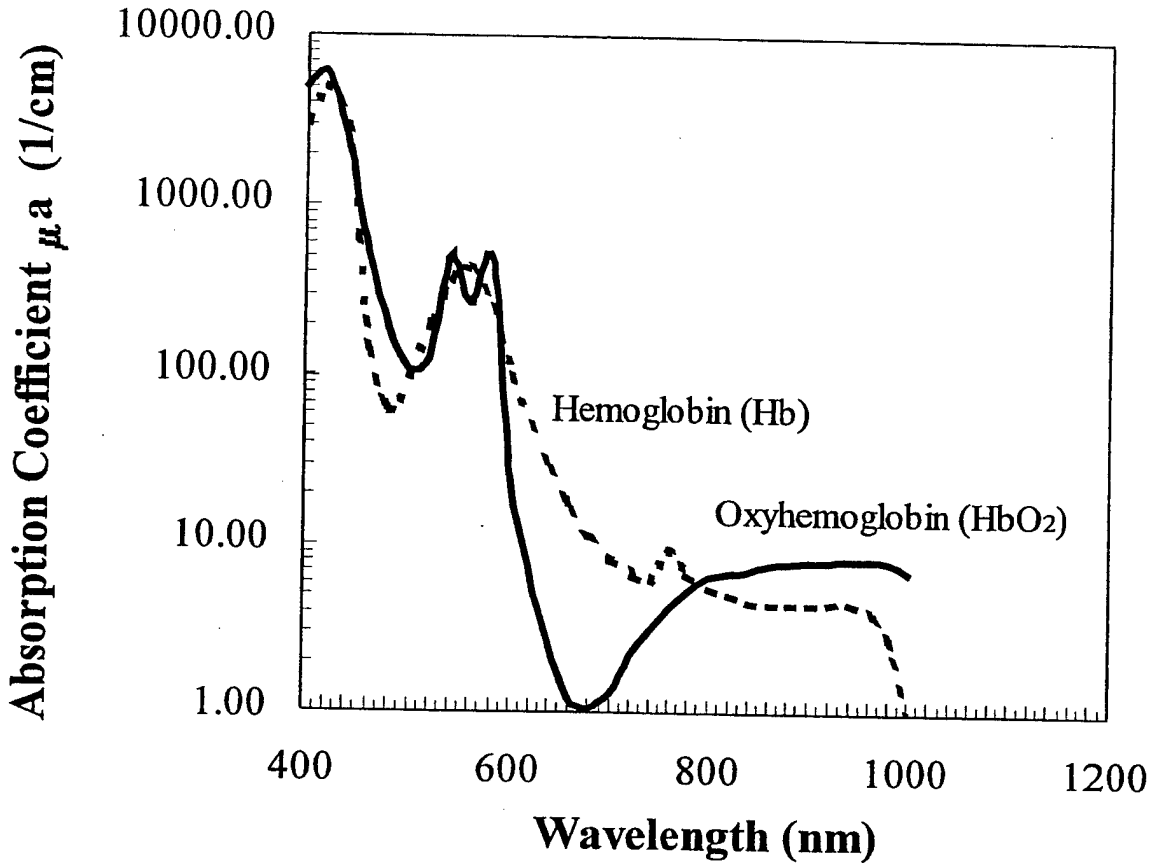

Fig. 7. Absorption spectra of oxy- and deoxyhemoglobin in the visible and near infra-red spectral range.

DESCRIPTION: State the goal of the project, including how it relates to improving health care and noting the advanced technology that will be developed or tested . Use succinct language to describe how the project goals will be achieved. **Do not exceed the space provided.**

Traumatic injury is the greatest cause of death in the US. Most trauma-related deaths occur within hours of initial therapy; many of these deaths are due to inappropriate fluid therapy, i.e. either under-resuscitation or over-resuscitation. We have recently found that cerebral oxygenation (CrSO2) as measured with noninvasive transcranial near infrared spectroscopy (NIRS) provides an effective index of cardiovascular status during shock and resuscitation. Further, we have designed and prototyped a new small, lightweight, microprocessor controlled infusion pump for field resuscitation.

These accomplishments have lead to this proposal and our current goal to develop a new product, a Resuscitation System, which integrates a small microprocessor pump, closed-loop fuzzy control and NIRS oximetry to optimize fluid infusions for the initial treatment of trauma.

The overall hypothesis to be tested is **Resuscitation of severe uncontrolled hemorrhagic shock is effectively achieved by fuzzy logic controlled titration of infusion to restore and maintain a target CrSO2.** We address our hypothesis with specific aims to:

1. Design and develop a functional prototype Resuscitation System which uses fuzzy control algorithms for adjusting infusions to restore and maintain target CrSO2.
2. Evaluate the efficacy of titrated resuscitation of uncontrolled internal hemorrhage using fuzzy logic controlled infusion to restore and maintain a target CrSO2 in chronically instrumented sheep. Control groups will be treated with standard of care large volume resuscitation and a no treatment control group.

The commercial potential is for all ambulances, life-flight helicopters and far forward military aid-stations to be equipped with this technology.

PROJECT SITE(S) (organization, city, state):

University of Texas Medical Branch
301 University Blvd.
Galveston, TX 77555

ORIGINA

No. 46
Unv. Texas Med. Branch/Kramer

Semi-annual Report for February 1, 2000 through July 31, 2000

Co-operative Agreement No. DA MD17-97-2-7016

Subagreement No. 19-FY99-UofTexas-Kramer

G. L. Kramer

PI signature

Aug 7, 2000

Date

Phone: 409) 772-3969

Fax: (409) 772-8895

Email: gkramer@utmb.edu

Introduction

Our overall long-term goal is to develop a new technological product, a Resuscitation System, which uses closed-loop control to optimize fluid infusions for the initial treatment of traumatic hemorrhage. The hypotheses to be tested were 1) monitoring brain oxygenation using non-invasive Near Infrared Spectroscopy (NIRS) provides an effective endpoint variable with which to guide infusion rates and 2) that fuzzy logic control provides the best control algorithm. In this semi-annual report, we present data that did not support the first hypothesis, and therefore we altered our plans and are using the other endpoints hepatic oxygenation and systolic blood pressure, which we have found effective. Completed experiments and their analysis have suggested several control algorithms that we continue to develop. These include dimensional decision tables, PID controller and fuzzy logic controller. On a positive note, Dr. Don Deyo of our group has made a new and significant redesign, improvement and simplification of our previously patented pressurized infusion system. We believe this new design has a superior commercial potential. Dr. Deyo's design may result in a new patent and an important product for both civilian and military treatment of trauma. The infusion algorithms developed by our research can be programmed into the pump, which would be the core component of a full Resuscitation System. A microprocessor controlled Resuscitation System could become part of telemedicine monitoring and trauma care and be most important for applications to combat casualty care and other non-hospital use. On the other hand, we are behind in our experimental timetable and also in our expenditures for a variety of technical and personnel issues. We are requesting a six-month extension with a no cost increase to complete the project. Details of results to date and amended plan follow.

Close to Bow?

BODY OF REPORT:

Historic Background and Current Guidelines: Advanced Trauma Life Support (ATLS) is a course taught by the American College of Surgeons for the initial care of hemorrhage and trauma by physicians and nurses(1). ATLS is as close to a US standard that is available. Actual prehospital and early emergency room trauma-care varies considerably at different US centers and even more so between the US and European systems based on physician training and beliefs as well as prehospital and ER resources. Treatment guidelines for military medicine can vary between service branches and units per local medical command. However, ATLS guidelines, modified somewhat for special logistic constraints of combat casualty care are often applied.

The ATLS guidelines for the initial treatment of hemorrhage and trauma are to control hemorrhage and infuse an isotonic crystalloid solution. The most commonly used solution is lactated Ringer's. Internal hemorrhage can rarely be immediately stopped, as this requires definite treatment, which is often surgery. Therefore, in most all cases fluid infusion is started before hemorrhage is controlled. If hemorrhagic shock has developed, it is considered necessary to infuse fluid to increase blood volume and hemodynamics before hemostasis is guaranteed. The amount of volume is controversial, but a sufficient volume needs to be infused that can provide enough venous return in order to produce a cardiac output that allows adequate arterial and blood flow to vital organs to preserve their function. The concept of the 'Golden Hour' of trauma care is that prompt early restoration of cardiovascular function in the first post injury hour can be critical to prevent subsequent organ morbidity or the development of irreversible shock. This emphasis on early volume therapy has lead to protocols of aggressive fluid infusion.

How much and how rapid the infusion should be is controversial. In the last 10 years there has been less emphasis on aggressive resuscitation, particularly after penetrating injury. Animal experiments mimicking uncontrolled internal hemorrhage due to aortotomy and arterial resection have shown that rapid increases in blood pressure secondary to rapid infusion can increase internal bleeding and mortality. Only one clinical trial to date has examined withholding or limiting intravenous fluids. Bickell et al, 1990 showed higher survival rates in which substantial fluid therapy was delayed until surgery began (2). Animal experiments suggest that the highest survival rates of uncontrolled hemorrhage occur with a limited resuscitation regimen that limits fluid in severe circulatory dysfunction to volumes sufficient to stabilize but not normalize (3, 4). This has resulted in policies of less aggressive therapy at many trauma centers. Some trauma centers and military medical units have different policies for volume therapy depending on the type of injury. Some infuse little fluid after penetrating injury, if mentation is present or systolic pressure is above 100 mnHg. Currently, there is no definitive means to guide fluid therapy.

Infusion Rates: ATLS guidelines for the treatment of hemorrhagic hypotension are to first infuse two liters of lactated Ringer's rapidly over 10 to 15 minutes. This would be an infusion rate of 133 to 200 mL/min for a 70 kg man. Such rates require one or two large bore catheters. More typically, civilian prehospital fluid therapy is delivered in volumes of less than a liter, and is often delivered over a short ≈10 minute urban transport time (5).

Response to Fluid Therapy: ATLS teaches that the hemodynamic response to the two liter bolus infusion can be a measure of how severe the shock is and whether ongoing bleeding is occurring. If there is no response the hemorrhage is considered severe and further volume, packed RBC's and surgery are likely to be indicated. If there is a sustained response and stability

then the hemorrhage may be modest and corrected and the need for surgery is considered less likely. One key question is should initial fluid therapy be directed by a set formula, adjusted to target endpoints or adjusted to the response of therapy? Such questions can only be answered when precise data on volume delivery and physiological responses can be monitored, recorded, and analyzed. Our experiments will address these questions in animals while a new Resuscitation System would gather the data in trauma patients.

Overview and Summary: We provide this overview of work done and results followed by details on the methods, results to date and the work to be done. The overall goal of the project continues to be the development of a Resuscitation System for monitoring and assessing level of circulatory shock and automated closed-loop fluid resuscitation. Such a Resuscitation System will provide definitive records between fluid therapy and responses and would also lend itself to online telemedicine monitoring and therapy decisions as well as detailed offline analysis.

The first hypothesis to be tested was monitoring brain oxygenation using non-invasive Near Infrared Spectroscopy (NIRS) provides an effective endpoint variable with which to guide infusion rates. The rationale was that using the target of brain oxygenation would provide a means of establishing adequate vital organ blood flow and overall cardiovascular stability, albeit at a lower than normal level. Data collected as part of this project strongly suggests that brain oxygenation will not provide a reliable endpoint to guide fluid resuscitation. After we submitted our NMTB proposal, the NIRS technology improved and we gained access to a newer model cerebral oximeter. The Somanetics dual channel INVOS 4100 has allowed us to measure both cerebral oxygenation and oxygenation at one additional site. Despite the lack of success with cerebral oxygenation the results were encouraging for two other endpoint variables: 1) hepatic oxygenation which was measured non-invasively with the NIRS oximeter and 2) systolic blood pressure which also lends itself to non-invasive measurement. These two variables appear to provide far more robust and useful endpoints. We will focus on these two endpoints for future studies and will incorporate one or both of them into the Resuscitation System.

The second hypothesis was that fuzzy logic control is superior to simple decision tables and a PID controller. We have not been able to evaluate this hypothesis yet. However, we have completed experiments and their analyses have suggested several control algorithms that we will continue to develop. We have found that normalization of systolic blood pressure or NIRS oxygenation are difficult to achieve even with massive resuscitation and that the use of subnormal target endpoints provides an adequate measure of cardiovascular stabilization. We have also compared large volume bolus infusions versus small volume bolus infusions versus continuous infusions at lower infusion rates. We find that the small bolus infusion is more efficient than the large bolus infusion. The continuous infusion approach is likely to result in fluid sparing while achieving the same endpoint. Volume sparing is an important consideration for field use and combat casualty care. We have compared various approaches to analyzing the target endpoints such as normalizing the physiological response to the volume of fluid infused or the initial level of the variable. The input from rate of change of the target variable (differential) has not been as useful as using the simple error signal alone. The error signal is equal to the difference between the measured variable and the target for that variable (proportional). We have had excellent success with the use of a 2 x 5 decision table, linking infusion rate to error signal or endpoint variable. We will test the prototype with fuzzy logic control once our experimental microprocessor controller is built.

Experimental Microprocessor Controller: This part of the project has had delays. We have had to redesign our closed-loop infusion system since our closed-loop PC based infusion system had interface problems with Baxter's commercial infusion pump, which we previously used. Baxter would not share their communication code with us and the computer control feature of the pump was discontinued and not fully supported by Baxter. Dr. Don Deyo has designed a controller from the ground up using LabView software that interfaces with a new Masterflex digital rotary pump. This controller has been designed to utilize a variety of target endpoint variables as inputs and a variety of control algorithms. Display and control panels and schematics appear in the Results section. Although good progress has been made the integration of the control component is not completed. We have not yet been able to fully use the controller in animal experiments. To maintain progress, we performed our first animal experiments with a 'simulated' closed-loop feedback using technician controlled infusion adjustments based on *a priori* designed decision tables and logic rules. This has allowed us to test our first hypothesis on using cerebral oxygenation and to evaluate several other infusion strategies.

Potential New Product and Invention: Dr. Donald Deyo has made a significant redesign, improvement and simplification of our previously patented pressurized auto-infuser system (6). We believe this new design has superior commercial potential and may result in an important product for the treatment of trauma, for both civilian and military. Dr. Deyo will file this as a formal record of invention and a commercialization plan with UTMB and NMTB. An initial declaration of the invention has been filed with UTMB's Technology Management Office along with a copy of this semi-annual report. We will make a functional concept-proving prototype of the Deyo invention once the experimental controller is completed. We will not prototype the original auto-infuser further.

Methods:

Our animal protocol received DOD approval three months after the start of the grant and this resulted in a delayed start. However, since starting the animal experiments we have made good progress, which has provided the necessary information to select a reliable endpoint variable and has helped design effective infusion algorithms.

Controller Development and Sheep Experiments: In the initial pilot experiments we found that NIRS monitoring of cerebral oxygen ($CrSO_2$) did not always provide a signal that improved with other indices of cardiovascular function. In fact, in some experiments $CrSO_2$ barely fell, presumably because of cerebral autoregulation. But in other experiments $CrSO_2$ did not improve with resuscitation, despite other improved variables. Thus we compared the use of the $CrSO_2$ endpoint (target of 50%) to other endpoints such as hepatic oxygenation (Hep SO_2) and systolic blood pressure target = 120mmHg. Results were correlated with 'gold standards' of cardiovascular function that have to be measured invasively, such as aortic blood flow and mixed venous oxygenation. If $CrSO_2$ had worked well, it would not have been necessary to evaluate other endpoint variables, but these experiments have saved the day as they provided us with two effective alternate endpoints for our Resuscitation System.

Experimental Series 1 Controlled Hemorrhage Comparison of Different Infusion Algorithms and Different Endpoints: Experiments were first performed in our model of controlled graded hemorrhage to produce different levels of hypovolemic shock and then resuscitation using bolus

infusions. We measured the response of the selected NIRS endpoint at 5 minutes after the bolus infusion in order to determine the need for and the size of the volume of the second infusion. Five minutes was deemed the time required to insure a NIRS response. When the more rapidly changing variable endpoint systolic blood pressure was used, a smaller bolus infusion was made every two minutes.

After an overnight fast, recording leads and catheters were connected from pressure transducers and flow meters (Baxter Vigilance Monitor) to the conscious sheep in its home cage on the experiment morning. Signals of blood pressure, cardiac output, (aortic blood flow), mixed venous S O_2, $CrSO_2$ and $HepSO_2$ received from pressure transducers, flow meters and a INVOS 4100 cerebral oximeter, respectively were continuously displayed and recorded after analog-digital-conversion using PowerLab Software and a Macintosh PC. After 60 min of baseline recording, we withdrew blood into a sterile titrated blood collection bag until mean-arterial-pressure decreased to 35-40 mm Hg. This produced a rapid and clinically relevant hemorrhage. All endpoint variables were continuously recorded and regression analysis was used to correlate variables from baseline through modest, moderate and severe shock, respectively, before resuscitation. Ten minutes after the hemorrhage was stopped, resuscitation was started to restore target variables using the different infusion algorithms listed in tables below. These were 'simulated' closed-loop resuscitation as Dr. Noddeland made the decision at every 2 or 5 min period using the decision/infusion algorithms as listed below in tables 1, 2 and 4.

Because of the lack of a mathematical model that relates volume infusion to any endpoint, we cannot analytically design the algorithm. Initially we used arbitrary target levels and endpoints that have been refined and tuned in subsequent experiments as described in the Results section.

In addition to performing a regression and correlation analysis during the induction of hemorrhagic shock, we performed a separate regression analysis for all variables during resuscitation or treatment. We compared results from four different 60-min resuscitation protocols using three different resuscitation endpoints (NIRS $CrSO_2$, NIRS $HepSO_2$ and SBP) in each of the six sheep, as well as one control untreated protocol. This resulted in a series of 24 experiments of hypovolemia and 18 experiments of resuscitation and 6 experiments with spontaneous compensatory responses alone. The endpoint variable was evaluated at predefined time-points. The endpoint value determined the size of the bolus infusion or the adjustment to the infusion rate for continuous infusion experiments. Dr. Noddeland designed the following decision tables.

Table 1

Rules for guiding infusion using NIRS endpoints and large bolus infusions: The same set of rules and targets were used for the NIRS liver and brain measurements in this large volume bolus series. A decision was made every 5-minute regarding the bolus size and whether to infuse a bolus or not. Each 5-minute period was divided into an infusion or intervention and the subsequent observation period.

NIRS endpoint value at timepoint	Intervention	Observation
less than 45 %	Bolus of Lactated Ringer's 200 mL given i.v. within 60 sec. from timepoint	About 4 min so that intervention + observation is exactly 5 minutes
45 – 50 %	Bolus of Lactated Ringer's 100 mL given i.v. within 30 sec. from timepoint	About 4 min so that intervention + observation is exactly 5 minutes
above 50 %	no intervention	5 minutes

Table 2

Rules for arterial systolic blood pressure (SBP) guided fluid resuscitation and small bolus infusions. The set of rules and targets were used for the more rapidly responding SBP measurement. A decision was made every 2-minute regarding the bolus size and whether to infuse a bolus or not.

SBP endpoint value at time-point **mmHg**	**Intervention: Bolus of Lactated Ringer's given i.v. within 30 sec. from time-point** **mL**	**Observation: From 1' 30" to 1' 50" so that intervention + observation is exactly 2 min** **min**
less than 50	100	2
50 – 59	80	2
60 – 69	70	2
70 – 79	60	2
80 – 89	50	2
90 – 99	40	2
100 – 109	30	2
110 – 119	20	2
120 and above	none	2

Table 3

Controlled Hemorrhage Studies: Sequence of timepoints bolus & continuous infusion studies. The variables $CrSO_2$, $HepSO_2$, aortic blood flow, arterial blood pressure, right atrial pressure and continuous cardiac output were recorded continuously using a PowerLab Macintosh AD system.

Time point	Definition	Blood sample	Comment
BL 1	Beginning of baseline period	Arterial blood gas, oximetry, Hct and protein analysis. Pulmonary blood gas and oximetry	thermodilution CO for comparison with Aortic blood flow. In vivo cal of SvO_2 Check zero press.
BL2	End of baseline period	Arterial blood gas, oximetry, Hct and protein analysis.	
Minutes-0 HEM-0	Start of hemorrhage		The aim is to hemorrhage the animal down to 35-40 mmHg MAP in 10 minutes
Minutes-10 HEM-10	Stop of hemorrhage Shock period starts		
Minutes-20 HEM-20 RES-0	10 minutes after STO Start treatment protocol per table 1 or 2.	Blood sample just before Hem20 Arterial blood gas, oximetry, Hct and protein analysis	
Minutes-50 RES-30		Blood sample just before Res-30 Arterial blood gas, oximetry, Hct and protein analysis	
Minutes-80 RES-60	Last treatment intervention	Blood sample just after RES-60 Arterial blood gas, oximetry, Hct and protein analysis	

Table 4

Rules for arterial systolic blood pressure (SBP) guided fluid resuscitation and continuous infusions: In the continuous infusion experiments, the maximum infusion rate was set at 1.43 mL/min/kg and was used when the target variables were lowest. This represents a max infusion rate of 100 mL/min for a typical 70-kg patient. It was deemed that this was a reasonable maximum value that was realistic to achieve, and was in keeping with the recent trend of less aggressive infusion rates. As the endpoint variable improved and approached target the infusion rate was decreased. At target levels and above, the infusion rate was set to a minimum value or the pumps lowest setting. The following table was calculated for 35 kg. sheep. An individual table was calculated for each animal.

	Endpoints			
	Liver NIRS	**Brain NIRS**	**Target SBP**	**Infus. rate**
Target =	**50%**	**48%**	**120 mm Hg**	**mL/min**
Max infusion if	**0-42**	**0-39**	**50**	**50.0**
80% Max if	**43-44**	**40-41**	**50-59**	**40.0**
60% Max if	**45-46**	**42-43**	**60-79**	**30.0**
30% Max if	**47-48**	**44-45**	**80-99**	**15.0**
10% Max if	**48-49**	**46-47**	**100-119**	**5.0**
Min infusion	**50+**	**48+**	**120+**	**1.5**

Preparatory surgery: All animals were instrumented one week before an experiment using general halothane anesthesia and aseptic surgery. Catheters were secured in the right and left femoral artery and veins and the pulmonary artery via the jugular vein (Swan-Ganz pulmonary artery catheter). The Swan-Ganz catheter is fitted with a fiber-optic port for continuous recording of mixed venous oxygen saturation in the pulmonary artery using an Oximetrix 3 System (Abbott Labs) or Baxter Vigilance system which also provides a measure of continuous cardiac output. Unfortunately, the continuous cardiac output did not have the response time needed. So it was necessary to also place a 16-20 mm Transit Time Doppler flow probe (SB 16-20) on the ascending aorta to allow continuous real-time monitoring of aortic blood flow as an index of cardiac output. Thermal dilution cardiac-output can be measured intermittently with the Swan-Ganz catheter for definite calibration.

Measured and Calculated Variables: Variables measured, using methods described in our previous publications, (7-9) included arterial pressure, central venous pressure, pulmonary arterial pressure, cardiac output, mixed venous oxygen saturation, standard blood gases of blood from the aorta and mixed venous (pulmonary artery), blood hemoglobin, and hematocrit. Blood flow is measured by a Doppler ultrasound flow probe using a Transonic Flow Meter Model

T206/8. Total intraperitoneal blood volume was directly measured after euthanasia in the uncontrolled hemorrhage experiments at autopsy.

Data analysis and statistics: Correlation linear regression analysis and sensitivity analyses were performed comparing $CrSO_2$, $HepSO_2$, SBP and aortic blood flow (cardiac output). These analyses were used to select the best endpoint and target for resuscitation, i.e. for titration of fluid therapy. Analysis were performed on all data for each experiment and then separated into two analyses during induction of shock and resuscitation. There provided different relationships between $CrSO_2$ and other physiologic variables during shock and resuscitation. This helped us to define the relative invalidity of using cerebral oximetry to diagnose shock and the more valid use of $HepSO_2$ and SBP to titrate fluid therapy

The experimental protocol for the efficacy studies allow repeated measures designed with each sheep serving as its own control. The units of analysis were the changes from pretreatment for particular treatments (or "time points"); both within-group and between-group comparisons (treatments) are of major interest; ANOVA models are employed to analyze the data.

Results and Discussion:

Tissue Oxygenation using Near Infrared Spectroscopy (NIRS): In 24 experiments of controlled hemorrhage we evaluated $CrSO_2$ with other oxygen endpoints of resuscitation, namely $HepSO_2$ and mixed venous SvO_2. Comparisons with aortic blood flow were used as an invasively measured 'gold standard' of cardiovascular function.

We performed a series of controlled hemorrhage studies in which we used either brain oxygen saturation ($CrSO_2$), n=6, liver oxygen saturation ($HepSO_2$), n=6 or systolic blood pressure (SBP), n=6 as the target variable to guide fluid therapy. We also performed six experiments of untreated hemorrhage. Hemorrhage was induced by rapid bleeding to reduce mean arterial pressure to 35-40 mmHg in 10 minutes; this resulted in a bled volume of 20-25 mL/kg. Infusions were delivered as intermittent bolus volume delivery every 5-min with NIRS targets and every 2-min with SBP target using *a priori* designed decision table. Representative experiment shown in Figure 1A and 1B.

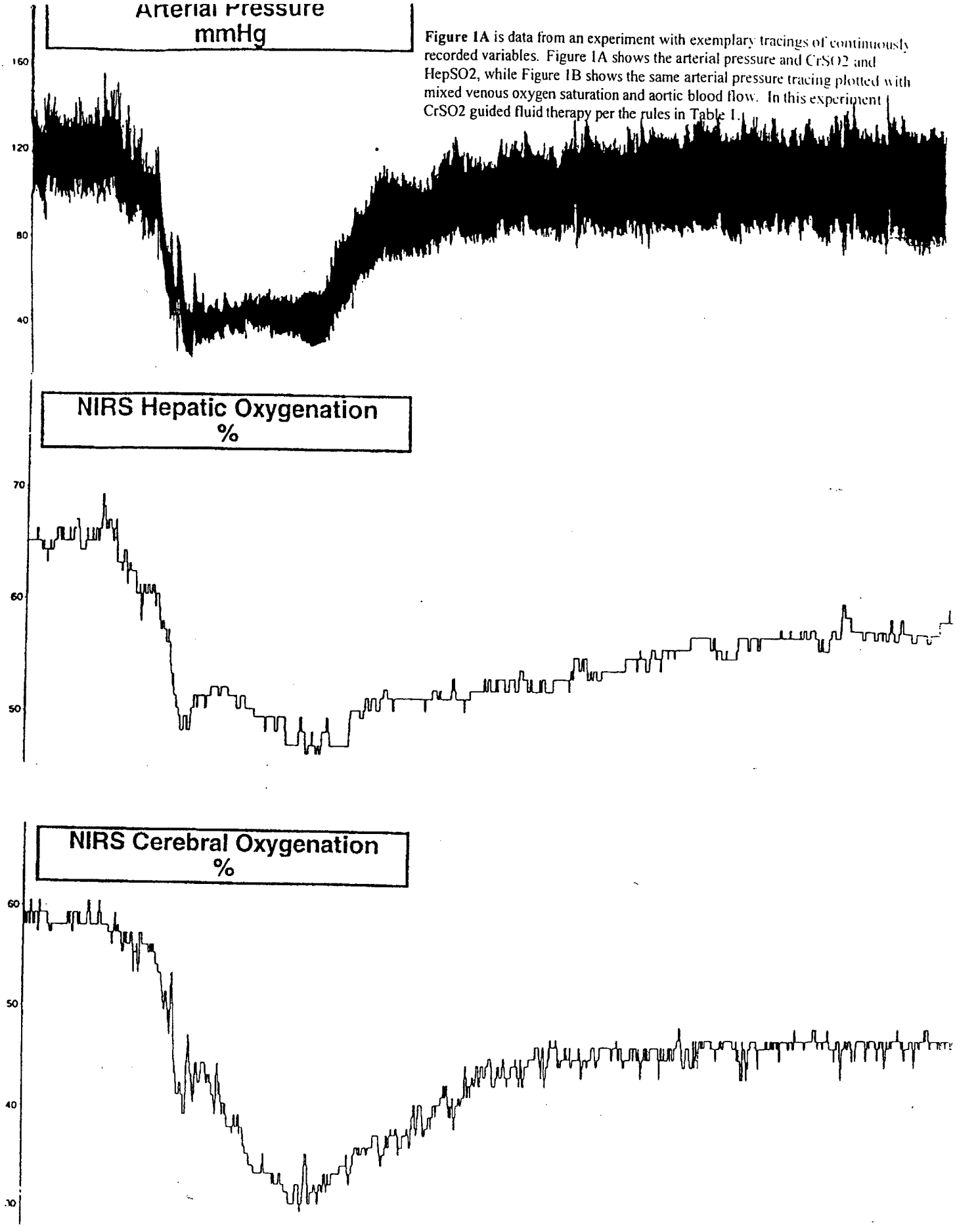

Figure 1A is data from an experiment with exemplary tracings of continuously recorded variables. Figure 1A shows the arterial pressure and CrSO2 and HepSO2, while Figure 1B shows the same arterial pressure tracing plotted with mixed venous oxygen saturation and aortic blood flow. In this experiment CrSO2 guided fluid therapy per the rules in Table 1.

Figure 1B

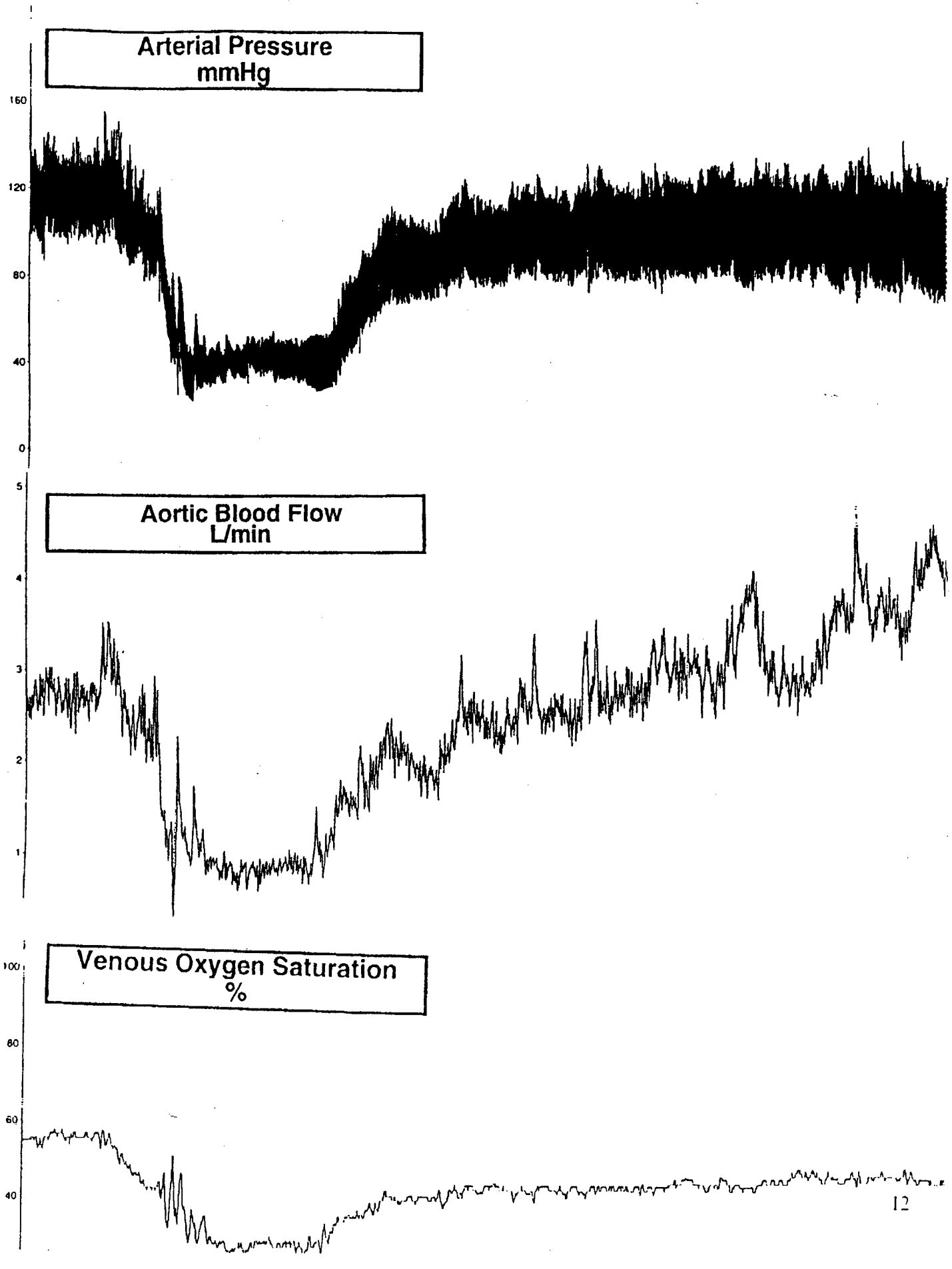
Arterial Pressure
mmHg
160
120
80
40
0
Aortic Blood Flow
L/min
5
4
3
2
1
Venous Oxygen Saturation
%
100
80
60
40

$CrSO_2$ has not proved to be as reliable an index of cardiovascular function as we had hoped for. We base this conclusion on several comparisons.

Inability to reach target: A $CrSO_2$ less than 50% used to represent borderline cerebral hypoxia (10-14). $CrSO_2$ = 50% was our initial target value, indicating a minimum cardiovascular function that was sufficient to provide vital organ blood flow. However, we found that sometimes baseline levels were below 50% (3 out of 24 experiments) and in 15 out of 18 resuscitation experiments $CrSO_2$ did not reach target levels. In some experiments $CrSO_2$ barely fell, presumably because of cerebral autoregulation. On the other hand, $HepSO_2$ always started above 50% and this target was achieved in 16 out of 18 resuscitation experiments.

Signal Quality and Failure: A subjective comparison of the signals for $CrSO_2$ and $HepSO_2$ usually provided comparable data showing declines with hemorrhage and improvement with resuscitation, Fig 1. However, paired comparison of $CrSO_2$ and $HepSO_2$ tracings showed that $CrSO_2$ could exhibit rapid variability and a comparatively noisier signal than the $HepSO_2$ signal. There were some outright failures in which several instantaneous and large increases or decreases to supranormal or subshock levels were recorded with NIRS and mixed venous oximetry. Outright failures were recorded in 3 out of 24 studies for $CrSO_2$, but in only 1 out of 24 studies for $HepSO_2$. However, both $CrSO_2$ and $HepSO_2$ were more stable than the mixed venous SO_2 measured with an indwelling pulmonary artery co-oximetric catheter. There were 9 out of 24 outright failures with SvO_2 monitoring. This may reflect that the pulmonary artery catheter moved into a wedge position or the sensor can be pushed next to the vessel wall during low flow states or with increased respiratory efforts.

Ability to distinguish between fluid therapy and non-treatment: In general more discrimination was exhibited with all other variables than with cerebral oxygenation. This may reflect better cerebral autoregulation. Figures 2-7 show the mean responses of all target variables, as well as aortic blood flow and mixed venous SvO_2 for each of the three resuscitated groups and the one untreated group. Treatment was started at 20 minute after starting the hemorrhage as guided by oxygenation of the brain, liver, or systolic blood pressure; one group was untreated.

Figure 2 - Systolic blood pressure rapidly declined to 55 to 65 mmHg with hemorrhage adjusted to reduce mean arterial pressure to 35-40 mmHg. SBP increased more rapidly with treatment than without, but SBP demonstrated slow spontaneous recovery even without fluid therapy, most likely due to compensatory mechanisms such as transcapillary refill. The group using brain oxygenation as endpoint received the greatest volume of fluid, Fig 9.

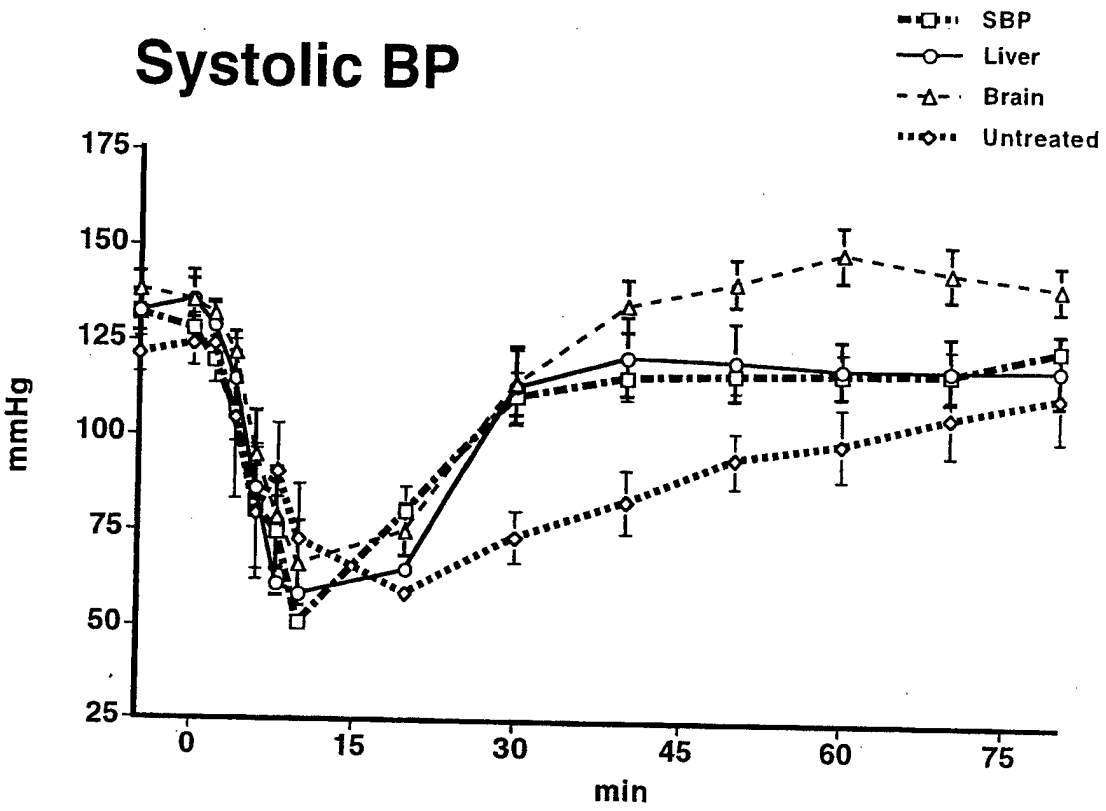

Figure 3 - Aortic blood flow declined to about 30% of baseline levels and then recovered more quickly with resuscitation than without. There was a trend for the treated animals to improve more quickly, but the data was not as clear as with systolic blood pressure. At the end of the experiment, after 60 minutes of treatment aortic blood flow was similar for all four groups.

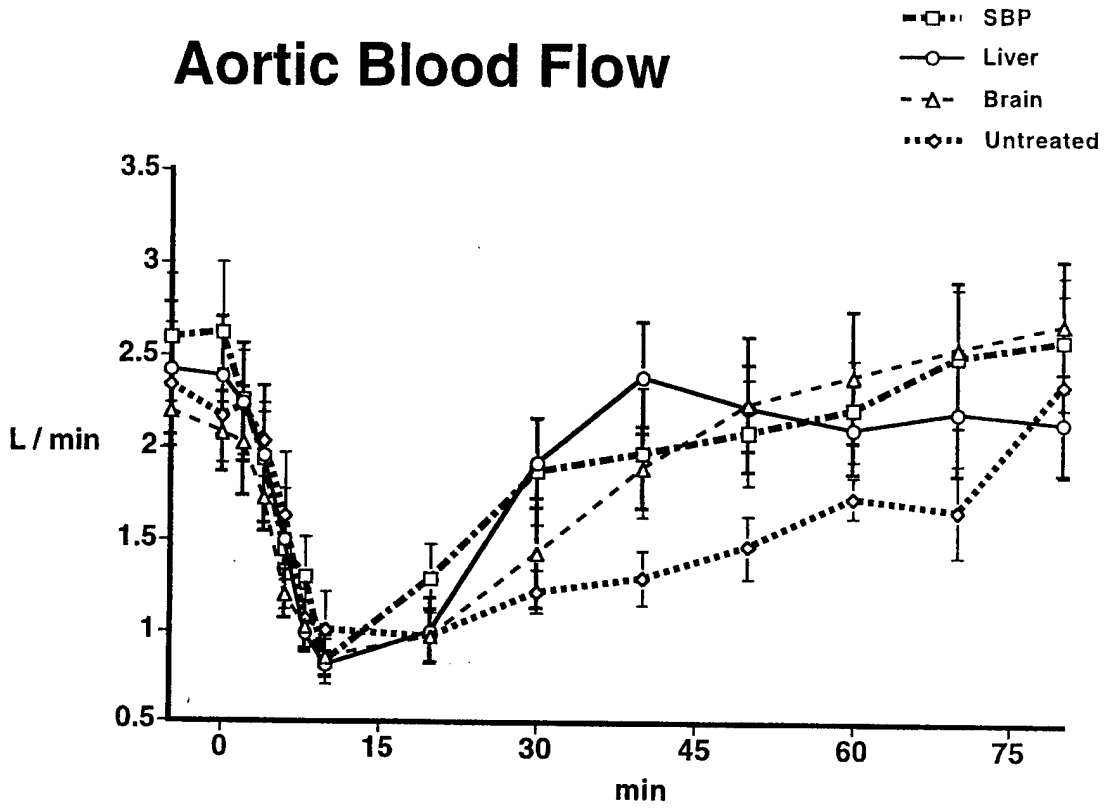

Figure 4 - Cerebral regional oxygen saturation CrSO2 as measured with an INVOSS 4100 declined from normal level of 50 to 60% to about 35%. Slow improvement was observed by all groups with little difference between treatment and non-treatment or between endpoint variable used. These data suggest that cerebral oximetry will not provide a robust endpoint by which to guide and adjust infusion rate.

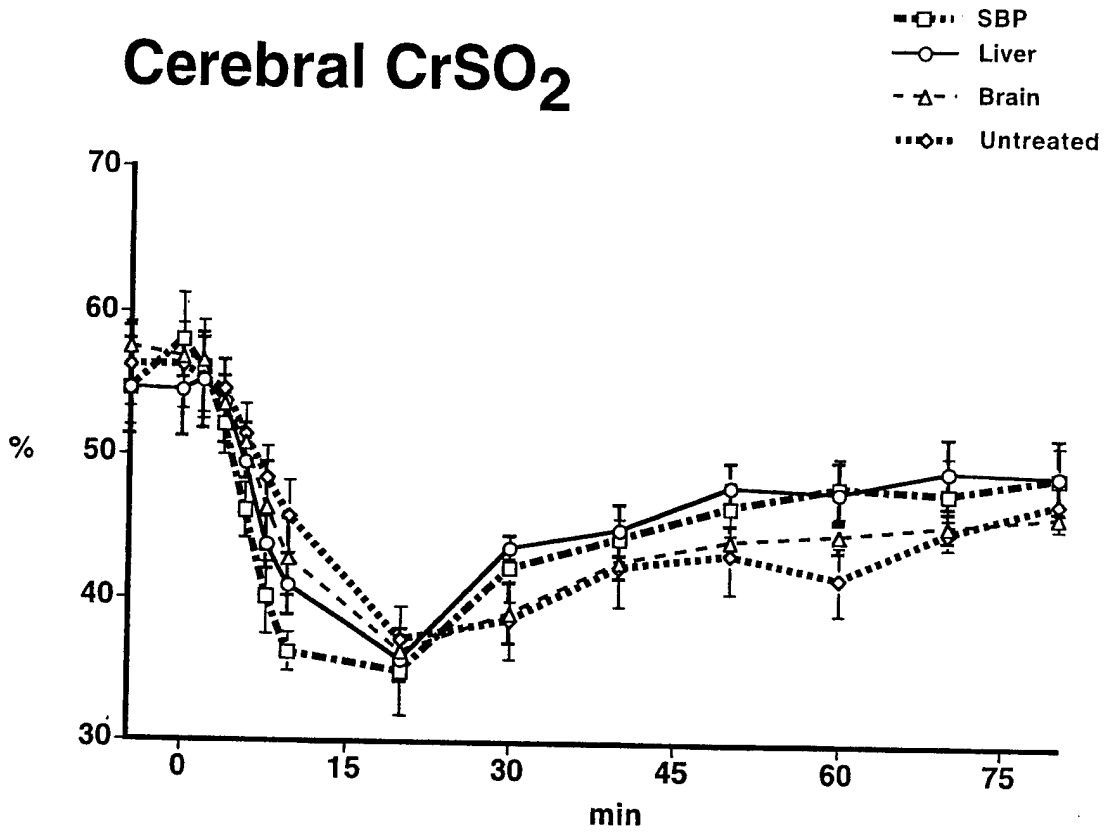

Figure 5 - Hepatic regional oxygen saturation HepSO2 as measured with an INVOSS 4100 rapidly declined from baseline levels of 60 to 65% to about 40%. As opposed to CrSO2 all groups of treated animals improved more rapidly than did untreated animals.

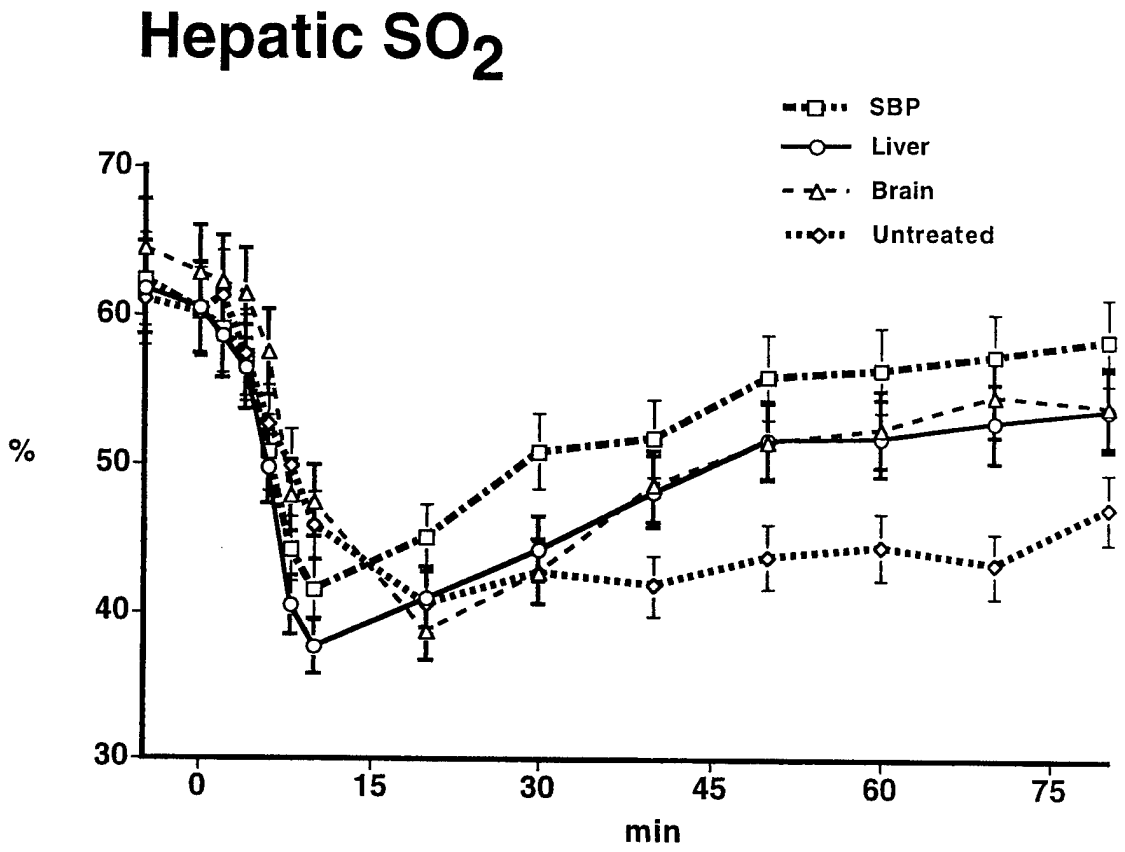

Figure 6 - Mixed venous SvO2 declined with hemorrhage and appeared to exhibit more variability than either of the NIRS measures of tissue oxygenation. There was a trend for more improvement with the treatment.

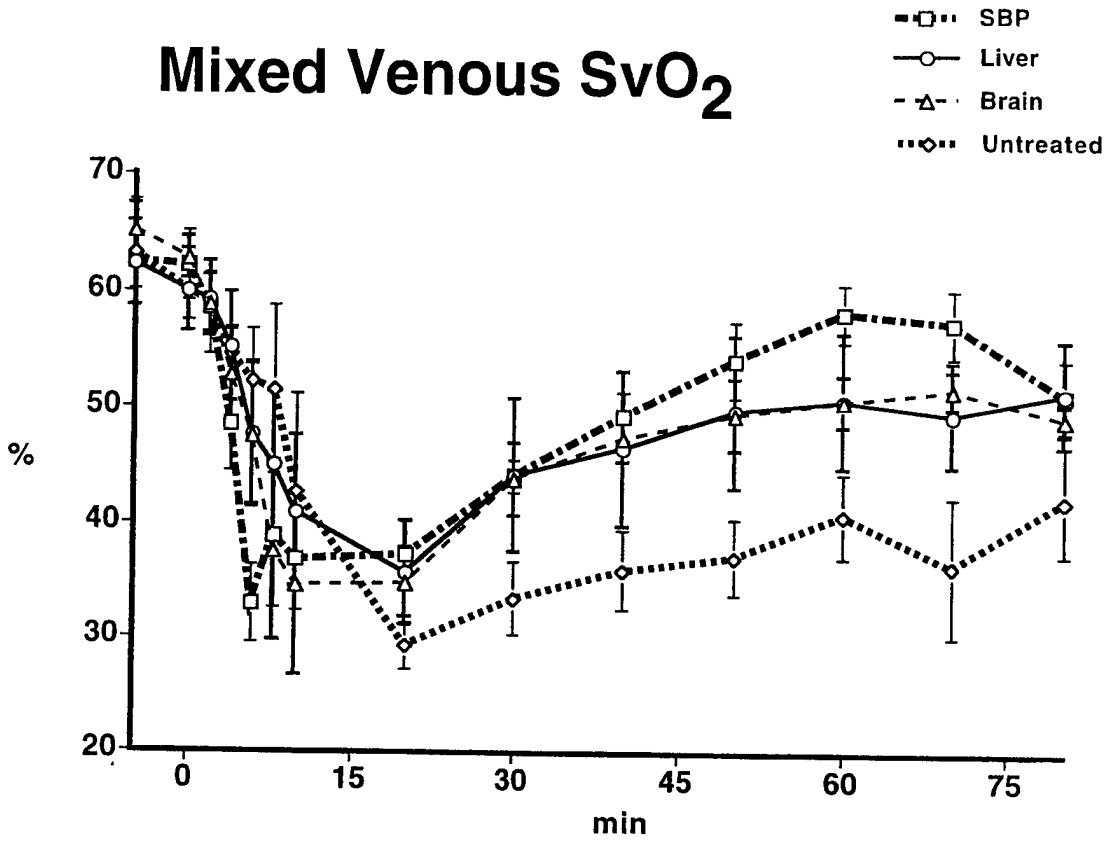

Figure 7 - Cumulative volume needed to resuscitate using large volume infusions and target endpoints of $CrSO_2$ and $HepSO_2$ of 50% (Table 1) as compared to small volume bolus infusions using SBP of 120 mmHg as endpoint. Large volume therapy guided by $CrSO_2$ or $HepSO_2$ or small volume therapy guided by SBP was based on algorithms shown in Tables 1 and 2. Each group had six animals. $HepSO_2$ and SBP targets were reached in the majority of experiments while $CrSO_2$ target was reached in just one out of six experiments.

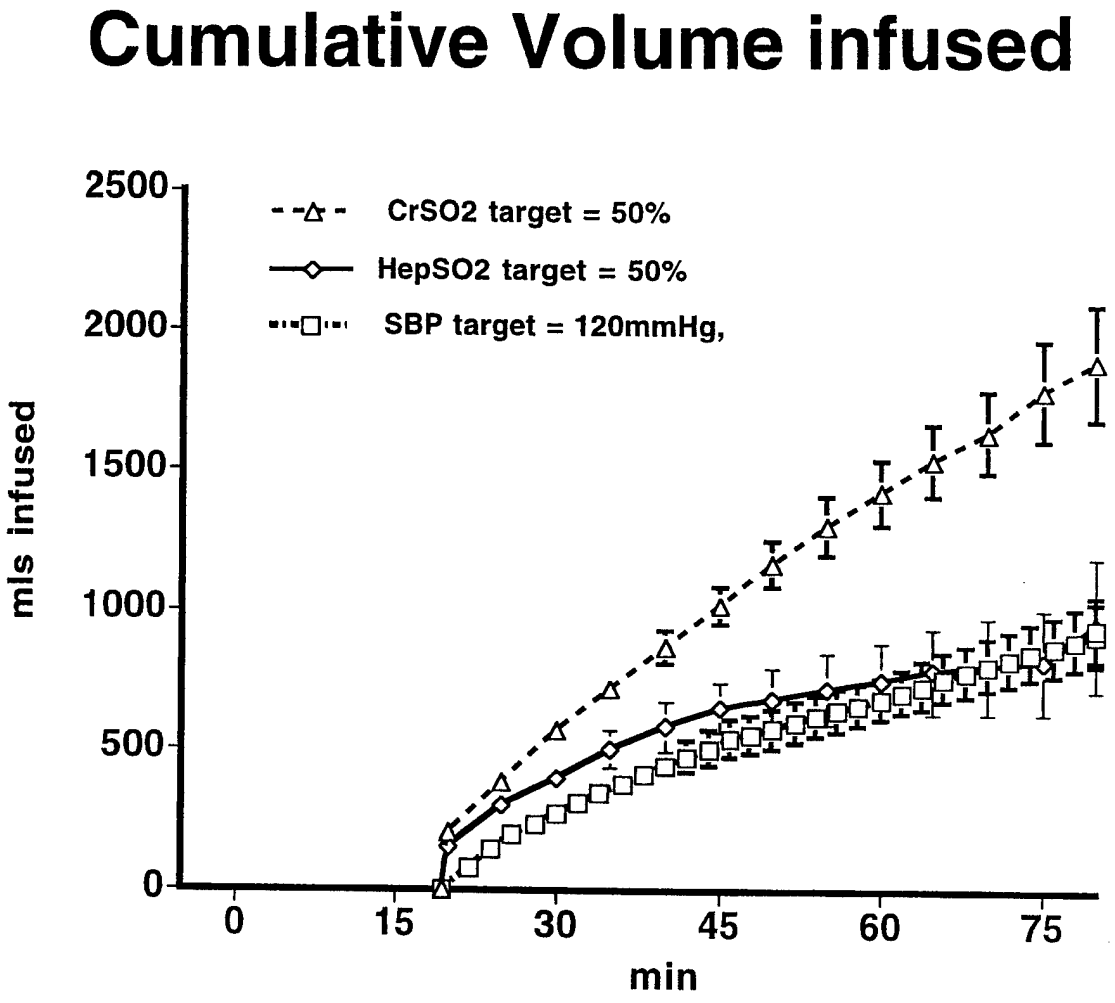

Correlation and Regression Analysis: We performed correlation and regression analysis of target variables versus each other and versus aortic blood flow as a more functional index of cardiovascular performance and the success of resuscitation. Correlation coefficients were calculated twice for each individual experiment, once during induction of hemorrhage at 2 min intervals and also during resuscitation at 10 min intervals. In nearly all experiments correlation coefficients were higher for hemorrhage than during resuscitation. However, the resuscitation correlation coefficients are the only ones that have relevance for guiding fluid therapy as baseline or preinjury levels would not be available in a clinical setting.

We present a summary of the mean z squared regression of four variables versus aortic blood flow during resuscitation in the following table. In the untreated group this represents regression correlation's during slow spontaneous recovery. We found that both $CrSO_2$ and $HepSO_2$ had higher levels of mean correlation with aortic blood flow (A/BF) than found with SvO_2 in 7 out of the 8 comparisons of mean values. This may reflect greater reliability of the non-invasive NIRS monitoring compared to an indwelling catheter. $HepSO_2$ was higher than $CrSO_2$ in 3 out of 4 mean comparisons and 14 out of 23 individual experiment comparisons. The highest correlation was often found with systolic blood pressure versus aortic blood flow.

Table 5

Correlation and regression (r squared) of variables versus aortic blood flow

Highest correlation within each group is bolded.

	Endpoint Groups, n = 6 each			
variable	**Brain**	**Liver**	**SBP**	**untreated**
$CrSO_2$ vs A/BF	0.717 ± 0.05	0.730 ± 0.12	0.655 ± 0.05	0.443 ± 0.15
$HepSO_2$ vs A/BF	**0.823 ± 0.04**	0.665 ± 0.15	**0.755 ± 0.04**	0.487 ± 0.09
SvO_2 vs A/BF	0.692 ± 0.13	0.534 ± 0.14	0.577 ± 0.13	0.439 ± 0.05
SBP vs A/BF	0.759 ± 0.08	**0.802 ± 0.09**	0.745 ± 0.08	**0.587 ± 0.11**

Table 6

Response Times: We calculated the time from the initiation of hemorrhage to the minimum value for each variable as an indication of response time in 24 experiments of controlled hemorrhage. Data shown in Table 6 suggests that systolic blood pressure is the most responsive variable, with NIR Liver oxygenation following by about 5 minutes and NIRS Brain oxygenation following by 8 minutes. Mixed venous O_2 and aortic blood flow had intermediate response times, but these two variables can only be measured by invasive technology at the present time.

Endpoint Variable	minutes to minimum, mean ± sem
Systolic BP	10.6 ± 0.7
SvO_2	13.9 ± 1.0
Ao BF	12.6 ± 0.7
NIRS Liver	16.0 ± 1.2
NIRS Brain	18.4 ± 1.1

Conclusions Regarding Target Variables: The original endpoint variable that we proposed to use in the design of our Resuscitation System was brain oxygenation as measured non-invasively by near infrared spectroscopy (NIRS). We previously used the INVOS 3100 but now we use the newer model INVOS 4100 cerebral oximeter (Somanetics). This device provides a non-invasive means of assessing cerebral oxygenation. It has two sensors designed to provide a measure of cerebral oxygenation in the two cerebral hemispheres. However, we used the second sensor to measure transcutaneous liver saturation. We believe that the use of systolic blood pressure or hepatic oxygenation measured via NIRS is superior to cerebral oxygenation for use as a resuscitation endpoint. We base this conclusion on 1) our experience and subjective evaluations of the signal quality; 2) higher correlation with gold standard variables such as aortic blood flow; 3) a greater ability to distinguish between animals being treated versus untreated and 4) a more rapid response time. We continue to monitor and record the $CrSO_2$ signal, but focus on using $HepSO_2$ and SBP as the endpoints to guide infusion. Future studies on this project will focus on using these two endpoint variables. Our original target levels were 50% for both brain and hepatic oxygenation and 120 mmHg for systolic blood pressure. We have amended these target values to be 47% for the brain and 100 mmHg for systolic blood pressure. Hepatic oxygenation of 50% does appear to indicate adequate cardiovascular stabilization. These target levels are indicative of cardiovascular stabilization, albeit at a level of subnormal hemodynamics.

Control Algorithms: A table of infusion rules is the simplest controller. It is basically a set of specific infusion rates for a range of endpoint variables. Examples of a 2 x 3, 2 x 5 and 2 x 9 dimensional decision tables are shown in Tables 1, 2 and 4. We first tested out this concept using both large and small bolus infusions with different endpoints. We are in the process of comparing bolus infusions with continuous infusion.

Large Bolus vs Small Bolus vs Continuous Infusion: We have consistently found that algorithms using a small bolus infusion every 2 minutes reaches the same endpoints with less total volume than do the algorithms in which larger volumes are administered every 5 minutes. In Figure 8 we plot the volumes required to reach 100 mmHg in three different groups treated with a large bolus infusion every 5 minutes and a small bolus infusion every 2 minutes. This suggested that continuous infusion would be more efficient and our ongoing testing of with bolus vs continuous appears to validate this as seen in Figure 9.

Figure 8 - Mean cumulative volume required to resuscitate hemorrhaged sheep to restore systolic blood pressure to 100 mmHg. Data is replotted from same experiments shown in Fig. 7. All resuscitated animals had systolic blood pressure improve to 100mmHg or better in 40 minutes or less. Large volume therapy guided by CrSO2 or HepSO2 or small volume therapy guided by SBP was based on algorithms shown in Tables 1 and 2. Each group had 6 animals. We speculate that rapid bolus infusion may transiently elevate microcirculatory pressures and leave to increases in fluid filtration and volume loss to the interstitium and via increased glomerular filtration in the kidneys. Data suggests that smaller bolus is more efficient and can be volume sparing

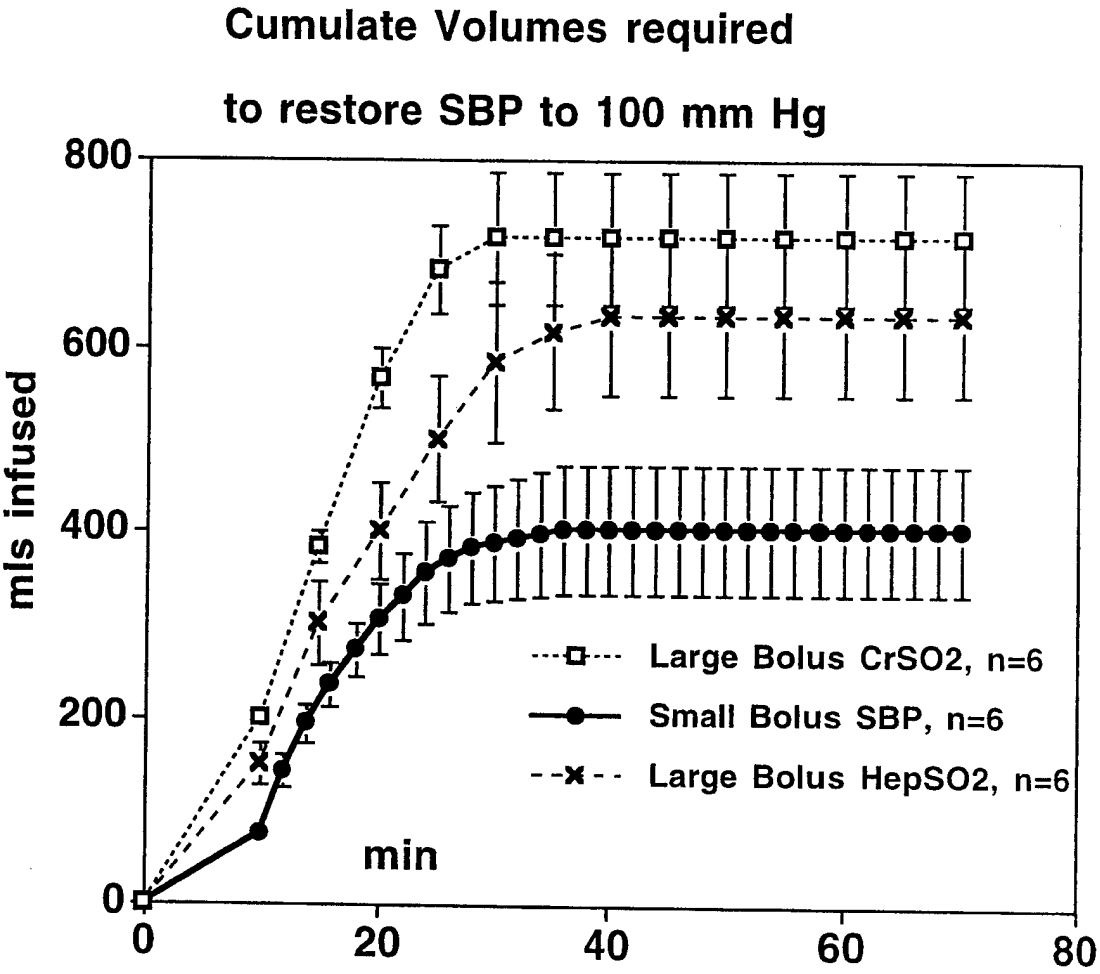

Figure 9 - Comparison of volume and the time that was required to restore blood pressure to 100 mmHg using either continuous infusion from the three most recent experiments or intermittent bolus infusions from the previously completed series. Data shown suggests that a continuous infusion algorithm might be more volume efficient than a bolus infusion algorithm. Our most recent data supports this conclusion.

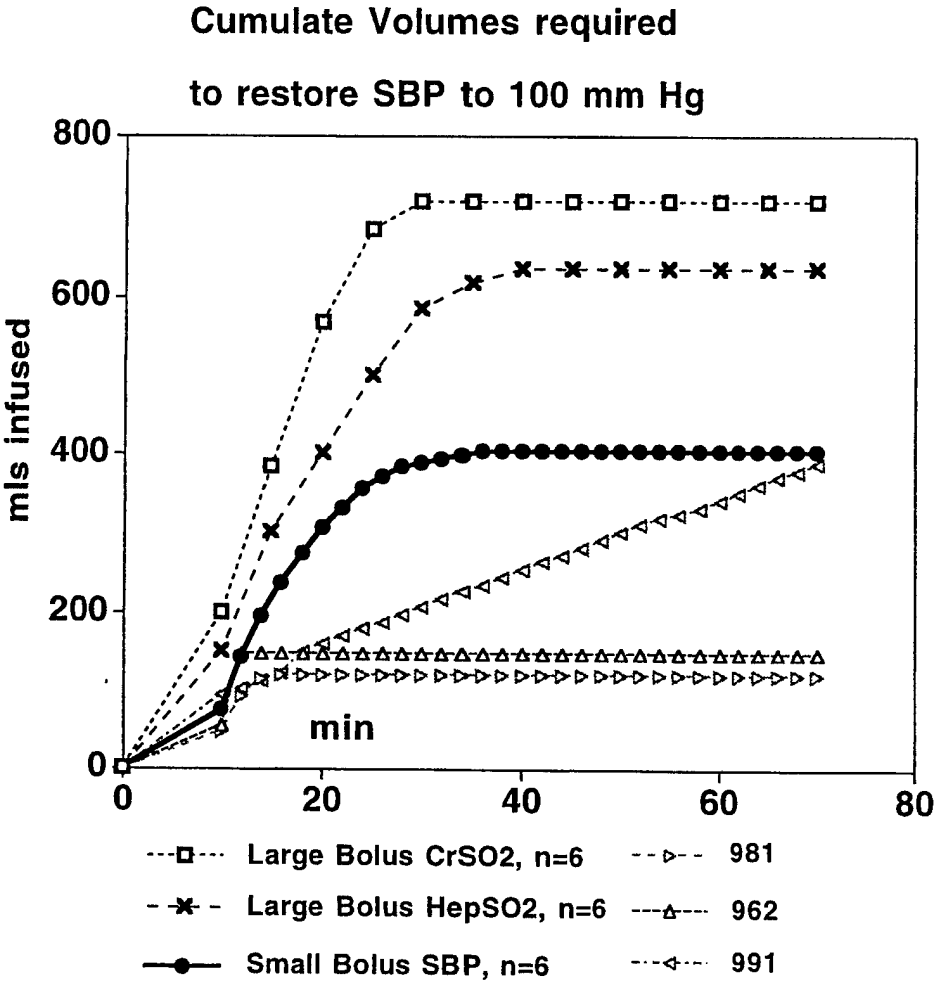

Endpoint Variables, Error Signals versus Normalized Endpoints: The ATLS guidelines suggest that the response to bolus therapy can be used to assess cardiovascular status. Our initial infusion algorithms are to set infusion rates proportional to an Error Signal or a target endpoint value minus actual endpoint value. Our decision tables are a simplified version of this. We reasoned that the response to infusion would be proportional to the infused volume and that the response would vary based on the level of hypovolemia. We plotted change in endpoint value versus volume infused, e.g. ΔSBP/infused volume and normalized change in endpoint variable $\Delta SBP/SBI_{initial}$ versus the level of shock. We also analyzed $\Delta SBP/SBI_{initial}$ per infused volume versus level of shock, data not shown. Unfortunately, no patterns were apparent with the level of shock or with early or late resuscitation. Responses varied greatly and no pattern suggesting useful information was gained from the response to relatively small bolus infusions or continuous infusion rates. This suggests that the use of the simple straightforward target level or its Error Signal is a more useful input to guide fluid therapy than the responses to the infused volume.

The Experimental Infuser and Controller: Dr. Don Deyo has made substantial progress on using LabView to implement the monitoring, infusion algorithms and pump controllers required for a Resuscitation System. This setup will be used experimentally to compare different automated closed-loop endpoint infusion algorithms to develop the best control algorithm and the selection of the optimal target endpoint for incorporation in the design of a future Resuscitation System prototype.

There are three major hardware components of the experimental infuser and three major components of the LabView program for each hardware component. The infusion pump is a commercial digital MasterFlex rotary infusion-pump. Sterilization of the rotary tubing provides a aseptic method of resuscitation. The physiological monitors are the INVOS 4100 oximeter used to measure transcutaneous hepatic oxygen saturation or a bridge amplifier that Dr. Deyo built that can be used with commercial clinical blood pressure transducers. An analog voltage input from the transducer amplifier or the INVOSS 4100 is connected via LabView A-D board to a Macintosh computer while a digital out signal is sent to the MasterFlex pump. The MasterFlex pump controller, the endpoint monitor and the infusion algorithm are all programmed in LabView. The input endpoint variable is compared to a target level for calculation of an Error Signal, (E(t) = target minus actual) for use by PID control or fuzzy control algorithms. Alternately, the input variable is compared to an array of ranges to set infusion based on a 2 x X decision table as illustrated in Table 4.

Figures show two of the interface user control panels and their underlying LabView schematics.

Figure 10 shows the front panel and user interface for monitoring the endpoint variable and setting target criteria. In the example CrSO2 is selected and the target has been set at 50% with changes in infusion set a 2% increments as in Table 4. The graph display shows CrSO2 over time, while the sliding scale shows the most recent 2-minute mean value which is used to calculate a new infusion rate every 1 minute.

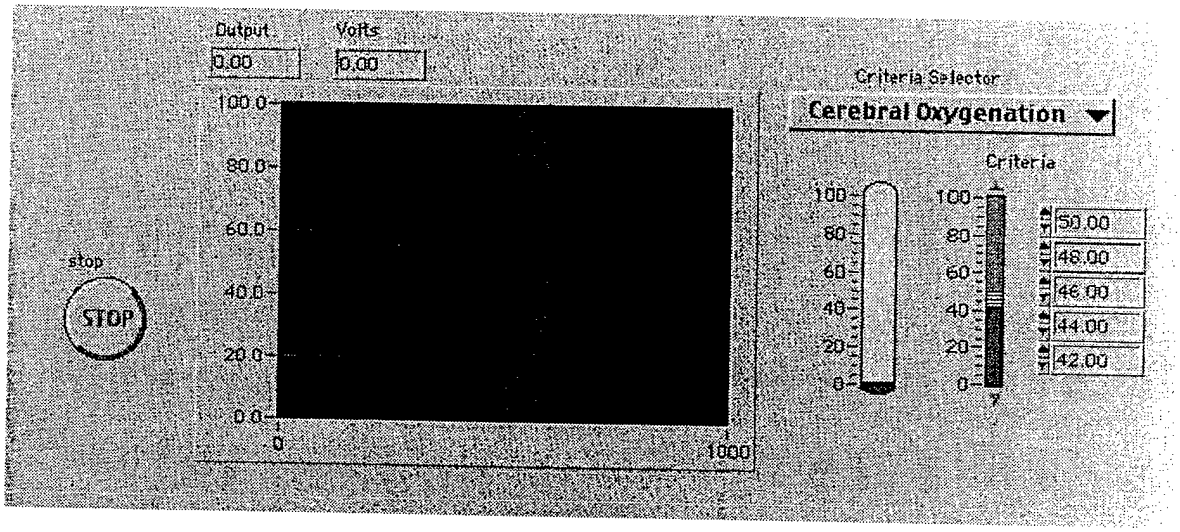

Figure 11 shows schematic of the monitor and controller. Analog voltage input from our endpoint device is shown at top left. To date we have programmed only with decision tables. Dr. Hao Ying is designing our first PID and Fuzzy Logic controllers and working with Dr. Deyo on their implementation.

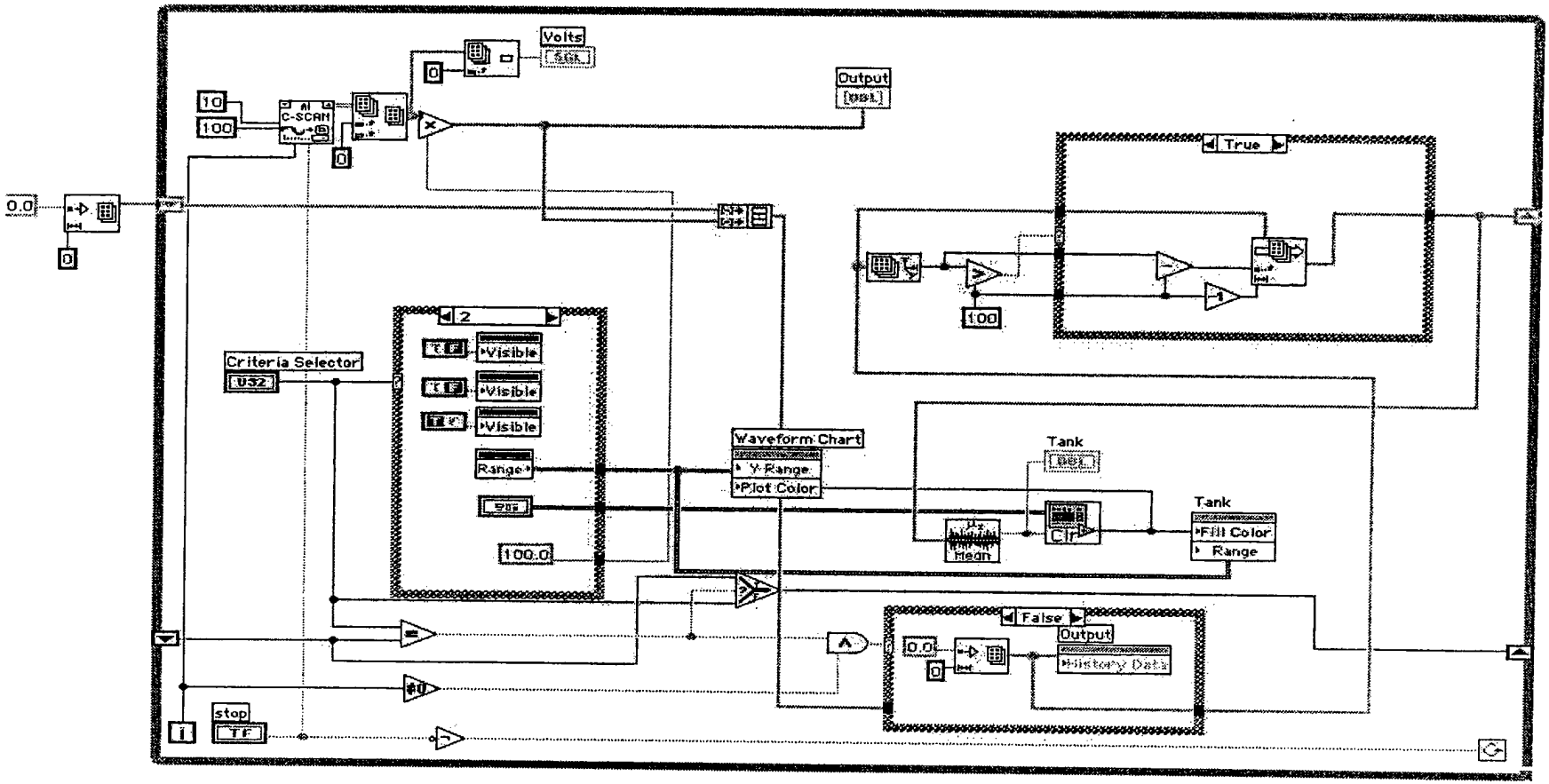

Figure 12 shows the front panel and user interface for the MasterFlex rotor pump controller. Lab view translates the desired infusion rate into revolutions per minute depending on the tubing size used in the pump.

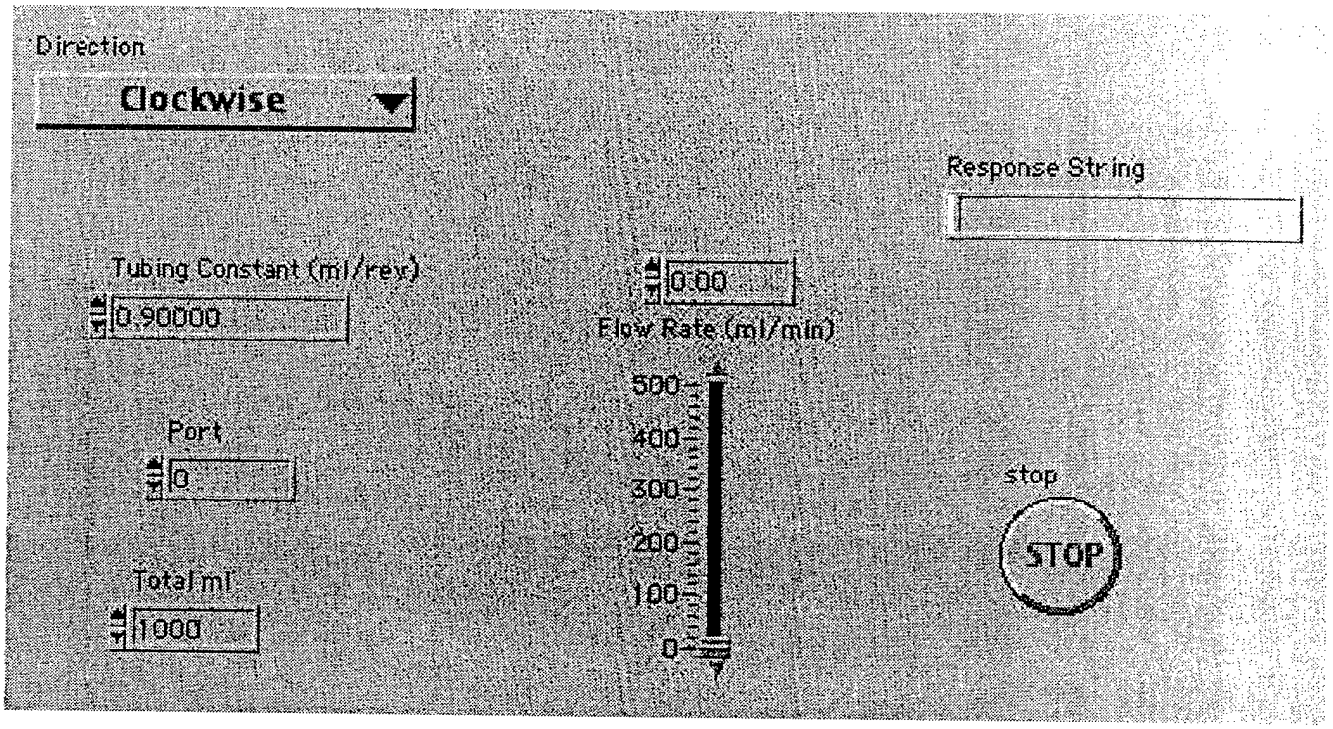

Figure 13 shows the schematic of the MasterFlex pump controller.

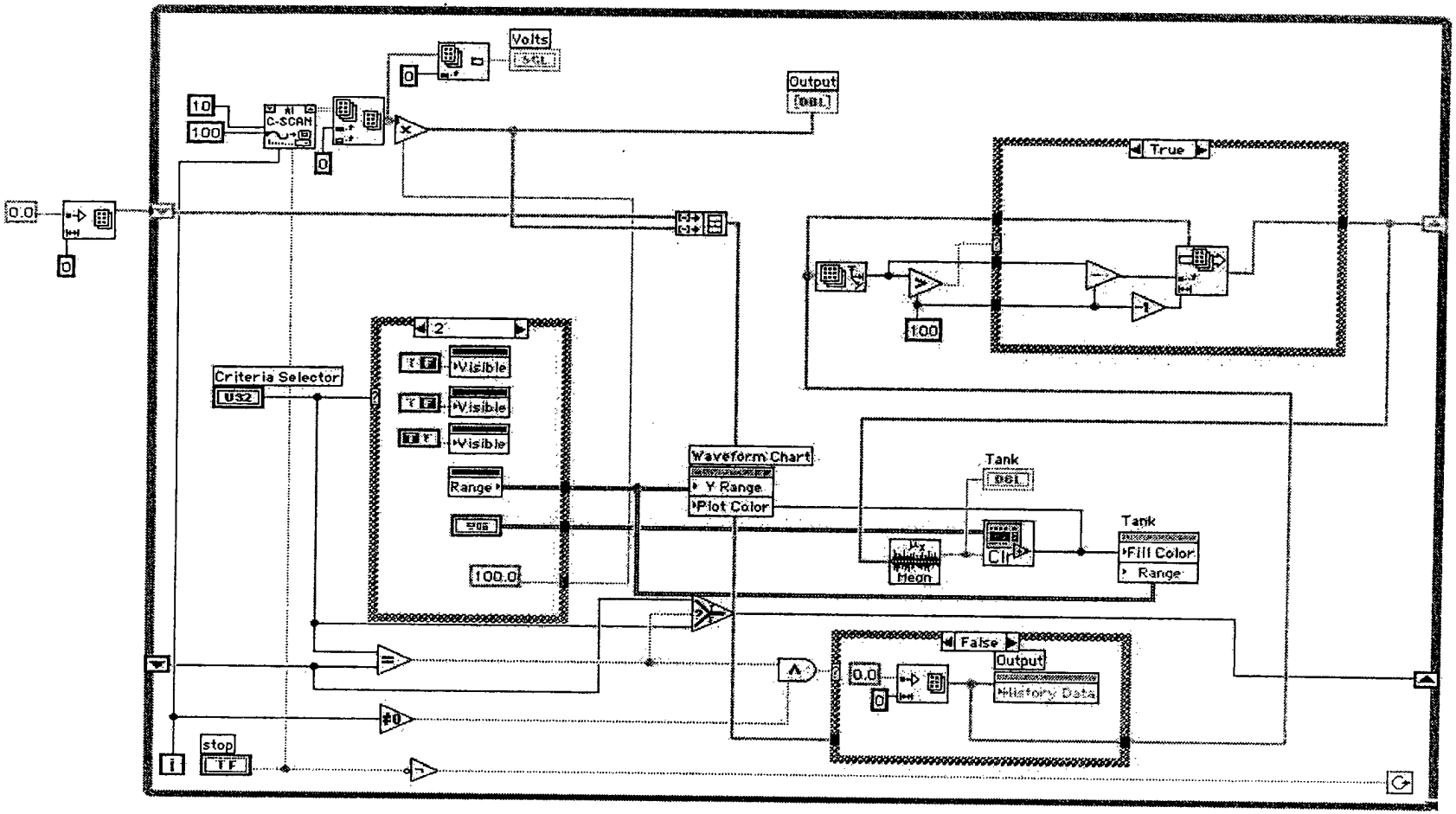

Proportional Integral Derivative (PID) controllers measure an error signal (E) for a specific time (t) which is the difference between a target level of an endpoint variable and its actual level. Infusion rate is set as a function of three constants (A, B and C).

$$\textbf{New infusion rate} = A \times E(t) + B \times \int E(t)\,dt + C \times dE/dt$$

For SPB and a target of 100 mmHg, based on our bolus studies we have chosen as the initial testing A = 1.8, B= 0 and C = 0.2. Maximum infusion is set at 100 mL/min per 70 kg and the minimum is set at 3 mL/hr. These constants will be tuned as needed.

Table 5

Fuzzy logic control approaches can be based on a series of rules or questions that are applied to an input variable and the function that is to be controlled. This is a simple schematic of a fuzzy logic controller that attempts to improve and maintain an endpoint variable at and above its target level. The simplest set of rules is a two by two matrix.

	Target variable is decreasing	Target variable is increasing
Endpoint is > or above target level	**-no change-**	**Decrease infusion**
Endpoint is < or below target level	**Increase infusion**	**-no change-**

Table 6

A more complex fuzzy logic controller might be a three-by-three or four-by-four decision table. We believe that this approach will provide the greatest control and the most efficient means of infusion therapy. PID controllers and Fuzzy Logic controllers will be tested.

	Endpoint decreasing > 10% / min	Endpoint decreasing < 10% / min	Endpoint increasing < 10% / min	Endpoint increasing > 10% / min
Endpoint > than target level	**Increase infusion** ⇑	**-no change-**	**Decrease infusion** ⇓⇓	**Min infusion .004 mL/kg/min**
Endpoint = 80-100% of target level	**Increase infusion** ⇑⇑	**Increase infusion** ⇑	**-no change-**	**Decrease infusion** ⇓
Endpoint = 60-79% of target level	**Increase infusion** ⇑⇑⇑⇑	**Increase infusion** ⇑⇑⇑	**Increase infusion** ⇑⇑	**-no change-**
Endpoint < 60% of target level	**Max infusion 1.5 mL/kg/min**	**Increase infusion** ⇑⇑⇑⇑	**Increase infusion** ⇑⇑⇑	**Increase infusion** ⇑

New Invention: Dr. Don Deyo has designed a new pressurized infusion pump that is a major improvement and significantly different design and concept than our previously prototyped pressurized infuser. The following is the non-enabling background and description of this invention. Under separate cover we will send a detailed confidential invention disclosure by the end of the month after filing with UTMB Technology Management Office. Proprietary details removed from the report are replaced with (----------). The invention has grown out of the development work funded by the NMTB contract. It is important to appreciate that this invention is the pump component that could be a stand-alone product or interfaced as part of the Resuscitation System we are developing. The experimental infuser and controller described on Page 25 are made up of a commercial rotary pump and do not include this new invention. That experimental infuser and controller are for experimental use only and to test and develop the infusion algorithms and the closed-loop endpoint resuscitation. Eventually, this new invention could be the important part of the functionality and proprietary protection for a Resuscitation System.

Need for New Invention: There is a need for a better means to monitor and control intravenous fluid therapy for pre-hospital treatments in the field and during ambulance and

Lifeflight transport. This is particularly true when dealing with life threatening hypovolemia as occurs after traumatic injury. "Under resuscitation" of hemorrhagic shock can lead to ischemia. increased morbidity and death. "Over resuscitation" can lead to increased internal bleeding and excessive edema and also may increase morbidity. A special need is for corpsman use during combat casualty care. Military field resuscitation has logistic constraints that limit the weight and 'cube' (volume) of equipment and fluid that are available for treating hemorrhagic shock.

Different causes of traumatic injury may dictate different fluid infusion regimens. For example: 1) Penetrating injury is often associated with significant internal hemorrhage that can be aggravated when blood pressure is rapidly increased with aggressive resuscitation. 2) Blunt injury is believed to respond well to aggressive resuscitation and increased bleeding is less of a concern. 3) Traumatic head injury weakens the brain's ability to auto-regulate blood flow. Even transient hypotension worsens clinical outcome in patients with head injury and thus. strict maintenance of normotension is a critical goal.

Currently fluid is dripped in from plastic intravenous bags and infusions sets. Infusion are sometime facilitated with a pressurized device or other means to squeeze the fluid bag. A thumbscrew or other restriction in the IV line controls rate. Adjustment of the drip rate as viewed in a drip chamber allows the rate to be roughly calculated, set and adjusted as needed. Unfortunately, paramedics and corpsman have many tasks to perform and fluid therapy is not tightly controlled. This is due to lack of an easy means to monitor fluid infusion rate and the lack of any standardized protocols that adjusts fluid therapy based on a patient specific response. Although drip rate may be manually adjusted this is often difficult to perform in a timely fashion in the field on during emergency transport.

There are small portable intravenous pumps available, but these are expensive complex devices that require significant electrical energy and battery power to move fluid rapidly. An improvement would be a simple, lightweight, small, low cost and more energy efficient pump.

One possible improvement is a pressurized canister that holds a fluid bag as described in US patent #5,938,636. In this set-up changes in canister pressure and modifications of the ideal gas laws are used to calculate the change in volume and infusion rate. However, as described in patent # #5,938,636, this device would require a specially made pressure container. A significant improvement would be to design a system that could use ---------- components. --------.

The present invention satisfies these requirements and is lighter, less expensive to manufacture and simpler in design than the previously described designs.

Invention Description: A device to turn an ordinary IV bag, ---------- and ---------- into a microprocessor controlled infusion pump. The invention has the following components:

This new pump could be interfaced with a physiological monitor of an important variable used to help diagnosis shock and guide fluid therapy. Closed-loop infusion algorithms would

use the variables to automatically titrate fluid therapy as appropriate for the physiological response of the patient. When the Pump is combined with the monitor and closed-loop control algorithms the product is a Resuscitation System that would precisely titrate fluid therapy to specific patient needs. A Resuscitation System such as this would optimize prehospital care in a manner that is timely effective and volume efficient. Such a Resuscitation System could be interfaced with telemedicine transmission for use on airplanes, boats or in the far forward combat field or rural field applications or other remote locations.

Future Plans and Schedule

Amended Plans and Timetable: We have had delays in work efforts and expenditures for several reasons. Animal experiments started late due to our protocol approval from DOD coming after our contract started. We have had to change our endpoint variable due to the ineffectiveness of using the $CrSO_2$ signal. Fortunately our experiments have established the effectiveness of Hepatic SO_2 and SBP. The design and testing of the controller has taken longer than expected. We previously built a PC based controller using Visual Basic, but it had to be abandoned due to the communication problems with the original pump we were using. Good progress has been made using the LabView software on a Macintosh computer, but its development has taken longer than originally planned for. Because of the delays, Dr. Ying's input on the fuzzy logic control was also delayed. We have had several planning sessions with him and have designed the initial rules of the fuzzy logic controller, Fig 5-6.

Our expenditures have also been less due to the delays, therefore, we request a six month no cost extension to finish the project. All personnel remain the same. Dr. Hao Ying recently accepted a new position as an Associate Professor, Department of Electrical and Computer Engineering at Wayne State University, Detroit, Michigan. His effort will be compensated per our NMTB budget, per the requirements that Wayne State University and UTMB have. He will work on designing the PID controller and Fuzzy Logic controller. We have had several meetings in order that the collaborations and work can be done remotely. Dr. Deyo and Dr. Ying have arranged to develop the fuzzy controller and PID controller for the LabView program using the remote access internet module as provided by LabView's software (Enterprise Network Connectivity™). This software enables Dr. Ying too remotely and in real-time develop, execute and modify the PID and fuzzy control programs on a computer here at UTMB from his PC at Wayne State University via a high speed internet connection. This has the added advantage that it may help our final prototype to be telemedicine ready for internet monitoring and control. We have rearranged this Phase I work schedule on an 18-month timetable.

Table 7- Time Table

Task	Month # 1-18	Sheep
Algorithm Design & Interfacing $HepSO_2$/SBP	1-8	0
Endpoint Testing and Algorithm Testing	1-6	6 sheep
LabView Controller built	1-7	

PID & Fuzzy Controller Development/ Final Algorithm selection	7-14 months	12 sheep
Efficacy Testing of LabView Infuser & Best Algorithm	13-16 months	24 sheep
Build Prototype Resuscitation Pump/System- new Deyo invention	15-18	
Experimental Failures	3-18	5 sheep
Data analysis, Report & Phase 2 preparation	17-18	
Total:	**18 months**	**47 sheep**

CONCLUSIONS

We continue to perform the key development work towards the goal of producing a prototype Resuscitation System. Results at this six-month mark include 1) Finding that the endpoints $HepSO_2$ and SBP are more robust than $CrSO_2$. 2) Simulated closed-loop algorithms successfully restored physiological endpoints to their target levels. 3) A small bolus and continuous infusion algorithms can be volume sparing and will be used in future algorithms. 4) Dr. Deyo has submitted a new invention disclosure to the UTMB Technology Management Office on the improved auto-infuser that will be prototyped.

Goals remaining to be accomplished are 1) Compare fuzzy logic control with PID control with decision tables and select best algorithm. 2) Test efficiency of 'best' algorithm with standard of care as described in original plan. 3) Build prototype of the new pressurized infuser.

REFERENCS

1. American College of Surgeons Committee on Trauma. *Advanced Trauma Life Support Program for Physicians, Instructor Manual.* Chicago, 1998.
2. Bickell WH, Matthew J, Wall MJ, Jr., Pepe PE, Martin RR, Ginger VF, Allen MK, Mattox KL: Immediate versus delayed fluid resuscitation for hypotensive patients with penetrating torso injuries. N Engl J Med 331(17):1105-9, 1994.
3. Owens TM, Watson WC, Prough DS, Uchida T, Kramer GC: Limiting initial resuscitation of uncontrolled hemorrhage reduces internal bleeding and subsequent volume requirements. J Trauma 39(2):200-7, 1995.
4. Stern SA, Dronen SC, Birrer P, Wang X: Effect of blood pressure on hemorrhage volume and survival in a near-fatal hemorrhage model incorporating a vascular injury. Ann Emerg Med 22(2):155-63, 1993.
5. Smith J, Bodai B, Hill A: Pre-hospital stabilization of critically injured patients: a failed concept. J Trauma 25:65-70, 1985.
6. Auto-infuser for resuscitation and method of infusion fluid injection. U. S. Patent 5,938,636: (1999). (UTMB) George C Kramer, Jerald M Henderson, Wendy R Feenstra, Domenico C Castaldo.
7. Kramer GC, Perron PR, Lindsey DC, Ho HS, Gunther RA, Boyle WA: Small-volume resuscitation with hypertonic saline dextran solution. Surgery 100(2):239–46, 1986.
8. Nguyen TT, Zwischenberger JB, Herndon DN, Traber DL, Prough DS, Watson W, Kramer GC: Hypertonic acetate dextran achieves high flow/low pressure resuscitation of hemorrhagic shock. J Trauma 38(4):602-608, 1995.
9. Elgjo GI, Poli de Figueiredo LF, Traber L, Traber D, Kramer GC: Hemodynamics and bleeding rates during severe uncontrolled hemorrhage in conscious sheep. Shock 5(2):20, 1996.
10. Lewis GD, Flemming JM, Widman RA: Infrared cerebral oximeter: summary of recent clinical case histories. SPIE 1641:194-201, 1992.
11. McCormick PW, Stewart M, Goetting MC, Balakrishnan G: Regional cerebrovascular oxygen saturation measured by optical spectroscopy in humans. Stroke 22(5):596-602, 1991.
12. McCormick PW, Stewart M, Goetting MG, Dujovny M, Lewis G, Ausman JI: Noninvasive cerebral optical spectroscopy for monitoring cerebral oxygen delivery and hemodynamics. Critical Care Medicine 19(1):89-97, 1991.
13. Pollard V, Prough DS, DeMelo AE, Deyo DJ, Uchida T, Stoddart HF: Validation in Volunteers of a Near-Infrared Spectroscope for Monitoring Brain Oxygenation in Vivo. Anesth Analg 82(2):269-277, 1996.
14. Pollard V, Prough DS, DeMelo AE, Deyo DJ, Uchida T, Widman R: The influence of carbon dioxide and body position on near-infrared spectroscopic assessment of cerebral hemoglobin oxygen saturation. Anesthesia & Analgesia 82(2):278-87, 1996.

DESCRIPTION AND PERFORMANCE SITES (FORM B)

DESCRIPTION:

The goal of the project is to demonstrate that digital sensors of X-rays, based on a new breakthrough, thin film, photoconductive material, lead iodide, will offer improved performance over current X-ray detector technology for digital mammography used in diagnostic and interventional procedures. This will be achieved by combining the large area, thin film, lead iodide photoconductor technology with the large-scale electronics-on-glass technology of amorphous silicon thin-film-transistor (TFT) arrays. The latter are used in laptop computers to control liquid crystal light valve arrays for displays.

The team will replace the liquid crystal with a lead iodide film that directly absorb X-rays and convert them into electric charge. The TFTs will switch this detected charge into integrated circuit (IC) electronic processors where the information will be digitized and formatted into high resolution X-ray images. Using vidicon test structures Radiation Monitoring Devices (RMD) has demonstrated that lead iodide has over 5 times better contrast resolution (than X-ray film/screen) at the high spatial resolution required for mammography [Shah 97]. RMD has further demonstrated that X-ray images can be produced on a test detector composed of an evaporated lead iodide film formed on a 5 cm x 5 cm glass sheet on which an array of 200 μm wide pixels of amorphous silicon TFTs [Street 98].

Varian will specify and provide RMD with glass substrates (fabricated by OIS) that are large enough for meaningful mammography imaging. These will be approximately 10 cm x 10 cm arrays of amorphous silicon TFTs contained in pixels, $\leq$ 140 μm wide, on the glass. This is an enabling step toward the 50μm pixels and 10 lp/mm resolution and the 20 cm by 25 cm sensors areas ultimately needed for full-breast mammography. The latter should be straight forward scaling with the lead iodide and glass substrate TFTs although the IC interconnection engineering and other aspects will be quite challenging. After RMD evaporates lead iodide films onto these substrates, Varian will further integrate these glass plates with IC processors with speeds sufficient for near real time (video) imaging.

Varian is one of the world's leading suppliers of glass X-ray sensor arrays where a scintillator cover layer converts X-rays into visible light. Underlying amorphous silicon arrays of photodiodes converts this light into charge that is switched by amorphous silicon TFTs. At 50 μm pixel sizes, there is insufficient room for both the photodiodes and the TFTs. Lead iodide circumvents this problem by being formed on top of the TFTs.

Martin Yaffe is one of the world's leading experts in digital mammography. Dr. Yaffe will compare the second generation sensors of this program with the first generation ones in his labs based on CCDs and amorphous silicon photodiodes. The latter are too small and/or too expensive and/or too complex for widespread use. In the second year, Dr. Yaffe will explore the unique advantages of the second generation sensor for near real time imaging in clinical tests. This should provide improved guidance for stereotactic core needle biopsies and allow contrast angiography of suspicious breast abnormalities. Dr. Yaffe will also provide overall project direction. The biomedical significance is that "digital mammography is the most promising technology toward improved control of breast cancer in large scale screening programs" according to the US Office of Women's Health [Shtern 96]. Lead iodide should make wide spread digital mammography practical. Over 40,000 US women will die this year of breast cancer. This equals or exceeds the US death rates due to either AIDS or prostate cancer.

PROJECT SITE(s) (Organization, City, State): Consortium/Contract Arrangement
Optical Imaging Systems (OIS), Northville, Michigan
Radiation Monitoring Devices (RMD), Watertown, Massachusetts
Sunnybrook Health Science Centre, Toronto, Ontario, Canada
Varian Associates, Palo Alto, California

VARIAN
medical systems

ORIGINAL MAY 12 2000

ginzton technology center

Wednesday, May 10, 2000

Thomas J. Callanan
Administrative Director
National Medical Technology Testbed
11354 Mountain View Avenue, Suite D
Loma Linda, CA 92354
(909) 558-6184

Subj: First Semiannual Report NMTB98-01 – Subagreement #: 29-FY98-Varian-Yaffee

Dear Tom:

The subject report is attached. Note that we are ahead of schedule on the tasks. The latter includes generating our first X-ray image with our new break through material. We are enthusiastic about our continuing work on this project.

Sincerely,

Larry Partain
Contract Research Manager

CC: E. Seppi, M. Yaffe, K. Shah, G. Zentai, G. Virshup, A. Shrewsbury, Files

3075 Hansen Way, M/S K-402, Palo Alto, CA 94304-1025 USA
650/424-5645 FAX 650/494-3279
email: larry.partain@grc.varian.com

ORIGINAL MAY 12 2000

DIGITAL MAMMOGRAPHY USING PHOTOCONDUCTOR (VATP-2747)

Semi-annual progress report
Covering the period 11/1/99-4/30/00

Cooperative Agreement No. DAMD17-97-2-7016

Subagreement No. 29-FY98-Varian-Yaffe

Report prepared 5/1/00

Martin J. Yaffe, Ph.D.
(416) 480-5715
(416) 480-5714 FAX
martin.yaffe@swchsc.on.ca

DIGITAL MAMMOGRAPHY USING PHOTOCONDUCTOR (VATP-2747)

INTRODUCTION

Digital radiographic imaging offers the potential to provide improvements in the diagnostic quality of images as well as to enable new applications that can offer valuable information for detection, diagnosis and treatment of disease or allow remote image interpretation (telemedicine). This is particularly true in breast imaging, where digital mammography systems have recently been introduced by four manufacturers. In preliminary clinical testing, these first generation systems have already begun to show some advantages associated with accuracy of breast cancer detection. These advantages arise from the wide dynamic range and good signal-to-noise characteristics of the x-ray detectors and from the ability to apply computer contrast enhancement in their display.

Despite these promising results, we have identified several limitations associated with the first generation detector technology which is based on the use of phosphors to absorb x rays and convert their energy to light. These detectors require three components: the phosphor, an optical detector in which the light is converted to electronic charge and some means of coupling the two. Some loss of spatial resolution occurs due to spreading of light in the phosphor or in the coupling material and there are inefficiencies at each stage of energy conversion. As the thickness of a phosphor is increased to improve the efficiency of x-ray absorption by the detector, the importance of the blurring phenomena generally increases. In addition, because of the multiple stages of energy conversion and collection in a phosphor- based detector, there are additional noise sources. Together, these give rise to a reduction in the signal-to-noise ratio (SNR). Alternatively, this can be described as a reduction in the detective quantum efficiency (DQE) of the detector.

In this project, we are investigating and developing high resolution x-ray detectors which are based on a new detector material, lead iodide (PbI_2), for use in digital mammography and other demanding applications in radiographic imaging. PbI_2 is a direct conversion detector; energy of the absorbed x-rays is converted directly to charge. The electronic signal produced can be collected by placing an electric field across the detector.

In our work, the PbI_2 will be deposited on a two-dimensional active matrix readout consisting of an array of detector electrodes (dels) formed on an amorphous silicon substrate. Because the signal is collected electrically, the lateral spread of charge that would give rise to blur, can be controlled by electrode design and biasing. This allows extremely high spatial resolution to be achieved with a detector that is as thick as is required to absorb x rays efficiently. Thus the system should provide excellent performance both at low energies such as those used in mammography and at the higher energies as used in general digital radiography. These factors and the reduction of noise because of the direct conversion process will lead to increased DQE of the detector. The resulting higher SNR should contribute to increased diagnostic accuracy and/or possible reduction of radiation dose.

OBJECTIVES (Year 1)

- to optimize the performance of PbI_2 layers
- to test the basic imaging properties of the PbI_2 material

- to demonstrate the feasibility of producing the PbI_2 /active matrix detector system
- to characterize the imaging performance of a prototype detector
- to consider the suitability of this detector for use in a quantitative breast digital angiography system.

RESEARCH

Since the onset of funding, the group has had one formal planning meeting during the SPIE medical Imaging Conference in San Diego and one informal meeting in Washington. The design specifications of the detector have been reviewed at these meetings and during frequent communications that have been conducted via conference call and e-mail. Data on performance of test structures and devices have been shared between Varian, RMD and Sunnybrook via e-mail.

The table below indicates our original work plan. The solid bars show the degree to which the tasks have been completed. At present, we are slightly ahead of our planned schedule in that x-ray images have been made of a test coating on a 10 x 10 cm panel. This activity has allowed us to identify several technical challenges that we will address in the 3rd and 4th quarters of the initial funded year.

Milestone	Task	Year 1				Year 2			
	Sunnybrook Program quarter -	1	2	3	4	5	6	7	8
1	Arrange/coordinate consortium meetings								
2	Critique Gen. 2 sensor specs vs Gen.1								
3	Evaluate prototype properties								
4	Clinical tests – 1st prototype								
5	Clinical tests – 2nd prototype								
	Radiation Monitoring Devices								
6	Develop 10 cm x 10 cm PbI_2 coating process								
7	Characterize PbI_2 on plates								
8	Deliver a-Si arrays coated with PbI_2								
9	Optimize PbI_2 coating process								
10	Assist with problems identified in clinical tests								
	Varian								
11	Procure 10 cm x 10 cm a-Si plates								
12	Integrate PbI_2 coated plates with ICs								
13	Obtain x-ray images with sensor prototype								
14	Assist with problems identified in clinical tests								

◆----------◆ Indicates predicted duration of task

▬ Indicates degree of completion of task

RMD – PbI_2 development

During the course of this project, RMD has been investigating approaches to improve properties of lead iodide films, specifically, their dark current and sensitivity. We have recently observed that by optimizing the substrate temperature used during evaporation, and thereby the grain size of the lead iodide layers, the electrical properties can be enhanced. We have grown over 25 films over the course of the project with film

thickness in 30-100 μm range. **Figures 1 and 2** show x-ray induced signal (70 kVp exposure) and dark current properties of a recent PbI_2 film (about 50 μm thick). Both the sensitivity and dark current properties are superior to the results obtained with earlier films.

Issues to be addressed in Quarters 3 and 4:
Compatibility of the new evaporation process with amorphous silicon technology. We will test evaporations onto readout arrays within the next month. Figures 1 and 2 show a different level of sensitivity of the detectors depending on whether the applied bias is positive or negative. The results for negative bias are consistent with theory, whereas the positively biased detector exhibits increased dark current and sensitivity. We believe that this is due to a phenomenon known as "photoconductive gain". While increased sensitivity is sometimes desirable, the high dark current is believed to be caused by charge injection from the biasing electrode and would result in increased noise in an imaging system. We are in the process of investigating this effect and have already begun developing an effective blocking layer to eliminate charge injection.

VARIAN
Varian has obtained amorphous silicon readout plates (10 cm x 10 cm) and are developing the readout electronics. A test deposition of PbI_2 has been performed at RMD and preliminary images have been produced as shown in **Figure 3.** Image quality is encouraging, in spite of some artifacts due to the readout ASICS.

Varian will continue the development of the image readout system and plans to deliver a "rough" version of the system to Dr. Yaffe's lab in 8/00 for testing. Dr. Yaffe's group will then test the detector by performing standard image quality measurements on it including MTF, noise power analysis, DQE, as well as testing dynamic range, linearity, uniformity and freedom from artifacts, as appropriate. As available, imporoved versions will also be provided to Dr. Yaffe.

After Dr. Yaffe has characterized the performance of the system(s) and performed images on anthropomorphic breast phantoms and contrast uptake phantoms, the team will determine whether the imaging system is ready to proceed to patient studies. Dr. Yaffe is already conducting a protocol where digital mammography (first generation system) is used for iodine contrast uptake studies in the breast where differential uptake has been seen in several lesions. The potential improvement in signal-to-noise ratio of the PbI_2 detector is attractive as a way to improve the sensitivity of this procedure.

CONCLUSIONS
The results acquired thus far are encouraging and we have a clear idea of how to overcome the problems that have been observed, (i.e. photoconductive gain, readout artifacts). Based on these results, we remain convinced that this detector system can offer significantly improved performance in imaging and dose efficiency as compared to first generation phosphor-based radiological imaging systems.

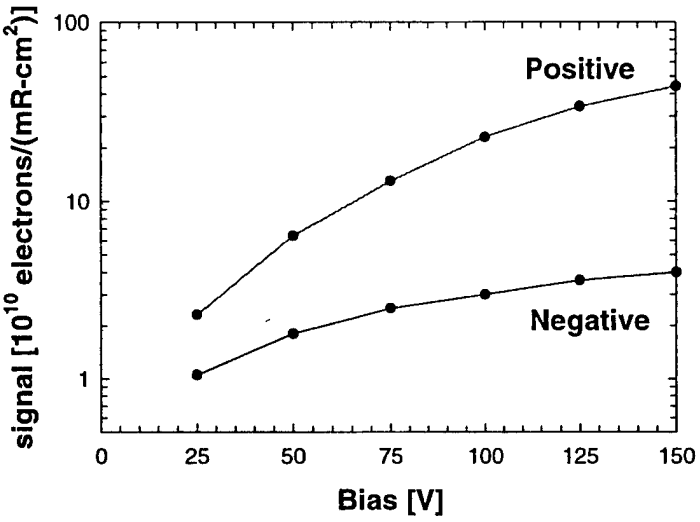

Figure 1. X-ray signal measured with PbI_2 film for both positive and negative bias on top Pd contact.

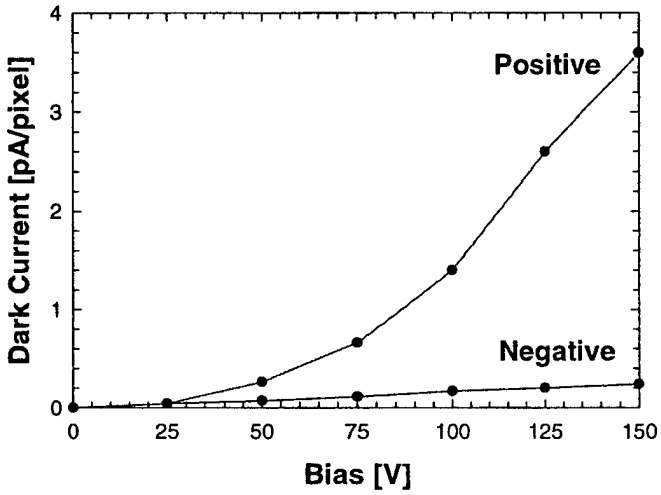

Figure 2. Dark current for PbI_2 film for positive and negative bias polarities. The dark current is scaled for a 100 μm pixel

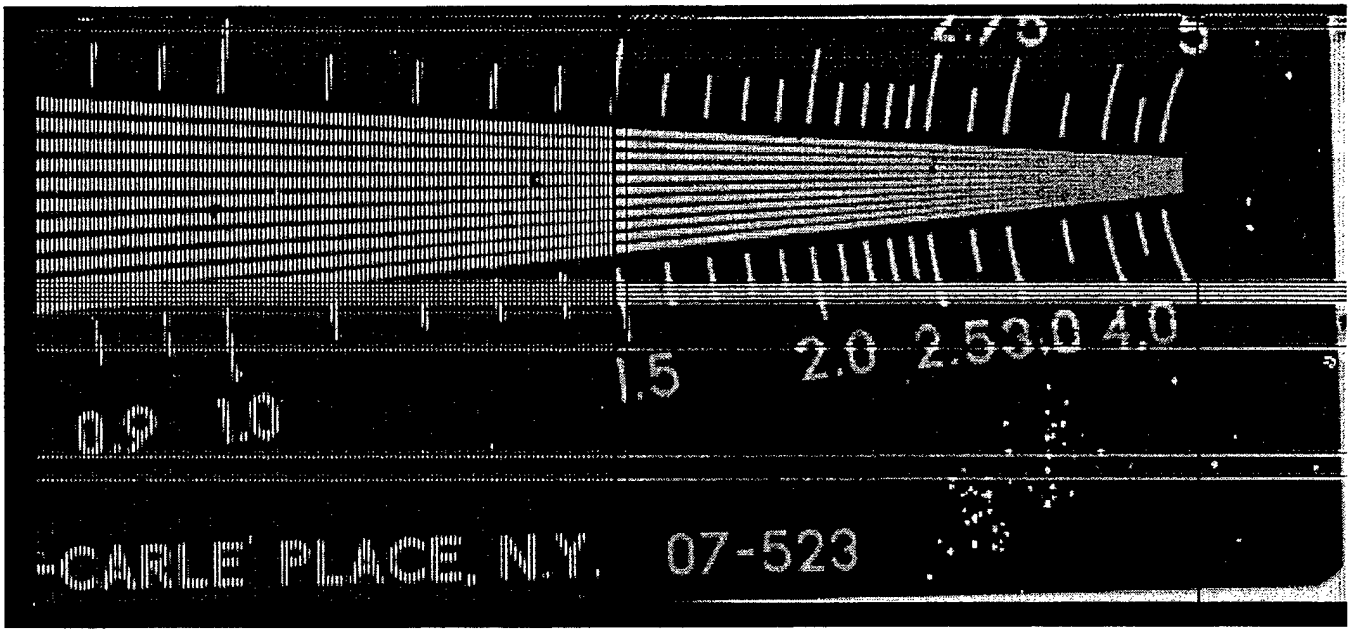

Figure 3. First preliminary X-ray image obtained at Varian from a 10 x 10 cm array coated with PbI_2 by RMD.

DESCRIPTION: State the goal of the project, including how it relates to improving health care and noting the advanced technology that will be developed or tested . Use succinct language to describe how the project goals will be achieved. **Do not exceed the space provided.**

The overall goal of this project is to further the development of two ophthalmic instruments that improve the quality and availability of medical care. One instrument, in a brief test of eye movements and pupil responses, generates measures to be used for detection, diagnosis and treatment monitoring of a wide range of pathologies that affect the central nervous system or neuromuscular junctions. The instrument can be used by unskilled personnel after only a brief training period, and the results are in digital form for easy telecommunication. The proposed work on this instrument involves the use of existing prototypes to collect data on normal patients and those with a variety of pathologies.

The second instrument automates the capture of images of the ocular fundus. It, too, can be operated by unskilled personnel after only minimal training. The images are in digital form for easy telecommunication. At present, a "proof of concept" prototype is in operation. The proposed work would carry the development to the pre-production stage.

PROJECT SITE(S) (organization, city, state):

Visual Pathways, Inc. and Bascom Palmer Eye Institute
Prescott, Arizona Miami, Florida

No consortium arrangements are involved.

JUN 27 2000

VISUAL PATHWAYS, INC.

SEMI-ANNUAL REPORT – JANUARY 1 – JUNE 30, 2000

Subagreement No: 1-FY99 - Visual Pathways, Inc. – Cornsweet

Principal Investigator: Dr. Tom Cornsweet

Project: Two Ophthalmic Instruments Suitable For Telemedical Applications

ORIGINAL

Subagreement No: 1-FY99-Visual Pathways, Inc.-Cornsweet
Principal Investigator: Dr. Tom Cornsweet
Project: Two Ophthalmic Instruments Suitable for Telemedical Applications

SEMI-ANNUAL REPORT – JANUARY 1 – JUNE 30, 2000

INTRODUCTION

The overall objective of this project is to further the development of two ophthalmic instruments that improve the quality and availability of medical care. The first system, the Fundus AutoImager™, automatically captures color, digitized, stereo images of the ocular fundus. Operating features include auto-alignment, auto-focus that allow for operation by technician-level personnel; imaging is achieved rapidly using infrared illumination, rather than intense flashes of white light and therefore eliminates the patient discomfort that is associated with some of the present fundus cameras. The second system, the VisPath Analyzer™, generates measures to be used for detection, diagnosis and treatment monitoring of a wide range of medical conditions that affect the visual pathways, central nervous system or neuromuscular junctions. The tests can be performed rapidly by technician level personnel. The output of both these systems is in digital form and can easily be used in telemedicine applications.

BODY

Visual Pathways, Inc. moved into office and laboratory facilities in Prescott, Arizona in January 2000. These facilities consist of about 2,000 square feet of office area and about 1,500 square feet of laboratory and shop area. During the month of January, office furniture and equipment was purchased and equipment and supplies were moved from storage to set up a complete machine shop, electronics shop and optics shop, including two darkrooms for optical systems development.

Development of two different instruments is proceeding under the present US Army/NMTB grant, the Fundus AutoImager™ (FAI) and the VisPath Analyzer™ (VPA). Progress on these two instruments will be described separately.

Fundus AutoImager™

Background: The FAI is an instrument that automates the process of obtaining digital images of the ocular fundus. Existing "fundus cameras" are extremely difficult to operate, require highly skilled operators, and the entire process is time-consuming, primarily because the operator must align the instrument precisely with respect to the patient's eye, in three dimensions, refine the alignment to avoid interference from light reflected from the cornea, position a target for the patient to look at so that the desired portion of the fundus is imaged, and then focus the fundus image. During these processes, the patient often moves, requiring a repetition of the process. The FAI automates all the alignment, target positioning, and focus functions, compensating for any patient movement. As a result, any relatively unskilled operator can learn to obtain excellent images after only a few minutes of training.

Progress: At the time the proposal for this grant was written, a working prototype of the FAI was able to perform automatic alignment but neither target positioning nor focusing was automated. During the process of implementing these functions, it became clear that the basic design of the instrument was sub-optimal and we therefore developed a new design for the FAI during the months preceding and the first month of the grant period (January 2000). During February through April, a new prototype was constructed, as shown in **Figure 1,**

in the Appendices. As of this writing, algorithms for automatic alignment, focus, target positioning and image registration (for color imagery) have been written and tested. Currently we are constructing software to handle secondary issues, such as handling of blinks, automatic setting of certain thresholds, etc.

Because this prototype was intended only as a test bed to evaluate our new methods of alignment and focus, the lenses and video camera are "off the shelf" items and do not provide optimal image quality.

As of this writing, the FAI operates as designed. The operator selects a target location or set of locations and performs a rough alignment, using a trackball to approximately center an image of the patient's pupil on the computer screen. The alignment system then automatically precisely centers the image of the pupil, finds the optimal positioning of the illuminating light with respect to the pupil, and automatically adjusts this position if the patient moves. The image of the fundus is then automatically focused and a set of digitized images is collected. All of the alignment and focusing operations are carried out under infrared illumination, so that the patient experiences no discomfort, and for most patients, there is no need to dilate the pupils with drugs.

These collected images consist of stereo pairs taken either under infrared illumination (for monochrome images) or, if the operator has so chosen, stereo pairs of color images. (If color is chosen, a brief flash of visible light is delivered for each member of the stereo pair).

Work is now beginning on an improved version of the prototype described above, one that is intended to be as close as possible to a production instrument. The new instruments will be used for beta testing. The functioning of the beta prototypes will differ from the existing one in two respects. First, the optics that form the fundus image will be designed for optimal resolution. This work is currently being carried out by Optical Research Associates, Pasadena, California, an optical design firm. Second, the present, standard, CCD camera will be replaced by a high resolution camera (at least 1024 x 1024 pixels, yielding 4.4 micrometers per pixel at the fundus). We have developed specifications for the camera, and vendor selection is currently under way.

Future Tasks: As described in the Conclusions Section of this report, we are about to enter into a strategic partnership agreement with a company that is actively marketing a unique internet-facilitated health care delivery system, Digital Disease Detection and Tracking (3DT)™. In particular, they intend to purchase a significant number of FAIs over a five-year term, to screen diabetics for retinopathy, using a protocol established by the National Institutes of Health (NIH), which requires the examination of stereo images of seven specified regions of the ocular fundus. We have therefore included in the design of the FAI the capacity to collect, automatically, stereo images of each of those regions. Early in August, we plan to collect such sets of images from a group of 100 patients, either at the VA hospital in Prescott, or the Indian Health Service Hospital in Phoenix. These images will be collected with the existing FAI prototype to validate the accuracy of the locations of the seven images and to identify any limitations of the instrument that might call for modifications.

Concurrently, the mechanical and electronic design required for a production version of the FAI will be undertaken. The design, and the building of five beta prototypes, will be carried out under a contractual agreement between Visual Pathways, Inc. and Phoenix Analysis and Design Technologies, Inc. (PADT), Gilbert, Arizona. VPI personnel will work closely with PADT throughout this process of instrument prototyping. A copy of the PADT Program Evaluation and Review Technique chart for the Fundus AutoImager is shown in **Figure 2**, in the Appendices.

VisPath Analyzer™

Background: The VisPath Analyzer™ (VPA) is an instrument designed to automate the detection and evaluation of a wide range of pathologies that affect the central nervous system and the eye. A variety of targets are presented to either or both of the patient's eyes and the resulting eye movements and pupil responses are recorded and analyzed.

At the time the proposal for the NMTB grant was written, five prototypes of the VPA were being used for various research projects in clinics at the University of Iowa, University of Indiana, and a Neuro-Ophthalmology clinic in New Jersey, in addition to one prototype at Visual Pathways, Inc. These prototypes have had one significant shortcoming, which was described in the NMTB grant proposal, namely that the lenses through which the patient viewed the targets were of low quality, resulting in blurred, colored, and distorted targets. We proposed to replace these lenses with ones of high quality, and then to collect extensive data on a large number of patients.

Progress: The optical design firm Optical Research Associates, Pasadena, California, was hired to design appropriate lenses. On January 26, 2000 they provided us with the design shown at full scale in **Figure 3**, in the Appendices. We then contracted with Harold Johnson Laboratories, Gardena, California to fabricate the lenses. Five pair of these lenses (two per instrument) were delivered by June 13, 2000. Pairs of these lenses have now been mounted in two prototypes and kits to retrofit the remaining three prototypes have been constructed. (The resulting appearance of the targets is now excellent and distortion is less than 1% over the entire field of view).

In consultation with Dr. Randy Kardon at the Neuro-Ophthalmology clinic at the University of Iowa, in whose clinic the data will be collected, we have developed a protocol for a series of tests that, based upon our previous experience with the instrument and our knowledge of the effects of various pathologies, is our current best estimate of a series that will provide optimal detection of a wide variety of disorders. The details of the series are presented in Appendix i. The software to perform these tests is now complete and we expect the software for analysis of results to be complete by July 1, 2000. (All of these tests are essentially modifications of tests that are currently implemented on VPA prototypes). A photo of the VisPath Analyzer, **Figure 4**, is found in the Appendices.

Future Tasks: We plan to begin data collection during the last week in July 2000. Because these data will be the first extensive clinical data collected with the instrument, we will analyze them at the end of each week and implement any modifications to the tests that the analyses suggest.

CONCLUSIONS

General and Personnel: Company facilities are now in place and fully functional. In addition to the Company's President and Chief Scientific Officer positions, we have hired an Administrative Assistant, currently working on an 80% basis and intend to bring her to full time status with additional funding. We have an Electronics Engineer on about a 50% basis and intend to increase him to about 75%, and will be hiring two assembly Technicians in the near future. We have hired a Software Engineer full time, to begin July 1 and have another Software Engineer consultant working on a 75% basis. Our additional personnel needs include an Accountant, Mechanical Engineer/Industrial Designer and a Director of Manufacturing Engineering. We also

will require the services of a Regulatory Affairs consultant to begin preparation of documentation related to Food and Drug Administration 510(k) filing on the FAI and VPA products.

Business and Financial: The Company registered with the US Securities and Exchange Commission (SEC) to raise capital through the sale of its Common stock, under a Regulation D (506) which allows for raising up to $5 Million. This offering is restricted to accredited investors only. Discussion has been initiated with two investment fund managers. Meanwhile, five private, individual investors have purchased stock, totaling $150,000.

In January the Company entered into discussions with Inoveon Corporation, a privately-held company based in Oklahoma City that has developed, and is marketing proprietary software and encryption technology in its Digital Disease Detection and Tracking (3DT)™ service. They presently are using a fundus camera made by Zeiss and have been placing systems in remote Indian Health Service hospitals and clinics, as well as in Veteran's Administration facilities for imaging of diabetic patients for retinopathy. The images they collect are transmitted via Internet to Vanderbilt University in Nashville, where retina expert readers interpret the images, make the diagnosis and treatment recommendation, and transmit their findings back to the clinic, whereby a mobile laser system can deliver the photocoagulation therapy to prevent blindness. They have a marketing plan for imaging and treatment of age-related macular degeneration (AMD), the leading cause of blindness in people over age 60. There now are photodynamic therapies in late-stage clinical trials, so that what was an untreatable condition only a year ago, can now be treated with increasing success. As with diabetic retinopathy, the earlier the detection and treatment intervention, the more likely it is that the treatment will be effective.

Inoveon is 30% owned by Wesley-Jessen Vision Care, a leading supplier of specialty contact lenses and a publicly-traded company (NASDAQ symbol: WJCO). Novartis, the large Swiss pharmaceuticals firm, through its wholly-owned subsidiary, Ciba Vision, recently announced it will acquire Wesley-Jessen for $785 Million in cash.

Our negotiations with Inoveon have resulted in agreement on basic terms and formal documents are now in preparation by our lawyers at Ryley, Carlock & Applewhite in Phoenix. Once consummated, this agreement calls for Inoveon to provide VPI with development funding of approximately $650,000 in milestone payments, and five-year sales forecasts and minimum purchase commitments of one model of the FAI. These minimums, if met, will result in approximately $20 Million in revenues to VPI over the five-year period. VPI will be free to market its own model of the FAI, on a worldwide basis.

The Company believes that it will be both time and cost-effective to engage the services of a professional engineering firm experienced in opto-electronics and in instrument prototyping, to assist VPI in completion of the design and construction of the Fundus AutoImager beta prototypes. In this way, VPI can move the product, and all necessary design drawings and documentation, more rapidly into full production. VPI has received a proposal from PADT to complete the development and production of five beta prototypes, three of which will be provided to Inoveon for their use in clinical validation in diabetic retinopathy imaging.

REFERENCES
Not Applicable

APPENDICES

Appendix i

INITIAL VPA TEST SEQUENCE

The following tests will be performed in sequence, with a pause between each, during which the patient can exit the instrument.

Instructions to the patient are as follows: "Place your head in the headrest and look into the instrument, where you will see a lighted target. The target may move or flash. If the target moves, follow it with your eyes".

1) Swinging Pulse, Full Field: This test measures pupil responses to flashes of light, evaluating amplitude, latency, constriction velocity, re-dilation velocity, and Relative Afferent Pupillary Defect (RAPD).

   Disks of light 30 degrees in diameter and centered on the fixation point are flashed alternately to the right and left eyes. The flashes are of 0.2 second duration with a 2.0 second separation between flashes. The alternation is repeated until each eye has been stimulated four times. Horizontal diameters of both pupils are recorded 60 times per second. (Total test time = 18 seconds).

   The data are analyzed as follows:

   Mean amplitudes, latencies, maximum constriction velocities and maximum re-dilation velocities are computed for each pupil and for lights delivered to each eye, as are the differences between eyes for each of those measures.

   RAPD is computed as follows: The ratio of mean amplitudes of response for flashes to the left/right eye is computed. Previously collected data for the average patient show an approximately linear relationship between response amplitude and log stimulus intensity over the range of interest. From this relationship, the ratio of stimulus intensities to the two eyes of a normal subject necessary to produce the new patient's ratio of amplitudes is found and presented as the magnitude of the RAPD in db units.

2) Accelerating Circle: This test determines the presence or absence of capability for smooth pursuit eye movements, and the target speed at which smooth movement breaks down.

   A small, bright "x", visible to only one eye, moves smoothly in a circular path of a 12 degree diameter, starting at a low speed and smoothly accelerating. The horizontal and vertical movements of both eyes are recorded 1000 times per second. (Total test time = 15 seconds).

   The data are analyzed as follows:

   The target speed at which smooth following breaks down into saccadic movements is determined and displayed. In addition, differences between the positions of the two eyes as a function of velocity are measured and displayed, indicating phorias or tropias during pursuit movement.

3) Smooth Spiral/Cover-Uncover: This test measures phorias and tropias, and evaluates binocular coordination over a full field of view 45 degrees in diameter.

A small, bright "x" is initially visible to both eyes at optical infinity. After three seconds, the target is extinguished in one eye. After another three seconds, the target, still visible to only one eye, begins to move smoothly in a spiral pattern that expands until it covers a 45 degree field. The speed of movement is selected to be significantly lower than the smooth pursuit breakdown speed determined in the Accelerating Circle test. The target is then centered again and made visible to both eyes for three seconds and then the above sequence is repeated while the target is visible only to the other eye. Vertical and horizontal movements of both eyes are recorded 1000 times per second. (Total test time for both eyes = 120 seconds).

Data are analyzed as follows:

If a saccadic movement follows within one second of the offset of the target to either eye (after the three second binocular period), then the amplitude and direction of the saccadic movement are reported as the amplitude and direction of the tropia. The eye to which the target was being presented before that saccade is reported as the normally non-fixating eye.

If no tropia is detected, then any (smooth) displacement of the non-viewing eye that occurs during the three-second monocular period is reported as the amplitude and direction of a phoria.

Horizontal and vertical components of the differences between the directions of gaze of the two eyes during the spiral movement are displayed as a function of the location of the target, to reveal how imbalances are distributed over the field of motion.

4) Saccadic Clock/Screening Perimetry: This test evaluates the amplitudes, velocities, and latencies of saccadic eye movements in the cardinal directions, and also detects scotomas in regions of the retina most frequently affected by glaucoma.

The test is carried out with stimuli delivered to one eye only, the other being in darkness. A small spot of brightness 6 db above threshold is overlaid on a background at 31 Apostils (a standard background brightness for perimetry). Initially the spot is straight ahead. Every two seconds, the spot jumps to a new location, and the patient is asked to follow it if it moves. Stimuli are delivered in locations such that if the eye follows it, saccadic movements of 12 degree amplitude will be evoked from straight ahead to each of the eight cardinal positions (N, E, S, W, NE, SE, NW, SW), and also the target will jump to positions where accurate scotomas and nasal step scotomas frequently appear in the early stages of glaucoma. The sequence of target positions is unpredictable to the patient. Horizontal and vertical components of the positions of both eyes are recorded 1000 times per second. The test is performed on each eye. (Total test time for each eye = 60 seconds).

Results are analyzed as follows:

Horizontal and vertical components, latencies, and velocities of saccadic movements of both eyes are measured for movements to each of the cardinal positions. These measures are also compared between the two eyes.

Regarding perimetry (scotoma detection), if the target jumps to a position on the retina where there is no scotoma, then, after a latency of about 250 m.s., the patient will make a single saccadic movement that results in the approximate re-fixation of the target. However, if the target jumps into a scotoma, because the patient sees the target disappear but not reappear, he or she makes a saccadic movement in a random direction, which will almost always bring the target on to seeing retina, resulting in a second saccadic movement to the target position. Thus, the perimetry data analysis consists of mapping those positions on the retina that evoked more than one saccadic movement. (Saccadic movements one degree or smaller are ignored in the analysis).

5) Convergence/Near Reflex: This test evaluates convergence eye movements and the near pupil reflex.

The target, a light asterisk on a dark background, appears initially visible to both eyes at optical infinity. It then appears to move smoothly toward the patient until it appears six inches away, dwells there for one second, then moves smoothly back to infinity. This sequence is repeated twice. Horizontal and vertical components of the positions of both eyes are recorded 1000 times per second, and the horizontal diameters of both pupils are recorded 60 times per second. (Total test time = 30 seconds).

Results are analyzed as follows:

The smoothness and accuracy of the evoked vergence movements are measured.

Measured horizontal pupil diameters are determined jointly by actual pupil diameters and by the foreshortening effect on the images of the pupils as convergence proceeds. Therefore, pupil diameters are corrected for the foreshortening effect and then displayed as a function of apparent target distance and vergence angle.

PATENTS

No patents have been issued on VPI's products to date. Patents are in preparation for both the Fundus AutoImager and the VisPath Analyzer. The Company is working with a highly-regarded intellectual property firm in Phoenix, Cahill, Sutton & Thomas.

PUBLICATION OF ABSTRACTS, MANUSCRIPTS, BROCHURES, etc

There have been no scientific publications by Visual Pathways, Inc. on these products to date. No product brochures have been produced to date. Materials were produced for an exhibit in May 2000 at the American Telemedicine Association meeting in Phoenix. The exhibit, sponsored by USAMRAA, TATRC and NMTB, was developed and attended by NMTB, who in turn invited its prospective strategic partner, Inoveon Corporation. Several important medical contacts, as well as potential business contacts were made during this two-day exhibit. A copy of the Fundus AutoImager Features/Benefits chart from the ATA2000 exhibit is shown as **Figure 5**. **Figure 6** is copy of the Visual Pathways, Inc./Inoveon Corporation Diabetic Retinopathy ATA2000 chart. A copy of the VisPath Analyzer chart from the ATA2000 exhibit is shown as **Figure 7**.

Publications are anticipated for the FAI, as clinical validation of the beta prototypes is completed, in collaboration with Inoveon Corporation. Publications on the VPA are anticipated as data collection is completed, in collaboration with Dr. Randy Kardon at University of Iowa.

Tom N. Cornsweet, PhD
Principal Investigator

6/30/00
Date of Report

Visual Pathways, Inc.
P O Box 10458
Prescott, AZ 86304-0458
520. 778.5002 (Voice)
520. 778.5004 (Fax)
tomc@vispath.com

NMTB.SemiAnnReport.7.1.00

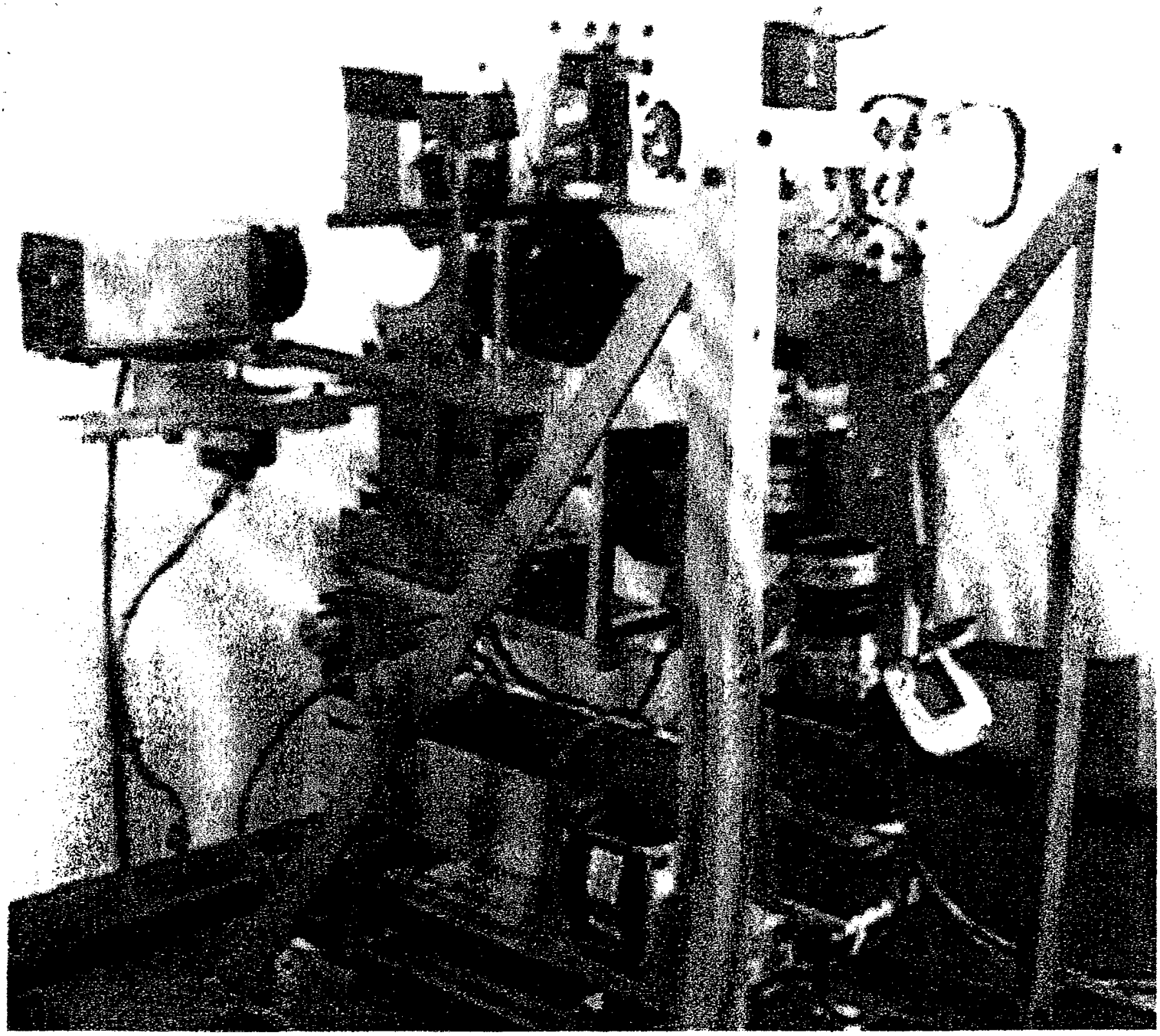

FIGURE 1

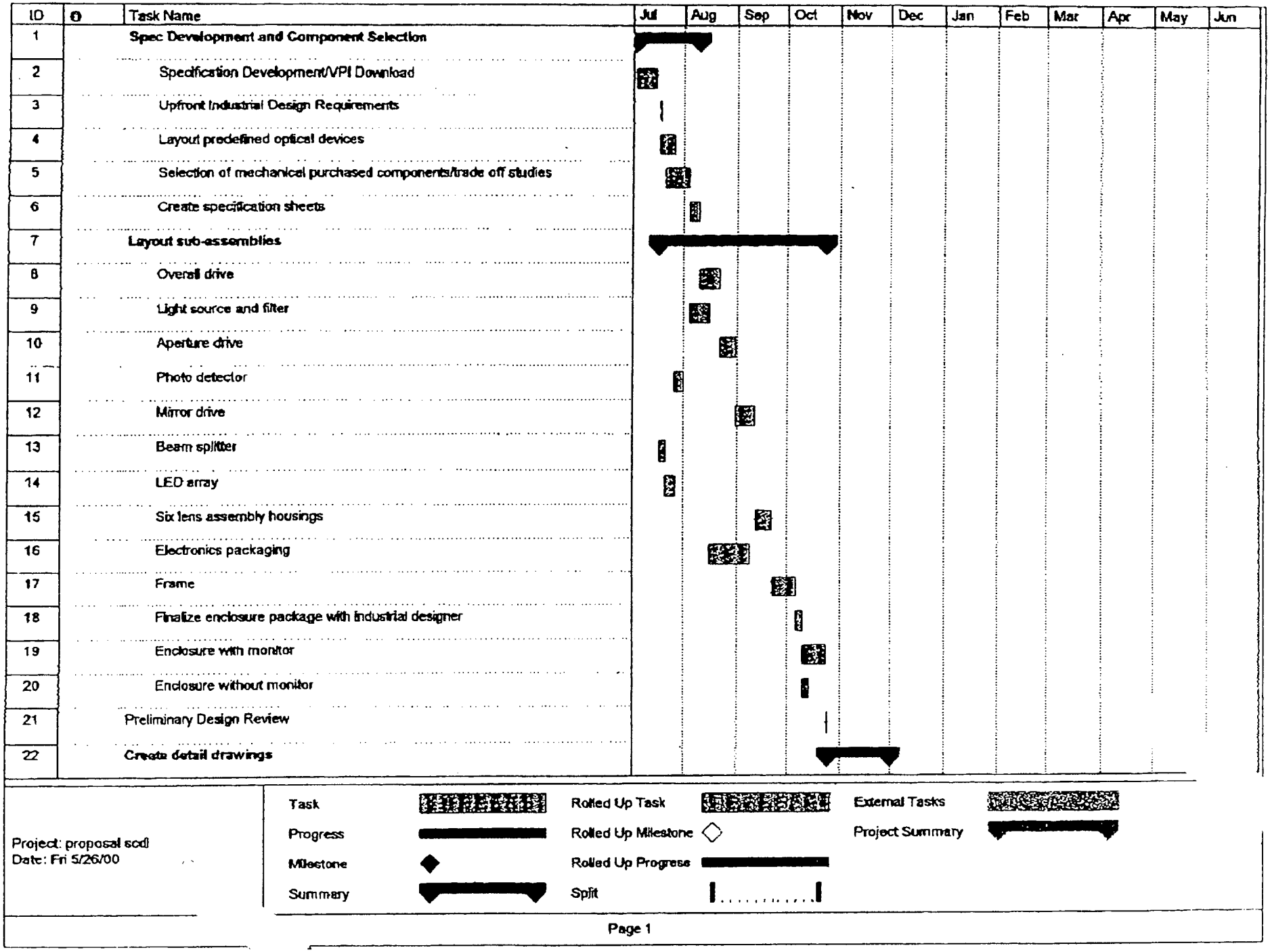
ID
Task Name
Jul
Aug
Sep
Oct
Nov
Dec
Jan
Feb
Mar
Apr
May
Jun
1 Spec Development and Component Selection
2 Specification Development/VPI Download
3 Upfront Industrial Design Requirements
4 Layout predefined optical devices
5 Selection of mechanical purchased components/trade off studies
6 Create specification sheets
7 Layout sub-assemblies
8 Overall drive
9 Light source and filter
10 Aperture drive
11 Photo detector
12 Mirror drive
13 Beam splitter
14 LED array
15 Six lens assembly housings
16 Electronics packaging
17 Frame
18 Finalize enclosure package with industrial designer
19 Enclosure with monitor
20 Enclosure without monitor
21 Preliminary Design Review
22 Create detail drawings
Project: proposal scdl
Date: Fri 5/26/00
Task
Progress
Milestone
Summary
Rolled Up Task
Rolled Up Milestone
Rolled Up Progress
Split
External Tasks
Project Summary
Page 1

FIGURE 2(A)

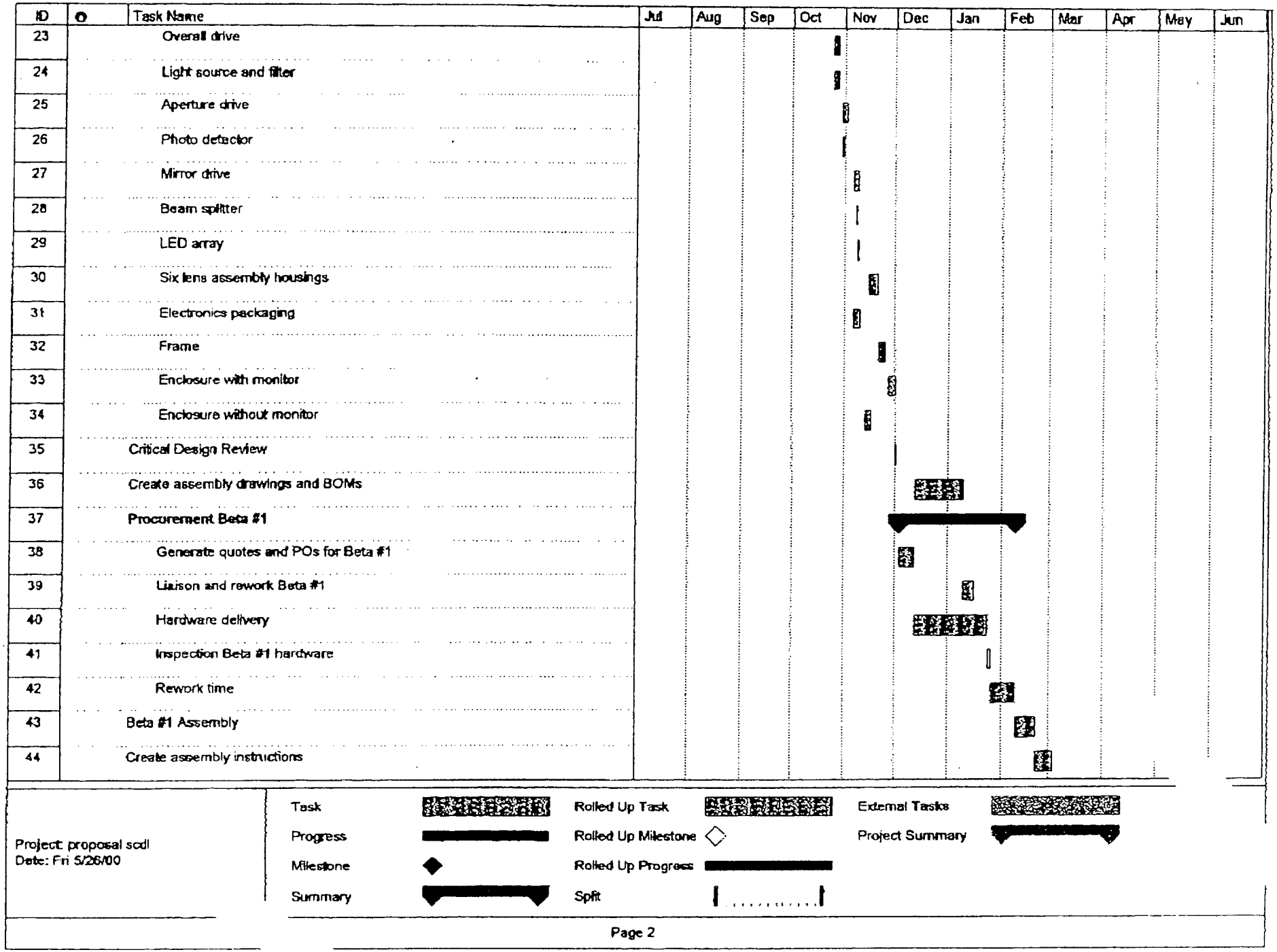
ID
Task Name
Jul
Aug
Sep
Oct
Nov
Dec
Jan
Feb
Mar
Apr
May
Jun
23 Overall drive
24 Light source and filter
25 Aperture drive
26 Photo detector
27 Mirror drive
28 Beam splitter
29 LED array
30 Six lens assembly housings
31 Electronics packaging
32 Frame
33 Enclosure with monitor
34 Enclosure without monitor
35 Critical Design Review
36 Create assembly drawings and BOMs
37 Procurement Beta #1
38 Generate quotes and POs for Beta #1
39 Liaison and rework Beta #1
40 Hardware delivery
41 Inspection Beta #1 hardware
42 Rework time
43 Beta #1 Assembly
44 Create assembly instructions
Project: proposal scdl
Date: Fri 5/26/00
Task
Progress
Milestone
Summary
Rolled Up Task
Rolled Up Milestone
Rolled Up Progress
Split
External Tasks
Project Summary
Page 2

FIGURE 2(B)

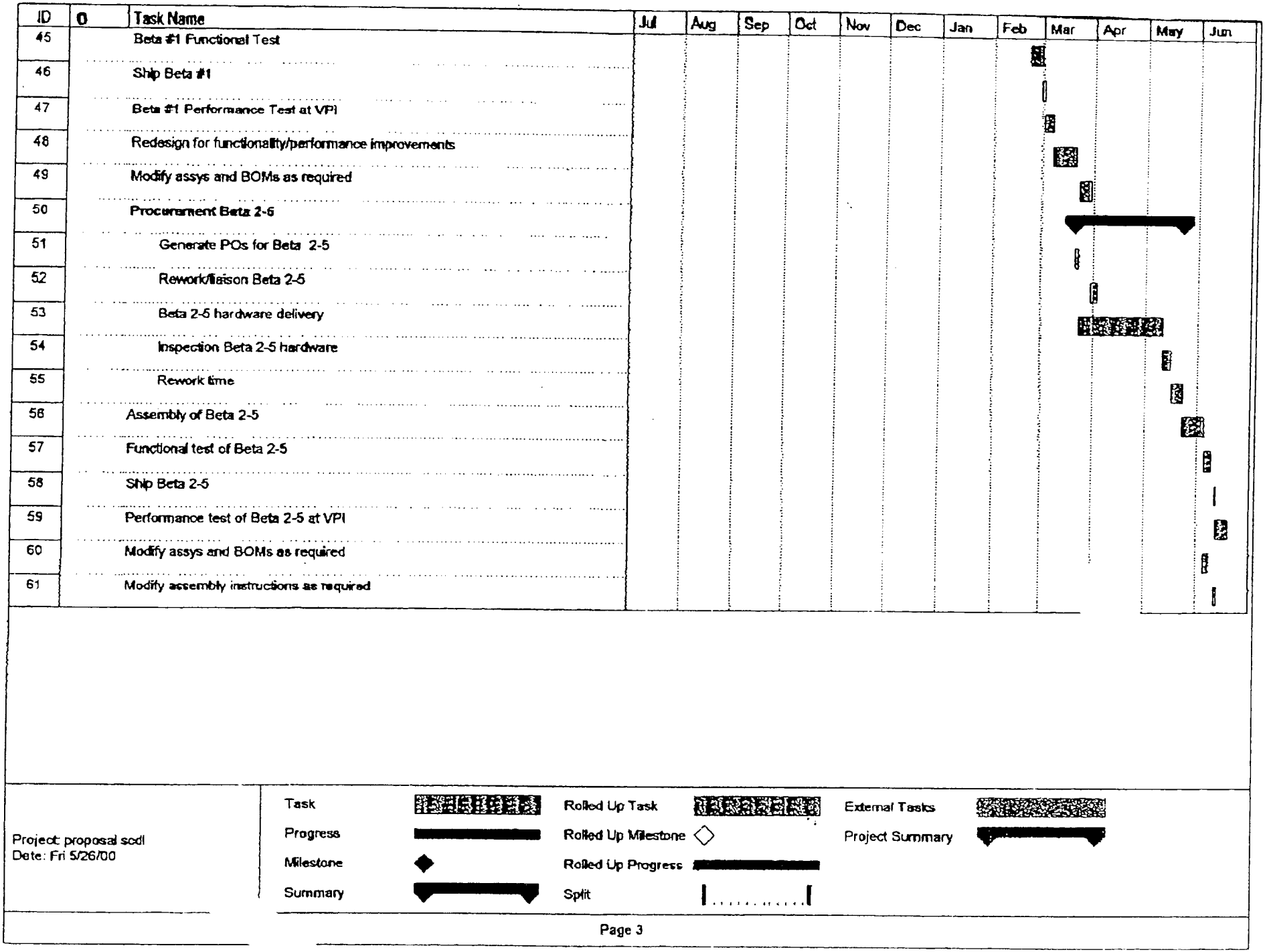
ID
0
Task Name
Jul
Aug
Sep
Oct
Nov
Dec
Jan
Feb
Mar
Apr
May
Jun
45 Beta #1 Functional Test
46 Ship Beta #1
47 Beta #1 Performance Test at VPI
48 Redesign for functionality/performance improvements
49 Modify assys and BOMs as required
50 Procurement Beta 2-5
51 Generate POs for Beta 2-5
52 Rework/liaison Beta 2-5
53 Beta 2-5 hardware delivery
54 Inspection Beta 2-5 hardware
55 Rework time
56 Assembly of Beta 2-5
57 Functional test of Beta 2-5
58 Ship Beta 2-5
59 Performance test of Beta 2-5 at VPI
60 Modify assys and BOMs as required
61 Modify assembly instructions as required
Project: proposal scdl
Date: Fri 5/26/00
Task
Progress
Milestone
Summary
Rolled Up Task
Rolled Up Milestone
Rolled Up Progress
Split
External Tasks
Project Summary
Page 3

FIGURE 2(C)

DIMENSIONS ARE IN MILLIMETERS

ASSEMBLY TOLERANCES

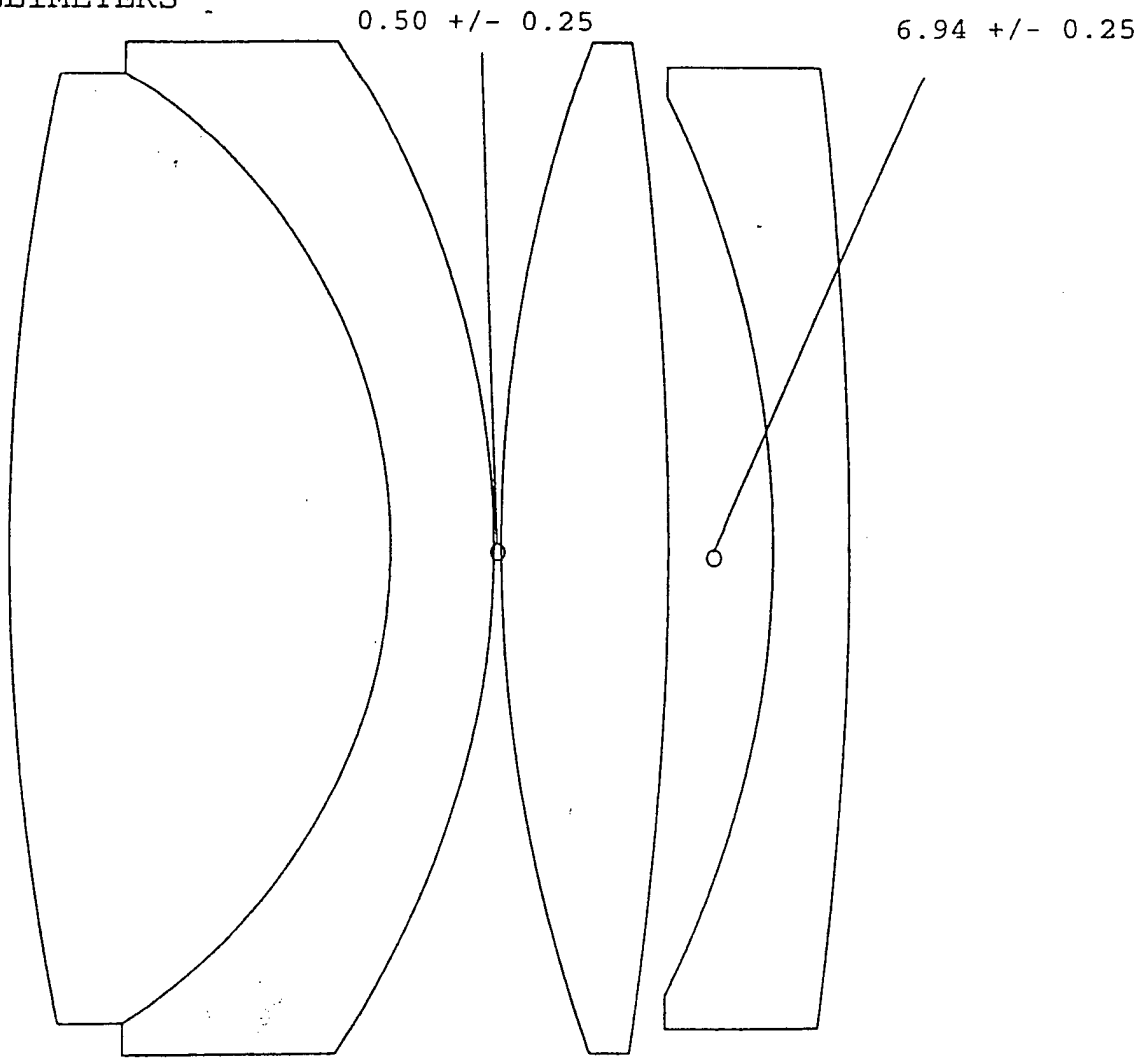

CENTERING TOLERANCE:
0.10 mm TYPICAL

TILT TOLERANCE:
4.0 ARC-MINUTES TYPICAL

VGA Viewing Lens Final Scale: 2.00 ORA 21-Jan-00

VPI.VisPathAnalyzer.Photo.BMP

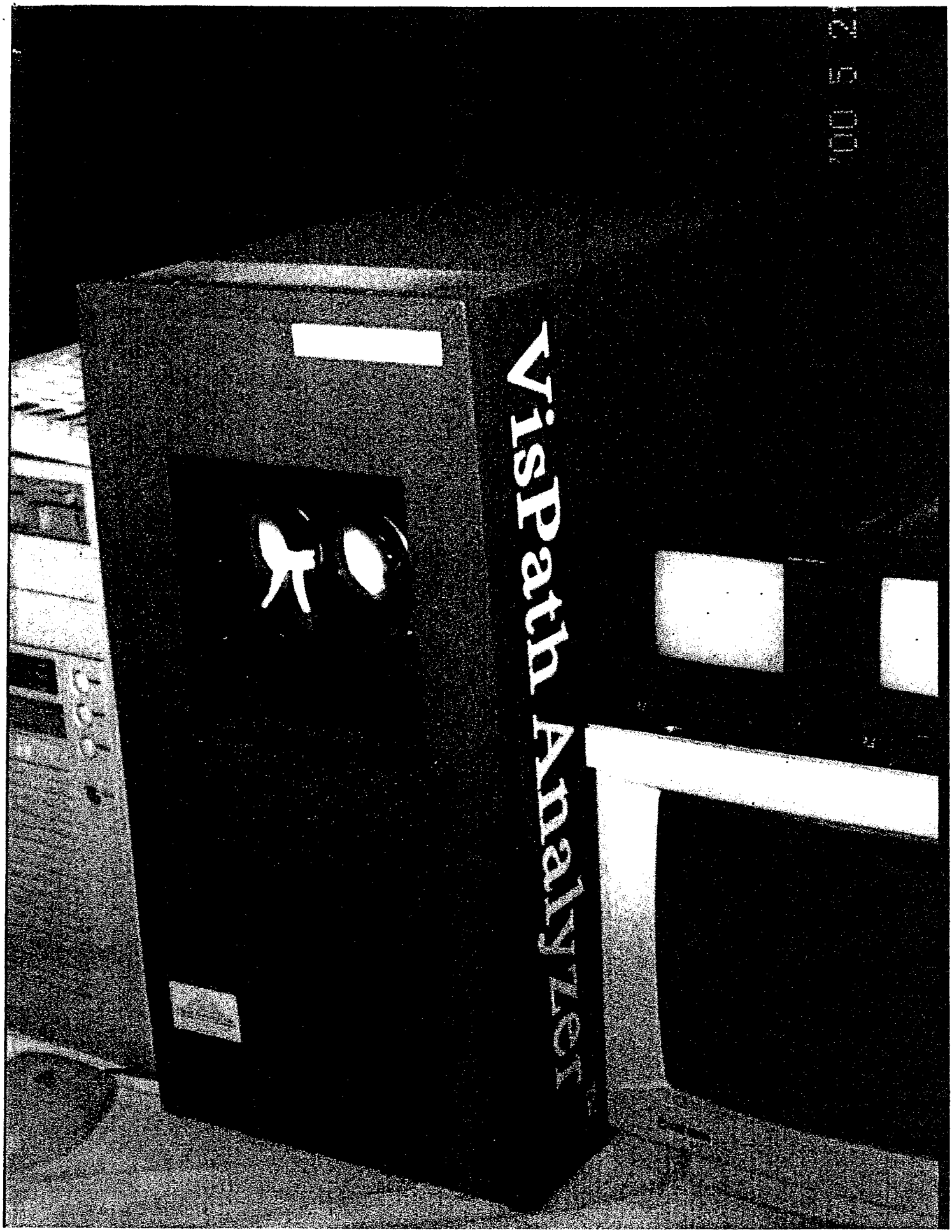

FIGURE 4

Fundus AutoImager™

Performance Features	*Benefits*
Digital Image Output	Transfer High-Quality Images via Internet; Store on Disk or Print Hard Copy
Non-Mydriatic for Most Procedures	Patient Comfort
Automatic Alignment	Minimal Operator Training; Ease; Speed
Automatic Focus	Minimal Operator Training; Ease; Speed
IR Alignment and Focus	Patient Comfort
Automatic Stereo Image Control	Operator Ease, Speed, Repeatability
Automatic Target Positioning	Minimal Operator Training; Ease; Speed
Infrared Imaging (w/o Flash if Monochrome)	Patient Comfort

Typical Imaging Sessions:

Single 30° Color Stereo Image: Less than 1 minute per eye

Multiple (e.g., DRS7) Stereo Images: Less than 2 minutes per eye

Visual Pathways, Inc.
"A New Vision In Eye Care"
609 West Gurley Street
Prescott, AZ 86305
Phone: (520)778-5002
Fax: (520)778-5004
Email: garybuck@vispath.com

FIGURE 5

Bringing The New Standard of Care
For
Diabetic Retinopathy
Management
inoveon
Visual Pathways, Inc.
"A New Vision In Eye Care"

FIGURE 6

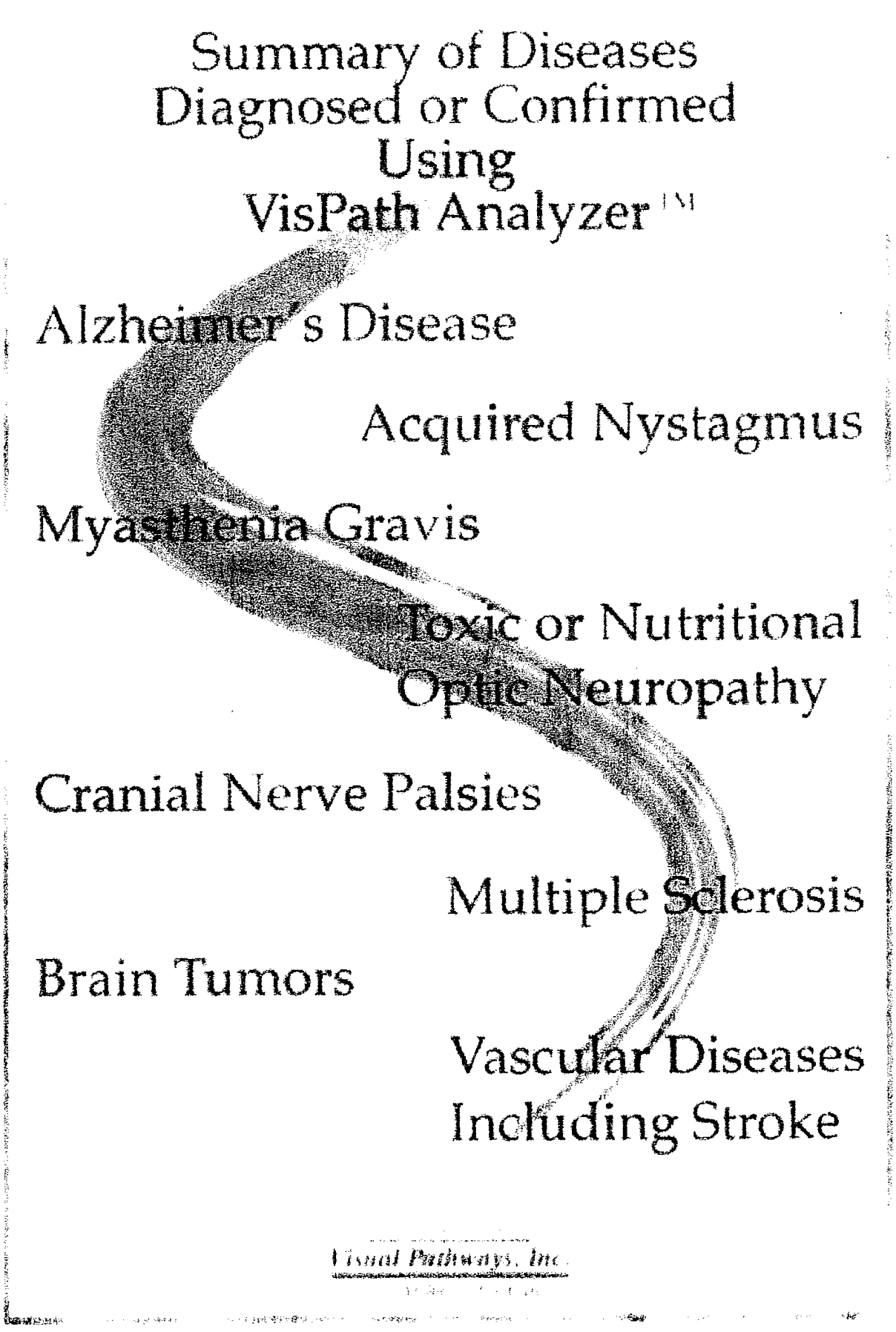
Summary of Diseases
Diagnosed or Confirmed
Using
VisPath Analyzer™
Alzheimer's Disease
Acquired Nystagmus
Myasthenia Gravis
Toxic or Nutritional
Optic Neuropathy
Cranial Nerve Palsies
Multiple Sclerosis
Brain Tumors
Vascular Diseases
Including Stroke
Visual Pathways, Inc.

FIGURE 7